Editors
Michele Barone
Andrea Gaddi
Claude Leroy
Larry Price
Pier-Giorgio Rancoita
Randal Ruchti

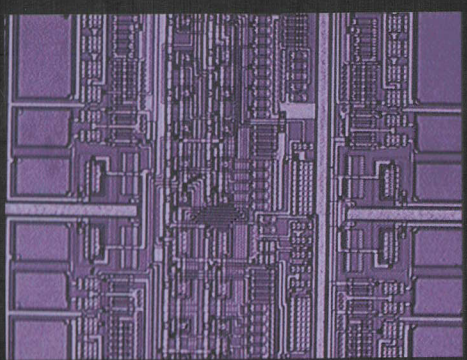

Astroparticle, Particle and Space Physics, Detectors and Medical Physics Applications

Proceedings of the 10th Conference

Astroparticle, Particle and Space Physics, Detectors and Medical Physics Applications

Proceedings of the 10th Conference

This page intentionally left blank

Astroparticle, Particle and Space Physics, Detectors and Medical Physics Applications

Proceedings of the 10th Conference

Villa Olmo, Como, Italy 8 – 12 October 2007

Editors

Michele Barone
NCSR Democritos, Greece

Andrea Gaddi
CERN, Switzerland

Claude Leroy
Université de Montréal, Canada

Larry Price
ANL, USA

Pier-Giorgio Rancoita
INFN-Milano-Bicocca, Italy

Randal Ruchti
University of Notre Dame &
US National Science Foundation, USA

World Scientific

NEW JERSEY · LONDON · SINGAPORE · BEIJING · SHANGHAI · HONG KONG · TAIPEI · CHENNAI

Published by

World Scientific Publishing Co. Pte. Ltd.

5 Toh Tuck Link, Singapore 596224

USA office: 27 Warren Street, Suite 401-402, Hackensack, NJ 07601

UK office: 57 Shelton Street, Covent Garden, London WC2H 9HE

British Library Cataloguing-in-Publication Data
A catalogue record for this book is available from the British Library.

ASTROPARTICLE, PARTICLE AND SPACE PHYSICS, DETECTORS AND MEDICAL PHYSICS APPLICATIONS
Proceedings of the 10th Conference

ISBN-13 978-981-281-908-6
ISBN-10 981-281-908-8

Printed in Singapore by Mainland Press Pte Ltd

Organizing Committee

E. Borchi	INFN and University of Florence
C. Leroy	University of Montreal
L. Price	ANL
P.G. Rancoita	INFN Milano-Bicocca
R. Ruchti	University of Notre Dame

Industry Organizing Committee

M. Barone	Democritos Athens
A. Gaddi	CERN

Session Oraganizers and International Advisory Committee

D. Abbaneo	CERN
S. Baccaro	ENEA-Rome
P. Binko	ISDC and University of Geneva
A. Capone	INFN and University "La Sapienza", Rome
C. Fabjan	CERN
S. Giani	CERN
V. Hagopian	Florida State University
K. Kudela	Slovak Academy of Science
E. Nappi	INFN-Bari
S. Pospisil	CTU Prague
P.L. Riboni	ETHZ-Zurich
T.J. Ruth	TRIUMF
J. Seguinot	College de France, Paris
V. Sossi	University of British Columbia, Vancouver
S. Volonté	HQ ESA
R. Wischnewski	DESY

Plenary Session Organizers

A. Capone and R. Wischnewski	Astroparticle and Underground Experiments
S. Giani	Software Applications
E. Nappi and J. Seguinot	Advanced Detectors and Particle Identification
L. Price	High Energy Physics Experiments
R. Ruchti	Accelerator and Computer Data/Networking Developments
V. Sossi	Radiotherapy and Medical Imaging
S. Volonté	Space Experiments

Parallel Session Organizers

D. Abbaneo	Tracker and Silicon Tracker
S. Baccaro	Radiation Damage
P. Binko and S. Giani	Software Applications
A. Capone and R.Wischnewski	Astroparticle and Underground Experiments
V. Hagopian	Poster Session
K. Kudela	Energetic Particles in Heliosphere and Earth Magnetosphere
C. Leroy	Calorimetry
E. Nappi and J. Seguinot	Advanced Detectors and Particle Identification
S. Pospisil	Medical Application Instrumentation
L. Price	High Energy Physics Experiments
V. Sossi	Radiotherapy and Medical Imaging
S. Volonté	Space Experiments

Organizers of Industry Participation and Exhibition

M. Barone	Demokritos Athens
A. Gaddi	CERN

Secretariat

A. Cazzaniga	Villa Olmo
A.M Barilli	Villa Olmo
C. Stefanetti	Villa Olmo
N. Tansini	Villa Olmo

PREFACE

The exploration of the subnuclear world is done through increasingly complex experiments covering a wide range of energy and performed in a large variety of environments going from particle accelerators, underground detectors up to satellites and space laboratory. The achievement of these research programs calls for novel techniques, new materials and new instrumentation to be used in detectors, often of large scale. Therefore, particle physics is at the forefront of technological advance and also leads to many applications. Among these, medical applications have a particular importance due to health and social benefits they bring to the public. The International Conference on Advanced Technology and Particle Physics is held every two years. The Conference held during the week 8-12 October 2007 at the "Centro di Cultura Scientifica A. Volta" was the Tenth Edition and again welcomed a large participation. There were about 290 participants representing 130 institutions from 28 countries. The Participants were experienced researchers but also graduate students and recent postdoctoral fellows, students receiving financial support from the Conference organization.

The conference allows a regular review of the advances made in all technological aspects of the experiments at various stages, data taking, upgrade or in preparation. The open and flexible format of the Conference is conducive to fruitful exchanges of points of view among participants, permits the measure of the progresses made and indicate research directions.

The medical sessions gave an interesting example of merging advanced technology, particle physics and numerical techniques. Industries specialized in advanced technologies were present at the Conference through a show of their products (organized by M. Barone and A. Gaddi)

Plenary and parallel sessions covered Advanced Detectors and Particle Identification (organized by E. Nappi and J. Seguinot), Astroparticle Physics and Underground Experiments (organized by A. Capone and R. Wischnewski), Space Experiments (organized by S. Volonté), Heliosphere and Earth Magnetosphere (organized by K. Kudela), Calorimetry (organized by C. Leroy), Software Applications (organized by P. Binko and S. Giani), High Energy Physics Experiments (organized by L. Price), Accelerator and Computer Data/Networking Developments (organized by R. Ruchti), Medical Application Instrumentation (organized by S.Pospisil), Radiotherapy and Medical Imaging (organized by V. Sossi), Radiation Damage (organized by S. Baccaro) and Tracking Devices (organized by D. Abbaneo). The organization of the Industry Participation was done by M. Barone and A. Gaddi. Four afternoons afforded parallel poster sessions, including one session of poster presentation. The poster sessions have always received special attention by the organizers of the conference. These sessions were organized by V. Hagopian. The number of posters accepted, more than 70, shows the great success of these sessions. The dedication of several rooms to the poster sessions allowed numerous discussions by various interested parties. The posters were divided into three general categories as follows: 1.

Astroparticle, Underground Experiments, Space Physics and Cosmic Rays. 2. High-Energy Physics Experiments, Trackers, Calorimetry, Software and Data Systems. 3. Advanced Detectors and Medical Physics Applications. Each poster submission was reviewed for relevance to the conference and accepted or rejected. The final poster papers accepted for publications have been included in the appropriate section of the Proceedings, as function of their topic. From the quality of the material of the posters, as well as the poster presentation, it is clear that a lot of effort went into the preparation of each presentation. We would like to thank the poster presenters for their fantastic effort that made the posters a truly important part of this Conference.

We would like to thank the staff of the Centro A. Volta for the excellent support provided to the Conference organization at Villa Olmo. In particular, we would like to extend our appreciation and thanks to the Secretariat of Centro di Cultura Scientifica A. Volta for their help and efficiency with the organization of the Conference and its running. We are particularly indebted to Dr G. Castiglioni, President of Univercomo, who by providing sponsorship allowed the Conference organizers to largely reduce or waive the registration fees for the graduate (MSc and PhD) students.

The organizers would like to thank the strong support of INFN and ESA which made the conference possible.

Finally, we would like to thank the speakers for the high quality of their contributions and the participants for their enthusiasm in attending the Conference and contributing to the discussions.

Michele Barone
Andrea Gaddi
Claude Leroy
Larry Price
Pier-Giorgio Rancoita
Randal Ruchti

December 2007

CONTENTS

This page intentionally left blank

Advanced Detectors and Particle Identification

Organizers:

E. Nappi
J. Seguinot

GEM detectors activity at the Laboratori Nazionali di Frascati of INFN

M. Alfonsi*, G. Bencivenni, P. de Simone, D. Domenici,
F. Murtas, M. Pistilli and M. Poli Lener

Laboratori Nazionali di Frascati,
40, Via Enrico Fermi, 00044 Frascati (RM), Italy
** E-mail: matteo.alfonsi@lnf.infn.it*

After ten years of development for high energy physics experiments, GEM detectors demonstrated great robustness, long-term stability of operation, remarkable flexibility and capability to accomplish different tasks in harsh environments.
This technology has entered the field of triggering devices with its application in the innermost region of the upstream Muon station of the LHCb experiment. Such application has required for an R&D on fast and high yield CF_4-based gas mixtures, performed by our group in Frascati in collaboration with the INFN of Cagliari, leading to an improvement in the time resolution of a factor of three (down to 3 ns r.m.s.).
Exploiting our established experience, we are starting an R&D on large-size GEM detectors. In the framework of the KLOE experiment upgrade, we are developing a completely new and competitive category of ultra-light, full sensitive vertex detector for high energy experiments, based on a fully cylindrical GEM detector. Moreover several GEM detectors have been realized for photon beam diagnostic and more recently a luminometer is under construction for accelerator machine studies.

Keywords: GEM, CGEM, tracking

1. Overview of the main activities

The first application of detectors based on Gas Electron Multiplier (GEM) technology [1] is the COMPASS experiment [2], where they operate as tracking device exploiting the excellent spatial resolution and high rate capability of this kind of detector, but little interest has been devoted to the time performance.
An intense R&D on this aspect has been performed by our group in collab-

oration with the INFN of Cagliari [a], during the development of a detector for the harsh region around the beam pipe of the upstream muon station of LHCb experiment.
Section 2 describes the study of new fast CF_4-based gas mixtures that allowed us to achieve such result.
The LHCb experience has been a precious background for new R&D on this technology: large size GEM detector can find important applications in the upgrade of LHCb apparatus as well as in other experiments.
In particular, in the framework of the KLOE experiment upgrade, we are developing a completely new and competitive category of ultra-light, full sensitive vertex detector, based on a fully cylindrical GEM detector.
This is reported in section 3.
Finally, minor activities include the study of GEM detectors as imaging devices for medical application and beam diagnostic. A luminometer based on GEM technology is under construction. This will be installed in DAFNE accelerator in Frascati for machine studies during the incoming upgrade, where the *crab waist* beam crossing technique can open the way for high luminosity kaon and beauty factories.

2. LHCb GEM detectors

LHCb GEM detectors instrument the high-irradiated region around the beam pipe of the upstream muon station [3,4].
Two layers of triple-GEM detector with pad readout are foreseen in this region (12 stations, 24 chambers), with the digital information coming from corresponding pads in each layer logical OR-ed through the front-end electronics. The total area is less than 1 m^2, but about the 20% of the total triggered muon will come from this device. In fact the response of this detector contribute in the first level trigger decision of the experiment, so a critical issue is a high efficiency in bunch crossing identification.
The requirements of the double layer are a rate capability better than 0.5 MHz/cm^2, an efficiency in 20ns time window greater than 96%, a cluster size lower than 1.2 pads per crossing particle, and the capability of sustain 10 year of operation in LHCb environment without damage or loss of performance.
To fulfill the demanding time resolution that comes from the 20ns time window requirement, a specific study of new fast (high drift velocity, high ionization yield) gas mixtures based on CF_4 has been performed with small

[a] Ca-INFN: W. Bonivento, A. Cardini, R. Oldeman, D. Pinci, D. Raspino, B. Saitta

size prototypes [5]. The choice of the $Ar/CO_2/CF_4$ (45/15/40) gas mixture, together with an optimization of the geometry of the final detector, allowed us to achieve time resolution better than 3ns r.m.s. (Fig. 1), to be compared to the 10ns r.m.s. time resolution of standand Ar/CO_2 gas mixtures, and to fulfill all the experiment requirements.
Accurate aging and robustness measurements were successfully performed with a high intensity X-ray beam in our laboratory and with the high rate hadronic beam (low momenta pions with a proton contamination) of the Paul Scherrer Institute (PSI) in Zurich. Moreover a global irradiation test of the final LHCb chambers has been performed at the irradiation facility of the ENEA-Casaccia with a ^{60}Co source, in order to test compatibility of the gas mixture with the construction materials. Performance of irradiated chambers, measured afterwars on a beam test at CERN, shows no significant losses after an integrated charge of about 2.2 C/cm^2, equivalent to about 12 years of operation at LHCb environment [6].
The production and the quality controls of the 24 chambers were completed at the end of 2006 and the installation is foreseen by the end of this year [7]. In Fig. 2 the efficiency of one of the twelve stations is shown, as measured, with the official LHCb DAQ electronics, on a test on SPS beam configured with a 25ns bunch crossing time structure, to simulate LHCb running condition.

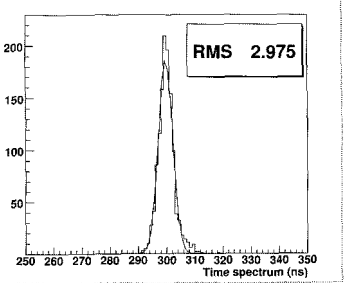

Fig. 1. The best time resolution obtained with LHCb GEM detectors

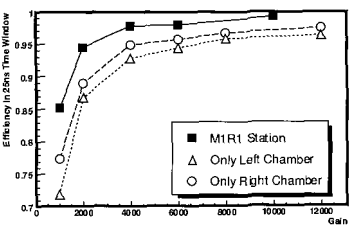

Fig. 2. Efficiency as a function of gain, measured in the last test on SPS beam

3. Cylindrical GEM detectors for KLOE upgrade

In the framework of the upgrade of the KLOE experiment in Frascati we are developing a novel idea for an ultra-light cylindrical triple-GEM (C-GEM)

detector [8], for vertex and inner tracking purposes.
The proposed detector will play a crucial role in the study of the K_S rare decays and the measurement of the neutral kaon interferometry.
The main requirements are a moderate detector spatial resolutions, $\sigma_{r\phi}$ $\sim$200μm and σ_z $\sim$500μm, but a very low material budget inside the active area, 1.5% of X_0 for the whole sub-detector.
The inner tracker will be composed by five C-GEM layers. Each C-GEM is realized inserting one into the other the required five cylindrical structures made of thin (50$\div$100 μm) polyimide foils: the cathode, the three GEMs and the anode readout.
The first small-size prototype ($\sim$90 mm diameter and $\sim$250 mm active length) has been built using LHCb GEM foils and a 50μm thick Kapton foil, with a 5 μm thick copper deposition, as anode and cathode electrodes. Such cylindrical electrodes are obtained gluing, inside a vacuum bag, the polyimide circuits rolled up on machined PTFE cylinders that act as moulds. Then cylindrical electrodes are inserted one into the other and glued to fiberglass flanges, used as mechanical support. After the assembly, the C-GEM prototype has been installed in a stretching system equipped with a gauge meter allowing the monitoring and control of the applied mechanical tension.
The C-GEM prototype, operated with an Ar/CO_2 = 70/30 gas mixture, has been characterized with an X-ray gun ($\sim$6 keV) measuring the current on the anode. Neither dark current nor sparks up to a gain of 10^4 have been observed (Fig. 3), in a wide range of stretching tension, that resulted to be not a critical parameter.
The construction procedure of cylindrical GEM electrodes implies the presence of a singularity along the gluing junction line (3 mm wide), made of bare Kapton with neither copper nor holes. The effect of this singularity is to create distortions of the transfer field lines above and below the singularity itself, but without generating dead zones.
A preliminary simulation study shows (Fig. 4) that electrons, generated in the conversion gap by a track, are still efficiently driven in the multiplication holes of the GEM. The track detection efficiency for MIP, practically 100% all over the GEM foil, slightly drops to $\sim$98% for the pessimistic case of tracks crossing perpendicularly in the middle of the junction line [9].
The next prototype under costruction, with a strip readout and equipped with front-end electronics, will allow us to understand the effective relevance of this issue. In fact the success of the small size C-GEM has opened the way for the construction of a full scale prototype of the first layer of

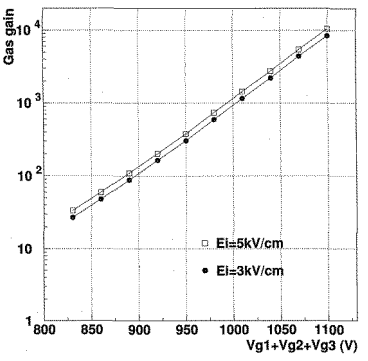

Fig. 3. Gain vs. gem voltages measured on C-GEM prototype with an X-ray tube

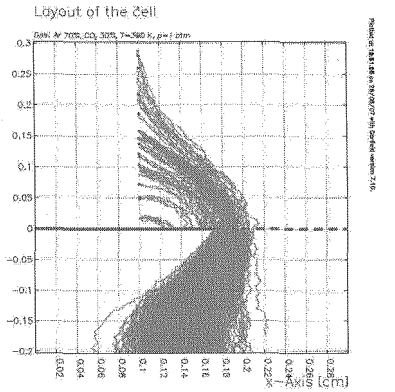

Fig. 4. Simulation studies of the gluing junction line

the inner tracker.

4. Conclusions

Laboratori Nazionali di Frascati has developed an established experience in the Gas Electron Multiplier technology, contributing with two major projects, the LHCb GEM detectors and the KLOE cylindrical GEM vertex tracker, investigating new aspects and introducing innovative applications.

References

1. F. Sauli, Nucl. Instrum. Meth. **A386** (1997) 531.
2. COMPASS collaboration, Nucl. Instrum. Meth. **A577** (2007) 455–518.
3. LHCb Muon System Technical Design Report, LHCb TDR 4, CERN LHCC 2001-010, (2001).
4. LHCb Muon System Technical Design Report - Addendum 2, CERN-LHCC-2005-0012, (2005).
5. M. Alfonsi et al., Nucl. Instrum. Meth. **A518** (2004) 106.
6. M. Alfonsi et al., IEEE Trans. Nucl. Sci. 52 (2005) 2872
7. M. Alfonsi et al., Nuclear Science Symposium Conference Record, IEEE, 2005 Volume 2, 811–815
8. G. Bencivenni et al., Nucl. Instrum. Meth. **A572** (2007) 168–169.
9. G. Bencivenni et al., Nucl. Instrum. Meth. **A581** (2007) 221–224.

Current Results on the Development of a Carbon Nanotube Radiation detector*

M. Ambrosio*
INFN Sezione di Napoli ambrosio@na.infn.it

A. Ambrosio, G. Ambrosone, L. Campajola, G. Cantele, U. Coscia, G. Iadonisi, D. Ninno, P. Maddalena, E. Perillo, A. Raulo, P. Russo and F. Trani
Dipartimento di Fisica, Universitá "Federico II" di Napoli and INFN

E. Esposito
Istituto di Cibernetica "E. Caianiello" and INFN

F. Buonocore, A. Di Matteo
STMicroelectronics

S. Santucci, M. Passacantando
Dipartimento di Fisica, Universitá dell'Aquila and INFN

M. Allegrini
Dipartimento di Fisica, Universitá di Pisa and INFN

P.G. Gucciardi
CNR - IPCF Sezione di Messina and INFN

S. Patané
Dipartimento di Fisica della Materia and TFA, Universitá di Messina and INFN

F. Bobba, A. Di Bartolomeo, F. Giubileo, L. Iemmo, A. Scarfato and A. M. Cucolo
Dipartimento di Fisica, Universitá di Salerno and INFN

Recent searches on carbon nanotubes lead in within INFN (GINT experi-

*This work is supported by Istituto Nazionale di Fisica Nucleare

ment) demonstrate enunciated characteristic of fotoconductivity of such material if illuminated from radiation, in particular from UV. Moreover the material can be easily managed to cover wide sensitive areas and finely structured through nanolitography. Therefore the way is open to a great number of applications in which UV, visible and near IR (150-1100 nm) radiation detectors cover particular importance. The applications would go from space physics (IR and UV detectors) to the high energies physics (Cerenkov detectors) to the UHECR physics (fluorescence light detectors) and to the medical instrumentation (not ionizing radiations).

Keywords: Nanotube, radiation detectors, fotoconductivity

1. Introduction

Carbon nanotubes (CNTs) are a class of interesting nanomaterials with simple chemical composition and atomic bonding configuration, and yet rich and diverse physical properties. A SWNT is a nanoscale seamless cylinder formed by rolling a single atomic layer of graphitic sheet with hexagonal lattice. As there are an infinite number of ways of rolling a sheet into a cylinder, the large variety of possible helical geometries, defining the tube chirality, provides a family of nanotubes with different diameters and microscopic structures. The electronic and transport properties, are certainly among the most significant physical properties of carbon nanotubes, and crucially depend on the diameter and chirality. This dependence on the atomic configuration is quite unique in solid-state physics.

In view of future bottom-up approaches, one of the main issues is the CNT growth onto selected areas during the fabrication of the device. Recently some of us demonstrate an under Scanning Electron Microscopy (SEM) electron beam technique is straightforward easy shaping, straightening, bending and soldering nanotubes into desirable configurations.[1] Submicrometric catalyst patterns have been fabricated by atomic force nanolithography and the subsequent selective growth of carbon nanotubes has been successfully verified.[2] Finally has been demonstrated[3] that CNTs can easily produce field emission effects applying relatively low voltage respect to any other material.

Photoconductivity of individual ropes and films of CNTs has been also investigated in the visible[4] and IR[5] spectral regions Photon induced charge carrier generation in single wall carbon nanotubes and subsequent charge separation across the metalcarbon nanotube contacts is believed to cause the photoconductivity changes.[4] Results under UV region at our knowledge are still missing. This region is of particular interest for the space and astroparticle physics. Future detectors for future experiments must cover

large area of finely pixelled cathodes sensitive to single photons in the wawelenght range of 200 - 400 nm to detect fluorescence and Cerenkov light or cosmic radiation at a reasonable cost.

In this scenario the GINT collaboration Project, as reported in this paper, is exploring the use of carbon nanotube-based devices to provide new opportunities for obtaining large area and highly sensitive radiation detectors.

1.1. *Characteristics of CNT device used*

The carbon nanotubes (CNTs) have been grown on substrate of silicon nitride in the region between two platinum electrodes (distance 3 mm) by means of Chemical Vapor Deposition (CVD) technique. A 3 nm thick-Ni film has been deposited on the Pt/Si_3N_4 substrate using a thermal evaporation under a pressure of 10-6 Torr. The Ni-deposited substrate has been inserted in a quartz CVD reactor and was pumped down to less than 10-5 Torr using a turbo molecular pump. In order to form the catalytic particles in the nanometer size the substrate has been pre-treated in NH_3 gas with a flow rate of 100 sccm for 20 min at 500 °C and 700 °C of temperature. The CNTs have been grown on the solid substrate by adding C_2H_2 at a flow rate of 20 sccm for 10 min at the same temperature of the NH_3 pre-treatment temperature.

The structural analysis has have been carried out by High Resolution Transmission Electron Microscopy (HRTEM, JEOL JEM 2010) and micro-Raman spectroscopy. While HRTEM features unique imaging capabilities, Raman spectroscopy has the advantage of being a noninvasive technique suitable for in situ, real-time analysis of optoelectronic devices. Figure 1A (red line) shows the Raman spectrum of a MWCNT sample grown at 700 °C. We observe the D and the G bands (1300 - 1400 and 1530 - 1640 cm^{-1}, respectively typical of carbon materials, together with the fingerprint of the silicon substrate (520 cm^{-1} and 980 cm^{-1}). Compared to amorphous carbon nanofibers (Figure 1A, black line), the MWCNTs show a much narrower D band (full width at half maximum of 72 cm^{-1} against 263 cm^{-1}), as well as a strong 2D mode at 2653 cm^{-1}. The picture in Figure 1B shows a well graphitized nanotube. The external diameters typically range between 15 and 25 nm, the inner diameters between 5 and 10 nm. The number of walls varies between 6 and 15 (9 for the tube of Figure 1B). Each nanotube is characterized by an external layer, 2 - 4 nm thick, of polycrystalline carbon. The nanotubes length is in the 10 μm range, as measured by Scanning Electron Microscopy shown in Figure 1C.

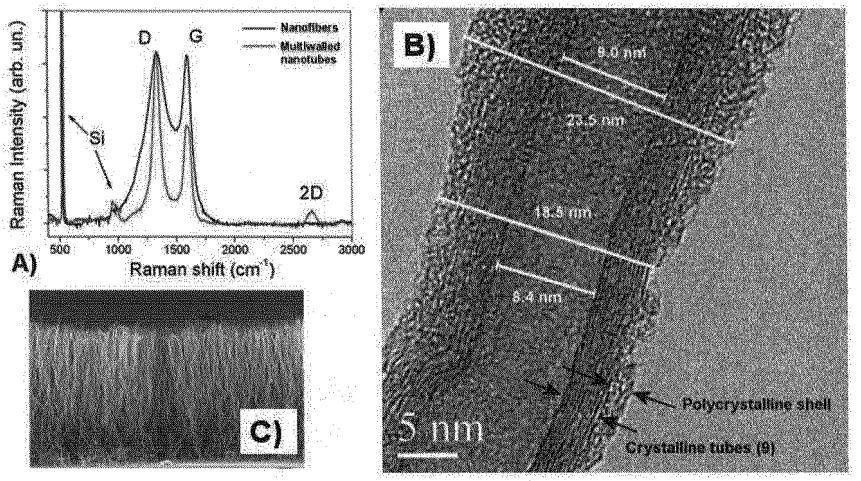

Fig. 1. A) Raman spectrum of MWCNTs (red/grey line) compared to amorphous carbon nanofibers (black line). B) HRTEM picture of an individual MWCNT. C) SEM overview.

I order to allow the carbon-nanotubes growth with a definite pattern, we developed the following procedure based on a lift off process with a Bi-Layer Resist Processing. A thin film of the assisting material (COP) is first deposited. A layer of resist PMMA is spined over this layer and patterned through photolithography. This way the assisting material layer is exposed. This layer is then wet etched so as to undercut the resist. The metal is then deposited on the wafer, by a thermal evaporation process. The resist is removed taking away the unwanted metal with it. The assisting layer is then stripped off too, leaving the metal pattern alone. Result is shown in figure 2.

1.2. *The field emission investigation*

For their high aspect ratio, extremely small radius of curvature, unique electric properties, high chemical stability and mechanical strength, carbon nanotubes (CNTs) can be extraordinary field emitters and interest in their applicability for field emission (FE) devices has been steadily growing since their discovery.

For the measurement of the FE current we used the nanometric probe of an high vacuum Omicron AFM/STM system as anode; the voltage was applied and the current was measured by means of a SMU (source-

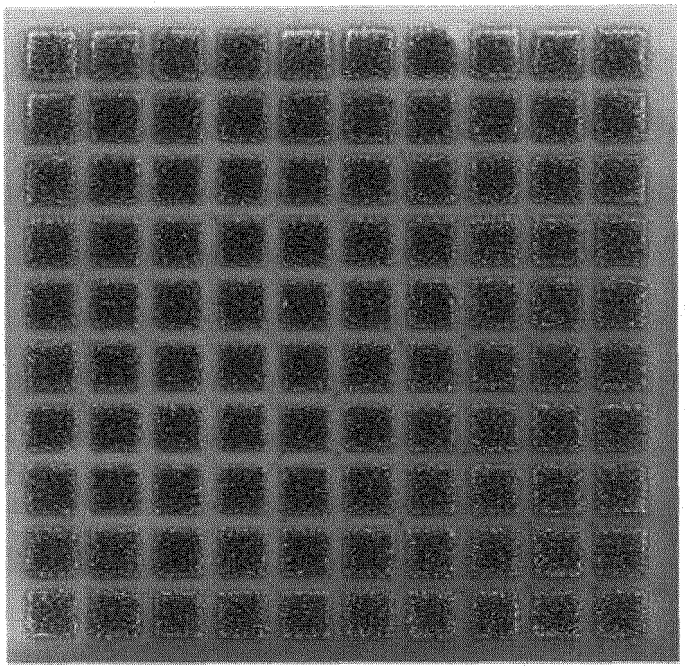

Fig. 2. An example of CNTs grown on a nanopatterned substrate. Each CNT insula is 4x4 micron square

measurement unit) of a Keithley 4200-SCS. Voltage sweeps were performed on the allowed voltage range of -210 V to +210 V and the current flowing through the tip was measured with an accuracy better that 1 pA.[6]

An example of current-voltage characteristics is shown in figure 3, where a series of 5 sweeps are recorded using a Pt-coated AFM tip at d $\sim$ 2 μm from the CNT film surface and in a high vacuum of $\sim$ 10-8 mbar. The figure shows also a very good stability (10 % at one sigma) of the emission current over a time of two days, a characteristic very important for the utilization of the CNT emitters in technological applications. A field enhancement factor $\sim$ 40-50 and a turn-on field E turn-on $\sim$ 15 V/μm at an inter electrode distance of 1 μm have been estimated from our measurements.[7]

1.3. *Photoconductivity*

In order to investigate the possibility to use Carbon Nanotubes as light detectors, MWCNTs have been produced and their response to the incident light radiation has been studied. In our device, MWCNT are grown be-

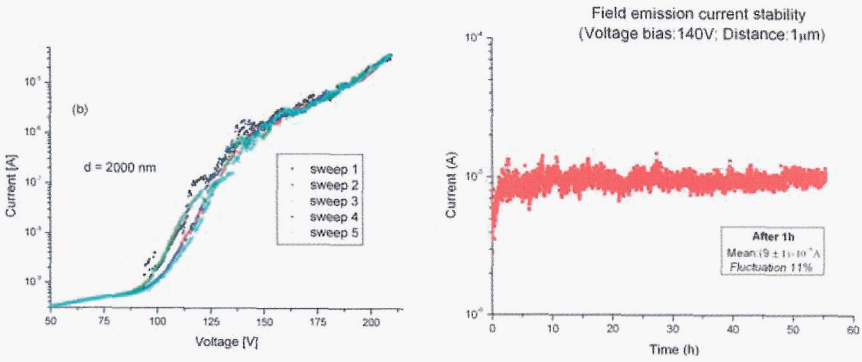

Fig. 3. **Field emission current versus bias voltage** (tip-CNT distance d = 2 μm) and field emission current versus time (d = 1 μm and Vbias = 100V)

tween two platinum electrodes deposited on a 500 micron silicon substrate insulated by means of 30 nm Si3N4 layer. A drain voltage applied between platinum electrodes collects drift charges through the nanotube layer.

In the test configuration the free surface of the device is exposed to white light from an incoherent light source. Under light flashes, charges are generated in the CNTs layer and collected by means of the electrical field applied between the electrodes. Since the very preliminary test of this working configuration, our new sensor has shown high sensitivity to light so that the variation of the drift current corresponding to light flashes can be observed on a standard oscilloscope without any electronic amplifier or complicated read-out electronic. Signals can be then registered and studied to evaluate the charge amount generated as a function of the illumination conditions.

Figure 4 represents an example of the signals we collected. In this case the light source is constituted by a low-power white LED fed by a squared electrical signal (black trace in the figure). The red trace here represents the sensor photoresponse as visible on the oscilloscope screen. A variation of the drift current collected between the platinum electrodes is clearly observed.

The photoconductive properties of MWCNTs deposited on different kind of substrates have been investigated under continuous white light radiation varying the power density in a wide range (0.1 - 340 mW/cm^2), as well as under monochromatic radiation in the 400-1100 nm range. In figure 5 the photocurrent, Iph, obtained by subtracting the current measured under light from the dark current, shows a non linear behaviour as a function

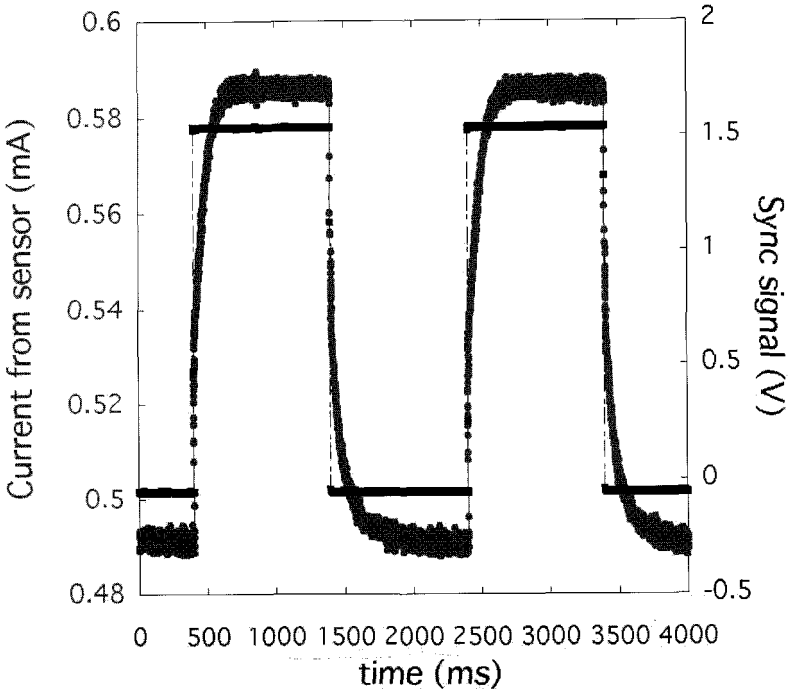

Fig. 4. Photoresponse (red/grey) of a sample of Carbon Nanotubes to white light. The shape of the light flashes is represented by the back trace in the graph.

of the bias voltage, V, in the 0.100 - 340 mW/cm^2 power density range.

1.4. *Response to pulsed light*

The response of CNTs to UV radiation has been analyzed by using a N pulsed laser (337.1 nm, 300 ps pulse duration and 10 Hz repetition rate) beam. A drain voltage, ranging from -20V to +20 V, is applied to one of the electrodes and the drain current is collected by the other electrode and processed with a standard nuclear electronics chain. Energy spectra recorded at various Vdrain are reported in figure 5, showing significant changes in the energy resolution.

The drained charge vs. Vdrain is reported in figure 6A. A sort of saturation clearly appears starting from Vdrain about 15 Volts.

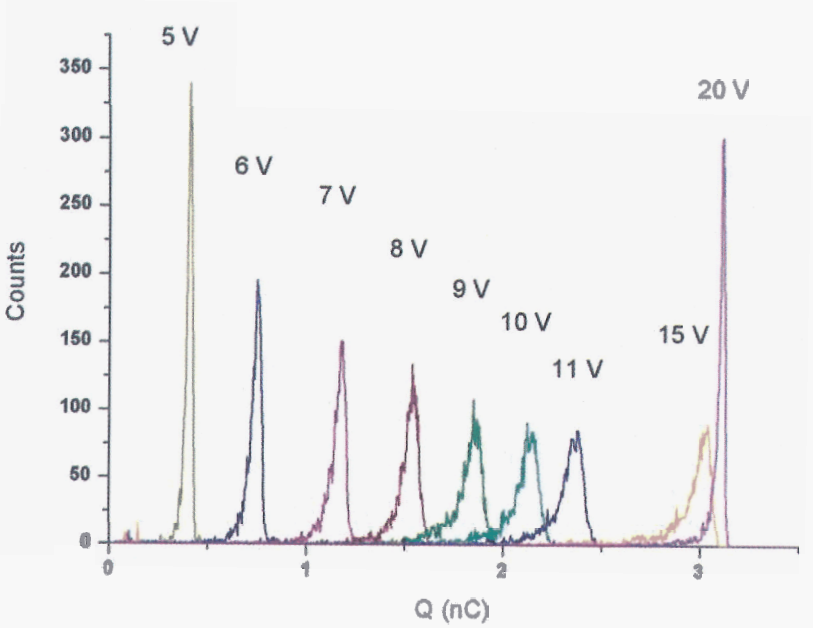

Fig. 5. The photocurrent generated at various drain voltages under continous white ligth illumination.

This investigation has been performed at various wavelenghts and results are shown in figure 6B. The conversion efficiency depends strongly from the light wavelenght and increases towards UV frequencies.

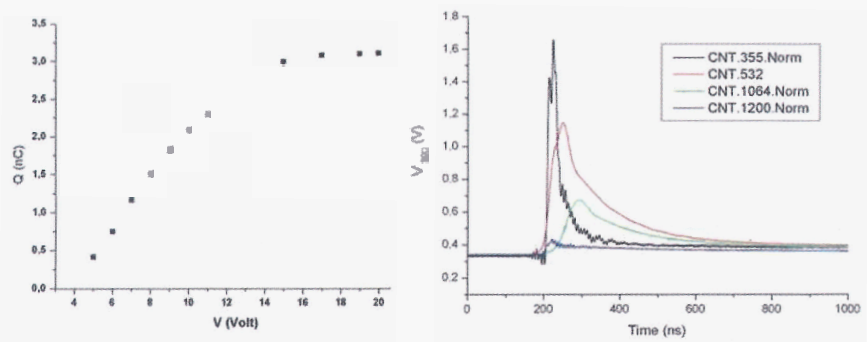

Fig. 6. A) Drained charges vs Vdrain. B) Typical pulses at various wavelenght.

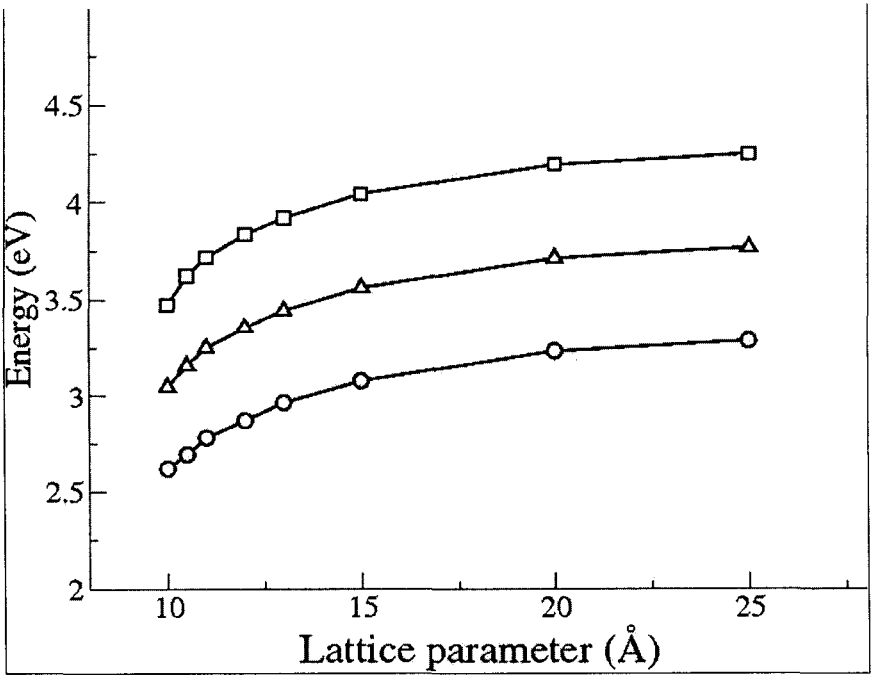

Fig. 7. Ionization potential (squares), electron affinity (circles) and work function (triangles) for (panel b) (5,5) nanotube array, as a function of the array lattice parameter. Lines are guides for the eyes.

1.5. *Theorethical aspects*

H-passivated (5,5) finite size carbon nanotubes have been studied using ab initio techniques. From our calculations it emerges that the EA and IP in finite carbon nanotubes are controlled by two concurrent effects. The first one is similar to a quantum confinement effect in that it gives a variation of both EA and IP with the nanotube length; the second is a purely electrostatic effect due to the formation of edge dipoles. In the case of a nanotube array, the third element that come into play is the array density through which the number of dipoles per surface area may be varied (Figure 7). Both EA and IP can either increase or decrease (with respect to the isolated nanotube) depending on the dipoles density and orientation. At least in principle, with a nanotechnological control on both the nanotube length and array density there are margins for tuning the electron affinity and the ionization potential.

Acknowledgments

We acknowledge the CNR-Istituto per la Microelettronica e Microsistemi, Sez. di Catania for the TEM measurements. F. Bonaccorso, B. Fazio and C. Vasi are acknowledged for fruitful discussions and M. Biasiucci, M. Longobardi and S. Piano for their useful support on the field emission measurement.

References

1. H. Murakami, M. Hirakawa, C. Tanaka, H. Yamakawa, Appl. Phys. Lett. 76 (2000) 1776-1778
2. W. B. Choi D. S. Chung, J. H. Kang, H. Y. Kim, Y. W. Jin, I. T. Han, Y. H. Lee, J. E. Jun, N. S. Lee, G. S. Park, J. M. Kim, Appl. Phys. Lett. 75 (1999) 3129-3131.
3. J. Kong, N. R. Franklin, C. Zhou, M. G. Chapline, S. Peng, K. Cho, H. Dai, Science 287 (2000) 622-625
4. H. Murphy, P. Papakonstantinou, T. I. T. Okpalugo, J. Vasc. Sci. Technol. B 24 (2006) 715-720.
5. J. S. Moon, J. H. Park, T. Y. Lee, Y. W. Kim, J. B. Yoo, C. Y. Park, J. M. Kim, K. W. Jin, Diam. Relat. Mater. 14 (2005) 1882-1887
6. F. Bonaccorso, C. Bongiorno, B. Fazio, P. G. Gucciardi, O. M. Marag A. Morone, C. Spinella, Appl. Surf. Sci (2007), in press.
7. S. J. Tans, A. R. M. Verschueren, C. Dekker, Nature 393 (1998) 49-52
8. C Jarlskog in *CP Violation*, ed. C Jarlskog (World Scientific, Singapore, 1988).
9. L. Maiani, *Phys. Lett.* B **62**, 183 (1976).
10. J.D. Bjorken and I. Dunietz, *Phys. Rev.* D **36**, 2109 (1987).
11. C.D. Buchanan *et al*, *Phys. Rev.* D **45**, 4088 (1992).
12. A. Di Bartolomeo, A. Scarfato, F. Giubileo, F. Bobba, M. Biasiucci and A. M. Cucolo, A local field emission study of partially aligned carbon-nanotubes by AFM probe, cond-mat/0702682, February. 2007, submitted for publication on "Carbon".

MONOLITHIC SENSORS IN DEEP SUBMICRON CMOS TECHNOLOGY FOR LOW MATERIAL BUDGET, HIGH RATE HEP APPLICATIONS

C. ANDREOLI, L. RATTI

Università degli Studi di Pavia, Dipartimento di Elettronica,
Via Ferrata, 1, I-27100, Pavia, Italy and
Istituto Nazionale di Fisica Nucleare, Sezione di Pavia,
Via Bassi, 6, I-27100, Pavia, Italy
E-mail: claudio.andreoli@unipv.it, lodovico.ratti@unipv.it

M. MANGHISONI, G. TRAVERSI

Università degli Studi di Bergamo, Dipartimento di Ingegneria Industriale,
Viale Marconi, 5, I-24044, Dalmine (BG), Italy and
Istituto Nazionale di Fisica Nucleare, Sezione di Pavia,
Via Bassi, 6, I-27100, Pavia, Italy
E-mail: massimo.manghisoni@unibg.it, gianluca.traversi@unibg.it

This work aims at discussing the development of monolithic active pixel sensors (MAPS), which are considered as possible candidate detectors for the inner layers at the future large colliders. In such devices the triple well option, available in deep submicron CMOS technologies, is exploited to implement analog and digital signal processing at the pixel level. In this scheme, the charge collecting electrode is laid out using a deep n-well (DNW) and a full readout chain for capacitive detectors is integrated in the elementary cell. In particular, this work is concerned with the design and performance of DNW monolithic sensor prototypes fabricated in a 130 nm CMOS technology, including different test structures and performing pixel-level charge amplification, shaping and data sparsification.

Keywords: MAPS; CMOS deep submicron; sparsified digital readout.

1. Introduction

Monolithic Active Pixel Sensors (MAPS) in CMOS technology are regarded as a promising solution for charged particle tracking applications at future high luminosity colliders (such as the Super-B Factory and the ILC). In fact, in recent years, many research groups involved in the development of detectors for HEP applications [1], [2], [3], [4], have focussed their attention

on these devices, because of their good performances in terms of material budget in the interaction region and radiation hardness. In CMOS MAPS, actually, the sensitive volume is, typically, 10 to 20 μm thick, therefore allowing thinning down the substrate to a few tens of microns and keeping multiple-scattering to a minimum. As a result, the front-end electronics can be integrated in the same substrate as the sensitive element, thus further reducing the interconnections complexity and the amount of material. Furthermore, the pixel element can also be made very small, in order to increase the spatial resolution, while the use of deep submicron CMOS processes ensures high functional density and versatility, a high radiation hardness degree, low power consumption and low fabrication costs.

2. Deep n-well MAPS concept

In the proposed MAPS prototypes, a deep n-well (DNW), which is made available in deep submicron CMOS processes in order to shield n-channel devices from substrate noise in mixed-signal circuits, is used to collect the charge released in the substrate. The DNW-MAPS sensor structure is illustrated in Fig. 1. Based on this approach, the larger size of the collecting electrode, if compared to conventional MAPS, allows the integration, inside the elementary cell, of a full readout channel for capacitive detectors, which usually comprises a charge preamplifier, a shaper and a threshold discriminator [5], [6]. As it may be observed, the DNW is used to house NMOS transistors of the analog section, while additional n-well regions can be safely used for the integration of PMOS devices, as long as they are kept significantly smaller than the DNW. In this way, the use of a charge-sensitive preamplifier decouples the charge sensitivity from the sensors capacitance, while the large scale of integration of deep submicron

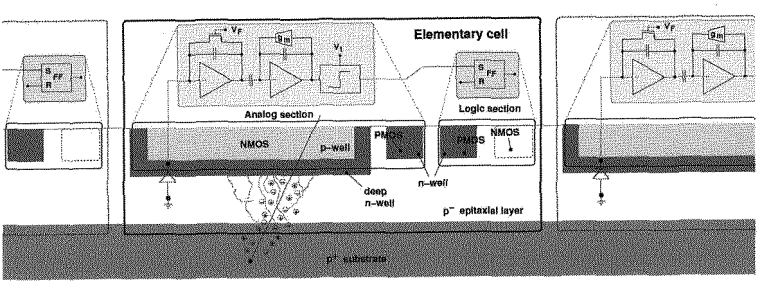

Fig. 1. Simplified cross-sectional view of a DNW-MAPS.

CMOS processes can be exploited to perform both analog and digital signal processing functions at the pixel level, including continuous-time charge amplification and shaping and data sparsification.

3. Apsel2M and Apsel2T chips characterization

In this section we will report on the extensive measurements performed on two DNW-MAPS prototypes, the Apsel2M and Apsel2T (Active Pixel Sensor ELectronics) chips, fabricated in a 130 nm triple-well CMOS technology provided by STMicroelectronics, which have been designed in order to demonstrate the feasibility of DNW monolithic sensors. Results from the test of the first two chips belonging to the Apsel series have already been published [5], [6]. The readout channel integrated in the elementary cell consists of a charge preamplifier, an RC-CR shaper with programmable peaking time (0.5, 1 and 2 μs), a threshold discriminator and a latch. The Apsel2M chip contains an 8×8 matrix of 50 μm pitch MAPS with injection capacitance on selected pixels, in order to evaluate the gain and noise of the matrix elements, and two 3×3 matrices with a fully accessible central pixel, which can be used to study the pixel behaviour as if it were in a larger matrix. The Apsel2T chip contains four 3×3 matrices, differing in testing modalities and in the charge collecting electrode size, and two single pixels. All of these structures have been fully characterized in terms of charge sensitivity and equivalent noise charge (ENC) by means of charge injection through an external pulse generator. As an example of the performed measurements, Table 1 shows the results (averaged over 3 test chips) of the gain and noise characterization of one of the Apsel2 channels, featuring a collecting electrode area of about 860 μm^2 and a capacitance of about 460 fF. The threshold dispersion and the ENC of the pixels in the 8×8 matrix have also been evaluated by measuring the latch firing rate as a function of the discriminator threshold. By fitting the turn-on curve with an error function, we measured the pixel noise and the threshold dispersion in the matrix (see Table 2). All of the performed measurements confirmed the viability of the triple well option for MAPS fabrication and indicated,

Table 1. Gain and noise measurements on a single Apsel2 channel.

Peaking time [μs]	ENC [e^- rms]	Gain [mV/fC]	dENC/dC_D [e^-/pF]
0.5	53	620	135
1	51	590	135
2	52	560	129

in particular, that a reduction of the threshold dispersion (of, at least, a factor of 2) is needed in the next detector version.

Table 2. Noise and threshold dispersion in the Apsel2M 8×8 matrix.

Peaking time [μs]	Average ENC [e^- rms]	Threshold dispersion [e^-]	Gain [mV/fC]
0.5	46	89	610
1	45	97	580
2	45	102	550

4. Design and operation of the SDR0 chip

In this section we will discuss the design and performance of a different DNW monolithic sensor, the SDR0 (Sparsified Digital Readout) chip, designed in the same 130 nm CMOS technology as the Apsel chips and whose main goal is to prove the feasibility of pixel-level data sparsification in MAPS, in view of applications to the International Linear Collider experiments. The elementary cell of the SDR0 sensor is based on a relatively large deep n-well acting as the collecting electrode, read out by a charge sensitive preamplifier followed by a threshold discriminator. Note that, as compared to the Apsel2 series chips, no shaping stage was included, in order to meet spatial resolution constraints [7]. The SDR0 chip also comprises a digital section, including a 5-bit time stamp register, and a number of blocks implementing the sparsification logic. Post-layout simulations performed on the SDR0 elementary cell predict that both the ENC and the threshold dispersion should be of the order of 30 electrons, while a power consumption for the analog section of about 5 μW and a charge sensitivity of 780 mV/fC are expected. Fig. 2 shows a block diagram of the logic employed for the readout of a 16×16 matrix. It is based on a token-passing scheme which was implemented in the FPIX readout circuit [8]. The chip includes several test structures, namely a 16×16, an 8×8 and a 3×3 matrices of 25 μm pitch MAPS and three single pixel channels. The 16×16 and 8×8 matrices, which are read out by means of the token-passing scheme shown in Fig. 2, are chiefly conceived for the sparsified readout architecture test, while the other structures have been designed with the main purpose of testing the functionality and noise behaviour of the analog processor.

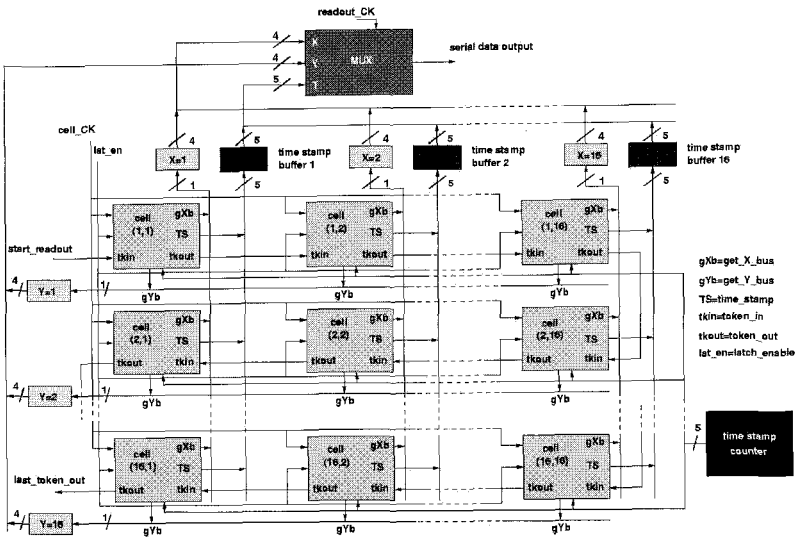

Fig. 2. Digital readout architecture of the SDR0 sensor.

5. Conclusions

This work discussed the design of monolithic active pixel sensors (MAPS) in deep submicron triple-well CMOS processes, based on the use of a deep n-well (DNW) as the charge collecting electrode. In particular, it reported on the extensive measurements performed on two test chips (Apsel2M and Apsel2T) and on the design and operation of another DNW monolithic sensor, the SDR0 chip, whose experimental characterization is planned for the last quarter of 2007. Based on the outcomes of the SDR0 prototype tests, the design of a new MAPS chip with sparsified digital readout, this time including 256×256 cells and suitable for testing on an accelerator particle beam, is being planned.

References

1. G. Deptuch, et al., IEEE Trans. Nucl. Sci. NS-49 (2002) 601.
2. H. S. Matis, et al., IEEE Trans. Nucl. Sci. NS-50 (2004) 1020.
3. D. Passeri, et al., Nucl. Instr. and Meth. A 518 (2004) 482.
4. G. Verner, et al., Nucl. Instr. and Meth. A 541 (2005) 166.
5. L. Ratti, et al., Nucl. Instr. and Meth. A 568 (2006) 159.
6. G. Rizzo, et al., Nucl. Instr. and Meth. A 565 (2006) 195.
7. L. Ratti, et al., IEEE Nucl. Sci. Sym. Conf. Rec. (2006) 681.
8. D. C. Christian, et al., Nucl. Instr. and Meth. A 549 (2005) 165.

First Results from the development of a new generation of Hybrid Photon Detector: EBCMOS

R. BARBIER*, P. DEPASSE

Université de Lyon, Université Lyon 1, Lyon, F-69003, France ; Institut de Physique Nucléaire de Lyon, CNRS/IN2P3, Villeurbanne, F-69622, France

J. BAUDOT, W. DULINSKI, M. WINTER

IPHC-IN2P3, Université Louis Pasteur Strasbourg, 23 rue du Loess, Strasbourg F-67037, France

N. ESTRE*, N. LAURENT*, C.T. KAISER†

* *PHOTONIS France SAS, avenue Roger Roncier BP 520, 19106 Brive cedex, France;*
† *PHOTONIS Netherlands BV, Roden B.O. Box 60, 9300 AB Roden, The Netherlands*

S. KATSANEVAS

IN2P3-CNRS, 3 Rue Michel Ange, Paris, 75016, France

The proximity focusing Hybrid Photon Detector (HPD) concept is implemented to develop a single photon sensitive Electron Bombarded CMOS (EBCMOS). The first demonstrator has been produced by the collaboration between the EBCMOS group of IPNL, the CMOS sensor group of IPHC and the R&D department of PHOTONIS. The prototype characteristics (dark current, gain, spatial and energy resolutions) are presented. The futur developments of this type of photo detector are discussed.

Keywords: EBCMOS, MAPS, hybrid photo detector, fluorescence, bioluminescence, single molecule tracking.

1. Introduction

This development is related to the design and the integration of a Monolithic Active Pixel Sensor (MAPS) into a photosensitive proximity focusing vacuum-based tube. This Hybrid Photo Detector is dedicated to the fluorescent and the bioluminescent high speed imaging. The project is de-

*Corresponding author: rbarbier@ipnl.in2p3.fr

veloped within the framework of the GIS (Grouping of Scientific Interest) PHOTONIS-IN2P3.
The first goal of this project was to produce and characterize a demonstrator based on a large scale back-thinned MAPS, sensitive to a single photon with a micrometric spatial resolution.

2. The EBCMOS demonstrator

2.1. *Demonstrator description*

The Minimum Ionizing MOS Active sensor (MIMOSA[1]) chips are developed by the IPHC team and are dedicated to the tracking of the charged particles in HEP experiments. The first mega-pixel sensor (17 μm pitch, 1024x1024 pixels, 3.5 cm^2) of the MIMOSA chip family, named MIMOSA5[2], have been back-thinned (MIMOSA5B[3]) and post-processed in order to be sensitive to low energy electrons. This process has been done within the framework of the SUCIMA FP5 European Project[4]. The precise characteristics of MIMOSA5B and his capabilities on low energy electron detection are presented in Refs 3,5,6.
The back-thinned MIMOSA5B chip is mounted in the die cavity of a ceramic carrier. The cathode-sensor gap is of the order of one millimeter. A tunable high voltage is put on the cathode ($\leq$ 10 kV). The cathode is a standard multi-alkali S20 type and provides a quantum efficiency equals to $15 \pm 2\%$ for a 520 nm wavelength. A picture of the first EBMIMOSA5 is presented in Fig. 1. The sensor encloses the cathode with a useful diameter of 18 mm.

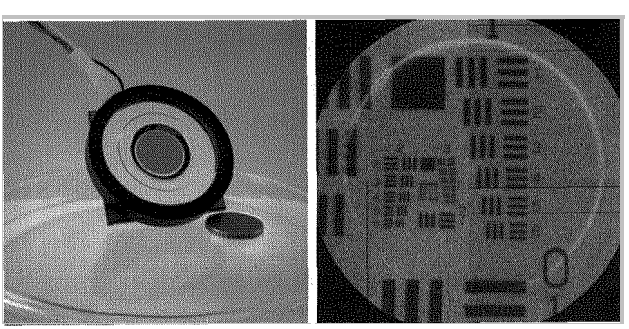

Fig. 1. On the left, the demonstrator EBMIMOSA5 with S20 photocathode. On the right, example of a *1951 USAF* resolution test chart imaging. The USAF target is mounted on a binocular with a magnification factor equals to 1.3. The illumination is tuned to 200 μLux and the high voltage to 4 kV.

2.2. *Photo-electron response and gain linearity*

The first characterization of the demonstrator is dedicated to single photo-electron energy measurement. The readout method and signal processing of MIMOSA5 are presented in Ref. 7. The readout clock is fixed at 10 MHz which corresponds to 27 ms exposure time for one frame. The signal selection is performed on a seed pixel and the charge deposited by the photo-electron is measured by the charge sum over the 5x5 pixels. The figure 2 shows the *signal-over-noise* ratio of the 25 pixels for a single photo-electron event. In the same figure, the linearity of the response with respect to the high voltage (3-8 kV) is presented.

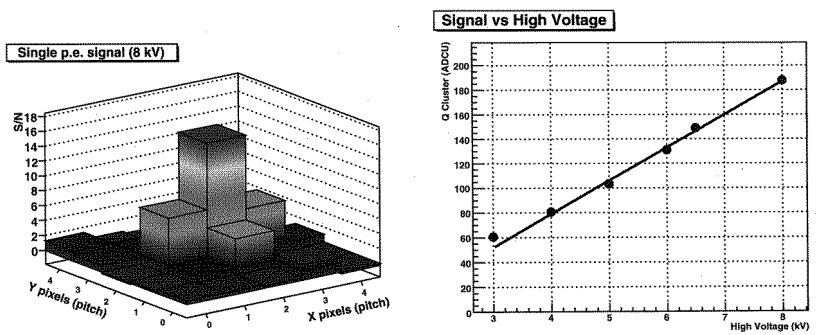

Fig. 2. On the left, signal over noise ratio of 25 pixels for a single photo-electron event at HV=8 kV: the charge sharing around the central pixel (called *seed*) is clearly visible. On the right, linearity of the sensor response *w.r.t* the high voltage.

2.3. *Dark Current measurement*

The drawback of proximity HPDs is the dark current from the cathode due to thermionic or field effects. The dark current obtained at 6 kV and 10°C is equal to 650 $\pm$ 25 photo-electrons per 27 ms per 2.5 cm^2. This corresponds to a dark current rate close to 100 Hz/mm^2. Cooling the EBCMOS window from 20°C to 10°C reduces the dark current by a factor of 2. No real improvement is observed when cooling below 10°C.

2.4. *Spatial resolution*

The point-spread function (PSF) of the tube is characterized with an optical test bench which provides a 2 μm diameter spot[a] on the photocathode plane. The spot can be precisely positionned with a 3D micro-controlled displacement. The pulse duration of the LED source is calibrated and fixed to 500 ns in order to obtain an average of one photo-electron into a selected sub-window (5x5 pixels). The PSF is obtained by computing, for single photo-electron events, the distribution of the position of the seed pixel. A Full Width at Half Maximum equals to 27.1 $\pm$ 0.1 μm has been measured at HV=8 kV.

2.5. *Photon counting capability*

One of the strong advantage of EBCMOS against EMCCD is its capability to count the number of photo-electrons in the same cluster. Figure 3 presents the charge sum over the 5x5 sub-window without any seed selection. The histogram exhibits a well defined Poisson distribution of the photo-electrons peaks. The peaks corresponding to 0, 1, 2 and 3 photo-electron events are resolved.

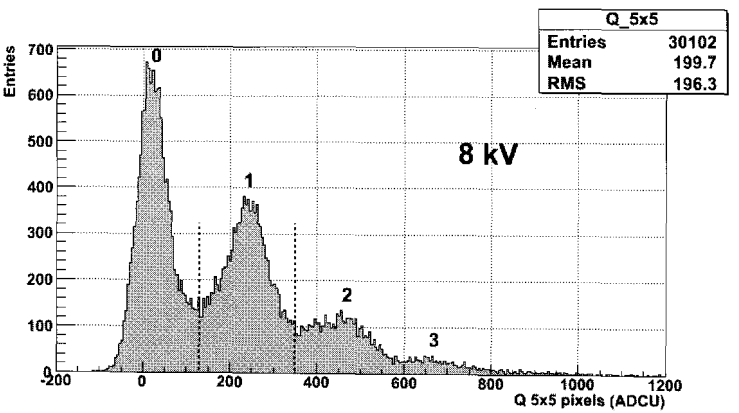

Fig. 3. Multi-photo-electron spectrum in ADC unit for the 5x5 pixel cluster.

[a]The spot is obtained by imaging a 100 μm diameter pinhole through an inverted MITUTOYO long working distance 50X objective.

3. Conclusion and Future plane

3.1. *Tracking concept for bioluminescence and fluorescence imaging*

The first results obtained on the EBMIMOSA5 demonstrate the concept of proximity focusing vacuum-tube on a back-thinned CMOS sensor. Single photon and multi-photon sensitivity with 27 μm resolution (FWHM) has been obtained with a back-thinned chip which is not optimized for this application. The characterization of the demonstrators is now focused on the main goal of this project: the tracking of fluorescent molecules. Cross comparisons between existing devices on fluorescence imaging of cell division (in zebrafish eggs) and on bioluminescence of calcium flow in drosophila brain are scheduled for the end of 2007.

3.2. *Future plans*

To overcome the limitation of the MIMOSA5 for the considered applications, we will produce in 2008 a Large-scale Ultra-fast SIngle PHoton trackER (LUSIPHER) with a dedicated back-thinned CMOS chip (medium-scale 400x800 pixels, 10 μm pitch, 8 analogue outputs and 40 MHz clock frequency, ST 0.25 μm process). A new acquisition ethernet board is currently developed to achieve 1000 frames per second (the equivalent data flow is equal to 3.6 Gb/s). LUSIPHER will be our first prototype dedicated to ultra-fast single photon tracking in fluorescence and bioluminescence experiments of single molecule tracking.

4. Acknowledgments

We would like to thank the acquisition team of CMOS sensor IPHC group for providing support on their USB2 DAQ board and technicians and engineers involved in this project at IPNL, IPHC and PHOTONIS.

References

1. R. Turchetta, et al., *Nucl. Instr. and Meth. A* **458** 677 (2001).
2. Yu. Gornushkin, et al., *Nucl. Instr. and Meth. A* **513** 291 (2003).
3. G. Deptuch, *Nucl. Instr. and Meth. A* **543** 537 (2005).
4. M. Caccia, et al., *Nucl. Phys. B (Poc. Suppl.)* **125** 133 (2003).
5. G. Deptuch, *Nucl. Instr. and Meth. A* **570** 165 (2007).
6. W. Dulinski, *Nucl. Instr. and Meth. A* **546** 274 (2005).
7. G. Claus, et al., *Nuclear Science Symposium Conference Record, 2004 IEEE 16-22 Oct.,* **Vol. 3** 1512 (2004).

THE MEMS PROJECT

ROBERTO BATTISTON
Dipartimento di Fisica e Sezione INFN di Perugia
Perugia, State ZIP/Zone, Italy

We report on the results of the first three years of the INFN/FBK-irst "MEMS Project", a program aiming to develop innovative silicon based radiation detectors using MEMS-like technologies.

1. Introduction

The potential for new discoveries is often linked to the availability of new measurement techniques. In the field of particle physics, a relevant example is the development, started in the 70's, of silicon detectors based on the CMOS technology derived from the microelectronics applications. It has been instrumental for the development of modern tracking detectors and imaging calorimeters used both at accelerators as well in space experiments. The technologies at the basis of the Micro Electronic Mechanical Systems (MEMS) open the possibility of developing completely new detectors for particle and fundamental physics, exploiting not only the electrical properties of Silicon, but also its mechanical and thermal characteristics. In order to explore further the potential of MEMS application for particle physics, in 2004, INFN and the Provincia Autonoma di Trento (PAT), have agreed to a collaborative effort, the MEMS research project, which is finalized the development of new radiation detectors. The MEMS project is driven by a "dual goal": on one side, to respond to the requirement of frontier research in the field of particle and fundamental physics, on the other side to identify consumer applications for these technologies .

During the last 10 years INFN and ITC-irst (now FBK-irst), the main PAT research Institute, have collaborated on a number of projects, both for ground based and space based research applications: the success of this collaboration is based on the fact that each Institute contributes with competences which are complementary. On one side INFN is very active in identifying demanding research applications, in the context of international collaborations. On the other side the FBK-irst laboratory has reached a level of organization and production quality, which is close to industry. In addition, one of the goals of the FBK-irst is to bridge the gap between the research and applications, a gap, which in Italy is particularly significant. For this reason the

MEMS project could become an example of good practice in the field of technology transfer in Italy, providing "turn key" new products for the industry, which are motivated from frontier research innovations

Since the fall of 2003, the start of the project, we have identified four pilot projects, which have been chosen because of their potential in revolutionizing four corresponding research fields:

- Three dimensional silicon detectors (3DSi)
- Solid state single photon detectors, also called Silicon Photo Multipliers (SiPM)
- Array of cryogenic bolometers for measuring the CMB
- Cryogenic, thick silicon for the search of rare events

These projects have been developed in collaboration with Italian INFN groups, active in the field of radiation detectors developments also through the support of the Vth INFN Committee. In the following we review the main results obtained on the pilot MEMS projects during the first two and half years of the program.

2. 3D-Silicon radiation detectors

2.1 Introduction

Planar silicon radiation, collect the charge on the wafers surfaces: the generation volume, the electric field intensity and the path traveled by the charges, all depend on the wafer thickness. Tri-dimensional (3D) silicon detectors are based on electrodes running perpendicular to the wafer surface, partly or fully across its thickness. In this way, while the generation volume is still determined by the detector thickness, but the drift volume and the interelectrode distance determines the electric filed. Since this distance can be reduce to few tens of micron, these detectors can be operated at a much lower depletion voltage, while the charge collection is much faster than in the case of traditional detectors. This geometry also assures full charge collection and lower intrinsic noise. The development of these detectors , started by S. Parker et al. at the end of the 90's, requires MEMS technologies, in particular the Deep-Reactive Ion Etching (DRIE). The fabrication of 3D detectors is based on laser drilling of holes, while the electrodes are realized by Schottky contacts using metal deposition. Thanks to their electrode geometry, 3D detectors are intrinsically radiation resistant. For this reason they are a good candidate for replacing pixel detectors on Inner Tracking Systems. Due to the lack of edge

effects and their intrinsic speed, they also find interesting applications in the field of medical or industrial X ray imaging, as well on DNA sequencing using radioactive tracers.

2.2 Development at FBK-irst

For the MEMS project, we have produced three lots of ~1.6 kΩcm , p-type, <111>, 380 μm wafers, using 3D-STC (Single Type Column) fabrication technology, with 180 μm deep DRIE holes (fabricated at CNM, Barcellona, Spain and IBS, Peynier, France). Surface insulation is obtained by a combination of *p*-stop and *p*-spray[1-3]. IV characteristics show an average columnar density <1pA with a detector yield of about 90%. The first two batches have been irradiated using the TRIGA facility of the Jozef Stefan Laboratory in Lubiana, Slovenia, at fluences up to $5*10^{15}$ n/cm^2 which were followed by a 15 days, ambient temperature annealing.

The electrical tests (IV and CV) were performed in darkness, at 23°C. From the analysis of the data, we observe that these 3D detectors are completely depleted below 1000 V even with fluences of $1*10^{16}$ n/cm^2, while a planar detector would require one order of magnitude higher V_{depl}.

Charge Collection Efficiency (CCE) has been measured using a 90Sr β source. Already at 0 V we observe a CCE of 27%, an effect characteristic of the 3D geometry. At 190 V we obtain 100% CCE with good S/N separation.

The next technological step will include the implementation of two types of alternated *n* and *p* column (*Double Type Column*, DTC, technology), starting from the opposite side of the wafer and stopping at 50 μm from the surface (Fig. 1) . For more information on the 3D detectors at FBK-Irst, you are invited to look at the web page http://tredi.itc.it/.

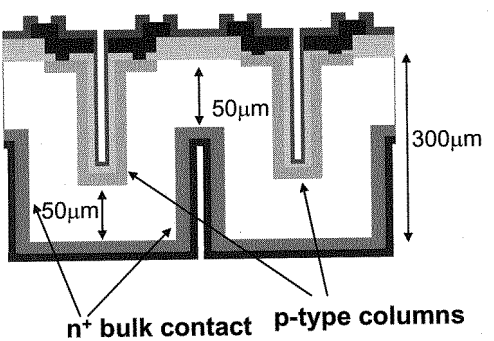

Figure 1: Layout of a 3D-dtc detector with alternating columns

3. Silicon Photomultipliers, SiPM

3.1 Introduction

Silicon Photomultipliers (SiPM) are arrays of semiconductor photon detectors (micropixel) operating in Geiger mode[4] (Fig. 2) The micropixels, having typical sizes of tens of microns, are built on a common substrate; all of them are interconnected through an integrated, decoupling resistor R to a common polarization strip. The polarization voltage is chosen 10-20% above the breakdown voltage, ensuring a high probability for a free charge to start a Geiger discharge. The discharge is self-quenched when the voltage goes below the breakdown voltage, due to the voltage drop across the resistor R. Each micropixel behaves like a binary counter for single photons. The array provides an output signal, which is the analog sum of the digital micropixel signals, measuring the intensity of the incoming radiation. The fabrication of the SiPM is based wafers having an epitaxial layer. The thickness of this layer (few micron) and the wafer resistively are chosen to ensure a good Q.E. for the wavelength of interest and a quick charge collection. The heart of the device is the inversely polarized *n+/p* junction. The additional *p* region contributes to control the discharge phenomenon, limiting its development within the planar junction volume. The junction depth is limited to the minimum needed for a good Q.E. (Fig.2c). In order to limit the operation voltage to a few tens of Volts, the doping level of the additional *p* layer has to be carefully chosen. In order to limit breakdown phenomena at the junction edge, an *n*-guard ring is added, to improve the decoupling among nearby micropixels. The size of the guard ring is critical, since it influence the geometrical efficiency of the device. The integrated resistor is made of polysilicon, a widely used technology at FBK-irst.

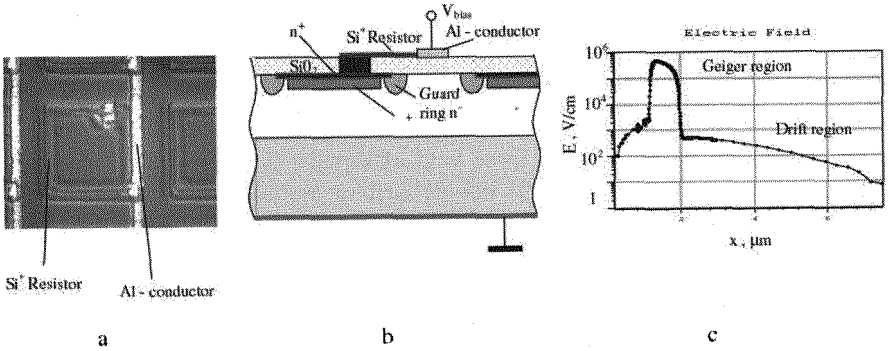

Figure 2: (a) SEM microphotography of a SiPM micropixel, (b) schematic section of the micropixel (c) electric field dependence through a vertical section of the micropixel.

The performances of SiPM are very interesting, in particular if compared to other kind of photomultipliers (see Table 1): high gain (~ 10^6) with low operating voltages (a (~ 30V), operational stability, insensibility to the magnetic field, excellent time resolution (< 30ps), single photon detection, possibility to operate at room temperature although best noise performances are obtained at lower temperatures (up to -70°C). The SiPM dynamic range is directly proportional to the number of micropixel in the array; for this reason it is important to build very small but highly efficient, micropixels.

Currently, the limiting factor for the SiPM in the single photon detection mode is the noise rate due to the dark current, typically few MHz/mm^2 (@300 K) or 1 KHz/mm^2 (@100 K). Due to the random properties of the noise signals, increasing the threshold of the output signal to value corresponding to two (or more) simultaneous pulses reduces the noise rates by order(s) of magnitude.

For these reasons the SiPM is quickly becoming a very interesting device for all applications where the detection of very low optical signals is required. Among the many application we recall the detection of single UV photons, the detection of signal from scintillating fibers in trackers of calorimeters both in high-energy physics as well as in medical imaging and optical telecommunications.

3.2 Development at FBK-irst

Three batches of SiPM have been developed at FBK-irst within the MEMS program [5-6]. The first and the second were devoted to develop the technology, checking the performances reported in the literature. The study of the noise and the cross talk among micropixels were among the goal of these production batches. The process requires 10 photolithography masks, with micron size features. The third batch is the first production batch with geometries optimized for specific applications.

The detailed characterization of the first two technology batches has provided important information on the devices produced at FBK-irst, allowing a detailed comparison with devices of the same type produced elsewhere.

The devices produces three kind of signals: (i) single pulses due to a single micro cell activation, (ii) double (triple) amplitude pulses due to the simultaneous activation of few micro cells (expected for instance in case of optical cross-talk and (iii) pulse of smaller amplitudes, following a normal (large) pulse (typical of after-pulses). Integrating the signals over 100 ns, in order to fully include the width of single pulses, we obtain the spectrum shown in Fig. 6.

Table 1. Comparison of SiPM produced at FBK-irst with other solid-state photomultipliers.

	PMT	APD	HPD	SiPM
Photon detection efficiency:				(geom.eff. 0.5)
Blue (450 nm)	20%	50%	20%	30%
Green – Yellow (550 nm)	a few%	60÷70%	a few%	35%
Red (650 nm)	<1%	80%	<1%	30%
Gain	10^6÷10^7	100÷200	10^3	10^6
Operation voltage	1÷2 kV	100÷500 V	20 kV	25 V
Operation in the magnetic field	problematic	OK	OK	OK
Threshold sensitivity (S/N » 1)	1 ph.e.	~ 10 ph.e.	1 ph.e.	1 ph.e.
Timing /10 ph.e.	~ 100 ps	a few ns	~ 100 ps	30 ps
Dynamic range	~ 10^6	large	large	~ 10^3/mm^2
Complexity	High: vacuum, high voltage	Medium: low-noise electronics	very high: hybrid technology, very high volt.	relatively low

The large peak, dominating the spectrum, corresponds to single "monochromatic" pulses and shows the good performance of the detector; the tail corresponds to events with larger charge deposition due to optical cross-talk and/or after pulses. The gain (corresponding to the peak position) grows linearly with the polarization voltage, reaching about 10^6 at about 3V above the breakdown. The measured dark count is of the order of one MHz at the breakdown voltage (32 V), and reaches 2-3MHz at 3V over-voltage. The width of the stability plateau is about 4-5 V.

In order to measure the SiPM Photo Detection Efficiency (PDE) we have done two kind of measurements. After illuminating the device with a suitable light source we have measured the DC value of the current: the difference between the measured value and the dark current is proportional to the number of detected photons, through the gain, which has to be known. The second method consists in the measurement of the counting rate: the difference between the measured rate and the dark rate measures the number of detected photons.

The two methods give a good agreement: the result obtained for a device having a 20% active area is shown in Fig. 3.

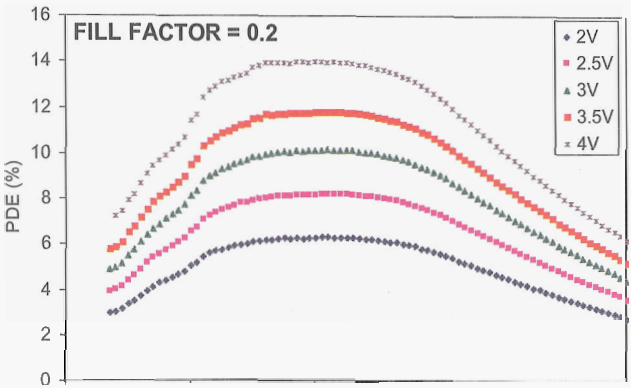

The figure shows the PDE as function of the light wavelength and for different polarization voltages. In order to understand the shape of the curves it is necessary to analyze the factors influencing the PDE: the geometrical efficiency (Ae), the quantum efficiency (QE) and the avalanche probability (Pt). Ae is independent form the polarization voltage as well from the wavelength and determines the maximum value that the PDE can reach (0.2 in this case). Pt depends both from the polarization voltage (the ionization yield increases with the voltage) as well as from the wavelength (different absorpition depth at different wavelengths). QE depends from the wavelength since both the transmittance of the antireflective coating and the internal quantum efficiency depends on the wavelength. The PDE dependence from the voltage is due only to Pt, while the wavelength dependence depends both on Pt as well as QE. QE has been measured on diodes from the same wafers. QE is close to 100% for wavelength of 420 nm, while quickly drops below 400 nm. From this result, we understand that the PDE dependence around 400 nm is limited by Pt. For wavelengths greater than 600 nm the QE is the limiting factor.

The measurement of the timing characteristics of the SiPM has been done in collaboration with CNR Pisa, using a laser which can provide 60 fs pulses at a rate of 80MHz with a jitter lower than 100 fs between pulses[7]. The results of the analysis of the time structure of the measured pulses are shown in Fig. 4 as a function of the breakdown voltage. An excellent single photon time resolution of

70 ps has been measured at 3-4V above breakdown; the time resolution has been observed to improve with $N^{-1/2}$ with the number of incident photons, N.

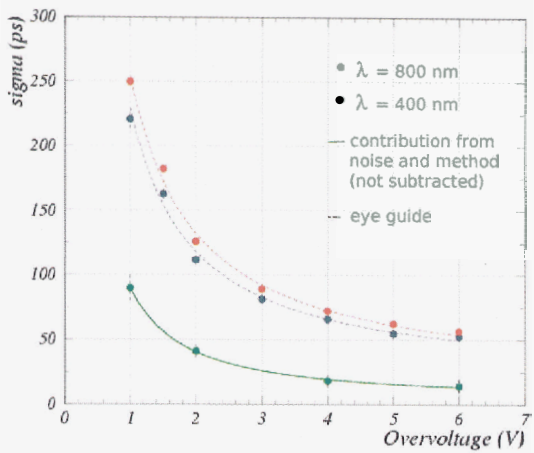

Figure 4: SiPM timing resolution as a function of the polarization voltage (refereed to the breakdown voltage)

In 2007 we have produced a third batch, using the technology derived from the first runs and implementing various geometries suitable for applications which ranges from PET, fiber tracking, calorimetry, Cerenkov light detections an so on. In particular the first arrays of SiPM have been produced, with up to 32 channel each (Fig.5).

The yield observed on this first large production run exceed 90%, with several thousand of SiPM produced, and the properties measured are very uniform among different devices from the same wafer. Applications of the FBK-irst SiPM for scientific applications are steadily increasing, as it has been presented at this conference.

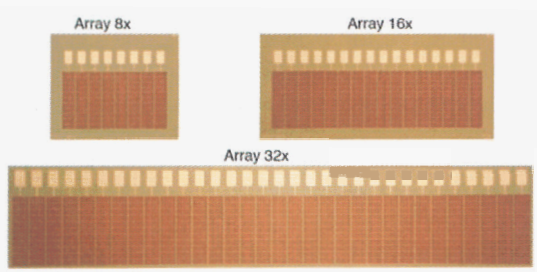

Figure 5: SiPM arrays produced at FBK-irst in 2007 (third batch)

4. Development of arrays of cryogenic microbolometers

4.1 Introduction

Bolometers are a versatile kind radiation sensor used since long time in various fields of physics and astrophysics as well as in industrial applications, like medical and environmental. Cryogenic bolometers are used since years in the search of rare nuclear decays, and FBK-irst has a solid experience in the development of this kind of sensors in collaboration with the INFN group of Milano working on double beta decay and neutrino mass determination.

Within the MEMS project we started the development aiming to the development of bolometers arrays for the imaging of the CMB radiation and of its polarization. A promising technology is the so-called *Kinetic Inductance Detectors* (KID), superconducting devices sensitive to the deposition of RF radiation, which changes their electrical properties. If KIDs are used as elements of an array of resonant circuits, the intensity of RF radiation is determined by the variation of the resonators properties.

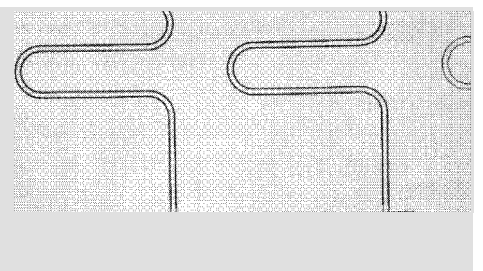

Figure 6: Microwave resonators coupled to a CPW line.

4.2 Development at FBK-irst

After some initial tests of structures Niobium based superconducting devices, which have shown problems in the purity of the evaporated Nb layer, we have concentrated our efforts on Al resonators deposited by sputtering. Various geometries have been built to study the influence of the substrate on the phase noise. One interesting structure is shown in Fig.6, where the conductor and the surrounding ground plane are separated by a 4 micron deep trench. These devices have been sent to the AIF laboratory in Cardiff for the first cryogenic tests at low temperature. Al strips have a lower superconductive transition temperature than Nb, around 1.2 K; they should then be tested in the 100 mK range.

5. Cryogenic Silicon Time Projection Chamber

5.1 Introduction

Silicon detectors for radiation detectors are traditionally based on doped semiconductors operating at ambient temperature. This technology limits the active volume of the detectors (depletion layer) to few mm with fairly large depletion voltages. In various applications one would need much larger active volumes: this can be obtained operating at cryogenic temperatures. At the "freeze-out" temperature the depletion is complete even for intrinsic silicon a there is no need to apply large voltages to remove the carriers generated inside the bulk. In this way it is also easier to model the electric fields in the bulk and to design focusing and amplification structures. At low temperature the electrons mean free path in silicon is 5-10 micron, much larger than at room temperature. The development of large volume detectors, in the range of 1 Kg of mass, would open application windows on fields like solar neutrino physics, coherent neutrino scattering, dark matter search, fast neutron detectors and so on. Preliminary results on the properties of thick silicon have been reported in the past, showing promising performances. For instance a 1 cm thick diode operating at 90 K at LNL has shown very low dark current, in the range of tens of fA @ 100 V of bias, detecting X and Gamma particles.

5.2 Development at FBK-irst

The goal of the development at FBK-irst was to develop for the first time large semiconductor active volumes, making use of the milliseconds electrons lifetime of high resistivity silicon (20 kΩ cm) operated at cryogenic temperatures with meter long attenuation lengths. A Schottky junction has been developed, after trying different kind of metals for the barrier, concentrating on Au/Si junctions. We then tried FZ wafers having resisitivities higher than 30 kΩcm and thickness of 1.5 mm. We tried both n and p wafers. After measuring the basic parameters on these wafers, construction of 1 cm thick wafers started; manipulating these large wafers has required modifications to the fab-line processes and solving various technical problems. Fig. 7 shows the photograph of two 1 cm thick wafers, built with the Au/Si barrier technology. Fig. 7b show the I-V characteristics of n type substrates at ambient temperature. The rectifying diode properties and the capability of these devices to stand high reverse voltages are clearly visible.

During 2006 we tested *B* and *P* diffusion-doped *pn* junctions on 1 cm thick wafers: from the I-V characteristics for the 4 large diodes on a 1 cm thick wafer we measure that only few volts are sufficient to substantially deplete the device.

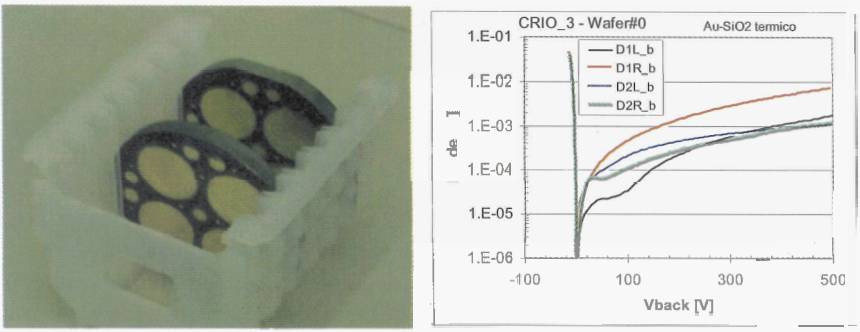

a) b)

Figure 7: a) 1 cm thick n wafers with Au/Si Shottky barrier b) I-V characteristics at room temperature of the four large area diodes

We then built 1 cm thick *n*-type high resistivity wafers, purchasing a *n*-type ingot with resistivity > 30 kΩcm: from this ingot we cut 12 wafers. The sensors were characterized cryogenically at LNL, using both gamma sources and cosmic rays. At liquid He temperatures we measured dark current are at the level of 1 pA/cm^2 or less. Capacitance measurements confirmed the complete depletion due to the "freeze-out" effect. The measured charge collection efficiency show that with an *n*-type substrate full efficiency starts already at 100 V. *p*-type substrates, having higher resistivity, show the same behavior already from 70 V. Using these devices we have measured 4.2keV (FWHM) of resolution for a 59keV gamma ray produced by an *Am* source. These results are very encouraging, and we are now developing improved charge collection/amplification structures as well as drift structures.

Acknowledgements

The MEMS project is based on the collaborative effort of a large number of researchers both from FBK-irst as well as from INFN. The author would like to particularly thank: Giovanni Ambrosi, Bianca Angelini, Pierluigi Bellutti, Maurizio Boscardin, Luciano Bosisio, Ubaldo Bottigli, Giacomo Bressi, Gianni Carugno, Gianmaria Collazuol, Piero dal Piaz, Paolo de Bernardis, Alberto del Guerra, Nicoleta Dinu, Sadakazu Haino, Maria Ionica, Gabriela Llosa, Sara Marcatili, Benno Margesin, Alessandro Monfardini, Marco Petasecca, Andrea Papi, Claudio Piemonte, Mario Zen, Nicola Zorzi.

References

1. A. Pozza, M. Boscardin, C. Piemonte, G.-F. Dalla Betta, L. Bosisio, S. Ronchin, N. Zorzi NIM A 570 (2007) 317.2.
2. M. Boscardin, L. Bosisio, G. F. Dalla Betta, C. Piemonte, A. Pozza, S. Ronchin, C. Tosi, N. Zorzi, NIM A, vol. 572, (2007), 284.
3. S. Ronchin, M. Boscardin, C. Piemonte, A. Pozza, N. Zorzi,G. F. Dalla Betta, G. Pellegrini, L. Bosisio, NIM A, vol. 573, (2007) 224.
4. G. Bondarenko et al, NIM A 242,(2000),187.
5. C. Piemonte, NIMA 568 (2006) 224.
6. C. Piemonte, R. Battiston, M. Boscardin, G.-F. Dalla Betta, A. Del Guerra, N. Dinu, A. Pozza, N. Zorzi, IEEE Transaction on Nuclear Science, Vol. 54, n. 1, (2007), pp. 236
7. G. Collazuol, G.Ambrosi, M.Boscardin, F.Corsi, G.F.Dalla Betta, A.Del Guerra, M.Galimberti, D.Giulietti, L.A.Gizzi, L.Labate, G.Llosa, S.Marcatili, C.Piemonte, A.Pozza, N.Zorzi, presented at the XI VCI, Vienna 19-24 February 2007, Nucl Instr and Methods A (2007), in press.

Quality Assurance of Pixel Hybrid Photon Detectors for the LHCb Ring Imaging Cherenkov Counters

LAURENCE CARSON* on behalf of the LHCb RICH collaboration

*Department of Physics and Astronomy, University of Glasgow, Glasgow, G12 8QQ, United Kingdom
E-mail: l.carson@physics.gla.ac.uk
www.physics.gla.ac.uk

Pion/kaon discrimination in the LHCb experiment will be provided by two Ring Imaging Cherenkov (RICH) counters. These use arrays of 484 Hybrid Photon Detectors (HPDs) to detect the Cherenkov photons emitted by charged particles traversing the RICH. The results from comprehensive quality assurance tests on the 550 HPDs manufactured for LHCb are described. Leakage currents, dead channel probabilities, dark count rates and ion feedback rates are reported. Furthermore, measurements carried out on a sample of tubes to determine the efficiency of the HPD pixel chip by measuring the summed analogue response from the backplane of the silicon sensor are described.

Keywords: LHCb; RICH; Pixel HPD.

1. Introduction

The LHCb experiment [1] is one of four experiments that will run at the Large Hadron Collider (LHC) at CERN, Geneva. When data taking begins in 2008, LHCb will commence the study of rare processes in the B-hadron system with the aim of discovering New Physics. Accurate and reliable Particle Identification (PID) will be crucial to the success of the LHCb physics program. To this end the LHCb detector includes two Ring Imaging Cherenkov (RICH) detectors [2] which are capable of identifying pions, kaons and protons over a wide momentum range of 1–100GeV/c.

Both RICH detectors make use of arrays of 484 pixel Hybrid Photon Detectors (HPDs) [3] to detect the Cherenkov photons which are emitted by charged particles as they traverse the RICH. The HPDs must meet stringent performance requirements if they are to provide PID capability over the lifetime of the LHC. This paper reports the results of comprehensive quality assurance tests on all 550 HPDs which were manufactured for LHCb.

2. The Pixel Hybrid Photon Detector

The pixel HPD aims to combine the advantages of vacuum and silicon technology by encapsulating a silicon sensor inside a vacuum-sealed tube. Figure 1 shows a schematic diagram of an HPD.

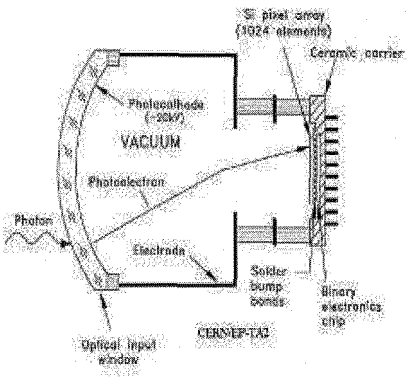

Fig. 1. Schematic of the pixel hybrid photon detector.

The principle of operation of an HPD is as follows: an incoming Cherenkov photon reaches the quartz window of the HPD, and strikes the layer of S20-type multialkali photocathode material which is deposited on the vacuum side of the window. This liberates a photoelectron, which is then accelerated and focused by a 20kV electric field toward the anode. The anode consists of a pixellated silicon diode which is bump-bonded to a binary readout chip. The readout chip has 8192 pixels. During LHCb running these are ORed in groups of 8 to make 1024 superpixels.

The HPD manufacturing process involved a number of different international companies, with the final stages carried out by Photonis-DEP[a]. The quality assurance tests were carried out by LHCb between October 2005 and July 2007 using dedicated Photon Detector Test Facilities (PDTFs).

3. Final Results from Quality Assurance Tests on All HPDs

All 550 HPDs which were manufactured for LHCb have now been tested at the PDTFs. Table 1 shows some of the specifications that were set out in the contract between LHCb and DEP for the performance of the manufactured HPDs, and also shows the actual average performance of the HPDs from tests carried out at the PDTFs. The collective performance of the HPDs in the areas most crucial for their physics performance is further illustrated

[a]Photonis Netherlands B.V., Dwazziewegen 2, P.O. Box 60, NL-9300 AB Roden, Netherlands. Formerly Delft Electronic Products.

Table 1. Selected contract specifications and actual HPD performance.

Property	Specification	Average Performance
Working Pixels	95% minimum	99.8%
Photoelectron Detection Threshold	$1500e^-$ maximum	$1064e^-$
Photoelectron Detection Noise	$100e^-$ typical	$145e^-$
Photoelectron Detection Efficiency	85% typical	88%[a]
Leakage Current at 80V reverse bias	1μA typical	1.49μA
Quantum Efficiency at 270nm	20% minimum	30.9%[b]
Dark Count Rate	$5kHz/cm^2$ typical	$2.54kHz/cm^2$
Ion Feedback Probability	1% maximum	0.03%

Note: [a] From tests carried out on 2 HPDs, see Sec. 4. [b] See Ref. [4].

in Figs. 2 and 3. Note that the whole sample of 550 HPDs contained only 12 HPDs (i.e. 2.2% of the sample) which had a performance issue serious enough to disqualify them from use in the RICH.

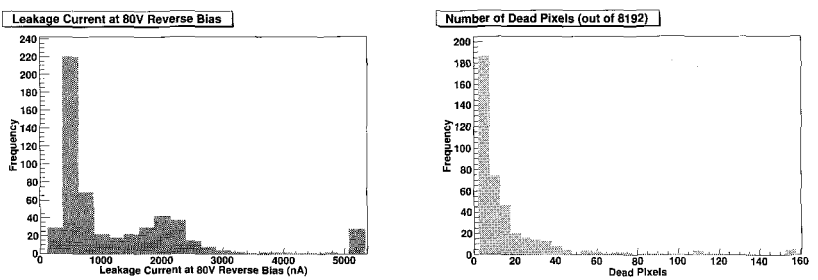

Fig. 2. Left: Silicon sensor leakage current (nA) at 80V reverse bias. Right: Number of dead pixels (out of 8192).

It can be seen that the leakage current is normally less than 1μA, which is the typical leakage current specified in the contract. The dead pixel probability is always less than the contract maximum of 5%, which corresponds to 410 dead pixels. No HPD exceeds the contractual maximum of 1% ion feedback probability. Some HPDs do exceed the contractual maximum dark count level of $5kHz/cm^2$, but these tubes were not rejected as the dark count level is still 1,000 times lower than the level where it would adversely affect the physics performance of the RICH. In addition, the higher dark count rate is correlated with the improved quantum efficiency of the tubes.

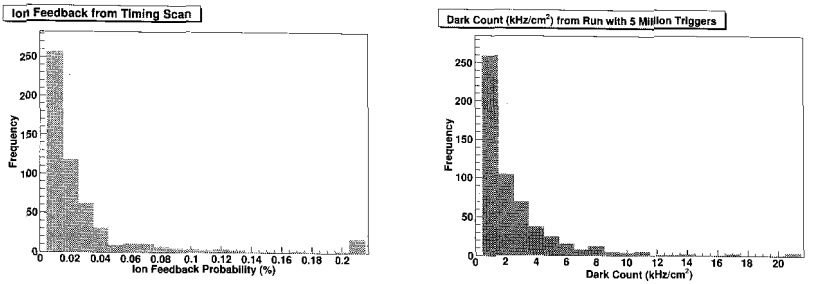

Fig. 3. Left: Ion feedback probability (%). This measures the quality of the vacuum inside the HPD by measuring the number of ions created by photoelectrons as they pass through the vacuum. Right: Dark count levels (kHz/cm^2). This is the noise level seen when the high voltage is on but no light is incident on the HPD.

4. Backpulse Measurements

The number of photoelectrons seen by the chip will be lower than the number arriving at the backplane of the silicon sensor because some photoelectrons do not deposit enough charge within the readout window of the chip to reach the detection threshold. This is due to charge-sharing and backscattering effects, and defines the photoelectron detection efficiency η_{Si} of the HPD pixel chip. A specialised test to measure η_{Si} (the "backpulse measurement") was carried out on two HPDs. This measurement involves shining light from an LED onto the quartz window, and counting the number of photoelectrons this produces by two different methods. Firstly, one counts the number of hits registered by the digital readout chip, as measured by the standard PDTF Labview software. This is then divided by the number of photoelectrons found by measuring the amount of charge deposited at the backplane. The number of photoelectrons at the backplane is measured by fitting a custom-defined function [5] to the charge spectrum acquired at the backplane. A typical spectrum (black dots) and fit (green line) is shown on the left of Fig. 4.

Figure 4 (right) shows the η_{Si} values obtained for one HPD (named H630005) using a digital readout window of 50ns. The average value across the two tubes is $\eta_{\mathrm{Si}} = (94 \pm 2)\%$. The errors on each η_{Si} value are estimated by considering the change in the light output level of the LED during a single measurement, and by examining the stability of the fit to the backpulse spectra. Note that η_{Si} is independent of the amount of light input (x-axis). Measurements were also carried out on H630005 (only) using a

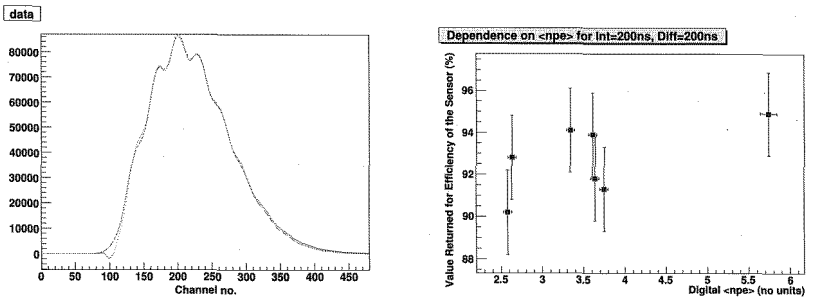

Fig. 4. Left: Fit to backpulse spectrum. The 2nd, 3rd and 4th photoelectron peaks can be clearly seen, with the other peaks appearing as shoulders due to the high noise level. Right: η_{Si} results for tube H630005. This HPD has $\eta_{\mathrm{Si}} = (92 \pm 2)\%$.

digital readout window of 25ns, as this is what will be used during LHC running. These yield $\eta_{\mathrm{Si}} = (88 \pm 2)\%$, which as expected is lower than the 50ns value.

5. Conclusions

All HPDs required by the LHCb RICH detectors, including spares, have now been produced and thoroughly tested. Only 12 out of 550 HPDs fail to meet the performance requirements. The remaining HPDs meet all specifications and exceed them in certain key areas, for example ion feedback probability, number of working channels and quantum efficiency. The manufacture and testing of the whole sample of HPDs required for LHCb has proceeded according to plan. Commissioning of the HPDs in the RICH detector has commenced, with all components on schedule to be ready for the first LHCb data during 2008.

References

1. LHCb Collaboration, *LHCb Reoptimized Detector Design and Performance*, CERN LHCC 2003-030 LHCb, 9th September 2003.
2. LHCb Collaboration, *LHCb RICH Technical Design Report*, CERN LHCC 2000-037 LHCb, 7th September 2000.
3. M. Moritz, *et al.*, IEEE Trans. Nucl. Sci. NS-51 (3) (2004) 1060.
4. R. Lambert, *Quantum Efficiency of Hybrid Photon Detectors for the LHCb RICH*, in these proceedings.
5. T. Tabarelli de Fatis, Nucl. Instr. and Meth. A **385** (1997) 366.

Fast photon-detection for COMPASS RICH-1

P.Abbon[k], *M.Alexeev*[a†], *H.Angerer*[i], *R.Birsa*[o], *P.Bordalo*[g], *F.Bradamante*[n], A.Bressan[n], *M.Chiosso*[l*], *P.Ciliberti*[n], *M.L.Colantoni*[m], *T.Dafni*[k], *S.Dalla Torre*[o], E.Delagnes[k], *O.Denisov*[m†], *H.Deschamps*[k], *V.Diaz*[o], *N.Dibiase*[l], *V.Duic*[n], W.Eyrich[d], *A.Ferrero*[l], *M.Finger*[j], *M.Finger Jr*[j], *H.Fisher*[e], *S.Gerassimov*[i], M.Giorgi[n], *B.Gobbo*[o], *R.Hagemann*[e], *D.vonHarrac*[h], *F.H.Heinsius*[e], *R.Joosten*[b], B.Ketzer[i], *K.Königsmann*[e], *V.N.Kolosov*[c+], *I.Konorov*[i], *D.Kramer*[f], *F.Kunne*[k], A.Lehmann[d], *S.Levorato*[n], *A.Maggiora*[m], *A.Magnon*[k], *A.Mann*[i], *A.Martin*[n], G.Menon[o], *A.Mutter*[e], *O.Nähle*[b], *D.Neyret*[k], *F.Nerling*[e], *S.Panebianco*[k], D.Panzieri[a], *S.Paul*[i], *G.Pesaro*[n], *C.Pizzolotto*[d], *J.Polak*[f], *P.Rebourgeard*[k], *F.Robinet*[k], E.Rocco[l], *P.Schiavon*[n], *C.Schill*[e], *W.Schoenmeier*[d], *W.Schröder*[d], *L.Silva*[g], *M.Slunecka*[j] F.Sozzi[n], *L.Steiger*[j], *M.Sulc*[f], *M.Svec*[f], *F.Tessarotto*[o], *A.Teufel*[d], *H.Wollny*[e]

[a]*INFN, Sezione di Torino and University of East Piemonte, Alessandria, Italy*
[b]*Universität Bonn, Helmholtz-Institut für Sthralen- und Kernphysik, Bonn, Germany*
[c]*CERN, European Organization for Nuclear research, Genva, Switzerland*
[d]*Universität Erlangen-Nürnberg, Physikalisches Institut, Erlangen, Germany*
[e]*Universität Freiburg, Physikalisches Institut, Freiburg, Germany*
[f]*Technical University of Liberec, Liberec, Czech Republic*
[g]*LIP, Lisbon, Portugal*
[h]*Universität Mainz, Institut für Kernphysik, Mainz, Germany*
[i]*Technishe Universität München, Physik Department, Garching, Germany*
[j]*Charles University, Prague, Czech Republic and JINR, Dubna, Russia*
[k]*CEA Saclay, DSM/DAPNIA, Gif-sur-Yvette, France*
[l]*INFN, Sezione di Torino and University of Torino, Torino, Italy*
[m]*INFN, Sezione di Torino, Torino, Italy*
[n]*INFN, Sezione di Trieste and University of Trieste, Trieste, Italy*
[o]*INFN, Sezione di Trieste, Trieste, Italy*
[+]*on leave from IHEP, Protvino, Russia*
[†]*on leave from JINR, Dubna, Russia*

[*] *e-mail: michela.chiosso@to.infn.it*

A fast photon-detection system for the detector RICH-1 of the COMPASS Experiment at CERN SPS is in operation since the 2006 run. It is based on the use of Multi-Anode Photomultipliers (MAPMTs) coupled to individual fused silica lens telescopes and fast read-out electronics. It has been designed taking into account the high photon flux in the central region of the detector and the high rate requirements of the COMPASS Experiment. We present the photon-detection design and construction, together with its characterization

and measured performances based on the data collected in 2006.

Keywords: particle identification; RICH; COMPASS; multi-anode photo-multiplier.

1. Introduction

COMPASS is high luminosity experiment,[1] at CERN SPS, dedicated to hadron physics, with an extend research program both dedicated to the nucleon spin structure, collecting data with the muon beam, and to the hadron spectroscopy, using hadron beams. For both scientific programs, as for many other particle and nuclear experiments, a very efficient particle identification (PID) is mandatory. In the COMPASS spectrometer hadronic particle identification in the multi-decade GeV/c range is performed by RICH-1,[2] a large size RICH counter in operation since 2001.
During years 2001-2004 RICH-1 was fully instrumented with Multi-Wires Proportional Chambers (MWPCs) equipped with CsI photocathodes for single photon detection, operated at low gain, and thus read-out by long integration time amplificators, as imposed by the presence of CsI photocathodes. This results in a detection system with long memory, not adequate for extremely high rates. To overcome these limitations and to cope with the higher trigger rates, of up to 100 KHz, foreseen by the COMPASS experiment from 2006 on, an ambitious upgrade project has been developed and implemented during the SPS shut down period, between Autumn 2004 and Spring 2006. In particular, the central detection region, corresponding to 25% of the active surface, has been equipped with the new fast photon-detection system based on MAPMTs, while in the peripheral region the existing MWPCs with CsI photocathodes are unchanged, but read-out by a new electronic system based on APV preamplifiers and flash ADC chips.[3] We focus here on the fast photon-detection system, presenting the detector design and construction, as well as its characterization and performances based on the 2006 data.

2. General description of the photon-detection system

Multi-anode photo-multiplier tubes (MAPMTs) by Hamamatsu, type R7600-03-M16, with 16 anode channels, have been chosen to detect single photons at high rates: they have bialkali photocathodes with 18x18 mm^2 active surface and UV extended glass window, to enlarge the range of the detectable Cherenkov light spectrum (200-700 nm). MAPMTs are coupled to individual telescopes of two lenses in order to increase the geometrical

acceptance; image distortion is avoided by an accurate telescope design; lenses are made of fused silica to match the wavelength range of the PMT. A custom voltage-divider compact circuit, which also provides connections between MAPMT anodes and the read-out chain, has been realised; it is based on the standard circuit[4] proposed by Hamamatsu, which, as proved by laboratory test, ensures high efficiency in single photo-electron detection also at high rate: in fact no gain reduction has been observed up to rates larger than 5 MHz per anode.

3. The read-out electronics

The whole electronics system is arranged in a very compact setup, free from cable connections to minimise the electrical noise and to take into account the limited space in front of the RICH-1 detector. The small analog boards, each populated with two MAD4 preamplifier-discriminator chips,[5] are directly linked via a connector to the voltage divider boards. A deck board, the Roof board, provides services to eight MAD4 boards: power, threshold settings and input/output data transfer from and to the digital board; it also acts as a mechanical fixation of the other elements of the read-out system. The digital data from the Digital RICH ElectronIc Sampling (DREISAM) boards are transferred via optical links to the HOT-CMC receiver boards, explicitly developed for this project, mounted on the common read-out driver of the COMPASS experiment: the COMPASS Accumulate, Transfer and Control Hardware (CATCH).[6]

The main task of the front-end electronics is to amplify the signals from the MAPMTs, to discriminate them and send the differential LVDS signals to the digital board. Low noise level and good efficiency in single photo-electron detection are required. In Fig. 1 typical threshold curves for three

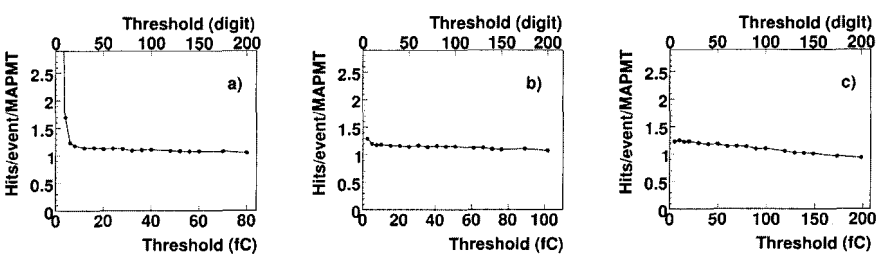

Fig. 1. Threshold curves for three different DAC resolutions: a) 0.40 fC/digit; b) 0.50 fC/digit; c) 0.99 fC/digit; Signals are generated by single photo-electrons

different DAC resolutions are shown. In the second plot, corresponding to the currently used DAC resolution of 0.5 fC/digit, there is a wide range of threshold settings, outside the noise and crosstalk region, and with negligible photo-electron losses. A small electronic noise, in the range of 5-7 fC, has been measured in laboratory; it has to be compared with typical photo-electron signals of 500 fC.

The DREISAM board hosts eight F1 TDC chips[7] for the read-out of four MAPMTs. The F1-TDC is a high-resolution dead-time free TDC chip, that can provide time measurement with different resolution modes: normal, high and latch mode. For our application a normal resolution mode with a digitisation bin width of 108.7 ps has been chosen. In the selected mode the F1 chip can operate at input data rates of up to 10 MHz per channel and trigger rates of up to 100 kHz. The time resolution of the complete readout-chain, including MAPMT, has been measured in laboratory to be about 290 ps.[8]

4. Performances in the real environment

The new fast photo-detection system has been successfully commissioned at the beginning of the 2006 data taking. In this section we present its performances and preliminary characterization based on the 2006 data.

In Fig. 2, left, the time spectrum obtained during the data taking for a

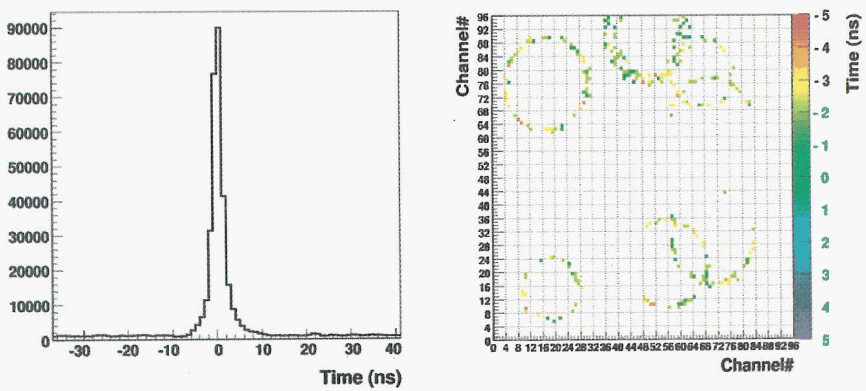

Fig. 2. **Left: Physics signal and background, in** real environment; Right: Hadron Cherenkov rings from the online single event display.

whole quarter of the MAPMT detector system is shown. The visible peak is due to Cherenkov photons generated in the radiator gas by particles scat-

tered in the triggered physics event. The standard deviation of about 1 ns has been confirmed in a Monte Carlo simulation and it is due to the different geometrical path lengths of the photons. The background below the peak is determined by uncorrelated Cherenkov photons mainly generated by beam halo muons. Thanks to the very good time resolution of the whole read-out system, an excellent background suppression can be obtained, applying an offline cut of a few ns around the signal peak. The excellent time resolution can also benefit to the correct assignment of hits to rings, as it can be nicely seen in the online event display shown in Fig. 2, right, where multiple hadron Cherenkov rings detected in a single physics event are shown. It is possible to appreciate a time resolution of the order of 1 ns within a single Cherenkov ring. The average number of detected photons per ring at saturation is about 56 and the angle resolution obtained is about 0.3 mrad.

5. Conclusions

A fast photon-detection system has been designed and successfully implemented, as a part of a global upgrade project of the COMPASS RICH-1, between November 2004 and May 2006, during the SPS shut down period. The system has been operated during 2006 data taking period: its performances entirely fulfill the expectations.

Acknowledgments

We acknowledge help from the CERN/PH groups PH/TA1, TA2 and DT2 and TS/SU and the supported of the BMBF (Germany) and of the European Community-Research Infrastructure Activity under the FP6 program (Hadron Physics, RII3-CT-2004-506078).

References

1. P. Abbon et al., COMPASS Collaboration, (Nucl. Instr. Meth. A 577, 2007, 455)
2. E. Albrecht at al., (Nucl. Instr. Meth. A 553, 2005, 215)
3. M. J. French et al., (Nucl. Instr. Meth. A 466, 2001, 359)
4. HAMAMATSU, *Multianode Photomultiplier Tube assembly H8711, Technical Data.*
5. F. Gonnella and M. Pegoraro, (CERN-LHCC-2001-034, 2001, 204).
6. H. Fisher et al., (Nucl. Instr. Meth. A 461, 2001, 507).
7. TDC-F1 Functional Description, ACAM MesselekTronik, D-76297 Stutensee (www.acam.de).
8. R. Hagemann, Diploma Thesis, University of Freiburg, August 2007.

Implementation of High-Resolution Time-to-Digital Converters on two different FPGA devices

R. Cicalese*, A. Aloisio, P. Branchini, R. Giordano,
V. Izzo, S. Loffredo

Dipartimento Scienze Fisiche, Università di Napoli Federico II and I.N.F.N. Sezione di Napoli - Italy,
Via Cintia 2 - 80126 Naples, Italy
**E-mail: cicalese@na.infn.it*

This paper describes the development of two high precision Time-to-Digital Converter (TDC) in two different SRAM-based FPGA devices. The time conversion is based on a course counter for long range and on a stabilised delay line for the time interpolation within the system clock cycle. In the first method, dedicated carry lines are used to perform fine time measurement, while in the second one a differential tapped delay line is used. In this paper we compare the two architectures and show their performance in terms of stability and resolution.

1. Introduction

Time to Digital Converter (TDC) has been widely used in many applications such as particle detection in high energy physics, laser range finder, frequency counter and on-chip jitter measurement. For many years the main methods used to achieve the hundreds of pico-seconds resolution have been based on time-stretching, Vernier and tapped delay line. These technique were designed both in ASIC and FPGA devices. However, the design process of an ASIC device not only can be expensive, especially if produced in small quantities but also the design process is complex due to the long turn-around time and layout phase. On the other hand, low cost, fast development cycle and commercial availability are several driving motivations for using general purpose Field-Programmable Gate Arrays (FPGAs) to implement the TDC without using any external circuits. One of the first TDC realized on an FPGA-based approach was proposed by Kalisz [1] et al. in 1995. They made use of the difference between a latch delay and a buffer delay of QuickLogics FPGA and achieved a time resolution of 100 ps. In

2003, a TDC was implemented in an ACEX 1 K FPGA from Altera by Wu [2] et al. This TDC used cascade chains of the FPGA and offered a time resolution of 400 ps. In the same year, Szymanowski, et al. implemented a high-resolution TDC with two stage interpolators in a QL12X16B from QuickLogic [3] . The TDC had 200 ps resolution and standard measurement uncertainty below 140 ps. In 2004, a TDC was implemented in a general purpose FPGA device by using dedicated carry lines in the FPGA to perform time interpolation by Qi An [4] et al.

2. Principle of operations

We have designed two types of TDC architectures in different Xilinx FPGAs. Both approaches use the classic Nutt [5] method based on the two stage interpolation. The timing acquisition process consists of three phases. First, the time interval (Δt_1) between the rising edges of the start signal and the succeeding reference clock is measured. Secondly, a coarse counter is activated to measure the time interval (Δt_{12}) between the two rising edges of the reference clock immediately following the START and the STOP signals. Finally, the same procedure for measuring the time interval (Δt_2) between the rising edges of the STOP signal and the succeeding reference clock is also performed. The time interval between the START and STOP signals, (Δt), may be determined as ($\Delta t_1 + \Delta t_{12} - \Delta t_2$). The dynamic range for fine conversion of (Δt_1) and (Δt_2) is limited to only one reference clock cycle. The principle of operations is presented in Fig.1 as a conceptual timing diagram.

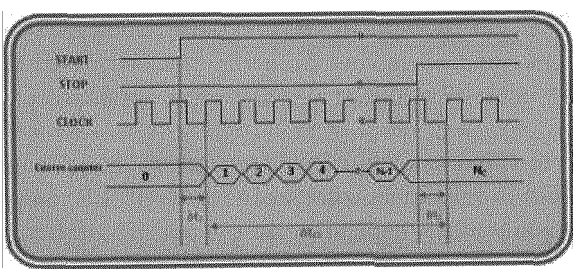

Fig. 1. Measurement of time interval T with the Nutt method.

In the FPGA available today, there are chain structures that the vendors designed for general-purpose applications. A few well-known examples are carry chains, cascade chains, sum-of-products chains, etc. These chain

structures provide short predefined routes between identical logic elements. They are ideal for TDC delay chain implementation. In our works, the fine TDC for the measurement of the short intervals, (Δt_1) and (Δt_2), have been performed in two different methods:

1. The first architecture, shown in Fig.2 (a) uses carry chain delays, like the one present in the newest available Xilinx Virtex 5 FPGA. The START signal after each delay unit is sampled by the pertaining flip-flop on the rising edge of the STOP signal.

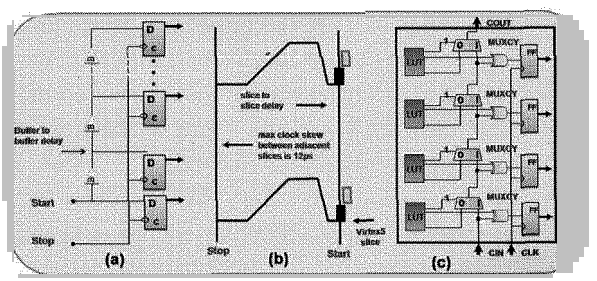

Fig. 2. **Carry chain delay line: (a) logic block diagram; (b) Layout** obtained using a Xilinx Virtex 5 FPGA; (c) simplified block diagram of the Virtex 5 slice.

2. The second architecture, shown in Fig.3 (a),
uses two rows of slightly different cell delays and it makes a differential delay line by using the Xilinx Virtex II' s slices. During the time-to-digital conversion process, the STOP pulse follows the START pulse along the line, and all latches from the first cell up to the cell where the START pulse overtakes the STOP pulse are consecutively set.

To implement the designs in FPGA, one must address one major problem: in the FPGA development software, a logic cell (LE) can be physically placed in nearly any place, depending on the optimization algorithm used. When left up to the program, routing between LEs may also be unpredictable to the user. If the logic cells used for the architectures are placed and routed in this fashion, the propagation delay of each delay step will not be uniform. To avoid this, the designer is forced to place and route the logical resources by hand. The two layouts are presented respectively in Fig.2 (b) and Fig.3 (b). In Fig.2 (c) and Fig.3 (c) simplified block diagrams of the two Virtex 5 and Virtex II are shown.

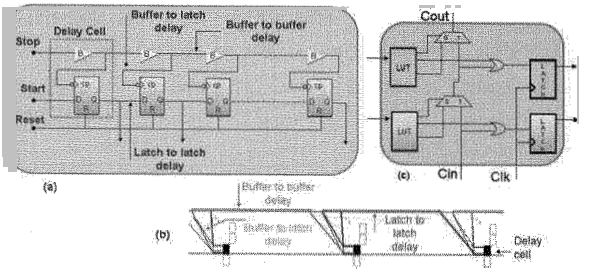

Fig. 3. **Vernier delay line: (a) logic block diagram; (b) layout obtained** using a Xilinx Virtex II FPGA; (c) simplified block diagram of the Virtex II slice.

3. Test bench results

Preliminary tests have been made on our delay lines using the first architecture on a Xilinx Virtex 5 [6] demo board and the second one on the Xilinx Virtex 2 [7] demo board. Each TDC structure has 64 steps. The external clock frequency we used in the tests was 100 MHz. To execute our tests we have used an architecture based on an embedded microprocessor Fig.4.

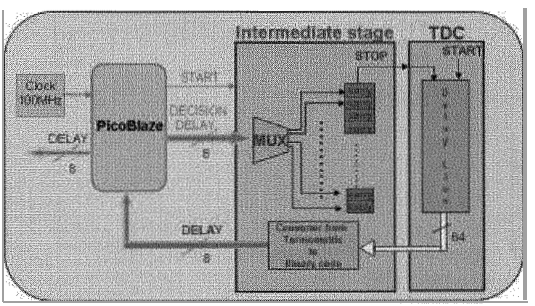

Fig. 4. Communication between PicoBlaze and the TDC delay line.

PicoBlaze is a FPGA based microprocessor which has an 8-bit address and data port to access a wide range of peripherals. PicoBlaze allows the user to input a delay value via a RS232 link. The intermediate stage receives data bus, decodes it and establishes which is the value delay. Each signal is connected to the respective carry. In this way arrival time (STOP) is changed by using carry of various lengths. Carry chain has been used to generate the delays because for each step they can be considered fixed for the particular physical technology, rail voltage and temperature range. So

the time interval between START and STOP has been determined and then it is measured by TDC. Fig.5 shows a test result of the second architecture TDC output as a function of the signal input time.

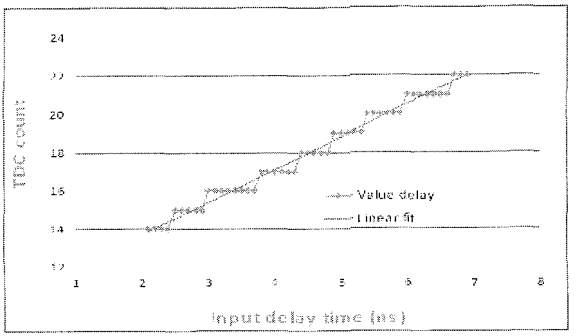

Fig. 5. TDC output as function of the input time delay.

More than 1000 measurements were made for each point and the average of each set of measurements was plotted. A simple linear fit shows that the least significant bit (LSB) bin size of the TDC structure in this device was about 0.5 ns. One would also expect some non-uniformity due to internal layout structure of the device.

References

1. J. Kalisz, R. Szplet, and A. Poniecki, *Field programmable gate array based time-to-digital converter with 200-ps resolution*, IEEE Trans. Instrum. Meas., vol. 46, no. 1, pp. 5155, Feb. 1997.
2. J. Wu, Z. Shi, and I. Y. Wang, *Firmware-only implementation of time-to-digital converter in field programmable gate array,*in Proc. IEEE Conf. Rec. NSS., vol. 1, 2003, pp. 177181.
3. R. Szymanowski and J. Kalisz, *Field programmable gate array time counter with two-stage interpolation*, Rev. Sci. Instrum., vol. 76, 2005. 045 104.
4. Jian Song, Qi An, and Shubin Liu, *A high-resolution Time-to-Digital Converter Implemented in field programmable gate array*, IEEE Trans. Instrum. Meas., vol. 53, no. 1, Feb. 2006.
5. J. Kalisz, *Review of methods for time interval measurements with picosecond resolution*, Metrologis, vol.41, pp.99-145.
6. *Virtex-5 User Guide (2007, Feb.)[Online].* http://direct.xilinx.com/bvdocs/userguides/ug190.pdf
7. *Virtex-II Platform FPGA User Guide (2007, March). [Online].* Available: http://direct.xilinx.com/bvdocs/userguides/ug002.pdf

PERFORMANCE OF THE HIGH MOMENTUM PARTICLE IDENTIFICATION DETECTOR IN ALICE AT LHC

GIACINTO DE CATALDO
INFN Sez. Bari, Via Orabona 4, 70126 Bari I, and CERN CH-1211, Geneva 23 Switzerland

ON BEHALF OF THE ALICE-HMPID COLLABORATION
CERN CH-1211, Geneva, Switzerland

The ALICE High Momentum Particle Identification Detector (HMPID) is a proximity focusing ring imaging Cherenkov detector (RICH), 10 m^2 of active area for the hadron identification at high transverse momenta: $1 < p_t < 3$ GeV/c for charged π and K, $1 < p_t < 5$ GeV/c for p. It has been installed in ALICE since September 2006 in view of the first collisions expected mid-2008. After a short description of the detector and the online data quality monitoring this paper focuses on the HMPID particle identification (PID) capabilities even in the higher expected track multiplicity $dN_{ch}/d\eta$=6000, simulated in central Pb-Pb ALICE events.

1. Introduction

ALICE - A Large Ion Collider Experiment – is designed to study the physics of strongly interacting matter and the quark-gluon plasma (QGP) in nucleus-nucleus collisions at the LHC [1]. The p-p physics will be study as well as reference data for the nucleus-nucleus analysis.

The HMPID, designed with an acceptance of the 5% of the central barrel coverage ($|\eta| < 0.6$ and azimuthal coverage 57.61 deg), can significantly contribute to the ALICE combined PID with its capabilities in the 1 – 5 GeV/c of p_t momentum range.

1.1. *The Ring Imaging Cherenkov detector in ALICE*

In this paragraph only the detector working principles are briefly presented. A detailed detector description can be found in [2].

The HMPID is a RICH based on a 1.5 cm thick C_6F_{14} (perfluorohexane) liquid radiator, multi-wires proportional chambers (MWPC) operated with CH_4 and CsI pad photo-cathodes. Cherenkov photons, emitted when a fast charged

article traverses the radiator, are detected by the photon counter based on a thin layer (300 nm) of CsI deposited onto the MWPC pad cathode.

2. The online data quality monitoring

In order to ensure stable PID performance the HMPID is endowed with both a Detector Control System (DCS) and an Online Data Monitoring system (ODM). The ODM is based on MOOD [3] a framework developed at CERN.

A fraction of the DAQ data stream intercepted are displayed online, before transferred to the mass storage. Reference plots and histograms are filled and used to alert the operator about possible malfunctioning on the front-end and/or readout electronics or on the detector in general.

In specific, among other parameters, the pad map, the cluster multiplicity (set of contiguous pads), related charge distributions and the MWPC gas gain will be monitored.

In addition, a detector status word (SW) which is being coded in the DCS, displayed with the ODM histograms, will account for the detector status respect to the ancillary subsystems (gas, cooling, HV-LV, and C_6F_{14}). By crosschecking the SW and ODM histograms a quick diagnostic about the source of possible malfunctioning, can be done.

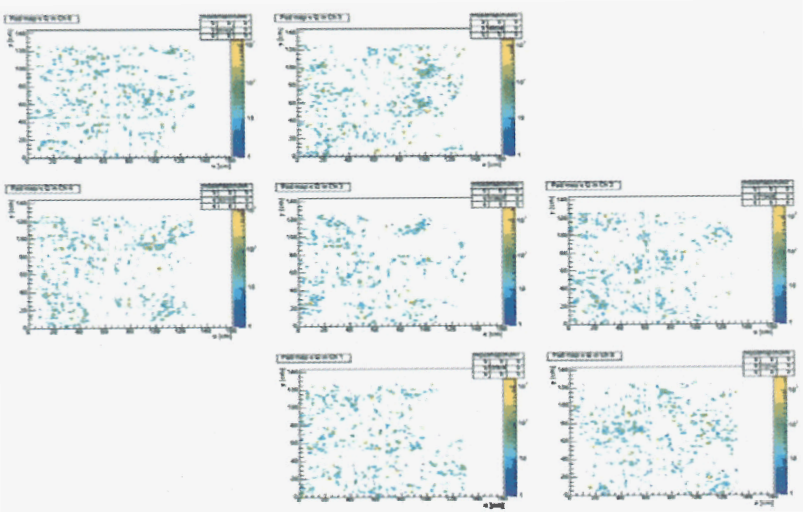

Figure 1. The online monitoring pad map of the seven HMPID modules is shown for a single minimum bias Pb-Pb ALICE event at 5.5TeV c.m.s. in a 0.2 T magnetic field.

In Figure 1, a pad map of a simulated 5.5 TeV/nucleon pair Pb-Pb minimum bias event @ 0.2T magnetic field is shown. It is as it will appear to the operator in the online monitoring environment. For a normally working detector, overlapping a certain number of events, a uniformly populated map will appear.

In the Figure 2, the expected single electron (s.p.e) pulse-height distribution in ADC channels for ten simulated events is shown. By the average pulse-height A_0 of the Furry fitting function, the MWPC gas gain can be calculated [2].

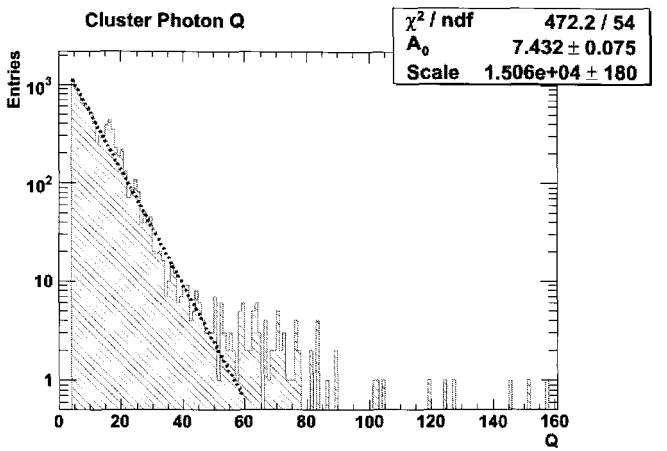

Figure 2. For ten simulated Pb-Pb ALICE events at 5.5TeV c.m.s. in a 0.2 T magnetic field, the expected charge distribution for the s.p.e fitted with a Furry distribution is shown. The average pulse high for the single electron A_0 provides the MWPC gas gain

3. Particle identification

The identification in the HMPID of charged particles of known momenta requires the particle's track to be extrapolated from the central tracking devices (ITS, TPC and TRD, for a total X/X_0 of 38% including the TOF material budget) and associated with the corresponding cluster of the minimum ionizing particle (m.i.p.) in the HMPID cathode plane.

The extraction of the mean Cherenkov angle is based on the Hough Transform Method (HTM) [4]. Starting from the photon cluster coordinates, HTM associates the corresponding Cherenkov angle. Reiterating on the pattern's photons (on the average eighteen photons are expected) finally the HTM provides the average angle $<\theta_c>$.

The probability that a given reconstructed $<\theta_c>$ belongs to the probability density function of the particle type $i = \pi$, K, p is

$$P(<\theta_c>) = \text{Gauss}(<\theta_c>, \theta_{ci}, \sigma_{\theta c,i}),$$

where $\text{Gauss}(<\theta_c>, \theta_{ci}, \sigma_{\theta c,i})$ is the ordinate in $<\theta_c>$ of the normalised Cherenkov angle distribution, centred on the theoretical value θ_{ci}, with $\sigma_{\theta c,i}$ the parameterised standard deviation from the beam test data. The probability that the given particle with $<\theta_c>$ is of the type $i = \pi, k, p$ can be then calculated as

$$P_i = \frac{\text{Gauss}(<\theta_c>, \theta_{ci}, \sigma_{\theta c,i})}{\Sigma_{i=\pi,K,p}\text{Gauss}(<\theta_c>, \theta_{ci}, \sigma_{\theta c,i})}$$

Finally, to identify the particle a significance level on P_i (typically 0.10, 0.05, and 0.01) is applied.

In order to study the PID performance in terms of identification efficiency and contamination [5], even in the higher expected track multiplicity, central Pb–Pb ALICE events at 5.5 TeV per nucleon pair c.m.s energy, with $dN_{ch}/d\eta$ = 6000 (~13% of pad occupancy), have been fully simulated.

The identification efficiency and the contamination for the three species at a fixed momentum, are:

$$Eff_i = N_i^{found}/N_i^{tot};$$

$$Cont_i = (N_j^{found} + N_k^{found})/(N_i^{found} + N_j^{found} + N_k^{found}), \quad i \neq j \neq k \ (i = \pi, K, p);$$

where N_i^{found} is the number of identified particles of i-type, while N_i^{tot} is the total number of simulated events for particle of i-type. In order to calculate $Cont_i$ the dependence of the expected particle production ratios vs. momentum, has been estimated with HIJING.

In Figure 3, the efficiencies and contaminations computed for π in the momentum range 1.2–4 GeV/c, for k in the momentum range 1.2–3 GeV/c and for p in the momentum range 1.2–5 GeV/c, are shown. The lower limit of the momentum range is chosen to have also the proton velocity above the Cherenkov threshold, while the higher limit is chosen to still separate protons from the rest with at least $2\sigma_{\theta c}$.

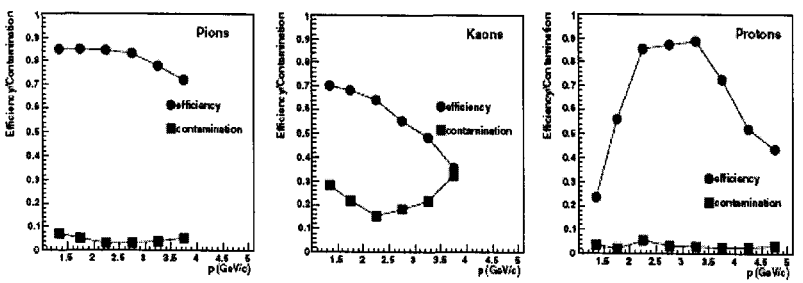

Figure 3. Efficiency and contamination vs. momentum for charged pions, kaons, and protons.

3.1. *The HMPID contribution to the physics*

The identified particle yields in the intermediate momentum region can shed light on the baryon-meson anomaly, antibaryon/baryon ratios as well as information about early times in heavy-ion collisions through correlation measurements [6].

In fact one of the most striking experimental results from RHIC (200 GeV Au-Au collisions) shows for the measured nuclear modification factor a different suppression pattern for mesons and baryons in the p_t range 1-5 GeV/c (baryon-meson anomaly) [6]. Even though, the intermediate momentum region, as defined at RHIC, is expected to shift at LHC, quark coalescence models are able to reproduce the measured p/π ratios, thus HMPID data can offer deeper understanding of microscopical mechanisms of hadronization in the presence of hot quark matter produced in heavy ion collisions [7].

4. CONCLUSION

The HMPID particle identification performance was studied via simulated central Pb-Pb ALICE events ($dN_{ch}/d\eta$ = 6000) at 5.5 TeV per nucleon pair in c.m.s. energy in the momentum ranges $1< p_t< 3$ GeV/c for charged π and K and $1< p_t < 5$ GeV/c for p. The identified particle measurements in the HMPID could significantly contribute to various aspects of the physics goals in ALICE. In particular, identified particle yields in the intermediate momentum region can shed light on baryon-meson anomaly and antibaryon/baryon ratios.

References

1. ALICE Physics Performance Report Vol. 1, CERN/LHCC 2003-049
2. ALICE HMPID Technical Design Report, CERN/LHCC/ 98-19
3. http://ph-dep-aid.web.cern.ch/ph-dep-aid/MOOD/Documentation/MOODv2/tutorial/index.html
4. Di Bari D (ALICE Collaboration) 2003 *Nucl. Instrum. Methods* A **502** 300
5. Cozza D *et al* (ALICE Collaboration) 999 *Nucl. Phys.* A **661** 702
6. ALICE Physics Performance Report Vol 2 Part 1, CERN/LHCC2005-030
7. V.Greco, C.M.Ko, P.Levai, Phys.Rev.Lett.90,202302,2003
   R.J.Fries, B.Muller, C.Nonaka, S.A.Bass, Phys.Rev.Lett.90,202303,2003

HYDROGENATED AMORPHOUS SILICON DEPOSITED ON THE ASIHTEST CIRCUIT FOR RADIATION DETECTION

M. DESPEISSE [1]
[1] *CERN, CH-1211 Geneva, Switzerland*

G. ANELLI [1], P. JARRON [1], D. MORAES [1], A. NARDULLI [2], N. WYRSCH [3]
[2] *Institute for Particle Physics, ETH, CH-8093 Zurich, Switzerland*
[3] *IMT, Rue A.-L. Breguet 2, CH-2000 Neuchatel, Switzerland*

Radiation detectors were developed by depositing 20 μm thick hydrogenated amorphous silicon (a-Si:H) sensors directly on top of the so-called aSiHtest integrated circuit. This circuit was designed in a quarter micron CMOS technology as a global test circuit for this detector technology. The sensor leakage current turned out to be limiting the performance of the whole detector. Its detailed study is presented together with design techniques to reduce it. Direct detections of 10 to 50 keV single electrons were demonstrated on integrated thin strip structures with a pitch down to 10 μm. Results are shown to understand the potential of the technology for ionizing radiation detection.

1. Thin Film on ASIC technology for radiation detection

In addition to state-of-the-art silicon detectors, a number of innovations aimed at improving radiation detection speed, spatial resolution, radiation hardness or costs are being developed to greater maturity [1]. Their development is of primary interest for future high energy physics experiments and for biomedical imaging where alternative solutions to standard silicon detectors will be needed [2]. In this context, we studied the emerging Thin Film on ASIC (TFA) technology, which consists in the deposition of a hydrogenated amorphous silicon (a-Si:H) sensor directly on top of the readout integrated circuit [3]. a-Si:H is widely industrialized in thin films (< 1 μm) and it was shown to potentially offer radiation hard alternatives to silicon devices [4]. The vertical integration of the a-Si:H sensor on the electronic readout enables a level of integration comparable to monolithic pixel detectors while it still presents the advantages of the hybrid pixel approach as the sensing device and electronic readout can be designed, optimized and biased separately. However, sensors thicker than nowadays standard a-Si:H devices have to be deposited and fully depleted to provide adequate signal to noise ratio for particle detection. Sensors

with a thickness above 50 μm can be grown but they would require more than 1.1 kV for full depletion and certainly be very hard to deplete [5]. Sensors with thickness of up to 30 μm were deposited in our studies. They are thick in comparison to standard a-Si:H device but thin compared to standard crystalline silicon detectors (which are above 150 μm). Fewer charges are thus expected to be created by the passage of a particle through a TFA detector than through a silicon detector, resulting in the most important limitation of the TFA technology. The development of this technology requires full depletion of the deposited a-Si:H sensors and the design of very low noise pre-amplifiers (< 100 e⁻ rms) able to read out the small signal induced by a particle.

2. The aSiHtest detector

The TFA detector is built by consecutive depositions of n-doped, intrinsic and p-doped (n-i-p) a-Si:H films on top of the readout circuit (Fig. 1). Depositions were done by Very high Frequency Plasma Enhanced Chemical Vapor Deposition at 200 °C at the Institute of Micro-technology in Neuchatel. The doped layers are deposited very thin (~ 30 nm) because of a high defect density so that the diode and i-layer thicknesses are equal. A transparent conductive oxide (TCO) is deposited on the a-Si:H sensor p-layer, defining the detector's common top electrode.

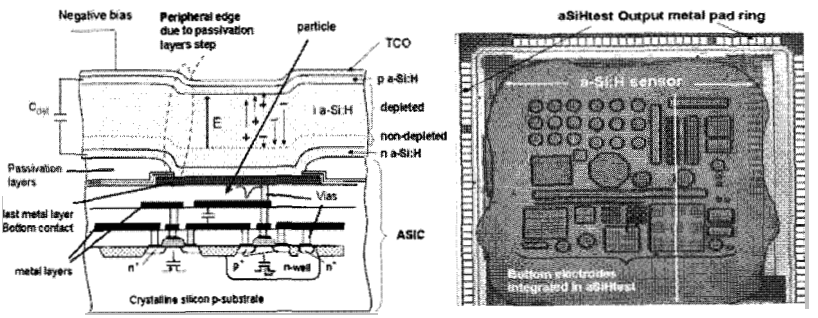

Fig. 1. Left: Schematic cross section of a TFA detector based on the deposition of n-i-p a-Si:H layers and TCO electrode on top of a CMOS circuit with 3 levels of metal. Right: A TFA detector made of a 20 μm thick a-Si:H sensor and an aSiHtest circuit.

Sensors were successfully deposited on the AFP and Macropad circuits, results are presented in [5]-[6]. The aSiHtest circuit was designed in a quarter micron CMOS technology as a global test chip to fully characterize the TFA technology. TFA detectors were built on this circuit with 20 μm thick a-Si:H sensors (Fig. 1). In standard CMOS technologies, integrated circuits are

protected with passivation layers which cover its surface. Openings in these layers are made to allow external access to metallic pads designed in the topmost metal layer, and in the case of TFA detectors to provide back contacts to the a-Si:H diodes. The metal pads and the openings define the detector segmentation. The openings are usually done inside the pads and the 5 μm thick passivation layers induce unevenness on the circuit (Fig. 1). The different metal structures integrated in the aSiHtest are designed with passivation layers opened either on their top (inside the pad) or on top and all around the metal pad, in order to study the impact of the passivation layers step on the detector performance. These different metal structures segment the TFA detector in either strips or pixels. They are either connected to current mirror stages which provide a selectable current gain of 10^2 to 10^5 to study the leakage current of the a-Si:H sensor or to active feedback pre-amplifiers to perform radiation detection. The Integrated pre-amplifiers exhibit either a 5 ns peaking time and an equivalent noise charge (ENC) of 160 e^- rms or a 25 ns peaking time for an ENC of 70 e^- rms (for a 1 pF maximum input capacitance).

3. Leakage current mechanisms

The high reverse voltages needed to deplete the "thick" deposited a-Si:H sensors and the deposition on a non-flat ASIC surface were shown to strongly increase the sensor's leakage current [5]-[6], enhancing mechanisms negligible in standard a-Si:H devices. These high currents prevent the full depletion of the sensors, limiting the active volume of interaction and lowering the induced signal amplitude. The understanding of the mechanisms governing the leakage current in TFA detectors and their reduction are thus of primary interest for the development of the technology. The evolution of the leakage current density of 20 μm thick sensors deposited on aSiHtest circuit were measured on the different integrated structures as a function of the temperature and the results are presented in Fig. 2. A current induced by thermal generation enhanced by electric field E through Poole-Frenkel mechanisms can be expressed as [7]:

$$I = I_0 \exp(-E_A/kT) \quad (1); \qquad E_A = E_G/2 - \gamma\sqrt{E} \quad (2).$$

E_G is the material bandgap, E_A is the activation energy needed to activate ionisable defects, γ is the Poole-Frenkel constant, I_0 the maximum current (for E_A=0), T the temperature and k the Boltzmann constant.

Experimental data presented in Fig. 2 is well fitted by Eq. (1) and (2), showing that the leakage current in the TFA detector can be attributed to Poole-Frenkel reduction of the activation energy, enhancing the thermal generation of charges. The activation energy was extracted for different structures and it was shown to

decrease for increasing applied reverse voltages. Values equal to 0.49 eV and 0.42 eV were measured for 80 V and 160 V biases respectively, while it is expected to be at about 0.9 eV for no applied biases. Experimental results presented in Fig. 2 (right) show that reduction of the TFA detector dark current could then be obtained by opening the passivation layers on top and all around the metal pads, i.e. by planarization of the circuit surface. Standard openings in the passivation layers inside the metal pad lead to a non-planar profile of the a-Si:H sensor on top of the metal pad, inducing high electric field zones at the pixel periphery and thus increasing leakage currents. Significant reduction could also be obtained by a planarization process of the ASIC surface.

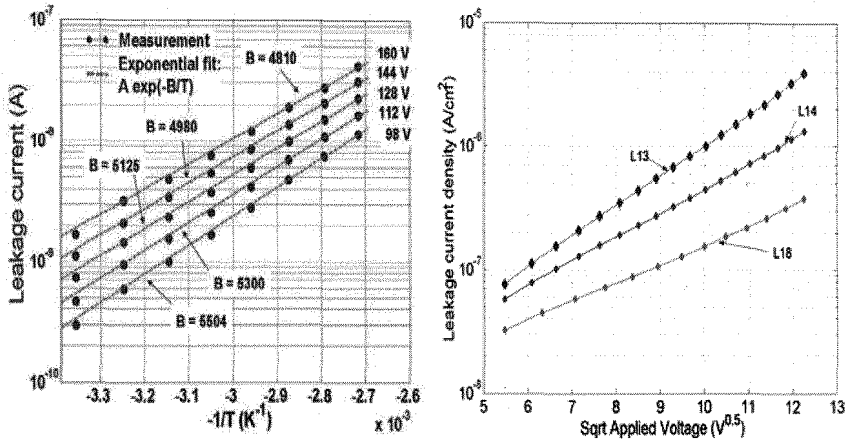

Fig. 2. Leakage current measured on a 20 µm thick a-Si:H sensor on top of an aSiHtest circuit. Right: for pixel pads with openings inside the metal pad (L13), at 6 µm outside the metal pad (L14) and at 40 µm outside the metal pad (L18). Left: Evolution with temperature.

4. Detection of 10 to 50 keV single electrons

Direct detections of 10 to 50 keV electrons were also carried out on the aSiHtest detectors. Results obtained on high resolution strip structures, 6.6 µm wide and separated by 4 µm to 13.4 µm, each connected to one of the implemented low-noise pre-amplifiers, are presented in Fig. 3. Most of electrons inducing a signal on the strip S2 do not induce a significant signal on the neighboring strips. Few signals seen on S2 induce a low signal on S1 (which is at 4 µm), but these events are rare (< 20 %) and can be explained by the tortuous path of few keV electrons in matter. Low charge sharing can therefore be considered on thin strip structures on the developed TFA detectors. This can be explained by the low diffusion coefficient of about 10^{-2} cm^2/s for electrons and 10^{-4} cm^2/s for holes [8] and by the fact that charges drift under very high

electric fields on short distances (thin sensor of 20 μm, maximum drift time of electrons of about 18 ns [5]) so that lateral diffusion of a charge packet will be small. A deviation perpendicular to the electric field of less than 1 μm rms for a charge packet created at the p-i interface in a 20 μm thick sensor can be expected. These results thus show a very interesting potential of the TFA technology for the detection of low energy electrons and for the construction of a high spatial resolution detector.

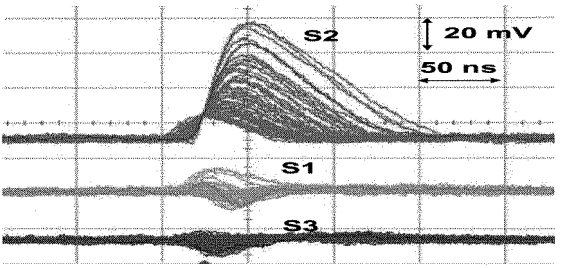

Fig 3. Signals created by 10 to 50 keV electrons on a 20 μm thick a-Si:H sensor deposited on aSiHtest circuit. The circuit is reverse biased with 240 V. Top: readout is done on 3 neighboring strips, S1, S2 and S3, trigger on S2. Bottom: ~ 100 superimposed signals created by electrons from the source.

5. Conclusion

N-i-p a-Si:H sensors with thicknesses up to 20 μm were successfully deposited on top of aSiHtest integrated circuits. Edge effects due to the non-flatness of the circuits were demonstrated to increase the sensor leakage current, limiting the detector performance, but specific design of the ASIC metal pads was shown to allow reducing these currents. Finally, direct detection of ionizing particles was performed on strips structures, demonstrating an interesting potential of the technology for high spatial resolution detection.

References

1. N. Wermes. Nucl. Instr. And Meth. In Phys. Res. A 541 (2005), 150.
2. M. Moll et al., Nucl. Instr. And Meth. In Phys. Res. A 546 (2005), 99.
3. P. Jarron et al., Nucl. Instr. And Meth. In Phys. Res. A518 (2004), 366.
4. J.R. Srour *et al.*, IEEE Trans. On Nucl. Sc., vol. 45, no. 6, (1998), 2624.
5. M. Despeisse *et al.*, Nucl. Instr. Meth. In Phys. Res. A518 (2004), 35.
6. D. Moraes *et al.*, J. Non-Cryst. Solids 338-340, 2004, 729.
7. J. B. Chévrier and B. Equer, J. Appl. Phys. 76 (11), 1994, 7415.
8. Q. Gu, *et al.*, Phys. Rev. Lett., Vol. 76, 1996, 3196.

^{210}Pb BREMSSTRAHLUNG EMISSION SPECTRUM FROM LEAD

SOFIJA FORKAPIĆ,
Department of Physic, Faculty of Sciences, University of Novi Sad, Trg D. Obradovića 4, 21000 Novi Sad, Serbia

IŠTVAN BIKIT, DUŠAN MRĐA, JAROSLAV SLIVKA, MIROSLAV VESKOVIĆ
Department of Physic, Faculty of Sciences, University of Novi Sad, Trg D. Obradovića 4, 21000 Novi Sad, Serbia

The 46.5 keV gamma intensity of ^{210}Pb in the background of germanium spectrometers can be easily reduced by inner lining of lead shield , but the bremsstrahlung from the 1.16 MeV maximal energy beta decay of ^{210}Bi (daughter of ^{210}Pb) will reach the Ge detector. The emission spectrum of this bremsstrahlung is calculated by numerically fitting the beta spectrum and integrating the Koch-Motz formula. The absorption of the bremsstrahlung spectrum in the lead and detection efficiencies for Ge detector are calculated by the effective solid angle algorithm, using correction for photopeak/compton ratio of cross sections in Ge.The calculated bremsstrahlung intensity is in good agreement with the experimental result derived in Max Planck Institute, Heidelberg.

1. Introduction

Although Pb-210 emits only a weak (4.05%) low energy γ-ray at 46.5 keV, its daughter Bi-210, is an almost pure β^- emitter ($E_{\beta max}$=1.16 MeV). The contribution of this bremsstrahlung to the background of lead shielded Ge detectors was experimentally studied by Heusser [1] without an attempt for quantitative explanation. In the present paper we describe a semi empirical method, for the estimation of bremsstrahlung intensity, induced by Pb-210, in the background of the GMX type "ORTEC" HPGe spectrometer .The ^{210}Pb content of the lead shield is measured [2] to be A_s=25±5 Bq/kg. The shield has cylindrical shape with outer diameter of Φ=410 mm, wall thickness of 120 mm and mass of 708 kg.

2. Calculations and results

The number of emitted bremsstrahlung photons in lead shield, per unit of energy and unit of time is obtained by the following formula

$$\frac{dR(E_\gamma)}{dE_\gamma} = A \cdot w(E_{\beta L}, E_{\beta\max})\, c(E_{\beta_L}) \times \int_{E_{\beta L}=E_\gamma}^{E_{\beta\max}} \rho_{Pb} \frac{N_A}{M_{Pb}} \bar{r}_\beta(E_\beta) \frac{d\sigma}{dE_\gamma}(E_\beta, E_\gamma) dE_\beta \quad \left[\frac{1}{s\,MeV}\right] \quad (1),$$

where: A is the total ^{210}Pb activity in the shielding material ($A=A_S \cdot m=25Bq/kg \cdot 708kg=17700Bq$), $w(E_{\beta L}, E_{\beta max})$ is the probability of electron emission in the energy interval ($E_{\beta L}$, $E_{\beta max}$), $E_{\beta L}$ is the lowest β electron energy contributing to the probability of bremstrahlung emission with energy E_γ ($E_{\beta L} = E_\gamma$) and $c(E_{\beta L})$

is the function that takes into account the collision-ionization losses in lead. It is simply the $\left(\frac{dE_{\beta L}}{dx}\right)_{rad} / \left(\frac{dE_{\beta L}}{dx}\right)_{coll}$ ratio dependence [3] on the electron energy.

Using the Bi-210(RaE) experimental β spectrum, often graphically presented in the literature [4], the probability of electron emission $w(E_{\beta L}, E_{\beta max})$ in the energy interval ($E_{\beta L}$, $E_{\beta max}$=1.16) is calculated from:

$$w(E_{\beta L}, E_{\beta \max}) = k \int_{E_{\beta L}}^{E_{\beta \max}} N(E_\beta) dE_\beta$$ where

$N_\beta(E_\beta) = a + b E_\beta + c E_\beta^{3/2} + d \cdot E_\beta^{\ 2} \cdot \ln E_\beta + g e^{-E_\beta}$ represents analytical function of energy distribution of emitted Bi-210 electrons $N(E_\beta)$, i.e. emission probability per unit energy interval . The total electron emission probability per radioactive decay is normalized to 1 : $k \int_0^{E_{\beta \max}} N(E_\beta) dE_\beta = 1 \rightarrow k = 0.107787$.

The probability of bremsstrahlung emission $d\sigma/dE_\gamma$ [cm^2/ MeV] depends of atomic number of medium , initial kinetic energy of electron E_β and energy of emitted photon E_γ [5]: $\frac{d\sigma}{dE_\gamma} = f(Z, E_\beta, E_\gamma)$ .The first factor under the integral $\rho_{Pb} \frac{N_A}{M_{Pb}}$ determines the number of lead atoms per unit of volume (ρ_{Pb} is density, N_A is Avogadro's number, M_{Pb} is atomic weight).

The function $\bar{r}_\beta(E_\beta) = \frac{1}{\rho_{Pb}} 0.412 \times E_\beta^{(1.265 - 0.0594 \ln E_\beta)}$ [cm] describes the mean range of the electrons with energy E_β (in MeV) [6]. From (1) the finite spectral intensity $\frac{\Delta R(E_\gamma)}{\Delta E_\gamma}$ is derived by varying $E_{\beta L}$ in bins of 50 keV. The results are presented in Table 1. The shape of emission spectrum is fitted by following simple function

$$\frac{\Delta R(E_\gamma)}{\Delta E_\gamma} = a + b \cdot E_\gamma + c \cdot E_\gamma^{2.5} + d \cdot E_\gamma^{0.5}$$

(Fig.1, upper curve) :, where E_γ is expressed in dimensionless units relative to 1 MeV, and $\frac{\Delta R(E_\gamma)}{\Delta E_\gamma}$ is than given in (1/(s · MeV)). Parameters have following values: a=514.31138, b=779.0155, c= - 68.607204, d=-1224.3796.

The emission spectrum is significantly modified by self absorption in the thick wall of lead shield. The self absorption effect and the detection efficiencies of HPGe detector were calculated by the "ANGLE" computer code [7], [8]. Having in mind the cylindrical shape of shield, it was assumed that shield represents a photon source with Marinelli geometry in Pb matrix. The total absorption peak efficiency ε_{Pb} was corrected for the contribution of Compton

events to the detector spectrum by multiplying it with the ratio $\frac{\sigma_{Ph}+\sigma_C}{\sigma_{Ph}}$, where σ_{Ph} is photo peak cross section and σ_C Compton scattering cross section in Ge, depending on photon energy [9].

Table 1. The bremsstrahlung emission spectrum

E_γ [MeV]	$\frac{dR(E_\gamma)}{dE_\gamma}\left[\frac{1}{s \cdot MeV}\right]$
0.05	274.1
0.07	245.1
0.1	214.3
0.15	157.6
0.2	118.9
0.25	91.24
0.3	73.28
0.35	56.62
0.40	43.83
0.45	34.62
0.5	26.34
0.55	19.94
0.60	15.41
0.65	10.70
0.70	7.371
0.75	4.904
0.80	3.091
0.85	1.838
0.90	0.9908
0.95	0.4920
1.00	0.2040
1.05	0.0565
1.10	0.00588

The "detected" bremsstrahlung intensities were derived from equation:

$$\frac{\Delta R(E_\gamma)_{DET}}{\Delta E_\gamma} = \frac{\Delta R(E_\gamma)}{\Delta E_\gamma} \cdot \varepsilon_{Pb} \cdot \frac{\sigma_{Ph}+\sigma_C}{\sigma_{ph}} . \qquad (2)$$

The "detected" spectrum, calculated for 22 points (Table 2), is on Fig.1. compared with the emission bremsstrahlung spectrum.

Table.2. expected bremsstrahlung intensities in spectrum of HPGe detector ("detected" bremsstrahlung intensities)

E_γ [MeV]	$\frac{\Delta R(E_\gamma)_{DET}}{\Delta E_\gamma}\left[\frac{1}{s \cdot MeV}\right]$
0.05	0.304
0.1	0.343
0.15	0.343
0.2	0.329
0.25	0.300
0.3	0.288
0.35	0.246
0.40	0.213
0.45	0.177
0.5	0.146
0.55	0.116
0.60	0.0927
0.65	0.0671
0.70	0.0473
0.75	0.0319
0.80	0.0209
0.85	0.0138
0.90	0.00817
0.95	0.00444
1.00	0.00201
1.05	0.000613
1.10	0.000068

The bremsstrahlung contribution to the spectral intensity up to 500 keV is about 20 % for our surface based detector, but it is important to note that relative contribution of Pb-210 bremsstrahlung to the background spectrum becomes greater for underground based detector, where the bremsstrahlung induced by muons is significant reduced.

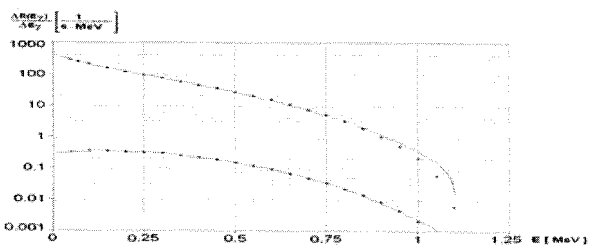

Fig.1. The comparison of emission bremsstrahlung spectrum (upper curve) and the expected bremsstrahlung intensities in background spectrum of HPGe detector(lower curve)

On Fig.2. the calculated bremsstrahlung spectrum for our detector (dots) is compared with one of the measured spectrum of Heusser (Heusser [1]) (upper spectrum) taken in the shallow underground laboratory.

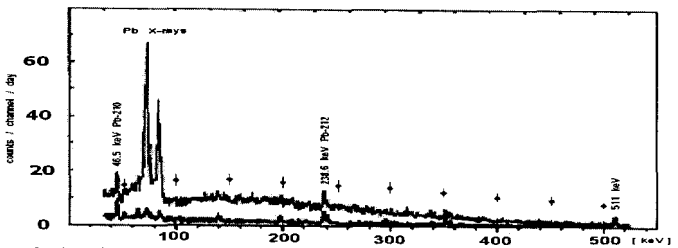

Fig.2. The calculated bremsstrahlung spectrum for our detector (dots with error bars) compared with the measured spectrum of Heusser[1] *(upper spectrum)*

Acknowledgment

The authors acknowledge to the Provincial Secretariat for Science and Technological Development of Autonomous Province of Vojvodina (project No 114-451-00631/2006-1) and Ministry of Science of Republic of Serbia (project : Nuclear spectroscopy and rare processes) at the financial support of this research.

References

[1] G.Heusser, in *Proceedings of the International Summer School on Low-Level Measurements of Radioactivity in the Environment: Techniques and Applications, Huelva, Spain 1993*, edited by M.Garcia-Leon and R.Garcia-Teonorio; World Scientific, Singaspore, 1994 pp.69-112

[2] J. Slivka, D. Mrdja, E. Varga and M.Veskovic, in *Proceedings of the 49th Conference of ETRAN, Budva, Serbia and Montenegro 2005,* edited by M.Milosevic, Z.Jaksic, D.Bozic and V.Potkonjak; Belgrade, 2005 pp. 56-57

[3] K. S. Krane, *Introductory Nuclear Physics* (John Wiley & Sons, New York, 1988), p. 197

[4] H. Semat and J.R.Albright, *Introduction to Atomic and Nuclear Physics* (Chapman and Hall, London, 1973), Fifth Edition, p. 444

[5] H. W. Koch, J. W. Motz, Rev. Mod. Phys. **4**, 920 (1959)

[6] P. Marnier and E. Sheldon, *Physics of Nuclei and Particles* (Academic, New York, 1969)

[7] L. Moens, J. De Donder, Lin Xilei, F. De Corte, A. De Wispelaere, A. Simonits and H. Hoste, Nucl. Instrum. Methods **187** (1981), p.451

[8] S.Jovanovic, A. Dlabac, N.Mihaljevic and P.Vukotic, in *Proceedings of the 19th Yougoslav Symposium for the Radiation Protection, Golubac, Serbia and Montenegro, 1997*, edited by M.Ninkovic, G.Joksic, M.Orlic and R.Kljajic; Belgrade, 1997 p.127

[9] M. J. Berger, J. H. Hubbell, S. M. Selzer, J. Chang, J.S. Coursey, R. Sukumar and D.S.Zucker, XCOM: Photon Cross Sections Database, Version 1.3, NIST Standard Reference Database 8, 2005.

COMMERCIAL WINDOW GLASS TESTED AS POSSIBLE HIGH DOSE DOSIMETER. ELECTRON AND GAMMA IRRADIATION

P.G. FUOCHI†, U. CORDA, M. LAVALLE
ISOF-CNR, Via P. Gobetti 101
Bologna, I-40129, Italy

A. KOVÁCS, M. BARANYAI
Institute of Isotopes, HAS, P.O.Box 77
Budapest, H-1525,Hungary

A. MEJRI, K. FARAH
Laboratoire deRadiotraitment, CNSTN
2020 Sidi-Thabet, Tunisia

The use of commercial window glass as possible high dose routine dosimeter has been investigated. Glass samples have been irradiated with doses in the range of 1–50 kGy using ^{60}Co γ source, 4 MeV and 12 MeV electron accelerators. The samples were given a post irradiation thermal treatment (150 °C for 20 min) in order to improve the post irradiation stability of the measured specific optical absorbance, since a rapid fading of the optical absorbance has been observed at room temperature immediately after irradiation. The optical absorbance measurements of the irradiated samples, kept in the dark and at room temperature, were carried on for several weeks. The samples submitted to heat treatment showed a decrease of about 10–15% of the specific optical absorbance that became much less pronounced after 10 days from the irradiation. The response of the window glass plates is energy and dose rate dependent. This study shows the feasibility of using commercial window glass as a routine dosimeter in a certain dose range after proper calibration in the irradiation plant where they are going to be used.

1. Introduction

The ionizing radiation-induced colour centres in many types of commercial glasses have been found suitable for radiation dosimetry [1, 2]. The use of glass samples as radiation dosimeters presents some advantages that make them attractive for the scope: they are recyclable (a thermal treatment at 300 °C for time >20 min is enough for re-use of the glass sample [3]), chemically inert, fast

†Corresponding author: P.G. Fuochi, E-mail: fuochi@isof.cnr.it; fax: +39-051-6399844.

to measure, with little or no dependence on humidity and their use does not require special preparation. Beside that window glass, a common material that can be found everywhere, has the advantage to be very cheap. If its behaviour under γ and electron irradiation is fully studied and well characterized it can become a suitable material for environmental and radiation processing dosimetry. The main disadvantage presented by all types of glass detectors is the undesirable strong post-irradiation fading even at low temperature [4]. To overcome this problem it is advisable to submit the glass dosimeters to post-irradiation thermal treatment at 150 °C for 20 min and then measure the optical density at adequate time intervals, in this way calibration curves can be obtained for different time intervals after irradiation and subsequent thermal treatment [4].

The aim of this work is to investigate: 1) the dose rate and radiation energy effects on the response of commercial window glass irradiated with 3.4 MeV and 8.4 MeV electrons and ^{60}Co γ rays, and 2) the fading behaviour of the irradiated samples after post-irradiation thermal treatment.

2. Experimental

A commercial glass sheet, which composition is reported in [4], was cut into pieces of approximately 11x30 mm with c.a. 3 mm thickness for irradiation and optical measurements. To avoid grease contamination on glass surface, which may affect the absorbance measurements, the samples were carefully cleaned with ethyl alcohol. A thermal treatment at 300°C for 1h was used to get rid of any spurious optical signal. The optical spectra of non-irradiated samples were measured against air and used as reference to the optical spectra of the corresponding irradiated samples in order to obtain the irradiation induced changes of absorption.

Irradiations of the glass samples were done using electron accelerators and ^{60}Co γ source having the characteristics reported in Table 1. Dosimetry was done using the Fricke and ethanol-chlorobenzene chemical dosimeters. Electronic equilibrium was achieved by enclosing the samples as well as the chemical dosimeters in plastic phantoms with wall thickness of 0.4 g/cm^2. Dose reported here is referred as dose to water. As for the electron irradiation care was taken to keep the temperature of the samples during irradiation ≤50°C.

Spectrophotometers and thickness gauge were used to measure the specific absorbance changes (absorbance/dosimeter thickness = mm^{-1}) produced in the glass.

3. Results and Discussion

Sets of three samples were irradiated at different doses in the range of 1–50 kGy.

Table 1. Characteristics of the facilities used for irradiations

	Nominal beam energy (MeV)	Energy* (MeV)	Beam characteristics and dose rate
Institute of Isotopes Budapest	4	3.4	LINAC 2.6 μs p.l. - 50 p.p.s. 2.17 Gy/pulse
ISOF-CNR Bologna	12	8.4	LINAC 2 μs p.l. - 50 p.p.s. 6.95 Gy/pulse
Tunisian semi-industrial ^{60}Co γ source		1.25	1 kGy/h 6 kGy/h

*In the case of the electron accelerator the energy refers to most probable energy.

Radiation causes displacement of atoms in the glass network, and induces free electron and holes which are then trapped in defects such as vacancies, interstitials atoms, impurities [4, 5]. These new electronic configurations (colour centres), give rise to the coloration of the alkali-silicate glasses with two large optical absorption bands at around 410 and 600 nm (Fig. 1). These bands have been attributed to "non-bridging oxygen hole centre" (NBOHC:≡Si–O•) [5-7] which most probably overlaps with the band of peroxy radical ≡Si–O–O• at 630 nm [6].

Both γ and electron irradiation did not affect the position of the absorbance bands [4], only the heights and the area of the bands changed due to increase of concentration of the colour centres with dose. Because of the rapid fading of the optical absorbance at room temperature after irradiation, the irradiated samples were submitted to post irradiation thermal treatment at 150°C for 20 min to improve their stability before optical measurements that were taken 24 h after irradiation and heat treatment (Fig. 1). Specific absorbances for the dose range 1–50 kGy at 410 nm are shown in Fig. 2 as dose response curves. The overall estimated uncertainty associated to these measurements is 9% at 95% confidence level.

The response of the glass to irradiation looks to be energy dependent more than dose rate dependent. This effect can be explained with the fact that for the same dose the higher the energy of the radiation the greater is the number of colour centres formed. At doses >40 kGy an almost horizontal plateau is reached. According to [8] the non linear dose dependence can be interpreted in terms of two different processes: first activation of pre-existing defects (precursors) forming colour centres which saturate with dose because of their limited concentration in glass, and then bond breaking that creates new defects in the glass network.

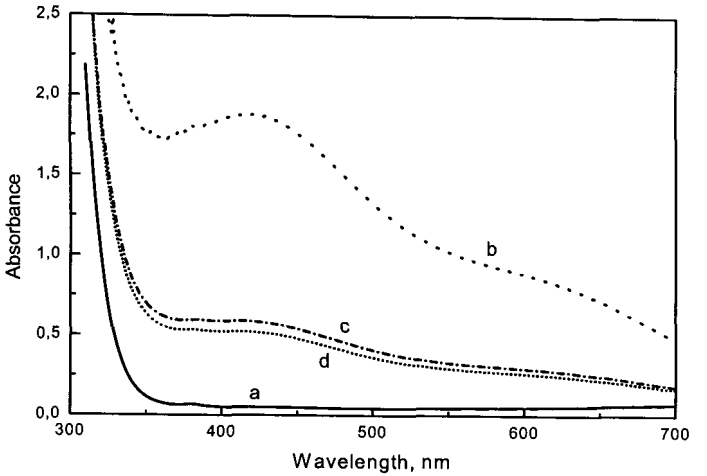

Figure 1. Optical absorption spectra of glass: a) unirradiated; b) after irradiation with 8.4 MeV electrons (25 kGy); c) after heat treatment (150°C for 20min.); d) 24 hours after heat treatment.

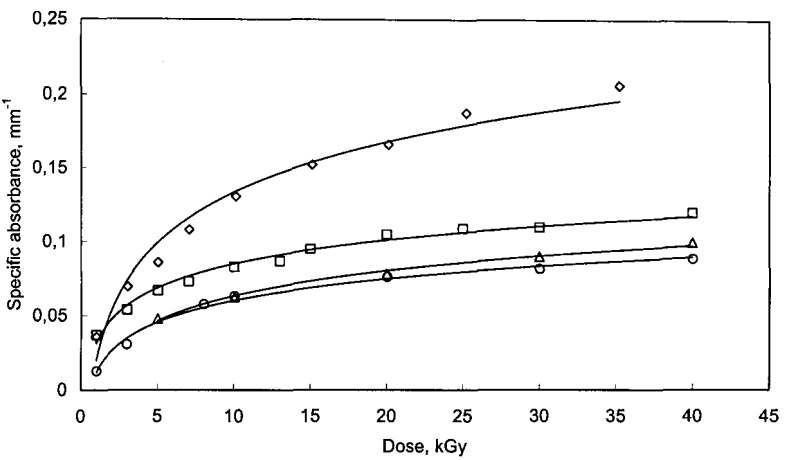

Figure 2. Response curves of irradiated glasses: (◇) 8.4 MeV electrons; (□) 3.4 MeV electrons; (△) γ rays 6 kGy/h; (○) γ rays 1 kGy/h. Optical measurements taken at 410 nm.

The optical fading of the irradiated and heat treated glasses kept in the dark at room temperature was followed for several weeks (Fig. 3). A 10–15% decrease of the optical absorbance was observed after 10 days from the irradiation, followed by a much slower decrease in the remaining days. The decay of absorption can be fitted by the sum of two first order decay kinetic curves and it is the depth of the

traps in this material that determines their decay characteristics [5].

Thus if the irradiated glasses get the reported thermal treatment they might be used as dosimeters in radiation processing. It should be borne in mind that evaluation of the absorbance has to be done at the same time when, after irradiation and heat treatment, the corresponding calibration curves have been obtained.

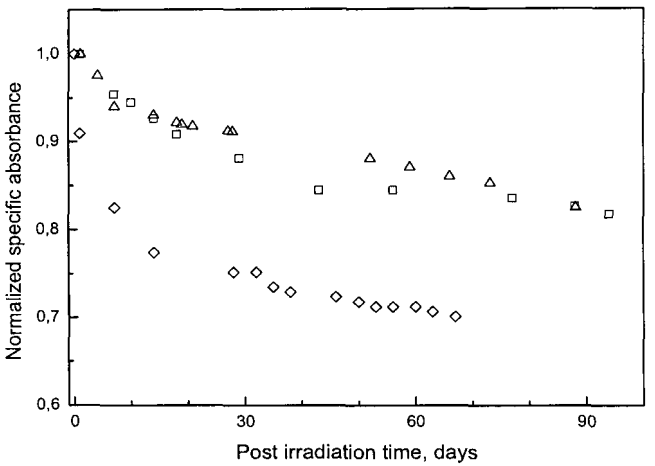

Figure 3. Post-irradiation fading of glass samples: (◇) 8.4 MeV electrons (25 kGy); (□) 3.4 MeV electrons (25 kGy); (△) γ rays (6 kGy/h, 30 kGy). Specific absorbance at 410 nm.

References

1. W.L. McLaughlin, in: E.R.L. Gaughran, A.J. Goudie (Eds.), Sterilization by Ionizing Radiations, Multiscience, Montreal, (1974), p. 219.
2. L.V.E. Caldas, C.N. de Souza, in: Proceedings of the International Symposium on High-dose Dosimetry for Radiation Processing, Vienna, Nov. 5-9, 1990. IAEA, Vienna, pp. 93-99.
3. V.A.C. Quezada, L.V.E. Caldas, *Radiat. Prot. Dosim.* **85**, 473 (1999).
4. K. Farah, A. Kovács, A. Mejri, H. Ben Ouada, *Radiat. Phys Chem.* **76**, 1523 (2007).
5. J. Bartoll, M. Nofz, R. Stösser, *Phys. Chem. Glasses* **41**, 140 (2000).
6. D.L. Griscom, M. Mizuguchi, *J. Non-Cryst. Solids* **239**, 66 (1998).
7. C.D. Marshall, J.A. Speth, S.A. Payne, *J. Non-Cryst. Solids* **212**, 59 (1997).
8. V.A. Mashkov, Wm.R. Austin, Lin Zhang, R.G. Leisure, *Phys. Rev. Lett.* **76**, 2926 (1996).

CERAMIC –MATRIX COMPOSITES FOR EXTREME APPLICATIONS

A.Ortona, D.Gaia, G.Maiola, T. Capelari
L. Mannarino, F.Pin, E.Ghisolfi

FN S.p.A. Nuove Tecnologie e Servizi Avanzati

S.S .35 Bis dei Giovi Km.15 – 15062 Bosco Marengo (Al)

Hi-tech systems whose components operate in working conditions characterised by a chemically aggressive environment and elevated temperatures (above 1000°C) are ever more numerous. If metallic materials are not suitably protected and cooled under these conditions, they operate at the limit of their capacity and therefore the integrity of the component can not be guaranteed. Their cooling may furthermore constitute considerable complications in terms of their design. Ceramic materials are a category of materials that bears such extreme working conditions well. However, these materials are actually scarcely used due to their fragility. This limit is overcome by Ceramic Matrix Composites materials (CMCs). All the technologies introduced in this study are developed at FN S.P.A.

1. CERAMIC MATRIX COMPOSITES

1.1. *CMC and fibre pull-out phenomena*

A CMC is a composite in which both the fibres and the matrix consist of ceramic materials. It is generally identified by the formula of its fibre and the matrix. (Eg. C-SiC = Carbon fibres and a Silicon Carbide matrix). In order to ensure that a CMC "deforms" above its maximum load, the presence of an interface between the fibre and matrix is necessary. Unlike polymeric composite materials, the matrix is often stiffer than the fibre and the interface between them must be the weak point of the CMC. The so-called fibre-pull-out phenomenon, which regulates the fracture of a CMC will appear under these conditions (fig. 1)

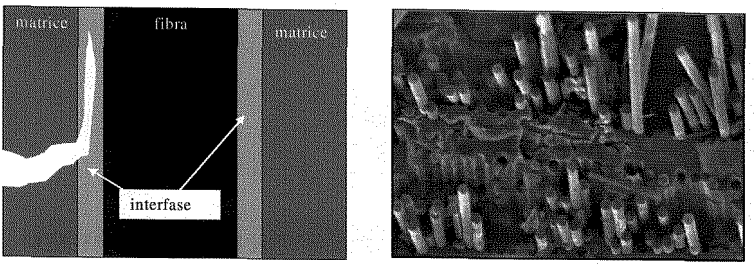

Fig. 1: Fibre pull-out.

Fibre-pull-out occurs when cracks propagate within the material. The propagation is guided by a preferential rupture in a third phase, named interphase, placed between the fibre (first phase) and the matrix (second phase). When cracks are near the fibre, their path is deviated along the aforesaid interphase, which is less resistant along the thickness. The result is that the material starts to break fibre by fibre. Moreover, each time a fibre breaks, in order to free itself from the matrix which sheathes it, energy is dissipated due to the friction [1].
It should be emphasized that the matrix begins to yield well in advance of material's failure, making the composite locally permeable to oxygen through the cracks (fig 2).

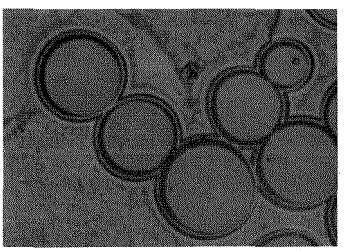

Fig. 2: interphase after oxidation

2. CERAMIC MATRICES AND RELATED MANUFACTURING TECHNIQUES

There are numerous ceramic matrix compositions that may be distinguished according to their constituting material. Among these, the main ones contain Carbon, carbides, oxides and glasses.
In the present study and for the uses described herein, we will only deal with the first two types and related manufacturing methods.

2.1 Chemical Vapour Infiltration (CVI)

The CVI process consists of decomposing a vapour or gaseous precursors by means of heat in a controlled atmosphere. The decomposed products are deposited on the hottest parts inside the reactor and therefore, intentionally on the preformed fibres. Composites produced by means of CVI always present residual porosity because this technique leads to the formation of closed porosity. The produced composites prove to be the best since a matrix with a controlled microstructure is deposited at relatively low temperatures by means of CVI. Isothermal CVI permits the production of both an interphase as well as the matrix.
The process, which is carried out at a low pressure (about tens of mbar), is based on the decomposition by means of heat of the following precursors:
Methane to deposit carbon, according to the following reaction: $CH4(g) \rightarrow C(s) + 2H2(g)$. Methyltrichlorosilane(MTS) to deposit silicon carbide according to the following reaction: $CH3SiCl3(g) \rightarrow SiC(s) + 3HCl(g)$.
In this way, C or SiC fibres progressively increase their diameter until empty spaces are almost filled [2].

2.2 Polymer Infiltration and Pyrolysis (PIP)

The PIP process, outlined in figure 3, consists of the impregnation of fibrous preforms (1) with a liquid polymer and its subsequent thermal curing treatment (2) by means of manufacturing techniques that are similar to those used for traditional polymeric matrix composites. A subsequent thermal pyrolysis treatment (3) converts the polymer into a ceramic. After pyrolysis, CMCs present elevated porosity since a consistent fraction of the polymeric mass (40-70%) is evacuated in form of low molecular weight oligomers and gaseous species. In order to obtain high density matrices it is therefore necessary to repeat the infiltration phases and pyrolysis various times (4).

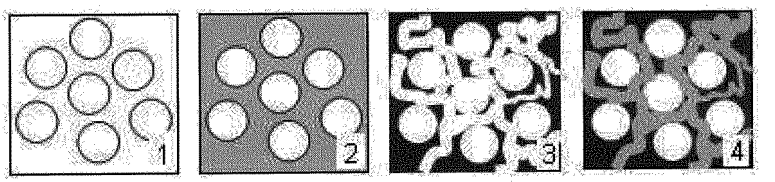

Fig. 3: PIP process

2.3 Silicon Infitration

The silicon infiltration technique is used for the realisation of SiC/SiC composites and consists of the initial preparation of a composite made of fibres and a slurry, containing a pre-ceramic polymer and SiC powder. The composite

is pyrolysed to transform the polymer into carbon. That preform is coated with a given quantity of metal silicon flakes, placed in a vacuum oven and subjected to a thermal treatment at a higher temperature than the melting point of the Silicon (1414°C). Under these conditions, fused silicon penetrates the porosity of the preform through its capillaries, infiltrating all the empty spaces. A certain quantity of silicon reacts with the carbon matrix to form SiC, while the rest remains in a metal form.
The presence of free metal silicon, confines the use at temperatures lower than the melting point of the silicon itself.

2.4 Forced filtration

Forced filtration consists of making a liquid, containing a colloidal suspension of micrometric SiC or C powder, it is than forced through a fibrous preform to fill the macro porosity among fibre bundles. The advantage of this technique is that it is carried out at room temperature, but it must always be followed by further densification, using the procedures described in the preceding paragraphs [3].

2.5 Main characteristics of CMCs

Table 2.1 shows a comparison among different CMC manufacturing techniques.

Properties	unit	CVI SiC-SiC	CVI C-SiC	CVI+FI+PIP SiC-SiC	CVI+PIP C-SiC
Fibre volume	%	42 - 47	42 - 47	40	
Density	g/cm^3	2,3 - 2,5	2,1 - 2,2	2,5	1.6
Porosity	%	10 - 15	10 - 15	8-10	10.15
Tensile strength	MPa	280 - 340	300 - 320	200	240-270
Strain at break	%	0,5 - 0,7	0,6 - 0,9	0,5	0,6-0,7
Young's Modulus	GPa	190 - 210	90 - 100	80-90	65-70
Flexural strength	MPa	450 - 550	450 - 500	350-400	-
Interlaminar shear strength	MPa	45 - 48	45 - 48	50-60	-
Thermal expansion coefficient (@ 21°C)	10^{-6} °K-1	4 = 4 ⊥	3 = 5 ⊥	-	1,5 = (at 1000°C)
Thermal conductivity (@ 21°C)	W/m°K	20 = 10 ⊥	14 = 7 ⊥	8 ⊥	-

table 2.1: CMC_s properties

3. APPLICATIONS

Carbon-Carbon (C-C) composites were the first material that demonstrated to be suitable for structural components resistant up to 1800°C.
Initially, they were designed for the construction of nozzles for rocket engines and they were also used for wing leading edges, fuselages spinners , hypersonic missile engine parts and high performance brakes.
In the 70's Silicon Carbide continuous ceramic fibres, used as reinforcement, were made available on the market. Thanks to that, the first silicon carbide-based CMCs came out and immediately proved to be very promising.
In longterm applications, such as in nuclear fusion reactors, SiC composites have been particularly studied because resistant to elevated temperatures, behave in a pseudo-tough manner and, most of all, behave excellently under neutron irradiation [4].

4. REFERENCES

[1] A. Ortona, S. Sguotti, G. Marino, B. Riccardi: "Compositi a matrice ceramica per applicazioni termostrutturali;
[2] S.Sivaram: "Chemical vapor deposition: thermal and plasma deposition of electronic materials"; ed. VNR ; 1995
[3] C.A.Nannetti, A.Ortona, B.Riccardi: "Manufacturing SiC-Fiber-Reinforced SiC Matrix Composites by Improved CVI/Slurry Infiltration/Polymer Impregnation and Pyrolysis", J.Am.Ceram.Soc., 2004;
[4] S.Ueda, S.Nishio. Y.Seki. R.Kurihara. J.Adachi. S.Yamazaki and DREAM design team: "A fusion power reactor concept using SiC/SiC composites"; J.Nucl.Mat. 258-263 (1998) 1589-1593.

THE CMS MUON SYSTEM AND ITS PERFORMANCE IN THE CMS COSMIC CHALLENGE

K. Hoepfner* on behalf of the CMS Muon Collaboration

CERN & RWTH Aachen University,
52074 Aachen, Otto-Blumenthal-Strasse, Germany
**E-mail: hoepfner@cern.ch*

This article describes the CMS muon system and its performance in a first CMS global run using cosmic ray muons.

Keywords: CMS, Muon system, Cosmic Challenge.

1. The CMS Muon System in the CMS Cosmic Challenge

The CMS muon system[1,2] is integrated in the iron return yoke of the CMS solenoid which provides a 4 Tesla magnetic field for the tracker and calorimeters. The magnetic field strength in the return yoke varies, thus different detection technologies are being used in the muon barrel and forward regions. Drift Tubes chambers (DT) provide precise tracking in the almost field-free barrel region, complemented by Resistive Plate Chambers (RPC) with a fast response. In the forward region, where the field is higher and non-uniform, and the particle flux can reach up to 1 kHz compared to the moderate flux of about 10 Hz in the barrel, Cathode strip chambers (CSC) provide the precision tracking in the forward region, again complemented by fast RPCs.

In summer and fall 2006 the CMS collaboration exercised a huge integration effort along with the first operation of the large solenoid magnet - the Magnet Test and Cosmic Challenge (MTCC). To operate the magnet, the CMS detector had closed for the first time. The magnet slowly ramped up to its nomimal magnetic field and the field was mapped precisely, a necessary ingredient for a proper reconstruction of the kinematics of pp collision events.

For the CMS muon system, the MTCC was an important milestone being the only opportunity before the start of the LHC to operate the

three subsystems (CSC, DT and RPC) together as an entity along with the alignment tools. Apart from integration aspects, it was one of the goals to verify the chamber and electronics performance in the magnetic field. Another aim was to record muon tracks traversing all subsystems to provide real data to exercise the muon reconstruction and to study the detector performance of the complete system.

For all three muon subsystems, detector installation and commissioning is ongoing and a subset of these detectors sufficient to achieve the goals has been used for the MTCC, including final cabling and final electronics. The numbers of chambers read out was mainly limited by the availability of low voltage power supplies.

In the barrel region two out of the five barrel wheels contributed with a total of three instrumented sectors, sectors 10 and 11 in the outermost wheel YB+2 along with sector S10 in the neighbouring wheel YB+1 (see Fig. 1). In total 14 DT and 21 RPC chambers were operated, corresponding to a fraction of 5% of the barrel's 60 sectors.

In order to trigger on cosmic ray muons, the algorithms which are designed to trigger on high momentum muons from the interaction point had to be adapted. The chamber output was transmitted to three trigger Sector Collectors (one per sector), where chambers within a sector are synchronized and subsequently fed to three DT Track Finders (DTTF) operating a special track finding algorithm for the MTCC situation, just taking a simple coincidence of any two muon chambers from the three sectors.

Local RPC readout and RPC barrel triggers were both available in phase 1 and 2. In MTCC phase 2 barrel RPC also participated in global readout.

Already before the MTCC all CSC chambers on the positive Endcap were installed and most off-chamber electronics was commissioned. For the MTCC the scope has been limited to a single trigger sector, TS5, on stations ME+1, ME+2 and ME+3 involving 36 chambers. This MTCC Trigger Sector forms a 60° slice which overlaps with sectors 10 and 11 of the Barrel Muon Detectors (see Fig. 1). Although the Endcap RPCs did not actively participate in the global system readout an attempt was made during the final days of Phase 2 to include the dedicated readout path through the CSC Trigger electronics.

The trigger electronics in the counting house was based on the CSC TrackFinder crate. A single Sector Processor (SP) module receives the trigger primitive data from the four peripheral crates. The SP is highly configurable and was most of the time operated in a local mode allowing various trigger selections ranging from single-chamber, coincidences, to actual

track-based. During the MTCC triggers were limited to single-chamber or coincidences between stations. The locally generated CSC cosmics trigger was distributed to the Local Trigger Control (LTC) and the Central Trigger Control (CTC) were it was ligned up with other trigger sources (DT and RPC) and used for the joint MTCC runs.

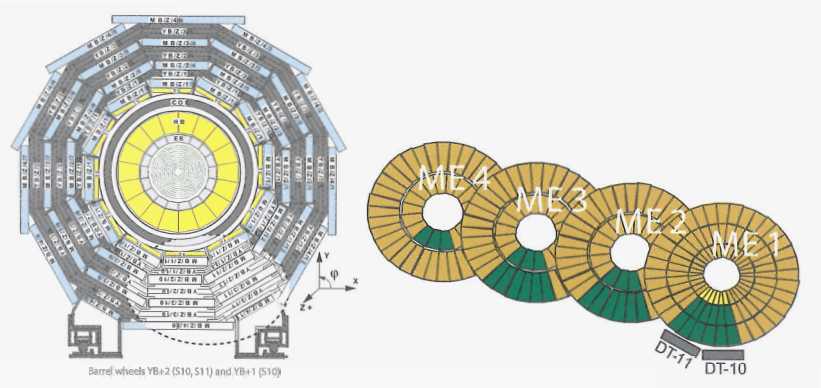

Fig. 1. The MTCC exploits in the barrel region three sectors in the wheels YB+1 (sector 10) and YB+2 (sectors 10, 11) instrumented with DTs and RPCs. From the four end-cap stations a 60 degree slice instrumented with CSCs is read-out in three stations.

2. Muon Detector Performance in the MTCC

Some highlights from the analysis of muon data recorded during the MTCC are outlined in the following paragraphs. More details can be found in.[3] RPC results are in a separated paper of this conference.

Using MTCC data, the CSC chamber performance was examined in several key aspects: the chamber gain (both gas gain and electronics gain), the pedestals stability and dispersion, the electronics noise as well as the shape and timing of signal pulses.

Given large samples of good CSC segments, it was also possible to check the reconstruction algorithms and compare alternatives and refinements, as well as to establish typical performance characteristics such as the efficiency and resolution. The segment reconstruction performed well after the tolerances to assign a hit to a segment were increased. The extrapolation to the following station showed a precision consistent with multiple scattering of relatively low-momentum cosmic-ray muons. The efficiency to detect a muon local trigger segment in a chamber was determined to

be $99.6 \pm 0.1\%$ (stat).

This study also verified known behaviors of the residuals, such as their tendency to increase with the strip width (since the coordinate measurement obviously depends on the strip width) and to be larger in layers 1 & 6 than in layers 3 & 4, which reflects the uncertainty in the linear fit, which contributes to the widths of the distributions.

For DT chambers, the influence of the magnetic field on the drift behaviour was a key aspect to be studied during the MTCC. For the determination of the muon position from the measured drift time, it is necessary to know and assume a constant drift velocity. However, in the innermost barrel chambers of YB±2 the - normally linear - drift behaviour is influenced by the existance of a magnetic fringe field which increases the drift path, reflecting in an apparent change of drift velocity, which is a critical parameter not only for the muon reconstruction but also for the functionality of the DT trigger. Earlier simulations calculated the expected magnetic field in the chamber volume and revealed a significant radial component in particular for the innermost MB1 barrel stations.[1]

Three different methods have been exploited to determine the drift velocity from those data, showing compatible results.[4] As an example, Figure 2 shows the drift velocity as a funtion of the muon track position along the CMS z-axis. For the chambers at B=4T in wheel YB+1 no dependence is seen, while chambers in wheel YB+2 do show a decrease in the drift velocity, clearly seen for the MB1 chambers, to a smaller extent, also for MB2. The overall variation in the MB1 chambers is of the order of ~3%, ranging from 54.8 μm/ns to 52.9 μm/ns.

3. Comparison between Data and Monte Carlo Simulation

The lessons learned from the MTCC are also of great interest for future cosmic muons which will be an important instrument of monitoring and aligning the CMS detector during LHC operation. Right before and during the start-up of the LHC operation, cosmic ray muons, although with a low flux in the underground cavern, will constitute a reliable particle source for detector commissioning, synchronization, and alignment. A cosmic muon generator CMSCGEN has been developed and included in CMSSW[5] and compared to the MTCC data. In the simulation the cosmics arrival time is distributed uniformly between -12.5 nanosecond and +12.5 nanosecond. The trigger conditions are modelled as a two chamber coincidence. After application of the usual calibration steps, the drift time spectra and local reconstruction agrees well between data and simulation. For data taken

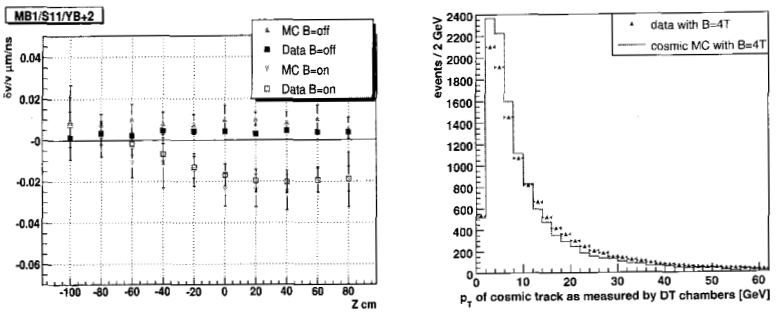

Fig. 2. Left: Variation along z of the drift velocity w.r.t. nominal value as measured from the track fitting. Right: The p_T spectrum measured from MTCC data in comparison to simulated cosmic ray muons.

with magnetic field the transverse momentum was determined from the curvature of the track and compared to simulated cosmic ray muons as seen on the right of Figure 2.

The distributions for data and simulation agree reasonably well with both having their maximum around 2-4 GeV. The momentum resolution for non-bunched cosmic ray muons when using the cosmic muon reconstruction has been measured to $\Delta p_T/p_T = 24\%$. The corresponding value for muons from pp interactions is expected to be 2.5 times better, around 10% for stand-alone muons in the muon system only.[1] It reflects the importance of synchronization. Clearly, cosmic challenge data would not yield the design resolution of the detectors.

References

1. CMS Muon Collaboration, *CMS, the Compact Muon Solenoid. Muon Technical Design Report*, (15 December 1997). CERN-LHCC-97-32, CMS TDR 3.
2. S. Dasu *et al.*, *CMS. The TriDAS Project. Technical Design Report, Vol. 1: The Trigger Systems.* CERN-LHCC-2000-038.
3. CMS Muon Collaboration, *The CMS Muon System in the Magnet Test and Cosmic Challenge*, (2007). CMS Note in preparation.
4. M. Fouz *et al.*, *Measurement of Drift Velocity in the CMS Barrel Muon Chambers at the CMS Magnet Test Cosmic Challenge*, (2007). CMS Note submitted.
5. P. Biallass, T. Hebbeker and K. Hoepfner, *Simulation of Cosmic Muons and Comparison with Data from the Cosmic Challenge using Drift Tube Chambers*, (2007). CMS Note submitted.

Quantum Efficiency of Hybrid Photon Detectors for the LHCb RICH

R. W. Lambert*†

Department of Physics and Astronomy, University of Edinburgh, Edinburgh, EH9 3JZ, United Kingdom
**E-mail: R.W.Lambert@ed.ac.uk*

The production of Hybrid Photon Detectors to be used as the single-photon sensors for the RICH detectors of the LHCb experiment has recently finished. We present the quantum efficiency measurements of the entire sample of 550 tubes. The manufacturer has succeeded in consistently improving the quantum efficiency of the employed S20-type multi-alkali photocathode above our expectations, by a relative 27 % integrated over the energy spectrum. We also report measurements of the vacuum quality using the photocurrent of the device as a monitor for possible vacuum degradation.

Keywords: Hybrid photon detector, LHCb, RICH, quantum efficiency

1. Introduction

To identify charged particles within the LHCb experiment, two Ring Imaging Cherenkov (RICH) detectors are employed.[1] Cherenkov photons from charged relativistic particles passing through the C_4F_{10} gas and Aerogel radiators in RICH 1 (upstream) and/or the CF_4 gas radiator in RICH 2 (downstream) are ring-imaged onto one of four photon detector planes covering a total area of 3.3 m^2. We require single-photon sensitivity over wavelengths of 200 – 600 nm with a spatial granularity of 2.5 mm by 2.5 mm.

The chosen photodetector technology is that of Hybrid Photon Detectors[2] (HPDs), see Fig. 1. An HPD is a pixelised vacuum photon detector with an encapsulated silicon sensor and bump-bonded[3] binary readout electronics.[4] An S20-type multi-alkali photocathode, deposited on the inside surface of a quartz entrance window, is biased to -20 kV with respect to the silicon anode. Electrostatic optics cross-focus the emitted electrons onto the encapsulated silicon sensor.

†on behalf of the LHCb RICH collaboration

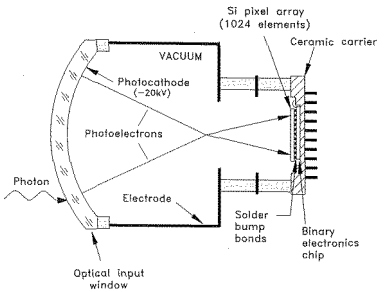

Fig. 1. A schematic of an HPD with electron optics highlighted. A total of 8192 channels are read out at 40 MHz via the integrated sensor/readout electronics.

The HPD photocathode quantum efficiency (QE), η_q is important for a high photon detection efficiency and therefore a high photon yield in the LHCb RICHes. The QE of a photocathode is here defined as the probability of any incident photon being absorbed to release a photoelectron and is measured through the ratio of the number of photoelectrons released to the number of incident photons.

The HPDs are manufactured in several stages in close collaboration with industry.[2] The final stage of encapsulation of the HPD, photocathode deposition, vacuum sealing and potting was performed by Photonis-DEP[a]. In this paper we will present the QE measurement techniques and results for the full sample of 550 HPDs.

2. Photonis-DEP measurements

The manufacturer, DEP, measures the QE of every HPD during production. In a similar technique to that reported in Sec. 3, DEP measures over wavelengths of 200 – 900 nm with 10 nm band-pass filters. They use white light sources without using any infra-red (IR) blocking filters to illuminate the centre of the photocathode up to 25 mm in diameter, and then compare to a calibrated reference measurement. The QE is measured with the HPD photocathode at −900 V. A separate measurement setup is employed for wavelengths up to 400 nm than for wavelengths beyond 400 nm.

DEP has demonstrated an ability to consistently improve the HPD QE during the production process (Fig. 2). The QE has been increased in the blue and UV, while the QE in the red, and the dip[5] in QE at 300 – 400 nm, has been reduced. Results are summarized in Table 1.

3. LHCb measurements

Independent tests to verify the QE results quoted by DEP have been performed by LHCb on a subsample of 60 HPDs or ∼10% of the production.

[a]Photonis Netherlands B.V., Roden. Formerly Delft Electronic Products (DEP).

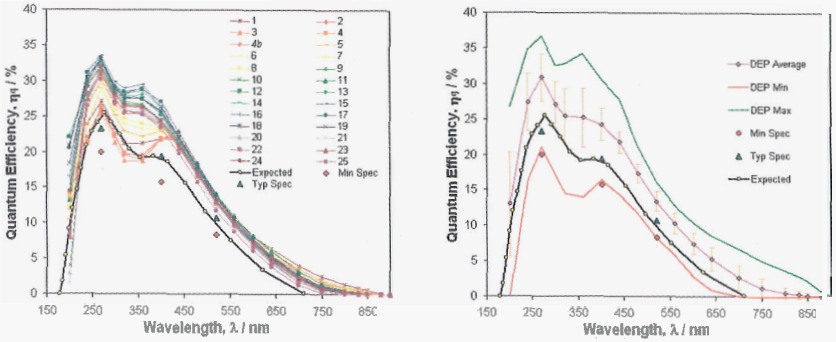

Fig. 2. The QE of HPD production batches. Left, average QE per batch, batch 1 to 25 in chronological order. Right, summary of entire sample. Vertical bars indicate the standard deviation of the DEP QE measurements, no error is included. Red and green solid curves are the extrema. Expectations result from initial measurements on pre-production HPDs.

Table 1. QE for production HPDs.

Detail	Typ. Specification	Mean	R.M.S. width	Unit	Increase
270 nm	23.3	30.8	3.4	%	32 %
400 nm	19.3	24.2	2.4	%	25 %
520 nm	10.7	13.4	1.3	%	25 %
Σ QE δE	0.762†	0.967	0.113	eV	27 %
Σ QE(Aerogel) δE ‡	0.076†	0.108	0.011	eV	41 %

Note: Errors are not included. †Expectations from pre-series and prototype HPDs. ‡Weighted for Aerogel performance.

These measurements took place at one of two purpose-built Photon Detector Test Facilities (PDTFs). A self-calibrating test method was employed between wavelengths of 270 – 800 nm, shown in Fig. 3. The repeatability is demonstrated in Fig. 4 (left). The results of all tests show an excellent agreement between DEP and PDTF measurements, Fig. 4 (right).

We have used the photocurrent-voltage (LIV) curve to identify HPDs which are adversely affected by lower vacuum quality, and to apply a correction to the QE measurement by DEP. Mechanisms for the introduction of residual gas involve diffusion (mainly of helium) through the quartz window, diffusion of gasses through imperfections in the tube body or the vacuum seal, and outgassing of the HPD internally. Any vacuum degradation is evident in the increase of ion-feedback within the HPD. As photoelectrons ejected from the photocathode travel through the vacuum of the tube they

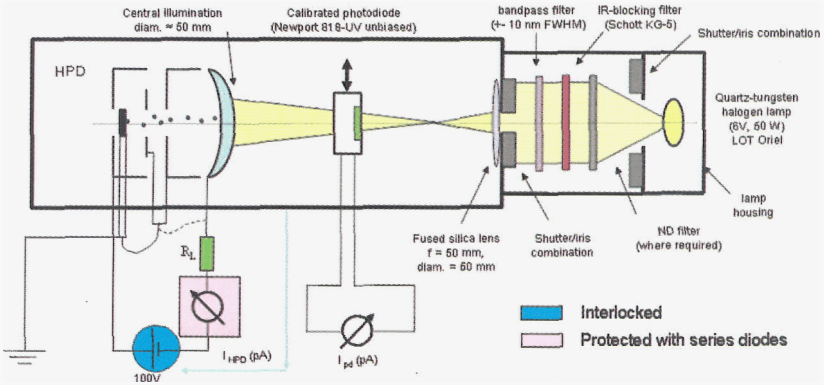

Fig. 3. QE design schematic. I_{HPD} and I_{PD} are the currents determined using the picoampere meter for the HPD under test and the reference PD respectively.

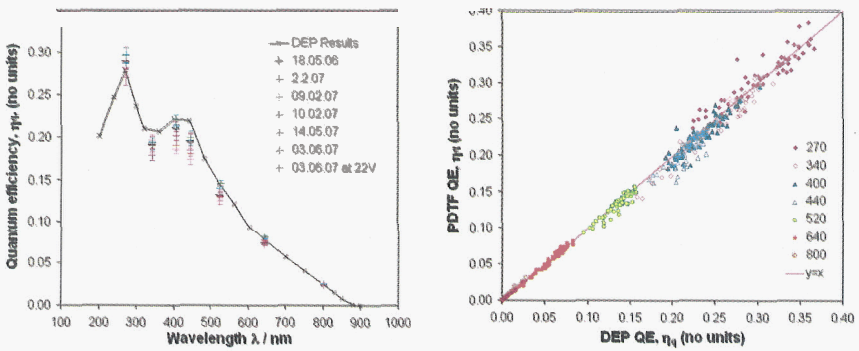

Fig. 4. Left, QE as a function of wavelength for a single HPD (H527009) at PDTF. Measurements were repeated over a year. Right, QE measurements from the PDTF for 60 HPDs in comparison DEP results. The typical 2 % errors are omitted for clarity.

may ionise residual gas molecules. The positive ions produced are accelerated towards the photocathode. When the ions impact they deposit their energy and result in multiple electron emission. This produces a small gain within the HPD, which is probed during the photocurrent measurement.

Examining the gain effects as a function of the photocathode potential we find the primary residual gas in HPDs with low vacuum quality is consistent with helium. For example, we find a plateau region between 20 V and 25 V; consistent with the first ionisation energy of helium, 24.6 eV.[6]

As the gain is voltage dependent, there is a systematic difference between PDTF and DEP measurements for HPDs exhibiting lower vacuum

quality. We obtain a correction factor to recover the true QE for the few affected HPDs from these LIV curves (as employed in Table 1 and Fig. 2).

4. Discussion

To a first approximation the emission of Cherenkov light is flat in the energy spectrum. An integration over energy of the QE will hence allow us to estimate the number of photons detected by the LHCb RICH system. We calculate the discrete sum which is given in Table 1. A 27 % increase is evident over our expectations from pre-series and prototype HPDs.

Next we note that the performance of the RICH for the three radiator materials will differ. Namely that for the Aerogel radiator in RICH 1 the Cherenkov emission is heavily weighted to the long-wavelength end of the spectrum. Factoring this in we obtain a second number for the performance of the HPDs for the Aerogel radiator given in Table 1. A 41 % increase is evident over our expectations.

5. Conclusions

The 550 HPDs required for the LHCb RICH experiment have now been produced. The QE has been measured both by the manufacturer and by LHCb. We observe an impressive improvement in the QE over the production time. Integrated across the energy spectrum the QE is substantially above our expectations, by a relative fraction of 27 %. This will directly improve the performance of the LHCb RICH detectors.

6. Acknowledgements

The LHCb RICH collaboration extend their thanks to their industrial partners, particularly the HPD manufacturer Photonis-DEP, who have produced the excellent devices we are pleased to present herein.

References

1. S. Amato *et al.*, the LHCb collaboration, *LHCb RICH, Technical Design Report 3*, CERN-LHCC-2000-037 LHCb, 2000.
2. T. Gys, Nucl. Instr. and Meth. A **567** (2006) 1, pp. 176-179.
3. M. Campbell *et al.*, IEEE Trans. Nucl. Sc. **53** (2006) 4, pp. 2296-2302.
4. K. Wyllie *et al.*, Nucl. Instr. and Meth. A **530** (2004) 1-2 pp. 82-86.
5. W. E. Spicer and A. Herrera-Gomez, SLAC-PUB-6306, SLAC/SSRL-0042 (1993) pp. 3295-3310.
6. R. G. Montague *et al.*, J. Phys. B: At. Mol. Phys. **17** (1984) pp. 3295-3310.

TIMING PERFORMANCE OF A VACUUM PHOTOTRIODE

DAWN E. LESLIE, IGNACIO YASELLI AND PETER R. HOBSON*
School of Engineering and Design, Brunel University, Uxbridge UB8 3PH, UK

The timing performance of a vacuum phototriode (VPT) has recently been simulated using SIMION 3D software [1] to develop an electron-optic model [2]. In this work, more precise treatment of the approximation is detailed and comparison is made with corresponding experimental data. The origin of the signals features is investigated and interpreted, affording a deeper understanding into the operation and timing potential of these devices.

1. Introduction

The electromagnetic calorimeter of the Compact Muon Solenoid detector (CMS) [3] at the Large Hadron Collider, CERN, uses large monocrystals of the scintillator lead tungstate coupled to sensitive photodetectors, which in the endcap are vacuum phototriodes (VPT) [4] manufactured in Russia by Research Institute Electron (RIE) [5].

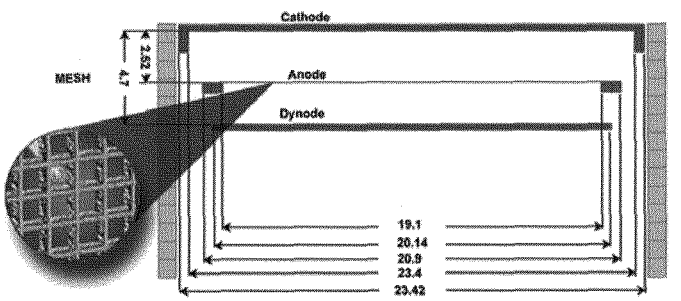

Figure 1. Illustration of VPT components (after Hobson and Yaselli [2]). The mesh anode has 50% transparency and a pitch of 10 micrometres.

The VPT characterised in this work (see Figure 1) was supplied by RIE and is a single gain-stage photomultiplier with a diameter of 26mm. In our experimental arrangement, the centre of the photocathode is illuminated by a 60ps pulse from a PicoQuant SEPIA 800 diode laser (λ = 435 nm). The

* Corresponding author: Tel. +44 1895 266799; Fax. +44 1895 272391; email. peter.hobson@brunel.ac.uk

relatively simple planar geometry and small inter-electrode spacing suggests that the VPT should be very fast, with good timing resolution.

2. Initial Computer Simulation: *SIMION 3D*

The amplitude of the induced current in the anode load resistor is proportional to the intensity of the light and the gain of the VPT, controlled by the bias of the terminals: the photocathode, anode and dynode. SIMION 3D [1] has been used in conjunction with a second program written by us to simulate the behaviour of the incident photoelectrons and the resulting secondary particles in the following manner: photoelectrons from the cathode are accelerated towards the anode mesh (50% transmission) by a high electric field. Those primary electrons which are transmitted are decelerated before being incident on the solid dynode. The dynode is manufactured from a material with a high secondary electron emission coefficient. We model the secondary electron emission from this electrode with a Poisson distribution having a mean value of 20 for an incident electron energy of 1keV. These secondary electrons are accelerated back towards the anode, where a fraction (75%) is collected. The remainder travel back to the dynode and are absorbed upon impact. In the event that these electrons have enough energy to produce tertiary electrons, the simulation is continued.

Using the SIMION 3D simulation, Hobson and Yaselli [2] demonstrated the reproducibility of some of the major features of the VPT response, namely the absolute gain in zero magnetic field and relative time shift. By applying Ramo's Theorem [6] the measured signal may be approximated by calculating the current, I, induced due to an electron moving to an electrode, i.e.:

$$I = q\mathbf{v}\cdot\mathbf{F_k}\,, \tag{1}$$

where $\mathbf{v}$ is the instantaneous velocity of the charge, q, and $\mathbf{F_k}$ is the field that would exist due to q at a distance, d from the induced electrode. The solid curve in Figure 2 shows an example of the output of this model i.e. the induced current on the anode, for an anode potential (V_A) of 1000V, the cathode potential (V_K) at ground and the dynode (V_D) at 800V, whilst the dashed line gives the signal following compensation for attenuation and multiplication factors which arise due to various components of the VPT. It may be seen that the zero-crossing time of the first bi-polar signal is in good agreement with the previously simulated arrival times of electrons at the anode (250ps) [2]. At later times, the signal generated by the secondary electrons emitted from the dynode due to: their direct absorption by the anode; their traversing the anode before being returned by the cathode; and their traversing the anode, returning through the mesh before being detected at the dynode. In order to best simulate the behaviour of the VPT in the experiment, the number of primary electrons has

been calculated to be 2.6×10^6. The resulting signal exhibits a similar shape, although of an increased magnitude.

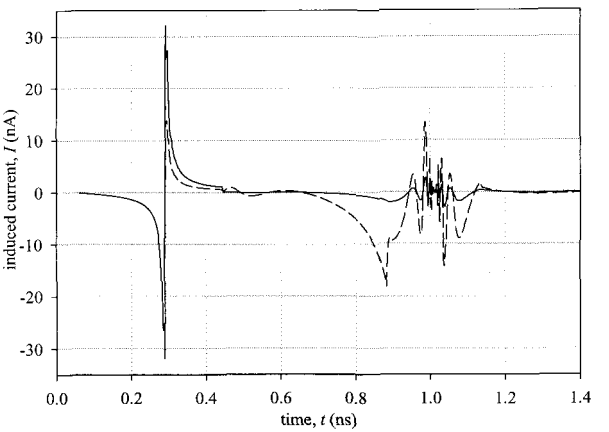

Figure 2: Simulation of current induced at anode by a single incident photoelectron: V_K =0V, V_A=1000V, V_D=800V.

3. Experimental Data

Due to experimental constraints, which require the anode of the VPT to be DC coupled to the 50Ω input of the digital oscilloscope (LeCroy WaveMaster 8300A, 3GHz, 10 Gsamples/second), the potentials used in the above simulation equate to experimental values of V_{KX}=-1000V, V_{AX}=0V and V_{DX}=-200V.

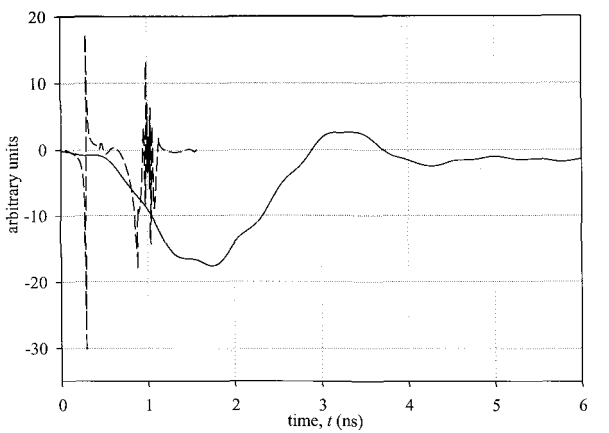

Figure 3. Comparison of simulation (---) and experimental data (— (average of 2000 sequential traces)): the time scale of the experimental data has been shifted by 2.84ns and the magnitude of the first negative peak, scaled to that seen in the simulation.

By shifting the time-zero of the experimental data by 2.84ns, and scaling the magnitude of the negative peak, these data may be compared with the initial simulation on the same axes (see Figure 3).

The results indicate that the initial signal, seen from the SIMION simulation, is reproduced, albeit with an apparent integration due to the finite bandwidth of the experimental setup, which is dominated by the effects of the stray impedances of the VPT. In order to approximate the behaviour of the experimental apparatus upon the signal, the SIMION output has been further processed using SPICE, as discussed below.

4. Further Simulation: *SPICE*

Our simulated current data, shown in Figure 3, has been used as input to SPICE (LTSpice v.2.21) [7], such that the affect of the experimental apparatus upon the signal may be determined. A piece-wise linear approximation was made to the induced current simulated by SIMION, which was then applied to the circuit shown in Figure 4 (inset) to reflect the experimental set-up.

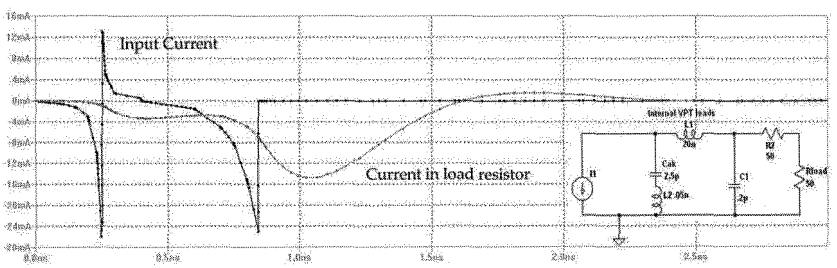

Figure 4. Comparison of input and output current in the 50Ω load resistor current from LT-Spice. The time origin of the load resistor current has been shifted to remove the effect of the delay line. Dots on the curves show the data points. Inset illustrates the circuit employed: The load resistor represents the connection to the digital oscilloscope; *Cak* represents the anode-cathode capacitance, and the value of *L1* is estimated from geometry of the internal connecting leads of the VPT; *C1* represents the stray capacitance between the VPT anode socket and ground.

The resulting signal is shown in Figure 4, from which it can be seen that a plateau appears in the signal at around 0.4ns after time-zero. This feature is also seen to appear between ~0.1–0.5ns in the experimental data (Figure 3).

Experiments have also been conducted to investigate the effect of variable V_A and V_D on the gain of the VPT. Maintaining constant potentials of V_K=0V and V_A=1000V whilst varying the V_D incrementally from 0 to 800V shows that the gain of the VPT increases to a maximum at V_D=600V, beyond which the

gain decreases, thereby confirming that the voltage gain is dependent on both the number of electrons and their velocity. By keeping the potential difference between the anode and dynode constant at 200V, it is evident that the voltage gain increases with increasing V_A. These general trends have also been confirmed from further computer simulation results.

5. Conclusions and Future Work

This paper has reported advances in the simulation process of the VPT using SIMION 3D. An experimental setup has been implemented in order to compare the simulated VPT with a production CMS VPT. Figure 4 demonstrated that the relationship between the simulated and the experimental data is that of integration due to the bandwidth limitation of the physical VPT. In order to show that the experimental timing performance of this device can match the simulated prediction, an impedance matched stripline to the anode should be built into the vacuum tube itself. With these simulation tools we are in a position to further optimise the geometric structure of vacuum photodetectors to provide very fast timing pulses for other applications.

Acknowledgments

This work is supported by the Science and Technology Facilities Council, UK.

References

[1] SIMION 3D v7.0 *Scientific Instrument Services Inc.* 1027 Old York Road, Ringoes, NJ 08551, USA

[2] Hobson, P R and Yaselli, I; *Nuclear Instruments and Methods in Physics Research A* **567** (2006) p226-229

[3] The Compact Muon Solenoid Technical Proposal, CERN/LHCC 94-38 (1994)

[4] Bell, K W et al; *Nuclear Instruments and Methods in Physics Research A* **469** (2001) p29-46

[5] National Research Institute Electron, Morisa Toreza Ave., 68, 194223 St. Petersburg, Russia

[6] Ramo, S; *Proceedings of the IRE* **27** (1939) p584-5

[7] LTSPICE, *Linear Technology*, 1630 McCarthy Blvd., Milpitas, CA 95035-7417, USA [Available: http://www.linear.com/designtools/software/]

APPLICATION OF THE CHANNELING RADIATION FOR PARTICLE IDENTIFICATION

M. BRIGIDA C. FAVUZZI, P. FUSCO, F. GARGANO, N. GIGLIETTO, F. GIORDANO, F. LOPARCO*, M. N. MAZZIOTTA*, N. MIRIZZI, S.RAINÒ, P. SPINELLI

Universitá degli Studi di Bari and INFN Sezione di Bari, Via E. Orabona 4, Bari, I-70126
**E-mail: mazziotta@ba.infn.it, loparco@ba.infn.it*

The channeling radiation is emitted by fast charged particles crossing a crystal with a regular lattice structure in a direction nearly parallel to a major crystal axis. The incident particles are trapped in the potential wells due the crystal planes, resulting in a coherence effect in the emitted radiation. Since the total energy of the emitted radiation depends on the square of the Lorentz factor, channeling radiation can be applied to discriminate between different particles with the same momentum in a collimated beam. To study this application of the channeling radiation, we have performed a beam test campaign at the CERN-PS T9 facility using a $500\mu m$ thick $\langle 110 \rangle$ silicon crystal. A NaI calorimeter has been used in conjunction with a magnetic field to detect the channeling photons produced in the crystal. The electron (positron) - pion identification performance and the energy spectra of channeling photons have been studied. The preliminary results will be shown and the perspectives will be discussed.

Keywords: Channeling radiation, particle identification

1. Introduction

When a parallel beam of charged particles crosses a crystal target along a direction nearly parallel to the main lattice axis, with the incident angle less than the channeling critical angle (Lindhard angle), the beam particles are trapped in the potential wells due to the crystal lattice, and coherent channeling radiation is emitted [1].

The channeling effect can be either planar or axial. The emitted radiation is strongly dependent on the charge sign because it is the result of the interaction of the beam particles with the positive ions of the lattice. The total emitted energy is proportional to γ^2, where γ is the Lorentz factor of the incident particle, while the average photon energy is proportional

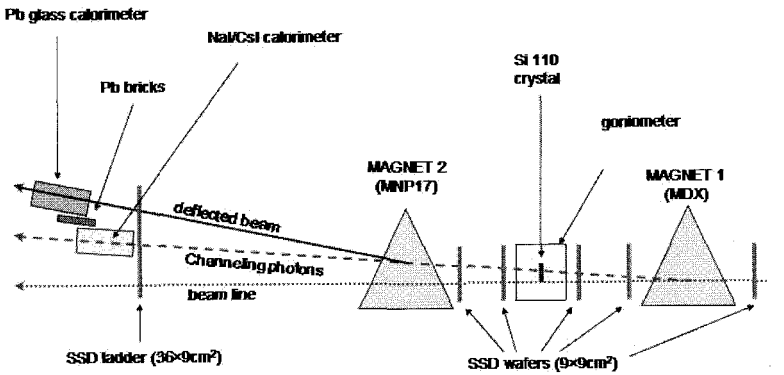

Fig. 1. Beam test setup. The plot is not in scale.

to $\gamma^{3/2}$. The typical energy spectra of channeling photons exhibit some characteristic peak frequencies depending on the particle and on the lattice parameters. Since the average emission angle of channeling photons is of the order of $1/\gamma$, in the case of ultrarelativistic particles they are emitted in a direction collinear to the beam.

Due to its features, the channeling effect can be used to discriminate in high energy unseparated beams between light radiating particles and heavy nonradiating ones. We have studied this possibility in a dedicated test, using a $500\mu m$ thick $\langle 110 \rangle$ silicon crystal exposed to a 5 GeV/c electron/pion beam at the CERN-PS T9 line.

Since a detectable channeling photon yield can be obtained from a reduced thickness crystal, the advantage of this particle identification technique is that small amounts of materials have to be disposed along the beam lines. On the other hand, since the Lindhard angle is of the order of $100\,\mu$rad in the $1 \div 10$ GeV energy region, highly collimated beams are needed.

2. Beam test setup

Figure 1 shows a schematic view of the experimental setup of our beam test. A $500\,\mu$m thick silicon $\langle 110 \rangle$ crystal (with a miscut angle less than $0.1°$, according to the specifications provided by the manufacturer) has been mounted on a goniometer that allowed to adjust its axis with respect to the beam direction. The goniometer was equipped with a linear stage and three rotative stages, that ensured a precision of $0.001°$. The motorized stages were controlled by means of a custom LabView software.

The channeling photons eventually produced in the crystal were detected by an electromagnetic calorimeter located downstream. Two kinds of electromagnetic calorimeters have been used: a NaI calorimeter, consisting of a single crystal (6″ diameter, 8″ length) readout by a 5″ diameter XP3550 photomultiplier, and a CsI calorimeter, consisting of 21 bars, each with dimensions $3 \times 3 \times 9\,\mathrm{cm}^3$, disposed in 7 layers. The 7 central bars were readout at both ends by a couple of PIN photodiodes ($18 \times 18\,\mathrm{mm}^2$ and $10 \times 10\,\mathrm{mm}^2$ cross sections), while the 14 side bars were readout only at one end by a single PIN photodiode ($18 \times 18\,\mathrm{mm}^2$).

The magnet labelled as MNP17, with a bending power of 0.5 Tm, was used to separate the beam particles from the channeling photons eventually exiting from the crystal. A lead-glass calorimeter was disposed along the trajectory of the deflected beam and was used to discriminate electrons (positrons) from hadrons and muons in conjunction with two beam Čerenkov counters. A set of scintillators were used for triggering purpose.

An additional magnet, labelled as MDX in the figure, with a bending power of 0.75 Tm was used to deflect the beam before it entered the crystal in order to reduce the bremsstrahlung background from the upstream materials in the electromagnetic calorimeter.

We also installed a telescope of SSD modules along the beam line, to measure the beam divergence and to eventually reconstruct the directions of the beam particles in the regions before and after the crystal. The first 5 modules consisted of a pair 400 μm thick SSD "wafers" with a cross section of about $9 \times 9\,\mathrm{cm}^2$, each composed by 384 strips with a pitch of 228 μm, oriented along horizontal and vertical directions. The last module, with a cross section of about $36 \times 9\,\mathrm{cm}^2$, was composed by a set of 4 "wafers" like the ones described above, for a total of 1536 vertical strips. Since the silicon modules introduced a consistent contribution to the bremsstrahlung background, after some test runs they were removed from the beam line.

3. Data analysis

We have performed several runs with electrons, positrons and pions at 5 GeV/c beam momentum, changing the orientation of the goniometer with respect to the nominal incoming beam direction.

In figure 2 a plot of the photon detection efficiency is shown for all the configurations investigated during our beam test campaign. The results shown in the figure have been obtained using the NaI calorimeter, after removing the SSDs from the beam line. The photon detection efficiency is defined as the fraction of events with a signal in the NaI calorimeter

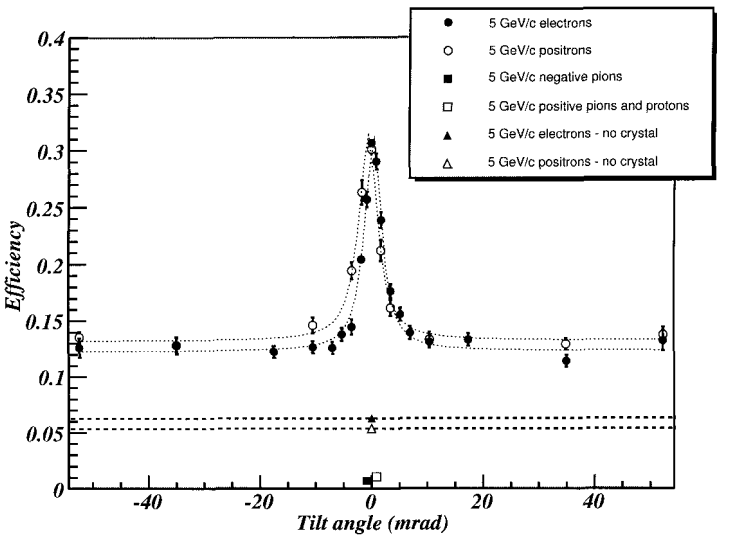

Fig. 2. Photon detection efficiency as a function of the tilt angle (evaluated with respect to the maximum position).

exceeding a threshold of 1.0 MeV (3σ of the pedestal distribution). The results shown in the plot have been obtained without making any correction to take into account the detector acceptance and its efficiency.

At the channeling peak we measured a photon detection efficiency of about 0.35 for both electrons and positrons, to be compared with the value of 0.13 at large angles. The width of the channeling peak is of about 4 mrad and is mainly due to the beam divergence, that is of about 2 mrad in the horizontal plane and 1 mrad in the vertical plane, while the Lindhard angle in $\langle 110 \rangle$ silicon is of about 100 μrad. On the other hand, in the pion runs the measured photon detection efficiency at the channeling peak is about 0.01. Since pions are expected to emit channeling radiation in the soft X-ray energy range, this result can be due to pedestal fluctuations. .

A few runs have been also performed with electrons and positrons after removing the crystal from the beam line, in order to measure the bremsstrahlung background due to all the materials disposed along the beam line. A background of about 0.06 photons/electron(positron) has been measured.

In figure 3 the photon intensity spectra measured with the NaI calorimeter are shown. The energy calibration of the calorimeter was done at

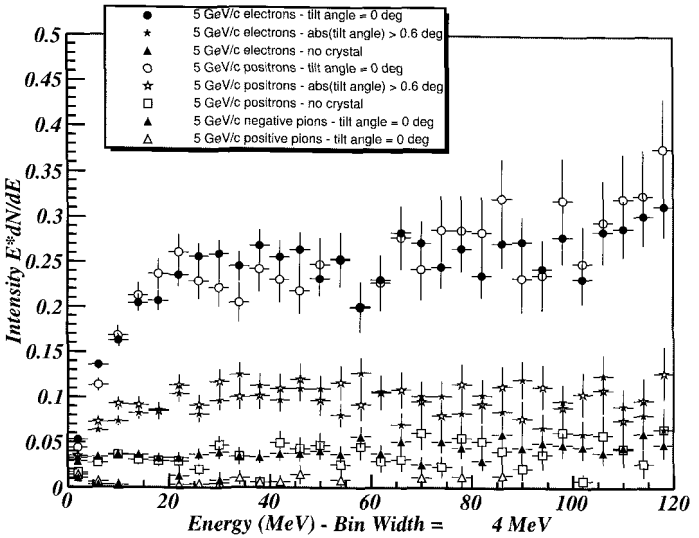

Fig. 3. Photon intensity spectra measured with the NaI calorimeter.

the BTF facility in Frascati, using an electron beam with energies up to 500 MeV and has been checked at CERN exposing the calorimeter to a beam of 5 GeV/c muons and pions (the most probable energy loss of a minumum ionizing particle in 8″ NaI is 97 MeV). The positron intensity spectrum obtained at the channeling peak shows a small peak around 25 MeV, that is consistent with the expected value of the first characteristic frequency.

4. Conclusions and future perspectives

We have measured the channeling radiation emitted by a 5 GeV/c beam of electrons (positrons) crossing a 500 μm $\langle 110 \rangle$ silicon crystal. A clear evidence of the channeling effect has been found for electrons and positrons, even though the beam divergence was larger than the expected channeling angle.

For the future, we are planning to perform a further beam test at the SPS, where highly collimated beams are available.

References

1. M. A. Kumakhov, Phys. Lett. **57** (1976), 17

INSTRUMENTATION OF THE FAST DETECTOR

A. BARCZYK, J.KIRKBY, L. MALGERI
CERN
Geneva, Switzerland

C. CASELLA, M. POHL
University of Geneva
Geneva, Switzerland

K. DEITERS, P. DICK
Paul Sherrer Institut
Villigen, Switzerland

J. BERDUGO, J.CASAUS, C. MANA, J. MARIN, G. MARTINEZ, E. SANCHEZ, C. WILLMOTT
Ciemat
Madrid, Spain

The Fiber Active Scintillator Target (FAST) is an imaging particle detector intended for high precision muon lifetime measurement. This measurement will lead to a determination of the Fermi coupling constant (G_F) with an uncertainty of 1ppm, one order of magnitude better than the current world average. This contribution presents a description of the detector instrumentation and the first results, which have validated the design of the system.

1. Introduction

The main goal of the FAST experiment is the precise measurement of the positive muon lifetime. This measurement will lead to a determination of the Fermi coupling constant (G_F) with an uncertainty of 1ppm, one order of magnitude better than the current world average [1]. The Fermi coupling constant is one of the input parameters in the electroweak sector of the Standard Model and the improvement in the uncertainty of its determination is important in order to test the theory. G_F can be directly obtained from the muon lifetime. Since the theoretical uncertainties have become negligible in the calculation of

the Fermi constant, the precision in the muon lifetime measurement is nowadays the dominant error.

The Fibre Active Scintillator Target (FAST) installed at Paul Sherrer Institut (PSI, Villingen, Switzerland) is a high granularity imaging particle detector. A DC π^+ beam, obtained from the PSI proton Synchrotron [2], is stopped in the target, the system identifies the $\pi^+ \rightarrow \mu^+ \rightarrow e^+$ decay chains and registers the time and space coordinates of each particle to obtain the lifetime distributions. In Fig. 1 a diagram of the target is shown.

In order to get the desired precision in muon lifetime analysis, a huge data sample of more than $2x10^{11}$ events is required. The system is able to work with overlapped observation windows and to manage a demanding trigger rate; therefore the required sample can be acquired in an affordable data taking period.

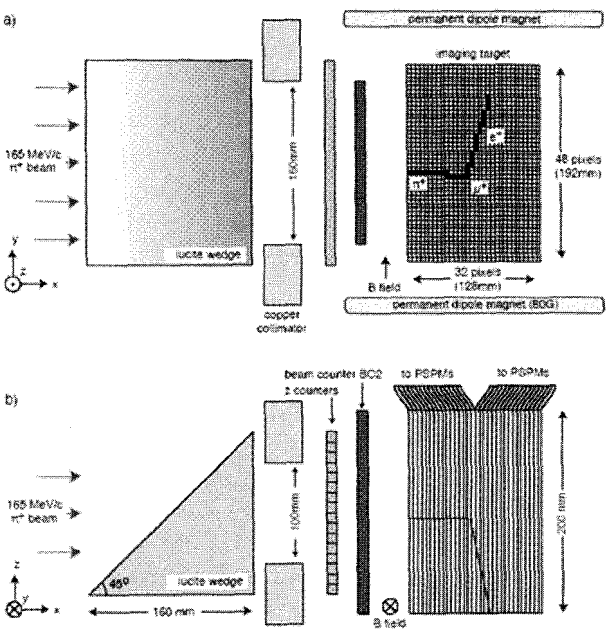

Figure 1. FAST target

A description of the detector instrumentation is presented in this contribution. The results obtained in 2006 are also presented; they are compatible with the current world average and have validated the system

design. The detector upgrades carried out throughout this year will lead to the experiment goal precision in muon lifetime determination.

2. The FAST Detector

A block diagram of the detector is shown in Fig. 2. The 128x192x200 mm^3 target consists of 1536 plastic scintillator bars that form a two-dimensional pixel array. The scintillating light is guided to photomultiplier tubes (PMTs) using wavelength shifting fibers. A total of 96 Hamamatsu 6568-10 multi-anode PMTs are used for complete target reading out. Each tube has 16 pixels arranged in a 4x4 configuration. The high voltage is controlled independently for each tube.

A set of 16 scintillator bars are placed horizontally in front of the target for Z-coordinate determination. An extra PMT is used to detect the scintillation light of the Z-counters.

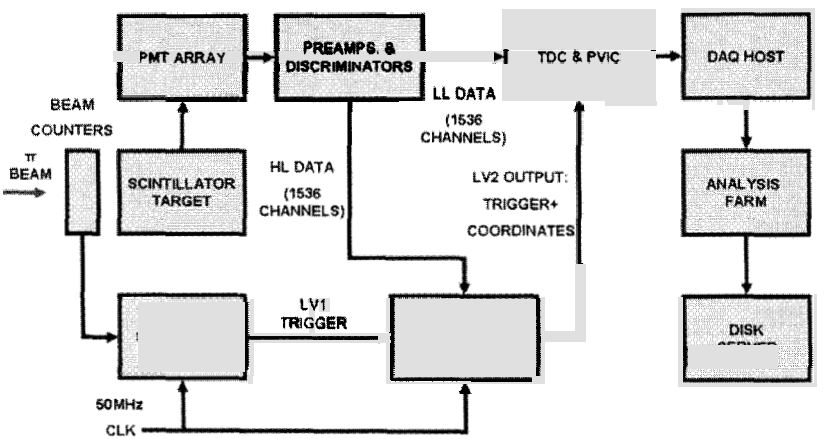

Figure 2. FAST detector layout

The front-end electronics can be separated in two different kinds of modules. Both of them have been developed specifically for FAST at PSI. The preamplifiers modules amplify the current pulses, which are provided by the PMTs outputs, into voltage pulses. Each preamplifier board has 16 channels matching one complete PMT. No multiplexers are used in the readout chain, so, each channel has its own preamplifier. The discriminator modules are used to perform the analog-to-digital conversion. Again one discriminator module has

16 channels. There are two different discrimination thresholds. The low level (LL) threshold outputs are set to be sensitive to all beam particles. However, the high level (HL) threshold outputs are set to be activated only with pions and muons and are used to provide a cleaner sample for the second level trigger system. The discriminator modules are allocated in several NIM crates next to the target. The thresholds voltages are set via the slow control system.

The time measurement is performed with C.A.E.N. 128 channel multi-hit TDC modules. These boards are based on the TDC32 chip [3], developed by the CERN microelectronics group for the LHC. Only 96 channels per module are used for pixel readout, the rest of channels are devoted to control issues. A long observation window of 30μs is programmed in the TDCs. A pre-trigger period of 10μs is observed before the beam particle in order to characterize the background. A period of 20μs, corresponding to 10 muon lifetimes is observed after the beam particle time. The TDCs are clocked with a high stability 30MHz rubidium atomic clock. The time resolution achieved with this clock frequency is 1,041ns, which is enough for the experiment purposes.

The TDC modules are VME format. There are 4 VME crates that allocate 4 TDC boards each. The PVIC modules provide a self-governing VME-to-PCI interface. They manage the reading out of the crates sending the data to the acquisition PCs. Each PVIC has a top bandwidth of 20MBps, so, with the current configuration of 4 PVIC links the maximum bandwidth of the system is 80MBps.

The data acquisition PCs collect data from the PVIC links and put together the event fragments in order to build the events. Since the data sample that is required to achieve the experiment goal precision is so huge, the events are not stored in raw format. The analysis PCs perform the calculation of the lifetime distributions on-line and store the histograms in disk. Only a small fraction of raw events are registered for data taking monitoring.

The trigger system is divided into two different levels. The first level trigger (LV1) is used to flag that a particle has entered the target. It uses a couple of beam counters, the Z-counters and the accelerator RF clock of 50MHz. The LV1 signal is also used as a global time reference for all the TDCs.

The second level trigger (LV2) performs a hardware event selection and data processing in order to reduce the trigger rate sent to the TDCs and the size of the events, i.e., the data throughput to be acquired by the DAQ system. The system processes 1536 discriminator HL outputs to find the pions and the subsequent muons inside a certain time window. This event selection is done in order to neglect the early muon decays, which cannot be processed by the

discriminators. In addition, the system defines a region of interest around the pion stop and triggers only the involved TDCs of the event, with the consequent bandwidth optimization. The stopping pixel of the muon is also given by the LV2 system to speed up the analysis program.

The Slow Control program is LabView based. It is used to control the high voltages, discriminator thresholds and trigger settings and to monitor temperatures and other parameters. In addition, a web-based program is used to monitor the data taking in detail.

3. First Results

Two long pilot runs during 2005 and 2006 have validated the detector operation. The average LV2 trigger rate during 2006 data taking was 30 kHz and a data sample of 10^{10} events was collected. The result obtained from this run is in agreement with the current world average with similar statistical error and controlled systematics [4]. For this year run, the DAQ has been upgraded to obtain a sustainable LV2 trigger rate operation of 120 kHz; this will make possible the collection of few times 10^{11} events in order to reach the desired precision in muon lifetime measurement.

4. Conclusion

The goal of the FAST experiment is the precise measurement of the muon lifetime. The instrumentation of the detector is presented in this contribution. The system design has been validated with two long pilot runs during the last two years. The upgraded system will meet the requirements to reach the final goal precision in muon lifetime determination.

References

1. J. Kirkby, M. Pohl et al, "Precision Measurement of the μ^+ lifetime (G_F) with the FAST Detector". PSI proposal R-99-06, May 27 1999
2. http://www.psi.ch
3. C.A.E.N. 128 CH. General Purpose Multihit TDC Technical Information Manual. Version 4, Jul. 2003.
4. FAST Collaboration, "Measurement of the Fermi Coupling Constant by FAST"; submitted to Phys. Let. B (arxiv: 0707.3904 [hep-ex])

FIRST RESULTS OF SILICON PHOTOMULTIPLIER STUDY PERFORMED AT THE UNIVERSITY "LA SAPIENZA" OF ROME

C. BOSIO [(1)], S. GENTILE [(1,2)], E. KUZNETSOVA [(1)], F. MEDDI [(1,2)] †

[(1)] *INFN Roma1, Piazzale Aldo Moro 2*
Rome, 00185, Italy

[(2)] *Department of Physics, University of Rome, "La Sapienza", Piazzale Aldo Moro 2*
Rome, 00185, Italy

First results on Silicon Photo-Multiplier (SiPM) properties study are presented. The current-voltage (I-V) characteristic and the response to low-intensity light were studied for samples produced by CPTA (Russia), Hamamatsu (Japan), ITC-irst (Italy) and SensL (Ireland).

1. Introduction

Silicon Photo-Multiplier (SiPM) is a novel type of avalanche photo detector with single photon counting capability proposed by Golovin and Sadygov in the 90's [1, 2]. The SiPM active area of usually from 1 to several mm^2 is divided in a matrix of about 500–1600 cells. The cells are connected in parallel and operated in reverse bias mode just above the breakdown value. The spatial extension of the breakdown electrical field involves thickness of ~1μm. The detector works in the Geiger mode limited by a passive quenching resistor $R_{quenching}$ implanted on the surface. Typically, $R_{quenching}$ is about several hundreds kΩ. A value of ~50ns is obtainable as recovery time. In spite of the binary response of each cell (typically ~10^5-10^6 electrons for each electron triggering the avalanche), the matrix works as an analogue device providing an output signal proportional to the number of fired cells. The dynamic range of SiPM is defined by the number of cells. The small size, capability to operate in a magnetic field, low bias voltage and reasonable price make SiPM to be a very promising device for many applications and therefore induces the intense development of the technology leaded by various manufactures (CPTA, HAMAMATSU, IRST, MEPHI, SENSL ...). Systematic studies done with

† Corresponding author. Email address: franco.meddi@roma1.infn.it

various types of SiPM would provide a start information for an optimal choice of the SiPM type for a given application.

2. Measurement setup

Fig. 1 shows a principal scheme of the measurement setup designed for the SiPM properties study. The setup allows performing measurements of the dark current as a function of bias voltage as well as studies of the SiPM response to low intensity light. The latter measurements are done using a LED (Light Emitting Diode) as the light source. The pulse light of about 6ns duration is coupled with an optical fiber on the SiPM. The signal from SiPM is read out with a Pre-Amplifier (PA) and digitized with an integrating ADC. A trigger synchronizes the LED pulse and the ADC gate. The measurements have been performed at room temperature (24°C ± 2°C) without any temperature control. Temperature variation during the measurements did not exceeded 2°C for each samples. The total variation for all samples was less than 4°C.

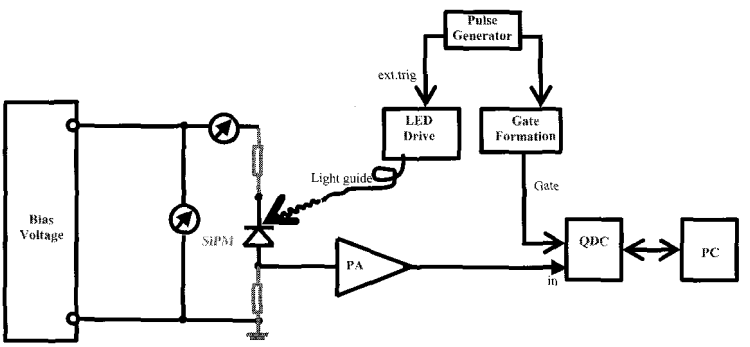

Figure 1. The static polarization circuit (on the left part), the pulsed light injection circuit (on the middle) and the readout via an integrating ADC circuit (on the right) are shown.

3. Measurement Results

Five Silicon Photo-Multipliers samples from different producers have been tested. Two produced by CPTA (Russia) and distributed one by Obninsk [3] University and another by Forimtech [4]. One sample was from Hamamatsu [5] (Japan) (S10362-11-025C). One sample was from ITC-irst [6] (Italy) (SIT6V1PD1). Finally, one sample was from SensL [7] (Ireland) (SPMScint1000). Fig. 2 shows the different surfaces of the SiPM detector as

seen at optical microscope. All studied types of SiPM have the active area of 1mmx1mm, but different cell size and geometry.

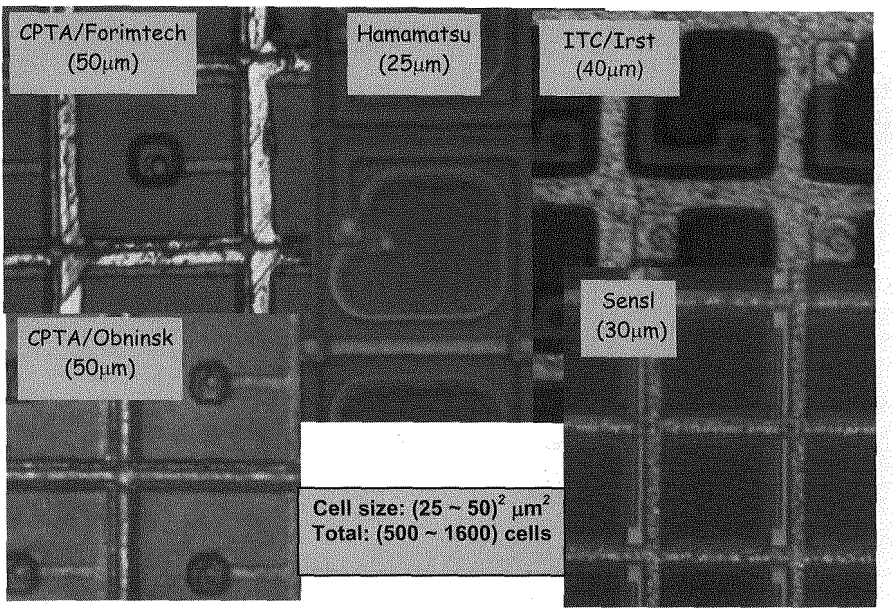

Figure 2. Summary of the surface views taken by a microscope of the five tested SiPM. To be noted that the shown photos are not in scale. The matrix structure is evident.

Five samples, one per each of the listed types, have been studied. Fig. 3 shows current-voltage characteristics of the SiPM samples. Fig. 4 shows an example of the SiPM response to low intensity light. The peaks clearly seen in the ADC spectrum correspond to the different number of cells fired at each light pulse, starting from the pedestal when no cells are fired. From distance between peaks the SiPM gain can be evaluated. The spectrum is fitted as a sum of Gaussian distribution. The normalization factors and standard deviations σ_i are individual for each Gaussian. The pedestal position μ_0 and the gain g are global parameters. The position μ_i of i^{th} peak is given by the relation $\mu_i = \mu_0 + i \cdot g$. The standard deviation σ_i obtained from the fit can be parameterized as $\sigma_i = [(\sigma_0)^2 + i < \sigma_{px}>^2]^{1/2}$ where σ_0 stands for pedestal standard deviation, $<\sigma_{pix}>$ stands for the standard deviation averaged over the active area of the matrix.

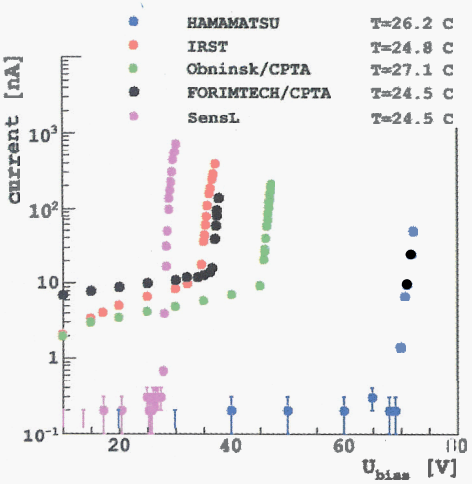

Figure 3. The current-voltage measurements show a similar behavior for tested SiPM giving breakdown voltage value ranging from 28V up to 70V.

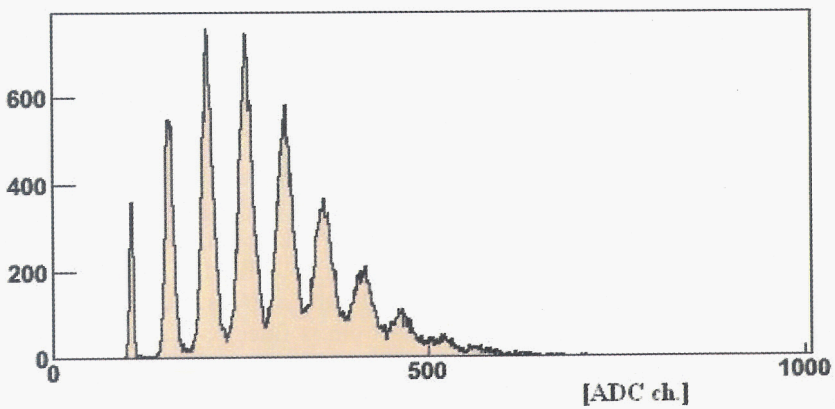

Figure 4. Typical charge spectrum (in terms of ADC counts) obtained from one SiPM pulsed by a low intensity LED light. On the reported spectrum the multi peak structure refers to the various numbers of fired cells in a particular triggered light pulse impinging the matrix.

In Fig. 5 are reported for all the tested SiPM the gain versus the quantity ($V_{bias} - V_{brd}$), i.e. at the applied bias voltage is subtracted the breakdown voltage.

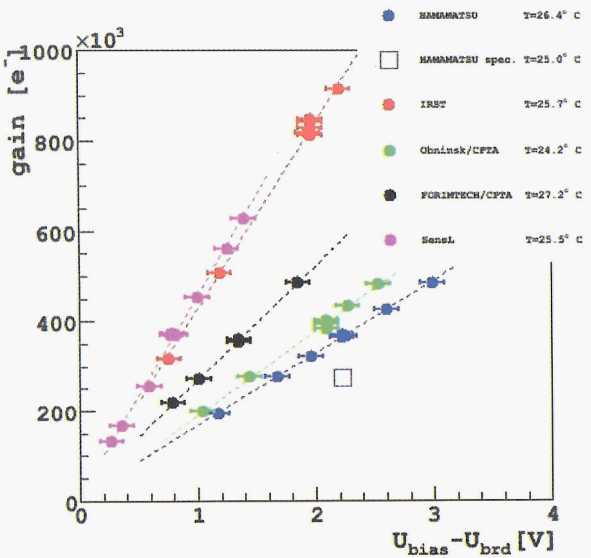

Figure 5. Gain as a function of the over voltage (V_{bias} - $V_{breakdown}$) for the tested SiPM is reported, at <T> ~ 24°C (see text).

4. Conclusion

First characteristics of SiPM produced from different manufactures have been measured and compared. Future extensions of the measurements are foreseen in near future including efficiency measurements at various wave lengths.

Acknowledgments

We would like to thanks the support received from: Valeri Saveliev, Roberto Battiston, Ivo Polak and Nicola D'Ascenzo.

References

1. V. Golovin et al. *Nucl. Instr. and Meth.* **A518,** 560 (2004).
2. Z. Sadygov et al., *Trans. Nucl. Sci.,* **43,** No.3, 1009 (1996).
3. CPTA, Russia, http://www.zao.cpta.ru
4. Forimtech SA, http://www.forimtech.ch
5. Hamamatsu, Japan, http://www.hamamatsu.com
6. ITC-irst, Italy, http://www.itc.it/irst
7. SensL, Ireland, http://www.sensl.com

STUDY ON NANOSTRIP GAS COUNTER FOR THE OPERATION UNDER INTENSE BEAM

HISAKO NIKO[†]

Nuclear Engineering, Tokyo University, 7-3-1,Bunkyo Hongo Tokyo, 113-8656, Japan

HIROYUKI TAKAHASHI

Nuclear Engineering, Tokyo University, 7-3-1,Bunkyo Hongo Tokyo, 113-8656, Japan

To cope with the high intensities of new generation beams such as the X-ray Free Electron Laser, a novel detector design ensuring a steady performance is needed. We are developing MicroStrip Gas Chambers (MSGCs) with grid electrodes between the anode and the cathode electrodes in order to obtain a stable electric field. While studying these MSGCs, we have developed the concept of a fine-pitch MSGCs under high counting rate. We are convinced that the very fine-Pitch MSGC or "NanoStrip" Gas Chamber (NSGC) are promising for very high counting rate applications, as well as for fine resolution with high pressure heavy gas. Our first trial for 50 μm pitch plate showed a gas gain sufficient to detect 8 keV X-rays. We keep studying the development of finer pitch NSGCs.

1. Introduction

MicroStrip Gas Counters (MSGCs) are the first and the oldest type of gas counters among micropattern detectors. However, we are still foreseeing a new possibility of this well-understood detector. A multi-grid-type MSGC (M-MSGC) [1-2] is equipped with several intermediate strips between the anode and the cathode strip. These strips are connected to an individual high voltage source to maintain intermediate potentials between anode and cathode. As a result, the electric field is stabilized by this grid potential, and therefore a very high gas gain can be achieved without discharge. We are trying to operate this type of detector in a charge-integrating mode, where pile-up pulses can also provide the intensity information of incident radiation. Although we lose the benefit of pulse counting, we can obtain a wide dynamic range in this operating mode.

[†] Work partially supported by Global COE "Nuclear Engineering and Management", Tokyo University

2. Motivations

We used an individual readout circuit from each cathode strip and connected each strip to the input channel of charge-integrating ASICs. The test M-MSGC had 400 μm anode pitch and 4 grids between the anode and the cathode. The detector has been tested at the KEK photon factory and at SPring-8 in Japan. Fig.1 shows a result obtained at SPring-8 facility. We irradiated 8 keV X-rays up to 10^{12} cps/mm^2. We observed linearity of the detector response up to 10^{10} cps/mm^2 in the charge-integrating operating mode.

However, when carefully investigating the position distributions, we observed some nonlinearities and hysteresis (a report about the experiment at KEK has been provided in a previous paper [3]). We suppose that these nonlinear behaviors are due to the space charge effect at a very high counting rate situation. We are convinced that the fine-pitch MSGC or the NanoStrip Gas Counter (NSGC) are suitable to suppress this effect. We suggest that the fine-pitch MSGC can share the total charge with several anode strips and that the average charge per anode strip can be reduced. This would lead to a MSGC having a wider dynamic range.

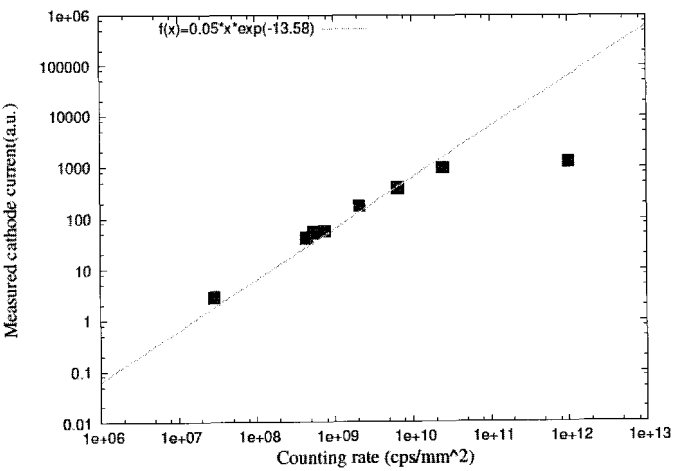

Fig.1: Counting rate characteristics of a charge-integrating mode operation

3. Experiments and Results

We decided to develop a fine-pitch MSGC able to achieve an enlargement of the area of avalanche. We fabricated a 50 μm pitch NSGC (Fig.2) using an electron beam drawing machine at the University of Tokyo. The latest

microfabrication technology allows us a sub-um scale electrode. We think this NSGC is promising for very high counting rate applications, as well as for a fine resolution with high pressure heavy gas.

We tested our first prototype NSGC at KEK with 8 keV X-rays collimated 100 μm and with a Ar (30 %) + CH_4 (70 %) gas mixture at 1 atm, and could obtain a pulse height spectrum at a gas gain of 280 (Fig.3).

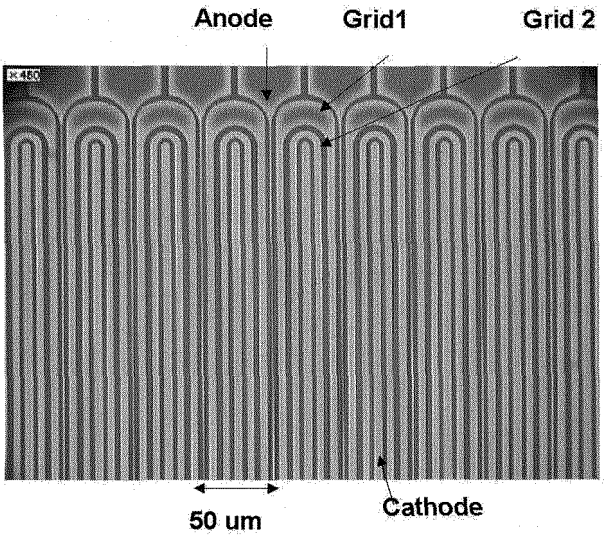

Fig.2: Photograph of fine-pitch M-MSGC

4. Current Works

We are designing a plate able to read signals from each cathode with charge-integrating operation mode. At the same time we are developing finer NSGCs (30 μm pitch with 500 nm width anode). With these plates, we consider that detector response linearity can be achieved up to more than 10^{10} cps/mm^2. Also, a higher position resolution (around 50 μm) can be obtained.

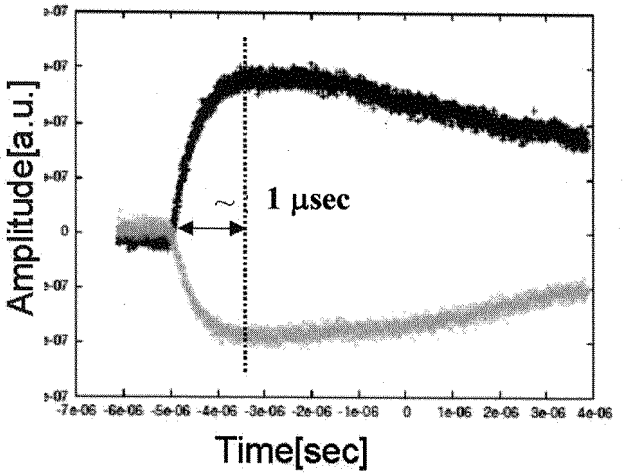

Fig.3 (a)

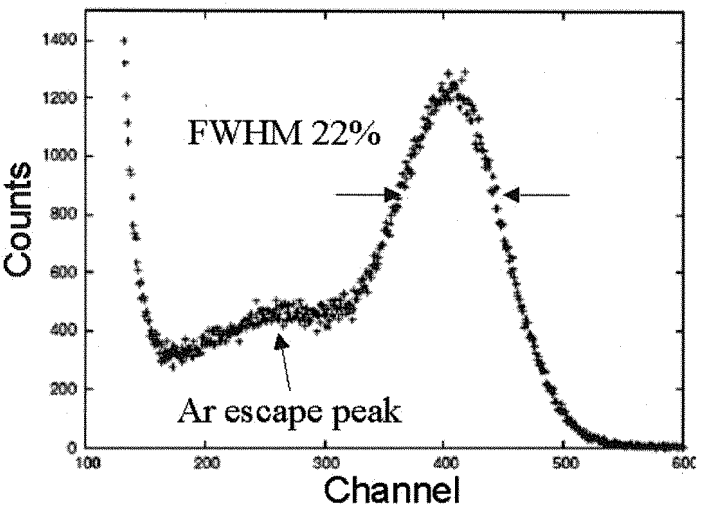

Fig.3 (b)

Fig.3: Results of the test of the NSGC with 8 keV X-rays collimated 100 μm and with a Ar (30 %) + CH_4 (70 %) gas mixture at 1 atm. (a) Waveform ,(b) Pulse height spectrum.

Acknowledgments

Layout is designed by Cadence Virtuoso accessible through VLSI Design and Education Center (VDEC)'s academic program. Photomasks are made using the University of Tokyo VDEC's 8-inch EB writer F5112+VD01 donated by ADVANTEST corporation.

References

1. H. Takahashi et al., Nucl. Instr.and Meth. A477(2002)13.
2. H. Takahashi et al., IEEE Trans on Nucl.Sci.48;(6)(2001)2317.
3. H. Takahashi et al., Nucl. Instr.and Meth. A 513(2003)201.

EXCITATION FUNCTIONS AND YIELDS FOR RE-186G PRODUCTION BY PROTON CYCLOTRON

E. PERSICO, M. L. BONARDI, F. GROPPI, C. ZONA, L. CANELLA, S.MANENTI, M. MARCHETTI
LASA, Università degli Studi di Milano and INFN-Milano, via F.lli Cervi 201 Segrate,I- 20090, Italy

K. ABBAS, U. HOLZWARTH, F. SIMONELLI
IHCP, Institute for Health and Consumer Protection, JRC-Ispra, via E. Fermi Varese, I-21020, Italy

Excitation functions and yields for the $^{181-186}$Re radionuclides were measured by the activation method on natural tungsten foils for the proton energies up to 17 MeV . A new data sets have been given for the investigated radionuclides. These results are compared both with the experimental literature values and the ones calculated by EMPIRE II code (version 2.19). In particular, the attention is focused on Re-186g due to its remarkable applications in Nuclear Medicine for metabolic radiotherapy of tumours.

1. Introduction

^{186g}Re is a γ-β emitter actually used in metabolic radiotherapy and with optimal possibilities to be used also in radioimmunoteraphy (RIT)[1], thanks to its suitable nuclear properties ($t_{1/2}$=90.64 h, $E_{max\beta}$ 1.07, 0.93 MeV, E_γ 137 keV)[2]. In particular the energy range of the β particles suggests that this radioisotope is a good candidate for cancers with small dimensions (from few millimetres to few centimetres). Presently ^{186g}Re is produced by neutron capture on enriched ^{185}Re in thermal nuclear reactors, leading to a relatively low specific activity A_S (activity/isotopic carrier mass). The possibility to use this radionuclide for therapeutic purpose is strictly linked to the possibility of increase the AS, approaching to the theoretical carrier free value of 6.9 GBq.μg^{-1}.

In order to improve the specific activity, ^{186g}Re can also be produced by proton bombardment of tungsten targets by the (p,n) nuclear reaction. This way to operate surely leads to an increase of the A_S due to the possibility to chemically separate the product from the target. However, even if several researchers had studied the excitation function of this nuclear reaction[3-9], there are large discrepancies in the literature data sets.

In order to assess the capacity of the ^{186}W(p,n)^{186g}Re way of production, a new excitation function was measured; in particular the experiments were carried out using thin natural tungsten foils. This leads to a production of several isotopes as

^{181}Re, ^{182m}Re, ^{182g}Re, ^{183}Re and ^{184g}Re together with, of course, ^{186g}Re. For each radionuclide, its own excitation function and experimental integral yield was measured at proton energies up to 17 Mev in the first case and 16.5 MeV in the latter one. Finally, the all the experimental values were compared to the excitation functions as calculated by the EMPIRE II nuclear reaction code.

2. Experimental

The excitation functions were measured by using the stacked foil technique while the experimental yields were measured by using thick tungsten foils in order to guarantee to total absorption of the proton beam. In each case, anyway, the high purity of the natural tungsten foils (Goodfellow Cambridge Limited, UK) were mandatory. As regard the cross-section, the stack of foils consisted of alternating aluminium (as energy degrader and catcher foils), W and, depending on the irradiation, one or two Ti beam monitor foils.

All the irradiations have been carried out with the cyclotron (K=38, beam current up to 60 μA) of JRC-Ispra at several energies but with typically 100 nA for few hours depending on the energy range under investigation: in the region of high and low energies the time irradiation was quite long (3 or 4 hours) while in the middle region, where according to the literature values the cross-section presents its maximum, the irradiation time was shorter.

The activity of rhenium radionuclides produced in the irradiated targets was measured by calibrated high purity germanium (HPGe) detectors (EG & G Ortec, 15% efficiency, 2.2 keV (FWHM) at 1.33 MeV). The spectra obtained were analysed by using the Gamma Vision s/w (EG & E Ortec) and each single peak was manually identified and fit. Mean proton beam incident energy and in general energy degradation in each foil was computed by the MonteCarlo based computer code Stopping and Range of Ions in Matter (SRIM) 2006 edition[10].

As regard the determination of the reliability of the incident energy, checks were made by the information in the monitor spectra by using the IAEA tabulated reaction ^{nat}Ti (p, x)^{48}V[11].

The overall uncertainty for cross-section and yield measurement results from the sum of several errors and considerations accounted during the evaluation process; first of all, the statistical error in the peak counts. To reduce this value under the threshold of 1%, the acquisition time of each spectrum (of several hundreds) must be the result of a balance between the dead time and the distance of the target from the detectors. Besides, in the final uncertainty was taken into account the error on the tungsten foil thickness, on the integrated charge (more or less around 2%) and, on the efficiency curve of the detector (calibrated in both energy and efficiency by certified sources of ^{133}Ba and ^{142}Eu). Finally, as regard the uncertainty of the mean incident energy, this value strictly depends on the beam energy value on the first target and the thickness of each foils (W, Al and Ti). At the end, the cross-section data obtained for the ^{nat}W(p,xn)^{18x}Re reactions have been compared both with the values reported in the literature and with the model calculation using EMPIRE-II version 2.19.

Results and discussion

The measured excitation functions are shown below compared with the literature values and the theoretical ones; it is important to stress that the energy range of these graphs is cut so that our data are more visible. In the end, where possible, the computation was carried out using more than one gamma emission.

Rhenium 186g: cross-section and yield

Rhenium-186g is the object of our research and in this occasion we will present its excitation function and its cumulative yield.

As regard the cross-section, this is the only case in which the data are presented divided by the natural isotopic abundance (28.6%). As we can see from Fig.1 our data just lie in the middle between the ones of Zhang and all other authors. Instead, in Fig. 2 calculated thick-target yield and the experimental one have been compared. The compute values have been calculated by measuring thin-target yield and then fitted by using an analytical way (Mathcad 13). The curve obtained was integrated at different energies in the case of total proton energies absorption, taking into account the self-absorption of photon at 137.15 keV[12]. As it is easy to observe, there is an agreement between the calculated values and the experimental ones as regard the behaviour.

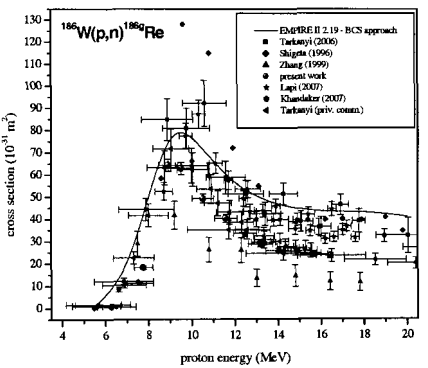

Figure 1: Excitation function of the $^{186}W(p,n)^{186g}Re$ reaction.

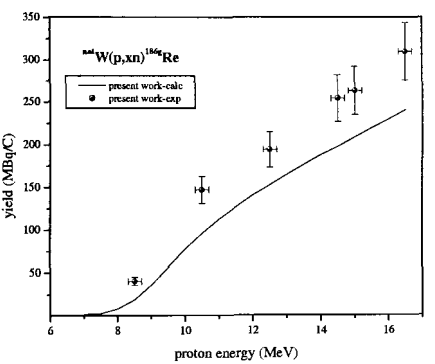

Figure 2: Calculated and experimental thick target yield for Re-186g on natural W target.

Rhenium 184g

In comparison with the literature data, it is possible to see in Fig. 3 good agreement at low energy with all authors but while the energy increases, good agreement is kept only with the Zhang values.

Rhenium 183

As we can see from Fig. 4, our set of data is in strong agreement with the one of Tárkányi, while others authors present values that are spread in comparison with our trend, at least at energies up to 17 MeV.

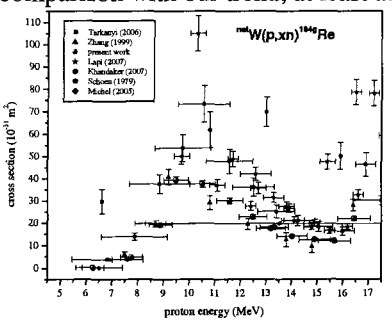

Figure 3: Excitation function of the $^{nat}W(p,xn)^{184g}Re$ reaction

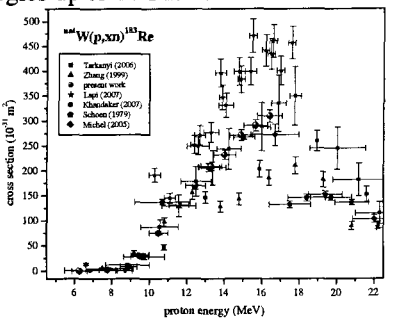

Figure 4: Excitation function of the $^{nat}W(p,xn)^{183}Re$ reaction

Rhenium 182m+g

As regard ^{182m}Re (Fig. 5), our data are in very good agreement at energies up to 12 MeV more or less. Then, some authors data present a slowly increase, Zhang a decrease while our values reach a plateau. For ^{182g}Re, instead, our data (Fig. 6) and the Lapi's ones are in good agreement while the others present a spread at energies higher and higher.

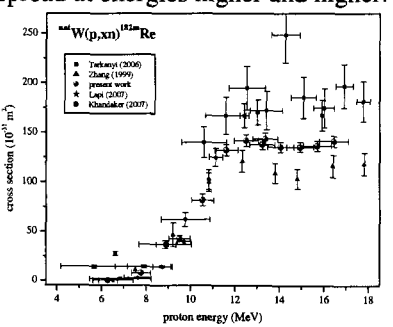

Figure 5: Excitation function of the $^{nat}W(p,xn)^{182m}Re$ reaction

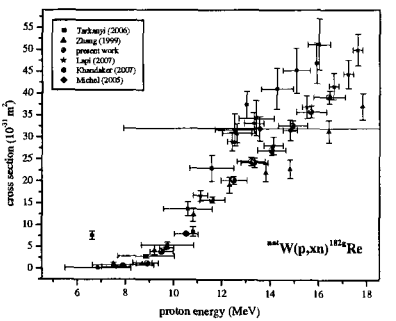

Figure 6: Excitation function of the $^{nat}W(p,xn)^{182g}Re$ reaction

Rhenium 181

As we can see from Fig. 7, at lower energies (up to 3 MeV more or less) there is strong agreement within all the authors, but even in this case, as the energy rises, the spread of the values becomes bigger too.

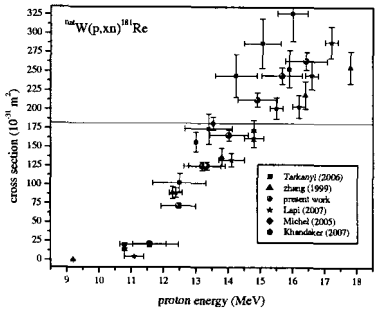

Figure 7: Excitation function of the $^{nat}W(p,xn)^{181}Re$ reaction

3. Conclusions

Cross-sections for the production of rhenium isotopes ($^{181-186}Re$) from natural tungsten target have been presented together with the thick-target yield of rhenium-186g. Thick-target yields of the other rhenium isotopes will be presented in a full extension version of this article. Anyway, what it is immediately clear from the results discussed above is: first of all the discrepancies between the authors as regard ^{186g}Re excitation function, and then the importance to verify the behaviour of thick-target yield of this nuclide bombarding an enriched tungsten target.

References

1. S. Kanuya, K. Yokoyama et al., Cancer Lett. 219 (2005), 41-48.
2. R.B. Firestone, C.M. Baglin and F.S.Y. Chu, Table of Isotopes, 8-th Ed., 1998 Update on CD-ROM, John Wiley and Sons, New York, USA, 1998.
3. S. Lapi, W.J. Mills et al., Appl. Radiat. Isot. 65 (2007), 345-349.
4. F. Tárkányi, S. Takács et al., Nuc. Instr. Meth. B 252 (2006), 160-174.
5. M.U. Khandaker, M.S. Uddin et al., available on line at http://arvix.org/ftp/nucl-ex/papers/0703/0703035 .pdf.
6. N. Shigeta, H. Matsuoka et al., Radioanal. Nucl. Chem. 205 (1996), 85-92.
7. X. Zhang, W. Li et al., Radiochim. Acta 86 (1999), 11-16.
8. R. Michel, A.S.M.F. Choedhury et al., in S.M. Quaim (ed.), NEA/NSC/DOC(2005)27, ONDC(GER)-0051, Jül-4194, FZJ, 2005, p. 31.
9. F. Tárkányi, A. Hermanne et al., private communication, submitted to Nucl. Instr. Met., B
10. J.F. Ziegler, J.P. Biersalc and U. Littmark, http://www.SRIM.org.
11. IAEA, TECDOC 1211, available on line at http://www-nds.iaea.org/reports-new/tecdocs/iaea-tecdoc-1211.pdf
12. http://physics.nist.gov/PhysRefData/Xcom/Text/XCOM.html

THE STATUS OF THE LHCb RICH SYSTEM

R. W. Plackett* on behalf of the LHCb RICH Group

Physics Department, Imperial College London
SW7 2AZ, United Kingdom
**E-mail: richard.plackett@imperial.ac.uk*
http://www.imperial.ac.uk/research/hep/

As the completion of the LHCb detector approaches we report on the status of the Ring Imaging Cherenkov (RICH) detectors that provide light hadron particle identification. The design and status of the two detectors RICH1 and RICH2 is explored and an overview is given of the photon detector technology the Hybrid Photon Detector. RICH1 is a more compact system working at lower particle momenta closer to the interaction point and is currently nearing completion. RICH2 is a larger detector operating at higher momenta and is complete and currently being commissioned.

Keywords: LHCb; Ring Imaging Cherenkov Detectors; Hybrid Photon Detectors.

1. LHCb

The LHCb experiment is designed to study the high yield of hadrons containing the b-quark at the CERN Large Hadron Collider (LHC). Its primary goals are to make precision measurements constraining the Standard Model description of CP violation and to study rare B-meson decay where the discovery potential of physics beyond the Standard Model is high. Most b-hadrons produced in LHC collisions are emitted at small angles with respect to the colliding beams. The LHCb detector is therefore designed as a single-arm spectrometer with a limited angular acceptance of about 300mrad. The ability to distinguish between pions and kaons in the final states of a variety of B-decay modes is essential and Ring Imaging Cherenkov[1,2] (RICH) detectors are used.

2. Ring Imaging Cherenkov Detectors

Charged particles traversing a transparent medium, faster than the speed of light in that medium, radiate Cherenkov light in a cone of half angle θ, given

by $\cos\theta = \frac{1}{n\beta}$ where n is the refractive index and β is the particle speed as a fraction of c. By focusing this cone of light to a ring, using a spherical mirror, it is possible to measure the ring radius and hence the Cherenkov angle θ. This gives the particle velocity that, combined with a measurement of its momentum, allows the particle's mass to be calculated. The Cherenkov light is uniform in photon energy and the intensity is very low, requiring efficient detection of single photons over a wide energy spectrum.

3. The LHCb RICH System

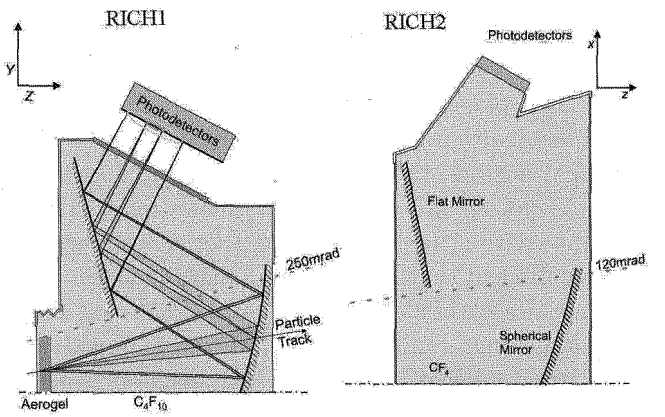

Fig. 1. The optical components of the (left) RICH1 and (right) RICH2 detectors. An example charged particle track is shown in the RICH1 detector to illustrate the way in which the two radiators operate in the same RICH detector.

LHCb requires separation of pions and kaons over a wide momentum range from 1GeV/c up to and beyond 100GeV/c. Owing to the performance limitations listed above there is a limited momentum range over which a radiator of a given refractive index can provide the required separation. LHCb uses three different radiators - silica aerogel (1-10GeV/c), C_4F_{10} gas (up to 60GeV/c) and CF_4 gas (up to and beyond 100GeV/c). The angular distribution of the particles of interest means it is not necessary for the CF_4 radiator to cover the entire LHCb acceptance. As a consequence the CF_4 radiator is contained in RICH2, downstream of the spectrometer magnet, covering a polar angle of about 100mrad, while aerogel and C_4F_{10} in RICH1 upstream of the magnet, cover the full acceptance.

The optical layout of both RICH detectors is similar and shown in Figure 1. In both detectors the Cherenkov cones produced in the radiators are focused using tilted spherical mirrors and reflected from plane mirrors onto photon detectors that are located outside the LHCb acceptance. In RICH1 the cones of light from the aerogel and C_4F_{10} gas radiators form concentric rings on the Hybrid Photon Detector (HPD) arrays. The two detectors share the pixel HPD[3] technology that was developed at CERN with partners in industry specifically for the LHCb RICH detectors.

4. RICH1

The design of RICH1[4] has been heavily shaped by the necessity to protect the HPDs from the fringe field of the LHCb spectrometer magnet, this has resulted in large iron shielding boxes above and below the RICH optics protecting the HPD planes. Between these shields the RICH optics shown in Figure 1 are held within an aluminium gas enclosure, this supports the flat and spherical mirrors, the aerogel radiator, the upstream and downstream particle windows and the quartz windows to the HPD planes. All of the components within the 250/300mrad (horizontal/vertical) LHCb acceptance are required to have a very low radiation length. This has led to the use of composite carbon fibre spherical mirrors that contribute only 1.5% of a radiation length and a carbon fibre and foam exit window.

RICH1 is currently being constructed. The magnetic shields, gas enclosure, mirrors, beryllium beampipe and acceptance windows have been installed, aligned and, where appropriate, leak tested. The outstanding tasks are to install the HPD planes above and below the gas enclosure and mount the quartz windows. The quartz windows and HPD electronics 'columns' are complete and ready to be installed and the mechanics required to support them is currently being prepared.

5. RICH2

Figure 1 demonstrates that the design of RICH2[5] is conceptually similar to that of RICH1, a gas radiator volume containing spherical focussing mirrors and flat mirrors taking the HPD planes beyond the LHCb acceptance. The major difference between the detectors is their scale. RICH2 is much larger, requiring a very stiff aluminium superstructure to rigidly hold the optical components in place. The downstream position of RICH2 reduces the effect of any scattering on the performance of LHCb allowing glass substrate mirrors to be used. The RICH2 spherical mirrors each comprise 21 hexagonal

segments and the flat mirrors 20 rectangular ones. The upstream and downstream acceptance windows were technically challenging to produce due to their size and the low scattering requirement. They were manufactured as carbon fibre and aluminum skinned foam sandwiches respectively.

RICH2 has been completed and is undergoing commissioning. The HPD planes have been successfully read out and control systems are currently being developed. RICH2 is the first LHCb sub-detector ready to be integrated into the LHCb global data aquisition system.

6. Hybrid Photon Detectors

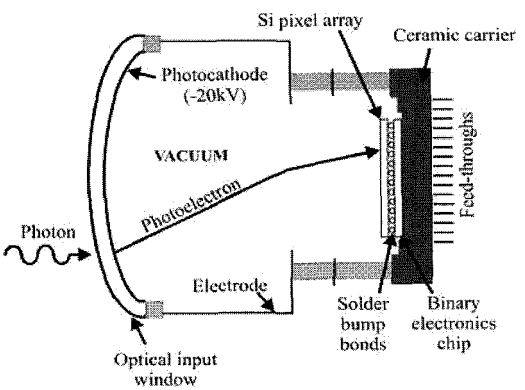

Fig. 2. A schematic cross-section of an HPD. Showing the path of a photon detected by the device and the design of the HPD itself.

Both RICH detectors use the Hybrid Photon Detector developed at CERN in partnership with Photonis-DEP. These photo-tubes provide a pixel size of 2.5×2.5mm with single photon sensitivity, operate at the LHC rate of 40MHz and have a signal to noise ration of 50:1. They operate, as shown in Figure 2, by accelerating a single photoelectron in a 20kV electrostatic field and detecting it with a pixelated silicon sensor. The sensor chip is bump-bonded[6] directly to a read out chip and both are encapsulated within the vacuum of the photo-tube itself. The tube has a quartz window to increase its UV sensitivity and an S20 multialkali photocathode. The production and initial testing of the 484 HPDs required for the RICH photon detector planes is now complete. The HPDs and the necessary power

and readout electronics have been mounted on columns that allow them to be hexagonally close packed to form the photon detector planes. All RICH1 and RICH2 columns have been mounted and tested and the RICH2 columns have been installed.

7. Projected Performance

The performance and read-out chain of the HPDs has been verified in experiments in charged particle beams.[7] This information informs our Cherenkov ring reconstruction simulations that currently predict the particle identification performance for pion and kaon identification is adequate for the physics program of LHCb.

8. Conclusions

The RICH system plays a vital part in the physics program of LHCb, providing light hadron identification unavailable to the other LHC experiments. The wide momentum coverage requires three Cherenkov radiators housed in two detectors RICH1 and RICH2. RICH1 contains silica aerogel and C_4F_{10} gas radiators and is nearing completion. RICH2 contains a CF_4 gas radiator and is undergoing commissioning. Both detectors use HPDs to provide a large pixelated area of single photon sensitivity. The production of the HPDs is complete. Simulation based on tests of the systems indicate the performance of the RICH detectors will meet the needs of LHCb. We look forward to taking data in 2008.

References

1. The LHCb Collaboration, *"LHCb RICH Technical Design Report"*, CERN LHCC 2000-037, September 2000.
2. The LHCb Collaboration, *"LHCb Reoptimised Detector Design and Performance Technical Design Report"*, CERN LHCC 2003-030, September 2003.
3. M. Campbell, F. Formenti, T. Gys, W. Snoeys and K. Wyllie, *"Development of pixel hybrid photon detectors for the RICH counters of LHCb"*, LHCb-98-035, January 1998.
4. The LHCb Collaboration, *"LHCb RICH1 Engineering Design Report"*,LHCb-2004-121, October 2005.
5. The LHCb Collaboration, *"LHCb RICH2 Engineering Design Report"*,LHCb-2002-009, March 2002.
6. M. Campbell *et al.*, IEEE Trans. Nucl. Sc. **53** (2006) 4, pp. 2296-2302.
7. M. Adinolfi *et al.*, NIM A **574**, (2007) 1, pp. 39-49.

Latest results from a mass–production sample of MRPCs for the ALICE TOF detector

A. Akindinov[a], A. Alici[b,c], P. Antonioli[c], S. Arcelli[b,c], M. Basile[b,c], G. Cara Romeo[c], L. Cifarelli[b,c], F. Cindolo[c], A. De Caro[d], D. De Gruttola[d], S. De Pasquale[d], M. Fusco Girard[d], C. Guarnaccia[d], D. Hatzifotiadou[c], H.T. Jung[e], W.W. Jung[e], D.S. Kim[e], D.W. Kim[e], H.N. Kim[e], J.S. Kim[e], S. Kiselev[a], G. Laurenti[c], K. Lee[e], S.C. Lee[e], M.L. Luvisetto[c], D. Malkevich[a], A. Margotti[c], R. Nania[c], A. Nedosekin[a], F.Noferini[c,f], P. Pagano[d], A. Pesci[c], R. Preghenella[b,c], G. Russo[d], M. Ryabinin[a], E. Scapparone[c], G. Scioli[b,c*], A. Silenzi [b,c], R. Silvestri[d], Y. Sun[g], M. Tchoumakov[a], K. Voloshin[a], M.C.S. Williams[c], B. Zagreev[a], C. Zampolli[c,f], A. Zichichi[b,c,f]

[a] *Institute for Theoretical and Experimental Physics, Moscow, Russia*
[b] *Dipartimento di Fisica dell'Università, Bologna, Italy*
[c] *Sezione INFN, Bologna, Italy*
[d] *Dipartimento di Fisica dell'Università and INFN, Salerno, Italy*
[e] *Department of Physics, Kangnung National University, Kangnung, Republic of Korea*
[f] *Museo Storico della Fisica e Centro Studi e Ricerche "Enrico Fermi", Roma, Italy*
[g] *World Laboratory, Lausanne, Switzerland*

The double–stack MRPC (Multigap Resistive Plate Chamber) strip is the basic element of the ALICE Time–Of–Flight (TOF) detector. A test of a sample of MRPC strips randomly chosen from two years of mass production (the TOF is made of 1638 strips) was carried out during the autumn of 2006 at the CERN Proton Syncrotron facility. In this paper the most relevant results on the performances of the MRPCs will be presented. The results confirm that these devices have a very good uniformity of response, a long streamer–free plateau, an efficiency higher than 99% and an "intrinsic" time resolution better than about 40 ps.

Keywords: MRPC, mass–production, efficiency, time resolution, uniformity

*Corresponding author G.Scioli, Physics Department Bologna, scioli@bo.infn.it

1. The ALICE Time–Of–Flight system

ALICE (A Large Ion Collider Experiment)[1] will study Pb–Pb collisions at a centre–of–mass energy of 5.5 TeV per nucleon pair. The purpose of this experiment is to investigate the behaviour of the nuclear matter at extreme densities and temperatures focalizing the attention on the QCD phase transition of nuclear matter into a deconfined state of quarks and gluons: the QGP (Quark Gluon Plasma) state.

In this scenario the particle identification is fundamental to study the QGP. The event–by–event hadron identification will allow to measure with high statistics the shape of p_t distributions and the $\pi/K/p$ ratio which can be used to probe the nature and dynamical evolution of the system produced in ultra–relativistic heavy–ion collisions at LHC energies.

The ALICE Time–Of–Flight (TOF) system[2] provides the charged particle identification in the intermediate momentum range (from 0.5 to a few GeV/c) and in the central pseudo–rapidity region ($|\eta| < 0.9$).

The TOF covers a cylindrical surface of polar acceptance $|\theta - 90°| < 45°$ and full coverage in the azimuthal angle ϕ. The inner radius of the TOF is 3.70 m from the interaction point. The whole system is divided into 18 SuperModules (SM) in ϕ; each SM is composed of 5 different modules.[3]

In particular the TOF has to cover an area of $\sim$ 150 m^2 and has to be highly segmented in order to keep the occupancy in Pb–Pb collisions below the 15% level, with a few 10^3 primary charged particles produced per unit of rapidity. In order to satisfy these requirements 157248 independent readout pads of size 2.5×3.7 cm^2 are needed and as the basic unit of the TOF system the double–stack Multigap Restive Plate Chamber (MRPC[3]) was chosen. These chambers, built with a strip geometry (120×7.4 cm^2 active area), are placed inside the modules (19 MRPCs for the outer and the intermediate modules and 15 for the central one) overlapped by 2 mm along the longitudinal edge of their active area and progressively tilted with respect to the axis of the cylinder. This is to avoid dead areas and to minimize the number of very oblique transversal paths, respectively.

2. Experimental results

During the last two years the MRPCs mass production was carried out in the INFN TOF laboratories in Bologna. To simplify, automate and speed up the MRPC assembly, a series of procedures were developed.[4] A test of a sample of 10 MRPCs randomly chosen from the 1638 ones of the mass production was carried on during the autumn of 2006 using the final

electronic chain from the front-end card with the NINO-ASIC[5] to the readout modules with the HPTDCs.[6]

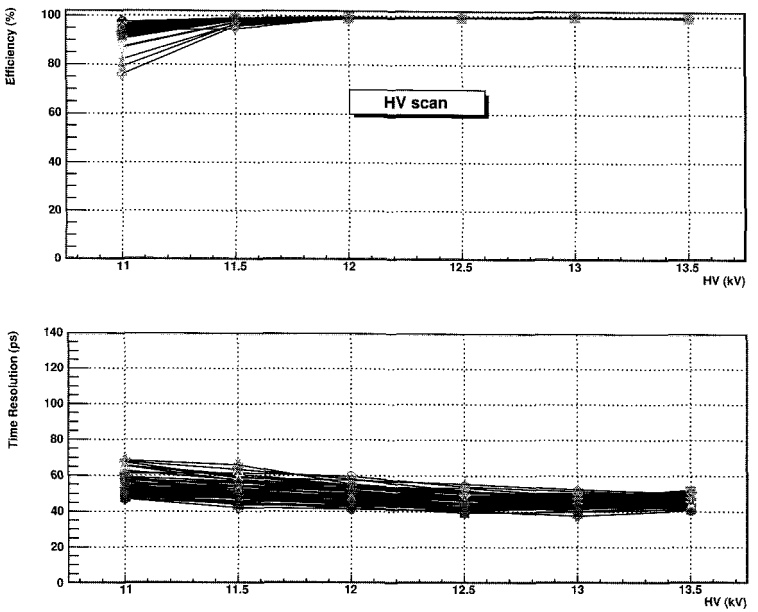

Fig. 1. Efficiency and time resolution as a function of the applied voltage for 55 readout pads randomly distributed on 10 MRPCs.

The tests were performed in the experimental area located at the PS-T10 beam line of the CERN Proton Syncrotron. The experimental set-up consisted of: *(i)* two fast scintillator bars ($2 \times 2 \times 10\ cm^3$), each equipped with two photomultipliers to provide an accurate time reference; *(ii)* two pairs of crossed scintillators, whose coincidence defines a 1 cm^2 area and provides the trigger; *(iii)* a device under test, i.e. an aluminium box (external dimensions of $19.5 \times 48 \times 129\ cm^3$) with 5 MRPCs. A mechanical frame was used to move the box with relative millimetric accuracy. This allowed to position the beam on different readout pads by remote control.

The aluminium box was filled with the MRPC standard gas mixture: 90% $C_2F_4H_2$, 5% SF_6, 5% C_4H_{10}.

The uniformity of response of the chambers was studied first by centering the beam on many different readout pads, randomly distributed along

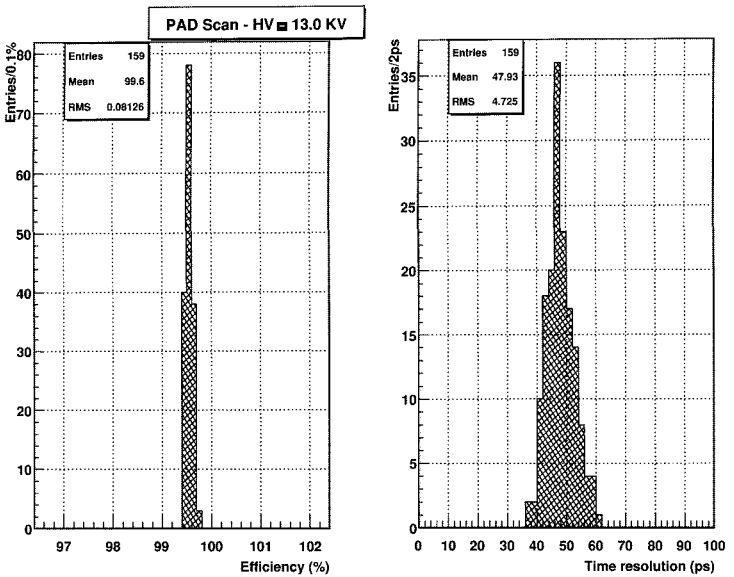

Fig. 2. Efficiency and time resolution distributions for 159 readout pads at a fixed voltage of 13.0 kV.

each MRPCs. The efficiency and time resolution as a function of the applied voltage for 55 channels belonging to the 10 MRPCs are shown in Fig. 1. It should be noted that in the HV range between 12.0 and 13.5 kV, the mean efficienty is higher than 99% and the mean time resolution is 50 ps. This means a very good uniformity and a long streamer–free plateau.

Then a scan over 159 readout pads was performed by fixing the high voltage value to 13.0 kV. The results are plotted in Fig. 2 where the efficiency (on the left) and the time resolution (on the right) are presented. As it can be seen the mean efficiency is 99.6% and the time resolution is about 48 ps. The RMS of the time resolution distribution (4.7 ps) gives an estimate of the uniformity of the devices.

To conclude, the strip B19, produced and tested at PS in 2004,[3] was tested again in 2006. This MRPC was used as reference in the cosmic ray telescope in Bologna continuosly running since 2 years. As it can be noted in Fig. 3 the detector's response was not affected by a so long "ageing" process.

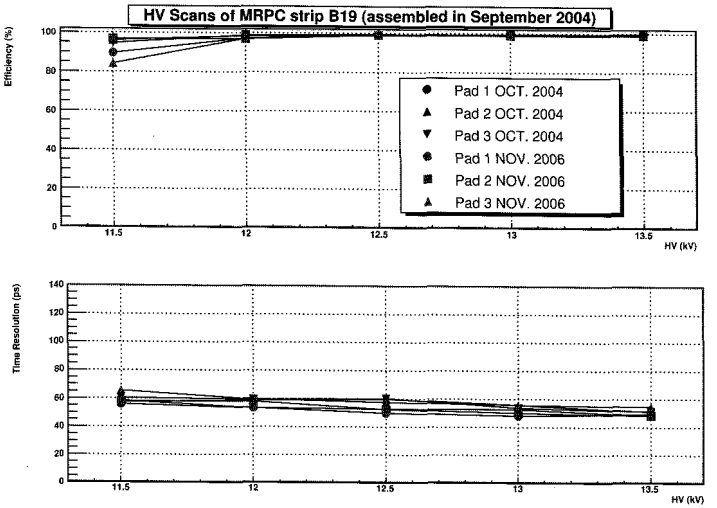

Fig. 3. Efficiency and time resolution for the MRPC B19 used as reference in the cosmic ray telescope in Bologna.

References

1. ALICE Collaboration, ALICE: Physics Performance Report, Volume I, J. Phys. G: Nucl. Part. Phys. 30 (2004) 1517–1763 and Volume II, J. Phys. G: Nucl. Part. Phys. 32 (2006) 1295–2040.
2. ALICE Collaboration, Technical Design Report of the Time–Of–Flight Detector CERN/LHCC/2000-12; Addendum CERN/LHCC/2002-16.
3. A. Akindinov et al.: The MRPC detector for the ALICE Time Of Flight system: Final design and performances, Nucl. Phys. Suppl. 158 (2006) 60–65.
4. A. Akindinov et al.: Quality assurance procedures for the construction of ALICE TOF detector, Nucl. Phys. Proc. Suppl. 158 (2006) 78–82.
5. F. Anghinolfi, P. Jarron, F. Krummenacher, E. Usenko, M.C.S. Williams: NINO: An Ultrafast Low-Power Front-End Amplifier Discriminator for the Time-of-Flight Detector in the ALICE Experiment, IEEE Transactions on Nuclear Science, Vol.51, No.5, October 2004.
6. A.V.Akindinov et al.: Design aspects and prototype test of a very precise TDC system implemented for the Multigap RPC of the ALICE-TOF, Nucl. Instrum. Methods, A533 (2004) 178-182.

FAST TIMED ACTIVE SHIELD FOR A GAMMA-RAY SPECTROMETER

NATAŠA TODOROVIĆ,
Department of Physic, Faculty of Sciences, University of Novi Sad, Trg D. Obradovića 4, 21000 Novi Sad, Serbia

DUŠAN MRĐA, IŠTVAN BIKIT, SOFIJA FORKAPIĆ, JAROSLAV SLIVKA, MIROSLAV VESKOVIĆ
Department of Physic, Faculty of Sciences, University of Novi Sad, Trg D. Obradovića 4, 21000 Novi Sad, Serbia

The operational problems of the gamma ray spectrometer shielded passively with 12 cm of lead and actively by five 0.5 m x 0.5 m x 0.05 m plastic veto shields are described. In the present paper we describe the new results of our ground based actively shielded extended range low level gamma spectrometer emphasizing the anticoincidence timing details which are unavoidable for the proper operation of the system After the new adjustment of active shield germanium system, total count rate in anticoincidence background spectrum was 0.38 c/s (50 keV-2 MeV), the achieved reduction factor with respect to the passively shield background spectrum is 2.42. The 511 keV reduction factor is 4.25.

1. Introduction

The fundamental aim of an active shield system is to eliminate the (mainly cosmic muon induced) background without loss of events from sample. Many researchers have described their active shield techniques [2, 3, 4, 5] , not mentioning the task of sample count losses and the timing set up. Moreover, for similar experimental configurations [5, 6], very different background reduction factors ~~(~~5 and 1.4, respectively~~)~~ are reported.

Cosmic and environmental gamma radiation interacted with both veto and germanium detectors generate coincident pulses which enable the rejection of the germanium events ~~by~~ with an anticoincidence circuit.

In the present paper we describe the new results of our ground based actively shielded extended range low level gamma spectrometer and compared with the values obtained in [1].

2. Experiment

On Figure 1 the schematic view of the gamma-ray spectrometer system is presented. The passive shielding is made of 120 mm thick low-active lead. The cylindrical passive shield with wall thickness has outer diameter of 41cm matching the inner dimensions of the "cube" of plastic scintillators (Fig. 1.). This thickness is less than the recommended thickness of 15 cm [7], but similar to the thickness reported by [6]. The ^{210}Pb content of the lead shield is measured [8] to be 25±5 Bq/kg. Monte-Carlo calculations by the "Photon" code [9] have been

performed in order to select the most appropriate material and the optimal thickness for the inner lining. It is found that Sn is more appropriate than the most frequently used Cd due to lower probability of neutron capture. The $^{113}Cd(n, \gamma)^{114}Cd$ reaction results in a prominent background peak at 558.2 keV and a lesser peak at 651 keV. Additional advantage is that Sn is not a toxic metal. The optimal thickness of Sn is found to be 3.5 mm. The Sn X-rays are reduced by 0.5 mm of Cu. The results confirmed that this solution is better than the use of thick copper layers which increase the background continuum [10]

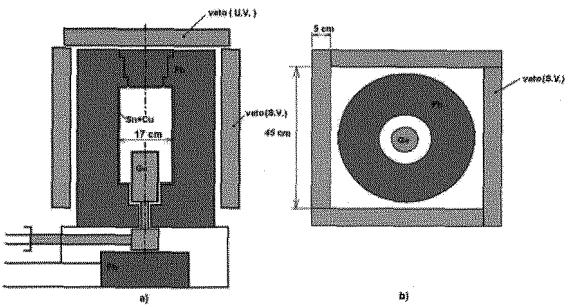

Figure 1. Vertical cross section (a) and horizontal cross section (b) of the passive and active shield

The germanium detector was the low background extended range (GMX) closed-end coaxial p-type, made by ORTEC corp. in a J type cryostat. The nominal relative efficiency is 36%, and due to the thin surface dead layer and the Be window it has a good efficiency even at 10 keV. The chamber inside the passive shield was flushed by nitrogen evaporating from the Dewar vessel. The integral count rate of the passively shielded detector, in the energy range of 50-1800 keV, is 0.9 c/s. This is a very good value for the ground based passive shield. Plastic scintillator detectors (type R500*50 N 500) made by SCIONIX (Netherlands) were arranged to surround the top (U.V .-upper veto) and four sides of lead shielding (S.V.- side veto). The active shielding consists of 5 plastic scintillators (0.5 m x 0.5 m x 0.05 m). The photomultipliers from all veto detectors have slow and fast (spectroscopic) outputs. The most probable dE/dx value for the cosmic muons in such a detector is about 10 MeV, which is sufficient to separate the pulses from cosmic radiation and environmental background (which ends at 2.6 MeV). The cosmic rays and environmental gammas interacting with both the veto detector and the Ge detector produce coincident pulses which will reject the appropriate GMX event by an anti-coincidence circuit [11] .

Using a computer controlled multichannel analyzer (MULTIPORT II module) with four irrespective internal ADC and GENIE 2000 CANBERRA softer, the investigation of anticoincidence mode of veto detectors and Ge-spectrometer-with respect to earlier settings [1] were done.

Also, in electronic circuit of plastic scintillators the fast amplifier (TFA) was added. The schematic view of the anticoincidence circuit, after this modification, is shown of Fig 2.

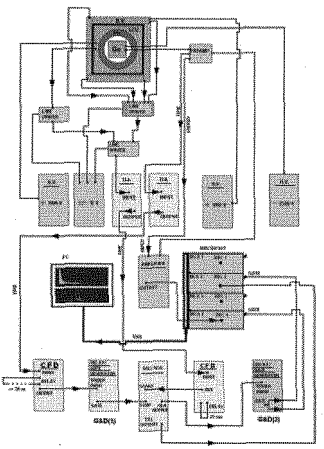

Figure 2.The electronic scheme of active shield Ge-spectrometer (yellow colour indicates the fast electronic circuit branch). TFA-timing filter amplifier, H.V.-high voltage, P.S.-power supply, MCA –multi channel analyzer, ADC –analogue digital converter, CFD-constant fraction discriminator, G&D-gate and delay generator, TAC/SCA-time to amplitude convector/single channel analyzer

In order to perform a detailed investigation of the delayed events contribution to the background gamma-spectrum, the adjustment of gain and pulse shape on the fast amplifier (TFA) in a veto detector branch and Ge detectors branch was done. The appropriate delay cable is inserted into a constant fraction discriminators (CFD) of germanium and plastic scintillators (length 20 m to CFD of Ge and 0.25 m to CFD of plastic veto). The precise «walk» adjustment on both discriminators was done. The TAC range set to 10 μs. In order to get the proper position of the true coincidence peak in the time spectrum, the signals from GMX detector are delayed by 1.1 μs (with the G&D(1)), relative to the signals from the plastic scintillatorrs.

The energy threshold of CFD (CFD was at constant fraction mode) for the GMX detector was set up to reject the events with energy less than 30 keV. For the plastic veto detectors the energy threshold was set at 3 MeV (higher than the environmental gamma-energy, but much less than the maximum deposited muon energy in plastic at 10 MeV). Thus only muon induced events were rejected with the new setup.

3. Experimental results

The time resolution of the system was considerably improved, Fig 3., with respect to [1]. The first peak of the double peaked time spectrum comes from saturated signals in the GMX TFA.

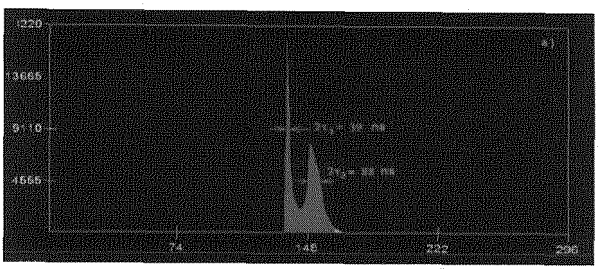

Figure 3. The background time spectrum, 9.8 ns/~~chn~~ ch (TAC range 10 μs, number of channels 1024)

After the new adjustment of the active shield germanium system, the total count rate in the anticoincidence background spectrum was 0.38 c/s (50 keV-2 MeV), the achieved reduction facto with respect to the passively shielded background spectrum is 2.42, and for first test this value was 3.03, Fig 4. The reduction factor for 511 keV is 4.25, whereas this factor was 3 in [1].

4. Test of the count rate losses with a source

We tested the count loss of our gamma spectroscopy system by the cylindrical sample of rough phosphate (m= 182,4 g , h=31 mm, d = 67 mm) in contact geometry with the Ge detector. The activity concentration of radio nuclide radium was A(^{226}Ra)= 700 ± 30 Bq/kg, and the activity of radium (with respect to the mass) was A= 130 ± 6 Bq . The total count rate with this sample in direct phosphate spectrum was 24.5 c/ s (50 keV - 2 MeV), and in anticoincidence spectrum was 24.0 c/s, and it was a value 27 times larger than the passively shielded GMX background count rate. The dead time in the anticoincidence phosphate spectrum was 0.06 %, the same value as for the direct phosphate spectrum.
Comparison of anticoincidence and direct spectra, Fig. 5, shows that there are no count losses with the source in anticoincidence mode.

According to these results it could be concluded that in the new setting up there are no count losses in source spectrum, which is significantly improved relatively to [1], where the source losses reach 20%. However, the integral counts reduction factor in the anticoincidence background spectrum with respect to the passive shield background spectrum is less (value 2.42) than the earlier

value (3.03) Although, the reduction of the annihilation line (~ 4.5) is worse than in [1] (~ 7). A possible explanation of these results is probably the impossibility to respond of MULTIPORT ADCs conversion circle delay, beginning after signals arrived, because of timing «bypass» gate and ADC signals.

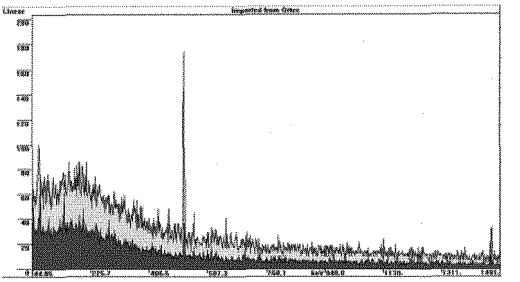

Figure 4 Background spectra compared: upper spectrum without active shield and lower spectrum with active shield.

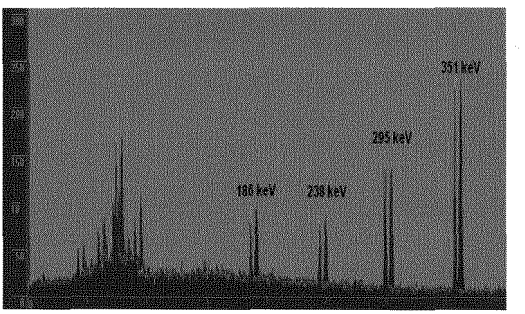

Figure 5 Low-energy region of phosphate spectrum of direct and anticoincidence spectrum (comparative view). The direct spectrum was shifted in right side in respect to the anticoincidence (for peak intensity comparison)

Acknowledgements

The authors acknowledge the financial support of the Ministry of Science of Republic of Serbia (project: Nuclear spectroscopy and rare processes, Number 141002B).

References

1. D. Mrđa, I. Bikit, N. Žikić-Todorović, S. Forkapić, J. Slivka, M. Vesković, First tests of the active shield for a gamma ray spectrometer, *Radiation Measurements* **42** (2007) 1361-1367.
   Hamajima,Y., Komura, K., 2004. *Appl. Radiat. Isot.* **61** 179.
2. Byun, J. I., Choi,Y. H., Kwak, S. I., Hwang, H. Y., Chung, K. H., Choi, S.
3. Park, D. W., Chang, W. L., 2003. *Appl. Radiat. Isot.* **58** 579.
4. Povinec,.P..P., Commanducci, J-F., Levy-Palomo, I., 2005. *Journal of Radioanalyitical and Nuclear Chemistry*, Vol. **263** 441.
5. Pointurier, F., Laurec, J., Blanchard, X., Adam, A., 1996. *Appl. Radiat. Isot.* **47**, 1043.
6. Hurtado, S., Garcia-Leon, M., Garcia-Tenorio, R., 2006. *Appl. Radiat. Isot.* **64** , 1006.
7. Nunez-Lagos, R., Vitro, A., 1996. *Appl. Radiat. Isot.* **47** 1011.
8. Slivka, J., Mrdja, D.,Varga, E. and Veskovic, M. , 2005. *Proceedings of the 49th Conference of ETRAN, Budva, Serbia and Montenegro 2005,* edited by Milosevic, M., Jaksic, Z., Bozic, D., and Potkonjak, V. Belgrade **56.**
9. Puzovic, J., Anicin, I., 1998. *Nucl. Instr. and Meth. in Phys. Res.* A **414** 279.
10. Vojtyla, P., Povinec, P., 2000. *Appl. Radiat. Isot.* **53** 185.
11. Heusser, G., 1994. Background in ionizing radiation detection – illustrated by Ge-spectrometry, Proceedings, World Scientific Singapore, pp. 16-28.

Test results of the ALICE-HMPID detector commissioning

G. VOLPE

Istituto Nazionale di Fisica Nucleare, Sezione di Bari,
Via E. Orabona 4, 70126 Bari, Italy
**E-mail: giacomo.volpe@ba.infn.it*

on behalf of the ALICE-HMPID collaboration

The ALICE High Momentum Particle Identification Detector (HMPID) consists of seven identical proximity focusing RICH counters. It covers in total 11 m^2, exploiting large area CsI photocathodes for Cherenkov light imaging. The detector is installed in the ALICE solenoid, ready for the data acquisition. By means of the Detector Control System, the Front-end (FEE) and the Readout (R/O) electronics, the MWPC high voltages, the cooling and the gas system have been tested. The HMPID module gas pressure, temperature, current and voltage trends have been monitored and archived in the ORACLE database. In this paper a comprehensive review on the test results is presented.

Keywords: LHC, HMPID, Detector Control System.

1. High Momentum Particle Identification Detector

The ALICE-HMPID detector[1] is dedicated to the identification of charged hadrons produced by Pb-Pb and p-p collisions at LHC. It consists of seven identical proximity focusing RICH counters, exploiting large surface CsI pad-segmented photocathodes, coupled with a MWPC, to detect Cherenkov photons, produced in the radiator (C_6F_{14}). The gas used in the MWPCs is CH_4.

2. HMPID - Detector Control System

The HMPID Detector Control System (DCS) has been implemented in the PVSS SCADA system[2] using the FW components[3] developed at CERN in the context of the JCOP project.[4] The HMPID DCS allows the detector operation via both the detector and device oriented views. The detector oriented view is built with software finite state machines (FSM) modeling the detector behavior. It allows the automatic operation and the detector integration in the general ALICE DCS. On the other side, DCS device oriented provides also the manual control down to the single device. This view resulted very useful during the detector commissioning activities. The DCS user interface (UI) is shown in the right panel of Fig. 1. It

has been developed by the HMPID group and adopted as standard UI in the ALICE DCS context. For each detector module, six subsystems are integrated and controlled:

- High Voltage (HV);
- Low Voltage (LV);
- C_6F_{14} Liquid Circulation System (LCS);
- physical parameters (e.g. temperature, pressure);
- cooling system;
- gas System;
- C_6F_{14} transparency measurement system.

By means of the DCS it is possible to control and to monitor, by remote stations, power-on power-off cycles, voltage, current, temperature and pressure trends. The monitored parameters values are archived in the ORACLE database to complement the physics data during the offline analysis. Since July 2007 the detector is fully powered on and remotely controlled. The DCS project is running on the production computers installed on the ALICE DCS network. Long term tests of the HMPID subsystems have been started and now are still underway. In the following a summary of these activities is provided.

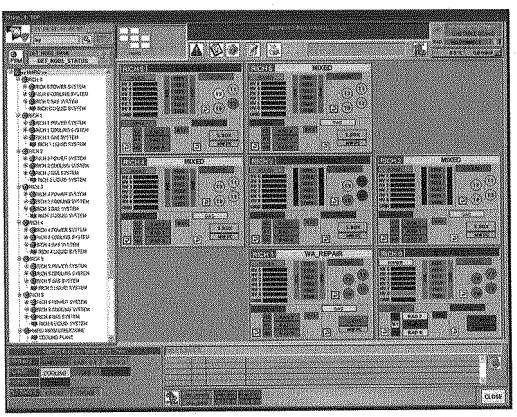

Fig. 1. DCS user interface.

3. High Voltage and Low Voltage systems

The High Voltage and Low Voltage systems provide power to the MWPCs, Front-end (FEE) and Readout (R/O) electronics, respectively. Each HMPID module is divided in six high voltage sectors. In this way a sector failure does not prevent the MWPC operation. During the normal run operation of the detector, the MWPC

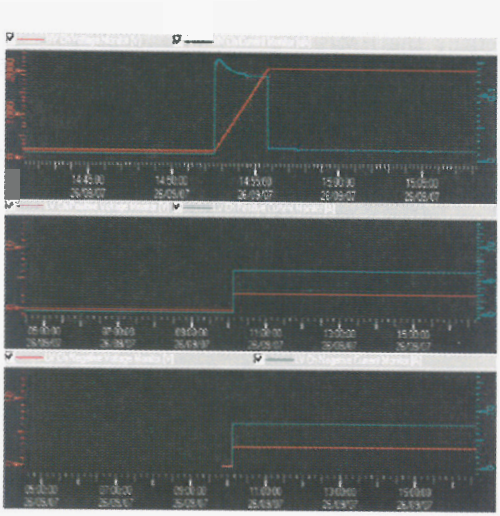

Fig. 2. **voltage** (red line) and current (blue line) vs time relative to HV (upper one) and LV channels.

high voltage values will be set at 2000-2150 V to get optimal photons detection efficiency. Each HMPID module is provided by six FEE sectors and by two R/O channels (right and left). One FEE sector is power by two LV channels (negative and positive). The normal operation values of voltage and current are 2.8 V for all FEE channels, 7.5 A for positive, 6.3 A for negative. For the two R/O channels, they are set to 5 V and in the range 12 - 13 A, respectively. By means of dedicated panels, operations of switch-on and switch-off and value settings are executed. Voltage and current trends are provided via dedicated panels. In Fig. 2 the values of voltage (red line) and current (blue line) of one HV MWPC sector (upper one) and of one LV sector (positive and negative) vs time are shown. The plots refer to one sector rump-up cycle during the switch-on of the detector. In the case of the HV, at the linearly increasing of the voltage, according to the RC circuit (cables + detector) behavior, corresponds an almost constant value of the current.

4. Cooling System

The FEE and R/O electronics dissipate about 350 W per module. Since the electronics is housed in a protective aluminum box, to prevent over-temperature the cooling system removes the dissipated heat. For each HMPID module four values of temperature are monitored. Two of them concern the MWPC aluminum frame, two the gas (argon) contained in the protective box, where the electronics is housed. In Fig. 3 the temperatures of the gas (green and yellow) and of the frame (blue and red) are shown. The initial increasing of the temperatures corresponds to the switch-on of the FEE and R/O electronics, while the temperature decrease is caused by a power-off cycle. Once the electronics is powered-on, the gas temperatures increase faster then the others, due to his smaller thermal

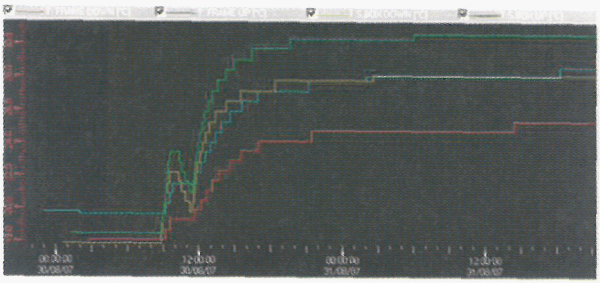

Fig. 3. Left: temperature in °C as a function of time.

capacity. Because of the presence of the cooling system, with a time constant of some hours the temperatures reach a constant value, of course lower than any harmful limit for the electronics. On these temperatures hardware and software interlocks protect the electronics against temporary failure of the cooling system. In this case the LV is switched-off on the entire module.

5. Gas System

The gas system provides the circulation of CH_4 in the MWPCs and of argon in

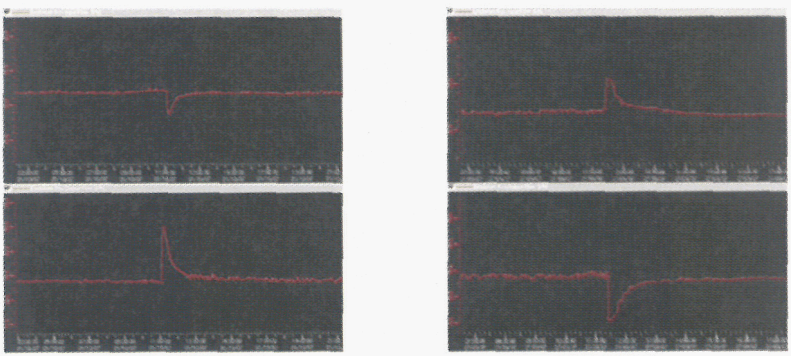

Fig. 4. argon inlet and outlet flows in enclosure box during one power-on (left) and power-off (right) cycle.

the enclosure boxes, where the electronics is housed. By means of the DCS, the values of the inlet and outlet gas flows are monitored along with the MWPC and enclosure box pressures. Software interlocks on these values ensure a protection system against overpressures. Fig. 4 shows the values of the incoming (up) and outgoing (down) argon flows vs time, relative to one module powering-on (left) and powering-off (right) cycle, respectively. The gas expansion due to the

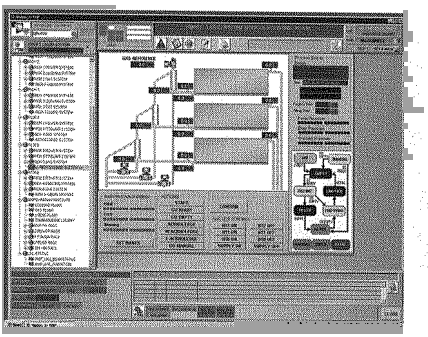

Fig. 5. liquid circulation system panel.

electronics power-on, results in a temporary decreasing of inlet gas flow and increasing of the outlet one. The opposite trend occurs during the gas contraction due to the gas cooling on the electronics power-off. Inlet and outlet flows reach normal values when gas thermodynamic equilibrium is restored.

6. Liquid Circulation System

The Liquid Circulation System (LCS) provides the circulation of C_6F_{14} liquid Cherenkov radiator in the seven modules of the HMPID. The liquid for each module is contained in three different vessels. By means of the DCS, pressure and temperature values of C_6F_{14} are monitored. Figure 5 shows the DCS panel of the liquid system, it corresponds to one detector module. The radiator containers and all the values are displayed.

7. Conclusion

On July 2007 the HMPID operation via the DCS has been successful carried out. Since then the entire system stability is monitored and the alarm-interlock thresholds are tuned. The archiving and retrieving of hundreds of parameters in the ORACLE database has proved to be an effective strategy if huge amount of data has to be managed. Nevertheless, to avoid that LSB fluctuation od ADCs on the parameter monitoring is in vain archived, smoothing algorithm are implemented. The HMPID detector is already installed in the ALICE solenoid ready to take data at LHC at CERN.

References

1. HMPID TDR: CERN/LHCC 98 - 19, ALICE TDR1, 14 August 1998.
2. http://itcobe.web.cern.ch/itcobe/Services/Pvss.
3. http://itcobe.web.cern.ch/itcobe/Projects/Framework/welcome.html/.
4. http://itco.web.cern.ch/itco/Projects-Services/JCOP.

Astroparticle and Underground Experiments

Organizers:

A. Capone
R. Wischnewski

C. Bozza	Nuclear Emulsion Scanning in OPERA: Methods and Results
M. Brinet	CHERCAM: a Cherenkov imager for the CREAM experiment
C. Corda	Gravitational waves from the R^1 high order theory of gravity
A.S. Cucoanes	The Double Chooz Experiment
M. Doro	Technical Solutions for the MAGIC Telescope
F. Ferroni	Challenging the Neutrino Mass with CUORE
L. Foggetta	A Modular DAQ System for Next Generation Bolometric ν Mass Experiments
E. Fokitis	Novel Techniques for Atmospheric Monitoring for EAS Detectors using High Resolution Spectroscopy
E. Fokitis	A Fluorescence /Air Cherenkov Telescope Prototype in Greece: Possibility to detect Escaping Taus from Helmos Mountain in Greece.
M. Giorgini	Search for Massive Rare Particles with the SLIM Experiment
C.-C. Hsu	PMT Characterization for MAGIC II Telescope
S. Kraft-Bermuth	Determining the Neutrino Mass with a Calorimetric Low-Temperature Detector - The Experiment MARE
P. Lombardi	The Borexino Detector: Construction and Performances
S. Maltezos	Design of a Wide Spectral Range and High-Resolution Spectrograph for Monitoring the Night Sky Background for Use in Air Fluorescence Telescopes
G. Matthiae	The Auger Experiment Status and Results
M. Pellicciari	Preliminary Results on Neutron Background induced by Muons in a Shallow Underground Laboratory: Baradello Underground Laboratory in Como
G. Riccobene	Acoustic Detectors in Submarine Large Scale Detectors
F. Salesa	Search of Point-like Sources with the ANTARES Neutrino Telescope
U. Schmitt	A tritium activity monitor for the KATRIN Experiment

M. Taiuti	Optical Module for Deep-sea Neutrino Telescopes
C. Timmermans	Radio detection of Cosmic Rays at the Pierre Auger Observatory
U. Ugolino	The Monitor online system of the OPERA muon magnetic spectrometer
L. Vála	Results from the NEMO 3 Experiment
J. Vogel	Search for Solar Axions with the CAST-Experiment
A.V. Zablotsky	Data Acquisition System for the Tunka-133 Array
D. Zaborov	Status report on the ANTARES project

NUCLEAR EMULSION SCANNING IN OPERA: METHODS AND RESULTS

CRISTIANO BOZZA
for the OPERA Collaboration
Dept. of Physics, University of Salerno and INFN, Via S. Allende, Baronissi (Salerno), 84081, Italy

The design of the OPERA experiment was also motivated and justified by the revival of nuclear emulsion handling and scanning in a modern, automatic fashion, as it took previously place, although at a smaller scale, for the CHORUS experiment. Nuclear emulsions are still the only detector to allow a very detailed topological study of an interaction / decay vertex at the sub-micrometer level. They are most suitable in experiments where topology is a non-ambiguous signature of a certain class of events. This is for instance the case of neutrino oscillation detection and measurement by the study of a tau-appearance signal.
The design and performance of the two different scanning systems used in OPERA (ESS and S-UTS) are discussed. Their unique features in terms of speed, precision, background suppression, particle identification, and kinematical reconstruction are shown in close connection with the technical details that make them possible. Unequalled precision, almost vanishing background, and a wealth of information about each single event are the results presented.

1. The ECC technique in OPERA

One way to detect and measure neutrino oscillation in an appearance experiment is to observe the characteristic topological signature of ν_τ CC events in an originally pure ν_μ beam. Assuming δm^2 about 2.5×10^{-3} eV^2, and a beam energy spectrum suitable for ν_τ CC interactions (CNGS: <E>~17 GeV, ν_τ CC threshold ~ 3.4 GeV), the typical flight length of a τ before decay is of the order of 1 mm. A sketch of the interaction topology in OPERA [1] is given in Fig. 1, with a typical τ decay chain (BR: ~18%).

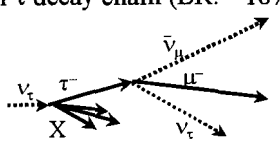

Figure 1: Tau decay topology. The dotted lines mark paths of neutral particles; the solid lines mark paths of charged particles (visible in emulsion).

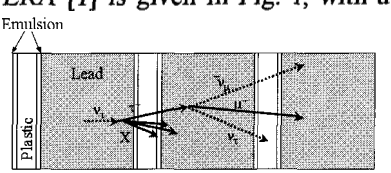

Figure 2: three consecutive cells of ECC used in OPERA. The neutrino beam is orthogonal to the plates (typical setup for automatic scanning; plates used to be parallel to the beam in manual scanning).

In order to produce high statistics in a neutrino beam of a long baseline experiment, dense material such as lead as a passive target material is mandatory. In the ECC (Emulsion Cloud Chamber) technique, plates of heavy material are interleaved with nuclear emulsion plates. OPERA uses lead plates, each 1 mm thick, as a target, and emulsion plates with a central transparent plastic foil, 205 μm thick, coated with 43 μm emulsion layers on both sides as a tracking device. Figure 2 shows the τ production-decay chain in the OPERA ECC.

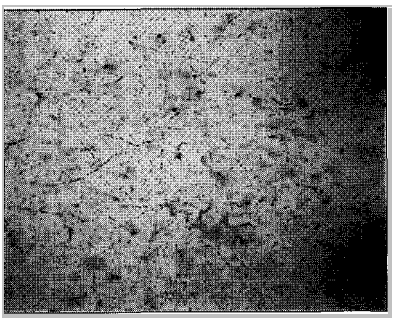

Figure 3: Emulsion image (390×310 μm^2). Black dots are particle track grains or "fog" grains (result of the chemical process of development, not of physical processes).

Topological reconstruction makes sense if particle tracks are well separated along typical path lengths. Detector precision of the order of 1 μm or better is mandatory to use topological signature. The choice of nuclear emulsion as a 3D tracking device arises naturally from this need. Ionising particles in emulsion sensitise AgBr crystals interspersed in a passive gel; after emulsion development, the sensitised sites act as crystallisation nuclei for grains of metallic Ag, seen as spots (0.6 μm diameter) aligned along particle paths (tracks). Fig. 3 shows a field-of-view of nuclear emulsion viewed by an optical microscope. Typical alignment residuals of a sequence of grains (a "microtrack") with respect to the average straight-line fit are about 70 nm. One drawback of the nuclear emulsion technique is the continuous sensitivity of emulsion before development, which leads to background pile-up. Good tracking precision is therefore also needed to discriminate event-related tracks from tracks produced by cosmic rays and environmental radioactivity during the history of each emulsion plate.

Until the early 1990's, nuclear emulsion plates were scanned manually, so that high statistics could not be achieved; however, as of the CHORUS experiment (WA95-CERN), automatic scanning systems [2] were developed in Europe (SySal, CERN-NIKHEF) and Japan (TS/NTS/UTS) that collected about 2×10^5 events in emulsion. This generation of automatic scanning systems had a maximum scanning speed about 1 cm^2/h for a single side of a plate.

2. The European Scanning System

European labs taking part in the OPERA experiment joined their efforts in the development of a next-generation automatic scanning system, the ESS [3,4] (European Scanning System). Its basic philosophy is to be mostly software-

based, and made with commercial components, profiting of ongoing technological evolution. A picture of an ESS microscope is shown in Fig. 4. The plate from which data is to be collected is placed on a stage able to move in 2 directions (X,Y axes); illumination comes from below, and a coaxial objective, mounted perpendicularly (Z axis) forms a real image on a CMOS camera with 1.2 Mpixel, operating at 376 frames per second. The pixel resolution is about 0.3 μm. At each field of view, while the X and Y axes are held still, the Z axis is moved to obtain an optical tomography (field depth ~3 μm, 15 images/view). A vision processor board takes data from the camera, pre-processing 2D images (2D FIR filtering/equalisation/binarisation), and sending them to the host workstation (which also hosts the motion control board). The scanning software (custom-made) uses the workstation CPUs to recognise grains and reconstruct 3D microtracks on-the-fly. The tracking software looks for local alignments of grains with a tunable tolerance (usually 0.23 μm). The sustained data flow from the camera is 97 MB/s (452 MB/s peak), and the overall scanning speed is 20 cm^2/h/side of each plate, with an efficiency about 90÷95% for microtrack pairs (on either side of the plate), for a background of 10 microtrack pairs/cm^2 with slope below 0.5 (slope is 0 for tracks perpendicular to the plate). Reconstructed microtracks are continuously sent to a central server (Batch Manager) that coordinates data taking of several microscopes, defining interesting areas and performing further processing by a dedicated cluster of processing machines (Data Processing Servers); data are then written to an Oracle-based DB. A station with 4 microscopes can produce up to 160 GB/day.

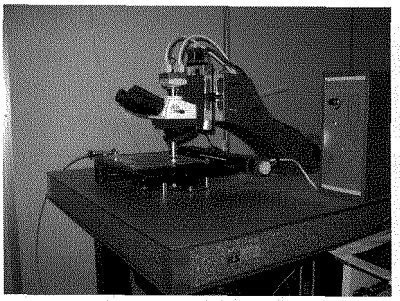

Figure 4: picture of the European Scanning System microscope.

3. The Japanese Scanning System

The last evolution of the automatic systems formerly used by Japanese groups in CHORUS is the S-UTS (Super-Ultra Track Selector) [5,6], shown in Fig. 5. The system is mostly hardware-based, using a custom camera (0.25 Mpixel, 3000 frames per second). The objective lens is mounted on a piezoelectric drive, capable of very high accelerations, to produce a high-repetition motion along the optical axis (Z). The plate is set on a stage that has a continuous motion on the X axis, synchronised with the alternating motion on Z. Scanning proceeds line by line, and the Y axis moves only at the end of each scan line to reach the next one. Accelerations along X are almost absent, and scanning has limited dead time. Images acquired are processed completely by a custom parallel processing

device, based on extensive use of FPGAs. Microtrack recognition is based on the observation that summing up all grain images in a tomographic sequence will give a peak when the piling is done according to a skewing angle compatible with real microtracks, no peak otherwise. With an acceptance on track slopes as large as 0.5, the system is able to scan at 50 $cm^2/h/side$ (72 $cm^2/h/side$ peak) with an efficiency of 95% (microtrack pairs), for a background of 10^4 microtrack pairs/cm^2. Each S-UTS is driven by a companion PC, where data are temporarily dumped; after each scanning task has been completed, the related results are processed locally to define interesting areas for the next plate; at the end of the process for each OPERA brick, data are written into an Oracle-based DB.

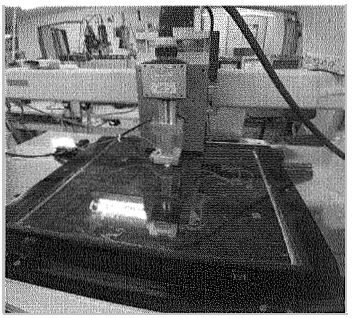

Figure 5: picture of the S-UTS at work in Nagoya

4. Data quality and analysis capabilities

Microtrack detection efficiency of the order of 90÷95% can be obtained on 43 μm thick emulsion layers. By aligning microtracks measured on several emulsion layers, tracks are reconstructed across a whole OPERA brick. The average alignment residuals of high momentum tracks over a cell of 1300 μm are of the order of 0.3 μm for vertical tracks, and grow to 0.7 μm at slope = 0.7 [7]. Topological reconstruction of events prescribes that reconstructed tracks approaching closer than a proper tolerance form vertices; of course, low momentum tracks suffer larger scattering; crossing tolerances of the order of 20÷50 μm allow reliable recognition of ν_τ CC vertices, with low background.

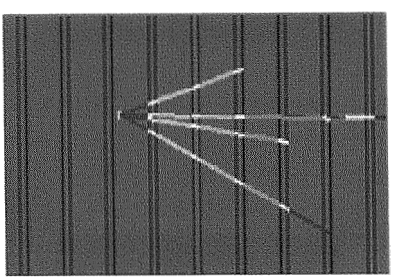

Figure 6: Geometrical and topological reconstruction of an interaction vertex, using the unique precision of nuclear emulsions.

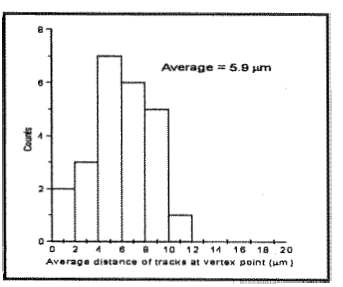

Figure 7: Average track distance from the vertex point (ν_μ interactions in a test exposure at the NuMi beam - FERMILAB).

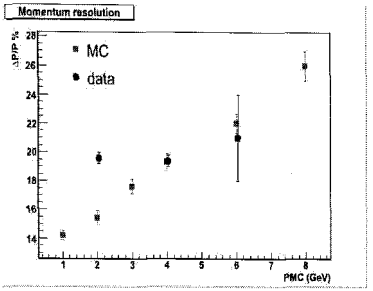

Figure 8: Comparison between resolution on momentum estimation from real data and from Monte-Carlo simulation.

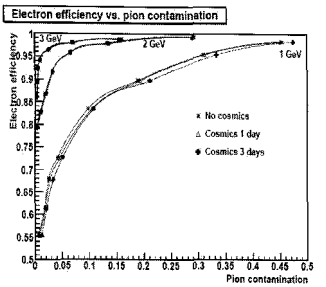

Figure 9: Example of performances in particle identification achievable through neural network analysis on emulsion tracks.

High momentum track slopes are determined with a precision as good as 1÷2 mrad, and decay kinks as small as 20 mrad, after flight paths shorter than 1 mm, can be easily detected. Fig. 6 shows a ν_μ interaction from a sample obtained in a test exposure at the NuMi beam at FERMILAB, and Fig. 7 shows the precision of track crossing at vertex point.

High precision is useful also in estimating kinematical parameters of tracks, e.g. by momentum determination through multiple Coulomb scattering. 26% relative uncertainty ($\Delta p/p$) resolution at momenta as high as 8 GeV/c is a routine-duty performance (Fig. 8).

Finally, event topology and precise measurement can help identify and disentangle electrons and pions [8]. Particle identification algorithms based on neural networks have been developed, and their misidentification rate is below 1% above 2 GeV/c (Fig. 9), using about 10 X_0 (thickness of one OPERA brick).

References

1. R. Acquafredda et al., *New Journal of Physics* **8** (2006), 303
2. C. Bozza (CHORUS Collaboration), *Nucl. Inst. Meth. Phys. Res.* **A478**, 411-414
3. L. Arrabito et al., *Nucl. Inst. Meth. Phys. Res.* **A568**, 578-587
4. N. Armenise et al., *Nucl. Inst. Meth. Phys. Res.* **A551**, 261-270
5. T. Nakano (CHORUS Collaboration), *2001 Internat. Europhys. Conf. High-Energy Physics*
6. T. Nakano, *BUTURI* **56**(6) (2001)
7. L. Arrabito et al., *Journal of Instrumentation* **2** P05004
8. L. Arrabito et al., *Journal of Instrumentation* **2** P02001

CHERCAM: a Cherenkov imager for the CREAM experiment

M. BRINET*, A. BARRAU, O. BOURRION, J. BOUVIER, B. BOYER, M. BUENERD, L. DEROME, L. ERAUD, R. FOGLIO, L. GALLIN-MARTEL, A. PUTZE, Y. SALLAZ-DAMAZ, J.-P. SCORDILIS

Laboratoire de Physique Subatomique et de Cosmologie, CNRS/IN2P3/UJF Grenoble, France

** E-mail: mariane@lpsc.in2p3.fr*

P. BHOYAR, O. GANEL, J.H. HAN, C.H. KIM, M.H. LEE, L. LUTZ, A. MALININE, E. S. SEO, P. WALPOLE, Y.S. YOON, S.Y. ZINN

University of Maryland, College Park, MD USA

R. BAZER-BACHI, J.N. PERIE

Centre dEtude Spatiale des Rayonnements, UFR PCA, CNRS Toulouse, France

A. MENCHACA-ROCHA

Instituto de Física, Universidad Nacional Autónoma de México, México

The CREAM experiment (Cosmic Ray Energetics and Mass) is dedicated to the measurement of the energy spectrum of nuclear elements in cosmic rays, over the range 10^{12} to 10^{15} eV. It has already begun to measure high energy cosmic rays at the frontier of the statistical limits accessible to balloon-borne experiments.[1] Measurements of the cosmic ray spectrum of nuclei from proton to iron in this energy range will provide invaluable data on cosmic ray spectral characteristics and/or abundance changes, which could be related to the acceleration limit in the shock front of supernovae. The individual elements separation, which is a key feature of CREAM, requires instruments with strong identification capabilities. A proximity focused type of Cherenkov imager, CHERCAM (CHERenkov CAMera), providing both a good signature of downgoing $Z = 1$ particles and good single element separation through the whole range of nuclear charges considered, has been developed and will be part of the third CREAM flight in December 2007. After a brief introduction, the main features and test results of the CHERCAM are being summarized.

Keywords: Cosmic Ray; Cherenkov Detector.

1. Introduction

CREAM experiment is dedicated to the measurements of the cosmic ray energy spectra in an energy range from 10^{12} à 10^{15} eV, with an individual identification of nuclei, from proton to Iron.

CREAM instrument has been designed such as to respect a certain compromise between the necessity to have as large an acceptance as possible – to accumulate a reasonable statistics – and the requirement of limited weight inherent in the balloon borne experiments.

The instrument includes a set of sub-detectors able to measure the energy and charge of particles in a redundant way.[2] A Timing Charge Detector (TCD) and a Silicon Charge Detector (SCD) provide a charge mesurement. Four successive layers of scintillating fibers (S0/S1) provide an additional determination of the charge, together with informations on particle trajectories. Another layer of scintillating fibers (S3) give the reference time. The particle energy is determined by a hadronique calorimeter, which provide an energy resolution almost constant over the three orders of magnitudes of energy covered. For the 2007 flight, a Cherenkov imager optimized for charge measurements will be added to the CREAM instrument.

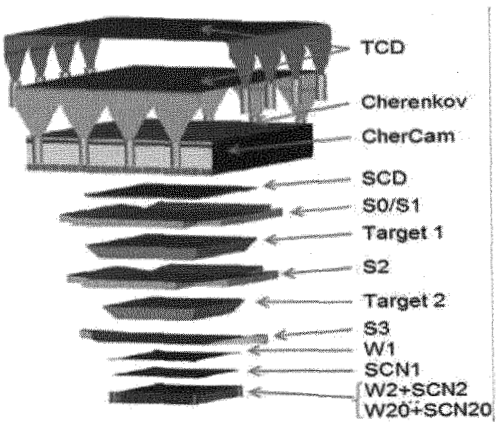

Fig. 1. Exploded view of CREAM instrument for the 2007 flight.

One of the main interest of this counter is that it will provide both a good albedo particles signature and a constant resolution over the whole range of charge under interest. The different flights configurations can be seen in Figure 1, where an exploded view of the detector is displayed, both for previous flights (l.h.s.) and for the coming one (r.h.s.).

2. CHERCAM architecture

CHERCAM[3] is a proximity focusing imager derived from the solution developed for AMS experiment, whose principle is illustrated in figure 2 (l.h.s.). Its mechanical structure, displayed in figure 3, is divided into two frames

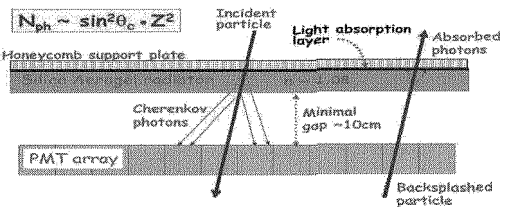

Fig. 2. Scheme of the Cherenkov imager principle

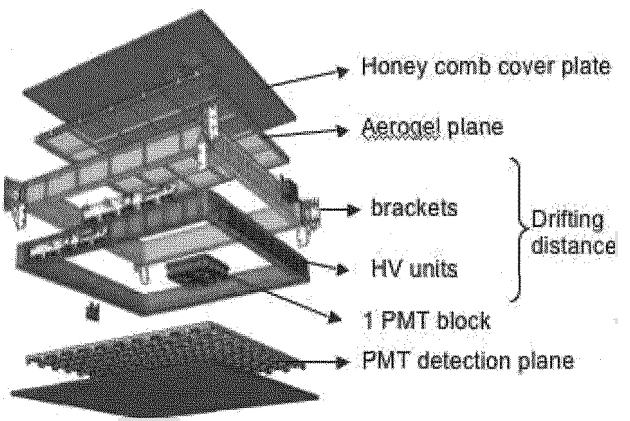

Fig. 3. CHERCAM mechanical structure.

(green and red in figure 3) for mechanical reasons. The upper frame includes the radiator plane and the Cerenkov photons drifting gap. The lower one contains the PMTs modules, the read-out electronics and the high and low voltage units.

The radiator plane is made of 200 silica aerogel tiles with a refraction index ~ 1.05, distributed on a $11 \times 11 \times 2$ cm^3 plane (see l.h.s. picture in figure 4).

The Cherenkov radiator plane is separated by a ~11 cm ring expansion gap, from a photon detector plane consisting of a 1600 photomultiplier (PMTs) tubes array (Photonis XP3112), backed with dedicated front-end electronics, power supply, and read-out electronics. The latter employs the same 16-channel ASIC circuit than the one used for the AMS Cherenkov imager.[4] The 1600 PMTs are distributed in 25 modules of 4 blocks, each block containing 16 PMTs. The detection plane, once assembled, is represented in figure 4 (r.h.s.).

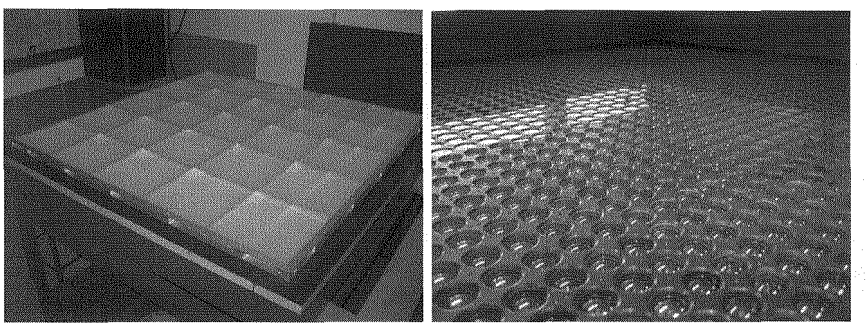

Fig. 4. CHERCAM aerogel plane (200 tiles, 10x10x105mm) (l.h.s.) and detection plane, made of 1600 PMTs. (r.h.s.)

3. Detector validations

The CHERCAM instrument underwent both beam tests and thermal and vacuum validations.

A module of 64 PMT has been tested at CERN in october 2006 and 2007, using pions, electrons and protons beams, with energy ranging from 100 to 300 GeV. It allowed to verify the basics functionalities of the detector. Examples of events are displayed in figure 5.

The analysis is still in progress but the preliminary results give a charge resolution for $Z = 1$ of 0.21 charge unit. The complete beam tests analysis will allow to check the basic CHERCAM functionalities and performance, as well as to determine the possible contribution of the ring imaging detector to the particle position reconstruction.

In addition, the behavior of the detector – which will have to be powered on ground in Antarctica, and then to work at $\sim$ 35 km in altitude – has been validated during long term vacuum (from 5 to 1000 mbar) and thermal ($[-10°C, +35°C]$) tests. High voltage units working conditions have in particular been checked and the counter operated without problem over the

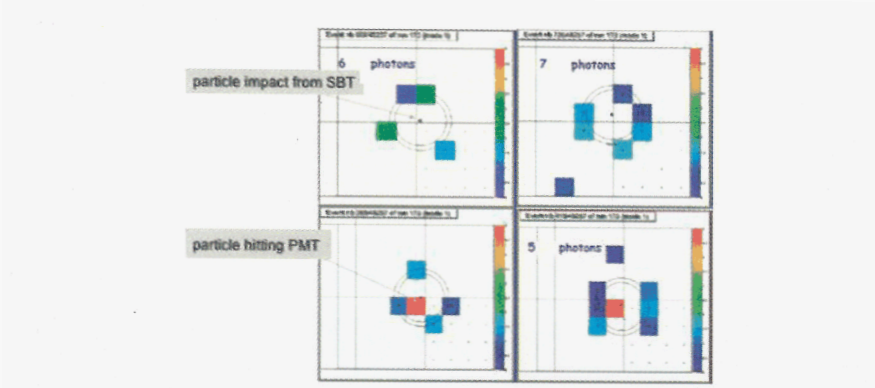

Fig. 5. Examples of events obtained during test beam at CERN in october 2006, with electrons.

total duration of tests (∼ 70 hours).

All tests have been conclusive and have shown the perfect working functionalities of the CHERCAM imager, including in operating conditions close to Antarctica flight ones.

4. Simulation

A full GEANT4 simulation of CHERCAM has been developed, to investigate the detailed features of the detector response and its performance in resolution. The simulation, illustrated in figure 6, includes the photomultipliers modeling and contains as physical processes: Cherenkov effect , Rayleigh scattering in the aerogel, optical refraction, reflection and absorption. The quantum efficiency of the PMT photocathode is taken into account according to the data given by the manufacturer.

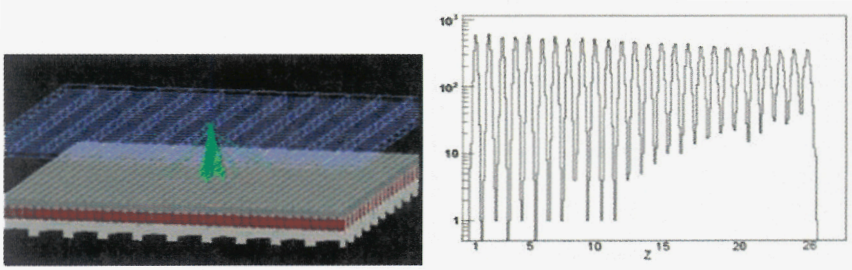

Fig. 6. L.h.s.: example of a simulated event. The green lines represent Cherenkov photons. R.h.s.: charge reconstruction, obtained with 44000 simulated events, uniformly distributed in charge.

Reconstruction codes are also being developed, with a special interest in the control of the geometrical efficiency determination.

The first results of the simulation show that a combination of incident particle hit position provided by the other detectors, and the Cherenkov ring overlap with the PMTs active areas, can provide a charge reconstruction better than $\Delta Z = 0.3$ over the full range of charges concerned (see figure 6).

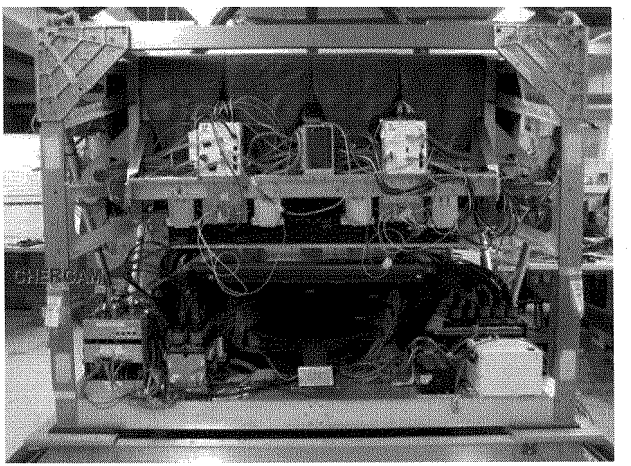

Fig. 7. *CHERCAM instrument integrated.*

5. Conclusion

CHERCAM instrument, designed and built in less than two years, has been shown to satisfy all the required tests and was succesfully integrated to the CREAM payload, as one can see in figure 7.

CREAM has just been transferred to MacMurdo base. Final tests are being performed on ice, waiting for an appropriate launch window in December 2007 and the first results of the experiment with CHERCAM instrument included are impatiently expected.

References

1. See for instance E. S. Seo et al, Nucl. Inst. and Meth. in Phys. A, Proc. 20th ICRC, 2007, in press, and references therein.
2. E. S. Seo et al., Adv. in Space Research, Vol. 33, Issue 10, 1777 (2004)
3. M. Buénerd et al., Nucl. Inst. and Meth. in Phys. A, Proc. 20th ICRC, 2007, M. Brinet et al, Nucl. Inst. and Meth. in Phys. A572, 410 (2007)
4. L. Gallin-Martel et al., Nucl. Inst. and Meth. in Phys. A504, 2783 (2003)

Gravitational waves from the R^{-1} high order theory of gravity

C. CORDA

INFN Sezione di Pisa and Universit di Pisa,
Via F. Buonarroti 2,I-56127, Pisa, Italy
European Gravitational Observatory (EGO),
Via E. Amaldi, I-56021 Pisa, Italy
E-mail: christian.corda@ego-gw.it

M. DE LAURENTIS

Politecnico di Torino
and INFN Sezione di Torino,
Corso Duca degli Abruzzi 24, I-10129 Torino, Italy
E-mail: mariafelicia.delaurenti@polito.it

This paper is a review of a previous research on gravitational waves from the R^{-1} high order theory of gravity. It is shown that a massive scalar mode of gravitational waves from the R^{-1} theory generates a longitudinal force in addition of the transverse one which is proper of the massless gravitational waves and the response of an arm of an interferometer to this longitudinal effect in the frame of a local observer is computed. Important conseguences from a theoretical point of view could arise from this approach, because it opens to the possibility of using the signals seen from interferometers to understand which is the correct theory of gravitation.

1. Introduction

The data analysis of interferometric gravitational waves (GWs) detectors has recently started (for the current status of GWs interferometers see[1–8]) and the scientific community hopes in a first direct detection of GWs in next years.

Detectors for GWs will be important for a better knowledge of the Universe and also to confirm or ruling out the physical consistency of General Relativity or of any other theory of gravitation [9–14]. This is because, in the context of Extended Theories of Gravity, some differences between General Relativity and the others theories can be pointed out starting by the linearized theory of gravity [15–20].

In this paper, which is a review of a previous research on gravitational waves from the R^{-1} high order theory of gravity [15], it is shown that massive scalar modes of gravitational waves from the R^{-1} theory generate a longitudinal force in addition of the transverse one which is proper of the massless gravitational waves and the response of an arm of an interferometer to this longitudinal effect in the frame of a local observer is computed. Important conseguences from a theoretical point of view could arise from this approach, because it opens to the possibility of using the signals seen from interferometers to understand which is the correct theory of gravitation.

2. A scalar massive mode of gravitational radiation in the R^{-1} high order theory of gravity

In [15] it has been shown that a massive scalar mode of gravitational radiation arises from the high order action

$$S = \int d^4x\sqrt{-g}R^{-1} + \mathcal{L}_m, \tag{1}$$

where R is the Ricci scalar curvature. Equation (1) is a particular choice with respect the well known canonical one of General Relativity (the Einstein - Hilbert action[21,22]) which is

$$S = \int d^4x\sqrt{-g}R + \mathcal{L}_m. \tag{2}$$

From the linearizated field equations arising by the action (1), in [15] it has been obtained a plane wave propagating in the z direction:

$$h_{\mu\nu}(t,z) = A^+(t-z)e^{(+)}_{\mu\nu} + A^\times(t-z)e^{(\times)}_{\mu\nu} + \Phi(t-v_G z)\eta_{\mu\nu}. \tag{3}$$

The term $A^+(t-z)e^{(+)}_{\mu\nu} + A^\times(t-z)e^{(\times)}_{\mu\nu}$ describes the two standard (i.e. tensorial) polarizations of gravitational waves which arise from General Relativity, while the term $\Phi(t-v_G z)\eta_{\mu\nu}$ is the scalar massive field arising from the high order theory.

3. A longitudinal force

For a purely scalar gravitational wave eq. (3) can be rewritten as [15]

$$h_{\mu\nu}(t-v_G z) = \Phi(t-v_G z)\eta_{\mu\nu} \tag{4}$$

and the corrispondent line element is the conformally flat one

$$ds^2 = [1 + \Phi(t - v_G z)](-dt^2 + dz^2 + dx^2 + dy^2). \tag{5}$$

But, in a laboratory environment on Earth, the coordinate system in which the space-time is locally flat [12,15,21,22] is typically used and the distance between any two points is given simply by the difference in their coordinates in the sense of Newtonian physics. This frame is the proper reference frame of a local observer, located for example in the position of the beam splitter of an interferometer. In this frame gravitational waves manifest themself by exerting tidal forces on the masses (the mirror and the beam-splitter in the case of an interferometer). The effect of the gravitational wave on test masses is described in this frame by the equation

$$\ddot{x^i} = -\widetilde{R}^i_{0k0} x^k, \tag{6}$$

which is the equation for geodesic deviation.

But, because the linearized Riemann tensor $\widetilde{R}_{\mu\nu\rho\sigma}$ is invariant under gauge transformations [12,15,21,22], it can be directly computed from eq. (4).

From [21] it is:

$$\widetilde{R}_{\mu\nu\rho\sigma} = \frac{1}{2}\{\partial_\mu\partial_\beta h_{\alpha\nu} + \partial_\nu\partial_\alpha h_{\mu\beta} - \partial_\alpha\partial_\beta h_{\mu\nu} - \partial_\mu\partial_\nu h_{\alpha\beta}\}, \tag{7}$$

that, in the case eq. (4), begins [15]

$$\widetilde{R}^\alpha_{0\gamma 0} = \frac{1}{2}\{\partial^\alpha\partial_0\Phi\eta_{0\gamma} + \partial_0\partial_\gamma\Phi\delta^\alpha_0 - \partial^\alpha\partial_\gamma\Phi\eta_{00} - \partial_0\partial_0\Phi\delta^\alpha_\gamma\}. \tag{8}$$

The computation has been performed in details in [15], the results are

$$\begin{aligned} \widetilde{R}^1_{010} &= -\tfrac{1}{2}\ddot{\Phi} \\ \widetilde{R}^2_{010} &= -\tfrac{1}{2}\ddot{\Phi} \\ \widetilde{R}^3_{030} &= \tfrac{1}{2}m^2\Phi, \end{aligned} \tag{9}$$

which show that the field is not transversal.

Infact, using eq. (6) it results

$$\ddot{x} = \frac{1}{2}\ddot{\Phi}x, \tag{10}$$

$$\ddot{y} = \frac{1}{2}\ddot{\Phi}y \tag{11}$$

and

$$\ddot{z} = -\frac{1}{2}m^2\Phi(t - v_G z)z. \tag{12}$$

Then the effect of the mass is the generation of a *longitudinal* force (in addition to the transverse one). Note that in the limit $m \to 0$ the longitudinal force vanishes.

4. The interferometer's response to the longitudinal component

We have to recall that the scalar wave needs a frequency which falls in the frequency-range for earth based gravitational antennas [12,15], that is the interval $10Hz \leq f \leq 10KHz$ (see refs [1–8]). For a massive scalar gravitational wave, this implies [12,15]

$$0eV \leq m \leq 10^{-11}eV. \tag{13}$$

Equations (10), (11) and (12) give the tidal acceleration of the test mass caused by the scalar gravitational wave respectly in the x direction, in the y direction and in the z direction [15].

Equivalently we can say that there is a gravitational potential [12,15]:

$$V(\vec{r}, t) = -\frac{1}{4}\ddot{\Phi}(t - \frac{z}{v_P})[x^2 + y^2] + \frac{1}{2}m^2\int_0^z \Phi(t - v_G z)ada, \tag{14}$$

which generates the tidal forces, and that the motion of the test mass is governed by the Newtonian equation

$$\ddot{\vec{r}} = -\bigtriangledown V. \tag{15}$$

To obtain the longitudinal component of the scalar gravitational wave the solution of eq. (12) has to be found.

For this goal the perturbation method can be used. A function of time for a fixed z, $\psi(t - v_G z)$, can be defined [12,15], for which it is

$$\ddot{\psi}(t - v_G z) \equiv \Phi(t - v_G z) \tag{16}$$

(note: the most general definition is $\psi(t - v_G z) + a(t - v_G z) + b$, but, assuming only small variatons in the positions of the test masses, it results $a = b = 0$).

In this way it results

$$\delta z(t - v_G z) = -\frac{1}{2} m^2 z_0 \psi((t - v_G z). \tag{17}$$

A feature of the frame of a local observer is the coordinate dependence of the tidal forces due by scalar gravitational waves which can be changed with a mere shift of the origin of the coordinate system [12,15]:

$$x \to x + x', \; y \to y + y' \text{ and } z \to z + z'. \tag{18}$$

The same applies to the test mass displacements in the z direction, eq. (17). This is an indication that the coordinates of a local observer are not simple as they could seem [12,15].

Now, let us consider the relative motion of test masses. A good way to analyze variations in the proper distance (time) of test masses is by means of "bouncing photons" [12,15]. A photon can be launched from the beam-splitter to be bounced back by the mirror. It will be assumed that both the beam-splitter and the mirror are located along the z axis of our coordinate system (i.e. an arm of the interferometer is in the z direction, which is the direction of the propagating massive scalar gravitational wave and of the longitudinal force).

In the frame of a local observer, two different effects have to be considered in the calculation of the variation of the round-trip time for photons [12,15]. The unperturbed coordinates for the beam-splitter and the mirror are $z_b = 0$ and $z_m = L$. So the unperturbed propagation time between the two masses is

$$T = L. \tag{19}$$

From eq. (17) it results that the displacements of the two masses under the influence of the scalar gravitational wave are

$$\delta z_b(t) = 0 \tag{20}$$

and

$$\delta z_m(t - v_G L) = -\frac{1}{2} m^2 L \psi(t - v_G L). \tag{21}$$

In this way, the relative displacement, is

$$\delta L(t) = \delta z_m(t - v_G L) - \delta z_b(t) = -\frac{1}{2} m^2 L \psi(t - v_G L), \tag{22}$$

Thus it results

$$\frac{\delta L(t)}{L} = \frac{\delta T(t)}{T} = -\frac{1}{2} m^2 \psi(t - v_G L). \tag{23}$$

But there is the problem that, for a large separation between the test masses (in the case of Virgo or LIGO the distance between the beam-splitter and the mirror is three or four kilometers), the definition (22) for relative displacement becomes unphysical because the two test masses are taken at the same time and therefore cannot be in a casual connection [12,15]. The correct definitions for our bouncing photon can be written like

$$\delta L_1(t) = \delta z_m(t - v_G L) - \delta z_b(t - T_1) \tag{24}$$

and

$$\delta L_2(t) = \delta z_m(t - v_G L - T_2) - \delta z_b(t), \tag{25}$$

where T_1 and T_2 are the photon propagation times for the forward and return trip correspondingly. According to the new definitions, the displacement of one test mass is compared with the displacement of the other at a later time to allow for finite delay from the light propagation. Note that the propagation times T_1 and T_2 in eqs. (24) and (25) can be replaced with the nominal value T because the test mass displacements are alredy first order in Φ. Thus, for the total change in the distance between the beam splitter and the mirror in one round-trip of the photon, it is

$$\delta L_{r.t.}(t) = \delta L_1(t - T) + \delta L_2(t) = 2\delta z_m(t - v_G L - T) - \delta z_b(t) - \delta z_b(t - 2T), \tag{26}$$

and in terms of the amplitude and mass of the SGW:

$$\delta L_{r.t.}(t) = -m^2 L\psi(t - v_G L - T). \tag{27}$$

The change in distance (27) leads to changes in the round-trip time for photons propagating between the beam-splitter and the mirror:

$$\frac{\delta_1 T(t)}{T} = -m^2\psi(t - v_G L - T). \tag{28}$$

In the last calculation (variations in the photon round-trip time which come from the motion of the test masses inducted by the scalar gravitational wave), it was implicitly assumed that the propagation of the photon between the beam-splitter and the mirror of our interferometer is uniform as if it were moving in a flat space-time. But the presence of the tidal forces indicates that the space-time is curved. As a result another effect after the previous has to be considered, which requires spacial separation [12,15].

For this effect we consider the interval for photons propagating along the z-axis

$$ds^2 = g_{00}dt^2 + dz^2. \tag{29}$$

The condition for a null trajectory ($ds = 0$) gives the coordinate velocity of the photons

$$v^2 \equiv (\frac{dz}{dt})^2 = 1 + 2V(t, z), \tag{30}$$

which to first order in Φ is approximated by

$$v \approx \pm[1 + V(t, z)], \tag{31}$$

with $+$ and $-$ for the forward and return trip respectively. Knowing the coordinate velocity of the photon, the propagation time for its travelling between the beam-splitter and the mirror can be defined:

$$T_1(t) = \int_{z_b(t-T_1)}^{z_m(t)} \frac{dz}{v} \tag{32}$$

and

$$T_2(t) = \int_{z_m(t-T_2)}^{z_b(t)} \frac{(-dz)}{v}. \tag{33}$$

The calculations of these integrals would be complicated because the boundary $z_m(t)$ is changing with time. In fact it is

$$z_b(t) = \delta z_b(t) = 0 \tag{34}$$

but

$$z_m(t) = L + \delta z_m(t). \tag{35}$$

But, to first order in Φ, this contribution can be approximated by $\delta L_2(t)$ (see eq. (25)). Thus, the combined effect of the varying boundary is given by $\delta_1 T(t)$ in eq. (28). Then, only the times for photon propagation between the fixed boundaries 0 and L have to be calculated. Such propagation times will be denoted with $\Delta T_{1,2}$ to distinguish from $T_{1,2}$. In the forward trip, the propagation time between the fixed limits is

$$\Delta T_1(t) = \int_0^L \frac{dz}{v(t', z)} \approx T - \int_0^L V(t', z)dz, \tag{36}$$

where t' is the retardation time which corresponds to the unperturbed photon trajectory:

$$t' = t - (L - z)$$

(i.e. t is the time at which the photon arrives in the position L, so $L - z = t - t'$).

Similiary, the propagation time in the return trip is

$$\Delta T_2(t) = T - \int_L^0 V(t', z)dz, \tag{37}$$

where now the retardation time is given by

$$t' = t - z.$$

The sum of $\Delta T_1(t-T)$ and $\Delta T_2(t)$ gives the round-trip time for photons traveling between the fixed boundaries. Then the deviation of this round-trip time (distance) from its unperturbed value $2T$ is

$$\delta_2 T(t) = \int_0^L [V(t - 2T + z, z) + V(t - z, z)]dz. \tag{38}$$

From eqs. (14) and (38) it results:

$$\delta_2 T(t) = \tfrac{1}{2}m^2 \int_0^L [\int_0^z \Phi(t - 2T + a - v_G a)ada + \int_0^z \Phi(t - a - v_G a)ada]dz =$$

$$= \tfrac{1}{4}m^2 \int_0^L [\Phi(t - v_G z - 2T + z) + \Phi(t - v_G z - z)]z^2 dz +$$

$$-\tfrac{1}{4}m^2 \int_0^L [\int_0^z \Phi'(t - 2T + a - v_G a)z^2 da + \int_0^z \Phi'(t - a - v_G a)z^2 da]dz, \tag{39}$$

Thus the total round-trip proper distance in presence of the scalar gravitational wave is:

$$T = 2T + \delta_1 T + \delta_2 T. \tag{40}$$

Now, to obtain the interferometer response function of the massive scalar field, the analysis can be transled in the frequency domine.

Using the Fourier transform of ψ defined from

$$\tilde{\psi}(\omega) = \int_{-\infty}^{\infty} dt\psi(t)\exp(i\omega t), \tag{41}$$

and recalling a theorem about Fourier transforms [15], it is simple to obtain:

$$\tilde{\psi}(\omega) = -\frac{\tilde{\Phi}(\omega)}{\omega^2}, \tag{42}$$

where

$$\tilde{\Phi}(\omega) = \int_{-\infty}^{\infty} dt\Phi(t)\exp(i\omega t). \tag{43}$$

is the Fourier transform of our scalar field. Then, in the frequency space, it results [15]:

$$\tilde{T}(\omega) = \Upsilon_l(\omega)\tilde{\Phi}(\omega), \tag{44}$$

where

$$\Upsilon_l(\omega) \equiv (1 - v_G^2)\exp[i\omega L(1 + v_G)] + \frac{1}{2\omega L(v_G^2-1)^2}$$

$$[\exp[2i\omega L](v_G + 1)^3(-2i + \omega L(v_G - 1) + 2\exp[i\omega L(1 + v_G)] \qquad (45)$$

$$(6iv_G + 2iv_G^3 - \omega L + \omega L v_G^4) + (v_G + 1)^3(-2i + \omega L(v_G + 1))],$$

is the response function of an arm of our interferometer located in the z-axis, due to the longitudinal component of the massive scalar gravitational wave propagating in the same direction of the axis.

For $v_G \to 1$ it is $\Upsilon_l(\omega) \to 0$.

5. Conclusions

In this paper, which is a review of a previous research on gravitational waves from the R^{-1} high order theory of gravity,[15] it has been shown that massive scalar modes of gravitational waves from the R^{-1} theory generate a longitudinal force in addition of the transverse one which is proper of the massless gravitational waves and the response of an arm of an interferometer to this longitudinal effect in the frame of a local observer has been computed. Important conseguences from a theoretical point of view could arise from this approach, because it opens to the possibility of using the signals seen from interferometers to understand which is the correct theory of gravitation.

6. Acknowledgements

We would like to thank Salvatore Capozziello for helpful advices during the work.

References

1. Acernese F et al. (the Virgo Collaboration) - Class. Quant. Grav. **23** 8 S63-S69 (2006)
2. Corda C - Astropart. Phys. **27,** No 6, 539-549 (2007);
3. Corda C -Int. J. Mod. Phys. D **16,** 9, 1497-1517 (2007)
4. Corda C - Int. J. Mod. Phys. A **22,** 13 2361-2381 (2007)
5. Sigg D (for the LIGO Scientific Collaboration) www.ligo.org/pdf_public/P050036.pdf
6. Abbott B et al. (the LIGO Scientific Collaboration) - Phys. Rev. D 72, 042002 (2005)
7. Ando M and the TAMA Collaboration - Class. Quant. Grav. **19** 7 1615-1621 (2002)

8. Willke B et al. - Class. Quant. Grav. **23** 8S207-S214 (2006)
9. Capozziello S - *Newtonian Limit of Extended Theories of Gravity* in *Quantum Gravity Research Trends* Ed. A. Reimer, pp. 227-276 Nova Science Publishers Inc., NY (2005) - also in arXiv:gr-qc/0412088 (2004)
10. Capozziello S and Troisi A - Phys. Rev. D **72** 044022 (2005)
11. Allemandi G, Capone M, Capozziello S and Francaviglia M - Gen. Rev. Grav. 38 1 (2006)
12. Capozziello S and Corda C - Int. J. Mod. Phys. D **15** 1119 -1150 (2006); Corda C - *Response of laser interferometers to scalar gravitational waves-* talk in the *Gravitational Waves Data Analysis Workshop in the General Relativity Trimester of the Institut Henri Poincare* - Paris 13-17 November 2006, on the web in www.luth2.obspm.fr/IHP06/workshops/gwdata/corda.pdf
13. Allemandi G, Francaviglia M, Ruggiero ML and Tartaglia A - Gen. Rel. Grav. 37 11 (2005);
14. Corda C - Astropart. Phys. 28, 247-250 (2007)
15. Corda C - J. Cosmol. Astropart. Phys. JCAP04009 (2007)
16. Corda C - Mod. Phys. Lett. A No. 22, 16, 1167-1173 (2007)
17. Capozziello S, Corda C and De Laurentis MF - Mod. Phys. Lett. A 22, 15, 1097-1104 (2007)
18. Corda C - Mod. Phys. Lett. A No. 22, 23, 1727-1735 (2007)
19. Brans C and Dicke RH - Phys. Rev. 124, 925 (1961)
20. Bonasia N and Gasperini M - Phys. Rew. D **71** 104020 (2005)
21. Misner CW, Thorne KS and Wheeler JA - "Gravitation" - W.H.Feeman and Company - 1973
22. Landau L and Lifsits E - "Teoria dei campi" - Editori riuniti edition III (1999)

THE DOUBLE CHOOZ EXPERIMENT

ANDI S. CUCOANES
FOR THE DOUBLE CHOOZ COLLABORATION[†]
III. Physikalisches Institut, RWTH Aachen University, 52056 Aachen, Germany

One of the main interests for nowadays neutrino physics is the knowledge of the mixing angle Θ_{13}. The present limit is given by the CHOOZ experiment. The Double Chooz Collaboration aims for a reactor antineutrino flux measurement with two identical detectors placed at ~250 m and respectively ~1 km from the reactor cores as the search for a non-vanishing Θ_{13} value. Within 3 years of data taking and a 0.6% relative detector uncertainty, the limit on $\sin^2(2\Theta_{13})$ is smaller than 0.025 at 90% C.L. The Double Chooz experiment is planned to start in spring 2009 and will rapidly improve the present constrain on Θ_{13} serving in this way as a guide for the future neutrino experiments.

1. Introduction

The general characteristic of the neutrino mixing is assumed to be the coupling between the flavor and the mass eigenstates through the PMNS matrix. Three mixing angles Θ_{12}, Θ_{23} and Θ_{13} are describing the magnitude of this effect. Since many years, a variety of experiments measuring solar, atmospheric, reactor and accelerator neutrinos, have determined the values of the oscillations parameters [1]. Still unknown, Θ_{13} is considered very small ($\sin^2(2\Theta_{13}) < 0.2$ at 90% CL) mainly by the CHOOZ experiment [2]. There are enough reasons for a big interest on the Θ_{13} parameter, for example a nonzero value is fundamental for leptonic CP violation searches.

Double Chooz attempts to improve the present knowledge of Θ_{13} by measuring the disappearance of the electron antineutrinos emitted by the two reactors (2*4.27 GW_{th} with an average of 80% loading factor) of the Chooz nuclear power plant.

To achieve this goal, a significant increase of the statistics and the reduction of systematic error below one percent are needed. Double Chooz uses two similar detectors, a near one at ~250 m and a far one at 1.05 km (close to the oscillation maximum) from the reactor cores. In fact, the near detector provides a non-oscillated reference for the antineutrino flux and spectrum.

[†] for a list of the collaborators and the institutions participating see [3]

The Double Chooz site is situated in the Ardennes, near to the France-Belgium border with the advantage of re-using the "old" CHOOZ experiment facilities for the far detector. The existing experimental hall is located underground, with 300 meters-water-equivalent (m.w.e.) overburden.

The near detector site will be at the bottom of a 40 m shaft, beneficiating of ~80 m.w.e. overburden. There are additional conditions fulfilled, as a minimum average distance from the cores and equal fluxes ratio seen by the both detectors. Also, the site must satisfy the reactor safety and security needs.

2. Sensitivity and the Background

The detection mechanism is based on the inverse β-decay $\bar{\nu}_e p \rightarrow e^+ n$ in liquid scintillator viewed by photomultiplier tubes. An event is characterized by two delayed energy depositions, a prompt one from the positron annihilation, followed by the neutron capture. The scintillator is loaded with 0.1% Gd. The Gd capture of the neutron generates a cascade of gammas with a total energy 8MeV, far above the radioactive background.

The main benefit of a multi-detector experiment as Double Chooz is the cancellation of the reactor-induced systematic errors, leaving only the relative normalization between the detectors. The uncertainties of the involved parameters must be carefully controlled. Such examples are: the number of free protons in the target (0.2%), the distance between the detectors locations and the "barycenter" of the neutrino emission in the reactors cores (0.15%).

For now, we assume a relative normalization error 0.6%. With 3 years of data taking, in the case of non oscillation, a sensitivity of $\sin^2(2\Theta_{13})<0.025$ at 90% CL for $\Delta m_{atm}^2=2.4\times10^{-3}$ eV^2 can be achieved.

Specific for reactor neutrino experiments are two categories of background.

One case is the accidental background, where two random events can occur close together in space and time and mimic the delayed coincidence. For example radioactivity in PMT glass, surrounding rock, or construction materials can mimic a positron signal. Then, cosmic muons may produce fast neutrons (via spallation) which after thermalization, can be captured on Gd.

A second category is represented by correlated background. Here, one event mimics both parts of the coincidence signal. Such cases are the atmospheric muons which produce, via spallation on C^{12}, fast neutrons and long-lived β-decaying isotopes as Li^9, He^8.

An efficient protection against the muons is given by the overburden of the detectors sites. A careful selection of the construction materials especially the PMT glass can avoid the naturally occurring radioactivity. Furthermore, Double

Chooz detectors consider active and passive shielding against background. A measurement of the accidental rate will be done in situ.

3. The Detector Design

The design of the two detectors foresees similar central regions. A starting point is the reduction of the background related effects which are known from the CHOOZ experiment. The detection efficiency as well as the scintillator stability are improved with respect to CHOOZ [3].

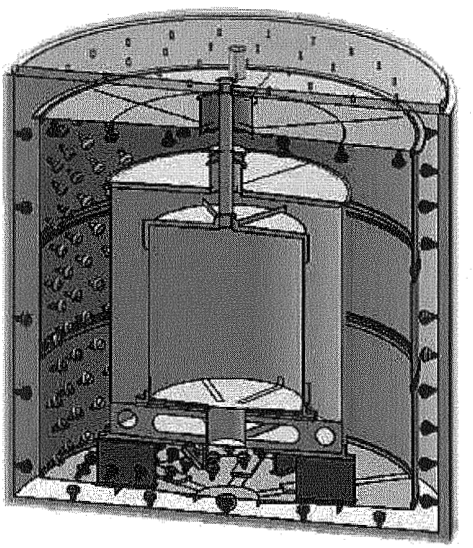

Figure 1. The design of the Double Chooz detector.

3.1. *The Central Region*

Two concentric acrylic cylindrical vessels form the central region of each detector. The **target** is the inner one containing 12 m^3 Gd loaded dodecane+PXE liquid scintillator. The outer cylinder, filled with unloaded dodecane+PXE scintillator, aims to catch those gamma energy depositions which escape the target volume. The target and **gamma catcher** cylinders are located inside a stainless tank, containing dodecane. The goal of this non-scintillating **buffer** is to reduce the random background generated by the PMT glass. The central detector is observed by 390 10" photomultipliers.

3.2. *The Veto Regions*

The **inner veto** will reduce the amount of untagged muons which pass through the central region. To achieve this goal, it was designed a 60 cm thick liquid scintillator layer surrounding the central region; the energy depositions are detected by ~80 8" photomultipliers.
In addition, the **outer veto** is placed over the top of the detector. It aims to tag the nearly-passed muons and to further the spallation neutrons which pass through the detector. More, the outer veto will improve the tracking capability for muons. This region consists of plastic scintillator planes.

3.3. *The Electronics, Trigger and DAQ*

Figure 2 provides a simplified sketch of the Double Chooz electronics and the distribution of the detector signals.

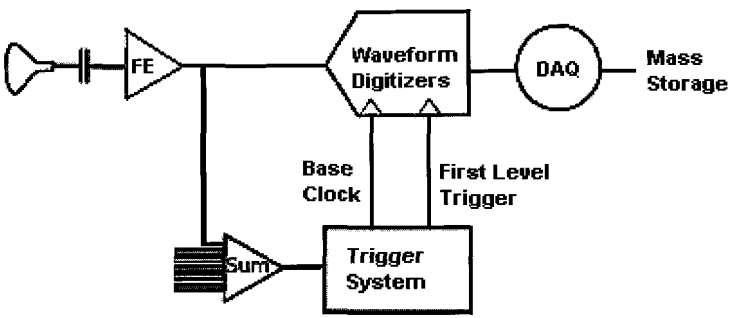

Figure 2. The simplified scheme of the electronics and DAQ

In order reduce the costs and the ground-loop effects, a single cable will carry the high voltage and the signal for each photomultiplier. **HV splitters** will be used for the decoupling of the signal. The **front-end electronics** handle the amplification and the filtering of the photomultipliers signals.
The **trigger** system has very high efficiency for antineutrino and background events. It will distribute a common clock signal to the detector components and provide a time stamp for the events. The trigger readout is followed by the **online filter** decision, which reduces the total data flow to a rate which can be handled by the data storage system.
Each photomultiplier pulse will be recorded with **waveform digitizers** which have a smart memory management in order to perform uninterrupted digitization and zero dead time (CAEN model V1721) [4].

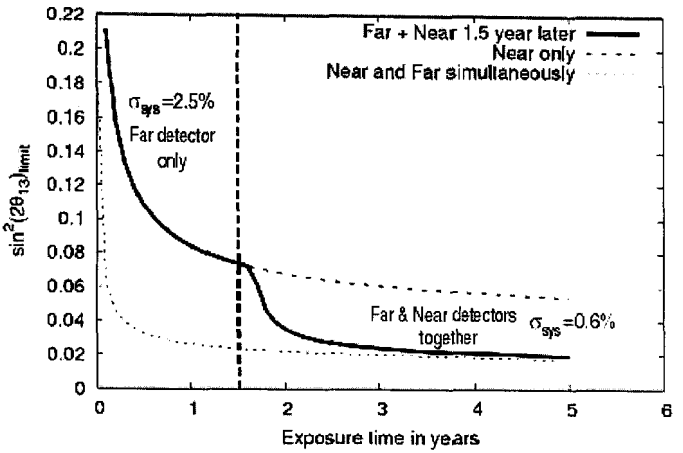

Figure 3. The $\sin^2(2\Theta_{13})$ sensitivity limit of Double Chooz (90% CL) function of time assuming zero value for Θ_{13}

4. Conclusions and schedule

Since now, the Double Chooz collaboration has made a considerable progress in designing and prototyping the detector components; the plan foresees the first data taking for the spring 2009. The existing infrastructure of the far lab will split the data taking period in two phases. The first one with far detector only, followed a year and half later by a second phase with both detectors involved. In short time a considerable progress will be achieved, e.g. the CHOOZ Θ_{13} limit can be surpassed in the first 6 months. The second phase will decrease the systematic uncertainty until ~0.6% (Figure 3) and the final sensitivity after 5 years of data taking will be $\sin^2(2\Theta_{13}) < 0.025$, an order of magnitude improvement over the current limit.

References

1. W. M. Yao *et al.* [Particle Data Group], Chapter 13: "Neutrino Mass, Mixing, and Flavor Charge", *J. Phys.* **G33**, 1 (2006).
2. M. Apollonio *et al.* [CHOOZ Collaboration], *Eur. Phys. J.* **C27**, 331 (2003).
3. F. Ardellier *et al.* [Double Chooz Collaboration], *arXiv:hep-ex/0606025*
4. CAEN Catalogue, available at http://www.caen.it

Technical Solutions for the MAGIC Telescope

M. DORO* on behalf of the MAGIC collaboration**

University of Padova & INFN
via Marzolo 8, 35131, Padova, Italy
**michele.doro@pd.infn.it*
***http://wwwmagic.mppmu.mpg.de*

The atmospheric Cherenkov telescope MAGIC for ground-based gamma-ray astronomy is operating since late 2003 on the Canarian island La Palma. The telescope's 17 m diameter mirror is composed of 964 light weight, square all-aluminum mirrors of 234 m^2 total area, which allows to lower the energy threshold to a value far beyond that of past generation of telescopes. The trigger system, based on ultra-fast decision logics (topological, time-coincidences, etc.) is designed to cope with very fast PMT signals (2 ns). Details of the MAGIC telescope will be presented, technical problems and solutions will be discussed as well as a report on three years of operations will be given.

Keywords: Style file; LaTeX; Proceedings; World Scientific Publishing.

1. The MAGIC Telescope

The MAGIC telescope is designed and operated by a collaboration of 150 physicists from 22 institutes from 7 countries. The telescope is fully operational since fall 2003 and is currently in its third observations cycle. The MAGIC telescope belongs to the Imaging Atmospheric Cherenkov Telescope (IACT) class of detectors and is currently the one with the world-largest mirror dish. IACTs allow to study from ground the Very High Energy (VHE) gamma–ray emission coming from cosmic sources of various classes, i.e. Supernova Remnants (SNR), pulsars, Active Galactic Nuclei (AGN), etc. Gamma-rays, as well as the many orders of magnitude more frequent charged cosmic rays, hitting the Earth atmosphere initiate atmospheric particle showers with a typical shower maximum around 8-12 km asl. The charged shower particles, mostly electrons and positrons, emit Cherenkov light in case their speed exceeds that of light in the atmosphere. The Cherenkov light illuminates nearly uniformly a dish of $\sim$ 120 m radius. If a telescope is located inside this Cherenkov-light pool, the light hitting

the mirror can then be reflected and focused onto a multi-pixel camera composed of a large number of photomultipliers. An image reconstruction algorithm allows the determination of major parameters of the primary particles, such as energy and direction, as well as its likeliness to be a hadron or a gamma-ray. As lower energy gamma-rays produce a lower density of photons at ground, a larger telescope mirror area is required to decrease the energy threshold of the telescope. In case of MAGIC, the 17 m reflector allows the reconstruction of primary gamma-rays above $\sim$ 70 GeV (zenith angle dependent) with a sensitivity of 10^{-11}ph cm^{-2} s^{-1} in 50 hours of observation and with an effective area, which is of the order of 10^5 m^2 (slightly depending on the energy).[1]

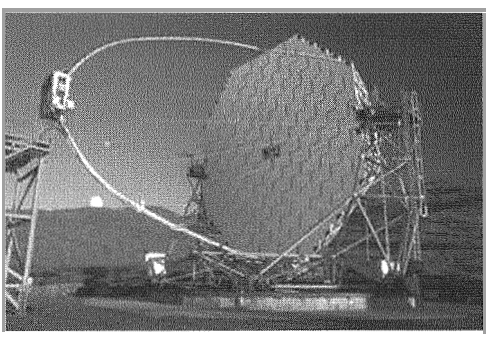

Fig. 1. The MAGIC telescope. La Palma (Spain) (28.75 N, 17.89 W)

2. Technical Solutions

MAGIC is located on the Canary island of La Palma (28.75 N, 17.89 W) at 2225 m asl. The observation conditions on site are amongst the best in the world, even if occasional strong winds, winter snowfalls and high humidity demand anyhow a strong technical effort to prevent damaging and ageing as the MAGIC telescope is too large to be protected by a dome.

The telescope construction incorporates a number of "firsts" used in IACTS: *a*) It has the worldwide largest mirror dish. *b*) It is the first time that a lightweight mirror dish has been constructed from carbon fiber reinforced plastics (CFRP). *c*) First use of diamond turned light weight all-aluminum sandwich mirrors. *d*) First use of an active mirror control to counteract small deformations of the 17 m ϕ mirror during positioning and tracking, *e*) First use of low gain hemispherical PMTs with diffuse lacquer coating

and special light catchers resulting in increased quantum efficiency and allowing prolonged operation during modest moon shine. *f*) First use of the transmission of the fast analog PMT signals over 160 m by means of optical fibers to a distant counting house. *g*) First use of a 2 GHz F-ADC digitization of the fast PMT pulses.
In the following, an overview on the technical solutions adopted for each subsystem is reported and discussed. A detailed design report of the initial design ideas can be found in Barrio et al.[2]

2.1. *The Mounting and Drive System*

The reflector frame satisfies at the same time three main demands: it is very large, it is light-weight and it allows for fast repositioning. The space frame is made from carbon fiber reinforced plastic (CFRP) tubes and has a weight of only 5.5 tons. The CFRP construction is about three times stiffer and has a less than a third of weight of an equivalent steel construction. The structure of an alt-azimuth design is mounted on a circular rail of 19 m ϕ. The telescope can be moved from $-80°$ to $105°$ in declination and $450°$ in azimuth. The camera at around 17 m distance from the reflector is carried by a single aluminum tubular arc. The weight of the camera is around half a ton, and the small bending, unavoidable during the telescope tracking, is corrected via a re-orientation of the mirror. Two motors control the motion in azimuth and one motor the zenithal motion, with a maximum power consumption of $\sim$ 7 kW per motor. The angular positions are controlled by absolute shaft-encoders of 14-bit precision/360°. In addition, a starguider camera, mounted at the centre (offset by 1 m) of the reflector, monitors the positioning of the telescope by viewing both the camera of the telescope and the corresponding section of the sky star-field.[3] The lightweight structure allows for very fast repositioning of the telescope to any position on the sky within $\sim$ 30 s. This challenging feature was designed to instantly react to Gamma-Ray Burst (GRB) alerts from dedicated satellites detecting GRBs in the KeV/MeV domain.[4]

2.2. *The Reflector and Details on its Construction*

The 17 m ϕ reflector (17 m focal distance) follows a parabolic profile which was chosen to maintain the temporal structure of the shower light flashes. The reflector of MAGIC I is tessellated and comprises 956 mirrors of a total area of 234 m^2. Each mirror is a square of 0.495 m side length and has a spherical profile whose radius of curvature is optimized for the position

in the telescope to best approximate the paraboloid. MAGIC I mirrors are grouped onto panels of 4 or 3 elements and each panel can be moved by the Active Mirror Control system (AMC).[5] The AMC was designed to correct small deformations of the mirror support dish during telescope positioning and tracking. The mirrors are an all-aluminum, light weight sandwich construction composed of an Al-skin and an Al-box and filled with a Hexcell honeycomb structure.[6] A heating wire mesh, embedded in the sandwich, can be switched on in case of dew or ice deposits on the mirrors. The total power consumption for heating the entire reflector is 40 KW. The reflecting aluminum surface of the mirror elements is diamond turned using the so-called fly-cutter technique, which provides an average roughness of 4 nm and a mean reflectivity of 85%. The surface of the mirrors was coated by a thin layer of quartz (with some admixture of carbon) for protection against corrosion and acid rain. Very little degradation ($< 3\%$/year) of the reflectivity was observed after 4 years exposure the atmosphere at La Palma. The well-adjusted mirror has, for an infinite point-like source, a point spread function (PSF) of the reflected spot of $\sim$ 10 mm ϕ at the camera of the telescope. New solutions will be adopted for MAGIC II, whose outermost rings of mirrors will be made of recently designed glass mirrors, produced by a cold-slumping technique. The central part of the reflector will be equipped by a modified version of the MAGIC I diamond-turned mirrors but of increased dimension ($1m^2$ area), improved water-tightness and lower weight. Also the surface quality of these new Al-mirrors is enhanced and should result in a PSF of 5 mm.[6]

2.3. *Camera and read-out*

The camera of the MAGIC telescope of a 3.6° field of view (FOV) comprises 576 photomultipliers with 396 1′ PMTs from Electron Tubes Ltd of type 9116 covering the inner section (up to 1.2° radius) and 180 PMTs of type 9117 and 1 1/2″ for the outer part of the camera. The PMTs of a hemispherical cathode were enhanced in quantum efficiency (QE) by a diffuse lacquer doped with P-Terphenyl shifting the short wave UV component of the Cherenkov light into the spectral range of maximum sensitivity. In order to minimize losses due to dead space between the densely packed PMTs we used hex-to-round light concentrators, which added a further increase of the QE by deflecting many photons such that their trajectory passed the semitransparent photocathode twice. The mean QE of the entire system (mirror, camera window, cone, effective PMT QE) between 300 and 600 nm was 15%. The 6 dynode PMTs were operated at a gain of $\sim 3 \cdot 10^4$

in order to allow also observations at modest moon shine.[8] Finally, the fast PMT signals are converted back into optical signals by means of large dynamic Vcsels operating in the analog mode and routed via 160 m long optical fibers to the 80 m away counting house. At the counting house the optical signals are converted back into electronic signals, split and routed to the trigger branch and to the fast digitization and recording system. The trigger is two-fold: in level–0 the PMT analog signals are converted into logical signals once the signals exceed a 5-8 overlapping photoelectrons threshold. Level–1 is dedicated to the time-coincidence topological reconstruction of the signal in the camera: when a number of pixels (adjustable by software) are activated at the same time according to the next-neighbor logic (2NN–6NN) a level-1 trigger signal is generated. The typical trigger rate is about 150-250 Hz interleaved by frequent calibration events. Upon a trigger the data received by the telescope camera are digitized by ultra-fast Flash-ADCs of 2 GHz sampling rate. This system has replaced since a year the original digitizing system of only 300 MHz sampling rate and allows a much better timing measurement and a considerable reduction of the night sky light background.

3. Future Prospects

The IACT technique is already well-established. The so-called III generations of IACTs will likely start observation around 2012-2015 (CTA in Europe and AGIS in USA). These new instruments will have a factor 10 increase in sensitivity by using a large array of IACTs of both large and small mirrors to allow observations on both the high energy and the low energy domain of VHE (hundred of TeV and few GeV respectively). Chances for additional improvements are promising as new technologies are emerging such as new high quantum efficiency photon detectors, low power GHz digitizers for each pixel, higher level triggers and better mirror optics.

References

1. J. Albert *et al.*, astro-ph/0705.3244
2. Barrio et al., *MAGIC Design report*, 1998
3. R. Mirzoyan *et al.*, ApJ. 27:509-511,2007.
4. D. Bastieri et al., astro-ph/0709.1380
5. A. Biland *et al.*, Procs. ICRC 2007, astro-ph/0709.1574.
6. M. Doro, Procs. 6th RICH, Trieste, 2007
7. D. Paneque, NIM A518:619-621, 2004.
8. J. Albert *et al.*, arXiv:astro-ph/0702475.

CHALLENGING THE NEUTRINO MASS WITH CUORE

F. FERRONI

Sapienza University & INFN,
Roma, OO185,Italy
**E-mail: fernando.ferroni@roma1.infn.it*

One of the fundamental questions still open in elementary particle is the nature of the neutrino mass. Whether Dirac or Majorana, its knowledge would deeply impact the development of the field. Double Beta Decay experiments are, although extremely challenging, the only way known that might give an answer to the question. In this paper one of the second generation experiment that aims to get the sensitivity for probing the inverted hierarchy will be discussed. It is CUORE, in preparation at the Gran Sasso underground laboratories of INFN.

Keywords: Style file; LaTeX; Proceedings; World Scientific Publishing.

1. Introduction

Mysteries about neutrinos are several and of different nature. We know that they are neutral particles with an extraordinary little mass compared to the one of all the others. Although they are massive we have not succeeded yet in measuring their mass. We do not know if the neutrino is a particle different from its antiparticle or rather as hypothesized [1] by Majorana in 1937 they are the same particle. Majorana observed that the minimal description of spin 1/2 particles involves only two degrees of freedom and that such a particle, absolutely neutral, coincides with its antiparticle. If the Majorana conjecture holds then it will be possible to measure an extremely fascinating and rare process that takes the name of Neutrinoless Double Beta Decay (0ν DBD). The net effect of this ultra rare process will be to transform two neutrons in a nucleus into two protons and simultaneously to emit two electrons. Since no neutrinos will be present in the final state the sum of the energy of the two electrons will be a line. The rate of this yet unobserved phenomenon will also allow a determination, although not precise, of the neutrino mass. A set of pioneering experiments [2] has been performed for this search. With the exception of one, all of them resulted into a negative

observation. The one claiming a positive evidence [3] (about 4σ) has not fully convinced the community and it is waiting for a possible confirmation. A new generation of experiments is in preparation [4] for challenging this difficult problem. In this paper, one of them will be described in some detail. It is CUORE [5], a concept extrapolated from a running prototype (CUORICINO [6]) that will be functional around 2010 with a sensitivity such to be able to probe the inverted hierarchy region as described by the most recent analyses [9] of the global neutrino data.

2. Majorana Neutrinos and Double Beta Decay

Neutrinoless double-beta decay is an old subject. What is new is the fact that, recently, neutrino oscillation experiments have unequivocally demonstrated that neutrinos have mass and that the neutrino mass eigenstates mix. Indeed the massive nature of neutrinos is a key element in resurrecting the interest for the Majorana conjecture.

The practical possibility to test the Majorana nature of neutrinos is indeed in detecting the process known as the Double Beta Decay (DBD) without emission of neutrinos.

Although the possibility [7] for this process was pointed out far in the past, the experimental search looked just impossible. The key element for the process to occur is in fact in the helicity flip needed. As long as the neutrino was thought to be massless this could just not happen. Nowadays we know that this is indeed possible. The discriminant between Dirac and Majorana neutrinos is in the lepton flavour conservation, required by Dirac and violated by Majorana. So that the observation of neutrinoless DBD would be the proof of the Majorana conjecture. The oscillation experiments have yielded valuable information on the mixing angles and on the mass differences of the three eigenstates. They cannot, however, determine the scale of the neutrino mass, which is fixed by the lightest neutrino mass eigenvalue. This can only be directly determined by beta decay end point spectral shape measurements, or in the case of Majorana neutrinos, by the observation and measurement of the neutrinoless double-beta decay half-life. The oscillation experiments yield values for the mixing angles and mass differences accurate enough to allow the prediction of a range of values of the effective mass of the Majorana electron neutrino. As a function of the oscillation parameters indeed we find that

$$m_{\beta\beta} = \Sigma m_{\nu_k} U_{ek}^2 = cos^2\theta_{13}(m_1 cos^2\theta_{12} + m_2 e^{2i\alpha} sin^2\theta_{12}) + m_3 e^{2i\beta} sin^2\theta_{13}$$

According to most theoretical analyses of of present neutrino experiment

results, next-generation DBD experiments with mass sensitivities of the order of 10 meV may find the Majorana neutrino if its mass spectrum is of the quasi- degenerate type or it exhibits inverted hierarchy.

3. Experimental techniques

The DBD's are extremely rare processes. In the two neutrino decay mode their half- lives range from $T_{1/2} \simeq 10^{18}y$ to 10^{25} y. The rate for this process will go as

$$1/\tau = G(Q,Z)|M_{nucl}|^2 m_{\beta\beta}^2.$$

The first factor (phase space) that goes like Q^5 is easily calculated. The second (nuclear matrix element) is hard to compute. Several calculation made under different approaches [8] exist and they differ by a lot. The experimental investigation of these phenomena requires a large amount of DBD emitter, in low-background detectors with the capability for selecting reliably the signal from the background. The sensitivity of an experiment will go as $S^{0\nu} \propto a(\frac{MT}{b\Delta E})^{1/2}\epsilon$. Isotopic abundance (a) and efficiency (ϵ) will make you gain linearly, while mass (M) and time (T) only as the square root. Also background level (b) and energy resolution (ΔE) behaves as a square root. In the case of the neutrinoless decay searches, the detectors should have a sharp energy resolution, or good tracking of particles, or other discriminating mechanisms. There are several natural and enriched isotopes that have been used in experiments with tens of kilograms. Some of them could be produced in amounts large enough to be good candidates for next generation experiments. The choice of the emitters should be made also according to its two-neutrino half-life (which could limit the ultimate sensitivity of the neutrinoless decay), according also to its nuclear factor-of-merit and according to the experimental sensitivity that the detector can achieve.

Double beta decay experiments can be divided into two main categories: measurement with source being separate from the detector and measurement with a detector that also acts as the source (Fig. 1).

When the source is the same as the detector (calorimetric type) , source mass is maximized while materials that could potentially contribute to the background is minimized. Also energy resolution can be optimized. However the absence of topological signature does not allow to reject on the event-by-event basis the background coming from photons. Conversely the other type of detectors (spectrometer type) can optimize the background rejection although at the cost of a reduced mass, a complicate geometry

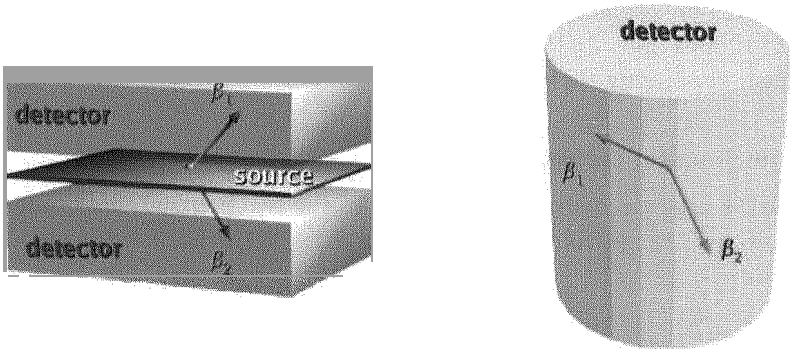

Fig. 1. Schematics of the two main technique for neutrino-less DBD search.

and a comparatively worse energy resolution. Bolometers belong to the calorimetric category. At low temperatures (the operating temperature for CUORICINO is 8 mK), the heat capacity of crystals is proportional to the cube of the ratio of the operating and Debye temperatures. The energy released in a single particle interaction within the crystal is clearly measurable as change in temperature of the entire crystal by using neutron transmutation doped (NTD) germanium thermistors which are optimized to operate at these temperatures.

A number of experiments are currently at various stages of development to probe the degenerate and into the inverted mass hierarchy region of the neutrino mass spectrum.

All of them are needed since it is imperative to carry out double beta decay searches in multiple isotopes, both to improve the nuclear matrix calculations necessary to extract the effective neutrino mass, and to ensure that the observation of a line at the expected energy is not a result of a yet unknown radioactivity line.

4. CUORICINO and CUORE

Cryogenic bolometers, with their excellent energy resolution, flexibility in material, and availability in high purity of material of interest, are excellent detectors for search for neutrinoless double beta decay. Kilogram-size single crystals (cubic crystals of 5cm side) (Fig. 2) for TeO_2 are now available

and utilized in CUORICINO in an array for a total detector mass of 40 kg. CUORICINO results from a total exposure of 11.83 kg-yr of ^{130}Te (Fig. 3)

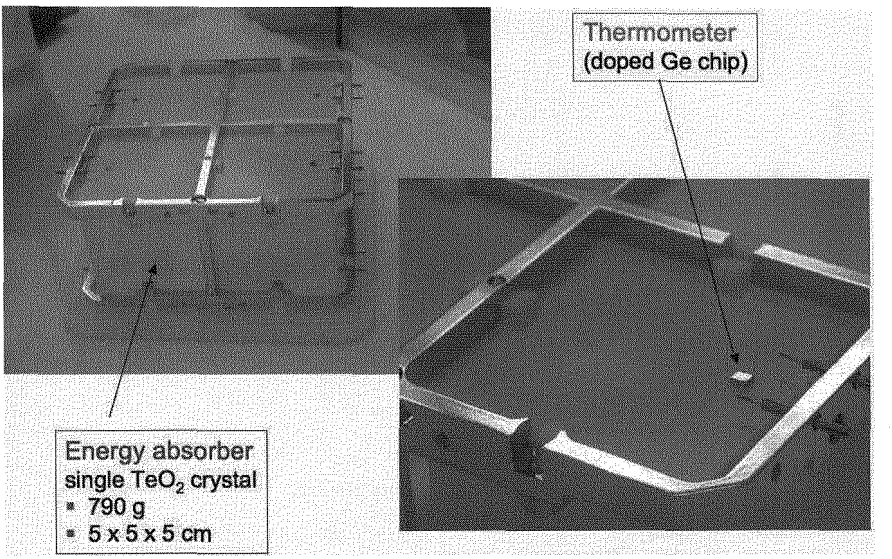

Fig. 2. Cuoricino 4-crystals building block.

show no evidence for a peak at 2530 keV, the expected Q-value for for ^{130}Te. The absence of any excess events above backgrounds in the region of interest gives a limit of $T_{1/2} \geq 3.0 \times 10^{24}$ yr(90%) C.L. on the 0ν decay rate of ^{130}Te. This corresponds to an effective neutrino mass of $m_{\beta\beta} \leq 0.20 - 0.98$ eV, the range reflecting the spread in nuclear matrix element calculations. The background measured in the region of interest is 0.18 ± 0.01 counts/keV/kg/yr. CUORE (Cryogenic Underground Observatory for Rare Events), to be located at the Gran Sasso National Laboratory of INFN (LNGS) , at a depth of 3400 m.w.e., will consist of 988 bolometers of TeO_2 crystals, with a total mass of 740 kg. Because of the high isotopic abundance (34%), 204 kg of ^{130}Te will be available for the relevant process without isotopic enrichment, a virtue that eliminates the requirement for the very expensive process needed in all of the other proposed next generation experiments, making CUORE both timely and significantly less expensive than other experiments. CUOREs modular design (see Fig. 4) and flexibility of cryogenic detector will also allow future searches in other isotopes of interest.

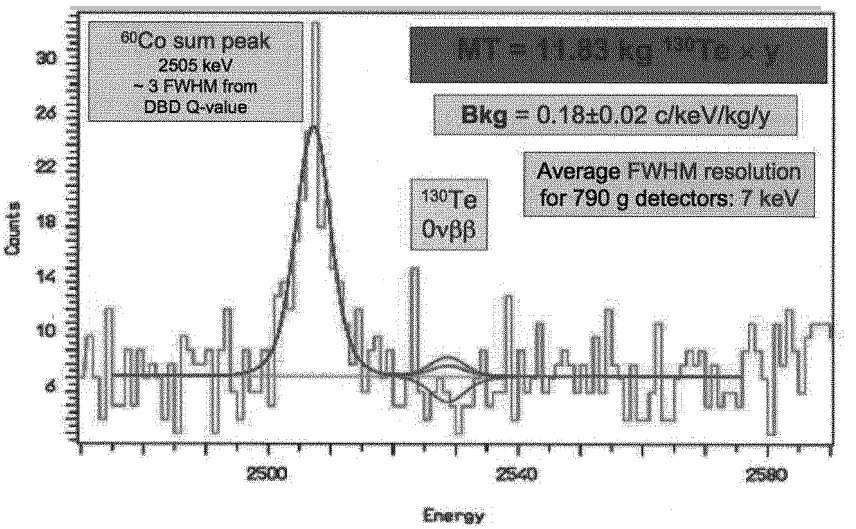

Fig. 3. Cuoricino results.

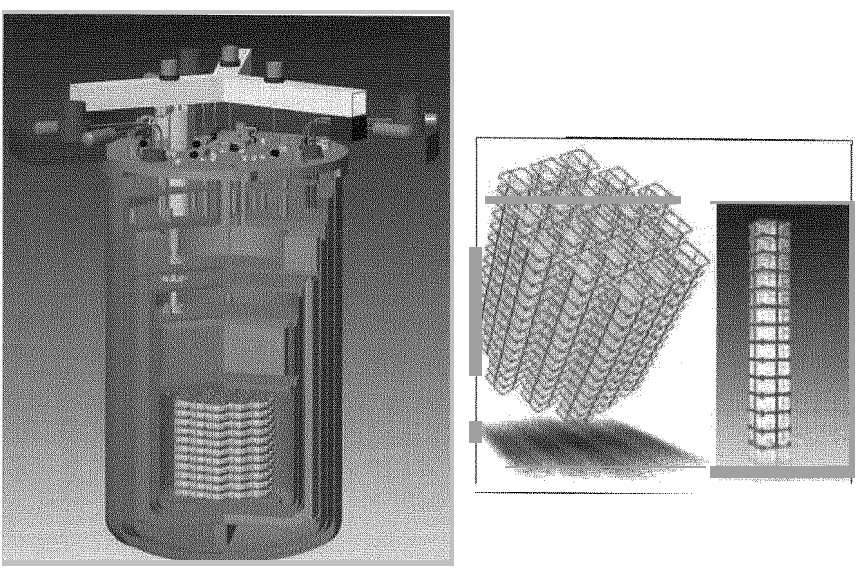

Fig. 4. Cuore detector.

The extrapolation from CUORICINO results to CUORE expectation is based on the following facts:

- a total mass 20 times larger
- a running time 10 times longer
- an energy resolution 50% better
- a background 20 times smaller

The major challenge in obtaining the desired sensitivity is the reduction of the background rate. This task can be accomplished in three main ways:

- by reducing the amount of material (Cu in our case) surrounding the crystals.
- by a proper cleaning procedure of all the materials that will be in contact or will look at the crystals.
- by finding a veto procedure to eliminate unwanted signals coming from outside the bolometer.

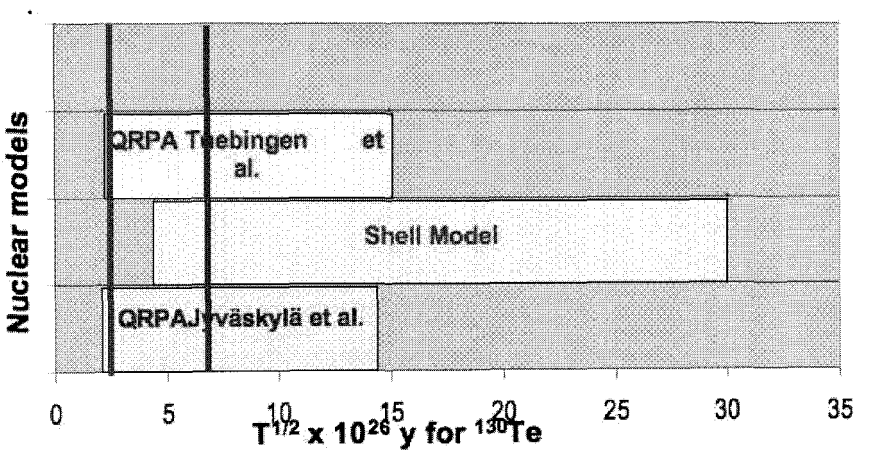

Fig. 5. CUORE projected sensitivity to $m_{\beta\beta}$. The range of $m_{\beta\beta}$ is between 20 and 50 meV. The matrix elements are taken from recent calculation of three different groups. The two lines correspond to a conservative (aggressive) Cuore background estimate.

The results so far available from the CUORICINO understanding, the dedicated *R&D* performed in a dedicated cryogenic facility running at LNGS and the MonteCarlo simulations indicate that a factor 10 has been

already secured.

The sensitivity, in term of neutrino mass and taking into account the entire set of matrix elements calculation available, shall be $m_{\beta\beta} \approx 19 - 100$ meV. The complex interplay between the measured lifetime and the uncertainty of the matrix elements in extracting a limit for the neutrino mass is shown in Fig. 5.

5. Conclusion

Neutrino physics is one of the leading field of the high energy research today. One of the top question that has to be answered is about the Dirac or Majorana nature of neutrino mass. The neutrino-less double beta decay search is the only experimental line that can answer this fundamental question and that might possibly be the sole chance to provide a measure of neutrino mass. Cryogenic bolometer, with its flexibility in material choice and the ability to scale up to the ton- scale makes it an ideal technology for large-scale detector for double-beta physics experiments. CUORICINO is currently running as the most sensitive experiment. Much of the technology has been tested for CUORE that will start taking data in 2010 with much a larger mass. The sensitivity of CUORE will allow probing a good portion of the mass region predicted in case of inverted hierarchy. The proof of the Majorana nature of the neutrinos might be achieved by CUORE together with a determination of the neutrino mass scale.

6. Acknowledgments

I am deeply indebted to Prof. E. Fiorini and all my colleagues in CUORE. The list of their names is found in [5].

References

1. E. Majorana, *Il Nuovo Cimento*, **14**, 171 (1937).
2. See for example presentations at Neutrino06 by M. Hirsch, F. Simkovic, S. Elliott, and A. Barabash.
3. H. V. Klapdor-Kleingrothaus et al., *Nucl. Instrum. Meth.*, **A522**, 371 (2004).
4. Ph. Adamson et al., EoI in the SuperNemo double beta decay program, 2004; I. Abt et al., GERDA Technical Proposal, 2005; C.E. Alseth et al., The proposed Majorana ^{76}Ge double beta decay experiment, *Nucl. Phys. Proc. Suppl.*, **138**, 217 (2005); H. Ejiri et al., Double Beta Decays and solar neutrinos with ^{100}Mo, 2005; D. Akimov et al., EXO: An Advanced Enriched Xenon double-beta decay Observatory, *Nucl. Phys. Proc. Suppl.*, **138**, 224 (2005).
5. R. Ardito et al., hep-ex/0501010.

6. R. Alessandrello et al., *Nucl. Phys. Proc. Suppl.*, **87**, 78 (2000).
7. W. H. Furry, *Phys. Rev.*, **56**, 1184 (1939)
8. V.A. Rodin, A Faessler, F. Simkovic, P. Vogel, *Nucl. Phys.*, **A766** 107 (2006) and Erratum; M. Kortelainen and J. Suhonen, *Phys. Rev.*, **C76** 024315 (2007); E. Caurier, F. Nowacki, A Poves, *arXiv:0709.0277*
9. A. Strumia and F. Vissani, *Nucl. Phys.*, **B276**, 294 (2005).
G. L. Fogli et al., *Prog. Part. Nucl. Phys.* , **57**, 742 (2006).

A MODULAR DAQ SYSTEM FOR NEXT GENERATION BOLOMETRIC ν MASS EXPERIMENTS

LUCA FOGGETTA[1,2,*] ANDREA GIULIANI[1,2] MICHELA PREST[1,2]
ERIK VALLAZZA[3]

1 Università degli Studi dell'Insubria - V.Valleggio 11-22100-Como-Italy
2 INFN - Milano Bicocca - Milano-Italy
3 INFN - Trieste – Italy

This work will describe the development and the present status of the new DAQ system for the MARE experiment. This kind of DAQ system is oriented to a run-time selection and digitization of analog signals coming from a huge number of microbolometers in a cryogenic environment, readout by an array of semiconductor thermistors. The main properties of this DAQ are a full analog signal sampling feature with high speed FPGA-controlled trigger logic for a fast hardware signal selection and trigger. This DAQ system has to be capable to collect and measure the beta spectrum of ^{187}Re with high statistics and energy resolution, essential for the neutrino mass determination.

1. Introduction

The measurement of the neutrino mass scale is crucial over two fronts: the progress in the comprehension of elementary particles and the solution of hot astroparticle problems. The experimental evidence of oscillating neutrino flavours involves a massive neutrino, a fact that represents a serious crack of the Standard Model building, after 30 years of almost boring successes. Laboratory experiments aiming at fixing the absolute neutrino mass scale are based on the study of proper nuclear processes. In this class of researches, only kinematical direct measurements permit to estimate neutrino masses in a model-independent approach with the nuclear β-decay. A next generation experiment based on the analysis of the ^{187}Re β-decay is MARE[1] (Microcalorimeter Array for a Rhenium Experiment). In the MARE approach, the source is embedded in a low temperature microcalorimeter to provide a measurement of the deposited energy. Since only the ν escapes from the detector, the measured energy is the total one minus the neutrino one; this β-decay is by far the most sensitive process due to the very low energy available to the particles in the final state. Natural Rhenium has a specific β-activity of the order of 1 Bq/mg, which is ideal for the typical size and time response of the thermal calorimeters in a cryogenic environment. Unfortunately, even taking advantage of this lowest Q-value β-process in nature[2]

(Q = 2.5 keV for ^{187}Re), it is very hard to get sensitivities much lower than 1 eV. One of the limits to the sensitivity on this calorimetric approach comes from the pulse pileup: unresolved pileup produces "background" close to the end-point. This effect leads to an irreducible statistical uncertainty on the neutrino mass determination and to systematic effects that follow the spectral shape distortions. These facts translate in very stringent requirements on the DAQ system.

2. The mare experimental setup

The MARE experiment will be developed in several steps: the initial one (MARE-1) to study detectors and DAQ, aiming to a few eV resolution; the final clue aims to the sub-eV setup (MARE-2). The MARE-1 experiment starts from the result of the MIBETA experiment (that collected statistics for a 2σ upper limit of 15eV)[3]. The microbolometer of MIBETA consisted of dielectric crystals of $AgReO_4$ (which are both the β source and the absorber): these crystals had a typical mass of 350μg and a β-activity around 0.5Bq. The MIBETA group has also shown to be able to develop relatively massive microcalorimeters with a record energy resolution (~5 eV FWHM) at the ^{55}Mn X-ray energies (5.9 keV and 6.4 keV). The MARE-1 experiment will use ~300 $AgReO_4$ crystals of about 450 μg each, readout by semiconductor neutron doped thermistors; the expected event rate is 0.3decays/s/crystal. Assuming an energy resolution of 10 eV FWHM and a time resolution of 100 μs for each element, the statistics gathered in three years will allow to set a limit of the order of ~2 eV on the neutrino mass.

3. Mibeta-2 daq

This kind of DAQ system has to acquire the thermistor analog signals coming from a huge number of bolometers in a cryogenic environment. The DAQ standards have to be user friendly and fail proof since it has to be installed in a large number of MARE sites.

A full analog signal sampling is necessary to perform pulse shaping optimization, pileup rejection and pulse parameterization: the analysis procedure extracts 17 pulse parameters and pileup information using both the time and frequency domain for each sampled pulse. The sampling procedure has to be a compromise between the desired Nyquist frequency and the electronics filtering hardware setup: the pulse pileup rejection efficiency strong depends on its recognition during the rise time of the first pulse in the pileup one. Thus the DAQ system has to digitize the whole length of the pulse (that lasts few milliseconds) with a pulse-pair resolving time of 100μs. In order to reduce the

load on the databus to the storage system the signal rejection can be accomplished in two steps: the hardware and the software pulse processing.
The former has to be fast enough to discriminate, during the sampling procedure, saturated pulses or simple pileup. The hardware Front Trigger Board detects over threshold pulses with a smart retrigger logic that acts in the decay time of the first pulse when the amplitudes of the secondary ones are a significant fraction of the first. The software process leads to precise pileup recognition in the off-line analysis by means of optimum-filter based algorithms, as the Wiener filter.
The DAQ core is represented by several 32-channel VME units, controlled by a SBS Bit3 Mod.620 module, linked in fiber channel to a DAQ Linux PC. The data are sent via NFS to a dedicated storage system. The DAQ units are composed of a custom-made Front-end Trigger Board (FTB, a VME mixed analog and digital board) and a commercial, hardware-triggered ADC. Each FTB is controlled by a Cyclone II Altera FPGA; the board is developed for a 2-level trigger/retrigger logic and for simultaneous pulses discrimination and tagging. The ADC module is an ICS-145, 32-channel, 16-bit, VME data acquisition card with a standard output rate of 2.5 MSample/sec and able to sampling up to 10 MS/sec. Its design has been optimized for offering high speed, precision and low channel crosstalk.
From the DAQ point of view, the ~300 readout channels will be grouped in sets of 32 channels each, corresponding to the maximum number of the ADC input channels. The 32 conditioned analog out lines corresponding to the 32 detector signals, will be connected to the corresponding FTB, which processes the signals and controls the respective ADC sampling operations. Each FTB will work as the corresponding ADC trigger generator; its analog part will amplify and discriminate (i.e. taking into account the baseline fluctuations) the 32 conditioned signals producing digital-coded signals (i.e. Time over Threshold). During the initial, arming phase, all the 32 detector signals are sampled and stored in a double switching circular buffer installed on the ADC for a pretrigger sampling. This feature allows the off-line optimizing procedure to achieve a more precise evaluation of the pulse parameters. When a "good" event is detected in one or more channels, the FTB will generate an OR trigger signal, sending it to the corresponding ADC. During the sampling time the FTB stores, in internal trigger registers, couples of triggered channels identification number and respective timestamp, which has been generated starting from the OR time. Since all the 32 channels are sampled in a synchronous way, this last FTB feature allows to keep, in the databuffer, the starting points of the initial sample for each fired channel, if a retrigger occurs. If subsequent triggered channels

need more samples than the ones the onboard data buffer offers, a fast retrigger mode has been developed to ensure the 2048 sampling points for each pulse. The hardware pulse rejection is performed if a retrigger occurs in the same fired channel during the 2048 sampling clocks; the FTB has the possibility to tag the corresponding couple in the onboard trigger register, thus discarding definitively the event.
The data dumping phase goes from the ADC sampling buffer to a NFS storage filesystem, starting when the DAQ-unit thread acknowledges the data ready signal from the ADC; the channel interlaced data are transferred in a full slave DMA mode. At the same time, the thread reads programmatically the couples channels/timestamps from the FTB. This data stream is subsequently deinterlaced and segmented, to extract the defined number of samples from each timestamp. This allows a quite complete independent storage of the data of up to the ADC maximum channel number. Recent tests demonstrated that the ICS-145 is capable of transferring up to 3.4 Msamples/sec/board in block transfer mode with all the 32 channels hit. This output rate allows a trigger rate from 80 Hz up to 640Hz depending on the number of active channels. The semi-hardware managed DMA transfer reduces the processor loads down to 15%, allowing some fast pre-analysis features, useful for the startup phase of the experiment.

3.1. *A focus on the software*

The DAQ software is developed with the theory typical of a multi-purpose DAQ: unlimited ADCs number and type (nowadays only hosted in VME environment), run-time setup changing (i.e. time scheduled preanalysis and SlowControl procedure with the use of dynamic function pointers and multithreadings), Slow Control integration (via Ethernet or USB bus) and easy further implementation (large use of abstract constructions).
The GUI is developed in Tcl/Tk with specific stand-alone DAQ and SlowControl panels for preliminary setup data consistency check and high level communication. The Tcl multi-language generalized script procedure permits an easy integration of external SlowControl software. The operative control of each DAQ unit runs in a separated thread with Round Robin kernel arbiter; the C low level protocols are contained in a C shared object triggered by the Tcl core; the GUI and the Slow Control software run in low priority kernel threads. An abstract structure permits to control the DAQ unit with different type ADC modules with the same high level routines: a global defined array of pointers to arrays of structures that contain coded information on specific modules address and data registers. This software memory mapping, shown in fig.1, of the

hardware register is a part of a kind of register extension used to complete the run-time information on the specific module, achieving a standard in controlling every kind of module. The mathematical and signal processing libraries are the CERNLIB, GSL, IPP and MKL. All of the instrumentation module drivers, low-level and high-level control and processing library are custom made.

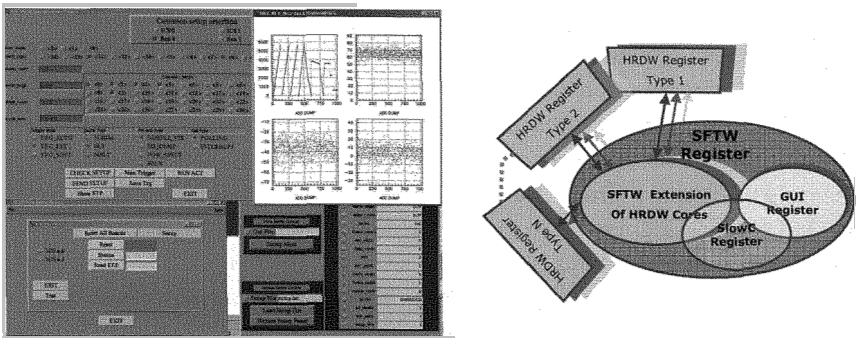

Figure 1 – On the right side: DAQ main panels. On the left: illustration of the software core register

4. Storage system

Up to now, the storage system is intended to be structured with a network of DAQ PCs in a multi-gigabit aggregate Ethernet connection to a high performance multiprocessor Linux-PC for the data analysis. One of its processors will be used as a server to give a NFS access to the DAQ PCs at the filesystem of the Direct Attached Storage unit and from this to the SCSI tape library for backup operation. The DAS storage unit will be connected by FiberChannel to the analysis PC to provide access to the RAID6 filesystem.

Acknowledgements

We greatly thank our informatics system experts Luca Carbone and Luca Paredi for their fundamental work in the storage system design.

Reference

1. MARE Collaboration. MARE: MICROCALORIMETER ARRAYS FOR A RHENIUM EXPERIMENT. The MARE Collaboration proposal. 2006. downloadable from: http://crio.mib.infn.it/wig/silicini/publications.html
2. C. Arnaboldi et al., *Phys. Rev. Let. 91*, BOLOMETRIC BOUNDS ON THE ANTINEUTRINO MASS, 161802 (2003)
3. M. Sisti, et al., *Nucl. Instr. Meth. Phys. Res. A*, NEW LIMITS FROM THE MILANO NEUTRINO MASS EXPERIMENT WITH THERMAL MICROCALORIMETERS **520** 125 (2004)

NOVEL TECHNIQUES FOR ATMOSPHERIC MONITORING FOR EAS DETECTORS USING HIGH RESOLUTION SPECTROSCOPY *

E. FOKITIS[1], P. FETFATZIS, S. MALTEZOS, N. ANTONAKAKIS SPYROPOULOS
Physics Department, National Technical University of Athens, Iroon Polytechniou 9 Zografou, Athens, 15780, Greece

A. ARAVANTINOS
Physics Department, Technological Educational Institute of Athens, Ag Spyridonos, Egaleo, Athens,12210, Greece

First, we present a system based on a pair of Fabry-Perot interferometer prototypes to be used for quantifying the aerosol and molecular scattering coefficients, in two separate channels. The system is considered in operation either for backscattering measurements or in bi-static mode giving unbiased measurements of the aerosol phase function. The advantages over existing methods are analyzed. Secondly, we present strategies based on high resolution spectroscopy for measuring atmospheric absorption coefficients at ionospheric heights, specifically at the wavelengths of the main nitrogen fluorescence lines produced by Extensive Air Showers at the troposphere.

1. Introduction

In this work, we aim to develop the receiver component, of a Lidar System for use in EAS detection, of Ultra High Energy Cosmic Rays (UHECR)[1]. A part of the experimental set up in EAS detection is the Atmosphere, which interacts in two ways in these measurements. Atmospheric parameters such as humidity, aerosols, pressure, clouds, etc affect the development of the Shower [2]. Secondly the detected optical signal, at first propagates in the Atmosphere. This signal, consists of two components, the Fluorescence and Cherenkov, which are detected generally in deferent ways or together [3]. The same parameters of the atmospheric conditions, affect the propagation of the prospective signal in a different way [4]. The knowledge of the atmospheric conditions and the specific parameters, can give us the conditions that the Shower expands and light

* This work has been funded by the project PENED 2003.
[1] Corresponding author: fokitis@central.ntua.gr

propagates (Cherenkov and Fluorescent). These types of data are essential in MC simulation and calculations, in order to reproduce and understand the registered events by the detectors of the Cherenkov and Fluorescent Light.

2. Lidar Design

The need for the knowledge of the mentioned parameters led us to search for the best way to Atmospheric Monitoring. The baseline design, used in most EAS telescopes, is the Elastic Lidar method [5][6]. The Lidar design, selected in the present work involves the following parts: The beam that is a Pulsed Laser beam from a Nd:Yag Laser. The collection system of the Lidar is a Newtonian telescope and will consist of a Primary Parabolic mirror that use Pyrex substrate and is coated with protected Aluminum, so its reflectivity will be high in a large range of wavelength, the focal length is f=1.6m and the diameter d=14''. The secondary mirror is Plane Elliptic with a diameter so that the angular dispersion is approximately the same with the one that comes from the beam diameter at the height of 2 - 5 km .

For the analysis of the backscattered light two Fabry Perot Etalons are going to be used. The first etalon mirror spacing is 50mm so that we can analyse the aerosols concentration in each atmospheric layer, via the backscattered light (Mie). The diameter of this etalon is D=40mm clear aperture. The Surface roughness is 0.4 nm and the Reflectivity Finesse is ($\mathcal{F}$) is $\mathcal{F}$=19.3 and finally reduces to the Effective Finesse of F_e=17.1 for parallelism finesse F_p= 43.3 The second Fabry Perot Etalon Mirror Spacing is under investigation so that we can analyse the scattering due to atmospheric molecules. The collimating lenses would be achromatic or aspheric in the same diameter with the etalons and the f number of the lenses will be a little larger than the f number of the telescope so that the lenses suit to the whole design of the system.

The recording system will be a CCD camera that should be considerably fast (gated in order of 200ns or less) so that can separate the backscattered light from a specific area of height. This can be achieved by the short exposure time and the triggering system, which takes the signal from the pulsed laser. The size of CCD can be found by the required resolution and the available CCD camera market.

3. Experimental

A sequence of laboratory activities is under way for the experimental study and understanding of the etalon response and for optimizing its cooperation with the corresponding mirror and a commercial CCD camera Nikon D40, - which are the fundamental parts of a Lidar system. The first set up, that tests etalon's

behavior, is from a Cadmium light source. The light propagates at the beginning via a small pinhole and meets the collimating lens that makes the light beam parallel to the etalon axes. In the same set up we have used two different etalons, 20mm and 50mm, in order to understand the responsè on that type of source. The experimental result shows, that the different cavity length can give other dispersive characteristics. From the theory, the Airy function (1) describes the procedure of multiple interference and via a parameterization can give us the expected inteferogram which can be used for the comparison with the experimental. Here for the Cadmium lines λ_1=508.7, λ_2=480.1, λ_3=467.9, we have a result by having the contribution of the above wavelengths and summing all the intensities.

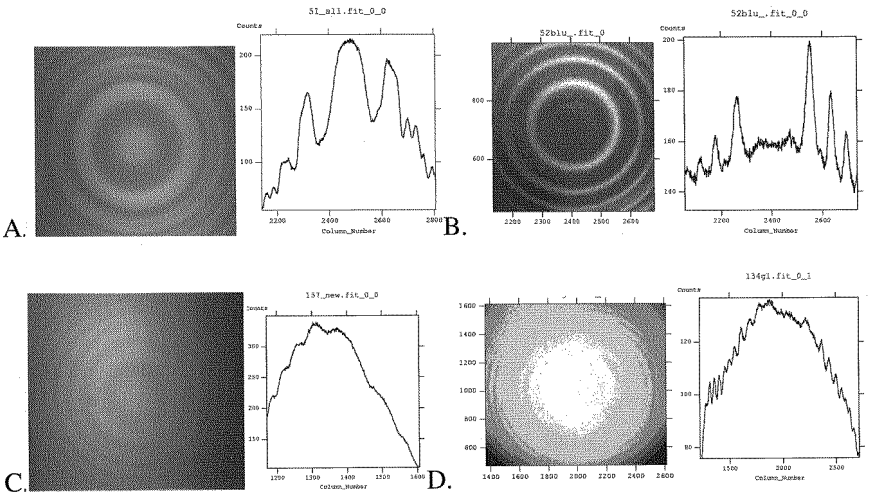

Figure 1. Fringe interference patterns left and their intensity diagrams right. A, B with 20mm etalon and C, D 50mm, A the fringes of all lines off Cadmium, B the same with filter in the blue region, C all lines off Cadmium and D via the Parabolic mirror.

Secondly, in a system with a He Ne laser, commonly the existence of the longitudinal modes is not desirable, but here can help us characterize the etalon. The longitudinal modes have a distance of 417MHz and the backscattered light from a Lidar will be at the same about linewidth for the molecules (Raleigh). For the aerosols we expect a very small broadening of the backscattered laser line(Mie). With the He Ne laser we did the experiments as mentioned below. At first the laser beam was pointed directly to the etalon, after passing from expander, so that the width of the beam would be able to give enough number of

fringes. Secondly the beam in the lab via a beam expander has been broadened and reflects at a part of the parabolic mirror (without using the whole surface). The beam before the reflection had been parallel to the mirror axes (off axes geometry).

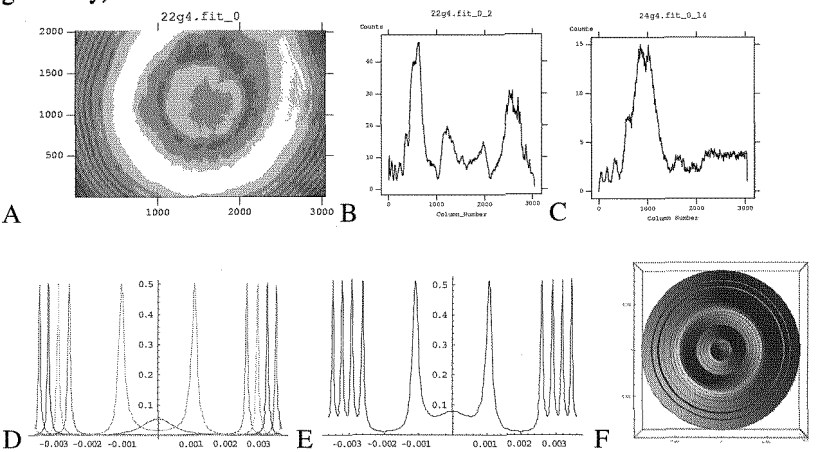

Figure 2. A. Fringe interference pattern 50mm etalon from a HeNe Laser source, after 130m propagation and light collection by Parabolic mirror. B & C. Intensity diagrams from the CCD pixlels. D. The Airy function Intensity via angle for each mode, E the sum of the Intensity of all modes, F the surface of revolution that comes from E.

And at third the same experiment took place outdoors without a beam expander and the broadening occurred by the large distance L_1=82m and L_2=130m. To meet the theory predictions at a first order approach, we use the Airy function(1).

$$I(\lambda,\theta)=\frac{\sqrt{Io}}{1+\frac{4R}{(1-R)^2}\sin^2\left(\frac{2\pi nd}{\lambda}\cos(\theta)\right)}\quad , \tag{1}$$

Here for the wavelengths of the He Ne Laser (Figure 2D) λ_1=632.79944nm, λ_2=632.98888nm, λ_3=632.8 , λ_4=632.80055nm, λ_5=632.801112nm, we have a result by the having the contribution (Figure 2E) of the above wavelengths and summing all the intensities (Figure 2F).

Conclusion and Prospects

From the Cadmium experiment we understood, the use of two different channels for the lidar in order to have the aerosol to molecular ratio from the

backscattered light. The reason is that the broadening of the backscattered light from aerosols (Mie) has a very small width in comparison to those from the molecules (Raleigh). The conclusion is that the spacer length of the etalon, of these channels should have a 5mm and 100mm in order to lead to an accurate monitoring. The project will continue with the use of a secondary in order to use the whole surface of the primary mirror, in a Newtonian telescope design and using a NdYAG laser that will at first be analyzed and a second analysis will follow after backscattering. OPO as well as other Laser systems are discussed in order to achieve better quality for the laser beam. The simulation procedure will be improved, until it describes the observed phenomena. The recording mean will be a camera that will be very fast so that can distinguish the atmosphere in height of 100-200m due to the short exposure time and the triggering system. The trigger pulse will be produced from the pulsed NdYAG laser.

Acknowledgments

This work has been funded by the project PENED 2003. The project is cofinanced 75% of public expenditure through EC - European Social Fund, 25% of public expenditure through Ministry of Development - General Secretariat of Research and Technology and through private sector, under measure 8.3 of OPERATIONAL PROGRAMME "COMPETITIVENESS" in the 3rd Community Support Programme.

References

1. 1.E. Fokitis, P. Fetfatzis, S. Maltezos, *"A Fabry Perot Interferometer prototype for Atmospheric Monitoring in EAS detection"*, 30th ICRC, Merida, Mexico, July 2007.
2. Sciutto S. J., *Physics of Astroparticles,* Brazilian Journal of Physics, vol. 37, no. 2B, June, 2007.
3. Fabian Schüssler,Ralph Engel, Ralf Ulrich, Michael Unger, www-ttp.physik.uni-karlsruhe.de/GK/DoktorandenSeminar/20062007/Schuessler.pdf.
4. Roberts M., *Atmospheric aerosol monitoring at the Pierre Auger Observat.*, 29th International Cosmic Ray Conference Pune 2005.
5. Allen Q. Howard Jr., George W. Lemire, and Martin S. Marshall, *Estimation of Aerosol Concentration from Elastic Scattering LIDAR Data,* IEEE 2003
6. E. Fokitis, S. Maltezos, A. Aravadinos, A. Ageranios, K. Patrinos, N. Maragos, *"Use of the Fabry Perot Interferometer for atmospheric and night sky backround monitoring in EAS detection"*, 29th ICRC, Pune, India, August 2005.

A FLUORESCENCE /AIR CHERENKOV TELESCOPE PROTOTYPE IN GREECE: POSSIBILITY TO DETECT ESCAPING TAUS FROM HELMOS MOUNTAIN IN GREECE

E. FOKITIS[1], P. FETFATZIS, S. MALTEZOS, V. GIKA, N. ANTONAKAKIS SPYROPOULOS, V. XIDI, A. GEORGAKOPOULOU

Physics Department, National Technical University of Athens, Iroon Polytechniou 9 Zografou, Athens, 15780, Greece

We consider the design of a combined Fluorescence/Air-Cherenkov telescope prototype with capability to detect, in separate channels, the fluorescence and air-Cherenkov contributions. This radiation comes from air shower caused by an escaping tau from a nearby mountain, after being produced in a cosmic tau-neutrino mountain mass interaction. The location of the telescope, near the 2.3 meter diameter "Aristarchos", is considered one of the darkest in Europe. In this work, we focus our design on the optical filter technology for the telescope, exploiting recent developments in the manufacturing such as rugate type optical filters, which promise the tailoring their spectral transmittance to optimize the optical signal-to-noise ratio.

1. Introduction

Several authors have studied the issue detection of earth skimming neutrinos. Some scenario discusses the detection of Earth-skimming tau neutrinos (ESTN) to be detected by the Fluorescence Detector (FD) of Pierre Auger Observatory [1]. Similar analysis has been carried out for the possibility of detecting this type of neutrinos using the Surface detector array of PAO [2]. At the FD, there is a small but potentially encouraging probability for detecting ESTNs. A more recent study in ref. [3] based on new and more detailed evaluation of the effective aperture of the FD concludes that there is a significant increase in the number of expected events with respect to the predictions of a previous semi-

[1] Corresponding author: fokitis@central.ntua.gr

analytical determination. The new results show the enhancement effect for neutrino detection from the presence of the near mountains. Another recent project [4] aims at a dedicated search for tau neutrino originating tau atmospheric showers. The pixel size is about $1^0 \times 1^0$ forming a total field of view (FOV) of $14^0 \times 16^0$. In this case, one could argue that finally, the architecture of the FD is an important factor in enhancing the probability of detection of such type of showers. The architecture of the telescope should match the spectral performance of the optical filters to be used. Although, the baseline selection for the major Fluorescence telescopes has been the absorption type optical filters, a total field of view of $14^0 \times 16^0$ opens the possibility of using multilayer interference filters since they promise to offer better merit function than the absorption filters. In addition, the spectral properties, and especially the spectral reflectivities of the mountainsides considered must be studied since this may affect the signal to noise ratio in the detection of air fluorescence or air Cherenkov radiation from the relevant ESTN showers. Therefore, taking the advantage of the Helmos mountain (Figure 1) in Greece, we aim to do a detailed study of the night sky background. After validation of the instrumentation developed for this purpose, we plan to explore the possibility to do similar measurements in Auger sites related mountains.

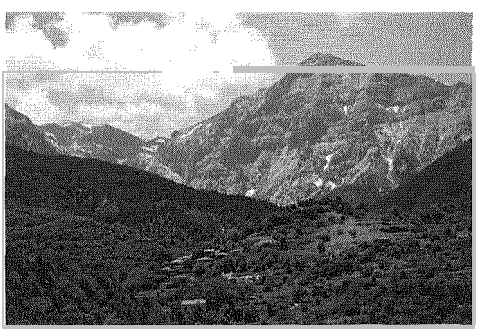

Figure 1. An image of Aristarhos telescope in the context of the mountain.

2. Optical filters of the EAS Telescope

2.1. *Mounting position of optical filters*

One possible position is at the entrance of the telescope. A second possible position is just in front of the PMT array. The first position is technically the best as the angular variation of the incoming rays is smaller, and therefore the interference filter performance is better. However, the cost in this case is larger. There is a performance advantage in placing the optical filters in the telescope

aperture if one considers using multilayer interference filters. This is due to the smaller angular spread of the rays entering the telescope in comparison to the case where the optical filter is placed just in front of the two-dimensional phototube camera. In the latter case, due to the reflection on the telescope mirror, the angular spread on the rays in the optical filter is considerably larger, and this leads to a deterioration of the interference filter performance [5]. In order to study this, we plan to test wide band interference filters having as pass-band the range 300-400 nm and cutoff above this range as described in [6].

2.2. *Optical filter technology considerations*

In addition, one would be interested to improve on the optical filter performance by producing notch filters which have two transmission peaks, namely one near the main Nitrogen fluorescence UV emission lines as is seen in Figure 2. This Figure is the result of a simulation for a multilayer optical filter design based of a sequence of SiO_2/Ta_2O_5 multilayer stack, selecting the three main lines or, rather, groups of lines, since in the rightmost peak, we have more than one line. As the phototube sensitivity, the optical glass of filters and the atmospheric transmittance deteriorate below 350 nm, one would be interested to seek for a more cost effective two band notch filter above 350 nm. Recently, the progress in manufacturing large area precision optical filters with improved productivity may be allowing, therefore, potentially affordable solution for mountain penetrating or Earth skimming High energy neutrino telescopes based on air Cherenkov and Fluorescence technique. The technique of the so-called Rugate optical filters may also improve the optical filter performance, and has a tendency to become the standard technique for precision optical filters.

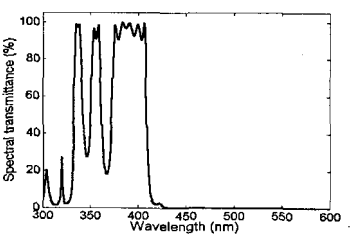

Figure 2. Simulation for a multilayer optical filter.

3. Optimizing the signal to noise ratio and study of the night sky background

We now discuss the plan to characterize prospective sites for installing Cosmic Ray Tau Neutrino Telescope (CRTNT) telescopes. In previous night sky background measurements we used a medium resolution spectrometer. However, this arrangement had the disadvantage of covering only about 100 nm of the desired wavelength (i.e. 300-780 nm) in one exposure, while there is interest in measuring the NSB with high resolution, i.e. resolution approaching the 1 Å, in reasonably small time interval. This is achieved with the echelle spectrometer of Figure 3, see this Conference [7]

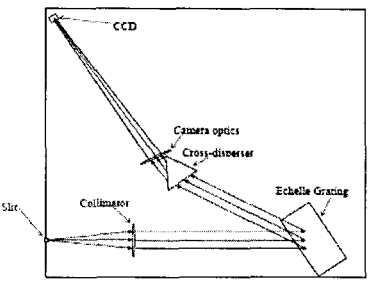

Figure 3. The echelle spectrometer that is going to be used for night sky background measurements.

The reflectivity of Helmos mountain surface has to be estimated before we install any regular facility in this location. The percentage of reflectivity depends mainly from the type of the surface and varies from 5 % for a broadleaf forest to 95 % for a snow-covered mountainside. Recording with a CCD sensor the radiation opposite and towards the mountainside we will be able to estimate the integrated reflectivity while putting narrowband and broadband notch filters we could estimate the reflectivity at specific wavelengths of interest.

4. Conclusion and Prospects

We discussed the prospects for improvement the optical filters and monitoring the spectrum of the sky brightness in prospective areas for installing Cosmic Ray Tau Neutrino Telescope (CRTNT) telescopes. It is argued, that for angular range of around 14^0x14^0, optical filters can be tailored to reduce the night sky background and therefore lower the threshold of the energy of the neutrino induced tau escaping from a mountain after been produced by a tau cosmogenic neutrino penetrating the mountain.

Acknowledgments

This project is co - funded by the European Social Fund (75%) and National Resources (25%) – (EPEAEK II) – PYTHAGORAS.

References

1. C. Aramo, A. Insolia, A. Leonardi, G. Miele, L. Perrone, O. Pisanti and D.V. Semikoz, *Earth-skimming UHE tau neutrinos at the fluorescence detector of Pierre Auger Observatory*, Astroparticle Physics, Pages 65-77, February 2005.
2. X. Bertou, P. Billoir, O. Deligny, C. Lachaud, A. Letessier-Selvon, *Tau neutrinos in the Auger Observatory: a new window to UHECR sources*, Astroparticle Physics, Vol.17, Pages 183-193, May 2002.
3. Gennaro Miele et al, *The aperture for UHE tau neutrinos of the Auger fluorescence detector using a Digital Elevation Map*, Physics Letters B 634, 137–142, 2006.
4. He Huihai et al, *Cosmic Ray Tau Neutrino Telescope (CRTNT) Prototype Experiment at Yangbajing*, Proc. 30th ICRC, *Merida*, July 2001.
5. Geranios A., Fokitis E., Petridis, A., and Vassiliou M., *Evaluation Method of Optical Filters used in Fluorescence Detectors,*Optical Engineering, Vol., 42, p. 759-764, N. 3, March 2003.
6. E. Fokitis et al, *Performance of optical pass-band interference filter for the Auger fluorescence detectors*, Proc. 27th ICRC, Hamburg, HE 148, August 2001.
7. N. Antonakakis Spyropoulos, P. Fetfatzis, E. Fokitis, V. Gika, S. Maltezos, *Design of a wide spectral range and high-resolution spectrograph for monitoring the night sky backround for use in air fluorescent telescopes*, Proc. 10th ICATPP, Como, October 2007.

SEARCH FOR MASSIVE RARE PARTICLES WITH THE SLIM EXPERIMENT

M. GIORGINI* on behalf of the SLIM Collaboration

Dept. of Physics, University of Bologna,and INFN
Viale C. Berti Pichat 6/2, I-40127 Bologna, Italy
**E-mail: miriam.giorgini@bo.infn.it*

The SLIM experiment is a large array of nuclear track detectors located at the Chacaltaya High Altitude Laboratory (5260 m a.s.l.). The preliminary results from the analysis of ~ 383 m^2 exposed for 4.07 y are here reported. The detector is sensitive to Intermediate Mass Magnetic Monopoles, $10^5 < M_M < 10^{12}$ GeV, and to SQM nuggets and Q-balls, which are possible Dark Matter candidates.

Keywords: rare particles; nuclear track detector; upper limit.

1. Introduction

Grand Unified Theories (GUT) of the strong and electroweak interactions predict the existence of magnetic monopoles (MMs), produced in the early Universe at the end of the GUT epoch, with very large masses, $M_M > 10^{16}$ GeV. GUT poles in the cosmic radiation should be characterized by low velocity and relatively large energy losses [1]. At present the MACRO experiment has set the best limit on GUT MMs for $4 \cdot 10^{-5} < \beta < 0.5$ [2].

Intermediate Mass Monopoles (IMMs) [$10^5 \div 10^{12}$ GeV] could also be present in the cosmic radiation; they may have been produced in later phase transitions in the early Universe [3]. The recent interest in IMMs is also connected with the possibility that they could yield the highest energy cosmic rays [4]. IMMs may have relativistic velocities since they could be accelerated in one coherent domain of the galactic magnetic field. In this case one would have to look for downgoing fast ($\beta > 0.1$) heavily ionizing MMs.

Besides MMs, other massive particles have been hypothesized to exist in the cosmic radiation and to be components of the galactic cold dark matter: nuggets of Strange Quark Matter (SQM), called nuclearites when neutralized by captured electrons, and Q-balls. SQM consists of aggregates of u,

d and s quarks (in approximately equal proportions) with slightly positive electric charge [5]. It was suggested that SQM may be the ground state of QCD. They should be stable for all baryon numbers in the range between ordinary heavy nuclei and neutron stars ($A \sim 10^{57}$). Nuclearite interaction with matter depend on their mass and size. In ref. [6] different mechanisms of energy loss and propagation in relation to their detectability with the SLIM apparatus are considered. In the absence of any candidate, SLIM will be able to rule out some of the hypothesized propagation mechanisms.

Q-balls are super-symmetric coherent states of squarks, sleptons and Higgs fields, predicted by minimal super-symmetric generalizations of the Standard Model [7]. They could have been produced in the early Universe. Charged Q-balls should interact with matter in ways not too dissimilar from those of nuclearites.

After a short description of the apparatus, we present the calibrations, the analysis procedures and the results from the SLIM experiment.

2. Experimental procedure

The SLIM (Search for LIght magnetic Monopoles) experiment, based on 440 m^2 of Nuclear Track Detectors (NTDs), was deployed at the Chacaltaya High Altitude Laboratory (Bolivia, 5260 m a.s.l.) since 2001 [8]. The air temperature is recorded 3 times a day. From the observed ranges of temperatures we conclude that no significant time variations occurred in the detector response. The radon activity and the flux of cosmic ray neutrons were measured by us and by other authors [9]. Another 100 m^2 of NTDs were installed at Koksil (Pakistan, 4600 m a.s.l.) since 2003.

Extensive test studies were made in order to improve the etching procedures of CR39 and Makrofol, improve the scanning and analysis procedures and speed, and keep a good scan efficiency. "Strong" and "soft" etching conditions have been defined [10]. Strong etching conditions (8N KOH + 1.25% Ethyl alcohol at 77 °C for 30 hours) are used for the first CR39 sheet in each module, in order to produce large tracks, easier to detect during scanning. Soft etching conditions (6N NaOH + 1% Ethyl alcohol at 70 °C for 40 hours) are applied to the other CR39 layers in a module, if a candidate track is found in the first layer. It allows more reliable measurements of the Restricted Energy Loss (REL) and of the direction of the incident particle. Makrofol layers are etched in 6N KOH + Ethyl alcohol (20% by volume), at 50 °C.

The detectors have been calibrated using 158 AGeV In^{49+} (see Fig. 1) and 30 AGeV Pb^{82+} beams. For soft etching conditions the threshold in

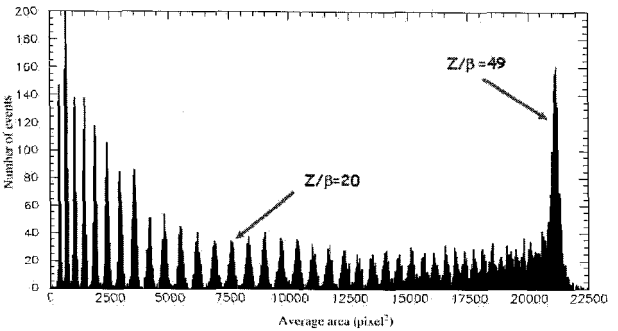

Fig. 1. Calibrations of CR39 nuclear track detectors with 158 AGeV In^{49+} ions and their fragments.

CR39 is at REL $\sim$ 50 MeV cm^2 g^{-1}; for strong etching the threshold is at REL $\sim$ 250 MeV cm^2 g^{-1}. Makrofol has a higher threshold (REL $\sim$ 2.5 GeV cm^2 g^{-1}) [11]. The CR39 allows the detection of IMMs with two units Dirac charge in the whole β-range of $4 \cdot 10^{-5} < \beta < 1$. The Makrofol is useful for the detection of fast MMs; nuclearites with $\beta \sim 10^{-3}$ can be detected by both CR39 and Makrofol.

The analysis of a SLIM module starts by etching the top CR39 sheet using strong conditions, reducing its thickness from 1.4 mm to $\sim$ 0.6 mm. Since MMs, nuclearites and Q-balls should have a constant REL through the stack, the signal looked for is a hole or a biconical track with the two base-cone areas equal within the experimental uncertainties. The sheets are scanned with a low magnification stereo microscope. Possible candidates are further analyzed with a high magnification microscope. The size of surface tracks is measured on both sides of the sheet. We require the two values to be equal within 3 times the standard deviation of their difference. A track is defined as a "candidate" if the REL and the incidence angles on the front and back sides are equal to within 15%. To confirm the candidate track, the bottom CR39 layer is then etched in soft conditions; an accurate scan under an optical microscope with high magnification is performed in a region of about 0.5 mm around the expected candidate position. If a two-fold coincidence is found the middle layer of the CR39 (and in case of high Z candidate, the Makrofol layer) is analyzed with soft conditions.

3. Non reproducible candidates

In 2006 the SLIM experiment found a very strange event when analyzing the top CR39 layer of stack 7408. We found a sequence of many "tracks" along a 20 cm line; each of them looked complicated and very different from usual

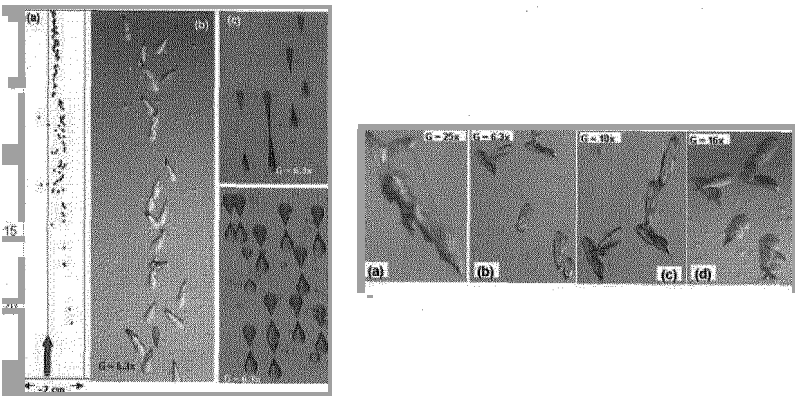

Fig. 2. Left: (a) Global view of the "event" tracks in the L1 layer of wagon 7408. (b) Microphotographs of the 22 cones at the top of Fig. 3a. (c) Normal tracks of 158 AGeV Pb^{82+} ions and their fragments (soft etching), and (d) of 400 AMeV Fe^{26+} ions and their fragments (strong etching). Right: Example of "tracks" in the L6 layer of wagon 7410: (a) after 30h of soft etching, (b) after 5h more of strong etching, (c) after 4h more of strong etching and (d) after 10h more of strong etching.

ion tracks, see Fig. 2left(a,b). For comparison Fig. 2left(c) shows "normal" tracks from 158 AGeV Pb^{82+} ions and their fragments and Fig. 2left(d) shows tracks from 400 AMeV Fe^{26+} ions.

Since that "event" was rather peculiar, we made a detailed study of all the sheets of module 7408, and a search for similar events and in general for background tracks in all NTD sheets in the wagons around module 7408 (within a $\sim$ 1 m distance from module 7408). We etched "softly" all the sheets in order to be able to follow the evolution of the etch-pits. A second event was found in the CR39 bottom layer (top face) of module 7410, see Fig. 2right. Some background tracks in other modules were found after 30 h of soft etching. We decided to further etch "strongly" the 7410-L6 layer in short time steps (5h) and to follow the evolution of the "tracks" by systematically making photographs at each etching step. After additional strong etching, the "tracks" began more and more similar to those in the 7408-L1 layer, see Fig. 2right(b,c,d). The presence of this second event/background and its evolution with increasing etching casts stronger doubts on the event interpretation and supports a "background" interpretation also of the "tracks" in module 7408. We made different hypotheses and we checked them with the Intercast Co. Since 1980 we analyzed more than 1000 m^2 of CR39 using different etching conditions and we have not seen before any of the above mentioned cases. It appears that we may have been hit by an extremely rare manufacturing defect involving 1 m^2 of CR39.

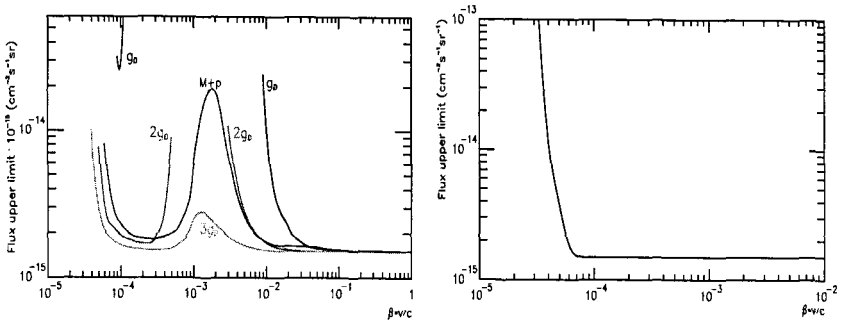

Fig. 3. Left: 90% C.L. upper limits for a downgoing flux of IMMs with $g = g_D$, $2g_D$, $3g_D$ and for dyons (M+p) plotted vs β. Right: 90% C.L. upper limits for a downgoing flux of nuclearites with $M_N \leq 8.4 \cdot 10^{14}$ GeV.

4. Results and Conclusions

We etched and analyzed 383 m^2 of CR39, with an average exposure time of ~ 4.07 years. No candidate passed the search criteria: the 90% C.L. upper limits for a downgoing flux of IMMs with $g = g_D$, $2g_D$, $3g_D$ and for dyons (M+p) are at the level of $\sim 1.5 \cdot 10^{-15}$ cm^{-2} s^{-1} sr^{-1} for $\beta \geq 4 \cdot 10^{-2}$, see Fig. 3left. The same sensitivity was reached also for nuclearites with $\beta \geq 10^{-4}$ (Fig. 3right) and Q-balls coming from above with galactic velocities.

References

1. G. Giacomelli, *Riv. Nuovo Cimento* **7 N12**, 1 (1984); *hep-ex/0005041*; *hep-ex/0702050.*
2. M. Ambrosio et al., *Eur. Phys. J. C* **25**, 511 (2002); *Eur. Phys. J. C* **26**, 163 (2002).
3. T.W. Kephart and Q. Shafi, *Phys. Lett. B* **520**, 313 (2001).
4. T.W. Kephart and T.J. Weiler, *Astrop. Phys.* **4**, 271 (1996).
   C.O. Escobar and R.A. Vasquez, *Astrop. Phys.* **10**, 197 (1999).
5. A. Witten, *Phys. Rev. D* **30**, 272 (1986).
   A. De Rujula and S. L. Glashow, *Nature* **312**, 734 (1984).
6. S. Balestra et al., *Czech J. Phys.* **56**, A221 (2006); *hep-ex/0601019.*
7. S. Coleman, *Nucl. Phys. B* **262**, 263 (1985).
   A. Kusenko et al., *Phys. Lett. B* **418**, 46 (1998).
8. D. Bakari et al., *hep-ex/0003028.*
9. H. Schraube et al., *Rad. Prot. Dos.* **84**, 309 (1999).
   A. Zanini et al., *Il Nuovo Cim.* **24C**, 691 (2001).
10. S. Balestra et al., *Nucl. Instr. Meth. B* **254**, 254 (2007).
11. S. Cecchini et al., *Radiat. Meas.* **40**, 433 (2005).

PMT Characterization for MAGIC II Telescope

Ching-Cheng Hsu

Max-Planck-Institut fuer Physik, Muenchen, 80805, Germany

** E-mail: cchsu@mppmu.mpg.de*

MAGIC, a 17m diameter Cherenkov telescope located on the Canary Island of La Palma, is the biggest IACT (Imaging Atmospheric Cherenkov Telescope) in the world. For lowering the energy threshold and improving the sensitivity, the MAGIC collaboration is currently building a second telescope (MAGIC II), using Photomultipliers(PMTs) with a better sensitivity. Various measurements of different characteristics of PMTs, such as single photoelectron spectrum(SPE), afterpulse, aging and photoelectron detection were performed. The results from selected PMT candidates of different companies will be presented here.

Keywords: Photomultipliers; MAGIC Telescope; Proceedings; IACT.

1. Introduction

The MAGIC telescope has been in scientific operation since the summer of 2004. Currently, it is the largest ground-based gamma ray telescope in the world. The main purpose of the MAGIC I design was to study high energy phenomena in the universe in the unexplored energy range down to 30 GeV. For improving the sensitivity further and also benefitting from the stereoscopic/coincidence operational mode, we are building a second telescope, MAGIC II [1], at about 85 meters' distance from the MAGIC-I telescope. The imaging camera will be equipped with high quantum efficiency (QE) photomultiplier (PMTs) and also Hybrid photodiodes (HPDs). The signals will be read out by a fast sampling system of 2 GSamples/s in order to reduce the background photons coming from the night sky and to achieve a better gamma/hadron separation by taking into account the timing profile of the Cherenkov light. Our goal is to lower the threshold by a factor two with advanced photon detectors and a fast readout system. PMTs are very suitable photon sensors for measuring very fast and low light level signals. Though PMTs have already been widely used in high energy physics before, their characteristics may differ from tube to tube. We have searched the

current market for the PMTs which fullfilled the following requirements:

- High quantum efficiency.
- Low gain ($2 * 10^4$), because of the moon observation.
- One-inch diameter and hemispherically shaped photocathode.
- Six-dynode structure for better timing characteristics.
- Low afterpulsing rate. It has been understood that lowering the trigger threshold is limited in part by the afterpulsing rate induced by single photoelectron pulses due to the night sky light. [2]
- Fast and short pulses.

To really understand each pixel, a variety of measurements were performed. The impacts on the future MAGIC II telescope will also be discussed.

2. The Quantum Efficiency Measurement

The Quantum efficiency is a quantity used to express the sensitivity of a photonsensor. For fast and low light level experiments, it becomes important to provide high signal-to-noise ratio photon sensors. To enhance the QE, we improve it by extending the spectral sensitivity in the short-wave UV range using a wavelength shifter (WLS) and, further, by increasing the overall quantum efficiency (QE), applying a layer of structured lacquer acting as a photon scatterer [3].

The photocathode was fully illuminated and the current produced by the anode was measured. We applied a potential difference of 200V between the photocathode and the first dynode. For eliminating the gain influence, we shorted all the 6 dynodes. Every charge collected inside the PMTs would produce anode current and be measured. In Figure 1, we plot the average QE curves of 20 coated and uncoated PMTs from different companies.

3. Single Photoelectron Spectrum

When a PMT is used to detect a very weak signal, the pulses from individual photoelectrons are well separated in time. Because of the secondary electron emission process in the first dynode, the single-electron pulses show very large amplitude fluctuations. We tuned the laser light density down to single photoelectron regime. The laser triggered the FADC to record the pulses from PMTs.

The single photoelectron pulses were extracted from FADC data and we integrated the charge for each pulse. We kept the single photoelectron

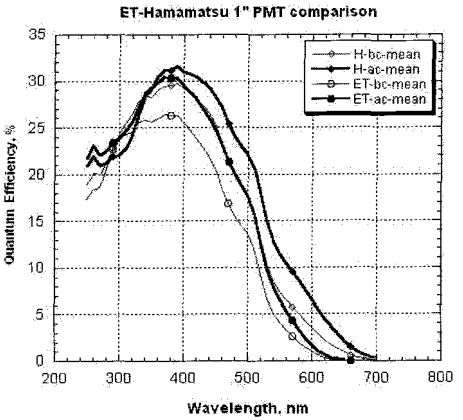

Fig. 1. PMT QE curves from different companies. H-bc and H-ac stand for Hamamatsu PMTs before and after coating. ET-bc and ET-ac stand for Electron Tubes PMTs before and after coating.

events smaller than 5% such that the probability to get two photoelectrons was smaller than 2% of the number of single photoelectrons.

From the SPE, we could also calculate the peak-to-valley (P/V) ratio. For the future MAGIC II telescope, we are going to reject pixels which have a P/V value lower than 1.3 .

4. Time Characteristics

The time characteristics of photonsensors are quite important for IACTs. Since the Cherenkov light flash is always quite short, usually a few ns, we need fast PMTs to reduce the background. We measured the pulse response width at half of the maximum (FWHM) of the anode current pulse delivered in reponse to a very short and narrow laser light pulse (about 40 ps). The pulse width depends on the light illumination level and is minimum when this level is so low that the probability of more than one photoelectron being emitted per light pulse is very small.

We measured with a 2GHz bandwidth amplifier (gain $\sim$ 100) followed by a fast oscilloscope (1.5 GHz in bandwidth, 5 G/s sampling rate). Most of the pulses had a rising time of appr. 600 $\sim$ 800 ps and a falling time of 700 $\sim$ 1000ps. The pulse width (FWHM) was around 1 $\sim$ 1.5ns.

The transit time spread (jitter) was measured, too. Because of the ge-

ometry of our tubes, we believe that the main reason for the difference is the cathode/first-dynode space. However, there is another important factor, i.e. the voltage applied between the electrodes. The time resolution of the tube could be defined as the FWHM of the probability distribution of this fluctuation. It is also proportional to $1/\sqrt{n}$, where n is the number of photoelectrons per pulse. We found the transit time jitter is about 960 ps, when the PMT has high gain $1.12 * 10^5$. We also found that if we lowered the gain down to $7 * 10^4$, the time jitter changed very little.

5. Aging Test

Exposing the PMTs to constant light intensity over a period of time will make the gain of the PMT decrease. This is important for IACTs, because the PMTs are constantly exposed to night sky background light (NSB). The gain of the PMTs drops because of the fatigue of the dynode. The lifetime of the PMT is defined as the time when the gain of the PMT drops to 50%. In order to speed up the measurement, all measured PMTs were illuminated by highly intense light. We tuned their gains such that they had the same initial anode current, i.e. $150\mu A$. The measurement was operated for approximately one week (10150 minutes) in total. We tested with 4 PMTs. Their lifetime was estimated to be $10 \sim 20$ years, assuming the NSB at La Palma to be 2 uA and 10% of the duty cycle of the telescope operation.

6. Afterpulsing

When the dynodes are bombarded by electrons, during the amplification process, some residual molecules which are resting on the surface of the dynode will be ionized and the positive ions will have the chance to fly back to the cathode. This process is the so-called afterpulse. We used a pulsed laser (wavelength 405 nm) as our light source and triggered the FADC externally. Once the FADC was triggered, there was a main pulse of about several tens of photoelectron coming from the laser and we searched for the afterpulses within the following 2 μs. Within this period, we applied different thresholds and then counted the number of afterpulses and normalized this number to the total number of main pulses and the number of photoelectrons in these main pulses. To check if the measurement depended on the intensity of the laser pulse, we measured the PMTs with two different intensities. All measured PMTs had an afterpulsing rate of about 0.2 % to 0.8 %.

7. Photon Detection Efficiency

In the above QE measurement, we measured all the photoelectrons emitted from the photocathode. Under normal operation, some of the photoelectrons are collected at the first dynode and they do not contribute to the amplified signal. The total photon detection efficiency is the ratio of the photoelectrons contributing to a measurable signal at the anode to that of all photoelectrons produced at the photocathode.

We measured two PMTs simultaneously, using the same diffuse light source with symmetric geometry in order to have a direct comparison of the photon detection efficiency of the two sensors. Afterwards, two PMTs were swapped in order to get rid of the small asymmetry of the illumination. Then we evaluated relative efficiencies by numbers of detected single photoelectrons. We found the photoelectron efficiency of the Hamamatsu PMTs to be high enough.

8. Conclusion

We set up procedures to measure the different properties of a sample of PMTs. For MAGIC II we selected Hamamatsu PMTs. The company Hamamatsu will deliver PMT modules which include a socket with a Cockcroft-Walton type High Voltage generator. The PMT socket and all the front-end analog electronics is assembled to form a compact pixel module. All will be embedded in the camera pixel cluster design.

References

1. F. Gloebel. Status of the second phase of the MAGIC telescope. *Proceeding of ICRC2007, Mexico*, 2007.
2. R. Mirzoyan, E. Lorenz, D. Petry, and C. Prosch. On the influence of afterpulsing in PMTs on the trigger threshold of multichannel light detectors in self-trigger mode. *Nucl. Instr. and Meth. Phys. Rev. A*, 387:74–78, 1997.
3. D. Paneque et al. A method to enhance the sensitivity of photomultipliers for air Cherenkov telescope . *Nucl. Instr. and Meth. Phys. Rev. A*, 504:109–115, 2003.

Determining the Neutrino Mass with a Calorimetric Low-Temperature Detector – The Experiment MARE

S. Kraft-Bermuth* for the MARE collaboration

University of Milano-Bicocca, Dept. of Physics, and INFN Milano-Bicoccca, Italy
**E-mail: Saskia.Kraft@mib.infn.it*
www.mib.infn.it

In the light of the recent cosmological discussion, the direct measurement of the lightest neutrino mass from single β-decay has become an important issue. Calorimetric low-temperature detectors measure the temperature rise induced by the energy deposition of the β-electron in an absorber of low heat capacity. It has been demonstrated in the past that observing the β-decay spectrum of ^{187}Re provides a suitable method to determine the mass of the electron anti-neutrino from β-endpoint measurements. In a first step, with the experiments MANU and MIBETA a sensitivity of $m_{\nu e} \leq 20\,eV/c^2$ was achieved. To compete with the sensitivity of $m_{\nu e} \leq 0.2\,eV/c^2$ aimed at with the KATRIN experiment, a new experiment MARE has been initiated. As a first stage, MARE-I will reach a sensitivity of $m_{\nu e} \leq 2\,eV/c^2$. With 300 detectors mounted, systematic effects of the calorimetric approach will be studied in detail. The second stage MARE-II will consist of several 10000 detectors and aim at a sensitivity of $m_{\nu e} \leq 0.2\,eV/c^2$.

Keywords: single β-decay, neutrino mass determination, calorimetric detectors

1. Introduction

Since the discovery of Neutrino oscillations, the fact of non-zero neutrino mass is established. Neutrino oscillation experiments have determined mass differences as well as mixing angles of the three neutrino flavours with small uncertainties. However, the absolute mass scale is still unknown. Although cosmological approaches as well as the neutrino-less double β-decay may be more sensitive, the kinematical neutrino mass measurement is the only model-independent method. It accesses the mass scale by precisely analyzing the kinematics of β-electrons emitted by isotopes with low endpoint energies. The most stringent results currently come from experiments with electrostatic spectrometers on tritium decay: The collaboration of Mainz/Troitsk has reached $m_{\nu e} \leq 2.2\,eV/c^2$. The next-generation exper-

iment KATRIN is designed to reach a sensitivity of $m_{\nu e} \leq 0.2\, eV/c^2$.[1] However, all experiments with electrostatic spectrometers are subject to similar systematic uncertainties, namely the fact that the β-electrons have to leave the tritium source before entering the spectrometer. Therefore, an entirely different method to determine the neutrino mass from single β-decay has been investigated. This method takes advantage of the β-decaying isotope with the lowest endpoint energy known to date: ^{187}Re has an endpoint energy of only 2.47 keV (compared to 18.6 keV for tritium), thus enhancing the count rate in the energy intervall of interest by a factor of about 10^3.

A calorimetric detector measures the temperature rise of an absorber after the energy deposited by the incident particle is thermalized. This detection principle is schematically displayed in Fig. 1: The incident particle deposits its kinetic energy E in an absorber with a heat capacity C at a working temperature T_a. After thermalization of the whole absorber, a temperature rise $\Delta T = E/C$ is induced. To realize a large temperature change, low heat capacities and thus low operating temperatures are essential. The temperature change is then read out by the resistance change of a temperature-dependent resistor $R(T)$. Rise times τ_{rise} are of the order of 0.01–10 ms. High dR/dT values for high resistance changes are realized either by specially doped semiconductors or by a superconductor operated at the transition temperature (transition edge sensor). The dynamic behaviour of the detector, i.e. the decay time τ, is determined by the thermal coupling constant k.[2] Typical values are $\tau \sim 0.1 - 10$ ms.

As in principle the whole deposited energy is finally transferred into heat after the decay of the inital electronic excitations, a more complete energy detection is achieved, which considerably reduces fluctuations in the detected amount of energy and therefore improves the energy reso-

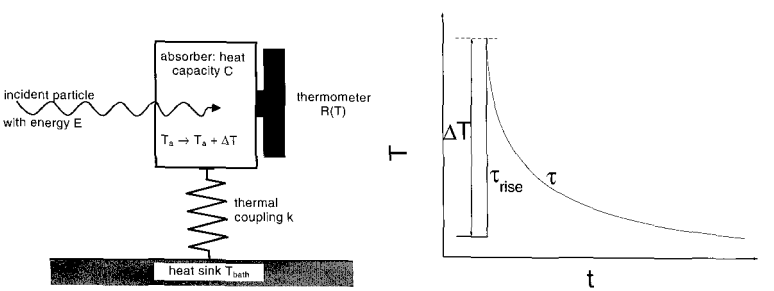

Fig. 1. Schematic principle of particle detection with a calorimetric low temperature detector (left side) and schematic temperature signal (right side).

lution. As the detection principle is almost independent of the absorber's material properties, a material containing the β-decaying isotope can be selected, thereby eliminating any systematic effects from electrons having to leave a source before reaching the detector. In addition, energy deposited in long-lived excited electron states will eventually contribute to the thermal signal. The energy resolution is limited by thermal fluctuations in the absorber: $\Delta E = \sqrt{k_B C T^2}$. For operating temperatures of ~100 mK, energy resolutions of 2–5 eV have been obtained for X-rays at 6 keV.

2. Calorimetric Rhenium Experiments

At low temperatures, the conductivity of compensated doped semiconductors is governed by the phonon-assisted variable-range hopping mode,[3] which leads to an exponential R(T) dependence. The absorbers are glued to the thermistors by means of an epoxy varnish. To use rhenium as an absorber, two possibilities can be exploited: Metallic rhenium is superconducting at temperatures of $T_C \sim 1.6$ K. At the typical operating temperature of around 100 mK, the heat capacity becomes sufficiently small to reach a high signal-to-noise ratio. However, superconducting absorbers are known to exhibit problems in thermalization due to phonon-trapping states with life times longer than τ. To avoid this drawback, dielectric rhenium compounds (perrhenates) with high Debye temperatures can be used.

To investigate the feasibility of a microcalorimetric rhenium experiment, two independent test experiments were performed: the experiment MANU in Genova[4] and the experiment MIBETA in Milan.[5] MANU used one detector with neutron transmutation doped germanium glued to a 1.6 mg single crystal of metallic rhenium, while MIBETA used an array of eight Si:P implanted silicon thermistors with $AgReO_4$ crystals with a total mass of 2.2 mg. The two experiments collected statistics corresponding to $1-2\times10^7$ β-decays, corresponding to a sensitivity of $m_{\nu e} \leq 20\, eV/c^2$. The systematic uncertainties in these experiments were still small compared to the statistical errors. The main sources were background contributions, the detector response function, the theoretical shape of the ^{187}Re β-decay spectrum, the Beta Environmental Fine Structure,[6,7] as well as pile-up.[8]

If the effect of pile up is kept negligible, the sensitivity improves as $\sqrt[4]{1/N_{ev}}$. Therefore, improving the present limit of the MIBETA and MANU experiments by a factor of 100 requires to increase the statistics by a factor of 10^8.

3. The Experiment MARE

Monte Carlo studies showed that for a neutrino mass experiment with sub-eV sensitivity, one will need large arrays of 10^4 elements, with an energy and time resolution of 1 eV and of 1 μs, respectively.[9] If each pixel has a source activity of 10 Hz, the measurement has to last up to 10 years to collect statistics of about 10^{14} β-decays in total. To realize such an extremely challenging project, the international collaboration MARE (**M**icrocalorimeter **A**rrays for a **R**henium **E**xperiment) has been founded in 2005.[8] The project is divided in two phases:

(1) MARE-I:
In a first step, an intermediate-sized experiment will be prepared by the two groups of Milan and Genova, based on their experiences with MIBETA and MANU, respectively. The main aim of this stage is to investigate the systematic effects for a number of around 300 pixels. After 3 years of measurement, MARE-I should reach a sensitivity of $m_{\nu e} \leq 2\, eV/c^2$, able to scrutinize the Mainz/Troitsk results.
The Milan group will continue to work with Si:P semiconductor thermistors produced by NASA (see[10,11] for a detailed description). One array contains 6 x 6 thermistors. With such thermistor arrays, an energy resolution of 3 eV has been obtained for 6 keV X-rays with Bi absorbers. To optimize the count rate, the mass of the $AgReO_4$ absorbers is increased to 500 μg. With a test array equipped with 10 crystals, an energy resolution of 28 eV at 2.5 keV was obtained. This will be improved by adapting the readout electronics to the resistance of the thermistors. By the end of 2007, two arrays will be running. The setup is designed to house 8 arrays for a total of 288 pixels, which will reach a sensitivity of $m_{\nu e} \leq 3\, eV/c^2$ after about 3 years with statistics of about 7×10^9 events.
The group in Genova is investigating transition edge sensors consisting of Ir layers or Ir/Au and Ir/Ag bilayers, which will be deposited directly onto metallic rhenium crystals by means of pulsed laser deposition. The steep rise in the transition allows for high dR/dT^2 and a rise time of only 10 μs. TES are read out by frequency-multiplexed SQUIDs, which makes the scaling to 10^4 pixels straightforward. With first test devices deposited on silicon, an energy resolution of 11 eV at 6 keV has been obtained. The sensitivity attainable in three years is about $m_{\nu e} \leq 2\, eV/c^2$ with statistics of about 3×10^{10} events.
(2) MARE-II:

During the second phase, the large-scale experiment will be carried out. Monte Carlo simulations show that with several 10^4 detector pixels which achieve an energy resolution of $\Delta E \leq 5$ eV and a rise time of $\tau_{rise} \leq 5\ \mu s$, a sensitivity of $m_{\nu e} \leq 0.2\, eV/c^2$ can be achieved within 10 years of measurement time. In parallel to MARE-I, different groups within the collaboration are developing different detector types to fulfill these demanding requirements. Transition edge sensors (TES) and Metallic Magnetic Calorimeters (MMC) have already been proven to be extremely sensitive. Both detector concepts have reached energy and time resolutions close to the requirements for MARE-II. While TES have already been integrated into large ($\sim 10^4$) arrays with multiplexed read-out, MMCs are more suitable for coupling to large-size absorbers. First tests with metallic rhenium absorbers give interesting results. Magnetic Kinetic Inductance thermistors represent a relatively new and promising technology with an inherent multiplexed read-out. Besides the sensor development, optimizing the rhenium-containing absorber and its coupling to the sensor remains the second focus of the R&D.

Within 3–4 years, the experience gained in MARE-I together with the ongoing R&D for MARE-II should define the optimal single pixel layout and absorber material as well as the design of the multiplexed 10^4 pixel array. Several of these arrays will then be mounted in different refridgerators run by the different groups. A staged approach of one 10^4 pixel array mounted per year would give a statistical sensitivity of $m_{\nu e} \leq 0.2\, eV/c^2$ after 10 years of data taking.

References

1. *KATRIN Design Report (2004)*, FZKA 7090, KATRIN LoI (2001), hep-ex/0109033
2. Chr. Enss (ed.), *Cryogenic Particle Detection*, Topics Appl. Phys. **99** (2005), Springer-Verlag Berlin Heidelberg 2005
3. N. F. Mott, Philos. Mag. **19** (1969) 835
4. F. Gatti, Nucl. Phys. B **91** (2001) 293
5. M. Sisti et al., Nucl. Instr. Meth. A **520** (2004) 125
6. F. Gatti et al., Nature **397** (1999) 137
7. C. Arnaboldi et al., Phys. Rev. Lett. **96** (2006) 042503
8. A. Monfardini et al., Nucl. Instr. Meth. A **559** (2006) 346
9. A. Nucciotti et al., Nucl. Instr. Meth. A **520** (2004) 148
10. R. P. Brekosky et al., Nucl. Instr. Meth. A **520** (2004) 439
11. C. K. Stahle et al., Nucl. Instr. Meth. A **520** (2004) 466

THE BOREXINO DETECTOR: CONSTRUCTION AND PERFORMANCES

PAOLO LOMBARDI[†]

I.N.F.N., Sez. di Milano, Via Celoria 16
Milano, 20133, Italy

Borexino, a real-time device for low energy neutrino spectroscopy has completed the construction phase at the middle of 2006 in the underground laboratories of Gran Sasso, Italy. The detector has been filled with 1300 tons of highly purified scintillator and 2400 tons of ultra-pure water as external shield and since May 16th is taking data. The experimental goal is the direct measurement of the flux of Be7 solar neutrinos of all flavors via neutrino-electron scattering in an ultra-pure scintillation liquid. The paper describes the design of the Borexino detector, the construction phases and the various facilities which play an essential role for its operation. Performances of the major sub-systems and the whole detector will be presented as well.

1. Introduction

Borexino is a liquid scintillation detector designed to observe solar neutrinos in real time. It is located 1.4 km (3500 meters water equivalent) underground, in the Gran Sasso National Laboratory in Italy [1]. The main observational target of the detector is the mono energetic (E = 862 KeV) ^{7}Be neutrinos that are believed to make up roughly 10% of the total solar neutrino flux. However, the possibility of observing the much less common pep neutrinos (E = 1.44MeV) is also foreseen. The Sun is an intense source of neutrinos that are emitted in nuclear reactions that provide its power. Borexino will directly observe only the electrons scattered by these neutrinos, not the total neutrino energy. Hence the observed energy spectrum for each type of neutrino will consist of a nearly flat signal ending at a shoulder, at 667 KeV for the 7Be neutrinos and 1.22MeV for the pep neutrinos. The Borexino experiment is made challenging by the fact that many naturally-occurring radioactive isotopes can decay to produce signals in these energy windows. Materials of extreme radio purity and a graded shielding design are mandatory.

[†] On behalf of the Borexino collaboration.

2. Overview of the Borexino Experiment

2.1. *Detector design*

The detector design is based on the principle of graded shielding (Figure 1); a stainless steel sphere (SSS) of 13.7 m diameter is the container of the scintillator and the mechanical support of the photomultipliers [2]. Inside this sphere, two nylon vessels separate the scintillator volume in three shells of radius 4.25 m, 5.50 m and 6.85 m. The inner nylon vessel (IV) contains the liquid scintillator solution, namely PC (pseudocumene, 1,2,4-trimethylbenzene C6H3(CH3)3) with a solvent and the flour PPO (2,5-diphenyloxazole, C15H11NO) as a solute at a concentration of 1.5 g/l (0.5 %). The second and the third shell contain PC with a small amount (5 g/l) of DMP (dimethylphthalate) that is added as a light quencher in order to further reduce the scintillation yield of pure PC. The OV is a barrier that prevents 222Rn emanated from the external materials (steel, glass, photomultiplier materials) to diffuse into the fiducial volume. The scintillation light is collected by 2212 photomultipliers that are uniformly attached to the inner surface of the SSS (Figure 1). The SSS is supported by 20 steel legs and enclosed within a large tank that is filled with ultra-pure water. The tank (Figure 1) has a cylindrical base with a diameter of 18 m and a hemispherical top with a maximum height of 16.9 m [3]. Besides being a powerful shielding against external background (rays and neutrons from the rock), the Water Tank (WT) is also used as a Cherenkov veto counter for muons. The muon flux, although reduced by a factor 10^6 by the 3500 meters water equivalent (m.w.e.) depth of the Gran Sasso Laboratory, is still significant for Borexino requirements and a strong additional reduction factor (about 10^4) is necessary [6]. Therefore the WT is equipped with 208 photomultipliers that collect the Cherenkov light emitted by muons in water [9]. In order to maximize light collection efficiency the whole external SSS surface and the internal WT surface are covered with a layer of Tyvek .

2.2. *Inner detector photomultipliers*

After several tests on the large area tubes available on the market, the 8" E.T.L. 9351 phototube, formerly Thorn EMI, was chosen for the Borexino inner detector. The 9351 tube has a hemispherical photocathode with a curvature radius equal to about 11 cm, resulting in a minimum projected area of 366 cm^2. The cathode coating is made of a layer of CsKSb and the multiplier structure consists of 12 linear focused dynodes (BeCu) [7]. The bulb of the tube is made of a low radioactive Schott 8246 glass that has been carefully studied and characterized underground at Gran Sasso by means of Ge detectors.

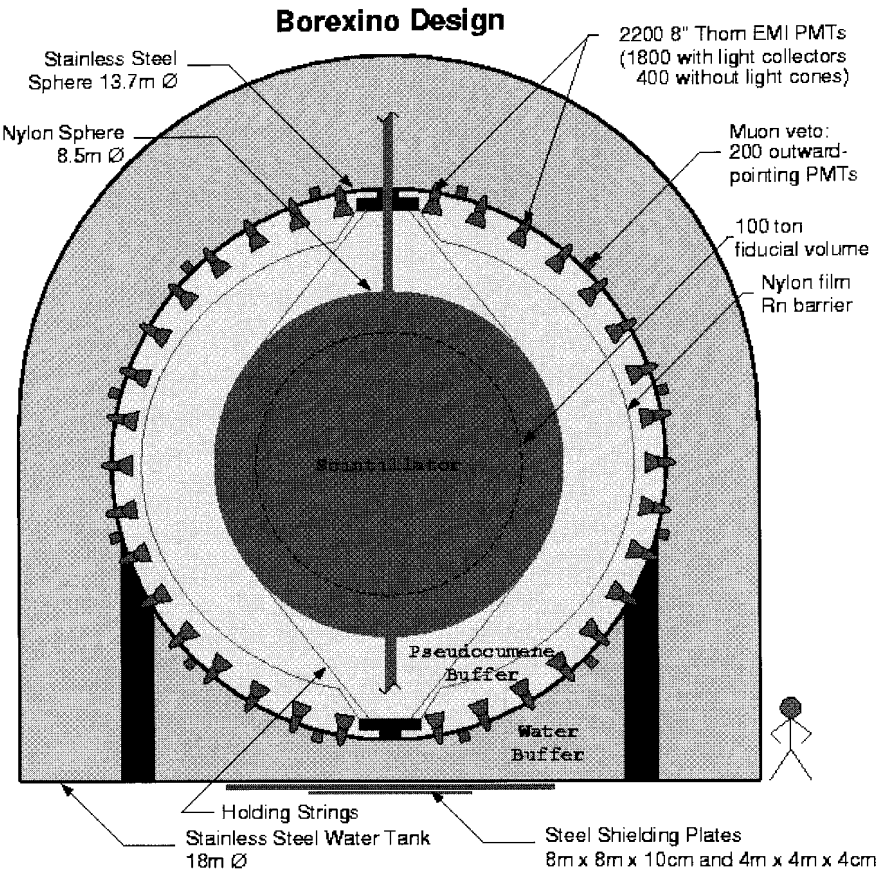

Figure 1. Scheme of the Borexino detector.

2.2.1. *Photomultiplier encapsulation*

The 2212 Borexino photomultipliers are mounted in the detector through equally spaced holes located on the 13.7m diameter stainless steel sphere already described in section 2.1. To assure a reliable operation of the PMTs both in water and PC, it was necessary to study and develop an encapsulation of the neck of the bulb and the divider in order to fulfil all the mechanical and environmental constraints [8]. The base and the neck of the tube are enclosed in a cylindrical stainless steel housing (Figure 2). This housing is fixed to the glass of the neck of the tube through the PC proof EP45HTepoxy resin from Master Bond, which acts as a structural adhesive and also as a protection barrier against the intrusion of PC. Phenolic resin is used as an isolating material (electrically decouples the device to avoid ground loops) and acts also as a groove for the

viton o-ring assuring the tightness between the tank and the sphere. All the 2200 feeds-through have been tested by means of a custom made spectrometer, using argon as a trace gas to evaluate the leak rate. It should be reminded that the feed-through is also designed to accommodate the underwater jam nut connector from Framatome company. The space inside the cylinder, left empty by the tube, is filled with an inert organic oil inserted inside the can through a 10 mm pipe port sealed afterwards with a swagelok cap.

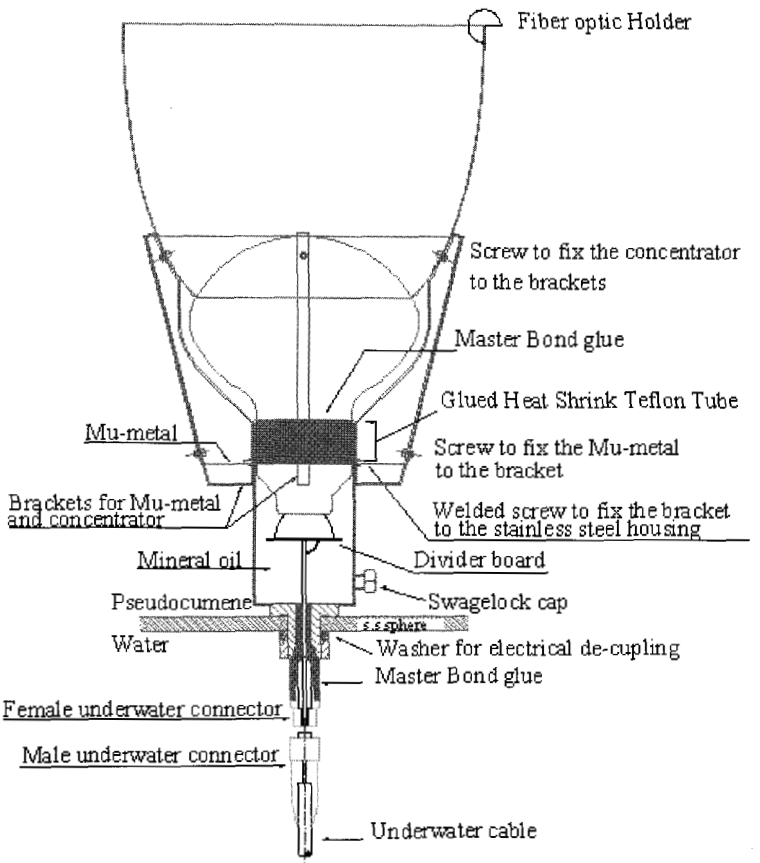

Figure 2. Photomultiplier encapsulation design.

This oil prevents water to condense on the divider without stressing the very delicate joint between the metal pin and the glass. A last barrier against PC is

assured by a heat shrink Teflon tube glued, with epoxy resin, between the glass neck of the photomultiplier and the steel can. In order to fully benefit this barrier, we exploited a patented technology of Gore which implies a preliminary surface etching of the Teflon film and allows a strong Teflon adhesion on other surfaces.

2.3. *Cables and connectors*

In Borexino, cables and connectors will be completely immersed in high purity water for a period of many years. This has required to find solutions and materials explicitly developed for submarine applications. The fundamental requirements are materials compatibility and electrical performances. Obviously, the radioactivity level of the materials is a major concern. Cables, that connect the photomultipliers directly to the electronics, are custom made RG 213 coaxial 50 Ω cables. The outer jacket is made of solid extruded high density polyethylene while a second barrier is realized with a laminated copper foil, bounded to the braid with a copolymer coating. All cables have an electrical length of 282.1 ± 0.25 ns (~57 m). Underwater connectors work in a non critical condition as concerns pressure, but an immersion time of many years without maintenance requires a very high confidence and experience in long term applications in submarine field. The company identified is Framatome which provided strong stainless steel connectors suitable for RG 213. Special attention was also dedicated to the connector cabling to optimize the overall electrical response of the line; dedicated tests were performed with a dual port network analyser.

2.4. *The outer detector*

As mentioned in section 2.1, high energy muons originating within cosmic ray interactions in the atmosphere are still able to penetrate to the depth of the Gran Sasso laboratory. Among the tagging methods, a key role is played by the Outer Detector (OD), a water Cherenkov detector composed of 208 additional photomultipliers installed in the volume of the Water Tank (WT), where a ultra clean water buffer is present for shielding purposes. The photomultipliers are 8" encapsulated THORN EMI 9351 photomultipliers, the same used for the internal detector, and are arranged on the outer side of the SSS and on the floor of the water tank. The photomultipliers work in water under almost 2 atmospheres of pressure at the WT bottom, therefore their mechanical arrangement, the connectors and the cables had to be designed and chosen to be reliable in these conditions. Unlike those mounted inside the sphere, OD photomultipliers are

equipped with a full encapsulation. A steel cone-shaped case, housing the photomultiplier, the voltage divider, the μ-metal shielding and a female HV connector. The sensitive photocathode is covered only by a transparent PET foil, so the photomultiplier retains an acceptance angle close to 180. The space between the case (including the PET foil on the front) and the photomultiplier is filled with mineral oil in order to minimize the refraction index discontinuities in the light path to the photocathode. In order to increase the light detection efficiency, most of the WT and SSS surfaces (95%) are covered with sheets of Tyvek, a white paper-like material, about 200 μm thick, made of pressed polyethylene fibres.

2.5. *Detector calibration systems*

2.5.1. *Photomultiplier calibration*

In Borexino, both time and charge calibration of the photomultiplier system is of utmost importance. Therefore, a multiplexed system of optical fibres has been developed for the precise photomultiplier calibration both in time and in gain. The solution of multiplexed fibre chains has been realized for the first time in a large underground detector. The solution adopted for Borexino is based on a simple idea: the light emitted by an external laser source is carried simultaneously to each photomultiplier tube by a dedicated system of optical fibres. The laser light is first distributed to 35 fibres which reach the Stainless Steel Sphere in 35 different points. Light enters the SSS via 35 purposely designed optical feeds-through and is again divided into 90 fibres each individually coupled to a photomultiplier. In this way radioactive contamination is avoided since no part of the system is immersed in the innermost part of the detector. Furthermore, light reaches the photocathode without crossing large amount of scintillator and/or buffer liquid, thus avoiding dependency on the medium characteristics.

2.5.2. *Internal source calibration system*

In order to carefully calibrate the detector a system for the insertion of radioactive and light sources in the Borexino bulk has been realised. This system must fulfil stringent requirements in terms of radio purity, cleanliness, mechanical strength and reliability, and must guarantee a complete air tightness while inserting, operating, and removing the sources from the detector. Sources, fibres and LED used for location are attached to the end of a series of neutrally buoyant stainless steel rods, each one meter in length, with an optional hinged section which allows the assembly to be rotated up to 90°. The rotation of the hinge is accomplished by pulling on a Teflon tether tube attached to the source

coupler. The entire assembly can also be rotated azimuthally 180° in either direction to map out cylinders in the inner vessel. The insertion operations are performed through a custom built glove box which resides in a class 10 clean room atop the Borexino water tank. Located between the glove box and the inner vessel tube is a load lock where the sources are attached to the spring loaded rod coupler. The insertion rods and Teflon tether tube pass through sliding seals since there is a significant pressure difference between the glove box and the load lock. The glove box, load lock, and the sliding rod seal, are continuously purged with LAKN during operations to avoid introducing any radioactive contaminants into Borexino during a calibration operation.

2.5.3. *CCD cameras system*

The system described above does not provide enough feedback to determine the position of the source to the level of precision required. Thus it was decided to equip every source with a LED, and use a system of seven digital cameras to find the position of said LED [12]. The cameras used are consumer grade Kodak DC290 digital cameras, each of which is equipped with a Nikon FC-E8 fish eye lens. During 2002, this system was tested with a string of LEDs hung in the center of Borexino and the ability to locate the sources to within 2 cm was verified. The camera system has also proved to be a valuable tool during the filling operations.

2.6. *Nylon vessels*

In the Borexino detector the scintillator volume is divided in three regions by means of two nylon vessels and one stainless steel sphere. The inner vessel is a thin-walled (0.125 mm thick), transparent nylon balloon, 4.25 m in radius, held in place at the center of the SSS. The Nylon is very transparent and has approximately the same index of refraction (1.53) as PC [4]. To avoid deposits of the long-lived 210Pb radon daughter, the vessel was constructed inside the Princeton University clean room, which was kept low in radon clean-room conditions [5]. The inner vessel is completely surrounded by a second, larger nylon membrane (Outer Vessel, OV) in order to square the effectiveness of the system as a barrier against radon atoms diffusing inward from outer parts of the detector. The two vessels were pre-assembled in this nested condition even before being shipped to Gran Sasso for installation and inflation to their final spherical shapes. The vessels must be held in place by a support structure; each nylon sphere is attached to a vertically oriented cylindrical "end region" at both top and bottom. To keep the vessels constrained in roughly spherical shapes, more than just two fixed attachment points are needed: each vessel is also held in place by two sets of ropes (one set attaching at each end region) that loop

vertically over and under them. A third set of ropes goes around each vessel horizontally, completing a coarse mesh.
The end regions are outfitted with sets of instrumentation for monitoring the detector. These include strain gauges that hold the rope ends to the end regions, for monitoring the buoyancies, temperature sensors in the buffer volumes, differential pressure gauges and a set of optical fibres to monitor the shape and position.

3. Performances and first results

We report a real-time spectroscopic observation of the mono-energetic (0.862 MeV) neutrinos (ν) from the radioactive decay of ^{7}Be in the Sun. These results constitute a scientific and technological breakthrough in the quest for the real time detection of low energy (below 2 MeV) solar ν that comprise more than 99% of the flux. Current spectroscopic data on solar ν are confined to energies greater than 5 MeV (0.01% of the total flux). The data used in this paper were collected for 47.4 live days between May and July 2007. Events are selected by means of the following cuts:

- The event must have a unique reconstructed cluster, in order to reject pile-up events and fast coincident events. The efficiency of this cut is nearly 100% because the very low triggering rate results in a negligible pile-up.
- Events with a muon flag, i.e. those with some Cherenkov light in the water tank detector, are rejected.
- After each muon that crosses the scintillator, all events within a time window of 2 ms are rejected. The measured muon rate in Borexino (muons that cross the scintillator and buffer volume) is 0.055±0.002 s−1. The dead time introduced by this cut is negligible.
- The events must be reconstructed within a spherical fiducial volume corresponding nominally to 100 ton in order to reject external background. Another volumetric cut (z<1.8 m) was applied in order to remove a small background from 222Rn daughters in the north pole of the inner vessel, resulting in a nominal fiducial mass of 87.9 t. The fiducial exposure in 47.4 days is 4136 day · ton.

When all cuts are taken into account in the analysis, we obtain the neutrino spectrum (Figure 3); fitting this spectrum our best value for the interaction rate of 0.862 MeV 7Be neutrinos is: 47 ± 7stat ± 12sys counts/(day · 100 ton) in the full electron recoil spectrum [13]. The first quoted error is 1σ statistical, while the second is the maximum systematic error due to the fiducial mass determination.

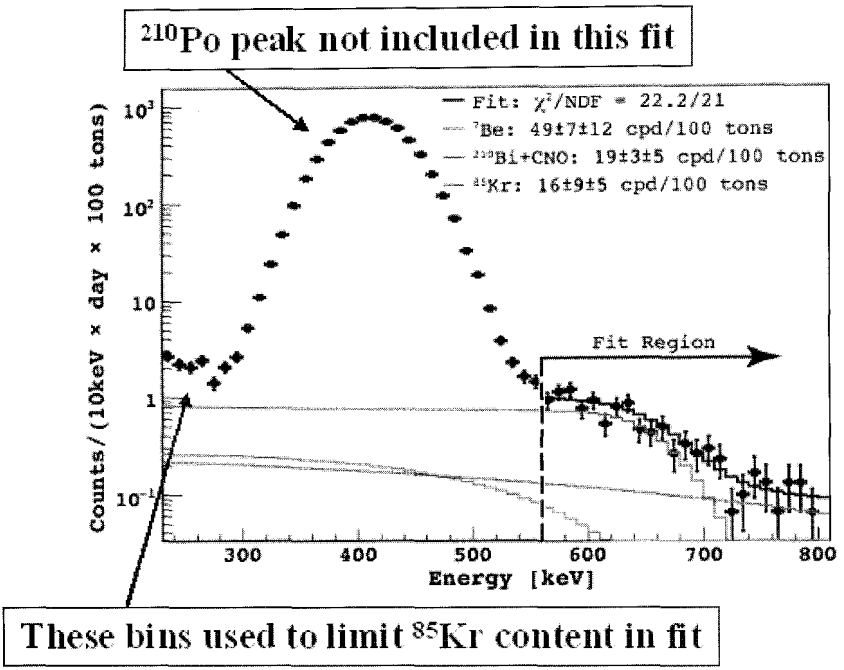

Figure 3. Fit of the ^{7}Be neutrino spectrum in Borexino.

Acknowledgments

I sincerely thank the funding agencies: INFN (Italy), NSF (USA), BMBF, DFG and MPG (Germany), Rosnauka (Russia) and I acknowledge the generous support of the Laboratori Nazionali del Gran Sasso. We gratefully acknowledge the valuable contribution from former collaborators and of all the technician.

References

1. G. Alimenti et al. (Borexino Collaboration), *Astropart. Phys.* **8**, 141 (1998).
2. G. Alimonti et al. (Borexino Collaboration), *Astropart. Phys.* **16**, 205 (2002).
3. C. Arpesella et al. (Borexino Collaboration), *Astropart. Phys.* **18**, 1 (2002).
4. A. Pocar,, *Ph.D. Thesis,* Princeton University (2003).
5. J. Benziger et al., *arXiv:physics/0702162*, accepted for publication in Nucl. Inst.Meth. A.

6. A. Ianni et al. (Borexino Collaboration)., *Nucl. Inst. Meth. A* **537**, 683 (2005).
7. A. Brigatti et al,. *Nucl. Inst. Meth. A* **537**, 521 (2005).
8. L. Oberauer et al., *Nucl. Inst. Meth. A* **530, 453** (2004).
9. Borexino Collaboration, "The Borexino Detector", paper in preparation.
10. F. Gatti et al. (Borexino Collaboration), *Nucl. Inst. Meth. A* **370**, 609 (1996).
11. G. Alimonti et al. (Borexino Collaboration), *Nucl. Inst. Meth. A* **440**, 360 (2002).
12. H. O. Back, PhD Thesis, Virginia Polytechnic Institute and State University, 2004.
13. C. Arpesella et al. (Borexino Collaboration), *Physics Letters B* PLB-D-07-00772R2 (2007).

DESIGN OF A WIDE SPECTRAL RANGE AND HIGH-RESOLUTION SPECTROGRAPH FOR MONITORING THE NIGHT SKY BACKGROUND FOR USE IN AIR FLUORESCENCE TELESCOPES

N. ANTONAKAKIS SPYROPOULOS, P. FETFATZIS,
E. FOKITIS, V. GIKA, S. MALTEZOS[1]

Physics Department, National Technical University of Athens, Iroon Polytechniou 9 Zografou, Athens, 15780, Greece

In this work we present the design of a compact, high-resolution echelle spectrograph for monitoring the Night Sky Background. This spectrograph is combined with a 25.4 cm telescope and uses an appropriate CCD camera as detector. It can operate in a wide spectral range from Ultraviolet to near Infrared (i.e. 300-780 nm) corresponding to the sensitivity spectral window of photocathodes used in the fluorescence telescopes. In the design we also made effort to compromise a sufficient sensitivity and a reasonable exposure time. This instrumentation could become a versatile tool for the operation and development of fluorescence telescopes used in Ultra High Energy Cosmic Ray Experiments.

1. Introduction

As we have mentioned in the previous ICRC we proceeded to the design and implementation of a dedicated and portable, spectroscopic facility in order to develop a diagnostics and optical noise experimental tool, useful for the statistical analysis of the signal and noise of Night Sky Background Radiation [1]. Our ground based instrumentation approach used existing technology in order to produce a more flexible apparatus that can be adapted by present and planned observatories of UHECRs. In previous measurements of the Night Sky Background Radiation at several locations in Greece we used a low-cost,

[1] Corresponding author: maltezos@central.ntua.gr

portable spectrometer based on a concave grating. The results from these measurements were satisfactory although the need for higher spectral resolution and wider spectral coverage in one exposure led us to adapt a more attractive design, based on an echelle grating. This echelle spectrometer is sensitive in the spectral range 300-780 nm, where the photomultiplier detectors typically used in EAS fluorescence installations are sensitive as also the EAS detectors, where the multi-alkali photocathodes have been proposed [2]. In next section, we present the design principles of the echelle spectrometer, while in section 3 preliminary measurements with the already-built prototype echelle spectrometer are discussed. Finally in Section 4, we report the conclusions and prospects for the future work.

2. Design of the Echelle Spectrometer

This high-resolution and very compact spectrometer uses an echelle grating with 46.1 grooves/mm and 32° blaze angle as the main dispersing element, while a Fused Silica prism with index of refraction equal to 1.477 at 350 nm was chosen for the cross-dispersion. Using the equations for an echelle spectrometer that are given in [3] and [4] we choose the most suitable components in order to record the spectral region from 300 nm to 780 nm in only one exposure with high resolution and in reasonably small time interval. From these equations the reciprocal linear dispersion (RLD) is about 1.0 nm/mm at 350 nm and the separation between two successive orders is such so the desired 2-D spectrum fills the CCD. A dSLR camera of the SBIG inc. with quite large CCD sensor, 12 mm x 9 mm, and pixel size about 7.4 μm x 7.4 μm is the light detector. According to camera's specifications the quantum efficiency is over 20% in the desired spectral region, while dark current is less than 1 e^-/pixel per s thanks to the additional thermo-electrical cooling of the camera. An f/5 UV-grade Fused Silica lens of 250 mm focal length is used to make the beam parallel before the echelle and a same one to project it on the CCD after its exit from the prism. The wavelength resolution is limited mainly by the f/number of the 25.4 cm telescope, which is f/4.7 and the slit width, which is 75 μm. Instead of the initial design, which was based in a classic Czerny-Turner mounting, we decide to replace the two mirrors with two UV-grade fused silica lenses. We made this decision for two reasons. Firstly, Fused Silica has very high transmission at the desired wavelengths as can be seen in Figure 1 (> 90 % from 250 nm to 1000 nm), much higher than the reflectivity of any mirror in that region. Secondly, in the Czerny-Turner mounting each mirror is tilted with respect to its incident chief ray and thus has off-axis aberrations, a problem that is avoided with the

use of lenses. The only sacrifice for this change is a few centimetres larger spectrometer. In Figure 2 a draw of the spectrometer is shown in respect with the design discussed above.

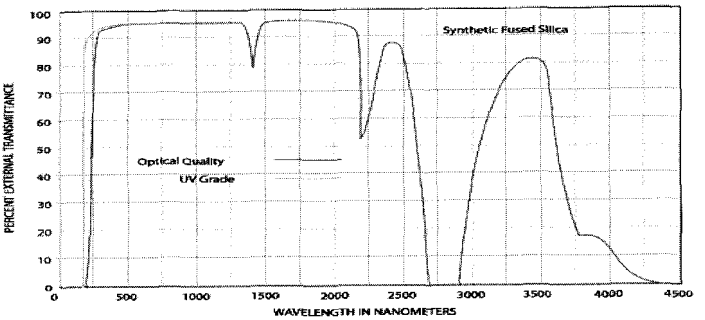

Figure 1. External transmittances for UV-grade and optical grade fused silica.

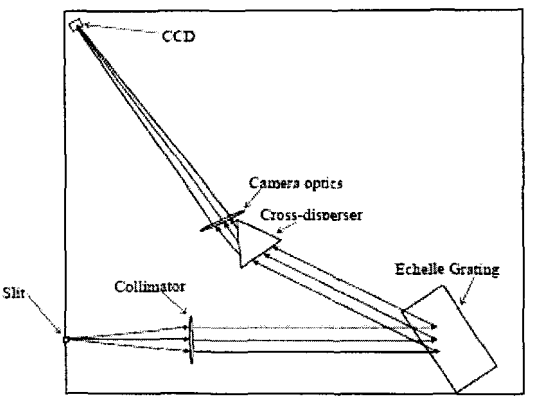

Figure 2. Design of the echelle spectrometer. For more information see the text above.

The choice of the type (diffraction grating or prism) and location (between the echelle and camera optics or between the collimator and the echelle) of the cross-disperser was done according to suggestions from [4] and [5]. The software for analysing the data from the pixels' matrix is IRIS and Visual Spec.

3. Laboratory Measurements

We set up a prototype echelle spectrometer for laboratory measurements, consisting of an echelle grating 31.6 g/mm and 63° blaze angle, a dispersing prism made of F2 glass and two lenses of 300 mm focal length each. For the

calibration purposes we used an Hg discharge lamp. As we see in Figure 3, in a single exposure we can record from 400 nm to 600 nm while in Figure 4 the FWHM of the 579 nm line is 0.06 nm and the reciprocal linear dispersion (RLD) of the 97th order is about 0.5 nm/mm.

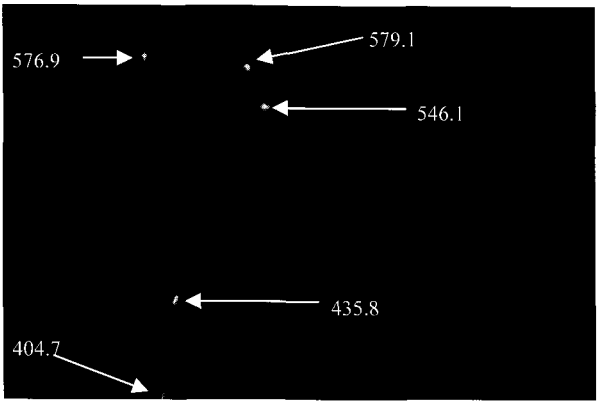

Figure 3. A 2-D picture of Hg spectrum as recorded from the camera.

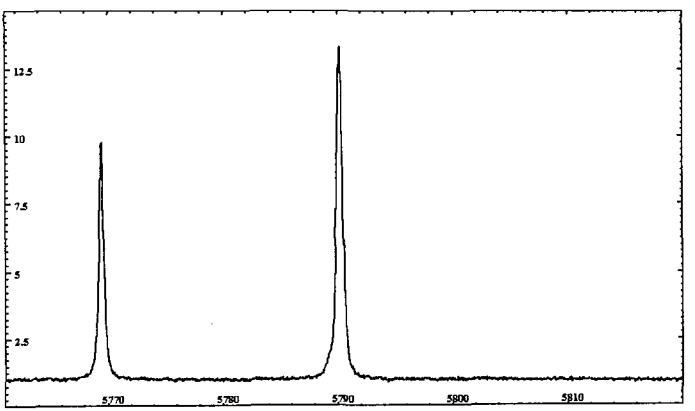

Figure 4. The spectral analysis of the 97th order where the doublet line 5769 Å – 5791 Å of Hg appears to be. The x-axis represents the wavelength in Å and the y-axis the relative intensity.

From these figures it becomes obvious the benefits of an echelle spectrometer by means of resolution and spectral coverage, as mentioned also in [3], [4], [5].

4. Conclusion and Prospects

In conclusion, we present a high-resolution portable instrument with capability to provide the night sky background in ground based EAS telescope locations. In particular, it can provide the NSB dependence on zenith angle and with further automation, it could give the NSB during nighttime at intervals around 15 min covering the range 300 to 780 nm, which covers the range of sensitivity of bi-alkaly and multi-alkali phototubes. The location where the measurements of the night sky background radiation will be done is situated in the mountain Helmos, near the "Aristarchos" telescope, which is considered as one of the darkest places in Europe. We are planning to insert the collected data in a database, which will be accessible to researchers, developing simulation Codes for EAS phenomena such as CORSIKA, so that spectrally meaningful estimators of night sky background can be developed.

Acknowledgments

This project is co - funded by the European Social Fund (75%) and National Resources (25%) – (EPEAEK II) – PYTHAGORAS. We would like to thank Buil C. author of IRIS and Desnoux V. author of Visual Spec for the free distribution of their software.

References

1. Fokitis et al. "A system of medium resolution for monitoring the night sky background in the visible and near UV range", in ICRC proc., Merida, Mexico, 2007.
2. G. Garipov et al. "The photomultiplier tubes in the light sensor of an orbital detector for studying the fluorescent radiation of extensive air showers", *Instrum. Exp. Tech.*, **48**, 92-95, 2005.
3. D. Schroeder. "Design Considerations for Astronomical Echelle Spectrographs", *PASP,* **82**, 1253, 1970.
4. D. Schroeder. "Astronomical Optics", Academic Press San Diego, 2000[2].
5. D. Walker and F. Deigo. "Design Philosophy of the Forthcoming Echelle Spectrographs for the AAT and LPO", *Mon. Not. R. Astron. Soc.* **217**, 355, 1985.

THE AUGER EXPERIMENT STATUS AND RESULTS

GIORGIO MATTHIAE
on behalf of the Pierre Auger Collaboration
University and Sezione INFN of Roma Tor Vergata Roma, Italy

The Auger experiment was designed to study the high-energy cosmic rays by measuring the properties of the showers produced in the atmosphere. The Southern Auger Observatory has taken data since January 2004. Results on mass composition, energy spectrum and anisotropy of the arrival directions are presented. The most important result is the recent observation of correlations with nearby extragalactic objects.

1. Introduction

The flux of cosmic rays, shown in Fig. 1 as a function of energy [1], follows approximately a power law $E^{-\gamma}$ with spectral index γ roughly equal to 3.

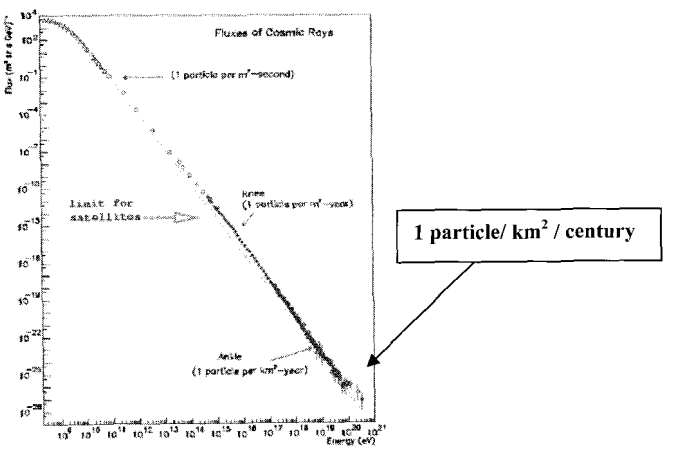

Figure 1. The flux of primary cosmic rays as a function of energy.

The spectrum exhibits interesting features, usually called the "knee" and the "ankle". At the energy of the "knee" (~ $3x10^{15}$ eV) the spectral index changes from approximately 2.7 to 3.1. The "ankle", a kind of undulation around a few 10^{18} eV, has been actively studied by recent experiments and will be discussed in the Section on the spectrum. In the region above 10^{19} eV the flux of the primaries is extremely low, of the order of 1 particle/ km^2/ century. Therefore the study of cosmic rays in this very high-energy region requires detectors with very large acceptance.

2. The Auger experiment

Two Observatories, one in the Northern and one in the Southern hemisphere are foreseen in the Auger project, to achieve a full exploration of the sky.

The Southern Auger Observatory [2] is located near the small town of Malargüe in the province of Mendoza (Argentina) at the latitude of about 35^0 S and altitude of 1400 above sea level. The region is flat, with very low population density and favorable atmospheric conditions. The Observatory is a hybrid system, a combination of a large surface array and a fluorescence detector.

The surface detector (SD) is a large array of 1600 water Cherenkov counters spaced at a distance of 1.5 km and covering a total area of 3000 km^2. Each counter is a plastic tank of cylindrical shape with size 10 m^2 x 1.2 m filled with purified water. Technical details of a tank are given in Fig. 2. The surface detector measures the front of the shower as it reaches ground. The tanks activated by the event record the particle density and the time of arrival.

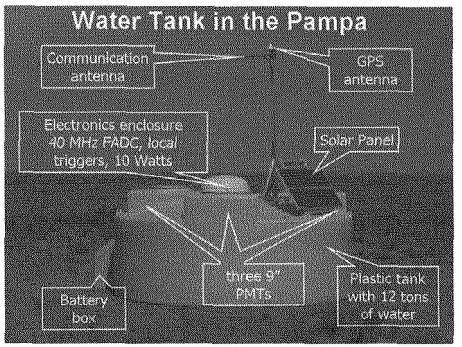

Figure 2. Picture of a water tank of the Surface Detector of the Auger Observatory. The insets give explanations on the various components of the system.

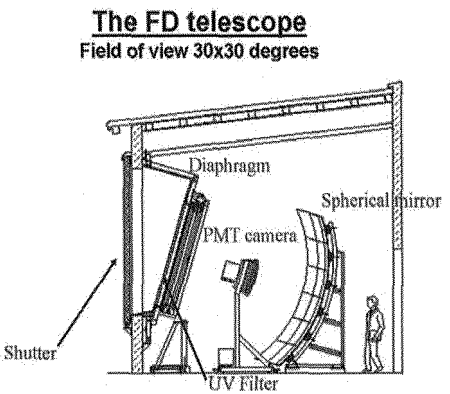

Figure 3. Sketch of a fluorescence telescope. The various components are indicated.

The fluorescence detector (FD) consists of 24 telescopes located in four stations which are built on the top of small elevations on the perimeter of the site. The telescopes measure the shower development in the air by observing the fluorescence light. Each telescope has a 12 m^2 spherical mirror with curvature radius of 3.4 m and a

camera with 440 photomultipliers. The field of view of each telescope is 30^0 x 30^0. UV filters placed on the diaphragm reject light outside the 300-400 nm spectrum of the air fluorescence. The FD may operate only in clear moonless nights and therefore with a duty cycle of about 12%. A sketch of a telescope is shown in Fig. 3.

Attenuation of the fluorescence light due to Rayleigh and aerosol scattering along the path from the shower to the telescope is measured systematically with the LIDAR technique.

An example of a longitudinal profile of a shower as measured by the FD is shown in Fig. 4 where the number of particles of the shower is plotted as a function of the atmospheric depth. In order to obtain the shower profile, the contamination due to Cherenkov light has to be subtracted. The empirical formula by Gaisser and Hillas is used to fit the data.

An example of an event of very high energy as observed by the SD is shown in Fig. 5.

The signal of each tank is expressed in units of Vertical Equivalent Muons (WEM) which represents the signal produced by a muon traversing the tank vertically.

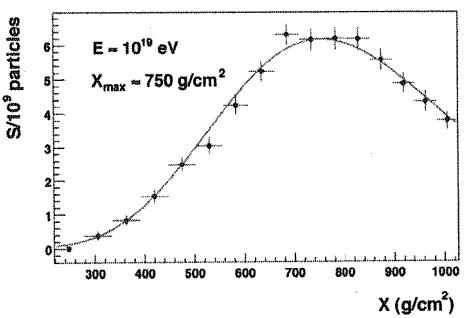

Figure 4. Example of a measured longitudinal profile of a high-energy shower.

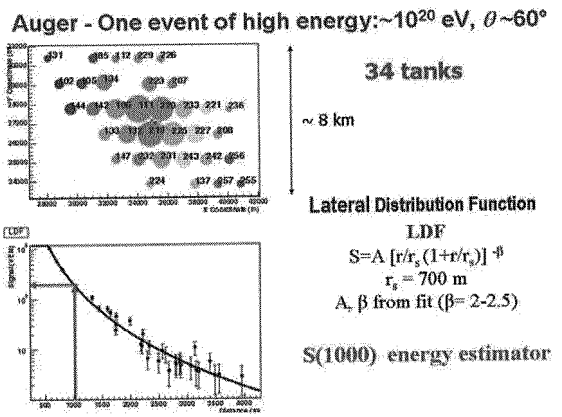

Figure 5. Example of a very high energy event as observed by the SD. The shower has activated 34 tanks distributed over an area of more than 50 km^2.

The flux of cosmic ray muons provides a continuous monitoring of the SD. From the magnitude and the time of the signal of the tanks one derives the direction of the axis of the shower and the point of impact at ground. The left bottom panel of Fig. 5 shows the signal, expressed in units of VEM as a function of the distance from the shower axis. A simple analytical expression known as Lateral Distribution Function (LDF) is then fitted to the data to obtain the signal at the distance of 1000 m from the axis. This interpolated quantity, S(1000), is a good energy estimator in the sense that it is well correlated with the energy of the primary [3].

The Southern Auger Observatory started to collect data in 2004 and will be completed early in 2008. The Northern Auger Observatory which is now being designed will be located in Colorado (USA).

3. Mass composition

The direct method to study the mass composition is based on the measurement of the longitudinal profile of the showers. It is well known that for a given energy protons are more penetrating than light/medium nuclei which interact essentially as a collection of nucleons. The depth of the maximum of the shower profile X_{max}, as measured by the fluorescence telescopes, is well correlated with the particle mass. The principle of the method is indicated in Fig. 6. The FD detector of Auger can measure X_{max} with systematic uncertainty of about 15 g/cm^2.

A compilation of earlier data on X_{max} for energies above 10^{14} eV is shown in Fig. 7 where expectations from simulation programs are also given for Fe nuclei, protons and photons. The value of X_{max} for protons is about 100 g cm^{-2} larger than for iron.

Recent data by Auger [4] are presented in Fig. 8 together with the predictions of various simulation programs. In spite of the still low statistics, the data indicate some change of regime at 2-3 EeV where the slope (elongation rate) changes. At the highest energies the trend is intermediate between protons and Fe nuclei with a mean mass number of about 5.

4. The energy spectrum

An important feature of the spectrum in the energy region above 10^{19} eV is the mechanism suggested by Greisen, Zatsepin and Kuz'min which is known as GZK

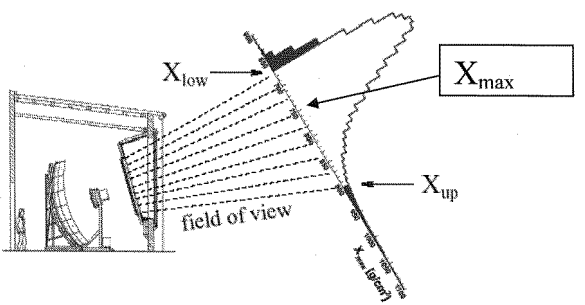

Figure 6. Illustration of the measurement of the quantity X_{max} by a fluorescence telescope of the Auger Observatory.

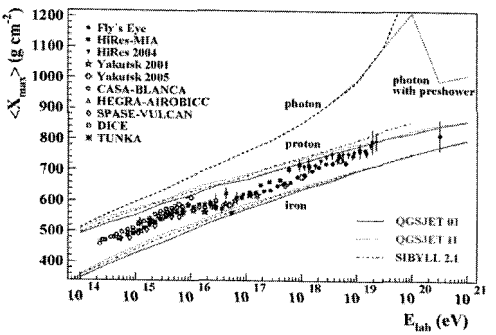

Figure 7. Compilation of earlier data on the quantity X_{max} as a function of energy. Prediction of various simulation programs for incident photons, protons and iron nuclei are also shown.

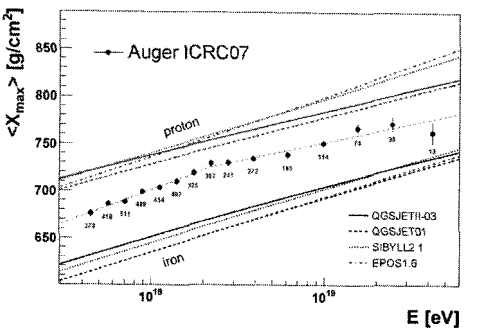

Figure 8. The Auger data on the quantity X_{max} are plotted as a function of energy and compared to predictions of simulation programs for protons and iron nuclei. The number of events for each data point is also shown. The errors shown are statistical.

cutoff. It is due to the interactions of the cosmic rays with the low energy photons of the Cosmic Microwave Background. Protons with energy above the threshold for photoproduction of pions (~ $4x10^{19}$ eV) will lose energy as they travel in space. The value of the energy where an integral power-law spectrum would be reduced to one half is $5.3x10^{19}$ eV [5]. The energy loss per interaction is about 15 – 20 %. At ~ $5x10^{19}$ eV most of the observed particles must have come from sources within 100 Mpc. Production of electron-positron pairs is also present but it is less effective than photo-pion production. However, this process is expected [5] to be responsible for a feature related to the so-called "ankle", a shallow minimum (or "dip") in the plot of the flux times E^3 which is centered at energies of a few 10^{18} eV.

In the past there was a controversy on the actual presence of the suppression due to the GZK cutoff. The AGASA data did not show a suppression, contrary to the preliminary data of HiRes. The experimental situation is now clarified by the final data of HiRes [6], shown in Fig. 9 and by the data of Auger. The HiRes data clearly show a steepening of the spectrum above $10^{19.6}$ eV with a fitted value of the spectral index $\gamma = 5.1 \pm 0.7$. The steepening agrees with the expectations from the GZK cutoff.

The method used by Auger to measure the energy spectrum exploits the hybrid nature of the experiment with the aim of using the data itself rather than simulations.

For each event, the energy estimator S(1000) is obtained as discussed in Section 2. The energy estimator S(1000) depends on the zenith angle because the effective atmosphere thickness seen by showers before reaching ground changes with the zenith angle. The value of S(1000) corresponding to the median zenith angle of 38^0 is used as reference and the zenith angle dependence of the energy estimator is determined assuming that the arrival directions are isotropically distributed. This procedure is traditionally called "Constant intensity cut".

The absolute calibration of S(1000) is derived from the hybrid events using the calorimetric energy measured by the FD which is then corrected for the missing energy (neutrinos and muons) using the mean value between proton and iron (10% correction at 10^{19} eV with uncertainty ± 2%). This absolute calibration, which defines the energy scale, is at present affected by a systematic error of about ± 20%, mainly due to uncertainties on the fluorescence yield and on the calibration of the FD telescopes.

The energy calibration, obtained from the subset of hybrid events (see Fig. 10) is then used for the full set of events with higher statistics as measured by the SD.

Three different measurements of the energy spectra were obtained by the Auger Collaboration as explained in detail in ref.7. The SD "vertical" spectrum is for zenith

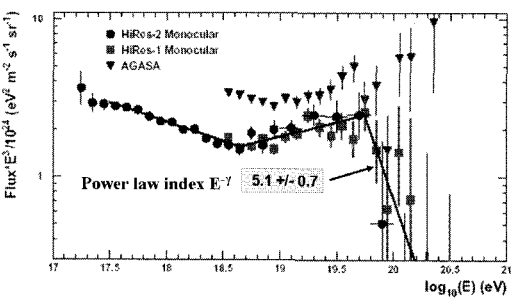

Figure 9. The final HiRes results on the energy spectrum are presented as Flux x E^3 and compared to the earlier AGASA data. The steepening due to the GZK cutoff is clearly seen. In addition the shallow minimum centered around $10^{18.6}$ eV is also evident.

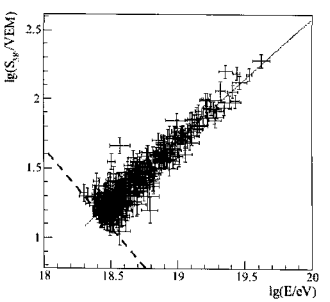

387 hybrid events are used to establish the absolute calibration of the energy estimator S in terms of the FD energy E_{FD}, as shown in the left panel.

The fitted line corresponds to
$E_{FD} = K \times S^B$
with B= 1.10 ± 0.02

Figure 10. Calibration of the energy estimator S(1000) using the energy from the FD.

angle $\theta < 60^0$, the SD "inclined" is for $60^0 < \theta < 80^0$. The SD spectra starts at the energy of $3x10^{18}$ eV where the efficiency goes to a plateau. The hybrid spectrum refers to FD events with at least one SD tank and starts at a lower energy (10^{18} eV).

The three spectra are consistent within statistics, as shown in Fig. 11 and therefore were combined in a single spectrum which is presented in Fig. 12.

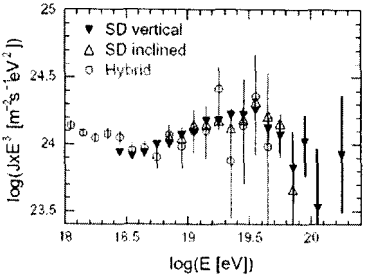

Figure 11. The Auger spectra (flux x E^3) from the SD and from hybrid events.

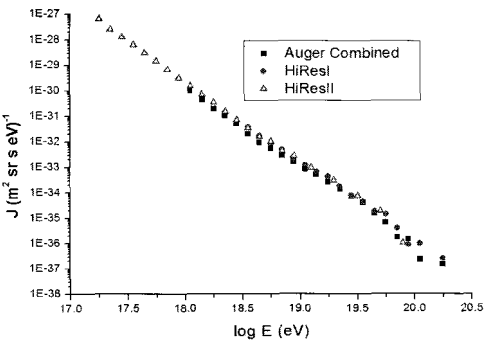

Figure 12. The combined Auger spectrum is plotted together with the HiRes data. The difference between the two sets of data can be attributed to ~10% difference in the energy calibration which in turns is due to different values used for the fluorescence yield.

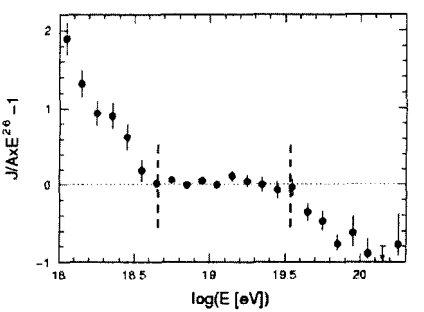

Figure 13. The relative difference of the Auger energy spectrum with respect to the form $E^{-2.6}$. The vertical dashed lines indicate the different intervals for the power law fits.

The "ankle", a barely noticeable undulation in Fig. 12, appears as a clear shallow minimum in Fig. 11 with shape and position similar to the predictions of ref.4. Above $\sim 10^{19.6}$ eV, the steepening expected from the GZK mechanism is also evident.

The structures present in the Auger spectrum are better analyzed by taking the relative difference of the data with respect to the reference form $J_s = A\, E^{-2.6}$. The result is presented in Fig. 13. Numerical values of the spectral index γ in the different energy intervals are given in Table 1.

Table 1. Numerical values of the spectral index γ of the power law fits in the different energy intervals. The energy values E_{ankle} and E_{GZK} correspond to the position of the breaks.

	Auger	**HiRes**
E_{ankle} (eV)	4.5×10^{18}	4.5×10^{18}
E_{GZK} (eV)	3.5×10^{19}	5.6×10^{19}
γ ($E < E_{ankle}$)	3.30 ± 0.06	
γ for ($E_{ankle} < E < E_{GZK}$)	2.62 ± 0.03	2.81 ± 0.03
γ for ($E > E_{GZK}$)	4.1 ± 0.4	5.1 ± 0.7

5. Anisotropy studies

In the study of anisotropy the Auger Observatory may exploit the good angular resolution of the SD which is better than one degree at high energy.

Observation of an excess from the region of the Galactic centre at the level of $4.5\,\sigma$, in the energy region 1.0 – 2.5 EeV and with angular scale of 20^0, was reported by AGASA [8]. The Auger Observatory is suitable for this study because the Galactic centre (constellation of Sagittarius), lies well in the field of view of the experiment. Some of the Auger results [9] on the observed and the expected number of events in the direction of the Galactic centre are shown in Table 2. Clearly the Auger data don't confirm the AGASA result.

Table 2. The number of observed and of expected events and the corresponding ratios are listed for different angular windows in the direction of the Galactic centre (energy between 1 and 10 EeV)

Angular window (degrees)	$N_{observed}$ / $N_{expected}$	**Ratio (errors: stat, syst)**
5	425/393	$1.08 \pm 0.07 \pm 0.01$
10	1662/1578	$1.05 \pm 0.04 \pm 0.01$
20	6365/6252	$1.02 \pm 0.02 \pm 0.01$

The Auger collaboration has done an extensive search for correlation of the high-energy events with known astrophysical objects. This study started early in 2004 and the results from data collected until August 2007 have been published recently [10]. During this period, the Observatory has increased in size. The total exposure is about 20% larger than for the yearly exposure of the Observatory once completed.

The simple plot of Fig. 14 already gives a hint that high-energy events are not distributed isotropically but rather tend to concentrate on the supergalactic plane where most of the nearby galaxies are located.

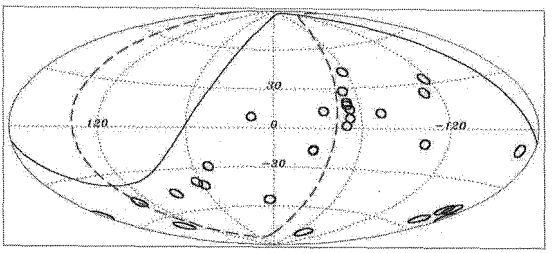

Figure 14. Plot in galactic coordinates showing the high-energy events as small blue circles. The supergalactic plane is indicated by the green dashed line.

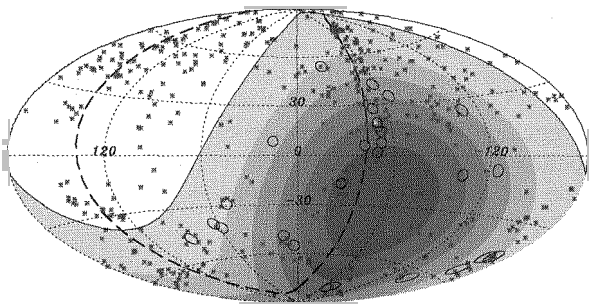

Figure 15. Plot in galactic coordinates showing the events with energy larger than 57 **EeV** as small circles of radius 3.2 degrees. The supergalactic plane is shown as a dashed line. The red crosses indicate the position of AGN within 71 Mpc. Cen A, one of the nearest AGN is marked in white. The white region of the sky is not accessible from the Southern Auger Observatory. Darker blue regions indicate larger relative exposure.

A more complete picture showing the data and the position of nearby AGN (from the catalog of ref.11) is reported in Fig. 15. Two events are correlated within less than 3 degrees with Cen A, a strong radio source at the distance of about 4 Mpc.

A sophisticated analysis described in ref. 10 has shown that a clear correlation, within an angle ψ about equal to 3 degrees, exists between the arrival directions of cosmic rays with energy above about 60 EeV and galaxies with active nuclei (AGN) at distances less than about 75 Mpc.

The results are summarized in Table 3. The first exploratory analysis has shown that 12 out of 15 events with energy above 57 EeV were correlated with AGN at distances less than 75 Mpc, within 3.1 degrees while only 3.2 were expected to be correlated by chance for an isotropic distribution.

As a consequence of this result, a prescribed test was defined to see whether the isotropy hypothesis had to be accepted or rejected. The same set of parameters and the same reconstruction algorithms were used. The second independent set (see Table 3, row #2) satisfied the test and the probability for this single configuration to happen by chance if the flux was isotropic is 1.7×10^{-3}.

A complete reanalysis of the data set gave the results reported in Table 3, row#3. Out of 27 events, 20 were found to correlate with a chance probability of the order of 10^{-5}.

Table 3. Results of the analysis for the first set, the second independent set, the reanalysis of the full set and for the full data set excluding the galactic plane region are reported.

	Number of events E > 57 EeV	Events correlated with AGN ψ = 3.1 degree	Events expected for isotropy
Exploratory scan 1 Jan 04- 27 May 06	15	12	3.2
Second independent set 27 May 06–31 Aug 07	13	8	2.7
Full data set (about 1.2 year full Auger)	27	20	5.6
Full data set excluding galactic plane region	21	19	5.0

The correlation becomes statistically more significant if the events in the region around the galactic plane (|b| <12 degrees) are removed. For this subset of 21 events, 19 are correlated with AGN. Elimination of the galactic plane region is motivated by the incompleteness of the catalog in this region and by the expected stronger effect of the galactic magnetic field which is known to be concentrated in the galactic disk.

The distribution of the separation angle between the direction of the 27 high-energy events and the nearest AGN is shown in Fig. 16. The histogram of the data shows a clear departure from isotropy.

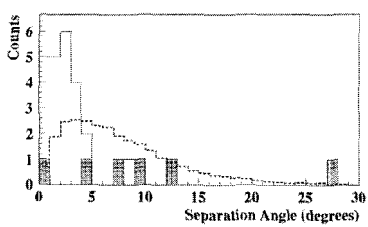

Figure 16. The angle between each event and the nearest AGN. The dotted histogram represents the expectation for isotropic distribution. The histogram shows the data while the 6 shaded areas represent the events removed because close to the galactic plane.

References

1. S.Swordy, *Space Science Reviews* **99,** 85 (2001).
2. J.Abraham et al., *Nucl. Instr. and Methods* **A523,** 50 (2004), B.Dawson (Auger Collaboration), *Proc. ICRC2007.*
3. D.Newton et al., *Astropart. Phys.* **26,** 414 (2007).
4. M.Unger (Auger Collaboration), *Proc ICRC2007.*
5. V.Berezinsky et al., *Phys. Rev.* **D74,** 043005 (2006) and refs therein.
6. R.U.Abbasi et al., *astro-ph*/0703099v1 (2007) and refs therein
7. Contributions of P.Facal San Luis, L.Perrone, M.Roth and T.Yamamoto (Auger Collaboration) to *Proc. ICRC2007*
8. M.Teshima et al., *Proc. ICRC2001* **1,** 337 (2001).
9. J.Abraham et al, *Astropart. Phys.* **27,** 244 (2007), E.M.Santos, *Proc. ICRC2007.*
10. J.Abraham et al., *Science* **318,** 939 (2007) and *astro-ph*/0712.2843 (2007).
11. M.P.Véron-Cetty and P.Véron, *Astron. & Astrophys.* **455,** 773 (2006).

PRELIMINARY RESULTS ON NEUTRON BACKGROUND INDUCED BY MUONS IN A SHALLOW UNDERGROUND LABORATORY: BARADELLO UNDERGROUND LABORATORY IN COMO

MONICA PELLICCIARI, E. ANDREOTTI, A. GIULIANI, M. GRASSI
Dipartimento di Fisica e Matematica, Università dell'Insubria, Como – Italy
A. CESANA, M. TERRANI
Dipartimento di Ingegneria Nucleare, Politecnico di Milano, Milano - Italy
G.L. RASELLI
INFN, Sezione di Pavia, Pavia – Italy

In the next future the relevance of shallow-depth underground laboratories as experimental sites for the study of low energy rare events of cosmic origin will increase. In such laboratories the natural background can give a relevant contribution to the recorded events and must be understood as much accurately as possible. In some kind of experiments, noticeably those aiming to dark matter detection, a main role is played by neutrons which can be generated by natural radioactivity or as the result of the interaction of muons with the rocks surrounding the detector. In this view we started a project aiming at studying such contribution both by measurements and Monte Carlo simulations.

1. Introduction

At present, the main experiments concerning most of the important open questions about dark matter and neutrino physics are located in very deep underground laboratories (thousands of meter water equivalent). This in order to suppress the background effects due to cosmic rays: in such laboratories the hadronic component of secondary cosmic radiation (CR) is suppressed and the muon component is strongly reduced to an amount which depends upon the rock cover of the laboratory. Several research groups have already studied (mainly by Monte Carlo simulation) the rate of survival of muon flux and its interference with the experimental results. In this kind of experiments one is looking for very rare and low energy events which can be easily masked or even simulated by cosmic radiation. Perhaps the most important effect from this point of view is the production of neutrons by muons within the last few meters of rock cover and in the detector itself. About this point the agreement between different simulations is not particularly good, but, due to the extremely low rate of surviving muons in deep underground laboratory, generally their contribution to the neutron flux is negligible with respect to other production ways, namely from natural radioactivity via (α,n) or spontaneous fission reactions.
Unfortunately, in order to investigate the most important open questions of contemporary physics, the sensitivity of the currently running experiments is by far too low, hence it will be mandatory to increase the detector masse of orders of magnitude to reach thousands of tons. Such detectors are no more compatible, for practical reasons, with deep underground laboratories. In such view it's clear that shallow underground laboratories will increase their importance like candidates for the location of next generation experiments. In these laboratories the contribution to the background of muon induced neutrons becomes important and can no more be

neglected. On the basis of the above considerations we started a project aiming at studying the muon induced neutrons field in a shallow laboratory, namely the Baradello Underground Laboratory – Insubria University.

2. Baradello Underground Laboratory

The laboratory is located in an artificial cave under Baradello Hill housing the water purification plant of the town of Como (northern Italy): the rock cover is about 100 m corresponding to about 300 m water equivalent. In the last years, the laboratory was characterized from the point of view of rock radioactivity, radon concentration, thermal and fast neutron background [1]. In particular, concerning neutron background, it was measured a thermal neutron flux of $(5.6 \pm 0.4) \times 10^{-6}$ cm^{-2} s^{-1} and a fast neutron flux integrated over energy range of $(1.9 \pm 0.8) \times 10^{-5}$ cm^{-2} s^{-1} , that means a suppression respectively of a factor 1000 and 100 with respect to sea – level external laboratories.

3. The project

The project that we are developing in Baradello Underground Laboratory foresees the validation of a Monte Carlo program for the simulation of muon induced neutron rate production and of their interaction with different materials. We will use known data with respect to the configuration of the mountain housing the cave and the rock composition, and new experimental data concerning:

- the muon flux from different directions at different points of the cave;
- the fast and thermal neutron flux at the same points;
- coincidence events between muons and fast neutrons;
- neutron production in high Z materials useful for γ-ray shielding.

4. First step: muon flux reduction factor

In order to better characterize the muon flux we carried out some measurements in the neighbourhood of our laboratory aiming at an estimation of the muon flux reduction inside the cave with respect to outside.

4.1 *NaI(Tl) measurements*

First of all, we acquired inside and outside the cave the muon spectra (around the vertical direction) with two standard NaI(Tl) detectors 3" x 3" and 4"x 4". In figure 1 we display the spectra obtained with the first detector. We used the natural radioactivity peaks at 1460 keV and 2614 keV for the calibration. From the spectra, it is possible to verify that the position of the bump which can be interpreted as due to muons crossing both the detector bases is consistent with the energy loss of relativistic charged particles in NaI: 1.7 MeV cm^2 g^{-1} [2]. It's also interesting to note the presence of a peak at about 4.8 MeV in the spectrum obtained inside the cave.

This peak is probably due to an U and Th contamination of the detector. Concerning its origin: it could be the sum of the energy of two particles emitted in the radioactive chains [3] or the energy of a photon emitted in the decay of an excited state of a nuclide produced by α particle interactions in the crystal itself, e.g. 4.835 MeV photon emitted by ^{26}Mg obtained from $^{23}Na(\alpha,p)$ reaction.

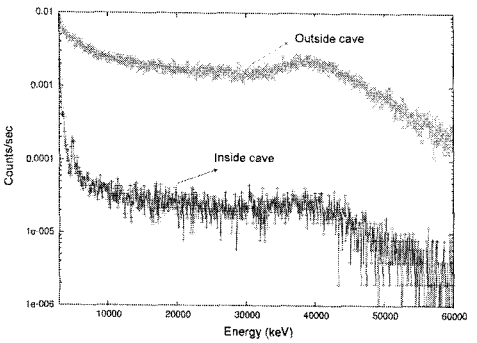

Figure 1: Comparison between 3" x 3" NaI (Tl) spectra inside and outside the cave

Table 1. Data concerning muon measurements with NaI (Tl)

NaI	Bump Area inside cave	Bump Area outside cave	Ratio: outside/inside
3" x 3"	0.61 ± 0.01	43.36 ± 0.51	71 ± 1
4" x 4"	2.01 ± 0.03	148.83 ± 1.18	74 ± 1

Table 1 reports data concerning the bump – area (Gaussian fit) inside and outside the cave and their ratio calculated from the spectra acquired with the different NaI. It's possible to appreciate the very good agreement of the results.

4.2 *Plastic scintillator measurements*

We repeated the measurements of muon intensity inside and outside the cave using a telescope made with two plastic scintillators (NE102 by Nuclear Enterprises - dimension of 33 x 20 x 1 cm^3) in coincidence. Measurements were performed placing the two slabs at different distances between each other. For distances greater than 10 cm, we found reduction factor of 65 ± 7, independent of distance, in fair agreement with the results obtained with the NaI(Tl) detectors.

4.3 *Hybrid Telescope*

In order to improve the selection of muons coming from a given direction with respect to NaI(Tl) detectors and to reduce the effect of secondary CR showers and random coincidences with respect to the plastic scintillator telescope, we realized an hybrid telescope: the 4" x 4" NaI(Tl) in triple coincidence with two plastic scintillators.

4.3.1 Muon flux characterization

We acquired vertical muon spectra inside and outside the cave in order estimate the muon flux reduction in the cave also with the hybrid telescope. Figure 2a) shows the comparison between the two registered spectra. Bumps corresponding to muons coming from a direction around the vertical are much better defined than in the previous cases and presumably the attenuation factor due to the laboratory cover is better determined. The estimation based on the Gaussian fit of the bump in the two spectra acquired with this structure, gave a reduction factor of 127 ± 1 significantly bigger than the previous values. This fact suggests that the contribution of secondary showers and casual coincidences can not be neglected in underground sites. We also acquired spectra outside the cave with the telescope inclined 45° right (corresponding to west inclination) and left (east inclination) with respect to the vertical. Preliminary data concerning these measurements are reported in table 2: it's possible to note the evidenced a modest east – west effect outside due to the geomagnetic field like reported in [4,5].

Table 2: Data concerning muon measurements with telescope inclined for East – West effect investigation

Telescope	Bump Area: West inclination	Bump Area: East inclination	Ratio: West/East
	0.1038 ± 0.0019	0.0901 ± 0.0014	1.152 ± 0.002

4.3.2 Muon flux and Baradello Hill shape

Our underground laboratory is located under a mountain with irregular shape, so the surviving muon flux hasn't the same intensity from all the directions. In this case it depends upon both from azimuth angle (ϕ) and zenith angle (θ) [6], so the orientation and the inclination of the detector are interesting ways to use for the characterization of the muon flux in correlation with rock cover. In order to have some data describing this fact to be used for Monte Carlo code validation, we started some measurements in the cave orienting and inclining the telescope. Following, the orientation of the telescope will be described in terms of cardinal points and inclination as degrees left and right with respect to the vertical. At present we completed data acquiring for 50° NW orientation with the telescope in vertical, inclined 45° left and 45° right. Table 3 summarizes the results and figure 2b) shows the comparison between the acquired spectra. It's interesting to note that the differences in the measured muon intensities are in very good agreement with the structure of the mountain, in fact from the map of the Baradello Hill and from the plant of the cave it's possible to note that in the first point of measurement:

- in the case of the left inclination, the telescope detects the muons coming from the side of the entrance to the cave where the rock cover is less than the one from the opposite side where the hill continues in a small chain;
- the rock cover from the vertical inclination is bigger than the left inclination but less than the right inclination due to the structure of the Baradello Hill.

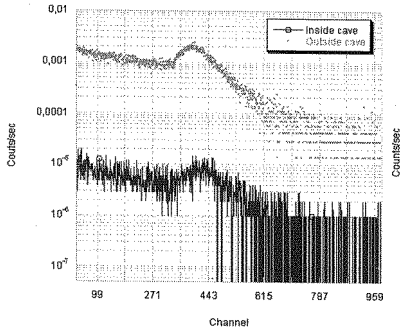

Figure 2a)

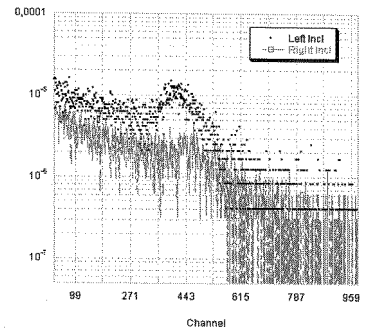

Figure 2b)

Figure 2a): comparison of the spectra acquired with telescope inside and outside the cave
Figure 2b): comparison between spectra acquired with telescope inclined right and left in the cave

Table 3. Data concerning muons measurements with hybrid telescope in the cave

Telescope	Bump Area: Left inclination	Bump Area: Right inclination	Bump Area: Vertical
	$(9.12 \pm 0.31)\cdot 10^{-5}$	$(1.93 \pm 0.21)\cdot 10^{-5}$	$(7.15 \pm 0.45)\cdot 10^{-5}$

5. Results and conclusions

Due to the relevance of neutrons induced by muons in shallow underground laboratories, a project aiming at the characterization and simulation of such contribution with Monte Carlo code is in developing at the Baradello Underground Laboratory (Como – Italy). Preliminary measurements for the characterization of the muon background in the site have been carried out with different detectors: NaI (Tl), telescope and hybrid telescope. As results we found that in the cave the muon flux is reduced by about two orders of magnitude with respect to outside sea level laboratories. From the results of our measurements and preliminary Monte Carlo simulations, we can foresee that with set – up for the acquisition in coincidence between muons and fast neutrons signals we will obtain some events/day.
At present, we have started some measurements aiming at the characterization of the surviving muon flux from different directions.

References

1. C. Brofferio et Al., *J. of Env. Rad.* 71, 159 (2004).
2. D.E. Groom, N.V. Mokhov, S.I. Striganov, *Atomic and Nuclear Data Tables* 78, 183 (2001).
3. H. Ohsumi et Al, *Nuc. Inst. And Meth. in Phys. Res. A* 482, 832 (2002).
4. M. Tokiwa1 et Al., *Proceedings of ICRC 2001,* 939 (2001)
5. G. Bressi et Al., *Europhys. Lett.,* 11 (3), 287 (1990)
6. D.-M. Mei, A. Hime, *Phys. Rev.* D **73**, 053004 (2006).

ACOUSTIC DETECTORS IN SUBMARINE LARGE SCALE DETECTORS

GIORGIO RICCOBENE[†]

INFN laboratory Nazionali del Sud
Catania, Via S.Sofia 64, 9513, Italy

FOR THE NEMO COLLABORATION

Underwater acoustic detection is a promising experimental tool to investigate the astrophysical neutrino spectrum at $E>10^{16}$ eV. Several collaborations are currently working in the field, despite technological constraints imposed by the hostile deep sea environment. We will present the results obtained by several running experiments (SAUND, ACORNE, BAIKAL, NEMO-OnDE, ...) and we will discuss the main projects of large-scale acoustic stations presently proposed and under construction. Interdisciplinary and technological issues connected to these pioneering works will be highlighted.

1. Present activities on acoustic neutrino detection

The detection of faint astrophysical ($E > 10^{18}$ eV) neutrino fluxes requires apparatuses having masses larger than 10 GTons. A promising experimental approach for the identification of such rare events is the detection of neutrino interactions in water through their acoustic signature [1]. At these energies neutrino interactions in water produce showers, which release instantaneously a macroscopic amount of energy in a small volume of matter. Ionization and sudden heating of water produce a bipolar pressure pulse, that expands perpendicularly to the shower axis. The amount of thermal energy converted into mechanical energy is proportional to the Gruneisen coefficient of water, whose value in deep Mediterranean water is typically 0.12. The maximum wave amplitude, calculated with thermo-acoustic models, scales linearly with the density of energy deposition: for a 10^{20} eV neutrino-induced shower it is of the order of 10 mPa at a distance of 1 km from the shower core [2]. The wave peak frequency is estimated to be in the range of few tens kHz. The acoustic technique could be very fruitful since the sound absorption length in water is, in this frequency range, of the order of km (the higher frequency the stronger is

[†] email: riccobene@lns.infn.it

sound absorption) [3]. Computer simulations of such processes, carried out by several groups, can be broken down into four key stages: the neutrino interaction, the evolution of the shower, the formation of the acoustic signal, and finally, the propagation of the acoustic signal and its detection above background [4,5,6].

On the side of experimental approach, activities range from studies at accelerator facilities, construction of dedicated underwater experiments and test sites, data taking and analysis using existing arrays of hydrophones. The SAUND Collaboration [2] has carried out a pioneering work on acoustic neutrino detection, analyzing data taken using a subset of 6 hydrophones of a military array deployed at 1600 m offshore from the Bahamas, covering an area of 7 km^2. The Collaboration set for the first time a limit on the flux of $> 10^{21}$ eV neutrinos and is now analyzing the data taken with a much larger subset of hydrophones (>60 hydrophones, covering about 1500 km^2). The Baikal collaboration developed two different experimental set-ups to detect acoustic signals in the NT200+ [7] site: a tetragon of hydrophones (1.5 m side) and a linear array of 4 hydrophones both deployed at about 200 m depth. The latter benefits also of a trigger, given by a surface array of 6 scintillators that detect downgoing showers. ANTARES has conducted preliminary studies on underwater noise using an autonomous module (AMADEUS) deployed at 2300 depth in a Site close to Toulon (France), which acquired few seconds of data. At present the collaboration aims at deploying 3 ANTARES strings equipped with 3 acoustic modules each [8]. The Acorne collaboration is working on the analysis of data taken using the Rona Military Array (Scotland). The collaboration is mainly working on developing strategies for signal identification (matched filters, coincidences, ...) through fast DSP analysis [9,10].

2. Acoustics detectors in NEMO Phase 1

The NEMO collaboration is carrying out, since 1998, an R&D program towards the construction of a km^3 underwater Cherenkov neutrino telescope in the Mediterranean Sea [11]. The NEMO detector design foresees the installation of an array of about 6000 photomultipliers (PMTs) displaced over a volume of about 1 km^3 at ~3000 m depth. In order to test the technological solutions developed to build the detector, the Collaboration installed an underwater Test Site 2000 m depth, 25 km offshore Catania (Eastern Sicily) that is used to deploy prototypes of the future km^3 detector (the so called NEMO Phase 1 project). Together with this activity, NEMO is carrying out the first studies for a

deep sea acoustic detector. This R&D has a two main goals: 1) testing underwater acoustic sensors (hydrophones) and associated electronics; 2) measure the background acoustic noise at large depth and its variation as a function of time and identify noise sources. The NEMO Group, in Collaboration with CIBRA Pavia [8], has therefore constructed and operated the experimental station OvDE (Ocean noise Detection Experiment). The detector was deployed on January 2005 at the NEMO Test Site, and it was switched off on November 2006 [12]. The OvDE apparatus was designed to perform long-term and on-line monitoring of the acoustic noise at large depth. The station was equipped with four large bandwidth hydrophones (30 Hz - 40 kHz) located on a tetragon of about 1 m side at about 2.5 m above the seabed. Hydrophones come from a special production of the commercial TC-4042C hydrophone, manufactured by RESON, having a receiving sensitivity of -195±3 dB re 1V/μPa (at 5 kHz) almost linear over a wide range of frequencies: from few tens hertz to about 50 kHz. Analog signals were digitized underwater, at 96 kHz sampling rate and 24 bits resolution, by means of a pair of stereo ADC. Signals were translated into optical and sent to shore through optical fibers. On shore, optical signals were reconverted into electrical and recorded using professional PCI audio boards installed on a PC. Data recording was performed with proprietary software (SeaRecorder, developed by the collaboration) that reads and keeps synchronized the two digital stereo streams coming from the underwater station. The strategy chosen for data recording was to save on a PC Hard Disk, 5 minutes of data every hour, corresponding to a load of 450 MB/hour. The present analysis carried out on the data recorded from June 2005 to December 2005 shows that the average PSD (Power Spectral Density) of acoustic noise is at the level of about 30 dB re $\mu Pa^2/Hz$ (i.e. acoustic noise in condition of sea state 1) in the frequency range between 20 kHz and 40 kHz, with an RMS of about 1 dB (figure 1). However impulsive signals (e.g. pingers, sonars, cetaceans) can rise this level of 20 dB and more. At lower frequencies the average noise and its RMS increase for several orders of magnitude, due to biological, seismic and, mainly, navigation noise. The tetragonal shape of the antenna, allowed also to reconstruct the acoustic source direction (in plane wave approximation): tracking tests indicate a good capability of the detector in identifying the acoustic source bearing and azimuth angles with a resolution of ~2° and ~10° respectively [13].

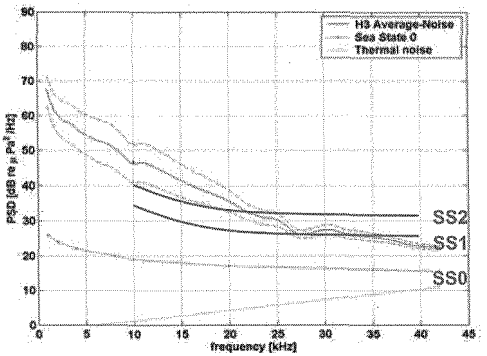

Figure 1. The Average Sound Pressure Density of acoustic noise measured with OvDE form June to December 2005 (after electronics noise subtraction). Between 30 and 40 kHz the sea noise is at the level of 30 dB per uPa2/Hz, close to the bibliographic reference of the acoustic noise in conditions of Sea State 1 [3]. The dip at 10÷12 kHz is attributed to wave reflections on the metallic vessel that hosts the hydrophone and its preamplifier. At 10 kHz a peak due, probably, to an underwater transponder is visible.

In December 2006 the Collaboration installed and successfully operated at the Test Site a small-scale technological demonstrator for the future km^3 neutrino telescope: a junction box and a "mini-tower" of 4 floors (250 m height) hosting 16 PMTs and its readout and data transmission electronics.

3. Acoustics on NEMO Phase 2

Following the successful operations of OvDE and NEMO Phase 1, the Collaboration is now constructing NEMO Phase 2: a full-scale tower made of 16 floors (750 m height) equipped with 64 PMTs, installed at 3500 m depth, in a marine site candidate for the construction of the future Mediterranean neutrino telescope. A submarine electro-optical cable was laid on July 2007 connecting a shore lab, located in the town of Capo Passero (South East Sicily), with the underwater site. A major improvement of Phase 2 will be the installation on each tower floor and at the tower base of two large bandwidth hydrophones dedicated both to the detector acoustic positioning system and to tests of neutrino acoustic detection. The acoustic positioning is a mandatory system in underwater neutrino telescopes, that has to identify the PMTs positions and allowing a better reconstruction of the Cherenkov light front produced by muons. On each floor Acoustic data will be digitised underwater at 192 kHz and 24 bits, and sent to the floor data acquisition and transmission electronic board (Floor Control Module board: FCMb) [15]. The electronics will receive digital data from 4 PMTs, 2 hydrophones and other slow control sensors

(oceanographic instrumentation, temperature sensors, etc), serializes them and drives a DWDM laser to transmit data on-shore, using a synchronous proprietary optical standard protocol. On shore, the data stream is reconverted into electrical using a twin FCM board, thus unpacked and distributed to the detector control and data analysis systems. Thanks to the use of the proprietary auto-synchronous protocol, and a common reference GPS clock signal distributed among all FCM boards, data from all tower floors will be synchronized and tagged with a "reference time" information with a resolution of about 1 ns. Hydrophone data received from each floor, parsed from the main data stream and tagged with the time information, will be sent to dedicated PCs. The PC farm for the acoustic positioning system will be main end user. The processed acoustic data will be also addressed to dedicated PCs in order to monitor the noise spectrum in real-time and to implement first-level trigger in order to recognize acoustic pulse shape and to identify the acoustic source position using TDoA analysis. A correlation between optical signals and acoustic pulses will be also possible.

References

1. G. Askaryan, Atom. Energiya **3**, 153 (1957).
2. J. Vandenbrouke, Astroph. J. **621**, 301 (2005).
3. R. J. Urick, Principles of Underwater Sound, Ed. Peninsula (1982).
4. V. Niess and V. Bertin, Astropart. Phys. **26**, 243 (2006)
5. T. Sloan, Journal of Physics: Conference Series **81**, 012001 (2007).
6. J. Perkin et al., Journal of Physics: Conference Series **81**, 012021 (2007).
7. V. Lyashuk, Journal of Physics: Conference Series **81**, 012001 (2007).
8. K. Graf et al, Journal of Physics Conference Series **81**, 012012 (2007).
9. S. Danaher et al., Journal of Physics: Conference Series **81**, 012011 (2007).
10. L. Thompson et al., Journal of Physics Conference Series **81**, 012023 (2007).
11. E. Migneco et al., Nucl. Inst. And Meth. **A567**, 444 (2006).
12. G. Riccobene et al, Journal of Physics Conference Series **81**, 012013 (2007).
13. CIBRA web page http:\\www.unipv.it\webcib.
14. F. Speziale, Diploma Thesis, University of Catania (2007).
15. F. Ameli et al, The Data Acquisition and Transport Design for NEMO Phase 1, to be published on TNS-IEEE.

SEARCH OF POINT-LIKE SOURCES WITH THE ANTARES NEUTRINO TELESCOPE

FRANCISCO SALESA[†], ON BEHALF OF THE ANTARES COLLABORATION
IFIC (CSIC-UV), Ed. Institutos de Investigación
València, AC 22085, Spain

The ANTARES underwater neutrino telescope is being deployed at 2500 m depth in the Mediterranean Sea at 40 km of the Toulon coast. The detector consists of an array of 900 photomultipliers distributed in 12 lines. The aim of the experiment is the detection of the high-energy (>1 TeV) cosmic neutrinos, detected from the Cherenkov light induced by the charged particle produced near or inside the instrumented volume from their interaction. The main goal of the ANTARES is to detect high energy neutrino point-like sources. It is helped in that by an angular resolution better than 0.3° above 10 TeV that enables the rejection of the dominating isotropic atmospheric neutrino flux. This work reviews the main searching algorithms developed by the collaboration, and their performances.

1. Introduction

Neutrino astronomy is a very recent and promising field of research. Unlike the traditional astronomy, the aim of the neutrino telescopes is the discovery of cosmic high-energy neutrino emitters. The discovery of cosmic neutrinos will help in the explanation of the origin of the cosmic rays and the acceleration mechanisms that take place in the astrophysical objects (AGN, GRB, etc.). Moreover, neutrino astronomy can shed light on some mysteries of astrophysics like dark matter or monopoles. This work is focused on the search for steady cosmic neutrino sources using specific searching algorithms (additional time-dependent analyses like GRB detection, follow a different approach in which time constraints can be applied to the data). The background from neutrinos and muons produced after the reaction of the cosmic rays in the Earth atmosphere is much higher than the expected cosmic neutrino signal. Therefore, it is crucial to have an algorithm able to point out an accumulation of events over this isotropic background.

[†] Corresponding author. Tel.: +34 963543542; fax: +34 963543488; e-mail:sagreus@ific.uv.es.

2. The ANTARES neutrino telescope

The ANTARES [1] detector is placed in front of the coast of Toulon (France) at 2500 m depth and 40 km off the beach. It will be composed by 900 photomultipliers distributed on 12 lines. At the moment 5 out of these 12 lines are deployed and taking data smoothly. Another 4 lines and 1 of instrumentation line are also deployed and they are waiting for an imminent connection. The detector is supposed to be finished in early 2008. At the moment ANTARES is the biggest neutrino telescope in the northern hemisphere, and it has started to collect neutrino candidates.

3. Point-like sources search methods

The search methods developed by the collaboration are of two kinds, binned and unbinned.

3.1. *Binned methods*

The grid and cluster methods are the most frequent approaches of binned [2] searches.
In the grid method the sky is divided in bins with an optimal size for searching or for upper limits. For each bin the expected number of background events can be estimated from Monte Carlo or from data when available. Then a study of the events accumulation due to a source can be done when comparing with the background. In order to claim a point-like source, the significance of the data is checked. This significance is directly related to the probability of the background to produce an excess of events. It is often expressed in terms of standard deviations of the normal probability distribution function. The number of source events necessary to claim a source is computed selecting a threshold criterion for this significance, for instance 3 or 5 standard gaussian deviations (σ). The other method, called the cluster method, follows exactly the same logic as the grid method except that instead of bins (square shape), cones (circular shape) are used. The study is done without any assumption about the energy spectrum and the flux normalization of the source. In addition, for the full sky search no assumption about the source location is done apart from the educated assumption of the power law emission of the source.
Binned methods have been widely used to analyze the data in other experiments as, for instance, in the AMANDA neutrino telescope. These methods constitute a robust approach since they do not have a sound dependence on the expected performances of the detector. Furthermore, these methods have a well known associated statistics (Poisson/Binomial).

3.2. *Unbinned methods*

The so-called unbinned methods take advantage of all the available information such as energy of the events, distribution of the events inside the bin, or any other information found to be relevant to discriminate the signal against the background, contrarily to the binned methods. For this reason, the unbinned methods use to show better performance than the binned ones. In ANTARES two different unbinned methods have been developed:

- Likelihood ratio (LR) method:

In this method [3] a simple pre-clustering algorithm selects a set of candidate clusters to be analyzed. This algorithm selects the events inside a cone of 1.25° around each event of the sample. This cone size is larger than the typical angular resolution, better than 0.3° above 10 TeV, which ensures that all relevant events are selected. The compatibility of the data is then evaluated with two hypothesis, H_0 (only background) and H_1 (background + signal). The unknown free parameters are: the source position (right ascension and declination), the spectral index of the source emitter and the flux normalization. The maximum likelihood ratio (LR) is selected as the statistical test of the method. With the candidate clusters, the LR method tries to find the best value for the test statistic, by maximizing the likelihood evaluated using an estimated density function that depends on the free parameters. The discovery is claimed when the test statistic is higher than a critical value which, as in the binned methods, is associated to a certain confidence level. This method needs the information from the Monte Carlo to build the estimated density functions such as the effective area, the muon energy estimation and the point spread function (PSF) of the detector.

- Expectation-Maximization (EM) method:

This algorithm [4] is a maximization likelihood procedure for finite mixture model problems, i.e., a model in which the probability density function (PDF) is composed by more than one component like in the problem of the search of point-like sources. As in the previous method, a simple pre-clustering algorithm runs previously in order to find a set of candidate clusters that exceed a maximal required number of events. The size selected for the cones is again 1.25°. As usual, the discovery is claimed when the test statistic is higher than a critical value which depends on the confidence level chosen. In this case the test statistic is the BIC (Bayesian Information Criterion). The EM method works in a iterative way divided in two steps, on one hand the expectation (E) step, where the expected value of the likelihood is estimated, and on the other hand, the maximization (M) step where the previous expected value is analytically maximized. In this method it is assumed a 2-dimensional Gaussian function for the PSF of the source signal. Therefore the free parameters are the position of the source (right ascension and declination) taken as the mean value of the 2-D Gaussian, the covariance vector, and the number of source events. Unlike the LR method, this method only uses the information of the neutrino track direction, and no further information about the

detector is used to estimate the density function which makes this method a very reliable technique.

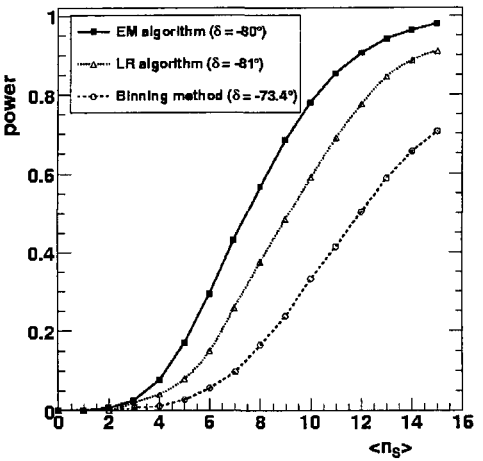

Figure 1. Discover probability at 5σ with respect to the mean number of detected events from the source, after 1 year of data taking. Three search methods are compared. Remark: The Monte Carlo for each case is different. The position of the source is not exactly the same.

To conclude, the unbinned methods and specifically the one based in the EM algorithm, present the best performances in order to detect the point-like sources emitting neutrinos, as can be seen in Figure 1. This figure also shows that the ANTARES detector is sensitive to a signal for a very small number of events.

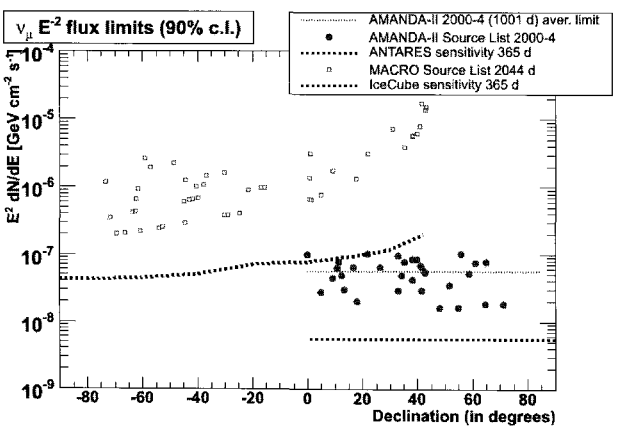

Figure 2. Sensitivity and upper limits for ANTARES and other experiments. For E^{-2} muon neutrino and anti-neutrino fluxes from point-like sources versus declination.

4. Conclusions

The methods explained in this work have shown that a point-like source discovery can be claimed even with a very few events per source. It is also important to notice that if no events are observed, then a restrictive sensitivity will be settled (see Fig. 2). Considering all the methods studied the EM seems to be the one with better performance for the point-like source seek.

Acknowledgments

This work was supported by the Ministerio de Educación y Ciencia under grant BES-2004-5387.

References

1. E. Aslanides et al. (ANTARES collaboration), preprint CPPM-P-1999-02, DAPNIA 99-01, IFIC/99-42, SHEP-HEP/99-06.
2. E. Carmona, Study of the event reconstruction and expected performances for point-like sources of the future ANTARES neutrino telescope, *PhD thesis*, University of Valencia, (2003).
3. A. Heijboer, Track reconstruction and point-like source searches with ANTARES, *PhD thesis, ISBN 90 6464 510 8*, (2004).
4. J.A. Aguilar, *in proceedings of the International Cosmic Ray Conference,* Mérida (2007), arXiv:0710.0252v1

A tritium activity monitor for the KATRIN Experiment

UDO SCHMITT

Institut für Kernphysik, Forschungszentrum Karlsruhe,
Postfach 3640, 76121 Karlsruhe
E-mail: Udo.Schmitt@ik.fzk.de
www.fzk.de

The **KA**rlsruhe **TRI**tium **N**eutrino experiment KATRIN is designed to measure the absolute neutrino mass scale by analyzing the endpoint region of the tritium beta-decay spectrum with a sensitivity of 0.2 eV/c^2 (90 % C.L.). A high-luminous windowless gaseous tritium source with an activity of $1.7 \cdot 10^{11}$ Bq will produce the decay electrons, their energy spectrum will be analyzed by a combination of two electrostatic retarding spectrometers with magnetic adiabatic collimation (MAC-E-filter). Fluctuations of the source column density and inelastic scattering processes within the source affect the energy distribution of the decay electrons. Hence, a precise and continuous monitoring of the source activity is necessary to correct the data taken by the main detector. A prototype of the beam monitor detector, based on a silicon drift diode, has been developed to measure an expected counting rate in the range of $10^6/(\mathrm{s} \cdot \mathrm{mm}^2)$. The detector element shall be moveable across the complete beam in a magnetic field of 0.8 T, resulting in a beam diameter of 20 cm. A precise sensor positioning device has been designed and built to be compatible with the primary beamline vacuum of 10^{-11} mbar.

Keywords: Neutrino mass; tritium beta decay; silicon drift detectors; DEPFET.

1. Introduction

The **KA**rlsruhe **TRI**tium **N**eutrino experiment KATRIN is designed to measure the absolute neutrino mass scale in a direct and model-independent way by analyzing the endpoint region of the tritium β-decay spectrum with a sensitivity of $m_\nu < 0.2\,\mathrm{eV/c^2}$ (90% C.L.). The experimental setup consists of four main components.[1] A high-luminosity windowless gaseous trititum source (WGTS) will provide the β-decay electrons with a maximum energy of 18.6 keV and an activity of $1.7 \cdot 10^{11}$ Bq. Most of these electrons have an energy far below the endpoint E_0 and do not carry any information on the neutrino mass, therefore they will be reflected by a prespectrometer

which operates at a reduced retarding voltage of 18.4 keV. Only the high-energetic electrons will be transmitted into the large main spectrometer, where a precise analysis with an energy resolution of 0.93 eV is performed. The transmitted electrons will be detected by the main detector, a monolithic segmented PIN diode with 145 pixels distributed over a diameter of 90 mm. The spatial resolution of 13 segments along the radius is very important, because the retarding voltage in the analyzing plane of the main spectrometer has a small dip towards its center due to the finite length of the apparatus. Using the spatial resolution of the main detector, one can reconstruct the radial position at which the electron has passed the analyzing plane and what effective retarding potential it has seen.

2. Motivation

Fluctuations of the tritium column density and associated inelastic scattering processes within the source affect the energy distribution of the decay electrons, in particular within the spectral endpoint region close to E_0. Since the main detector will only have a moderate energy resolution, these effects will have influence on the reconstructed energy spectrum and thereby the neutrino mass measurement.

The tritium source activity will be stabilized as accurately as technically feasible by controlling critical parameters like the source tube temperature and the tritium inlet rate down to the 0.1% level. In addition, the tritium purity of 95% will be measured continuously by in-situ Laser Raman spectroscopy. Nevertheless, a redundant monitoring system measuring permanently the actual source intensity is necessary to correct the main detector data. This system will consist of a rear source monitor for the integral β-activity and a forward beam monitor measuring the emission towards the spectrometers.

3. The forward beam monitor

The forward beam monitor will use a semiconductor detector with an active area less than 1 mm^2, since the high intensity of the source leads to a β-electron flux of the order of $10^6/(s \cdot mm^2)$ in an assumed magnetic field of 0.8 T at the designated measuring position. The permanent monitoring of the source intensity will be performed by placing the detector in a position at the very outer rim of the beam, a 'halo' which is not analyzed by the main detector. The inner part of the beam can only be probed during setup and calibration phases, since the detector support structure would partly

shadow the main detector.

The detector element shall be moveable across the full beam cross section using a positioning system which is based on two coaxial linear shifting devices. These linear motions are transformed into a two-dimensional movement by the sensor holder, which is scanning an area of 20 cm in diameter perpendicular to the beam axis. As detector element, we want to use silicon drift detectors (SDDs). These provide a high energy resolution and have successfully been operated at counting rates of several 10^5 counts per second,[2,3] thus they seem to be a suitable device to measure the high-luminous tritium source of KATRIN. Recently developed DEPFET macropixels[4] combine the electrical properties of silicon drift detectors with a pixel size that is close to the desired value around 0.1 mm^2. The active detector area can also be varied by using only a reduced number of drift rings instead of the full detector surface.

Electronic modules to operate the detector prototype have been developed. A preamplifier transforms the DEPFET drain current into a low-impedance voltage that can be fed into the data acquisition system. It has been designed using discrete components, because at a later stage, it is foreseen to build it as an encapsulated hybrid circuit which shall be mounted directly adjacent to the detector chip inside the beamline. Otherwise, the sensitive signals would have to be transmitted over a distance of 1.5 m to an electrical vacuum feedthrough before reaching the preamplifier. Although there is already a first amplification stage within the DEPFET, such a long distance between sensor and preamplifier would probably cause electrical interference problems and increase the noise level

During particle detection, electron-hole pairs are created in the fully depleted bulk and the drift field drives the electrons towards the potential minimum at the position of the internal FET gate, where they are accumulated. The potential of this internal gate, in combination with the biasing external gate, changes the drain current of the DEPFET.

After a certain number of events, the stored electrons have to be removed by applying a clear pulse sequence to the clear gate of the detector. The clear mechanism can either be triggered periodically and the frequency can be set according to the event rate. It can also be triggered dynamically by the DC component of the preamplifier output signal which is proportional to the 'fill level' of the internal gate. The clear pulse generator is then triggered by comparing the preamplifier output with a pre-defined threshold. This operation mode allows to adjust the maximum amount of charge collected in the detector and thus to reduce possible nonlinear behavior. Furthermore,

the clear pulse frequency is adapted automatically to the event rate. A bias circuit supplies the detector with the necessary voltages for the drift rings, the bulk depletion and the integrated readout FET.

The DEPFET macropixel prototype is currently being tested with an electron gun that produces monoenergetic electrons with an energy of up to 30 keV. Parameters like noise level and energy resolution are determined as a function of the detector temperature, the electron energy and the counting rate.

References

1. KATRIN Design Report 2004, FZKA scientific report 7090 (2005)
2. P. Lechner *et al.*, Silicon drift detectors for high count rate X-ray spectroscopy at room temperature, Nuclear Instruments and Methods in Physics Research A 458 (2001) 281-287
3. R. Alberti *et al.*, High-rate X-ray spectroscopy using a Silicon Drift Detector and a charge preamlifier, Nuclear Instruments and Methods in Physics Research A 568 (2006) 106-111
4. C. Zhang *et al.*, Development of DEPFET Macropixel detectors, Nuclear Instruments and Methods in Physics Research A 568 (2006) 207-216

OPTICAL MODULE FOR DEEP-SEA NEUTRINO TELESCOPES

M. TAIUTI*

Dipartimento di Fisica dell'Università di Genova
and
Istituto Nazionale di Fisica Nucleare, Sezione di Genova,
I-16146 Genova, Italy
**E-mail: mauro.taiuti@ge.infn.it*
www.ge.infn.it

In this paper I will discuss the main properties of the optical modules developed for neutrino telescopes and I will present the recent research activitiy to realize some prototype with improved performances. Different solutions have been investigated and few of them are very promising.

Keywords: Neutrino Telescope, Photodetector

1. Introduction

High-energy neutrinos are expected to be very promising probes to investigate the most energetic phenomena in the Universe. Neutrinos may easily escape even from thick sources, are hardly absorbed during their propagation and are not deflected in magnetic fields. They are therefore the ideal candidate particles to point back to the sources of high-energy cosmic rays.

However the expected low fluxes, estimated mainly from the measured cosmic ray fluxes and from theoretical model for several high energy sources (GRB, AGN, GZK, ...)[1] require a detector with a sensitive volume in the km^3-scale. Following the pioneering activity of the DUMAND collaboration,[2] a first generation of small scale detector instrumentation with photomultipliers (PMT) have been realized (AMANDA[3,4] in the South Pole and BAIKAL[5,6] in the Baikal lake) demonstrating the viability of the detection in deep water or ice of the Cherenkov light emitted by neutrino induced muons.

Following the success of AMANDA the larger size detector (of the order of 1 km^3) ICECUBE[7,8] is presently under construction at the South Pole.

A similar detector located in the northen emisphere would provide the full sky coverage, including the investigation of the Galactic Centre that has raised interest after the recent impressive results from HESS on the detection of TeV gamma rays.[9] The Mediterranean Sea offers optimal conditions to locate the telescope and three collaborations are currently operating: the ANTARES[10,11] Collaboration is building an underwater detector demonstrator of about 0.1 km^2 at about 2400 m depth, 40 km offshore Toulon; the NESTOR[12] Collaboration aims at the deployment of the first NESTOR tower with 10^4 m^2 effective area for $E_\mu \geq 10$ TeV and the NEMO[13,14] Collaboration deployed in 2006 a prototype of the NEMO tower and is presently planning the deployment at the Capo Passero site of a complete tower by the end of next year. The three collaborations are presently participating in the KM3NeT Design Study.[15]

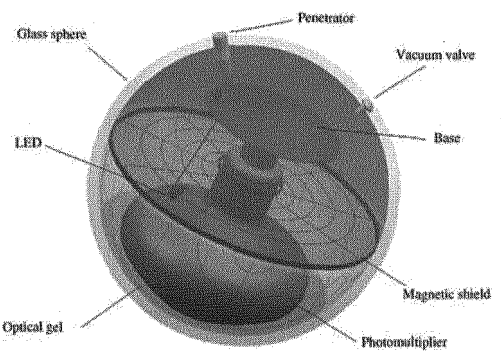

Fig. 1. The ANTARES Optical Module.[16]

2. The Optical Module

All the detectors mentioned above are based on the same detection principle inherited from their ancestor DUMAND:[17] the Cherenkov light emitted by the charged particle produced by the interaction of the neutrino with the Earth are detected by large area photomultipliers with low noise, high quantum efficiency and therefore good single photon detection, hosted in glass spheres together with the read-out electronics, the high-voltage power supply and the calibration system. As an example in Fig. 1 the ANTARES optical module[16] is reported. The comparison between the original DUMAND design and the solution adopted by the individual collaboration

shows that most of the effort has been dedicated to solving the problem of deploying a relative large number of optical modules. Almost each Collaboration has chosen a peculiar configuration for the detector:

- AMANDA and ICECUBE deploy in the polar ice strings where individual optical modules[18] are located at fixed distance;

the remaining detectors are deployed in water where the presence of optical noise generated by biological activitity and ^{40}K decay (in salt water) is reduced with local coincidences among nearby optical modules

- BAIKAL deploys in water strings where couples of optical modules[19] are located at fixed distance;
- ANTARES deploys strings where triplets of optical modules[16] are located at fixed distance;
- NEMO deploys towers where couples of optical modules are located at the end of horizontal bars 12 m long;
- NESTOR deploys more complex structures hosting twelve optical modules[20] in each floor.

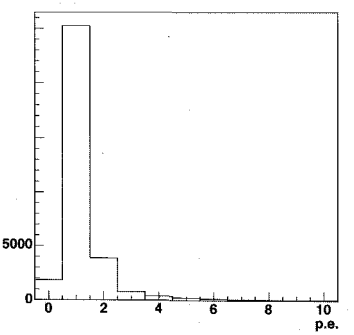

Fig. 2. Distribution of the number of detected photon by a single optical module equipped with a 10" photomultiplier

The efficient collection of the Cherenkov light emitted in water or ice is a main requirement. The result of the simulation of the response of a km^3 neutrino telescope in water is reported in Fig. 2. The plot shows that the optical modules must provide high efficiency in detecting very faint signal of the order of few photons. A further requirement for those telescopes working

in salt water is the suppression of the background originated from the decay of ^{40}K; simulations have shown that the major criterion for distinguishing signal from background is the identification of a coincidence of two or more photons in a single optical module or in nearby optical modules.

In Table 1 the photomultipliers adopted in each detector are reported. From initial relatively large area photomultiplier the experiments that are currently in the deployment phase oriented the choice on middle-sized photomultipliers: ICECUBE and ANTARES chose the 10" Hamamatsu single photon counter R7081 in its different versions; the same photomultiplier is being used in the R&D activity of NEMO. BAIKAL is testing optical modules with the 13" R8055 (Hamamatsu) and the 12" XP1807 (Photonis) and the same 13" R8055 (Hamamatsu) has been studied by the NESTOR Collaboration[21] as possible replacement of the previous R2018-03. For sake of completeness the table includes the hybrid photomultiplier QUASAR-370 adopted by the BAIKAL Collaboration.

Table 1. Comparison of adopted photomultiplier.

Model	size (")	dynodes	peak/valley ratio	TTS FWHM (ns)
R2018	15			
R2018-03	15	13	1.2	7
R5912-2	8	14	> 2	< 3
R7081-02	10	10	> 2	3
R7081-20	10	14	2.7	2.6
R8055	13	10	2.6	4.8
XP1807	12	11	2.3	5.0
QUASAR-370		-	2.1	3.8

3. The New Optical Module

The european KM3NeT aims at the definition of the Technical Design Report of the km^3 detector to be deployed in the Mediterranean Sea. Several new ideas have been developed in order to improve the performances of the optical modules and three of them are now the subject of this presentation.

3.1. *The Hybrid Solution*

This solution under development at CERN,[22] could be considered as the most recent attempt to apply the ideas that originated the Philips

"SMART" XP2600[23] and the later QUASAR-370. The X-HPD consists of a practically spherical glass envelope on which a semitransparent photocathode is evaporated and a cubic or spherical anode for the detection of the photoelectrons in the centre of the sphere. The central location of the anode brings about three main advantages: (1) the anode can detect photoelectrons in a large solid angle range ($\approx 3\pi$), (2) all photoelectrons have practically the same pathlength (the transit time spread is well below 1 ns), and (3) the photoelectron collection efficiency reaches values close to 100%. A prototype tube with 208mm diameter and an anode in form of a metallic cube has been fabricated. In the final version the anode will be a scintillator cube with plated faces and a small photodetector to readout the bottom. Crystals like YAP:Ce and LSO:Ce achieve light yields of 1520 photons per keV deposited energy, have short decay times (≈25 ns) and are compatible with the required bakeout cycles of a photocathode process.

The development of a sealed X-HPD with crystal anode and PMT readout is under way in close collaboration with the company Photonis.

3.2. *The Multi-PMT Solution*

The main idea is to segment the photocathode area in order to count the number of photons. This can be done by replacing the single 10" PMT by 12 3" PMTs.[24] The new design has an equal photocathode area compared to a 10" PMT but in this case a two photon event will, in more than 90 % of the cases, be registered as a coincidence between two separate PMTs. In Fig. 3 the response of the candidate Photonis XP53X2 is reported.

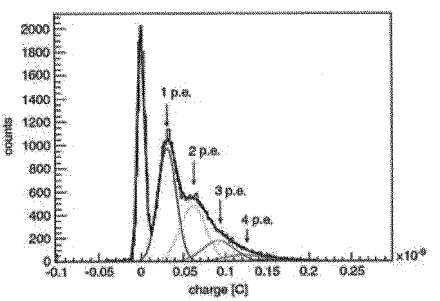

Fig. 3. Pulseheight distributions for the Photonis XP53X2 PMT.[24]

The measured peak/valley ratio is 2.4 comparable to large area single

photon counters. The design looks promising but it requires the complete re-definition of the read-out system. The conceptual design has been thoroughly discussed and the realization of a prototype is in progress.

3.3. *The Direction-Sensitive Optical Module*

The previous solutions do not take into account the information of the direction of the detected Cherenkov light. This information is not necessary at high energy when the trajectory length is comparable to the dimensions of the telescopes, but it become crucial when the reconstruction is based on the signal from few active optical modules that is for low energy neutrinos ($\approx 1TeV$) or tracks close to the edge of the detector.

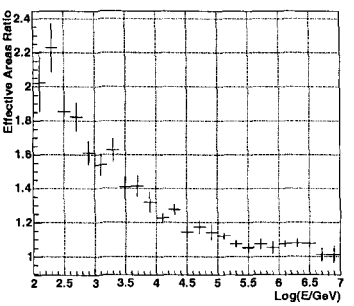

Fig. 4. The ratio of the effective areas of the NEMO-KM3 detector equipped with direction-sensitive optical modules and the standard NEMO-KM3 detector.

In Fig. 4 is reported the comparison of the detector efficiency in the NEMO-KM3 configuration with and without the direction-sensitive optical modules. It results that at neutrino energies lower than $10^4 GeV$ the use of the direction-sensitive optical module could improve the efficiency up to a factor 2. The prototype is based on a multi-anodic 10" photomultiplier coupled to a set of mirrors realized with plexiglas foils covered with an high reflective 3M plastic material with better reflectivity in the blue region than silver or aluminum. In Fig. 5 it is summarized how the device would work: all photons arriving from the same direction are collected on a single sector of the multi-anodic photomultiplier.[25]

We chose to subdivide the solid angle (close to 2π) covered by each optical module in four quadrants. This is a minimal configuration that allows to introduce the information of direction of the detected light without major

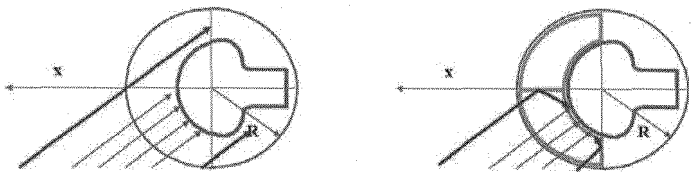

Fig. 5. Left: behaviour of the classical optical module: the Cherenkov light illuminates the whole photocathode surface. Right: the mirrors concentrates the light on a single sector of the photocathode surface.

modifications of the optical module lay-out and of the electronic read-out. The sensitive area of the photomultiplier has been kept equal to that of the 10" photomultiplier adopted in the optimized design of KM3. Therefore the new direction sensitive optical modules will work as four individual photomultipliers oriented in different directions with a total detection efficiency and total angular acceptance equal to that of a single 10" photomultiplier. A cross section of the prototype is shown in Fig. 6.

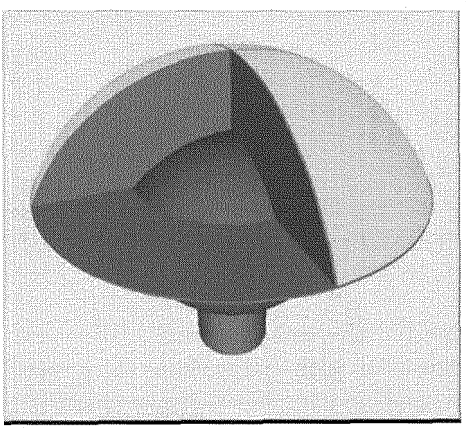

Fig. 6. The conceptual design of the direction-sensitive optical module based on a 4-anodic photomultiplier coupled to a light-guide system. The main components are the photocathode surface (red), the mirror system (gray) and the optical gel (yellow).

Hamamatsu manufactured two prototypes of the multi-anodic photomultiplier that are presently under test in Catania. The preliminary results look very promising. In Fig. 7 the response to a point-like single-photon beam is reported. The read-out of a single anode shows a rather good correspondence between the photocathode sector and the anode as well as

a rather good single-photon discriminitation. The measured TTS shows a FWHM of 4.5 ns. The photocathode uniformity is better than the standard 10" R7081 corresponding to a gain of 20% in collecting light efficiency.

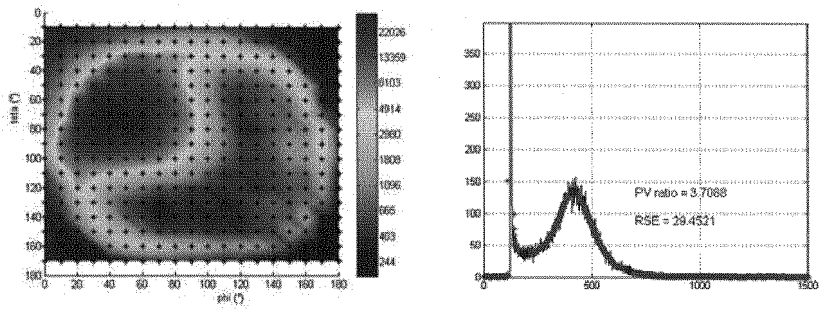

Fig. 7. Left: Single anod response to point-like illumination of the photocathode of the Hamamatsu multianodic 10" prototype in one-photoelectron regime. Right: typical single photoelectron response.

4. Conclusions

The realization of optical modules to be employed in neutrino telescope use a well established technology developed since the pioneering activity of DUMAND and most of the efforts have been devoted in the past to the search of the optimal design of the supporting structures. Recently, the European Consortium KM3NeT aiming at the definition of the Conceptual Design Report of a neutrino telescope to be realized in the Mediterranean Sea, is investigating new solutions that could better fit in the marine environment. Three different R&D activities, with the support of two of the leading industries in the field Hamamatsu and Photonis, aim at improving the amount of collected light and detecting the direction. Prototypes are expected to be developed and tested by the end of this year.

References

1. F. Halzen and D. Hooper, *Rept. Prog. Phys.* **65**, 1025 (2002).
2. `http://www.phys.hawaii.edu/dmnd/dumand.html`.
3. `http://amanda.uci.edu`.
4. E. Andres *et al.*, *Astropart. Phys.* **13**, 1 (2000).
5. `http://www.inr.ac.ru/INR/Baikal.html`.
6. I. A. Belolaptikov *et al.*, *Astropart. Phys.* **7**, 263 (1997).

7. http://icecube.wisc.edu.
8. J. Ahrens *et al.*, *Nucl. Phys. Proc. Suppl.* **118**, 388 (2003).
9. F. Aharonian *et al.*, *Nature* **439**, 695 (2006).
10. http://antares.in2p3.fr.
11. J. A. Aguilar *et al.*, *Nucl. Instrum. Meth.* **A555**, 132 (2005).
12. http://http://www.nestor.org.gr.
13. http://nemoweb.lns.infn.it.
14. E. Migneco *et al.*, *Nucl. Instrum. Meth.* **A567**, 444 (2006).
15. http://www.km3net.org.
16. P. Amram *et al.*, *Nucl. Instrum. Meth.* **A484**, 369 (2002).
17. S. Matsuno *et al.*, *Nucl. Instr. Meth.* **A276**, p. 359 (1989).
18. K. Hanson and O. Tarasova, *Nucl. Instrum. Meth.* **A567**, 214 (2006).
19. R. I. Bagduev *et al.*, *Nucl. Instrum. Meth.* **A420**, 138 (1999).
20. E. G. Anassontzis *et al.*, *Nucl. Instrum. Meth.* **A479**, 439 (2002).
21. S. Tsagli *et al.*, *Nucl. Instrum. Meth.* **A567**, 511 (2006).
22. A. Braem, C. Joram, J. Seguinot, P. Lavoute and C. Moussant, *Nucl. Instrum. Meth.* **A570**, 467 (2007).
23. P. C. Bosetti, An optical sensor for dumand ii.
24. P. Kooijman, *Nucl. Instrum. Meth.* **A567**, 508 (2006).
25. M. Taiuti, *Nucl. Instrum. Meth.* **A525**, 137 (2004).

Radio detection of Cosmic Rays at the Pierre Auger Observatory

C. Timmermans[1], for the Pierre Auger Collaboration[2]

[1] *Nikhef and Institute of Mathematics, Astronomy and Particle Physics, Radboud University, Nijmegen, the Netherlands*
**E-mail: c.timmermans@hef.ru.nl*

[2] *Av. San Martín Norte 304 (5613) Malargüe Prov. de Mendoza, Argentina*

When a cosmic ray enters the Earth's atmosphere, an avalanche of (charged) particles is created, which is called an air shower. Charged particles passing through the Earth's magnetic field emit electromagnetic radiation that can be detected by ground-based dipole antennas. The southern site of the Pierre Auger Observatory, located in Argentina, provides an excellent environment for testing various prototype radio detectors for cosmic-ray studies. The first results of prototype radio detectors will be discussed. The events obtained will be used to characterize the radio signal of air showers. The results of this initial phase provide an important milestone on the path to an engineering array of several tens square kilometers.

Keywords: Cosmic Rays; Air Shower; Radio Detection; Pierre Auger Observatory.

1. Introduction

The air shower created from interactions in the atmosphere initiated by a cosmic-ray particle emits electromagnetic radiation. Already since the late 1960s, synchrotron radiation in the Earth's magnetic field is known to be the dominant component of this EM-radiation [1]. As this radiation is emitted coherently, the amount of radiation depends roughly linearly on the number of particles in the air shower, and thus on the primary energy. This radiation can be measured at ground level using simple antennas, as was demonstrated first by Jelley in 1965 [2]. These pioneering efforts continued in the early 1970s, however, the state of the electronics did not permit proper measurements. Furthermore, shower to shower fluctuations were identified as a possible problem, whereas a good simulation program was

not available. With modern electronics, the measurement of EM-radiation emitted by the shower can be done in a sophisticated way. The revival of radio detection of air showers is evident from a number of recent papers, e.g. by the Lopes [3] and Codalema [4] collaborations, which use particle detectors to identify air showers and to trigger the antenna readout. We continue this development at the Pierre Auger Observatory, with the goal to understand this mechanism at the highest energies, and, afterwards to use this technique to obtain complementary information on the showers, as obtained by only the surface detector array.

2. Setup

At the southern site of the Pierre Auger Observatory [5], near Malargüe in Argentina several antenna-based air-shower detectors have been set up. The Pierre Auger collaboration operates the worlds leading detector system for the observation of the highest energy cosmic rays. Therefore, this observatory is particularly suited for an R&D program to develop radio detection beyond energies of 1 EeV [6]. As the aim is to understand radio detection at the highest energies and to develop a stand-alone radio detector several approaches are taken.

Wireless setups in which different antenna types are used without any external triggers are aimed toward understanding the problems of running a radio detector as an independent and stand-alone cosmic-ray measuring device. An example of such a setup is shown in the left part of Fig. 1.

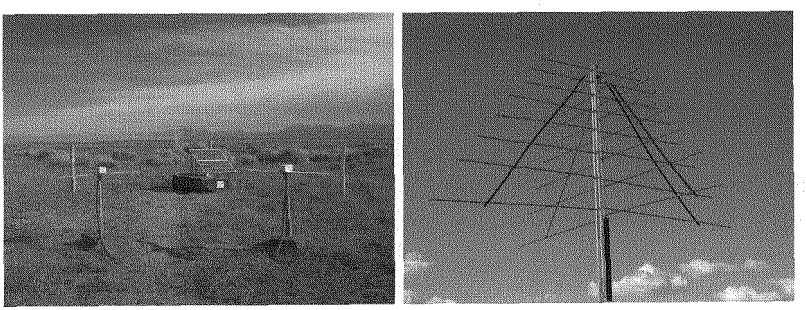

Fig. 1. Left: A standalone antenna setup near the center of the Pierre Auger Observatory. Right: LPDA antenna used to obtain the results presented here.

A setup in which three antennas are connected by signal cables to a central place 100 m away, where the data are filtered, amplified, digitized,

and stored onto a central PC is shown in the right part of Fig. 1. The trigger is created from the coincidence between signals originating from two scintillator detectors of 0.5 m^2 each. Offline, the data are correlated with those from the Auger Surface Detector (SD) using GPS time-stamps. The results presented below originate from this setup, using well known Log Periodic Dipole Antennas (LPDAs) and Low Noise Amplifiers (LNAs) [7] as shown in the right part of Fig. 1.

3. The Sensitivity of the setup

Fig. 2 shows the average noise level in the 50 to 55 MHz band as function of the local sidereal time for one of the LPDA's used in this setup. A clear structure is seen for the noise in both the North-South and the East-West arms. The time of maximum noise emission corresponds to the passing of the Galactic center overhead. It is clear that the setup is sensitive to the

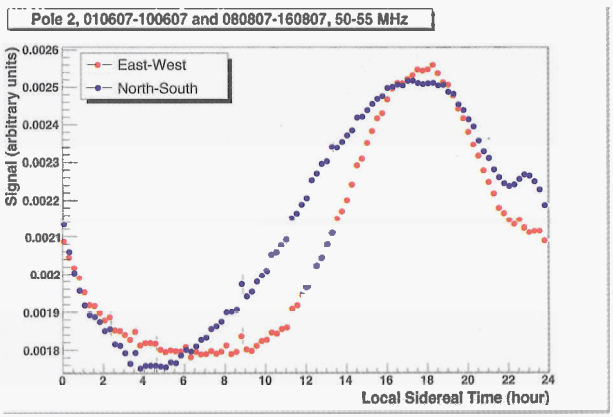

Fig. 2. Average signal in the 50-55 MHz band as function of local sidereal time.

Galactic background noise. Furthermore, the amplitude of the noise variation is a substantial fraction of the total signal. Therefore, the background noise level created by the readout electronics and external sources, is comparable to the Galactic background levels.

4. Measurement of high-energy cosmic rays

Signals originating from air showers produced by high-energy cosmic rays have been seen by the 3 antennas in the cabled setup. Here we will discuss

one of the most energetic events in more detail, which was measured to have an energy of 2.1 EeV, and a zenith angle of 58 degrees. The azimuthal angle was -69 degrees from the east; i.e. the ray was coming almost from the south. The distance of the shower to our antenna setup is approximately 300 meters. The envelope of the antenna data of this event in the 50-70 MHz

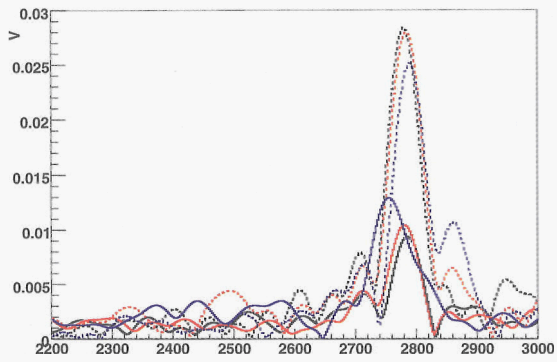

Fig. 3. The envelopes of the filtered data. The data of antenna 1 (black), 2 (red) and 3 (blue) are seen from the North-South arm (full lines) and the East-West arms (dashed lines).

band can be seen in Fig. 3, which clearly shows an enhancement of the measured signal in both polarization directions of all three antennas. From detailed Monte Carlo simulations, based on the geosynchrotron model [8] one expects that the signal strength in the North-South arm is only 50 % of that in the East-West arm, which is confirmed by our measurement. At this moment, we do not have an absolute calibration of the complete electronics chain, thus we cannot compare the absolute pulse heights.

We have used the antenna data to extract angular information of this event, independently of the SD information. As we only have 3 antennas, the assumption was made that the radio signal arrives in a plane perpendicular to the shower direction. The data of the individual traces is then shifted in time to accommodate different arrival times in the antennas. Afterwards, the resulting traces are multiplied to a single result of which the maximum is used as a discriminating parameter. The result is seen in Fig. 4, which shows good agreement with the measurement from the Auger SD. In general, the angular resolution obtained from these radio measurements is about 5

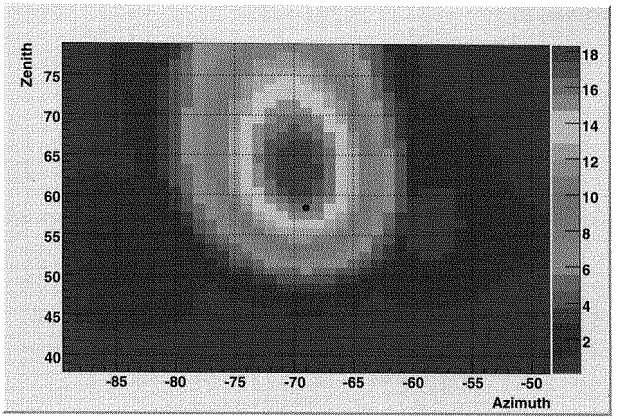

Fig. 4. Directional information with respect to the reconstructed direction (shown as the dot in the center) from the Auger surface detectors. The color code reflects the combined signal strength for all antennas in the specified direction. The coding is shown to the right of the plot in arbitrary units.

degrees, which can easily be improved by increasing the antenna baseline (currently only 100 m) and increasing the total number of antennas.

5. Conclusion and outlook

Five events which show clear signals in 3 antennas have been analyzed. One of which was shown above. More events have a clear signal in at least a single antenna. The measurements also provide detailed information on background conditions. This information will be used in the development of a stand-alone radio detector of cosmic rays.

References

1. H. R. Allan, Progress in Elementary Particle and Cosmic Ray Physics Vol. 10, 171-302 (1971) and references therein.
2. J. V. Jelley *et al.*, Nature 205, 327-328 (1965)
3. H. Falcke *et al.*, Nature 435, 313-316 (2005)
4. D. Ardouin *et al.*, Nucl. Instr. Meth. A 555, 148-163 (2005)
5. The Pierre Auger Collaboration, Nucl. Instr. and Meth. A, 50-95 (2004)
6. A. M. van den Berg *et al.*, Proceedings of the 30th Int. Cosmic Ray Conference (2007)
7. H. Gemmeke *et al.*, Intern. Journal of Mod. Physics A 21, 242-246, (2006)
   T. Asch *et al.*, Proc. VCI 2007, to be published
8. T. Huege, R. Ulrich, R. Engel, Astroparticle Physics 27, 392-405 (2007)

The Monitor online system of the OPERA muon magnetic spectrometer

U. Ugolino*, M. Ambrosio, R. Acquafredda, V. Masone

Istituto Nazionale di Fisica Nucleare, Section of Naples,
Via Cintia 2 - 80123 Naples, Italy
**E-mail: ugolino@na.infn.it*

The OPERA muon magnetic spectrometer has been designed for muon detection, tracking and timing. The 44 bakelite Resistive Chambers (RPC) planes, imbibed inside the magnet iron slabs, must provide the tracking of the muon curved in the magnetic field to ease the momentum and charge measurement provided by the HPT. Furthermore, it provides the momentum for muons stopping in the iron. RPC signals will be also used as start of drift tube acquisition thanks to the very good time resolution of RPC detectors. Due to the required performances the tracking detector must be fully efficient and stable. In this conditions an online monitor is mandatory to continuously control stability of run conditions. We report the main characteristics and performances of the monitor system for the OPERA spectrometer and capabilities of the software developed for settings and data acquisition.

1. Introduction

The OPERA (Oscillation Project with Emulsion tRacking Apparatus) experiment [1] has been proposed for an appearance search of $\nu_\mu \leftrightarrow \nu_\tau$ oscillations. The detector intercepts the CNGS (Cern Neutrino beam to Gran Sasso) [2] ν_μ beam searching for decay of τ particles whose presence will be an unambiguous signature of the $\nu_\mu \rightarrow \nu_\tau$ neutrino oscillations in the atmospheric sector. The event signature of the interaction is the so called *kink*, the angle between the tracks of the τ particle and the charged decay daughter. The kink must be identified analyzing the emulsion layers of the brick in which it has been registered. For the muonic decay mode the presence of the penetrating (often isolated) muon track allows an easier event vertex finding: the brick can be easily identified by reconstructing the muon trajectory and the ν_τ flavour can be determined by the sign of the charge of the muon as measured by its curvature in the magnetic muon spectrometer. It is a large dipolar magnet made of two walls of iron plates

in which are inserted 44 bakelite Resistive Plate Chambers (RPC), 8 m in height and 8.75 m in width, for muon detection. It is mandatory a full efficiency of the detector and a great apparatus stability in time. The most sensitive information concerning the RPC working conditions is its single counting rate that strongly depends from temperature, humidity, gas flow and mixture, power supply value and, most important, fabrication defects. In the Gran Sasso Underground Laboratory the cosmic ray rate is very low, about 80 muon/m^2/hour, so the RPC single counting rate is mainly due to the detector noise. By monitoring the noise trough the single counting rate an efficient monitor of detector working stability can be easily achieved. The developed system addresses exactly this request.

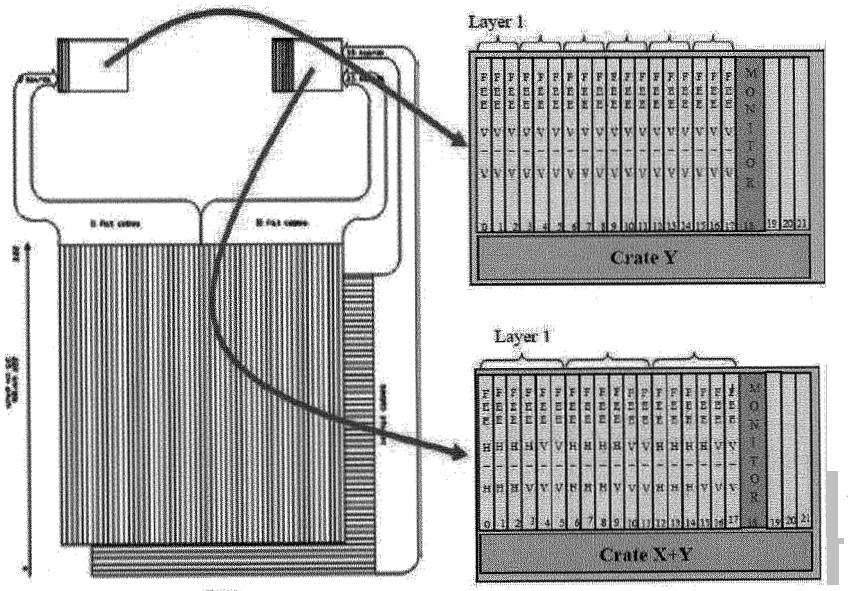

Fig. 1. Redout - FEB crates

2. The monitor system

The monitor system has been integrated inside the readout electronics grouped in crates on the top of the apparatus. Front End Boards (FEB) reading the RPC signals have been positioned in VME-like crates each housing 18 boards. Because each FEB reads two groups of 32 strips gen-

erating two separate Fast ORs, an individual 40 channel monitor board inserted in the 19th slot allows the readout of all FEBs housed in the crate (Fig. 1). The monitor system counts a total of 30 monitor boards, interfaced to the acquisition PC, on which the management software of the system is installed, by 9 serial-ethernet converters, net-configurable. A monitor program, developed in LabVIEW environment, allows the managing of the system constituted of 30 monitor boards for a total of 1200 channels of acquisition.

The user interface is a window from which it is possible to recall the interface of each Monitor board and the monitoring of the alarm and acquisition states of all boards. Recalling the interface of a single board (Fig. 2), it is possible the visualization of the graphical plots of the signal frequencies for the 40 channels and the management of the board settings.

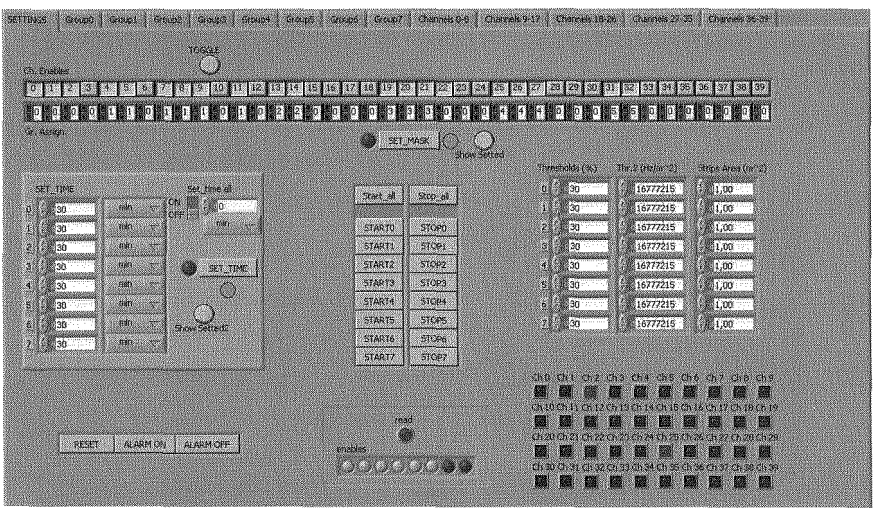

Fig. 2. Front Panel for each Monitor Board

The 40 input channels for each board can be grouped on common characteristics, such as the RPC belonging plane or the area covered from the strips. To each group it is possible to associate a different integration time in order to assure a greater statistic uniformity, because strips covering different plane surface portions will give different counting rates. It is possible grouping channels until a maximum of eight groups per board and associating a graph to each of them (Fig. 3). In this way the counting rate can

be normalized to the area covered by the strips and to the integration time and given directly in Hz/m^2.

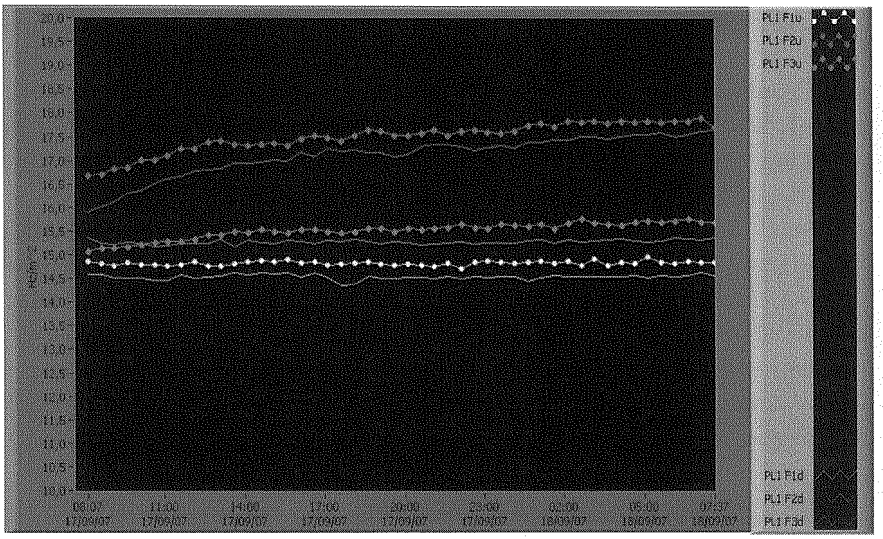

Fig. 3. One day rate acquisition

Moreover it is possible to visualize the frequency time course for every channel, with the respective alarm thresholds. The alarm thresholds are centered around to the average value of the frequency measured for each channel and may be fixed in percentage of rate by the operator. But it is also possible to set up, like alarm threshold, a frequency limit fixed by the user. For every Monitor and every group it is possible to give an independent start or stop to the acquisition, but it is however possible to give a common start or stop to all groups for each Monitor, or for every Monitor. The frequency diagrams, normalized in surface, give date and hour of acquisition on the abscissa.

All the settings are saved on an external file and loaded at the start run. The results of an acquisition are saved on a spreadsheet file created automatically from the program with a name indicating date and hour of the beginning of the acquisition (gg/mm/aaaa hh.mm), in order to create an history and easily go back to one determined acquisition. A last property of the Monitor system consists on the availability of a remote access and handling of the system for a continuous monitoring of the apparatus.

3. Conclusions

The described monitor developed for the OPERA experiment is now running successfully. It has been demonstrated that this kind of monitoring is particularly powerful in the underground environment being the information directly correlated to the running conditions. In particular the RPC single counting rate can be strictly related to the temperature inside the magnet, whose increase can be very dangerous for the RPC detector. The advantage of an on line monitor consists on the ability of sending immediately the alarm signal to people in shift for emergency intervention.

The developed system could monitor whatever apparatus producing NIM signals. Stated this capability and the usefulness of the system, the OPERA collaboration has decided to extend the control of the Monitor also to the VETO and XPC planes, originally excluded from this control.

The network configuration easly allows the control of 1200 input channels by a unique ethernet gate. The property of remote accessing allows the control and management of the system from everywhere trough internet.

Acknowledgments

We thank Dr. Giulietto Felici and electronic technicians of the Frascati National Laboratory for their continuous assistance and for the Timing Boards installed for the test. We also thank Dr. Roberta Cicalese and the electronic service (SER) of INFN Naples Unit for the participation to the electronic realization. Finally we are very grateful to Dr. Riccardo De Asmundis for his suggestions in the LabView program development and to Dr. Pasquale Migliozzi for his suggestions in the drawing up of this contribution.

References

1. R. Acquafredda et al., *First events from the CNGS neutrino beam detected in the OPERA experiment*, 2006 New J. Phys. 8 303

   The OPERA Collaboration: *Experiment Proposal: An appearance experiment to search for $\nu_\mu \leftrightarrow \nu_\tau$ oscillations in the CNGS beam*, CERN/SPSC 2000-028, SPSC/P318, LNGS P25/2000, July 10, 2000.

2. G. Acquistapace et al., CERN 98-02, INFN/AE-98/05, 19 May 1998;
   R. Bailey et al., CERN-SL/99-034 (DI); INFN/AE-99/05.

RESULTS FROM THE NEMO 3 EXPERIMENT

L. VÁLA*

IEAP, Czech Technical University in Prague,
Horská 3a/22, Prague, CZ - 128 00, Czech Republic
E-mail: ladislav.vala@utef.cvut.cz

The aim of the NEMO 3 experiment is the search for neutrinoless double beta decay and precise measurement of two-neutrino double beta decay of several isotopes. The experiment has been taking data since 2003. Since no evidence for neutrinoless double beta decay of ^{100}Mo and ^{82}Se has been found, a 90% C.L. lower limit on the half-life of this process and corresponding upper limit on the effective Majorana neutrino mass are derived. The data are also interpreted in terms of alternative models, such as weak right-handed currents or Majoron emission. In addition, NEMO 3 has performed precision measurements of the two-neutrino double beta decay for seven different isotopes. The most recent experimental results of NEMO 3 are presented in this paper.

Keywords: neutrino; double beta decay; NEMO; ^{100}Mo; ^{82}Se

1. Introduction

The neutrino oscillation experiments demonstrated in the last decade convincing evidence for neutrino oscillations proving the finite neutrino masses and mixing. However, these experiments are only sensitive to the difference in the square of the neutrino masses, $\Delta m^2_{ij} = |m^2_i - m^2_j|$, therefore they do not provide information on the absolute scale of the neutrino masses and are not sensitive to the nature of neutrinos Nevertheless, the detection and study of neutrinoless double beta decay is the only way able to answer the following fundamental questions: (i) neutrino nature (Majorana or Dirac particle?), (ii) absolute neutrino mass scale, (iii) type of neutrino mass hierarchy (degenerated, inverted, or normal?), (iv) CP violation in the lepton sector.

Double beta decay ($\beta\beta$) is a transition from nucleus (A, Z) to $(A, Z + 2)$ and it can occur in different channels: (a) two-neutrino double beta

*on behalf of the NEMO Collaboration

decay ($2\nu\beta\beta$) with emission of two e^- and two $\bar{\nu_e}$, (b) neutrinoless double beta decay ($0\nu\beta\beta$) with emission of two e^- and (c) neutrinoless double beta decay with Majoron emission ($0\nu\chi\beta\beta$) with two e^- and Majoron χ (massless Goldstone boson) in the final state. The mode (a) is a process of second order allowed in the Standard Model (SM) which has been observed for several nuclei. Nevertheless, processes (b) and (c) are violating lepton number conservation by two units and involve new physics beyond the SM.

The NEMO 3 experiment (NEMO = Neutrino Ettore Majorana Observatory) is devoted to the search for $0\nu\beta\beta$ decay and to the accurate measurement of $2\nu\beta\beta$ decay. For this goal, the experiment combines two detection techniques: calorimetry and tracking. Such approach allows us at the same time unambiguous identification of e^-, e^+, γ, and α-particles provided by a wire tracking chamber and energy and time measurements of particles with a calorimeter.

2. NEMO 3 detector

The NEMO 3 detector [1] is installed and currently running in the Fréjus Underground Laboratory (4800 m w.e.) in France. The experimental set-up is cylindrical in design, is divided into twenty equal sectors and with γ and neutron shielding it has about 6 m in diameter and 4 m in height.

The tracking wire chamber is made of 6180 open octagonal drift cells operating in Geiger mode (Geiger cells). It is filled with a gas mixture of 95% He, 4% ethyl-alcohol and 1% Ar. The Geiger cells provide a three-dimensional measurement of the charged particle tracks by recording the drift time and the two plasma propagation times.

The calorimeter, which surrounds the wire chamber, is composed of 1940 plastic scintillators coupled by light-guides to very low-radioactivity PMTs. The energy resolution σ_E/E of the calorimeter ranges from 6.0% to 7.5% for 1 MeV electrons, while the time resolution is 250 ps.

Seventeen sectors of NEMO 3 accommodate almost 10 kg of the following, highly enriched (95% - 99%) $\beta\beta$ decay isotopes: ^{100}Mo (6914 g), ^{82}Se (932 g), ^{116}Cd (405 g), ^{130}Te (454 g), ^{150}Nd (34 g), ^{96}Zr (9 g), and ^{48}Ca (7 g). In addition, three sectors are also used for external background measurement and are equipped with pure Cu and natural Te. All these isotopes are produced in the form of thin foils and are placed in the central vertical plane of each sector.

For the e^-/e^+ recognition, the detector is surrounded by a solenoidal coil which generates a vertical magnetic field of 25 Gauss. Moreover, NEMO 3 is covered by two types of shielding against external γ-rays and

neutrons. Finally, the whole experimental set-up is closed inside a "tent", which is supplied with radon-free air from a radon trapping facility. Radon is trapped and then decays inside a tank filled with 1 ton of charcoal cooled down to $-50°C$. This facility decreases the radon level of the air from the laboratory (15 – 20 Bq/m^3) by a factor of $\sim$ 1000. The radon trapping facility has been operating in the laboratory since October 2004.

3. Measurement of $\beta\beta$ decay and backgrounds

A candidate for a $\beta\beta$ decay is a two-electron event which is defined with the following criteria: two tracks coming from the same vertex in the source foils, the curvature of the tracks corresponds to a negative charge, each track has to be associated with a fired scintillator, and the time-of-flight has to correspond to the case of two electrons emitted at the same time from the same vertex. In addition a threshold of 200 keV is applied on energy of each electron. Finally, it is also required that there is no delayed Geiger cell hit close to the event vertex in order to suppress background from ^{214}Bi decay inside the tracking detector.

The energy window of interest for the $0\nu\beta\beta$ decay for both ^{100}Mo and ^{82}Se is set to $(2.8 - 3.2)$ MeV and the complete study of background contribution in this window has been performed. The level of each background component has been directly measured from data using different analysis channels. The dominant background during the first running period from February 2003 to September 2004, Phase I, was due to radon diffusion into the tracking wire chamber. Nevertheless, during Phase II (since November 2004 up to now), the radon level inside NEMO 3 has been reduced by a factor of ten thanks to the radon trapping facility. Remaining low radon activity inside NEMO 3 is due to degasing of detector components.

4. NEMO 3 results

4.1. $2\nu\beta\beta$ decay

The $2\nu\beta\beta$ decay of ^{100}Mo and ^{82}Se is measured with high acuracy with NEMO 3. The obtained half-lives for Phase I data (389 d) are $T_{1/2} = [7.11\pm0.02(stat)\pm0.54(syst)]\times10^{18}$ y for ^{100}Mo and $T_{1/2} = [9.6\pm0.3(stat)\pm 1.0(syst)] \times 10^{19}$ y for ^{82}Se [2]. The half-lives for the other five $\beta\beta$ isotopes have been also derived from data and are summarised in Tab. 1. Measurements of this process are important for nuclear theory as they allows us to reduce the uncertainties on the nuclear matrix elements (NME).

Table 1. Measured half-lives of $2\nu\beta\beta$ decay and S/B ratio.

Isotope and transition		$T_{1/2}$	S/B
^{100}Mo	(g.s. $\rightarrow$ g.s.)	$[7.11 \pm 0.02(stat) \pm 0.54(syst)] \times 10^{18}$ y	40
	(g.s. $\rightarrow 0_1^+$)	$[5.7^{+1.3}_{-0.9}(stat) \pm 0.8(syst)] \times 10^{20}$ y	3.0
	(g.s. $\rightarrow 2_1^+$)	$> 1.1 \times 10^{21}$ y at 90% C.L.	
^{82}Se	(g.s. $\rightarrow$ g.s.)	$[9.6 \pm 0.3(stat) \pm 1.0(syst)] \times 10^{19}$ y	4.0
^{116}Cd	(g.s. $\rightarrow$ g.s.)	$[2.8 \pm 0.1(stat) \pm 0.3(syst)] \times 10^{19}$ y	7.6
^{150}Nd	(g.s. $\rightarrow$ g.s.)	$[9.7 \pm 0.7(stat) \pm 1.0(syst)] \times 10^{18}$ y	2.4
^{96}Zr	(g.s. $\rightarrow$ g.s.)	$[2.0 \pm 0.3(stat) \pm 0.2(syst)] \times 10^{19}$ y	0.9
^{48}Ca	(g.s. $\rightarrow$ g.s.)	$[3.9 \pm 0.7(stat) \pm 0.6(syst)] \times 10^{19}$ y	15.7
^{130}Te	(g.s. $\rightarrow$ g.s.)	$[7.6 \pm 1.5(stat) \pm 0.8(syst)] \times 10^{20}$ y	0.25

4.2. $0\nu\beta\beta$ decay

In the case of ^{100}Mo, there are 14 events observed in the energy window of interest while 13.4 events were expected from backgrounds for combined Phase I and II data (693 d). The situation is similar for ^{82}Se as 7 events are observed and 6.2 expected for the same period. Thus, resulting half-life limits at 90% C.L. are $T_{1/2} > 5.8 \times 10^{23}$ y for ^{100}Mo and $T_{1/2} > 2.1 \times 10^{23}$ y for ^{82}Se. If using the NME from Refs. [3–5], the following limits on the effective neutrino mass are derived: $\langle m_\nu \rangle < (0.6 - 0.9)$ eV for ^{100}Mo and $\langle m_\nu \rangle < (1.2 - 2.5)$ eV for ^{82}Se. We determined also limits for alternative models assuming weak right-handed currents (V+A) and the $0\nu\chi\beta\beta$ decay channel [6]. All these results are given in Tab. 2.

Table 2. Limits at 90% C.L. for different $0\nu\beta\beta$ decay modes for ^{100}Mo and ^{82}Se.

Decay mode	^{100}Mo	^{82}Se
$0\nu\beta\beta$ (V − A) (g.s. $\rightarrow$ g.s)	$T_{1/2} > 5.8 \times 10^{23}$ y	$T_{1/2} > 2.1 \times 10^{23}$ y
	$\langle m_\nu \rangle < (0.6 - 0.9)$ eV	$\langle m_\nu \rangle < (1.2 - 2.5)$ eV
	$\langle m_\nu \rangle < (2.1 - 2.7)$ eV	$\langle m_\nu \rangle < (2.6 - 3.2)$ eV
$0\nu\beta\beta$ (V − A) (g.s. $\rightarrow 0_1^+$)	$T_{1/2} > 8.9 \times 10^{22}$ y	
$0\nu\beta\beta$ (V − A) (g.s. $\rightarrow 2_1^+$)	$T_{1/2} > 1.6 \times 10^{23}$ y	
$0\nu\beta\beta$ (V + A) (g.s. $\rightarrow$ g.s)	$T_{1/2} > 3.2 \times 10^{23}$ y	$T_{1/2} > 1.2 \times 10^{23}$ y
$0\nu\chi\beta\beta$ ($n = 1$)	$T_{1/2} > 2.7 \times 10^{22}$ y	$T_{1/2} > 1.5 \times 10^{22}$ y
$0\nu\chi\beta\beta$ ($n = 2$)	$T_{1/2} > 1.7 \times 10^{22}$ y	$T_{1/2} > 6.0 \times 10^{21}$ y
$0\nu\chi\beta\beta$ ($n = 3$)	$T_{1/2} > 1.0 \times 10^{22}$ y	$T_{1/2} > 3.1 \times 10^{21}$ y
$0\nu\chi\beta\beta$ ($n = 7$)	$T_{1/2} > 7.0 \times 10^{19}$ y	$T_{1/2} > 5.0 \times 10^{20}$ y

However, these results date back to 2006 because the NEMO Collaboration decided to perform blind analysis with mock data. We plan to open the box and update the results by the summer of 2008 and once again after

the end of the experiment by 2010.

4.3. *Double beta decay of ^{100}Mo to excited states*

The $\beta\beta$ decay of ^{100}Mo to excited 0_1^+ and 2_1^+ states of ^{100}Ru has been also studied with the NEMO 3 detector. The obtained half-life for the $2\nu\beta\beta$ decay to the 0_1^+ state is $T_{1/2} = [5.7^{+1.3}_{-0.9}(stat) \pm 0.8(syst)] \times 10^{20}$ y [7]. This value is in a good agreement with previous measurements [8,9]. In addition, the $T_{1/2}$ limits have been determined for the $0\nu\beta\beta$ and $2\nu\beta\beta$ decay to the 2_1^+ state and for the $0\nu\beta\beta$ decay to the 0_1^+ state (see Tabs. 1 and 2).

5. Conclusions

The NEMO 3 detector has been routinely taking data since February 2003. The $2\nu\beta\beta$ decays of ^{100}Mo and ^{82}Se have been measured with very high statistics and better precision than in previous experiments. The $2\nu\beta\beta$ half-lives have been obtained also for ^{116}Cd, ^{130}Te, ^{150}Nd, ^{96}Zr, and ^{48}Ca.

No evidence for $0\nu\beta\beta$ decay has been found in combined data for Phase I and II corresponding to 693 days. The $T_{1/2}$ limits at 90% C.L. for different modes of this decay are summarised in Tab. 2. We obtained currently the best limits for the $0\nu\chi\beta\beta$ decay of ^{100}Mo and ^{82}Se

At present time, the analysis of the Phase II data without radon is in progress and improved $2\nu\beta\beta$ and $0\nu\beta\beta$ results will be published in 2008. The expected half-life limits for the $0\nu\beta\beta$ decay by the end of the experiment in 2010 are $T_{1/2} > 2 \times 10^{24}$ y for ^{100}Mo and $> 8 \times 10^{23}$ y for ^{82}Se.

Acknowledgment

A portion of this work has been supported by the Grant Agency of the Czech Republic (grant No. 202/05/P293).

References

1. R. Arnold *et al.* (NEMO Collaboration), Nucl. Instr. and Meth. in Phys. Res. A**536** (2005) 79.
2. R. Arnold *et al.* (NEMO Collaboration), Phys. Rev. Lett. **95** (2005) 182302.
3. M. Kortelainen and J. Suhonen, Phys. Rev. C **75** (2007) 051303(R).
4. M. Kortelainen and J. Suhonen, Phys. Rev. C **76** (2007) 024315.
5. V.A. Rodin *et al.*, Nucl. Phys. A **793** (2007) 213.
6. R. Arnold *et al.* (NEMO Collaboration), Nucl. Phys. A**765** (2006) 483.
7. R. Arnold *et al.* (NEMO Collaboration), Nucl. Phys. A **781** (2007) 209.
8. A.S. Barabash *et al.*, Phys. Lett. B**345** (1995) 408.
9. L. De Braeckeleer *et al.*, Phys. Rev. Lett. **86** (2001) 3510.

Search for Solar Axions with the CAST-Experiment

J. Vogel[j,*], E. Arik[s], S. Aune[b], D. Autiero[a,†], K. Barth[a], A. Belov[k], B. Beltrán[f,‡], S. Borghi[a], G. Bourlis[17], F. S. Boydag[s], H. Bräuninger[e], J. Carmona[f], S. Cebrián[f], S. A. Cetin[s], J. I. Collar[g], T. Dafni[b], M. Davenport[a], L. Di Lella[a,§], O. B. Dogan[s], C. Eleftheriadis[h], N. Elias[a], G. Fanourakis[i], E. Ferrer-Ribas[b], H. Fischer[j], J. Franz[j], J. Galán[f], T. Geralis[i], I. Giomataris[b], S. Gninenko[k], H. Gómez[f], M. Hasinoff[l], F. H. Heinsius[j], I. Hikmet[s], D. H. H. Hoffmann[c,d], I. G. Irastorza[b,f], J. Jacoby[m], K. Jakovčić[o], D. Kang[j], K. Königsmann[j], R. Kotthaus[n], M. Krčmar[o], K. Kousouris[i], M. Kuster[c,e], B. Lakić[o], C. Lasseur[a], A. Liolios[h], A. Ljubičić[o], G. Lutz[n], G. Luzón[f], D. Miller[g], A. Morales[f,¶], J. Morales[f], T. Niinikoski[a], A. Nordt[c,e], A. Ortiz[f], T. Papaevangelou[a], M. Pivovaroff[r], A. Placci[a], G. Raffelt[n], H. Riege[a], A. Rodríguez[f], J. Ruz[f], I. Savvidis[h], Y. Semertzidis[p], P. Serpico[n], R. Soufli[r], L. Stewart[a], S. Tzamarias[q], K. van Bibber[r], J. Villar[f], L. Walckiers[a], K. Zioutas[p]

[a] *European Organization for Nuclear Research (CERN), Genève, Switzerland*

[b] *DAPNIA, Centre d'Études Nucléaires de Saclay (CEA-Saclay), Gif-sur-Yvette, France*

[c] *Technische Universität Darmstadt, IKP, Darmstadt, Germany*

[d] *Gesellschaft für Schwerionenforschung, GSI-Darmstadt, Plasmaphysik, Darmstadt, Germany*

[e] *Max-Planck-Institut für extraterrestrische Physik, Garching, Germany*

[f] *Instituto de Física Nuclear y Altas Energías, Universidad de Zaragoza, Zaragoza, Spain*

*Attending speaker, Julia.Vogel@cern.ch

†Present address: Institute de Physique Nucléaire, Lyon, France

‡Present address: Department of Physics, Queen's University, Kingston, Ontario

§Present address: Scuola Normale Superiore, Pisa, Italy

¶deceased

[g] *Enrico Fermi Institute and KICP, University of Chicago, Chicago, IL, USA*

[h] *Aristotle University of Thessaloniki, Thessaloniki, Greece*

[i] *National Center for Scientific Research "Demokritos", Athens, Greece*

[j] *Albert-Ludwigs-Universität Freiburg, Freiburg, Germany*

[k] *Institute for Nuclear Research (INR), Russian Academy of Sciences, Moscow, Russia*

[l] *Department of Physics and Astronomy, University of British Columbia, Department of Physics, Vancouver, Canada*

[m] *Johann Wolfgang Goethe-Universität, Institut für Angewandte Physik, Frankfurt am Main, Germany*

[n] *Max-Planck-Institut für Physik (Werner-Heisenberg-Institut), Munich, Germany*

[o] *Rudjer Bošković Institute, Zagreb, Croatia*

[p] *Physics Department, University of Patras, Patras, Greece*

[q] *Hellenic Open University, Patras, Greece*

[r] *Lawrence Livermore National Laboratory, Livermore, CA, USA*

[s] *Dogus University, Istambul, Turkey*

Solar axions can be produced in the Sun via the so-called Primakoff effect. The CERN Axion Solar Telescope (CAST) uses an LHC prototype magnet of about 9 T to reconvert these axions into photons.

The magnet is able to follow the Sun for about 3 hours per day. Three different X-Ray detectors are mounted on its ends to detect photons from axion-to-photon conversion: a Time Projection Chamber (TPC), a MICROMEGAS (MICROMEsh GAseous Structure) and a Charge Coupled Device (CCD). For the CCD an X-ray focusing device is used to improve the signal-to-background ratio significantly.

With the completion of CAST's first phase, the current limits on the coupling constant $g_{a\gamma}$ for axion masses up to 0.02 eV have been improved. In its second phase, CAST extends the axion mass range by filling the magnet with a buffer gas. Masses up to about 0.4 eV have already been covered and thus the experiment is entering the regions favored by axion models. This paper will present the status of CAST's second phase.

1. Introduction

Quantum Chromodynamics (QCD) is expected to violate the so-called Charge-Parity-Symmetry (CP-Symmetry). For physical laws, C-Symmetry is a symmetry under charge-conjugation transformation, while P-Symmetry refers to parity transformations. A combination of both was initially expected to be conserved, but it was found to be violated in the Kaon decay. Thus the electroweak theory violates CP-Symmetry, and also QCD was expected to do so, but up to now no experiment was able to observe the non-conservation of the CP-Symmetry in QCD. A solution to this so-called CP-Problem was formulated by R. Peccei and H. Quinn.[1] They introduced an additional symmetry, the Peccei-Quinn-Symmetry. When it is spontaneously broken, the resulting particle is an axion, which obtained its name by F. Wilczek[2] and S. Weinberg.[3]

If they exist, axions could have been created in the very early universe. But they could as well originate from cores of stars like our Sun nowadays. In order to prove or rule out the existence of the axion, several constraints from astrophysics and cosmology have been applied. Like this, the mass range, in which axions are still likely to exist, could be narrowed down to a window reaching from μeV up to some meV. In several experiments, it has been attempted to detect axions in and close to the remaining mass regions. Different methods have been applied in the quest for the postulated particle. Most of them, however, make use of the so-called Primakoff[4] effect, which allows for a conversion of axions into photons in the presence of a strong electromagnetic field.[5] One possible kind of experiment employing this effect are the helioscopes,[6] waiting for axions produced in the closest axion source available: the core of the Sun.

2. The Experiment

The CERN Axion Solar Telescope (CAST) of the European Organization for Nuclear Research CERN (Conseil Européen pour la Recherche Nucléaire) in Geneva, Switzerland, is one of these helioscopes. It utilizes a prototype of the Large Hadron Collider (LHC) magnets with a length of 9.26 m and a magnetic field of up to 9 T. Since it is mounted on a movable platform, the CAST magnet is able to follow the Sun for about 90 minutes during sunrise and sunset each day. In this experiment three different X-ray detectors are used. A Time Projection Chamber[7] (TPC) is waiting for the appearance of photons from axion-to-photon conversion arriving during sunset, while in the morning a MICROMEGAS[8] (MICROMEsh GAseous

Structure) detector and a Charge Coupled Device[9] (CCD) are used to prove the appearance of an axion by detecting an X-ray photon. Between the magnet and the CCD, an X-ray focussing device is installed. It is able to improve the signal-to-background ratio by a factor of about 150.

3. Status and Results

With the completion of CAST's first phase and no observable signal above background, the existing limits on the coupling constant $g_{a\gamma}$ have already been improved by a factor of 5 using only the data obtained in 2003.[10] Further improvements by a factor of 1.3 compared to the 2003 results could be achieved by including in the analysis the data taken in 2004. As the final result of CAST's first phase (vacuum in the magnet bores) an upper limit of $g_{a\gamma} < 8.8 \times 10^{-11}$ GeV^{-1} at 95 % CL for $m_a \leq 0.02$ eV was obtained.[11] For the given range of axion masses this limit supersedes the best astrophysical limit (Horizontal Branch star limit).

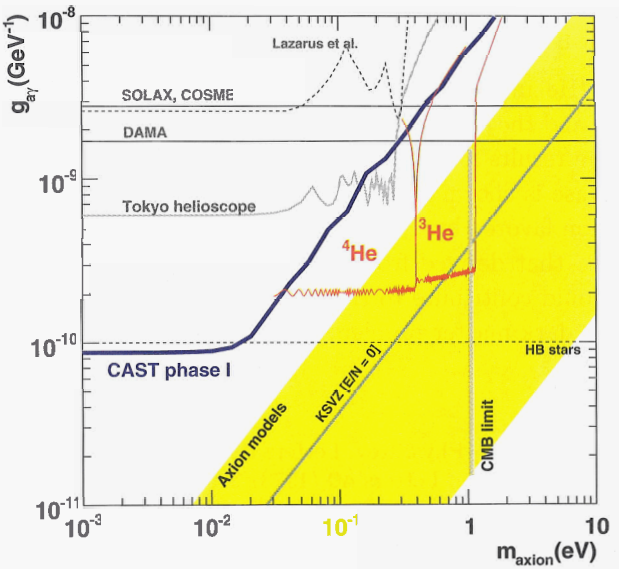

Fig. 1. CAST exclusion plot of the axion to photon coupling constant (at 95 % C.L.).The result for CAST's first phase[10] (thick blue line) is more stringent than other laboratory constraints of previous axion experiments. Theoretical models are represented by the shaded band. In addition, the prospects for the second phase of the CAST experiment (thin red line) are shown for both, ^{4}He and ^{3}He.

In order to extend the observable mass range, CAST has already been upgraded and since late 2005 data have been taken with the improved setup. The magnet bores have been filled with Helium (CAST Phase 2) in order to restore coherence between the photon and the axion field and thus allow for axion-to-photon conversion. By changing the pressure of the gas in appropriate steps, it is possible to scan axion masses up to 1 eV. In order to make this possible, novel so-called cold windows have been developed for the CAST experiment to assure that the inserted gas is kept in its designated region. Furthermore a complete gas system had to be designed for this purpose. Thus it was possible to apply daily changes in the pressure of about 0.082 mbar and access a total range from 0 to 13.256 mbar.

Due to the low temperature of the superconducting magnet, which is around 1.8 K, it is necessary to change to ^{3}He to go to higher pressures since ^{4}He is no longer gaseous under the given conditions. Additionally, the gas system used for the ^{4}He has to be upgraded since the data taking procedures will be changed. More pressure steps will be necessary and thus there will be more than one pressure step measured per day.

4. Conclusion

So far with ^{4}He in the magnet bores, axion masses up to 0.4 eV have been covered and the obtained data are being analyzed. The exclusion plot containing the results for CAST's first phase and the expected results for its second phase is shown in Fig.1. CAST is the first experiment entering the mass region favored by QCD axion models on a sensitivity level for $g_{a\gamma}$ comparable to that derived from astrophysical arguments. Axions in this mass range could contribute to the dark matter of the universe and could thus solve the dark matter problem in cosmology.

References

1. R. Peccei, H. Quinn, Phys. Rev. Letters **38** (1977) 1440.
2. F. Wilczek, Phys. Rev. Letters **40** (1978) 279.
3. S. Weinberg, Phys. Rev. Letters **40** (1978) 223.
4. H. Primakoff, Phys. Rev. Letters **81** (1951) 899.
5. P. Sikivie, Phys. Rev. Letters **51** (1983) 1415 [Erratum ibid. **52** (1984) 695].
6. K. van Bibber *et al.*, Phys. Rev. Letters **59** (1987) 759.
7. D. Autiero *et al.*, New Journal of Physics **9** (2007) 171.
8. P. Abbon *et al.*, New Journal of Physics **9** (2007) 170.
9. M. Kuster *et al.*, New Journal of Physics **9** (2007) 169.
10. K. Zioutas *et al.* [CAST Collaboration], Phys. Rev. Letters **94** (2005) 121301.
11. K. Zioutas *et al.* [CAST Collaboration], JCAP **04** (2007) 010.

DATA ACQUISITION SYSTEM FOR THE TUNKA-133 ARRAY

N.M. BUDNEV[2], O.B. CHVALAEV[2], O.A. GRESS[2], N.N. KALMYKOV[1], V.A. KOZHIN[1], E.E. KOROSTELEVA[1], L.A. KUZMICHEV[1], B.K. LUBSANDORZHIEV[3], R.R. MIRGAZOV[2], G. NAVARRA[5], M.I. PANASYUK[1], L.V. PANKOV[2], V.V. PROSIN[1], V.S. PTUSKIN[4], Y.A. SEMENEY[2], A.V. SKURIKHIN[1], B.A. SHAIBONOV(JUNIOR)[3], CH. SPIERING[6], R. WISCHNEWSKI[6], I.V. YASHIN[1], A.V. ZABLOTSKY[1], A.V.ZAGORODNIKOV[2]

1 Scobeltsyn Institute of Nuclear Physics of Moscow State University, Moscow, Russia
2 Institute of Applied Physics of Irkutsk State University, Irkutsk, Russia
3 Institute for Nuclear Research of Russian Academy of Science, Moscow, Russia
4 Institute of Terrestrial Magnetism, Ionosphere and Radiowave Propagation of Russian Academy of Science (IZMIRAN), Troitsk, Moscow Region, Russia
5 Dipartimento di Fisica Generale Universita di Torino and INFN, Torino, Italy
6 Deutsches Elektronen Synchrotron (DESY), Zeuthen, Germany

The new EAS Cherenkov array Tunka-133, with about 1 km^2 sensitive area, is being installed in the Tunka Valley. The investigated energy range is $10^{15} - 10^{18}$ eV. It will consist of 133 optical detectors based on EMI-9350 PMT. Optical detectors are grouped into 19 clusters with 7 detectors each. The detectors are connected to the cluster box with RG-58 cables. Every PMT signal is digitized in the cluster box with 200 MHz FADC. The cluster boxes are connected to the data acquisition center with a 1 Gb/s optical link. A detailed description of the data acquisition system (DAQ) system is presented.

1. Introduction

The elaborate study of the energy range $10^{16} - 10^{18}$ eV is of crucial importance for understanding of the origin and propagation of cosmic rays in the Galaxy. The maximum energy of cosmic rays accelerated in SN remnants seems to be in this energy range [1]. As pointed out in [2], in this energy range the transition from Galactic to extragalactic cosmic rays may occur. The new EAS Cherenkov array under construction in the Tunka Valley (50 km from Lake Baikal), with 1 km^2 area, was named Tunka-133 [3, 4]. It will allow studying cosmic rays by covering with a single method uniformly the energy range from 10^{15} to 10^{18} eV. Tunka Valley is known for its good weather conditions (especially during winter). Various EAS Cherenkov arrays – from Tunka-4 [5] to Tunka-25 [6,7] – have been operated at this place.

2. The Tunka-133 Array

The Tunka-133 array will consist of 133 optical detectors on the basis of PMT EMI 9350 (diameter of photocathode 20 cm). The 133 detectors are grouped in 19 clusters, each composed of seven detectors – six hexagonally arranged detectors and one in the center. The distance between the detectors is 85 m, similar to Tunka-25. Due to this fact the accuracy of EAS parameter reconstruction will be the same as for Tunka-25, which however had only an area of 0.1 km^2. The accuracy of the core location is ~6m, that of energy determination ~15%. The accuracy of the EAS maximum depth X_{max} determination (from the Cherenkov light lateral distribution steepness and pulse duration) is ~25 g/cm^2. The energy threshold of the array is close to 10^{15} eV. During one year operation (400 hours) Tunka-133 will record ~$5 \cdot 10^5$ events with energies above $3 \cdot 10^{15}$ eV, ~300 events with energies higher than 10^{17} eV and a handful events with energies higher than 10^{18} eV.

In addition to the Cherenkov detectors, 5-7 Auger-like water tanks (S = 10 m^2, depth = 90 cm) will be constructed for common operation with the Cherenkov array.

3. DAQ system

PMT's signals from the optical detectors arrive at the cluster DAQ where they are digitized by custom-made 4-channel-FADC VME modules with 200 MHz sampling rate, and connected to variable threshold comparators. A trigger system is implemented in each cluster; the cluster trigger is formed by a coincidence of pulses above threshold within a time window of 0.5 μs from at least three optical detectors. The time of the local trigger is measured by a cluster timer closely synchronized with the central DAQ.

Each cluster is connected to the central DAQ through a multi-wire cable with four copper wires (for power supply) and four optical fibers. Optical transceivers operating at 1 GHz are responsible for data transmission and synchronization of the cluster's clock. In the acquisition center optical links are connected to DAQ boards which are strictly synchronized among themselves. A DAQ board provides an interface between the 4 optical lines and 100 Mbit/s ethernet within the cluster DAQ and is connected to the master PC via switch.

3.1. *Optical detector*

An optical detector (fig. 1) consists of a metallic cylinder with 50 cm diameter, containing the PMT. The container has a plexiglass window on the top, heated

against frost. The angular aperture is defined by geometric shadowing of the PMT. The efficiency is close to 100% up to 30° and reduces to 50% at zenith angles > 45°. The detector is equipped with a remotely controlled lid protecting the PMT from sunlight and precipitation. Apart from the PMT with its high voltage supply and preamplifiers, the detector box contains a light emitting diode (LED) for both amplitude and time calibration and a controller. The controller is connected with the cluster electronics via twisted pair (RS-485). To provide the necessary dynamic range of 10^4, two analog signals, one from the anode and another one from the dynode, are read out. They are amplified and then transmitted to the central electronics hut of each cluster. The ratio of amplitudes of these signals is about 30. It is not planned to heat the inner volume of the optical detector boxes, therefore all the detector electronics is designed to operate over a wide temperature range (down to –40°C).

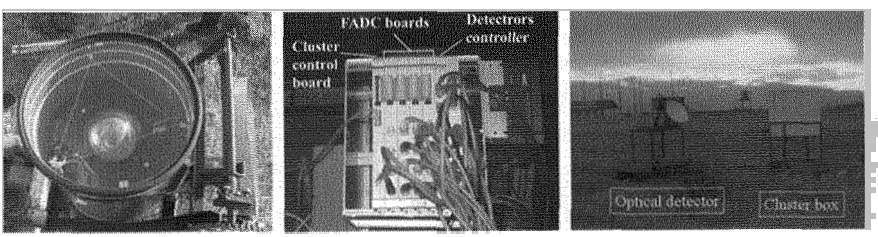

Fig. 1. Optical detector and cluster box photos (from left to right: top view of the optical detector, the cluster DAQ , the cluster center).

3.2. *The cluster DAQ system*

The cluster DAQ (fig. 1) consists of 4 FADC boards, a detector control board and a cluster control board. The detector control board provides extra service by controlling the detector and synchronously starting the calibrating LEDs. Optical transceivers, trigger module, time synchronization module and local timer are included inside the cluster control board, designed on the basis of a FPGA (XLINX Spartan XC3S200).

Every FADC board consists of four simultaneously digitizing ADCs which are logically divided into two channels (one per the anode and dynode signals from each optical detector), see fig. 2. Every FADC has 12 bit resolution and samples at 200 MHz. The digitized signal from each ADC is transferred to the FPGA which handles the data. A double-buffered FIFO memory for 1024 counts was realized inside the FPGA: while one buffer is waiting for readout, the second one is connected to the ADC outputs, thus minimizing the readout

dead-time. Receiving a trigger signal from the master device, 512 counts before and 512 after the trigger are readout. Only one signal (anode) from each channel is connected to the adjustable digital comparator, which works out the request to the trigger module. The anode signal is also connected to an amplitude analyzer, accumulating monitor histograms for every channel.

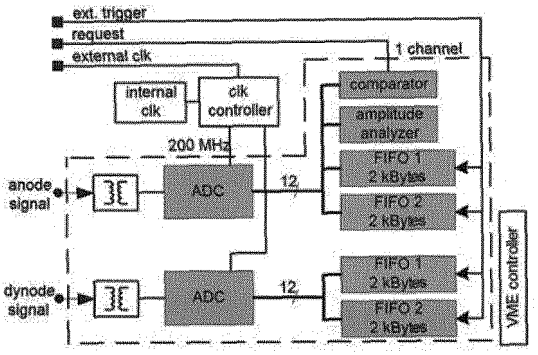

Fig. 2. Internal structure of FADC board (shown only one channel; the second one is identical).

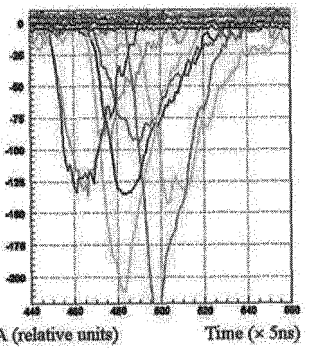

Fig. 3. Example of an event in a cluster (energy $(5\pm2)\cdot10^{17}$ eV)

3.3. *Time synchronization system*

Optical detectors (anode and dynode signals) are linked to the cluster DAQ with RG58 cables which have identical length, so they will not be further considered here. But the clusters are connected to the central DAQ via optical cables with unknown lengths. Every cluster has a local timer, used for the cluster event time; therefore offsets between cluster timers must be calibrated.

The time synchronization is implemented in two stages (fig. 4). Cable length and other propagation delays are measured in the first stage. The center sends to the cluster a special packet, returned by the cluster after decoding. The total time delay, divided by two, corresponds to the propagation delay. On the second stage, the center sends a timer reset command simultaneously to all cluster DAQs. The knowledge of the propagation delay allows to calculate differences between timers for every cluster. The accuracy of this time synchronization is about 10 ns. To avoid any mis-timing, the synchronization is being checked once per second by hardware.

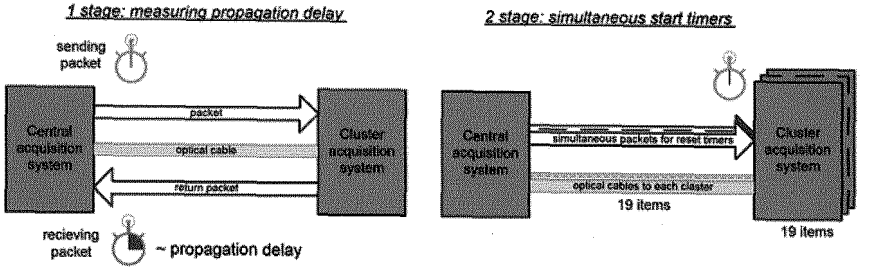

Fig. 4. Concept of the time synchronization system.

4. Conclusion

A 1-km^2 Cherenkov EAS array is under construction in the Siberian Tunka Valley. A data acquisition system was built and is under comprehensive testing now. The first cluster of the TUNKA-133 array (seven optical detectors) was successfully operated during the winter 2006 - 2007.

During the winter season 2007-08, four clusters will operate. Commissioning of the main part of the array is planned for autumn 2008.

Acknowledgments

The present work is supported by the Russian Ministry of Education and Science, by the Russian Fund of Basic Research (grants 05-02-04010, 05-02-16136, 06-0216520) and by the Deutsche Forschungsgemeinschaft DFG (436 RUS 113/827/0-1).

Refereces

1. V.S. Ptuskin and V.N. Zirakashvili, *Astron. Astroph.* 403, 1, 2003.
2. R. Aloisio, V. Berezinsky et.al., *Astropart. Phys.*, 27, 76, 2007.
3. N.M. Budnev et al., *Proc 29th ICRC Pune*, 8, 255, 2005, astro-ph/0511229.
4. D. Chernov et al., *Int. Journal of Modern Physics* A20, 6796, 2005, astro-ph/0411218.
5. S.V. Bryanski et al., *Proc. 24th ICRC Rome*, 2, 724, 1995.
6. N.M. Budnev et al., *Proc. 27th ICRC Hamburg*, 1, 581, 2001.
7. D. Chernov et al., *Int. Journal of Modern Physics* A20, 6799, 2005, astro-ph/0411139.

Status report on the ANTARES project

D. Zaborov* for the ANTARES collaboration

Institute for Theoretical and Experimental Physics,
Moscow, 117218, Russia
** E-mail: dmitry.zaborov@itep.ru*
www.itep.ru

The ANTARES collaboration has recently demonstrated a rapid progress in the construction of the 0.1 km^2-scale neutrino detector in the Mediterranean sea. At present the underwater setup consists of 5 active detector "lines" (of the 12 lines foreseen in the final configuration) and it is taking physics data with nearly nominal efficiency. Currently the atmospheric muon flux and its angular distribution are under intensive studies. Meanwhile over hundred upward-going neutrino events have been extracted from the largely overwhelming background originated by the downward going muons. Thus the concept and the design of the undersea experiment now appear to be confidently proved. The detector construction is to be completed in spring 2008.

Keywords: ANTARES, high-energy neutrino detection, deep-sea Cherenkov telescope, neutrino astronomy.

1. Introduction

ANTARES is a large water Cherenkov detector operating in Mediterranean sea 40 km offshore Toulon (France).[1] The setup is mainly sensitive to muon neutrinos, which are detected thanks to Cherenkov emission of muons produced when a neutrino eventually interacts with a medium nucleon via charge current. Thanks to the long range of high energy muons effective detection volume exceeds tenfold the actually instrumented detector volume. CC interactions of τ-neutrinos can sometimes be detected via $\tau \to \mu$ decay. Hadronic showers created in neutral current interactions of all neutrino types can be detected if fall into or close to the instrumented detector volume. The size and the design of the experimental setup guarantee a high efficiency of neutrino detection starting from sub-TeV energies. Excellent optical properties of Mediterranean water provide a high angular resolution, helping to disclose point-like neutrino sources on the background of

atmospheric neutrinos. The geographic location determines convenient sky coverage to look for neutrinos originated from the Galactic center and from the core of the Sun, as well as from other directions.

2. Detector design

The sensitive element of the ANTARES detector, so called ANTARES optical module,[2] is based on a 10-inch photomultiplier tube, which is enclosed in a special glass sphere to protect the vacuum device from the enormous outside pressure. The sphere also contains a mu-metal cage to shield the phototube from magnetic field of the Earth. The main building block of the setup, the ANTARES storey, includes a triplet of optical modules and a titanium container with a high-voltage power supply, readout and slow control electronics, all together mounted on a titanium frame. Twenty five storeys, connected by electromechanical cables (EMC) in a chain with a step of 14.5 m, form a detector line. Each line is anchored at the seabed, which is 2470 m deep, and held in nearly vertical position by a flotation buoy. The whole ensemble of lines is connected to the shore via a Junction Box, also installed on the seabed.

The ANTARES data acquisition system (DAQ) implements the "all-data-to-shore" concept, that implies using rather powerful computers underwater, high-bandwidth networking and onshore triggering.[3] The position and orientation of the detector elements are monitored by means of an acoustic positioning system, digital tiltmeters and compasses. Precise synchronization of the electronics spread over large volume is achieved by measuring round-trip delays in dedicated optic fibers. Several calibration systems and techniques ensure a sub-nanosecond precision of the Cherenkov pulse measurements. An important role is played by powerful light sources, LED Beacons, which provide the time calibration *in situ*.[4] A recently invented calibration method based on the use of ^{40}K decays in sea water is now adopted for precise monitoring of optical module sensitivities and cross-checking the time calibration.

3. Detector performance

Track reconstruction in ANTARES relies on directional properties of Cherenkov emission and the three-dimensional layout of the detector. Thanks to little light scattering in the sea water,[5] an angular resolution better than 0.3^o can be achieved. Energy reconstruction in ANTARES is based on track length (for sub-TeV muons) and Cherenkov light yield (for

multi-TeV muons and showers). The effective area of the complete detector will approach 0.1 km^2. The principal source of background for a neutrino telescope is the flux of atmospheric muons, which overwhelms the neutrino flux by six orders of magnitude. Luckily, atmospheric muons are all downward going, and a reliable reconstruction method is capable to single out the rare upward-going neutrino events. The orientation of the optical modules at 45^o to the vertical, facing down, also aims at the optimization of the efficiency of the upward-going neutrinos. In a sense, the whole telescope is looking through the Earth. Consequently, its field of view cyclically changes as a function of time following the rotation of the Earth.

4. Status of construction and operation

In the last few years the ANTARES collaboration has made a substantial progress in the construction of the unique undersea setup. A full-scale mechanical prototype line (Line 0) was built and deployed in March 2005 to test a new design of the EMC and the leak tightness of the electronics containers. Following the success of Line 0, several complete detector lines have been deployed and connected to the Junction Box. The short instrumentation line which had been used for various in-situ measurements for three years, MILOM,[6] was recently recovered from the seabed. The new instrumentation line, IL07, was built and deployed in July 2007. IL07 includes modified MILOM instruments: two acoustic Doppler current profilers (ADCPs); two conductivity-temperature probes; two CSTAR devices with improved sensitivity and horizontal mechanical mounting (which will measure optical properties of the water); a Sound Velocimeter; and a Seismometer. IL07 also includes two sensitive cameras with infrared flash, a device for measuring the concentration of the molecular oxygen (O_2 probe), and three acoustic detection storeys equipped with six hydrophones each.

Presently five ANTARES lines are operating underwater, forming together a three-dimensional array of 375 optical modules (see Fig. 1). Four more detector lines have been deployed and are awaiting underwater connection by a submarine. In general, the setup is operating well. Most of the optical modules work with about nominal efficiency, electronics is functioning well, the calibration systems achieve the desired performance. Though, a high level of bioluminescent activity resulted in a reduced efficiency of data taking in certain periods, e.g. in winter 2007. Presently, thanks to various improvements in the DAQ and trigger software, a highly-efficient data taking is ongoing. Every week the physics trigger delivers over 1 million muon events, of which about 10 are neutrinos. A dedicated GRB trigger is

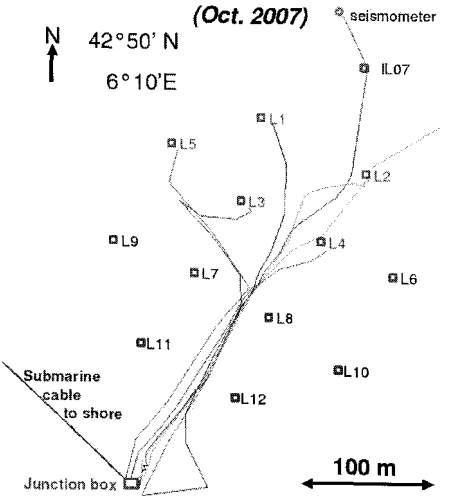

Fig. 1. Scheme of the ANTARES detector, as for October 2007 (top view). The five lines currently operating (L1-L5) are shown in red. Also shown are the four detector lines (L6-L9) and the instrumentation line IL07, which have been deployed but not yet connected, and the future positions of Lines 10, 11 and 12.

operating in parallel, providing full records of detector data within a few minutes after satellite GRB alerts. A dedicated point-source trigger, which maximizes the detection efficiency in the direction of the Galactic center, is operating since July 2007.

5. Data analysis

As for the time of writing these proceedings, the 5-line detector have collected almost 14 millions muon triggers during the live time of almost 200 days. The physics analysis is now particularly focused on the measurement of the atmospheric muon flux and its zenith angle distribution. First results have confirmed the feasibility of separating neutrino events from the background of atmospheric muons (see Fig. 2). Over hundred neutrino candidates have been selected in the data so far, allowing to start searching for point-like neutrino sources and producing first neutrino sky maps.[7] An alternative method of muon flux measurement, based on the use of time correlations between hits in different detector storeys, has been recently invented and is capable to provide, in addition, a measurement of the depth dependence of the muon flux.

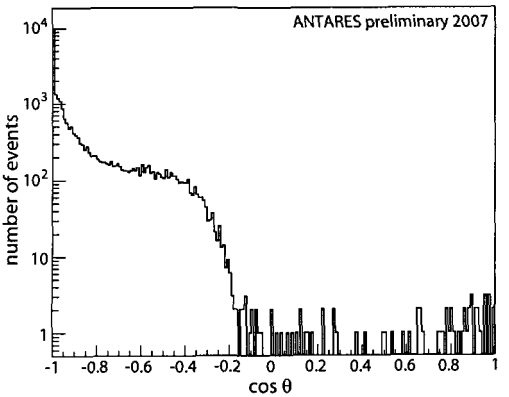

Fig. 2. Zenith angle distribution of reconstructed muons obtained with a subset of Line 1-5 data ignoring detector alignment (preliminary).

6. Outlook

The great effort of the international team of scientists and engineers from seven European countries has recently made ANTARES the largest neutrino telescope in the Northern hemisphere. The experiment has already collected millions of events, allowing for the measurement of atmospheric muons and neutrinos. While more and more data are accumulated, the vast field of physics topics opens up for ANTARES: search for high-energy neutrino sources in the Universe, indirect search for Dark Matter, and many others. The ultimate configuration of the setup, with 12 detector lines, is to be reached in March 2008.

References

1. ANTARES collaboration, *A Deep Sea Telescope for High Energy Neutrinos (Proposal)*, (1999), http://antares.in2p3.fr.
2. P.Amram et al. *Nucl. Instr. and Methods* **A484**, 369 (2002).
3. J. A. Aguilar et al. *Nucl. Instr. and Methods* **A570**, 107 (2007), astro-ph/0610029.
4. M. Ageron et al. *Nucl. Instr. and Methods* **A578**, 498 (2007), astro-ph/0703355.
5. J. A. Aguilar et al. *Astroparticle Physics* **23**, 131 (2005), astro-ph/0412126.
6. J. A. Aguilar et al. *Astroparticle Physics* **26**, 314 (2006), astro-ph/0606229.
7. F. Salesa, Point sources with ANTARES, *these proceedings.*

Calorimetry

Organizer: C. Leroy

This page intentionally left blank

Calorimetry at the LHC

Francesca Cavallari

Istituto Nazionale di Fisica Nucleare, Sezione di Roma,
Dip. di Fisica G. Marconi, Università La Sapienza,
Piazzale A. Moro 2, 00185, Roma, Italy
E-mail: Francesca.Cavallari@roma1.infn.it

The Large Hadron Collider (LHC) is the new CERN accelerator that will provide proton proton collisions at $\sqrt{s}$ =14 TeV. It will have two dedicated experiments: Alice, to study heavy ion collisions, and LHCb, to study b physics, and two general purpose experiments: Atlas and CMS. The LHC is an explorative machine to search for the Higgs boson and physics beyond the Standard Model. Calorimeters play a crucial role in these searches. In particular the electromagnetic calorimeters are fundamental in the search for the Higgs boson, depending on the mass range, either in the two photon decay channel or in the four leptons channel. Hadron calorimeters are important for super-symmetric particles searches where jets and missing transverse energy are expected. We present a review of the LHC experiments calorimeters and their expected performance.

Keywords: Calorimetry, high energy physics

1. The Large Hadron Collider

The Large Hadron Collider is the new CERN hadron collider that will provide proton-proton collisions at $\sqrt{s}$ =14 TeV. The design luminosity is 10^{34} cm^{-2}s^{-1} and the bunch crossing spacing is 25 ns. Two general purpose experiments will take data at the LHC: Atlas and CMS and two dedicated experiments will perform specific studies: b physics (LHCb) and heavy ion collisions (Alice).

The purpose of Atlas and CMS is to search for the Higgs boson and to study the physics beyond the Standard Model. In addition many standard particles, like top and beauty quarks, can be studied with high statistics.

The LHC will explore the existence of the Higgs boson from the present LEP limit[1] of 114.4 GeV. Depending on the H mass the analysis uses the H$\rightarrow \gamma\gamma$ decay or H$\rightarrow$ZZ(*)$\rightarrow$4 leptons. These channels have electrons or photons in the final state and require a very good energy and position

resolution. The electromagnetic calorimeters of Atlas and CMS have been optimized on the H$\rightarrow \gamma\gamma$ channel which is the most demanding.

In events with super-symmetric particles production tipically leptons, jets and neutralinos are present in the final state. So good energy and position resolution also for jets and missing energy is required. The hadronic calorimeters of Atlas and CMS have been optimized to have the best possible jet energy resolution and missing transverse energy (E_T^{miss}) resolution compatible with the framework of the experiment.

2. Requirements on the calorimeters at the LHC

The tipical energy of the photons in the H$\rightarrow \gamma\gamma$ channel is above 50 GeV. A di-photon invariant mass resolution of 1% is required to disentangle the H mass peak from the background. The detector must be granular to allow a good $\pi^0 \rightarrow \gamma\gamma$ separation and reduce the background. The H$\rightarrow$ 4 electrons channel requires full coverage in ϕ and $|\eta|$ up to 3. The range of the calorimeter must be able to reach about 2 TeV to cope with high mass resonances (like the Z').

The energy resolution of a calorimeter can be parametrized as:

$$\frac{\sigma(E)}{E} = \frac{a}{\sqrt{E}} \oplus \frac{b}{E} \oplus c \qquad (1)$$

where a takes into account the stochastic fluctuations, it is small for homogeneous calorimeters and higher for sampling calorimeters. This term limits the low energy performance. The b term is due to electronics noise and the constant term c takes into account the detector disuniformities or instabilities and the error on the calibration and it limits the high energy performance. The experiments have put a lot of effort to contain its effect.

The hadronic calorimeters must contain jets up to 1 TeV, so approximately 11 λ_I are required. They have to be hermetic not to spoil the E_T^{miss} resolution, so a coverage in $|\eta|$ up to 5 is required. They have to tag forward jets and measure their energy with satisfactory resolution for the E_T^{miss} computation. Thus both experiments have installed a forward calorimeter to extend the η coverage from 3 to 5.

The detectors must be compact, fast, radiation hard and reliable for at least 10 years.

3. The Atlas experiment

The Atlas experiment is the largest of the LHC experiments, it is 40 m long and 22 m tall. It is made of a large muon spectrometer with three

toroidal magnets, a silicon tracker with transition radiation tubes for particle identification inserted in a 2 T super-conductive solenoid field, a highly segmented liquid argon electromagnetic calorimeter and a tile calorimeter for hadronic activity. The solenoid coil is in the cryostat just in front of the electromagnetic calorimeter.

4. The Compact Muon Solenoid experiment (CMS)

The CMS experiment is made of a super-conducting solenoid, providing a 4 T magnetic field, which contains the silicon tracker and the calorimeters. Muon chambers are embedded in the iron return yoke. A crystal electromagnetic calorimeter and a sampling brass and plastic scintillator hadronic calorimeter are located inside the coil.

5. Electromagnetic calorimeters

5.1. *The Atlas electro-magnetic calorimeter*

The Atlas sampling electromagnetic calorimeter is made of liquid argon (LAr) and lead absorber plates shaped as an accordion and operated in a cryostat at 87 K. The signal is given by the ionization electrons collection, it is linear and uniform, stable in time and intrinsically radiation hard. The modules are longitudinally segmented: the front sampling is made of narrow strips for better separation of the π^0 photons, the middle sampling (16-18 X_0) collects most of the shower energy, the back sampling (2 X_0) catches the tail of high energy showers and helps to separate hadrons from electrons. A thin presampler is installed for $|\eta| < 1.8$. The calorimeter depth is $25X_0$ and the number of channels is about 170000.

Keeping the mechanical tolerance in the absorber thickness at 2 mm within $9\mu m$ was a challenge. The obtained precision guarantees uniform cell response and contributes to the constant term c for less than 0.2%.

The energy resolution of the LAr calorimeter measured in test-beams (see Figure 1) is $\sigma(E)/E = 10\%\sqrt{E} \oplus 0.17\%$. Long range non uniformities contribute to c for 0.44% giving a global constant term below 0.7%. The measured linearity is better than $\pm 0.1\%$ for electron energies between 10 and 180 GeV. In total 10% of the calorimeter modules have been exposed to test-beams.

The electronics calibration is sufficient to inter-calibrate the channels thanks to the high mechanical uniformity. Simulation shows that with 50000 $Z \rightarrow ee$ events (achievable in 0.1 fb^{-1}) the constant term can be contained to 0.7%.

5.2. *The CMS electro-magnetic calorimeter*

The CMS ECAL is a homogeneous calorimeter made of 75000 lead tungstate ($PbWO_4$ or simply PWO) crystals (X_0=0.89 cm). The crystals, developed after a long R&D phase, are 23 cm long, corresponding to 25 X_0. The light is fast but the light yield is small (LY$\simeq$ 100 γ/MeV). The light is measured via avalanche photodiodes (APD) in the barrel and vacuum phototriodes (VPT) in the endcaps, due to the higher level of radiation. Being a homogeneous calorimeter, the stochastic term is small, so the performance at high energy is limited by the constant term c.

Very stable cooling and high voltage systems guarantee a small contribution to c (0.1-0.2%). Due to the intrinsic fluctuations of the shower maximum depth, a potentially dangerous contribution to c could be the disuniformity of the light collection along the crystals. This has been contained to 0.3% by depolishing one of the crystal lateral faces. The radiation level in the detector causes transparency loss, thus reducing the signal level. A light injection system monitors transparency changes, keeping the effect on c below 0.2%.

Several ECAL modules have been tested with high energy electron beams. The energy resolution (see Figure 1) is $\sigma(E)/E = 2.8\%\sqrt{E} \oplus 125\ MeV/E \oplus 0.3\%$.

All the barrel modules have been inter-calibrated with 1-2% precision with cosmic rays and 25% of them have been calibrated to 0.4% with high energy electrons beams. At the LHC the calibration will be performed using physics events. The crystals with precise calibration will help understanding the calibration with physics events and especially the effect of the material in front.

5.3. *Detector performance and status*

The tracker material in front of the ECAL reaches about one X_0. In Atlas the solenoid coil adds 2-4 X_0 just in front of the ECAL that may cause energy loss and contribute to the stochastic term. High energy electrons traversing the tracker material emit Bremsstrahlung that generates separated cluster in the ECAL due to the magnetic field. So smart reconstruction algorythms are used to recover radiated energy. Photon reconstruction is also affected due to photon conversion that generates fake tracks, thus reducing the photon efficiency.

Full simulation studies of the H$\rightarrow \gamma\gamma$ channel show that the H mass resolution is as expected and it will allow a discovery in about 10 pb^{-1}.

Nevertheless this analysis requires a well calibrated and understood ECAL and a well aligned tracker to find the event vertex. So the commissioning phase and the ability to reach fast a good calibration level will be crucial.

Both calorimeters are built and installed. The CMS Endcaps are being assembled and will be finished by June 2008.

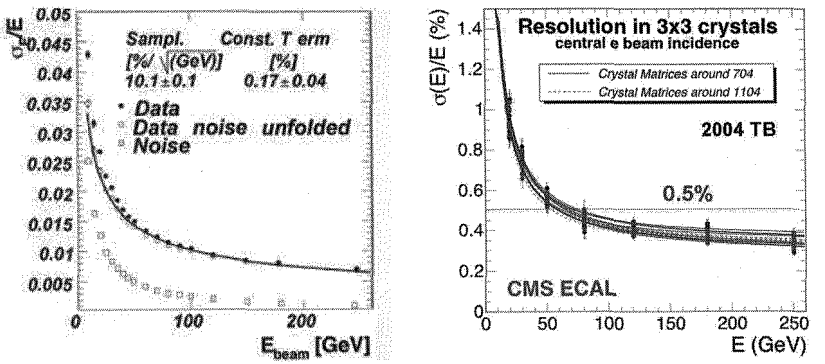

(a) (b)

Fig. 1. The Atlas (a) and CMS (b) ECAL energy resolution.

6. The hadronic calorimeters

6.1. *The Atlas hadronic calorimeter*

The Atlas HCAL is made of a Barrel and two endcap parts. The endcaps, closed in the same cryostat as the ECAL endcap, are made of copper plates and use LAr as an active medium, The Barrel HCAL is made of steel and plastic scintillator tiles arranged parallel to the beam line. The scintillation light is collected by wavelength shifting fibers (WLS) and read by PMTs at the back. The barrel covers up to $|\eta|$ =1.7 and two extended sections with the same technology surround the copper/LAr endcap calorimeter. The Atlas HCAL is non compensating (e/h$\simeq$1.4). It reaches 9.7 to 13 λ_I and the energy resolution in the barrel for pions is $\sigma(E)/E = 45\%/\sqrt{E} \oplus 1.3\%$.

6.2. *The CMS hadronic calorimeter*

The CMS HCAL is made of brass and plastic scintillator tiles arranged transversal to the beam line. WLS fibers are used to collect the light and

clear optical fibers carry the light to hybrid photo-diodes at the back. The design energy resolution for pions is: $\sigma(E)/E = 100\%/\sqrt{E} \oplus 8\%$.

The HCAL is 7 λ_I deep at $\eta = 0$. Another HCAL layer has been installed outside the solenoid to add 3 λ_I. This improves by 10% the energy resolution for 300 GeV pions and improves the linearity. The HCAL is non compensating (e/h$\simeq$1.4). The use of energy dependent ECAL and HCAL weights allows to improve the energy resolution and the linearity but the non compensation and the poor containment limit the performance. To improve the jet energy resolution CMS is studying particle flow algorythms, which measure charged particles in the tracker, photons in the ECAL and long lived neutral hadrons in the HCAL.

6.3. *Performance, Calibration and commissioning*

Both hadronic calorimeters have been calibrated at 3-5% level with radioactive sources. Many modules have been tested on test-beams also in combination with the ECAL. The detectors are all built, installed and have started taking cosmic rays data in the pit.

Simulation shows that currently the Atlas E_T^{miss} resolution is better than the CMS one. However recent studies on inclusive supersymmetric searches, where fully hadronic channels are analysed,[4] show that the Atlas and CMS potential is similar. Apparently what really counts in this analysis is the hermeticity and the correct Monte Carlo description of the gaps in the detector rather than the resolution.

7. The LHCb experiment

The LHCb experiment uses high B production rate at small angle to study CP-symmetry violation in the neutral B meson systems. It is a single arm spectrometer that covers the angle from the beam between 10 and 300 mrad. The detectors are assembled in two halves. The calorimeters must give electron/hadron separation, electron energy and position measurement for the first trigger level and for offline analysis.

The ECAL is a Pb/scintillator/WLS Shashlik calorimeter. The total length is 25 X_0. Just in front of the ECAL a scintillator pad detector and a pre-shower help the electron/hadron separation. The granularity dicreases with radial distance from the beam. Test-beam results show that the energy resolution is $\sigma(E)/E = 10\%/\sqrt{E} \oplus 1\%$, which is sufficient for hadron rejection and for π^0 reconstruction. A monitoring system with LED is used to compensate for radiation damage. The initial calibration will be

obtained using cosmic rays and then using energy flow and $\pi^0 \rightarrow \gamma\gamma$ decay.

The HCAL is made of iron and scintillator tiles mounted parallel to the beam line. It constitutes $5.6\lambda_I$ and has a resolution of $a = 80\%/\sqrt{E} \oplus 10\%$.

The calorimeters are installed in the pit and the commissioning phase has started.

8. The Alice experiment

The Alice experiment will study heavy ion collisions at the LHC, to investigate the quark-gluon plasma formation.

Alice has a photon spectrometer (PHOS) to study direct single photon and di-photon production in the collision initial phase and jet quenching via high p_T photons and π^0. Typical photon energies are between 0.5 and 10 GeV. It is made of 17000 PWO crystals read by APDs and operated at -25°C to optimize the response for low energy showers. Its depth is 20 X_0. It is at 4 metres from the interaction point and it covers $|\eta| < 0.12$ and 100° in ϕ. Its performance measured in test-beams is: $\sigma(E)/E = 3.3\%/\sqrt{E} \oplus 18\ MeV/E \oplus 1.1\%$. The first of the five modules is ready and installed.

9. Conclusions

It was a challenging adventure to build calorimeters with this number of channels and the required level of reliability for ten years or more in the LHC environment. The detector performance was estensively tested in test-beams and meets the design specifications. Most of the detectors are built and the commissioning phase has started. Preliminary simulation studies show that the obtained calorimeters performance allows to reach the desired physics goals. We are looking forward to seeing interesting physics with them.

References

1. The Aleph, Delphi, L3 and Opal Collaborations, the LEP Working Group for the Higgs Boson Searches, Phys. Lett. B 565 (2003) 61.
2. Atlas Collaboration, *The Atlas technical proposal*, CERN/LHCC/94-43.
3. CMS Collaboration, *The CMS Technical proposal*, CERN/LHCC/94-38.
4. M. Tytgat, *SUSY searches in all hadronic states with large MET at the LHC*, presented at SUSY07, Karlsruhe (Germany), July 26, 2007.
5. LHCb Collaboration, *The LHCb Technical proposal*, CERN/LHCC/98-4.
6. Alice Collaboration, *The Alice Technical proposal*, CERN/LHCC/95-71.

AN OFFLINE QUALITY CALORIMETRIC SELECTION FOR THE CDF TRIGGER

GIORGIO CORTIANA

INFN & University of Padova, Via Marzolo 8, 35131 Padova, Italy.

and the CDF L2CAL Upgrade Team

During the first part of the CDF Run-II, the Level-2 calorimeter trigger was implemented in hardware and based on a simple algorithm used since Run-I. This system has worked well at low Tevatron luminosity, however, as the accelerator instantaneous luminosity increases, the limitation due to the adopted clustering algorithm started to affect the data taking. In this paper, we present an upgrade path to the CDF Level-2 calorimeter trigger system, based on the Pulsar board, a general purpose VME board developed at CDF and broadly used during previous trigger upgrades. The design, the hardware and software implementation, as well as the advantages of this new system over the existing one, will be discussed.

1. Overview of the CDF trigger system

CDF Run-II trigger system has a three level architecture [1] designed to retain the most interesting events for physics according to the bandwidth limitation of the data acquisition system. Each trigger stage rejects a sufficient fraction of the events to allow processing at the next stage with minimal dead time.

The first level of the trigger system (L1) is a synchronous 40 stages pipeline and is based on custom-designed hardware. At this level, a limited set of information from tracking chamber, muon and calorimeter systems, is processed and used to select events. Level-2 (L2) processing is asynchronous and based on a combination of custom hardware and commodity processors. L2 looks for silicon detector information and construct more sophisticated event variables for event selection (i.e. clusters of calorimeter towers). Upon L2 accept, the full detector information is readout and sent to L3 processor farm for further processing. Only events accepted by L3 are sent to mass storage.

In this paper, we describe an upgrade for the L2 Calorimeter (L2CAL) trigger subsystem aimed at improving the L2 trigger rejection power at high Tevatron luminosities, as well as the system capability and flexibility to increase trigger collection efficiency for important high P_T physics processes.

2. CDF Calorimeter trigger

The calorimeter system of the CDF detector [1] has a cylindrically symmetric layout with a uniform segmentation in pseudorapidity (η) and azimuthal angle (ϕ). Hadronic (HAD) and electromagnetic (EM) calorimeter towers are summed into trigger towers with a width of $\Delta\eta$=0.2 and $\Delta\phi$=15°, so that, the entire calorimeter is represented in a 24×24 trigger tower map in the η-ϕ plane. Tower HAD+EM energy is projected in the transverse plane with respect to the beam axis to form the transverse energy (ET).

The calorimeter trigger is designed to identify electrons, photons, jets, and to perform event selections based on total event transverse energy (SumET) and missing transverse energy (MET). The trigger tower energy data is sent to both L1 and L2 calorimeter trigger systems (L1CAL and L2CAL, respectively) with 10-bit energy resolution, using a least significant count of 125 MeV resulting in a full scale ET of 128 GeV. However, due to intrinsic hardware features, the L1 calorimeter subsystem only uses 8-bit trigger tower energy information for processing, with the least significant and most significant bits dropped. L1CAL selects events based on the number of trigger tower above a given ET threshold, and on the values of SumET and MET.

The L2CAL subsystem receives all 10-bit trigger tower energy information. However, the previous existing hardware-based L2CAL system used SumET and MET values as provided by the L1CAL. The main L2CAL task was to identify clustered energy depositions yielded by jet, electron or photon production. It adopted a hardware-implemented algorithm which combines or links contiguous regions of trigger towers with non-trivial energy. Each cluster starts with a tower above a "seed" ET threshold (typically a few GeV) and all towers above a second lower "shoulder" threshold, in a contiguous region around the "seed" tower, are added to the cluster. The size of each cluster expands until no more "shoulder" towers adjacent to the cluster are found, and the cluster position is set to coincide with the "seed" tower position.

While the L2CAL system, described above, worked well during the first part of CDF Run-II, its features started to affect the data taking at high Tevatron luminosities, forcing the collaboration toward an upgrade of the system. At high luminosity (i.e. $>1.50\times10^{32}$ $cm^{-2}s^{-1}$), multiple proton-antiproton interactions occur in the same bunch crossing, increasing the occupancy of the calorimeter, and consequently the probability for a trigger tower to be above "shoulder" threshold. As a result, large number of trigger tower can be summed in a single mis-identified cluster, yielding high L2 accept rate for single-jet triggers, and sizable efficiency losses for multi-jet based triggers. Additionally, the

suboptimal resolution used for MET selections at L2 degrades sample purities, and can yield L2 bandwidth saturation.

3. L2 Calorimeter Trigger upgrade

The L2CAL upgrade by mean of a new hardware path delivers the full 10-bit resolution trigger tower energy information to the Level-2 decision CPU, where new cluster finding, including a recalculation of MET and SumET, is performed.

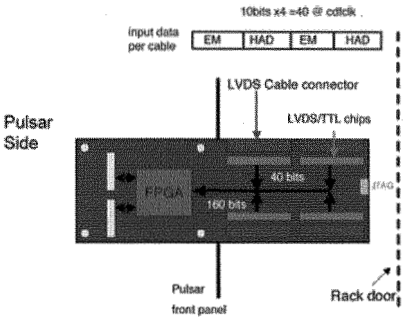

Figure 1: Schema of the custom mezzanine card used to interface LVDS cables from L1CAL to the Pulsar board.

A new hardware path has been designed based on the Pulsar board [2], a general purpose VME board developed at CDF and already used in previous CDF trigger system upgrades [3, 4]. Briefly, a Pulsar boards is constituted by a motherboard equipped with three powerful Altera FPGA (APEX 20K400BC-652-1XV [5]) and RAMs, which interface any user data with any industrial standard link (i.e. CERN S-LINK or Gigabit Ethernet) through the use of custom mezzanine cards. Two FPGAs are used for data input/output (DATAIO) operations, and interface to two mezzanine cards by means of bidirectional connections. DATAIO FPGAs are connected with a Control FPGA responsible for data serialization and merging. In our configuration, the control FPGA output data stream is formatted according to S-LINK standard.

In the old system one L2CAL board received four Low Voltage Differential Signals (LVDS) input cables from the L1CAL system, corresponding to 8 trigger towers energy information (both EM and HAD) at the CDF clock frequency (132 ns period). In the upgraded system [6] (Fig. 1 and 2), one new LVDS mezzanine card receives the same amount of input data.

Mezzanine cards (Fig. 1) are equipped with four LVDS 80-pin Honda connectors, LVDS/TTL signal converter chips, and an Altera Apex Device

(EP20K160E) controlling the flux of data from the mezzanine to the pulsar DATAIO FPGA. With four mezzanines per Pulsar board, 18 Pulsars are required to receive all the 288 LVDS cables from L1CAL (576 trigger towers). The three FPGAs in each Pulsar board process, merge, and convert the data into S-LINK format. A second set of S-LINK Merger Pulsar boards receives and merges the 18 S-LINK outputs into 4 S-LINK data stream for input to the L2 CPU. A highly integrated PCI interface, FILAR (Four Input Links Atlas Readout) move data from the SLINK channel to a 32-bit PCI bus.

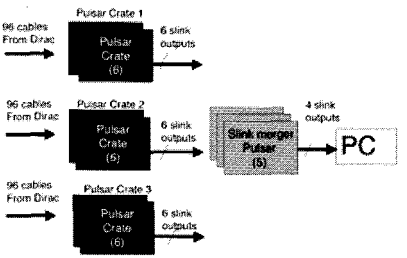

Figure 2: Pulsar cluster used to make trigger tower energy information directly available to L2 CPU.

4. Clustering Algorithms and Results

Algorithms for the L2CAL upgrade are executed, satisfying the L2 timing constraints, on the L2 PC (2 dual core AMD Opteron) processors.

New jet clustering is performed using a fixed cone algorithm: jets are formed starting from a list of towers, "seeds", above a programmable ET threshold, and their position is calculated by ET-weighting each tower inside a jet-cone centered at the "seed" tower position. MET is recalculated using full 10-bits energy resolution, and in addition, fast software emulations of the previous electron/photon clustering are in place.

The quality of the calorimetric trigger variables provided by the upgraded L2CAL system is near offline-like. This is shown by Figure 3, where L3 variables are compared to L2 ones as provided by the old and upgraded L2CAL systems. Given the enhanced capabilities provided by the L2CAL upgrade, CDF is re-optimizing and re-designing its trigger selections in order to fully exploit the increased quality of L2-objects, and the flexibility of software-based algorithms. In particular offline-like quality jet position measurement can be used for jet-track matching requirements, useful to implement b-jets and tau-lepton online-tagging [7].

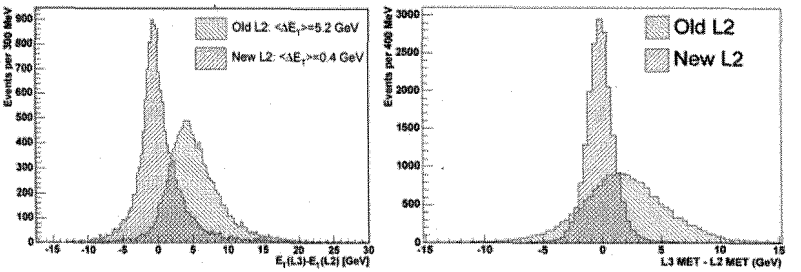

Figure 3: Difference between L2 and L3 jet transverse energy (left) and MET (right) for the old and upgraded L2CAL systems.

5. Summary

The L2CAL upgrade, fully commissioned in summer 2007 with minimal impact on CDF data taking ("parasitic commissioning"), constitutes a big step forward for the CDF triggering capability at Level-2, and thus a vital instrument for high-luminosity running foreseen for the next years. It improves the quality of jet and MET related quantities at Level-2, allowing a simultaneous trigger rate reduction, and trigger collection efficiency increase for important high P_T physics processes. The increased trigger selection flexibility is being exploited for the design and implementation of more powerful and sophisticated trigger paths.

References

1. R. Blair et al., "The CDF RunII Detector Technical Design Report", 1996, FERMILAB-Pub-96/390-E.
2. http://hep.uchicago.edu/~thliu/projects/Pulsar.
3. K. Anikeev et al., "CDF Level 2 Trigger Upgrade", IEEE Trans. on Nucl. Sci., Vol. 53, No 2, 2006 pp. 653 - 658.
4. J. Adelman et al. "First Steps in the Silicon Vertex Trigger upgrade at CDF", Nuclear Science Symposium Conference Record, 2005 IEEE Vol. 1, October 23 - 29, 2005, pp:603 – 607.
5. ALTERA Pub, "APEX 20K Programmable Logic Device Family", Data Sheet v.5.1, 2004.
6. A. Bhatti et al., "Level-2 Calorimeter Trigger Upgrade at CDF", FERMILAB-CONF-07-165-E.
7. S. Amerio et al., "Online b-jet tagging at CDF", FERMILAB-CONF-07-109-E (2007).

Data Preparation of the Calorimeter Based Algorithms of the High-Level Trigger for the ATLAS experiment at the LHC

A. Anjos, A. Bazan, D. O. Damazio*, B. Laforge, W. Lampl, S. Laplace, F. Ledroit, R. Lafaye, H. Ma, A. Ruiz-Martinez, C. Santamarina-Rios, R. Seuster, A. Solodkov, M. Wielers, H. Wilkens, I. Wingerter-Seez, X. Wu

*Corresponding author : * E-mail: damazio@mail.cern.ch*

The ATLAS detector trigger system needs to reduce the incoming rate of 40 MHz at design luminosity to around 200 Hz. The access to detector information must be fast so that trigger algorithms can run within a very short time budget (40ms at Level-2 and $\approx 4s$ at Event Filter). This work presents the modifications implemented to the calorimeter software data preparation which resulted in a gain of almost six times in data unpacking processing speed. Application to cosmic rays acquisition is also shown.

Keywords: Calorimeter, Trigger, Fast Processing, Cosmic Rays, ATLAS

1. Introduction

The ATLAS detector,[1] a general purpose experiment for the Large Hadron Collider (LHC) at CERN, is scheduled to start operation in 2008. The ATLAS trigger system needs to select around 200 Hz of potentially interesting events out of the 40 MHz bunch crossing rate.

ATLAS has a three-tier trigger system consisting of a hardware based Level-1 (LVL1) and a software based Level-2 (LVL2) and Event Filter (EF), together called High Level Trigger (HLT). The HLT algorithms fetch digital data from the readout chain of the detector. This data is decoded to form event quantities such as energy in calorimeter cells. Data must be organized in a convenient way so that the so-called feature extraction (FEX) which are simple fast reconstruction algorithms (eg: cluster finding) do not loose unnecessary time.

Recently, a smarter way of using the subdetector electronics readout lead to an important timing reduction. In preparation for pp collisions, the calorimeter based trigger reconstruction has been adapted for cosmic data taking. Results from these tests will be shown.

2. ATLAS Trigger System

The ATLAS LVL1 trigger uses the calorimeter and muon systems. Coarse granularity signals are used. A maximum latency of 2.5μs is admitted. It reduces the incoming rate to around 75 KHz (upgradable to 100 KHz).

The position of the object that triggered the LVL1 is passed to the LVL2. The LVL2 software algorithms typically operate only around these so-called Regions of Interest (RoI). Full detector resolution is used in these RoIs allowing for more precise online analysis. Around 2% of the detector data is used and an average event processing time of 40 ms is admitted. The rest of the event data is buffered by the data acquisition system in the ReadOut Buffers (ROBs), waiting for the final LVL2 decision.

The EF is the third processing level. Seeded by the LVL2 results, it will operate on full detector data at full granularity. It will also run in an unseeded mode. The average event processing time is of the order of 4s and offline like algorithms will run at this stage.[2]

3. ATLAS Calorimeter

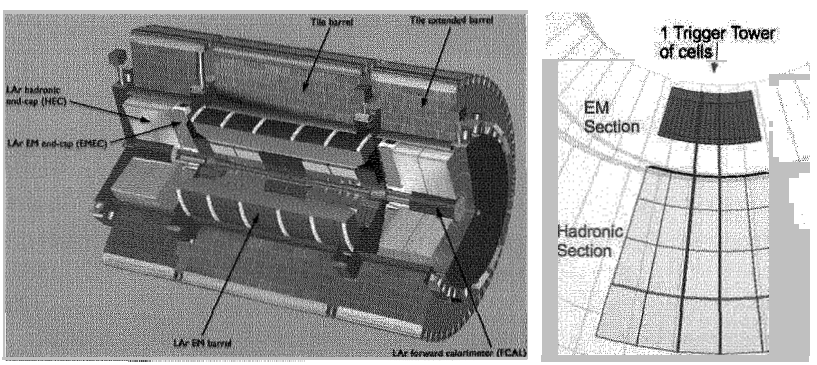

Fig. 1. **The ATLAS** Calorimeters different sectors (left) and the trigger tower definition within an RoI (right).

The ATLAS Calorimeters use different technologies to perform ElectroMagnetic (EM) and hadronic calorimetry (Figure 1 - left). The EM calorimeter is a lead/liquid-argon (LAr) detector. It covers $|\eta| < 3.2$. The hadronic calorimeter consists of an iron and scintillator up to $|\eta| = 1.7$. Over the range $1.5 < |\eta| < 4.9$ LAr calorimetry is again used. The hadronic part uses copper absorbers and extends up to $|\eta| = 3.2$. Above this region,

a high density forward calorimeter is used.[3] In total, the calorimeter system comprises more than 200K readout cells.

For the LVL1, coarse granularity projective regions from the collision center are defined by grouping together calorimeter cells. The analog signal pulses from such cells are combined to form $\Delta\eta \times \Delta\phi$ calorimeter sectors of 0.1×0.1 separated for EM and hadronic parts. These are the trigger towers (TT). The input for the cluster finding are the TT's for EM clusters and comprises several TTs for the jet finding. In case of an accept (EM TT transverse energy above a programmed threshold), this position is passed to the LVL2. Figure 1 (right) shows one TT (marked) within a calorimeter RoI processed at LVL2.

4. The LVL2 Electron and Photon Algorithm

The LVL2 electron and photon reconstruction reconstruction starts by searching for the hottest cell within the RoI. A fixed size ($\Delta\eta \times \Delta\phi = 0.075 \times 0.125$) cluster centered around this cell is built. Transverse shower shape variables and total EM transverse energy are calculated. These variables can be subsequently used to discriminate electrons and photons from jet background (See Figure 2).[4]

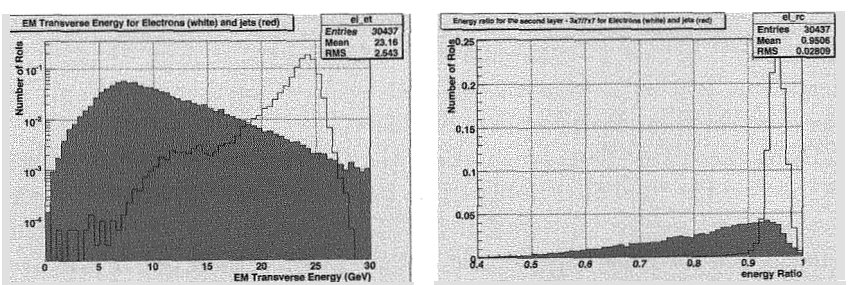

Fig. 2. Transverse EM Energy as calculated by the LVL2 electron and photon algorithm (left) and cluster confinement (shower shape calculated in the second EM sampling by dividing the energy in the 3×7 cells by the energy in 7x7) are shown for electrons with Et=25 GeV (blank histograms) and di-jets (shaded) with Et(hard)>25GeV.

The LVL2 calorimeter reconstruction starts by using a lookup table based on the detector geometry to find for a given RoI the ROB addresses

for data request. Upon data receipt, collections of cell objects with geometry and energy information are prepared. To optimize cells access for the subsequent reconstruction, cells are mapped by TT (from another lookup table). Cells in TTs outside the RoI are not accessed. A ROB contains data for many TTs and it is necessary to select only the RoI ones.

The initial implementation for the data access used offline like code. Unpacking (in this case, energy reconstruction from digital output) is performed by subdetector specific code. In this scheme, cell objects were organized in a vector which was deleted at the end of each event to avoid memory leaks. Actually, the lack of such cells in memory triggered the data unpacking. This represents important overhead as memory allocation, cell geometry association per readout channel and energy information decoding are performed online. Furthermore, as organizing cells by TT improves the timing of the subsequent reconstruction, online remapping of cells had to be performed. Since the cells were deleted after each event, this map had to be remade on an event by event basis.

The online implementation of the calorimeter reconstruction was changed to respect the channel ordering of the calorimeter hardware instead of forcing them to respect the TT map. Readout channel number translates to a cell index in the code. All $\approx 200k$ calorimeter cells are statically allocated in the memory in the initialization step, and thus the TT to cell lookup table now just needs to be prepared once. Online TT mapping per event is no longer necessary. This does not yield into an important load in terms of memory consumption.[5] A table keeps track of which ROBs (comprising 256 cells) were decoded per event. If another algorithm uses data from the same RoI, data will be reused.

Using the offline data preparation, the measured unpacking time was 9.86 ms and the total algorithmic (data unpacking plus feature extraction) time was 12.1 ms, as measured on 2.4GHz computer. Using the new implementation the data unpacking is 1.65 ms (a gain factor of 5.96) and the total algorithmic time is 3.77 ms (an improvement factor of 3.2). In the offline data unpacking, 81% of the time budget was used for data unpacking. Now, this represents 43% of the total processing time for this algorithm.

5. Application to Cosmic Data

To prepare for running with all its subdetectors during LHC operation, ATLAS performs cosmic ray commissioning runs.[6] At the LVL1 events are triggered by the muon barrel or the Tile calorimeter trigger.

Figure 3 (left) shows a plot from the online monitoring system for the

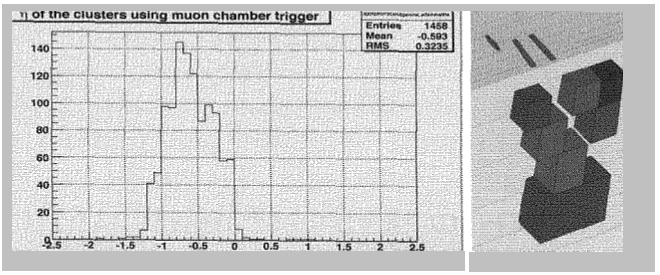

Fig. 3. **LVL2 algorithm monitoring plot for the cluster η position (left). 3D view of** a cosmic signal (right). Smaller (EM) and larger (hadronic) cells above noise are shown.

LVL2 algorithm with the LVL2 found cluster positions. For this run, the detector coverage was only on the negative η side. The figure (right) also displays a 3D view of the detector cells illuminated by a cosmic ray. Only cells above noise (100 MeV) are displayed for both EM and Hadronic sections. This was an important test which shows that the calorimeter algorithms at LVL2 and EF are ready to be deployed at ATLAS start-up.

6. Conclusions

Recently, a speed increase of ≈ 6 times was obtained for the data preparation step of the ATLAS calorimeter based trigger selection algorithms for electrons and photons. The same data preparation procedure is now used for all LVL2 and EF calorimeter data preparation requests.

The LVL2 and EF calorimeter based algorithms have been successfully tested during ATLAS cosmic ray commissioning runs this summer.

References

1. the Atlas Collaboration, *ATLAS Technical Proposal* (CERN, Geneva, Switzerland, 1994).
2. the Atlas Collaboration, *HLT Technical Design Proposal* (CERN, Geneva, Switzerland, 2003).
3. the Atlas Collaboration, *Calorimeter Performance Techinical Design Report* (CERN, Geneva, Switzerland, 1997).
4. S. Gonzales, T. H-Kozanecka and M. Wielers, *Selection of high-p_T electromagnetic clusters by the level-2 trigger of ATLAS* (Geneva, Switzerland, 2000).
5. the Atlas Collaboration, *Computing System Commissioning Note on Calorimeter Data Preparation* (D.O. Damazio and C. Santamarina-Rios, CERN - Note in preparation, 2007).
6. B. G. on behalf of the ATLAS Trigger/DAQ Collaboration, *Integration of the Trigger and Data Acquisition Systems in ATLAS* (CHEP, 2007).

STUDY WITH COSMIC AND TEST-BEAM PARTICLES OF SCINTILLATION-TILE DETECTORS READ OUT VIA SILICON PHOTOMULTIPLIER DEVICES

A. Calcaterra, R. de Sangro, G. Finocchiaro*, P. Patteri, M. Piccolo and M. Rama

Laboratori Nazionali di Frascati dell'INFN,
Via E. Fermi,40 - I-00044 Frascati (Rome) Italy
**E-mail: fnc@lnf.infn.it*

This paper describes measurements made using counters made of a small ($3 \times 3 \times 0.5\,\mathrm{cm}^3$) scintillation tile coupled to a Multi-Photon Pixel Counter (MPPC) produced by Hamamatsu and exposed to an electron beam at the Beam Test Facility in Frascati, and to cosmic rays. We show our first results for charge spectra and efficiency, and a preliminary measurement of device linearity.

Keywords: Silicon Photomultiplier, Scintillation counter, Hadron calorimetry
PACS: 29.40.Wk,29.40.Mc, 29.40.Gx

1. Introduction and motivation for this study

Silicon photomultipliers,[1] often called "SiPM" in literature, are semiconductor photon detectors built from a square matrix of avalanche photodiodes on common silicon substrate. The dimension of each single square microcell can vary from 20 to 100 μm. The applications of silicon photon detectors are very wide;[2] in particular, at the ILC, the demands imposed to calorimetry may be met only with a very fine transverse and longitudinal granularity of individual detection elements; scintillator tiles of 30 by 30 by 5 mm^3, and possibly thinner, being candidate detectors.

2. The Beam Test Facility in Frascati and the setup

The Beam Test Facility[3] exploits by means of a transfer line the DAΦNE ϕ-factory LINAC, and is optimized for the production of electron and positron bunches in a wide range of multiplicities, down to single-electron. The beam profile from the BTF has typical horizontal and vertical dispersions of $\sigma_h = 2\,\mathrm{mm}$ and $\sigma_h \leq 5 - 10\,\mathrm{mm}$, with some additional, wider halo in the horizontal plane, where the bending magnets act. The setup consists of

3 counters using MPPC detectors[4] and a 6-layer, two-dimensional tracker made of mechanically-quenched Resistive Plate Counters[5] with strip readout, yielding a spatial resolution extrapolated on the scintilator tiles of a few mm. The trigger is obtained for every beam pulse via a signal synchronous with the LINAC radiofrequency; it is thus unbiased, and completely independent from our measurements. The BTF equipment includes a Pb-glass calorimeter, placed downstream the user setup. The beam pulse is totally absorbed in the calorimeter, and the integrated signal from the PM gives a measurement of the number of electrons in every pulse (see Fig. 1). Unless

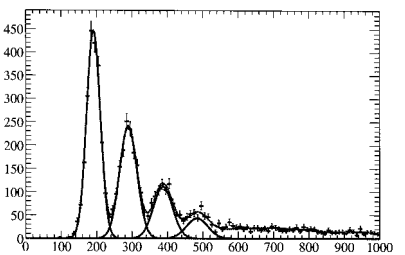

Fig. 1. Beam pulse multiplicity. 0-MIPs beam pulses appear at $\sim$ 200 counts.

otherwise stated, only events having a Pb-glass calorimeter signal in the second peak in Fig. 1 have been used in this work: those corresponding to beam pulses of multiplicity one.

The counters in these measurements were: n."1", a scintillation tile made of St. Gobain BC-400 coupled to the MPPC using a 1 mm thick green fiber, inserted into a groove machined along the tile center, and read by an MPPC with 1600 pixels in a square matrix of 1×1 mm (25 μm pixel pitch); n."2", a tile made of green-scintillating material, similar to Scionix EJ260, coupled as in n. "1" to an MPPC with 400 pixels (50 μm pixel pitch); n."3", a tile like counter "1", directly coupled without a fiber to a MPPC like the one in counter "2". In all 3 counters the MPPC were biased using a power supply HP6614C, with a stated accuracy of 0.03%, in quadrature with 12 mV.

3. Results from the BTF beam test

Fig. 2 shows the pedestal-subtracted charge spectra (in pC) for the three MPCC counters, each biased about 1 V above the MPPC breakdown voltage (V_{bias} = 72.0 V for counter 1, V_{bias} = 69.5 V for counters 2 and 3). One particle per beam pulse has been requested here (second peak in Fig. 1). The contribution from events having 2 particles per pulse is estimated at

$\sim$ 5%. The spectra show a very narrow peak at 0, barely visible in the picture, and a series of equally-spaced peaks, due to events firing 1, 2, 3, and more pixels in the MPPC's. The RMS noise, estimated by fitting with

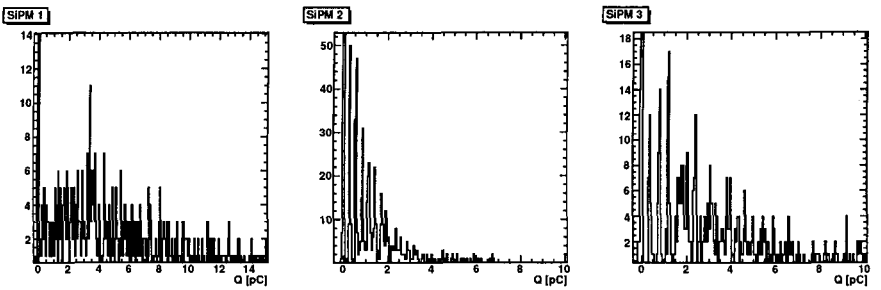

Fig. 2. Charge spectra from left to right for counter 1 (V_{bias} = 72.0 V), 2 and 3 (V_{bias} = 69.5 V for both).

a Gaussian the peak at 0 pC, is around 10 fC. The gain, measured by fitting the peak pitch, is $\sim 1 \times 10^6$ for counter 1, $\sim 1.6 \times 10^6$ for counter 2, and $\sim 2.2 \times 10^6$ for counter 3. Since the conversion constants for the cherge amplitudes of the 3 counters were very close, the gain difference indicates that the working points for `e.g.` the 2 400-pixels MPPCs (#2 and #3) were actually different. The effect of the scintillator material and the coupling geometry is instead to affect the peak populations, creating a bigger or smaller average number of peaks. A measurement of the gain as a function of the bias voltage V_{bias} is shown in the left plot of Fig. 3.

We measured the efficiency of counters 2 and 3 by correlating their charge signals (Fig. 3, right). Cutting above the pedestal (4σ's) for one

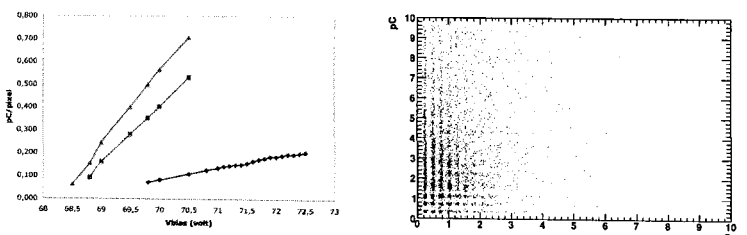

Fig. 3. Left: gain vs. bias voltage for the three counters. Diamonds and navy line are for counter 1, squares and green line for counter 2, triangles and red line for couonter 3. Right: charge from counter 3 (vertical axis) vs. charge in counter 2.

of the two, due to the very close proximity of the 2 scintillating tiles, we

evaluate the efficiency of the other one as the ratio of above-pedestal signals to the total for the events left by the former cut. These proximity-defined efficiencies are of $(84 \pm 1)\%$ and $(91 \pm 1)\%$ for counters 2 and 3 respectively. We attribute the difference in efficiencies to the different working point of the 2 MPPC's, which were identically biased at 69.5 V.

Fig. 4 shows the charge spectrum for counter 1 ($V_{bias} = 72.0\,\mathrm{V}$) in units of "pixels", for 1, 2, and 3-MIPs events. Fitting these data to Landau

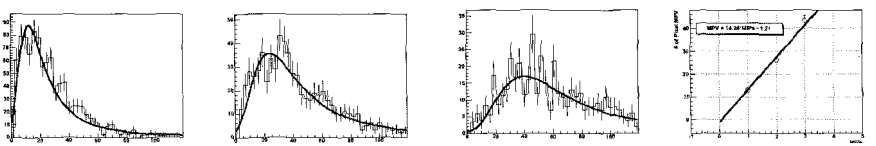

Fig. 4. From left to right: charge spectra in "pixel" units (see text) for 1-, 2-, and 3-MIPs events, and MPV vs. number of MIPs.

distributions we obtain the Most Probable Values (MPV's) depicted in the rightmost plot of Fig. 4 against the number of MIPs. The points show good linearity with an intercept close to 0. The most probable number of pixels per MIP is 14.

4. First results from the cosmic ray test

Our equipment is also set up to take data with cosmic rays, the trigger being given by the coincidence of two scintillators. After the test at the BTF discussed in the previous sections, the RPC-based tracker has been optimized to yield slightly better efficiency and spatial resolution $\mathcal{O}(1)$ mm; a temperature probe was also integrated in the DAQ system. The electronic noise is slightly worse ($\sim 20\,\mathrm{fC}$ vs. $10\,\mathrm{fC}$) than at the BTF test, due to reduced shielding of the experimental hall. This figure, however, is still adequate with respect to the typical charge of 300 fC in an MPPC pixel.

Using the RPC tracker we can define a fiducial region were cosmic muons should impinge on the MPPC's; the charge profiles as function of the track impact point on the scintillator tiles are shown in the left plot of Fig. 5. We studied the gain of our devices by fitting the pixel charge at different biasing voltages and temperatures. The gain variation with temperature for a particular biasing voltage in MPPC n.2 is shown in the middle plot of Fig. 5. The right plot of the same figure shows the gain as a function of V_{bias}, for temperatures T= 26 – 28°.

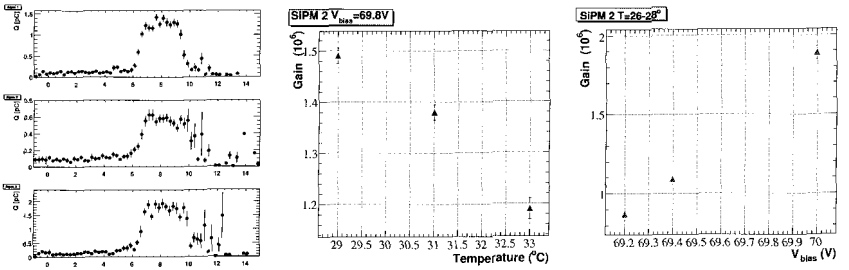

Fig. 5. Left: charge amplitude profile in the three counters as functions of the impact points predicted by the tracker; center: gain variation as a function of operating temperature in counter 2 for $V_{bias} = 69.8$ V; right: gain variation as a function of V_{bias} for T= 26 – 28°.

5. Conclusions and outlook

The results described in this paper, although still in an initial stage, encourage us to proceed with the study of the performance in a beam test and in cosmic rays of scintillation counters employing a SiPM as detection element: with a small and relatively fast assembly we have obtained charge spectra and efficiency, and a first very preliminary measure of linearity. We plan to increase the number of counters studied by an order of magnitude and to accumulate more data both at the BTF and in cosmic rays.

The authors of this paper wish to express their thanks to G. Mazzitelli and P. Valente, and all operators of the BTF facility for successful and time-efficient running, and to L. Daniello for his skill and dedication in the assembling of the MPPC counters.

References

1. B. Dolgoshein et al., Nucl. Instr. and Meth. A563 (2006) 368, and references therein.
2. For a recent review, see N. Otte in Proceedings of the SNIC April 2006 Symposium, SLAC, Stanford, available online at `http://www-conf.slac.stanford.edu/snic/default.htm`
3. G. Mazzitelli et al., Nucl. Instr. and Meth. A515/3 (2003) 516.
4. The present paper is about devices S10362-11-050U and S10362-11-025U, for a description and more types see for example `http://www.hahamatsu.it`.
5. A. Calcaterra et al., Nucl. Instr. and Meth. A565/2 (2006) 444.

MEASUREMENT OF THE DETECTION EFFICIENCY OF THE KLOE CALORIMETER FOR NEUTRONS BETWEEN 20 AND 174 MEV

P. GAUZZI and the KLONE Collaboration *

Università degli Studi La Sapienza *e Sezione INFN di Roma,*
Pl.e A.Moro, 5 - 00185 Rome, Italy
E-mail: paolo.gauzzi@roma1.infn.it

The detection efficiency of a KLOE calorimeter prototype to neutrons of kinetic energy of 21, 46 and 174 MeV has been measured by exposing it to the neutron beam of the The Svedberg Laboratory, Uppsala. The measurement of the neutron detection efficiency of a NE110 scintillator provided a reference calibration. At the lowest trigger threshold, the ratio between the calorimeter and scintillator efficiency ranges from 2.5 to 3.2.

Keywords: KLOE, neutrons, efficiency

1. Introduction

Detection of neutrons with energies from a few to hundreds MeV is usually performed with organic scintillators. The elastic scattering of neutrons on the hydrogen atoms produces recoil protons which originate a visible response. Typical efficiency is of ~ 1 %/cm of scintillator thickness [1]. When inserting an organic scintillator in a high Z material there is a sizeable cross-section for elastic and inelastic neutron interactions which could originate a large production of secondary particles and consequently increase the detection efficiency.

*The KLONE collaboration is: M.Anelli[a], G.Battistoni[b], S.Bertolucci[a], C.Bini[c], P.Branchini[d], C.Curceanu[a], G.De Zorzi[c], A.Di Domenico[c], B.Di Micco[d], A.Ferrari[e], S.Fiore[c], P.Gauzzi[c], S.Giovannella[a], F.Happacher[a], M.Iliescu[a,f], M.Martini[a], S.Miscetti[a], F.Nguyen[d], A.Passeri[d], A.Prokofiev[g], P.Sala[b], B.Sciascia[a], F.Sirghi[a].
Institutions: (a) Laboratori Nazionali di Frascati, INFN, Italy, (b) Sezione INFN di Milano, Italy, (c) Università degli Studi "La Sapienza" e Sezione INFN di Roma, Italy, (d) Università degli di Studi "Roma Tre" e Sezione INFN di Roma Tre, Italy, (e) Fondazione CNAO, Milano, Italy, (f) IFIN-HH, Bucharest, Romania, (g) The Svedberg Laboratory, Uppsala University, Sweden.

The KLOE calorimeter [2] is a high sampling lead scintillating fiber calorimeter mainly designed to detect low energy photons. It has been operated from 1999 to 2006 at the Frascati ϕ-factory DAΦNE, showing good resolutions and high efficiencies for electrons and photons detections and also good capability for $\pi/\mu/e$ separation.

A KLOE study of kaon interactions in the apparatus walls showed high efficiency for neutrons of $\sim$ 20 MeV thus suggesting a more systematic study of the calorimeter response to neutrons. Apart from the possibility to develop compact, inexpensive, fast and highly efficient neutron counters, this work has also been motivated by the prospects of the search of deeply bounded kaonic nuclei [3] and of the measurement of the neutron electromagnetic form factors in the time-like region [4] in the DAΦNE upgrade under study at Frascati.

This is being done by dedicated test beams and by detailed simulation.

2. Measurement at the The Svedberg Laboratory

The calorimeter prototype is composed of $\sim$ 200 layers of 1 mm diameter blue scintillating fibers glued inside thin grooved lead layers of 0.5 mm thickness. The final structure has a fiber:lead:glue volume ratio of 42:48:10 resulting in a density of $\sim$ 5 g/cm^3. The external dimensions **x,y,z** are $13 \times 65 \times 24$ cm^3 representing the horizontal direction, the coordinate along the fiber direction and the calorimeter depth, respectively. The calorimeter is readout at both fiber ends by photomultipliers, PMs, to reconstruct the **y** coordinate by time difference and it is organized in four planes in **z** for the first 16.8 cm. Each plane is subdivided in 3 columns in **x** originating cells of 4.2×4.2 cm^2. Larger readout elements are used in the rear part of the calorimeter. The readout elements in the lower (upper) end are called side A (B). Each PM signal is split in three replicas to measure the charge and time and to create two signals for the trigger as the analog sum of the PM charges of the first four planes. The discriminated analogic sums , $\Sigma A, \Sigma B$, are used for triggering. A reference counter for efficiency was built with a 5 cm thick bulk of NE110, of 10×20 cm^2 transversal dimensions, by coupling it at the two ends to two PM's. To trigger on the scintillator, the discriminated PM signals, $S1$ and $S2$, were used.

We have run two experiments at the The Svedberg Laboratory (TSL) high-energy neutron facility [5], one at high energy (174 MeV) in October 2006 and the other one at low energy (21.8 ,46.5 MeV) in June 2007. The cyclotron protons were directed on a ^{7}Li target generating a neutron beam geometrically shaped by an iron collimator block with a 2 cm di-

ameter cylindrical hole. The neutron energy spectrum is dominated by a peak at few MeV below the primary proton energy and a long tail down to thermal neutrons. The neutron beam time structure was in phase with the cyclotron RF which had a period of $\sim$ 45 (54) ns for high(low) energy running. The beam emerged from the collimator at 3 m distance from the target. To grant full beam acceptance we have run at distances of 5-6 m from the target and centered the beam in the middle of our detectors. Low intensity neutron beams of few kHz/cm^2 has been required to minimize the probability of double neutron counting. The neutron rate has been measured by an Ionization-Chamber Monitor, ICM, with an absolute accuracy of 10(20) % at high(low) energy.

All discrimination and trigger signals were formed with NIM logic while the DAQ was based on VME standard. We wrote on disk at a maximum rate of 1.7 kHz. The trigger was defined either as $\Sigma A \cdot \Sigma B$ or $SA \cdot SB$ and phase locked with the cyclotron RF replica. The common start to the TDC was provided by the trigger while the stop was given by delayed discriminated signals. Typical runs consist of $\sim 0.5 - 1.5 \times 10^6$ events.

For a given trigger threshold, assuming full beam acceptance and no background, the efficiency of the detector D ($CALO$ or $SCINT$) to the overall neutron spectrum has been determined according to the formula:

$$\varepsilon_D = \frac{R_{DAQ}^{(D)}}{R_n F_{live}} \tag{1}$$

where $R_{DAQ}^{(D)}$ is the acquired rate for the detector D, F_{live} is the fraction of DAQ live time, and R_n is the the neutron rate estimated by the ICM. The incoming neutron rate, R_n, is instead given by:

$$R_n(\text{kHz}) = \pi r^2 \cdot R_{ICM} F_{CAL} / F_{peak} \tag{2}$$

where R_{ICM} is the ICM rate counted by our scalers, F_{CAL} is the ICM calibration scale (flux/rate), F_{peak} is the fraction between peak neutron and total events, and $r = 1$ cm is the collimator radius.

The measured efficiencies at high energy for the reference counter and for the calorimeter are shown in Fig. 1 as functions of the trigger threshold. For the scintillator, the horizontal scale has been calibrated by fitting the spectra obtained with a β source. For the calorimeter, each cell has been calibrated by using minimum ionizing particles and then applying the energy scale determined with electron and photon beams [6].

This preliminary analysis shows that the calorimeter neutron detection efficiency ranges between 40 and 50 % at the lowest threshold. It corresponds to a sizeable enhancement with respect to the expected 15% based

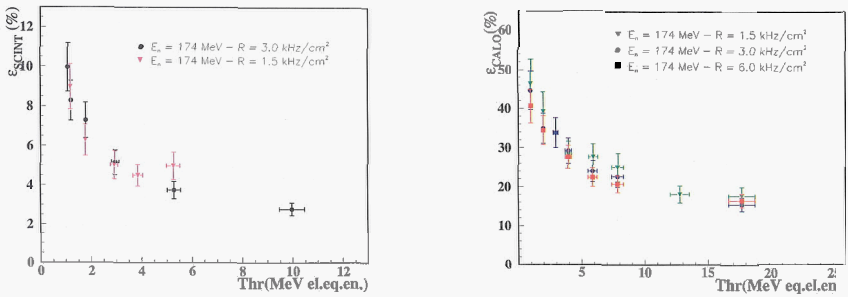

Fig. 1. Dependence on trigger threshold of: (left) ε_{SCINT}, (right) ε_{CALO} for the high energy data set.

on the amount of scintillator only as extrapolated by our measurement. We also performed a first preliminary analysis of part of the data taken at low energy. In these samples, we have to consider also the presence of a sizeable contribution of events coming from the area surrounding the collimator and that have been roughly measured (with an error as large as 100%) by the TSL experts. An horizontal scan outside the collimator area has been performed with the same Thin Film Breakdown Counter [5] used for the absolute calibration of the beam flux. Although the halo flux in the ICM area is only 4-5% of the signal flux, we have first indications of a very broad ($\sigma = 14 - 16$ cm) distribution of the halo when projected over the calorimeter or scintillator surfaces. Preliminary corrections of 0.80±0.13 (0.90±0.09) have been evaluated and applied to R_{CALO} (R_{SCINT}). The resulting efficiency at low energies for the calorimeter is then reported in Fig. 2.left. The distribution of $R_\varepsilon = \frac{R_{CALO}}{R_{SCINT}} F_L$, where $F_L = 8/5$ is the ratio between the equivalent scintillator thickness in the calorimeter and the reference counter, is shown as a function of the threshold in Fig. 2.right. This ratio is almost independent from any halo, and is sizably greater than one for all the three measured data sets.

To understand the origin of the efficiency enhancement, we have used the FLUKA [7] program for a detailed simulation of the calorimeter structure and of the neutron beam line. The primary reason for the efficiency enhancement appears to be the huge inelastic production of neutrons on the lead planes. For neutrons in the high energy peak (174 MeV), the probability to have an inelastic interaction is 31.4 % on the lead, compared to 7.0 % on the fiber and 2.2 % on the glue. A neutron shower-like effect is observed

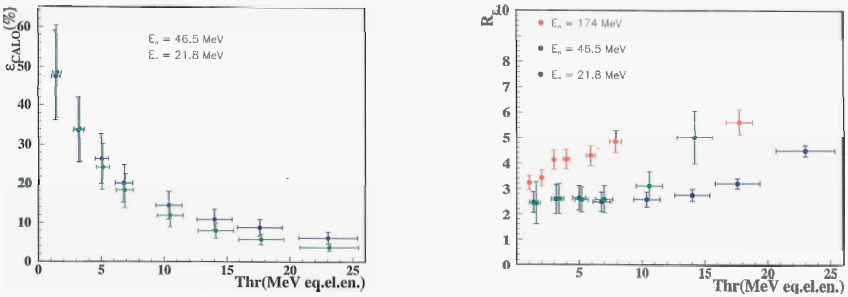

Fig. 2. **Calorimeter efficiency at low energies (left)**. Ratio of the counting rates normalized to the same active material thickness (right).

which originates many low energy neutrons and other secondaries, out of which protons and photons directly contribute to the visible response. The fine geometrical structure of the calorimeter and the high sampling frequency are also contributing to the high neutron detection efficiency. In average the simulation predicts a detection efficiency ranging between 50 and 60 %.

References

1. A. Del Guerra *Nucl. Instr. and Meth.* **135**, 337 (1976).
2. M. Adinolfi et al., KLOE Collaboration, *Nucl. Instr. and Meth. A* **482**, 364 (2002).
3. LOI_MARCH_AMADEUS.pdf in http://www.lnf.infn.it/lnfadmin/direzione/roadmap/.
4. loi_06.pdf in http://www.lnf.infn.it/conference/nucleon05/FF.
5. A.V. Prokofiev et al., PoS (FNDA2006) 016 (2006); A.V. Prokofiev et al., *Journal of Nuclear Science and Technology, Supplement* **2**, 112 (2002).
6. A. Antonelli et al., *Nucl. Instr. and Meth. A* **354**, 352 (1995).
7. A. Fassò et al., CERN 2005-10 (2005), INFN/TC_05/11, SLAC-R-773; A.Fassò et al., eConf C0303241 (2003), arXiv:hep-ph/0306267.

The CMS-HF Forward Calorimeter Commissioning

E. Gülmez

On behalf of CMS-HCAL Collaboration

Physics Department, Boğaziçi University,
Bebek, Istanbul, 34342 TURKEY
E-mail: gulmez@boun.edu.tr

The CMS HF Calorimeter was the first detector to be lowered into the cavern at UX5. It was placed in the garage position during the lowering of the rest of the big CMS pieces. The commissioning of the hardware parts is continuing, especially integrating the HF and completing the monitoring systems, such as, online laser, LED and radioactive source monitoring. Also a special monitor system for the radiation damage (raddam) of the quartz fibers is being implemented. Calibration measurements of the calorimeter had already started even before the lowering. Progress in the calibration work and current plans for the HF calorimeter during the low luminosity run will be summarized.

Keywords: Calorimetry, LHC, CMS, Forward Calorimetry, Diffractive Physics, Luminosity, Commissioning

1. Introduction

CMS forward hadron calorimeter (HF) was designed [1–3] to detect the forward particles with eta values from 3 to 5 for optimizing the identification of those processes that produce forward jets, especially processes involving heavy Higgs and SUSY particles. The Calorimeter will also improve the determination of the missing transverse energy.

The two cylindrical HF units for each end of the detector are 1.65 m long and have an active radius of 1.4 m. The HF is a sampling calorimeter with plastic clad quartz fibers embedded into iron absorber. Each unit is composed of 18 20-degree slices. Each slice has 24 towers. There are long (1.65 m) and short fibers (1.43 m) in each tower to sample the energy in hadronic and electromagnetic showers, respectively. Light produced in each fiber through Cerenkov radiation goes into its own photomultiplier tube (PMT). Phototubes used in the HF were selected and tested at the University of Iowa PMT test station [4–6].

Commissioning of the HF involves completing the hardware installation and lowering the detector into the underground cavity and also the calibration of the detector.

2. Calibration

Before lowering the CMS detector into the cavern, there was much work done above ground, especially in calibration. In 2004, during test beam studies, several slices of the HF were tested with electron, pion, and muon beams at energies varying from 30 GeV to 300 GeV. There were also tests with a ^{60}Co wire-source [7–9]. During these tests, data were taken while the wire-source was being inserted into the detector. Charge collection as a function of the position of the source inside the absorber provides information for the energy calibration of the detector. There is a clear difference in the number of counts between the wire-source positions inside the detector and at park position. These tests were carried out to understand the performance of the various hardware parts, absorber, PMTs, fibers, read-out boxes, etc. During 2006, LED and wire-source data were taken to understand the calibration constants of the calorimeter. With the experience gained in the 2004 Test Beam study, the analysis of the 2006 LED and wire sourcing data improved the calibration constants. These measurements were done in the Building 186 and then the HF was moved to SX5 prior to the lowering into the cavern [10]. Radiation damage tests also continued [11,12]. The online radiation damage monitoring system was tested and finalized for the installation into the HF detector. The lifetime of the PMTs were addressed earlier and the measurements done at the UI PMT test station showed that their photocathodes could provide more than 3000 C of charge with less than 50% degradation in the gain at 1100V [6].

Charge collected in the single photoelectron (SPE) peak provides one of the constants. This calibration constant is obtained using a single photoelectron spectrum of the phototubes accumulated with a source or an LED [7–9]. This is directly related to the PMT gains. PMTs were tested extensively at the University of Iowa PMT test station before installing them in the HF detector. Among these tests there were also measurements of the relative gains at 1100 V for all the PMTs [6]. PMT gains as a function of HV for over 200 PMTs were also measured. Using these gain values and the 2004 test beam data, it is shown that the relative gains measured at the University of Iowa PMT test station and the gains obtained from the SPE data are highly correlated [7]. These relative gain values were used to group the PMTs to be installed in different tower positions (the lower the

gains are, the closer to the beam they are). It also confirms the reliability of using the SPE peaks in monitoring the gains with the LED system. In the earlier versions of the CMS Software package the calibration constant related to the integrated charge per photo electron is taken as 5.92 and 4.35 fC/p.e. for the long and short fibers, respectively. On the other hand, measured values for the nominal PMT HV of 1100 V is about 16.75 and 11.06 fC/p.e. for the long and short fibers, respectively [13].

The energy calibration in terms of the amount of charge collected per unit energy of a particle is done with the help of the wire sourcing and the measured value is about 0.21 and 0.34 GeV/fC for the long and short fibers, respectively [13]. Of course, some of these measurements were done at higher HVs than the nominal value of 1100 V. All the results were extrapolated to the nominal HV value. These studies helped us understand the operation of the QIE elements, pedestals, and the noise in the system. Specific values for these quantities were determined from the data. Consistency of the calibration constants means that the three calibration constants: charge per photo electron, energy per unit charge and photo electrons produced per GeV energy, should result in unity when they are multiplied all together. (The first two are determined from the data. The third could be estimated from the standalone shower library. A better estimate would be to use the unity condition mentioned.) A value of 0.25 p.e. per GeV means the constants are consistent within 10% [12,13].

3. Lowering into the cavern

The CMS HF Calorimeter was the first detector to be lowered into the cavern at UX5 in Fall 2006 (Figure 1) [14]. The HF detector was lowered into the cavern without any problem and placed in the garage position during the lowering of the rest of the big CMS pieces. Various cables, patch panels, and other electrical and mechanical pieces were either installed or in the process of being installed. In general, the commissioning of the hardware parts is continuing. Especially, integrating the HF and completing the monitoring systems, such as, online laser, LED, and radioactive source monitoring. Also a special online monitoring system for the radiation damage (raddam) of the quartz fibers is being implemented.

Both HF units are the first detectors ready for the overall data taking test (Global Run). During the Global Run and also other data acquisition test runs, the HF system has been tested for overall debugging of the data acquisition and also to determine the pedestals of all the channels. LED runs were also used to make sure that there are no missing channels.

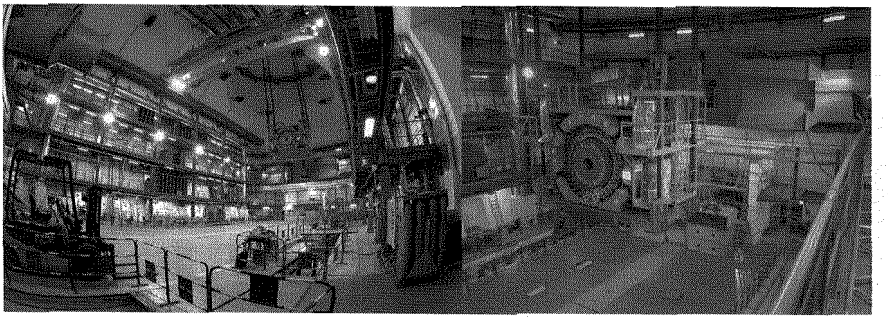

Fig. 1. HF+ was lowered into the cavern UX5 in November 2006.

4. Conclusion

It is not likely that there will be any data taking runs during 2007 due to problems in the LHC. For the same reason, the schedule for the next year is also uncertain. The HF calorimeter is considered to be a candidate for luminosity measurements, in addition to some possible ideas about diffractive physics.

Acknowledgements

Valuable comments and helpful suggestions of A. Penzo, K. Cankocak, T. Yetkin, and Y.Onel are greatly appreciated. This work was partially supported by Turkish Atomic Energy Agency (TAEK), Bogazici University Scientific and Technological Research Fund (06B302), and Bogazici University Foundation. I also thank the University of Iowa for its support.

References

1. "Design, Performance and Calibration of the CMS Forward Calorimeter Wedges," CMS HCAL Collaboration, **CMS NOTE-2006/044, (2006).**
2. "Radiation-Hard Quartz Cerenkov Calorimeters," U. Akgun and Y. Onel, *"AIP Conference Proceedings of XII International Conference on Calorimetry in High Energy Physics," edited by S. R. Magill and R. Yosida, pp 282-289(2006).*
3. "Present Status of CMS HF Quartz Fiber Calorimetry," Y.Onel, *"Proceedings of 10th International Conference on Calorimetry in High Energy Physics, CALOR 02, March 25-29, 2002, Cal Tech, CA, USA," ed. by R.Y. Zhu, World Scientific, pp. 504-520(2002).*
4. "Comparison of PMTs From Three Different Manufacturers for the CMS-HF Forward Calorimeter," U. Akgun, E. W. Anderson, A. S. Ayan, E. Gülmez,

M. Miller, Y. Onel, I. Schmidt, ve D. Winn, IEEE TRANSACTIONS ON NUCLEAR SCIENCE, **51, (2004)1909.**

5. "Selection and Testing of 2000 Photomultiplier Tubes for the CMS-HF Forward Calorimeter," E. Gülmez, U. Akgun, A. S. Ayan, P. Bruecken, F. Duru, A. Mestvirishvili, M. Miller, J. Olson, Y. Onel, I. Schmidt, E. W. Anderson, and D. Winn, *Proceedings of IMTC 2004 Instrumentation and Measurement Technology Conference, Como, Italy, May 18-20, 2004, (2004)1870.*
6. "Complete tests of 2000 Hamamatsu R7525HA phototubes for the CMS-HF Forward Calorimeter, U. Akgun, A. S. Ayan, P. Bruecken, F. Duru, E. Gülmez, A. Mestvirishvili, M. Miller, J. Olson, Y. Onel, I. Schmidt, Nucl. Instr. And Meth. **A550, 145(2005).**
7. "Comparison of PMT relative gains measured at the University of Iowa and at CERN," K. Dindar, M. Deliomeroglu, E. Gülmez, U. Akgun, A. S. Ayan, Y. Onel, and I. Schmidt, CMS Internal Note **IN-2005/045, (2005).**
8. "Variation of relative gains as a function of HV for the Hamamatsu R7525HA PMTs used in the HF Forward Calorimeter," E. Gülmez, U. Akgun ve Y.Onel, CMS Internal Note **CMS IN-2005/06, 2005.**
9. "Using single photoelectron spectra in the calibration of the CMS-HF Calorimeter," E. Gülmez, *et al., Proceedings of 9th ICATTP Conference on Astroparticle, Particle, Space Physics, Detectors and Medical Physics Applications., World Scientific pp 339-342 (2006).*
10. "Calibration of HF," Taylan Yetkin, All US CMS Meeting - 4/27/2007.
11. "Radiation Hardness Studies of high OH- Content Quartz Fibers Irradiated with 24 GeV Protons," J. P. Merlo and K. Cankocak, Proceedings of 9th ICATTP Conference on Astroparticle, Particle, Space Physics, Detectors and Medical Physics Applications., World Scientific, pp 838-842(2006) and "Radiation-hardness studies of high OH- content quartz fibres irradiated with 24 GeV protons," J-P Merlo and K. Cankocak, CMS Conference Report **CR-2006/005, (2006).**
12. "Radiation-hardness measurements of high OH- content quartz fibres irradiated with 24 GeV protons up to 1.25 Grad." K. Cankocak, N. M. Bakirci, S. Cerci, E.Gülmez, J.P. Merlo, Y. Onel, F. Özok, I. Schmidt, N. Sönmez, CMS Note, **CMSNOTE 2007/003 (2007).**
13. "HF Calibration status, Michal Szleper, DPG Meeting CMS Week, 02/25/07.
14. "HF: Status and Program, Aldo Penzo, Project Manager's Meeting, CMS Week, 02/26/07.

UPDATE ON THE HADRON CALORIMETER OF THE CMS EXPERIMENT AT CERN*

VASKEN HAGOPIAN

Department of Physics, Florida State University
Tallahassee, Florida, 32306, USA

The construction and assembly of the Hadron Calorimeter is now complete and commissioning is almost done. The hadron calorimeter inside the CMS detector is made of scintillator and copper absorber covering the $|\eta|$ range of 0.0 to 3.0. The forward calorimeter, made of quartz fibers and iron absorber, covers the $|\eta|$ range of 3.0 to 5.0. Recent test beam effort is aimed at understanding of the performance of the Hadron Calorimeter in conjunction with the lead tungstate crystal Electromagnetic Calorimeter. Recent test beam results using production modules help us improve resolution. Work has started on several upgrade fronts for the high luminosity LHC.

1. Introduction

The Hadron Calorimeter[1] is a major sub-system of the CMS detector. The Hadron Calorimeter will detect jets, single hadrons and μ's. It is required for the discovery of the Higgs between masses of 100 to 1,000 GeV and for searches of Dark Matter associated with large missing energy. Astronomical measurements of the rotation curves of galaxies as well as the distribution of microwave background of the sky require the existence of Dark Matter. The calorimeter is crucial in measuring missing energy for dark matter searches as well as for many standard physics processes. The Hadron Calorimeter (HCAL) Central Barrel (HB) is 9 meters long, one meter thick and 6 meters in the outer diameter. The HB consists of two half barrels of 18 wedges each made of brass and scintillator. The two End Caps (HE) are also made of brass and scintillator, with a diameter of 0.8 to 6.0 meters and a thickness of 1.8 meters. Both HB and HE are inside the 4-tesla solenoid coil. The η-ϕ segmentation of HB and HE is 0.087×0.087, except near $\eta = 3.0$, where the size of the segmentation is doubled. The depth segmentation for HB is one unit while for HE; it varies from one to three. The two forward calorimeters (HF) are made of quarts fibers imbedded in iron cover the η range of 3.0 to 5.0. HB is only 6.5 interaction lengths thick at η=0 and will not contain the particle showers, so additional scintillators are placed inside the muon barrel system, outside of the solenoid coil, to measure the HB energy leakage. This system is called HO and both Monte Carlo studies and test beam

*For the CMS HCAL Collaboration (about 35 institutions and 250 physicists)

results show that it improves the energy measurement by reducing the tails of the energy distribution substantially. To correct for the radiation damage at η above 2.0, HE has extra longitudinal segmentation to allow correction for signal loss. The light from scintillators is transported by means of plastic fibers to the Hybrid Photo Detectors (HPD's) for HB, HE and HO. The signals for HF are Cherenkov radiation in quartz fibers read by conventional phototubes[1]. The essential electronics elements are QIE's (charge integrator and encoder), HTR's (trigger and readout module) and event builder card (DCC- data concentrator card)[2,3]. The Hadron Calorimeter is now installed in the CMS detector and is being commissioned (connecting cables, optical fibers, cooling pipes, etc). It will be ready to take data on day one of the experiment.

The electromagnetic calorimeter (ECAL) in front of HCAL is made of finely segmented lead tungstate scintillating crystals contributing one interaction length to hadron calorimetry. This combination is highly non-compensating, which poses unique problems in energy measurement and resolution.

2. Test Beam Effort in 2006 and 2007

Recent test beam effort measured the response of the calorimeter as a function of particle identity and energy with the goal of improving the energy measurement resolution. The test beam used production modules to account correctly for the material between ECAL and HCAL. Figure 1 is the test beam setup in CERN with electron beams of 2 to 150 GeV, muon at 100 to 225 GeV and hadrons of 2 to 300 GeV. The normal beam line is limited to momentum above 10 GeV/c. In order to obtain even lower energies a tertiary beam was constructed with time of flight and Cherenkov counters to identify each beam particle. In 2006 the barrel HCAL and ECAL were deployed on the rotating table. In 2007 the endcap HCAL and ECAL were used and the analysis is now in progress. Below are some of the results from the 2006 test beam. Each detector was calibrated by 50 GeV electrons. Figure 2 shows the detector response as a function of beam momentum for various particles. As expected the response to π^+ and π^- are very similar. K^+ and K^- (not shown) are also similar to π's. The low momentum proton and antiproton response is not the same as pions because p and pbar available energy for a particular beam momentum is different from π's. In addition p and pbar interactions in the calorimeter produce different amounts of π^0s and both ECAL and HCAL detector response to photons (and electrons) is substantially different from charged π's.

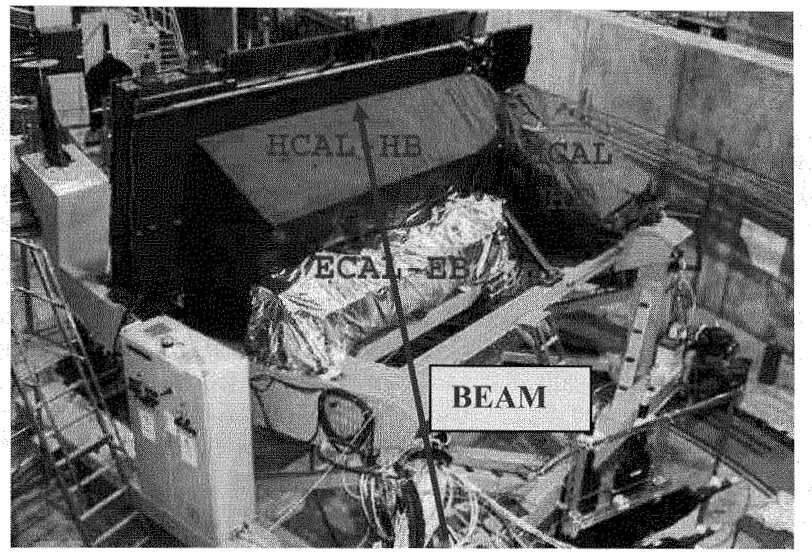

Figure 1. HCAL-ECAL test beam in CERN H2 area.

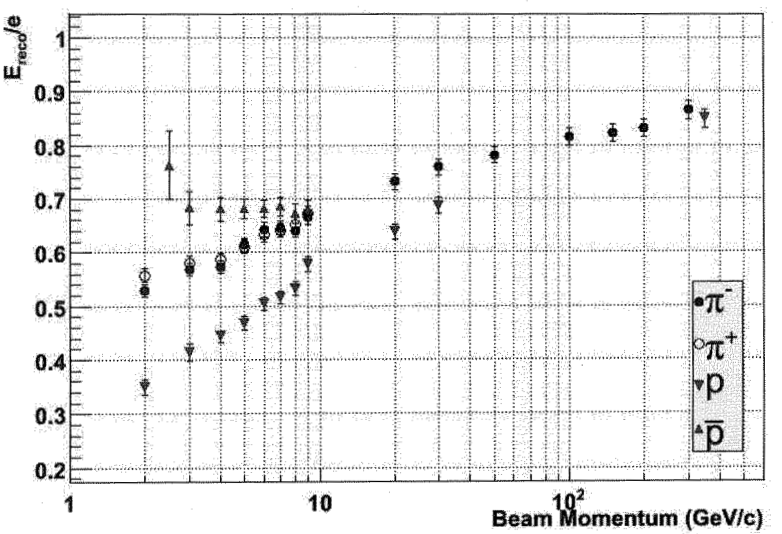

Figure 2. ECAL+HCAL response to various particles and beam momenta. The detectors were calibrated by 50 GeV electrons.

3. Energy Calibration

The energy calibration is a multidimensional puzzle. HCAL and ECAL can be calibrated individually but the response together is very different to different particle species. In addition the outer calorimeter HO beyond the magnet coil cannot be independently calibrated, but only in combination with ECAL + HCAL barrels. Both HB and EB were calibrated by 50 GeV electrons. Pions deposit less energy than electrons as seen in Figure 3(a). To calibrate ECAL and HCAL together, first HB only π/e response is corrected in ECAL. Next using the corrected HCAL energies and the known beam momentum in the test beam, π/e for ECAL is estimated and corrected. After these corrections are applied, the response for the combined ECAL+HCAL system still depends nonlinearly on the ECAL energy fraction. Finally, this non linearity is corrected. Figure 3(a) shows the energy correction and figure 3(b) shows the energy resolution with and without correction. A substantial improvement is noted with the stochastic term dropping from 130% to 90%.

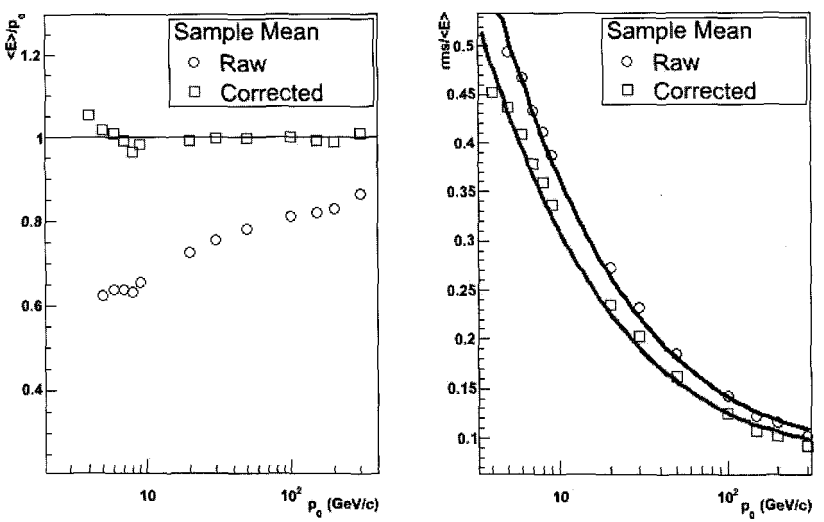

Figure 3. Measured energy and resolution σ/p versus p before and after correction.

4. HCAL Upgrades

Even though the CMS detector has not taken any collider data, the HCAL collaboration is already considering upgrades, especially for the SLHC that will

have a much higher luminosity. At the higher luminosity the scintillators will suffer unacceptable radiation damage near $|\eta| = 3$ and other parts of the detector may also suffer. Several upgrade efforts are progressing at this time and will be reported elsewhere.

5. Conclusion

The CMS HCAL Collaboration has designed, built, installed and is now commissioning the HCAL system. Detector components have been placed in the CERN external test beams and the performance matches the design. HCAL has already observed cosmic muons during global commissioning of the detector. It will be ready on day one of collider data taking.

Acknowledgments

A detector of this complexity cannot be designed and built without the effort of many people, who have worked very hard during the past decade. We also would like to acknowledge the many funding agencies that have supported this effort including the US DOE, US NSF, Hungarian RMKI-KFKI, and The Scientific and Technical Research council of Turkey, Turkish Atomic Energy Agency, Bogazici University Research Fund and the Russian Ministry of Education and Science and the Russian State Committee for Atomic Energy.

References

1. HF is the topic of another contribution to this conference and will not be presented in this paper.
2. THE HADRON CALORIMETER OF THE CMS EXPERIMENT AT THE LARGE HADRON COLLIDER. V. Hagopian, For the CMS HCAL Collaboration. Proceeding of the 9th International Conference on Astroparticle, Particle, Space Physics, Detectors and Medical Physics Applications, Como, Italy, 17-21 Oct 2005. Ed. Barone, Borchi, Gaddi, Leroy, Price, Rancoita and Ruchti. Published by World Scientific Press pp 348 – 352 (2006).
3. DESIGN, PERFORMANCE AND CALIBRATION OF THE CMS FORWARD CALORIMETER WEDGES. G. Bayatian, et al. CERN-CMS-NOTE-2006/044, Feb 2006. Submitted to European Journal of Physics.

STATUS AND PERFORMANCE OF THE ALICE/PHOS ELECTROMAGNETIC CALORIMETER*

MIKHAIL IPPOLITOV, ANDREY VASIL'EV†

Russian Research Center "Kurchatov Institute", Kurchatov sq.1, 123182 Moscow, Russia

The PHOS is a high resolution electromagnetic calorimeter in the ALICE experiment at the LHC. The PHOS is dedicated for measurements of gammas and neutral mesons in a wide dynamic range with high energy and spatial resolutions. The PHOS is subdivided into 5 independent rectangular modules. The module is segmented into 3584 detection channels (64x56 matrix). Each channel consists of a 22x22x180 mm^3 lead-tungstate crystal, coupled with 5x5 mm^2 avalanche photo diode. The first PHOS module was assembled, commissioned and tested with 2 GeV/c electrons at CERN on the T10 PS secondary beam-line.

1. Introduction

The Large Hadron Collider (LHC) at CERN is designed to produce collisions of hadrons and nuclei at extremely high energy.

ALICE (A Large Ion Collider Experiment) [1] is an experiment at the LHC optimized for the study of heavy-ion collisions at a centre - of - mass energy ~5.5 TeV/nucl. The prime aim of the experiment is to study in detail the behavior of matter at high densities and temperatures. At these conditions the creation of a new state of matter, called quark - gluon plasma (QGP), in which quarks and gluons behave almost as free particles, is expected.

One of the most direct ways to explore QGP properties are direct thermal photons because they do not interact with surrounding matter. Direct photons contribute only small part of the total photon yield while the dominant part of final photons comes from final hadrons, mainly from π^0 and η. Direct thermal photons, emitted from QGP in thermal equilibrium, dominate in energy range up to few GeV [2-3]. It is expected, that ALICE will collect sufficient number of Pb + Pb events so that statistical error will be small and one can expect extraction of thermal direct photons in the range below 10 GeV/c. Direct

* This work was supported by Russian Federal Atomic Energy Agency and Federal Agency of Science and Innovations

† Work was partially supported by INTAS grant Nr 03-52-5747

photon measurements in ALICE experiment will be performed with the dedicated electromagnetic calorimeter PHOS (PHOton Spectrometer) [4].

The second physics objective of the PHOS is investigation of jet quenching and neutral jet identification. It requires measurements of high energy π^0 and η mesons.

High particle multiplicities up to ~8000 charged particles per unity of pseudorapidity are typical for central lead on lead collisions at LHC [1-3]. It requires the use of very dense and heavy material having small radiation length and Moliere radius as a medium for detector. Lead tungstate scintillating crystals were chosen for the PHOS detector. Indeed, this material is suitable for construction compact and high granularity calorimeters – it is a dense (density 8.3 g/cm^3, Moliere radius 2 cm, radiation length 0.89 cm), fast and relatively cheap. Its emission spectrum is well adapted to the spectral sensitivity curves of the most commonly used photo detectors.

2. The PHOS description

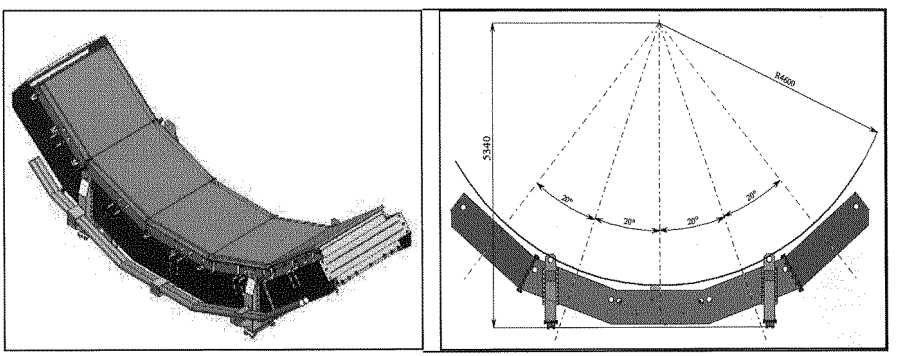

Figure 1.Schematic view of the ALICE/PHOS electromagnetic calorimeter. From the left: modules situated on the PHOS cradle, from the right: front view of the PHOS cradle.

The photon spectrometer PHOS (see figure 1) in the ALICE experiment [4] is designed to detect, identify and measure with high resolution the 4-momenta of high energy inclusive photons in a wide energy range from 200 MeV up to 100 GeV. In addition it is able to detect neutral mesons through their 2 photon decay channels. The PHOS will be positioned on the bottom of ALICE set-up at a distance 460 cm from the interaction point and will cover pseudorapidity range $-1.2 < \eta < 1.2$ and 100° in azimuthal angle. Its total area is approximately 8 m^2 and crystals weigh is 12.5 t. All the PHOS modules will be situated on the top of the PHOS cradle (see figure 1).

2.1. *Detection unit*

The PHOS consist of 17920 detection channels of $PbWO_4$ crystals. Detection channel is presented in figure 2. Each crystal is coupled to 5x5 mm^2 Hamamatsu S-8148(S-8664-55) avalanche photodiodes (APD). APD was mounted in low noise charge sensitive preamplifiers (CSP) – see figure 2. The crystal is 22x22x180 mm^3 in dimensions (20 radiation length in depth, one Moliere radius in perpendicular to the length direction). The APD was glued to crystal with glue with refractive index n_d=1.7. To improve light collection crystals are wrapped with TYVEK. To increase the light yield and decrease noise, crystals with APD and CSP will be operated at a temperature -25°C. The temperature stability will be within 0.2^0 C. At this temperature APD has gain M=50 at HV ~320-350V, dark current less than 1nA and capacitance C less than 80 pF. The CSP has JFET 2SK932 in the input. The APD+CSP ENC noise equivalent is ~500e^-, CSP sensitivity 0.833 V/pC, linearity range 0.1-5V and 64 mW power consumption.

Crystals were produced by North Crystals Company, Apatity, Russia. All crystals were tested in RRC "Kurchatov Institute" and around 11 000 crystals at present were accepted for PHOS assembling.

Monitoring of the channels was carried out by LED monitoring system with long term stability better than $1.2x10^{-3}$.

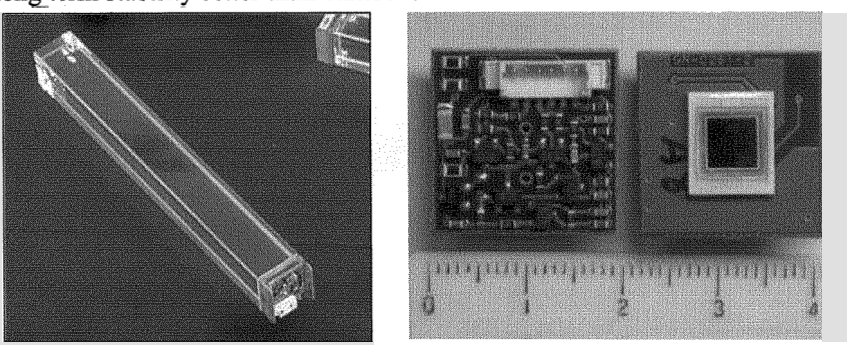

Figure 2. On the left: detection channel, on the right charge-sensitive preamplifier with APD

2.2. *Module*

The PHOS is subdivided into 5 separate rectangular modules. Each module (see figure 3) is segmented on 3584 detection channels (56x64). The module subdivided in 2 separated and thermo insulated volumes - cooled and warm volumes. The minimal mechanical unit in the module is a strip unit (see figure 3), consisting of 16 detection channels, grouped in 2x8 matrix. All 224 strip units in the module will be located in the cooled volume.

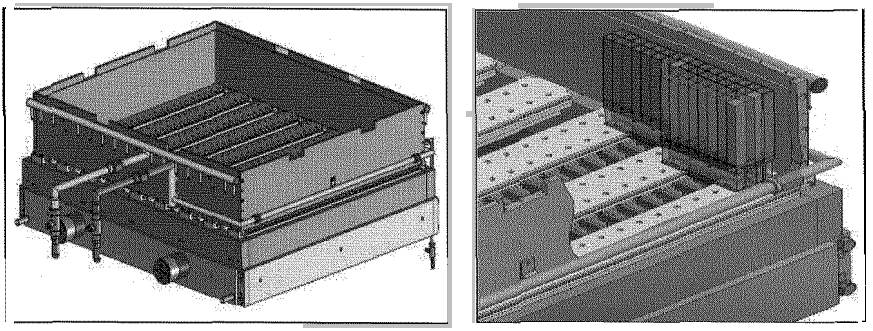

Figure 3. On the left: general view of the open PHOS module without thermoinsulation and crystal array; on the right: strip units in the working position inside the module.

2.3. *Front end electronics*

Front-end electronics (FEE) [5] is situated inside the warm volume. The 32 readout channels FEE card serves 2 strip units. Important feature of FEE is a programmable high voltage (HV) bias system, which deliver HV for each APD with a precision 0.2 V. Voltages are delivered from a common input voltage 390 V. Dual gain (gain ratio 16/1) semigaussian shapers together with 10-bit sampling ADC ensure 14-bit dynamic range up to 80 GeV. The sampling frequency is selectable between 1 and 20 MHz. The ADCs are Altro-16 chips, developed for ALICE TPC[6], with multi-event buffer, zero suppression, pedestal memory and processing scheme. Each FEE card deliver fast 2x2 OR signals for Trigger Region Unit cards (TRU). Each TRU card generate L0 and L1 trigger signals from 14 FEE cards which corresponds to array of 16 x 28 crystals.

3. Beam-test results

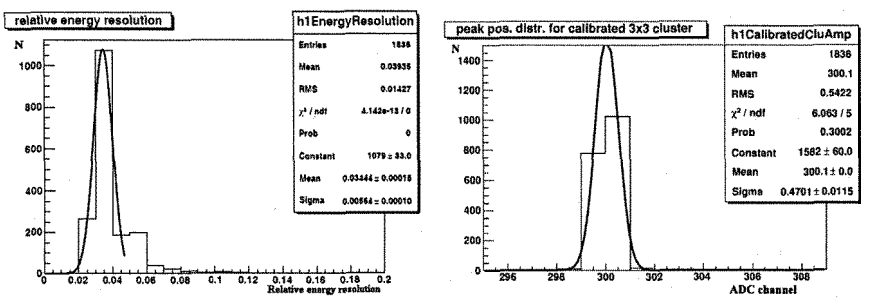

Figure 4. On the left: distribution of relative energy resolution at 2 GeV; on the right- distribution of peak position of different 3x3 cluster sums.

In 2006 the first PHOS module was assembled and tested with 2 GeV/C electron beam at the CERN PS T-10 beam-line. The crystal matrix was cooled down to -17°C. Gains of ~2000 channels were defined. In calibration process high-voltage for each channel was selected by iteration procedure. After 3rd set of HV 0.16% precision in 3x3 sums peak position was achieved (see figure 4). The mean value of APDs high voltage was 350 V.

The energy resolution was measured in the momentum range 1-5 GeV/C for small subset of channels and is consistent with the previous measurements [6]. The distribution of energy resolutions for large amount of detectors measured at 2 GeV/C is presented in figure 4.

4. Conclusion

The production of the ALICE/PHOS electromagnetic calorimeter is going well. The first (from five) PHOS module is assembled, tested and ready for installation in the ALICE experiment. The PHOS cradle was produced in Czech Republic and already installed in ALICE setup.

Assembling of modules 2 and 3 is already started. Some mechanical and electronics parts for assembly of modules 2 and 3 either ready for delivery to CERN or already delivered. FEE cards is in production and will be delivered to CERN by end of 2007. New cooling system was produced and ready for delivery to CERN.

Production and assembly of modules 4 and 5 are scheduled for years 2008-2010.

Acknowledgments

The authors wish to thank all the members of the ALICE/PHOS group for their extremely hard work to ensure progress and success of the PHOS project.

References

1. ALICE TP, CERN/LHCC 95-71, LHCC/P3, 15 December 1995
2. ALICE PPR, Vol. I, CERN/LHCC 2003-049, 7 November 2003.
3. F.Arleo et al., hep-ph/0311131, Hard Probes in Heavy Ion Collisions at the LHC, p.367-493
4. PHOS TDR, CERN/LHCC 99-4, Alice TDR 2, 5 March 1999
5. H.Muller et al., NIM A518 (2004) 525-528
6. R.Esteve Bosch et al, Proc. IEEE NSS/MIC, November 2002, Norfolk, Virginia
7. D.Aleksandrov et al., NIM A550(2005) 169-184.
8. M.Ippolitov, A.Vasil'ev in Proc. 9th ICATPP Conference, Villa Olmo, Como, Italy 17-21 October 2005, p.353

PERFORMANCE OF THE ATLAS LIQUID ARGON FORWARD CALORIMETER IN BEAM TESTS

P.KRIEGER*

Department of Physics, University of Toronto,
Toronto, Ontario M5S 1A7, Canada
E-mail: krieger@physics.utoronto.ca

A beam test of three final ATLAS Forward Calorimeter modules (FCal) is described. The data were taken at CERN in the summer of 2003, using electron and hadron beams with energies from 10 to 200 GeV. The response of the FCal to single electrons and hadrons is derived.

1. The ATLAS Forward Calorimeter

ATLAS is one of two general purpose detectors that will take data at the Large Hadron Collider at CERN, starting in 2008. The experimental programme includes searches for the Higgs Boson and searches for supersymmetry. For the former, in certain mass regions, the tagging of energetic forward jets is important, For the latter, calorimetric hermeticity is crucial. The ATLAS Liquid Argon Forward Calorimeter (FCal) is designed primarily for the detection of jets, either tagging jets, or jets that would otherwise escape detection and degrade the resolution on missing transverse energy. The ATLAS FCal is a liquid argon calorimeter that is integrated into the endcap cryostat that also houses the electromagnetic and hadronic endcap calorimeters, extending the calorimetric coverage from $|\eta|$ of about 3.1 to 4.9. This region of the detector is close to the beam pipe, where the particle flux from minimum bias events places severe constraints on the calorimeter design. In particular, liquid argon gaps must be very narrow, to avoid problems due to positive ion buildup that would distort the electric field in the gap, degrading the detector performance.[2] Since constructing very narrow LAr gaps in a parallel plate structure is difficult, this constraint is accommodated by use of an electrode structure with thin annular LAr gaps

*On behalf of the ATLAS Forward Calorimeter Group

oriented parallel to the beamline. Individual gaps are formed by a structure consisting of a copper tube, acting as the cathode, and an absorber rod acting as the anode. This rod is positioned concentrically, and electrically isolated, by a helically-wound radiation hard plastic (PEEK) fibre. The FCal consists of three modules: the FCal1, FCal2 and FCal3, which sit one behind another inside a support tube that forms a structural part of the endcap cryostat. The FCal1, which sits closest to the interaction point, is designed for EM calorimetry. It has copper anode rods, and the 12,260 electrodes are positioned within a copper matrix made of a stack of copper plates with precision drilled holes to accept the electrode tubes. The FCal2 and FCal3 modules are designed for hadronic calorimetry and are made primarily of tungsten, with 10,200 and 8224 electrodes, respectively. A copper skeleton is used, consisting of electrode tubes installed between two endplates. The space between the tubes is filled with specially formed tungsten alloy slugs and the anode rods are made of pure tungsten. The LAr gaps in the FCal1, 2 and 3 are 250 μm, 375 μm and 500 μm, respectively.

In each module, electrodes are positioned within the absorber matrix in an hexagonal array, with a spacing optimized for energy resolution. This leads to a detector with a fine lateral segmentation that can be exploited in the energy reconstruction.[3] The module structure is illustrated in figure 1, which shows a schematic partial view of the front face of the FCal1 module alongside a photo of the rear face of the FCal3 module. For high voltage distribution and signal readout, electrodes are ganged together in groups of 4, 6, or 9 on the FCal1, FCal2 and FCal3, respectively, using interconnect

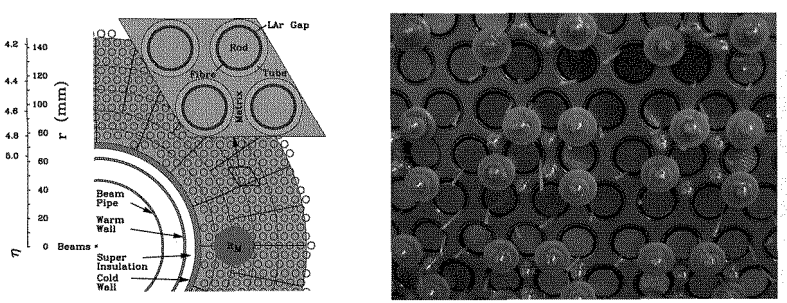

Fig. 1. Forward calorimeter electrode arrangement. The left-hand plot shows a schematic view of a portion of the front face of the FCal1, also illustrating a single electrode group and indicating the size of the Molière radius in this device. The right-hand figure shows a photograph of the rear (non-readout) face of a hadronic (FCal3) module. Also visible are PEEK retention washers and the ends of the PEEK fibres.

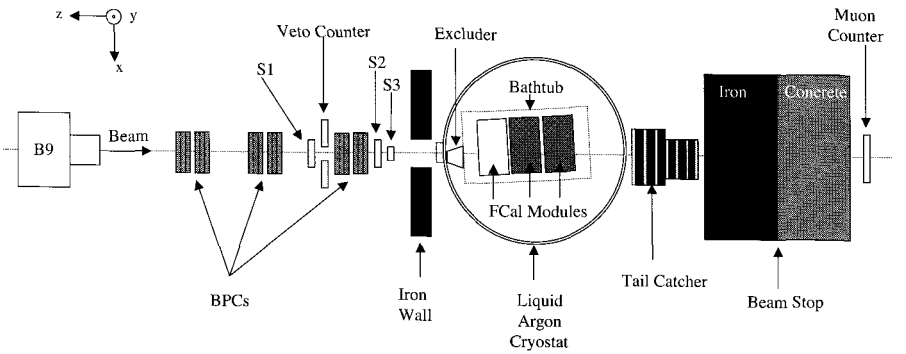

Fig. 2. Beamline instrumentation used for FCal calibration testbeam

boards at the readout face of each calorimeter module, which are installed onto pins inserted in the ends of the anode rods. For most channels, four such groups are summed on a transformer summing board before the signals are sent to the cryogenic feedthrough.

2. Forward Calorimeter Beam Test

Beam test data were taken using the three production FCal modules for the C-side of ATLAS. The tests were done in the H6 beamline at CERN, with electron and hadron beams of energies from 10 to 200 GeV. Because the support tube that houses them in ATLAS was not available, the modules were placed on a purpose-built stand. The FCal readout used prototype electronics, with 25 sampling of the shaped signals, as in ATLAS. Signal reconstruction was done with the optimal filtering method[4] as will be the case in ATLAS.

The beamline instrumentation is illustrated in figure 2. Coincidence of the three scintillators, $S1$, $S2$ and $S3$ was used for triggering. Three stations of beam positioning chambers (BPCs) provided tracking information. Additional counters provided other information for use in offline analysis, for example, for beam-cleaning similar to that employed previously.[5]

Electron energy reconstruction was done by summing the energy of all cells within an 8 cm radius cylinder centred on the beam particle impact point, which was reconstructed using information from the BPCs. Noise contributions were accounted for by using knowledge of the average noise for each channel, run-by-run, obtained from analysis of random-triggered events. For each energy sum, a noise sum over the same channels was

also performed, allowing the noise contribution, which varied from 12.5 to 15.5 ADC counts, to be removed when fitting the resolution function. Signal shapes are non-Gaussian due to the calorimeter response being dependent on the impact point relative to the closest electrode;[5] this effect is the dominant contribution to the constant term in the resolution function. Energy spectra are fitted with a double-Gaussian, which provides a good description of the signal, and a contribution for residual hadron contamination, the shape of which is taken from the analysis of hadron data taken at the same energy. The response linearity and resolution are shown in figure 3. The response is linear to within 0.5%. The linearity fit yields the EM scale factor for the FCal1. Previous measurements of the relative response of FCal1 and FCal2 prototypes,[5] along with simulations, set the EM scales for the FCal2 and FCal3, which are needed as the starting point for hadronic calibration. The result of a fit to the energy resolution, using the function $\sigma_E/E = a/\sqrt{E} \oplus b$, is overlaid. The fit values for the sampling and constant terms agree well with the results of the prototype tests, and with expectations for ths design.

For pions, the energy sum was done within a 16 cm radius cylinder. After correcting for the relative EM scales of the three modules, the total hadronic energy is summed using a flat weighting technique, with one weight per module.Weights were derived from the 200 GeV sample by minimizing the resolution with the constraint that the average reconstructed energy equal the beam energy. Noise was dealt with as described earlier and varied between 5 and 6 GeV. The reconstructed energy for 200 GeV pions is shown in figure 4, alongside a plot of the corresponding noise-subtracted energy resolution. Overlaid, in each case, are results of an alternative weighting scheme, also used in past analyses,[3,6] which exploits the fine transverse

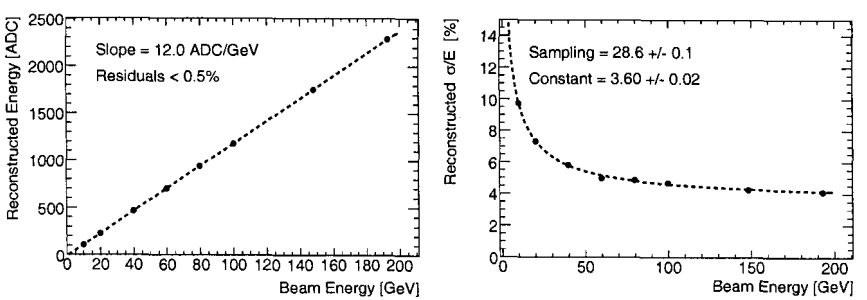

Fig. 3. ATLAS Forward Calorimeter performance for electrons: linearity and resolution.

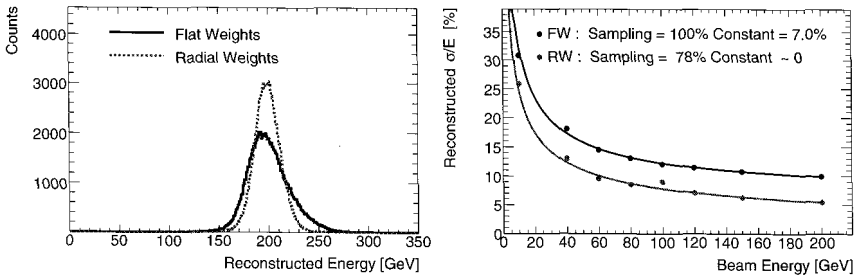

Fig. 4. ATLAS Forward Calorimeter performance for hadrons.

segmentation of the FCal modules. In this "radial weighting" scheme, cell energies at the appropriate EM scale are summed using weights that are a function of the radial distance from the beam impact point. The results of the resolution fits are shown on the plot; the potential improvement, with radial weighting, is apparent. However, the ATLAS requirement of $100\%\cdot\mathrm{GeV}^{1/2}/\sqrt{E} \oplus 10$ % is achievable with the simpler technique.

For all results, the statistical uncertainties are relatively small, while the systematics remain under investigation.

3. Acknowledgments

I would like to express my thanks to my colleagues in the Forward Calorimeter group, as well as to those members of the ATLAS Liquid Argon group, particularly in the cryogenics and electronics communities, who provided necessary expertise during the beam tests.

References

1. ALEPH,DELPHI,L3 and OPAL Collaborations, *Phys. Lett.* **B 565** (2003) 61.
2. J.P.Rutherfoord, *Nucl. Inst. Meth.* **A 482** (2002) 156.
3. A.Savine, in *Proceedings of CALOR2000*, Frascati Physics Series, 2000.
4. W.E.Cleland and E.G.Stern, *Nucl. Inst. Meth.* **A 338** (1994) 467.
5. J.C.Armitage et al., *Electron Signals in the Forward Calorimeter Prototype for ATLAS.* Submitted to *J. Inst.*
6. M.Schram, in *Proceedings of the* 9^{th} *ICATPP Conf.*, World Scientific, 2006.

THE MEASUREMENT OF SPECTRAL CHARACTERISTICS AND COMPOSITION OF RADIATION IN ATLAS WITH MEDIPIX2-USB DEVICES*

M. CAMPBELL[A], Z. DOLEŽAL[B], D. GREIFFENBERG[C]. E. HEIJNE[A], T. HOLY[D], J. IDÁRRAGA[E], J. JAKŮBEK[D], V. KRÁL[D], M. KRÁLÍK[F], C. LEBEL[E], C. LEROY[E,†], X. LLOPART[A], G. LORD[E], D. MANEUSKI[G], O. OUELLETTE[E], V. SOCHOR[F], S. POSPÍŠIL[D], M. SUK[B], L. TLUSTOS[A], Z. VYKYDAL[D], I. WILHELM[B]

[A]*CERN, CH-1211 Genève 23, Switzerland*

[B]*Faculty of Mathematics and Physics of the Charles University in Prague, V Holesovickach 2, CZ-18000, Praha 8, Czech Republic*

[C]*Freiburger Materialforschungszentrum, Albert-Ludwig-Universität Freiburg, Stefan-Meier-Strasse 21, D79104 Germany*

[D]*Institute of Experimental and Applied physics, Czech Technical University in Prague, Horská 3a/22, CZ-12800 Praha 2 - Albertov, Czech Republic*

[E]*Université de Montréal, Montréal (Québec), Canada H3C 3J7*

[F]*Czech Metrology Institute in Prague, IIR, Radiova, CZ-10200, Praha 10, Czech Republic*

[G]*Glasgow University, Department of Physics and Astronomy, Glasgow G12 8QQ, Scotland, UK*

This work was carried out within the CERN Medipix Collaboration

* The work of the Montreal Group was financially supported by NSERC, Canada. This work has been also financially supported by the Czech Ministry of Education, Youth and Sports in frame of the long term research program MSM 6840770029 and 1P04LA212.

† Corresponding author: Claude Leroy (Claude.Leroy@cern.ch)

A network of devices to perform real-time measurements of the spectral characteristics and composition of radiation in the ATLAS detector and cavern during its operation is being built. This system of detectors will be a stand alone system fully capable of delivering real-time images of fluxes and spectral composition of different particle species including slow and fast neutrons. The devices are based on MEDIPIX2 pixel silicon detectors that will be operated via active USB cables and USB-Ethernet extenders through an Ethernet network by a PC located in the USA15 ATLAS control room. The installation of 14 devices inside ATLAS (detector and cavern) is in progress.

1. Introduction

The precise evaluation of spectral characteristics and composition of radiation in and around the ATLAS detector is necessary for understanding the performance of various detector systems and to predict their useful lifetimes. The results of these measurements may prove to be an important feedback for data analysis and improvement of data taking strategy, particularly in the early phase of operation. In this project, it is proposed to install a system of a minimum of 14 detecting devices. This system is capable of providing quantitative real-time information on the fluxes and flux distributions of the main radiation species in the experiment including slow and fast neutrons.

Three tasks can be identified from an operational point of view [1]:

1. Measurement of the radiation field inside the ATLAS detector volume.
2. Measurement of background radiation in the experimental hall and in the detector surroundings.
3. Measurement of the real performances of the different sub-detectors (e.g., "particle/energy" leakage, punch through, etc.).

The proposed system is based on a network of MEDIPIX2-USB devices connected to a PC located in the USA15 control room.

2. The Medipix2-USB device

The Medipix2 hybrid silicon pixel device was developed by the Medipix2 Collaboration. It consists of a semiconductor detector (active part) bonded to the readout chip Medipix2 [2]. This position-sensitive device is composed of a pixellated 300 μm thick semiconductor detector with 256x256 pixels, each of 55 μm x 55 μm area. Each pixel is connected to its respective readout chain (preamplifier, double discriminator and digital counter) integrated on a readout chip. The assembled hybrid pixel device is glued on a printed circuit board (motherboard). The detector is controlled by the Universal Serial Bus (USB) [3] through the Pixelman software package [4] using a PC (or a laptop). Settings of the pulse height discriminators provide noise suppression and at the same time

determine the input energy of radiation to be detected. The pixel counter counts interacting quanta of radiation falling within the preset energy window. Thus, only particles with preselected energy are counted. Hence, the devices can be used for position and energy sensitive (from 5 keV up to tens of MeV) spectroscopic detection of radiation. They are also capable of counting particle fluxes at rates in excess of GHz per cm^2. The Medipix2-USB device is routinely used as a small, portable, PC controlled device. The read-out speed of 5 Mbits/s (5 fps) is suitable for real-time applications. The device can be externally triggered.

The Medipix2-USB devices can operate in two modes [5]. The first, so-called "counting mode" is usable for high count rates (above $5x10^3$ events per second per cm^2). In this mode, the number of interactions in individual pixels is counted at different threshold settings yielding the fraction of radiation with the corresponding ionizing power. Calibration of the devices enables the conversion of the individual counts measured into fluxes of respective types of radiation and dose rates. The second mode is the "tracking mode", applicable at low detection rates. It is based on "electronic visualization" of tracks and traces of individual quanta of radiation in the sensitive silicon volume.

3. Medipix2-USB in ATLAS

A network of Medipix2 devices will be installed within the ATLAS detector and cavern [1]. Four devices will be located between the moderator (JM) shielding and Liquid Argon (LAr) calorimeter (two on each of the two sides of the ATLAS detector). Similarly, two devices on each side will be installed along the TileCal (scintillator/iron hadronic calorimeter). Four devices will be placed near the ATLAS muon chambers and two devices will be located near the very forward (JF) shielding.

The ATLAS detector is designed to study events with very specific topologies and the trigger menu is, of course, optimized for investigation of the Standard Model and beyond. The ATLAS detector is basically blind to the low energy radiation with possibly rather isotropic distributions. The low energy radiation that tells about the radiation environment within the ATLAS detector and in the cavern has to be measured by other means. The Medipix2 device will fulfill that role, being used for the real-time measurement of the composition and spectroscopic characteristics of the radiation field inside the ATLAS detector and cavern. The detection capabilities of the Medipix2 device can be selective regarding the energy of the incoming radiation. Also, the different types of particles can be determined from studies of the pattern of identifiable-shaped

tracks left by the particles in the detector. Electrons, muons, charged hadrons and neutrons can be differentiated using a Medipix2 device [1].

The interactions with surrounding materials of particles produced by the high rate head-on collisions of protons at high luminosity at the LHC will yield large amounts of neutrons covering a large spectrum of energies, from fast to thermal. A precise knowledge of the neutron field at various locations in ATLAS is desirable as neutrons contribute to radiation damages inflicted to electronics and equipment, to the background signal in different ATLAS sub-detectors, and to the generation of SEE effects possibly affecting the electronic devices and control functions operating in the ATLAS environment. The neutron detection capabilities of the Medipix2 device have been demonstrated for the detection of thermal or very slow neutrons with LiF converter [6] and for fast neutrons (or neutrons with energy higher than hundreds of keV) with CH_2 converter [7]. The possibility to record in real-time the microscopic details of muon trajectories and pion interactions has been demonstrated for Medipix2-USB devices [8].

4. Medipix2-USB detection capabilities

Medipix2 devices have demonstrated specific capabilities for particle identification relying on pattern recognition techniques. Images of Medipix2-USB device responses are characteristic of illuminations by specific radiation, resulting from different charge deposition mechanisms.

4.1. *Electrons, photons, α-particles*

As an example, Figs. 1a)-1c) show the measurement of electron, alpha particles, and photons with a Medipix2-USB device. Calibration of the energy thresholds was performed with photons of low energies, from ^{241}Am sources and X-rays [9], making all their deposition in a single pixel. The photons detection efficiency is about 80% at 12 keV and about 1% at 150 keV. As the electrons detection efficiency is 100%, the photon efficiency curve as a function of photon energy follows the absorption curve of photons in silicon [9].

4.2. *Neutrons*

The Medipix2 device can be used for neutron detection. For detection of thermal or very slow neutrons [6], the silicon sensor is partially or totally covered with a neutron absorbing material which converts the energy into radiation detectable in silicon.

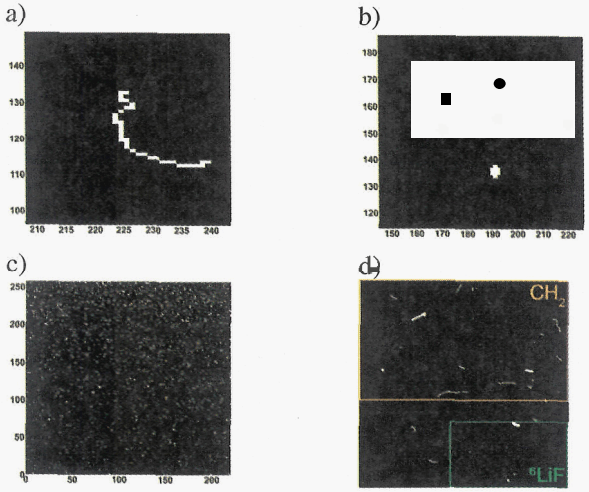

Fig.1 Measurement of a) electrons, b) alpha, c) photons, and d) neutrons with a Medipix2-USB

A film of ^{6}LiF is often used and exploits the reaction n + ^{6}Li → α (2.05MeV) + ^{3}H (2.72 MeV). The lower part, right hand side, of Fig. 1d) is covered with a LiF film and detects thermal and slow neutrons. The thermal neutron detection efficiency is ≤5% for a thick converter (~7mg/cm^2, [7]). For fast neutrons (or neutrons with energy higher than hundreds of keV) detection, the silicon sensor is partially or totally covered with a film of hydrogen-rich material, such as polyethylene (CH_2) [7]. The neutrons are detected by recoil protons in the elastic scattering of neutrons on nuclei in a CH_2 film converter covering the detector. In Fig. 1d), the top half area is covered with a CH_2 film, 1.3 mm thick, and detects fast neutrons. One can clearly recognize long and rather thick tracks (Bragg peak energy deposition) of recoiled protons and big tracks and clusters generated via ^{28}Si(n,α)^{25}Mg, ^{28}Si(n,p)^{28}Al nuclear reactions in the body of the silicon detector. Electrons and photons are also seen although the huge background due to gamma rays which always accompany neutrons can be highly suppressed with threshold setting. The detection efficiency is ≤10^{-4} from recoil proton and of about 10^{-5} from direct (n,α), (n,p) interaction in silicon 300 μm thick. The uncovered part of the device serves for subtraction of the electrons, photons and α-particles signal background from the neutron signals.

4.3. *Muons and pions*

The capability of Medipix2-USB to allow the real-time measurement of microscopic details of muon trajectories and pion interactions from a hadronic

beam has been demonstrated at CERN-SPS ([8] first reported measurement) for devices placed parallel to the particles of a beam. The muons resulting from the decay of pions produce typical minimum ionizing particle (mip) trails in the sensor. With the absence of nuclear interactions for these mips, the tracks are continuous and monotonously tilted downwards, crossing the rows of pixels of the detector matrix with regular stretches of overlapping rows. Incoming particles (mostly pions) produce interaction patterns characterized by large energy deposition around a vertex with recoil fragments remaining in the detector sensitive volume traveling all the way in the pixel matrix or traveling along a short path before leaving the sensitive volume depending on recoil angles. All particles have additional hit pixels along the trail which indicate large energy transfers or delta rays generation. By analyzing such pixel trail, the precision on track coordinates of the corresponding particles can be significantly improved, possibly down to submicrometer scale.

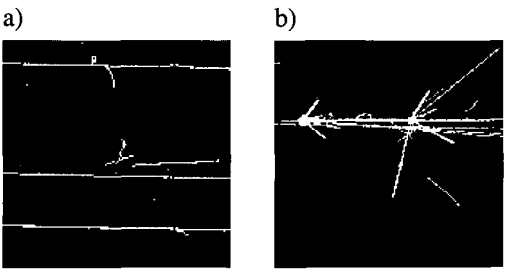

Fig. 2 Meaurement of a) muons and b) pions with a Medipix2-USB device at CERN-SPS.

5. Charge sharing

The shape of a track in a Medipix2-USB device depends on the nature of the interaction in the detector sensitive volume and is influenced by the charge sharing effect. This effect among adjacent pixels originates from the lateral spreading of charges from the interaction of an ionizing particle in the silicon detector. The response to single particle hit in the form of a cluster of adjacent pixels can be effectively used to improve the spatial resolution of the incident particle and then exploited for tracking. Alpha particles were used to understand the effect as they deposit large amounts of energy in a very confined space. The energy dependence of the charge sharing induced by α particles incident on a Medipix2-USB device shows a monotonic increase of the cluster size with the α-particle energy as α-particles of higher energy create a larger number of pairs resulting in an increased charge sharing [10].

A model [10] was presented for understanding the charge sharing using the Medipix-2-USB response to incident strongly ionizing particles such as α-particles. The lateral spread can be explained in terms of plasma effect, charge column erosion and funneling on top of diffusion and drift process. Figure 3 illustrates the lateral spread (cluster radius) of the charge from the interaction of 3.0 MeV and 4.2 MeV α-particles as a function of the bias voltage and the result of the fit based on the model [10, 11].

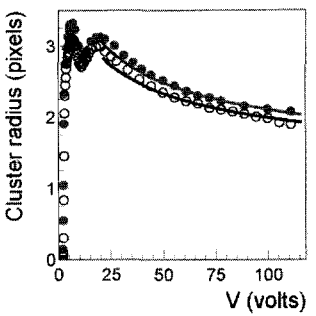

Fig. 3. Results of charge sharing model (full lines) applied to data taken with 3.0 MeV (○) and 4.2 MeV (●) alpha particles entering the back side of the Medipix2-USB detector. The agreement is excellent.

6. Conclusions

The Medipix2-USB device allows the visualization of particle signature morphologies that are characteristic of illuminations by a specific radiation. The images reflect the different charge deposition mechanisms. Then, the Medipix2-USB device, with its pattern recognition capabilities allows the detection of a variety of particles produced in proton-proton collisions at LHC in counting and tracking modes. The installation of a network of Medipix2 devices within the ATLAS detector and cavern is in progress. A number of general tasks are identified for such a system, the most important being the analysis of radiation background (neutrons, X-rays, γ-rays, ions,...). The proposed system will become a precious device to provide real-time information about the content of the LHC generated background radiation and to validate background radiation simulation studies, starting to give relevant information from the first particle collision onwards. Moreover, the same system will be used to monitor the evolution of activation during beam-on periods and to monitor the background during beam-off periods. Elements of the system will serve during data taking to provide information on the composition of cascades, possibly leaking out of calorimeters. As the dynamic range of the system is very large it will also be

used where relatively high dose rates are expected. On-line measurement with Medipix2-USB devices will also effectively contribute to the estimates of SEE effects possibly affecting the electronic devices, circuits and control functions operating in the ATLAS experiment conditions.

References

1. M.Campbell, C. Leroy, S. Pospisil, M. Suk, MPX-USB-ATLAS-2006, ATL-R-MA-0001; and T. Holy, J. Jakubek, S. Pospisil, J. Uher, Z. Vykydal, Z. Doležal, M. Suk, I. Wilhelm, M. Campbell, E. Heijne, X. Llopart, L. Tlustos, C. Leroy, B. Mikulec, M. Nessi, C. Buttar, V. O'Shea, K. M. Smith, both available at https://edms.cern.ch/document/815615/1, CERN (2006)
2. Z.Vykydal, J. Jakubek, S. Pospisil, Nucl. Instr. and Meth. A563 (2006) 112.
3. T. Holy, J. Jakubek, S. Pospisil, J. Uher, D. Vavrik, Z. Vykydal, Nucl. Instr. and Meth. A563 (2006) 254.
4. Z. Vykydal, J. Jakubek, T. Holy, S. Pospisil, Proceedings of the 9th IATPP Conference, Villa Olmo, Como 2005, Italy, 779.
5. Medipix Collaboration: http://medipix.cern.ch/MEDIPIX.
6. Jakubek J., Holy T., Lehmann E., Pospisil S., Uher J., Vacik J., Vavrik D., Nuclear Instruments and Methods in Physics Research, A 546 (2005) 164-169; Jakubek J., Holy T., Pospisil S., Rypar V., Uher J., Vykydal Z, Proceedings of Nuclear Science Symposium IEEE 2005 published on CDROM, 23-29th October 2005, Puerto Rico, USA.
7. J. Uher, J. Jakubek, U. Köster, C. Lebel, C. Leroy, S. Pospisil, R. Skoda, Z. Vykydal, Proceedings of the 9th IWORID Conference, Erlangen, submitted for publication in Nucl. Instr. and Meth. A (2007).
8. R. Field and E. Heijne, Nucl. Instr. and Meth A577 (2007), 595.
9. M.Fiederle, D. Greiffenberg, J. Idarraga, J. Jakubek, V. Kral, C. Lebel, C. Leroy, G. Lord, S. Pospísil, V. Sochor, M. Suk, Proceedings of the 9th IWORID Conference, Erlangen, submitted for publication in Nucl. Instr. and Meth. A (2007).
10. M. Campbell, E. Heijne, T. Holy, J. Idarraga, J. Jakubek, C. Lebel, C. Leroy, X. Llopart, S. Pospisil , L. Tlustos, Z. Vykydal, Proceedings of the 9th IWORID Conference, Erlangen, submitted for publication in Nucl. Instr. and Meth. A (2007).
11. M. Campbell, E. Heijne, T. Holy, J. Idarraga, J. Jakubek, C. Lebel, C. Leroy, X. Llopart, S. Pospisil , L. Tlustos, Z. Vykydal, Proceedings of the Nuclear Science Symposium IEEE 2007, Hawaii, USA.

PERFORMANCE OF THE CMS ELECTROMAGNETIC CALORIMETER

N. PASTRONE on behalf of the CMS ECAL Group

I.N.F.N. Torino, Via P. Giuria 1, 10125 Torino, Italy
E-mail: nadia.pastrone@to.infn.it

The Large Hadron Collider at CERN will allow the study of pp interactions at a center of mass energy of 14 TeV. The main physics goals of the Compact Muon Solenoid (CMS) experiment are the discovery of the Higgs boson and the search for new physics. Experimental conditions and physics goals set demanding constraints on the Electromagnetic Calorimeter (ECAL), made of about 76000 Lead Tungstate scintillating crystals, to be able to achieve a high precision in photon and electron energy measurement. ECAL performance has been studied using an electron test beam, before final commissioning in the experiment. The most relevant results are presented.

Keywords: Calorimetry; CMS

1. Challenges and choices

The Electromagnetic Calorimeter[1] (ECAL) of CMS has been designed to optimize the detection of the most promising low mass Higgs two photons decay channel. It is a hermetic homogeneous calorimeter made of lead tungstate ($PbWO_4$) scintillating crystals, mounted in a central barrel, closed by two endcaps, covering the full acceptance $|\eta| < 3$.
The small Moliere radius (2.19 cm) and the short radiation length (0.89 cm) allow a compact design and high granularity inside the 4 T magnetic field of the experiment. 80% of the light is collected in the 25 ns LHC bunch crossing time. ECAL will be operated in a severe radiation environment, affecting crystal transparency. To follow and correct a variation of signal during LHC cycles, a fiber-distributed laser system monitors the light response of each crystal, with a stability of 0.1%. The relative low light yield of $PbWO_4$ ($\sim$50 photons/MeV) requires the use of photodetectors with internal gain. Avalanche Photo Diodes (APD) and Vacuum Photo Triodes (VPT) have been chosen respectively for the barrel and the endcaps, resulting in a yield of about 4.5 photoelectrons/MeV.

Innovative solutions were developed to place the front-end electronics and the trigger primitive generation on the detector with the advantage of minimizing external noise contribution, reducing the number of optical links to send data to the off-detector readout. High radiation tolerant custom ASICs have been designed in 0.25 μm CMOS technology to satisfy the demanding requirements of wide dynamic range, good resolution, high speed and low power dissipation. A dynamic range of 15 bit was obtained sending the signal in parallel to the three amplifiers ($\times$1, $\times$6, $\times$12) MGPA chip and choosing the highest not saturated digitized ADC signal, sampled at 40 MHz. The ADC outputs with the selected amplifier gain information (12+2 bits) for 25 crystals are stored into a pipeline waiting to be read out from DAQ, on receipt of the Level 1 trigger accept. On each group of 25 crystals, trigger primitives are generated and sent to the off-detector readout to be processed by the regional trigger system within the 3 μs latency of the on-detector data pipeline. The energy reconstruction over the wide dynamic range requires a good linearity and pulse shape matching across gains, while the correlated noise and crosstalk must be minimized. The electronic noise must not exceed 50 MeV/channel.

2. Test beam results

Extensive measurements were carried out with test beam in 2004 and 2006 on ten barrel supermodules (SM=1700 crystals), using electrons with energies between 20 and 250 GeV. In parallel, each of the 36 ECAL barrel SMs has been tested for inter-calibration purpose with cosmic muons. To properly take into account the light yield fluctuations, preliminary estimates of the start-up inter-calibration coefficients were obtained from laboratory measurements, test beam pre-calibration of some supermodules, and the commissioning of all supermodules with cosmic rays reaching an overall precision of about 2%, and up to 0.5% with electron [2].

2.1. *Detector response*

The amplitude A of the signal collected in each crystal channel is reconstructed using a digital filtering technique. A linear combination of many discrete time sample values S_i with weights w_i, $A = \sum_i w_i S_i$, is used to minimize the contribution of electronics noise. The determination of the optimal set of weights makes use of a representation $f(t)$ of the time development of the signal pulse as in Fig. 1 *left.*

The rise time of about 50 ns (two clock units) corresponds to 10 ns of crys-

tal decay time and 40 ns of MGPA shaping time. Real data are affected by (high frequency) noise correlations between time samples, while any low frequency (e.g. pick-up) noise is taken away by pre-sample measurements. The best results for test beam data have been obtained with a set of 3 + 5 weights, with 3 pre-sampling weights used to subtract pedestal noise on event-by-event followed by five consecutive digitization samples, as shown in Fig. 1 *left*. The measurement of the electronics noise is made by applying the amplitude reconstruction procedure to data (pedestal events) taken with a random trigger. The distribution of such noise measurements for a large number of individual channels gives a mean width $\sigma_{1\times1}$ of 41.5 MeV with a rms dispersion of 3.3 MeV. The calorimeter response is reconstructed by summing the energy deposits in matrices of either 3×3 (or 5×5 crystals), with crystal channels intercalibrated at gain 12 using 120 GeV electrons. A distribution of this measured summed noise gives a mean width $\sigma_{3\times3} = 127$ MeV (Fig. 1 *right*) and $\sigma_{5\times5} = 213$ MeV. This corresponds to, respectively, about 3 and 5 times the single channel noise, as expected in the absence of channel-to-channel correlated noise.

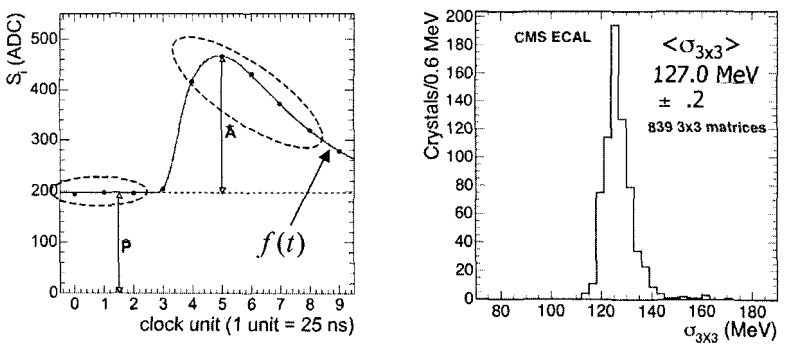

Fig. 1. Amplitude reconstruction with digital filtering technique(left). Noise reconstruction for 3×3 crystal arrays (right)

2.2. *Energy resolution*

A uniform energy measurement response of ECAL is essential for precision physics. The energy of electrons and photons reaching the ECAL will be reconstructed by summing the channels corresponding to matrices of 3×3 or 5×5 crystals centered on the crystal with the largest energy deposit. The variation of energy containment with the incident electron impact position

on the central crystal leads to a degradation of the energy resolution. The energy contained in such matrices depends on the position of the impact on the central crystal. To achieve the desired energy resolution and uniformity of response when the incident electrons are distributed over the full crystal front face a correction must be applied on event-by-event basis.
Central beam incidence is defined as electrons incident within an area of 4×4 mm^2 around the point of maximum shower containment. For such a small central area of incidence, there is no observable dependence on the incident position of the energy contained in the finite crystal array.

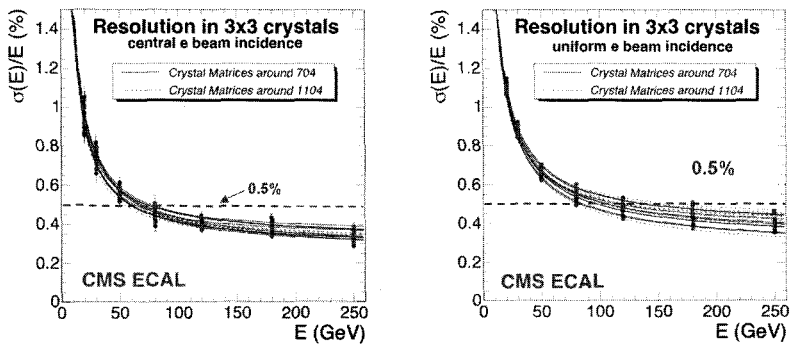

Fig. 2. Resolution obtained for 18 different crystals as a function of the energy reconstructed by summing in 3×3 crystals after applying a beam hodoscope cuts of 4×4 mm^2 (left) and for quasi-uniform incidence (right)

The energy dependence of the energy resolution, for data taken at 20, 30, 50, 80, 120, 180 and 250 GeV, is fitted by the following functional form:
$\left(\frac{\sigma}{E}\right)^2 = \left(\frac{S}{\sqrt{E}}\right)^2 + \left(\frac{N}{E}\right)^2 + C^2 \quad (E \text{ in } GeV)$
where S is the stochastic term, N the noise and C the constant term. The fit is performed with the noise term fixed for each crystal at the value measured in the pedestal runs.

In a crystal array of 3×3 crystals, a fractional energy resolution $\frac{\sigma}{E}$ with a stochastic term of $\frac{2.8\%}{\sqrt{E}}$, a noise term of $\frac{125}{E}$ and a constant term of 0.30%, with E in GeV, has been obtained, well in agreement with the designed values. The energy resolutions for 3×3 arrays centred on crystal 704 and 1104 are shown in Fig. 2, together with the fitted resolution function, both for central beam incidence *left* and for almost uniform incidence *right*. Compared to the results obtained for central incidence a slightly larger dispersion of the stochastic and constant terms is observed

for uniform incidence. The resolution nevertheless remains better than 0.5% for electrons of energy greater than about 100 GeV.

2.3. *Linearity*

During the 2006 test campaign the beam line was equipped to be able to measure the incident electron energy with high precision. The aim was to measure at best ECAL non-linearity as a function of the beam energy. Central events on each crystal with maximum energy deposit were selected, within an area of 4×4 mm^2 around the point of maximum shower containment. The reconstructed energy was obtained fitting the 5×5 array energy distribution with a gausssian with an exponential low energy tail. A preliminary differential non-linearity (deviations from a linear fit of reconstructed energy versus beam energy normalized to the largest measured energy) is shown in Fig. 3. The maximum deviation is of the order of 0.3 %.

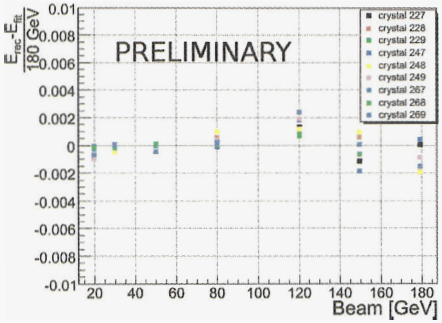

Fig. 3. Preliminary differential non-linearity measurement

3. Conclusions

Extensive test beam studies demonstrate that CMS ECAL will meet its ambitious design goal for energy resolution, uniformity of the response and noise levels. ECAL barrel commissioning is in progress, while endcaps are under construction getting ready for the LHC first data taking.

References

1. M. Ryan on behalf of the CMS ECAL Group, this proceedings
2. V. Tancini on behalf of the CMS ECAL Group, this proceedings

Assessment of the Čerenkov light produced in a $PbWO_4$ crystal by means of the study of the time structure of the signal

L. Cavallini, C. Mancini, A. Mecca and D. Pinci*
Università "La Sapienza" and INFN Sezione di Roma, Italy
** E-mail:davide.pinci@roma1.infn.it*

N. Akchurin, L. Berntzon, H. Kim, Y. Roh and R. Wigmans
Texas Tech University, Lubbock, USA

A. Cardini
INFN Sezione di Cagliari, Italy

R. Ferrari, S. Franchino, G. Gaudio and M. Livan
Università di Pavia and INFN Sezione di Pavia, Italy

J. Hauptman
Iowa State University, Ames, USA

L. La Rotonda, E. Meoni, A. Policicchio and G. Susinno
Università della Calabria and INFN Sezione di Cosenza, Italy

H. Paar
University of California at San Diego, La Jolla, USA

A. Penzo
INFN Sezione di Trieste, Italy

S. Popescu[1] and W. Vandelli
CERN, Geneva, Switzerland
[1] *on leave from IFIN-HH, Bucarest, Romania*

On beam tests were carried out on $PbWO_4$ crystals. One of the aims of this work was to evaluate the contribution of the Čerenkov component to the total light yield. The difference in the timing characteristics of the fast Čerenkov

signals with respect to the scintillation ones, which are emitted with a decay time of about 10 ns, can be exploited in order to separate the two proportions. In this paper we present the results of an analysis performed on the time structure of signals, showing how it is possible to detect and assess the presence and the amount of Čerenkov light. Since Čerenkov light is emitted only by the electromagnetic component of a hadronic shower, its precise measurement would allow to account for one of the dominant sources of fluctuations in hadronic showers and to achieve an improvement in the energy resolution of a hadronic calorimeter.

Keywords: Čerenkov light, $PbWO_4$ crystal, high energy particle calorimetry.

1. Introduction

The possibility of evaluating the amount of Čerenkov light produced by fast particles in an hadronic calorimeter represents a promising method to detect the electromagnetic fraction of an hadronic shower.[1,2] Long and detailed on-beam tests were performed on $PbWO_4$ crystals, which represents an attractive material for detecting electromagnetic showers on high energy colliders because of its high density and fast response.[3–5] One of the main purposes of the test was to evaluate the contribution of the Čerenkov component to the total light yield. In order to assess the presence of Čerenkov light and to evaluate its ratio to the scintillation one, two of their main differences were exploited:

(1) While the scintillating light is emitted isotropically, the Čerenkov light is produced in a cone with an opening angle $\cos\theta = 1/\beta n$ as shown in Fig. 1.
(2) The emission process of the scintillating light, produced by the molecular de-exitation, has a characteristic decay time (about 10 ns for $PbWO_4$ crystal) while the Čerenkov light is produced prompt after the particle crossing.

2. Study of the signal time structure

In order to evaluate the effects of Čerenkov photons to time structure of the PMT signals, during the on-beam tests the PMT signal pulse shapes were acquired with a very fast Flash ADC (effective sampling frequency of 800 MHz) or with a 10 Gigasample/s oscilloscope.

2.1. *Signal timing properties*

The timing properties of the signals have been analysed by two simple methods shown in Fig. 2. In a first method the leading edge of the signal

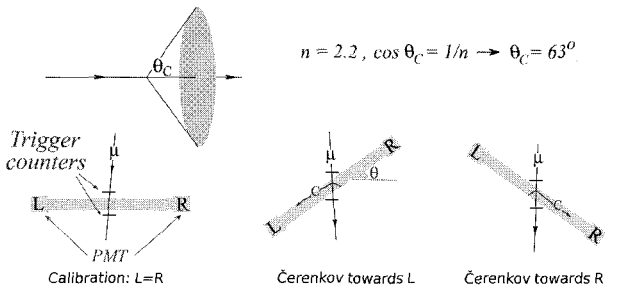

Fig. 1. Directionality of the Čerenkov light and sketch of the setup used to study the difference of the responses on the two crystal sides.

is fitted to a Fermi-Dirac function:

$$V(t) = A\left[\frac{1}{e^{(t-t_L)/\tau_L}+1} - 1\right]$$

An increase in the Čerenkov content of the signal will manifest itself as a decrease in the value of τ_L, since the leading edge is becoming steeper. In a second method we evaluated the time at which the pulse height crosses a certain threshold level (e.g. 30 mV in Fig. 2 right). An increase of the Čerenkov component will shift that point to an earlier moment.

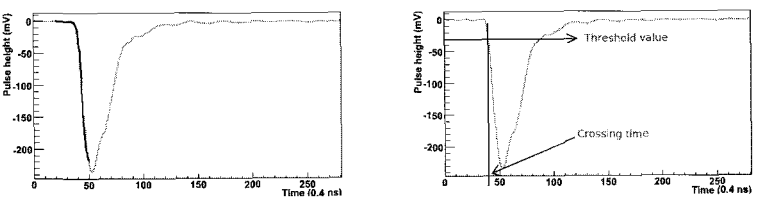

Fig. 2. Methods to determine the time structure of the signal. On the left the leading edge is fitted with a Fermi-Dirac. On the right the time at which the pulse height exceeds a certain threshold is used to this purpose.

In Fig. 3 the *leading constant* and the difference between the R and L *crossing times* are shown as a function of the crystal angle respectively on the left and on the right. The effects of Čerenkov photons on the signal timing are visible on both the variables.

The precision shown for the data at 0°, is completely dominated by photo-electron statistics and are such that the used variables do not provide

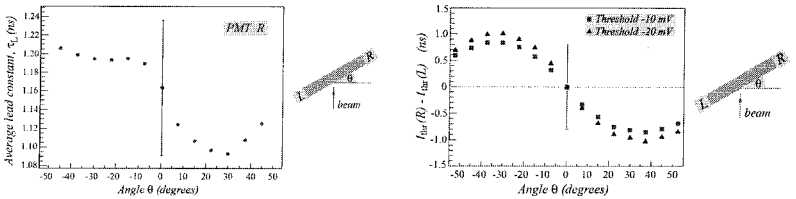

Fig. 3. Left: angular dependence of the *leading time* τ_L. Right: difference of the times needed by the signals in L and R to reach a fixed threshold as a function of the angle.

statistically significant information about the contribution of Čerenkov light to the signal in question on a event by event basis.

The difference between the crossing times on L and R was also measured by means of a standard CAMAC discriminator and a TDC without any offline pulse shape analysis (Fig. 4). Although a maximum time difference

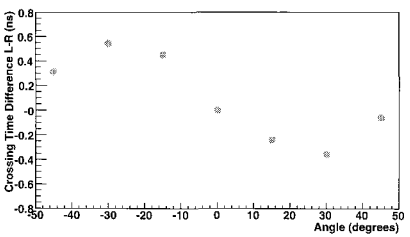

Fig. 4. Results of the measurement of the crossing time difference by means of standard CAMAC electronics.

of only about 1 ns was found, the effect is clearly visible.

2.2. *The qRatio method*

A third method to evaluate the Čerenkov contribution to the total light yield is to calculate the ratio between the light collected in the first few instants of the signal and the total one. This charge ratio (*qRatio*) is expected to increase when the Čerenkov light is collected because the signal becomes faster and higher. In Fig. 5 very preliminery results on the behaviour of qRatio as a function of the angle are shown for the R side signals. The value of qRatio is almost constant over the whole range of angles in which no Čerenkov light is collected by the PMT R. For $\theta < 0$ it starts to increase reaching its maximum for $\theta \simeq -30^o$. The maximum value is about 10%

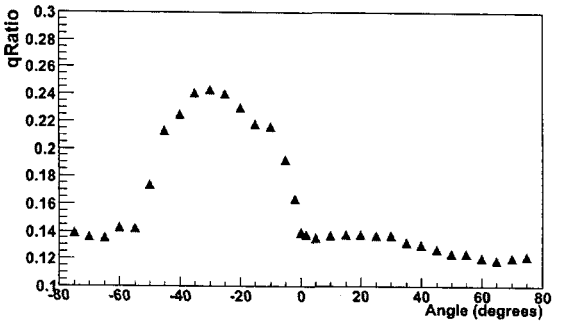

Fig. 5. Results of the qRatio analysis (see text) for the crystal R side.

(once offset-subtracted) which is equal to the ratio between the Čerenkov and the total light calculate with signal shape analysis.[3] No effects due the increase of the effective particle path are found for large angles.

3. Conclusion

Several variables sensitive to the effects of the Čerenkov light correlated with the signal time structure were studied. The prompt Čerenkov photons give rise to a fast signal whose time characteristics can give information about their presence and their amount. The use of the qRatio method, which adds to the effects on the signal timing the effects on the increase of total charge can represent a promising way to assess the Čerenkov contribution to the total light yield also in homogeneous $PbW0_4$ calorimeters.

References

1. N. Akchurin *et al.*, Nucl. Instr. and Meth. A 537 (2005) 537.
2. N. Akchurin *et al.*, (DREAM Collaboration), Dual-readout calorimetry with lead tungstate crystals, Nucl. Instr. and Meth. 2007, submitted for publication.
3. N. Akchurin *et al.*. "Contributions of Čerenkov light to the signals from lead tungstate crystals" in press on Nucl. Instr. and Meth. A.
4. N. Akchurin *et al.* "Dual-Readout Calorimetry with Lead Tungstate Crystals" in press on Nucl. Instr. and Meth. A.
5. N. Akchurin *et al.* "Measurement of the contribution of neutrons to hadron calorimeter signals" in press on Nucl. Instr. and Meth. A.

LUCID, THE LUMINOSITY MONITOR FOR ATLAS – A STATUS REPORT*

JAMES PINFOLD†

Centre for Particle Physics, University of Alberta, Edmonton, Alberta T6G 0V1, Canada.

In addition to the main ATLAS detector, three smaller systems are being built to provide good coverage in the very forward region . These are closely connected to the luminosity determination in ATLAS, but are also foreseen to study forward physics. If ordered according to their distance from the ATLAS interaction point, the first system is LUCID the main luminosity monitor of ATLAS located at a distance of 17 m from the interaction point. This detector is now nearing the end of construction at CERN. The LUCID detector and its status with regards to construction, testing and installation are described in this document.

1. Introduction

In addition to the main ATLAS detector, three smaller systems are being built to provide good coverage in the very forward region [1]. These are closely connected to the luminosity determination in ATLAS, but are also foreseen to study forward physics. If ordered according to their distance from the ATLAS interaction point (see Figure 1), the first system is a Cerenkov detector called LUCID that is the subject of this paper. LUCID is the main luminosity monitor in ATLAS and is located at a distance of 17 m from the interaction point. The second system is a zero degree calorimeter (ZDC), which is located at a distance of 140 m from the interaction point. This corresponds to the location, where the LHC beam pipe is divided in two and the ZDC is located between the beam pipes just after the split inside an absorber. The most remote detector is the ALFA system which consists of scintillating-fibre trackers located inside Roman Pots at a distance of 240 m from the ATLAS interaction point. Additional detectors are being considered at an even further distance of about

* This work is reported by James Pinfold on behalf of the LUCID Collaboration (Alberta, Bologna, CERN, LUND).

420 m from the interaction point, but they are just mentioned in this brief introduction since no decision has been taken yet concerning them.

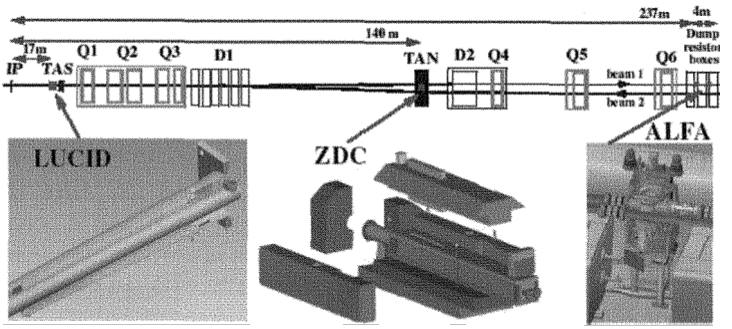

Figure 1 Placement of the forward detectors along the beam line around the ATLAS interaction point (IP).

2. The LUCID Detector

The luminosity can be measured by several detectors in ATLAS but LUCID (or *LUminosity measurement using Cerenkov Integrating Detector*) will be the only detector that is dedicated to luminosity monitoring. Its main purpose is to detect inelastic *pp* scattering in the forward direction, both in order to measure the integrated luminosity of the ATLAS runs and to monitor online the in- 45 stantaneous luminosity and beam conditions. Potentially, LUCID could also be used for diffractive studies, for example as a rapidity-gap veto or as tag for the diffractive signal [2].

When the luminosity is ~10^{32} cm^{-2} s^{-1} or less, the detector will only have to count the number of bunch crossings producing an interaction. At the LHC design luminosity, however, most bunch crossings will result in multiple interactions and the detector will have to measure how 50 many of these have occurred. The basic principle of the detector is that the number of interactions in a bunch crossing is proportional to the number of particles detected in LUCID. This holds even when most of the detected particles originate from secondary interactions.

Since there is no Landau tail in the measurement of Cerenkov light, it is in principle possible to determine the number of particles that have entered a Cerenkov tube by using pulse height measurements (so-called particle counting mode). The probability that several particles enters the same tube is, however, quite low (typically a few percent at a luminosity of ~10^{33} cm^{-2} s^{-1}). Simulations show that a simpler measurement of counting only the number of tubes with a signal above a preset threshold (so-called hit counting mode) gives a measurement with an acceptable systematic error for online measurements.

These measurements will be done with different scalers for each bunch in the LHC so that the luminosity of the individual bunches can be monitored online. A pre-scaled LUCID trigger will make it possible to record a sub-set of the LUCID events for offline analysis and a more precise luminosity determination using charge and time to digital converters for particle counting.

LUCID is a relative luminosity detector. Well known physics processes measured by other detectors will be used to perform the calibration. The most accurate calibration will be obtained with the ALFA detectors that measure elastic Coulomb scattering. During the initial period of LHC running the calibration procedure will utilize calculations based on LHC machine parameters. Physics processes can also be used, such as W and Z counting [3] and exclusive muon pair production via two photon interactions [4]. The goal is to use the LUCID detector to measure the luminosity with an error better than 5%. The main requirements for the LUCID detector are:

- Good acceptance to minimum-bias events;
- Sufficient time resolution to measure individual bunch-crossings;
- Resistance to very high radiation levels;
- Low sensitivity to soft background particles;
- The ability to count individual particles;
- Pointing capability in order to suppress, as much as possible, signals from tracks which do not point to the interaction point.

The concept of a luminosity detector consisting of an array of Cerenkov tubes (cones) was developed by the CDF collaboration [5]. The main challenges in using this type of detector at the LHC are the much higher radiation and background levels as well as the requirement for the detector to srvive the high temperatures experienced during beam pipe bake-out. ATLAS has approved the construction of a detector with a minimum number of read-out channels for the initial low luminosity phase of the LHC running (up to few 10^{33} cm^{-2} s^{-1}) and then to upgrade the detector to a larger coverage if it can be demonstrated that the detector works well at the LHC design luminosity.

2.1. *The Detector Design*

The LUCID detector is schematically depicted in Fig. 2. It consists of twenty aluminium tubes that surround the beam pipe and that point towards the ATLAS interaction point. The 1.5 *m* long mechanically polished tubes with a diameter of 15 *mm* are placed in a light-weight aluminum gas vessel that ensures that the tubes are filled with C_4F_{10} (providing a Cerenkov threshold of 2.8 *GeV* 90 for pions and $10MeV$ for electrons) at a constant pressure of ~1.3 *bar*. There are two

detectors installed, one in each end cap region of ATLAS, at a distance of approximately 17 *m* from the interaction point, covering the pseudo rapidity range 5.6 → 6.0.

The Cerenkov light emitted by a particle traversing the tube has a half-angle of 3 degrees and it is reflected on average three times before the light is measured by photo-multipliers tubes (PMTs) that match the size of the Cerenkov tubes. The signal amplitude from these PMTs can be used to distinguish the number of particles per tube and the fast time response provides unambiguous measurements of individual bunch crossings. LUCID is situated in a high radiation area and although the PMTs have quartz windows and are radiation hard, their performance is expected to degrade after several years of operation at nominal LHC luminosity. It is therefore foreseen to upgrade the detector after some years of running. The Cerenkov light in the upgraded detector could be taken out with radiation hard quartz fibers to the outside of the shielding, in a low background radiation level region, where the fibers would be read out with multi anode PMTs. In this read-out scheme, a Winston cone at the end of the tube focus the light onto a bundle of fused silica fibers having 0.8 *mm* diameter. In order to gain experience with this type of read-out, four of the twenty Cerenkov tubes are read out by fibers in this manner.

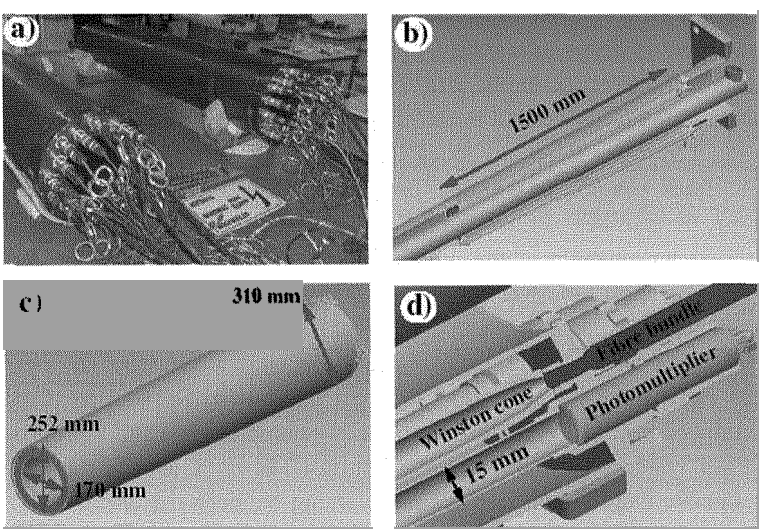

Figure 2 a) Picture of the two LUCID vessels fully assembled and ready to be installed in ATLAS. b) Sketch of LUCID integrated in the cone supporting the beam pipe. c) Design of the gas vessel. d) Expanded view of the readout area showing the coupling between the Cerenkov tubes and PMTs and the tubes and fibres via a Winston cone.

The 16 electrical signals from the PMT readout are fed into a custom designed front end card containing a fast amplifier and a differential line driver. These analog signals pass through a constant fraction discriminator (CFD), which registers a hit each time the PMT is above a preset threshold. A charge to digital converter (QDC) allows offline analysis of the signal amplitudes in a sub sample of the triggered events. One of the digital outputs of the CFD card is fed into a multi hit time to digital converter (TDC) for offline timing analysis, with a second output going to a custom designed 9U VME card called LUMAT (LUMinosity And Trigger card). LUMAT is a luminosity monitor, trigger and ROD card which uses a FPGA to calculate the luminosity for each bunch crossing using different algorithms and stores one scaler value per bunch crossing per luminosity algorithm. LUMAT is the core of the LUCID online processing and sends the pattern of LUCID hits to the ATLAS ROS, pending a first level trigger request, as well as providing a separate LUCID trigger. The LUCID readout buffer will be sent to the ATLAS TDAQ via the S-link interface to be written in the ATLAS event record to be available for the offline analysis.

2.2. *Experimental beam and radiation test results*

A six-tube prototype detector, dedicated purely to test beam measurements, has been validated in beam tests at DESY. The prototype was used to study the light collection efficiency of both read out schemes with either PMTs directly connected to the Cerenkov tubes or bundles of optical fibre coupled to Winston cones attached to the Cerenkov tubes. The light output was studied as a function of angle, track position in the tube, pressure, Cerenkov tube polish, PMT type, fibre type, the number of fibres and the Winston cone design parameters. Fig. 3 (left) shows an example of the number of photoelectrons created in the PMT when the Cerenkov tube was placed in a coaxial electron beam with energy 6 GeV. This test was performed using a Cerenkov tube with a larger diameter than the PMT window resulting in two peaks depending on whether the beam particles missed the PMT window or went through it. On average Cerenkov light produced in the gas resulted in about 70 photoelectrons and light produced in the PMT window gave about photoelectrons. The PMT used in the prototype had a concave window with a thickness varying between 0.8 and 2 *mm*. In the final detector a PMT window with a constant thickness of 0.8 *mm* is used. One of the main objectives of the test beam measurements was to validate the Monte

Carlo simulations of the detector. A comparison of a measurement of the average number of photoelectrons with the simulated detector response shows that he agreement is excellent, indicating that the light collection is correctly simulated.

The radiation hardness of the detector and its read-out is an important issue, although for the first luminosity stage of the LHC machine the total dose per year seen by LUCID will be less than one tenth of the dose at full LHC luminosity (7 *Mrad* per year). The body of the detector is made 140 of aluminum and is extremely radiation hard. However damage to other components may be a concern (for instance, the PMTs, the optical fibres, the signal cables, the power cables and certain seals and bonds in the detector that were made using epoxy). Radiation testing of these components has been performed using both a strong gamma source and a reactor. The gamma exposure so far corresponds to about 3 years of LHC running while the neutron exposure corresponds to five years at nominal luminosity. So far there have been no serious problems observed in any of the materials tested. The dark current of the PMTs increased but their gain and light collection efficiency were not affected. In addition, significant radiation annealing effects were observed indicating that dose rate effects are important.

2.3. *LUCID Installation in ATLAS*

The LUCID detector is fully assembled and mechanically tested for gas leaks and light tightness. The front end and readout scheme has already been validated in the test beam at DESY. The calibration using LED light injected in each Cerenkov tube has been successfully tested in the fully assembled detectors. The detector is therefore ready to be installed along with the ATLAS beam pipe.

References

1. ATLAS, ATLAS Forward Detectors for Measurement of Elastic Scattering and Luminosity Determination (ATLAS TDR, in preparation); ATLAS Forward Detectors for Luminosity Measurement and Monitoring (CERN-LHCC/04-10, LHCC I-014); Zero Degree Calorimeters for ATLAS (CERN-LHCC/07-01, LHCC I-016). 340
2. T. L. Cheng and P. Teixeira–Dias, ATL-PHYS-PUB-2006-029, .
3. M. Dittmar *et al.*, Phys. Rev. **D36** (1994) 7284.
4. A.G. Shamov and V.I. Telnov, Nucl. Instr. and Meth. **A494** (2002) 51.

5. D. Acosta *et al.*, Nucl. Instr. and Meth. **A461** (2001) 540.
6. H. Stenzel, ATL-LUM-PUB-2007-001. 345
7. S. Ask *et al.*, Nucl. Instr. and Meth. **A568** (2006) 588–600.
8. F. Anghinolfi *et al.*, Hadron beam test of a scintillating fibre tracker system for elastic scattering and luminosity measurement in ATLAS, JINST **2 P07004** (2007) 588–600.

CMS ECAL intercalibration with cosmic rays and 2006 test beam electrons

Valentina Tancini on behalf of the CMS ECAL group

Universita' degli Studi di Milano Bicocca and INFN Milano Bicocca, Milano, Dipartimento di Fisica G.Occhialini, Piazza delle Scienze 3 20126 Italy
**E-mail: valentina.tancini@mib.infn.it*

The CMS Electromagnetic Calorimeter (ECAL) calibration foresees dedicated protocols both before and during the data taking. Up to now test beam electrons and cosmic muons have been used to precalibrate ECAL. During the summer 2006, nine ECAL supermodules have been exposed to a high energy electron beam at the CERN SPS north area facility and the intercalibration coefficients of the 1700 channels have been measured for each supermodule. The reproducibility of the intercalibration has been tested by measuring a supermodule twice. Different calibration methods based either on single crystals or on matrices of crystals energy reconstruction have been used. The intercalibration coefficients obtained have also been compared with those calculated by means of the cosmic ray muons.

Keywords: calorimetry, LHC, CMS, electromagnetic, calibration, higgs

1. The Electromagnetic CALorimeter

The CMS experiment is equipped with a hermetic homogeneous electromagnetic calorimeter. It is made of 61200 lead tungstate ($PbWO_4$) crystals mounted in the central barrel part and closed by 7324 crystals in each of the 2 endcaps. The crystal material has been chosen for its fast response and its resistance to irradiation as well as its high density (8.3 g/cm^3), short radiation length ($X_0 \simeq 0.89\ cm$) and small Moliere radius ($R_M \simeq 2.19\ cm$), allowing a compact detector to be built. Silicon avalanche photodiodes (APDs) are used as photodetectors in the barrel and vacuum phototriodes (VPTs) in the endcaps. The barrel is divided into two halves, each composed of 18 supermodules containing 1700 crystals. There are 4 modules in each supermodule separated by aluminum webs. The individual crystals have a truncated-pyramid shape with a lateral size of approximately 1 R_M and a length of 25.8 X_0. The crystals are organized in a quasi-projective

geometry, their principal axes making a 3° angle with respect to a vector from the nominal p-p interaction vertex, in both the azimuthal and polar angle projections. ECAL has been designed to provide the granularity and the excellent energy resolution which are required to detect the decay of the Standard Model Higgs boson into two photons.

2. The intercalibration

Calibration is composed of a global component, giving the absolute energy scale, and a channel-to-channel relative component, which is referred to as intercalibration. The intercalibration is a severe challenge to achieve the most accurate energy resolution for electrons and photons. The design goal for the energy resolution, in order to find the Higgs via its decay into two photons, is 0.5% at high energies. The main source of channel-to-channel response variation in the barrel is the crystal-to-crystal variation of scintillation light yield which has an RMS of 13%. In the endcaps the variation has a RMS of 25% and is mainly due to differences in the VPTs response. Preliminary estimates of the intercalibration coefficients are obtained from laboratory measurements of crystal light yield with ^{60}Co source (4.5%), test beam precalibration of some supermodules ($< 0.5\%$), and the commissioning of all supermodules with cosmic rays ($< 2\%$). After the start-up the intercalibration will use the ϕ-independence of the energy depositions of minimum bias events (2.5% in few hours), the reconstruction of $Z \rightarrow e^+e^-$ (0.5% with $\simeq 3\ fb^{-1}$) and $\pi^0/\eta \rightarrow \gamma\gamma$ (1% with $10 - 100\ pb^{-1}$) events, and the momentum of the electrons from W decays as measured in the tracker (0.4% with $5\ fb^{-1}$).

3. Experimental setup at the 2006 test beam

During the summer 2006, test beam data have been taken in H4 beam line at SPS. The ECAL supermodules were installed on a movable table allowing the electron beam to be directed to all the crystals of the supermodule with the same quasi-projective geometry foreseen for the LHC running. The transverse incidence position of the beam electrons was determined by four planes of fiber hodoscopes situated upstream the movable table with a precision of 150 μm. The supermodules were fully equipped with the final versions of the readout electronics, high and low voltage regulations, cooling system, temperature and laser monitoring systems, DAQ and DQM. The energy of the electrons varied from 20 to 250 GeV. Intercalibration coefficients of nine supermodules have been computed with different techniques.

4. The single crystal technique (S1)

The energy deposition of impinging electrons on a single crystal depends on the electron impact point because of the variation of the shower containment. Since the S1 algorithm is based on the energy measured in a single crystal, this dependence has to be corrected for with an appropriate fitting procedure. The position dependence can be factorized into the two coordinates with 4th order polynomials. The corrected response is computed event by event. The distribution is fitted with a gaussian plus an exponential left tail and the peak is chosen as the estimator of the crystal response. Only electrons falling in a 3×3 mm^2 window around the position of maximum containment are selected. The statistical precision, evaluated dividing the data sample in two subsamples and applying the full procedure independently to both, is $\simeq 0.2\%$ (Fig. 1). By measuring a supermodule twice, the intercalibration coefficients resulted reproducible of $\simeq 0.2\%$. (Fig. 2). The reliability of the S1 algorithm at different energies has been demonstrated by exposing part of a supermodule to both 90 and 120 GeV electrons; the consistency $\simeq 0.4\%$.

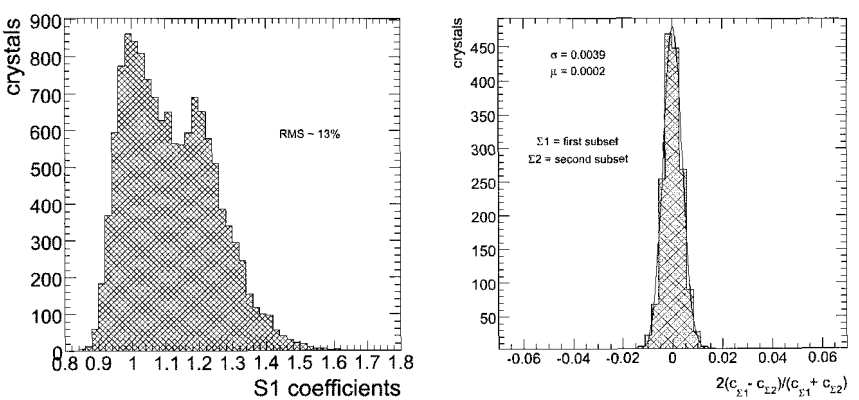

Fig. 1. Left: Distribution of the S1 intercalibration coefficients. The RMS of 13% is consistent with the expected initial miscalibration. Right: The difference of two sets of calibration coefficients corresponding each to half of the statistics. The present statistical precision is 0.2%.

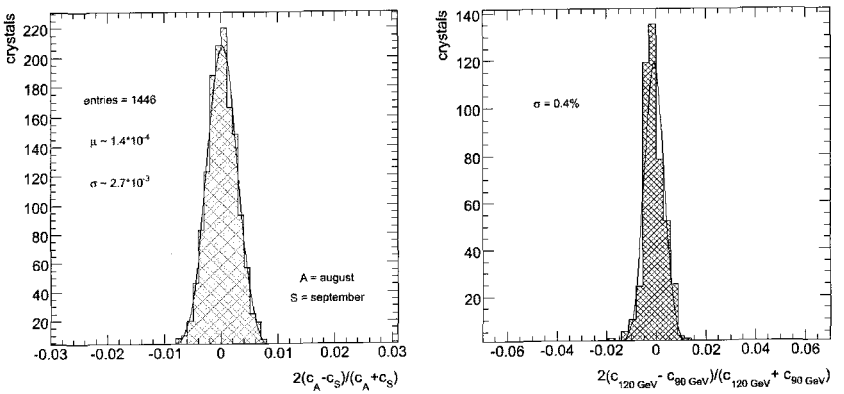

Fig. 2. Left:Comparison between August and September S1 intercalibration coefficients for the supermodule 22 that was under beam twice. The reproducibility is measured to be 0.2%. Right: Distribution of the difference between intercalibration coefficients calculated at 90 GeV and 120 GeV respectively. The consistency is $\simeq 0.4\%$.

5. Algorithms for the in situ intercalibration

The algorithms for the in situ intercalibration are based on the comparison between the energy deposited in a cluster of crystals and the nominal electron energy. While in the inverted matrix technique a χ^2 minimization procedure is used and combined with a iterative procedure, in the L3 technique the cluster response is aligned event by event with the electron known energy. The reliability of both algorithms has been demonstrated with the test beam dataset and measured from the comparison with the S1 technique after the correction for the η trend of the containment: an agreement of $\simeq 0.2\%$ has been reached. (Fig. 3).

6. Intercalibration with cosmic rays

The procedure exploits the equalization of the responses of the different crystals to the cosmic muons energy. Muons well aligned with the crystal axes provide a reference signal of 250 MeV. The data acquisition is triggered by the coincidence of two scintillators arranged in a pointing geometry. The supermodules are inclined by 10° with respect to the horizontal position in order to increase the rate of aligned muons at large η. Not aligned muons are rejected by vetoing on energy deposition in the crystals surrounding the one with the maximum energy deposit. The APDs gain is increased by a factor 4 to achieve a reasonable veto efficiency. Events with sizeable energy

deposit either in one single crystal or in two nearby crystals (at constant η or ϕ) are selected. The comparison between the S1 intercalibration and the results of the combined single crystals and crystal pairs shows an accuracy of 1.5% when excluding the edge crystals (Fig. 3).

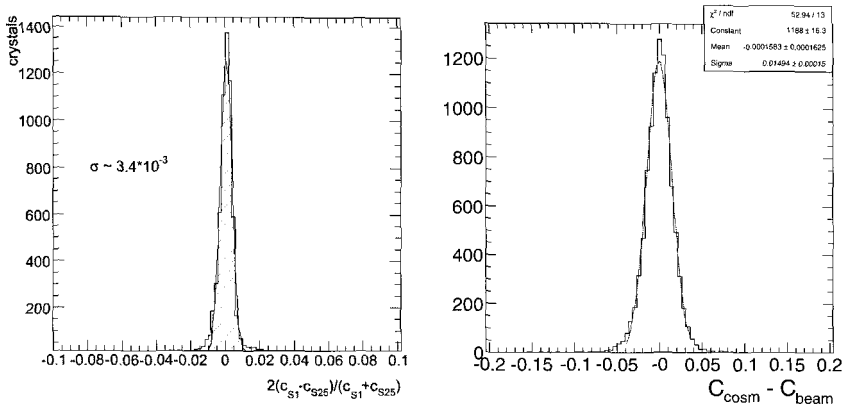

Fig. 3. Left: Comparison between the S1 and the inverted matrix intercalibration techniques. The consistency between the two algorithms is $\simeq$ 0.2%. Right: Comparison between the intercalibration with the S1 technique and the intercalibration based on the cosmic muons. The consistency between the two procedures is $\simeq$ 1.5%.

7. Conclusions

During the test beam of summer 2006 intercalibration coefficients for nine supermodules of ECAL have been computed by means of the single crystals techinique. The intercalibration coefficients resulted reproducible in time (0.2%) and independent from the beam energy (0.4%). The S1 algorithm has been used to test the reliability of the crystal cluster techniques, that will be used in situ (0.2%). The precalibration with cosmic rays, applied on all supermodules, gave results consistent with the other techniques (1.5%).

References

1. P. Govoni, V. Tancini "The intercalibration of the CMS electromagnetic calorimeter at the testbeam" (proceeding of HCP 2007 in preparation).
2. A. Ghezzi "Calibration of the CMS Electromagnetic Calorimeter by Cosmic Ray Muons" (proceeding of HCP 2007 in preparation).
3. CERN/LHCC 97-33 CMS Collaboration "The electromagnetic calorimeter project. Technical design report."

Study and Development of the Multi-Pixel Photon Counter for the GLD Calorimeter Readout

Satoru Uozumi *for the GLD Calorimeter Group*

Faculty of Science, Shinshu University,
Matsumoto, Nagano 390-8621, Japan
**E-mail: satoru@azusa.shinshu-u.ac.jp*

The Multi-Pixel Photon Counter (MPPC) is a novel semiconductor photon sensor belonging to the Pixelated Photon Detector (PPD) family, which also includes the Silicon-Photomultiplier. Since it has many remarkable features, we are studying and developing the MPPC, aiming to utilize it to read out a strip-scintillator calorimeter for a future linear collider experiment. We have measured the gain and photon detection efficiency of the 1600 pixel MPPC, which are comparable to the performance of conventional photomultipliers, and its dark noise rate and cross-talk, which are acceptably small. The dynamic range, a weak point of the MPPC, is confirmed to be enhanced thanks to a short recovery time. After ensuring the acceptable performance of 1600 pixel MPPCs, we built a calorimeter test module with a scintillator-strip structure and full MPPC readout, and exposed it to positron beams to evaluate its performance. Results of the beam test show good performance of the calorimeter prototype. These results indicate that the MPPC is a promising device not only for calorimeter readout, but also for photon detection in various other fields.

Keywords: MPPC; calorimeter; scintillator-strip;

1. Introduction

The International Linear Collider (ILC) is a future e^+e^- collider, and the GLD is one of several detector concepts proposed for the ILC.[1] At the ILC, precise jet energy measurement is a key issue, since many physics processes dominantly decay into multi-jet final states. To improve the jet energy resolution, we adopt the Particle Flow Algorithm (PFA).[1] This method significantly improves the jet energy resolution, typically achieving around $\sigma/\sqrt{E} = 30\%$, but it requires finely segmented calorimeter for the separation of particles within a jet. To realize a calorimeter of fine granularity, a scintillator-strip structure is proposed for the GLD calorimeter. The GLD

calorimeter has a sandwich structure of plastic scintillator and absorber layers. The scintillator layers have a strip structure to achieve fine granularity as shown in Figure 1. The size of the scintillator strips is 1×4 cm^2 with a thickness of 2 mm, and the strips are aligned in orthogonal directions in successive layers. The signals from each scintillator strip are read individually, giving of order ten million channels in total. Since the number of required photon sensors is huge and the calorimeter is placed in a 3 Tesla magnetic field, conventional photomultipliers cannot be used for the readout. However, the Multi-Pixel Photon Counter (MPPC) has ideal characteristics for this environment. The MPPC[2] is a type of Pixelated Photon Detector (PPD) which has been developed for three years and has recently been commercialized by Hamamatsu Photonics. The MPPC consists of 100~1600 APD pixels. Each pixel operates in the limited Geiger mode with a bias voltage of a few volts above the breakdown voltage (70-80 V). A picture and the structure of the MPPC are shown in Figure 2. The MPPC has many advantages with respect to conventional photomultipliers or other semiconductor photon sensors, including high gain and photon detection efficiency, compact size, low cost, and insensitivity to magnetic fields. To utilize the MPPC for the GLD calorimeter readout, we have studied and developed it, collaborating with Hamamatsu Photonics to achieve sufficiently good performance for GLD calorimeter readout.

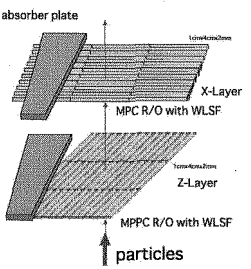

Fig. 1. The scintillator-strip structure of the GLD calorimeter.

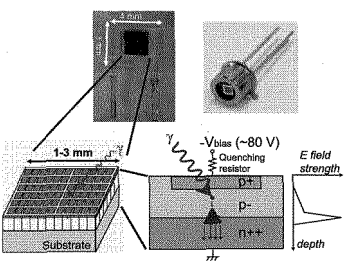

Fig. 2. Pictures and structure of the MPPC.

2. Basic performance of the 1600 pixel MPPC

We have measured basic properties of the 1600 pixel MPPC. Figure 3 shows the result of measurements of MPPC gain, dark noise rate, inter-pixel cross-talk probability and photon detection efficiency. The measured

gain is fitted with the formula Gain $= C\Delta V/e$, where $\Delta V = V_{\rm bias} - V_0$ is called the over-voltage. The gain is typically $(2-9) \times 10^5$, which is almost comparable to that of conventional photomultipliers. It is also found that the breakdown voltage depends on temperature with a coefficient $\Delta V_0/\Delta T = 56.0 \pm 0.1$ mV/K. The dark noise is caused predominantly by thermal electrons, giving rise to a temperature dependence as seen in Figure 3. In the temperature range $-20 \sim 30$ °C, the rate is always of order 100 kHz, which is acceptable for the purpose of calorimetry at the linear collider. Inter-pixel cross-talk is caused by infrared photons generated in the avalanche. The observed cross-talk rate is of order 0.1, which is not negligible but still acceptable for this application. The Photon Detection Efficiency was measured and is shown in Figure 3. The PDE increases with the over-voltage to a maximum of ~18 %, which is comparable to the quantum efficiency of conventional photomultipliers. We have also measured the

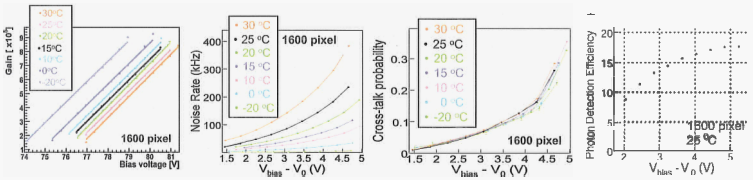

Fig. 3. **The gain, dark-noise rate,** inter-pixel cross-talk probability and photon detection efficiency of the 1600-pixel MPPC.

variation in performance within a sample of hundreds of 1600 pixel MPPCs. Figure 4 shows the observed variation of breakdown voltage, pixel capacitance and noise rate. These variations are less than 10 %, which is small enough for real large scale use. We have measured the recovery time

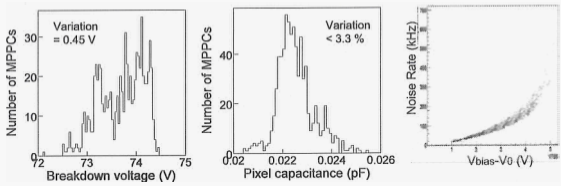

Fig. 4. Variation of breakdown voltage, pixel capacitance and dark noise rate. Variation of first two are measured in a sample of 800 1600 pixel MPPCs, while the variation of dark noise is measured in a sample of 450 pieces.

of the 1600-pixel MPPC using strong laser pulses. The setup and result are shown in Figure 5. A strong laser pulse is directed into the MPPC, and after a delay of Δt, a second strong laser pulse is injected. By measuring the MPPC output from the second laser pulse at various delay times, we can measure the time constant of the recovery. The recovery time is measured to be 4 ns, independent of the applied bias voltage. We measured the

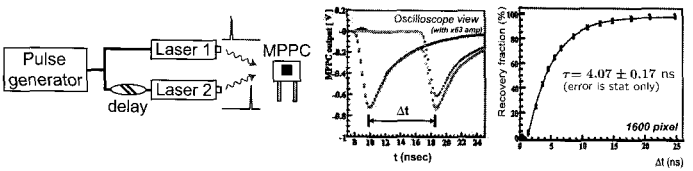

Fig. 5. Setup and result of the recovery time measurement. The middle plots show the pulse shape of the MPPC output to the laser pulses: black is the response to only laser-1, green only for laser-2, red is for the sequential input of laser-1 and 2, and blue shows the net pulse shape for laser-2 by subtracting black from red.

response curve, namely the relation between light input and MPPC output, with various widths of light input pulses. The results are shown in figure 6. We have confirmed that the dynamic range of the MPPC can be enhanced by a wider input pulse, thanks to the quick recovery. This is an advantage of the MPPC, however knowing the width of the light signal is crucial to calculate the correct response curve.

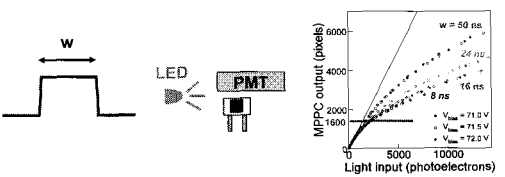

Fig. 6. Scheme and result of the response curve measurement. w is the width of the rectangular pulse provided to the LED.

3. The Scintillator-strip Electromagnetic Calorimeter Prototype

As a second step, we built a prototype of a scintillator-strip calorimeter with full MPPC readout, and exposed it to positron beams with an energy of 1 - 6 GeV to evaluate its performance. Figure 7 shows the structure of the prototype. It consists of 3 mm thick scintillator and 3.5 mm thick tungsten

layers. The scintillator layers consist of 18 strips, and an MPPC is attached to the end of each strip. Figure 7 also shows preliminary results of the beam test. The statistical and constant contributions to the energy resolution are measured to be $\sigma_{\text{stat}} = 13.4 \pm 0.1\%$ and $\sigma_{\text{const}} = 2.5 \pm 0.1\%$, respectively, which is consistent with the performance achieved in simulation. Deviations from linearity are sufficiently small, within $\pm 1\%$, even before a correction for MPPC signal saturation. This world's first trial of this type of calorimeter proves that the MPPC is useful for calorimetric use.

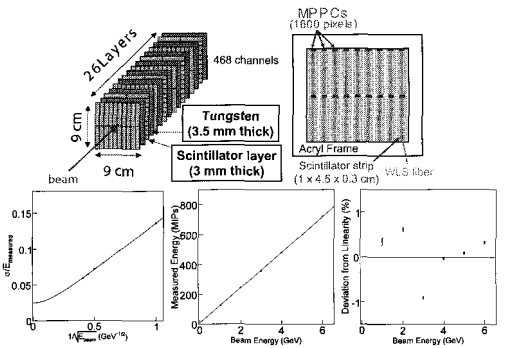

Fig. 7. Drawings of the scintillator-strip calorimeter prototype with full MPPC readout, and preliminary results of the beam test performed using 1-6 GeV positron beams. Plots shows σ/E, measured energy, and the deviation from linear response as a function of the beam energy E, or $1/\sqrt{E}$.

4. Conclusion

As a result of extensive study and development, we find that the performance of the 1600-pixel MPPC is sufficient to be used in the readout of the GLD calorimeter. We conclude that the MPPC is a promising photon counting device not only for calorimetric use, but also in various other fields. However further development of the dynamic range, stability, radiation hardness, and temperature dependence are necessary for actual use at the GLD calorimeter. Such improvements of the MPPC's performance are being actively pursued.

References

1. GLD Detector Outline Document, GLD collaboration
http://ilcphys.kek.jp/gld/documents/dod/glddod.pdf
2. Hamamatsu Photonics K.K.
http://jp.hamamatsu.com/products/sensor-ssd/4010/index_en.html

THE CALICE TILE HADRON CALORIMETER PROTOTYPE WITH SIPM READOUT: DESIGN, CONSTRUCTION AND FIRST TEST BEAM RESULTS

N. WATTIMENA
on behalf of the CALICE collaboration
FLC, DESY, Notkestr. 85,
Hamburg, 22607, Germany
E-mail: nanda.wattimena@desy.de

The CALICE collaboration has constructed a test beam hadronic calorimeter (HCAL) with 7608 scintillator tiles, individually read out by novel multi-pixel Geiger mode photodiodes, so called SiPMs, and tested it in electron and hadron beams at CERN. This prototype is the first device which uses SiPMs on a large scale; its purpose is to establish the technology and to record hadron shower data with unprecedented granularity for the validation of simulation models and the development of clustering algorithms.

Keywords: Hadronic Calorimeter; Silicon Photomultiplier; test beam.

1. The Tile Hadron Calorimeter Prototype

The CALICE tile hadron calorimeter prototype (HCAL) is a 38-layer sampling calorimeter made of a plastic-scintillator steel sandwich structure with a lateral dimension of about 1 m^2. Each layer consists of 1.6 cm thick steel absorber plates and a plane of 0.5 cm thick plastic scintillator tiles housed in a steel cassette with two 2 mm thick walls. The total thickness corresponds to 4.5 λ. The tile sizes vary from 3×3 cm^2 for 10×10 tiles in the center of the module, to 6×6 cm^2 in an intermediate region and 12×12 cm^2 in the outer region for the first 30 layers. The tile pattern of one such high granular active HCAL layer is shown in Fig. 1, right. For the last 8 layers the 3×3 cm^2 are replaced by 6×6 cm^2 tiles, due to cost reasons. Thus, the total number of channels in this prototype is 7608.[1]

The edges of all scintillating tiles are chemically matted to reduce the light crosstalk between the cells to less than 2 %. Each scintillator is individually read out by a SiPM (from MEPhI/PULSAR), directly mounted

on the tile itself. Due to the green sensitivity of the photo detector a 1 mm diameter wavelength-shifting (WLS) fiber (Kuraray Y11(300)). The WLS fiber, inserted into a groove in the tile, is used to couple the scintillation light into the SiPM. A mirror at the other end of the WLS fiber and reflection foil (VN2000 superradiant from 3M) covering the scintillator faces minimize light losses. The picture of one fully equipped 3×3 cm^2 size scintillating tile can be seen in Fig. 1, left.

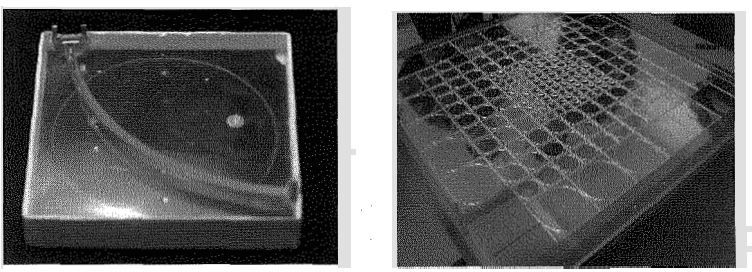

Fig. 1. 3×3 cm^2 scintillating tile with WLS fiber and SiPM (left) and one active HCAL layer with 216 tiles (right)

The readout electronics consists of 18 channel front end ASICs with preamplifier shaper and sample-and-hold chain mounted on the cassettes, multiplexed and read out by an off-detector VME based ADC system common for all CALICE detectors. The ASICs provide a high gain operation mode for auto-calibration of the SiPM gain by observation of single photoelectron signals, and include DACs for the channel-by-channel adjustment of the SiPM bias voltage. A versatile LED calibration system provides light signals up to an equivalent of 200 minimum ionizing particles (MIP) to each tile. The HCAL is mounted together with the CALICE silicon-tungsten electromagnetic calorimeter prototype (Si-W ECAL) on a movable stage for transverse scans and inclined incidence through the high granularity zone. The calorimetric system is completed by a tailcatcher and muon tracker (TCMT).[2]

2. Silicon Photomultiplier

The SiPMs were developed, manufactured and tested by MEPhI/PULSAR in Russia. The photosensitive area (1.1×1 mm^2) holds 1156 pixels. The detectors are reversely biased with a voltage of $\sim$ 50 V and have a gain

of $\sim 10^6$ that is determined by the charge $Q_{\text{pixel}} = C_{\text{pixel}} \cdot \Delta V$ collected in a pixel, where the voltage $\Delta V = V - V_0$ above breakdown voltage V_0 is in the order of few Volts and the pixel capacitance is typically 50 fF.[3] An incoming photon creates an electron-hole pair in the depletion region of a pixel, which are pulled apart by the applied electrical field. The field is strong enough to make the initial electron produce an avalanche of further charge carriers. This process is passively quenched by a resistor of few MΩ. Even though the signal of a single pixel is digital, the total signal, which corresponds to the sum of all fired pixels, is analogue and thus, proportional to the number of impinging photons.

For the HCAL, more than 10000 SiPMs have been characterized in an automatic setup, with calibrated LED light. The bias voltage working point was chosen as the one that yields 15 pixels for a MIP-like LED signal. Gain, relative efficiency, dark rate, inter pixel crosstalk, noise above a threshold of $\frac{1}{2}$ MIP and the non-linear response function of fired pixels vs light intensity over the full dynamic range were determined for each SiPM.[4]

2.1. *Detector performance*

Out of 7608 readout SiPM during the 2007 test beam period 1.6 % were dead due to bad soldering connections. The electronic noise with non-biased SiPMs shows a gaussian spectrum with $<$ 1 photoelectron width. In addition to this noise one has to account for the SiPM dark rate of few MHz, due to thermally created charge carriers in the sensitive volume. Thus, after carefull voltage adjustment the overall noise occupancy is 10^{-3}, with an average energy of 1.3 $\frac{\text{MIP}}{\text{hit}}$.

The photo-detection efficiency of $10 - 15$ % is mostly limited by the geometrical efficiency.

As the breakdown voltage depends on temperature, and all SiPM characteristics depend on ΔV, the SiPM signal is temperature and voltage dependent. The SiPM gain is found to vary between $-1.7\ \frac{\%}{^\circ C}$ and $+2.5\ \frac{\%}{0.1\,V}$, while the overall SiPM amplitude changes between $-4.5\ \frac{\%}{^\circ C}$ and $+7\ \frac{\%}{0.1\,V}$ for a SiPM with gain of 10^6. This sensitivity to temperature and voltage decreases with increasing gain.[3]

2.2. *Calibration and Monitoring*

The calibration procedure of a calorimeter cell consists of two independent steps: MIP calibration and correction for the non-linear SiPM response.

The MIP calibration relates ADC channels to the response of a minimum

ionizing particle. It is used to equalize the response of all channels by means of a physics process and at the same time defines the threshold ($\frac{1}{2}$ MIP) used to suppress cells without signal, which yields a MIP hit efficiency of about 93 %.

Due to the limited number of pixels and the finite pixel recovery time $\tau = C_{\text{pixel}} \times R_{\text{pixel}}$ of $50 - 500$ ns, SiPMs exhibit saturation behavior. This behavior is measured for each SiPM before mounting on a scintillator tile. One example measurement plotted versus the linear response of a photomultiplier tube (PMT) is shown in Fig. 2, left. The reference curves, measured at ITEP are used for the individual saturation correction of each SiPM.[5]

As the SiPM saturation behavior occurs at the pixel level, the gain calibration, relating ADC channels to the single pixel signal, is needed to scale the individual amplitude of each channel to the pixel scale.

3. Test beam experience

The HCAL was assembled and commissioned at DESY, where also an initial calibration of the active layers was obtained in the electron test beam. In 2006 and 2007, together with the CALICE silicon-tungsten electromagnetic calorimeter (Si-W ECAL) and the CALICE tailcatcher & muon tracker (TCMT), the HCAL was exposed to electron and hadron beams of 6–50 GeV and 6–180 GeV, respectively, in the H6 beam line at the CERN SPS. In addition high intensity muon beams were available for calibration. Detector operation proved very stable, with more than 90 % up-times and 270 million events were recorded. Mounting the ECAL and the HCAL on a movable stage, allowed to take data under different beam impact angles, ranging from 0° to 30°, and at different beam impact positions.

In August 2006 the first 15 active HCAL layers were installed in double sampling structure, thus the first data was taken with less than the design granularity. By October 2006 eight more modules were produced, commissioned and sent to CERN, during the last data taking period in summer 2007 the full HCAL was instrumented.

3.1. *First Physics Results*

The electron data are used to validate the calibration and the detector understanding in terms of simulations. Dedicated electron runs have been taken with the HCAL alone, removing the ECAL. After correcting the non-linear response of the SiPM using the test bench data and the in-situ channel-by-channel gain calibration, the calorimeter response is shown to

be linear within 6 % up to 45 GeV electron beams during the August 2006 data taking period (Fig. 2, right) and is likely to be better for the rest of the data. This is by far sufficient for the hadron shower measurement.

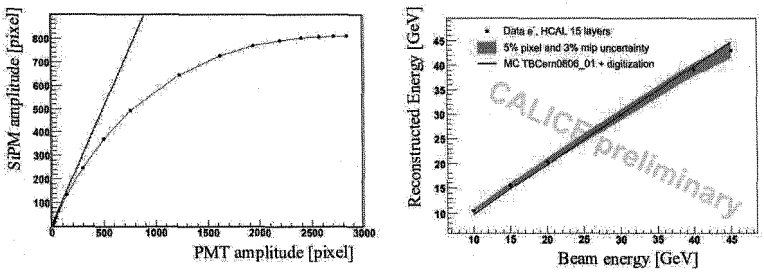

Fig. 2. Typical SiPM response function shows saturation behavior (left). Linearity better than 6 % can be gained back for up to 45 GeV electron beams (right)

The hadron analysis has just started, data show reasonable qualitative agreement with expectations. Thanks to the high granularity of the HCAL a rich substructure of hadronic showers can be observed. These data can be used, for example, to determine event-by-event the electromagnetic energy fraction for weighting procedures, and to test clustering algorithms.

References

1. G. Eigen, *AIP Conf. Proc.* **867**, 565 (2006).
2. C. Adloff *et al.*, *arXiv:0707.1245 [physics.ins-det]* (2007).
3. B. Dolgoshein *et al.*, *Nucl. Instrum. Meth.* **A563**, 368 (2006).
4. M. Danilov, *arXiv:0704.3514 [physics.ins-det]* (2007).
5. E. Garutti, *AIP Conf. Proc.* **867**, 574 (2006).

Inter-calibration of the CMS Barrel Electromagnetic Calorimeter Using $\pi^0 \to \gamma\gamma$ Decays

Y. YANG

On behalf of the CMS ECAL Group

256-48, High Energy Physics, Caltech
Pasadena, 91125, CA, USA
**E-mail: yongy@hep.caltech.edu*

Inter-calibrating the electromagnetic calorimeter (ECAL) of the CMS detector *in situ* at the LHC to achieve the energy resolution approaching 0.5% at high energy is going to be important to fully exploit the physics reach of the detector, particularly for the discovery of the Higgs boson in the two-photon decay channel. In this paper we evaluate the potential of a calibration technique that makes use of photon pairs produced in neutral pion decays, $\pi^0 \to \gamma\gamma$. Such photon pairs will be selected from the QCD events accepted by the Level-1 triggers using an online filter farm. Assuming a Level-1 trigger rate of 12.5 kHz, the rate of suitable neutral pions is found to be about 0.9 kHz.

We show that 95% of the barrel electromagnetic calorimeter can be calibrated to at least 1% (0.5%) precision after several days (weeks) of data-taking in the low-luminosity scenario of LHC, $\mathcal{L} = 2 \cdot 10^{33}\,\mathrm{cm}^{-2}\,\mathrm{s}^{-1}$. In addition, we show that a 1% calibration precision is achieved with π^0 decays produced in the π^- test beam runs during November 2006. The obtained calibration constants are successfully used for the reconstruction of 50 GeV electrons from the test beam data.

Keywords: CMS; ECAL; Calibration

1. Introduction

The Compact Muon Solenoid (CMS) barrel electromagnetic calorimeter consists of 61200 lead tungstate crystals arranged in 170 η−rings of 360 crystals each. The ECAL energy resolution has been determined in test beams to be $\frac{\sigma(\mathrm{E})}{\mathrm{E}} = \frac{2.9\%}{\sqrt{\mathrm{E(GeV)}}} \oplus \frac{0.130\ \mathrm{GeV}}{\mathrm{E}} \oplus 0.4\%$ [1], for electrons incident on the center of crystals. For electrons and photons with energies above 100 GeV, the energy resolution is dominated by the constant term. As a consequence, the performance of the CMS ECAL at the LHC will

depend mainly on the quality of its calibration and monitoring. Achieving the design-goal calibration precision of 0.5% will be particularly important for a discovery of the Higgs boson in the decay channel $H \rightarrow \gamma\gamma$, one of the primary goals of the LHC physics program. Several other calibration strategies have already been considered by the CMS ECAL community [2]. In this paper, we investigate the feasibility of inter-calibrating the CMS ECAL barrel region ($|\eta| < 1.479$) with photon pairs produced by $\pi^0 \rightarrow \gamma\gamma$.

2. Selection of π^0 Candidates in the ECAL Barrel

A sample of about four million fully simulated QCD events is used for selection and calibration exercise. The low-luminosity scenario, $\mathcal{L} = 2 \cdot 10^{33}\,\mathrm{cm}^{-2}\,\mathrm{s}^{-1}$, is assumed.

Photon pairs produced in neutral pion decays are planned to be selected on an online filter farm from all events accepted by the Level 1 (L1) trigger. To facilitate the future transition to the demanding environment of the online filter farm, the selection of π^0 candidates decays is based on ECAL variables from localized regions around the π^0 candidates.

The energy of photon candidates is defined as the sum of energies deposited in crystals forming the 3×3 matrix centered on the crystal with the highest energy deposit, $S_9 \equiv \sum_{3\times3} C_i \cdot E_i$, where C_i denotes the crystal's calibration constant and E_i the energy deposited in this crystal. The direction of flight is obtained by calculating the weighted averages of the positions of the constituent crystals.

Only photon candidates with a transverse energy above 1 GeV are considered. The S_4/S_9 and S_9/S_{25} ratios are required to be above 0.9. Here, the quantities S_9 and S_{25} correspond to the energies deposited in the 3×3 and 5×5 crystal matrices centered on the crystal with the highest energy deposit, respectively. The quantity S_4 is the highest value of energies deposited in the four possible combinations of 2×2 crystal matrices containing the most energetic crystal. The π^0 candidates are then selected by requiring more than 3.5 GeV transverse energy. To remove pairs with one or more converted photons, a cut on the sum of energy depositions around the π^0 candidate is also applied. The average energy of the selected π^0's is found to be about 8 GeV.

2.1. *Selection Efficiency and Purity*

The obtained invariant mass distribution is fitted to a combination of a Gaussian and a polynomial function (see Figure 1).The selection efficiency

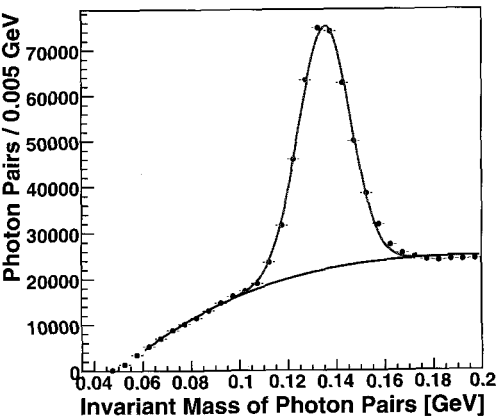

Fig. 1. The $\gamma\gamma$ invariant mass distributions together with the results of the fit to a combination of a Gaussian and a polynomial.

is then calculated as the ratio of the number of selected π^0's which match with generator-level π^0's within $\pm 3\sigma_{fit}$ around the mass peak to the total number of simulated QCD events which passed L1 trigger. However, the signal-to-background ratio (S/B) is estimated using a narrower window of $\pm 2\sigma_{fit}$ because the calibration performance is dominated by photon pairs near the peak. The total π^0 rate is found to be 0.87 ± 0.03 kHz, assuming a L1 event rate 12.5 kHz [3], while the S/B ratio is found to be about two.

3. Calibration with $\pi^0 \rightarrow \gamma\gamma$ Decays

Several calibration algorithms have been studied and found to produce consistent results. One them is described below.

For a given crystal, the invariant mass distribution is obtained from all π^0 candidates for which one of the photons is centered on this crystal. Iteratively, the calibration constants are updated according to the peak positions of such distributions. The energy and direction of each photon candidate are recalculated using the updated calibration constants. An initial miscalibration, typically about 4%, is applied before the first iteration. The calibration precision is then estimated as the R.M.S. of the distribution of the products of the initial miscalibration and final calibration constants.

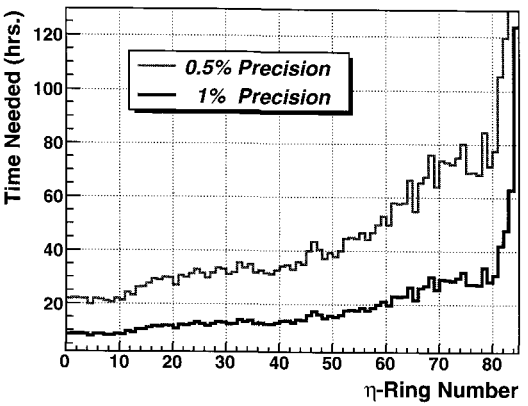

Fig. 2. Time of continuous data-taking required to achieve calibration precisions of 1% and 0.5% for crystals in different η-rings.

3.1. *Performance of the $\pi^0 \rightarrow \gamma\gamma$ Calibration*

Before crystal-to-crystal calibration, a correction depending on η and ϕ index of crystals is applied in order to remove the systematic effects due to the gaps between the ECAL modules and due to the implementation of a noise-suppression algorithm. The dependence of the calibration precision on the number of selected signal π^0 decays, n_{π^0}, and S/B ratio is determined by varying n_{π^0} and S/B separately. Then we translate the obtained results into the time needed to achieve a given level of calibration precision for different η regions of ECAL. Figure 2 shows that the time required to achieve a 0.5% precision ranges from about 20 hours for $|\eta| \simeq 0$ to about 130 hours for $|\eta| \simeq 1.4$.

3.2. *π^0 Calibration in Test Beams*

Further calibration studies are carried out using π^0 decays produced in the π^- test beam runs performed in November 2006 (see Figure 3). The average energy of the selected π^0 candidates is found to be about 8GeV. Using a sample of approximately 140 π^0's per crystal we achieve a calibration precision of $1.0 \pm 0.1\%$, which is consistent with the statistics-limited expectation of 0.9%. Thus, no noticeable limiting factors on the calibration performance are observed. This study also confirms that the CMS ECAL is capable of reconstructing the low-energy photons produced in $\pi^0 \rightarrow \gamma\gamma$ decays. In addition, It has been verified that the calibration constants obtained from π^0 calibration can be applied at higher energy(e.g. 50 GeV electrons) without

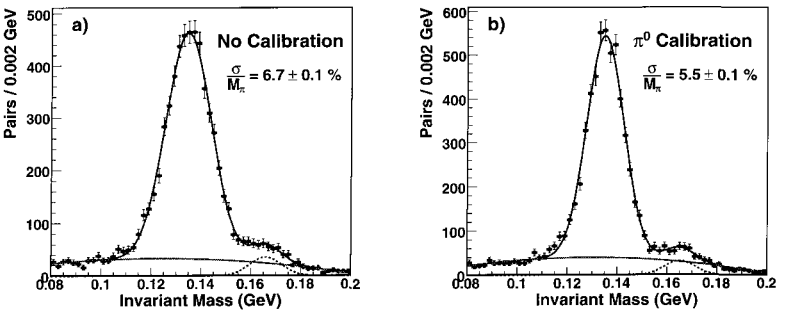

Fig. 3. Reconstructed π^0 mass peak a) before and b) after applying the π^0 calibration constants. Each distribution was fitted to a double-gaussian plus a second order polynomial function and the obtained peak resolution is indicated on the plots.

loss of accuracy.

4. Conclusions

We have presented the results from a study of the potential for a calibration of the CMS barrel ECAL with photons from $\pi^0 \rightarrow \gamma\gamma$ decays. We have shown that the majority of the barrel calorimeter, up to $|\eta| < 1.4$, can the be inter-calibrated to at least a 1% (0.5%) precision after about 30 (130) hours of continuous data-taking in the low-luminosity scenario of LHC. The π^0 calibration method has been successfully applied to the test beam data.

Acknowledgments

I would like to thank all my colleagues from the CMS ECAL collaboration. This work was supported in part by the U.S. Department of Energy Grant No. DE-FG02-92-ER40701.

References

1. P. Adzic *et al.* [CMS ECAL Collaboration], "Results of the first performance tests of the CMS electromagnetic calorimeter," Eur. Phys. J. C **44S2**, 1 (2006).
2. G. Daskalakis, "CMS ECAL Calibration Strategy," AIP Conference Proceedings, Vol. 867 pp. 400-407.
3. CMS Collaboration, "The CMS Physics Technical Design Report, Volume 2," pp. 541-564, CERN/LHCC 2006-021 (2006).

High Energy Physics Experiments

Organizers:

L. Price
High Energy Physics Experiments
R. Ruchti
Accelerator and Computer Data/Networking Developments

M. Ryan	The CMS Electromagnetic Calorimeter
B. Storaci	The Magnetic Distortion Measurement System of the LHCb RICH 2 Detector
D. Strom	Aspects of the SiD Detector Design for the International Linear Collider
R. Trentadue	Resistive Plate Chamber performance during the CMS Magnet Test Cosmic Challenge
S. Xella	Implementation and performance of the tau trigger in the ATLAS experiment

Quality assurance procedures for the construction of ALICE TOF SuperModules

A. Akindinov, S. Kiselev, D. Malkevich, A. Nedosekin, M. Ryabinin, M. Tchoumakov, K. Voloshin, B. Zagreev

Institute for Theoretical and Experimental Physics, Moscow, Russia

A. Alici[a,*], P. Antonioli, S. Arcelli[a], M. Basile[a], G. Cara Romeo, L. Cifarelli[a], F. Cindolo, D. Hatzifotiadou, G. Laurenti, M.L. Luvisetto, A. Margotti, R. Nania, F. Noferini[b], A. Pesci, R. Preghenella[a], E. Scapparone, G. Scioli[a], A. Silenzi [a], M.C.S. Williams, C. Zampolli[b], A. Zichichi[a,b]

Sezione INFN, Bologna, Italy

[a] *also Dipartimento di Fisica dell'Università, Bologna, Italy*

[b] *also Museo Storico della Fisica e Centro Studi e Ricerche "Enrico Fermi", Roma, Italy*

* *E-mail: Andrea.Alici@bo.infn.it*

A. De Caro, D. De Gruttola, S. De Pasquale, M. Fusco Girard, C. Guarnaccia, P. Pagano, G. Russo, R. Silvestri

Dipartimento di Fisica dell'Università and INFN, Salerno, Italy

H.T. Jung, W.W. Jung, D.S. Kim, D.W. Kim, H.N. Kim, J.S. Kim, K. Lee, S.C. Lee

Department of Physics, Kangnung National University, Kangnung, Republic of Korea

Y. Sun

World Laboratory, Lausanne, Switzerland

This paper describes the set of quality assurance procedures developed to check the status of the ALICE TOF SuperModules. Some preliminary results are presented as well.

1. Introduction

A large Time–Of–Flight (TOF) array [1] is the main detector devoted to Particle Identification for the ALICE experiment at the CERN LHC. It will allow hadron identification in the central region ($| \eta | \leq 0.9$) in the momen-

tum range from 0.5 GeV/c up to a few GeV/c.
The ALICE TOF is based on 1638 Multigap Resistive Plate Chamber (MRPC) [2,3] arranged in 90 modules. The whole structure is divided into 18 sectors in ϕ, called SuperModules (SM); five modules are grouped in a line to form one SM. At both ends of each SM special crates host the TDC boards as well as the power supply modules for front–end and readout electronics.

2. Test on the MRPC detectors and TOF modules

The great challenge of the ALICE TOF MRPC production was to garantee the same excellent performances obtained so far for all the prototypes. All the MRPC detectors have been tested during production for HV, signal short circuits and gas–gap width [4]; the overall fraction of rejected chambers is at the percent level. The whole production, as well as the modules assembly, is performed at the INFN Bologna Laboratories. The modules finished are then sent to the CERN laboratory to be arranged inside a SM.
A second level of quality assurance tests concern the TOF modules. The gas tightness is a fundamental demand; this is checked in Bologna after the MRPC insertion, when they arrive at CERN and after the SM assembly operations. Accepted leakage rates are less than 1 mb/h (the average measured value is < 0.2 mb/h). The signal connection between the MRPCs and the front–end channels is checked injecting a pulse directly on the MRPC via a special trace on the cathode printed circuit. This pulse will induce a signal on the pads and as a consequence on the full readout chain. This check is performed after the module assembly in Bologna and after the transport to CERN.
Once at CERN, all the modules are operated under cosmic rays in the Cosmic Ray Facility shown in Fig. 1 to study their global preformances. The facility contains a stack of 5 modules; two arrays of scintillator tiles with MRS APD light readout [5] placed at the top and at the bottom of the stack are used to tag cosmic rays. Modules on this facility undergo a one–week gas and HV conditioning; once the working voltage is reached a map of the modules is done with dedicated cosmic runs.

3. Test on crates and readout electronics

The ALICE TOF crates are custom VME 9U crates [6], each one containg a 12–slot VME64X bus. Two of these crates are placed at each end of a SM and house a Data Readout Module (DRM), that acts as VME master,

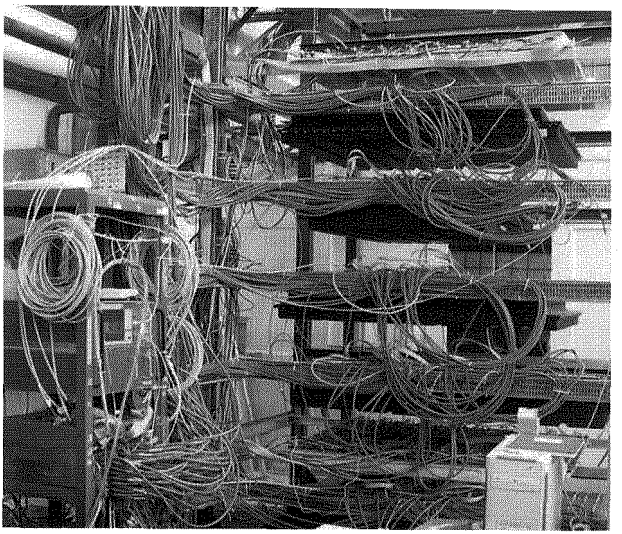

Fig. 1. Picture of the Cosmic Ray Facility at CERN with a stack of 5 TOF modules.

a Local Trigger Module (LTM) for trigger purposes, a Clock and Pulser Distribution Module (CPDM) hosted only in one crate every two, and 9 or 10 TDC Readout Modules (TRMs). The high–current low voltage for the VME boards is supplied by DCDC Converter modules placed inside the crate and designed to operate in a magnetic field (up to 5kGauss) and moderate radiation environment. Each crate fully equipped with all the VME boards is burned out and stressed for at least one week before being accepted. The crate performances including the readout electronics and the cooling system are checked during this commissioning test.

4. Test on Supermodules

A SM is assembled arranging the 5 modules on an assembly table and joining them together with aluminium supports. During and after cabling a new set of tests starts:

- *Gas system.* Gas–pipe tightness is checked before and after connecting the pipes to the modules. The pipes are filled with compressed air with an overpressure up to 100 mb; no leakage should be measured.
- *Cooling system.* The front–end cards (FEA) and the crate cooling pipes are first tested with air pressure at about 100 mb once the assembly of the SM is completed; if ok, the two complete systems are tested with water at

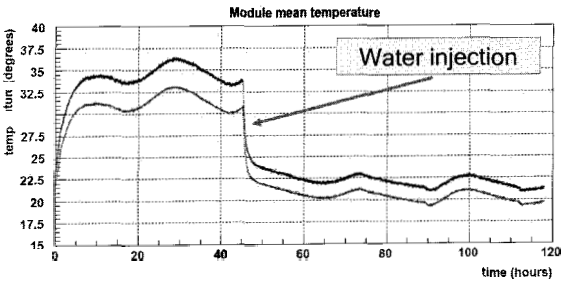

Fig. 2. Temperature test over a SM.

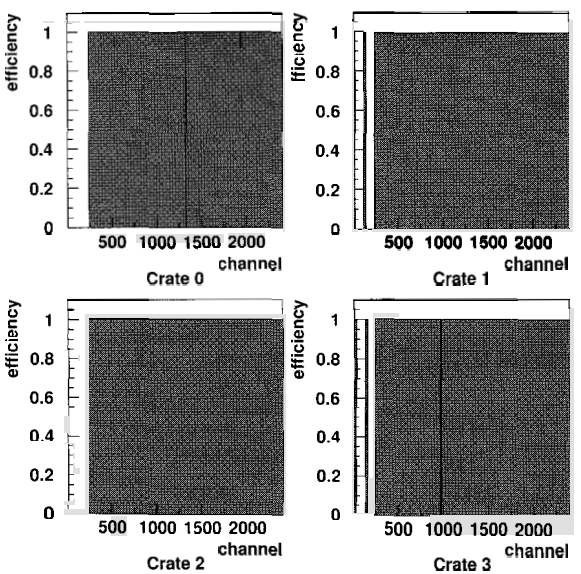

Fig. 3. **Result of pulser** test on SM10; from the plot only 2 dead channels over a total of 8736 can be seen.

10 bar for 20 minutes. Several tests have shown that both cartes and FEAs (Fig. 2) can be cooled to temperatures below the 25 ^oC limit required inside the ALICE magnet.
- *LV system.* Because of different cable lengths connecting the FEAs with the crates, all the LV channels have to be tuned in order to feed each FEA with the correct voltage. The LTM capability to provide the signal for the setting of the threshold voltages for more than 90 FEAs is also checked at this time.
- *HV test.* An HV up to 3kV is applied to all the MRPCs.
- *New pulser tests.* The test consists in inducing a pulse signal directly on the MRPC pickup pads and in checking the presence of the corresponding hits on the TDCs at the end of the electronic readout chain.
Fig. 3 shows the results of a pulser test over a full SM (4 crates); from the plot only two dead channels can be seen. Complementary to these tests are the noise tests, where data for a total time of about 1 second are collected without pulsing the dectector, searching for hot electronic channels. Most of bad and hot channels could be restored; the fraction of the remaining channels after the test of 11 SMs (96096 channels) is at the level of few channels over a thousand.

5. Conclusion

At the present 11 ALICE TOF SMs have been assembled and tested. Two of them are already installed in the ALICE experiment and in autumn 2007 also the others will follow. The complete installation is foreseen in the first months of 2008. Most of the tests described in this paper are repeated once the SM is installed as part of the commissioning procedure.

References

1. ALICE Collaboration, Time of Flight System, Addendum to ALICE TDR8, CERN/LHCC 2002–16.
2. E. Cerron Zeballos, I. Crotty, D. Hatzifotiadou, J. Lamas Valverde, S. Neupane, M.C.S. Williams and A. Zichichi, Nucl. Instr. and Meth. A 374 (1996), 132
3. G. Scioli, these Proceedings
4. A. Akindinov et al., Nucl. Phys. B 158 (2006) 78–82
5. A. Akindinov et al., Nucl. Instr. and Meth. A 555 (2005) 65–71
6. L. Colombini, M. Lippi, A. Mati, G. Passuello, S. Petrucci, M. Pieracci, G. Selmi and C. Tintori. Sep 2005, 5pp. Prepared for 11th Workshop on Electronics for LHC and Future Experiments (LECC 2005), Heidelberg, Germany 12–16 September 2005

Accelerator Neutrino Physics and Low Energy Tests of The Standard Model with High Intensity Neutrino Beams

V. Antonelli*

Department of Physics, Milano University and I.N.F.N. Milano Section, Via Celoria 16, 20133 Milano, Italy
**E-mail: vito.antonelli@mi.infn.it*

P. Ferrario

IFIC, CSIC-Universitat de València, Apt.Correos 22085, E-46071 Valencia, Spain

Neutrino physics will offer a possibility of improving the determination of Standard Model parameters in the region of medium and low energies, different from the one usually explored by colliders like LEP. In fact, in the near future many facilities will provide us with very high intensity artificial neutrino beams designed to solve some of the problems still open in neutrino physics. It could be interesting to use these high intensity beams also to recover the value of the Standard Model parameters like the Weinberg angle at low energies. A similar possibility had already been studied in literature in the case of neutrino factories. Here we present an analyis of this possibility also for experiments like the superbeams and beta beams, showing the feasibility of such a program.

1. The future of Accelerator Neutrino Physics and of Standard Model Precision Tests

It has been stressed many times in literature that the search for new physics should follow two main paths: not only the higher energy, but also the high–intensity frontier [1]. Neutrino (ν) experiments will play also in future an important role in this program. In order to pass from disappearance to appearance experiments and to fully determine the pattern of ν masses and mixing, dedicated high–intensity artificial ν beams will be required [2]. They could be used not only to study ν properties, but also as a sensitive probe of electroweak interaction. The potentiality of a high energy neutrino factory to measure many strong and electroweak processes has been shown already [3]. With our analysis we started addressing the issue whether with a *low energy* but sufficiently intense ν beam one can perform equally inter-

esting measurements and, in particular, extract in a competitive way the values of Standard Model parameters like the electroweak mixing angle.

There will be three stages in the future of accelerator ν experiments. In the first the already running or just commissioned long baselines (MINOS, the CERN/Gran Sasso beam and the first phase of T2K), using conventional ν beams from the decay of a secondary meson beam, will search for signals of ν_τ appearance and should improve θ_{13} knowledge down to about 7 degrees. In the second stage (beginning of the next decade) the "superbeams" should reach beam intensities about hundred times higher, exploiting very high–intensity and relatively low energy primary proton beams. Examples of such facilities are the second phase of T2K at JParc, NOνA in the States and a possible high–energy superbeam at CERN. If θ_{13} is in a region between about 1 and 3 degrees, it could not be determined by superbeams and would, instead, be accessible to new generation of experiments using ν from decays of a *primary* beam (having the advantage of higher intensity and a better control on the ν energy spectrum). Two possible kinds of primary beams are envisaged for this third stage: either a neutrino factory, i.e. relatively high energy (tens of GeV) muon beam, or a β–beam, i.e. relatively low–energy (few GeV) radioactive nuclei.

2. Theoretical Framework

At the typical energies of a neutrino factory (tens of Gev) the better channel to extract Weinberg angle is the ν elastic scattering on electrons [3]. The alternative offered by CC/NC deep-inelastic scattering ratio, that is competitive at a neutrino factory [3], could be considered also at relatively lower energies, but in this case the accuracy of the meaurement is significantly limited by the uncertainty related to parton distributions [4]. For lower energies (around one, or at most a few GeV), typical of superbeams and of low–energy β beams, a different possibility must be considered. The Fig. 1 shows that in the region of $E \sim M_N$ (quasi)–elastic contribution to the total cross section becomes of the order of magnitude of the inelastic one, while the total cross section is still reasonably large. Therefore (quasi)–elastic scattering could offer a promising opportunity to perform competitive measurements of Weinberg angle at low energies. We have performed a systematic study (not available before in literature) of the feasibility of this idea. For a detailed study of the theoretical framework we refer the interested reader to [5,6]. The main obstacle is the fact that (quasi)–elastic cross sections strongly depend on different hadronic form factors, parametrizing our partial ignorance of the hadronic part of the interaction. There are eight

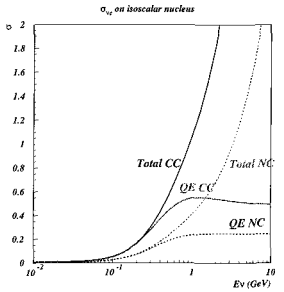

Fig. 1. ν–nucleon cross sections vs. energy.

independent form factors [7] entering the results. It was absolutely not evident a priori whether the uncertainty in their values could completely destroy the possibility of extracting $\sin^2\theta_W$ from these cross sections or not. The possibility of getting a positive answer to this question is one of the most important result of our analysis. In principle the number of quantities that should be extracted from the analysis is quite high (8 form factors in addition to the Weinberg angle) and we should have at our disposal 6 physical observables, corresponding to the different interaction channels for ν and $\bar{\nu}$ beams with nucleons. However, if the kinematical reconstruction is good enough, one can study the number of events in different angular bins, parametrize the form factors and try to fit these parameters as well as $\sin^2\theta_w$. In [5] and [6] we have shown that it is possible to find an analytic expression for $\sin^2\theta_w$ dependent only on measurable quantities (cross section combinations) and we have also performed a theoretical study of the error one expects to have in the extraction of the weak mixing angle. The result is encouraging (an accuracy of the order of $10^{-3} - 10^{-2}$ for $\sin^2\theta_w$). However, for real experimental situations, a more quantitative numerical estimate is needed.

3. Analysis and Results

3.1. *Physical situation and experimental caveats*

The detector choice is driven by the two main experimental requirements: the need of a mass sufficient to guarantee the desired statistics and the possibility of detecting CC and NC events with a ν beam energy between one and a few GeV. This second constraint essentially rules out water Cherenkov detectors, because the Cherenkov threshold implies that only protons with recoil momentum $p > 1.1$ GeV can be detected, removing most of the cross

section. The situation is much better in the case of liquid Ar TPC [8]. The constraint that the recoiling proton leaves a sufficiently long track to be distinguished from nucleon motion due to nuclear effects gives a cut on the proton energy $E - m \sim 50$ MeV i.e. $p \geq 300$ MeV. With a beam energy of the order of 1 GeV, about 75% of the scattering events survives this kinematic cut. In the real experimental setup it will not be possible to detect recoiling neutrons and, therefore, one is left only with proton contributions to NC current events and with only four, instead of six, independent cross sections. With a near detector at a few hundreds of meters from the source, it would be possible to obtain fluxes by many orders of magnitude larger than those at the far detector used for oscillations studies. However, in a realistic analysis one should keep in mind that an Argon TPC might have difficulties in handling interaction rates much larger than a few events per spill. This would put a bound on the maximum flux.

3.2. *Main steps and results of the analysis*

To estimate the accuracy in the determination of Weinberg angle, we have generated a set of fictitious events (treated as the experimental input of our analysis), using for the magnetic and electric nucleon form factors the expressions recently introduced in [10] and for the axial and strange form factors the functional forms of ref. [7]. We have considered a ν energy of $E = 1$ Gev and assumed values of the incoming ν and $\bar{\nu}$ fluxes equal to $\Phi_\nu = 10^{16}/(m^2 yr)$ and $\Phi_{\bar{\nu}} = 5 \times 10^{14}/(m^2 yr)$, typical for the T2K (second phase) superbeam, supposing to use a near detector located at about 300 m from the source. We have assumed to use a liquid Ar detector with a mass of the order of 10 KTons. The scattering events have been generated by using Poissonian distributions of the events. To extract the form factor and the Weinberg angle values we have used the minuit fit program, minimizing a χ^2 function obtained by comparing in the different kinematical bins our fictitious experimental data with the expected theoretical number of events (computed as functions of the form factors and of the Weinberg angle).

At a first stage we assumed to know the expression of the form factors and we have tried to perform a global fit of the parameters entering these expressions together with the weak mixing angle. To fit simultaneously such an high number of parameters (22) is a difficult task. It is reasonable to restrict the fit to the values of the Weinberg angle and of a significant subset of form factors, proving that the uncertainties in the values of the remaining form factors do not affect significantly the results of the analysis. An exhaustive analysis of different possible combinations will be discussed

in [9]. Here we limit ourselves to a few remarks. The accuracy on Weinberg angle is fully satisfactory in most cases. An interesting example is to let $sin^2\theta_W$ and the forward value of the strange magnetic form factor $G_M^S(0)$ as free parameters and repeat their fit by varying the value of the forward strange axial form factor. The choice of these 2 form factors is motivated by the fact their forward values are the only ones to be affected by a significant uncertainty. The output of this analysis, in very good agreement with the experimental input, is $sin^2\theta_W = 0.2309 \pm 0.0019(stat.) \pm 0.0024(syst.)$. Another significant result is obtained by fixing the values of the electric form factors (known with quite a good accuracy) and of the strange magnetic one and fitting together the Weinberg angle and the 2 magnetic form factors. We get $sin^2\theta_W = 0.2293 \pm 0.0006$ (with a difference with respect to the value used to generate data of about 3 σ and a relatively low uncertainty in the fit). It is easier in general to fit, together with the value of the weak mixing angle, the electric form factor of proton and the magnetic form factor of neutron. Unfortunately the results of the analysis exhibits a significant dependence on the explicit functional form assumed for the form factors. This is one of the main indetermination sources to take into account in the analyses of the real data that will be produced in the different experiments. In order to by pass this difficulty one can use a neural network to fit the different form factors. This part of the analysis is under investigation and the preliminary results are encouraging [9].

4. Acknowledgments

The authors would like to thank G. Battistoni and S. Forte who collaborated with them in the study on which this work is mainly based. V.A., is deeply grateful to the organizers, and mainly to Prof. Rancoita, for the invitation and for the stimulating human and scientific atmosphere.

References

1. B. Foster, Nucl. Phys. Proc. Suppl. 147 (2005) 3.
2. A. Blondel, A. Cervera-Villanueva, A. Donini, P. Huber, M. Mezzetto and P. Strolin, Acta Phys. Polon. B 37 (2006) 2077.
3. M. L. Mangano et al., arXiv:hep-ph/0105155.
4. G. P. Zeller et al. [NuTeV Collaboration], Phys. Rev. Lett. 88 (2002) 091802 [Erratum-ibid. 90 (2003) 239902]. S. Davidson *et al.* JHEP 0202 (2002) 037.
5. P. Ferrario, Laurea thesis, Milan University (July 2005).
6. V. Antonelli, G. Battistoni, P. Ferrario, S. Forte, Nucl. Phys. Proc. Suppl. 168 (2007) 192.
7. W. M. Alberico, S. M. Bilenky and C. Maieron, Phys. Rept. 358 (2002) 227.
8. S. Amerio et al., Nuclear Instruments & Methods A526 (2004) 329.
9. V. Antonelli, G. Battistoni, P. Ferrario, S. Forte, in preparation.
10. R. Bradford et al., Nucl. Phys. Proc. Suppl. 159 (2006) 127.

The Muon Ionisation Cooling Experiment - MICE

M. APOLLONIO

University of Oxford and John Adams Institute,
The Denys Wilkinson Building, Keble Rd.
OX1 3RH, Oxford, UK
E-mail: m.apollonio@physics.ox.ac.uk

Muon Cooling is discussed, showing its importance both for a future Neutrino Factory and the Muon Collider. The physics cases are introduced and a comparison of the two facilities is done, which illustrates similarities and differences. R&D programs, with special emphasis on the presently starting cooling experiment MICE, are discussed.

Keywords: Neutrino Factory, Muon Collider, Muon Cooling, Emittance.

1. Two Physics Cases

Neutrino Factory. In the last decade neutrino experiments have produced compelling evidence that neutrinos have mass and mix their flavours. This effect can be described by means of a unitary matrix [1], containing three mixing angles and a phase expressing possible CP violation. At present most of the parameters have been measured with precisions better than 10% [2], however we are still missing some important elements to complete the general description, namely: (1) the neutrino mass hierarchy $sign(\Delta m^2_{23})$, (2) the value of θ_{13}, presently there is only an upper bound, (3) the CP violating phase, δ, is completely unknown.

A non-zero value for θ_{13} would allow to measure δ, paving the way to CP violation studies in the leptonic sector. Albeit that some of these questions will be addressed in the next years by several experiments, the high intensity (10^{21} muons/year) together with clean neutrino production would make a Neutrino Factory (NF) the ultimate tool to determine the aforementioned parameters with an unprecedented precision.

Muon Collider. The second case refers to a future Higgs Factory (at about 0.1 TeV) or to the search for physics beyond the Standard Model at higher

energy scales (1 to 4 TeV), in a post LHC scenario. With respect to hadronic devices, the advantage of leptonic machines is represented by the clean event signature, however e^+e^- colliders suffer from radiation processes which impose the use of linear apparatuses [3] in lieu of circular machines. A major advance would be represented by a Muon Collider (MC), where muons offer several advantages over the electrons [6]: (1) the $1/m^2$ suppression in radiative processes which would allow the use of recirculating accelerators with an obvious reduction in size and costs, (2) the $(m_\mu/m_e)^2 = 4.3 \times 10^4$ enhancement in cross section for the s-channel annihilation to Higgs boson, making MC a unique tool to study electro-weak symmetry breaking and (3) the dramatic reduction of beamstrahlung processes, highly detrimental for electron machines at high energies while almost negligible for muons.

2. The Need for Cooling

Both cases mentioned in Sect. (1) rely on the possibility of accumulating muons in storage rings: in the NF they decay along straight sections, producing neutrinos towards a far detector, while in the case of the MC muons are kept circulating to collide at some interaction points where detectors are placed. The baseline designs for both facilities require some scheme of phase space compression (*cooling*) of the beams prior to acceleration [4,5] [6].

Muons are tertiary beams, resulting from hadronic interactions of protons on a target, and the following decays of pions. From this production mechanism muon beams have a large dispersion and divergence which is described in terms of emittance. The normalized 6D emittance can be defined from the beam covariance matrix, V, of phase space vectors (x, p_x, y, p_y, t, E) characterizing each muon of the beam:

$$\epsilon_{6D}^N = \frac{1}{m_\mu c} \sqrt[6]{det(V)}, \tag{1}$$

Reducing emittance (both in transverse and longitudinal phase space) is a pre-requisite to accommodate a substantial fraction of muons in the accelerating stage of the complex, maximising transmission. The short lifetime of the muon (τ_μ=2.2 μs) prevents the use of traditional techniques (*e.g.* stochastic cooling) leaving ionisation cooling as the only viable solution. This fundamental technology for high intensity muon storage rings was proposed more than 20 years ago [7], albeit its feasibility yet has to be proven. The transverse normalized emittance change per unit length can be expressed as a sum of a pure cooling term and a multiple scattering

one [4]:

$$\frac{d\epsilon_T^N}{dX} = -\frac{\epsilon_T^N}{\beta^2 E}\langle\frac{dE}{dX}\rangle + \frac{\beta_t(0.014GeV)^2}{2\beta^3 E m_\mu X_0} \tag{2}$$

Eq. 2 tells us that, in order to minimize the impact of multiple scattering, the transverse β_t function should be as low as possible (*e.g.* in a focus of the channel) and also the radiation length of the material should be high. Cooling is effective as long as the actual emittance of the beam is above its equilibrium value, where the two competing processes equal each other. This happens when:

$$\epsilon_T^N(equilibrium) = \frac{\beta_t(0.014GeV)^2}{2\beta m_\mu X_0}\langle\frac{dE}{dX}\rangle^{-1} \tag{3}$$

The figure of merit $X_0 \cdot \langle\frac{dE}{dX_0}\rangle$ justifies the use of liquid hydrogen as the best absorbing material and this is the choice adopted by MICE. However other choices (like LiH or He), albeit slightly less effective, are perfectly legitimate and imply less demanding engineering and safety issues.

In the NF the need for cooling, motivated by the finite acceptance of the accelerating section, could be relaxed by choosing machines with larger acceptances. Trading between large apertures and length of the cooling section requires a careful evaluation of the costs. At present the US Feasibility Study II B envisages a scheme with an 80 m long cooling section capable of a factor 2 reduction in transverse normalized emittance [5].

If cooling is a strong option for the NF, it becomes a necessity for the MC, where several order of magnitude reduction in 6D emittance is advocated [8].

3. MICE: the Muon Ionization Cooling Experiment[a]

So far the only approved experiment aimed at demonstrating the feasibility of muon cooling is MICE [9], presently in its contruction phase at RAL[b]. It is a program aimed at testing the performance of an ionization cooling channel for a variety of momenta (140, 200, 240 MeV/c) and initial emittances (ϵ_T^N = 1, 6, 10 mm rad). The overall picture of MICE is illustrated in Fig. 1 where the eighteen superconducting coils and the cooling section in the middle are displayed. The design for the cooling channel comes from the US Feasibility Study II [4] and is a SFOFO lattice with three liquid hydrogen absorbers interspersed with two RF systems, each made of four 201

[a]MICE comprises international institutions from UK, Europe, US, Japan and China.
[b]Rutherford Appleton Laboratory, Chilton (Didcot) UK

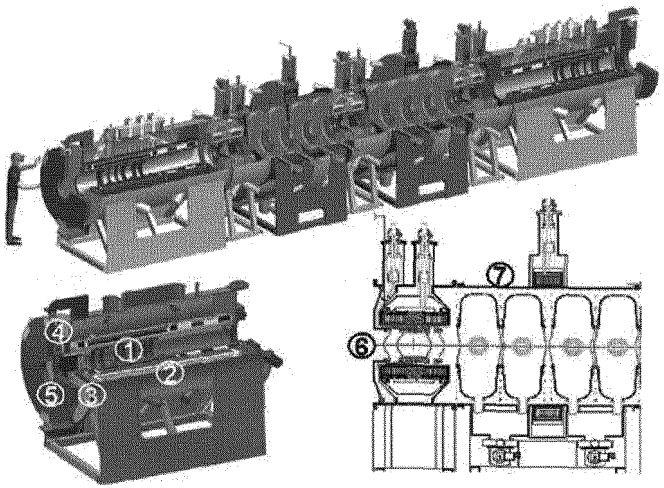

Fig. 1. (top) the MICE experiment. The cooling section is visible in the middle with its three liquid hydrogen absorbers and the two RF systems. The two spectrometers are located in the upstream and downstream edges.(left inset) a close view of the spectrometer: (1) tracker, (2) super conducting solenoid (endcoils, central solenoid, matching coils), (3) patch panel for tracker readout, (4) diffuser system and (5) iron shield. (right inset) cross section of the cooling cell: (6) Absorber and Focus Coil (AFC) module, (7) RF and Coupling Coil (RFCC) module.

MHz conventional cavities. Six absorber focus coils and two RF coupling coils provide the alternating B field. This configuration produces a small value for the beta function at the absorbers, contained maxima in the RF regions and a reduced growth of angular momentum in the absorbers (see Fig. 2). In MICE the emittance will be measured, before and after the cooling section, on a single particle basis. This requires a complete tracking and particle identification system: the former defining the kinematical parameters $(x, x\prime, y, y\prime, E)$, the latter providing the required high level of beam purity and the sixth phase-space coordinate t. Two fibre trackers placed upstream and downstream the cooling channel sit in a 4T field generated by 1.3 m long superconducting solenoids, whose uniformity ($\Delta B/B$ <1%) is ensured by endcoils. Four additional coils provide the proper matching with the cooling lattice. Before and after the trackers a combination of time of flight counters, Čerenkov detectors and electromagnetic calorimeters will be used to define the muon phase with respect to the RF cavities and to separate muons from electrons and pions.

Demonstration of cooling in MICE poses several challenges: these in-

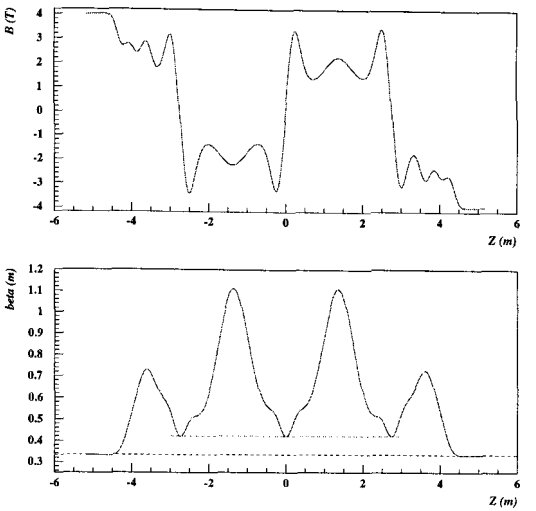

Fig. 2. (top) B_z field component along the z axis for the MICE SFOFO channel. (bottom) β function for the above optics with $P_z = 200$ MeV/c: the horizontal dashed lines indicate the values inside the spectrometer solenoids (33 cm) and at the absorbers (42 cm).

clude RF operations at high gradient (up to 16 MV/m) in a strong magnetic field (up to 3 T), safety issues related to the use of liquid hydrogen and the need for a precise (0.1 %) determination of emittance (see Sect. 4). A detailed description of the experiment follows in the next sections.

3.1. *Beamline*

MICE beamline is shown in Fig. 3 (a). The titanium blade of an oscillating target dips in the halo of the ISIS 800 MeV/c proton beam during the last 2 ms of the synchrotron cycle. Pions created via hadro-production are then captured by a quadrupole triplet and selected in momentum by a dipole (see Fig.3 (b)). Pions decay into muons in a solenoid[c], and are transported towards MICE by means of another dipole (selecting a momentum about half of the first) and by two triplets of quadrupoles.

Just before the first tracker and inside the bore of the upstream solenoid

[c]Provided by PSI, Switzerland (5 m long, 12 cm bore, 5T magnetic field).

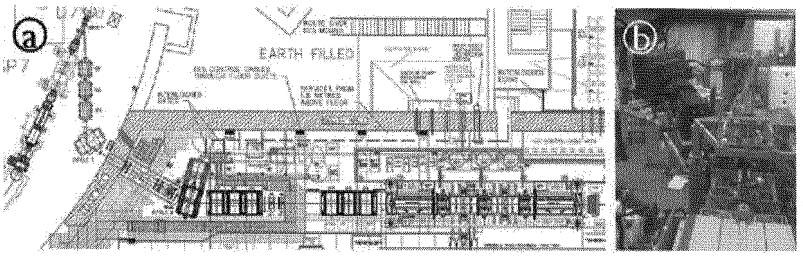

Fig. 3. (a) Top view of MICE beamline, from target to experiment. (b) bottom to top: target station, first triplet of quadrupoles and first dipole in the ISIS vault.

a layer of diffusing material (typically lead) is used to inflate the initial emittance in a controlled fashion [10]. A mechanical system is under construction which will provide the remotely controlled insertion of five different thicknesses, covering all the possible cases in (emittance,momentum) space.

3.2. *Particle Identification Detectors (PID)*

The precision required for the emittance measurement in MICE (see Sect. (4)) calls for a clear rejection of particles other than muons. Current studies show how the 99.9% required purity can be reached. The particle identification system relies on a combination of three different types of detectors (see Fig. 4):

- Time of Flight devices (TOF0, 1, 2)
- Threshold Čerenkov detectors (CKOVa, b)
- Muon Calorimeters (KL, SW)

TOF detectors. All three TOFs have a similar structure and operating principles: a (x,y) matrix of hodoscopes defines the passage of the muon in the transverse plane with a high time precision (about 70 ps). The first two devices (TOF0 and TOF1), located respectively after the second and the third set of quadrupoles, provide the trigger of the experiment. Their precise timing and the 10 m baseline helps in muon discrimination too. TOF1 will be also used to determine the time of the muon with respect to the RF system phase. TOF2, sitting at the downstream end of the experiment, will be used to select throughoing muons in order to measure genuine cooling (against scraping and decay spurious effects).

Čerenkov detectors. Two threshold devices located between TOF0 and before the last quadrupole triplet, complement the time of flight counters providing $\pi - e - \mu$ separation up to 300 MeV/c. After successful tests

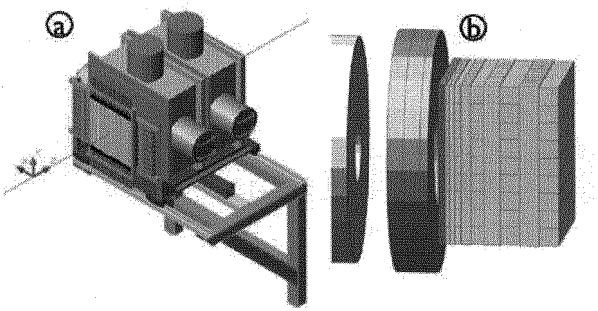

Fig. 4. (a) TOF0 counter and CKOVa,b detectors. (b) rendering of the muon calorimeters at the downstream end: KL fibre preshower (gray layer), SW scintillating bars calorimeter (yellow).

(summer 2006) TOF0,1 and Čerenkovs are being assembled and their installation is foreseen by the end of the year.

Calorimeters. The purpose of these detectors is separating muons from decaying electrons. A sandwich of scintillating fibres and lead grooved layers serves as a pre-shower (KL), which is followed by a fully sensitive block of scintillating bars (SW). The pre-shower degrades electrons while the scintillator provides a precise measurement of muon range. Both prototypes have been tested at the Frascati Beam Test Facility and are currently being assembled.

3.3. *Tracking Spectrometers*

The trackers, used to determine the kinematic parameters of throughoing muons, represent the core of the emittance measurement system: five stations are distributed over 1 m length, which are constituted by planes of scintillating fibres defining three views (u,v,w) orthogonal to the z axis. Tests conducted on prototypes showed a spatial resolution of 440 μm and the 4T field of the spectrometer solenoids should guarantee the resolution in momentum necessary for the 0.1 % precision on the final emittance measurement ($\sigma_{P_T} \simeq 1.5$ MeV/c for $P_T = 10$ MeV/c). Tracker production is well advanced and the first unit will be in place for the first beam. Solenoids are on their way to be delivered, tested at Fermilab and eventually installed by the first half of 2008 at RAL (Fig. 5).

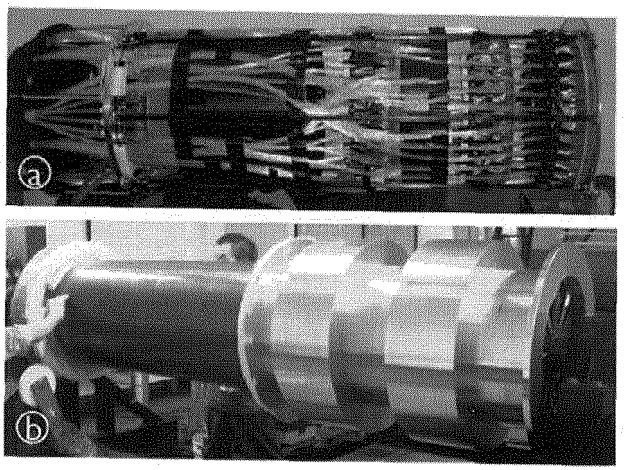

Fig. 5. (a) four station protoype of the MICE tracker. (b) spectrometer solenoid coils being wound.

3.4. *The Cooling Cell*

Eq. 2 describes ionization cooling as an instantaneous process in which momentum is reduced both in transverse and longitudinal components. In a real machine the z component of momentum has to be restored. This is accomplished by means of RF cavities between the absorbers. Four 201 MHz copper cavities will be used, which will operate in the large magnetic field produced by a coupling coil (CC) surrounding the system (we refer to this set as an RFCC module). Tests conducted at Fermilab MTA facility have shown RF protoypes can operate at 16 MV/m gradient without magnetic field; coming crucial measurements are expected to assess performances in intense B field environment.

The absorber-focus-coil (AFC) module performs the twofold task of momentum reduction and minimisation of the beta function, both ensuring the minimum equilibrium emittance. The use of liquid hydrogen as ionizing medium (as discussed in Sect. (2)), dictates some important constraints like the use of thin metal container windows, safety and hydrogen storage. Absorber bodies and thin windows are currently under test at KEK and Fermilab as part of the MuCool Program.

Fig. 1 shows the RFCC and AFC modules in the cooling cell.

4. Emittance Measurement

As described in Sect. (2), the demonstration of cooling in MICE is based on the determination of the kinematical properties of single muons, construction of the covariance matrix from an ensemble of particles and comparison of emittances determined before and after the cooling section. Fig. 6 (left) displays an ICOOL [11] simulation showing the emittance evolution through the channel: cooling in MICE is expected to be modest (around 10%) which requires a high precision in emittance determination (0.1% absolute).

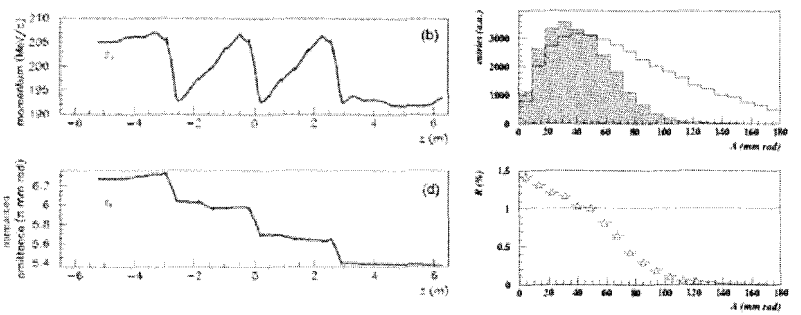

Fig. 6. (left) muon $< P_z >$ as a function of z along the channel (ICOOL simulation) for a 6 mm rad beam (top), and transverse normalized emittance through the channel (bottom), showing the 10 % variation between the upstream and the downstream tracker. (right top) Amplitude distributions before (empty histogram) and after (dashed histogram) the cooling channel for a 20 mm rad muon beam. (right bottom) ratio of the above hisograms showing the phase space enhancement at low amplitudes.

The aforementioned approach exploits only partially the important feature of MICE as a single particle experiment. An alternative approach (as described in [12]) is based on the use of a single particle feature: its (normalised) amplitude. Fig.6 (right) shows the distinctive feature of cooling, which reshapes initial distributions by depleting higher amplitudes enhancing phase space density.

5. Schedule

MICE will be built following a staged schedule to suit both experimental needs and funding availabilty. The current program foresees a first beam in January 2008. The tracker (without magnetic field) and the main PID devices will be on site. A first run (STEP I) with these detectors will allow a characterization of the beam. Measurement of emittance will be possible

with the installation of the first spectrometer solenoid (STEP II). STEP III will allow to assess the biases between the two spectrometers, preparing the experiment for the actual evaluation of cooling (STEP IV-V-VI). In STEP IV a first measurement of cooling will take place with the first AFC module. The focusing optics will be tested too, both in flip and non-flip modes (values of β at foci varying from 42 to 5 cm). STEP V will show the capability of restoring momentum by means of RF cavities. The final configuration (STEP VI) will test the functioning of a full cooling cell.

6. Conclusions

MICE will be the first apparatus to demonstrate the feasibility of ionisation muon cooling with momentum recovery. The great engineering challenges and the high precision required in the emittance measurement are to be tackled to reach for a successful result which will open the way to new accelerating machines based on muons. Tests on solid absorbers can be considered which could provide additional information for future facilities.

References

1. Z. Maki, M. Nakagawa, S. Sakata, Prog. Theor. Phys. 28 (1962) 970; Particle Data Group, Review of Particle Physics, Eur. Phys. J C3 (1998) 1
2. W. M. Yao et al. (Particle Data Group), J. Phys. G 33, 1 (2006)
3. T. Abe *et al.* "Linear Collider Physics Resource Book for Snowmass 2001", FERMILAB-Pub-01/058-E, June 2001
4. S. Ozaki *et al.* "Feasibility Study-II of a Muon Based Neutrino Source", http://www.cap.bnl.gov/mumu/studyii/FS2-report.html
5. J. S. Berg *et al.* "Cost-effective Design for the Neutrino Factory", Phys. Rev. Special Topics - Accelerators and Beams 9, 011001 (2006)
6. C. M. Ankenbrandt *et al.* "Status of Muon Collider Research and Development and Future Plans", Phys. Rev. Special Topics - Accelerators and Beams, Vol. 2, 081001 (1999)
7. A. N. Skrinsky, V.V. Parkhomchuk, Sov. J. Part. Nucl. 12, 223 (1981)
8. R. Palmer *et al.* "A complete Scheme for a Muon Collider", e-Print: arXiv:0709.2864
9. The MICE Collaboration, "An International Muon Ionization Cooling Experiment (MICE)", Proposal to the Rutherford Appleton Laboratory, 10 January 2003, http://mice.iit.edu/mnp/MICE0021.pdf
10. M. Apollonio, J. Cobb "Optimal Size for the MICE Diffuser", MICE-NOTE-BEAM-0176
11. R. C. Fernow et al., "ICOOL Reference Manual v2.96", Brookhaven National Laboratory, 10 April 2006.
12. M. Apollonio, "Measuring Single Particle Amplitudes with MICE", Proceedings of PAC07, Albuquerque, New Mexico, USA

Luminosity measurement using Cherenkov Integrating Detector (LUCID) in ATLAS

D. CAFORIO

Dipartmento di Fisica, Università di Bologna, and INFN, Bologna, Italy
E-mail: Davide.Caforio@bo.infn.it
www.bo.infn.it

LUCID (LUminosity measurement using Cherenkov Integrating Detector) is a Cherenkov counter designed to monitor the luminosity in the ATLAS experiment. Since the final accuracy of the measurement of some crucial physical quantities in the LHC program will depend on the precision of the luminosity measurement, it is mandatory to push the latter to its best. This in turn implies the need to monitor the beam conditions. In this paper an overview of LUCID is given. After a description of the detector, an insight into the luminosity measurement strategy in ATLAS is given, as well as a description of the calibration strategy of LUCID.

Keywords: luminosity; LUCID; ATLAS.

1. Introduction

Measuring luminosity is important as it correlates the number of events N of any physical process to its cross-section σ:

$$N = \sigma \times \mathcal{L} \tag{1}$$

A similar relation holds between the event rate ($R = \frac{dN}{dt}$) and the instantaneous luminosity L.

Luminosity may represent the main source of systematics on cross section measurements. As an example, in fig. 1 the expected uncertainty in the measurement of the cross-section of the Higgs boson at LHC is plotted against its mass for various processes [1]. Dropping the uncertainty in the luminosity by one half gives, in the region of interest, a drop by one half in the uncertainty on the cross-section.

Measuring the instantaneous luminosity is also important to monitor the beam and to use it efficiently. For each filling of the LHC, the luminosity is

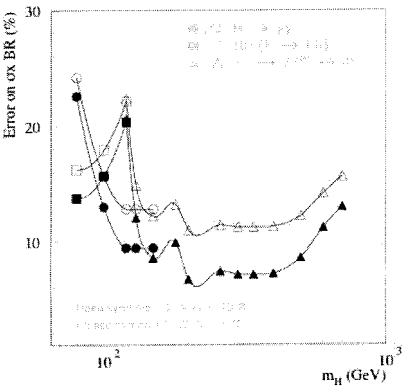

Fig. 1. Relative precision on the measurement of the Higgs-boson rate ($\sigma \times$BR) for various channels, as a function of m_H, assuming an integrated luminosity of 300 fb^{-1}. The luminosity is assumed to be known to 10% (open symbols) or to 5% (black symbols) [1].

expected to evolve with time according to the power law [1]:

$$L = L_0 \, e^{-\frac{t}{\tau}} \tag{2}$$

where $\tau \simeq 14$ h. Luminosity is thus expected to decrease by 1% every 10 minutes and can be considered as constant over a period of one minute.

Thanks to its good time resolution, LUCID can give luminosity values for every bunch crossing. It can then be used to check the stability of the bunches and reject the bad ones.

2. The ATLAS strategy

The ATLAS collaboration strategy in measuring the luminosity consists of various steps.

A first estimate of the absolute luminosity can be obtained from the machine parameters. Previous experience has shown that the typical accuracy reachable with this method is of the order $5 - 10\%$. An improvement is expected on the mid term from the measurement of the rate of well known physics channels. On the longer term a dedicated detector, ALFA, will measure the absolute luminosity in dedicated runs with specific beam optics and low luminosity ($L \simeq 10^{27}$ cm^{-2} s^{-1}).

The relative luminosity will be measured by LUCID, a Cherenkov counter designed to work in the full dynamic range of LHC from low ($L = 10^{27}$ cm^{-2} s^{-1}) to full luminosity ($L = 10^{34}$ cm^{-2} s^{-1}).

3. LUCID

3.1. *Concept*

LUCID counts the average number of charged particles per bunch crossing by detecting the Cherenkov light emitted in a gaseous radiator.

The detector implementation will be performed in two phases, for low ($L \simeq 10^{33}$ cm^{-2} s^{-1}) and high ($L \simeq 10^{34}$ cm^{-2} s^{-1}) luminosity respectively. The first phase consists of two conical shaped aluminum vessels 1.5 m long and about 30 cm in diameter. The vessels are placed around the beam pipe 17 m away from the interaction point, on both sides. 20 aluminum tubes, filled with C_4F_{10} at a pressure of 1.3 bar, are positioned inside each vessel to form two concentrical rings pointing to the *pp* interaction region. The coverage in pseudorapidity is $5.5 \leq |\eta| \leq 6.1$. Cherenkov light is emitted

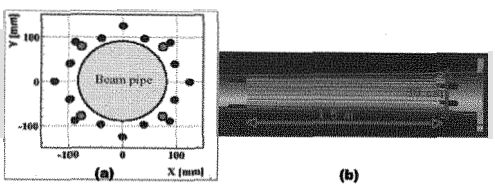

Fig. 2. (a) Transverse and (b) longitudinal view of the LUCID vessel.

under an angle of about 3° and reaches the end of the tubes after an average of 3 reflections. For each vessel, 16 tubes out of 20 are read out by PMTs directly coupled to the tubes; 4 are read out by fiber bundles coupled to a Multi Anode PMT (MAPMT). In the second phase, when the radiation will be much higher, all PMTs will be replaced by fibers and the number of tubes will be increased to 168.

LUCID characterisrics can be summarized as follows:

a) good background rejection thanks to the Cherenkov threshold and projective geometry;
b) fast detector response ($\sigma_t \simeq 3$ ns) for single bunch crossing luminosity measurement;
c) capability of particle counting thanks to the lack of Landau fluctuations;
d) radiation hardness.

Undesidered background can be rejected thanks to the Cherenkov threshold which suppresses low energy particles. The detection threshold

in C_4F_{10} is 25 GeV for pions and 10 MeV for electrons. The number of Cherenkov photons is directly proportional to the path of the charged particle in the gas. In a *pp* interaction, primary particles (mostly pions) travelling along the whole tube length coexist with a large number of secondary particles hitting the tubes with larger angles. The IP pointing geometry reduces the signal produced by secondary particles both due to their shorter paths and to the higher number of reflections of the light they produce.

After the project approval in February 2007, LUCID was constructed and assembled by the Alberta University (Canada) and Bologna University (Italy) groups.

LUCID is located in a region where the absorbed doses are expected to be 0.7 Mrad/y in phase I and 7 Mrad/y in phase II [2]. Radiation hardness tests on the PMTs have successfully been conducted during the summer of 2007 at the National Physical Laboratory (Teddington, London) and at the ENEA (Casaccia, Roma) facility in order to verify that the response of the PMTs is not affected by the surrounding radiation. After irradiation with neutrons (equivalent to 10 years of operation at low luminosity or 1 year at high luminosity) and gamma rays (equivalent to 30 years of operation at low luminosity or 3 years at high luminosity), no significant changes in the PMTs characteristics were observed [3].

3.2. *Calibration*

Since LUCID is a relative luminosity monitor, it must be calibrated with absolute luminosity measurements.

In the first LHC days, LUCID will be calibrated with the luminosity given by the machine parameters (proton currents and transverse dimensions of the beam).

On the mid term, a better accuracy can be obtained by using well known physics processes: given the theoretical cross section σ and the numebr of reconstructed events N, $\mathcal{L}$ is then given by equation 1. A typical QED channel

$$pp \rightarrow (p + \gamma^*) + (p + \gamma^*) \rightarrow p + (\mu^-\mu^+) + p$$

has the advantage of a small theoretical uncertainty (1%) but the drawback of low frequency ($<<$ 1 Hz), even at high luminosity [4]. Electroweak channels with W or Z decaying into leptons have higher frequencies (6 Hz for $Z \rightarrow \mu^+\mu^-$, 60 Hz for $W \rightarrow \mu\nu$ at $L = 10^{34}$ cm^{-2} s^{-1}) but also larger systematic uncertainties ($\Delta L/L \sim 4 - 6\%$) mainly due to the protons' PDFs [5–7].

On a longer term (after LHC shutdown in 2009), the ALFA detector will measure the absolute luminosity from elastic pp scattering in low luminosity ($L = 10^{27}$ cm^{-2} s^{-1}) dedicated runs with specific beam optics. The ALFA detector consists of scintillating-fiber trackers located in Roman Pots, 240 m away from the IP. Roman Pots allow to detect elastic pp interactions in the Coulomb-Nuclear interference region by detecting the scattered protons at $1 - 2$ mm from the beam axis. The expected accuracy is 2-3 % [2].

4. Conclusions

In this paper the features of LUCID, a relative luminosity monitor based on the Cherenkov effect, are presented. The stretegy pursued by the ATLAS collaboration will lead to measure luminosity with an expected accuracy of 2-3 %.

LUCID is the only subdetector in ATLAS specifically dedicated to measure the instantaneous luminosity. After four test beams at DESY and CERN as well as radiation hardness tests, LUCID is now ready to be installed.

Acknowledgments

I wish to thank the following people for their support and assistance: M. Bruschi, R. Di Sipio, L. Fabbri, P. Faccioli, B. Giacobbe, P. Giovannini, M. Piccinini, J. Pinfold, C. Sbarra, A. Sbrizzi, R. Soluk, J. Soukup, R. Spighi, S. Valentinetti, M. Villa, Y. Yao, A. Zoccoli.

References

1. ATLAS Collaboration, *The ATLAS Physics TDR (Vol. I)* CERN/LHCC/99-14.
2. ATLAS Collaboration, *ATLAS Forward Detectors for Luminosity Measurement and Monitoring Letter of Intent* CERN/LHCC/2004-010 (22 March 2004).
3. S. Valentinetti, *Test di resistenza a radiazioni sui fotomoltiplicatori del rivelatore di luminosità LUCID dell'esperimento ATLAS a LHC* (Master Thesis, Bologna 2007).
4. ATLAS Collaboration, *The ATLAS Physics TDR (Vol. II)* CERN/LHCC/99-15.
5. *CMS-NOTE-2006-124*, (October 2006).
6. *CMS-NOTE-2006-082*, (23 May 2006).
7. *CMS-NOTE-2006-068*, (14 October 2006).

THE CMS MAGNET COMMISSIONING AND THE DEVELOPMENT OF AN IMPROVED CMS CONDUCTOR SUITABLE FOR FUTURE PROPOSALS

D. CAMPI, B. CURE, A. GADDI, H. GERWIG, A. HERVE', S. SGOBBA
CERN, Geneva
Switzerland

P. FABBRICATORE
INFN Genova
Italy

F. KIRCHER
CEA Saclay
France

The success of the CMS Magnet commissioning has clearly shown the reliability of the conceptual choices for the cold mass. The reinforced conductor and the multi layer winding open the path for the conception of Large Magnet for HEP of the next generation. The paper will report about the basic results of the test campaign and then, after some critical considerations about the choices made for the CMS coil construction, possible improvements for the conductor construction are outlined. The main goal being to preserve long term RRR, and thus stability, of the insert and simplify the welding process to join the reinforcement alloy to the insert.

1. Introduction

The Compact Muon Solenoid (CMS) is a multi-purpose detector due to operate at the Large Hadron Collider (LHC) presently being constructed at CERN in the Geneva region. LHC will provide collisions of two 7 TeV proton beams with a designed luminosity of 10^{34} cm^{-2} s^{-1}. The CMS detector, being installed about 100 m underground in one of the four experimental halls, includes the magnet [1] comprising a 12.5-m long, 6-m inner diameter, 4-T superconducting solenoid and of a 12000-t, 1.5-m thick iron yoke to bend the charged particles providing their momentum measurement. To test the magnet a commissioning campaign has been done during August-October 2006.

2. The CMS superconducting solenoid

The main design parameters of the solenoid are recalled in Table 1.

Table 1. Main Parameters of the CMS Coil

Parameter	Value
Magnetic length	12.5 m
Free bore diameter	6.0 m
Central magnetic induction	4.0 T
Maximum induction on conductor	4.6 T
Nominal current	19.1 kA
Average inductance	14.2 H
Stored energy	2.6 GJ
Stored energy per unit of cold mass	11.6 kJ/kg
Operating temperature	4.5 K

The most challenging engineering choices of the design, which had to be checked during the commissioning, were a combined conductor (cable, co-extrusion in pure aluminium, plus a mechanical reinforcement) [2], a cold-mass made of 5 modules, mechanically, electrically and cryogenically coupled, and the indirect cooling the coil in the thermosiphon mode. A passive protection of the coil, by the means of a quench back process, which is generated into the external cylinder in case of a fast discharge or a quench, has been retained as well. The quench back process initiates a distributed quench as a result of the induced currents in the conductor and the external cylinder. Nevertheless, a classical resistive dump circuit with a discharge voltage of 600 V is connected to the coil to extract about 50 % of the stored energy.

The powering circuit of the coil comprises a bipolar thyristor power converter, which covers the range of voltage from +26 V to -23 V, with a nominal current of 20 kA, two main breakers to disconnect the power source and leave the coil in on its dump resistor (in case of a fault on the power converter or in case of a quench of the coil), a dump resistor which consists of three elements. These elements can be put either in series or in parallel through contactors, so as to adjust the value of the dump resistor.

Consequently, the discharge of the magnet performs in three modes: partial or total ramp down through the power converter using the reverse voltage of -23 V, slow discharge through the dump resistor with a value of 2 mΩ (elements in parallel) to be followed by a fast discharge generated once the current is under 4 kA, and the fast discharge trough the dump resistor with a value of 30 mΩ

(elements in series) only when a quench or a dangerous situation is detected in the magnet.

3. Cool-down and magnet commissioning

The cool-down of the solenoid was started on 2 February 2006 and the 220-t cold mass was smoothly brought from ambient temperature to 4.5 K in 24 days. The main parameter to be monitored during the cool-down is the difference of temperature along the coil. The maximum acceptable value was set to 40 K, but in practice, this value never reached more than 22 K. At the end of the cool-down the RRR value of the whole coil of 420 was measured between 273 K and 10 K that gives the RRR around 1850 for the pure aluminium stabilizer (starting from about 3000 for the virgin billets).

Two magnet test campaigns took place in August and October 2006. During the first campaign, the magnet was progressively charged up to its nominal field. Current ramps were done up to 2, 3.2, 7.5, 12.5, 15, 17.5 and 19.1 kA (corresponding to the target central field of 4.0 T). After a flattop of about one hour at each current level, the magnet was discharged either in slow or fast mode. It is only above 7.5 kA that a fast discharge can induce a quench of the magnet by quench-back effect. The first results of this campaign are reported in [3]. During the second campaign, the main goal was to measure the magnetic field inside the bore of the magnet and in some parts of the iron yoke. Measurements were done for a central field of 2, 3, 3.5, 3.8 and 4 T, with current flattops typically two-days long. These long flattops were also used to set the control parameters of the coil for the long-term operation.

4. Commissioning results

4.1. *Thermal measurements*

Main points of the thermal measurements have been the inlet temperature at the phase separator (4.45 K), the average temperature of the inner part of the coil (around 4.7 K) and the static heat loads at 4.5 K, resulting in 154 W on the cold mass alone, plus 20 W on the phase separator, and in addition, twice 0.4 g/sec for the current leads at zero current. The gross total has been measured to be 194 W at zero current and 226 W at nominal current.

At the nominal current, the coil temperature increases around 0.3 K at the beginning of a slow discharge because of the eddy currents in the conductor and the structure. It has been demonstrated also the good operation of the

thermosiphon, which was working with a filling factor of the phase separator around 25 % in volume.

4.2. *Electrical measurements*

Several points were checked during the commissioning:

- Coil insulation to ground: the value measured at various stages of the tests with a 2.2 kV voltage test value has always been larger than 50 MΩ.
- Apparent coil inductance: the value measured through the induction voltage is decreasing while increasing the current, as the iron yoke reaches the saturation region. At low current, the apparent inductance of the coil is 14.7 H, and then decreases down to 13.3 H at 18 kA.
- Electrical joint resistance: the measured values are ranging from 0.7 to 1.6 nΩ at 10 kA, with no measurable magneto-resistive effect. This corresponds to a maximum dissipation in each joint of 0.6 W at the nominal current.

4.3. *Current fast discharge*

During all the tests, the coil did not exhibit any natural quench, but a fast discharge above 7.5 kA induces a quench of the coil through the quench-back process. It is worth mentioning that although CMS has the highest density of stored energy per unit of cold mass compared to any similar superconducting magnets ever built (11.5 kJ/kg), these values are fully compatible with a safe behaviour of the magnet in case of quench. In fact, studies are starting to see how such a concept can be used or adapted to large coils for field up to 5 T [4].

4.4. *Magnetic measurements*

The extensive results of the magnetic measurements are reported in reference [5]. Using a fieldmapper with 3-D Hall probes, it was possible to measure the field within the whole aperture of the magnet from 2 to 4 T central field with a relative accuracy inside the coil at the level of 0.7 10^{-3}. Other 3-D Hall probes and flux loops were used to measure the local field and the magnetic flux density in the yoke.

5. Towards an improved conductor for future detectors

5.1. *R&D made so far*

In 2004, at the end of the coil modules construction, the CMS Magnet team started a small R&D program mainly with the aim of keeping available in

industry the expensive tooling that had been used to produce and wind the conductor. For economical reasons the efforts were concentrated on the improvement of the mechanical parameters of the conductor to target, in a generic way, solenoids of similar dimensions with higher field.

The choices consisted mainly in replacing the high purity aluminum of the stabilizer (Al 99,998%) with a cold drawn Al-0.1wt%Ni alloy, developed for the Atlas thin solenoid [6, 7], and replacing the reinforcement alloy AW-6082 by a higher strength alloy EN AW-7020 (ALZn4.5Mg1). The results of preliminary test with pure aluminum are described in [8] and have been very encouraging because they have demonstrated the possibility of cold working at 20 % a large section, as that of the insert of CMS, without degrading the bonding with the Rutherford cable.

5.2. *Considerations from the CMS construction in view of new projects*

The successful commissioning of CMS in 2006 and the appearance of HEP projects with coils similar to CMS and a field of 5T, has induced the CMS Magnet team to reconsider, a posteriori, all the technical choices made in the early nineties, which have allowed CMS to reach the specific stored energy of 11.6 kJ/kg which was never achieved before for this kind of magnets.

In [4] all the points are described in detail, but the main conclusion is that if one wants to target 5T keeping a similar enthalpy margin of 1.5 to 2 K, and strain in the conductor of 0.15%, most of the basic technical choices concerning winding, impregnation and conductor can be kept. A good improvement could be done by replacing the pure Al of the insert with the Al-0.1wt%Ni alloy. This change doesn't target the increase of the mechanical behavior of the conductor but the possibility of having an high strength alloy which could always work in the elastic domain and thus prevent degradation at long of its RRR.

5.3. *Next steps in the CMS Conductor improvement*

In the next months it is now envisaged to produce 200 m of the new insert to demonstrate extrudability of the CMS section with 0.1% Ni doped Aluminum and non degradation of the critical current of the cable, then check cold working at 20% of the insert section without degrading the bonding with the cable, and confirm invariance of the RRR after cycling.

In parallel, an investigation of the alternative methods to the Electron Beam Welding technique to reinforce the insert, like soft soldering, laser beams and friction stir welding could be done with a goal to simplify the welding process avoiding vacuum around the welding. Some of these techniques were already

taken into account in the past, but their state of the art needed development whose timing was not compatible with CMS construction planning.

6. Conclusions

The CMS Magnet has been very successfully commissioned in the surface hall SX5 in summer 2006 and is now installed in its final position in the underground experimental cavern ready to be cooled before the end of this year. The critical review of the technical choices made for CMS shows that they are mostly suitable to build similar coils with 5T field. An R&D program to improve long-term invariance of the conductor RRR as well as the investigation of simpler welding techniques to join the reinforcement to the insert is envisaged in the first half of the next year.

References

1. CMS Magnet Collaboration, "The magnet project: Technical Design Report", CERN, volume CERN/LHCC97-10, CMS TDR 1,1997
2. B. Blau, D. Campi, B. Curé, R. Folch, A. Hervé, I .L. Horvath, F. Kircher, R. Musenich, J. Neuenschwander, P. Riboni, B. Seeber, S. Sequeira-Tavares, S. Sgobba, and R.P.Smith., "The CMS conductor", *IEEE Trans. Appl. Supercon.*, Vol 12, No 1 pp 345-348, Mar 2002
3. D. Campi et al., "Commissioning of the CMS magnet", *IEEE Trans. App. Superconduct.*, Vol 17, No 2, June 2007
4. A. Hervé, D. Campi, B. Curé, P. Fabbricatore, A. Gaddi, F. Kircher, S. Sgobba, "Experience gained from the construction, test and operation of the large 4-T CMS coil", submitted for publication to Proc. 20th Int. Conf on Magnet Technology, Philadelphia, 2007
5. V. Klyukhin et al., "Measurement of the CMS magnetic field", submitted for publication to Proc. 20th Int. Conf on Magnet Technology, Philadelphia, 2007
6. K. Wada et al., "Development of high-strength and high-RRR aluminium-stabilized superconductor for the Atlas thin solenoid", IEEE Trans. App. Superconduct., Vol 10, pp 373-376, Mar 2000
7. D. Campi, private communication, Jul 2007
8. S. Sgobba et al., "Toward an Improved High Strength, High RRR CMS Conductor", IEEE Trans. App. Superconduct., Vol 16, pp 521-524, Jun 2006

Commissioning the CMS experiment

Tiziano Camporesi* representing the CMS collaboration
PH department, CERN, Geneva , Switzerland
** Tiziano.Camporesi@cern.ch*

The CMS experiment is getting ready to take data at the LHC accelerator at CERN. Due to late delivery of the experimental caverns the detector had to be pre-assembled on the surface and lowered in large segments. This has constrained the commissioning strategy of the experiment. Global commissioning has started in Spring of 2007 and has progressed in parallel with the construction and assembly of detector and services underground. This paper describes the strategy adopted in order to commission components of the system in incremental steps in order to be ready to accept collisions from LHC with a well debugged and understood system, including the detector, acquisition system, trigger, software, computing and data shipping.

Keywords: HEP; Proceedings; CMS;commissioning;LHC

1. The CMS experiment

The CMS experiment is being assembled in one of the experimental cavern of the LHC accelerator complex at CERN in Geneva , Switzerland. The geological structure of the area where the cavern has been located (around the Interaction point 5 of the old LEP accelerator) has been known to be causing civil engineering difficulties and, from inception, the experiment has been designed so to allow its pre-assembly on the surface in segments which could be lowered as complete units through the cavern shaft. An artist view of the detector can be seen in Fig. 1.

The total number of elements to be lowered is 13: 6 endcap disks (3 on each side named YEs, 2 very forward calorimeters named HF, and 5 barrel wheels called YBs). Each element carries a sign identifying on which side of the interaction point it is located and an order number. The central barrel wheel carries the superconducting solenoid which has been designed to generate a uniform field of 4 Tesla.

Such structure allows for easy maintenance access: each element carries its own services (Low voltage, cooling, safety) and is connected to the elec-

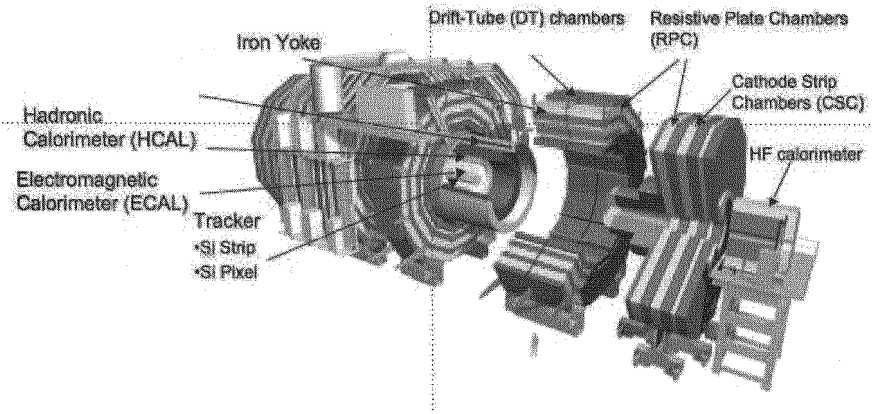

Fig. 1. Overview of the CMS detector

tronics houses located in the adjacent service cavern via cable chains which can move with the element.

The late delivery of the experimental cavern (late spring 2006) and the constraints to be ready for the LHC beam in may 2008 has led to a specific commissioning strategy: the commissioning of parts of the detector had to be carried out while services, and the rest of the detector, were being built/installed.

The first element to be lowered in the experimental cavern was the HF+ detector (November 2, 2006), followed by the +side endcap elements in December 2006. By January the first 2 barrel wheels were lowered followed by the heaviest element, the central barrel wheel YB0 carrying the CMS solenoid, on February 28 2007. The barrel hadron calorimeter -a brass-scintillator sampling calorimeter-, preassembled on the surface in two rings was inserted in the solenoid immediately afterwards.

The 36 supermodules of the Electromagnetic barrel calorimeter -comprising 61200 $PbWO^4$ crystals- were successfully inserted by the end of July 2007.

The last elements of CMS, the 3 disks of the negative side endcap will be lowered by the end of the year.

The tracker -comprising 220 m^2 of silicon microstrips-, described in fig 2, is ready to be transported to the experimental site and will be inserted once the cabling of the electromagnetic and hadronic calorimeter will be completed. This cabling is ongoing and is foreseen to terminate in November.

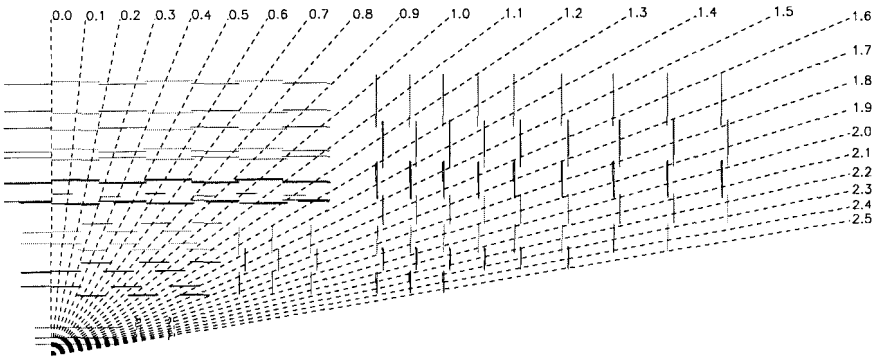

Fig. 2. Schematic layout of CMS tracker

All of the subdetectors of CMS have front end electronics installed on the detector: information is carried on optical fibers from the experimental cavern to the service cavern. The readout is performed by an off-detector electronic chain. Such electronics is all located in the service cavern which houses two floors of counting rooms. Only the muon detectors (Drift Tubes and RPC for the barrel and Cathode Strip chambers and RPC for the endcaps) have a first data concentration performed by so called sector collectors located on the towers attached to the CMS elements.

The readout is performed by Front End Data concentrators (FEDs) which collect the information sent on the fiber-optic links. The FEDs feed the data to the central DAQ electronic chain shown in Fig 3 . The central DAQ chain provides Event Building (Builder Units), a software level of filtering (High Level Trigger), Storage of the events (Storage manager) and an overall layer of control (Run Control)-for more details see ref.[1]).

To date all the hardware for the central DAQ has been installed and commissioned. The ultimate performance of the system should be able to sustain a first level trigger rate of 100 KHz with corresponding filter unit capacity. To date only 2/8 of the PC filters are installed: the remaining PCs will be available by late 2008.

Another important element of the CMS hardware chain is the first level trigger electronics. A schematic view of the Level 1 trigger is shown in fig. 4. The subdetector hardware builds locally trigger information (calorimetric clusters of energy for the calorimeters and track stubs for the muon detectors). The calorimeters feed their info to Regional Calorimeter Trigger modules, which in turn provide information for the Global Calorimeter trigger module. The Muon detectors feed their information to Regional Trigger

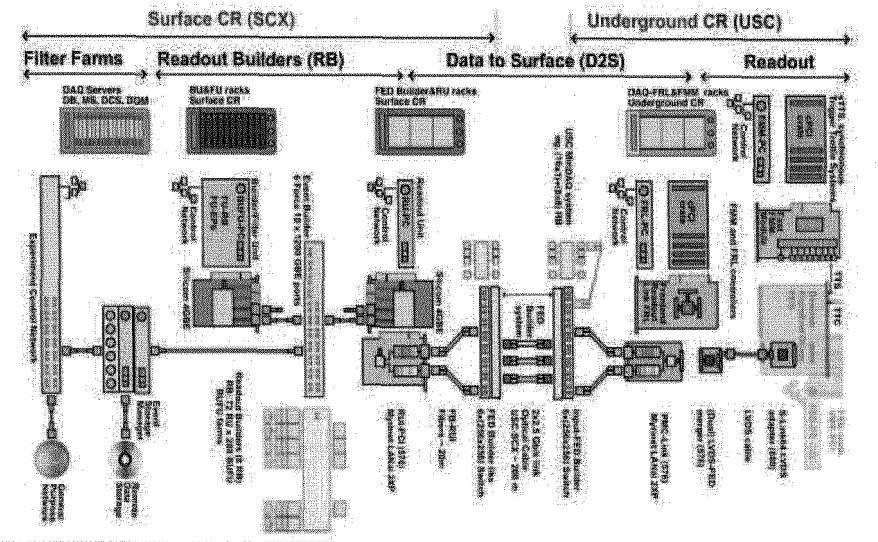

Fig. 3. CMS data acquisition layout

modules which identify tracks which in turn feed the Global Muon trigger module. The information from the Global calorimeter and Global muon triggers are sent to the Global trigger module which provides the trigger to the experiment(see ref.[2] for a complete description of the CMS trigger, timing and control system). To date more than 80% of all the off-detector electronics has been installed in the service cavern or on the towers as shown in table 1.

Table 1. Installed off-detector electronics:FEDs are the boards which concentrate the data arriving form the front ends and feed the data fragments to the central event builder, FEC and CCS are the timing and control distribution cards for tracker and ECAL respectively, TPGs are trigger primitive generation board which generate the local trigger components to be used by the central trigger,.

	FEDs	Other	TPGs	Tower electronics
Tracker	100%	100% FECs	n.a	n.a.
ECAL barrel	100%	100% CCS	80%	n.a.
HCAL (HE, HB, HF)	100%	50% HLX (Lumi)	100%	n.a.
Drift Tubes	40%	60%	50%	80%
CSC	75%		100%	100%
RPC	100%	100%	100%	50%

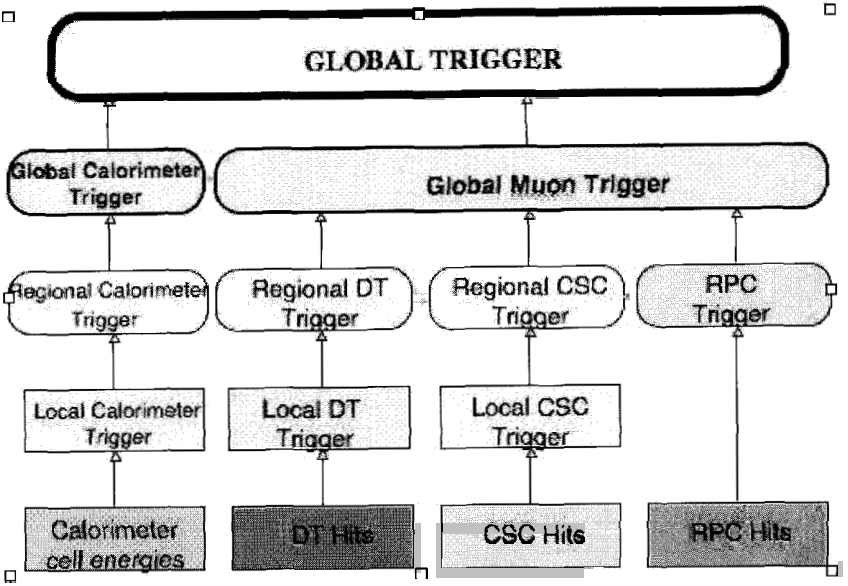

Fig. 4. CMS first level trigger components

2. Commissioning strategy

The commissioning has progressed through several phases: all subdetector have been commissioned stand-alone prior to the installation into the CMS elements. The necessity to commission the superconducting coil on the surface has created the occasion to make a full integration test of all the CMS subdetectors in summer 2006. After lowering into the experimental cavern, each element has to be connected to the cable chains and equipped of all services (power, cooling, safety equipments). The installation of services has determined the pace of global commissioning: in order to progress temporary power outlets have been installed which has allowed piecewise commissioning of small portions of the subdetectors. This partial availability of powered front-ends has allowed commissioning of the functionality of the whole data acquisition chain from front-end to data delivery to remote computer centers. Since May 2007 regular global integration exercises take place each end of the month: such global runs have allowed commissioning of the functionality of the whole system from triggering to the transfer to the tiered computing facilities around the world (Tier0, Tier1s and Tier2s) including offline reconstruction of the data.

2.1. *Subdetector local commissioning*

All subdetectors have commissioned locally their devices at construction time.

Tracker The tracker has been assembled in a dedicated facility during 2007 and around 20% of it has been operated triggered by a cosmic ray telescope. During summer 2007 five millions cosmic tracks have been recorded both at room temperature and with the detector cooled down at several operating temperatures. The performance recorded is excellent: signal/noise ratio of 27,31,31 have been achieved respectively for TIB(the inner part of the tracker),TOB(outer part) and TEC (endcap disks). The efficiency obtained from the analysis of cosmic tracks exceeds 99.7% as shown in Fig. 5, with less than 0.2% of dead or noisy strips.

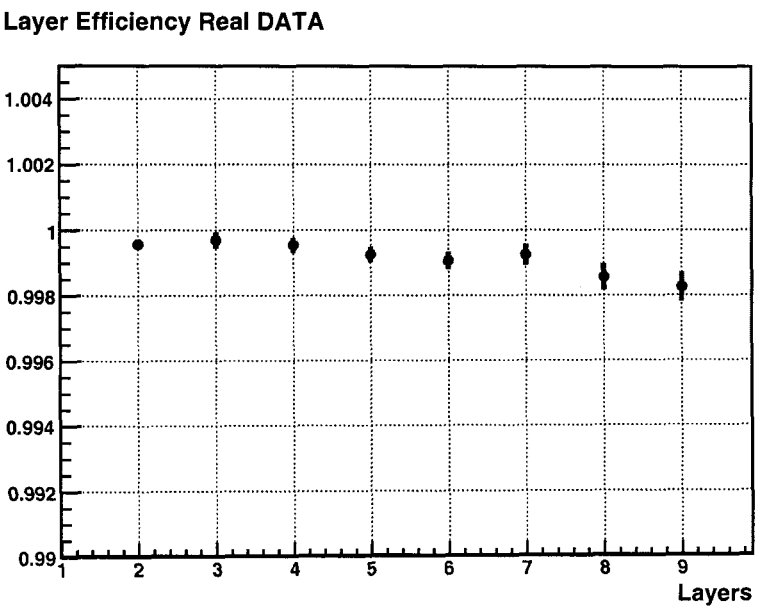

Fig. 5. Tracker efficiency measured with cosmic rays on 20% of the full detector. The first three layers belong to the TIB(Tracker inner barrel) and the last 5 to the TOB(Tracker Outer Barrel)

Electromagnetic Calorimter The 36 Electromagnetic calorimeter supermodules have been calibrated using cosmic tracks. The crystal to crys-

tal intercalibration obtained from the cosmic ray exposure has been cross checked with the one obtained on the electron beam (for 9 Supermodules) and found to be consistent at the level of 1.5% averaged over the whole supermodule as shown in Fig. 6. The exposure to an electron test beam of more than 15000 crystals (9 Supermodules) has shown order of 0.5% constant term in the resolution of the calorimeter is achievable. The installed calorimeter has only 28/61200 channels dead or with some problem.

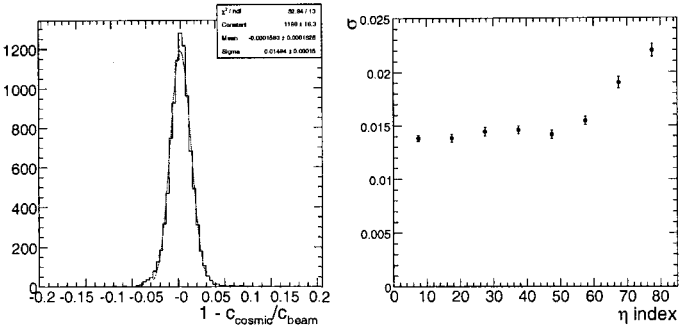

Fig. 6. Barrel Electromagnetic calorimeter crystal to crystal intercalibration accuracy: (left) distribution of comparison between calibration coefficients obtained with cosmic muons and 120 GeV electrons over a whole supermodule, (right) the same comparison averaged over azimuth-angle versus pseudorapidity

Hadron Calorimeter The hadron calorimeter has been systematically calibrated using radioactive sources -which will be used to monitor the detector response throughout the life of the experiment- and several wedges have been exposed to hadron and electron beams over the years. In 2006 a combination of barrel electromagnetic Supermodule arranged in front of a Hadron calorimeter wedge as in CMS has been exposed to hadron and electron beams ranging in energy from 2 GeV to 300 GeV. The beam was equipped with sophisticated particle identification devices which have allowed mapping the combined response for various particle species as shown in Fig. 7. Such results will allow fine tuning of the simulation of the calorimetric response of CMS. In 2007 a combination of a preshower prototype, a few towers of the Electromagnetic endcap calorimeter and a prototype of the endcap hadron calorimeter has been exposed to hadron and electron beams with energies ranging from 2 to 300 GeV. Such tests besides providing invaluable data to optimize the CMS simulation has also allowed

verifying the readiness of the Data acquisition setups of the three subdetectors as the operation was done using the standard CMS DAQ framework.

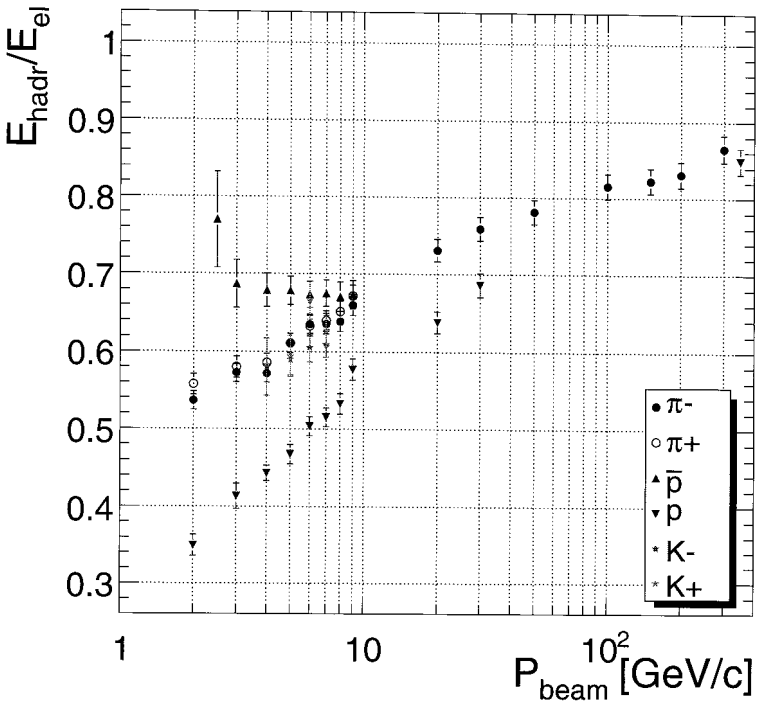

Fig. 7. Reponse of the combined Ecal and Hadcal to low momentum particles of different species

Muon The Muon detector chambers (RPC,CSC and Drift tubes) have been commissioned individually in the construction labs and recommissioned using cosmic rays in situ once installed in CMS. An example of the performance obtained by the DTs on the point resolution monitored with cosmic rays after insertion in the CMS yoke is shown in Fig. 8.

2.2. *Magnet commissioning before lowering*

Most of the experimental apparatus has been pre-assembled on the experiment site surface building. The necessity to commission the magnet before

Table 2. Major milestones for future global exercises GRE[a] and CCR[b]

	DAQ	Slow control	L1 trigger	High level Trigger	Data quality	Computing	Detectors
GRES Sep. 07	XDAQ 3.11 MiniDAQ Runcontrol 3.04 Filter farm reconstruction	Local subdetector control	GT,GMT, CSCTF, RPCTF DTTF Rate <1KHz	Unpacking and DIgi	Automatic start Shifters Final GUI Remote monitoring	Digi at Tier0 Data to Tier1 and Tier2	5 Sectors DT 7 Wedges HB 1 HF 4sectors RPCB CSC Front ends
GREN Nov. 07	Run control 3.1 XDAQ rel.4 Run from final DAQ farm slice	Safe (24/7) operation YE+, YB+ and YB0	RCT, GCT EB mip trigger HCAL trigger 10 KHz rndm trigger	Local reco LV1 confirmation Frontier CondDB	Geometrical Navigation in GUI	Several primary datasets	>1 wheels DT 30-50% EB 8 sectors RPCB
CCR0T Dec. 07	Config everything from DB				Full suite Subdet and trigger DQM code	Data to Tier0 Tier1s and Tier2s and CAF	some tracker
GREF Feb. 08	All DAQ tasks fault tolerant Run in final Control room 10 KHz, 8 Slices	Central control	jet calo trigger 50 Khz rndm Trigger	Full bandwidth DQM and error reporting	Error report and persistency Archival and retrieval of DQM info		All YE+ YB+, YB0, YB- some YE-
CCR4T Apr. 08	Phase in final filter farm		All trigger HW and SW ready for LHC	Complete cosmic Trigger menu	LHC DQM environment GUI, trends and correlation with conditions	Calibration and alignment in CAF	All CMS B field on (lessEE and ES)

Note: [a] technical global integration exercises are labelled **GlobalRunEndX** where X is the initial of the month

Note: [b] Long stable runs aimed at accumulating large statistics of Cosmic rays triggers are labelled **CMS Cosmic Run**

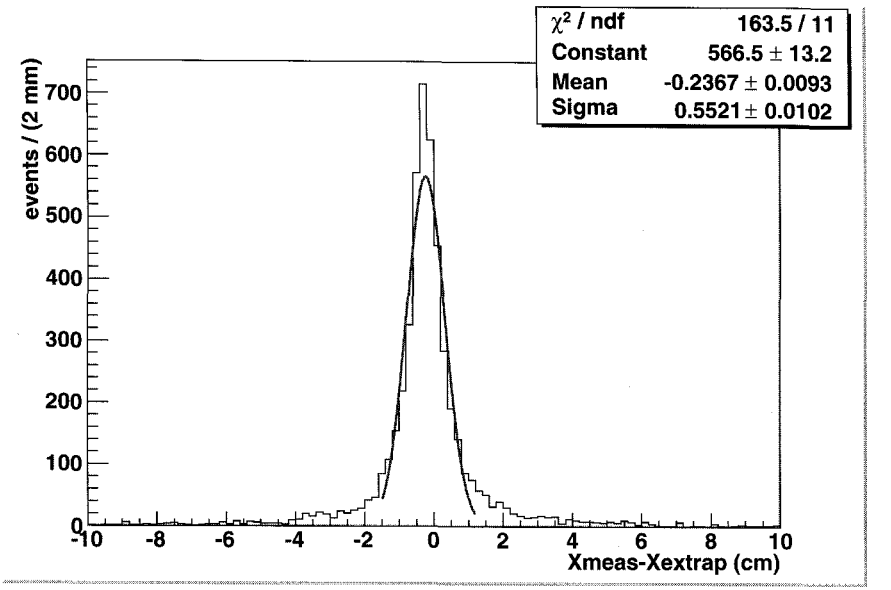

Fig. 8. Single point resolution for Drift tube system measured in situ with cosmic rays

lowering the CMS elements has created the opportunity for the first global commissioning exercise: during summer 2006, once the CMS elements had been closed in order to allow the training of the superconducting coil, portions of all the CMS detectors (typically less than 5% of the total) have been temporarily connected to an ad-hoc counting room installed nearby and were successfully readout and triggered using the final trigger and DAQ hardware. This test was very successful and managed to accumulate around 20 millions cosmic triggers which have been very valuable to debug and commission the readout hardware and software (see ref.[3]). The magnet has operated flawlessly up to the nominal field of 4 Tesla and several detailed and high precision field maps have been collected. This exercise has allowed understanding of the cross-synchronization of the subdetectors and trigger and has been the first exercise of real data (cosmic muons) across the whole detector.

2.3. *Global runs*

From May 2007 for 3 to 5 days every last week of the month a global run has taken place involving increasing participation of subdetector elements, trigger elements and increasing complexity of functionality for all

software aspects related to the data flow and quality control. In Fig. 9 the number of subsystem participating in global runs as a function of time is displayed. Until September 2007 each subsystem could participate with only a very limited amount of front-ends (less than 4%) due to the limited power available. All the services for the positive endcap and 3 of the barrel wheel (including the central one) will be available for the run at the end of November which will see for the first time 30-50% of subdetectors powered and readout. An exception is constituted by the tracker which will be inserted in the barrel at the end of November. A long cosmic-ray run is scheduled for when a major fraction of the tracker cables will be connected to the counting rooms: this is likely to happen before or just after the end of the year. That will be the first occasion when more than 50% of CMS will be readout. The achievements of the global runs are fully satisfactory:

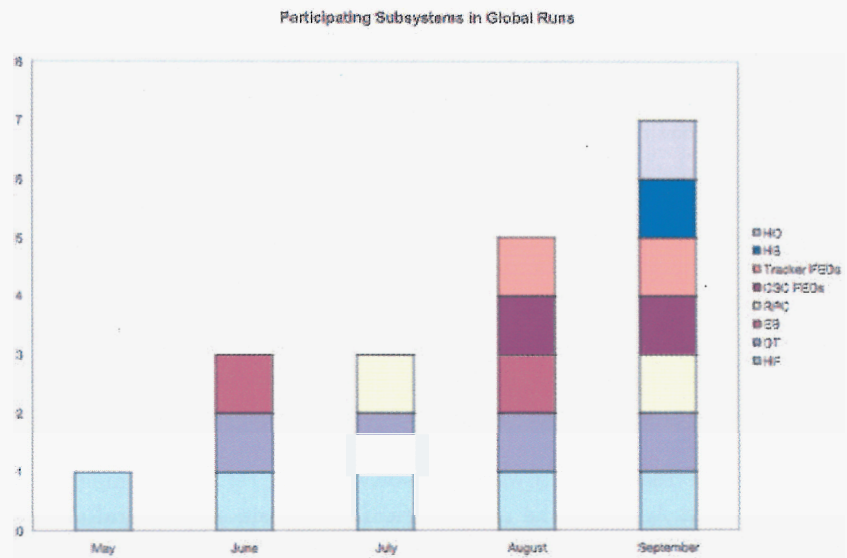

Fig. 9. Increasing complexity of global runs: HO= had. calorimeter tail catcher, HB= Had. calorimeter barrel,CSC=Cathode Strip Chambers, RPC=Resistive Plate chambers(barrel),Eb= Electromagnetic calorimeter barrel. DT= Drift tubes, HF=Very forward HAD. calorimeter. Label FEDs means that only the front end concentrator card was readout without any live Front-end connection

at every run we have, naturally, found problems which have been typically been fixed immediately or in any case in time for the next global run. Some of the main achievements are listed below:

- Readout of ECAL, HB, HF, HO, HE, DT,RPC,CSC and LUMI front ends (<5% of powered front ends)
- Readout of ~200 Front end data concentrator of Tracker (~ 50% of total)
- Commissioned run control software,Initialize and configure detectors from Database
- Integrated real time DQM framework
- High level trigger (HLT)unpacking and reconstruction with state of the art CMS offline software
- Streaming after HLT
- Data flow to Tier0, Tier 1 and Tier2 (latency typically less than 1 hour)
- Shift at Remote center (FNAL) with shifters looking at data as transferred to TIER1

All basic functionalities have been commissioned: now the accent is on increasing the scale of the test, improve the fault tolerance of the system, consolidate the data quality monitoring aspects in view of running with complex event topology, streamline the error reporting and so on.

3. Preparing for running at LHC

The coil is now connected to the power system, the cryogenics installed and the cool down initiated. It will be powered with some limited current (the detector being still open) in November 2007. In January the beam pipe will be installed in the CMS interaction point. The main milestone ahead is a long cosmic run with detector closed and the magnet powered to full field in April 2008. Such cosmic run will take place in LHC data taking mode: if LHC will deliver beam in early summer 2008 this run will continue seamlessly into LHC data taking. Table 2 shows the major milestones to be achieved in the global runs between now and then.

References

1. CMS DAQ Technical design report, CERN/LHCC/2002-26, CMS TDR 6.2, 15 December 2002
2. CMS Trigger Technical design report. CERN/LHCC 2000-38, CMS TDR 6.1, 15 December 2000
3. proceedings of the 2007 Europhysics Conference on High Energy Physics July 2007 (to be published): "The CMS Magnet Test and Cosmic Challenge "

THE STATUS OF THE ATLAS SIMULATION PROJECT FOR THE LHC STARTUP

A. Dell'Acqua, M.V.Gallas and A. Di Simone
CERN, Geneva

Z. Marshall
Columbia University

A. Rimoldi
University of Pavia and INFN

V. Tsulaia
University of Michigan

I Ueda
University of Tokyo

S. Vahsen
LBNL, Berkeley

The commissioning phase for the ATLAS experiment, being now so imminent the LHC startup, is a challenge for every development performed up to now. Along this line, the simulation program is nowadays operational and running with full functionality within the ATLAS common framework Athena. The latest developments concern an enhanced versatility, to cope with the increasing needs of developers and users, an easiness in use by a big community such as ATLAS reaching now more than 2000 potential users. Emphasis in this talk is towards the new functionality recently added, validation and production strategy as well as improved robustness and maintainability.

Keywords: ATLAS; Geant4; Simulation; HEP

1. Introduction

A common framework for event processing, Athena [1], is the basis for all ATLAS applications. An application is a set of services and algorithms as-

sembled and configured at runtime, steered using scripts written in Python, an Object Oriented scripting language which adds interactivity to the primarily C++ based applications. The simulation program for ATLAS has been developed in this environment. The main results, recent developments, the validation and production strategies in terms of performance figures, and robustness and maintainability are summarized in this paper.

2. G4Atlas

The application used in ATLAS to setup the simulation is named G4Atlas. It is the only application required and supported by the experiment for simulation, and is written entirely in C++. It is a fully featured OO GEANT4 simulation suite based on dynamic loading and action on demand, so that all functionality is added using plug-in modules. The Python application that sets up the appropriate conditions to run the simulation is called PyG4Atlas, and its role is to add flexibility for configuring the different setups, interactivity, and introspection for all settings needed at runtime. With these tools we are able to handle all daily user requests and to set different geometry configurations by setting parameters at runtime with no code manipulations.
The robustness of the resulting applications has been proven in many Grid productions with negligible failures rates. The different geometry setups implemented are handled similarly: the full ATLAS detector, all available cosmic-ray setups, and the combined test beam geometries are simultaneously available and usable for immediate simulation purposes.

3. Detector Description

The description of the complex geometry of ATLAS is derived from primary numbers and alignment constants (stored in a dedicated database) using a libraty called GeoModel, which is decoupled from the simulation framework (G4Atlas). This allows to use the *exactly* same geometry in simulation, digitization, and reconstruction applications. The GeoModel description is optimized for a large numbers of volumes ($\sim 10^6$) with extensive use of parameterized volume-based solutions.
In the initialization phase, the GeoModel tree is translated into the GEANT4 geometry. Despite major optimization, the total amount of memory required currently exceeds 90 MB. Presently, three flavours of detector descriptions are simultaneously available: the ideal detector, the misaligned detector, and the misaligned detector with material distortions. In addition,

special descriptions for the commissioning and combined testbeam setups are available. The simulation application can deal with the different configurations, leaving to the user the possibility to choose at runtime which setup to simulates.

4. Baseline for the simulation application as of August 2007

The recently adopted version of Geant4 for productions of full physics samples throughout 2007 is 8.3.patch01. The standard physics list adopted for productions is QGSP_EMV. Physics-wise this list behaves like QGSP_GN under G4 7.1, from the CPU viewpoint we observe an increasing degradation (in 8.2 QGSP_EMV is about 20% slower than QGSP_GN in 7.1). Table 1 shows the results of preliminary studies performed to compare the performance of different available physics lists when of full physics samples are run. In the table the CPU time/event for the different samples is shown.

Table 1. CPU time per event, in kSI2K, measured in Athena release 13.0.20, with different physics lists and different physics samples

Channel	QGSP	QGSP_BERT	QGSP_EMV	QGSP_GN
susy	1977.46	2685.78	1409.95	1094.42
$Z \rightarrow ee$	2148.36	2654.16	1145.22	1051.14
$Z \rightarrow \mu\mu$	1673.24	2394.72	1016.15	834.61
$Z \rightarrow \tau\tau$	1642.88	2251.98	1082.72	794.38
$H(130) \rightarrow 4l$	2038.36	2762.86	1294.62	1064.3
MB	670.83	824.09	384.3	311.41
jets	1548.94	2224.83	1067.77	854.33

A coherent revision of range cuts in subdetectors has been recently done for performance optimization. The adopted range cuts are presently set to $50\mu m$ in the Inner Detector and Muon Spectrometer, and to $30\mu m$ in the Calorimeter System. These settings seem to offer the optimal balance between performance and good physics description of all samples. Dedicated studies are ongoing.

5. Validation

The validation process is parallel to the simulation development. Its aim is to spot as soon as possible any non-optimal performance, internal inconsistency, or even inaccurate description of the detectors or physical processes.

The validation process uses single particle and physics events in restricted samples for quick feedback or larger samples for validation activities (using also reconstruction) [3]. The overall approach for validation is threefold:

- Continuous measurement of the performance in terms of the CPU time and memory consumption.
- Comparisons with real data from old standalone test beams for the different subdetectors, and from the 2004 Combined Test Beam.
- Physics performance studies with reconstruction of full physical events.

5.1. *Particles in calorimetry*

Electrons in the ATLAS Liquid Argon barrel calorimeter are well described by Geant4 both for energy response and resolution. Longitudinal and radial profiles are also well described. In the forward calorimeter a recent steady improvement was observed, even making the resolution a bit too good when compared to the data. Muons are also well described in the ATLAS barrel calorimeter by simulation: we observe that the mean energy deposits in Tile and LAr calorimeter stay within 2% of their expected values. Adding the Bertini nuclear cascade model to the Geant4 physics list, a better description of longitudinal and lateral shower profiles has been observed.

5.2. *Tile calorimeter and hadronic physics*

Comparison between Geant4 and Fluka with respect to real data was recently done using a common source of geometry and the same format of digitization output, allowing common digitization and analysis. GDML+FLUGG+FLUKA (with a Fortran-C++ interface) was used to create FLUKA-hits with the material and the geometry extracted from the G4 simulation of the test-beam. Electrons with Geant4 seem to have a better agreement with data. Pions agree (2%) with data when using Geant4 with Bertini or FLUKA. Bertini and FLUKA give reasonable agreement with data in longitudinal shower shapes, and after adding Bertini, higher energy in lateral shower halos has been observed. In conclusion, our preliminary results seem to indicate that Geant4 needs Bertini for good data reproducibility in hadronic showers.

6. Performance

Studies about the optimization of the ATLAS simulation software are underway. At each Athena release a set of robustness tests are performed for

different physics samples, from single particle to a compilation of physics sets. Memory consumption per event is also measured, comparisons figures are discussed, and the impact of different set of simulation parameters is carefully evaluated through dedicated tests. Library profiling is also performed using dedicated tools, and the results monitored through the release cycle.

7. Conclusions

The ATLAS simulation application is a mature project that is flexible, robust, and successful, but which still needs to be revised, tested and validated before the LHC startup. The different subdetector implementations are continuously updated and optimized. Beyond the present release we have planned for the LAr Calorimeter a revision of the entire endcap region for what concerns material, positions and dimensions. The sagging of the calorimeter is going to be implemented in the near future, as well as the description of imperfections throughout it. The HV imperfections are to be described and a uniform interface for all the LAr subdetectors should be implemented. The Tile Calorimeter needs a careful description of distortions while the muon system should provide a cure to revising active and passive material overlaps. Finally the forward detectors, already in implementation status, should finalize their simulation and integrate it in the full ATLAS simulation.

Acknowledgments

The authors want to thank all ATLAS developers in the detector groups and all organizations that gave financial support for the realization of this project. We are also extremely grateful to colleagues from the Geant4 Collaboration for helping in problem solving and for sharing their experiences with us, in particular J. Apostolakis.

References

1. Athena framework:
http://atlas.web.cern.ch/Atlas/GROUPS/SOFTWARE/OO/architecture/-General/Documentation/AthenaDeveloperGuide-8.0.0-draft.pdf
2. ATL-SOFT-2004-006 , *The Simulation of the ATLAS Experiment: present Status and Outlook.* by D. Costanzo, A. Dell'Acqua, M. Gallas, A.Nairz, A. Rimoldi, J. Boudreau, V. Tsulaia
3. ATL-SOFT-PUB-2005-004, *Validation of the GEANT4-Based Full Simulation Program for the ATLAS Detector* by D. Costanzo, A. Dell'Acqua, M. Gallas, A.Nairz, N. Benekos, A. Rimoldi, J. Boudreau, V. Tsulaia

CMS DATA AND WORKFLOW MANAGEMENT SYSTEM

A. FANFANI[A], B: BONACORSI[A], W:BACCHI[A], G. CODISPOTI[A], N. DE FILIPPIS[B], A POMPILI[B], S. MY[B], M. ABBRESCIA[B], G. MAGGI[B], G DONVITO[B], L.SILVESTRIS[B], F.CALZOLARI[C], S.SARKAR[C], D.SPIGA[D], M.CINQUILI[D], S:LACAPRARA[E], M:BIASOTTO[E] ,F.FARINA[F], M.MERLO[F],S. BELFORTE[G], C.KAVKA[G], L. SALA[H], J. HARVEY[I], D. HUFNAGEL[I], F.FANZAGO[I], M.CORVO[I], N.MAGINI[I], J REHN[I], Z. TOTEVA[I], D. FEICHTINGER[J], L. TUURA[K], G. EULISSE[K], B. BOCKELMAN[L], C.LUNDSTEDT[L], R. EGELAND[M], D. EVANS[N], D. MASON[N], O.GUTSCHE[N], L.SEXTON-KENNEDY[N] , D.W. DAGENHART[N],A. AFAQ[N], Y. GUO[N], S. KOSYAKOV[N], L. LUEKING[N], V. SEKHRI[N], I. FISK[N], P.MCBRIDE[N], L. BAUERDICK[N],J.BAKKEN[N], P.ROSSMAN[N],E. WICKLUND[N],Y. WU[N],C. JONES[O], V.KUZNETSOV[O], D. RILEY[O], A. DOLGERT[O], F VAN LINGEN[P], I. NARSKY[P], C. PAUS[Q], M. KLUTE[Q], G.GOMEZ-CEBALLOS[Q], J. PIEDRA-GOMEZ[Q], M.MILLER[Q], A MOHAPATRA[R], C LAZARIDIS[R], D. BRADLEY[R], P. ELMER[S], T. WILDISH[S], F. WUERTHWEIN[T], J. LETTS[T] ,D. BOURILKOV[U],B. KIM[U], P. SMITH[V], J.M. HERNANDEZ[W], J. CABALLERO[W], A. DELGADO[W], J.FLIX[X] ,I. CABRILLO-BARTOLOME[Y], M. KASEMANN[Z], A FLOSSDORF[Z], H. STADIE[Z] ,P KREUZER[1], A KHOMITCH[1], C. HOF[1], C. ZEIDLER[1],S. KALINI[1] , A TRUNOV[2] ,C.SAOUT[2],U.FELZMANN[2], S. METSON[3], D. NEWBOLD[3], N. GEDDES[4],C. BREW[4],J.JACKSON[4], S.WAKEFIELD[5] , S. DE WEIRDT[6], V.ADLER[6],J MAES[6], P. VAN MULDERS[6], I.VILLELLA[6], G.HAMMAD[7], N. PUKHAEVA[8], T. KURCA[8], I.SEMNENIOUK[9], W GUAN[10], J A LAJAS[11], D. TEODORO[11] ,E. GREGORES[12], M. BAQUERO[13] A. SHEHZAD[14], M .KADASTIK[15], O. KODOLOVA[16] ,Y. CHAO[17], C. MING KUO [17], C. FILIPPIDIS [18], G. WALZEL[19] , D. HAN[20] , A. KALINOWSKI[21] , N. M. GIRO DE ALMEIDA[22] , N. PANYAM[23]

(A)Bologna University and INFN Bologna, Italy ;(B)INFN Bari, Italy;(C) INFN Pisa, Italy;(D) INFN Perugia, Italy; (E)INFN Legnaro, Italy;(F) INFN Milano-Bicocca, Italy;(G) INFN Trieste, Italy;(H) INFN Rome, Italy,(I)CERN Geneva, Switzerland;(J) PSI Villige, Switzerland, (K)North eastern University MA,USA ;(L) University of Nebraska NE,USA; (M)University of Minnesota MN, USA; (N)FNAL Batavia IL, USA ;(O)Cornell University NY, USA ;(P) California Institute of Technology CA, USA ;(Q) MIT, Boston, USA ; (R)University of Wisconsin WN, USA;(S) Princeton University, Princeton, NJ, USA ;(T) University of California San Diego, USA;(U) University of Florida, USA ;(V)University of Purdue, USA, (W)CIEMAT Madrid, Spain; (X) PIC, Spain;(Y)IFCA; Spain, (Z)DESY Hamburg, Germany; (1) RWTH Institute Aachen, Germany;(2) Karlsruhe FZK Germany, (3)University of Bristol, UK ;(4)RAL, UK;(5)Imperial College London, UK, (6)Vrije University of Bruxels, Belgium (7)University libre de Bruxels Belgium, (8) IN2P3 Lyon, France ; (9) GRIF Paris, France, (10) IHEP, Beijing, China, (11)UERJ Rio de Janeiro,(12) SPRACE Sao Paolo, Brasil, (13)Universidad de Los Andes, (14) Quaid-E-Azam University,(15) NCPB Tallin, Estonia, (16) Moscow University, Russia, (17) ASGC, Taiwan, (18) Demokritos, Greece,

(19)Hephy-Vienna, Austria, (20)KNU, South Korea, (21)Warsaw University, Poland, (22)LIP-Lisbon and LIP-Coimbra, Portugal, (23)TIFR Mumbai, India

CMS expects to manage many tens of peta bytes of data to be distributed over several computing centers around the world. The CMS distributed computing and analysis model is designed to serve, process and archive the large number of events that will be generated when the CMS detector starts taking data. The underlying concepts and the overall architecture of the CMS data and workflow management system will be presented. In addition the experience in using the system for MC production, initial detector commissioning activities and data analysis will be summarized.

1. Introduction

CMS [1] uses a number of event data formats, starting from the detector data (RAW) data to successive degree of processing that refine this data.

A multi-Tier hierarchical distributed model [2] is adopted in CMS for serving and archiving of the RAW and reconstructed data. The Tier-0 centre at CERN accepts data from the CMS online system, archives the data, performs prompt first-pass reconstruction and distributes raw and processed data to Tier-1s. The Tier-1s are typically large regional computing centers and provide services for data archiving, scheduled data processing operations (reconstruction, calibration, skimming) and other data-intensive analysis tasks. Tier-2s centers provide capacity for analysis, calibration activities and Monte Carlo simulation.

CMS uses Grid technologies in the context of Worldwide LHC Computing Grid (WLCG) that provide a large amount of distributed computing, storage and network resources for data processing.

2. Data management system

The CMS data management is based on a set of loosely coupled components which allow physicists to discover, access and transfer event data, as illustrated in Figure 1.

2.1. *CMS catalogues*

The CMS catalogues used to define and discover data are the Dataset Bookkeeping System (DBS) and the Data Location Service (DLS).

- The DBS maintains the semantic information associated to datasets, it keeps track of the data parentage and allow to discover which data exists and how are organized in term of files/file-blocks.
- The DLS maps file-blocks to sites holding a replica of them. It is used to find the location of desired data.

DBS supports the existence of local and global instances, for private and public data, and the migration of data between them.

DBS and DLS are integrated in a single service that is implemented as a Tomcat-based Java server with an Oracle or MySQL back-end.

2.2. *Local data access*

The local file catalogue provides access information for the files at a site's storage with simple rules to build physical paths from logical names and access protocols. CMS application interface to storage with a POSIX-like interface.

2.3. *Data placement and transfer system*

The Physics Experiment Data Export (PhEDEx) project [3] manages the transfers of data among sites, dealing with grid file transfer services and different storage systems. PhEDEX interacts with the CMS catalogues cross-checking with the DBS the file-level information for datasets mentioned in transfer requests and update the DLS as data transfers complete.

Technically is based on software agents that run autonomously at sites and exchange information via a central database.

PhEDEx has been exercised in progressively increasing complexity and scale during several years of use in daily production and computing challenges. In the last 18 months PhEDEX transferred 20 PB. In July 2007 the average global daily transfer rate was 100 TB/day or 1.2 GB/s. Around 70 sites are involved at present.

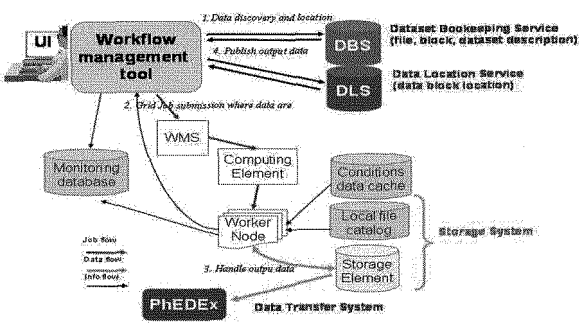

Figure 1. CMS data and workflow management services.

3. Workload management system

The CMS Workflow management system manages large scale data processing and reduction processing which is the principal focus of HEP computing. An example of distributed processing workflow that illustrates the interactions with data management components and the Grid middleware is shown in Figure 1. The basic steps are: i) data discovery and location via DBS/DLS, ii) job submission where the data are located, iii) handling of the output data stored on local storage or passed to the transfer system (PhEDEx), iv) publication of the produced data with the relevant provenance information in DBS/DLS.

3.1. *MC production*

CMS has a long term need to perform large-scale MC simulation and it provide a way for testing the tools and infrastructure needed to process large amounts of events that will be available at detector startup.

The MC production system consists of three components: the Request system (ProdRequest), acts as a front-end application for production request submissions into the production system; the Production Manager (ProdManager), manages these user requests, performing accounting and allocating work to a collection of Production Agents (ProdAgents). The ProdAgents themselves are defined internally in terms of autonomous components that communicate via an asynchronous and persistent message system. This set of loosely coupled components cooperates to carry out production workflows in grid environment. ProdAgents are responsible for job submission, job tracking, error handling and automatic resubmissions as well as data merging and publication into the CMS cataloguing system and the data transfer systems.

Production scale of more than 20K/day jobs has been reached by running several ProdAgents in parallel over last year by 4-8 operations teams. A production yield of 2 million events per day, with a job efficiency of about 75%, is routinely reached. More than 40 sites have been used for production with high job efficiency. Performance in the production system is greatly affected by the unreliability and instability of global Grid services and sites (local storage and batch systems).

3.2. *Tier-0 workflow*

The CMS Tier0 is responsible for all data handling and processing of real data events in the first period of their life. Data written by DAQ in specific format

(streamer files) are automatically transferred to the Tier-0 site. At Tier-0 the repacking of the streamer files, converting them into RAW data and splitting into physics primary datasets, occurs. The output RAW data are archived on tape. Prompt reconstruction reads RAW data and stage out reconstructed data, with merge if necessary. These workflows are managed by ProdAgent and its evolution to into a much wider system to support Tier-0 activities. Files are registered in DBS/DLS. The RAW and reconstructed data are transferred from Tier-0 to dedicated Tier-1s sites with PhEDEx.

Experience using the system is being gained with initial detector commissioning activities (monthly Global Data taking), that however deals with small data volume, as well as dedicated stress tests at data nominal rates scale.

3.3. *User Analysis*

A tool, CRAB (CMS Remote Analysis Builder) [4], has been developed to provide a user friendly interface for CMS physicists interactions with data management and Grid submissions. CRAB support both direct submission to Grid and submission with a CRAB server that aim at improving automation and scalability of the whole system.

CRAB has been used to analyse data during the past CMS challenges: studies of the CMS physics discovery potential based on MC simulation, analysis of Magnet Test cosmic challenge and Tracker real data, etc.

4. Conclusions

CMS is making progress towards implementing and testing a system for handling organized and analysis workflow in its distributed environment for the coming critical first year of LHC data taking.

References

1. CMS Collaboration, "The Compact Muon Solenoid Computing Technical Proposal", CERN/LHCC 1996-045(1996)
2. CMS Collaboration, "The Computing project Technical Design Report", CERN/LHCC-2005-023 (2005).
3. J. Rehn et al. "PhEDEX high throughput data transfer management system, Proc. Int. Conf. on Computing in High Energy and Nuclear Physics (Mumbai) vol 2 (Macmillan India ltd.) p. 1027 (2006)
4. F.Fanzago et al. "CRAB: a tool to enable CMS Distributed analysis" Proc. Int. Conf. on Computing in High Energy and Nuclear Physics (Mumbai) vol 2 (Macmillan India ltd.) p. 1110 (2006).

The large-angle photon veto detector for the P326 experiment at CERN

R. Fantechi*

INFN - Sezione di Pisa,
Pisa, Italy
**E-mail: Riccardo.Fantechi@pi.infn.it*
www.pi.infn.it

The P326 experiment at CERN plans to measure BR($K^+ \to \pi^+\nu\bar{\nu}$) with an uncertainty of $\approx$ 10%. The π^0 rejection factor should be at the level of 10^8 to achieve the required signal to noise ratio. For the construction of the large-angle photon veto system, a test program of different technological solutions has started. A module based on lead and scintillating fibers has been constructed and it has been tested together with a lead/ scintillator with WLS readout prototype originally developed by CKM at Fermilab and with some lead glass blocks formerly used in the OPAL calorimeter. Preliminary results on the inefficiency to electrons are presented.

Keywords: Detector; Photon veto;

1. Introduction

The P326 experiment [1] has been proposed to measure the branching ratio of the rare decay $K^+ \to \pi^+\nu\bar{\nu}$. An accurate measurement of this BR allows a precise test of the Standard Model and a 10% accurate evaluation of $|V_{td}|$. Furthermore, given its sensitivity to physics beyond the Standard Model, one can also observe clean signals of new physics. Presently the only existing measurement is based on three signal events collected by the E787(E949) [2] experiment at BNL, giving $BR(K^+ \to \pi^+\nu\bar{\nu}) = (1.47^{+1.30}_{-0.89}) \cdot 10^{-10}$.

2. Experimental requirements

The experiment is particularly demanding. The kaon beam should have a high intensity in order to collect significant statistics in a reasonable time. The proposed beam has a high momentum (75 GeV/c with $\sigma(p)/p \approx 1\%$) and it will be produced by 400-GeV protons from the CERN SPS. The

main advantage of an high energy beam is the high energy of the photons from π^0 decays, which will improve the photon detection efficiency. The experimental layout is shown in Fig. 1.

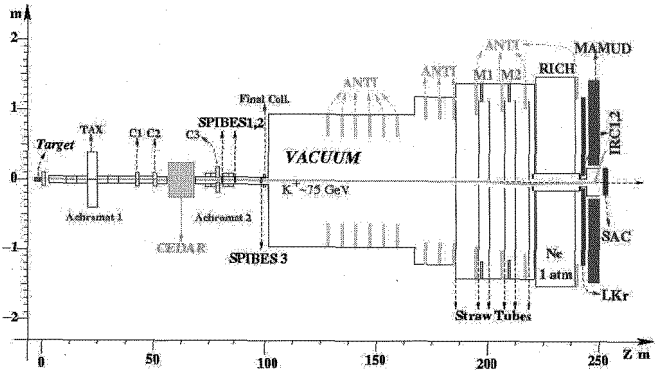

Fig. 1. The P326 experimental layout.

The rejection power for the most common background channels should be around 10^{12} to have the expected signal to noise ratio of about 10. This is most important in the two-body decays $K^+ \to \pi^+\pi^0$ and $K^+ \to \mu^+\nu$, where the combined use of missing mass cuts and particle identification should be used. In the case of $K^+ \to \pi^+\pi^0$ an hermetic system of calorimeters should be used, with a very low detection inefficiency ($\lesssim 10^{-4}$) over a large energy range.

The two photons from the π^0 decay exhibit energy correlation: one low energy photon, detected with somewhat poor inefficiency at a large angle, is paired with a high energy one, hitting the forward, very efficient, detector.

A simulation has been performed, taking into account the kinematics of the decay and it has shown that an inefficiency of 10^{-4} down to 200 MeV is well enough to reach the expected level of rejection.

3. Photon Vetoes

The Photon Veto system should be able to detect photons with high efficiency in order to reject the background decays, mainly from $K^+ \to \pi^+\pi^0$. The average inefficiency for the π^0 should be $\approx 10^{-8}$. Different detectors will be used for different angular regions: below 15 mrad, the LKr calorimeter and small calorimeters in the very forward direction and around the beam

pipe will be used. For an hermetic coverage up to 50 mrad, a system of 12 ring calorimeters (Large Angle Vetoes) will be used.

4. Large Angle Vetoes

The veto system is composed of 12 modules of annular shape located along the decay vacuum tube; the total active surface is $\approx 27m^2$. The photon energy to be detected varies from $\approx$ 10 MeV to $\approx$ 25 GeV, depending on the angle of incidence and on the module hit. For comparison, in any of the three technologies described below, the detected energy of a minimum ionizing particle is below 100 MeV.

For the construction of these detectors, three options have been taken into consideration and prototypes have been built or provided to test for the response and inefficiency in an electron beam.

One design consists of a sandwich of lead sheets and scintillating tiles with WLS fiber readout. An assembly of 16 wedge-shaped modules forms the veto counter. An example of such a detector, using 80 layers of 1-mm thick lead sheets and 5-mm thick scintillating tiles, was designed for the (now canceled) CKM experiment at Fermilab. Tests at the Jefferson Lab showed that the inefficiency of the detector for 1.2 GeV electrons was at most $3 \cdot 10^{-6}$ [3].

Another solution is based on the design of the KLOE calorimeter [4], and consists of 1-mm diameter scintillating fibers sandwiched between 0.5-mm thick lead foils. The fibers are arranged orthogonal to the direction of particle incidence and are read out at both ends. Two U-shaped modules form a veto station.

The third option is to use the lead glass modules already used in the barrel of the OPAL calorimeter and which could be available in a more than sufficient quantity. Each block is a kind of truncated pyramid with an height of 37 cm and with trapezoidal bases of about 11*11 cm. A 4-cm long light guide couples the lead glass block to a Hamamatsu R2238 photomultiplier. A veto station could be composed of four or five layers of blocks radially arranged with the long axis perpendicular to the beam axis. The blocks will not touch each other and the different layers will be arranged such as to have the complete coverage of the solid angle as well as a minimum thickness in radiation lengths.

In order to determine the best choice in terms of detection inefficiency, we have asked for the loan of the CKM prototype, taken few of the OPAL lead glasses and built a lead-fiber prototype.

4.1. *The lead-fiber prototype*

One U-shaped module was built in Frascati in fall 2006. The inner radius (60 cm) and length (310 cm along the inner face) are identical to the specifications for one of the upstream veto stations. The prototype has a radial thickness of 12.5 cm, about a third of the final one, but sufficient for the transverse containment of low-energy electron showers incident along the center line of the module. Layers of the module were constructed by rolling 1-mm grooves into 0.5-mm lead foils and gluing scintillating fibers into the grooves. The longitudinal depth of the module is determined by the width (25 cm) of the lead foils. The desired radial thickness was obtained by stacking 99 layers. The ends of the module were milled and then fitted with light guides, with a segmentation in the plane transverse to the fibers of six cells along the depth and three along the radius. In the region covered by the last two cells in depth, scintillating fibers in alternating grooves were replaced by lead wires, in order to have the back part of the detector with less fiber density, without complicated modifications to the lead-foils grooving machine.

5. The tests

The three prototypes were tested at the Frascati Beam Test Facility. This is an electron transfer line leading off the DAΦNE linac. It can provide electrons or positrons, in 10-ns pulses with a repetition rate of 50 Hz, with $50MeV < E < 750MeV$ and mean multiplicities from < 1 to 10^4 per pulse.

A "tagging system" has been built to define without ambiguity the arrival of an electron on the device to be tested. It is composed of two beam profile measuring devices, two tagging counters to define the beam and two veto counters (scintillators with an hole inside), mounted on the same support and well aligned along the beam axis. The tagging efficiency of this system varies with the momentum; the global tagging efficiency for 1-electron events depends also from the Poissonian probability to have one electron in the beam. Fig. 2 shows the effect of the tagging: out of all events with different multiplicities, the loose selection (only with the two defining counters) is shown in red and the tight, final one, using also the vetoes, is plotted in black.

Table 1 gives the total statistics obtained in the June-July 2007 run.

The determination of the inefficiency was done looking for tagged events with an energy deposit less than 50 MeV, which were declared inefficient. Table 1 shows the numbers of inefficient events and the preliminary results for the inefficiency to electrons. Fig. 3 summarizes these results. All three

Table 1. Statistics accumulated in the June-July 2007 run

	Energy	P(1e-)	Eff. (tag*1e-)	Tagged Events	Ineff. Events	Inefficiency
Fiber prototype	200 MeV	23.6%	3.4%	69689	8	$11.5^{+4.8}_{-3.4} \cdot 10^{-5}$
	350 MeV	35.9%	9.0%	220702	5	$2.3^{+1.3}_{-0.8} \cdot 10^{-5}$
	500 MeV	36.3%	14.7%	414632	3	$7.2^{+5.6}_{-3.1} \cdot 10^{-6}$
CKM prototype	200 MeV	29.5%	3.7%	65165	2	$3.1^{+3.1}_{-1.5} \cdot 10^{-5}$
	350 MeV	31.8%	8.8%	221162	3	$1.4^{+1.0}_{-0.6} \cdot 10^{-5}$
	500 MeV	29.0%	17.6%	192412	1	$5.2^{+0.8}_{-3.2} \cdot 10^{-6}$
Lead Glass	200 MeV	30.2%	3.9%	25069	3	$12.0^{+9.2}_{-5.2} \cdot 10^{-5}$
	500 MeV	26.0%	17.1%	91511	1	$1.1^{+1.8}_{-0.7} \cdot 10^{-5}$

solutions give a value for the inefficiency below the requirements for the P326 Large Angle Veto system.

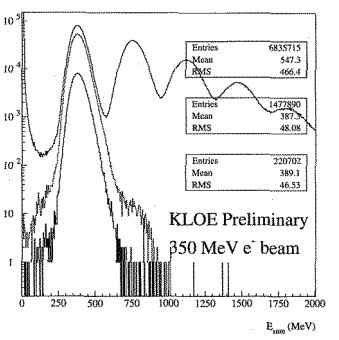

Fig. 2. Effect of the tagging system

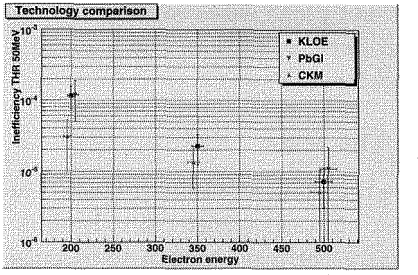

Fig. 3. Inefficiency vs energy for the 3 solutions

6. Conclusions

For the P326 experiment at CERN, three technologies for the construction of a large angle photon veto system with an inefficiency of 10^{-4} have been tested with prototypes at the Beam Test Facility in Frascati. The preliminary results for the inefficiency to electrons show that all three could satisfy the requirements of the experiment.

References

1. G. Anelli et al., *Proposal to measure the rare decay $K^+ \to \pi + \nu\bar{\nu}$ at the CERN SPS*, CERN-SPSC-2005-013 (2005)
2. V.V. Anisimovsky et al., Phys. Rev. Lett. **93** (2004) 031801
3. E. Ramberg et al., IEEE Trans. Nucl. Sci. **51** (2004) 2201
4. M. Adinolfi et al., Nucl. Instrum. Meth. **A482** (2002) 364
5. G. Mazzitelli et al., Nucl. Instrum. Meth. **A515** (2003) 524

The CDF RUN II Silicon Detector: Aging Studies

Ignacio Redondo Fernández on behalf of the CDF collaboration

Division of Experimental High Energy Physics, CIEMAT,Avda. Complutense, 22 , Madrid, 28040, SPAIN

E-mail: redondo@fnal.gov

The CDF Run II silicon detector is the largest operating silicon detector in High Energy Physics. Its 750,000 channels spread over 6 m^2 of silicon microstrip sensors allow precision tracking and vertexing. The CDF silicon detector played a critical role in the discovery of B_s mixing and is used extensively for the current Higgs Boson searches. The observed effects of aging are presented followed by the expected performance to the end of the Tevatron Run II program, where 5.8-8.5 fb^{-1} is expected to be delivered. The impact of radiation damage upon the performance of the detector is shown including the status and expectations of the two inner most layers which have already inverted. The infrastructure (cooling, power supplies) aging problems dealt with during the 2007 sumer shutdown are also discussed.

Keywords: silicon ; radiation damage ; vertex detectors; HEP.

1. The CDF Silicon Detector in Run II

The Collider Detector at Fermilab (CDF) [1] is one of two multi-purpose particle physics detectors at the Tevatron collider at Fermi National Accelerator Laboratory (FNAL). The silicon vertex detector is one of the core components of CDF allowing for precision tracking and vertexing. It is used in the CDF Silicon Vertex Trigger (SVT) [2], the first hardware displaced vertex trigger implemented at a hadron collider detector. The detector is divided into three sub-detectors: Layer 00 (L00), SVX-II, and the Intermediate Silicon Layers (ISL).

The **L00 detector** [4] is installed directly on the Tevatron beam pipe with sensors as close as 1.35 cm to the beam pipe axis. L00 uses radiation hard, single-sided sensors, from Hamamatsu (at radius 1.62 cm) and SGS Thomson (at radius 1.35 cm) fabricated with design rules similar to those in use at the Compact Muon Solenoid (CMS) silicon tracker. It also includes two Micron oxygenated modules. The L00 sensors can be biased up to 500 V, limited by the maximum range of the power supplies.

SVX-II [5] is the core of the silicon detector and is the only component used in the hardware trigger for events with displaced vertices [2]. The SVX-II detector has 5 layers of double-sided sensors located at radii from 2.5 cm to 10.6 cm. Three layers are made of Hamamatsu silicon with the n strips perpendicular to the p strips. The remaining two layers are Micron sensors with a 1.2 ^{o} angle between the p and n strips. The maximum bias voltages that can be applied to Hamamatsu and Micron sensors are 170 V and 70 V, respectively. It is limited by the breakdown voltage of the integrated coupling capacitors and subtle sensor effects.

ISL [6] provides an extended forward coverage and links tracks between the CDF wire chamber and SVX-II. The ISL detector has one central layer at radius of 22 cm and two forward layers at radii of 20 cm and 28 cm. It is made of double-sided sensors with strips at a stereo angle of 1.2^o.

2. Radiation Damage

The Tevatron had delivered an integrated luminosity of 3.2 fb^{-1} per experiment at the end of 2006 running, already exceeding the design specification for the silicon detector to be radiation hard up to 3 fb^{-1}. The accelerator is expected to continue running through 2009 with the expectation to deliver from 5.8 fb^{-1} to 6.8 fb^{-1}. The option to run in 2010 is currently under discussion having been recently endorsed by FNAL and the two experiments. The CDF silicon detector is located in an intense **radiation field**. Measurement of the ionizing radiation dose at various points of the detector was done early in Run II [7] by means of >1000 thermal luminescent dosimeters (TLDs) spread over entire detector volume. An extrapolation of the measured dose using an inverse power law in r gives an estimate for the ionizing radiation dose of 300±15 kRad/fb^{-1} at a radius of 3 cm with a 20 % variation over z. This means that L00 and the inner layer of SVX-II have already received doses of ~3.2 MRad and ~1.3 MRad, respectively, after 3.2 fb^{-1} of Run II luminosity. The flux to luminosity factor has been measured using the increase of leakage current of the sensors themselves resulting in 0.93±0.26 (10^{13} 1 MeV n eq.)/cm^2/fb^{-1} for the inner layer of SVX (2.5 cm radius). The inner sensors of L00 (1.35 cm) see 2.5 higher flux. The integrated fluence in L00 after 8 fb^{-1} will be of the order of what is expected for the LHC strip trackers.

The performance of the readout electronics located inside the detector is not expected to be seriously compromised by the integrated radiation dose. The SVX3D chip [3] noise is predicted to increase by 17 % after 8 fb^{-1} while the light output from the Dense Optical Interface Module, DOIM [8]

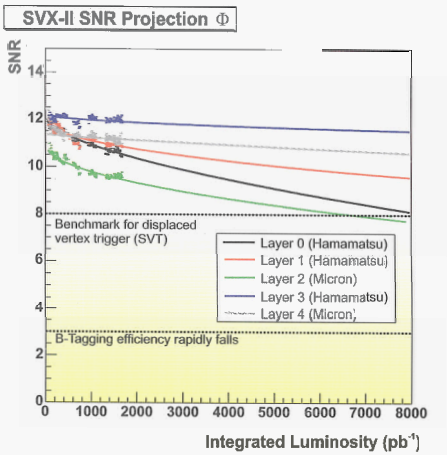

Fig. 1. Measured S/N ratio for the 5 SVX layers as a function of the luminosity. The shading indicates the expected drop of b-tagging efficiency based on RUN I experience. The SVT S/N specification is 8 but this is expected to be a soft limit.

is expected to degrade by 10 % [9].

Radiation damage to silicon sensors manifests itself in two ways which affect the detector's performance. Defects in silicon crystals due to radiation damage lead to an increase of the sensor leakage current and, as a consequence, to an increase of sensor shot noise. In addition, signal quality degrades as crystal defects cause degradation of charge collection efficiency via trapping and changes in the time response of the sensor. Damage to the bulk causes the number of effective charge carriers to change, gradually decreasing the voltage required to deplete the sensor until type inversion, after which the depletion voltage increases. The inner layer of SVX-II is of most concern for this type of damage because it is located at a radius of only 2.54 cm from the beam and its maximum bias voltage is limited to 170 V (unlike to 500 V for radiation hard L00). These two effects, in combination with increasing chip readout noise, cause a degradation of the signal-to-noise ratio (S/N). Therefore, two major concerns for the longevity of the CDF silicon detector are the degradation of signal-to-noise ratio and the ability to fully deplete the silicon sensors.

Studies of the S/N ratio and depletion voltage evolution have been carried out, and indicate functional silicon sensors for the lifetime of Tevatron Run II. The signal, S, is measured from hits on tracks collected with J/Ψ triggers in normal physics data which provide a clean track sample. The fitted Landau peak is path-corrected. The noise, N, is estimated using special calibration runs with beam. Fig. 1 shows the measured S/N ratio for the 5 SVX layers as a function of the luminosity along with extrapolations [10] that suggest appropriate S/N up to 8 fb^{-1}.

For single-sided sensors (L00) the depletion voltage is measured from runs with a dedicated track trigger to minimize sacrificed data. S is mea-

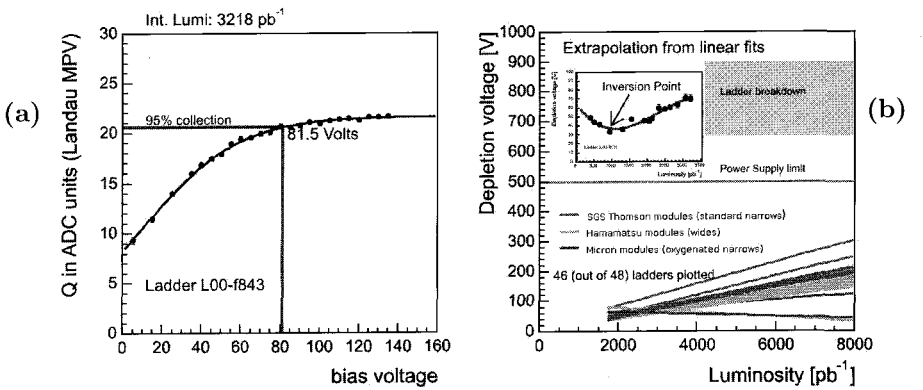

Fig. 2. (a) Peak of the path-corrected landau peak from hits collected with one L00 module vs. applied bias voltage. The red lines indicate the measured depletion voltage. (b) L00 depletion voltage vs Luminosity. The inset shows the measured depletion voltage vs. luminosity for one L00 module. The main plot displays the linear extrapolations up to 8 fb^{-1} from fits to data after inversion for all L00 modules.

sured as the applied voltage changes from 2 V to the operation voltage. This data are shown for one L00 module in Fig. 2 (a). The depletion voltage is defined as the 95 % of the plateau value. The evolution with luminosity of the depletion voltage for one L00 module is shown in the inset of Fig. 2 (b). All L00 modules have passed inversion but for the two Micron oxygenated ones which are close to inversion. The data after 1.8 fb^{-1} are well fitted with a straight line, which is used to extrapolate to 8 fb^{-1}, as shown in Fig. 2 (b). The expected increase in depletion voltage from the data will not reach the 500 V maximum depletion voltage. The method for double-sided sensors before inversion uses the n-side noise drop as the p-stops between the n-strips deplete. Since this method becomes unreliable close to inversion, signal scans of the inner layer of SVX-II (L0) have been taken recently. The average depletion voltage at the end of 2006 running was ~55 V, and showed an increasing trend, indicating that this layer has also undergone inversion. However, a larger luminosity lever arm is required to extrapolate from the data. A prediction based on the Hamburg model [11], which describes reasonably well the noise and signal scan data, suggests this layer will survive until the end of RUN II.

3. Infrastructure Aging

Both the power supply and cooling system are critical to the survival of the detector. The 2007 summer shutdown has allowed CDF to significantly improve the situation of both systems. The Aluminum pipe cooling the

optical transmitters reading out one half of ISL/L00 had suffered a leak in May 2007, which made impossible to operate that part of the system. It is suspected that the leak was caused by the acidification of the coolant (water/10 % glycol) during the 2006 shutdown which was only identified in March 2007 when the pH had reached 2 and conductivity was 3300 μSi/cm. The coolant was neutralized by draining (pH 2.8, 700 μSi/cm) and deionizing with resin (pH 5, 5 μSi/cm). The SVX cooling system (water/30 % glycol) has always stayed above pH 4. Ion chromatography analysis shows that the main source of acid was the oxidation of glycol into carboxylic acids, mainly formic acid. The repair was performed from the inside of the pipe using medical equipment (borescopes/cathethers) and brass wires to deposit DP190 epoxy in the corroded areas. This was required due to its location next to the detector which makes impossible to access the outside of the pipe. After the repair the full system could be operated and readout.

The CAEN power supply modules (mod. A509, A509H, A510) had a failure mode in which the aging of one capacitor in the 12 V inner supply resulted in a slow drop of the delivered voltages. Over time the voltage would became erratic affecting the performance of the readout chips. All the modules (47 out of 112) that showed dropping voltages were repaired by replacing the capacitor.

4. Summary

The two inner layers of the CDF silicon detector have passed type inversion, but data and predictions indicate that the sensors will continue to perform well through the end of Run II. The 2007 shutdown allowed CDF to rejuvenate the power supply and cooling systems. The CDF Run II Silicon detector is ready for the luminosity to be delivered by the Tevatron during the next 2-3 years.

References

1. D. Acosta *et. al.*, Phys. Rev. **D71**, 032001 (2005).
2. W. Ashmanskas *et. al.*, Nucl. Instrum. Meth. A **518**, 532 (2004).
3. M. Garcia-Sciveres *et. al.*, Nucl. Instrum. Meth. A **435**, 58 (1999).
4. C.S. Hill *et. al.*, Nucl. Instrum. Meth. A **511**, 118 (2003).
5. A. Sill *et. al.*, Nucl. Instrum. Meth. A **447**, 1 (2000).
6. A. Affolder *et. al.*, Nucl. Instrum. Meth. A **453**, 84 (2000).
7. R.J. Tesarek *et. al.*, Nucl. Instrum. Meth. A **514**, 188 (2003).
8. S. Hou, Nucl. Instrum. Meth. A **511**, 166 (2003).
9. R.S. Lu *et. al.*, Nucl. Instrum. Meth. A **552**, 219 (2005).
10. A. Mitra, Nucl. Instrum. Meth. A **573**, 273 (2007).
11. S. Worm *et. al.*, Nucl. Instrum. Meth. A **549**, 126 (2005).

Implementation and performance of the ATLAS Trigger Muon "Vertical Slice"

S. Grancagnolo*, G. Cataldi, E. Gorini, M. Primavera, G. Siragusa, S. Spagnolo, A. Ventura

Università del Salento and I.N.F.N. Lecce, Dipartimento di Fisica, via Arnesano, 73100 Lecce, Italy
** E-mail: sergio.grancagnolo@le.infn.it*

G. Usai

"Enrico Fermi Institute", University of Chicago, USA

A. Krasznahorkay, Z. Tarem

CERN, Geneva, Switzerland

N. Panikashvili, S. Tarem

"Technion Israel Institute of Technology", Israel

M. Biglietti, G. Carlino, F. Conventi

Università degli Studi di Napoli "Federico II" and I.N.F.N., Napoli, Italy

T. Kohno

"University of Oxford", UK

M. Bellomo, D. A. Scannicchio, V. Vercesi

"Università di Pavia and I.N.F.N.", Pavia, Italy

T. Del Prete

"Università di Pisa" and I.N.F.N., Pisa, Italy

K. Nagano, K. Tokushuku, Y. Yamazaki

KEK, Tsukuba, Japan

A. Sidoti A. Di Mattia, S. Falciano, C. Luci, L. Luminari, F. Marzano, A. Nisati,

E. Pasqualucci
Università di Roma I "La Sapienza" and I.N.F.N., Roma, Italy

The ATLAS experiment at the Large Hadron Collider has a trigger system designed to keep high effiency for interesting events while achieving a rejection of low transverse momentum physics of about 10^7, thus reaching the ~200 events/s storage capability of the Data Aquisition system. A three-levels structure has been implemented for this purpose, as described in this work for the case of the muon trigger system. After describing the implementation, some performance results are presented in terms of final trigger rates, resolutions, efficiencies, background rejection and algorithm latency.

Keywords: ATLAS, HLT, Trigger, Muons

1. Introduction

High-p_T muons are important for many known processes, that can be used for monitoring and calibration ($Z \rightarrow \mu\mu$), and for several new phenomena (Higgs, SUSY), predicted at the energy of the Large Hadron Collider (LHC). Therefore the muon trigger system is of primary importance. The detector dedicated to the identification of muons is the Muon Spectrometer (MS). It consists of resistive plate and thin gap trigger chambers (RPC and TGC) and precision detectors consisting of monitored drift tubes (MDT) and cathode strip chambers (CSC).

The Muon Trigger "Vertical Slice" consists of three main trigger selection levels, one hardware, Level 1 (LVL1) and two software, Level 2 (LVL2) and Event Filter (EF), referred as High Level Trigger (HLT). Decision on each event is based on reduced-granularity detector data for interesting regions at LVL1, full-granularity and precision, but only for same LVL1 regions, at LVL2, and full event data, as in offline, at EF.

2. Level 1 trigger

LVL1 selects active detector regions (Region of Interest, RoI) in the event, using RPC for $|\eta| < 1$ and TGC for $1 < |\eta| < 2.4$. Six programmable thresholds of the muon p_T are applied: a low p_T scheme (for 6, 8, 10 GeV/c) and a high p_T (11, 20, 40 GeV/c) level triggers. Overall barrel LVL1 acceptance is 83% for low p_T, and 79% for high p_T particles, while is close to 1 for the endcap. The rates depend on the machine luminosity: at the low luminosity of $10^{33}\mathrm{cm}^{-2}\mathrm{s}^{-1}$ with the low p_T threshold, the expected rate is about 11 kHz, both for the barrel and the endcap, while at the high luminosity of $10^{34}\mathrm{cm}^{-2}\mathrm{s}^{-1}$ with the high p_T threshold, the expected rate is about 2 kHz for the barrel and close to 8 kHz for the endcap.

3. Level 2 trigger

Many different software algorithms compose the LVL2 trigger. The names are chosen to explain their role in the trigger chain. The basic algorithm is *muFast*, that confirms/rejects LVL1 result and refine muon p_T evaluation, using MDT precision measurements. The following steps are executed within a 10 ms latency time: "global pattern recognition", involving trigger chambers and positions of MDT tubes (without using drift time); "local segment reconstruction" involving drift time measurements for each station; fast "p_T estimate" via a look-up-table. To refine the *muFast* p_T, the algorithm *muComb* combines information from Inner Detector (ID) data, allowing to sharpen the threshold at low p_T. Efficiencies for LVL2, with respect to LVL1, in the barrel is above 80% for muons with p_T at the selection edge and well above 90% for muons with higher p_T.

4. Event Filter

The Muon Event Filter consists of three algorithms: *MOORE*, *MuId StandAlone* and *MuId Combined*. They are offline packages fully integrated in the ATLAS software framework. Imported in the trigger environment, they became *TrigMOORE*. TrigMOORE can work in two different modes: wrapped, scanning full detector data, and seeded, starting from RoI seeded by LVL2 (full trigger chain) or alternatively by LVL1 (for trigger studies).

The role of MuId StandAlone is to extrapolate MS tracks to the production point. Muon momenta are measured with a resolution $\Delta p_T/p_T < 10\%$ up to 1 TeV. Tracks are reconstructed also in the ID by one dedicated software. MuId Combined uses these informations, thus enhancing momentum resolution to about $< 3\%$ for p_T up to 50 GeV/c. In Tab.2 are reported, for different threshold level, the rates extrapolated with single muon samples.

4.1. *Efficiency from $Z \rightarrow \mu\mu$ sample*

This sample can be used to extract MS trigger efficiency directly from data. One μ with $p_T > 20$ GeV and $|\eta| < 2.4$, reconstructed in both ID and MS, is used as a tag; the other μ is required only in the ID, and used as a probe to check if it is observed in the MS. The separation between the two muons must be $\Delta\phi > 0.3$ and the invariant mass must be close to the Z mass ($|M_{\mu\mu} - M_Z| < 10$ GeV). Two p_T selections are studied for this muon: $p_T > 1$ GeV to check the overall trigger efficiency and $p_T > 20$ GeV to check trigger measurement over threshold.

4.2. *Trigger Menus*

Different kinds of physic events need to share available bandwidth, that is limited. Flexible trigger menus allow to avoid saturation from few processes, and guarantee the possibility to organize the analysis depending from luminosity conditions. When the rates are too high, prescale factors (PS) can be applied to low p_T thresholds at LVL1, and leave the HLT in pass through (PT) mode. The HLT capabilities are studied flagging the events without rejection. Express streams, not prescaled, at fixed thresholds, are used for calibration and monitoring purposes. A possible Trigger Menu for LHC startup is shown in Tab. 1 for different muon p_T thresholds.

Table 1. A typical Muon Trigger Menu for 10^{31} luminosity (LHC startup).

	Level 1		Level 2		Event Filter	
Threshold		rate (Hz)		rate (Hz)		rate (Hz)
mu_4(*)	PS=1000	1k	PT	1	PT	1
mu_6		224		98		48
mu_6	PS=200	224	PT	1	PT	1
mu_10		112		13		7
mu_10	PS=100	112	PT	1	PT	1
mu_15		19		4		2
mu_15	PS=20	19	PT	1	PT	1
mu_20i		14	PT(muIsol)	14	PT	14
mu_40		8	PT	8	PT	8
2mu_6		4	PT	4	PT	4
2mu_20		<1	PT	< 1	PT	1
Total						88

Note: mu_4 correspond to a totally opened threshold, normally used for cosmic runs.

4.3. *A trigger chain example*

Trigger software works with objects called *Trigger Elements* (TE). *Feature Extraction Algorithms* (FEX) are activated by input TE produced by previous trigger levels. FEX access the detector data and compute physical quantities, Features, that are then associated to the output TE. Selection is done in *Hypothesis Algorithms*, that validate or reject TE according to trigger menu requirements.

In-flight decays of pions and kaons are the main source of LVL1 trigger rate at low p_T. One goal of the muon HLT is to reject such fake muons while having high selection efficiency on prompt muons up to p_T of 6 GeV/c.

A track from such decays appears with a kink, and the χ^2 of the fit is worse than prompt muon tracks. Another handle could be the ratio of the

p_T values in ID and MS for combined tracks: for prompt muons this ratio is closer to one. In general, all possible kinematic parameters and statistical techniques must be used to distinguish and reject tracks from π/K decays.

Table 2. Single muon rates at Event Filter for different threshold levels in the barrel and in the endcap, and for different luminosity conditions.

	Rates (Hz), low p_T threshold, L=10^{33}cm^{-2}s^{-1}			
	6 GeV/c		8 GeV/c	
	Barrel	Endcap	Barrel	Endcap
b	580	720	200	290
c	290	360	90	130
t	0.05	0.07	0.04	0.06
W	2.9	4.0	2.8	4.0
π/K	1640	1180	350	310
Total	2530	2260	640	740
	Rates (Hz), high p_T threshold, L=10^{34}cm^{-2}s^{-1}			
	20 GeV/c		40 GeV/c	
	Barrel	Endcap	Barrel	Endcap
b	68	110	2.7	4.4
c	26	44	0.94	1.6
t	0.21	0.32	0.05	0.08
W	22	33	4.1	6.9
π/K	46	45	0.16	0.2
Total	160	230	7.9	13.1

5. Conclusions

ATLAS and LHC are under completition and first collisions are expected by the end of 2007. A big effort will be required to the trigger, to reach the required performances of background suppression and high efficiency for events signal of new physics. The Muon Trigger Vertical Slice, designed with the three level system, should be able to cover such difficult role, remaining within the tiny window allowed by data access and latency time.

References

1. ATLAS Collaboration, ATLAS High-Level Trigger Data Acquisition and Controls CERN/LHCC/2003-022, 2003
2. ATLAS Muon HLT Review, [Online] https://twiki.cern.ch/twiki/bin/view/Atlas/MuonHLTReview and references therein

TEST OF REAL-TIME IDENTIFICATION OF SPARSE DATA PATTERNS IN SILICON PIXEL DETECTORS

MARCIN JASTRZAB[*a,b], ANTONIO BULGHERONI[c], MASSIMO CACCIA[b], CHIARA CAPPELLINI[b], GRZEGORZ CHWIERUT[a], WOJCIECH KUCEWICZ[a], FABIO RISIGO[b]

[a]*Electronics Department, AGH-University of Science and Technology, Al. Mickiewicza 30, Krakow 30-059, Poland*

[b]*Dipartimento di Scienze CC.FF.MM., Università dell'Insubria, via Valleggio 11, 22100 Como, Italy*

[c]*Dipartimento di Fisica, Università di Roma 3 e INFN Sezione di Roma 3, via della Vasca Navale 84, 00146 Roma, Italy*

Vertex reconstruction and Flavour Tagging in an experiment at the International Linear Collider (ILC) do require detectors well beyond the state-of-the-art and systems integrating up to 1 billion pixels. A data sparsification algorithm, applied to silicon pixel detectors to distinguish between signal and noise and providing an input for the off-line data analysis, has been developed and tested at different levels. The full exercise has been completed on algorithms implemented on the equipment computer. Real time implementation on the FPGA chip steering the DAQ system is currently being commissioned. Results are expected to be far reaching especially in terms of constraining the front-end architecture and electronics to get an on-sensor implementation. Moreover these developments are expected to be of relevance in the domain of radiolabeled biological sample imaging.

1. Introduction

1.1. *Monolithic Active Pixel Sensors in High Energy Physics*

Research and Development of Monolithic Active Pixel Sensors is focused on different technologies and architectures tailored to every specific application. The key figures steering the development for ILC may be outlined as follows:

- Single point resolution at the micron level
- Thickness/layer at the 0.1% of radiation length
- Tolerance to radiation levels of $\approx 10^{12}$ n/cm^2/year and $\approx 5 \times 10^{12}$ e/cm^2/year
- Occupancy from background hits well below 1%.

* corresponding author: jastrzab@agh.edu.pl

The latter requirement is actually extremely constraining since it implies full detector readout, or a time stamping of the hits, in time slots not exceeding 100 μs in the closest layer.

Irrespective of the extreme detector modularity, in 1 Gigapixel detector this specification can be accomplished only through architectures implementing on-chip real-time identification of sparse cluster of fired pixels, reducing dramatically the data transfer volume and time.

The easiest possible design to accomplish this task relies on parallel column readout of all of the pixels in a module, with the identification of pixels over threshold and zero suppression by the end-of-column logic. In this scheme, the emphasis is on single pixels rather than on clustering. Whether viable in most technologies and possibly effective in terms of circuitry, a scheme neglecting the correlation between neighboring pixels in a cluster could affect the overall performance in terms of resolution and data volume.

1.2. *The sparsification algorithms*

Real time data reduction is a non trivial issue and sparsification algorithms are expected to have an impact on the detection efficiency, on the spectrometric capabilities and possibly on the spatial resolution. An exemplary illustration is provided by Figure 1.

The correlation plot in Figure 1 shows very clearly the effect of different sparsification algorithms on the total detected cluster pulse height.
A selection based on single pixel signal over threshold provides a lower cluster pulse height with respect to a minimum bias algorithm, based on the sum over 8 (or 24) cells surrounding a seed pixel.

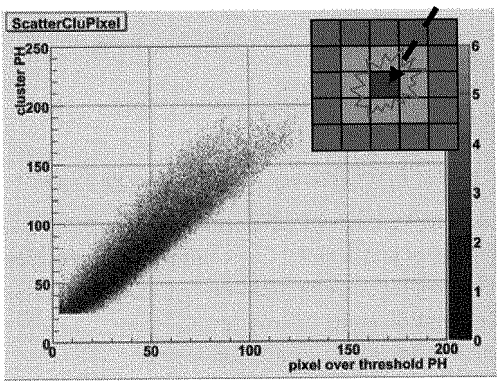

Figure 1. Signal pulse height with clustering versus pixel over threshold

The relevance of the threshold setting for single pixel over threshold procedure is becoming more critical for the systems with low S/N ratio as explained in 2.1. Since spatial resolution is based on the mean value, pulse height weighted, of the single cells entering the cluster, an incomplete accounting of the pixels carrying a signal may have an impact on the most relevant figure of position sensitive detectors.

2. Sparsification algorithm tests

2.1. *Software based on-line sparsification*

The potential disclosed by sparsification was investigated in a series of experiments on low activity ^{3}H detection in biological samples. The algorithms were implemented in a dedicated Labview [1] program. The baseline detector was a 1 Mpixel, high granularity CMOS sensor called Mimosa5 [2,3]. The data were readout by the FPGA steered SUCIMA DAQ [4].

The results obtained during the measurements are presented in Figure 2. To investigate the signal deposition around the seed pixel in the cluster, the spectrum of the pulse height in the 8 surrounding pixels has been analyzed.

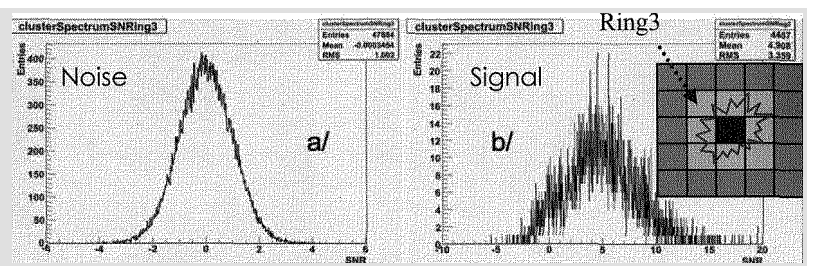

Figure 2. The collected charge spectra of the seed pixel crown for noise a) and signal b) events.

The spectra show that, unless the signal over noise ratio is increased by a significant factor, a pixel-over-threshold sparsification suffers from irreducible limitations: assuming a low threshold value (at the 1 noise unit level), the recorded charge of a genuine cluster is minimally biased but the number of output pixels by pure stochastic fluctuations is significant, increasing the data volume. On the other hand, increasing the threshold would naturally induce the opposite effect, reducing spurious hits but possibly affecting the reconstructed point position in a systematic way.

The software implementation of sparsification on one hand provides high flexibility to implement different algorithms, on the other hand severely limits the duty cycle of the system, possibly improved by the hardware implementation of the optimal algorithm.

2.2. *Hardware based – real time sparsification*

The preliminary results obtained with the EUDRB DAQ are presented in this section. The EUDRB (EUdet Data Reduction Board) has been developed by INFN Ferrara within the P-ILC project and it is the baseline system for the pixel telescope of the EC – EUDET project [5]. The board is compliant with different sensor matrices. The EUDRB is a highly flexible system, mastered by an Altera Cyclone II FPGA chip. For the time being a pixel over threshold sparsification procedure was implemented for Mimosa5 in VHDL language for the FPGA chip. One of the system features is the real-time sensor image monitoring and signal histogram calculation.

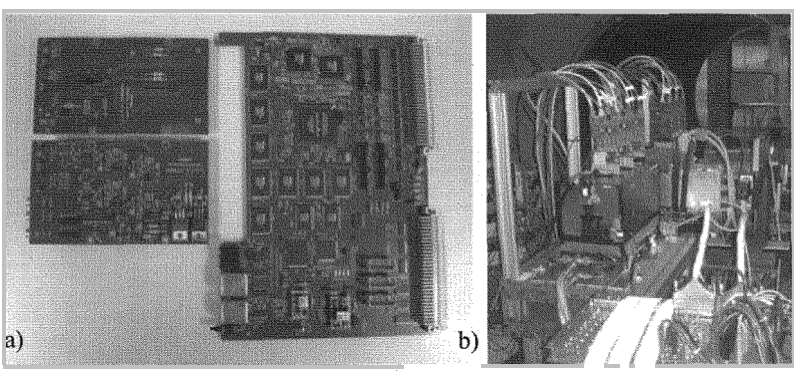

Figure 3. a) EUDRB Data Acquisition System first prototype July 2006, b) EUDET pixel telescope demonstrator, commissioned at DESY (June 07), used with HE hadron's beam at CERN (Sept. 07).

The hardware implementation of the real-time sparsification increases the duty cycle to nearly 100%, essentially because no overhead is introduced and sparsified data are transmitted to the equipment computer during one full frame readout requiring 26ms for Mimosa5.

The VHDL firmware consists of:

- pedestal and noise calculation,
- threshold calculation (in σ units for each pixel),
- signal over threshold data selection,
- data transmission of the selected pixels to the PC

Exemplary illustrations of the EUDRB potential are shown in Figure 4, displaying in real time the hit pattern from a ^{3}H loaded water droplet and from a focused light source.

On-line results have been cross checked against off-line analyses of non-zero suppressed data, qualifying the implementation. On the short timescale, minimum bias algorithms will be implemented and tests on the spatial resolution performed relying on the EUDET telescope.

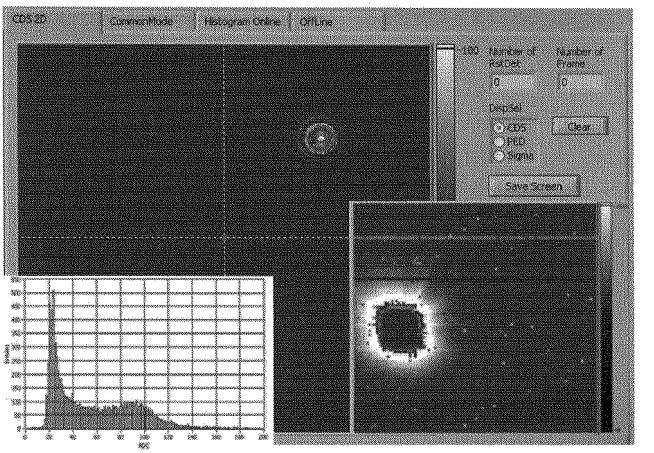

a) b)

Figure 4. a) EUDRB based analysis output from Picoquant PLS500 LED source, together with the histogram, b) result from ^{3}H droplet deposited on the surface of Mimosa5 sensor.

3. Conclusions and outlook

The performed experiments and comparison prove that sparsification at the hardware level for future HEP experiment and beyond is due. The main outcome is expected to be a guideline to the detector designers, specifying the boundary conditions for the development of architectures integrating on-chip sparsification procedures.

References

1. http://www.ni.com/labview/
2. G. Deptuch, Nucl. Inst. and Meth. in Phys. Res. A 543 (2005) 537-548
3. C. Cappellini et al, Imaging of biological samples with Silicon Pixel Detectors, proceed. of 9th iWoRiD workshop,22-26 July Erlangen 2007
4. A.Czermak, et al, Data Acq. System for Silicon Ultra Fast Cameras for Electron and Gamma Sources in Med. App. (Sucima Imager), World Scientific proceed. of 8th ICATPP confer, 6-10 Oct. 03, Como, Italy.
5. T. Hass et al, Nucl. Inst. and Meth. in Phys. Res. A 569 (2006) 53-56

Commissioning of the ATLAS Inner Detector with cosmic rays

E. Klinkby on behalf of the ATLAS collaboration
Niels Bohr Institute, HEP

The tracking of the ATLAS experiment is performed by the Inner Detector which has recently been installed in its final position.[1] Various parts of the detector have been commissioned using cosmic rays both on the surface and in the ATLAS pit. The different calibration, alignment and monitoring methods have been tested as well as the handling of the conditions data. Both real and simulated cosmic events are reconstructed using the full ATLAS software chain, with only minor modifications to account for the lack of timing of cosmics events, the lack of magnetic field and to remove any vertex requirements in the track fitters. Results so far show that the Inner Detector performs within expectations with respect to noise, hit efficiency and track resolution.

Keywords: Cosmics, ATLAS, Inner Detector, Commissioning

1. Introduction

Doing next year, the Large Hadron Collidor at CERN goes into operation providing proton-proton collisions at 14 TeV in the center-of-mass system. Bunches are collided every 25 ns with an expected average number of collisions $\sim$25 per bunch crossing when operating at the design luminosity. The high rate and energy set strong requirements for the tracking. In ATLAS the requirements are met by the Inner Detector operating in a 2 T magnetic field. The Inner Detector has a typical layered structure consisting of three sub-detectors based on different detector technologies to best cope with the requirements. Each sub-detector consists of a barrel part and two end-caps - the measurement accuracies quoted below corresponds to those of the barrel detectors from which most of the results presented below originates.

Closest to the interaction point is the very radiation hard and fine segmented pixel detector (Pixel) providing three measurements for each track of 12 μm precision in $r\phi$ and 110 μm in the (rz) plane. The next sub-detector met by a traversing particle consists of four silicon layers of the SemiConductor Tracker (SCT) - a silicon micro-strip detector with a readout pitch of 80 μm, which yields a binary resolution on the detector of $\sim$ 21 μm.

The cylindrical volume extending from a radius of 56 cm to 107 cm is covered by the gaseous Transition Radiation Tracker (TRT). Based on the principle of transition radiation the TRT consists of 73 layers of straws interleaved with radiator material providing both continuous tracking as well as electron identification by their transition radiation signature. The intrinsic measurement accuracy is expected to be 170 μm in the $(r\phi)$ plane. Presently the Inner Detector is installed in the pit and commissioning is ongoing. Results from standalone sub-detector measurements at the surface as well as combined tests in the ATLAS cavern are presented below.

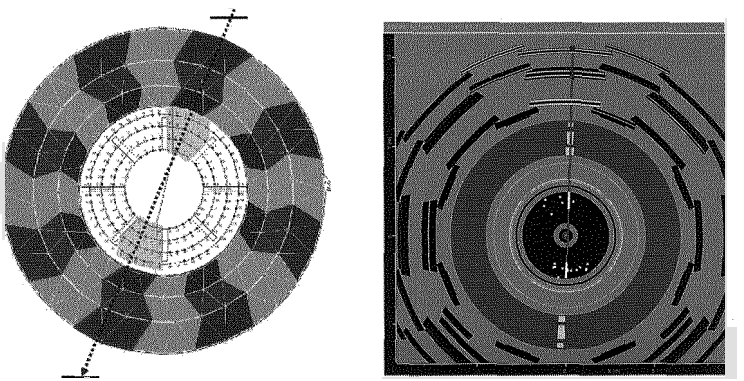

Fig. 1. Left: Setup for cosmic data taking at the surface. Scintillator plates are placed above and below the detector. Only the shaded sectors are read out. Right: Event display showing an event from cosmics in the pit. Note how the track is formed based on the information of many sub-detectors.

2. Commissioning using Cosmic rays: At the surface

For the most part, cosmic rays at the surface consist of low energy muons (average 2GeV) produced in the atmosphere. Since the arrival time of such muons is random, the surface setup for the integrated TRT cosmics included scintillator plates used for triggering. Plates were placed above and below the sub-detectors (see figure 1) in such a way that a coincidence would require a particle passing near the center of the detector and therefore to some extent, resemble a particle produced in a beam collision - at least with respect to which detector parts are passed. Offline, the full event reconstruction is performed on real cosmic data as well as simulations of the same using as much as possible standard ATLAS software packages. Minor updates were needed to cope with the fact that the cosmic events are

not synchronized with the ATLAS clock, and for the tracking to perform without vertex constraints or magnetic field. The resulting hit efficiencies for the TRT- and SCT barrel tests were within expectations - see figure 2. Additional tests using a random triggers to record noise levels were also successful - results for the SCT (barrel and endcap) and the Pixel (endcap) are shown in figure 3. After alignment and calibration the resolution of the TRT and SCT tracks are $\sigma = 59\ \mu m$ and $\sigma = 170\ \mu m$ respectively which is within expectations (see figure 4). The reason that SCT the uncertainty is larger than the ATLAS expectations is partly due to the low momenta of the cosmic rays, and partly that no magnetic field was applied, and therefore the particle momentum could not be measured and effects of multiple interactions could not be corrected for. As for the TRT, the fact that the expectations for the final ATLAS setup are reached at the cosmics tests indicate that improvements with respect to the design value can be expected in the final setup.

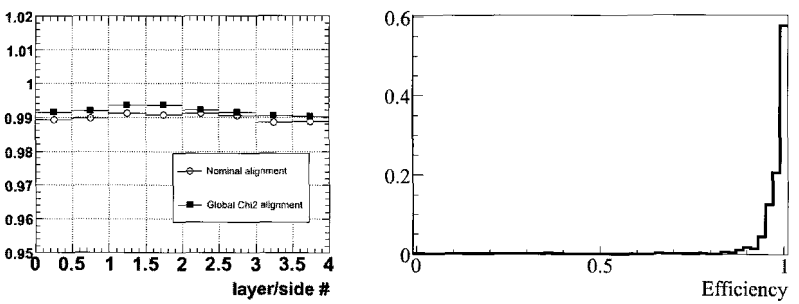

Fig. 2. Hit efficiencies of the SCT(left) and TRT(right) as measured in tests on the surface.

3. Commissioning using Cosmic rays: In the pit

Recently the Inner Detector has been installed in the ATLAS pit and tests performed with parts of the SCT and TRT integrated into the ATLAS data acquisition. Figure 5(a) shows an event from the test run. The muon chambers and tile calorimeter are used as triggers and this has caused some difficulties: This usage of the tile calorimeter was not part of the design requirements and the timing of the different muon modules has not been made uniform yet. However these issues presently being addressed. Simultaneously a different approach is being prepared for the next runs, where scintillator plates will be placed on top of the ATLAS detector. For practical reasons however the area covered with scintillators will be small,

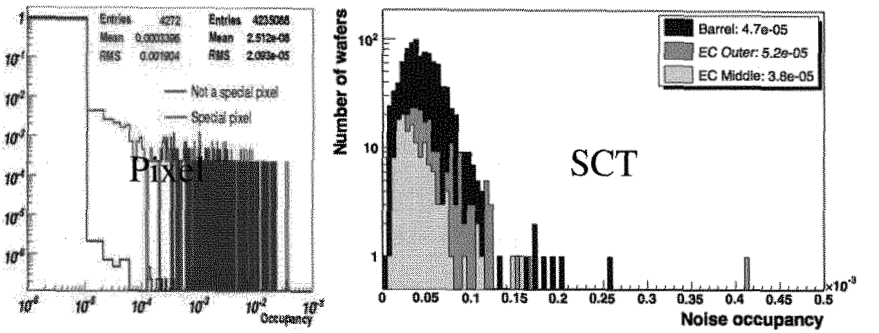

Fig. 3. Noise levels of the Pixel and SCT sub-detectors as measured in tests on the surface. The latter was tested only under "warm" conditions, where the noise occupancy is expected to be larger than during ATLAS operation.

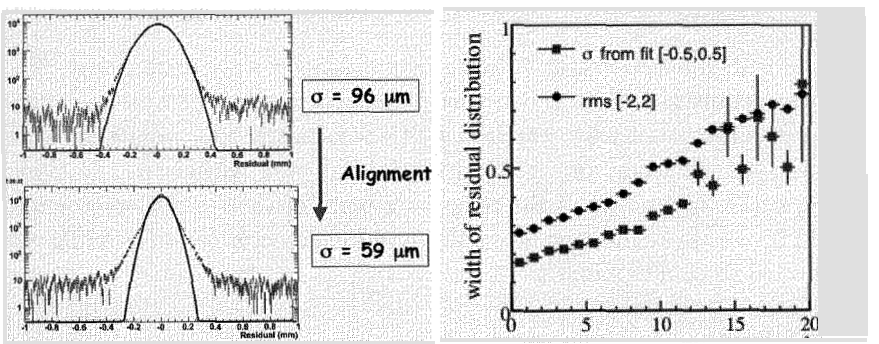

Fig. 4. Left: SCT track residuals before and after alignment. Right: σ of the TRT track residual distribution as a function of the unbiased χ^2 for each given hit (i.e. the χ^2 of the track removing the contribution of the hit under evaluation). Both plots stem from tests performed at the surface.

causing a low event rate from this cosmic trigger. The results of the most recent cosmic run in terms of TRT noise and resolution are shown in figure 5.

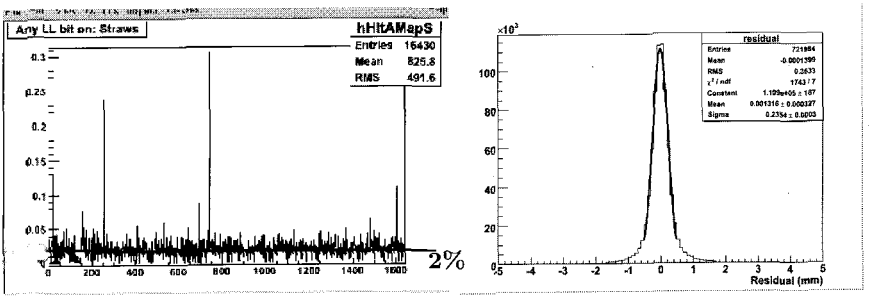

Fig. 5. Left: Noise levels of the various straws in one TRT ϕ sector. Level is generally below the expected 3%. Right: TRT track residuals as measured in the ATLAS cavern. The resolution is worse than the specifications (170 μm) due to the fact that multiple scattering is unaccounted for.

4. Conclusions

The ATLAS Inner Detector is being commissioned with cosmic rays. The full data acquisition chain is being used and cosmics data as well as simulation is reconstructed with standard ATLAS software. The results in terms of noise, hit efficiency and track resolution fall well within specifications. However the integration of the remaining parts of the Inner Detector into the ATLAS data acquisition is ongoing and the detector commissioning will proceed in to coming months.

References

1. ATLAS: Detector and physics performance technical design report. Volume 1 CERN-LHCC-99-14

ENERGY LOSS AND DAMAGE PRODUCTION BY HEAVY IONS AND STRANGE QUARK MATTER IN SILICON *

SORINA LAZANU

National Institute for Materials Physics,
POBox MG-7, Bucharest-Măgurele, Romania, e-mail: lazanu@infim.ro

IONEL LAZANU

University of Bucharest, Faculty of Physics, Department of Atomic and Nuclear Physics
POBox MG-11, Bucharest-Măgurele, Romania, e-mail: ionel.lazanu@gmail.com

In this contribution the peculiarities of the behaviour of strange quark matter in respect to ordinary ions in silicon are investigated, and a tentative to identify possible observable effects of degradation is made.

1. Introduction

Strange quark matter is a hypothetical state of matter with unusual properties: stability, large mass range, low charge to mass ratio. The main objective of the present contribution is the investigation of the peculiarities of the behaviour of strange quark matter in respect to ordinary ions in silicon and the identification of possible observable effects of degradation. Starting from the predicted characteristics of the SQM, we consider the interaction processes of ordinary ions and SQM in silicon, putting into evidence those phenomena which produce irreversible bulk degradation in material and effects at the device level.

2. Short review on strange quark matter (SQM)

Strange quark matter is another state of matter [1, 2]. As it is known, quarks and gluons carry colour charges. The confinement character of the strong force prohibits the isolated existence of single quarks, but they can cluster in pairs or small groups, as mesons, baryons, or antibaryons. There is no basic physical principle known which excludes the existence of larger baryons. Strange quark matter is so-called because of the admixture of a large number of delocalized

* work in the frame of CERN RD50 Collaboration.

quarks (u,..., u, d,..., d, s,..., s). The mass range for this kind of matter may lie anywhere between the masses of light nuclei and that of neutron stars. SQM should be considered stable or relatively stable based on the following possible arguments [3 ÷ 5]:

1. The (weak) decay of an s-quark from SQM into a d-quark would be suppressed or forbidden if the lowest single particle states are occupied.
2. The strange quark mass is lower than the Fermi energy of the u or d quark in such a quark droplet; the opening of a new flavour degree of freedom tends to lower the Fermi energy and hence also the mass of the strangelet.
3. SQM should have relatively small positive integer charge and the neutrality is realized by the existence of electrons, analogous to the case of atoms.

The unusual properties: stability, large mass range, low charge to mass ratio, low energy, are considered as characteristic for SQM. In particular, the low Z/A ratio has been recognized as a crucial signature for the experimental identification of strangelets. If for ordinary nuclei the Z/A ratio is usually between 0.33 ÷ 0.67, in colour flavour locked SQM (structures where quarks with different colour and quantum numbers form Cooper pairs), this is $\sim 0.3 \times A^{-1/3}$ and thus in ordinary strangelets it is approximately constant for small A, $A^{-2/3}$ for large A, reaching $A^{-1/3}$ only asymptotically.

If strange quark matter is absolutely stable or quasistable, the SQM produced in the early moments of the universe in the quark – hadron transition at about $T \approx 100$ MeV survives the evolution and in principle could exist as heavy isotopes with an unusual high mass and low charge in terrestrial or stellar matter, in cosmic rays, or could be produced in collision experiments of heavy ions at high bombarding energies.

In experiments devoted to the study of primary CR nuclei, anomalous events have been observed [6 ÷ 8], with values of charge Z = 14 and mass numbers A = 350 and A = 450 respectively, with Z = 46 and A > 1000 and with Z = 20 and A = 460, and have been reported. Recently, two events were put in evidence in the AMS-01 data: ^{16}He: Z = 2, A~16 and ^{54}O: Z = 8, A = 54+8(−6) [9]. A short-lived strangelet candidate with mass 7.4 GeV and charge Z = −1 was separated by the NA52 experiment [10].

3. Effects in silicon due to heavy ions and SQM

The incident ion interacts with the electrons and with the nuclei of the semiconductor lattice. It loses its energy in several processes, which depend on the nature of the particle and on its energy. The effect of the interaction of the incident particle with the electrons of the target is ionisation. The nuclear interaction between the incident particle and the lattice nuclei produces bulk

defects, depending on the nonionising energy loss (NIEL). The recoil nucleus (or nuclei in the case of inelastic processes) is displaced from the lattice site into interstitial positions. Then, the primary knock-on nucleus, if its energy is large enough, can produce the displacement of a new nucleus, and the process continues as long as the energy of the colliding nucleus is higher than the threshold for atomic displacements. The primary mechanism for defect formation during irradiation in semiconductors is the collision of the incoming particle with the atoms of the crystal, which leads to the departure of an atom to a rather large distance from its original site, i.e., to the formation of separated Frenkel pairs (vacancies and interstitials) as well as of the Si_{FFCD} defect, that introduces a new type of symmetry in lattice [11, 12],

$$Si \xrightarrow{G} V + I + Si_{FFCD}$$

In silicon, the primary defects (V and I) are mobile over a broad temperature range, including room temperature, and diffusing they are trapped by other primary defects or by impurity atoms forming secondary defects or migrate to sinks. The main characteristics of the kinetics of defects are summarised in Ref. [12].

The knowledge of the dynamics of defects in silicon during and after irradiation permits the determination of the effects produced at the p-n junction detector level. Due to the low radiation flux of particles from background and to the effects induced by every ion, the main modification in the detector parameters is observed in the leakage current.

4. Results and discussions

The competition between nuclear and electronic stopping produced in a material by ions is a function on energy. It must be mentioned that at low incident ion kinetic energy, nuclear stopping is the dominant process and this behaviour depends on Z and A, so it is very different for hypothetical SQM in respect to ordinary ions. This behaviour could be observed in Figure 1.

The bulk degradation due to nuclear interactions, the NIEL, is represented in Figure 2 for a great number of ions and for all hypothetical candidates for SQM versus the kinetic energy of the ions

Also, the spatial distribution of the degradation simulated using the SRIM 2006-02 MC programme put in evidence major differences between ordinary ions and corresponding exotic cases, candidates for SQM.

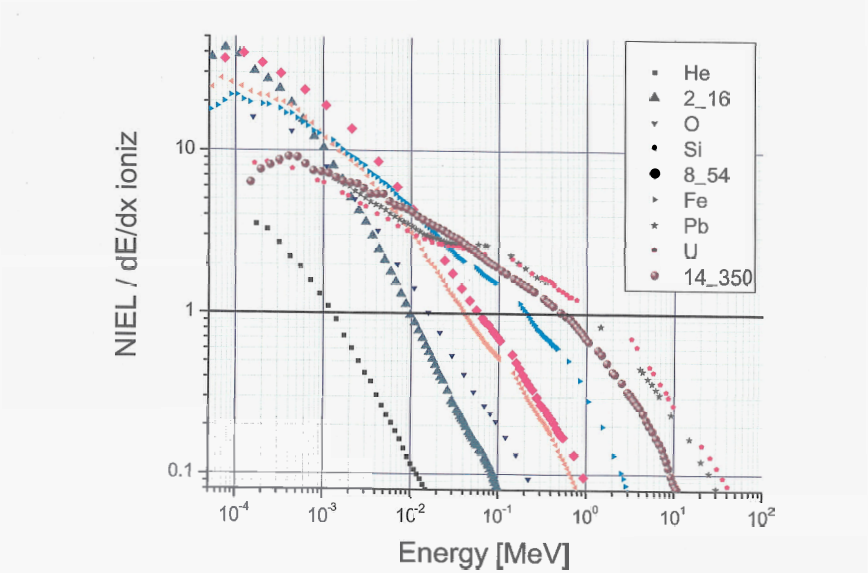

Figure 1. Energy dependence of the ratio between NIEL and ionisation for ordinary ions and hypothetical SQM

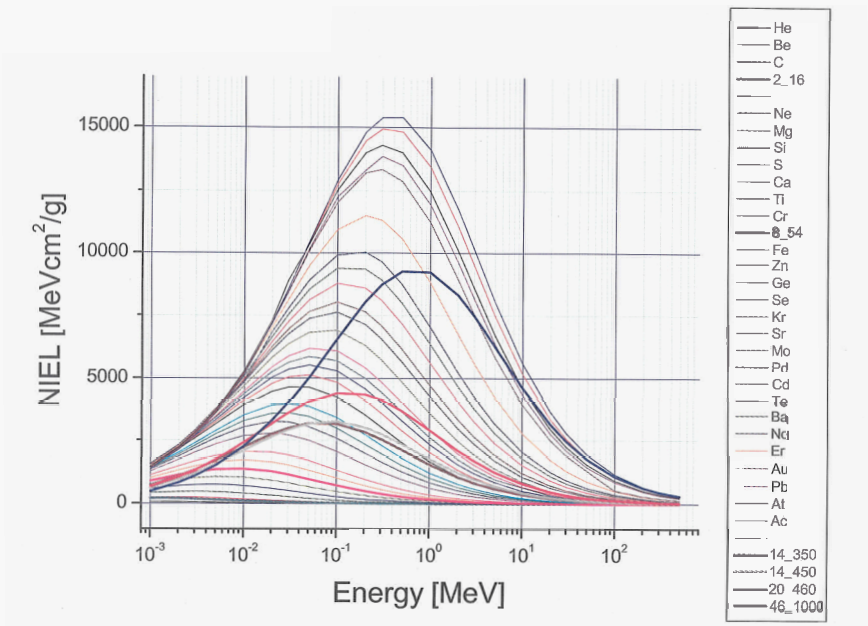

Figure 2. Energy dependence of NIEL for ordinary ions and hypothetical candidates to SQM

In the calculations, analytical approximations [13] and MC simulations [14] have been used.

The effect at the device level is the increase of the density of the leakage current. So, for example, in a detector exposed for two years to a continuous flux of protons from cosmic rays, the passage of one SQM ion (Z=14, A=350) with energy 10 MeV produces an increase in the current density up to about 10^{-4} A/cm^3 from an initial value of $2x10^{-9}$ A/cm^3.

5. Summary and possible conclusions

A very different behaviour of SQM ions was put in evidence in their interaction in silicon, in respect to ordinary ions. These aspects were observed in: NIEL, as a measure of bulk degradation, number of primary VI pairs per incident ion, characteristics of the interaction region. For the region where the incident ion deposits its energy, a significant increase of the density of the leakage current was estimated. More detailed studies are necessary to put in evidence aspects of experimental interest.

Acknowledgments

This work was partially supported by the Romanian National University Research Council, under grant no. 28 /2007.

References

1. R. Klingenberg, *J. Phys. G: Part. Phys.* **25**, R273 (1999).
2. C. Greiner and J. Schaffner-Bielich, "*Physics of Strange Matter*", World Scientific, Singapore, 1999.
3. J. Madsen, *Proc. Workshop on Exotic Physics with Neutrino Telescopes*, EPNT06, Uppsala 2006, editor:Carlos P. de los Heros, 57-62.
4. J. Madsen, *Phys. Rev. Lett.* **87,** 172003 (2001).
5. X. Ma, *J. Phys. G: Nucl. Part. Phys.* **32**, S575 (2006).
6. T. Saito, et al., *Phys. Rev. Lett.* **65**, 2094 (1990).
7. P.B. Price et al., *Phys. Rev.* **D18,** 1382 (1978).
8. M. Ichimura et al., *Nuovo Cim.* **A106**, 843 (1993).
9. Ke Han, http://home.physics.ucla.edu/calendar/conferences/sqm2006
10. R. Klingenberg et al., *Nucl. Phys.* **A610** 306c (1996).
11. S. Goedecker et. al., *Phys. Rev. Lett.* **88**, 235501 (2002).
12. I. Lazanu, S. Lazanu, *Phys. Scr.* **74**, 201 (2006).
13. S. R. Messenger et. al., *IEEE Trans. Nucl. Sci.* **50**, 1919 (2003).
14. SRIM – 2006.02 package (www.srim.org).

Implementation and Performance of the High-Level Trigger electron and photon selection for the ATLAS experiment at the LHC

F. Monticelli on behalf of the ATLAS e/gamma group *

UNLP, Universidad Nacional de La Plata,
La Plata, Argentina
E-mail: Fernando.Monticelli@cern.ch

The ATLAS three-tier trigger system faces the challenge to reduce the incoming rate of 40 MHz to $\sim$ 200 Hz. It consists of hardware based Level-1, and a software based High-Level Trigger (HLT).[1] In this talk an overview of the selection algorithms for electrons and photons will be given as well as the expected performance. The electron and photon trigger menu and the strategy for the initial phase of LHC exploitation.

Keywords: High Level Trigger; ATLAS; electron; photon.

1. Introduction

The ATLAS experiment will start taking data in 2008 at the Large Hadron Collider (LHC), currently under construction at CERN.

ATLAS[2] is a multipurpose detector, designed to explore the fundamental nature of matter and to search for new particles such as the Higgs boson and possible unforeseen new physics processes.

The ATLAS detector is equipped with the inner detector (Pixel, SCT silicon strips and TRT straw tubes), the Liquid Argon (LAr) electromagnetic calorimeter, the Tile hadronic calorimeter and the outer muon system. In total there are more than 100 million readout channels.

*Anduaga X., Baines J., Benslama K., Berry T., Coura Torres R., Damazio D., De Santo A., Dova M., Emeliyanov D., Enoque Ferreira de Lima D., Flacher H., Fonseca-Martin T., Gaumer O., Goncalo R., Grabowska-Bold I., Hryn'ova T., Khoriauli G., Kilvington G., Konstantinidis N., Ledroit F., Losada M., Monticelli F., Moreno D., Padilla C., Parodi F., Perez Reale V., Pinzon G., Riu I., Rodriguez D., Rogriquez Y., Santamarina C., Schiavi C., Seixas J. M., Sivoklokov S., Sutton M., Tripiana M., Wang M., Watson A., Wielers M., Woehrling E.-E., Wu X., Ozcan E.,

The high number of detector channels, leads to a mean event size of $\sim$ 1.5 MB. The trigger and data acquisition system (TDAQ) will reduce the incoming rate to $\sim$200Hz which is the rate allocated for offline processing.

2. The ATLAS High Level Trigger

In the ATLAS experiment, the reduction of the 40MHz incoming rate down to the 200 Hz maximum event data storage rate will be provided through three different trigger levels.

The hardware based first level trigger (LVL1) performs a preliminary rejection using only reduced granularity data coming from the calorimeters and the muon detector. It operates within a latency $\sim 2.5\mu$s, producing an average output rate of 75kHz upper limited to 100kHz. Further event selection is done by the software based second level trigger (LVL2) and event filter (EF), collectively referenced as the HLT. The reconstruction at LVL2 is seeded by the LVL1 result using full granularity of the ATLAS subdetectors, processing data contained in the regions of the detector identified by the LVL1 as regions of interest (RoIs), each correspond to $\sim$2% of the detector. The LVL2 is designed to have an output rate less than 2kHz, with a mean processing time of 40ms. The EF, seeded by the LVL2 results, uses more complex reconstruction.

The main two concepts characterizing the event selection at the HLT in ATLAS are the RoI guided and step wise reconstruction. This event selection mechanism reduces the amount of data to be processed at each trigger stage. Another feature of the ATLAS HLT event selection strategy is the early rejection achieved by alternating reconstruction algorithms and the so-called hypothesis algorithms which decide if the candidate fulfills certain identification criteria. The event can be rejected after any hypothesis step.

3. Electron and photon selection

Electron and photon reconstruction mainly exploits data coming from the electromagnetic calorimeter and the Inner Detector (ID) tracking systems. The starting point for the electron and photon chains are the triggered LVL1 electromagnetic cluster candidate. The first step in the e/γ chain is a fast clustering algorithm which is seeded by the LVL1 RoIs.In the next step a hypothesis algorithm uses this information to perform preliminary particle identification. In case the event is accepted, the e/γ chain then continues with the EF processing. For electrons track reconstruction is performed in

the ID. There are two main tracking algorithms being studied: IDScan and SiTrack[4] which have very similar performances. In the next step, cluster to track association is done using the matching between the cluster positions with the corresponding η and ϕ values of the tracks extrapolated to the calorimeter surface. In the subsequent step a particle identification is done based on the p_T of the track, the E_T/p_T ratio and the position match between the calorimeter cluster and the extrapolated track. The EF re-uses the available offline algorithms with more precise calibrations and alignment constants than at LVL2. Electron and photon trigger menus have been set to be fully efficient in all the pseudorapidity region $0 < |\eta| < 2.5$.

4. Performance of electron and photon trigger

Electron and photon trigger menus have been extensively studied for luminosity L$\approx 10^{33} cm^{-2} s^{-1}$. It was demonstrated they are well set-up to trigger on events produced at HLT. Table 1 shows the trigger efficiency w.r.t. to the offline selection for a low mass Higgs decaying into two photons selected by either the trigger which efficiently selects photons above a transverse energy of ET=60GeV (g60) or by the trigger which requests two isolated photons selected efficiently with ET>20GeV (2g20i). In the same table the respective expected background rate is also shown. Table 2 shows the expected electron trigger efficiencies for Z$\rightarrow e^+e^-$ and for Exotic Gravitons G$\rightarrow ee$ of 500GeV invariant mass.

Table 1. Photon trigger efficiencies w.r.t. to the offline photon selection for $H_{120} \rightarrow \gamma\gamma$

Trigger Level	2g20i		g60	
	Eff	Rate	Eff	Rate
L1	96.4±0.5%	150 ±10 Hz	92.9±0.4%	1200 ±80 Hz
L2	94.6±0.7%	5 ±1.7 Hz	86.8±0.6%	35 ±14 Hz
EF	93.8±0.8%	2 ±1 Hz	84.7±0.6%	16 ±9 Hz

In March and May 2007 the timing of the LVL2 and EF algorithms were measured in a so-called technical run. During this period the trigger software was run in playback mode on simulated events using a subset of the final HLT farm. Figure 2 show the LVL2 and EF total time measured for accepted events. The LVL2 timing obtained in the technical run in May 2007 was around 100ms with a large RMS. The EF mean processing time was 1.57s. Work is ongoing to improve further the timing performance of the HLT algorithms.

Table 2. **Electron trigger efficiencies** w.r.t. offline electron selection for Z→ e^+e^- and G→ ee

Sample	Z→ e^+e^-	G→ ee	
Trigger Level	e25i	2e15	e60
L1	96.0%	99.9±0.1	99.9±0.1
L2	84.4%	84.4±0.5	96.1±0.2
EF	84.0%	73.0±0.6	92.1±0.3

Note: Using IDScan algorithm for tracking

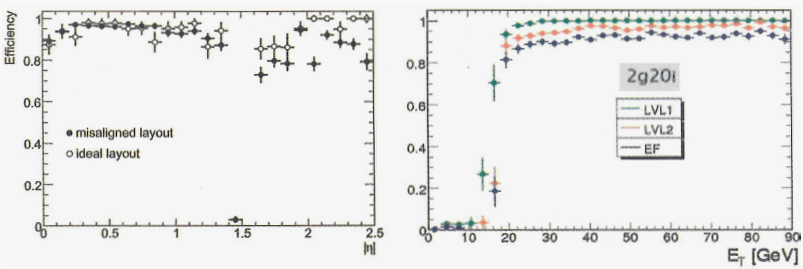

Fig. 1. **(a) e25i trigger efficiency vs pseudorapidity** $|\eta|$ w.r.t. offline; (b) g20i trigger efficiency vs p_T after each trigger level w.r.t. offline

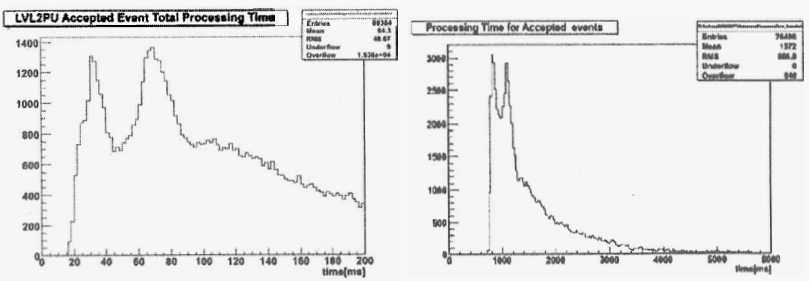

Fig. 2. Total time for accepted events measured for (a) LVL2 and (b) EF

5. Strategy at start up

At start-up an initial luminosity of L≈ $10^{31} cm^{-2} s^{-1}$ is expected. The start-up trigger menu for electrons and photons has to provide the data samples needed to commission the trigger and detectors and provide useful data to be used for physics analysis. Therefore, a good selection of the physics

channels $J/\Psi \rightarrow ee, Y \rightarrow ee$, Drell-Yan, $Z \rightarrow ee, W \rightarrow e\nu$, and direct photon production will be crucial. The aim is to select events with at least one electron above $\approx$ 10 GeV or one photon above $\approx$ 20 GeV in addition to the relevant double-object triggers, e.g. for selecting $J/\Psi, Y$, and Z events. As the data as well as the trigger and detector performance need to be understood the trigger selections use loose selection criteria. The photon triggers will use the same loose cuts for the calorimeter based selections. A range of signatures are foreseen in the trigger menu to adapt to running conditions. If the rate is too high triggers with higher thresholds are defined and/or pre-scales can be adjusted. To ensure the selection of important physics channels, redundant triggers are present, for example, a dedicated J/Ψ trigger. For $W \rightarrow e\nu$, triggers which combine electrons and missing transverse energy are available. With time the trigger and detector performance will be understood and gradually the trigger selections can be tightened and some redundancy triggers can be dropped.

6. Conclusions

The ATLAS trigger performance of electrons and photons at low luminosity (L=$10^{33} cm^{-2} s^{-1}$) has been discussed. It has been shown the triggers are well set-up for the various physics processes with electrons and photons in the final state. The HLT algorithms have been tested using simulated events in a subset of the final HLT farm. This has been an important test for the timing performance and a final test to ensure the algorithms are set-up for being run in the real HLT online environment.

References

1. ATLAS HLT/DAQ/DCS Group, ATLAS High-Level Trigger, Data Acquisition and Controls Technical Design Report, CERN/LHCC/2003-022, ATLAS-TDR-016 (2003).
2. ATLAS Collaboration, ATLAS Detector and Physics Performance Technical Design Report, CERN/LHCC/99-14, ATLAS-TDR-014 (1999).
3. G. Comune et al, The Algorithm Steering and Trigger Decision mechanism of the ATLAS High Level Trigger, ATLAS Internal Note, ATL-DAQ-2003-031, Proceedings CHEP03, La Jolla, California, March 24-28, 2003.
4. N. Konstantinidis et al, Fast Tracking for the ATLAS LVL2 Trigger, ATL-DAQ-CONF-2005-001, proceedings of the Computing in High Energy Physics and Nuclear Physics 2004 Conference, Interlaken, Switzerland, 27 September - 01 October 2004; C. Schiavi et al

THE CMS ECAL LASER MONITORING SYSTEM

T. J. ORIMOTO*
On behalf of the CMS ECAL Group
Charles C. Lauritsen Laboratory of High Energy Physics,
California Institute of Technology
Pasadena, CA 91125, USA
* *E-mail: toyoko@hep.caltech.edu*

Light monitoring will play a crucial role in maintaining the energy resolution of the CMS electromagnetic calorimeter, by providing transparency corrections for its 75,848 lead tungstate ($PbWO_4$) crystals. To maintain the resolution of the calorimeter, the variation in the light output of the $PbWO_4$ crystals in the harsh radiation environment of the LHC is corrected for by using a light monitoring system. The design of the light monitoring system, as well as the performance during test beams, is discussed.

Keywords: CMS, electromagnetic calorimeter, light monitoring.

1. Introduction

Elucidating the origins of electroweak symmetry breaking, and in particular discovering the Higgs boson predicted by the Standard Model, is the main motivation for building the Compact Muon Solenoid (CMS) experiment at the Large Hadron Collider (LHC). One of the design goals of the CMS electromagnetic calorimeter (ECAL) was to optimize the resolution for the discovery of the Higgs in the distinctive, yet challenging, diphoton channel.

The CMS ECAL is a high-resolution, high-granularity scintillating crystal calorimeter, consisting of 75,848 lead-tungstate ($PbWO_4$) crystals.[1] $PbWO_4$ crystals were chosen because of their short radiation length, small Molière radius, and fast speed as a scintillator. The design energy resolution of the ECAL has a constant term of 0.5%, and to maintain this constant term, *in situ* calibration and monitoring of the crystals must be performed. Exposure at the level of the nominal LHC luminosity causes a decrease in crystal transparency due to radiation induced absorption. The changes in transparency are monitored with a high precision, laser-based light monitoring system, the performance of which is described here.

2. Radiation Induced Crystal Transparency Change

At the LHC design luminosity of 10^{34} $cm^{-2}s^{-1}$, the CMS detector will be exposed to a very harsh radiation environment. The $PbWO_4$ crystals are radiation hard up to a high integrated dosage, but nonetheless suffer from dose-rate dependent radiation damage, resulting in a decrease in crystal transparency. Previous studies have shown that the scintillation mechanism of $PbWO_4$ crystals is not affected by radiation, and the loss of light output is due only to the absorption caused by radiation induced color centers.[2]

During irradiation, the annihilation and creation of color centers reach an equilibrium, depending on the applied dose rate. Although the crystals will self-recover in absence of radiation, this recovery takes place on the order of days, while the time cycle of the LHC operation is 12 hours. Therefore, changes in crystal transparency, and therefore calorimeter response, due to radiation damage must be corrected for to maintain the energy resolution of the detector. Typical variations in the crystal light output, measured using an electron beam, can be as large as 5% in the ECAL barrel and even greater in the endcaps for radiation levels at LHC design luminosity.

3. The Laser Monitoring System

The CMS ECAL utilizes a laser monitoring system to monitor the light output of the crystals. With this system, we can measure the change in transparency of each crystal continuously during LHC operation, with very high precision. In order to maintain the constant term in the ECAL resolution to 0.5%, the measurement of the transparency change must be made with an accuracy of greater than 0.2%. The ECAL readout electronics require that the laser pulse width be shorter than 40ns and stable at a level better than 10%. Sychronization with the LHC clock requires that the laser pulse timing be stable to a few ns. In addition, the pulse energy must be on the order of 1mJ/pulse, which is equivalent to 1.3 TeV in the dynamic range of the system, to provide sufficient light to monitor the entire ECAL in approximately 20 minutes.

To meet these requirements, a dual-stage, laser system has been designed, constructed and commissioned by the Caltech and Saclay groups.[3] The monitoring light source consists of two sets of Nd:YLF laser pumped Ti:Sapphire lasers, which provide two wavelengths, available using a 3×1 optical switch. The selected wavelength is then sent to each ECAL monitoring element using a 1×88 optical switch. Fig. 1 shows a schematic of

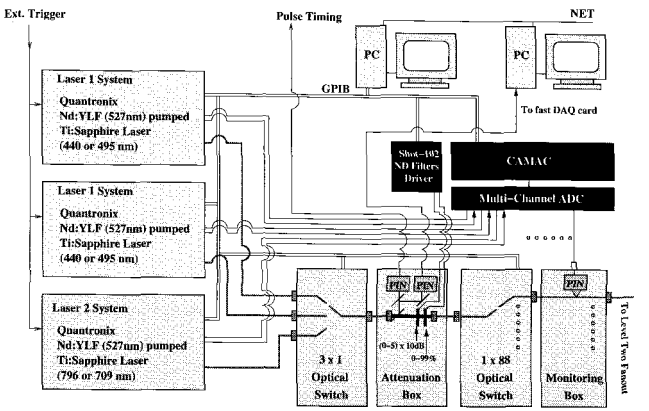

Fig. 1. Schematic diagram of the CMS ECAL laser monitoring source. Two laser systems provide light at 440nm and 800nm.

the light distribution system.

In 2006, a software feedback system was implemented so that the long term stability of the laser pulse intensity and FWHM width are maintained at the level of a few percent, with a laser pulse timing jitter of less than 2ns. The long term stability was observed in more than 2,000 hours of test beam data, as shown in Fig. 2. With an integrating sphere based light distribution system, the stability of the normalized monitoring response is about 0.1%. With such performance, even small changes in transparency can be monitored with precision.

4. Performance Results from Test Beams

The performance of the monitoring system and the transparency correction were tested during dedicated irradiation runs at test beams in 2006 and 2007. These dedicated studies were performed by emulating the dose rates expected at the LHC by irradiating the crystals with an electron beam at high rates. During the irradiation periods, the crystals were regularly monitored with laser runs. Fig. 3 (left) shows the changes in crystal transparency during the damage and recovery cycles in test beam data.

Prior studies have shown that the decrease in scintillation signal response due to a particle traversing a crystal is directly proportional to the decrease in the injected laser light monitoring signal. The loss in the response of the crystals to electron beam runs can be correlated with the loss in response to laser runs, by the equation, $E(t)/E(t_0) = [L(t)/L(t_0)]^{\alpha}$,

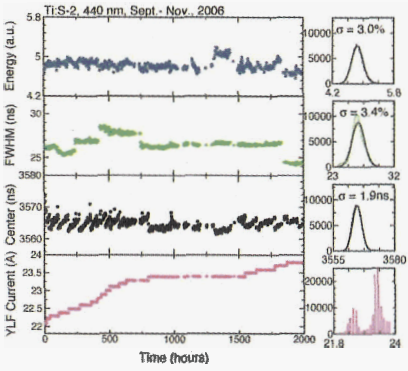

Fig. 2. Stability of the laser monitoring system, as measured in test beam data.

where $E(t)/E(t_0)$ corresponds to the normalized electron beam response, $L(t)/L(t_0)$ is the normalized response to laser runs, and α is the correlation constant which relates these two responses. Fig. 3 (middle) shows the fit for α for one of the ECAL barrel crystals, from test beam data. The spread of α values, as shown in Fig. 3 (right), has been measured to be around 5% in a sample of 28 crystals in prior test beam data. (Data from the 2006 test beam is still under analysis.) Such a small dispersion will allow us to use the same α parameter for all ECAL crystals during the first years of LHC operation. The energy resolution before and after the monitoring corrections, for 120 GeV electrons, reconstructed by summing the energy in 3×3 crystals, is 0.93% and 0.53% as measured with test beam data.

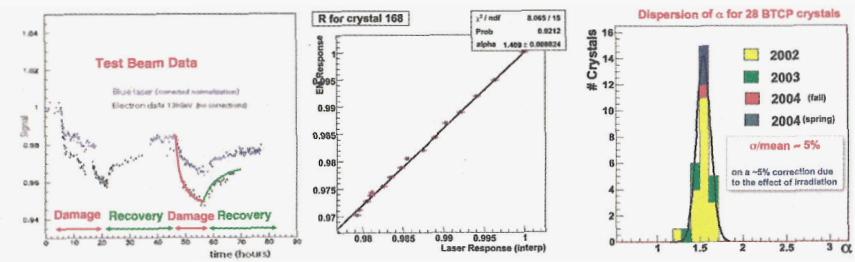

Fig. 3. (Left) The changes in responses to electron beam and laser runs during the damage and recovery cycles of the crystals, as seen in test beam data. (Middle) The correlation between the responses to electron and laser test beam data, for one of the ECAL barrel crystals. (Right) The distribution of α values for 28 different ECAL crystals.

5. Laser Monitoring Dataflow and Commissioning at CMS Point 5

During LHC running, laser data will be collected during "abort gap" events, which occur for $3\mu s$ every $90\mu s$. The gap events, containing laser data amongst other data, will be sent to a filter farm, at which point the events will be sorted. The laser events will then be analyzed in a PC farm to extract data relevant for the transparency correction. The data is then inserted into the "online" database, located at CMS Point 5. Next the data is then transferred to the "offline" database, during which any necessary corrections will be applied to the laser data. During the offline reconstruction of CMS data, the values in the database will be used to compute and apply the transparency correction to physics events.

6. Conclusion

The CMS ECAL laser monitoring system has been commissioned and tested at test beams at CERN, and is currently being commissioned at CMS Point 5 underground. The laser monitoring system will provide corrections for light output fluctuations caused by variations in crystal transparency during the radiation damage and recovery process. The stability of the system has been exhibited to be on the order of 0.1%. With such performance, even small changes in transparency can be monitored with precision.

7. Acknowledgements

I would like to acknowledge the CMS ECAL group for their effort and dedication. I would also like to thank my colleagues from the laser monitoring group, particularly A. Bornheim, C. Rogan, and R.Y. Zhu, for their input and support.

References

1. "The Electromagnetic Calorimeter Technical Design Report", CMS Collaboration, CERN/LHCC 97-33, 1997.
2. "Radiation Induced Color Centers and Light Monitoring for Lead Tungstate Crystals", X. Qu, L. Zhang, R.Y. Zhu, IEEE Trans. Nucl. Sci. NS-47 (2000).
3. "Performance of the Monitoring Light Source for the CMS Lead Tungstate Crystal Calorimeter", IEEE Trans. Nucl. Sci. Vol. 52 No. 4 (2005) 1123-1130.
4. "ECAL Monitoring Light Source at H4", D. Bailleux, A. Bornheim, L.Y. Zhang, K.J. Zhu, R.Y. Zhu, and D. Liu, CMS IN 2003/045.

HIGH ACCELERATING FIELD SUPERCONDUCTING RADIO FREQUENCY CAVITIES.

R.S. ORR[†]

Department of Physics, University of Toronto, 60 Saint George St., Toronto, Ontario M5S 1A7, Canada.

K. SAITO, F. FURUTA, T. SAEKI, H. INOUE, Y. MOROZUMI, T. HIGO, Y. HIGASHI, H. MATSUMOTO, S. KAZAKOV, H. YAMAOKA, K. UENO, M. SATO

KEK, High Energy Accelerator Research Organization, 1-1 Oho, Tsukuba 305-0801, Japan.

We have conducted a study of a series of single cell superconducting RF cavities at KEK. These tests were designed to investigate the effect of surface treatment on the maximum accelerating field attainable. All of these cavities are of the ICHIRO shape, based on the Low Loss shape. Our results indicate that accelerating fields as high as the theoretical maximum of 50MV/m are attainable.

1. Introduction

1.1. *The Proposed International Linear Collider*

Although a final decision must await the results from the LHC, there is a general consensus in the high energy physics community that the next accelerator should be a linear e^+e^- collider with an initial centre of mass energy of 500 GeV upgradeable to 1 TeV. In 2005 it was decided that the machine should be a cold one, based on niobium superconducting radio frequency cavities. These cavities are the kernel of the machine. The present Reference Design [1] envisages a machine which is of order 31 km long, and incorporates 17,000 cavities, each of which is 1.2 m long. The cost of these cavities is a major driver of the overall cost of the machine. Any reduction in the cost would be extremely beneficial for the timely approval of the project. Figure 1 shows a typical superconducting 9-cell radio frequency cavity.

[†] Supported by the Japan Society for the Promotion of Science

1.2. *Cavity Designs*

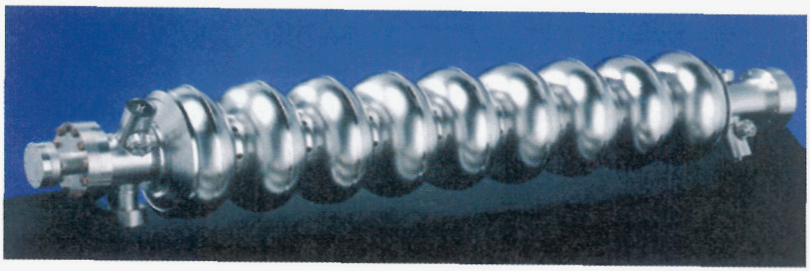

Figure 1. A TESLA 9-cell cavity as specified in the baseline ILC design.

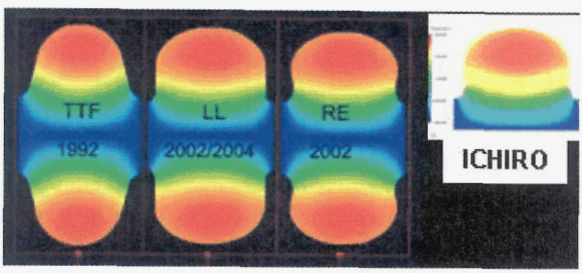

Figure 2. Comparison of shape and magnetic field distribution in the TESLA, Low Loss, Re-entrant, and ICHIRO cavity shapes.

The ILC baseline design requires a working gradient (accelerating field) of 31.5 MV/m and an acceptance gradient, for use in the machine, of 35 MV/m. If one assumes a distribution of gradients with an rms of ±5%, this implies a mean gradient of 40 MV/m.

Due to continuous improvements in surface preparation, it is now possible to design cavities whose accelerating field will be limited by the peak magnetic field, rather than field emission from the surface. This has led to the development of cavities such as the Re-entrant (RE) at Cornell and the Low Loss (LL) and ICHIRO (IS) cavities at DESY and KEK [2]. These new shapes are compared to the TESLA (TTF) shape in Figure 2. The important difference between the new shapes and the TTF, is that the ratio of the peak magnetic field to the accelerating field, $H_P/E_{acc}\,(Oe/MV/m)$, has been reduced from 42.6 (TTF) to 35.6 (IS). This, in principle, should allow the IS cavity to reach a maximum accelerating field of $50\,MV/m$.

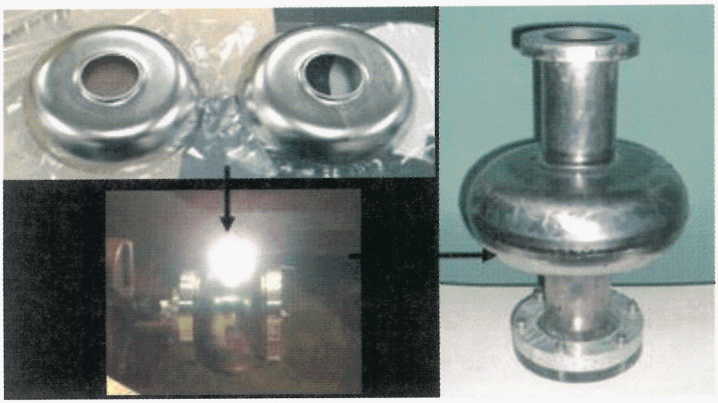

Figure 3. Deep drawn niobium cups (top left) are electron beam welded to produce the IS single cell structure shown on the right..

In addition to the baseline design, the ILC also has an Alternate Configuration. This assumes an operating gradient of 36MV/m, and an acceptance gradient of 40MV/m. Using the same consideration of a ±5% rms spread, this implies a mean gradient of 45MV/m. Such a increased gradient would reduce the ILC tunnel length by about 5 km, which would give a few percent reduction in the cost of the machine. A few percent is still a sizable sum, given the cost of the ILC. Perhaps more importantly, going to a higher maximum gradient would increase the number of acceptable cavities at the baseline acceptance gradient. The study described here was designed, using single cells of the ICHIRO shape, to determine whether such a distribution of high gradients was possible, as a precursor to performing the same study on 9-cell ICHIRO shape cavities

2. ICHIRO Single Cell (IS) Tests

2.1. *Single Cell Manufacturing Process*

For the purposes of studying the performance of the KEK surface treatment in achieving high gradients, we produced a series of six single cell ICHIRO cavities from sheets of high purity small grain niobium. The niobium sheets were supplied by Tokyo Denkai and were trimmed in the KEK machine shop. The dies for producing the deep drawn cups were also produced at KEK, and supplied to a local tool and die company. As shown in Figure 3, these deep

drawn cups were electron beam welded, at KEK, to produce the IS structure shown on the left of Figure 3.

2.2. *Surface Treatment of the IS series*

The maximum attainable accelerating field, E_{acc}, in RF cavities is a sensitive function of the surface preparation. As the field in a cavity is increased from small values, there are two major processes which can limit the performance; field emission and multi-pacting. These are discussed later. For the moment it is sufficient to say that avoiding these performance limiting effects depends on having a very smooth, clean interior surface in the cavities.

Table 1. Summary of KEK surface treatment procedure

Treatment	Process	Removal Thickness (μm)	Purpose
Centrifugal Barrel Polishing (CBP)	Mechanical grinding by stones and water	135 – 235	Remove defects of Nb material and smooth EBW seam.
Light Chemical Polishing (CP)	Chemical reaction	10	Remove dust after CBP and prepare smooth surface for EP
Annealing / degassing	750 °C for 3 hours by furnace		Release mechanical stress and degas hydrogen
Electro-Polishing (EP)	Chemical + electronic reaction	80	Prepare very smooth surface
High-Pressure Rinsing (HPR)	Rinse with pressured Ultra-Pure Water (UPW)		Remove particles and make clean surface
Baking	120 °C for 48 hours with pumping vacuum		Defuse oxidized layer

Over the past two decades a collaboration between DESY, JLAB, Cornell, and KEK has produced a more or less standard procedure for this surface preparation. However, the different groups do have somewhat different procedures, but all of them recognize that electro-polishing and high pressure rinsing with ultra-pure water, are the key to achieving high gradients. The IS series aimed at consistently achieving gradients in the region of the theoretical

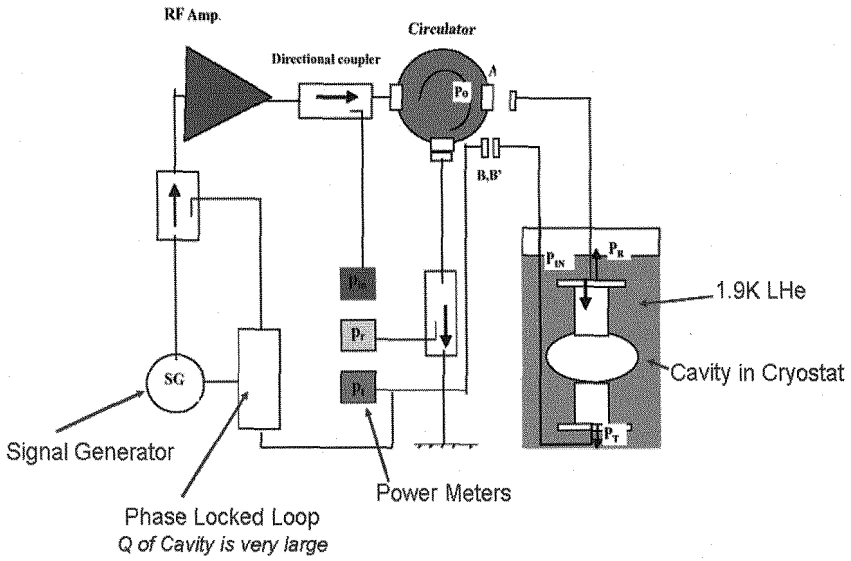

Figure 4. Schematic of the experimental setup used for vertical test of the IS cavity series

maximum of $50\,MV/m$, and a process developed at KEK [3] was used for the surface preparation. The process is summarized in Table 1.

The centrifugal barrel polishing is a process peculiar to this KEK recipe. Its purpose is to remove any surface defects on the niobium surface. Mechanical grinding has been used in the past. The KEK innovation is to use an automatic process. The cavity is filled with a slurry of water and polishing stones, and then put in a special rotary machine, which rotates the cavity at about 100 rpm for 12 hours. This process is repeated three times with successively finer polishing stones. The light chemical polishing is done for one minute at $25^{\circ}C$, and uses a mixture of $HF(46\%):\ HNO_3(60\%):\ H_3PO_4(85\%)$. The details of the effect of the final step of baking are not completely understood [4]. Empirically it is found that the Q-value of cavities falls off at high E_{acc}, unless this is done. One possibility is that an oxide layer formed by the previous processes is removed by diffusion during the baking.

2.3. *Vertical testing of the IS cavities*

The maximum attainable gradient of the cavities is determined by measuring the Q of the cavity as a function of the E_{acc}. A schematic of the experimental setup is shown in Figure 4. The cavity is immersed in liquid helium in a cryostat

at $1.9K$. RF power is applied to the cavity and the input, transmitted and reflected power are measured. As the input RF power is increased, the E_{acc} in the cavity increases. The Q of the cavity is just the fractional power lost in one radian of oscillation,

$$Q_0 \equiv \frac{\omega U}{P_{loss}}, \tag{1}$$

where ω is the resonant frequency, U is the stored energy, Q_0 is the unloaded Q value, and P_{loss} is the dissipative loss in the cavity. The Q value can be measured by disconnecting the RF source, and using an oscilloscope to measure the decay time τ of the energy in the cavity,

$$\tau = \frac{Q_L}{\omega}. \tag{2}$$

The Q value measured is actually the loaded Q_L which includes losses in the input and output RF couplers, but this can be related to the unloaded Q_0 [4]. The value of P_{loss} can be calculated from energy conservation,

$$P_{loss} = P_{in} - P_r - P_t. \tag{3}$$

Then the accelerating field can be calculated from,

$$E_{acc} = Z\sqrt{Q_0 P_{loss}} = Z\sqrt{Q_t P_t}. \tag{4}$$

The results are usually plotted as an excitation curve of the Q value against E_{acc}. Figure 5 is an example of such an excitation curve. This particular curve shows the behaviour of a well prepared cavity. The Q value falls off smoothly as E_{acc} increases, with no rapid drops in Q due to multi-pacting or field emission. This particular excitation curve may be taken as an existence proof that a correctly prepared IS cavity is indeed capable of reaching the theoretical maximum accelerating field.

After the initial surface preparation, excitation curves were measured for the six IS cavities. These excitation curves are shown in Figure 6. Three of the cavities have smooth excitation curves out to about the theoretical maximum. Another three have excitation curves which drop off much more steeply, an indication of field emission.

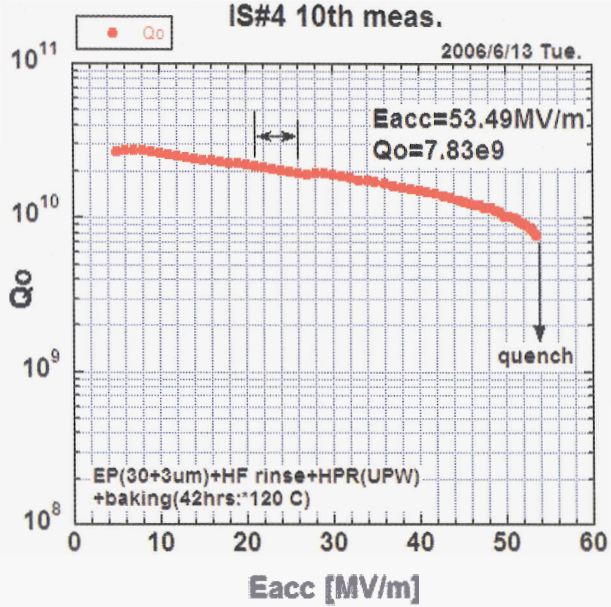

Figure 5. Excitation curve of Q versus $Eacc$ for a single cell cavity. The cavity quenches at 53.5 MV/m.

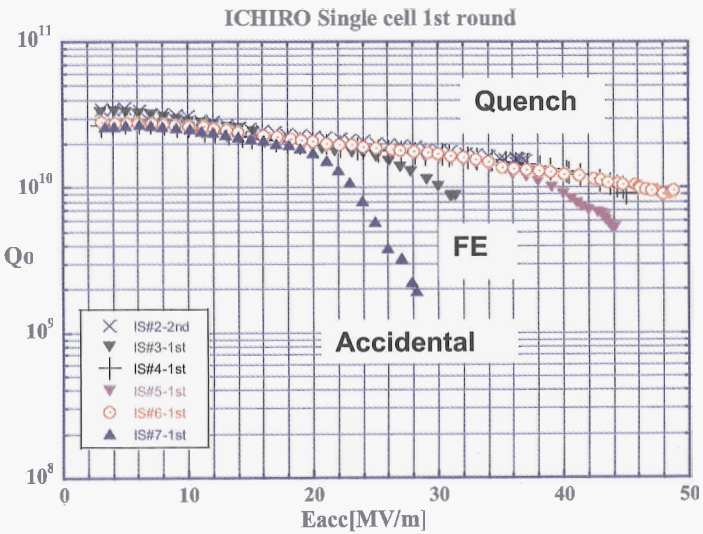

Figure 6. Excitation curves of the first measurements on the six IS single cell cavities.

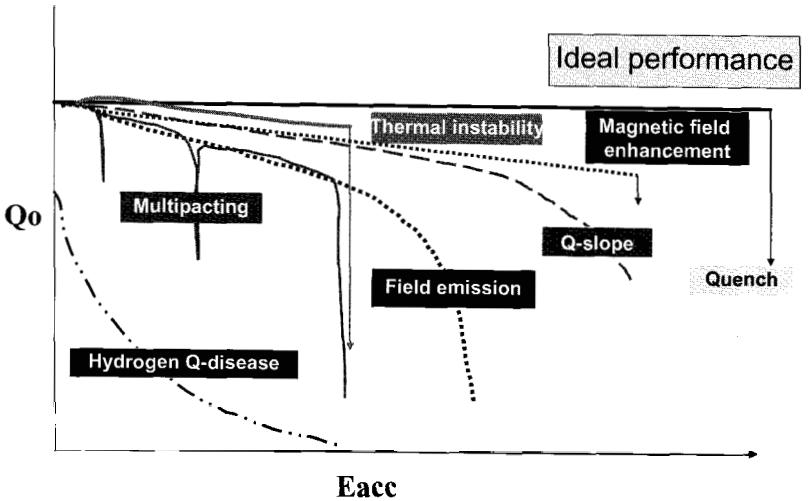

Figure 7. Various limitations on the performance of superconducting radio frequency cavities.

The possible behaviours for a well prepared cavity, including various pathologies, is shown in Figure 7. Naively, as the RF power input is increased, one would expect the horizontal line labeled "Ideal Performance"; E_{acc} increases at constant Q until the magnetic field exceeds the critical value, and the cavity quenches. In fact, experimentally the Q value falls off with increasing E_{acc}. This fall has two regions with different slope, as shown in the curve labeled "Q-slope". Various sources of these slopes have been discussed, but there is no clear theoretical understanding [4]. Since the surface of the cavity is not perfectly smooth, small defects may lead to local magnetic field enhancement, which can cause a critical field induced quench below the theoretical maximum, corresponding to the curve labeled "Magnetic Field Enhancement". The curve labeled "Thermal Instability" is due to a similar phenomenon, where internal electromagnetic field induced heating of small impurity defects cause a cavity to quench.

"Hydrogen Q-Disease" is a pathology where the formation of niobium hydrides form a lossy surface on the cavity, leading to a very low Q value [4]. For the cavities tested, by far the most important curves are those labeled "Multipacting" and "Field Emission". Both of these phenomena are caused by electrons emitted from the surface of the cavity absorbing the input RF power, and thus limiting the Q-value and E_{acc} attainable. The electron emission is either

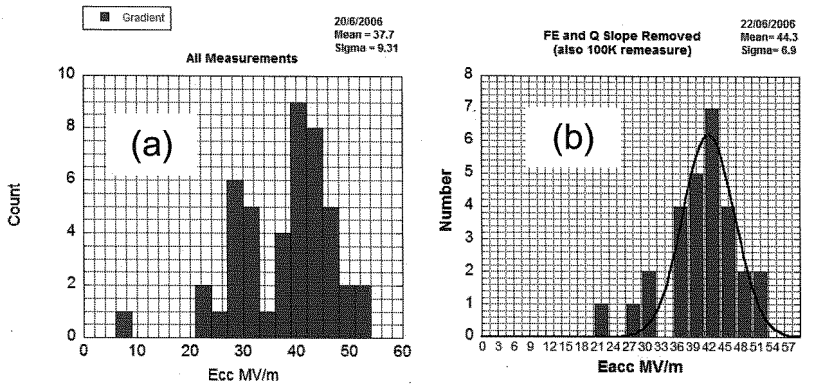

Figure 8 Accelerating field measured after cycling the six IS cavities through the surface preparation several times. (a) is all measurements, and (b) is after the removal of measurements during which there was severe field emission.

from defects or contamination on the cavity surface. Multi-pacting is a resonant phenomenon where, at a particular electric and magnetic field, emitted electrons describe resonant orbits originating and ending on the surface of the cavity. Field emission is non-resonant, and corresponds to more and more electrons tunneling out of a point on the cavity surface as the E_{acc} increases. These field emitted electrons are accelerated in the cavity and finally cause a quench by local heating at their impact point. Due to Bremsstrahlung, field emission is accompanied by copious X-ray emission, which is monitored by proportional counters outside the cryostat.

The six IS cavities were cycled through the surface preparation and measurement process several times. Figure 8(a) shows the distribution of the maximum E_{acc} reached. There is one very low value, due to miss-assembly in the clean room. The remaining measurements form two populations, the lower corresponding to field emission, and the upper to successfully prepared cavities. If the measurements with a high level of field emission, indicated by intense X-ray emission, and a rapid drop off of Q with increasing E_{acc}, are removed, we obtain the distribution shown in Figure 8(b). Fitting a Gaussian to this distribution indicates that this is indeed a statistical Gaussian and gives an estimate of the distribution of E_{acc} which could be obtained in single cells of this design, when subject to proper surface preparation. The fitted Gaussian has a mean of $44.3\,\mathrm{MV/m}$. This is in agreement with the requirement $45\,\mathrm{MV/m}$ mentioned in the introduction.

The large number of cavities undergoing severe field emission is attributed to the fact that the electro-polishing was done using a very old acid mixture. This could lead to precipitates of sulphur on the cavity surfaces, which are not removed in the subsequent high pressure rinse set. When we subjected the cavities to a second short electro-polishing step using fresh acid, the result was a distribution of $E_{acc} = 47 \pm 2\,\mathrm{MV/m}$.

In conclusion, we believe that these results are an existence proof of the possibility of producing cavities which operate at E_{acc} well above the baseline ILC design using the TESLA shape of cavities. It remains to be shown that 9-cell cavities which reach these voltage gradients can be consistently produced. Work is going on to demonstrate this [5].

References

1. ILC Reference Design Report, *http://www.linearcollider.org/cms/?pid=1000437.*
2. J. Sekutowicz et al., JLAB-TN-02-023, June 2002.
3. F. Furuta et al., Proceedings of LINAC 2006, Knoxville, Tennessee, USA, pp 299.
4. H. Padamsee, J. Knobloch, T. Hays, *RF Superconductivity for Accelerators*, Wiley, 1998.
5. T. Saeki et al., Proceedings of LINAC 2006, Knoxville, Tennessee, USA, pp 794.

OVERVIEW OF THE PLENARY SESSIONS ON ACCELERATOR AND COMPUTER/NETWORKING DEVELOPMENTS

R. C. RUCHTI

Department of Physics, University of Notre Dame, Notre Dame, IN 46556 USA and U.S. National Science Foundation, Arlington, VA 22230 USA

The goal of these plenary sessions is to present the status of developments in particle accelerators and computing and networking important for advanced scientific research. Topics can range from new acceleration schemes and technologies to Grid Computing and high speed, globally distributed networking. For ICATPP-10, it was decided to concentrate on three different particle accelerator approaches. These included hadron colliders (LHC), e+e- colliders (ILC), and developments toward muon colliders and neutrino factories (MICE). This paper summarizes some of the highlights of these sessions.

1. Introduction

Particle Physics is at the horizon of discovery with the planned start up of the Large Hadron Collider (LHC) at CERN in 2008. Once operational, the machine will provide collisions of proton beams at a CM energy of 14 TeV and a luminosity of $L = 10^{34}\text{cm}^{-2}\text{s}^{-1}$. Steve Myers presented the current status of the machine and its development plans.

In the era beyond LHC, a number of opportunities are being considered. One is an upgrade to the LHC to higher luminosity (called the SLHC) for which the luminosity will approach $L = 10^{35}\text{cm}^{-2}\text{s}^{-1}$. Other strategies involve lepton colliders (for e+e- and μ+μ-) and neutrino factories. At ICATPP-10 reports were presented on two aspects of these efforts – one on R&D on superconducting radiofrequency cavities for the International Linear Collider (ILC) by Bob Orr, and the other a presentation of the status of the Muon Ionization Cooling Experiment (MICE) by Marco Apollonio.

2. LHC Preparations

At present the LHC is being readied for operation in the next calendar year. The focus of Myers' presentation was on the status of the machine preparations, some of the challenges faced in this process, and the planning to reach the

design luminosity. Magnets: all of the dipole magnets for the machine have been in place as of April 2007 and the field quality is on target and well within allowed tolerances. Cool down and power up of seven out of eight LHC sectors is scheduled in parallel for the last months of 2007 into early 2008. Acceleration systems: the 400 MHz RF system is in cool down in preparation for power cavity testing in November 2007.

2.1. *Challenges*

Challenges: There was a failure of a heat exchanger tube at high pressure in the low β quadrupole triplets that focus the beams for collision – this problem has been resolved and the repairs are complete. The energy stored in the LHC beams is considerable (transverse energy density of order $1MJ/mm^2$) and protection for machine components and detectors depends significantly upon collimation. Production of collimators is now progressing well and all are to be produced by April 2008. During cool downs, vacuum leaks have occurred and repairs are in progress or complete. The helium inventory needs to be increased significantly to a level of 140 tonnes for machine operation, so effort is underway to increase the supply rate. The problem of failure of RF Fingers in the Arc Plug-In Modules has been diagnosed as due to out of tolerance preset bending angles of the fingers. The assemblies are being repaired with a tool that corrects to the proper finger geometry. Search for such failures (blockages) in the accelerator was expedited with a novel scheme – an RF Mole: a "ping-pong" ball containing a 400 MHz resonant circuit was inserted into the accelerator beam pipe and tracked, as it was moved through the pipe by airflow, using beam position monitors.

2.2. *Planning*

Planning: The schedule is ambitious with 7 sectors simultaneously under cool down and power testing in the closing two months of 2007. Machine checkout is scheduled for start in April 2008 and Beam Commissioning to 7 TeV per beam starting in May. Myers summarized his views as follows: many problems have been encountered and nearly all have been resolved; there may be more problems to come as machine preparations continue; the next few months are critical during the cool down of the sectors – the cool down must be leak free (vacuum); his recurring nightmares are polarity errors and aperture limitations; if there are no more serious problems, the plan is to move on to the next phase which is operating with beam in 2008; the accelerator group is very well

prepared for commissioning with beam and have an excellent team that was trained on LEP.

Several stages of operation are planned over several years to reach design luminosity.[a] Accelerator parameters for the first (Stage A) physics run are summarized in Table 1.

Table 1. Accelerator parameters for the initial LHC physics run (Stage A).

Parameters			Beam levels		Rates in 1 and 5		Rates in 2	
K(b)	N	β* 1,5 (m)	L(beam) proton	E(beam) (MJ)	Luminosity (cm-2s-1)	Events/ crossing	Luminosity (cm-2s-1)	Events/ crossing
1	10^{10}	11	1 1010	10-2	1.6 1027	<< 1	1.8 1027	<< 1
43	10^{10}	11	4.3 1011	0.5	7.0 1028	<< 1	7.7 1028	<< 1
43	$4\ 10^{10}$	11	1.7 1012	2	1.1 1030	<< 1	1.2 1030	0.15
43	$4\ 10^{10}$	2	1.7 1012	2	6.1 1030	0.76	1.2 1030	0.15
156	$4\ 10^{10}$	2	6.2 1012	7	2.2 1031	0.76	4.4 1030	0.15
156	$9\ 10^{10}$	2	1.4 1013	16	1.1 1032	3.9	2.2 1031	0.77

3. Superconducting RF cavity development for the ILC

One of the dominant cost drivers of the International Linear Collider will be its length and the RF cavities needed to accelerate the electron and positron beams to energies of 250 GeV or higher per beam. The machine design is based on superconducting (cold) RF technology, so R&D on niobium cavities with high gradient and reproducible performance characteristics is essential. Several developmental programs are underway, and Bob Orr presented the results of his work with colleagues at KEK on cavity development. Figure 1 taken from Orr's presentation shows an estimation of the relative cost of an ILC as a function of accelerating gradient.[b]

Challenge: The baseline ILC cavity design (BC) has a gradient of 31.5MV/m. To achieve this performance over many such structures requires an average performance of 35MV/m for an individual structure (35MV/m ± 5% with a cutoff for acceptance at 31.5MV/m). An alternate cavity design (AC) could allow for a gradient of 40MV/m and requires an average performance of 45MV/m. Breakthroughs in cavity R&D over the last decade have allowed this

[a] S. Myers, *LHC Status and Preparation for Operation*, Plenary Talk at ICATPP-10.
[b] R. Orr, *High Voltage Gradient Superconducting RF Cavities*, these Proceedings.

type of performance level to be reached – first with chemical polishing; high pressure rinsing; electropolishing; and lastly new cavity shapes. Orr presented the range and application of these techniques to reach gradients of ~50MV/m in an Ichiro Cavity.

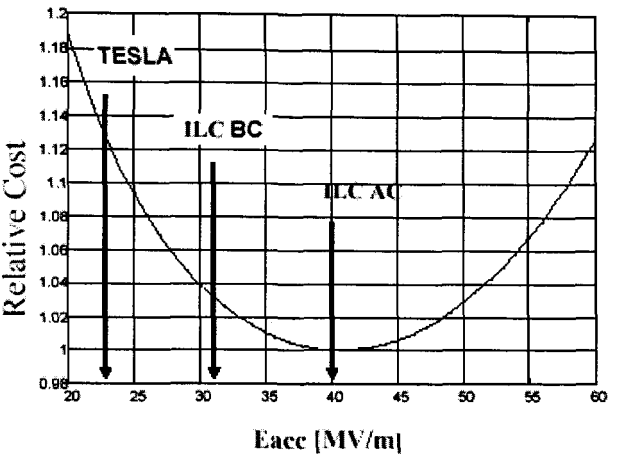

Figure 1. Relative Cost of the ILC as a function of accelerating gradient in the RF Cavities for TESLA, ILC Baseline (ILC BC), and an ILC Alternate (ILC AC).

4. Developments toward muon beam accelerators

If the physics that emerges from the LHC in the next half decade reveals that significant new phenomena lie in the TeV to multi-TeV range, then systematic studies of this realm would be accessible with a muon collider. Muon beams are also a vehicle to a neutrino-factory. Each of these facilities would rely on the development of controlled beams of muons, whose origin lies in the decays of mesons produced from proton interactions in a target. There are several challenges: the muons produced are divergent from the source and the transverse phase space must be "cooled" to allow the formation of a controlled beam suitable for subsequent acceleration and interaction; and this must be done very rapidly as the proper time for muon decay is 2.2μsec. So cooling and acceleration systems must be overlapped in space to accommodate these requirements.

Marco Apollonio discussed the preparations for MICE (the Muon Ionization Cooling Experiment) now being installed at the Rutherford Appleton Laboratory to demonstrate muon ionization cooling. The muon beam is derived

from mesons produced from the ISIS accelerator at RAL. The plan is to demonstrate, by 2010, the ionization cooling of muons with a cooling channel consisting of an interleaved system of liquid hydrogen absorbers, to create energy loss via ionization, RF cavities for longitudinal momentum restoration and magnet coils for coupling and focusing. Instrumentation includes particle identification through time-of-flight measurement, Čerenkov detectors, calorimetry and two magnetic spectrometers with scintillating fiber tracking and Visible Light Photon Counter readout for the measurement of the emittance and amplitude of particles before and after the cooling channel. Figure 2 shows the evolution of MICE from an initial configuration to measure beam properties through the final configuration with full cooling channel and full instrumentation.[c]

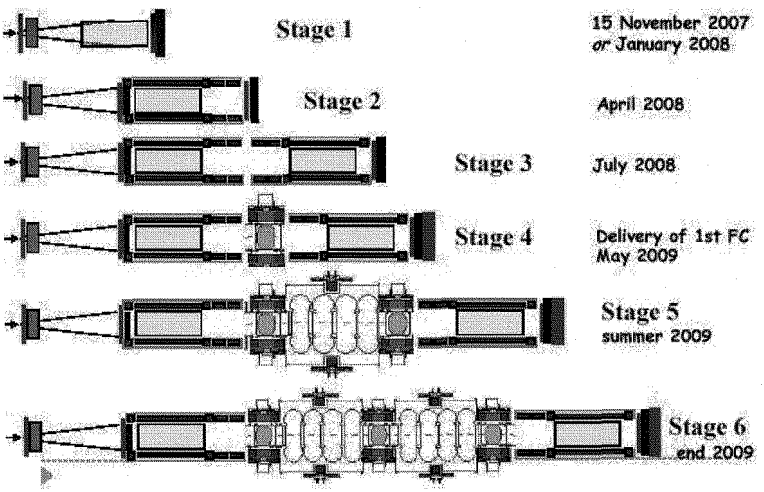

Figure 2. Evolution of the MICE Experiment, from an initial study of targeting and beam properties with one spectrometer [Stage 1] through the fully instrumented cooling channel configuration having spectrometers up and downstream [Stage 6].

Acknowledgements

R. Ruchti wishes to thank the invited speakers Marco Apollonio (Oxford), Steve Myers (CERN) and Bob Orr (Toronto) for their important contributions to ICATPP-10 and this plenary session.

[c] M. Apollonio, *Muon Cooling and the MICE Experiment*, these Proceedings.

The CMS Electromagnetic Calorimeter

M. Ryan

Imperial College, London

On behalf of the CMS ECAL group

The CMS experiment at the CERN Large Hadron Collider has placed great emphasis on precise calorimetry. The electromagnetic calorimeter (ECAL) contains 75000 scintillating lead tungstate crystals that are read out using sophisticated electronics; this paper describes these technologies and how they were implemented in the calorimeter. The results of pre-calibration measurements for the detector modules are detailed. Installation of the ECAL into the underground cavern has commenced and the commissioning process and its status are discussed. The experiment is scheduled to start in 2008 and prospects for the first year of operation and running are given.

Keywords: Lead Tungstate; CMS; Calorimetry

1. Introduction

The electromagnetic calorimeter (ECAL) [1,2] of the CMS experiment is a high precision scintillating crystal calorimeter and will play a key role in the wide LHC physics programme. This paper describes the technical details of the calorimeter, the pre-calibration measurements that have been made and the status of installation and commissioning in preparation for the first LHC run in 2008.

2. The Electromagnetic Calorimeter

2.1. *Mechanical Design*

The ECAL is divided into sections; a barrel section and two endcap sections. The barrel covers the pseudo-rapidity region $\eta < 1.48$ and is constructed from 61200 lead tungstate crystals. The crystals are grouped into units, called supermodules, of 1700 crystals. There are 36 supermodules in the barrel.

The endcaps cover the pseudo-rapidity region $1.48 < \eta < 3.0$. Each

endcap is made from two 'Dees' and 7244 crystals. The crystals are grouped into modules of 25 crystals, known as supercrystals. The inner and outer boundaries of the endcaps are made more circular by the addition of smaller units known as partial supercrystals.

2.2. *Lead Tungstate*

Lead tungstate ($PbWO_4$) [3] is a dense, fast and radiation-tolerant scintillating crystal. These three properties of the crystal make it an ideal choice for the CMS ECAL. The short radiation length ($0.89cm/X_0$) and small Molière radius (2.2cm) allow a compact calorimeter to be constructed. The scintillation decay time is very fast with 80% of the scintillation light collected within 25ns (in the LHC bunches of protons collide every 25ns).

The crystal also has very good resistance to radiation. The dose rates that the crystals will receive during LHC operation will be very high. Some loss of transparency does occur during irradiation however due to the formation of colour centres. This damage recovers in the absence of irradiation which means that the transparency of the crystals will fluctuate during a LHC run cycle. The crystal transparency will be monitored by injecting laser light into each crystal during gaps in the bunch structure and the crystal response corrected accordingly [1].

2.3. *Read-Out Electronics*

Lead tungstate has a comparatively low light yield, so photodetectors with gain are employed to detect the scintillation light. In the barrel, silicon avalanche photodiodes (APDs) [1] are used. In the endcaps, the higher radiation levels preclude the use of APDs and the approximately axial magnetic field allows the use of vacuum photo-triodes (VPTs) [1].

The photodetectors are connected to a multi-gain pre-amplifier (MGPA) and a radiation hard ADC. A Front End board takes the signals from groups of 25 channels and ASIC chips perform basic energy sums, known as trigger primitives, for each bunch crossing. The trigger data are converted to an optical signal and sent off-detector to the Trigger Concentrator Card. Upon receipt of a trigger accept, the full crystal data are read out. These data are also converted to an optical signal and sent to the Data Concentrator Card.

3. Pre-Calibration of the Calorimeter

The energy reconstructed in the calorimeter can be decomposed into the following factors [2]:

$$E = G \times F \times \sum_i A_i \times c_i \tag{1}$$

where G is a global scale factor, F accounts for energy losses from bremsstrahlung, A is the ADC count in a channel and c is the inter-calibration constant for that channel. The key to achieving the ECAL design performance is obtaining a precise channel to channel inter-calibration of 0.5%. This level of precision may only be achieved with *in-situ* physics events but a series of pre-calibration measurements were carried out to provide good calibration at start-up.

3.1. *Laboratory Measurements*

Before the crystals are assembled into supermodules various parameters are checked using an automated quality control system [4]. One of the parameters that is checked is the crystal light yield and is measured using a Co^{60} source and a photo-multiplier tube. From the light yield measurements, an initial estimate of the calibration constants can be made:

$$\frac{1}{c_i} \propto LY \cdot M \cdot \epsilon_q \cdot c_e \tag{2}$$

where LY is the crystal light yield, M the electronics gain, ϵ_q the quantum efficiency of the photo-multiplier and c_e the electronics calibration constant. The precision of the measured calibration coefficients was determined by comparing crystals that were also measured in the test beam. A precision of 4.5% was achieved.

3.2. *Cosmic Rays*

The cosmic ray method of pre-calibration was proposed to ensure that all supermodules could be pre-calibrated before insertion into CMS. A MIP traversing the full length of a crystal will deposit 250 MeV. For this test, the gain of the APDs is set 4 times higher than normal to ensure a good signal to noise ratio. This allows the use of a veto to reject events where a MIP crosses several crystals without the need for a dedicated trigger system. The inter-calibration coefficients are obtained by normalising the response of each crystal to the MIPs. All supermodules have been calibrated in this way and a precision on the calibration coefficients of around 1.5% was achieved [5]

3.3. *Test Beam*

During the summer of 2006, 9 supermodules (a quarter of the barrel detector) were calibrated to high precision in 120 GeV electron beams at CERN. The supermodules were equipped with the final CMS versions of the DAQ, data monitoring and detector monitoring systems. The short term reproducibility of the coefficients was approximately 0.2% [5] (see Fig. 1).

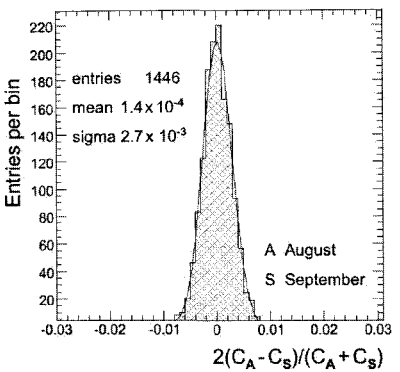

Fig. 1. The short term reproducibility of intercalibration coefficients as measured for a supermodule using electron beams.

4. Commissioning and Outlook

Installation of the barrel detector has been completed and the ECAL has participated in combined data-taking tests in unison with the hadron calorimeter and muon sub-detector systems (see Fig. 2). These test are invaluable for gaining experience in many aspects of detector operation and readout, such as trigger and timing generation and distribution.

When the LHC begins operation in 2008 one of the first and most urgent tasks for the ECAL group will be in-situ calibration of the detector. Three strategies have been identified to achieve this [2]. The first is a rapid method that uses the fact that mean energy deposition in the ECAL averaged over a large number of minimum bias events, is uniform in ϕ. Pairs of rings of crystals will be calibrated in this way, with an ECAL-wide calibration of 2-3% achieved within 10 hours, assuming a jet rate of 1kHz.

Achieving the target precision on intercalibration will require around

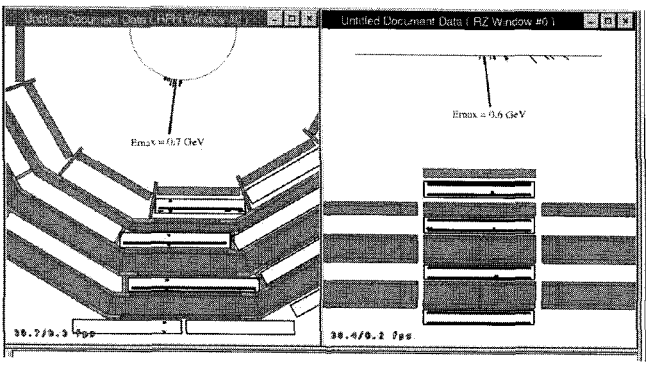

Fig. 2. One of the first cosmic ray muons seen in the ECAL detector during a commissioning run. The muon's track can also be seen in the muon detectors.

two months of data taking at an average luminosity of $2\times10^{33}\mathrm{cm}^{-2}\mathrm{s}^{1}$ and will rely on measurements of isolated electrons from $W \rightarrow e\nu$ decays. The third method, currently being investigated, uses the reconstructed mass of $\pi^0 \rightarrow \gamma\gamma$. Current simulation results suggest this will provide a much speedier approach to the desired precision.

5. Summary

The CMS electromagnetic calorimeter is a key detector of the CMS experiment and its installation into the experiment has been completed. All barrel supermodules have been calibrated using cosmic rays and a precision on the intercalibration coefficients of 1.5% was achieved. Nine supermodules (a quarter of the detector) have been calibrated using electron beams and an intercalibration precision of 0.2% was achieved.

The detector is now being commissioned in unison with larger fractions of the CMS experiment and the CMS collaboration look forward to taking the first data when the LHC becomes operational in 2008.

References

1. The CMS Collaboration, The Electromagnetic Calorimeter Technical Design Report, CERN/LHCC 97-033 (1997)
2. The CMS Collaboration, CMS Physics, Technical Design Report, Volume I: Detector Performance and Software (2006)
3. A. Annenkov *et al*, Nucl. Instrum. Methods Phys. Res. A490, 1-2 (2002) 30-50
4. E. Auffray *et al*, Nucl. Instrum. Methods Phys. Res. A456, 3 (2001) 325-41
5. F. Ferri, P. Govoni, CMS Conference Report CR-2007-012 (2007)

THE MAGNETIC DISTORTION MEASUREMENT SYSTEM OF THE LHCb RICH 2 DETECTOR

B. STORACI* on the behalf of the LHCb RICH Collaboration.

CERN
CH-1211 Geneve 23 Switzerland
Università degli Studi Milano Bicocca
Piazza della Scienza 3 I-20126 Milano (MI) Italy
**E-mail: Barbara.Storaci@cern.ch*

The Ring Imaging Cherenkov detector of the LHCb experiment will use Hybrid Photon Detectors (HPDs) to detect the Cherenkov photons. This paper reports on the characterization of image distortions in the HPDs due to the presence of a controlled and variable magnetic field. A video projector shines a well defined pattern onto an HPD which is subject to such a field. We present a detailed description of the experimental set-up and of the analysis algorithms developed to achieve a spatial resolution better than 1 mm^2.

1. Introduction

The LHCb experiments relies on two Ring Imaging Cherenkov (RICH) detectors[1] for the particle identification of the decay products of b-hadrons. The Cherenkov photons are detected by 484 Hybrid Photon Detectors[2] (HPDs) which cover a 3.3 m^2 surface area with a granularity of 2.5 $\times$ 2.5 mm^2. An HPD consists of a vacuum tube operating at a high–voltage of -20kV; Cherenkov photons converted to photoelectrons in an S20 photocathode are accelerated towards a pixelised silicon anode bump–bonded[3] to the encapsulated front-end electronics.[4] Two additional electrodes determine the shape of the accelerating electric field.

In the presence of a stray magnetic field from the LHCb dipole magnet, the photoelectron trajectories inside the HPD are deviated by the E $\times$ B Lorentz force, hence the photon image in the silicon detector is, to first approximation, distorted by the combination of a lateral displacement and a rotation around the tube axis. To reduce the amount of magnetic flux density inside the HPDs, four large soft–iron boxes enclose the matrices of photon detectors while a single cylindrical tube, made from high magnetic

permeability alloy, surrounds each individual HPD. This always results in a measured magnetic field at the photocathode less than 10 Gauss, with the absolute value dependent on the position of the HPD within the shielding box.[5]

In order to recover information on the actual photon impact point on the photocathode of the HPD, a correction factor for the magnetic distortion is required. The ultimate goal is to achieve an accuracy in the correction procedure such that the residual uncertainty due to magnetic distortions is negligible in comparison to the pixel size, i.e. $2.5 \times 2.5\,\mathrm{mm}^2$. The generality of the implemented algorithms in the pattern recognition procedure should allow the use of the same software both to identify the pattern before and after the magnetic distortion effect, and for internal alignment of the RICH subcomponents.

2. Experimental Set–up

The study of the HPD magnetic distortions relies on the projection of a well–defined pattern of light onto each HPD array. The generality of the pattern recognition procedure must be combined with a configurable light source. A LED "beamer" (Mitsubishi PK–10), working with the DLP technology and compatible with a magnetic field of 1 kGauss, is chosen to projects a hit pattern with well–defined fiducial marks onto the photon–detector arrays. In addition, to control the overall alignment, reference points will be beamed on three independent "pencil" photomultiplier tubes, Hamamatsu H3164–10.

A laboratory apparatus has been commissioned with the same beamer components used in the final RICH 2 system but with only a single HPD column of 16 tubes. A light-tight environment ensures that only the projected pattern impinges upon the HPDs. The projected pattern was an array of dots, projected as a square pattern of points on the HPD plane, separated by a distance of 12.5 mm, with each point having and RMS size of 5 mm.

All data presented in this paper were taken in the so-called "LHCb" mode of the HPD pixel chip. Vertical columns of pixels are segmented into eight finer pixels, making an effective pixel size at the photocathode of approximately 2.5 mm (horizontal) by 0.31 mm (vertical). In the LHCb mode, these pixels are OR-ed together in the chip. This is one feature that can break the symmetry in the resolution of the reconstructed beamer spot size in the two directions.

3. Preliminary Analysis and Simulation

A first goal of the analysis was to study the characteristic of ion–feedback events. These events result from photoelectrons which ionize residual gas molecules in the HPD tube vacuum, ions which then drift to the photocathode and result in multiple electron emission. These electrons then produce a characteristic large and delayed after–pulse. The study of ion–feedback was carried out by analysing the behaviour of two variables: the number of hits per event and the maximum cluster size per event[a]. These two variables are correlated, hence $\sim$ 87% of the ion–feedback contribution is removed simply with a cut on the number of hits and a fine selection is then performed on the maximum cluster size distribution to remove a further $\sim$ 6% of the contribution, see Fig. 1. It is clear that this set of cuts provides an

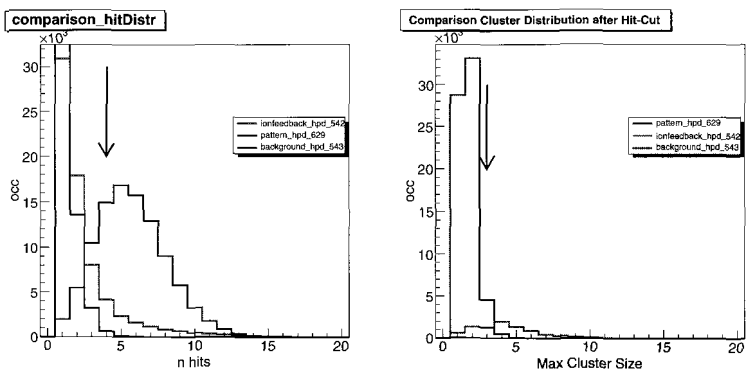

Fig. 1. Comparison of the ion–feedback and background behaviour with the signal from a beamer pattern. The arrows signify the selected (threshold) values. Left: A comparison for the number of hits per event. Right: The maximum cluster size distribution for only events with more than four hits per event.

effective background[b] reduction. A ratio of signal to noise better of than 30 is achieved with a pattern of 16 points, by accepting only events with more than four hits per event and with a maximum cluster size less than three. Moreover, the most important reduction of the background is achieved by triggering the HPD readout from the external photomultipliers.

[a] A cluster is defined as a set of contiguous hits and the size is defined as the number of hits that belong to that cluster.

[b] Possible sources of additional background can be dark counts and stray photons not related to the beamer operation.

A simulation was run to check the analysis performance in the worst possible conditions. The study was carried out by convolving the ion–feedback contribution with the pattern signal. In this simulation, ion–feedback events are added, event per event, to an HPD pattern signal. The ion–feedback effect increases the mean value and the uncertainty on the number of hits per event. We are able to reduce by one half the ion–feedback background by taking only the events with a maximum cluster size of two.

4. Data Analysis

A center of gravity procedure on each detected point was used to improve the spatial precision. To define a basic cluster, i.e. contiguous hits surrounded by empty cells, it is mandatory to remove all the hits that do not contribute to a pattern point. Unfortunately the level of background is a function of a number of HPD parameters such as the HPD quantum efficiency (Q.E.) or the HV value, therefore subtracting a uniform background proved not to be suitable. Therefore to solve this problem, a "maximum local search" algorithm was developed, then followed by an "advanced clusterization" algorithm. The maximum local search algorithm is based on a recursive function to find a maximum in a neighborhood of $r \times c$ cells[c]. The maximum is accepted only if it is greater than the local statistical median value (computed in a square of 3×3 cells) and the total statistical median, computed on the entire HPD to avoid that points belonging to a uniform background are taken as maximum.

After a complete scan of the accumulation image the advanced clusterization procedure is applied around each maximum. This is performed using a recursive function that searches for local maxima around the reference maximum. The search can be limited to a region around this maximum setting two variables which represent the two sizes of the rectangular window centered on the reference maximum[d].

Having found all the clusters, the final image is obtained using a center–of–gravity procedure on each cluster. An example of the analysis is shown in Fig. 2. The resolution of the reconstructed spot size is 0.93 (vertical) by 0.63 (horizontal) mm^2.

[c]For all the data presented, the values of r and c are respectively 5 and 5
[d]For all the data presented in this work the window size is again 5×5

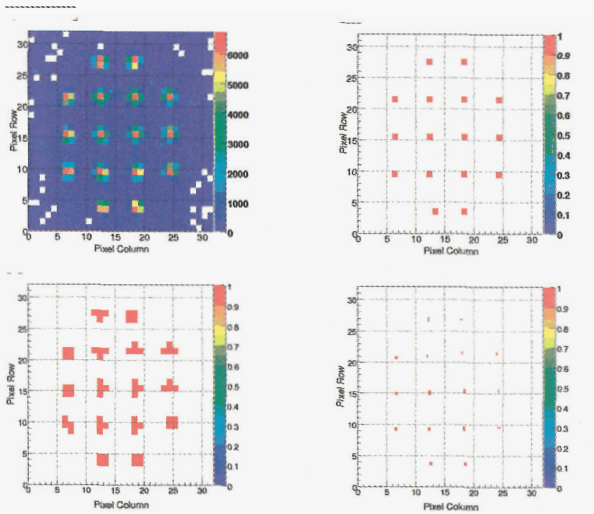

Fig. 2. An example of the pattern recognition analysis. Upper–left: Accumulation of raw beamer data. Upper–right: Maxima found with the maximum local search. Lower–left: Cluster made with the advanced clusterization. Lower–right: Center of gravity result.

5. Conclusions

The LHCb RICH magnetic distortion measurement system has been successfully set up and used to acquire data. The magnetic distortion analysis software has been optimized to compensate the displacement of the electron trajectories in the presence of a magnetic field and is able to reconstruct the pattern with an uncertainty of 0.93 mm vertically and 0.63 mm horizontally, even when ion–feedback is superimposed on the pattern signal. We verify that the ion–feedback process is characterized by large clusters, usually with a cluster size greater than three. Using this characteristic it is possible to reduce the contribution of ion–feedback in a sample of data simulated with both ion–feedback and pattern contributions. We have demostrated that if the background is properly tackled there is no resolution loss with respect to the ideal case.

References

1. L. Coll., *LHCb : Technical Proposal* (CERN, Geneva, 1998).
2. T. Gys, *Nucl. Instrum. Methods Phys. Res., A* **567**, 176 (2006).
3. M. Campbell, *IEEE Trans. Nucl. Sci.* **53**, 2296 (2006).
4. K. Wyllie et al, *Nucl. Instrum. Methods Phys. Res., A* **530**, 82 (2004).
5. M. Patel and M. Losasso, *Nucl. Instrum. Methods Phys. Res., A* **553**, 114 (2005).

ASPECTS OF THE SID DETECTOR DESIGN FOR THE INTERNATIONAL LINEAR COLLIDER

D. STROM* for the SiD Collaboration

*Department Physics, University of Oregon***,
Eugene, OR 97403-1274, USA
**E-mail: strom@physics.uoregon.edu*
***Author list: http://www-sid.slac.stanford.edu/*

The SiD (Silicon Detector) is one of four detector concepts being studied for the proposed International Linear Collider. The SiD is a compact, highly granular detector, that is designed to provide excellent jet energy resolution when used with particle flow algorithms. The high granularity is also advantageous for analysis of final states with tau leptons. In addition, its compact design allows for a large magnetic field that can mitigate the expected machine backgrounds allowing the first layer of the vertex detector to be close to interaction region. In this talk special emphasis will be given to two of the SiD subsystems, the electromagnetic calorimeter based on a silicon-tungsten calorimeter with integrated electronics and the Chronopixel option for the vertex detector. The electromagnetic calorimeter allows for very good separation of photons from charged particles. The Chronopixel vertex detector is designed to operate well in a high background environment.

Keywords: Linear Collider, Electromagnetic Calorimeter, Vertex Detector.

1. Introduction

The International Linear Collider is an electron-positron collider that will initially operate at a center-of-mass energy of 500 GeV with the possibility of an upgrade to 1000 GeV. The ILC will provide a complementary physics program to that expected at the LHC[1] that can build on the expected LHC discoveries.

In the last few years the ILC has made strides towards becoming a reality. The Global Design Effort has recently produced a Reference Design Report[2] and is working on producing a Engineering Design Report. If all goes well, construction of the ILC could begin as early as 2012. Recently the International Linear Collider Steering Committee (ILCSC) put out a call for Letters of Intent which will be used to select two groups to produce

Engineering Design Reports.

The SiD group will produce a Letter of Intent over the course of the next year. The SiD detector design is motivated by the desire to make the best use possible of the luminosity that will be provided at the ILC while maintaining a realistic cost budget. For physics involving hadronic final states, the emphasis is on jet energy resolution at the 3-4% level. For the analysis of τ leptons produced in reactions involving new physics such as SUSY, highly granular detectors are needed to perform tau polarization at high energies. Finally, excellent heavy flavor tagging is needed to separate b and c quark jets for the study of Higgs branching ratios.

The usefulness of a vertex detector at the ILC will be constrained by its inner radius because of the large number of soft e^+e^- pairs produced in the intense field of the colliding beams. To contain these pairs near to the interaction region a strong solenoidal field is needed. The target field for SiD is 5T; cost considerations then require a relatively compact detector. With a high-field, compact, detector, the energy and direction of hadronic jets can best be determined with highly granular calorimeters and a particle flow algorithm. In these algorithms the central tracker is used to measure the momentum of charge particles, the photons are measured in a granular electromagnetic calorimeter and neutral hadrons, defined in this context as neutrons, anit-neutrons and K^0_Ls, are measured in the hadron calorimeter. In this scheme, the direction of all charged hadrons is properly measured before being bent by the magnetic field. In addition the reconstruction of individual particles allows the use of sophisticated jet finders.

In this article we consider candidates for two of the subsystems of the SiD detector. After a brief overview of the SiD detector, the silicon-tungsten electromagnetic calorimeter that is designed to allow separation of energy depositions from closely spaced photons and charged hadrons is considered. Finally, we consider one of the options for the vertex detector.

2. Overview of the SiD Detector

Over the course of the next year a baseline configuration for SiD will be defined. For the SiD concept studies[3] the pixelated vertex detector and central tracker each have 5 layers for a total of 10 tracking layers. The tracker size is limited by the inner radius of the electromagnetic calorimeter of 1.25 m. The silicon-tungsten electromagnetic calorimeter has 30 layers with $(3.5\,\mathrm{mm})^2$ transverse segmentation. The hadron calorimeter consists of 34 layers of steel about 1.1 X_0 sampling for a total of 4 interaction lengths. Currently two options for sampling are considered, gaseous sampling (Resistive Plate

Chambers, RPCs, or Gaseous Electron Multipliers, GEMs) and scintillator readout with solid state devices such as silicon photo-mulltipliers. Transverse segmentation as small as 1 cm × 1 cm is used in the simulation. The hadron calorimeter is enclosed in a coil with a radius of 2.5 m. Outside of the coil there is a muon filter with 48 layers of 5 cm thick absorber.

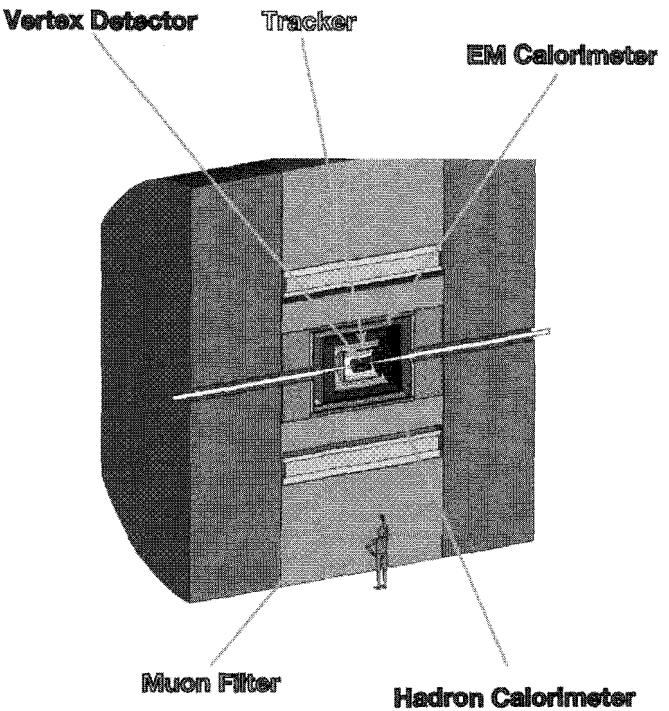

Fig. 1. The SiD detector.

3. The SiD Electromagnetic Calorimeter

The main criterion for selecting a technology for the electromagnetic calorimeter is its ability to separate energy depositions from charged and neutral particles. This is needed for both the particle flow measurements and for the reconstruction of tau lepton final states. In addition, the calorimeter should have sufficient longitudinal sampling to separate neutral hadrons from electromagnetic showers and it should be able to identify charged hadrons that begin showering in the electromagnetic calorimeter.

The ability to separate energy depositions from charged and neutral particles depends on the size of the electromagnetic showers, characterized by the Molière radius, (R_m), and the granularity of the detector. R_m depends on the type of material used, in the of case of this tungsten alloy, and the gap between layers. With a 1 mm gap and 2.5 mm thick 93% tungsten alloy, we estimate $R_m \simeq 14\,\text{mm}$.

Since there is considerable shower structure inside of the R_m,[4] it is useful to have transverse segmentation of $\frac{R_m}{4} \simeq 3.5\,\text{mm}$. This can be achieved by using silicon as the active medium in the calorimeter.

The energy resolution is given by the number of samplings and the thickness of the silicon. Cost considerations as well as the impact on R_m prevent us from considering tungsten thinner than 2.5 mm. We plan to use 2.5 mm plates at the front of the detector (perhaps 20 layers) and 5.0 mm plates deeper in the detector (perhaps 10 layers). This gives us an energy resolution of approximately $17\%/\sqrt{E}$ for 300 micron thick silicon detectors. Using thicker silicon would reduce the Landau fluctuations from electrons and positrons in electromagnetic showers, but requires higher bias voltages. Given the large amount of silicon in the calorimeter ($\sim 2000\,\text{m}^2$) we want to make the sensors as easy to produce as possible.

The main challenge in building such a detector is in the details of design. In SiD, the design is being developed by a Brookhaven, UC-Davis, Oregon, SLAC collaboration. To keep the gap between layers small we use integrated electronics as shown in Fig. 2. The individual pixels on the silicon sensor are connected via traces on a second layer of metal to the electronics readout chip called KPiX. The KPiX chip will be bump bonded to the pads on the wafer and will be connected to the outside world via a thin polyimide cable as shown in Fig. 3.

At the ILC beam will be delivered to the interaction point in bunch trains that are approximately 3000 bunches long. During the bunch train the charges and times measured in each hit pixel are buffered. Simulations show that except for angles below 120 mrad, only 4 buffers are needed for each channel.

An important feature to the KPiX chip is its large dynamic range. Using a clever range switching technique[5] it can record signals as large as 10 pC while maintaining a reasonable signal-to-noise ratio for minimum ionizing particles that typically deposit about 3.5 fC in the silicon. The KPiX chip includes a sophisticated calibration system and it is planned to keep any contribution from the constant term in the energy resolution of the electronics to below 1%. Another important feature of the KPiX is its power-pulsed

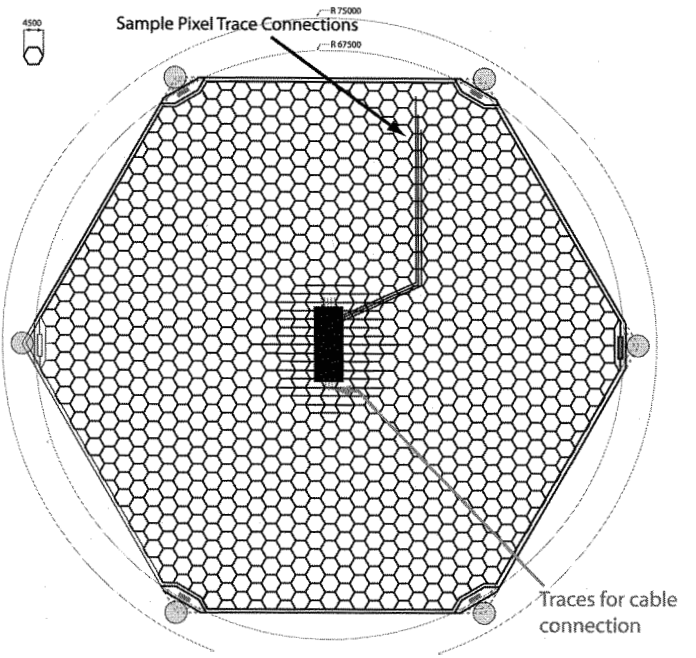

Fig. 2. Illustration of sensor layout and connections to KPiX readout chip.

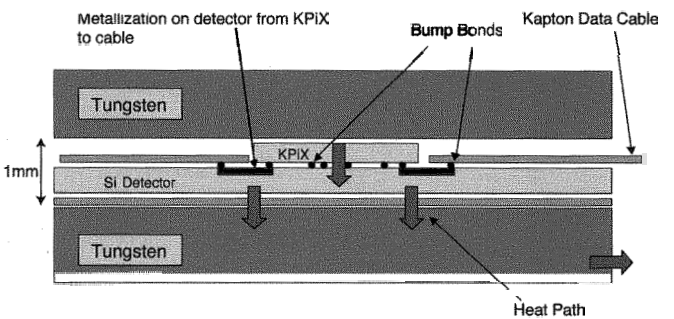

Fig. 3. Illustration of sensor layout and connections to KPiX readout chip.

mode that allows the current in the noise sensitive front end to be reduced between bunch crossing. The average power for a 1024 channel KPiX will be 20 mW. This is small enough for the heat produced by the chip to be removed through thermal conduction through the tungsten.

We have procured a first version of prototype sensors with 757 channels and hexagonal pixels with a long dimension of 5 mm. A production of a second round of sensors with 1024 channels and smaller pixels (long dimension 4.5mm, area = $(3.63\,\mathrm{mm})^2$) is underway. Measurements on the first prototypes of crucial sensor parameters such as stray capacitance and sensor depletion voltages are all as expected. The second prototypes will have reduced stray capacitive couplings to the second metal layer because half-sized pixels are used in central part of the sensor.

The KPiX prototype chips are currently being produced in 64 channel versions. It is possible that the KPiX chip can be used throughout the SiD detector. A number of features have been added to the chip to allow for these uses. For the tracker, nearest-neighbor triggering capability has been added, and there is an effort to reduce the noise to below 2000 electrons. For the hadron calorimeter the ability to run with either positive or negative input currents has been added. This allows for its use with either the RPC or GEM option for the HCAL and for use with RPCs in the return yoke of the magnet that serves as a muon filter.

Results from a recent test of the KPiX with a strip detector in the End Station A at SLAC are shown in Fig. 4.

Currently, bump bonding tests with prototype 64 channel KPiX chips and the first prototype detectors are underway. We expect to have a 1024 channel KPiX prototype within the next year and plan to build a 30 layer testbeam module.

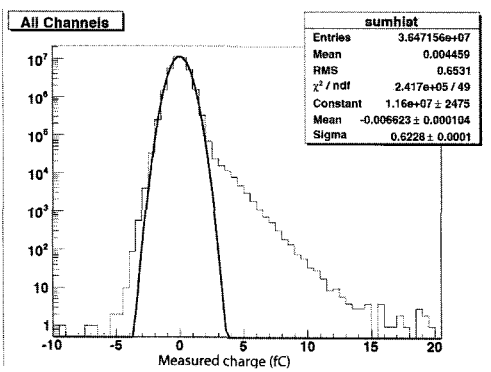

Fig. 4. Response of a strip detector readout with the KPiX chip in a test beam at SLAC's end-station A.

4. The Chronopixel Option

The importance of a good vertex detector is illustrated by the excellent physics program of the SLD experiment at SLAC when compared to the LEP program with relatively higher luminosity.[7] To precisely reconstruct secondary vertices from b and c hadrons, it is necessary to have a device that can operate close to the interaction region. The layout of one quadrant of the SiD vertex detector is shown in Fig. 5.

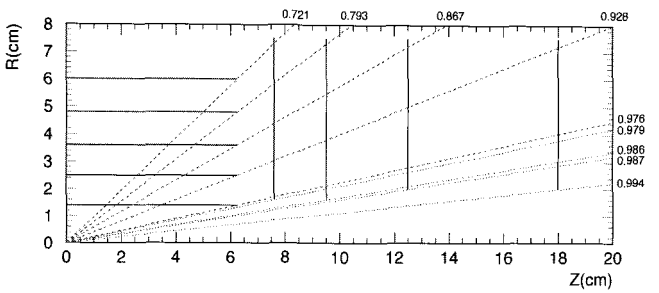

Fig. 5. The layout of one quadrant of the vertex detector in SiD. The dotted lines correspond to different values of $\cos\theta$

The nominal rate of background at the ILC is expected to be about 0.03 hit-cluster/mm^2/bunch in the innermost layer of device. This rate precludes designing a detector that integrates over all of the 3000 bunches in the train. The idea behind the Chronopixel detector that is being developed by a collaboration between Oregon, Yale and Sarnoff Corporation[6] is to be able to tag the bunch crossing associated with each hit. This would reduce the effective occupancy to about 10^{-5} for normal operation and allow operation of the detector in background conditions 10 times the nominal one.

To achieve tagging of each bunch crossing we use the same strategy as was employed in the KPiX chip: each pixel contains enough buffer memory to store as many hits as are expected during the bunch train. This means that the only activity during the bunch train is within a given pixel.

In the final device we plan to have pixels smaller than $20\,\mu$m $\times$ $20\,\mu$m with four 12 or 13 bit memories in each pixel. To reach this density it will be necessary to use a 45 or 60 nm CMOS process. Our initial prototypes will have $50\,\mu$m $\times$ $50\,\mu$m implemented in 180n nm CMOS with 2 memories of 13 or 14 bits. The extra bits allow for a parity check of the results. The circuit

for the initial prototype, with somewhat more than 500 transistors/pixel, has been designed and is ready for fabrication.

The functionality that is contained in each pixel is shown in Fig. 6. The 180 nm in-pixel circuit has been designed to be scalable to smaller feature size. For example, no capacitors in the signal path are used. One challenge for the designer is to mitigate the expected errors in the threshold voltage of the comparator. In the first prototype we have tried two pixel designs. One allows for up to 8 evenly spaced thresholds, the other for up to 32 thresholds. An automatic calibration can be performed simultaneously in all cells before the start of each bunch train. These schemes should allow the thresholds to be set with a precision of 0.2mV or better.

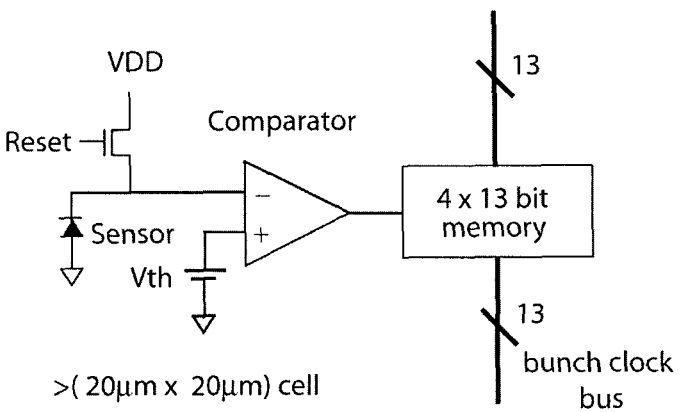

Fig. 6. Schematic diagram of the electronics contained in a single cell of the Chronopixel detector. The prototype version 180 nm CMOS has only two buffers and a $50\mu m \times 50\mu m$ footprint.

The sensitive part of the detector will be highly resistivity epitaxial layer. In order to collect charge from the entire area of the pixel, a process with a deep p-well will be needed as shown in Fig. 7. A relatively thick layer will be needed to reach occupancies from random noise of less than 10^{-5} as can be seen from Tab. 1. For the initial prototypes the TSMC process used will have a $7\,\mu m$ epitaxial layer and no deep p-well. As a result the pixels in the prototypes will be only sensitive over a small fraction of their area. This will allow a proof of principle test and should allow us to optimize the electronic circuit.

If the pixels were reset with a "hard reset" after each bunch crossing,

the noise introduced by the resets would be $\sqrt{kTC}$ where C is the total capacitance of the pixel and input transistor. In the prototype C is approximately 16fF. In this case the reset noise would be approximately 50 electrons. To reduce this noise two strategies are employed. The first is to use a so called soft reset.[8] The soft reset is especially well suited to cases like ours where the occupancy is very low. In these instances the reset noise can be reduced by a factor of 3 or more. In addition, a negative feedback circuit will be used to help "cool" the pixels during the reset operation.

In the ultimate device, with smaller feature size, the input capacitance is likely to be reduced and the sensitivity increased, giving us a better signal-to-noise ratio. If we can reach 25 electrons with the prototype pixels, better signal-to-noise should be possible in the ultimate device

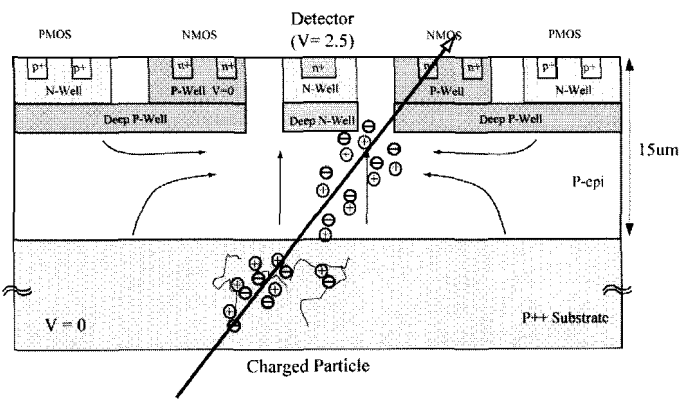

Fig. 7. Schematic diagram of the electronics contained in a single cell of the Chronopixel detector. The prototype version 180 nm CMOS has only two buffers and a 50μm $\times$ 50μm footprint.

Table 1. Expected signal and thresholds for different thicknesses of epitaxial layers.

Epilayer Thickness (microns)	Electrons at 99% Efficiency (electrons)	Threshold (electrons)	Acceptable Noise (noise)
4	40	20	4
7	125	63	13
10	250	125	25
15	400	200	40
20	550	275	55

5. Conclusion

The SiD detector represents a reasonable option for a general purpose detector to be built in conjunction with the ILC. Two promising options for detectors have been discussed. For the electromagnetic calorimeter, a silicon-tungsten device with integrated electronics is attractive. For the vertex detector, the Chronopixel project offers an option that is especially robust against machine backgrounds.

Acknowledgments

This work was supported by the US Department of Energy. I wish to thank my SiD colleagues for their help in preparing this report.

References

1. G. Weiglein *et al.* [LHC/LC Study Group], Phys. Rept. **426** (2006) 47 [arXiv:hep-ph/0410364].
2. Eds. James Brau, Yasuhiro Okada, Nicholas Walker, "Executive Summary; International Linear Collider Reference Design Report", August 2007.
3. SiD Detector Outline Document, http://www-sid.slac.stanford.edu/ .
4. G. Abbiendi *et al.* [OPAL Collaboration], Eur. Phys. J. C **14** (2000) 373 [arXiv:hep-ex/9910066].
5. D. Strom et al., IEEE Trans. Nucl. Sci. **52** (2005) 868.
6. Sarnoff Corporation, Princeton, NJ.
7. K. Abe *et al.*, Nucl. Instrum. Meth. A **400** (1997) 257.
   J. E. Brau [SLD Collaboration], Nucl. Instrum. Meth. A **418** (1998) 52.
   ALEPH,DELPHI,L3,OPAL and SLD Collaborations, Phys. Rept. **427** (2006) 257 [arXiv:hep-ex/0509008].
8. R. Turchetta, et al., NIMA 560 (2006) 139-142.

Resistive Plate Chamber performance during the CMS Magnet Test Cosmic Challenge

R. Trentadue*, RPC CMS Collaboration

Università degli Studi di Bari,
Bari, 70126, Italy
www.ba.infn.it

The CMS detector at the CERN Large Hadron Collider (LHC) is equipped with a redundant muon system based on Drift Tubes Chambers (barrel region) and Cathode Strip Chamber (endcap region), and Resistive Plate Chamber (RPC). During the summer and fall 2006 a first integrated test of an entire CMS slice was performed at the SX5 experimental surface hall. The RPC chambers were operated with cosmic rays. The results on the RPC performance are reported.

Keywords: Style file; LaTeX; Proceedings; World Scientific Publishing.

1. Introduction

During the summer and fall 2006 for the first time the CMS detector was closed and the magnet was ramped up to its nominal value for commissioning and field mapping purposes. In this occasion, a slice composed by portions of the muon and the calorimeter systems was operated under cosmic rays with the objectives to study the global CMS behavior by combining information from different sub-detectors. Also prototypes of the final readout, data acquisition and control system protocols were employed. The main purpose of the test for the muon system was to establish the trigger capability, study the chambers performance, optimize the synchronization and operation procedures. In this paper we only report results on the performances of the RPC barrel system.

2. Experimental set up and methods

In the barrel iron yoke, the RPC muon chambers form six coaxial sensitive cylinders (all around the beam axis) approximated with concentric dodecagon arrays and subdivided into 5 wheels. In the following the wheels will be denoted by the notation "W_i" where $1 = 1{,}5$ and the relative sector

number runs from 1 to 12. For the purpose of this test, 3 sectors, two belonging to wheel W_{+2} and one to wheel W_{+1}, were employed. In total 23 chambers (5 % of the full RPC system) were operated. The final CMS gas mixture was used, i.e. 95.5% $C_2H_2F_4$, 4% i-CH_{10}, 0,5% SF_6.

In view of detector commissioning and its maintenance during the LHC shut down periods, the development of a special RPC trigger for cosmic ray muons is particular important. For this purpose, an additional board, the RPC Balcony Collector (RBC) was designed and implemented in the system with a selectable majority level from 1/6 to 6/6. More details on the RBC trigger electronics can been found in [1].

During the test also a DT trigger, based on the track segment reconstruction in the DT muon chambers, was available. In this case an unbiased study of the RPC detector performance was possible since the event selection was independent on the RPC operation conditions.

Many million of events have been collected with different trigger conditions. However for most of the purpose of this paper, mainly event triggered by DT were used.

3. Study of the noise

The use of RPCs as trigger detector requires an extreme low intrinsic noise level to allow the proper functioning of the algorithm and to limit the number of fake triggers in the output data flow. It is therefore crucial to study the noise behavior of the detector in running conditions similar to the final ones to establish whether the CMS requirements have been fulfilled.

A fast evaluation of the noise level can be achieved preliminarily considering data from calibration streams taken at the beginning of each data taking run. All the results given in this section refer to a nominal operation high voltage of 9200 V and a threshold value of 220 mV, which according to previous test results, this value is the best one to maximize the efficiency and maintain a low noise figure. In the Fig. 1 the overall noise distribution for all the chambers under test is plotted for different values of the magnetic field. No dependence with the B field is evident, reassuring that the system behavior is not affected by external running conditions.

4. Efficiency studies

The DT track segments are three dimensional reconstructed objects obtained by analyzing the the hits in each of the three super-layers out of which the DT chamber are made of [2]. An unbiased study of the RPC

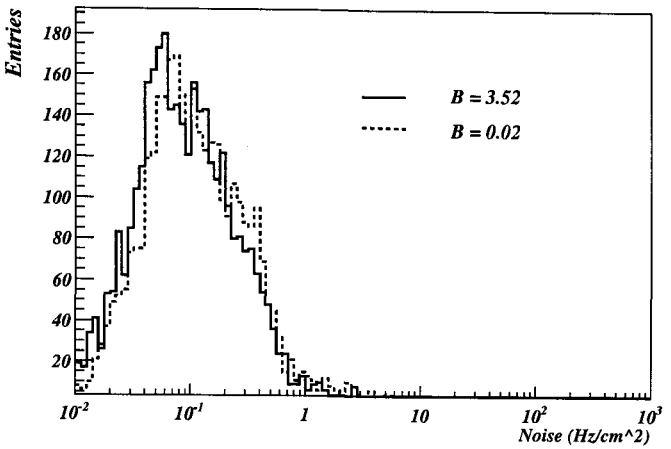

Fig. 1. Overall noise distributions for different magnetic field values.

system performance can be obtained by relying on those physics objects available in the date samples. The DT track segments are linearly propagated until the contiguous RPC chamber is reached and the impact point is computed. The corresponding RPC strip is then evaluated. The global efficiency for each chamber under test can be evaluated by making use of the results of the DT track segment extrapolation. A chamber is consider efficient if a fired strip is found in a region of $\pm$ two strips width with respect to the computed impact point.

A general view of the plateau efficiencies is given in the distribution of Fig. 2 where each bin correspond to half chamber. Also, superimposed the number of masked strip per chamber is shown (dashed line). It is evident the relevant effect of the masked strip on the global efficiency value for few chambers.

5. Cluster size study

The RPC trigger performance depend strongly on the cluster size, defined as the sample of adjacent fired strips per event inside the detector. The cluster size value should be less than 2 strips to avoid big uncertainty in determining of the muonic pattern and the associated transverse momentum. The cluster size is studied in relation to the track impact position. For this purpose the strip corresponding to the extrapolated DT segment

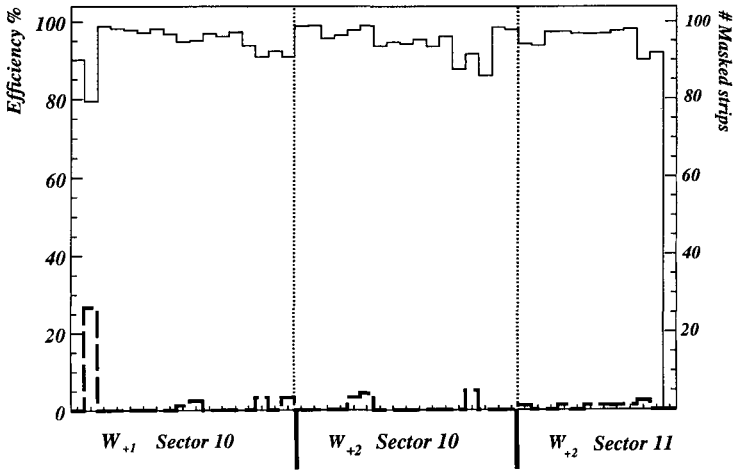

Fig. 2. Distribution of the plateau efficiencies for all the chambers in operation. Superimposed (dashed line) the number of masked strip per chamber.

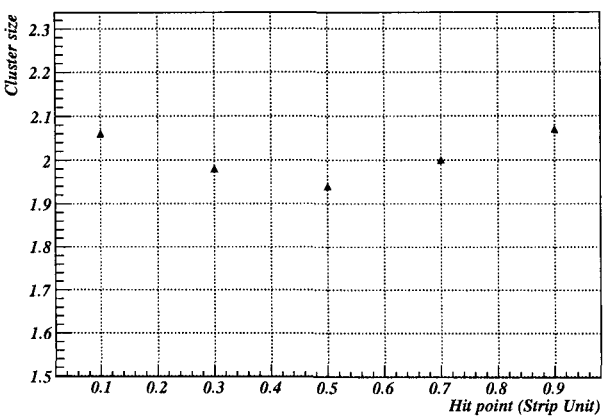

Fig. 3. Mean cluster size versus the impact point on the strip. The center of the slide is considered as reference

is divided into five slices. The average cluster size is then computed for all events where a particular slice is involved. The result is reported in fig. 3.

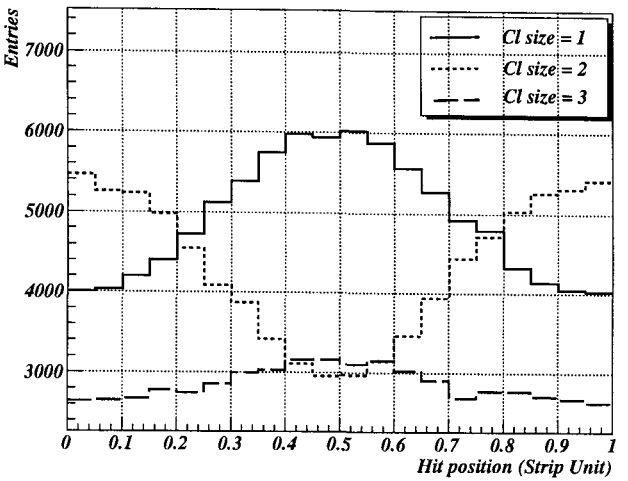

Fig. 4. Cluster size as function of the hit position on the strip fired.

Cluster size is minimum for track crossing the center of the strip, while it increases if the edges are interested. This is shown reported in fig. 4, where the expected impact point distributions for clusters of different sizes are given.

6. Conclusion

Three barrel sectors of the RPC CMS system have been successfully tested during the MTCC 2006. The study of detector performance has given results according to the expectancy. Noise, cluster size and efficiency have been studied. Cluster size studies have been useful to implement a more realistic model in the simulation software.

References

1. *An RPC-based Thecnical Trigger for the CMS esperiment Proceeding of the 12 Workshop on Electornics for LHC and Future Experiments, Valentia, Spanish, 25 Sept. 2006.*
2. *CMS Collaboration,* "CMS MUON Technical Design Report", *CERN/LHCC 97-32*

Implementation and performance of the tau trigger in the ATLAS experiment

M.Bosman[1], P.Casado[1], M.Dam[2], S.Demers[3], O.Igonkina[4], C.Osuna[1], E.Perez[1], R.Soluk[5], D.Strom[4], E.Torrence[4], A.Watson[6], S.Xella[2] *

[1] *Institut de Fisica d'Altes Energies (IFAE)*
Edifici Cn, Campus UAB, E-08193 (Spain)
E-mail: bosman@ifae.es

[2] *Niels Bohr Institute, University of Copenhagen*
Blegdamsvej 17, DK-2100, Copenhagen
E-mail: xella@nbi.dk

[3] *Stanford Linear Accelerator Center (SLAC)*
2575 Sand Hill Road, Menlo Park, CA 94025, USA
E-mail: demers@slac.stanford.edu

[4] *University of Oregon*
1226 University of Oregon, Eugene, OR 97403-1226, USA
E-mail: strom@physics.uoregon.edu

[5] *University of Alberta*
Edmonton, Alberta, Canada T6G 2G1
E-mail: soluk@phys.ualberta.ca

[6] *School of Physics and Astronomy, University of Birmingham*
Edgbaston, Birmingham B15 2TT, England, UK
E-mail: Alan.Watson@cern.ch

Triggering on hadronic taus at the LHC is a difficult task due to the high rate and occupancy of the events. On the other hand, the tau trigger increases the discovery potential of ATLAS in many physics channels, among others the Standard Model or SuperSymmetric Higgs (charged or neutrals) production. In order to cope with the rate and optimize the efficiency on important physics channels, the results of the current simulation studies indicate that the ATLAS tau trigger should be used either with relatively high transverse momentum thresholds alone, or with more relaxed threshold requirements in combination with other triggers, like the missing transverse energy trigger or a leptonic or

*Corresponding author, presenter at ICATPP

jet trigger.

In this contribution we describe the ATLAS tau trigger, and we present some of the current results from the simulation studies, focusing both on early physics and on physics at high luminosity.

Keywords: Atlas; Tau; Trigger.

1. The ATLAS tau trigger

In ATLAS, tau leptons are triggered either via the leptonic trigger (electron, muon), when they decay leptonically, or via the tau trigger, when they decay hadronically. In this section we will focus on the latter, describing the working principles and the performance as in the most up to date ATLAS simulation.

1.1. *The ATLAS Level 1 tau trigger*

The Level 1 trigger (LVL1) is a hardware trigger. This implementation satisfies the strong constraints in processing time due to the high input event rate $\sim$ 40 MHz and the required background rejection factor of 500. The decision time on an event at this level is of the order of μsec.

The way a tau is searched at LVL1 is depicted in Fig. 1 left. A 2x2 tower electromagnetic (EM) cluster and a 2x2 hadronic (HAD) cluster are used to identify a Region of Interest (RoI). In this core region, a 2x1 or 1x2 tower EM energy plus the 2x2 HAD energy are required to be above a transverse energy (E_T) threshold. The highest of the 4 possible combinations in the core of the RoI is taken as the energy of the tau candidate. The 12 towers in the outer EM part of the RoI are used to apply isolation criteria.

The hardware scheme for collecting and setting the scale of the tau jet energy at LVL1 inevitably biases and smears the tau transverse energy reconstructed with respect to the true tau visible transverse energy. This results in a rather slow turn-on of the efficiency for taus. This can be seen in Fig. 1 right, showing trigger efficiency for Level 1, and all other levels of the tau trigger, for one of the available tau trigger signatures, tau20i, optimized for taus with visible E_T above 20 GeV.

The handle for reducing the rate at LVL1 in the tau trigger is high energy threshold requirement for tau candidates . Additionally, missing E_T or another lepton or jet trigger can be required.

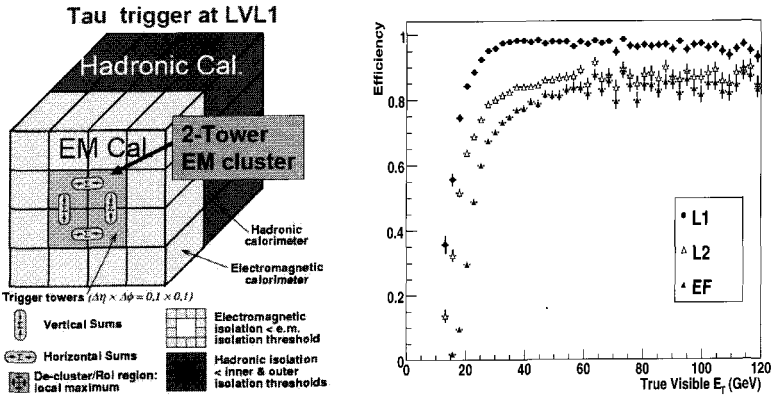

Fig. 1. Region of interest for the Level 1 Tau Trigger (left) and Trigger efficiency on W$\rightarrow \tau\nu$ events for the trigger signature tau20i (right). Efficiency is normalized to true taus with visible E_T above 20 GeV, matched to offline reconstructed tau candidates.

1.2. *High Level Tau Trigger*

The Level 2 Trigger (LVL2) and the Event Filter (EF) parts in the tau trigger are software triggers. More decision time (tens of milliseconds at LVL2, a fraction of a second at EF) and more algorithm flexibility are allowed. The fine granularity and the precision electronics from the calorimeter can be used. Additionally, tracks are reconstructed. Hence signal over background ratio can be enhanced, allowing a richer sample of interesting physics events with tau(s) in the final state to be saved on tape.

At the second level trigger, the tracking and calorimeter informations collected within a LVL1 RoI are used to created a refined tau candidate. The characteristics of a tau jet, such as low charged track multiplicity, narrowness, isolation, are imposed, to suppress further background QCD jets. Additionally, the energy of the tau candidate is estimated more accurately with respect to LVL1.

At the Event Filter (EF) level, offline reconstruction and calibration procedures for taus are used, on RoIs refined by LVL2. The tau identification used at EF is calorimeter based, analysing the shape of the shower, and matching tracks. An alternative algorithm, which builds a cluster around a reconstructed "leading" track is being developed in analogy to offline reconstruction, in order to better trigger on low E_T taus.

According to current studies, an additional background rejection factor of 20 to 50 with respect to LVL1 can be achieved at the HLT, while

keeping the overall trigger efficiency on signal with respect to good offline reconstructed taus above 60%, for a given E_T threshold. This is seen also in Fig. 1 right.

2. Tau trigger menus for physics

Some examples of possible tau triggers rates and efficiencies for low ($10^{31} cm^{-2} s^{-1}$) and high ($10^{33} cm^{-2} s^{-1}$) luminosity periods are shown in Tab. 1 and Tab. 2.

The main physics goal of the low luminosity period from the tau trigger point of view is to collect enough data to understand tau identification as soon as possible, and provide a solid backup for discovery searches at higher luminosities using tau leptons in the final state.

Therefore during the low luminosity period the tau trigger aims at collecting a large sample of W bosons decaying into tau and neutrino, and this can be achieved using a single tau trigger in combination with the request of large missing E_T (denoted as MET in tables). This avoids heavy prescaling of the trigger and depletion of the soft E_T tau samples from W. Rates will be of the order of 10 Hz at 10^{31}.

Additional triggers at low luminosity, providing low rate unprescaled triggers with low pT requirement, are the egamma/muon combined with tau triggers, requiring two objects in the event. They can be used to collect Z bosons decaying into two taus, in addition to single electron or muon triggers. The combination of 2 signatures allows to use lower thresholds. A combination of tau trigger and b jet trigger plus additional jet(s) trigger is under study, and seems to provide a good trigger for taus from top decays in $t\bar{t}$ production.

At higher luminosities single or double tau triggers aim at ensuring high discovery potential for new, heavy particles decaying into tau lepton(s), like SM Higgs or beyond SM charged or neutral Higgs. While the tau combined with missing E_T trigger has always been considered the trigger menu for tau final states at high luminosity, recent studies show that double tau triggers or a tau trigger combined with leptonic or jet trigger provide valuable additional triggers. At high luminosity also the more complex signatures like tau plus lepton plus jets or tau plus lepton plus MET will become very important as jets only or MET only might not give a sufficient rate.

A small subset of possible tau trigger menus for different luminosities is shown in Tab. 1 and Tab. 2. The efficiency of the single tau signatures on a tau offline reconstructed candidate matched to a true tau with visible E_T and η in acceptance is typically 60%.

Table 1. Example of tau menus for 10^{31} cm^{-2} s^{-1}

Selection	L1 (Hz)	EF (Hz)	Goal
tau20i + MET 30	500	6	W$\rightarrow \tau\nu$
tau60	80	11	high pt searches
tau20i + e10	1300	1	Z$\rightarrow \tau\tau$
tau20i + mu6	50	3	Z$\rightarrow \tau\tau$
tau20i+3j23	314	1	$t\bar{t}$

Table 2. Example of tau menus for 10^{33} cm^{-2} s^{-1}

Selection	L1 (Hz)	EF (Hz)	Goal
tau45i + MET 45	1.4K	15	H$^{\pm} \rightarrow \tau\nu$, H$\rightarrow \tau\tau$, new resonances
tau25i + e25i	10K	10	H$\rightarrow \tau\tau$, SUSY particles
tau25i + mu20	2K	10	H$\rightarrow \tau\tau$, SUSY particles

3. Conclusions

The ATLAS tau trigger is an important trigger for many discovery physics channels at the LHC. A lot of effort within the tau trigger group is devoted to the optimization of the tau trigger selection, and to the trigger menu definition for low and high luminosity periods of data taking, to ensure good unprescaled triggers for important physics channels.

Radiation Damage

Organizer: S. Baccaro

M.A. Caponero	Characterisation of FBG Sensors under Ionizing Radiation for High Energy Physics and Space Physics
A.Cemmi	Radiation effects on platinum nanostructured electrocatalysts for polymer electrolyte fuel cells
C. Consolandi	Determination of the Hall Coefficient for Neutron Irradiated Samples down to Cryogenic Temperatures and its Dependance on Resistivity at Room Temperature.
I. Di Sarcina	Thin-film Optical Materials under High Dose γ Irradiation
K.K. Gan	Study of the Radiation Hardness of VCSEL and PIN Arrays
C. Grah	Radiation Hard Sensors for the BeamCal of the ILC
X. Liang	Gamma-ray Irradiation Effects on Luminescent Glasses for White LED Applications
J.-P. Merlo	On line monitoring of radiation damage and recovery in quartz fibers using reflected light
F. Nessi-Tedaldi	Studies of Lead Tungstate Crystals exposed to Large Proton and Pion Fluences
A. Ranieri	Measurements of Noise and Static Parameters of CMOS Devices after 3 MeV Proton Irradiation up to 120 Mrad
A. Ruzin	Study of Lithium Diffusion into SiliconGermanium Crystals
A. Sopczak	Radiation Hardness Studies in a CCD with High-speed Column Parallel Readout

This page intentionally left blank

CHARACTERISATION OF FBG SENSORS UNDER IONIZING RADIATIONFOR HIGH ENERGY PHYSICS AND SPACE PHYSICS

MICHELE ARTURO CAPONERO
ENEA, FIM Research Center Frascati, via Frascati 45
Frascati 00044 RM, Italy

STEFANIA BACCARO
ENEA, FIM Research Center Casaccia, via Anguillarese 301,
00123 Rome,Italy

DOMENICO DONISI
Università degli Studi di Roma "La Sapienza", via Eudossiana 18
00184 Rome Italy

FABIO FABBRI
ENEA, FIM Research Center Frascati, via Frascati 45
00044 Frascati RM,Italy

MARIO PILLON
ENEA, FIM Research Center Frascati, via Frascati 45
00044 Frascati RM, Italy

Fiber optic sensors technology could find applications in various radiation environments. Different authors have shown the FBG behaviour in terms of λ_B-shift, Bragg peak intensity and spectral width at Full-Width Half-Maximum (FWHM) under high total dose radiation. In this paper we show the dose-rate dependencies irradiating fiber Bragg grating filters at two dose rates

1. Introduction

FBG sensors have found several applications for structural monitoring of civil and industrial engineering structures, used either to monitor strain straight stuck on the structure, or to monitor various physical parameters (acceleration, temperature, ...) applied on the structure by mean of specific mechanical interface. FBG sensors can be by now considered a proved alternative to

classical sensors, offering moreover unrivalled features such as the complete immunity to electromagnetic interferences, long term measurements stability, small mass, ease cabling. Such features, with particular respect to immunity to electromagnetic disturbances, make of great interest the use of FBG sensors in harsh radioactive environments, both for structural monitoring of critical mechanical components and for control of physical parameters of plant parts. Exposure of optical fibres to ionizing radiation results in optical transmission attenuation; such effect, though to be carefully considered, does not prevent use of FBG sensors in radioactive environment thanks to their pure spectroscopic principle of operation. The main problem to be faced in applying FBG sensors in radioactive environment is the effect of integrated dose to diffracted spectra [1], basically consisting in increase of FWHM, peak intensity lowering and peak wavelength shift. Some works [2], [3] about such effect on non-commercial custom sensors have already been reported. In this paper we investigate the effect of γ-radiation on standard commercially available FBG sensors, adopting two different dose rates to evaluate response dependence on such parameter.

2. Experiment

The experimental set-up is shown in Fig. 1. A commercial interrogation system was used to record the reflection spectra in situ during γ-irradiation with a controlled temperature. Two FBG sensors (S1 and S2) with nominal Bragg wavelength respectively of about 1534 and 1550 nm, reflectivity (R) of 88.6% and 92.3% and bandwidth of 0.15 and 0.25 nm are placed in front of the γ-source of the Calliope plant for 15 days. The gamma Calliope plant is a pool-type irradiation facility equipped with the 60Co γ-source in a high-volume (7x6x3.9 m3) shielded cell. Present source has a cylindrical geometry, with 60Co pencils in the rack circumference. The emitted radiation consists of two γ photons with energy 1.17 MeV and 1.32 MeV, mean energy being 1.25 MeV. The maximum licensed activity is 3.7•1015 Bq and the present activity is 1.05•1015 Bq. This plant has a possibility to select the dose rate for sample irradiation. Maximum dose rate (along the rack longitudinal axis) is 9400 Gy/h. There are three kinds of dosimetry available to determine the dose rate at the Calliope plant: the Fricke absolute dosimetry (20-400 Gy), the alanine dosimetry (about 500 kGy) and the Red Perspex dosimetry (5-40 kGy). Irradiation tests are performed in charge particle equilibrium and according to various demands of the user (possibility to perform temperature controlled tests) [4]. The relative distance (x2-x1) between the two sensors is of about 40 cm: the dose rate is of 1349 Gy/h for S1 sensor and 285 Gy/h for S2 sensor.

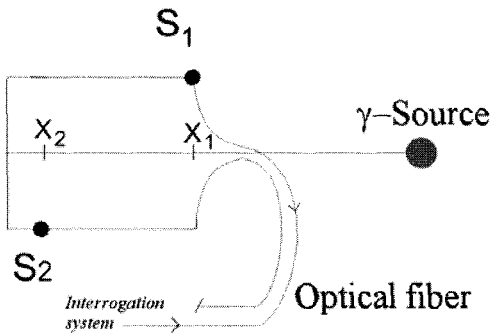

Figure 1. Schematical view of the experimental set-up

In Fig. 2 and 3 is plotted the intensity of the signal of sensor S1 and S2 under γ-radiation. In both cases it is evident the exponential decay of the intensity for a total dose radiation of 100 kGy.

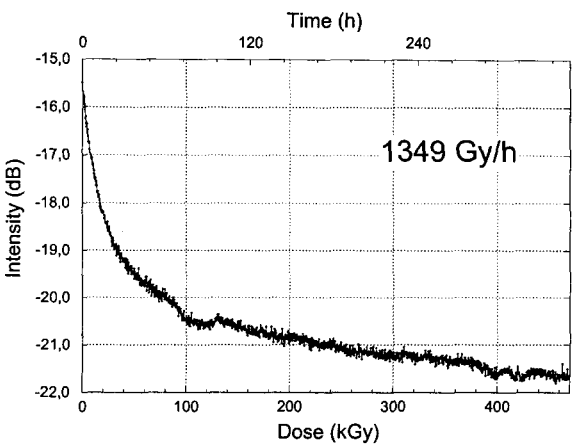

Figure 2. Intensity profile of the Bragg reflection peak for sensor S1

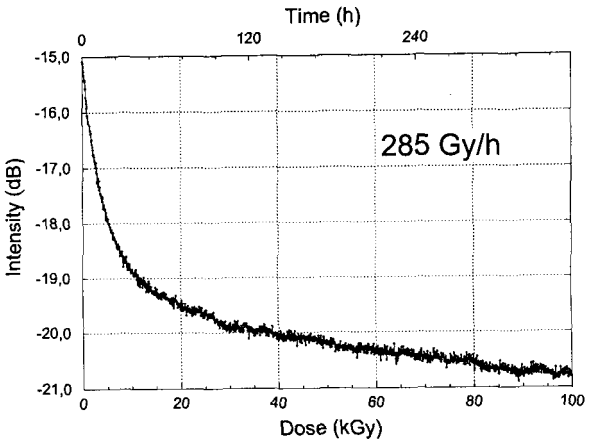

Figure 3. Intensity profile of the Bragg reflection peak for sensor S2

In Fig. 4 and 5 is plotted the shift of the Bragg peak of the signal of sensor S1 and S2 under γ-radiation: shift occurs toward higher wavelengths. The fluctuations correspond to the periodic thermal cycles from day to night.

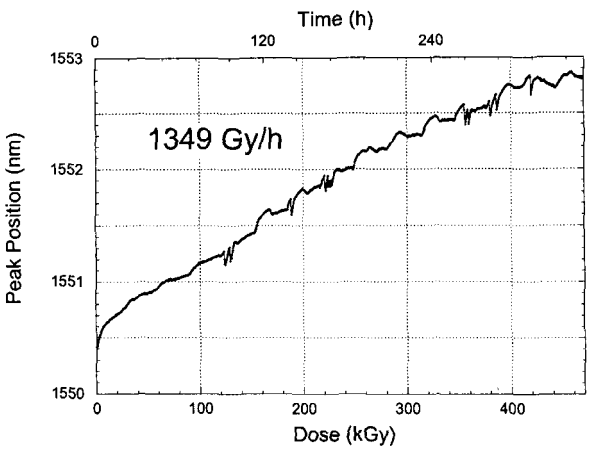

Figure 4. Wavelength shift of the Bragg reflection peak for sensor S1

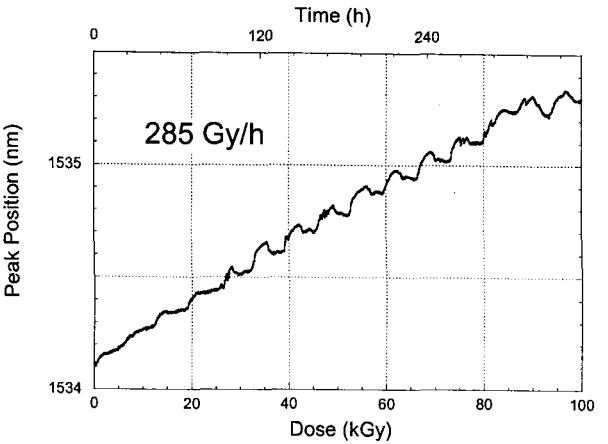

Figure 5. Wavelength shift of the Bragg reflection peak for sensor S1

In Fig. 6 are shown the overlapping normalized spectra for the sensor S2 for different values of absorbed dose to show how the γ-radiation does not affect the full-width at half-maximum of the reflection Bragg peak. It is quite evident how the irradiation does not act on the FBG spectrum shape but only induces an optical transmission degradation and a λ_B-shift. This last one can be interpreted as an increase of the average value of the refractive index modulation which translates into a Bragg peak wavelength increment. By observing the secondary lobes shape of the FBG spectra after irradiation it is possible to state that γ-radiation also does not affect the apodization profile of the sensor.

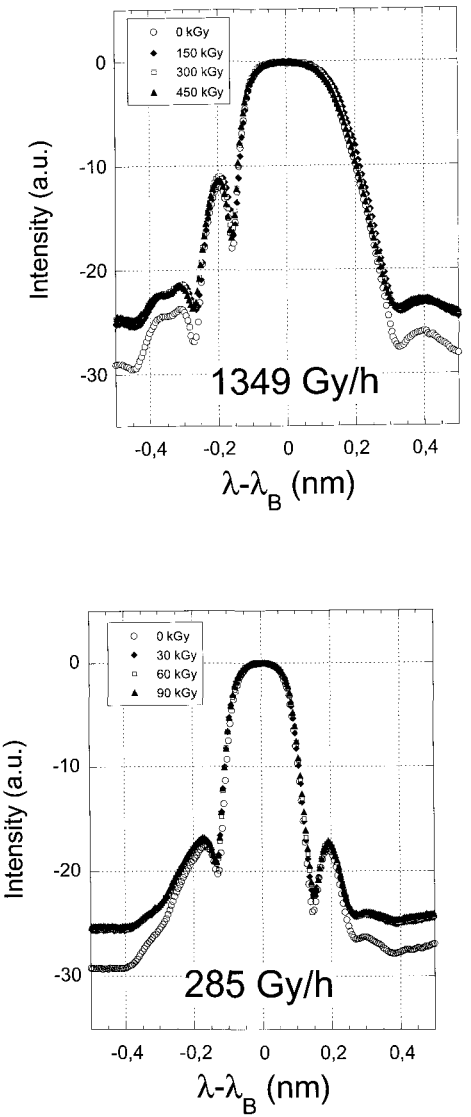

Figure 5. Overlapping normalized spectra for S1 (top) and S2 (bottom) sensors under γ-radiation.

3. Conclusions

FBG sensors technology brings promising alternatives to classical electronic instrumentation in nuclear environments. FBG filters are key devices in WDM

optical links. Our results show the radiation tolerance of FBGs under two different gamma dose rates. In particular we carried out the γ-radiation and dose rate influence on the most important FBG parameters reporting that the FWHM and the spectral shape is stable under gamma radiation and no dose rate dependency is observed. On the other hand, the Bragg peak position shifts toward higher wavelength with an observed total dose of about 100kGy. Currently a new measurement campaign is starting to observe the FBG spectral response under a higher total dose γ-radiation.

References

1. A. Gusarov, F. Berghmans, O. Deparis, A. Fernandez Fernandez, Y. Defosse, P. Mégret, M. Decréton, and M. Blondel, "High total dose radiation temperature effects on temperature sensing fibre Bragg gratings," IEEE Photonics Technology letters, no. 9, pp. 1159-1161, 1999.
2. A. Fernandez Fernandez, B. Brichard, F. Berghmans, and M. Decréton, "Dose-rate dependencies in gamma-irradiated in-fibre Bragg gratings," IEEE Trans. on Nuclear Science, vol. 49, pp. 2874-2878, December 2002.
3. A. Gusarov, A. Fernandez Fernandez, S. Vasiliev, O. Medvedekov, M. Blondel, and F. Berghmans, "Effect of gamma-neutron nuclear reactor radiation on the properties of Bragg gratings written in photosensitive ge-doped optical fibre," Nucl. Instr. Methods in Phys. Res. B, 2001.
4. S. Baccaro, A. Cecilia, A. Pasquali "Gamma Irradiation facility at ENEA-Casaccia Centre (Rome) Technical Report ENEA RT/2005/28/FIS (ISSN/0393-3016)", 2005.

RADIATION EFFECTS ON PLATINUM NANOSTRUCTURED ELECTROCATALYSTS FOR POLYMER ELECTROLYTE FUEL CELLS

A.CEMMI[a], C. PAOLETTI[a], A. POZIO[a], S. BACCARO[b]

[a]*ENEA Casaccia Research Center TER, Via Anguillarese 301, 00123 Rome*

[b]*ENEA Casaccia Research Center FIM, Via Anguillarese 301, 00123 Rome*

L.GIORGI[c], E. SERRA[c]

[c]*ENEA Casaccia Research Center FIM-MAT TEC, Via Anguillarese 301, 00123 Rome*

Polymer Electrolyte Fuel Cells (PEFCs) offer low weight and high power density and are being considered for automotive and stationary power production besides space and electronic applications. In this work, gamma radiation effects on carbon materials (carbon powder and multiwalled carbon nanotubes) used as substrates in PEFCs electrodes, were studied. The enhancing of free radicals formation (especially on carbon powder) was observed and studied by EPR spectroscopy. This evidence leads to a significant activation of carbon materials because paramagnetic sites represent the preferential position for platinum electrocatalyst nucleation. Galvanostatic techniques were applied to deposits platinum nanoparticles on carbon substrates while FEG-SEM characterization and cyclic voltammetry (CV) were carried out to study the morphology and the electrochemical performances of PEFCs electrodes.

1. Introduction

1.1. *PEFCs generalities*

Polymer Electrolyte Fuel Cells (PEFCs) are electrochemical devices that convert the chemical energy of a reaction directly into electrical energy. The basic physical structure or building block of a fuel cell consists of an electrolyte layer in contact with a porous anode and cathode on both side. In a typical fuel cell, gaseous fuels, i.e. hydrogen and oxygen (from air), are fed continuously to the anode (negative electrode) and to the catode (positive electrode) compartment, respectively.

Therefore, the electrochemical reactions take place at the electrodes to produce electric current. The electrolyte in the PEFCs is an ion-exchange membrane (fluorinated sulfonic acid polymer or other similar polymers) which is an excellent proton conductor. The desired function of the ion-exchange membrane is to provide an ion conductive gas barrier. The only liquid in this type of fuel

cell is water, thus corrosion problems are minimal. Water management in the membrane is critical to achieve efficient performances. In fact, to maintain the membrane well hydrated, the fuel cell must operate such that the by-product water does not evaporate faster than inside produced. Because of the limitations on the operating temperature imposed by the polymer and because of problems with water balance, maximum PEFCs working temperature is around 70-90°C.
However, PEFCs deliver high power density, offering low weight and extremely reduced volume. The immobilized solid electrolyte membrane simplifies sealing in the production process, reduces corrosion and provides for longer cell and stack life. PEFCs operating at low temperature allow to faster start-ups and immediate response to the power demand changes. The PEFC system is believed to be suitable for vehicular power applications as well as for smaller scale stationary power supplies and electronic devices.
In the field of space engineering, fuel cells have been applied to spacecrafts, like GEMINI, since the 1960s. Because fuel cell produces water as a by-product from electricity generation, it is very attractive for manned operations in a closed environment. Furthermore, because of fuel cells present high potentiality related to the very high energy densities of fuel gases, these systems are still advantageous for application to large spacecrafts in short-term missions [1–3].
For the above mentioned reasons, nowadays PEFCs are beginning to receive again considerable attention in aerospace applications: one example is the Stratospheric Platform Project [4–7]. In fact, a light weight and a long duration generating system is now required to maintain the altitude and position of an aircraft or airships in the stratosphere. Lately, a lot of missions, among which transfer vehicle in low-Earth orbit, are proposed providing PEFCs on- board [9, 10].

1.2. *Aim of the work*

The PEFCs gas diffusion electrodes are catalyzed by deposition of platinum nanoparticles on carbon substrates. Such particles must be localized on the electrode surface to achieve high electrocatalyst utilization. The traditional techniques for the electrocatalyst deposition (impregnation followed by chemical reduction of metal precursors) do not allow a surface localization and therefore it is necessary to deposit high quantity of platinum [11-12].
In order to reduce platinum quantity and improve electrocatalyst performances, platinum nanoparticles are usually deposited on high surface carbon substrates. Recent studies show that the use of an electric field to deposit the catalyst particles allows to have platinum nanoparticles localisation only in active reaction sites, accessible both to electrons and protons (carbon

substrate/electrocatalyst/ membrane triple interface), lowering highly platinum loading (< 0.1 mg cm^{-2}) [13-15].
In this work, we aim to enhance carbon substrate performances in platinum deposition by gamma-rays irradiation. In fact, radiation induces the free radicals formation: this paramagnetic sites are preferential position to the platinum nucleation.
The effect of dose and dose rate were also investigated by means of the electron paramagnetic spectroscopy (EPR).
Electrocatalysts were prepared by single pulse galvanostatic polarizations (GED), electrochemical activities were studied by cyclic voltammetries (CV) and morphological analysis were carried out by scanning electron microscopy (FEG-SEM).

2. Experimentals

2.1. *Materials*

Carbon Black Vulcan XC72R (CB Vulcan, 191 m^2g^{-1}) and SuperP (CB SuperP, 60 m^2g^{-1}), *in-house* Gas Diffusion Layer (GDL) and Multiwalled Carbon Nanotubes (CNTs, 50 m^2g^{-1} Aldrich) are used in this work as raw substrate materials.

2.2. *Irradiation*

Carbon substrates were irradiated at the Calliope ^{60}Co plant, placed in the Research Centre ENEA-Casaccia (Rome, Italy) at the increasing doses from 50 kGy to 1 MGy at dose rate of 500 Gy/h, 1270 Gy/h and 4530 Gy/h.
The radiation induced free radicals formation was investigated by EPR measurements performed at room temperature after at least 50 min from the stop of irradiation or followed in time in order to investigate the radical decay kinetic.
A Bruker EMS104 ESR analyzer (9.8 GHz) was used and the adopted parameter settings are the following ones: microwave power 10 mW, scan width 200 G, modulation amplitude 16 G, sweep time 10.5 s, filter time constant 20.5 ms, receiver gain 30 dB, field offset and receiver offset 0.
The EPR peak-to-peak intensity is proportional to the free radicals number present on investigated materials.
For each sample EPR spectrum was normalized to the mass and, in order to evaluate the free radical concentration effectively due to gamma radiation, the signal associated to radicals present in the un-irradiated filler was subtracted to each measurement.

2.3. *Electrode preparation and electrochemical characterization*

Platinum nanoparticles were electrodeposited on the CBs and CNTs substrates by galvanostatic polarization at constant current (GED), from 5 mM H_2PtCl_6 + 1 M H_2SO_4 aqueous solution.

In Fig.1a, a typical pulse profile is shown: t_p is the polarisation time and i_p is the applied current density. Charge electrodeposition (Q_{ED}) is calculated as the product between i_p and t_p.

The following parameters t_p= 300 s and i_p varying from 0.1 to 0.6 mA cm^{-2} are used to prepare the electrocatalysts.

In order to obtain CBs and CNTs electrodes, platinum was electrodeposited onto a rotating glassy carbon disc electrode (RDE), with a geometric surface of 0.125 cm^2. An homogeneous alcoholic suspension of CBs or CNTs and Nafion solution was sprayed over the cleaned glassy carbon surface and then dried.

The GED depositions were carried out in a standard three-electrode cell: an high purity (99.9999 %) platinum foil served as the counter electrode, an Ag/AgCl saturated electrode (SSC) used as the reference electrode and the RDE as the working electrode.

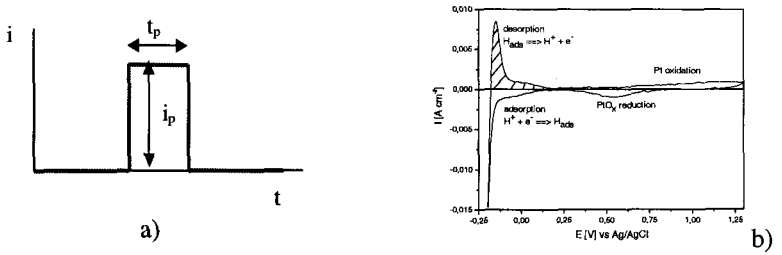

Figure 1 . a) GED profile b) Typical CV of platinum on carbon substrate in 1 M H_2SO_4 solution.

Cyclic voltammetries were recorded in 1 M H_2SO_4 with potential cycled between -0.2 and +1.3V vs. SSC (Fig.2). The electrochemical real surface was calculated from the density charge required for hydrogen desorption from platinum surface. Electrodeposition tests and electrochemical characterisations were done using a potentiostat-galvanostat PAR EG&G mod. 273A. All experiments were carried out at room temperature.

3. Results and discussion

In Fig.3 EPR spectra of CBs Vulcan and SuperP are reported. CBs morphology, porosity and surface area are key parameters for the EPR signal [16, 17]. In fact,

as you can see, the line shape is completely different: rather broad and asymmetric for the first, narrow and symmetric for the second.
The broad lines are due to radicals associated with polymer aromatic chains, while the narrow signals are due to the oxygen functional groups on carbon aggregates surface. Moreover, EPR spectra before and after irradiation present the same shape for both CBs.
These results, supported by SEM analysis, allow to assign an unhomogeneous and not ordered structure for CB Vulcan and a more finely dispersed aggregates distribution for CB SuperP.

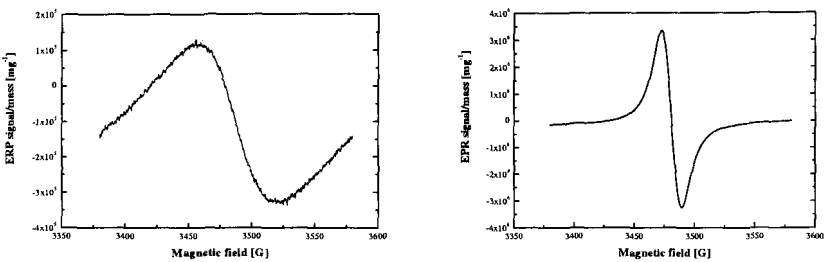

a) b)

Figure 3 . EPR spectra of CB a) Vulcan and b) SuperP.

In Fig.4 the EPR signals vs dose for the carbon substrates at 1200 Gy/h and at 4500 Gy/h are reported. Analyzing these trends, for each samples it is possible to single out the different conditions that produces a significant increase of the radicals species.

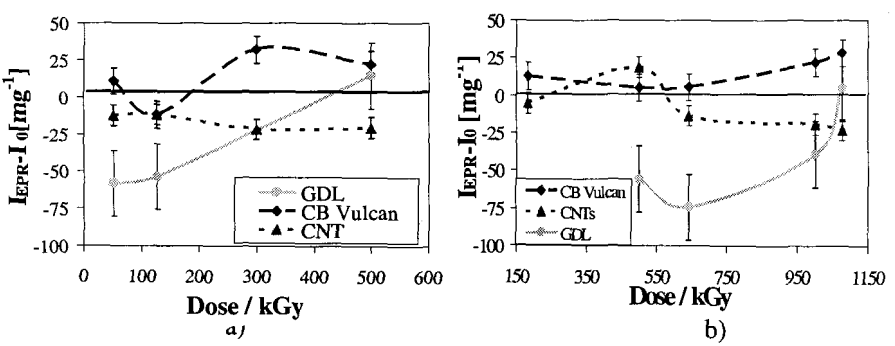

Figure 4 . EPR signal dependence on dose at a) 1200 Gy/h and b) 4500 Gy/h.

For CB Vulcan at 1200 dose rate, electrochemical results (Fig.5) confirm the evidences of EPR spectroscopy. In fact, the best electrochemical performances

are obtained for the 300 kGy irradiated sample, showing the highest EPR peak-to-peak intensity, while the 126 kGy irradiated sample presents the worst results.

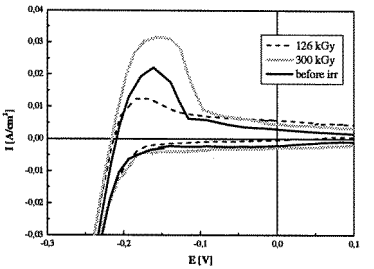

Figure 5 . Vulcan CV profiles depending on dose.

Morphological analysis (Fig.6) of irradiated carbon substrates show that platinum is more uniformly dispersed on the whole surface. Moreover, platinum particles present an homogeneous size distribution as well as a fine nanostructured surface. This evidence might be caused by the significant effect of radiation regarding induced free radicals formation on carbon materials above discussed.

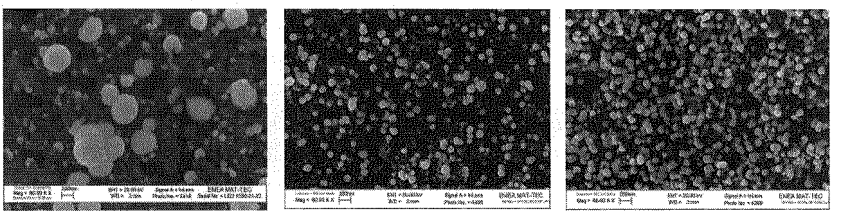

Figure 6 . CB Vulcan SEM images a) before irradiation b) at 126 kGy and c) at 300 kGy.

4. Conclusions

CB Vulcan, CB SuperP, CNTs and GDL are used as platinum electrocatalysts carbon substrates in PEFCs.

By means of gamma-rays irradiation it is possible to induce free radicals formation, enhancing carbon substrates performances related to the following platinum deposition.

The dose and dose rate conditions, leading to the best activation results for each carbon materials, were singled out.

As EPR spectroscopy results, a narrow and symmetric spectrum is presented by CB SuperP, indicating a finely dispersed aggregates distribution, while a broad and asymmetric spectrum by CB Vulcan, related to unhomogeneous and not ordered structure.

Free radicals formation improves platinum electrodeposition yield, increasing the electrochemical real surface.
On irradiated carbon substrates platinum deposits show homogeneous nanoparticles size and uniform distribution.

Acknowledgments

We are grateful to Mr. A.Pasquali for his appreciable support on samples irradiation and dosimetric measurements performed at *Calliope* plant (ENEA, Casaccia).

References

1. W.E. Simon and D.L. Nored, *Proceedings of The IEEE*, **75 (3),** 277 (1987).
2. M. Warshay and P.R. Prokopius, *J. Power Sources,* 29 (1990) 193.
3. W.E. Simon, *Space Shuttle Technical Conference*, NASA CP-2342, 1985, p. 702.
4. P.L. Loyselle, T.M. Maloney and H.M. Cathey Jr., *Proceedings of the 34th Intersociety Energy Conversion Engineering Conference*, Paper No. 1999-01-2588 (1999).
5. M.L. Davis, R.K. Allgeier Jr., T.G. Rogers and G. Rysavy, *The Development of Cryogenic Storage Systems for Space Flight*, NASA SP-247 (1970).
6. O.A. Velev, *Proceedings of the 35th Intersociety Energy Conversion Engineering Conference*, Paper No. AIAA-2000-2873 (2000).
7. H. Naito, K. Eguchi, T. Hoshino and S. Okaya, *American Institute of Aeronautics and Astronautics*, Paper No. 99-3913 (1999).
8. J.P. Fellner, Z.A. Johnson and D.F. Pickett, *Proceedings of the 35th Intersociety Energy Conversion Engineering Conference*, AIAA 2000-2871 (2000).
9 H. E. Van Dam and H. Van Bekkum, *J. Catal.* **131**, 335 (1991).
10 M. Watanabe, M. Uchida and S . Motoo, *J. Electroanal.Chem,* **229**, 395 (1987).
11 N. Giordano, E. Passalacqua, L. Pino, A. S . Arico', V. Antonucci, M. Vivaldi and K.Kinoshita, *Electrochimica Acta* **36**, (1991) 1979.
12 H. G. Petrow and R. J . Allen, U.S. Patent no. 4,044,193 (1977).
13 J.H. Ye and P.S. Fedkiw, *Electrochim. Acta* **41**, 221 (1996).
14 Kinoshita K., *J. Electrochem. Soc.* **137**, 845 (1990).
15 S. Liu, Z. Tang, E. Wang and S. Dong, *Electrochem. Comm.* **2**, 800 (2000).
16 M. Debowska, J. Rudzinska-Girulska,, A. Jezierski, A. Pasternak and R. Pozniak, *Radiation Physics and Chemistry* **58**, 575 (2000).
17 F.Boulic et al., *J. Phys. D: Appl. Phys.* **31**, 1904 (1998).

DETERMINATION OF HALL COEFFICIENT FOR NEUTRON IRRADIATED SAMPLES DOWN TO CRYOGENIC TEMPERATURES AND ITS DEPENDANCE ON RESISTIVITY AT ROOM TEMPERATURE.

C. CONSOLANDI[1,2], S. PENSOTTI[1,2], P. G. RANCOITA[1], M. TACCONI[1]

[1] *INFN-Istituto Nazionale di Fisica Nucleare sezione di Milano-Bicocca*
20126 Milan, Piazza Della Scienza 3, Italy
[2] *University of Milano-Bicocca*
Milan, Piazza della Scienza 3, Italy

Hall coefficients, Hall mobilities and resistivities of n-type samples with resistivities of $\approx$ 56 and 2500 Ω cm were measured before and after irradiation with fast neutrons, as a function of temperature from 300 down to 11 K. In addition, measurements of samples with resistivity of $\approx 157\,\Omega$ cm were carried out before and after irradiation at room temperature. The fast neutron fluences ranged from 6.1×10^{11} n/cm^2 up to 1.0×10^{15} n/cm^2. The Hall mobility sign was observed to change (from negative to positive) only for the highest resistivity samples at neutron fluences above 1.1×10^{14} n/cm^2.

1. Introduction

In recent years and nowadays, intensive investigations have been and are carried out, regarding the radiation-induced damages on the electrical characteristics of silicon devices after irradiations with charged and neutral particles (for a review, e.g., see [1]). Hall effect and resistivity measurements have confirmed the decrease of the majority carriers concentration and the increase of resistivity (ρ) with increasing particle fluences, similarly to what was observed in investigations of radiation-induced damages inflicted to silicon detectors employing high-resistivity n-type substrates. For n-type silicon samples with high-resistivities, the sign of the Hall coefficient R_H changes from negative to positive at large neutron and Kr-ion fluences at room temperature; while, for low-resistivities no change of sign is observed (see Sect. 4.5 of [1] and references therein). The Hall coefficient after irradiation has mostly been determined at room temperature. In the present investigation, the Hall coefficients, Hall mobilities and resistivities of n-type

silicon bulk samples with resistivities of ≈ 56 and $2500\,\Omega\,\mathrm{cm}$ have been determined before and after irradiations with fast neutrons and, in addition, as a function of temperature from 300 to 11 K; while for samples with resistivity of $\approx 157\,\Omega\,\mathrm{cm}$, at room temperature only.

2. Samples characteristics and experimental measurements

The n-type samples have an area of $1.0 \times 1.0\,\mathrm{cm}^2$, thickness of $400\,\mu\mathrm{m}$ and resistivities of ≈ 56, 157 and $2500\,\Omega\,\mathrm{cm}$. These samples contain an oxygen concentration of $6.4 \times 10^{17}\,\mathrm{cm}^{-3}$, $4.7 \times 10^{17}\,\mathrm{cm}^{-3}$ and $0.7 \times 10^{17}\,\mathrm{cm}^{-3}$ respectively.

The samples were irradiated with fast neutrons at the $\Sigma\Sigma$-facility of Bucarest [2]. The mean neutron kinetic-energy was $\approx 0.827\,\mathrm{MeV}$; within the energy range 10 KeV–18 MeV, the flux was $3.385 \times 10^9\,\mathrm{n\,cm^{-2}\,s^{-1}}$. The obtained fluences ranged from $6.1 \times 10^{11}\,\mathrm{n/cm^2}$ up to $1.0 \times 10^{15}\,\mathrm{n/cm^2}$.

All samples were measured using the four-point probe technique. They were mounted on a base that guaranties thermal-conduction and electrical-insulation. The contacts were made at the four corners of the sample by means of ultrasonic thermo-compression bonding of aluminium-silicon[a] wire with a diameter of $100\,\mu\mathrm{m}$.

The resistivity is determined using the Van der Pauw method [3]:

$$\rho = \frac{\pi t}{\ln 2}\frac{V}{I} f, \tag{1}$$

where V is the mean potential difference, I is the current value, t is the sample thickness and f is a geometrical factor. The Hall coefficient is determined by measuring the potential difference between the contacts at the two diagonals of the sample, located inside a magnetic field ($\approx 3\,\mathrm{kG}$) perpendicular to its surface. The numerical value of the Hall coefficient is given by:

$$R_H = \frac{Vt}{IB}, \tag{2}$$

where V is the mean potential difference of the two diagonals and B is the value of the magnetic field. The Hall mobility μ_H is defined as the ratio of the absolute value of the Hall coefficient and the resistivity:

$$\mu_H = \frac{|R_H|}{\rho}. \tag{3}$$

[a] Al 99%, Si 1%.

For an extrinsic compensated n-type non-irradiated sample [4], the resistivity is given by:

$$\rho = \frac{1}{e\mu_e n} \tag{4}$$

and, in the limit of low magnetic field, the Hall coefficient is given by:

$$R_H = -\frac{r_H}{en}, \tag{5}$$

where e is the electric charge, n is the concentration of majority carriers, μ_e is the electron mobility and r_H is the Hall scattering factor that depends on the dopant concentration and on temperature [5–7]. The Hall mobility is then $\mu_H = r_H\mu_e$, so that, within a 20% due to the variation of r_H, the electron mobility is equal to the Hall mobility.

The measurements were performed using a constant current source (DC mode) with the power supplied by a generator current (Keithley 220). An electrometer was used to control the current flowing in the sample (Keithley 617). The potential difference was measured by means of a digital multimeter with high input impedance ($> 10\,\mathrm{G\Omega}$) (Keithley 196). These instruments are connected with the sample by an Hall Effect Card (Keithley 7065) that controls all the contacts of the circuit. The magnetic field is supplied by an electromagnet (Oxford instrument) capable of generating 3 kG, with the possibility to invert the sing of the magnetic field. All samples were measured inside a cryostat (ADP) able to reach a minimum temperature of 11 K. The temperature is kept constant by a temperature indicator-controller (Scientific Instruments Model 5500). All instruments are connected to a computer for the data acquisition.

3. Experimental Results and Discussion

3.1. *Temperature Scan of non-irradiated Samples*

A temperature scan of ρ, R_H and μ_H was performed from 300 down to 11 K for non-irradiated samples with resistivities of $\approx$ 56 and 2500 Ω cm. Before irradiation, they are expected to follow an extrinsic region behavior [8] in the temperature range from $\approx$ 300 K down to $\approx$ 100 K (low resistivity). As expected, we found that the Hall coefficient is almost constant in this region [see non-irradiated data in Figs. 1 (I) and (II)]. For the lowest (highest) resistivity, at temperatures lower than $\approx$ 70 (60) K, the freeze-out of carriers starts and $|R_H|$ increases. In the temperature interval from 300 to 100 K, we can estimate that the concentration of majority carriers is:

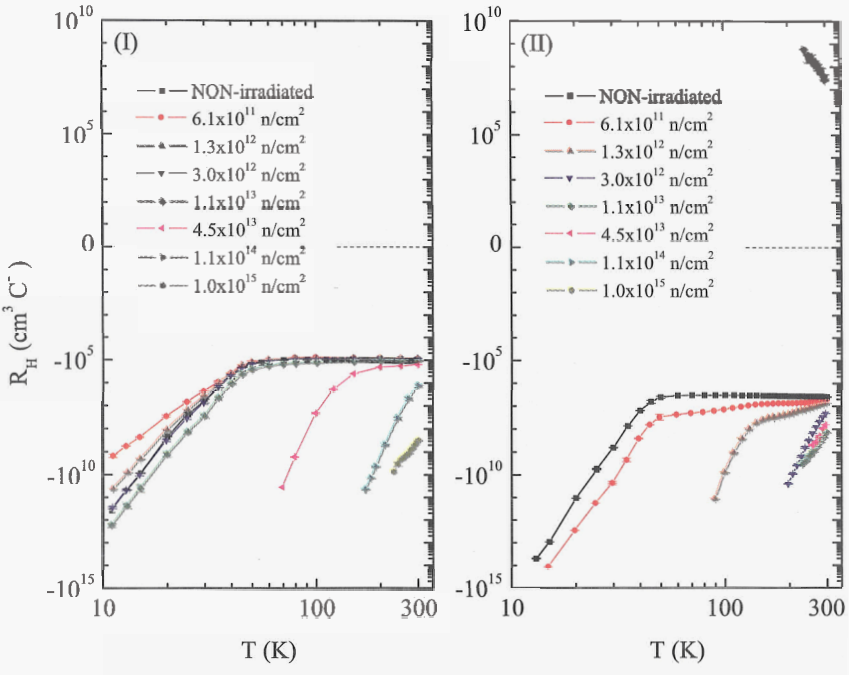

Fig. 1. **Temperature dependence of Hall coefficient for non-**irradiated and irradiated samples with resistivities of $\approx 56\,\Omega\,\mathrm{cm}$ (I) and $2500\,\Omega\,\mathrm{cm}$ (II).

$$n = (5.5\text{–}7.0) \times 10^{13}\,\mathrm{cm}^{-3} \quad \text{and} \quad n = (1.5\text{–}1.8) \times 10^{12}\,\mathrm{cm}^{-3}$$

for samples with resistivities of ≈ 56 and $2500\,\Omega\,\mathrm{cm}$, respectively.

In the same interval [see Eq. (4) and resistivity measurements in Figs. 2 (I) and (II)], the electron mobility follows the expected power-low dependence on temperature:

$$\mu_e \propto T^{-m}, \tag{6}$$

where the exponent m is ≈ 2 in agreement with literature [7].

Finally, the Hall mobilities [Figs. 2 (III) and (IV)] of non-irradiated samples decrease with increasing temperature.

3.2. *Temperature scan of irradiated Samples*

A temperature scan from 300 down to 11 K was also carried out for irradiated samples [Fig. 1, and 2]. From 300 down to 70–60 K (depending on the resistivity), the region in which $|R_H|$ is almost constant gradually reduces with increasing neutron fluence. This region is absent at the two

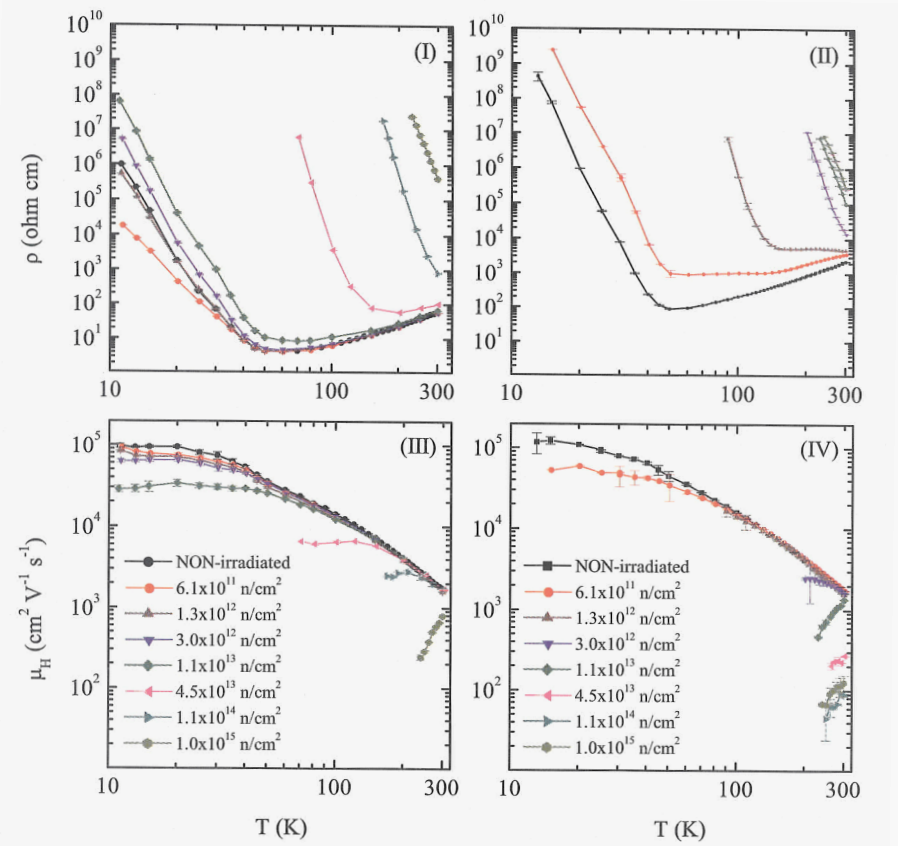

Fig. 2. **Temperature dependence of resistivity (I) and (II),** Hall mobility (III) and (IV) for non-**irradiated and irradiated samples with resistivities of ≈** 56 and 2500 Ω cm, respectively.

(five) largest fluences for samples with resistivity of ≈ 56 (2500) Ω cm. In addition, above 1.1×10^{14} n/cm^2 the sign of the Hall coefficients becomes positive for samples with resistivity of ≈ 2500 Ω cm before irradiation.

Furthermore in the same temperature interval, for the samples with the lowest resistivity, $|R_H|$ and ρ values of the first three fluences do not exhibit a significant variation with regard to the values before irradiation; but for temperatures lower than ≈ 50 K, we found that, for the first and the second fluences, $|R_H|$ and ρ values are lower than the corresponding non-irradiated ones. Finally, for the fast neutron fluence of 3×10^{12} n/cm^2 the values of $|R_H|$ and ρ are greater than those of the non-irradiated samples. It has to be remarked that for the samples with resistivity of ≈ 2500 Ω cm, ρ's exhibit

almost the similar dependence on temperature for the last three neutron fluences [Fig. 2 (IV)].

In addition, we have observed that, for all temperatures, the Hall mobilities of the non-irradiated samples are larger than the irradiated ones: for these latter samples, μ_H's gradually decrease with increasing fluence and temperature, except at the (four) largest fluence(s) where they increase with increasing temperature.

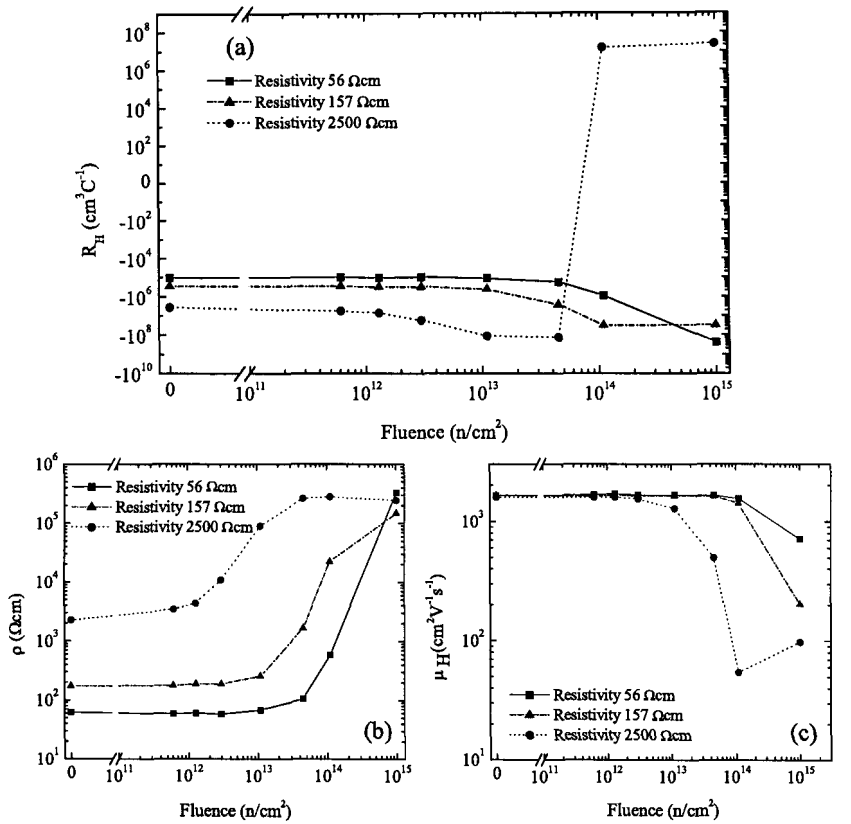

Fig. 3. Values of Hall coefficients (a), resistivity (b) and Hall mobility (c) for non-irradiated and irradiated samples with resistivities of $\approx$ 56, 157 and 2500 Ω cm, at room temperature.

At room temperature, the Hall coefficients, resistivities and Hall mobilities of samples with resistivity of $\approx$ 157 Ω cm were also determined before and after irradiations with fast neutrons: they are shown in Fig. 3 together

with those with resistivities of $\approx$ 56 and 2500 Ω cm. $|R_H|$ was found to increase with increasing fluence for all samples. As previously discussed, for the highest resistivity samples we observe a change of sign at the fluence of 1.1×10^{14} n/cm^2, in agreement with what observed by other authors (e.g., see [1,9,10]); while no change of the Hall coefficient sign was observed for the samples with resistivities of $\approx$ 56 and 157 Ω cm, in agreement with previous investigations (e.g., see [1,11]). Furthermore, ρ increases with increasing fluence for all types of samples. However, the values of the most irradiated ones achieve the same order of magnitude. Finally, μ_H decreases for all samples with increasing fluence.

4. Conclusions

With the present investigation, we have determined the behavior of Hall coefficients, resistivities and Hall mobilities of n-type silicon bulk samples with resistivities of $\approx$ 56 and 2500 Ω cm (before irradiation) from room temperature down to 11 K and after irradiations with fast-neutron fluences up to 1.0×10^{15} n/cm^2. No change of the Hall coefficient sign was observed for samples with resistivity of $\approx$ 56 Ω cm, but the sign was reversed for samples with resistivity of $\approx$ 2500 Ω cm at fluences above 1.1×10^{14} n/cm^2.

Furthermore, at room temperature, no change of the Hall coefficient sign was also observed for samples with resistivity $\approx$ 157 Ω cm in agreement with previous investigations (e.g., see [1,11]).

References

1. C. Leroy and P.G. Rancoita, Rep. Prog. Phys. 70 (2007) 493.
2. T.Angelescu et al.,Nucl. Instr. And Meth. A 345 (1994) 303-307
3. P.Blood and W. Orton. *The Electrical Characterization of Semiconductors: Majority Carriers and Electron States.* Accademic Press 1992
4. C. Hamaguchi. *Basic Semiconductor Physics.* Spinger-Verlang Berlin Heidelberg 2001.
5. I. G. Kirnas et al., Physica Status Solidi A, 23, 2, 1974, K123-K127.
6. N. N. Dmitrenko et al., Physica Status Solidi A 26, 1, 1974, K45-K48 (182K)
7. S. Adachi *Handbook on physical Propertes of Semoconductors* Kluwer Academic Publishers 2004.
8. S. M. Sze and Kwonk K. NG *Physics of semiconductors devices, 3rd Edition* Wiley-Interscinece 2007.
9. N. Croitoru et al., Nucl. Instr. And Meth. B 124 (1997) 542.
10. U. Biggeri et al., Nucl. Instr. And Meth. A 400 (1997) 113.
11. P.F. Lugakov, T.A. Lukashevich and V.V. Shusha, Phys. Status Solidi A 74, (1982) 445.

THIN-FILM OPTICAL MATERIALS UNDER HIGH DOSE γ IRRADIATION

ILARIA DI SARCINA, GIUSEPPE FERRARA,
ANGELA PIEGARI

ENEA, FIM - Advanced Physics Technology and New Materials, Via Anguillarese 301, Rome, Italy

Optical instruments are widely used in satellites for planetary and interplanetary missions where they are exposed to very high radiation levels. In this work a set of thin-film optical coatings, fabricated by Physical Vapor Deposition, have been exposed to high γ radiation dose in the *CALLIOPE* ^{60}Co radioisotope source at ENEA Casaccia Research Centre, in order to simulate the hostile radiation environment of interplanetary missions. Their optical behavior after irradiation has been analyzed.

1. Introduction

Optical and electronic instruments, employed in space science, are exposed to high energetic particles that might induce damage on their performance [1]. Such particles are generated from both primary (galactic cosmic rays, Van Allen belts and the solar activity) and secondary particles (knockout protons, neutrons, α particles, recoil nuclei and γ rays) [2]. Thin-film optical coatings are widely used in space instruments and in addition to the optical behavior, also their resistance to radiation exposure is critical for a correct operation.

In this work a set of optical materials, commonly used in thin-film devices for the ultraviolet and near infrared spectral range, have been exposed to γ irradiation up to 280kGy, in order to simulate the dose absorbed during a several-year interplanetary mission. The radiation damage on optical performance was investigated by carrying out spectrophotometric measurements before and after γ-ray exposure.

2. Thin-film optical samples

Materials widely used in either Extreme and Deep Ultraviolet (EUV-DUV) or Near Infrared (NIR) spectral range were selected. The analyzed samples are divided in two main groups, as reported in Table 1, that contain transparent conductive oxides, metals and semiconductors. The materials for the extreme

ultraviolet are often used for highly reflecting mirrors while, in the infrared, transparent conductive oxides are used for heat rejection devices.

All samples were fabricated by depositing thin film materials on Suprasil quartz substrates, using PVD techniques (radiofrequency and ion-beam sputtering) [3]. The selected substrate was already studied in the past by the authors and showed very good performance also at high dose radiation exposure[4].

Table 1. Analyzed thin film optical materials.

Spectral range	Material
UV	Al_2O_3, Mo, C, Si
NIR	ZnO:Al, ITO, Si

3. Radiation test and results

Optical samples were irradiated at the CALLIOPE ^{60}Co Source [5] by performing exposure cycles up to 280kGy total dose. Their performance, in terms of transmittance T and reflectance R, in the ultraviolet-visible-near infrared spectrum was investigated, spectrophotometric measurements were performed on all samples before and after radiation exposure, by both UV/VIS/NIR Lambda 900 and Spectrum GX FT-IR Perkin Elmer spetrophotometers.

Transmission measurements carried out in the past on Suprasil quartz have shown the absence of radiation damage on its optical properties, thus every induced variation will be attributed to the damage of the material deposited on the substrate.

High dose irradiation tests (up to 15kGy) performed on (about 300nm thick) Al_2O_3 samples confirmed the results [4] obtained at lower dose exposure. An almost linear decrease of transmittance especially in the UV region (λ<400nm) was detected as the radiation dose increases, with no variation in reflectance. This decrease of 1-2% indicates an increase of film absorption.

A different behavior was noticed on the metal film: a relevant transmittance increase (about 5%) and a corresponding reflectance decrease was observed for a 30nm-thick molybdenum layer. In Figure 1 the R+T curve for different radiation doses is reported, the complement to 100% of this quantity represents losses in the film. The variation induced by an increasing dose indicates an increase of losses that could be ascribed to a higher film absorption but also other phenomena occur that cause the transmittance increase.

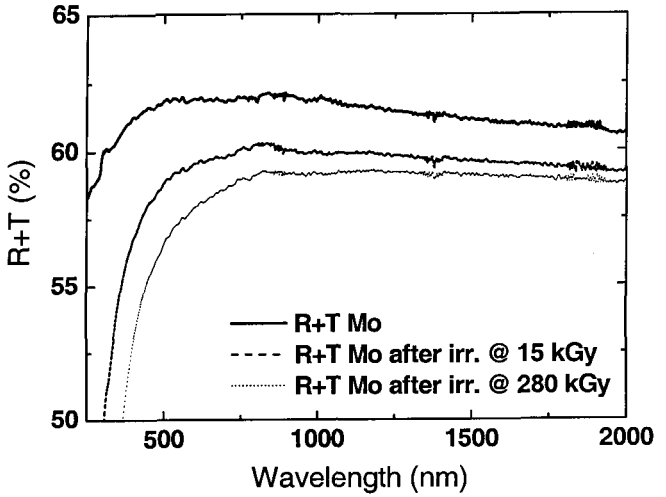

Figure 1. R+T variation of Molybdenum sample in different irradiation conditions.

Carbon and Silicon samples show no variations in the whole spectrum after the irradiation cycle. Carbon transmittance and Silicon reflectance curves, before and after γ exposure, are reported in Figure 2a and 2b. Silicon was irradiated as bulk material because the silicon film is easily oxidized.

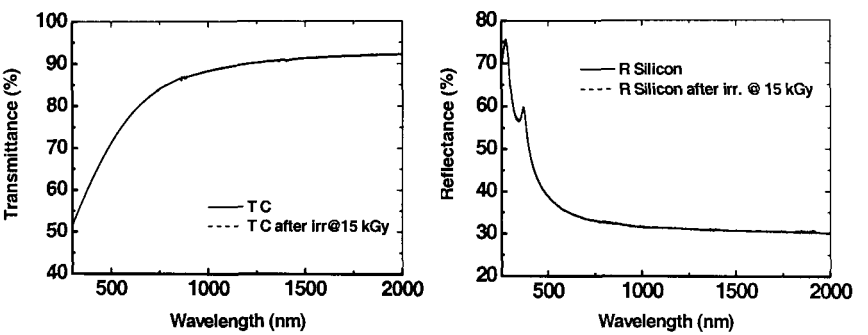

Figure 2. Transmittance spectra of Carbon film (a) and reflectance spectra of Silicon film (b) before and after irradiation.

Concerning NIR analysis, (400-800nm thick) transparent conductive films were studied. The behavior of a ZnO:Al sample after different dose rate exposure is presented in Figure 3, where the transmittance curve shows an

almost negligible variation (<1%) in the whole analyzed spectrum, in fact a slight increase of the NIR transmittance can be noticed at very high dose values. This effect could be due to the film oxidation.

More sensitive appears the ITO (In_2O_3:Sn) film behavior. This sample shows a shift of the transmittance curve towards infrared wavelengths when the dose increases (Figure 4), this red shift is probably due to a thickness modification or to the presence of inclusions in the film structure.

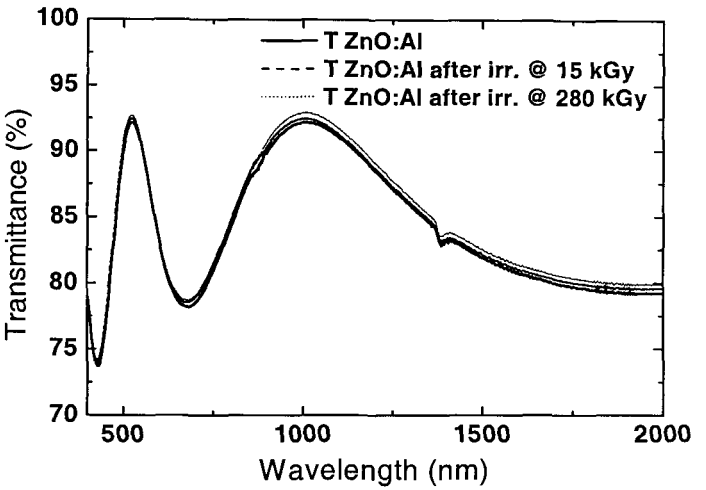

Figure 3. Transmittance spectra of ZnO:Al film before and after irradiation exposure.

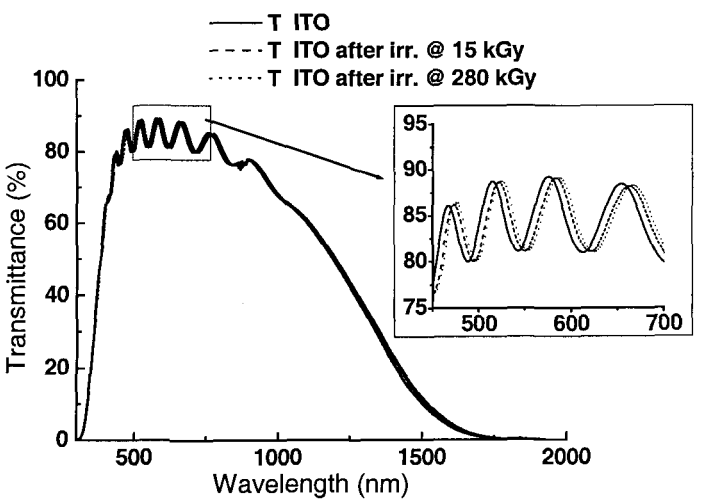

Figure 4. ITO transmittance before and after high dose irradiation exposure.

However it should be noticed that ITO films deposited with different process conditions did not undergo any change. A similar infrared shift was observed by the authors for Y_2O_3 samples in previous γ radiation damage tests [4, 6].

Conclusions

The analyzed materials show very different behaviors when exposed to γ radiation. Some of them are absolutely non affected by the irradiation, independently from the dose level. In a few cases a decrease of transmission is noticed corresponding to an increase of absorption, while in other samples an increase of this value was detected. Moreover some oxide films show an infrared shift of optical performance. All that means the interpretation of results is quite difficult and additional analysis is needed to understand the physical phenomena that are induced by the radiation on these thin-film materials.

References

1. M. Fernández-Rodríguez et al., *Ellipsometric analysis of gamma radiation effects on standard optical coatings used in aerospace applications*, *Thin Solid Films* 455-456, 545-550 (2004).
2. E.R. Benton and E.V. Benton, *Space radiation dosimetry in low-Earth orbit and beyond*, *Nucl. Instr. and Meth.* ***B*** **184**, 255 (2001).
3. R.F. Bunshah et al., *Deposition Technologies for Films and Coatings* (1982).
4. I. Di Sarcina et al., *Behavior of thin film materials under γ irradiation for astronomical optics*, *Astroparticle, Particle and Space Physics, Detectors and Medical Physics Applications* 802-806 (2006).
5. S. Baccaro et al., *γ irradiation facility at ENEA-Casaccia Centre, Roma*, *ENEA Report* ***RT/2005/28/FIS*** (2005).
6. S. Baccaro et al., *Effect of γ irradiation on optical components*, *IEEE Trans. Nucl. Science* **52**, **5**, 1779-1784 (2005).

STUDY OF THE RADIATION HARDNESS OF VCSEL AND PIN ARRAYS

K.K. GAN, W. FERNANDO, H.P. KAGAN, R.D. KASS, A. LAW, A. RAU, D.S. SMITH[†]

Department of Physics, The Ohio State University, Columbus, OH 43210, USA

M.R.M. LEBBAI, P.L. SKUBIC

Department of Physics and Astronomy, University of Oklahoma, Norman, OK 73019, USA

B. ABI, F. RIZARDINOVA

Department of Physics, Oklahoma State University, Stillwater, OK 74078, USA

The silicon trackers of the ATLAS experiment at LHC (CERN) use optical links for data transmission. VCSEL arrays operating at 850 nm are used to transmit optical signals while PIN arrays are used to convert the optical signals into electrical signals. We investigate the feasibility of using the devices at the Super LHC (SLHC). We irradiated VCSEL and GaAs PIN arrays from three vendors and silicon PIN arrays from one vendor. All arrays can be operated up to the SLHC dosage except the GaAs PIN arrays which have very low responsivities after irradiation and hence are probably not suitable for the SLHC application.

1. Introduction

Optical links are now widely used in high energy physics experiments for data transmission. The links substantially reduce the volume of metallic signal cables freeing up valuable detector space. In addition, the fibers eliminate the cross talk between metallic cables and electrical ground loops between the front-end electronics and the data acquisition system. The wide bandwidth of opto-electronics is well suited for multiplexing many input channels and allows for introduction of error checking and error recovery transmission protocols. These features are especially important in experiments where radiation can induce Single Event Effects (SEE) in the digital electronics. The silicon trackers of the ATLAS experiment at the Large Hadron Collider (LHC) use VCSELs to

[†] Work partially supported by the U.S. Department of Energy under contract No. DE-FG-02-91ER-40690.

generate the optical signals at 850 nm and PIN diodes to convert the signals back into electrical signals for further processing. The devices have been proven to be radiation-hard for operation at the LHC.

The LHC will start operation in 2008. However, an upgrade of the collider, Super LHC, is already being planned for 2015. The SLHC is designed to increase the luminosity of the LHC by a factor of ten to 10^{35} $cm^{-2}s^{-1}$. Accordingly, the radiation level at the detector is expected to increase by a similar factor. In this paper, we present a study of the radiation-hardness of the VCSEL and PIN arrays for the SLHC application.

2. SLHC Fluences and Test Setup

We use the Non Ionizing Energy Loss (NIEL) scaling hypothesis to estimate the SLHC fluences [1-3] at the present optical link location (PP0) of the pixel detector of the ATLAS experiment. The estimate is based on the assumption that the main radiation effect is bulk damage in the VCSEL and PIN with the displacement of atoms. After five years of operation at the SLHC (3,000 fb^{-1}), we expect the silicon component (PIN) to be exposed to a maximum total fluence of 1.5 x 10^{15} 1-MeV n_{eq}/cm^2 [4]. The corresponding fluence for a GaAs component (VCSEL) is 8.2 x 10^{15} 1-MeV n_{eq}/cm^2. We study the response of the optical link to a high dose of 24 GeV protons. The expected equivalent fluences at LHC are 2.6 and 1.6 x 10^{15} p/cm^2, respectively. For simplicity, we present the results from the irradiations with dosage expressed in Mrad using the conversion factor, 1 Mrad = 3.75 x 10^{13} p/cm^2 for silicon and 4.57 x 10^{13} p/cm^2 for GaAs. The expected dosages are therefore 69 and 34 Mrad, respectively.

We irradiated optical modules instrumented with one silicon PIN and two GaAs VCSEL arrays from various vendors using 24 GeV protons at the T7 facility of CERN. The PIN and VCSEL arrays coupled to radiation-hard ASICs produced for the current pixel optical link [5], the DORIC (Digital Opto Receiver Integrated Circuit) and VDC (VCSEL Driver Chip). Furthermore, the opto-boards were mounted on a shuttle system which enabled us to easily move in and out of the beam for annealing of the VCSEL arrays. The test system monitored various parameters of the opto-boards throughout the irradiation. In 2007, we also irradiated GaAs PIN arrays from three vendors. These devices were biased during the irradiation but not monitored due to space constraint.

3. Radiation-Hardness of VCSEL and PIN Arrays

We characterized the LIV (Light-Current-Voltage) curves of the VCSEL arrays before the irradiation. In 2006, we irradiated the arrays fabricated by three

vendors, Optowell, Advanced Optical Components (AOC, 2.5 Gb/s), and ULM Photonics (two varieties, 5 and 10 Gb/s) [6]. All arrays produced large optical power, in excess of 1 mW for the VCSEL current of 7 mA, the rated maximum current of the ULM 10 Gb/s array. This latter array also required higher voltage, ~ 2.3 V, to produce this current. The 5 Gb/s array required somewhat lower voltage to produce this current and the arrays from the AOC and Optowell, required significantly lower voltage. The latter arrays are therefore more suitable for operation at the SLHC because we expect to fabricate the driver and receiver chips using the 0.13 μm process with a thick oxide option which has a maximum operating voltage of 2.5 V. Given that it requires ~ 0.2 V to operate the transistors in the driver chip, the maximum drive current in the ULM arrays is therefore ~ 7 mA. This implies a lower optical power and less efficient annealing of arrays with radiation damage. In 2007, the AOC 2.5 Gb/s arrays were replace by two new devices operating with higher speed, 5 and 10 Gb/s. Figure 1 shows the LIV curves of the these arrays. These arrays produced large optical power and the required forward voltage to produce 7 mA is significantly less than 2.5 V and hence is suitable for operation at the SLHC.

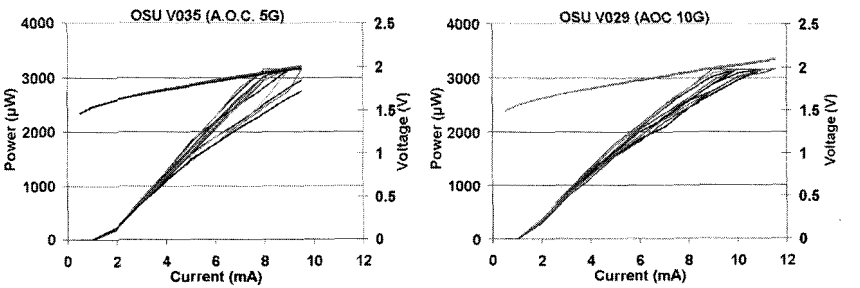

Figure 1. LIV curves of the 5 and 10 Gb/s VCSEL arrays by AOC before irradiation.

The test system monitored the optical power of the VCSEL arrays vs. dosage. In the 2006 irradiation, we found that all arrays continued to produce good optical power up to the SLHC dosage but the degradation with dosage was quite drastic [6]. We believe that the arrays would have performed better should we used a less intense beam and allowed more time for annealing. This is the program we followed in the 2007 irradiation. Figure 2 shows the optical power vs. dosage for the various arrays. The power decreased during the irradiation as expected. We annealed the arrays by moving the opto-boards out of the beam and passing the maximum allowable current (~ 10 mA per channel) through the arrays for several hours each day. The optical power increased during the annealing. Unfortunately, there was insufficient time for a complete annealing.

However, all devices continued to produce good optical power up to the SLHC dosage of 34 Mrad, except ULM 5 Gb/s which was least radiation-hard, consistent with the observation of 2006.

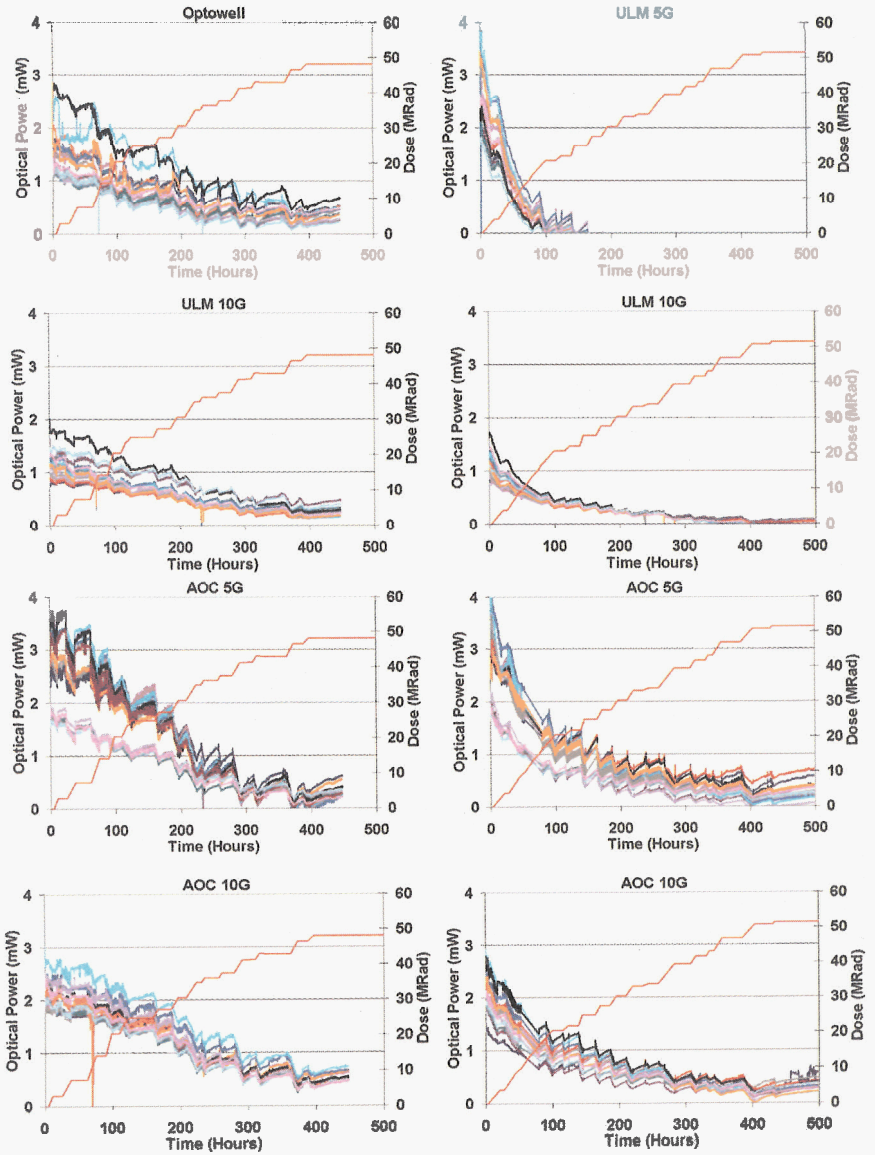

Figure 2: Optical power as a function of time (dosage) for various VCSEL arrays that transmitted data to the control room. The power decreased during the irradiation but increased during the annealing as expected.

We irradiated silicon PIN arrays by Truelight in 2006 and found that the responsivities decreased by 65% after the radiation, which is acceptable for the SLHC application. In 2007, we irradiated GaAs VCSEL arrays by AOC, Optowell, and ULM and found that the responsivities decreased by by ~ 90% which is not acceptable for the SLHC application.

4. Summary

We have irradiated VCSEL and PIN arrays from various vendors to the SLHC dosage. The GaAs VCSEL arrays from three vendors have been found to have the radiation hardness suitable for the SLHC operation. The responsivities of silicon PIN arrays decrease by ~ 65% while that for GaAs devices decrease by ~ 90% which are not suitable for the SLHC application.

Acknowledgments

The authors are indebted to M. Glaser in the use of the T7 irradiation facility at CERN.

References

1. I. Gregor, "Optical Links for the ATLAS Pixel Detector", Ph.D. Thesis, University of Wuppertal, (2001).
2. A. Van Ginneken, "Nonionzing Energy Deposition in Silicon for Radiation Damage Studies," FERMILAB-FN-0522, Oct 1989, 8pp.
3. A. Chilingarov, J.S. Meyer, T. Sloan, "Radiation Damage due to NIEL in GaAs Particle Detectors," Nucl. Instrum. Meth. A 395, 35 (1997).
4. The fluences include a 50% safety margin.
5. K.E. Arms et al., "ATLAS Pixel Opto-Electronics," Nucl. Instr. Meth. A 554, 458 (2005).
6. K.K. Gan et al., "Bandwidths of Micro Twisted-Pair Cables and Fusion Spliced SIMM-GRIN Fiber and Radiation Hardness of PIN/VCSEL Arrays," in Proceedings of the 12th Workshop on Electronics for LHC and Future Experiments, Valencia, Spain, 2006, edited by M. Letheren and S. Claude (CERN-2007-1), p. 223.

Radiation Hard Sensors for the BeamCal of the ILC

C. Grah

for the FCAL Collaboration

Deutsches Elektronen-Synchrotron DESY
Zeuthen, D-15738, Platanenallee 6, Germany
**E-mail: christian.grah@desy.de*

BeamCal is an electromagnetic sampling calorimeter in the very forward region of the detectors at the ILC. BeamCal will be hit by a large fraction of electron-positron pairs stemming from beamstrahlung. The sensors used for BeamCal have to withstand very high levels of total ionizing dose. We report on the investigations of radiation hard sensor materials for BeamCal of the FCAL collaboration. Artificial diamond, radiation hard silicon, SiC and GaAs sensors are under consideration. Static measurements of the current-voltage characteristics, response to minimum ionizing particles and test beam measurements are part of our investigations.

Keywords: ILC, forward region, BeamCal, CVD diamond, radiation hard silicon, GaAs, CCD, charge collection distance, irradiation

1. Introduction

The International Linear Collider, ILC, will be a future linear electron-positron accelerator.[1] Due to the very small beam sizes and high beam intensity at the ILC the creation of beamstrahlung will be a new phenomenon. These beamstrahlung photons are emitted under a very low angle of less than one mrad, but a fraction of the photons can convert into electron-positron pairs which will hit the forward region of the detectors at the ILC. The FCAL Collaboration[2] develops the systems in the forward region independently from one of the detector concepts. In Fig. 1 a design of the very forward region for the example of the Large Detector Concept, LDC,[3] is shown for the collider baseline concept of a crossing angle of 14 mrad between the incoming and outgoing beams.

The major systems in this region are LumiCal, which will measure the integrated luminosity to a relative precision of better than 10^{-3} using bhabha events, and BeamCal, which will give a fast feedback signal of

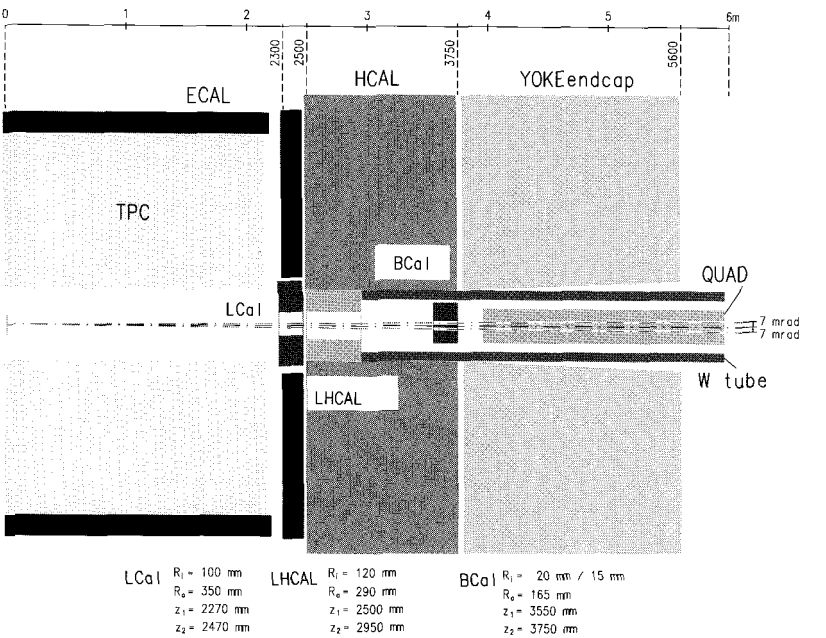

Fig. 1. The forward region of the Large Detector Concept.

the instantaneous luminosity. Both system with also optimize the hermeticity of the detector and guarantee efficient electron detection down to lowest polar angles. Details of the forward region are given in Ref. 4.

2. The Beam Calorimeter BeamCal

BeamCal will be a compact electromagnetic calorimeter using tungsten as absorber and a radiation hard sensor material as sensitive layers. Each of the 30 layers of BeamCal will consist of a 3.5 mm thick absorber layer followed by a sensor layer, which includes a segmented sensor and a readout plane which routes the interconnection lines from the segments to the outer radius of the BeamCal, where the readout electronics will be placed. Fig. 2 shows the expected dose rate per year in the sensor layer with the highes energy deposition, which is after $6\,X_0$ in this case. The energy deposition is strongly dependent on the geometry and magnetic field configuration. In the shown example a DID-like magnetic field configuration was chosen, where the magnetic field is parallel to the incoming beam.[5] According to these GEANT4 simulations the sensors for the BeamCal should be qualified

for a total ionizing dose of 10 MGy per year. Another requirement for the sensors for the BeamCal is the linearity of the response over at least four orders of magnitude of particle fluences. This arises due to the task of giving efficiently a veto signal of single high energetic particles (e.g. electrons) in the acceptance region of BeamCal on top of the high amount of background from beamstrahlung pairs.

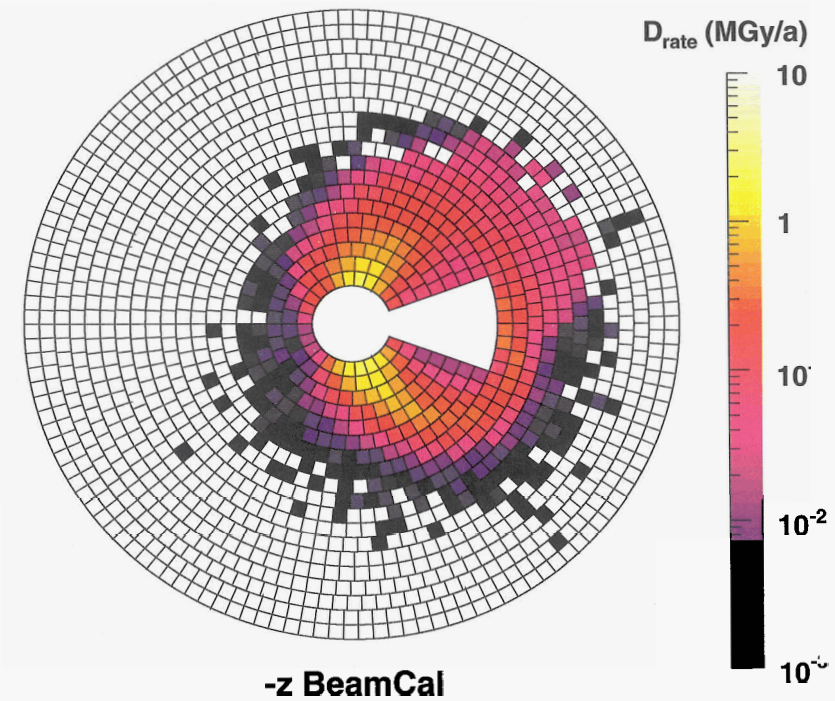

Fig. 2. The expected dose rate for the BeamCal sensor layer with highest energy deposition. The shown case assumes a 100 % running time of the accelerator per year, nominal beam parameters[6] at 500 GeV and a DID-like magnetic field configuration. The not instrumented areas are for the outgoing beam (left) and the incoming beam (right).

3. Sensor Materials under Investigation

The FCAL Collaboration investigates several materials as possible sensors for the BeamCal. Requirements are:

- radiation hardness against a total ionizing dose of up to 10 MGy
- a linearity of the response over at least 4 orders of magnitude of particle fluences
- if possible, no additional cooling or other support to keep the required compactness of BeamCal.

3.1. *CVD Diamond*

Chemical Vapor Deposited diamond can be produced as a polycrystalline material on wafer sizes. It is under investigation since several years[7] and is very radiation hard. We investigate pCVD diamond material from the manufacturers Element 6 and the Fraunhofer Institute for Applied Solid State Physics IAF. The samples are of about 1 cm^2 size and typically 300-500 μm thick. The properties of good classified samples are a high resistivity of about 10^15 Ωcm and a detectable signals of minimum ionizing particles using a part of the spectrum of a Sr^90 source. The signal is usually quantified as the Charge Collection Distance, CCD, which gives the mean drift distance of radiation induced free charge carriers. The pCVD material is not 100 % efficient showing CCDs between a few ten μm of CCD up to 150 μm and more. This corresponds to a measured charge of CCD $\times$ 36 eh-pairs/μm. The dependence of the CCD on the applied electric field saturates at about 1 V/μm. In a hadron test beam at the CERN PS it could be shown that the linearity of the response of this material is within 30 % over a range of 1 MIP to 10^6 MIPs/($cm^2$10 ns).

In a high dose irradiation test beam at the S-DALINAC of the technical university of Darmstadt it was possible to show that after 7 MGy of absorbed total ionizing dose from a 10 MeV electron beam, the sensors were still operational. The dark current of the samples increased slightly but still remains on the level of a few pA at 500 V. The overall signal size decreased significantly during this irradiation.

First tests of a monocrystalline sensor of about 0.25 cm^2 size and 340 μm thickness show a 100 % efficient charge collection at low electric fields of about 0.2 V/μm. The leakage current was below the sensitivity of our setup (¡10−13 A). This material has very promising properties but as of today it is only available in sizes of less than 1 cm^2.

3.2. *GaAs, SiC and Radiation Hard Silicon as Sensor Material*

Gallium arsenide is a semiconducting material with a band gap of about 1.42 eV with a higher radiation hardness than silicon. The Siberian Institute of Technology was able to supply us with sensor prototypes in a realistic BeamCal shape, featuring 88 pads of about 5 mm × 5 mm size and a thickness of 500 μm. The segmentation of the material is done by a metallization in the desired structure, the same procedure as used for diamond sensors. An individual pad shows a typical leakage current of 1 μA at 500 V. The CCD of the not irradiated material is about 250 μm at 0.4 V/μm. It is noteworthy that due to the high density of the material the induced signal from a MIP is about a factor of two higher than for silicon. First results from the high dose irradiation test beam show a degradation of the signal after about 1 MGy and an increase of the leakage current by about a factor of two. A first prototype of a SiC sensor was not usable as a detector for MIPs, due to the low resistivity. A prototype of a radiation hard silicon sensor made of mCz material was measured in laboratory and in the test beam. Without using further means of cooling the signal to noise ratio started to decrease until after about 100 kGy no signal was detectable due to the high leakage currents at room temperature. The signal size remained constant until then.

4. Conclusion

BeamCal is a very important part of the instrumentation in the very forward region of the ILC detectors. One of the challenges for this electromagnetic sampling calorimeter is the development of radiation hard sensors, which are able to survive the expected level of total ionizing dose of up to 10 MGy per year. The FCAL collaboration investigates several different possible materials. Sensor prototypes made of poly- and monocrystalline CVD diamonds, radiation hard silicon, GaAs and SiC are under test. These tests include laboratory measurements as current-voltage characteristics, response to minimum ionizing particles and the dependence of the response on parameters like the applied electric field or the absorbed dose. Test beam measurements prove the linearity of the response of pCVD diamond up to highest particle fluences of 10^6 particles per $\mathrm{cm}^{-2}\mathrm{s}$ $10\,\mathrm{ns}^{-1}$. High dose irradiation show that these samples are operational after up to 7 MGy of absorbed dose. GaAs samples show a significant decrease of their response after about 1 MGy and an increase of their leakage current by about a

factor of two. First tests using radiation hard silicon show that additional measures, like e.g. cooling, have to be considered to operate the sensors to doses of 100 kGy and beyond. A SiC prototype showed no detectable MIP response. We will investigate such a material if it will be possible to obtain material with a higher intrinsic resistivity.

5. Acknowledgments and Appendices

The author would like to thank all involved members of the FCAL collaboration. The Fraunhofer Institute IAF and the GSI in Darmstadt. Furthermore the Siberian Institute for Technology and the BTU Cottbus. Also thanks to the S-DALINAC crew of the technical university of Darmstadt and the CERN staff for their support during our test beams. This work was partly supported by EUDET.

References

1. ILC Global Design Effort and World Wide Study,*The ILC Reference Design Report*, 2007, available at http://www.linearcollider.org/.
2. The FCAL Collaboration, http://www-zeuthen.desy.de/ILC/fcal/.
3. The LDC Group,*The Detector Outline Document for the Large Detector Concept*, 2006, available at http://www.ilcldc.org/.
4. H. Abramowicz et al., *Instrumentation of the Very Forward Region of a Linear Collider Detector*, IEEE transactions of Nuclear Science, 51, p, 2983 2004
5. B. Parker and A. Seryi, *Compensation of the effects of a detector solenoid on the vertical beam orbit in a linear collider*, Phys. Rev. ST Accel. Beams 8, 041001 (2005).
6. T. Raubenheimer et al., *Suggested ILC Beam Parameter Ranged*, available at http://www-project.slac.stanford.edu/ilc/acceldev/beamparameters.html.
7. H. Kagan,*Radiation Hard Diamond Pixel Detectors*, these proceedings.

GAMMA-RAY IRRADIATION EFFECTS ON LUMINESCENT GLASSES FOR WHITE LED APPLICATIONS

X.LIANG, C..ZHU, Y.YANG, G.CHEN

Key Laboratory for Ultrafine Materials of Ministry of Education, School of Materials Science and Engineering, East China University of Science and Technology, Shanghai 200237, China

S.BACCARO

ENEA Casaccia Research Center FIM-FIS ION, Via Anguillarese 301, 00123 Rome

In the present work, silicate glasses co-doped with Tb^{3+} and Sm^{3+} ions are prepared and their photoluminescence properties are determined by excitation and emission spectra. The high-energy g-ray irradiation effects on luminescent properties of these glasses are examined and the redox processes involved are illustrated. Especially, the possibility of gamma irradiation as a tool to modify the color rendering index of glasses is discussed.

1. Introduction

The electronic transitions of 4f-4f and 4f-5d of rare earth ions (REn+) cause a wide sharp fluorescence pattern from the ultraviolet (UV) to infrared region, which attracts a large interest of researchers [1, 2]. In particular, luminescence materials doped with REn+ are widely used in a variety of applications, which include white light emitting diode (W-LED) and other emission display devices [3]. So far, W-LED develops quickly as the fourth generation lighting device, and shows a broad prospect for replacing the traditional incandescent and fluorescent lamps, due to its advantages such as longer lifetime, smaller volume, lower energy consumption, environmental protection and so on [4]. Conventionally, W-LED is manufactured using phosphors which are excited by a blue-emission LED chip. However, a great deal of attention is paid to luminescent materials that are excited by the UV light in order to exclude the participation of the LED chip in the emission of white light. Especially, luminescence glasses have some advantages over phosphors, such as lower production cost, simpler manufacture procedure, etc. In our present work, Tb^{3+} and Sm^{3+} co-doped glasses have been synthesized. The measured excitation and emission spectra indicate that this type of glasses can be effectively excited by the UV light and emit stable green and orange-red light, which then generate a white light. From the literature it is well known that γ ray irradiation can induce oxidation-reduction effect on some multi-valent ions in glasses which is

significant to modify the color rendering index of glasses. Thus we investigate the effect of γ ray irradiation on the valent state of Tb^{3+}/Sm^{3+} in glasses.

2. Experiment

The composition of luminescent glass samples is shown in Table 1. All samples were prepared using a conventional melt quenching method. High-purity powders of SiO_2, $CaCO_3$, and $BaCO_3$ (all analytically pure), Tb_4O_7, and Sm2O3 (99.99%) were well mixed in an agate mortar. Then, each 50 g batch was melted in an alumina crucible at 1550 °C for 2 h in air. The melt was then poured into a preheated stainless steel mold to form a 2 mm thick glass plate. To ensure their thermal and structural stability, all glasses were annealed at 500 °C for 2 h.

Table 1. Composition and irradiation dose of analyzed samples (mol%)

Sample	Composition	Irradiation dose/kGy
Si1	$50Si0_2$-37CaO-13BaO: $0.125Tb_4O_7$, $0.5Sm_2O_3$	0
Si2	$50Si0_2$-37CaO-13BaO: $0.125Tb_4O_7$, $0.5Sm_2O_3$	1000
Si3	$50Si0_2$-37CaO-13BaO: $0.125Tb_4O_7$, $0.5Sm_2O_3$	1300
Si4	$50Si0_2$-37CaO-13BaO: $0.125Tb_4O_7$, $0.5Sm_2O_3$	1500

In order to measure the characteristics of glasses, both faces of each sample were polished.

γ ray irradiation tests were carried out at the Calliope ^{60}Co source (ENEA-FIS/ION, Italy) in a dosimetric point corresponding to the dose rate of 4056.78 Gy/h at doses 1000, 1300, 1500 kGy, respectively.

The transmittance spectra were measured by Perkin Elmer Lambda 950 UV/VIS spectrometer (ENEA-FIS/ION, Italy).

The excitation and emission spectra were recorded on a JASCO FP-6500 spectrometer (ECUST, China).

3. Results and Discussion

The emission spectrum of pristine sample Si1 excited by the 375 nm light is shown in Figure 1a. The Tb^{3+} emission bands include the peaks at 416, 438 (purple), 488 (blue), and 544 nm (green, strongest), which are assigned to the electronic transitions of $^5D_3 \rightarrow {}^7F_5$, $^5D_3 \rightarrow {}^7F_4$, $^5D_4 \rightarrow {}^7F_6$, and $^5D_4 \rightarrow {}^7F_5$, respectively. The Sm^{3+} emissions are at 564 (green), 602 (orange-red, strongest), and 648 (red) nm, and correspond to the $^4G_{5/2} \rightarrow {}^6H_{J/2}$ (J=5, 7, 9) electronic transitions [5].

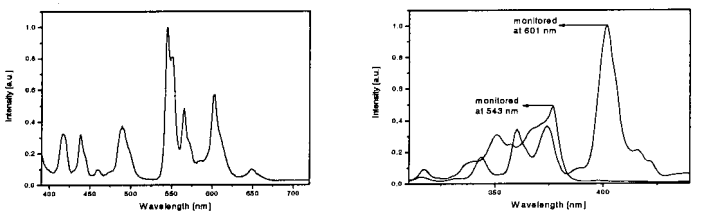

a) b)

Figure 1. a) Emission spectrum of sample Si1 excited by 375 nm light; b) Excitation spectrum of sample Si1 monitored at 543 and 601 nm.

The excitation spectra of Si1 glasses (figure 1b) show that the excitation peak at 377 nm, monitored at 543 nm, is due to the transition from the ground level $^7F_6$ to $^5D_2$ of Tb^{3+} ion while that at 374 nm, monitored at 601 nm, corresponds to the $^6H_{5/2} \rightarrow {}^4K_{13/2}$ electronic transition of Sm^{3+} ion. Based on excitation spectra, it is believed that the UV radiation around 375 nm could be used to efficiently excite the luminescence glasses and it nicely matches the requirements for W-LED applications.

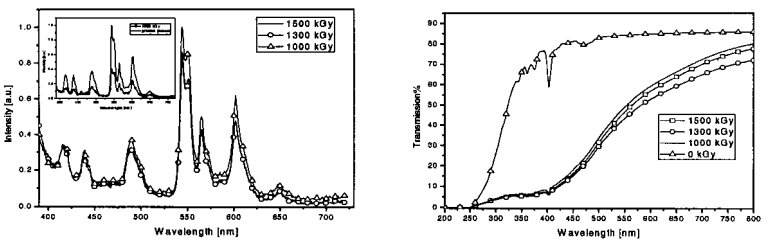

a) b)

Figure 2. a) Emission spectra of irradiated samples excited by 375 nm; b) Transmission spectra of samples before and after irradiation.

Figure 2a displays the emission spectra of irradiated glasses (Si2-4). The inset shows emission spectra of Si1 and Si2 in order to compare emission intensities before and after irradiation. One can clearly see that the emission intensity after irradiation becomes much weaker. It is known that the gamma ray irradiation can induce defects in glasses. The damage of glasses induced by radiation is evaluated by comparing their transmission spectra in the ultraviolet and visible regions measured before and after irradiation, as shown in Figure 2b. From this figure it can be seen that irradiation induced absorption cover almost the whole UV-VIS region and increase with the irradiation dose. The emergence of defects

would promote the nonradiative transition process of Tb^{3+}/Sm^{3+} and the holes could enhance the probability of refraction and reflection of light, which may be the main reason of the emission intensity reduction.

It is widely acknowledged that some types of rare earth ions would capture free electrons and generate the ions with lower valency while the holes could be trapped by oxygen ions. For our Tb^{3+} and Sm^{3+} co-doped glasses, the Tb^{3+} ions were introduced from Tb_4O_7 while the glasses were melted in air. Therefore, there is some higher valent Tb state (Tb^{4+}) in the final glasses. The potential redox processes may be as follow:

$$Sm^{3+} + e^{-} \rightarrow Sm^{2+} \quad (1)$$

$$Tb^{4+} + e^{-} \rightarrow Tb^{3+} \quad (2)$$

Though there is a notable decrease in the emission intensity with increasing irradiation dose, a regular increase in the intensity ratio of the Tb^{3+} 544 nm emission and the Sm^{3+} 60_2 nm line is observed (Table 2). This changing ratio means the enhanced emission of Tb^{3+} step by step by irradiation. In other words, the quantity of Tb^{3+} ions in glasses increases. So it is believed that the redox process of Tb ions (Equation 2) has occurred during irradiation. At the same time, the adjustment of intensity ratio is very important for illumination applications because the desired emission characteristics need to match those of the International Commission on Illumination (CIE) chromaticity diagram.

Table 2. Ratio of the intensities of the green to the orange-red emissions of samples

Glass NO.	Si2	Si3	Si4
Ratio	1.611 1	1.704 8	1.828 3

Based on work previously reported, in most glass systems, trivalent Sm^{3+} could be changed to divalent Sm^{2+} by X ray, γ ray or β ray irradiation at high dose [6, 7]. In theory, the emission peaks of Sm^{2+} are located at 684, 697 nm ($^5D_0 \rightarrow {}^7F_{0,1}$) and 727, 763 nm ($^5D_0 \rightarrow {}^7F_{1,3}$) [6], respectively. However, there seems to be no change in the positions of emission peaks in Figure 3, which means that divalent Sm^{2+} does not appear. Therefore we suppose that the redox process as shown in Equation 1 does not apply during irradiation. Such a selective redox process may be related to the ability of REn+ to capture an electron. This ability is different for Sm and Tb ions. It is known that trivalent state is the characteristic valence state for Lanthanide, including Tb and Sm atoms. As losing 3 electrons to form trivalent ion needs less ionization potential, Tb/Sm atom has the trend to be as the stable trivalent Tb^{3+}/Sm^{3+}. From another perspective, the capacity of

capturing electron from anion or cation is related to the relative alkalinity which can be measured by ionic potential (Φ). The larger the ionic potential, the weaker the relative alkalinity, and the stronger the attraction to an electron. For lanthanide, the ionic potential becomes larger with the decreasing ionic radius. Since the ionic radius of Tb^{4+} is about 84.3 pm, smaller than that of Sm^{3+} (96.4 pm), the Φ of Tb^{4+} would be larger than that of Sm^{3+}. In our glasses where Tb^{4+}/Tb^{3+} and Sm^{3+} co-exist, Tb^{4+} ions dominate the process of capturing an electron. Therefore, there is a conversion of Tb^{4+} ions to Tb^{3+} while Sm^{3+} ions are not affected.

4. Conclusions

To summarize, silicate glasses co-doped with Tb^{3+} and Sm^{3+} ions were synthesized by the melt-quenching method. All luminescent glasses can be effectively excited by the UV light and the main emission peaks are located at green and orange-red parts of the visible spectrum. In our glasses where Tb^{4+}/Tb^{3+} and Sm^{3+} co-exist, Tb^{4+} ions dominate the process of capturing an electron. Therefore a conversion of Tb^{4+} ions to Tb^{3+} applies while due to the lower ionic potential the Sm3+ ions are not affected. The intensity ratio of green to orange-red emissions can be tuned by varying γ ray irradiation dose. Thereby, these glasses give a possibility to generate the white light emission by the UV light excitation with the modified color rendering index.

References

1. P. I. Paulose, G. Jose, V. Thomas, N. V. Unnikrishnan, M. K. R. Warrier, *J. Phys. Chem. Solids.* **64**, 841 (2003).
2. M. Nogami, T. Enomoto, and T. Hayakawa, *J. Lumin.* **97**, 147 (2002).
3. E. Malchukova, B. Boizot, G. Petite, D. Ghaleb, *J. Non-Cryst. Solids.* **353**, 2397 (2007).
4. Y. Q. Li et al., *Chem. Mat.* **17**, 3242 (2005).
5. X. Liang, Y. Yang, C. Zhu, S. Yuan, G. Chen, A. Pring, F. Xia, *Appl. Phys. Lett.* **91**, 091104 (2007).
6. E. Malchukova, B. Boizot, D. Ghaleb, G. Petite, *Nucl. Instrum. Meth. Phys. Res. A.* **537**, 411 (2005).
7. E. Malchukova, B. Boizot G. Petite, D. Ghaleb, *J. Lumin.* **111**, 53 (2006).

On line monitoring of radiation damage and recovery in quartz fibres using reflected light

Jean-Pierre Merlo *

Department of Physics and Astronomy, University of Iowa,
Iowa City, IA 52242 , USA
Jean-Pierre.Merlo@cern.ch

In a detector exposed to high flux of particles (100 Mrad and more) and whose fibres are the active elements one has to know the level of radiation accumulated to calibrate the fibre read-out. This is the case for the forward calorimeter of the CMS experiment at LHC (HF) made of iron as absorber and quartz fibres generating and transmitting Cerenkov light to PMTs.. The light spectrum detected is centered near 450 nm (blue). The important transmission variations at these wavelength (few tens %) due to radiation damage and recovery led us to monitor on line the blue light transmission with special fibres called Raddam fibres. Injecting blue light in a 2.5m long fibre, we used the ratio of reflected signal at the two ends to determine the absorption of the fibre. This paper will describe the principle, the construction and tests of this device.

Keywords: radiation, fibre, quartz, attenuation

1. Introduction

Light transmission of irradiated radiation hard quartz fibres (high OH-content) have been measured and published by the University of Iowa and Turkish groups.[1,2] The results obtained from exposures to electrons[1] and to protons,[2] present close behaviours. There is a moderate attenuation in the band 400-520 nm and a high recovery of damage near 450 nm. The damage and its recovery varie exponantially with dose; fast in the first hours and slow after. For example in the FSHA 600730800 fibre manufactured by the US firm Polymicro Technology Inc. one observes for the blue (450nm) transmission of a 2m long fibre:

*on behalf of the authors: N Bakirci, A. Braem, K. Cankocak, S. Cerci, I. Dumanoglu, S. Erturk, M. Glaser, A. Heering, E. Isiksal, A. Kayis-Topaksu, A. Mestvirishvili, Y. Onel, F. Ozok, H. Ozkurt, A. Penzo, I. Schmidt, M. van Stenis, E. Vlassov.

- a decrease of 30 % in light transmission resulting from a dose accumulation of 20 Mrad (radiation damage).

- an increase in light transmission by 22 % ten days after the stop of an irradiation to 100 Mrad in 200 days (damage recovery).

One must pay attention to the damage recovery effect in a detector whose fibres are the active element as HF-CMS.[3] In such a detector the secondary shower particles produced in the absorber cross the fibres and generate Cerenkov light in the UV-blue. The fibres transmit this light to the PMT's and the effective detected spectrum is in the range 400-500 nm where the pecular effect of damage recovery occurs near 450 nm. The calibration of the system fibres-PMT's will depend of the level of fibre irradiation and of the time spent after the stop of data taking, due to the damage recovery. What is necessary to know is the effective calibration of the system fibres-PMT's at the time of data taking. In 2003 we proposed to install a dedicated device[4] to estimate on line the transparency of the fibres.

We have called this monitoring system "Raddam device" and we will describe below its principle, the installation in the HF-CMS detector and the various tests done.

The Raddam device uses the light reflexion at the two end of a fibre to measure its transparency. This system installed in the HF calorimeter could be used in other irradiated installations..

2. Radiation damage and recovery monitoring with reflected light: Raddam principle

- The light is injected through a thin fibre glued to the fibre going to the PMT inside a capillary tube. At the opposite side of the capillary the Raddam fibre, 2.5 m long, two ends polished, received the light (Figure 1). For HF-CMS this length corresponds to a regular fibre read by PMT's. One uses blue light wave shifted from a nitrogen laser, corresponding to the PMT's sensitivity.

- Reflections occur at the two ends of the Raddam fibre, signal S_1 at the entrance, independent of dose, and S_2 at the far end, coming 25 ns later. S_2 depends of the fibre transparency related to radiation damage and recovery. Then the ratio $R = S_1/S_2$ measures the fibre transparency. R depends of the dose accumulated D, and of the post irradiation time t for recovery.

- At LHC and in HF-CMS, R is stable when pulses are near the middle of the DAQ clocks. Nevertheless in HF the Raddam data will not be registered on line but soon after a break in data taking using the HF-DAQ logics.

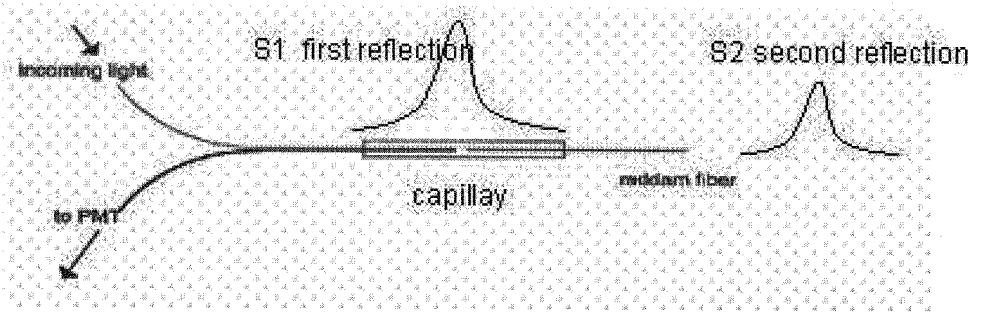

Fig. 1. Experimental set-up

- HF is segmented in wedges, The fibres coming from the HF iron absorber are assembled in bundles going to the PMT's. In 7 bundles of 8 wedges one fibre is cut and equipped as " Raddam fibre ". In total there are 56 Raddam fibres in the entire system which will provide radiation damage information.

3. The damage recovery at 450 nm

In an iron-fibre calorimeter like CMS-HF the Cerenkov light is detected by PMT's sensitive in the 400-500 nm range. Near 450 nm the damage recovery is maximum and gamma is close to 1 [see Equation (1)]. The knowledge of the evolution of light transmission in fibres after a break in data taking is important for the calibration measurements.[3]

One can easily derive the increase of transmitted signal $I_D(t)$ after an irradiation to a total dose D in time t_{irr}.[2]

$$I_D(t)/I(D) = exp[A(D)(L/4.343))(\gamma t^{\eta}/(t_{irr}^{\eta} + \gamma t^{\eta}))] \qquad (1)$$

As an example we present below the values of the ratios $I_D(t)/I(D)$ at 455nm for four post irradiation times t in a 2 m long fibre irradiated up to 100 Mrad in 4800 hours.

Using parameters $\gamma = 0.9$, $\eta = 0.25$ and A = 1.6 dB/m one gets:

o This table shows the amount of the correction to apply to a calibration performed at a post data taking time t to get the real calibration at the data taking time.

$t(h)$	2.4	24	240	2400
$I_D(t)/I(D)$	1.06	1.12	1.22	1.37

o If the fibre transparency is not measured strictly at the time of the irradiation or during LHC data taking it has to be done soon after a stop of irradiation or data taking.

4. On line measurement of a 1m long fibre in a 24 GeV/c proton beam using HF-DAQ

To check the response of raddam fibres we have installed a one meter long fibre in the PS 24 GeV/c proton beam delivered in the IRRAD facility.

The fibre is 1% tilted relative to the beam to get 1m swept. The beam delivered $10^{16}p/cm^2/h$ corresponding to a dose rate of 2.6 Mrad/h.

A laser nitrogen light (337nm) is shifted in the blue by a piece of blue scintillation fibre inserted in a feedthrue connector. This blue light (spectrum centered on 450 nm) is injected in the 1 m irradiated fibre out of the proton spill to avoid mixing with Cerenkov light produced by protons.

At LHC there are collisions every 25 ns. The DAQ shares the signals in 25 ns time slices.

o As S_2 comes 25 ns later than S_1 the two reflected signals are in two or three consecutive 25 ns time slices.

With 400 registered events we got the ratio $R = S_1/S_2$, with 0.5 % statistical error. This number of events was registered in 2 min at the PS.

The Figure 2 shows the history of the variation of the ratio $R(t) = S_1/S_2(t)$ in function of time. This irradiation was not continuous. One sees clearly the increase and decrease of R(t) corresponding to irradiation periods and fast decrease when the beam stopped. One can see even short beam stops inducing change in ratio (Figure 2).

The ratio R depends of dose D in irradiation periods, $D = doserate \times t$

The attenuation A is calculated from the ratio of reflected light signals at the fibre ends:

$$R(D) = \frac{S_1}{S_2(D)} \tag{2}$$

The first reflected signal S_1 is independent of dose D or time t.

$$\frac{I(\lambda, D)}{I(\lambda, 0)} = \frac{R(0)}{R(D)} = \frac{S_2(D)}{S_2(0)} \tag{3}$$

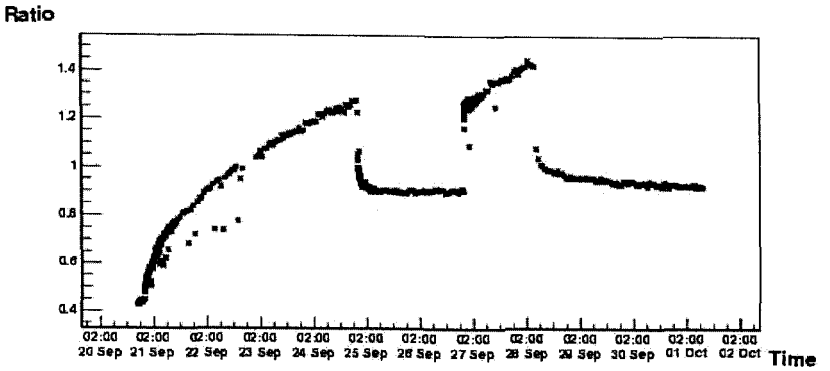

Fig. 2. History of irradiation and recovery

The attenuations calculated from these ratios agree with our previous measurements.

$$A(\lambda, D) = -\left(\frac{4.343}{L}\right) Log\left[\frac{I(\lambda, D)}{I(\lambda, 0)}\right] \tag{4}$$

On Figure 2, the radiation damage recovery in function of post irradiation time t. One can see the steep decrease of R when the irradiation stops. In this last plot is the main effect.

5. Summary

o The Raddam system using reflected light has been tested with LHC DAQ readout of CMS-HCAL,

o The results agree with previous transmission measurements.[1,2]

o The calibration results done after a break of data taking have to be corrected in function of post irradiation time.

o The reflection of light injected in a quartz fibre can be used to monitor irradiation area or devices.

References

1. I.Dumanoglu et al. NIM A490 (2002) 44-455
2. K.Cankocak et al. CMS note 2007-03, submitted to NIM.
3. CMS-HF collaboration HF CMS note 2006/044
4. K. Cankocak et al, Feasibility of Radiation monitoring in HF-CMS using reflection on fibre ends, Note CMS IN 2003/05

STUDIES OF LEAD TUNGSTATE CRYSTALS EXPOSED TO LARGE PROTON AND PION FLUENCES

P. LECOMTE, D. LUCKEY, F. NESSI-TEDALDI* and F. PAUSS

Swiss Federal Institute of Technology (ETH)
CH-8093 Zürich, Switzerland
*E-mail: Francesca.Nessi-Tedaldi@cern.ch
www.ethz.ch

D. RENKER

Paul Scherrer Institute (PSI)
CH-5232 Villigen, Switzerland
www.psi.ch

Lead Tungstate crystals are widely used for calorimetry in several high-energy physics experiments, in particular where performance has to be ensured in a high radiation environment and large particle fluxes. Results obtained with hadrons are thus crucial for operation at LHC. Preliminary results are presented here on a comparative study of Lead Tungstate *performance after irradiation with 24 GeV/c protons and 290 MeV/c positively charged pions.*

Keywords: Lead Tungstate, *crystal calorimeter, hadron damage*

1. Introduction

A series of irradiation tests on Lead Tungstate crystals[1–3] has allowed us to establish that hadrons cause a specific, cumulative damage to their light transmission, while their scintillation properties remain unaffected. We obtained those results through the exposure of several crystals to different fluences of 20 and 24 GeV/c protons up to the full integrated fluence expected at the LHC. We also performed complementary γ irradiations at a ^{60}Co source to disentangle the damage due to the associated ionising dose. Crystals used at the LHC will however be exposed mostly to high charged pion fluxes with energies ≤ 1 GeV. The scaling from proton damage results to such a pion-rich spectrum had to be experimentally determined.

2. The irradiation tests

A previously γ-irradiated crystal, labelled *w* in Ref. 1, was cut for this study into three equal length sections (which we label *w1*, *w2* and *w3*) with dimensions $\sim 2.4 \times 2.4 \times 7.5$ cm^3, after thermally annealing the γ damage.

The middle section, *w2*, was irradiated with 290 MeV/c pions. The irradiation was performed in the high-flux secondary pion beam line $\pi E1$ at the Paul Scherrer Institute 590 MeV Cyclotron. Details about the beam line can be found in Ref. 4 and about beam purity in Refs. 5 and 6. The crystal was irradiated with an Aluminium foil covering its entrance face, for fluence determination from activation measurements, whose details are given in Ref. 7. The crystal was irradiated up to a total fluence $\Phi_\pi = (5.67 \pm 0.46) \times 10^{13}$ cm^{-2}. The average flux on the crystal was $\phi_\pi = 4.13 \times 10^{11}$ cm^{-2} h^{-1}.

The first, *w1*, and last, *w3*, sections were irradiated with 24 GeV/c protons. For this purpose, they were placed at the same time, one in front of the other, into the IRRAD1 facility[8] of the CERN PS accelerator T7 beam line, with the beam entering through the small *w1* face, so that the hadronic cascade could develop through both crystals. Details of the procedure can be found in Ref. 1. The proton fluence on the crystal front face was $\Phi_p = (1.17 \pm 0.11) \times 10^{13}$ cm^{-2}.

3. Measurements and Results

Since hadron damage, as we have experimentally proven, only affects light transmission in the crystals,[2] the results shown here focus on this observable. Details to the measuring technique and precision can be found in Ref. 1, while details of this irradiation test can be found in Ref. 7. Measurements started one month after the end of irradiation, when the

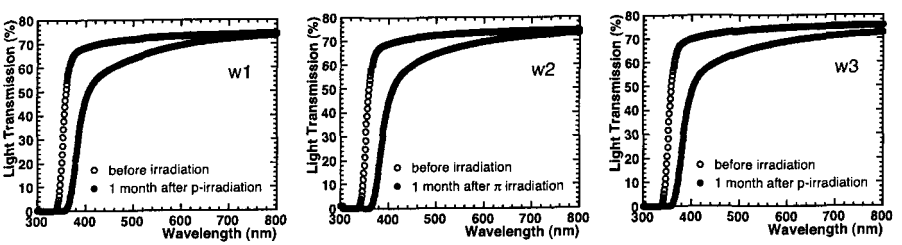

Fig. 1. Longitudinal Light Transmission data as a function of wavelength for the three crystals, measured 1 month after irradiation, compared to the Transmission before irradiation.

crystal radioactivity levels had dropped to a sufficiently low level for handling.

As a function of wavelength, the light transmission measured through the length of the crystal shows, after irradiation, the same behaviour for pions and protons (Fig. 1). In particular, the same band-edge shift is observed, which is characteristic for hadron-irradiated Lead Tungstate. It should be noted that similar damage amplitudes for the three crystals have been obtained on purpose through an appropriate choice of fluences for the two irradiations.

We quantify the damage through the induced absorption coefficient at the wavelength of 420 nm, which corresponds to the peak of the scintillation emission,

$$\mu_{IND}^{LT}(420\text{ nm}) = \frac{1}{\ell} \times \ln \frac{LT_0}{LT} \tag{1}$$

where LT_0 (LT) is the Longitudinal Transmission value measured before (after) irradiation through the length $\ell = 7.5$ cm of each crystal.

The evolution of damage with time for all three crystals is shown in Fig. 2, where it can be appreciated that pion damage follows the same pattern as observed for proton-irradiated crystals.[1] The data, as indicated by the lines, are well fitted by the same function used in Ref. 1, namely a sum of a constant plus two exponentials with time constants $\tau_1 = 17.2$ days and $\tau_2 = 650$ days. A similarly good fit is obtained through the form

$$\mu_{IND}^{LT,\,j}(420\text{ nm}, t_{\text{rec}}) = B_0^j \left(e^{-t_{\text{rec}}/\tau_2} + B_2\right) + B_1^j e^{-t_{\text{rec}}/\tau_1}. \tag{2}$$

where t_{rec} is the time elapsed since the irradiation and j, ($j = 1, 2, 3$) is

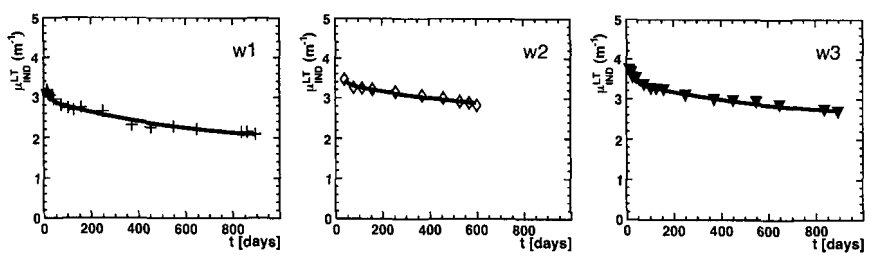

Fig. 2. Damage evolution as a function of time for crystals *w1* and *w3* after proton irradiation, and for crystal *w2* after pion irradiation, quantified through $\mu_{IND}^{LT}(420\text{ nm})$.

the crystal index. Here, B_2 is the same for all three crystals, and thus, for $t >> \tau_1$, this parametrisation yields a damage amplitudes ratio between crystals which is independent from elapsed time. The fits being almost indistinguishable, the comparison between crystals remains independent of the selected fit function. From Fig. 2 it is evident that most of the damage does not recover on a time scale of several years, while one should bear in mind that in Ref. 1 it was verified already, through irradiations at fluxes different by a factor up to 20, that the damage amplitudes and their recovery do not depend on flux.

For a more detailed damage comparison beyond the single values at 420 nm in Longitudinal Transmission, we have studied the evolution of induced absorption as a function of depth in the crystal. For this purpose, we have determined, analogously to Eq. 1 for LT, the transverse induced absorption coefficients $\mu_{IND}^{TT}(420\text{ nm})$ from measurements of the Transverse Light Transmission (TT) performed sideways at various positions along the crystals length. The profiles for this quantity are plotted in Fig. 3(a).

In Ref. 1 it was advocated that damage could be proportional to the density of stars, i.e. of inelastic hadronic interactions caused by a projectile above a given threshold energy. The very high local ionization, along their brief tracks, from fragments created in nuclear collisions was in fact supposed to be a possible distinctive mechanism for hadron damage. A qualitative confirmation of this hypothesis was already found in the Rayleigh-scattering behaviour of proton-damage reported on in Ref. 1. The comparison e.g. of the damage profile from protons in *w1* and *w3* with the simulated

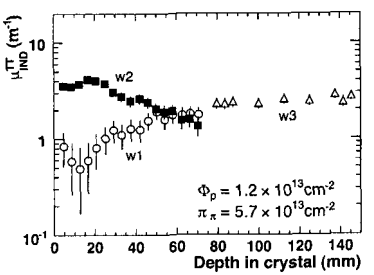

(a) Profile of induced absorption $\mu_{IND}^{TT}(420\text{ nm})$.

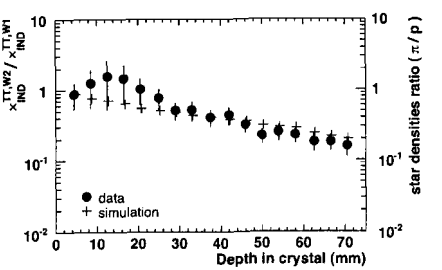

(b) Profile of normalised π- over p-induced damage ratios compared to the one of simulated pion-to-proton star density ratios

Fig. 3. Results from Transverse Light Transmission measurements

star densities profile in Fig.3 of Ref. 1, shows an agreement that confirms in a striking way the hypothesised mechanism.

We can thus answer the pending question from Ref. 1, whether the total track length of stars constitutes an additional factor that has to be taken into account to scale damage to a different particle spectrum. For this purpose, in Fig. 3(b) we have normalised the measured transverse damage from pions in *w2* and the one from protons in crystal *w1* to their respective particle fluences, and we have plotted their ratio as a function of depth. We also plotted the corresponding ratio of star densities obtained from the FLUKA simulations described in Ref. 1 and 9. The measured ratios and the star densities ratios are in agreement throughout, within the experimental uncertainties. Thus, for the considered particle types and energy range, we have established that the damage simply scales with the ratio of simulated star densities. The need for the total track length of stars as an additional scale factor is ruled out.

4. Conclusions

Irradiation studies with 20-24 GeV/c protons and ^{60}Co photons in a fluence regime as expected at the LHC demonstrate that hadrons cause a specific, cumulative damage in Lead Tungstate, which solely affects the crystals light transmission while their scintillation properties remain unaffected. With a pion irradiation we prove that the damage amplitudes caused by 24 GeV/c protons and 290 MeV/c pions in Lead Tungstate scale according to the star densities those particles cause in the crystals.

5. Acknowledgements

We warmly acknowledge the help of several people. The accelerator staff and in particular R. Steerenberg at CERN and A.-Ch. Mezger at PSI provided excellent beam conditions. M. Glaser and F. Ravotti helped with the proton irradiation and dosimetry facilities at CERN. F. Jaquenod and F. Malacrida performed the dosimetric measurements at PSI. M. Huhtinen contributed in the early phases of preparatory work.

References

1. M. Huhtinen, P. Lecomte, D. Luckey, F. Nessi-Tedaldi, F. Pauss, *Nucl. Instr. Meth.* ***A545*** *(2005) 63-87.*
2. P. Lecomte, D. Luckey, F. Nessi-Tedaldi, F. Pauss, *Nucl. Instr. Meth.* ***A564*** *(2006) 164-168.*

3. F. Nessi-Tedaldi, Proc. 9th Conf. on *Astroparticle, Particle and Space Physics, Detectors and Medical Physics Applications*, Como (Italy, 17-21 October 2005), Eds. M. Barone et al., World Scientific (Singapore, 2006), p.857-863.
4. *PSI Users Guide: Accelerators Facilities*, Paul Scherrer Institute, Villigen PSI (Switzerland, 1994) and *SIN Users Handbook*, SIN, Villigen (Switzerland, 1981).
5. C. Furetta, S.J. Bates, M. Glaser, F. Lemeilleur, E. Léon-Florian, C. Leroy, M. Tavlet, *Nucl. Phys. Proc. Suppl. 44 (1995) 503-509.*
6. E. Frlež et al., *Nucl. Instr. Meth.* ***A 526*** *(2004) 300-347.*
7. P. Lecomte, D. Luckey, F. Pauss, F. Nessi-Tedaldi and D. Renker, *preprint ETHZ-IPP-2007-02 (ETH Zurich, Switzerland) and arXiv:0709.4409, submitted to Nucl. Instr. Meth.*
8. M. Glaser, L. Durieu, F. Lemeilleur, M. Tavlet, C. Leroy, P. Roy, *Nucl. Instr. Meth.* ***A426*** *(1999) 72-77.*
9. M. Huhtinen, CERN (Geneva, Switzerland), private communication and http://indico.cern.ch/conferenceDisplay.py?confId=a03642

MEASUREMENTS OF NOISE AND STATIC PARAMETERS OF CMOS DEVICES AFTER 3 MEV PROTON IRRADIATION UP TO 120 MRAD

G. CRAMAROSSA, DE ROBERTIS, F. LODDO, C. MARZOCCA, A. RANIERI
DEE-Politecnico di Bari and INFN Bari, Via Orabona, 4 70126 Bari, Italy

L. CARRARESI, F. A. MIRTO
Dipartimento di Fisica dell'Università and INFN Firenze, Via G. Sansone, 1 50019 Sesto Fiorentino, Firenze, Italy

Deep submicron CMOS technologies nowadays open several interesting perspectives for analog applications in the field of High Energy Physics (HEP) at hadrons colliders like LHC. However, the exposure to ionizing radiation, typical of HEP applications, influences the static characteristics and the noise performances of deep-submicron MOS transistors employed in detector front-end circuits. The results of characterization measurements before and after protons irradiation carried out on CMOS devices with different form factors (W/L ratio), from a 0.13 μm commercial process at two different dose values, will be presented.

1. Irradiation conditions and experimental setup

In the literature, all the relevant data on effects caused by using protons on CMOS devices are mostly reported for energy values greater than some tens of MeV [1, 2]. Here we report data taken by using protons at 3 MeV, which release all their energy in about 100 μm of silicon, that is a significant fraction of the bulk thickness for a commercial silicon die. The proton beam line used for our tests, available at the Physics Department of Firenze University, produces a monochromatic protons beam of low energy up to 6 MeV. To reach two desired dose values, 12.5 Mrad and 120 Mrad respectively, the beam has been set up to provide a dose rate of about 1.7 Krad/s.

The devices considered in our experiments have been manufactured in a commercial CMOS process and feature an effective minimum gate length of 120 nm. In particular the test chips contain single MOSFETs with different aspect ratios W/L, designed according to the so called enclosed layout topology (ELT) to prevent post-irradiation leakage currents [3]. The maximum voltage applied to

the devices for the considered technology is 1.5V and the drain current I_{DS} has been limited to 1mA, which is usually an upper limit in the high-density integrated circuit designed for our particular applications. The gate-referred noise voltage spectrum (PSD) of the Device Under Test (DUT) has been measured by using a low-noise two-stage amplifier, suitably designed to read-out and amplify the drain current noise of the MOSFET under test[4].
The transistors have been kept under "worst case" bias conditions during the irradiation, i.e. all terminals grounded for PMOS transistors and all terminals grounded except the gate, which was kept at Vdd=1.5 V, for NMOS transistors. To better reproduce the physical operating conditions at the collider, after the irradiation, performed at room temperature, the annealing process has been prevented by keeping the devices at a temperature of about -4°C until the post-irradiation measurements have been carried out.

2. Pre and post-irradiation measurements of the static characteristics

Fig. 1 shows the comparison between the transfer curve $I_{DS}(V_{GS})$ measured for a PMOS and a NMOS device with the same aspect ratio W/L=100/0.24, before and after the irradiation with both the applied doses.
Since the discrepancies between pre and post-irradiation measurements appears to be very small for both devices, the good radiation tolerance of the considered technology combined with the proposed layout technique is confirmed. Note also that the effect of irradiation on the leakage current (I_{DS} at V_{GS} = 0) and the threshold voltage shift of both devices is negligible.

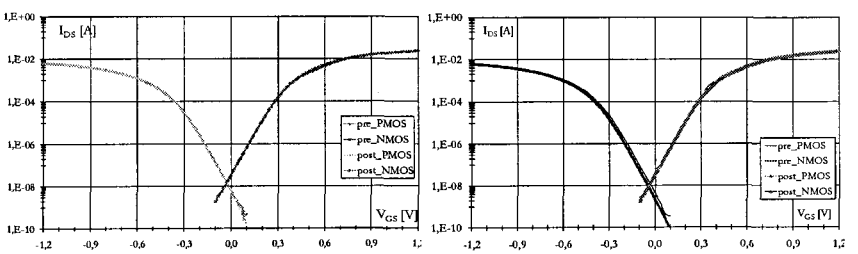

Fig. 1: Comparison of the transcharacteristics for PMOS and NMOS devices with expect ratio of W/L=100/0.24 for a total absorbed dose of 12.5 Mrad (left) and 120 Mrad (right) at V_{DS} = 0.3V

3. Pre and post-irradiation noise measurements

The general expression of the equivalent gate-referred noise spectral density $v_{in}^2/\Delta f$, for a MOSFET device is reported in equation (1):

$$\frac{\overline{v_{in}^2}}{\Delta f} = 4 \cdot K_B \cdot T \cdot n \cdot \gamma \frac{1}{g_m} + \frac{K_f}{C_{ox} \cdot W_{eff} \cdot L_{eff}} \frac{1}{f^{\alpha_f}} + 4 \cdot K_B \cdot T \cdot R_G + 4 \cdot K_B \cdot T \frac{g_{mb}^2}{g_m^2} R_B \qquad (1)$$

where the K_B is the Boltzmann's constant and T is the absolute temperature [5, 6]. The evaluation of the irradiation effects on the flicker noise parameters K_f and α_f is one of the main goals of our work. To evaluate these parameters measurements of the noise power spectral density (PSD) have been performed on the devices under test before irradiation, obtaining the following results. For instance in Fig. 2 we have compared the power spectral density of the equivalent input noise for the N and P devices with an aspect ratio of W/L= 1000/0.12, at a chosen bias point placed nearby the moderate inversion region. As already well known from the literature [7], in this region of operation the PMOS transistor exhibits better noise characteristics with respect to the NMOS counterpart at low frequencies, where flicker noise dominates, whereas in the high frequency part of the spectrum, where the dominant contribution to the PSD is due to thermal noise, the NMOS device is less noisy than the PMOS one, thanks to its higher transconductance values.

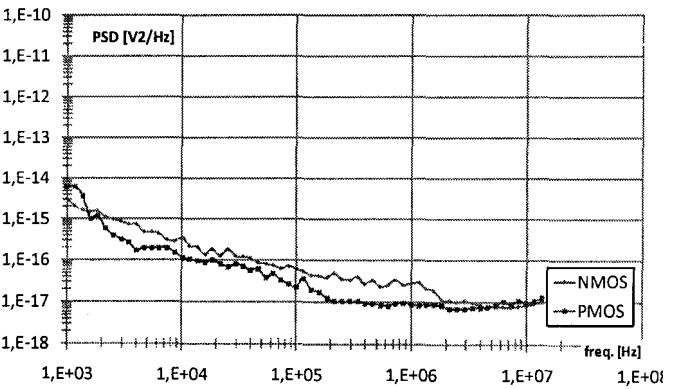

Fig. 2: Spectral density of equivalent input noise for NMOS and PMOS devices with W/L=1000/0.12 @ IDS = 152 μA and VDS = 330mV

In Fig. 3 the equivalent input noise of two NMOS devices, featuring the same width W=1000μm, but different channel length L, is depicted. As we can see, the 1/f noise increases as 1/L, as predicted by eq. (1). As a consequence, the difference between the values of the noise corner frequency is also apparent for the two devices.

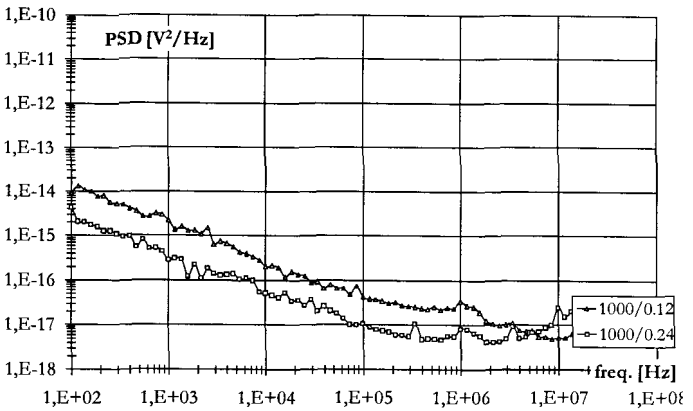

Fig. 3: Spectral density of equivalent input noise for two NMOS devices with W/L=1000/0.24 and W/L=1000/0.12 @ I_{DS} = 330 μA and V_{DS} = 300mV

From the slope of the noise spectral density curve at low frequencies the α_f parameter has been extracted for the MOSFETs of both kind characterized by W=1000μm, considering all the available lengths and different bias currents. The results do not allow to spot a clear dependence of the α_f parameter neither on the channel length nor on the bias drain current, at least in the operating inversion region analyzed. In our measurements we also found that $\alpha_{fN} < \alpha_{fP}$ still holds, as highlighted by other authors even for different technologies [8, 9, 10]. In Table 1 the average values of the α_f parameter measured for both devices have been reported.

Table 1. Average values of the measured α_f parameter for both NMOS and PMOS devices

	NMOS	PMOS
α_f	0.746±0.028	0.866±0.065

By applying a fitting method we estimated the value of the K_f parameter for N and P devices having an aspect ratio of 1000/0.12 measured at two biasing current values of 152μA and 235 μA. The obtained values for such parameter are listed in Table 2.

Table 2. K_f parameter for NMOS and PMOS devices with W/L=1000/0.12.

K_f [J $Hz^{(1-\alpha f)}$]	NMOS	PMOS
I_{DS} = 152μA	10.09E-25	20.22E-25
I_{DS} = 235μA	9.12E-25	34.21E-25

In our case the NMOS devices feature smaller values of K_f with respect to the PMOS ones, even though in the low frequency region they exhibit definitely larger noise levels, as it is apparent from Fig. 2, due to the smaller value of the slope parameter α_f. For other technologies with larger or even equal L_{min} values, the vice versa has been found for what concerns the relative value of the K_f parameters associated to NMOS and PMOS transistors. We have measured the K_f parameter before and after the irradiation at two different biasing current values for a PMOS device with W=1000μm and L=0.48μm for an absorbed total dose of 120 Mrad, and the obtained result is shown in Table 3.

Table 3. K_f parameter value measured for a PMOS device before and after a dose of 120 Mrad

PMOS 1000/0.48	I_{DS}=100μA	I_{DS}=200μA
Pre-rad	45.19E-26	46.47E-26
Post-rad (120 Mrad)	30.12E-25	37.13E-25

References

1. S. Gerardin *et. al.*, *IEEE Transactions on Nuclear Science*, Vol. **53**, No. 4 (2006).
2. E. Simoen, *IEEE Transactions on Nuclear Science*, Vol. **50**, No.6 (2003).
3. F.Faccio, *et.al., IEEE Transactions on Nuclear Science*, Vol. **52**, No. 6 (2005)
4. G.Cramarossa, Thesis, Bari 2006, to be published.
5. P.R. Grey, R.G. Meyer, *Analysis and Design of Analog Integrated Circuits*, Wiley & Sons Inc.,New York, 4'th Ed.
6. S. Tedja, *et.al., IEEE Transactions on Nuclear Science* Vol. **39**, No. 4 (1992).
7. M. Manghisoni *et.al., IEEE Transactions on Nuclear Science*, Vol. **53**, No. 4 (2006).
8. G. De Geronimo *et. al., IEEE Transactions on Nuclear Science* Vol. **52**, No. 6 (2005).
9. M. Manghisoni *et. al., IEEE Transactions on Nuclear Science* Vol. **52**, No. 6 (2005).
10. M. Manghisoni et. al., *IEEE Transactions on Nuclear Science* Vol. **53**, No. 4 (2006).

STUDY OF LITHIUM DIFFUSION INTO SILICON-GERMANIUM CRYSTALS

ARIE RUZIN
Faculty of Engineering, Tel Aviv University, 69978 Tel Aviv, Israel

NIKOLAI ABROSIMOV
Institute for Crystal Growth (IKZ) 12489 Berlin, Germany

PIOTR LITOVCHENKO
Institute for Nuclear Research, Ukraine Academy of Science, Kiev, Ukraine

In this study lithium atoms were diffused into single crystal, Czochralski grown silicon-germanium. It is shown that the diffusion coefficient has a considerable dependence on germanium concentration. In addition the surface concentration of lithium in silicon germanium is significantly higher than the values reported for float zone grown pure silicon crystals. The study compares direct and indirect characterization methods used to determine the lithium profile in silicon germanium. The $Si_{1-x}Ge_x$ semiconductors used in this study contain 2.6% and 5.4% (atomic concentration) of germanium and have measured resistivities of 100-200 Ω×cm.

1. Introduction

Epitaxial layers of silicon-germanium were studied extensively for some years for applications in the microelectronics VLSI industry [1-3]. However the demands of the VLSI industry translate into thin layers of mainly strained semiconductor with rather high doping levels. Recently bulk grown silicon-germanium draws increasing attention for applications of detection and imaging of X -and Gamma-ray photons, heterojunction solar cells [4], and possibly for microwave devices. In X- and gamma-ray detectors the active volume of the detector determines the detection efficiency, thus the conventional epitaxial layer of up to a few microns thickness are not useful. The thicknesses of interest for such detectors start at several hundreds of microns. In addition, the large active volume implies that the electric field has to extend throughout the device, namely the depletion layer has to be several hundreds of microns thick. To

obtain such depletion layers without reaching breakdown voltage limits the resistivity of the semiconductor should be preferably in the range of kΩ×cm.
Currently only few laboratories grow successfully single crystal, bulk silicon-germanium. The main challenge is to keep the germanium concentration uniform. The float zone process in known in general to yield material with high resistivity, but up to now the diameter of the $Si_{1-x}Ge_x$ grown ingots grown by float zone (FZ) is about 10 mm [5]. The Czochralski (Cz) grown silicon-germanium crystals are grown with ingot diameters of about 40 mm and recently the control over the material resistivity has improved a great deal [6]. However, the resistivity reproducibility, uniformity and control remain challenges. Currently it is possible to grow Cz-$Si_{1-x}Ge_x$ samples with resistivities of up to several hundreds Ω×cm.
Lithium has already been shown to behave as a shallow donor-like dopant and to diffuse rapidly in silicon and germanium crystals [7,8]. The method of lithium auto-compensation of p-type silicon was implemented successfully in SiLi detectors. However lithium was diffused into float zone grown silicon, which has relatively low oxygen concentration. Attempts to diffuse lithium into Cz-grown silicon were not very successful probably due to a significant oxidation of the lithium atoms in the lattice and the formation of non mobile complexes with oxygen. On the other hand in silicon-like alloy, namely silicon-germanium with low germanium content, the germanium atoms create local strains. Such strains should enhance the diffusion of lithium which diffuses through interstitial positions.
The characterization of lithium diffusion was almost always performed by indirect measurements of lithium concentration. Such was the method of measuring the p-n junction depth used by Fuller et al. [9]. The same author later proposed another, improved method based on the measurement of lithium ion drift under the influence of electric field [10]. The method is very similar to the Haynes-Shockley method [11], and the diffusion coefficient is calculated from the Einstein relationship, however the drift of the lithium atoms is monitored indirectly by the measurement of the p-n junction location. Keffous *et al.* used Cu deposition under light from a solution of CuSO4:5H2O and hydrofluoric acid [12]. It is known that the Cu atoms from the solution are absorbed selectively to the lithium rich, n-type surface. The measurement of the junction depth was done by SEM observation of the surface, and by four point probe measurements, where sheet resistivity was measured after consecutive polishing steps. Although it is known that lithium atoms can form complexes with oxygen atoms rather than becoming interstitial dopants with low ionization energy, it

was assumed in all cases that *all* the lithium atoms act as regular dopants. The assumption can be justified by the use of high quality, float zone grown silicon with low oxygen concentration.

Samples used in this study were Cz-grown $Si_{1-x}Ge_x$ single crystals with atomic germanium concentration of 2.4% and 5.6% and resistivities of 100 to 200 Ω×cm. The samples were diffused with lithium at temperatures 300°C and 320°C for 15 and 10 minutes, respectively. In one sample the lithium was partially drifted following the diffusion process. Then the samples were characterized by secondary ion mass spectrometry (SIMS), spreading resistivity profiling on a polished bevel, and by atomic force microscope in the contact potential difference mode (CPD).

The secondary ion mass spectrometry was performed after the remaining oxidized layer of the lithium was sputtered away from the surface. The sensitivity of the SIMS system to lithium is a few times 10^{15} cm^{-3}.

2. Results and discussion

Following the exposure to air most of the lithium layer is oxidized and washed away, but some residuals remain, therefore secondary ion mass spectroscopy characterization was performed after removal of the lithium residuals from the $Si_{1-x}Ge_x$ surface by sputtering. The concentrations of lithium atoms measured after 10 minutes diffusion at 320°C in two samples, with x= 0.024 and 0.056 are shown in figure 1.

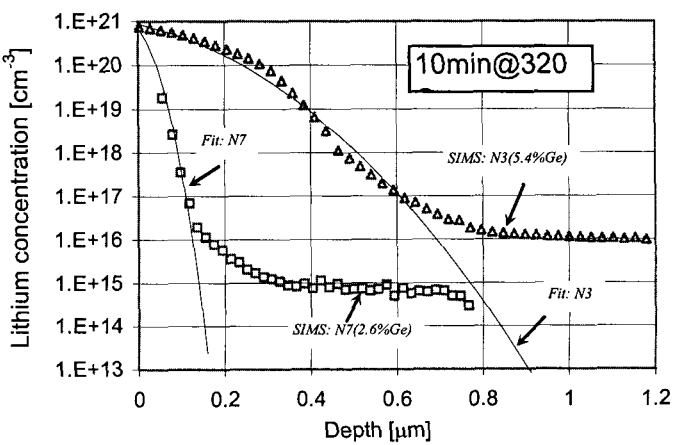

Figure 1. Lithium concentration in $Si_{1-x}Ge_x$ crystals following 10 minutes diffusion at 320C. The concentration was measured in samples with 2.4% and 5.4% Ge (atomic concentration). The solid lines describe diffusion equation fits.

The solid lines describe fits of the experimental data to the diffusion equation from an infinite source:

$$N(t,x) = N_S \times erfc\left[\frac{x}{2\sqrt{D \cdot t}}\right] \quad (1)$$

where $N(t,x)$ is lithium concentration at distance x from the surface after time t; D is the diffusion coefficient at a given temperature in [cm^2/sec]; and N_S is lithium surface concentration. The best fits were achieved using the following parameters: $D_{N3}=2.3\times10^{-13}$ [cm^2/sec], $N_{S,N3}=1\times10^{21}$ [cm^{-3}], $D_{N7}=7\times10^{-15}$ [cm^2/sec], and $N_{S,N7}=7\times10^{20}$ [cm^{-3}]. It is clearly seen, both from the data curve and the fit parameters that the diffusion coefficient under similar diffusion conditions increases significantly with the increasing germanium concentration. The fitted diffusion coefficients are also much lower than the values reported in FZ silicon at similar temperatures [12]. Another interesting feature is the concentration of lithium at the surface. The concentration is higher than the solubility limit reported in FZ silicon, thus either the lithium atoms segregate or the solubility of lithium in $Si_{1-x}Ge_x$ crystals is considerably higher than the solubility reported in FZ silicon [12]. The dependence of surface concentration of lithium on germanium concentration of the alloy is less pronounced than that of diffusion coefficient; however with only two germanium concentrations available for this experiment no solid conclusions can be drawn.

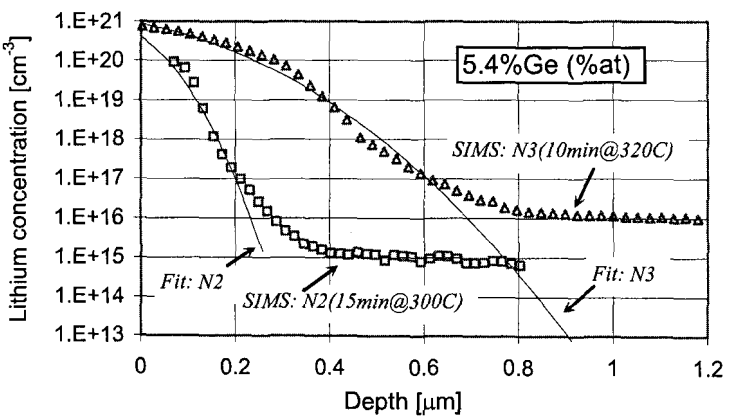

Figure 2. Lithium concentration in $Si_{1-x}Ge_x$ crystals with 5.4% Ge atomic concentration. The concentration was measured on similar samples following 15 minutes diffusion at 300C, and following 10 minutes diffusion at 320C. The solid lines describe diffusion equation fits.

The dependence of diffusion parameters on temperature can bee seen on figure 2. The material used in both experiment is from the same wafer with 5.6% germanium. Once again, the dependence of lithium diffusion coefficient on temperature is very pronounced whereas the dependence of surface concentration is vague.
Additional, indirect measurement of diffusion depth was performed using spreading resistivity measurement of the samples on a surface polished at approximately 2° bevel. The results shown in figure 3 indicate junction depths of 16 μm and 4 μm on samples with 5.4 and 2.6 percents germanium concentration, respectively.

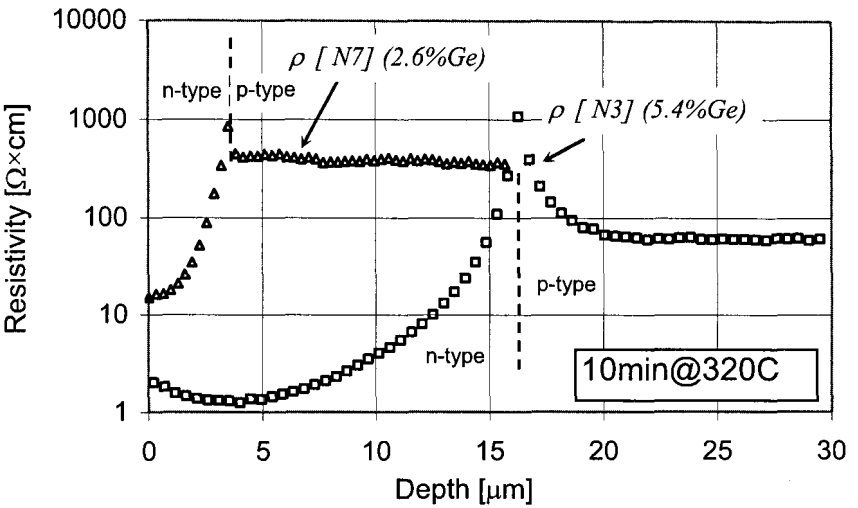

Figure 3. Spreading resistivity measured on a 2° polished bevel of lithium diffused $Si_{1-x}Ge_x$ crystals following 10 minutes diffusion at 320C. The samples contain 2.6% and 5.4% germanium (atomic percentage).

The resistivity of the lithium rich, n-type region near the surface indicates the concentration of *active* lithium. It is clearly seen in figure 3 that following identical diffusion procedure the surface resistivity of the sample with 5.4% germanium is approximately an order of magnitude lower than that of the sample with 2.6% germanium concentration. Thus there is much more active lithium in the sample with higher germanium content.
Spreading resistivity results of similar samples with 5.4% germanium after diffusion at 300°C (15 minutes) and 320°C (10 minutes) are shown in figure 4. The junction depth following 320°C diffusion is 16 μm and following 300°C diffusion only 5 μm. It should be noted that although the junction depth

difference is somewhat larger in this experiment than in the one shown in figure 3. The surface resistivity difference is smaller. In other words at a given germanium concentration, diffusion temperature affects greatly the diffusion coefficient, but less the active lithium concentration near the surface.

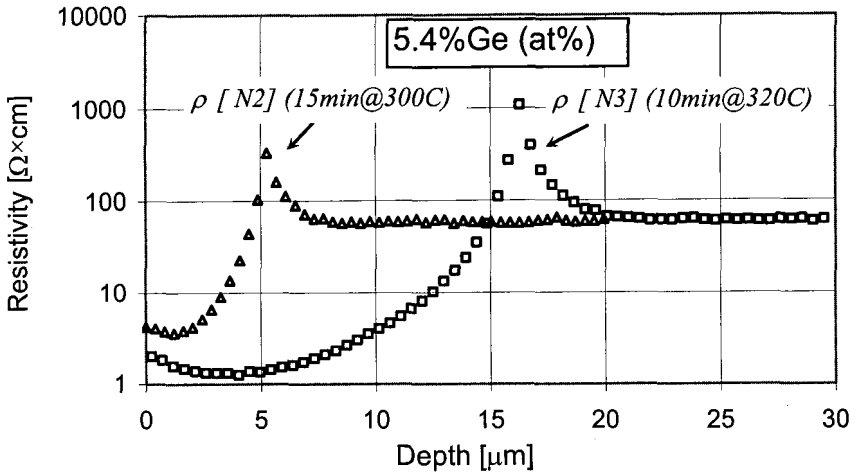

Figure 4. Spreading resistivity measured on a 2° polished bevel of lithium diffused $Si_{1-x}Ge_x$ crystals with x=0.054 (5.4% germanium), following 10 minutes diffusion at 320C and 15 minutes at 300C.

The direct measurement of lithium concentration was performed by secondary mass ion spectrometry (SIMS), and the results indicate clearly that the diffusion coefficient depends on temperature and germanium concentration. Indirect measurements performed by spreading resistance point to the same effect. However, there is a significant divergence of the values obtained by direct and indirect methods. While the SIMS results indicate diffusion of less than 1 μm depth, the spreading resistivity results show much deeper penetration of lithium. It should be said that the limit of SIMS sensitivity is a few times 10^{15} cm^{-3} whereas the maximum concentration of active lithium estimated from the spreading resistivity results is of the same order of magnitude. In addition atomic force microscope was used in contact potential difference mode (CPD) on the 5.6%Ge sample diffused for 10 minutes at 320°C. The results indicate that the n-region in the sample is about 15 μm thick, in agreement with the spreading resistivity results. The discrepancy of the direct and indirect characterization methods is under further investigation.

Acknowledgments

This work is supported by grant 965/05 of the Israeli Science Foundation. The authors wish to thank Dr. V. Dubovoj for his assistance in lithium diffusion experiments.

References

1. M. Miyamoto, N. Sugii, Y. Hoshino, Y. Yoshida, M. Kondo, Y. Kimura, K. Ohnishi, *IEEE Trans. On Electron Dev.* 54 (9), 2460 (2007).
2. F. Schwierz, J. J. Liou, *Solid State Elect.* 51 (8) 1079 (2007).
3. Z. Q. Ma, N. Y. Jiang, G. G. Wang, S. A. Alterovitz, *IEEE Electron Dev. Lett.* 26 (6) 381 (2005).
4. T. Matsui, C. W. Chang, M. Kondo, K. Ogata, M. Isomura, *Appl. Phys. Lett.*, 91 (10) (2007).
5. I. G. Atabaev, N. A. Matchanov, E. N. Bakhranov, *Phys. Of Solid State* 43 (12) 2234 (2001).
6. O. V. Smirnova, V. V. Kalaev, Y. N. Makarov, N. V. Abrosimov, H. Riemann, *J. of Crystal Growth* 287 (2): 281 (2006).
7. C. S. Fuller and J. A. Ditzenberger, *Phys. Rev.* 91, 193 (1953).
8. C. J. Wen, R. A. Huggins, *J. of Solid State Chem.* 37 (3) 271 (1981).
9. Fuller, Theuerer, and van Roosbroeck, *Phys. Rev.* 85 678 (1952).
10. C. S. Fuller and J. C. Severiens, *Phys. Rev.* 96, Num.1 21 (1954).
11. J. H. Haynes and W. Shockley, *Phys. Rev.* 81 835 (1951).
12. A. Keffous, T. Hadjersi, A. Cheriet, K. Bourenane, N. Gabouze, Y. Boukennous, F. Kezzoula, M. Amini. Zitouni, H. Menari, *J. Vacuum* 81 417 (2006).

RADIATION HARDNESS STUDIES IN A CCD WITH HIGH-SPEED COLUMN PARALLEL READOUT

ANDRÉ SOPCZAK

Lancaster University, UK; On behalf of the LCFI Collaboration;
E-mail: Andre.Sopczak@cern.ch

Charge Coupled Devices (CCDs) have been successfully used in several high energy physics experiments over the past two decades. Their high spatial resolution and thin sensitive layers make them an excellent tool for studying short-lived particles. The Linear Collider Flavour Identification (LCFI) collaboration is developing Column-Parallel CCDs (CPCCDs) for the vertex detector of the International Linear Collider (ILC). The CPCCDs can be read out many times faster than standard CCDs, significantly increasing their operating speed. The results of detailed simulations of the charge transfer inefficiency (CTI) of a prototype CPCCD are reported and studies of the influence of gate voltage on the CTI described. The effects of bulk radiation damage on the CTI of a CPCCD are studied by simulating the effects of two electron trap levels, 0.17 and 0.44 eV, at different concentrations and operating temperatures. The dependence of the CTI on different occupancy levels (percentage of hit pixels) and readout frequencies is also studied. The optimal operating temperature for the CPCCD, where the effects of the charge trapping are at a minimum, is found to be about 230 K for the range of readout speeds proposed for the ILC. The results of the full simulation have been compared with a simple analytic model.

Keywords: LCFI, CPCCD, CCD, charge transfer inefficiency, radiation damage

1. Introduction

Particle physicists worldwide are working on the design of a high energy collider of electrons and positrons (the International Linear Collider or ILC) which could be operational sometime around 2019. Any experiment exploiting the ILC will require a high performance vertex detector to detect and measure short-lived particles, yet be tolerant to radiation damage for its anticipated lifetime. One candidate is a set of concentric cylinders of Charge-Coupled Devices (CCDs), read out at a frequency of around 50 MHz.

It is known that CCDs suffer from both surface and bulk radiation damage. However, when considering charge transfer losses in buried chan-

nel devices only bulk traps are important. These defects create energy levels (traps) between the conduction and valence band, and electrons are captured by them. These electrons are also emitted back to the conduction band after a certain time.

It is usual to define the Charge Transfer Inefficiency (CTI) as the fractional loss of charge after transfer across one pixel. An initial charge Q_0 after being transported across m pixels is reduced to $Q_m = Q_0(1 - \mathrm{CTI})^m$. For CCD devices containing many pixels, CTI values around $\mathbf{10^{-5}}$ are important. Previous results for a CCD with sequential readout have recently been reported.[1] The expected background rate at the future ILC near the interaction point leads to radiation damage in the CCD detector. The trap concentrations used in the simulation are listed in Fig. 1. They correspond to about 3 years of operation for the 0.17 eV traps and several more years for the 0.44 eV traps.

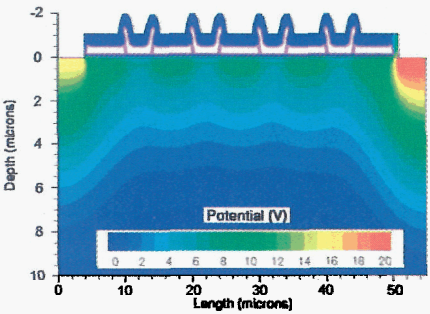

$E(eV)$	C (cm^{-3})	σ_n (cm^2)
0.17	1×10^{12}	1×10^{-14}
0.44	1×10^{12}	1×10^{-15}

Fig. 1. Left: Detector structure and potential at gates (nodes) after initialization. The pixel is located around between 20 and 40 μm length. Right: Energy levels E, trap concentrations C, and electron-capture cross-section σ_n used in simulation.

2. Simulations

The UK Linear Collider Flavour Identification (LCFI) collaboration[2] has been studying a CCD with high-speed (50 MHz) column-parallel readout produced by e2V Technologies. It is a two-phase buried-channel CCD with 20 μm square pixels.

Simulations of a simplified model of this device have been performed with the ISE-TCAD package (version 7.5), particularly the DESSIS program (Device Simulation for Smart Integrated Systems). The simulation is essentially two dimensional and assumes a 1 μm device thickness (width) for calculating densities. The overall length and depth are 55 μm and 20 μm respectively (Fig. 1).

Parameters of interest are the readout frequency, up to 50 MHz, and the operating temperature between 130 K and 300 K although simulations have been performed up to 440 K. The charge in transfer and the trapped charge are shown in Fig. 2.

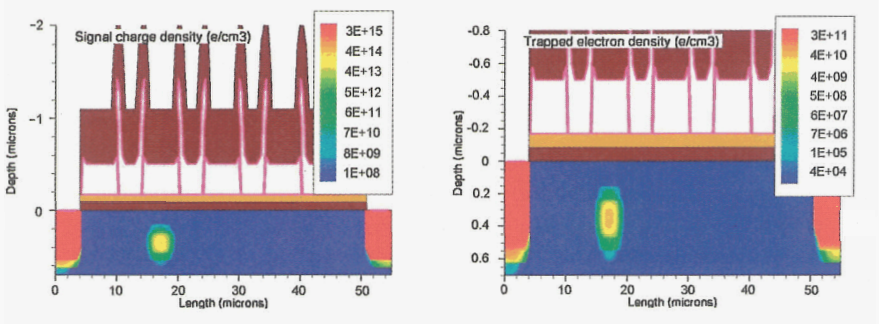

Fig. 2. Left: Signal charge density. Right: Trapped charge density.

Charge Transfer Inefficiency is a measure of the fractional loss of charge from a signal packet as it is transferred over a pixel, or two gates. After DESSIS has simulated the transfer process, a 2D integration of the trapped charge density distribution is performed independently to give the total charge under each gate.

This CTI study, at nominal clock voltage, focuses only on the bulk traps with energies 0.17 eV and 0.44 eV below the bottom of the conduction band. These will be referred to simply as the 0.17 eV and 0.44 eV traps. The 0.17 eV trap is an oxygen-vacancy defect, referred to as an A-centre defect. The 0.44 eV trap is a phosphorus-vacancy defect, an E-centre defect, as a result of the silicon being doped with phosphorus and a vacancy manifesting from the displacement of a silicon atom bonded with a phosphorus atom.[3]

3. Simulation Results

The CTI dependence on temperature and readout frequency was explored and Figure 3 shows the CTI for simulations with partially filled 0.17 eV and 0.44 eV traps at different frequencies for temperatures between 130 K and 440 K, with a nominal clock voltage of 3 V. The CTI value depends linearly on the trap concentration for a large concentration variation as also shown in Fig. 3. The CTI values for a variation of the 0.17 eV trap level by 0.005 eV and for 0.1% and 1% hit (pixel) occupancy are shown in Fig. 4. Figure 5 shows the results of a study of a clock voltage induced CTI in order to find the optimum clock voltage with a low power consumption and keeping the CTI at an acceptable level.

4. Comparisons with an Analytic Model

The motivation for introducing an analytic model is to understand the underlying physics through making comparisons with the TCAD simulations.

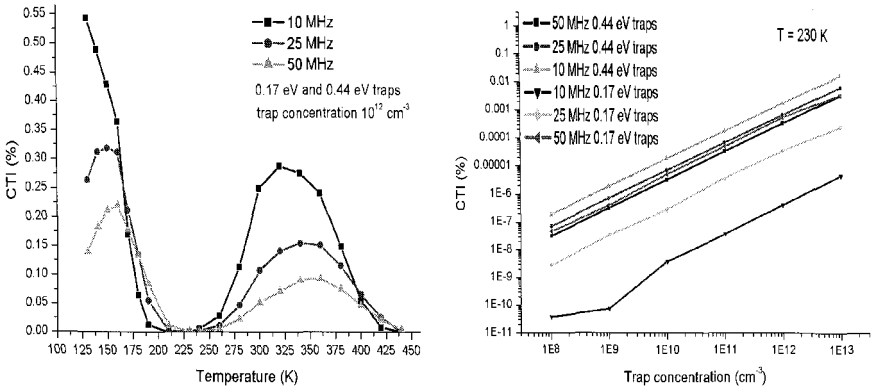

Fig. 3. Left: CTI values for 0.17 and 0.44 eV traps at clocking frequencies 10, 25 and 50 MHz. Right: CTI values for a large range of trap concentrations.

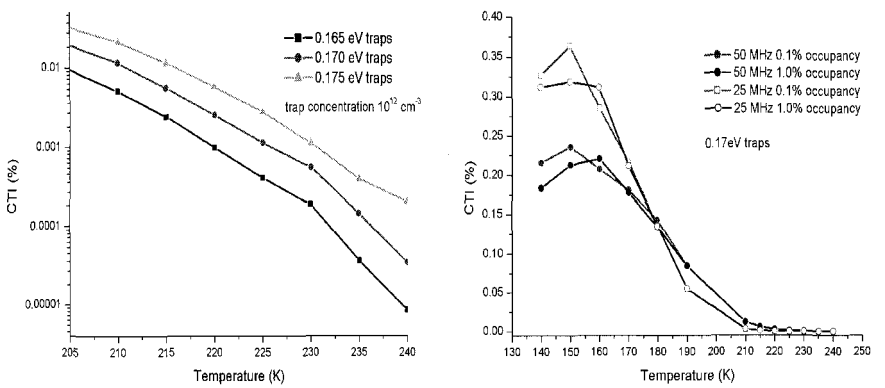

Fig. 4. Left: CTI values for 0.165, 0.170 and 0.175 eV traps. Right: CTI values for 0.1% and 1% hit (pixel) occupancy.

This might then allow predictions of CTI for other CCD geometries without requiring a full simulation. A simple analytic model[1] has been adapted to the CPCCD characteristics. Figure 5 compares the full TCAD simulation for 0.17 eV traps and clocking frequency of 50 MHz to this Analytic Model. It emphasises the good agreement between the model and full simulations. As an application the variation of hit occupancy is also shown.

However, there are limitations with the analytic model. They could relate to a breakdown of the assumptions at high temperatures, to ignoring the precise form of the clock voltage waveform, or to ignoring the pixel edge effects. Further studies are required.

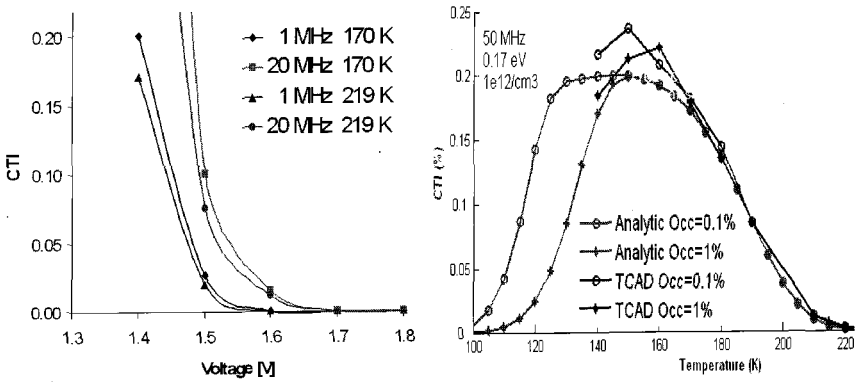

Fig. 5. Left: Clock voltage induced CTI. Right: CTI values for 0.17 eV traps at clocking frequency 50 MHz. Comparison of the analytic model with the full TCAD simulation for two hit (pixel) occupancies of 0.1% and 1%.

5. Conclusions and Outlook

The Charge Transfer Inefficiency (CTI) of a CCD with high-speed column parallel readout has been studied with a full simulation (ISE-TCAD DESSIS) and compared with an analytic model. The 0.17 eV and 0.44 eV trap levels have been implemented in the full simulation and variations of the CTI with respect to temperature and frequency have been analysed. At low temperatures (< 230 K) the 0.17 eV traps dominate the CTI, whereas the 0.44 eV traps dominate at higher temperatures. Good agreement between simulations and an analytic model adapted to the CPCCD has been found. The optimum operating temperature for the CPCCD prototype in a high radiation environment is found to be about 230 K for clock frequencies in the range 10 to 50 MHz. Our prototype CPCCD has recently operated at 45 MHz and a test-stand for CTI measurements is in preparation. The development of a high-speed CCD vertex detector is on track as a vital part of a future ILC detector.

Acknowledgments

This work is supported by the Science and Technology Facilities Council (STFC) and Lancaster University. I would like to thank my LCFI colleagues and in particular Salim Aoulmit, Khaled Bekhouche, Chris Bowdery, Craig Buttar, Lakhdar Dehimi, Michael Koziel, Dzmitry Maneuski, Konstantin Stefanov and Tuomo Tikkanen for significant contributions to this work.

References

1. A. Sopczak et al., IEEE Trans. Nucl. Sci., 54 (2007) 1429.
2. LCFI collaboration homepage: http://hepwww.rl.ac.uk/lcfi
3. K. Stefanov et al., IEEE Trans. Nucl. Sci., 47 (2000) 1280.

Radiotherapy and Medical Instrumentations

Organizers:

S. Pospisil
Medical Application Instrumentation
V. Sossi
Radiotherapy and Medical Imaging

G. Bartesaghi	Fricke Gel Dosimeter Tissue-Equivalence: a Monte Carlo Study
C. Cappellini	Optimised Operation of the MIMOSA5 Pixel Sensor for Biological Sample Imaging
V. Chmill	Silicon Photo Multipliers Characterization: Recent Achievements and Latest Results. Investigation of SiPM for Photon Counting Applications.
D.B. Crosetto	Ignored Discovery now proven Capable of Saving Millions of Lives from Premature Cancer Death demands rethinking the Direction of Research
J. Dammer	Real-time X-ray μ-imaging of Living Organisms
R. De Leo	The Axial 3-D Pet Concept implemented by Wave Length Shifter Strip Hodoscopes
A.R. Faruqi	Application of Pixel Detectors in Structural Biology
P. Le Dû	Ultra-fast Timing and the Application of High Energy Physics Technologies to Biomedical Imaging
M.L. Magliozzi	First Results of Small Animal Imaging SPECT Detector for Cardiovascular Disease Studies on Mice
A. Nardulli	Development of a Low Noise Optoelectronic Integrated Readout with N-I-P a-Si:H Photodiode Array for Positron Emission Tomography
S. Nill	The use of modern electronic flat panel devices for image guided radiation therapy: Image quality comparison, intra fraction motion monitoring and quality assurance applications
S. Scazzi	Neutron Imaging in a Hospital Environment.
M. Thomas	Implementation of Image-guidance Techniques in Radiation Therapy
E. Vallazza	A Double Layer Silicon Detector for Single Photon Counting

FRICKE GEL DOSIMETER TISSUE-EQUIVALENCE: A MONTE CARLO STUDY

M. VALENTE, G. BARTESAGHI, G. GAMBARINI
Physics Department of the University of Milan and INFN, Milan, Italy

D. BRUSA, G. CASTELLANO
FaMAF, Universidad Nacional de Córdoba and CONICET, Córdoba, Argentina

M. CARRARA
Istituto Nazionale Tumori, Milan, Italy

Gel dosimetry has proved to be a valuable technique for absorbed dose distribution measurements in radiotherapy. FriXy-gel dosimeters consist of Fricke (ferrous sulphate) solution infused with xylenol orange. The solution is incorporated to a gel matrix in order to fix it to a solid structure allowing good spatial resolution and is imaged with a transportable optical system, measuring visible light transmittance before and after irradiation. This paper presents an evaluation of total photon mass attenuation coefficients at energies in the range of 50 keV-10MeV for the radiochromic FriXy gel dosimeter sensitive material. Mass attenuation coefficient estimations have been performed by means of Monte Carlo (PENELOPE) simulations. These calculations have been carried out for the FriXy gel sensitive material as well as for soft tissue (ICRU) and pure liquid water; a comparison of the obtained data shows good agreement between the different materials.

1. Introduction

Radiochromic Fricke (ferrous sulphate) and Xylenol Orange infused gels, shaped in thin slices [1], constitute a dosimetric tool in continuous improvement that gives noticeable results [2].

One of the most important required characteristics in dosimetry is the tissue-equivalence: it is important to evaluate the dosimeter response for different type of radiations as well as for the range of energies in which the dosimeter will be used.

Nowadays, photon beams are widely employed in radiotherapy. The tissue-equivalence for photon beams can be ensured by checking the total mass attenuation coefficient. The basis-vector model (BVM) [3] assumes that attenuation coefficients of any biological substance can be approximated by a

linear combination of mass attenuation coefficients of the various basic substances. The partial attenuation coefficient for photoelectric absorption is proportional to the molecular photoelectric cross section, being independent of the density of the material. Analogous definitions apply for the other interaction processes. Then, the total mass attenuation coefficient is obtained as the weighted linear combination of the cross sections from the components.

Several experimental arrangements and techniques have been designed for mixture compounds mass attenuation coefficient measurements. Monte Carlo (MC) methods have demonstrated to be a simple and useful technique for radiation-matter parameters evaluation [4]. In this work, a dedicated MC subroutine has been employed to perform total photon mass attenuation coefficient determinations.

2. Materials and Methods

The mass attenuation coefficient and the mass energy-absorption coefficient are basic quantities used in calculations of the penetration and the energy deposition by photons (x-ray, gamma rays and bremsstrahlung) in biological, shielding and other materials. These coefficients are defined in ICRU Report 33 (1980) and have been discussed in detail [5]. As a first approximation, compound and mixture mass attenuation values can be obtained by simple additivity, i.e., combining values for the elements according to their proportions by weight. However, due to radiative losses (bremsstrahlung production, annihilation in flight, etc.), simple additivity could be no longer adequate [5].

The mass attenuation coefficient (μ) is defined by:

$$I = I_0 \, e^{-\mu x} \qquad (1)$$

where I stands for transmitted intensity, I_0 stands for the incident intensity and x stands for the sample thickness. Then, Eq. 1 can be rewritten as :

$$\ln[I(x)] = \ln[I_0] - \mu \, x \qquad (2)$$

Eq. 2 is a linear equation for the thickness of the target, in which the slope is the mass attenuation coefficient. In order to ensure good tissue-equivalence for photon beams it is necessary to compare total photon cross-sections, which are correlated to total mass attenuation coefficient by:

$$\frac{\mu}{\rho} = \frac{N_{Av}}{A}\left(\sigma_{Ph} + \sigma_{Co} + \sigma_{PP} + \sigma_{Ray}\right) = \frac{N_{Av}}{A}\sigma_T \qquad (3)$$

where N_{Av} is the Avogadro's number and A is the mean molecular weight.

Monte Carlo codes are widely applied for several calculations due to their simplicity and accuracy. In this work, MC calculations have been performed using the PENELOPE package. The simulation main program has been based on the sample PENCYL provided in the 2003 PENELOPE distribution. Target samples in form of thin layers of different thicknesses and monochromatic incident photon beams (1mm spot) have been considered, according to the usual experimental arrangements. In order to check the FriXy gel tissue-equivalence, three sample compositions (FriXy gel sensitive material, soft tissue (ICRU) and pure liquid water) have been simulated. In particular, the composition of a FriXy gel sample (200g) has been set as follows: Ultra pure water: 192g, Xylenol orange: 0.0251g, Ferrous sulphate: 0.0392g, Sulphuric Acid: 2.78ml, Gel Powder (Porcine skin): 6.00779g.

The proposed dosimetry method consists in evaluating the transmission intensities $I(x)$ for several thicknesses and different energies, employing every time the same source, a monoenergetic photon beam and a fixed quantity of incident particles, since in practice I_0 remains constant during the experiments. In order to ensure accurate results, 10^7 primary tracks have been considered, which was enough for this purpose. With the aim of evaluating the mean mass attenuation coefficients, five different target thicknesses for each energy (in the range from 50keV to 10MeV) have been considered. The dedicated subroutine allows to place a detector beyond the target, which can detect the transmitted particles discriminating energy, scattering angle and type of particle. With this information it is possible to determine the transmitted beam intensities $I(x)$, allowing a straightforward determination of the mean mass attenuation coefficient by means of Eq. 2.

3. Results

The adapted subroutine simulates the transmitted intensities $I(x)$ as the fraction of primary particles crossing a material slab at 0° deflection angle. For each target composition (pure liquid water, soft tissue (ICRU) and FriXy gel sensitive material), μ values have been obtained by means of a linear fit (Eq. 2).

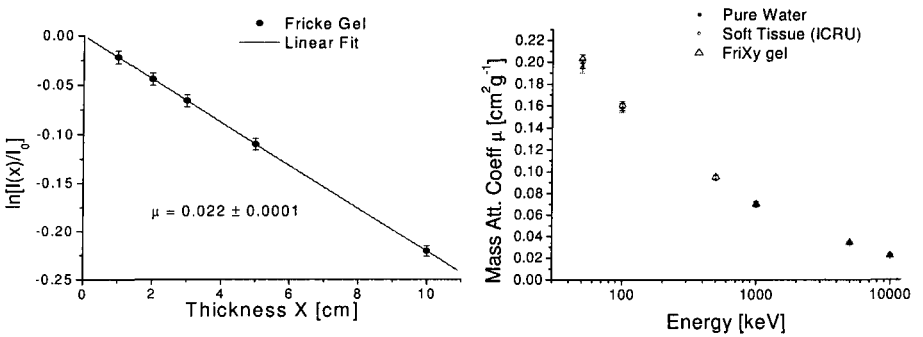

Figure 1. On the left: example of linear regression for total mass attenuation coefficient determination (10MV photon incident beam). On the right: Total Mass Attenuation Coefficient for FriXy gel sensitive material and reference materials (water, soft tissue).

Going on as established in the proposed method, the obtained results for the total mass attenuation coefficient corresponding to different compounds have been calculated (see Figure 1).

The similarity of the found profiles is encouraging, since they are a first indicator of tissue equivalence between the different simulated materials. In view of these results, in-phantom dose distribution have been obtained by means of MC calculations. A dedicated MC subroutine has been developed for a linear accelerator irradiation simulation [6]. For an 18MV linear accelerator photon beam, the obtained results for depth-dose distributions and isodose curves are shown in Figures 2. Similar results have been obtained for every sample compound corresponding to several energies in the range from 50keV to 10MeV.

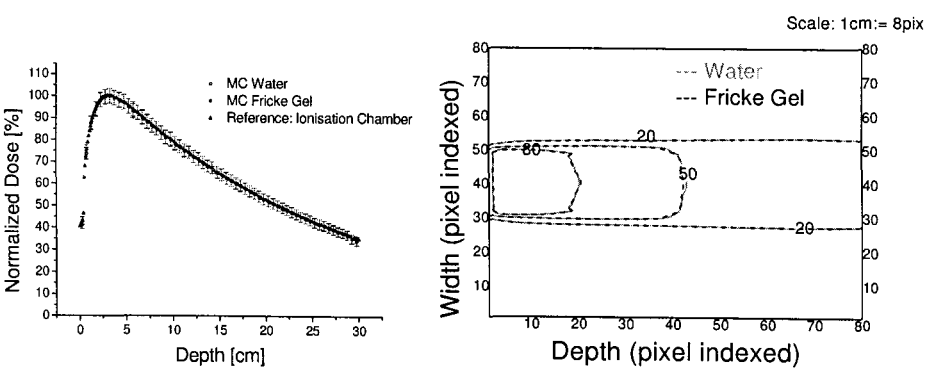

Figure 2. On the left: in-phantom depth dose (normalized) profiles for a 18MV photon beam from a linear accelerator (Varian 2100C). On the right: in-phantom normalized isodose curves for the same photon beam.

4. Conclusions

The obtained results for the photon total mass attenuation coefficient show a good agreement between FriXy gel sensitive material and reference materials (water and soft tissue). Differences between FriXy gel and reference materials have been found generally lower than 3%, but occasionally up to 5% for low energies (Figure 1). Total photon mass attenuation coefficients have been determined with a mean absolute accuracy of 5% or less in the range of 50keV to 10MeV. The overall obtained errors for total mass attenuation coefficients indicate that the number of primary tracks considered when performing MC calculations was large enough for the actual purposes.

In view of the correspondence between total cross section and mass attenuation coefficient (Eq. 3), the reported results ensure the FriXy gel good tissue-equivalence for photon beams in the considered range (50keV-10MeV), as shown in Figure 2. The obtained results show also a good agreement with previous works [4,5,7].

Acknowledgments

This work was partially supported by I.N.F.N. (Istituto Nazionale di Fisica Nucleare).

References

1. G. Gambarini, G. Gomarasca, A. Pecci, L. Pirola, R. Marchesini, S. Tomatis, *Nucl. Instrum. Meth. A* **422**, 643 (1999) .
2. S. Tomatis, M. Carrara, G. Gambarini, R. Marchesini, M. Valente, *Nucl. Instrum. Meth. A* **580**, 506 (2007) .
3. J. Williamson, S. Li, S. Devic, B. Whiting, F. Lerma, *Med. Phys.* **33**, 4115 (2006) .
4. F. Salvat, J. Fernández-Varea, J. Sempau, PENELOPE, A code system for Monte Carlo simulation of electron and photon transport. NEA France, 2003.
5. J. Hubbell, S. Seltzer, Tables of X-Ray Mass Attenuation Coefficientsand Mass Energy-Absorption Coefficients. Report 5632, NIST.
6. G. Gambarini, D. Brusa, M. Carrara, G. Castellano, M. Mariani, S. Tomatis, M. Valente, E. Vanossi, *J. of Physics: Conference Series* **41**, 466 (2006).
7. J. Hubbell, *Rad. Res.* **70,** 58 (1977).

OPTIMISED OPERATION OF THE MIMOSA5 PIXEL SENSOR FOR BIOLOGICAL SAMPLE IMAGING

C. CAPPELLINI*,
M. CACCIA, V. CHMILL, M. JASTRZAB, F. RISIGO
Dipartimento di Fisica e Matematica, Università dell'Insubria, Como, Italia
**E-mail: chiara.cappellini@uninsubria.it*

A. BULGHERONI
Dipartimento di Fisica, Università di Roma 3 e INFN – Roma 3, Roma, Italia

The potential of position sensitive solid state detectors for imaging radiolabelled samples has been widely investigated. Critical figures for the exploitation are the stability of the operation, the noise level and an efficient rejection of noise generated hits. Preliminary results on the operation of the MIMOSA5 monolithic active pixel sensor are reported.

Keywords: Biological imaging; Silicon Pixel.

1. Introduction

Radioactive labelling is a widely used tracking method to follow the distribution of bioactive molecules throughout biological samples, in order to localize specific cell populations, proteins and, in general, molecules of biological interest (ref. 1). In the standard panel of radiolabels (^{3}H, ^{14}C, ^{35}S, ^{32}P and ^{125}I) tritium is the most used since it can be easily bound to organic molecules, being chemically equivalent to hydrogen; moreover, the soft energy spectrum maximises the image quality. However, for the same reason, efficient detection is a real challenge.

The potential of silicon pixel detectors for imaging radiolabelled samples has already been demonstrated (ref. 2–4). A direct comparison between two general purpose sensors, MIMOSA5 and MEDIPIX2 (ref. 3,5), characterized by complementary technologies and architectures was performed and already reported (ref. 6). The results do confirm the advantage of real time granular sensors against films and phosphor imaging screens and set the basis for an optimized, customized development. Basic figures related to

^{3}H imaging have been measured using the RPA506 and RPA507 tritium standards. They are produced by Amersham[a] and consist in two columns of 8 active dots of 4 mm^2 area and specific activities ranging from 0.1 $\frac{nCi}{mg}$ to 109 $\frac{nCi}{mg}$.
The advantage of silicon pixel sensor has is assed in terms of *dark counting rate* and *effective activity*. The dark counting rate is made out of two components:

- a stochastic term, related to the electronics noise and to the cosmic ray flux;
- a non-stochastic component related to either pixels featuring an extremely high leakage current or an unstable behavior and to events with an abnormal occupancy, possibly due to bias supply instabilities or pickup signals.

The effective activity (strongly related to the sensitivity to low energy electrons) measures the ^{3}H event density rate per unit of specific activity.
In the following the results obtained imaging tritium standards with the MIMOSA5 sensor will be presented, together with a dedicated procedure to evaluate the reduction in the dark counting rate resulting from the sensor cooling.

2. System stabilization

The cooling system is made up of a laboratory cooling thermostat, pumping a mixture of water and alcool (in volume ratio of 1:2) into a copper coil coupled with an aluminium stirruf for the sensor. This apparatus, setting up the heat exchanger housing in a thermal isolated box, allows to keep the MIMOSA5 in a controlled ($\pm$ 0.1 °C) temperature in a range from - 20 °C to + 35 °C.
During the measurements, the system was stabilized at room temperature and cooled down to either 12 °C or 4 °C, requiring typically 2 hours for the thermalisation process.

3. Basic operation procedure

The MIMOSA5 is a high granularity monolithic CMOS active pixel detector with full analog output. Its main characteristics are summarized in Table 1 and in ref. 3.

[a] `http://www.amersham.com/.`

Table 1. Main characteristics of the MIMOSA5 sensor.

Technology	Monolithic
Active Volume	0.015 mm thin, undepleted
Architecture	Full Analog, 3 transistor/cell
Output channels	4
Granularity	17 μm
Active Area	$\approx$ cm scale

Its sensitivity to tritium was made possible back illuminating the sensor thinned down to 15 μm, namely to the thickness of the epitaxial layer (ref. 7). After this process, the MIMOSA5 is expected to have a high detection efficiency, featuring an equivalent noise charge (ENC) of $\approx 35\ e^-$ r.m.s. at room temperature (ref. 8–10), to be compared to a most probable value from a ^{3}H decay of 1000 e^-, distributed over a cluster with a core of 3x3 pixels (ref. 11).

Because of the extremely low activities of the ^{3}H standards, the number of expected decays within an exposure time of 25 ms/frame is quite low and images result from the information contained in typically 10^5 and 10^6 frames. As a consequence, sparsification at the earliest possible step in the data acquisition chain is of utmost importance, for the optimization of both the mass data storage and the frame rate. In order not to affect the efficiency, a loose selection has been applied in real time on the cluster seed candidates, tagged and saved together with the nearest 24 neighbours. The off-line data analysis is based on two steps addressing both the non stochastic and the stochastic components of the dark counting rate:

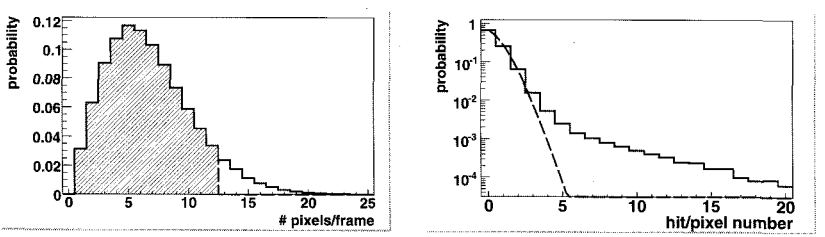

(a) (b)

Fig. 1. *Distribution of the number of events per frame (Figure 1(a)) and the number of hits per pixel (Figure 1(b)). In the Figure 1(a) the shared area reprfesents the accepted frames; in Figure 1(b) the black line represents the Poisson fit.*

- **Non stochastic component:** a recursive rejection of both the entire frames recording a number of events in excess of a paramentrised cut and of the single pixels presenting a dysfunctional behaviour has been developed. The method is described in Figure 2: a frame is rejected if it contains a number of clusters 2 σ away from the most probable value of the events per frame distribution (Figure 1(a)); moreover a pixel is masked if its behaviour differs from what can be expected by a Poissonian distributed number of background hits per pixel (Figure 1(b)).

- **Stochastic component:** a preliminary cut of 5.75 σ on the signal over noise ratio of the seed has been applied; this choice has been performed in order to maximise the background hit rejection and relying on the plots shown in Figure 2. A bayesian discrimination alghoritm against the hypothesis that each cluster is noise generated has then been applied. It has been developed following the method described in ref. 12 and summarized in ref. 6.

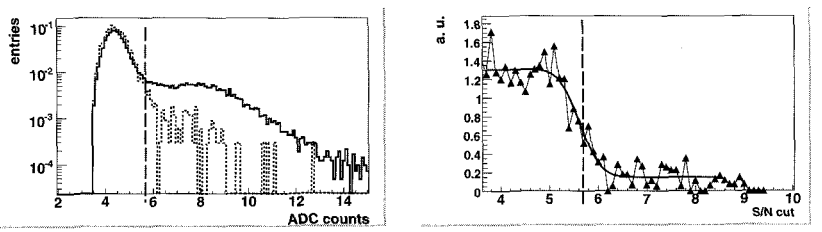

(a) (b)

Fig. 2. *Signal over noise spectra of the seed pixel for an empty and a tritium run (Figure 2(a)) and relative ratio (Figure 2(b)). The plots are normalized to the number of entries.*

4. Experimental results

The noise spectra recorded at different temperatures are shown in Figure 3. A slight decrease ($\approx$ 10%) in the most probable value as a function of the temperature is clear, with a strong impact on the rejection algorithm, where the variation is amplified by a factor corresponding to the selection threshold. The right hand side non gaussian tail at 27 °C is related to spatial in-homogenities of the sensor. This effect is mostly removed at 4 °C, making

more evident the contribution to the left hand side,due to the temperature independent noise, related to all the DAQ electronics placed outside the cool box and corresponding to the "lowest achievable limit". Applying the selection rules described above for the non stochastic noise, the number of rejected frames decreases from $\approx$ 10% at room temperature to $\approx$ 3% at 4 °C, while the number of masked pixels decreases from $\approx$ 2.5% to $\approx$ 1%. The spread among different quarters in the number of rejected frames and masked pixels is also decreasing from $\approx$ 7% to $\approx$ 0.01% and from $\approx$ 3.6% to $\approx$ 0.85%, thus resulting in a net improvement of the sensor uniformity.

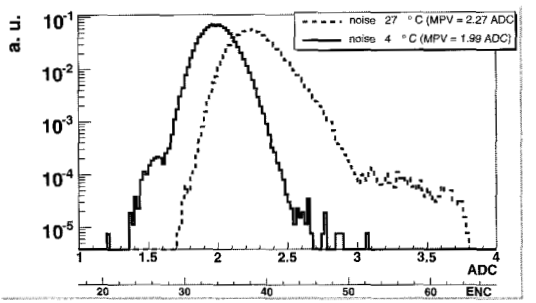

Fig. 3. *The noise spectra recorded at different temperatures.*

The image of the RPA506 standard recorded at 4 °C is shown in Figure 4; it refers to an effective exposure time of 3700 s that corresponds to 42 hours wall clock, because of the low duty cycle of the system.

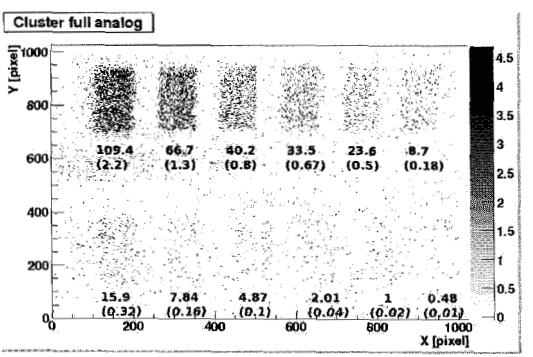

Fig. 4. *Imaged acquired at 4 °C. The activities are expressed in* $\frac{nCi}{mg}$ *and in* kBq *in the brackets.*

Table 2. Counting rates recorded at 4 °C temperature

	Dark Counting $[\frac{counts}{mm^2 \cdot s}]$	Effective activity $[\frac{counts}{mm^2 \cdot s \cdot \frac{nC}{mg}}]$
Raw data	$9.0 \cdot 10^{-1} \pm 3.0 \cdot 10^{-3}$	$6.3 \cdot 10^{-3} \pm 1.52 \cdot 10^{-4}$
Before stochastic rejection	$3.3 \cdot 10^{-3} \pm 1.7 \cdot 10^{-4}$	$1.3 \cdot 10^{-3} \pm 3 \cdot 10^{-5}$
After stochastic rejection	$6.6 \cdot 10^{-4} \pm 7.8 \cdot 10^{-5}$	$7.5 \cdot 10^{-4} \pm 2.3 \cdot 10^{-5}$

5. Conclusion

A cooling system has been commissioned and used to study the dark counting rate of the MIMOSA5 pixel detector as a function of the sensor temperature. Results do confirm an expected net reduction in the spurious counting rate, as demostrated in Table 2, where the left-over background hit density essentially matches what can be espected for the cosmic ray flux.
Incredibly high stability and sensor uniformity have been achieved cooling the sensor down to 4 °C, thus leading to a sensitivity to tritium of $\approx 10^{-2} \frac{dpm}{mm^2}$ to be compared to 30 $\frac{dpm}{mm^2}$ on ^{14}C for the BAS Fuji film. This is confirming the enormous potential of the proposed technology.

References

1. T. Nagata, *Progress in Histochemistry and Cytochemistry* **37**, 59 (2002).
2. J. Cabello, *Physics in medicine & biology* **52**, p. 4993(August 2007).
3. G. Deptuch *et al.*, *Nucl. Instrum. Meth. A* **A511**, 240 (2003).
4. G. Mettivier, M. C. Montesi and P. Russo, *Nucl. Instrum. Meth. A* **516**, 554 (2004).
5. Medipix collaboration web site `http://www.cern.ch/medipix`.
6. C. Cappellini, A. Bulgheroni, M. Caccia, V. Chmill, M. Jastrzab, F. Risigo and E. Scopelliti, *to be published in Nucl. Instrum. Meth. A* (2007).
7. W. Dulinski, A. Braem, M. Caccia, G. Claus, G. Deptuch, D. Grandjean, C. Joram, J. Séguinot and M. Winter, *Nucl. Instrum. Meth. A* **546**, 274 (2005).
8. G. Deptuch, *Nucl. Instrum. Meth. A* **543**, 537 (2005).
9. R. Turchetta, J. D. Brest, B. Casadei, G. Claus, C. Colledani, W. Dulinski, Y. Hu, D. Husson, J. P. Le Normand, J. L. Riester, G. Deptuch, U. Goerlach, S. Higueret and M. Winter, *Nucl. Instrum. Meth. A* **458**, 677 (2001).
10. Y. Gornushkin *et al.*, *Nucl. Instrum. Meth. A* **A478**, 311 (2002).
11. Y. Gornushkin *et al.*, *Nucl. Instrum. Meth. A* **A513**, 291 (2003).
12. G. Borisov and C. Mariotti, *Nucl. Instrum. Meth. A* **A372**, 181 (1996).

SILICON PHOTO MULTIPLIERS CHARACTERIZATION: RECENT ACHIEVEMENTS AND LATEST RESULTS. INVESTIGATION OF SiPM FOR PHOTON COUNTING APPLICATIONS

V. CHMILL*, M. CACCIA, C. CAPPELLINI, F. RISIGO

Physics and Mathematics Department, University of Insubria, Via Valleggio 11, 22100, Como, ITALY
**E-mail: valeriy.chmil@uninsubria.it*

M. JASTRZAB

Department of Electronics, UST-University of Science and Technology, al. Mickewicza 30, 30-059 Krakow, POLAND

Within RAPSODI (European founded project - coop 32993) a novel type of Silicon Photo-Multiplier (SiPM) from different suppliers was investigated. The main parameters: dark count rate, amplification, dynamic range, quantum detection efficiency and optical cross talk have been studied for qualifying of the detectors. Results demonstrate the possibility to apply this detection technology for intense photon fluxes detection as well as for low plurality ones.

Keywords: SiPM, silicon photo multiplier, detector, photon counting.

Introduction.

The Silicon Photomultiplier (SiPM) Technology, originally developed in Russia[1] and consisting in a high density ($\sim 10^3/\mathrm{mm}^2$) matrix of diodes with a common output load. Each diode is operated in a limited Geiger mode, in order to achieve gain at the level of 10^6 and comparable to well known PMT's. As a consequence, these devices are sensitive to single photons even at room temperature and feature a dynamic range well above 100 photons/burst, matching the boundary conditions in many processes of radio-diagnostics and radio-detection. Moreover, the SiPM measures the light intensity simply by the number of fired diodes, with an unprecedented time resolution at the 100 ps level and a dead time per diode limited to 100 ns. All of the above advantages imply that Silicon Photo-Multipliers

are an enabling technology for integration, miniaturization, and array formats in photon counting. Preserving the analogue information that relates to the deposited energy would add a considerable value in photons flux measurements.

1. Characterization of SiPM

Tests have been performed on existing devices with the main goal to define an exhaustive protocol and to produce a comparative study. Three kind of detectors were under test, from different manufacturers: SensL[2] (2 generation and 2 different topology), Hamamatsu[3] (2 different topology) and CPTA (2 generation). The characterization of detectors is a major task for all of the applications where SiPM are used, on the other hand the definition of main parameters is strongly application dependent. For example the Dark Counting Rate (DCR) is a main parameter for low event ratio application and thermo stability is essential for dosimetry in medical fields. For this reason the following exhaustive protocol has been developed with the intention to focus on subsets of it, depending on the considered application.

- Geometrical parameters (number of cells, size of detectors and occupancy factor).
- IV measurements.
- Noise measurements:
  - Dark Counting Rate (DCR).
  - Optical cross-talk.
  - Dependence on the environmental parameters.
- Analysis of a photon spectrum.
  - Resolution power (how many photons can be distinguished).
  - Gain.
  - Working point optimization (at low and large flux).
  - Noise measurement (not DCR).
  - Optical cross-talk (deviations from the Poisson distribution).
  - Dependence on the environmental parameters (Temperature).
- Linearity and dynamic range definition.
- Spectral response measurement.
- Photon Detection Efficiency.

2. Measurements results

The full protocol has been fulfilled for five sensors produced by three different companies: SensL, Hamamatsu and CPTA.

2.1. *Geometrical parameters definition*

The geometrical parameters are resumed in Table 1.

Table 1. Geometry parameters of the detectors under test.

Sensor	Number of cells	Size of detectors	Fill factor
SensL#1, 2	620	1x1 mm^2	
SensL#3	3640	3x3 mm^2	
Hamamatsu#1	400	1x1 mm^2	59%
Hamamatsu#2	1600	1x1 mm^2	37%
CPTA#1	556	1x1 mm^2	60%
CPTA#2	556	1x1 mm^2	60%

2.2. *I-V measurement*

The typical result of an I-V measurement is shown in Figure 1. There are major parameters that can be defined: the leakage current, the quenching resistor value, the working region and break down voltage. The breakdown

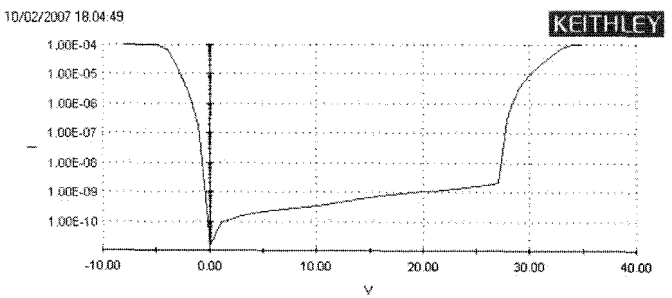

Fig. 1. I–V measurement for SensL SiPM.

voltage is identified as the voltage corresponding to the sudden increase in the current. In Figure 1 this is around 27.3 V with a corresponding leakage current of few nanoampers. The value of the quenching resistor can be estimated by the slope of the linear region.

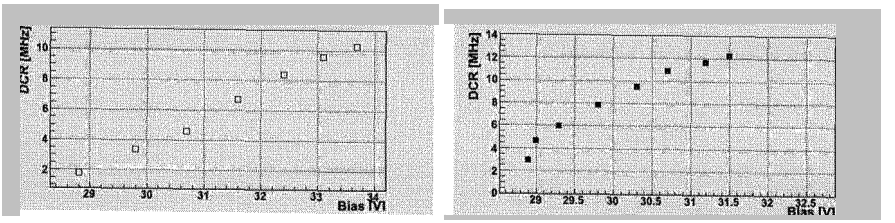

Fig. 2. DCR for SensL detectors: first (left side) and second (right side) generations.

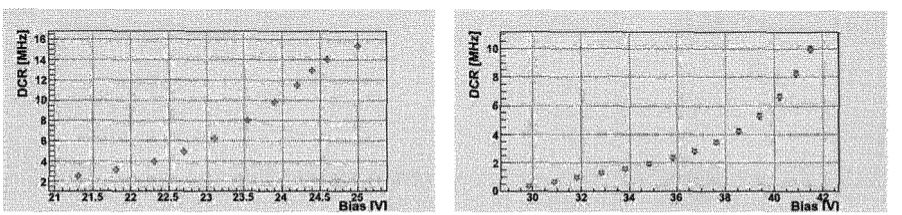

Fig. 3. DCR for CPTA detectors: first (left) and second (right) generations.

CPTA detectors presented in Figure 3. The minimum DCR was observed for Hamamatsu detectors; generally it was factor 5 less compared to SensL or CPTA.

2.4. *Optical cross-talk*

Optical cross-talk measurement was performed analyzing the "step-function" of DCR vs. threshold. The threshold starts from half of single photon amplitude and rising up to 3-4 photoelectrons. Sharpness of steps is a clear indication of reverse bias current which is smallest for Hamamatsu

and biggest for SensL, this is in a good agreement with data from I-V measurements. The plot of step-function for different detectors is presented in Figure 4.

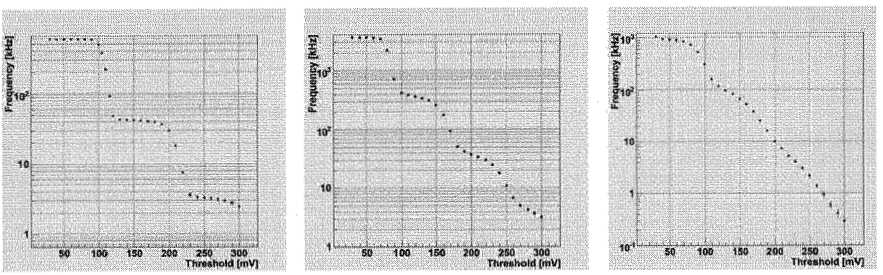

Fig. 4. **DCR vs.** threshold for Hamamatsu, CPTA and SensL detectors from left to right respectively.

2.5. *Dependence on the environmental parameters*

The sensor temperature dependence was measured with different thresholds in photo electrons units and with respect to different overvoltage for second generation of SensL detectors. It was important to prove possibilities to use bias optimization and other method of analysis, which was impossible to use without cooling the detector. Results of measurement for SensL detector are shown in Table 2.

Table 2. **DCR versus temperature for differe**nt threshold.

Voltage	Threshold	DCR [MHz]	
		T=−4°C	T=10°C
30 [V]	0.5 [ph.e$^-$]	3.14±0.15	5.68±0.16
	1.5 [ph.e$^-$]	0.59±0.007	1.41±0.1
31 [V]	0.5 [ph.e$^-$]	4.27±0.16	7.27±0.17
	1.5 [ph.e$^-$]	1.14±0.1	2.48±0.12

2.6. *Analysis of Photon spectrum*

The typical photon spectra obtained with a low plurality flux from the pulse light emitting diode is shown for three sensors in Figure 5. The reso-

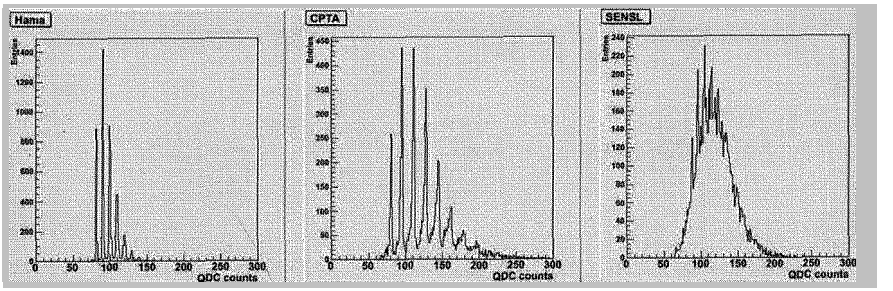

Fig. 5. Typical low plurality spectra for Hamamatsu, CPTA and SensL sensors.

lution power can be defined as the possibility to distinguish single photon peaks and it is obviously affected by their spread and by the background level spoiling the spectrum; the first is due to DCR and the second to the leakage current. The greater resolution power is featured by the Hamamatsu device, while for the SensL one it is hardly impossible to distinguish the different photons due to the high DCR and leakage current. From the analysis of the low plurality spectra it is also possible to evaluate the gain of the sensor by measuring the distance from the different peaks. Results are shown in Figure 6 (left column) where the gain has been evaluated as a function of the bias voltages. The different photon peaks should follow a Poisson distribution; a dedicated analysis on the multipeak spectra has been developed. The algorithm automatically defines the deviations from the Poisson distributions which are directly related to the crosstalk. When the sensor is shined with a high plurality of photons it is possible to evaluate the optimal working conditions by means of the maximum signal over noise ratio defined as the measurement mean value divided by its spread. Results are shown in Figure 6 (right column).

2.7. *Linearity and dynamic range definition*

The SiPM dynamic range has been investigated relying on the PDL 800-B pulsed led source produced by PicoQuant.[4] The led output (510 nm) is focalized and coupled to the sensor through an FC connected fiber in order to allow the geometrical reproducibility of the set up. The source has been qualified in terms of photons exiting the fiber using the calibrated H-5783 PMT produced by Hamamatsu. The digitized output of SensL SiPM for different LED intensities is shown in Figure 7 for different bias voltages. Using different biasing conditions the gain of the sensor is strongly chang-

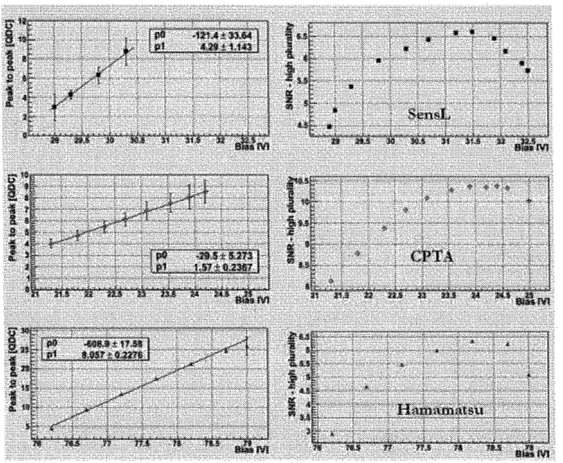

Fig. 6. **Gain evaluation from low plurality photon spectra at different bi**asing conditions. (left column) Optimization of the working conditions (right column).

ing and this definitely affects the dynamic range. The possibility to find a proper setting for which the device response is linear over all the range is demonstrated **by the lowest curve referring to Vbias = 27.8 V.**

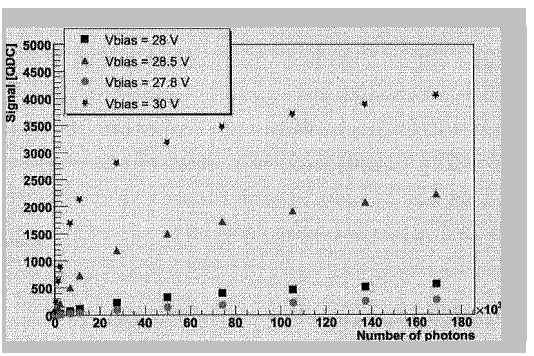

Fig. 7. Response function (linearity).

2.8. *PDE evaluation*

An indication on the Photon Detection Efficiency (PDE) through a calibrated detector and presuming a reproducible geometry was measured us-

ing calibrated Hamamatsu Photomultiplier Tube and FC connector with reproducible geometry to have exactly the same light collection. The PDE for three detectors, illuminated by pulsed LED is shown in Figure 8. Spectral response was measured for an application specified wavelength which is 510 nm. The result is in a good agreement with data specified for Hamamatsu detectors which give us an indication of going right way in PDE measurements.

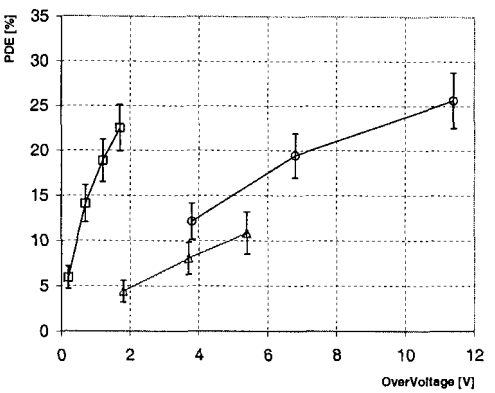

Fig. 8. PDE for Hamamatsu (squared), CPTA (circle) and SensL (triangle).

3. Conclusion

Characterization procedure nearly completed. An algorithm of bias optimization was developed and proved. Next major steps on characterization: Improve the PDE (using neutral filters combinations). Improve the linearity (again with neutral filters). Check the PDE in the Blue spectrum for using light directly from scintillator without wavelength shifter.

References

1. A.Akindinov et al., *Nucl. Inst. and Meth.* **A387**, 231 (1997).
2. Photon Counting Sensors `http://www.SensL.com`.
3. Multipixel Photon Counter `http://www.sales.hamamatsu.com`.
4. Picosecond Pulsed Diode Laser Driver `http://www.picoquant.com/getfs.htm?products/pdl800b/pdl800b.htm`.

IGNORED DISCOVERY NOW PROVEN CAPABLE OF SAVING MILLIONS OF LIVES FROM PREMATURE CANCER DEATH DEMANDS RETHINKING THE DIRECTION OF RESEARCH

DARIO B. CROSETTO

3D-Computing, Inc.900 Hideaway Place, DeSoto, TX 75115, USA
E-mail:Crosetto@3d-computing.com

A discovery described in articles for the past ten years regarding the increase of 400 times efficiency over current PET has been validated by a third party (Siemens). Its importance lies in the possibility to save millions of lives from premature cancer death through early detection and use of low radiation enabling safe screening of high-risk patients. Because the discovery has been ignored for a decade and has now been validated, rethinking the direction of research is demanded. Technical-Scientific objectives should be consistent with social objectives. Grant assignments should be based on estimates and verification of the number of lives saved, cost per life saved, time to achieve those results and how well supported, with solid scientific arguments, is the research. A conservative estimated result is 100,000 lives saved per year in the U.S. alone at a cost less than half of the current $64 billion annual expense for cancer treatment: a cost to society of only $250,000 per additional life saved versus the current cost of $10 million. Benefits to the patient can be achieved immediately with no need to wait for additional discoveries. A plan to accelerate benefits to the patient is provided.

1. Identifying Social Objectives

Statistical data show that during the past half century the heart disease death rate has been cut by more than half while there has not been a substantial reduction in cancer death [1]. Cancer kills prematurely (under age 75) one person in the world every 5 seconds, one every 100 seconds in the U.S. The U.S. alone has spent over $200 billion on cancer research during the past 40 years [2]. According to PubMed, an online database from National Cancer Institute (NCI), the cancer research community has published 1.56 million papers. In spite of these impressive numbers, a significant reduction in premature cancer death has not been achieved:

- In order to solve this problem it is imperative to prioritize the social objective of **substantial reduction in premature cancer death, now.**
- A second social objective, to avoid spending money without achieving significant results, must be to **analyze the reasons for the missed results, and correct them.**

2. Identifying Technical-Scientific Objectives

A constant goal in medicine is to identify abnormal biochemical activity associated with a specific pathology and to observe the abnormality directly as soon as possible in the diseased organism. Cancer is detected unequivocally in most cases using histological invasive examination revealing information about changes in shape, structure, metabolism and other biological processes of cancer cells. A fundamental goal of technological research should be to provide physicians with **a non-invasive means to diagnose cancer with a level of accuracy similar to that obtained with histological examination.** The technique should also be safe for the patient, economical and should detect cancer cells at a very early stage of development.

3. Verifying that the Social Objective is Achieved

It is necessary to establish clear procedures for evaluating if different research projects or interventions **truly address the social objective of reducing premature cancer death.** Only research projects or interventions that can show a substantial reduction in cancer death supported by scientific arguments should be taken into consideration. **All projects should first estimate and then experimentally verify the impact of the proposed solution on a representative sample of 10,000 people age 50-75,** selected from a population in a location with a constant cancer death rate of 50 deaths per year recorded over the previous 20 years. Funding will continue for solutions showing a reduction in premature cancer death as stated in the proposal.

Initial funding should be assigned by evaluating not the number of articles published by the applicant but based on the following five parameters:

1. Cost of the project (per experiment as described above)
2. Number of estimated lives saved (among the sample of 10,000 and when extended to a larger population)
3. Estimated cost for each additional life saved
4. Estimated time to achieve the claimed results
5. How well supported, with solid scientific arguments, are the project or intervention and the above four estimated figures

During the implementation of the various research phases, **the consistency between social and technical-scientific objectives must not be modified** toward other non-priority objectives. For example, a study showing the discrepancy between the publicly declared social objective of reducing cancer death with its technical-scientific implementation into a Type A PET, prioritized

for profit and not for the benefit of the patient is reported in the left column of page 693-694 [3]. When the research project cannot provide significant estimated figures and solid scientific arguments relative to these five parameters, neither in the estimation phase, nor in the experimental phase, this will indicate that the social objective is not a priority and funding should be suspended.

4. The Most Promising Intervention for Substantially Reducing Premature Cancer Death Now

Experimental data show that cancer is curable when diagnosed at an early stage and life is saved in 90% to 98% of the cases, while during the past half century the use of new drugs has not achieved a substantial reduction in cancer death. Therefore, **the most logical short term solution is to target the improvement of early detection through safe, economical and noninvasive medical diagnostic method.** Such a method would ideally be capable of identifying the development of the very first cancerous cells with high sensitivity and accuracy in order to avoid "false positives" and "false negatives."

Discovery of drugs that can cure **late stage** cancer is certainly desirable as well, so research for such drugs should not be stopped. However such drugs should only be considered long term solutions.

Regrettably, although early detection is a valid solution, data shows that it has not been pursued adequately.

5. Comparison of Current Medical Diagnostic Technologies

Cancer manifests itself in various ways. It can cause a change in tissue density, in anatomy, in temperature and/or in nutrient consumption rate (metabolism) of the cancerous cells. Therefore devices have been built to visualize information based on each of these properties. The most common are:

- Techniques that measure tissue density (CT, Computed Tomography; X-ray; MRI, Magnetic Resonance Imaging; Ultrasound; etc.) –However, the development of cancer does not always show tissue density change and 1 cm^3 of tissue is about 1 billion cells, too many to qualify as early detection.-
- Techniques that measure the difference in temperature or fluorescence (TIR, Thermal Infrared; LIF, Light-Induced Fluorescence spectroscopy). -Such differences are difficult to distinguish, in particular for those located a few mm below the skin surface.-
- Techniques that measure the ratio between cytoplasm and nuclei of the body cells and the distance between nuclei to detect changes in structure in the tissue (histological examination). -Such techniques allow microscopic

examination of cells with a resolution of one micron and observation of the result of chemical reactions with monoclonal antibodies to detect markers specific to tumors: however histological examination is invasive and cannot be used for screening.-

- Techniques that by means of cell nutrient marked with a radioisotope, **measure body cell metabolism in order to detect minimum abnormal metabolism** (SPECT, Single Photon Emission Computed Tomography and PET, Positron Emission Technology). –**Cancerous cells take up to 70 times more nutrient than normal cells.**-

Of the above possibilities, it is logical to **consider most reliable the one based on the last type of technique because the difference in metabolism of a cancer cell and a normal cell is high enough (up to 70 times) to be easier to detect early in its development.** This leads to the logical conclusion that one must invest in the technique that measures metabolism.

SPECT technique is very inefficient; fewer than one out of 200,000 signals from the tumor markers are captured by the device: it is not suitable for early detection and requires high radiation dosage to the patient, not acceptable for annual screening. The PET technique works by administering a nutrient compound to the body cells (molecules of glucose, oxygen, carbon, etc.) tagged with a radioisotope (tracer) and monitoring its path through the patient's body by means of a device that can capture signals emitted (photons) by the decay of the radioisotope. (See Figure 1).

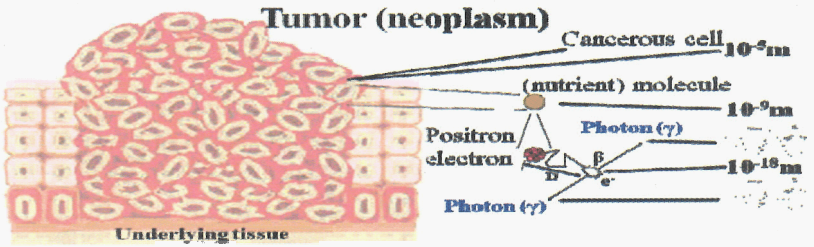

Figure 1 Schematic view of the dimensions and relationship between cancerous cells, molecule of cell nutrient, atoms, positron and the generation of a pair of photons emitted in opposite directions when the latter is annihilated with an electron. PET's task is to detect the pair of photons

The International Commission for Radiation Protection (ICRP) recommends that examinations used for annual screening of asymptomatic people at high risk must administer a radiation dose of less than 100 mrem. This leads to the logical conclusion that one must invest in and improve PET ability to capture as many signals as possible emitted by the tracer (or tumor marker).

6. Limits of Current PET

Over 4,000 current PET (Positron Emission Tomography or PET/CT) in use today, costing over $2 million each have severe limitations because they capture inaccurately only 1 out of 10,000 signals emitted by the tumor markers located on the molecules of body cell nutrient. This low efficiency does not allow detection of minimum abnormal metabolism; consequently tumor size must be large to be detected. Limits in efficiency due to the construction of the current PET are detailed in several articles [4], [5], [6] [7], [8], [11]. This low efficiency also requires a high radiation dose, which is hazardous to the patient and makes is unsuitable for annual screening of asymptomatic people at high risk. Therefore it has a low chance to save lives.

A major change in the overall approach to the construction of current PET should be made such that the priority is the benefit to patient's health, not to benefit business (see details at page 693-694 of [3] and Appendix of reference [11]). It should be prioritized for measuring minimum abnormal metabolic activity for early detection that saves lives, rather than measuring tumor dimension mainly to justify, through its shrinkage, chemo and radiotherapy which data show does not save lives (at best prolongs live for a short time). As a matter of fact, the over 4,000 current PET cannot contribute to a substantial reduction in cancer death, do not provide a real benefit to the patient and increase instead health care cost. Higher cost with no return to the patient just achieves higher profit for a few people.

7. A Solution for Safe Screening Targeted at Early Cancer Detection in Existence, But Ignored for Ten Years

A solution for safe screening targeted at early cancer detection has been in existence for over a decade, as documented in several publications [6], [3], [4], [5], [7], [8], [9], [10], [11], [12], [13]. It is an innovative technology that allows building a device over 400 times more efficient than current PET. One example of the implementation of this innovative technology is in the construction of a cost-effective apparatus called 3D-CBS (Three-Dimensional Complete Body Screening). Such staggering **improvement in efficiency enables early detection of cancer that in combination with safe annual screening** (within the radiation dose of 100 mrem recommended by the ICRP) of asymptomatic people at high risk, **provides a substantial reduction in cancer death**. Its key innovations are in four main areas:

1. Increased detector length –longer Field of View (FOV)
2. Improved and simplified detector assembly

3. Innovative electronics which enable other innovations:
   a) executing precise algorithms for photon identification
   b) accurately measuring the impact point and energy of oblique photons
   c) reducing the initial number of the electronic channels, and
   d) simplifying the method for identifying events in time coincidence
4. Innovations in the visualization of the information obtained

The synergy of coupling several innovations, such as in the detector, sensors and the electronic system, enables execution of real-time algorithms for more accurate and efficient photon identification at a lower cost per photon captured.

Validation of the possibility of increasing the efficiency of current PET over 400 times has been done beginning in 1995:

- in scientific and logical demonstrations for the reviewers of grant proposals (to National Institutes of Health –NIH-, Department of Energy –DOE-, National Science Foundation –NSF-),
- in scientific and logical demonstrations in the book [6] and articles [4], [9] presented at the 2000 IEEE-NSS-MIC Conference in Lyon (France),
- in hardware demonstrations of the innovative architecture of the electronic system at the 2001 IEEE-NSS-MIC Conference in San Diego (CA)
- in irrefutable scientific demonstrations at the meetings attended in person and by conference calls with the President, Vice President, Director of Advanced Research Group and Director of the Electronics Group of Siemens in 2002
- in the report [14] of a panel of scientists in an International Open Scientific Review (via web) in 2003 that confirms the claims and discovery (shown feasible with the innovative sections working in hardware).

8. Discovery Validated by Experimental Results Obtained by Siemens

THE "**JUDGE**" IN SCIENCE IS LOGICAL REASONING AND/OR THE RESULT OF EXPERIMENT and not the opinion of a reviewer unsupported by scientific arguments.

Science does not advance through the approval by a majority of scientists, it is not a popularity contest. Science advances because someone understands the law of nature and demonstrates the proof. For example the pendulum clock was invented by Galileo's observation that the period of each swing of a lamp in a cathedral was exactly the same. In another example, a child can demonstrate that Aristotle and thousands of scientists were wrong claiming that the speed of a falling object is related to weight. He can just repeat the experiment suggested by Galileo of dropping a big and a little stone from a tower to show that they hit

the ground at the same time. However, all scientists took Aristotle's claim as the truth until Galileo came up with a brilliant idea to show Aristotle's mistake.

Similarly the observations described in [6] show that current PET is very inefficient and that **improving crystals that are already over 90% efficient will not improve it much further. Still scientists in academia and industries continued for over 40 years trying to improving crystals and not the other sections, such as electronics that were less than 10% efficient.**

The discovery is proven by logical arguments in articles, [6], [5], [7], by simulation, by construction in hardware of the innovative parts and by proof by experimental results from third parties that my claims were correct. Scientific explanations[a] published in 2000 should have induced scientists to reflect on the contradictions pointed out in those figures.

That should have been sufficient to make scientists realize they had been wrong for decades to believe those who convinced the world that in order to improve PET, only the crystal should be improved. Instead reviewers of my grant proposals did not use "logical reasoning", did not support their rejection claims with scientific arguments. They just repeated the mistaken theory like those who repeated Aristotle's mistake until the Middle Age. A prominent example of this theory is Stephen DeRenzo, who received millions of dollars in grants for improving crystals, after reviewing my book [6] in 2000 and then stating: "The main loss of events at high event rates is due to dead time in the detector, not the electronics. That is why we are working on new scintillators with good stopping power, high light output, and sub-ns decay time. We do not view the electronics as a problem, either in terms of performance or cost".

I still hoped that the process of trying to solve the contradictions I pointed out in my two figures would lead scientists to understand that my claims were right. When leaders of Siemens paid a visit to my office in 2002, they could not accept that their PET could be far more efficient if they improved other sections of PET as I pointed out rather than the crystals. Unfortunately, just as people trusted Aristotle, they trusted people like DeRenzo and invested millions of dollars in fabricating the close to ideal LSO crystal. Anyone can imagine how the leaders of Siemens would have felt after investing millions of dollars in plants to manufacture the expensive LSO crystal, upon hearing my claims to use economical crystals and improve the electronics and other sections of PET.

---

[a] Figure 3-4 page 23, [6] (or Figure 3, [7] showing the ideal vs. actual coincidence detection of current PET system and the efficiency improvement solution and Figure 14-1 on page 136, [6] (or Figure 1, [10]) showing where photons are lost in current PET and how to capture over 400 times more accurately the number of photons.

They very strongly tried to counter my claims with many measurements and arguments (presented by the President, the Director of PET, the Director of Advanced Research Group and the Director of the Electronics Group) intended to prove to me that their electronics and other sections of PET were fine and that there could not be room for a substantial efficiency improvement. Moreover, they had already built 31 prototypes exploring all the possibilities of their current technology. They made many statements during our several meetings in 2002 such as: ***"...the detector* [at Siemens] *is extremely well characterized..., In fact, very accurate test results... We believe that we're making a very appropriate trade-off of light collection and information extraction, AND THAT IT IS NOT LIMITED BY THE ELECTRONICS"***.

However, those statements had to be retracted in 2007 when Siemens published on their own web site "*ultra-fast detector electronics significantly improved* [by 70%] *count rate performance, image quality, signal-to-noise ratio, lesion detectability and patient scanning flexibility.*" (See testimonials at www.crosettofoundation.com).

Although many reviewers from scientific journals and government agencies (who denied funding during the past decade) and top industry leaders who did not believe (though other scientists approved as shown in review reports and articles [14], [7]) that it is possible to substantially increase PET efficiency not by improving the crystals, but by using cheaper crystals and improving other sections of PET such as the electronics. In the end logical reasoning and experiment won, proving the viability of the discovery advancing science.

This admission by Siemens with experimental results that they could eliminate 70% inefficiency in their PET is a **first achievement.** However, a meaningful benefit to the patient (due to early detection and low radiation dose that enables annual screening) will only be reached with a **second achievement** when there will be the admission that my other claims to increase efficiency of current PET by 40,000% will also be recognized. Then patients will benefit from early detection, proven to be effective in reaching a substantial reduction of premature cancer death. There are no technical obstacles to achieving these results using my innovations. This can be proven now by building a device such as the 3D-CBS using materials already commercially available ten years ago.

9. Further Innovations That Must Be Considered

There is a need to change the direction of research not only in how quantitative information is acquired and processed by PET, but also in how it is displayed to the physician.

Such data should be displayed as a number, or a code, related to the *quantity* of signals detected per unit of time. Only PET devices that accurately capture all possible photons from the radiotracer provide reliable data that can be used for quantitative information. This is far superior to the display of a picture as done by the current 4,000 PET devices showing the darkening of spots by placing one dot on top of another related to only one signal out of every 10,000 from tumor markers, which does not allow early detection.

In this case the absurd contradiction is that manufacturers of current PET expect physicians to interpret abnormal metabolism from the darkening of a spot. This would be equivalent to a TV weather reporter who tries to impose on his viewers a high resolution map of a region expecting them to understand from dots drawn one on top of the other (each dot related to a rain drop), how much rain fell in one day. Once a black spot is drawn in an area, no new information is actually added by the subsequent dots. For sure the viewers will complain to the TV station and something will change very quickly. In fact, TV weather stations do show numbers indicating how many inches of rain fell within a given time. (See Figure 2).

The new 3D-CBS device, because of its high sensitivity can instead visualize information consisting of a number, or a code, **related to the QUANTITY of signals detected per unit of time**, related to precise information on minimal abnormal metabolism or other biological processes that allows making more accurate diagnosis and early detection of anomalies. This number could represent, but is not limited to, the difference or ratio between the expected metabolism in an area and the value measured by PET. (See Figure 3)

A gradient of colors would provide an intuitive immediate overview of the entire body, showing where the "hot" spots are. Several other functions should be provided such as: zoom, 3-D rotation; a software tool to subtract data coming from organs that obscure weaker but more important concentrations of the tracers in the nearby organ. For example, the bladder typically has a high concentration of radiotracers and obscures the prostate. The 3D-CBS is capable of acquiring data continuously and simultaneously from most of the length of the body with high sensitivity and to process data in real-time. This allows showing a sequence of images related to biological processes similar to a video.

Such capability could never be offered with current PET with 16 cm FOV due to lack of simultaneous recording of information over a long FOV. It would be difficult even for a point source, because information on minimum abnormal metabolism would be unreliable due to the low efficiency in capturing photons.

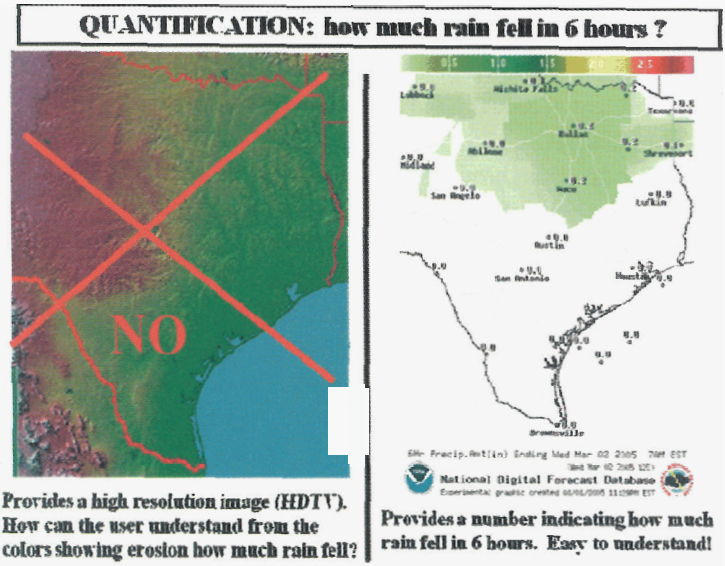

Figure 2 Analogy of the TV weather report that absurdly expects viewers to understand how much rain fell from a high resolution picture on the left rather than from numbers as displayed in the picture on the right.

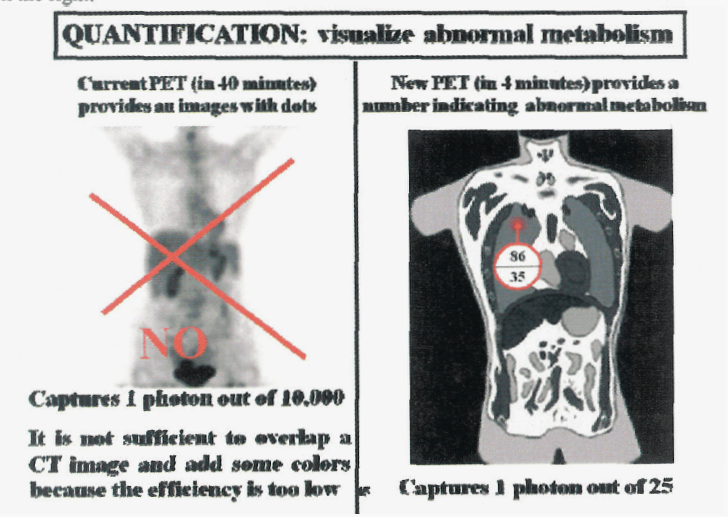

Figure 3 The way the information is displayed must change. A fine-grained photo of pixels, one on top of another as shown on the left does not provide accurate information about abnormal metabolism (nutrient consumption). The physician, radiologist, oncologist, should have coded colors for a quick overview of alarming spots and more detailed quantitative information showing the abnormal metabolism on a background profile of organs as shown on the right.

10. Reducing health care costs while saving more lives

The U.S. alone spends $64 billion a year on cancer treatment [2] without achieving a substantial reduction in premature cancer death [1].

The words "screening for cancer" are not necessarily synonymous with driving health care costs through the roof. Rather than emotional responses, we should instead analyze different solutions and change the direction of research toward a solution that saves more lives now at a lower cost, as the "verification parameters" in Section 3 state.

The $64 billion is mainly spent on drugs for treating cancer at an advanced stage. Even with a much reduced budget for early detection, a better result in number of lives saved from premature death is guaranteed. When early detection is achieved, drug use drops and the cost for post-surgical treatment decreases because it is needed for a shorter period of time, in particular when the problem is solved mainly by the removal of an early stage cancer with surgery.

The problem can be analyzed like any other cost/benefit problem. Clearly the main beneficiary should be the patient. Companies (drugs, etc.) in the business of cancer treatment at an advance stage will suffer. Therefore, they will transform their activity to early detection, surgical improvements, and drugs for treating cancer at an early stage.

Lower health care costs with a higher return in lives saved are supported by the following:

- Experimental data show that when cancer is diagnosed at an early stage it is curable and life is saved in 90% to 98% of the cases ("Early-stage ovarian cancer is more than 90% curable; late stage is 75% deadly" [2])
- Despite the fact that cancer grows without always showing a change in tissue density, there is widespread screening with techniques such as mammogram which are based on measuring differences in tissue density
- Knowing that there is a better chance to detect cancer by a change in metabolism than a change in tissue density or other signals, PET should be preferred over mammogram, CT, etc.
- Knowing that the current PET devices are very inefficient, it is obvious that a 40,000% increase in efficiency is highly desirable.
- Having had third parties (such as Siemens) validate the author's discovery confirms the claim that current PET efficiency can be increased by 40,000% by extending the FOV and improving other sections of the PET.

It is logical to use technology based on molecular imaging that provides a combined 40,000% increase in efficiency with respect to current PET, which in turn is more reliable than other technologies based on measuring tissue density, temperature, etc. Because it is more efficient, it is also logical to expect early detection that is better than mammogram, or CT (which claims some efficiency on its own). It is reasonable to conservatively predict not the 90% to 98% of lives saved as experimental data show from early detection, but a mere 33% in lives saved which would still provide a staggering improvement compared to the insignificant results obtained during the past half century.

Granting a current reduction in premature cancer death of 2% per year (although this result is mainly due to smoking cessation or diet change, and a very small percentage is due to research) and estimating only an extremely conservative 33% death rate reduction because of early detection obtained from screening with a 40,000% more efficient technology. Detailed calculations[b] show that it will cost about $1.5 billion to screen 3.64 million people (at $400/exam) and save 6,000 lives. More astonishing is the **fourth achievement** that can be reached of **only $250,000 (plus costs for surgery and post-surgery) per additional life saved while the actual cost during the last years has been about $10.5 million per person** (calculated as $64 billion/6,000 lives).

So the cost to achieve the same 2% death rate reduction of 6,000 people per year would be only $1.5 billion instead of $64 billion. In addition, the opportunity then exists to save not 6,000 people per year from premature death, but 100,000 per year at a cost of $24 billion, that is still less than half the current annual expense for cancer treatment. Furthermore, there is an additional gain to the economy from people age 50-75 brought back to productivity instead of incurring high expense for treatments of late stage cancer.

After reflecting on the above, it is clear that current beneficiaries of the $64 billion spent on cancer treatment are not the patients but the "cancer industry"

11. Rethinking the Direction of Research to Avoid Past Errors

Rethinking the direction of research to move in the right direction in cancer research means discarding faulty models, unclear objectives, wrong

[b] Statistical data show that the cancer death rate among the population age 50-75 is 0.5%. In order to save 6,000 lives from premature cancer death with early detection estimated conservatively to be only 33% efficient requires examining 3,640,000 people per year in the age-group 50-75).

assumptions, and distorted information about technology and techniques inappropriate to solve the problem.

The primary objective should not be the market or profit (building a PET that measures shrinkage of tumors detected at an advanced stage to justify the use of chemo or radiotherapy), but rather patients' health (building a PET with the capability to detect the minimal abnormal biological process).

Wrong assumptions are based on the belief that measuring shrinkage of a tumor at an advanced stage saves lives, while experimental data prove that early detection significantly saves lives.

Technology should not focus, on improving spatial resolution for measuring tumor dimensions, but rather on achieving high efficiency for measuring minimal abnormal metabolism (with minimal radiation dose at the lowest examination cost).

11.1. *Faulty models are built on contradictions*

Dissemination of inappropriate unscientific beliefs/opinion regarding the best technique for early cancer detection misleads funding agencies and researchers. For example:

- focusing on the improvement of crystals that are already at over 90% efficiency while other sections of PET are at less than 10% efficiency;
- believing that increasing sensitivity cause more "false positives", while what is called "increased sensitivity" is in reality "increase in noise."

In order to achieve the highest impact of premature cancer death reduction in the shortest possible time, **social and technical-scientific objectives must be consistent and stated by legislators and in cancer organization mission statements. Each one must have in their verification process the procedure described in Section 3 that measures results in cost/benefits to the patient.** No matter how many physicians or how many scientists these organizations appoint to their review panel for grant committees, all these people should make sure that the true judge is logical reasoning and ultimately the experiment and not their opinion. The authority is not theirs, but it is the law of nature that they have to serve. If they make a mistake, they should leave the task of being on a review committee to others who better understand the law of nature.

12. Specific Technical Corrections Needed to Accelerate Social Objective Achievement

The following are specific technical corrections that will help to eliminate some confusion in the field (See pages 693-694, [3] for an in-depth study:

1. The word "**Tomography**" should be eliminated from Positron Emission Technology literature. The concept of "tomography" has misled thousands of scientists. Tomography, from the Greek meaning "slice" or cut, is the wrong approach to Positron Emission Technology using a technique that reconstructs images using a tomographic technique. Since tracer photons are emitted in all directions, we should capture as many as we can, reconstructing the "*voxel*" (volume pixel) in three dimensions
2. The Technical parameter "**spatial resolution**" should be eliminated from the specification of PET because PET measure dynamic biological processes, not spatial dimension
3. The 2x2 PMT "**block detector**" with no light sharing between blocks should be abandoned in the construction of PET [5], [6], [11]
4. **The FOV should be extended** by using economical crystals and not the use of expensive, close to ideal crystals and shortening the FOV [6]
5. The technique representing PET information by **darkening spots** by placing one dot on top of another related to only 1 signal out of 10,000 from tumor markers should be abandoned in favor of quantitative reporting.

13. Conclusions

The author's discovery has been described in many documents [4], [5], [6], [11] during the past ten years, proven with logical arguments, with simulation, with hardware construction of the innovative parts shown working at the IEEE Conference in San Diego in 2001, at the Open International review in 2003, and validated by third parties (Siemens) that "*detector electronics significantly improved* [by 70%] *count rate performance, image quality, signal-to-noise ratio, lesion detectability and patient scanning flexibility.*"

It has been shown that extending the FOV of current PET, using economical crystals, using all other innovations in detector assembly, real-time photon detection algorithm, coupling between detectors, sensors and electronics, etc., as described in the referenced material is possible all at once. In addition to the validation that may come now from other third parties, the fact that the innovations that allow achievement of the claimed results can be built with material commercially available ten years ago, prove that it was a discovery.

The specific type of unscientific answers inconsistent with science and the interest of the patient that have accumulated for ten years from NIH,

IEEE, and reviewers from other funding agencies and scientific journals are an insult to human intelligence. Continuing to prefer technologies hundreds of time less efficient is a detriment to humanity because of the millions of lives needlessly lost prematurely [15].

By the same token, **there are no scientific arguments that invalidate my claims that not just 70% efficiency improvement but over 40,000% improvement can be achieved with respect to the current 4,000 PET** in use today and that all four achievements described in this paper can be reached. The verification process of Section 3 will contribute to obtaining results through competition among the best solutions.

In summary the discoveries derived from analyzing facts, identifying contradictions and errors, observing the law of nature, applying logical reasoning, verifying them with calculation and experimentally with hardware construction of the innovative parts leads to the following four benefits that are all achievable immediately:

1. The 70% PET efficiency improvement obtained by improving the electronics proves that the study of Figure 14-1 on page 136 of [6], is correct and that PET **efficiency can be increased hundreds of times if the focus moves from the crystal** (already at 90%) **to other sections** (at less than 10% efficiency)
2. The 40,000% PET efficiency improvement is validated by the previous achievement and is obtained by extending the FOV and implementing at once all innovations described in the references. It provides the advantage of early detection and of low radiation enabling a safe screening on asymptomatic people at high risk. This is what saves lives, which, with a conservative estimate of only 33% in place of the 90% to 98% reported by experimental data will allow **achievement of a substantial reduction of 100,000 premature deaths annually in the U.S. alone**.
3. **The quantitative, reliable information on abnormal metabolism**, based on accurately capturing 1 out of 25 signals from tumor markers (versus 1 out of 10,000) should be provided (versus only qualitative information).
4. The research and interventions that lower health care cost **to $0.25 million** (plus cost of surgery and post-surgical treatment) **per additional life saved from premature cancer death should be pursued instead of that which now costs over $10 million per additional life saved**

In order to accelerate achievement of the goal of a substantial reduction in premature cancer death, I am donating 80% of the income from my patents in this field:

1. To pay for the construction of 3D-CBS devices to be donated at no cost to hospitals,

2. To provide free screening examinations to low income people
3. To pay for education and dissemination of information aimed at a substantial reduction in premature cancer death

Now that this discovery, ignored for a decade, has been proven capable of saving millions of lives from premature cancer death, rethinking the direction of research must commence.

Acknowledgments

I would like to thank the Chairman of the Conference, P.G. Rancoita, the Industry Organizing Committee, M. Barone and the Medical Application Instrumentation Session Organizer, S. Pospíšil for accepting this contribution at the ICATPP 2007 Conference and M. Bentley for editing assistance.

References

[1] : National Center for Health Statistics. National Vital Statistics http://www.cdc.gov for U.S. and ISTAT for Italy, http://www.mortalita.iss.it/

[2] Leaf, Clifton,: "Why we're losing the war on cancer" FORTUNE magazine, March 22, 2004, pp.76-94

[3] Crosetto, D.: "Rethinking Positron Emission Technology for Early Cancer Detection" Book: Editor: World Scientific, 2006, pp. 692-696

[4] Crosetto, D.: A modular VME or IBM PC..." IEEE-NSS-MIC, 2000-563,

[5] Crosetto, D.: Nucl. Ins. & Met. in Phys. Sec. A, vol. 436 (1999) pp. 341-385

[6] Crosetto, D.: 400+ times improved PET efficiency... ISBN 0-9702897-0-7.

[7] Crosetto, D.: The 3D-CBS... IEEE-NSS-MIC-2003. Conf. Record. M7-129.

[8] Crosetto, D.: "Come Vincere il Cancro" Editor Clavilux, 2005, www.clavilux.it

[9] Crosetto, D.: Real-time, programmable, IEEENSS-MIC, 2000-567.

[10] Crosetto, D.: "Development of an Innovative Three-Dimensional Complete Body Screening Device - 3D-CBS" Book: Ed.: World Scient., 2004, pp. 350-359

[11] Crosetto, D. Saving lives through early cancer detection: Breaking the current PET efficiency barrier with the 3D-CBS." www.3d-computing.com/pb/3d-cbs.pdf

[12] Crosetto, D.: "3D-Flow DAQ IBM PC board for Photon Detection in PET and PET/CT" IEEE-NSS-MIC-2003. Conference Record. M3-130

[13] Crosetto, D.: "Channel Reduction and Time Coincidence IBM PC board for PET" IEEE-NSS-MIC-2003. Conference Record. M6-131

[14] See Final Report of the committee who reviewed Crosetto's innovative technology at www.3d-computing.com/pb/Review_rep.pdf.

[15[See web site www.crosettofoundation.com

REAL-TIME X-RAY μ-IMAGING OF LIVING ORGANISMS

JIRI DAMMER, TOMAS HOLY, JAN JAKUBEK, MARTIN JAKUBEK, STANISLAV POSPISIL AND DANIEL VAVRIK

Institute of Experimental and Applied Physics, Czech Technical University in Prague Horska 3a/22, CZ-12800 Prague 2, Czech Republic

ROBERT HANUS

Institute of Organic Chemistry and Biochemistry, Academy of Sciences of the Czech, CZ-16610 Prague 6, Czech Republic

FRANTISEK WEYDA

Institute of Entomology, Academy of Sciences of the Czech republic Branisovska 31, CZ-37005 Ceske Budejovice, Czech Republic

We present an X-ray μ-radiographic system developed for dynamic high spatial resolution imaging of living small animals. Our system is based on a micro-focus X-ray tube and the hybrid single photon counting silicon pixel detector Medipix2 (matrix 256 x 256 sq. pixels of 55 μm pitch). As soft tissue exhibits low contrast in classical absorption radiography, we exploit a new method of phase-enhanced imaging. Picture quality is further improved by statistical data analysis and extended calibration of individual pixel's response. Computing tomography provides 3D images of studied samples from radiographic projections. For 3D reconstruction of measured objects we use iterative algorithms which are advantageous for low statistics data, low or incomplete number of projections and complex physical model. This diagnostic system allows real-time observation of inner processes in living organisms and dynamic diagnose of living animals for biological studies. The obtained results and real-time stream video capability is demonstrated on samples of a mouse and living worm, caterpillar, etc.

1. Introduction

A new experimental setup devoted to digital high resolution X-ray transmission imaging [1] was applied to μ-radiography and μ-tomography of small organisms. This setup had been designed for X-ray imaging as well as for the observation of real-time processes in living organisms [2]. The single photon counting pixel device Medipix2[a] was used as image area. Hamamatsu μ-focus X-ray tube or FeinFocus μ or nano-focus X-ray tube were used as X-ray source.

[a] See also www.cern.ch/medipix and www.utef.cvut.cz/medipix

X-ray imaging of biological samples consisting of soft tissues is particularly difficult due to low differences in beam attenuation. This difficulty can be overcome by using highly sensitive and broad (unlimited) dynamic range images hybrid semiconductor pixel detectors like Medipix2 [3]. This device provides no leakage current (zero noise) and unlimited dynamic range which allow to reach high sensitivity and enhanced contrast. In combination with state-of-the-art point like X-ray sources and advanced data imaging analysis it is possible to refine spatial resolution of the system below 1 μm. The capability of the system assembled is demonstrated below on small animal and organic samples.

1.1. *The X-ray μ-imaging system*

The presented system (Fig. 1) contains a μ-focus X-ray tube with tungsten anode[b], a sample holder (enabling three-dimensional translation and rotation) and the pixel detector Medipix2[c]. The main advantages of the Medipix2 pixel detector include: high sensitivity to low energy X-ray photons; position sensitive and noiseless single photon detection with preselected photon energies; photon counting[d] in each pixel performed by digital counter (therefore there is no dark current); digital integration (providing unlimited dynamic range and absolute linearity in device response to number of photons); high speed digital communication and data transfer.

The response of each individual detector pixel was calibrated for different absorber thicknesses to suppress the beam hardening effect in the given object and to compensate pixel inhomogeneity across the whole pixellated sensor [4]. A set of perfectly flat aluminium foils of various thicknesses ranging from 50 to 500 μm was used for calibration. By altering the distance between the sample and the detector, an additional (geometric) magnification from 1× to 30× could be set.

1.2. *Phase-shift contrast enhanced imaging*

In addition to conventional beam attenuation we exploited phase-shift effect in the transmitted beam. Variations of the refractive index across the sample

---

[b] We used either a model Hamamatsu L8601 and Hamamatsu Photonics operated at 40 - 90 kV and 100 - 240 μA, the tube emission spot size is was 5 μm; or FeinFocus FXE-160.51, spot size was <1 μm operated 10-200kV and 50μA - 1mA.

[c] 300-μm thick silicon sensor chip and 256 × 256 pixels with 55-μm pixel pitch.

[d] In contrast, change-integrating devices, such as CCDs, show dark current (noise), limited range and non-linear response.

result in differences in phase shift of the transmitted X-ray beam. Induced phase gradients produce changes in the beam direction [5]. These phase effects cause changes in recorded transmission image observed as edge enhancement. Combined with conventional absorption transmission imaging, phase-sensitive imaging can be thus used for high-sensitive high spatial resolution edge contrast enhanced μ-radiography system of the tabletop scale [6].

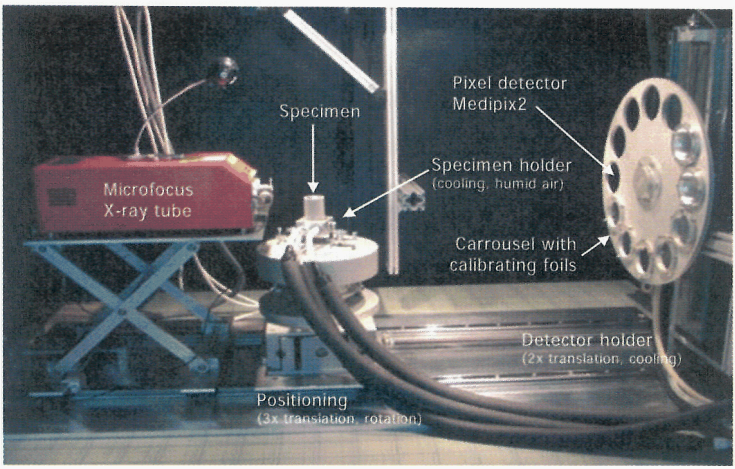

Figure 1. Experimental setup for X-ray μ-radiography and μ-tomography: μ-focus X-ray tube, automatic sample holder and calibration carrousel with images behind.

2. Biological samples used for imaging

The X-ray μ-radiography system can be significantly exploited for μ-imaging of soft tissue and a subject of in-vivo biological studies. For illustration, transmission images we show of a white worm (Fig. 2), parasitic caterpillar and parasite of pupae of Horse-chestnut [7] (Fig. 3) and termites (Fig. 4). Exposure time range was 100 ms - 5 sec per frame. Such frames (about 300 up to 1000) were used for real-time video.

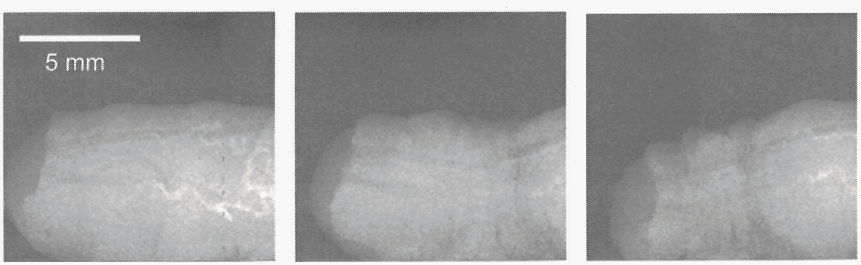

Figure 2. Sequence of X-ray μ-images of living white worm; exposure time 100 ms/frame.

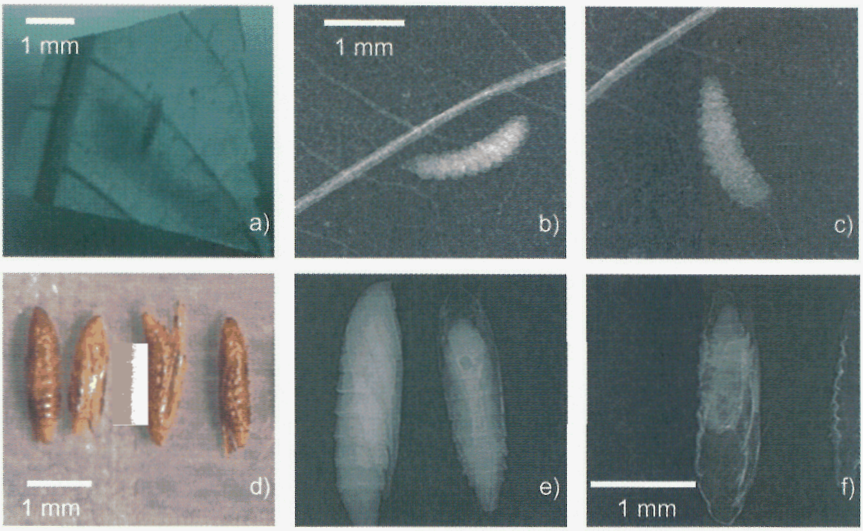

Figure 3. a) Infrared photography of a leaf miner inside a leaf; b), c) Sequence of X-ray μ-images of living caterpillar inside a leaf; d) Photography of a living pupae of leaf miner; e) X-ray μ-image of living pupae; f) X-ray μ-image of a living entomoparasite inside pupae.

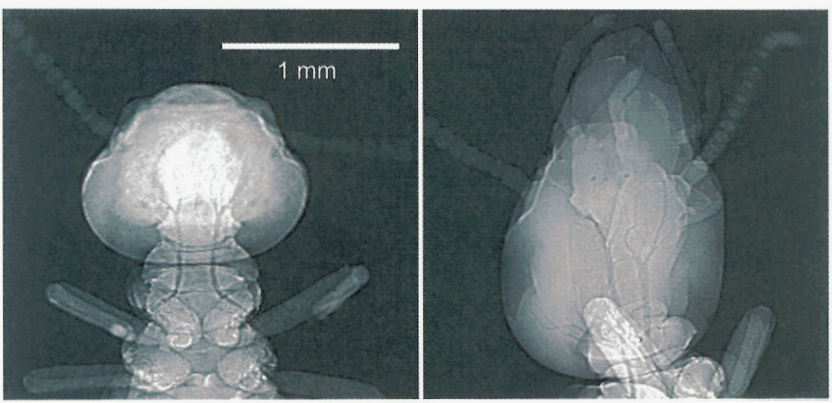

Figure 4. X-ray μ-images of the head of a living termite before (left) and after (right); its metamorphosis from worker to soldier caste; exposure time 5 sec.

By scanning the sample under several angles[e] and by suitable image reconstruction, high resolution tomographic images can be obtained with real μ-scale resolution. 3D-images of mouse bones are shown in Fig. 5 for demonstration.

[e] We used 20 projections (angles) for image of termites up to 180 projections for mouse bones. As more are projections, as better are 3D image reconstructions.

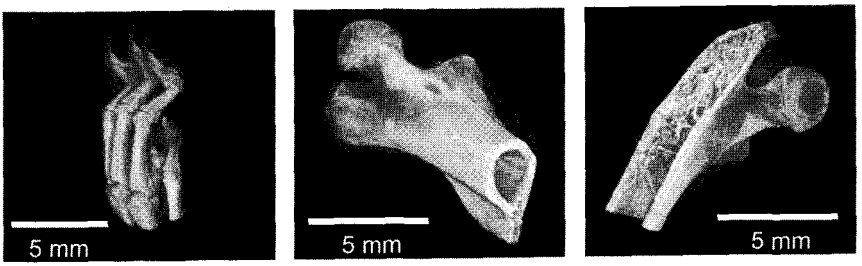

Figure 5. μ-tomographs of mouse bones. 3D images are computed from 180 projections.

3. Conclusions

In-vivo X- ray imaging of a table scale were realized using μ-focus X-ray tube and the performance of the state-of-the-art Medipix2 detector. Routine laboratory measurement are thus possible including in-vivo and time-dependent studies in biological samples [6, 8] such as living worms, caterpillars and termites.

Acknowledgments

This work was realized out in frame of the CERN Medipix Collaboration and was supported in part by the Research Grant Collaboration of the Czech Republic with CERN No. 1P04LA211, by the Fundamental Research Center Project LC06041 and the Research Programs 6840770029 and 6840770040 and Grant No. 2B06005 of the Ministry of Education, Youth and Sports of the Czech Republic. We thank A. Cejnarova and C. Granja from the IEAP CTU in Prague for proof-reading this paper.

References

1. J. Jakubek, D. Vavrik, T. Holy, M. Jakubek, Z. Vykydal, *Nucl. Instrum. Methods Phys. Res. A.* **563**, 278-271(2006).
2. J. Dammer et al., *Amer. Inst. of Phys. V 958*, 136-138 (2007).
3. X. Llopart, M. Campbell, R. Dinapoli, D. San Segundo, & E. Pernigotti, *IEEE Trans. Nucl. Sci.* **49**, 2279–2283 (2002).
4. J. Jakubek, *Nucl. Instrum. Methods Phys. Res A* **576**, 223-234 (2007).
5. R. Fitezgerald, Phase sensitive X-ray imaging, *Phys. Today* (2000).
6. J. Jakůbek, C. Granja et al., *Nucl. Instrum. Methods Phys. Res. A* **571**, 69-72 (2007).
7. F. Weyda, Digital Imaging of Horse Chestnut Leafminer, *(Proceedings of the XVII. Czech and Slovak Plant Protection Conference)*, 541-544 (2006).
8. R. Hanus, J. Dammer et al., *Journal of Microscopy* **576**, 223-234 (2007).

THE AXIAL 3-D PET CONCEPT IMPLEMENTED BY WAVE LENGTH SHIFTER STRIP HODOSCOPES

R. DE LEO, E. NAPPI
INFN-Bari and Phys.Dept., Bari University -70122 Bari, Italy

A.BRAEM, E.CHESI, C.JORAM, J.SEGUINOT, P.WEILHAMMER
CERN, PH Department, CH-1211 Geneva, Switzerland

W.LUSTERMANN, D.SCHINZEL
ETH Zürich, CH-8092 Zürich, Switzerland

I.JOHNSON, D.RENKER
Paul Scherrer Institut, CH-5232 Villigen, Switzerland

S.ALBRECHT
University Hospital Geneva, CH-1211 Geneva, Switzerland

The 3D HPD-PET concept is based on stacks of ~15 cm long axially oriented scintillator bars read out at both ends by a segmented HPD. The x and y spatial resolution of this concept are linked to the transverse sizes of the scintillators, while the z axial resolution to their length Lc and to the effective scintillation light attenuation length λ_{eff}. To improve this last resolution without decreasing Lc or λ_{eff}, we propose an alternative read out of the axial coordinate based on hodoscopes of thin wavelength shifter (WLS) strips, oriented orthogonal to the axis of the crystals, and singularly read out by G-APDs. A voxel resolution of about 10 mm^3 is expected. The validity of the method has been proved and its performance has been measured using PMTs and G-APDs to read out the LYSO (LSO) scintillators and wavelength shifting strips 2 mm wide. Axial resolutions of about 2.5 mm (FWHM) have been obtained for γ-rays of 511 keV.

1. Introduction

The HPD-PET concept [1,2] consists of ~15 cm long LYSO crystals with a cross section of 3.2×3.2 mm^2, axially oriented, separated by 0.8 mm, and stacked in matrices of 16x13 crystals, optically coupled at both ends to one pixelized HPD. The axial z-coordinate of the scintillation point is obtained from the ratio of the photoelectrons in the two HPDs, the transaxial x- and y-coordinates from the hit crystal.

In the WLS HPD-PET concept [3] the z-coordinate is obtained in a different way, by layers of thin wavelength shifter (WLS) strips stacked between the scintillator crystals and orthogonal to these (Fig. 1). The WLS strips are

arranged as z-hodoscopes placed in the 0.8 mm wide air gaps between the crystals. The role of the scintillators is now limited to detect the x and y coordinates and to measure the deposited energy. Crystals with long absorption lengths can be employed, which ensure better energy resolutions. The WLS strips are excited by the scintillation light (e.g. LSO: $\lambda \sim 420$ nm) which is not trapped in the crystal by total internal reflection (see Fig. 1). Part of the scintillation light escaping from the crystal bars is absorbed by the WLS strips and re-emitted as fluorescence light at about 490 nm (Y-11 WLS). A fraction of the fluorescence light trapped in the strip by total internal reflection propagates to the two end faces of the strip. One end face of the WLS strips is mirror-coated reflecting the light to the opposite end, where it is detected by compact fast photo sensors.

If only the signal from one WLS strip with width d closest to the photon interaction in the LYSO crystal is detected one obtains a digital spatial resolution ($\sigma = d/\sqrt{12}$) which can be tuned by varying d. For hits where the conversion of a 511 keV photon in the LYSO crystal is seen by more than one WLS strip, the z-coordinate can be determined by a centre of gravity algorithm requiring that the readout electronics provides analogue information. For such events one might expect that the z-resolution is even better than digital resolution. G-APDs are very good candidates for the readout of the WLS strips.

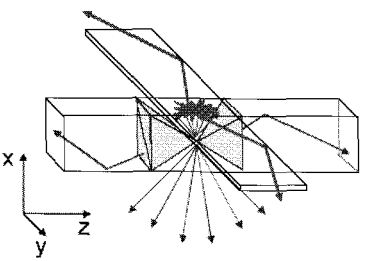

Figure 1. Details of scintillation and fluorescence light trapping. Only one crystal and one WLS bar are shown.

2. Experimental procedures

Two different and independent approaches, shown in Fig.2, have been followed to assess the potential of the WLS based z-readout.

2.1. *Pulsed low energy electron source*

In order to vary the energy deposition in the scintillator crystal and its position,

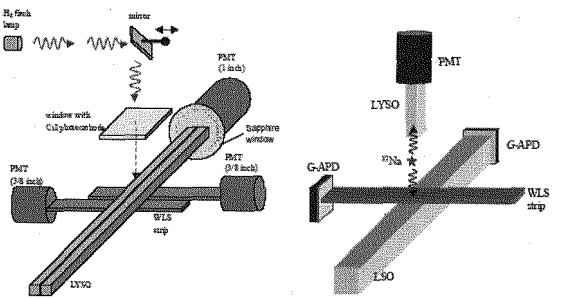

Figure 2. Details of scintillation and fluorescence light trapping. Only one crystal and one WLS bar are shown.

we used a set-up based on a pulsed source of low energy electrons which impinge on the crystal. The electrons are produced by illuminating a semitransparent CsI photocathode with short light pulses (~10 ns) from a H2 flash lamp. The negative potential of the photocathode *Ucath* ($10 \leq Ucath \leq 27.5$ kV) defines the kinetic energy of the electrons when they hit the crystal surface. The total energy deposition is controlled through the number *Ne* of electrons in the pulse. Two LYSO:Ce crystals ($3.2\times3.2\times100$ mm^3) were mounted side by side, with one of their end faces optically coupled through a Sapphire window to a single PMT. The other end faces are mirror-coated with a vacuum evaporated Al film. Two 60 mm long WLS strips (3×1.1 mm^2) were mounted orthogonal to and underneath the two crystals with a small air gap of about 0.1 mm. An Aluminum foil under the strips reflects the small fraction of non absorbed light back onto the strip. The strip end which is not read out was also coated with a reflective Aluminum film. The set-up allows continuously varying the deposited energy and displacing the beam spot in a controlled way in order to measure the z-resolution of the WLS based readout. The beam spot at the level of the crystals has Gaussian shape with FWHM of 1.8 mm, both in the x and y coordinate. The available intensity of the collimated H2 flash lamp allowed energy depositions up to about 425 keV per pulse. The measurements were performed in vacuum.

In first approximation, the total energy deposited in the crystal per bunch is: $Edep = Ne \cdot e \cdot Ucath$. For relatively small numbers of electrons per bunch ($Ne < 30$), the fluctuation $\sigma(Ne) = \sqrt{Ne}$ dominates over the photon statistics and the intrinsic resolution of the scintillator. The number of electrons in the bunch and hence the deposited energy can therefore be determined from $Ne = (Q/\sigma(Q))^2$ with Q and $\sigma(Q)$ being the charge amplitude and its fluctuation, respectively, measured with the PMT connected to the LYSO crystal. Absolute calibration of

the PMT gains was performed by determining the response of the PMTs to single photoelectrons generated by a pulsed LED. This allows converting the measured charge to the number of detected photoelectrons. The analysis is complicated by two low energy effects: (1) A fraction (~45%) of the electrons is back scattered from the LYSO crystal without depositing their full energy. (2) The light yield of LYSO scales with the deposited energy in a non-linear way described by the Relative Light Output function *RLO*. A straightforward Monte Carlo model, based on measured back scattering and light yield data is used to describe the two effects and to derive from the measured charge and its fluctuation, Q and $\sigma(Q)$, the actually converted energy. We estimate the relative precision of the converted energy to be ±10%.

Photoelectron yields of 1160 and 42 pe's, values extrapolated to a converted energy of 511 keV, have been deduced for a scintillator crystal and for the sum of the two WLS strips, respectively, yields a photoelectric yield of 1160 pe. The WLS value guarantees full detection efficiency even for deposited energies of 100 keV.

The z-coordinate can be reconstructed using the yield ratio of the two WLS strips. Fig. 3 shows the reconstructed z coordinate versus the position of the beam spot derived from the mirror position (see Fig. 2, left). In the region of the WLS strips indicated in the figure, the reconstructed z coordinate varies linearly with the mirror position. Outside the WLS strips, signals are seen only in the closer WLS strip resulting in a constant value for the reconstructed coordinate. The width of the *zrec* distribution as function of the converted energy is shown in Fig. 4. It shows the expected $1/\sqrt{Econv}$ dependence. Extrapolation to 511 keV leads to a σ_z-resolution of 1.1 mm (2.7 mm FWHM).

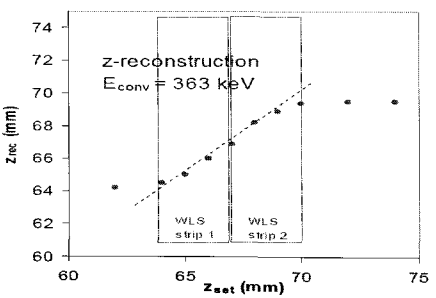

Figure 3. Reconstructed z-coordinate (for a converted energy of 363 keV) versus the z-coordinate of the electron beam. The position of the two 3 mm wide WLS strips is indicated. If the beam spot is placed besides the strips, such that the light is detected only by one strip, the reconstruction algorithm produces a constant value.

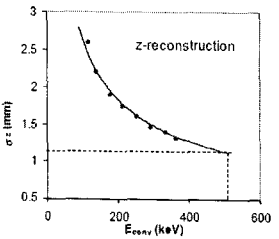

Figure 4. The reconstruction precision is plotted versus the converted energy. Extrapolations to 511 keV indicates a precision of σ_z=1.1 mm.

2.2. *Radioactive 22Na source*

In the second set-up a smaller LSO crystal (3×3×50 mm^3) and an orthogonal WLS strip (same type and dimensions as above) were exposed to annihilation photons from a ^{22}Na source. Both the crystal and the WLS strip were read out at one end by a G-APD of 3×3 mm^2 size. A small LYSO crystal (2×2×12 mm^3) read out by a PMT served to tag the second annihilation photon. The non-read end of the LSO crystal was closed with white Teflon tape and 3 of the long sides were covered with reflecting foil (V2000 from 3M). The upper side of the strip was covered with a reflecting foil and the non-read end with Teflon tape.
For the 511 keV γ-rays an energy resolution of 11.5% FWHM was obtained, in good agreement with the value estimated from photoelectric yield measurements performed on the electron source set-up, discussed before. The photoelectric peak corresponds to 43.5 pe's.

3. Conclusions

We propose a detector concept for PET scanners where long axially oriented scintillators are read out on one or both ends. The axial z-coordinate is derived from a hodoscope made of thin WLS strips slotted in between the crystals. Our measurements, performed with two different and independent set-ups, using classical PMT and G-APD for the readout, proved the feasibility of this geometrical configuration and demonstrated that a z-resolution better than σ_z = 1.1 mm can be achieved at $E\gamma$ = 511 keV. Given the transverse size of the scintillators, a voxel resolution of about 10 mm^3 (FWHM) appears fully realistic.

References

1. J. Séguinot et al., Il Nuovo Cimento C **29,** Issue 04, pp 429-463.
2. I. Vilardi et al., Nucl. Instr. And Meth. **A 564** (2006) 506–514.
3 A. Braem et al., Nucl. Instr. And Meth. **A 580** (2007) 1513.

APPLICATION OF PIXEL DETECTORS IN STRUCTURAL BIOLOGY

A.R.FARUQI
MRC Laboratory of Molecular Biology,
Hills Road,
Cambridge CB0 2QH, U.K.

Abstract

Silicon pixel detectors (both hybrid and active pixel sensors), are potentially useful for electron microscopy and x-ray crystallography. By direct detection of x-rays or electrons, these detectors eliminate the intermediate step of light conversion required by CCDs, which reduces the spatial resolution. Pixel detectors offer excellent spatial resolution, high efficiency and fast readout speeds. The main emphasis of this review is on electron detection in the context of electron microscopy with a brief section on x-ray crystallography.

1. *Introduction*

The two main techniques used in structural biology for structural analysis are electron cryo-microscopy (cryoEM) and x-ray crystallography. There is a rapidly growing number of large structures being tackled with cryoEM due partly to technical advances in microscopy. CryoEM is a stand-alone technique but it can also be considered as complementary to x-ray crystallography though the resolution attained is somewhat lower. On the other hand, an important advantage with cryoEM is that it is not necessary to obtain good quality crystals as are required for x-ray crystallography. Large amounts of data are needed to obtain a structure, most of which are very radiation sensitive so it is vital to use an efficient detector for data collection. Although film, which has been used for many years in cryoEM has excellent resolution and efficiency for electrons (though not x-rays), it requires lengthy processing before the data is available. The replacement of film by electronic detectors would be very desirable as data is available immediately providing rapid feedback to the user leading to possibly more efficient use of specimen [1,2]. Phosphor-coupled CCDs are indirect electronic detectors, operating by first converting the energy of the incident electron to light photons and subsequently recording the optical image on a low-noise CCD. Light scattering in the phosphor and the optical interface lead to an unacceptable loss of resolution in the image, i.e. reduces the modulation transfer function (MTF). Eliminating this intermediate light conversion step should, in principle, and in practice does, lead to improved resolution and signal-to-noise ratio (SNR)[1,3].

2. *Pixel Detectors*

Two main types of direct detection devices have been studied for electron microscopy and x-ray crystallography. Firstly hybrid pixel detectors (HPDs), of which Medipix2, developed within the Medipix collaboration based at CERN is a good example [4-6]. Secondly, monolithic active pixel sensors (MAPS) designed at Rutherford Appleton Laboratory were tested for electron microscopy [7]. In the following sections we will describe some basic properties of these detectors, some applications and prospects for future developments.

Although operationally distinct, the two types of detectors nevertheless share some common properties. For instance, both detectors are made possible by the availability of high density microelectronics device integration in CMOS technology, which allows a large number of features to be packed into small spaces and to have small pixel sizes. In both cases the primary electron deposits energy resulting in the creation of a number of electron-hole pairs, which constitutes the signal. There are, however, a number of significant differences in design and, more importantly, in performance. For HPDs the process of electron detection and subsequent readout of the result are separated into two layers of silicon. A detector layer, which is typically silicon (p-i-n diode) but could be made from a higher density material, is 300 μm in thickness (in the detectors under review); it is fully depleted by a suitable voltage applied across the detector layer. The holes created initially are forced by the drift field towards the bump-bond and the readout electronics. In MAPS, on the other hand, the detection and readout are integrated into the same layer of silicon. There is a relatively thin sensitive layer (4-20 μm) of high resistivity silicon which acts as the detector but has a number of collection diodes built into the pixel. The charge from the primary event, collected in the diodes, constitutes the signal [7].

3. *Simulation of electron trajectories in silicon*

Detector performance can be predicted by employing a simulation programs to model the behaviour of electrons in silicon. A simulation of electrons within the energy range 60 -300 keV in 300 μm thick silicon and CdTe is shown in Fig.1 [8]. The faint vertical lines in the figure are drawn at a spacing of 55 μm, chosen to be the same as the pixel size in Medipix2. For the lowest energy, i.e. 60 keV, the lateral spread of the primary electron is restricted to well under one pixel. At higher energies, the lateral spread increases progressively until, at 300 keV, the spread is over a number of pixels. The lateral spread results in a worsening of spatial resolution, which has also been confirmed experimentally. At 300 keV, a small fraction of the primary electrons are transmitted through the sensor - potentially causing damage to the readout chip.

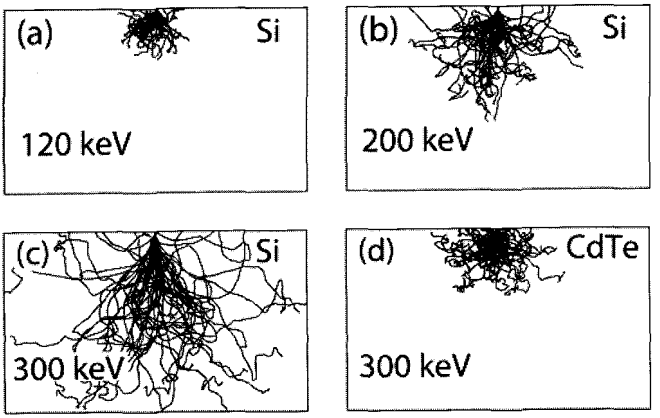

Fig. 1. Monte Carlo simulation of electron trajectories of electrons in the range 60-300 keV in silicon and 300 keV in CdTe [8].

4. *Spatial resolution*

The resolution, also expressed as the modulation transfer function (MTF), of Medipix2 was measured at 40, 80 and 120 keV using a standard knife-edge method [8]. As expected from simulations, the resolution is best for the lowest energy (40 keV) but is still very good at 120 keV. The setting of the pixel thresholds has a very dramatic effect on the resolution: at the lowest energy settings the resolution is poor and at high thresholds it is better. The setting of the optimum thresholds is a compromise between resolution (MTF) and efficiency (DQE – see below). The MTF at Nyquist frequency, where Nyquist frequency is given by $(2*\text{pixel size})^{-1}$, is plotted in Fig.2 (a) as a function of pixel thresholds. Various symbols represent the experimental measurements, which agree well with predictions given as solid curves [8].

5. *Detective Quantum Efficiency (DQE)*

The DQE of a detector is a measure of efficiency and the amount of noise added by the detector and can thus be used as a figure of merit for the detector [8]. The DQE of a detector is defined as:

$$DQE = (S/N)^2_{output}/(S/N)^2_{input}$$

The DQE at Nyquist frequency can be calculated as follows:

$$DQE\ (Nyquist) = DQE\ (0) \times MTF\ (Nyquist)^2/NTF\ (Nyquist)^2$$

Where NTF refers to the noise transfer function. The maximum value of MTF at Nyquist frequency for a pixellated detector is $2/\pi$ (=0.636) so that the maximum value of DQE at Nyquist, which has a DQE (0) of 1.0 and NTF of 1.0, is given by $4/\pi^2$ (0.404). Fig.2 (b) shows the DQE (Nyquist) as a fraction of the maximum possible value as triangles along with the theoretically predicted continuous line. The dotted line gives the experimental values for DQE (Nyquist). An outstanding feature of Medipix2 is that the DQE is independent of the electron dose.

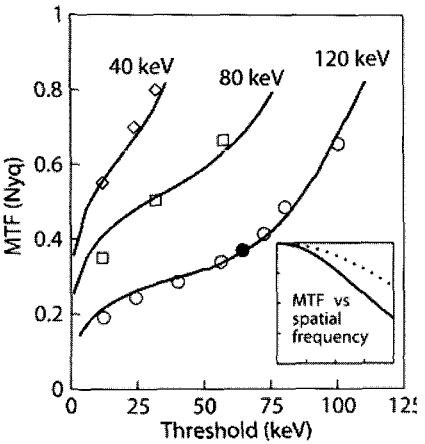

Fig. 2 (a) left: MTF in Medipix2 as a function of pixel thresholds at 40, 80 and 120 keV [8]

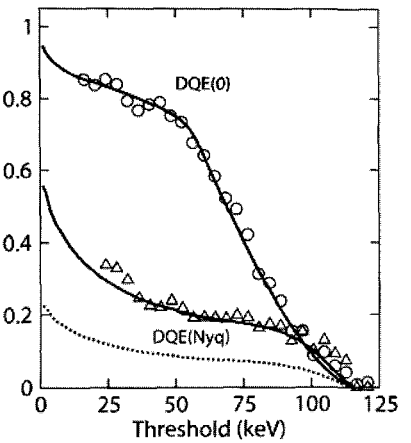

Fig. 2 (b) right: DQE at zero frequency and at Nyquist frequency in Medipix2 as a function of threshold at 120 keV [8]

6. *Single Particle Imaging*

An example of single particle imaging is taken from a recent publication [9]. The particle studied, Rotavirus, is a spherical virus with icosahedral symmetry, implicated in gastroenteritis. Fig.3 (a) is an image of the Rotavirus in a single frame with approximately 1.6 counts per pixel or approximately 1.5 electron per pixel. This dose, which is extremely low, corresponds to an electron dose of only ~0.03 electron/Å^2 at the specimen. Since it is possible to use up to 5-10 electron/Å^2 in cryo-imaging, Medipix2 could be used for specimen alignment purposes provided the contrast of non-stained specimen is not very much lower. When the sum of 100 frames is taken with approx.1.6 counts per pixel and the images have been aligned to within 1/4 of a pixel before being added (i.e. each image was expanded by a factor of 4 before being aligned) the image shown in Fig.3 (b) is obtained [9].

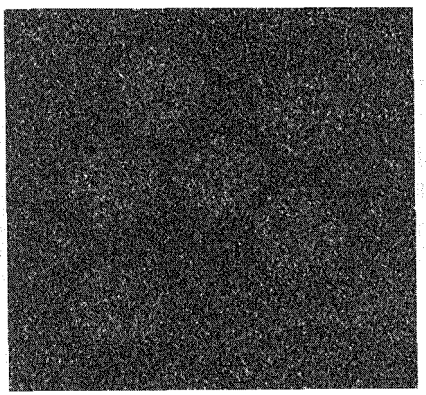

Fig. 3 (a) Image of Rotavirus taken with Medipix2 at extremely low electron dose: 1.6 electron/pixel

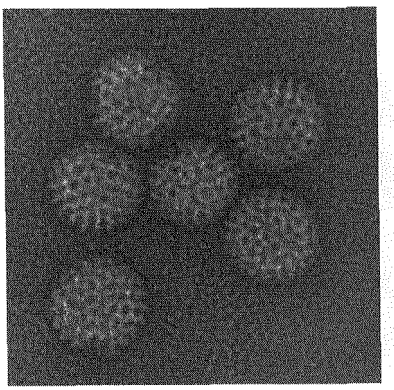

Fig. 3 (b) Similar Rotavirus image to (a) but imaged with 160 electrons/ pixel [9]

7. *Future Prospects for Medipix2*

The high sensitivity of Medipix2 combined with noiseless readout makes it an ideal detector in the lower range of energy of interest, *viz* 40-120 keV. The detector thickness, 300 μm of silicon, is sufficiently thick to prevent primary electrons from reaching the readout electronics and cause radiation damage[10]. Since the readout is noiseless it is possible to accumulate data by summing a number of individual images without any deterioration in signal-to-noise ratio, potentially increasing the dynamic range to an arbitrarily high figure. This could be very useful, for example, in recording electron diffraction data where weak and strong spots occur in the same pattern. Image contrast can be improved for non-biological specimen, which are not susceptible to radiation damage, by using high exposures.

The solution to poor resolution at 300 keV is unlikely to be solved without changing the detector material from silicon to either cadmium telluride (CdTe) or gallium arsenide (GaAs), both of which have much greater stopping power. The predicted behaviour of 300 keV electrons in CdTe is very similar to 120 keV electrons in silicon (Fig.1). The expectation is that, once the technology of producing satisfactory grade of CdTe has been achieved, it should be possible to obtain better resolution at 300 keV. The reduced range of the 300 keV electrons would also mean that radiation damage would be less of a problem even with the current Medipx2 readout chips (although future versions of the Medipix2 chip may be much more rad-hard).

The total size of the detector used in the present tests was a Quad chip, consisting of 512 by 512 pixels. In order to fulfil our criteria for the 'acceptable' detector, the size would need to be increased by a factor of 8 in both directions, to arrive at the required number of pixels: 4k by 4k. A start has been made to tile an array of Quads into larger areas, in a project called High Resolution Large Area X-ray Detector (RELAXD) by Panalytical [11], an industrial company, which has been closely associated with the Medipix2 chip. The existing Medipix2 chip is only 3-side buttable so it is not possible in its present form to consider larger area tiling. The plan is to modify the Medipix2 chip to make it 4-side buttable, thus making larger area detectors possible. The concept of the super-tiling is simple enough in principle – the wire connections from the readout chips are taken out through the silicon to the back-side of the wafer rather than to one side as was the case in the original design. The plan is to use the existing Medipix2 readout but to use through-wafer connections. The plan in the first phase is to design a detector with a 3 x 3 array of Quads, i.e. with 1.5k x 1.5k in the detector. Depending on the experience with the first design, more challenging designs, with larger arrays, could be undertaken in future.

8. *Applications to x-ray crystallography*

Some of the detector requirements for x-ray crystallography using synchrotron radiation are similar to those for electron microscopy. The x-ray energies used are typically 12-20 keV so the 300 μm thick sensor provides adequate detection efficiency. Since large macromolecular structures crystallise into large unit cell crystals it is necessary to record ~500 or more orders of diffraction spots – leading to a requirement for at least 2kx2k pixels in the detector. Spatial resolution or point-spread function needs to be extremely high to resolve closely packed spots. Since very weak spots could lie adjacent to very strong spots it is vital not to have any 'blooming' effects as seen on CCDs. A large dynamic range is essential for recording the weak and strong spots in the same exposure.

Most of the above mentioned requirements are fulfilled by a hybrid detector, PILATUS 6M and some of it's predecessors [12], designed and built at the Paul Scerrer Institute, Switzerland. There are about 6 million 172 μm pixels in the detector with a 20 bit counter in each pixel. Modular in construction the detector relies on tiling a large number of single chips (90,000) into modules, which are tiled to create a detector with a dimension of 431 mm x 448 mm with only ~7% dead space. The readout of data is massively parallel taking only 2 ms for the entire frame.

The rapid readout is an extremely useful feature for the rotation method for data collection. During such data collection the crystal is rotated at a constant speed. With traditional data collection with CCDs it is necessary to stop the

rotation during readout and close the beam shutter to avoid radiation damage to the crystal. Re-starting the crystal rotation introduces a degree of ambiguity in the angular position of the crystal. With the fast readout in PILATUS 6M it is not necessary to stop the rotation and interrupt the data collection – a significant advantage.

9. *Pixel Detectors, MAPS*

The second type of direct imaging detector considered in this review is a monolithic active pixel sensor (MAPS). The detection volume is contained in a high resistivity, p^- epilayer, ~4 μm in thickness grown on top of low resistivity p^{++} bulk silicon with n^+ diodes implanted in the epilayer. The p^{++} substrate does not have any function in the electron detection process but gives strength and support to the thin epilayer. As there are no electrical fields (other than potentials created due to different doping) in the epilayer and the signal electrons are only able to travel by diffusion. Any electrons diffusing towards the p^{++} bulk layer are reflected back into the epilayer due to the potential difference at the boundary and electrons diffusing towards the n^+ region are trapped in a potential well and unable to escape. MAPS detectors use this process to read out the signal by making the n^+ into a readout node as discussed below. A schematic diagram showing a single pixel layout is shown in Fig.4. The particular sensor used in the first tests was designed at the Rutherford Appleton Laboratory in complementary metal oxide semiconductor (CMOS) technology [7,13].

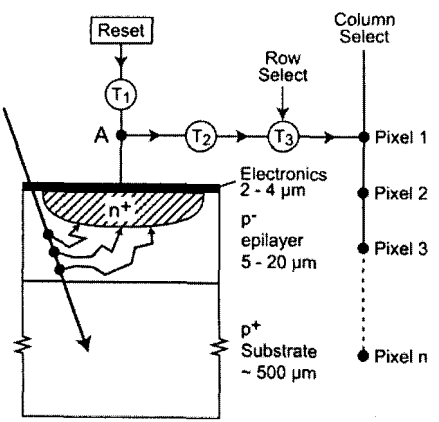

Fig. 4 Single pixel schematic diagram for a CMOS detector [7].

Tests were carried out to establish the viability of the first MAPS for electron microscopy at energies within the range 40-300 keV [14]. The main object of the tests, similar to the tests on Medipix2, was to measure the performance of MAPS in terms of spatial resolution, efficiency and SNR and susceptibility to radiation damage. The resolution was measured by recording the image of an electron microscope grid, which can be considered as a series of 'knife-edges'. The image in Fig. 5(c) shows an image of the grid recorded with a dose of ~6 primary electrons/pixel; the Fourier transform of the image is used as a measure of resolution. Comparing the results with film, which has very good resolution, about 50% of film. Single electrons were recorded, as shown in Fig.5 (a) by reducing the electron dose to .06 primary electrons/pixel when the likelihood of double counts is negligible. Integrated signal from single electron events can be used to obtain signal to noise ratio – which was ~20.

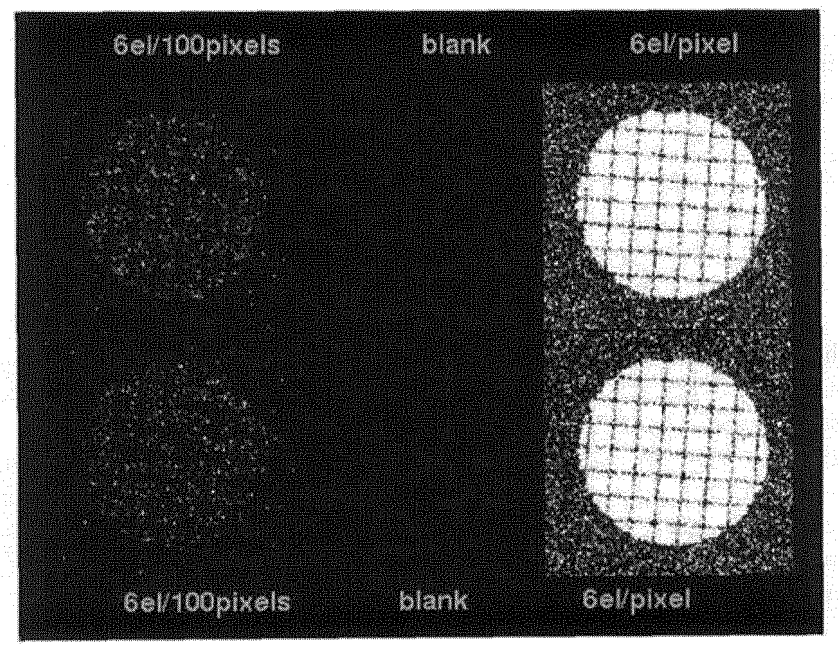

Fig.5 (a - left) and (c - right) Single electron events imaged on a MAPS detector at 120 keV using very low doses (left). Higher doses used to image an EM grid on the right . [14]

10. *Radiation Damage*

Radiation damage was tested on a rad-hard sensor, the STAR250, produced by Fillfactory [15]. The main conclusion from this experiment was that, if a rad-hard sensor was used for electron microscopy it retained a residual contrast was 82% after an integrated dose of 1 Mrad ($8x10^{10}$ 300 keV electrons/mm^2). The lowered contrast can be explained more clearly by pointing out the greatly increased dark levels. - any subsequent signal needs to be measured above this new raised 'baseline'.

11. *Summary and outlook for MAPS*

Although the signal from MAPS-type detectors for electrons are much smaller than in Medipix2, and there is some readout noise the signals are sufficiently large to give a reasonable SNR for single electron recording. An important feature for recording electrons with 300 keV energy is that the resolution is better than at 120 keV due to the smaller spread of charge in the epilayer. The pixel design is flexible enough to allow pixel size between 5 – 40 μm, to be applicable in different applications.

The performance of existing sensors can be improved in three ways:

1. Reduce the amount of material in the sensor [16]
2. Obtain large areas by stitching a number of sensors [17],
3. Design pixel layouts to be rad-hard to ~1 Mrad [18].

The DQE and resolution of MAPS is very good and likely to improve as suitably back-thinned detectors become available. Combining the radiation resistance of the rad-hard STAR250 sensor into the MAPS detector would produce an extremely useful device, but with only 512 x 512 pixels. As already discussed, a larger format sensor, with 4k square array is essential for many applications. New developments in CMOS designs may allow stitching together a number of smaller (1024 x 1024) sensors into a larger sensor with an adequate number of pixels.

References

1 A. R. Faruqi, R. Henderson, and S. Subramaniam, *Ultramicroscopy* **75,** 235 (1999).

2 A. R. Faruqi, R. Henderson, *Current Opinion in Structural Biology* , **17, 1,** (2007).

3 A. R. Faruqi and S. Subramaniam, *Quarterly Reviews of Biophysics 33, 1 (2000).*

4 X. Llopart and M. Campbell, *Nucl. Instr. and Meth* A **509,** 157 (2003).

5 http://medipix.web.cern.ch/MEDIPIX.

6 H.Krüger, *Nucl. Instr. and Meth.* A**551**,1 (2005)

7 M. L. Prydderch, Waltham, N.J., Turchetta, R., French, M.J., Holt, R. Marshall, A., Burt, D., Bell, R., Pool, P., Eyles, C. and Mapson-Menard, H. , *Nucl. Instr. Meth.* **A512,** 358 (2003).

8 G. McMullan, D. M. Cattermole, S. Chen, R. Henderson, X. Llopart, C. Summerfield, L. Tlustos, and A. R. Faruqi, *Ultramicroscopy* **107,** 401 (2007).

9 G. McMullan and A. R. Faruqi, Nucl Instr. and Meth. (2007) submitted.

10 A. R. Faruqi, R. Henderson and Tlustos, L., *Nucl. Instr. and Meth.* **546,** 160 (2005).

11 K. Bethke, R. Vries, V. Kogan, J. Vasterink, R. Verbruggen, P. Kidd, P. Fewster, and J. Bethke, *Nucl. Instr. and Meth.* A**563,** 209 (2006).

12 C. Broennimann, E. F. Eikenberry, B. Henrich, R. Horisberger, G. Huelsen, E. Pohl, B. Schmitt, C. Schulze-Briese, M. Suzuki, T. Tomizaki, H. Toyokawa, and A. Wagner, *J. Synchrotron Rad.* **13,** 120 (2006).

13 http://mi3.shef.ac.uk/.

14 A. R. Faruqi, R. Henderson, M. Prydderch, R. Turchetta, P. Allport, and A. Evans, *Nucl. Instr. and Meth.* **546,** 170 (2005).

15 A.R.Faruqi, R. Henderson, J.Holmes, *Nucl. Instr. and Meth* **A565,** 139 (2006).

16 R. R. Meyer, A. Kirkland, *Ultramicroscopy* **75,** 23 (1998).

17 http://www.towersemi.com/.

18 J. Bogaerts, Dierckx, B., Meynants, G. , Uwaerts, D., IEEE *Trans.Elec.* Dev. **50,** 84 (2003).

ULTRA-FAST TIMING AND THE APPLICATION OF HIGH ENERGY PHYSICS TECHNOLOGIES TO BIOMEDICAL IMAGING

CHIN-TU CHEN, CHIEN-MIN KAO, QUIGGUO XIE
Biological Sciences Division, University of Chicago (USA)
Email: cchen3@uchicago.edu

HENRY FRISCH, MARY HEINZ, HAROLD SANDERS AND FUKUNG TANG
Enrico Fermi Institute, University of Chicago (USA)
Email: frisch@hep.uchicago.edu

JOHN ANDERSON, KAREN BYRUM,GARY DRAKE AND CAMDEN HEARTLY
Argonne National Laboratory (USA)
Email: byrum@hep.anl.gov

PATRICK LE DÛ AND CHRISTOPHE ROYON
DAPNIA CEA Saclay (France)
Email: pledu@cea.fr

JEAN FRANÇOIS GENAT
CNRS/IN2P3 (France)
Email: genat@.in2p3.fr

JERRY VA'VRA
Stanford Linear Accelerator (USA)
Email: jjv@slac.stanford.edu

We propose to apply the ultra fast Time Of Flight technique (TOF) developed for High Energy Physics (HEP) particle detectors to biomedical imaging. The similarity of the problem in the two fields as well as the remarkable opportunities in biomedical imaging to use technologies developed in HEP have the potential to make major advances in the medical world, in particular for Positron Emission Tomography (PET). We will describe and present some preliminary results of the development of a new complete read-out chain able to manage signals from various types of modern photo detectors (MCP, APD, SiPM). This innovative architecture is made of a fast front-end electronics ASIC with novel Digital Signal Processing (DSP) concepts able to reach the Pico-second timing resolution, a time-to-digital converter, a pipelined digital readout and an integrated

trigger/filter with real-time data treatment and display. In parallel with the hardware development, we have begun a systematic program to simulate system characteristics from the initial particle interaction to the final digital data, including a bit-by-bit mapping of the front end/data acquisition system. The introduction of these techniques and tools, common in HEP, has the potential to make improvement to biomedical imaging systems.

1. Introduction

In HEP, the resolution in time measurements translates into resolution in space, which turn in a second step into impact momentum and energy measurement. Nowadays, silicon strips and pixels detectors have reduced the ultimate position resolution to few microns. But, time resolution has not yet follow this evolution and not much changed since the 60's in large scales Time Of Flight detectors in term of resolution as well as technologies (thick scintillators or crystals, PMT's, Lecroy TDC's). Improving time measurement is fundamental and can affect many fields like particle and nuclear physics, astrophysics, laser accelerators and biomedical imaging. To improve the situation, we need to understand what are the fundamental limiting underlying physical processes - e.g. sources line widths, photon statistics, e/photon path length variations. Recent studies [1,2,3] shows that few picoseconds are reachable for HEP and we guess around 30-40 picoseconds for Medical Imaging.

2. From HEP to medical imaging

Basic science instrumentation like High Energy Physics is developing state of the art techniques and tools, which can be transferred very efficiently in bio-medical imaging field. For example:

- New scintillating crystals and photon detection materials. (The Crystal Clear Collaboration: from the CMS PBO4 to the LuAp)
- Highly and compact light transducers: Photomultipliers (PMT), Avalanche Photo Diode (APD) and now Silicon Photomultipliers (SiPM).
- Highly integrated fast, low noise and low power electronics (preamp, shaper..)
- Dead timeless signal treatment (pipeline read-out) and digital processing techniques.
- Real Time event selection (trigger) and collection (data acquisition) with high level of parallelism and event filtering.
- Modern computing and modular simulation software using worldwide recognized standards like GEANT.

3. HEP Calorimeter versus PET

The most typical example with a lot of similarities and few differences between the two fields is the Positron Emission Tomography imaging (PET) which looks like a standard HEP calorimeter. Similarities are : the geometry and granularity, the detector are made of crystal and scintillators, the transducers are PMT, APD's, read-out by compact and fast electronics (40 MHz) and the data volume produced is of the order of Gbit/sec. The few differences are like the energy range (511 Kev), free running electronics, multiple vertices and low event rate of 10KHz.

4. Time of flight for PET imaging

Current PET technologies are constrained by several crucial limits in their capabilities. For example, the best human PET systems currently available offer a spatial resolution around 2-4 mm, and the best animal PET systems have resolutions of about 1-1.5 mm. The system sensitivity, defined as the ratio of detected coincidence events to all annihilation events, for the most advanced PET systems in existence ranges from only 2-4\% (human PET) to 6-8\% (animal PET). These limitations in spatial resolution and system sensitivity pose many restrictions on what types of PET studies we can perform today, both in medical diagnosis and therapy and in biomedical research and development. It is essential to find innovations in order to bring PET beyond these barriers. It is also highly desirable that these novel technologies be relatively low-cost.

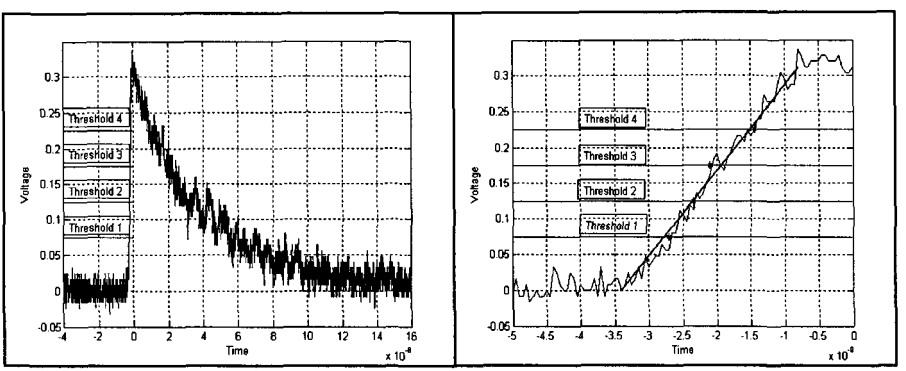

Fig. 1. DSP Multi-threshold method.

The time points on the leading edge of an event pulse are determined with respect to preset thresholds. A least-square fit of the time points obtained with a straight line is determined. The intercept of this line with the signal baseline defines the event time.

As we will discuss below, accurate time-of-flight measurements of the two coincidence photons in PET would qualitatively change the above picture. Our goal of 30 psec resolution on the time difference between the photons would limit each coincidence event to a space point with a resolution of 4.5 mm, rather than having a complete uncertainty along the line of response. It would also reduce substantially the effects of scattering and random coincidences. Lastly, HEP-style pipeline electronics would allow data-selection and reconstruction in close to true real-time.

5. Reaching the ultimate timing resolution

In a previous complete study [4] which compare the contribution of each element of a classical electronics read-out chain, it clearly appears that the Constant Fraction Discriminator (CFD) and the Time to Digital Converter (TDC) are the two main critical limiting factors. With modern technology, sophisticated DSP techniques can be readily implemented, and upgraded, by using FPGA's.

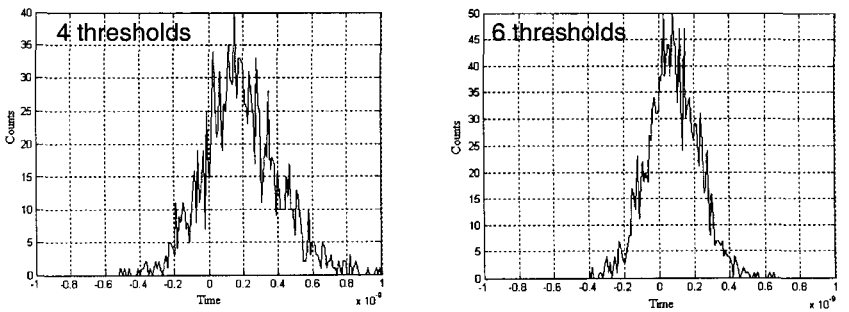

Fig. 2. Timing coincidence estimated.
For 4 thresholds: 360 psec FWHM (estimated single channel σ= 108 psec)
For 6 thresholds : 240 psec FWHM (estimated single channel σ = 72psec)

First, we focus on the determination of the event time (Fig.1). We are building a substantial waveform library that contains pulses generated by PET detectors employing different scintillation materials, crystal geometries, photo-detectors, and readout electronics. The pulse library contains more than 20,000 event records digitized waveforms of the event pulses produced by a pair of LSO/PMT modules. The set up of the test stand is made of two PMT's (Hamamatsu R9800@-1300V bias) with LSO crystal (size is 6.25x6.25x25 mm^3) sit on top of

its window. The LSO is coupled to the PMT through its 6.25x25 mm^2 surface and the other five sides are wrapped with Teflon tape. The two PMT pulses are simultaneously digitized by using a Tektronics TDS6154C digital oscilloscope at a 50 ps sampling interval. The DSP results reported below use a dataset that contains 1500 records of pulses having energy above ~350 keV. The timing coincidence histogram shown in Fig.2 is the histogram of the differential arrival time of the two 511 keV photons detected by placing a FDG source between two such modules. The single-channel timing is the estimation of the timing precision of each module from the coincidence timing measurement. I assumed the two modules are identical; therefore, the coincidence timing resolution will be sqrt (2) times the single-channel timing precision. The DSP method examined can yield a coincidence timing resolution of ~300 ps FWHM, which is comparable with measurements made using analog CFD's. We note that the reported DSP results include the effects of crystal size, shot noise in the PMT and electronics noise, as well as the effect of the 50 ps finite sampling interval of the oscilloscope.

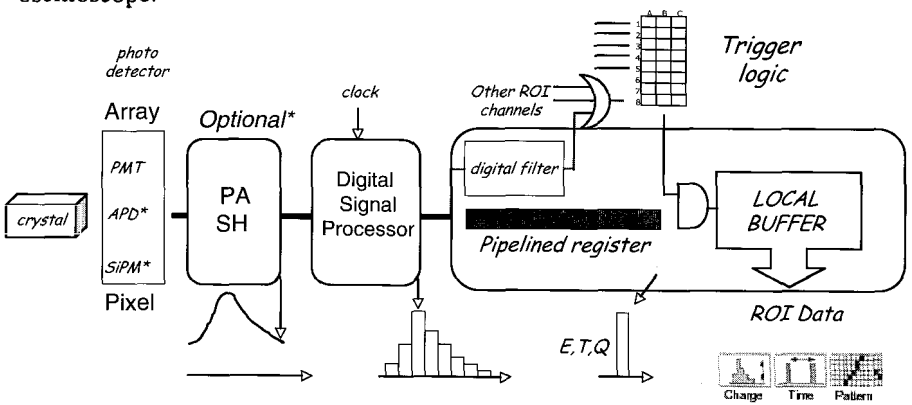

Fig. 3. Conceptual architecture of a full digital and dead timeless electronics for PET.

Another very promising possibility under investigation and comparison with the precedent one would be to use an analog sampling followed by an analog to digital conversion, and Digital Signal Processing[5]. In the context of picosecond timing, analog pulse sampling in the 10 psec range starting from a signal pedestal until its decay after the peaking, provides information to get accurately simultaneously the instant of the first electrons arrival and the pulse amplitude. In practice, a deep-submicron CMOS based vernier timing generator locked on a 500 MHz clock, for instance, can provide 10-20 psec spaced controls to 100-200 analog storage elements (of the order of few hundreds fF capacitors each) for a total duration of a few ns, long enough to get efficiently pedestal, rising edge,

and the peaking value of any pulse to be acquired. A full architecture implementation [6] of such electronics is presented in Fig.3.

6. Conclusions

Improving drastically the timing resolution toward the Picosecond level for HEP and few ten of Psec for Medical Imaging is hard, but not impossible! Adding TOF capabilities will have a fundamental impact on relevant detectors (HEP Particle ID and PET scanners). There is a long way to go but the first results are very encouraging. Join efforts between HEP and MI community is a very efficient way to reach this challenging goal.

Acknowledgments

We would like to thanks Dr. W.W. Moses from Lawrence Berkeley National Laboratory for useful discussion and support.

References

1. T. Credo, H. Frisch, H. Sanders, F. Tang, K. Byrum, G. Drake MCP-PMT Anode Development for Picosecond-Resolution Time-of-Flight Detectors-2006 Nuclear Science Symposium and Medical Imaging Conference, Poster N23-4, Oct 29 – Nov 4, 2006 San Diego, CA, USA.
2. F. Tang, J. Anderson, K. Byrum, G. Drake, H. Frisch, J-F. Genat, M. Heintz, H.Sanders - Development of Front-end Electronics for Picosecond Resolution TOF Detectors. TWEPP07 proceedings to be published. Dobyns JS, Lipscomb PR, Cooney WP. Management of thumb duplication. Clin Orthop 1985; 195: 26–44.
3. J.Va'Vra – SLAC (private communication)
4. W. W. Moses, IEEE Trans. Nucl. Sci., 50-5 (2003) 1325.
5. H. Frisch, J.F. Génat,, F. Tang Picosecond timing using fast analog sampling . Ultra fast Timing collaborative Group; Internal Note (Nov 2007)
6. P.-E. Vert & al., Proc. 14th IEEE-NPSS Real Time Conference, Stockholm, Sweden, 4-10 May 2005, 2005.

FIRST RESULTS OF SMALL ANIMAL IMAGING SPECT DETECTOR FOR CARDIOVASCULAR DISEASE STUDIES ON MICE

M.L. MAGLIOZZI[†]

Istituto Nazionale di Fisica Nucleare and Università La Sapienza, Rome, Italy

M. BALLERINI, E. CISBANI, S. COLILLI, F. CUSANNO, R. FRATONI, F. GARIBALDI, F. GIULIANI, M. GRICIA, M. LUCENTINI, F. SANTAVENERE, S. TORRIOLI, P. VENERONI

Istituto Superiore di Sanità and Sezione INFN Sanità, Rome, Italy

S. MAJEWSKY

Jefferson Lab, Newport News VA, USA

S.P.G. MOK, B.M.W. TSUI, Y. WANG

Johns Hopkins University, Baltimore MD, USA

G. MARANO, M. MUSUMECI, S. PALAZZESI

Istituto Superiore di Sanità, Rome, Italy

G. CICCARIELLO, G. DE VINCENTIS

Università La Sapienza, Rome, Italy

R. ACCORSI

The Children's Hospital, Philadelphia, USA

We have developed a compact, open, Dual Head pinhole SPECT system for high resolution molecular imaging with radionuclides of mice, dedicated mainly to preclinical study of stem cells capability to recover myocardial infarction.

The gamma detector is made of pinhole tungsten collimators, pixellated scintillators, matrix of multi-anode PMTs and individual channel readout. Measurements have been performed on phantoms and live mice devoted initially to test and calibrate the system and to optimize protocols.

[†] Corresponding author. *E-mail address*: lucia.magliozzi@iss.infn.it

The implemented system and the first results will be presented, demonstrating the effectiveness of our dedicated SPECT detector for small animal imaging.

1. Introduction

Cardiovascular disease is the leading cause of disability and mortality for both men and woman in the western countries. Various stem cells hold promise for the treatment of human cardiovascular disease; results of clinical trials are somewhat disappointing emphasizing the need of preclinical investigation as a means of better understanding the basic mechanism. Effective stem cell studies demand that location and number of cells be tracked in vivo, over few weeks.

In this aspect the use of small animals in biomedical research may play a leading role. Mice in particular are favourite animal subjects: they are economical, reproduce rapidly, and can provide models of human disease. Additionally, the development of the heart and vasculature in mice and humans seems to be regulated by similar genes and signaling pathways.

Over the last few years, functional in vivo imaging has emerged as effective alternative to the widely used invasive techniques such as biopsy, where large numbers of animals are required, and follow up studies are generally not possible in the same animal. The higher sensitivity of PET and SPECT imaging over other modalities and their applicability to both small animals and humans makes these techniques attractive for in vivo imaging; however simultaneous achievement of high resolution and high sensitivity is challenging. SPECT has (relatively) limited sensitivity due to the collimation but PET, that uses electronics collimation, has intrinsic limitations in terms of spatial resolution, is more complex and expensive.

We have developed a compact, open (for multimodality purpose), Dual Head pinhole SPECT system for high resolution molecular imaging with radionuclides of mice, for the study of stem cells capability to recover myocardial infarction; it will be used for monitoring both stem cells homing and their therapeutic effects (in terms of modifications of myocardial perfusion images). The gamma detector is made of pinhole tungsten collimators, pixellated scintillators, matrix of multi-anode PMTs and individual channel readout.

Tomographic images of Rod Phantom were acquired to characterize system spatial resolution; measurements have been performed on live mice devoted initially to test and calibrate the system and to optimize the measurement protocol for cardiovascular disease studies. Results of thoracic bone scan and myocardial perfusion acquisition on live mice are presented.

2. SPECT System Description

The SPECT system is equipped with a 2.5-cm-diameter acrylic cylindrical bed-holder (3 mm thick) that keep the mouse horizontal. The holder is coupled to a rotating stepping motor that ensure mouse rotation.

The system could be manually adjusted to optimize the distance between the pinhole and the axis of rotation, giving the possibility to resize the camera parameters depending on measurements requirements.

System setting is choose ensuring high resolution acquisition of the upper head and high sensitivity of the lower module. Detector characteristic and design performance parameters are listed in Table 1.

Table 1. Dual head detector components and design performance parameters.

	Upper Head	Lower Head
Pinhole Diameter (mm)	0.5	1.0
NaI(Tl) Scintillator, 6mm thick : - pitch (mm)	1.5	1.2
- dimension (mm)	10 × 10	20 × 15
Photomultiplier Array	(2 × 2) H8500	(4 + 4) H8500
Resolution (mm)	0.8	1.4
Efficiency (cps/microCi)	0.5	1.7
Magnification Factor	3	2.7
Field of View (mm)	33	37

3. Experimental method

To test the tomographic spatial resolution capabilities of our detector, a miniature acrylic resolution phantom, 2.5 mm in diameter, was manufactured, as show in Figure 1. It consists of 6 sectors, each containing equally sized sets of capillaries (0.8, 0.9, 1.0, 1.1, 1.2, 1.3 mm). The total activity in all filled capillary was ~4.5 mCi of ^{99m}Tc-pertechnetate. The single pinhole projection data were acquired in 60 angular intervals over 360 degree at 2 min/projection.

Three-month-old VFB/N male mice, weighted 30 g, were intraperitoneally anesthetized. Care was taken to minimize the volume of injected tracers into the tail vein (0.02-0.05 ml) to avoid significant changes in the whole blood volume of the mice. The single pinhole projection data were acquired in 60 angular intervals over 360 degree.

Thoracic bone scan was performed to evaluate system image quality. Mouse was injected with 2 mCi of ^{99m}Tc-MDP. After tracer injection, 1 ml of physiological saline was administered intraperitoneally, to ensure a better contrast of bone to soft tissue due to kidney clearance of tracer. Tomographic

acquisitions started 2 hour after tracer administration. Projection data were acquired at 2 min/projection.

Myocardial perfusion scan was also performed. Live mouse was injected with 6.7 mCi of ^{99m}Tc-MIBI; acquisitions started 1 hour after tracer administration to ensure a better contrast of heart to soft tissues. Projection data were acquired at 60 sec/projection.

Tomographic acquisition of a set of 2 point like sources (~1 mm in diameter) positioned as far as possible and away of the axis of rotation was performed for geometric calibration of SPECT detector.

4. Results

Upper head projection data were reconstructed using a 3D pinhole OS-EM algorithm[1] which takes into account system geometric misalignment parameters, including the center-of-rotation error, the tilt angles between the axis-of-rotation and the detector plane in the 3D space. Reconstruction matrix size was $90 \times 90 \times 90$ with a voxel size of 0.25 mm.

A 3D Butterworth filter was used for the post-reconstruction.

Figure 1 shows reconstructed image of Rod Phantom. 0.8 mm holes can be easily separated, leading to a sub-millimetre spatial resolution as designed.

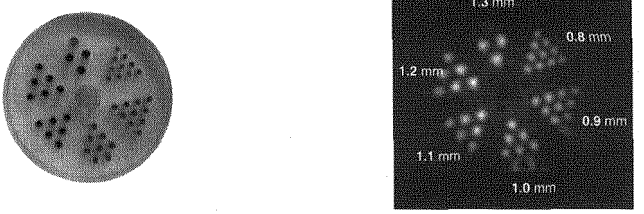

Figure 1. Miniature acrylic resolution phantom (left), and reconstructed image (right), sum of 21 trans-axial slices. 0.8 mm capillaries are clearly separated.

The result of reconstructed image of thoracic bone scan, front (left) and lateral view (right) is presented Figure 2.

Figure 2. Front (left) and lateral view (right) of reconstructed image volume of thoracic bone scan. Data were acquired in 120 minutes, 2 hours after injection of 2 mCi of ^{99m}Tc-MDP. Tracer uptake in spine, shoulder-blade and ribs are visible.

Tracer uptake in spine, shoulder-blade and ribs are visible. Images show also tracer localization in liver, probably due to the non optimal hepatobiliary clearance of radiotracer.

Mid-ventricular short-axis slice (left) and horizontal long-axis slice (right) obtained from reconstructed projection of myocardial perfusion images are shown in Figure 3. Left and right ventricular cavities and corresponding walls can be easily identified.

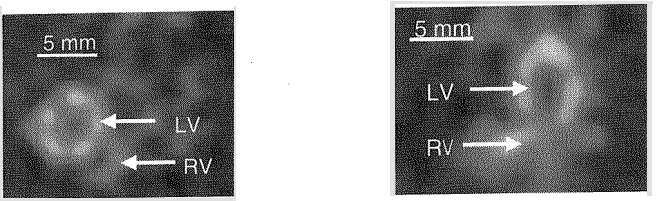

Figure 3. Mutual perpendicular cross section through sub-millimetre-resolution 3-dimensional myocardial perfusion image volume of living mouse. Data were acquired during 60 minutes, starting 1 hour after administration of 6.7 mCi of ^{99m}Tc-MIBI. Short-axis slice (left) showing myocardial perfusion in right ventricular (RV) and left ventricular (LV) wall. Horizontal long-axis slice (right).

5. Conclusion and Outlook

The characterization of the upper head of the above described SPECT system has demonstrated spatial resolution capability better than 0.8 mm at reasonable efficiency. Analysis of lower head data as well as the combined reconstruction from the two sets of projections are in progress.

Our current efforts aim to improve both resolution and sensitivity. Actually we are moving to a gated acquisition system and we are improving[3] the intrinsic resolution by means of new promising scintillators (continuous $LaBr_3$:Ce) or rugged material (0.5-0.8 mm pixellated CsI:Na, CsI:Tl) as well as evaluating the possibility of using multi pinhole collimation. Moreover, we will increase the number of detector heads, taking into account the possibility of using our system in a multimodality framework.

Activity is also ongoing, on the biological side, to probe the reproducibility of pinhole SPECT measurements of global and regional ventricular function in infarcted as well as in wild type mice.

References

1. Y Wang and BMW Tsui, *IEEE Trans Med Imag.* **26(3)**, 298 (2007).
2. Hamamatsu H8500 and H9500 specifications, www.hamamatsu.com.
3. E Cisbani et al., *Nucl. Instr. Meth.* A571, 169 (2007).

DEVELOPMENT OF A LOW NOISE OPTOELECTRONIC INTEGRATED READOUT WITH N-I-P A-SI:H PHOTODIODE ARRAY FOR POSITRON EMISSION TOMOGRAPHY

ALESSANDRO NARDULLI [1]

[1] *ETH-Zurich, CH-8093 Zurich, Switzerland*

M. DESPEISSE [2], G. DISSERTORI [1], S. DUNAND [3], P. JARRON [2], W. LUSTERMANN [1], D. MORAES [2], D. SCHINZEL [1], N. WYRSCH [3]

[2] *CERN, CH-1211 Geneva, Switzerland*

[3] *IMT, Rue A.-L. Breguet 2, CH-2000 Neuchatel, Switzerland.*

Detection of scintillation light from LSO crystals used in Positron Emission Tomography is traditionally based on photo multipliers. The proposal is to develop a novel photo sensor, which is based on vertically integrating an hydrogenated amorphous silicon (a-Si:H) film on a pixel readout chip. The a-Si:H film is deposited with a n-i-p diode structure. Section 1 compares different circuit topologies, at the transistor level, in order to fulfill the noise requirement for the circuit. Quantum Efficiency results of a-Si:H photodiodes deposited on glass and on integrated circuits are reported in section 2.

Introduction

The optoelectronic integrated readout system studied in this paper is developed to detect the output light coming from LSO crystals, used in Positron Emission Tomography (PET), for the energy conversion of 511KeV incoming photons [1]. The output light has a wavelength λ of 420 nm. An a-Si:H film is deposited using a n-i-p diode structure on top of the readout chip [2].

The proposed structure has 9 pixels per crystal: the crystal dimensions are 2x2x15 mm^3 and the pad width of the pixels is 600 μm. Assuming an intrinsic light output for the LSO crystal of 25000 photons per MeV [3], a Quantum Efficiency (QE) for the a-Si:H photodiodes of 75% (see Section 2), a fill factor of 65 %, we can estimate to 650 the number of electrons per pixels at the input of the preamplifier. The project is very challenging because of the imposed signal to noise ratio: a very low input signal, a detector capacitance of 7 pF and a leakage current of hundreds of pico-ampere per pixel. The total equivalent noise charge (ENC) must not exceed 60 e^-. Due to the dependence of series

noise on input capacitance, the white noise term due to the input MOS transistor is expected to be the dominant noise source [4].

1. The read out electronics

1.1. *The regulated cascode structure*

The cascode structure is often used as preamplifier stage for charge sensitive amplifiers (CSA) in detectors: it is characterized by an output resistance of $Rcasc = g_{m2} r_{ds2} r_{ds1}$ and an open loop gain of $(g_m r_{ds})^2$. The regulated cascode [5] uses an additional MOS transistor in a local feedback loop to increase the gain and the equivalent output resistance of the cascode: the schematic is highlighted with a red circle in figure 1. The overall output resistance becomes therefore: $R'_{casc} \sim g_{m3} r_{ds3} g_{m2} r_{ds2} r_{ds1}$. The resulting open loop gain of the amplifier is $g_{m1} R'_{casc}$. In comparison with the normal cascode amplifier, the regulating MOS transistor in the local loop increases the gain by a factor $g_m r_{ds}$. Since the open loop gain increases, the approximation that the dominant pole is only function of the feedback parameters is valid. With detector capacitances of several pF, the dominant pole shifts to higher frequencies. This increases the closed loop gain in the frequency region of interest. For relatively high input bias currents (several mA) the pulse gain increases from 400mV/fC to 950mV/fC.

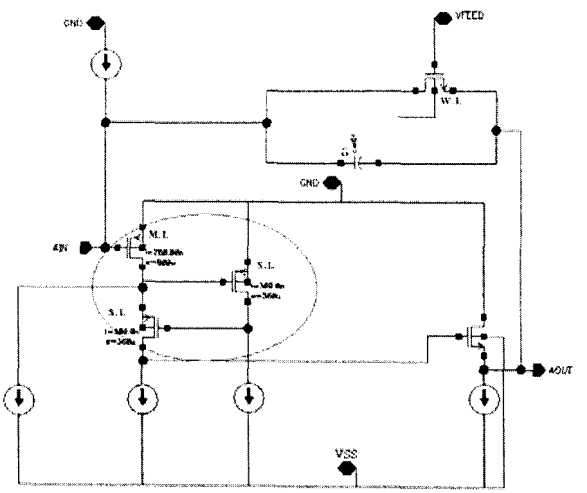

Figure 1: Schematic of the charge sensitive preamplifier with the regulated cascode structure circled in red and the active feedback on top.

1.2. *Choice of the input transistor*

Input noise matching means to adequately choose the basic design parameters, i.e. gate width W and length L for the input transistor to obtain a minimal ENC for a given detector capacitance [4]. In order to minimize the ENC due to thermal noise, an input transistor with minimal channel length has to be chosen. The input transistor has to be operated in moderated inversion which is often the case in CSA because noise optimization of the input transistor often leads to a large W/L ratio, once the bias current is fixed. In addition, for gate lengths close to the minimum of the technology, the excess noise factor Γ drops from values bigger than 3.5 in strong inversion to below 1.5 in moderate inversion, as it has been experimentally shown for 0.25 μm CMOS technology [6].

1.3. *Noise analysis*

This subsection analyzes the series and parallel noise. The dominant noise source is the series noise, in particular the thermal noise of the MOS input transistor operated in moderate inversion. Other non-dominant sources of noise i.e. flicker noise, gate induced current (GIC) noise and thermal noise of the input bias transistors have been calculated. Their contribution is at the level of few per cent. The parallel noise, due to the leakage current in the feedback loop, has been calculated as well: this term is proportional to the square root of the peaking time and it can become the dominant term for slower applications. The noise results obtained with HSPICE simulations are cross-checked with a mathematical model based on the EKV [7]. The data in figure 2 compare the noise of the two different structures using HSPICE simulations. The figure shows only the moderate inversion region of the PMOS input transistor.

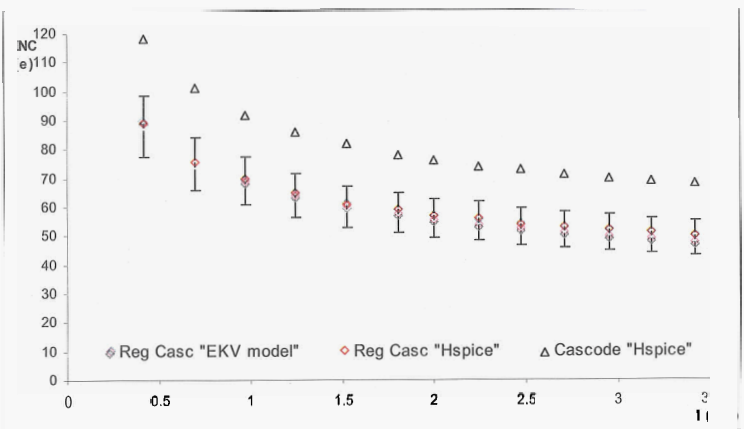

Figure 2: Plot of ENC versus bias current of input PMOS for regulated cascode (red and blue circles) and standard cascode (triangle) structure.

This fixes the limits in the plot for the bias current at 3.5 mA.
The results (fig.2) for the regulated cascode structure obtained with HPSICE simulations (red) are compared with simplified EKV model calculations (blue). The difference between the two models is 5 to 10 %. The advantage of regulated cascode in CSA is to guarantee sufficiently high open loop gain even when one deals with very high input capacitance and bias current. Noise optimization in fact leads to an increase of the input bias current with consequent reduction of the output resistance r_{ds} and of the gain of the stage $g_m r_{ds}$.

2. Quantum Efficiency measurements

The standard a-Si:H diode exhibits a maximum quantum efficiency at 550 nm and most devices (solar cells) are actually optimized for this wavelength. However, since the output light of the LSO crystal peaks at a wavelength of 420 nm, the a-Si:H diodes have to be optimized for this wavelength. The response of a photodiode in the UV region is mainly controlled by the top layers. To reduce the optical loss in these layers it is possible to increase the optical band gap by alloying amorphous silicon with carbon; an alternative is a reduction of the thickness of the Indium Tin Oxide (ITO) and the p-layer. Studies performed by the institute IMT of Neuchatel on samples deposited on glass have shown that reducing the deposition time to 45'', for the ITO layer, optimizes the quantum efficiency at wavelengths from 350 to 450 nm [8]. This deposition time corresponds to an estimated reduced thickness of the layer of 28 nm.

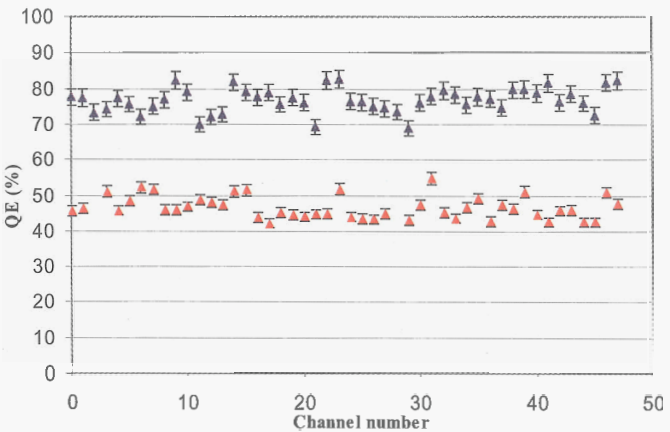

Figure 3: Quantum Efficiency of standard (red) and optimized (blue) a-Si:H photodiodes measured at 405 nm for 48 different pixels in AC condition. The average values of the QE are respectively 46% and 77%.

For the reduction of the optical loss the thickness of the p-layer has to be reduced as well. The optimized photodiodes have a deposition time for the p-layer of 4' to 5' compare to 10' of a standard p-layer. Results for standard and optimized a-Si:H photodiodes deposited on CMOS circuits, measured with a pulsed laser source at 405 nm for 48 different pixels are presented in figure 3 and confirm the preliminary results obtained after deposition of a-Si:H photodiodes on a glass substrate. An average QE of 77% has been reached for photodiodes deposited on integrated circuits.

Conclusions

The regulated cascode used in CSA has been proven to be very useful when high gain and low noise are required. The increase of the closed loop gain in the region of frequencies of interest shows a pulse gain increase of ~2.5 compared to the simple cascode configuration. The voltage noise referred to the output is increasing by less than 2 times in the regulated cascode configuration. Therefore the ENC at the input of the two structures shows a significant reduction for the regulated cascode compared to the cascode. The other noise sources are not varying significantly for the two structures.
First measurements of quantum efficiency of optimized photodiodes deposited on glass have shown that a QE up to 80% is possible with a-Si:H. These results of Quantum Efficiency are confirmed by a-Si:H n-i-p photodiodes deposited on chip.

References

1. L. Eriksson *et al.*, "Experience with scintillators for PET: towards the fifth generation of PET scanners", NIM in Phys. Res A 525 (2004), pp.242-248.
2. M. Despeisse *et al.*, "Hydrogenated amorphous silicon sensors based on Thin Film on ASIC technology", IEEE-NSS CR 2005 pp. 1389-1394.
3. A. Kriplani *et al.*, "Light output meas. of LSO single crystals and 4x8 Arrays: comparison of exp. with MC simulations", IEEE-NSS CR 2003.
4. Z.Y. Chang, W. Sansen, "Low noise wide-band amplifiers in bipolar and CMOS technology", Kluwer Academic Publisher pp.173-178.
5. T. Burger, Q. Huang, "On the optimum design of regulated cascode operational transconductance amplifiers", ISLPED 98.
6. G. Anelli, "Advanced VLSI Design Techniques" African Regional course Kumasa 2003.
7. C. Enz *et al.* "An analytical MOS transistor model valid in all regions of operation and dedicated to low voltage and low current applications". Anal. Integ. Circ. and signal processing 8, 83-114 1995.
8. N. Wyrsch "Vertical integration of hydrogenated amorphous silicon devices on CMOS circuits" Mater. Res. Soc. Symp. Proc. Vol. 869 2005.

The use of modern electronic flat panel devices for image guided radiation therapy: Image quality comparison, intra fraction motion monitoring and quality assurance applications

S. Nill* and J. Stützel and P. Häring and U. Oelfke

German Cancer Research Center, Department of Medical Physics, Heidelberg, BW, Germany
**E-mail: s.nill@dkfz.de*
http://www.dkfz-heidelberg.de/fs05/e0401

With modern radiotherapy delivery techniques like intensity modulated radiotherapy (IMRT) it is possible to delivery a more conformal dose distribution to the tumor while better sparing the organs at risk (OAR) compared to 3D conventional radiation therapy. Due to the theoretically high dose conformity achievable it is very important to know the exact position of the target volume during the treatment. With more and more modern linear accelerators equipped with imaging devices this is now almost possible. These imaging devices are using energies between 120kV and 6MV and therefore different detector systems are used but the vast majority is using amorphous silicon flat panel devices with different scintilator screens and build up materials. The technical details and the image quality of these systems are discussed and first results of the comparison are presented. In addition new methods to deal with motion management and quality assurance procedures are shortly discussed.

Keywords: IGRT, cone beam CT, 4D.

1. Introduction

The aim of modern radiotherapy is to deliver a more conformal dose distribution to the tumor while better sparing the organs at risk (OAR) compared to 3D conventional radiation therapy. To achieve this goal it is very important to know the exact position of the target volume during the treatment. This is only possible by applying image guided radiotherapy (IGRT) with the aim to monitor all tumor motions during the treatment course and use the acquired information to improve the patient's therapy. Tumor motion management and patient setup errors can be divided into two categories. There is the correction of random and systematic errors during the patient positioning process (inter fraction motion) and the more complex error due

to tumor movements during the therapy (intra fraction motion). To deal with both classes of errors a lot of research efforts were done to integrate imaging modalities into the treatment devices or at least into the treatment room. With such devices it is now possible to acquire anatomical images of the patient in the treatment position prior or even during the treatment.

Within this article four different imaging systems are presented and the relevant physical parameters for the imaging process are given. To evalute the image quality different phantoms were scanned and the results are presented. In addition new quality assurance and motion management procedures for one out of the four devices are shortly discussed.

2. Methods

One possible method to obtain images of the patient prior or even during the therapy is the availability of a computed tomography device (CT) in the treatment room. Several systems have been developed to achieve this goal. The straight forward solution is the installation of the standard CT scanner directly in the treatment room see Fig. 1(a) where the other methods are more technical challenging. Jaffray[1] for example proposed the integration of kilo voltage imaging components into the linear accelerator structure (Fig. 1(c)). Pouliot[2] used the megavoltage treatment beam in combination with a flat panel detector to acquire 3D data sets of the patient (Fig. 1(d)). Both solutions have the advantages that they could be integrated into already existing or even installed linear accelerators. This is not the case for the Tomotherapy unit (Fig. 1(b)). The Tomotherapy device, developed by Mackie,[3] is a new device which not only delivers the treatment with a modulated fan beam but also uses a standard CT ring detector for the image acquisition process.

Section 2.1 gives a detail technical description of each of the four different imaging devices. Section 2.3 and section 2.4 shows exemplarily one possible method to use electronic flat panel devices (EPI) in combination with the treatment beam for quality assurance applications and motion management.

2.1. *Technical description of the different imaging devices*

For each of the evaluated devices the setup and the imaging beam properties as well as the reconstruction parameters are reported in the next four subsections.

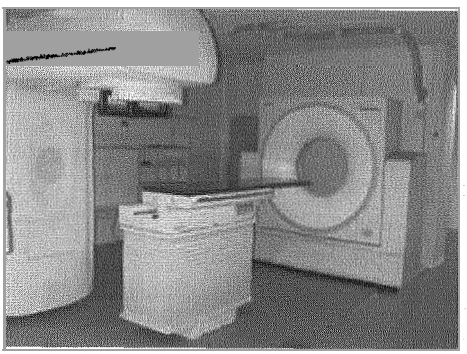

(a) Primatom

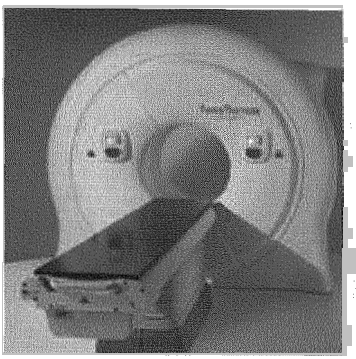

(b) Tomotherapy

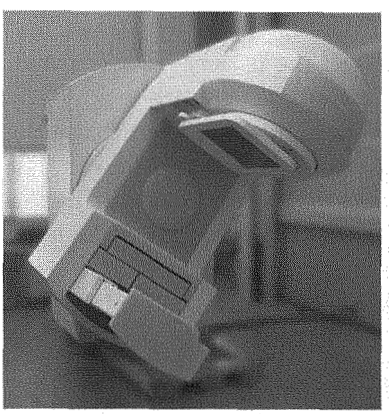

(c) kV cone beam

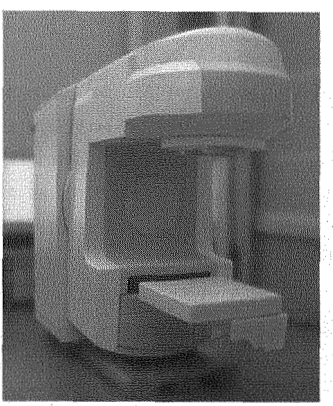

(d) MV cone beam

Fig. 1. Evaluated systems.

2.1.1. *Primatom*

The Siemens in room CT solution Primatom (Fig. 1(a)) is a combination of a Primus linear accelerator and a diagnostic single slice Siemens Somatom Emotion CT scanner. The patient support table has to be rotated by 90 or 180 degree depending on the installation prior to the scanning process. Therefore this system can not be used for intra-fraction motion correction methods. The x-ray tube, with a total filtration of 6.4 mm aluminum at central axis to harden the beam, is mounted on a ring gantry opposed an arc-shaped solid state detector. The latter features 672 channels and is made out of scintillating ceramic material, so called Ultra Fast Ceramics (UFC), that is based on Gd2O2S (Gadolinium oxysulfide). For the reconstruction

process a H40s kernel in combination with a 512x512 reconstruction matrix was used. The resulting slice thickness was 4 mm with a quadratic pixel size of 0.75 mm. The Primatom system was considered the gold standard for the performed image comparison.

2.1.2. *Tomotherapy*

Helical tomotherapy developed by Mackie[3] combines a linear accelerator and a helical CT scanner. The geometrical setup for image acquisition is analogous to that of spiral CT device where the image source rotates on a ring gantry while the patient couch moves simultaneously. The Tomotherapy devices uses a 6 MV photon beam for patient treatment but a reduced voltage of 3.5 MV for imaging purposes. A HI-ART II systems was used to acquire the presented images. The arc-shaped xenon detector, mounted on the gantry at a distance of 145 cm to the source, consists of 1476 ionisation cavities.[4] These 0.32 mm thick and 2.54 cm long cavities are separated by tungsten septa of the same thickness. The charges produced in two adjacent xenon cavities at a time are read out together, yielding the signal of one detector channel of 1.28 mm effective size. Due to the primary collimation the maximum available field of view (FOV) is 40 cm. Since the detector array has a 110 cm radius of curvature, its geometrical center is slightly out of focus with the source. This is done deliberately since by having the photons impinged on the tungsten septa an increased number of electrons will be produced which results in the detection of a higher signal by the ionisation chambers. This xenon detector has a particularly high efficiency compared to other existing detectors for mega voltage radiation. A fixed 4mm collimation of the jaw in y-direction at the isocenter defines the slice thickness. TomoTherapy by default provides a 512 x 512 reconstruction matrix resulting in a voxel size of 0.78 mm.

2.1.3. *kV cone beam*

The kV cone beam Artiste prototype system is based on the inline concept.[5] It combines a conventional linear accelerator (linac) with a kV cone beam imaging system consisting of a x-ray tube and a electronic flat panel device (Fig. 1(c)). The x-ray tube is mounted at 180 degree to the treatment beam and the flat panel device is positioned directly below the multi-leaf collimator. The diagnostic kV beam is produced by a Siemens Optitop 150/10/20 HL-100 x-ray tube and the images are acquired with a amorphous silicon Flat Panel Imager (FPI) RID 1640 by PerkinElmer, Optoelectronics, based

on Gd2O2S:Tb (Lanex Fast). The source detector distance is approximately 137 cm. The x-ray tube features a 40 kilo Watt (kW) source with a nominal focal spot value of 0.6. To harden the x-ray spectrum a total filtration of 2.5 mm aluminum inside the tube, an adjacent 0.2 mm copper plate and another 1 mm copper in the cover is used. With the standard imaging geometry a typical FOV of 27 cm can be reconstructed. The common problem of scatter for CBCTs is addressed by using a standard scatter grid of 80 line pairs per cm (lp/cm) which was mounted in front of the detector. The reconstruction with a Shep-Logan filter was performed resulting a 512 x 512 matrix with a pixel size of 0.75 mm and a final slice thickness 4 mm.

2.2. *MV cone beam*

The Artiste prototype system can be used either in the kV imaging mode or the MV cone beam mode (Fig. 1(d)). For the MV imaging mode the 6 MV treatment beam in combination with a Siemens Optivue 1000 ART flat panel device is used to acquire the phantom data sets. The source to detector distance is 145 cm. The same reconstruction parameters as for the kV cone beam images were applied.

Table 1. Imaging properties for all four devices. The reported dose levels are further referenced as low, normal, high.

	Primatom	Tomo Therapy	Artíste kVCB	Artíste MVCB
Beam energy [MV]	0.130	3.5	0.121	6.0
Detector	scintillating ceramics	xenon	amorphous silicon	amorphous silicon
Geometric beam shape	fan	fan	cone	cone
Hardware scatter reduction methods	septum	-	anti scatter grid	-
Dose levels $CTDI_w$ [cGy]	1.5	1.0 1.5,3.0	1.0 1.5, 3.0	3.0 8.2, 17

Table 1 shows a brief comparison of the most important imaging parameters of the evaluated systems. The dose measurements were performed inside a cylindrical water phantom with a diameter of 16 cm with two inserts (1 cm below surface and in the center of the phantom) for a small ionization chamber. The dose levels are based on the three available imaging protocol settings of the Tomotherapy unit. For all dose levels (low, normal, high) different phantoms including a homogenous water phantom,

a inhouse low-contrast and detail phantom and the Siemens Cone beam phantom were scanned and evaluated. To evaluate the spatial resolution capability the modulation transfer function (MTF) is determined using the method proposed by Boone.[6]

2.3. *Quality assurance*

For the delivery of highly complex treatment techniques like intensity modulated radiation therapy (IMRT) a very strict quality assurance program must be performed prior to the delivery of each patient treatment plan. For this process normally either multiple ionization chambers or even ionization chamber arrays are used to measure the delivery dose at multiple points inside a body phantom. The measured doses are then compared with the prediction of the treatment planning systems (TPS). The measurement process can be quite time consuming. One other possible solution is not to measure the dose deposited inside the phantom but to measure the fluence output of the machine directly. This can be either achieved by putting a radio sensitive film directly below the treatment head or using the available imaging panel of the kV imaging system in Fig. 1(c). With this setup the kV panel can not only be used to acquire kV images but also to reconstruct the fluence output of the treatment machine in almost real time (15 Hz readout frequency). Using a convolution based approach by Häring[7] the measured arbitrary units can be compared with the planed values. Not only the fluence can therefore be verified but it is also possible to detect the positions of the beam shaping elements. For one patient the results of the comparison are shown in the result section.

2.4. *Motion management*

Currently the treatment options of moving targets especially for tumors inside the lung are limited by the tolerance dose of the surrounding normal tissue. The standard approach to treat moving targets is to increase the area of the treatment beam to make sure that the target is always covered by the radiation field independent of the breathing phase of the patient. With the introduction of 4D CT by Vedam[8] it is possible to reconstruct the target position for the different breathing phases (e.g. inhale and exhale position) and use this information already during the treatment planning process to improve the target coverage and reduce the dose to the normal tissue. But by using this information inside the TPS it became of paramount importance to validate the breathing pattern with the patient in treatment

position. Using the kV cone beam imaging system Sonke[9] and Dietrich[10] developed a method to perform 4D CT reconstructions using the cone beam projections. For one patient the reconstruction results are presented in the results section.

3. Results

3.1. *Image quality*

Figure 2 gives an overview of the image quality achieved with the four devices. For all four devices the result for the dose level "normal" are shown. It is important to note that the doses applied with the MV cone beam system was approximately 5 times higher than for all the other devices. Comparing the image quality it can be seen especially in the third row that the Primatom system provides superior soft tissue contrast and only the kV cone beam system can still resolve some of the low contrast inserts at this dose level. A significant reduction of the image quality from the kV cone beam system to the Tomotherapy unit and especially the MV cone beam unit can be observed.

The spatial resolution is determined using the wedge shown in the last row of Fig. 2. Figure 3(a) shows the edge function based on the MTF slice from the Primatom data set and the derived fit. In Fig. 3(b) the MTF for all dose levels and for all devices are plotted. The MTF is independent of the selected dose level for all devices. The spatial resolution is reduced compared to the Primatom 0.05 MTF value by a factor of 1.2, 2 and 2.4 for the kV cone beam system, the Tomotherapy unit and the MV cone beam device.

3.2. *Quality assurance*

Figure 4 shows the results for a typical IMRT fluence profile in one direction. The values from the TPS system are shown in black. The uncorrected raw data values from the EPI always overestimates the delivered monitor units. After applying the convolution technique by Häring[7] the calculated values agrees with $\pm$ 0.5 MU with the planned values. Using this method an almost real time verification of the delivered 2D fluence distribution during the patient treatment is possible.

3.3. *Motion management*

If all available projections are used to reconstruct the 3D dataset of a moving target no sharp edges are visible in the dataset due to the breathing

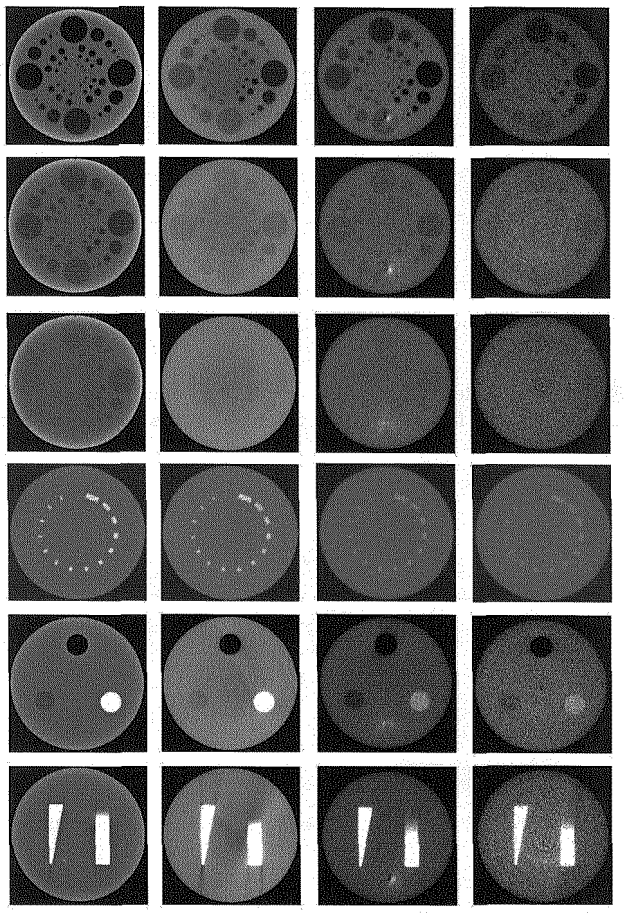

Fig. 2. The Siemens ConeBeam Phantom V2.5. From top to bottom: Contrast slice I (inserts have CT-numbers -200 HU, -120 HU, -90 HU, -60HU relative to the basic material, which has 35HU at 120 keV), Contrast slice II (-45 HU, -30 HU, -25 HU, - 20 HU), Contrast slice III (-15 HU, -10 HU, -5 HU, -3 HU), Spatial resolution slice, Noise and scaling slice, MTF slice. The images were acquired with the following devices from left to right: Primatom (1.5cGy), kV cone beam (1.5cGy), Tomotherapy (1.5cGy), MV cone beam (8.2cGy) at dose level normal.

motion (in Fig. 5 the diaphragm in the left picture is smeared out). Using the method developed by Dietrich[10] it is possible to reconstruct selected breathing phases to asses the tumor motion with the patient in treatment position. In both pictures a sharp edge of the diaphragm is visible. The observed motion of 5 mm agreed well with the measured motion of the

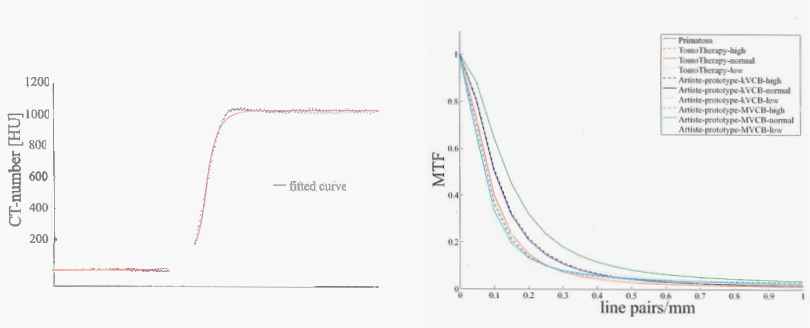

(a) Edge function (b) MTF

Fig. 3. a) Edge function derived from Siemens Cone beam phantom (Primatom data set). b) Modulation transfer function for the different devices and for different dose levels.

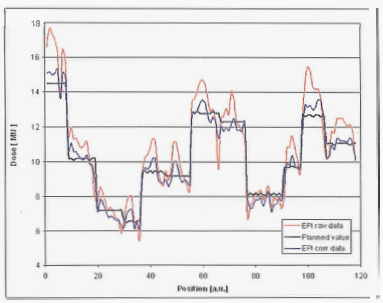

Fig. 4. **Comparison of predicted, uncorrected and corrected monitor units based on EPI measurements.**

diagnostic 4D CT scan. With this information and the quasi static reconstructed 3D datasets the target could be positioned correctly to take into account possible baseline shifts which are very important for the treatment of lung tumors.[11]

4. Conclusion

Based on the available results for the scanned phantoms the standard CT scanner is superior to all the other evaluated devices especially for the soft tissue achievable with low imaging doses. The kV cone beam system and the Tomotherapy unit are providing reasonable soft tissue contrast and spatial resolution for almost the same and slightly higher imaging doses. The MV cone beam system delivers considerably higher dose to the patient to get adequate images. The integration of flat panel devices into treatment units

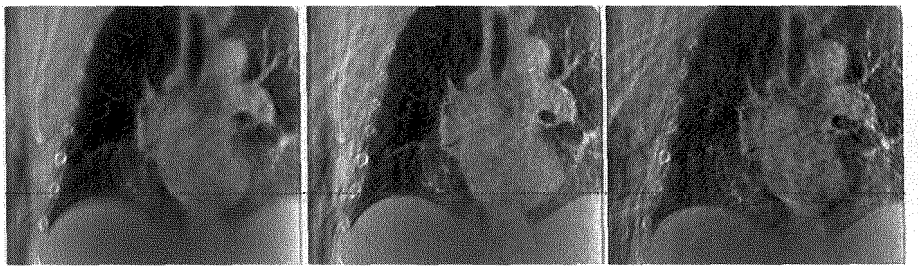

Fig. 5. Left: All projections. Middle: at exhale. Right: at inhale. The observed motion between the inhale and exhale phase is 5 mm.

not only enables IGRT but also provides the possibility to improve quality assurance and motion management procedures.

5. Acknowledgments

The presented work was partially supported by Siemens Medical Solutions Oncology Care Systems.

References

1. D. Jaffray, J. Siewerdsen, J. W. JW and A. M. AA, *Int J Radiat Oncol Biol Phys* **53**, 1137 (2002).
2. J. Pouliot, A. Bani-Hashemi, J. Chen, M. Svatos, F. Ghelmansarai, M. Mitschke, M. Aubin, P. Xia, O. Morin, K. Bucci, M. Roach, P. H. P, Z. Zheng, D. Hristov and L. Verhey, *Int. J. Radiat. Oncol. Biol. Phys.* **61**, 552 (2005).
3. T. Mackie, T. Holmes, S. Swerdloff, P. Reckwerdt, J. Deasy, J. Yang, B. Paliwal and T. Kinsella, *Med. Phys.* **20**, 1709 (1993).
4. S. Meeks, J.F.Harmon, K. Langen, T. Willoughby, T. Wagner and P. Kupelian, *Med.Phys.* **32**, 2673 (2005).
5. U. Oelfke, T. Tücking, S. Nill, A. Seeber, B. Hesse, P. Huber and C. Thilmann, *Medical Dosimetry* **31**, 62 (2006).
6. J. Boone and J. Seibert, *Med.Phys.* **21**, 1541 (1994).
7. P. Haering, S. Nill, E. Janisch, S. Klemm and B. Rhein, *Med.Phys.* **34**, p. 2477 (2007).
8. S. Vedam, P. Keall, V. Kini, H. Mostafavi, H. Shukla and R. Mohan, *Med. Phys.* **48**, 45 (2003).
9. J. S. JJ, L. Zijp, P. Remeijer and M. van Herk M, *Med. Phys.* **32**, 1176 (2005).
10. L. Dietrich, S. Jetter, T. Tücking, S. Nill and U. Oelfke, *Phys. Med. Biol.* **51**, 2939 (2006).
11. S. Korreman, T. Juhler-Nottrup, A. Boyer, B. Loo, A. Pedersen, L. Specht and H. Nyström, *Rad. Oncol* **84**, 85 (2007).

NEUTRON IMAGING IN A HOSPITAL ENVIRONMENT

S. SCAZZI*, D. BOLOGNINI, V. MASCAGNA, A. MATTERA, M. PREST
Università dell'Insubria di Como and INFN di Milano Bicocca, Italy

G. BARTESAGHI, V. CONTI
Università degli Studi di Milano and INFN di Milano, Italy

A. MOZZANICA
Università degli Studi di Brescia and INFN sezione di Pavia, Italy

P. CAPPELLETTI, M. FRIGERIO, S. GELOSA, A. MONTI, A. OSTINELLI
Fisica Sanitaria, Ospedale S. Anna di Como, Italy

G. GIANNINI, E. VALLAZZA
INFN, sezione di Trieste and Università degli Studi di Trieste, Italy

F. BASILICO, P. MAURI
Istituto di tecnologie biomediche, CNR Milano, Italy

BNCT is a technique exploiting the capture conversion process of thermal neutrons in the reaction $^{10}B(n,\alpha)^{7}Li$ to treat extended and radioresistant tumours. One of its main limitations is the lack of specificity of the boron compounds with respect to tumour cells, which needs to be studied with a dedicated neutron beam. This work, developed within the INFN PhoNeS project and carried out at the radiotherapy unit of the S. Anna Hospital in Como with a Varian Clinac 2100C/D, describes the possibility of neutron imaging, performed with the neutrons produced by a Linac detecting the alpha particles with a non depleted self-triggering microstrip silicon detector. Several trials have been made with solutions of ^{10}B at different percentages, obtaining a minimum sensitivity of 1.9 nmol/cm^2. The paper describes the detector, the measurement setup and the first results with biological samples.

Keywords: Neutron imaging; Boron concentration.

1. Introduction

Nowadays the standard radiotherapic treatments are not able to take care of all types of tumours; in the case of extended tumours such as the ones in the stomach, in the liver and in the lungs, or located near vital organs, such as brain tumours, it would be better to use a very selective technique whose main goal is to preserve the healthy cells: Boron Neutron Capture Therapy (BNCT) is one possible answer to these requirements.
To employ BNCT, the boron has to be carried inside the tumour cells and then irradiated with a neutron flux $> 5\times10^8$ n/cm^2/s with an energy range < 10 keV.
This technique exploits the neutron capture process of the ^{10}B in the reaction ^{10}B(n,α)^{7}Li; the particles emitted in this reaction have a very short range in matter releasing their whole energy inside the cell in which the reaction takes place. For this reason it is very important to find a selective carrier able to concentrate itself in the tumour cells. Neutron imaging, in the sense of the capability of detecting the presence of boron inside biological samples, plays a considerable role in the study of the carriers.
The second problem in BNCT is that a flux with the features described above can be produced only by a nuclear reactor and this makes this treatment of difficult use. The INFN PhoNeS (Photo Neutron Source) project is working to develop a converter+moderator system to maximize the neutron flux photoproduced by a LINAC high energy radiotherapy photon beam [1] . In this way it will be possible to have a useful neutron flux for BNCT in every hospital environment with a standard linear accelerator for radiotherapic treatments.

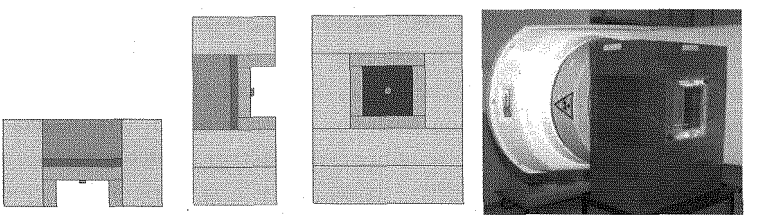

(a) Top (b) Side (c) Front (d) Photo

Fig. 1. Top 1(a), side 1(b) and front 1(c) view of the PhoNeS prototype simulated with MCNP and a picture 1(d) of the prototype positioned next to the head of the Linac.

2. The detector and the setup

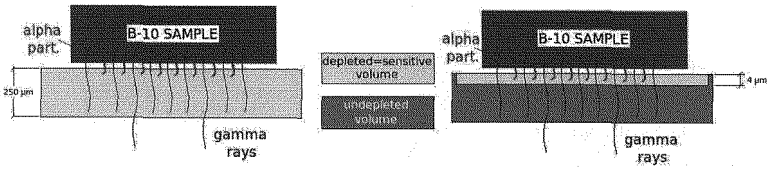

Fig. 2. Schematic drawing of the neutron imaging detector: a depleted detector which detects also photons and a not depleted one, seeing only the αs produced by the ^{10}B reaction.

The converter+moderator system, whose structure is presented in fig. 1(a)- 1(c), has been simulated with MCNP4B-GN. The system (fig. 1(d)) is made of different materials: a lead layer to stop the photons and to produce the neutrons through the giant dipole resonance; a polyethylene layer and a box of heavy water to thermalize the produced fast neutrons; the prototype is wrapped in graphite to stop the neutrons which drift out from the prototype and to concentrate the neutron beam inside the PhoNeS cavity.

The characterization of the spectrum in terms of energy and intensity has been performed with a real time scintillator system (energy) and the activation method (intensity) as described in [2] .

Even if the first prototype flux (1.3×10^7 n/cm^2/s) is not high enough for BNCT, it is ideal to perform neutron imaging with the scheme shown in fig. 2. Some samples doped with boron have been positioned on the surface of a silicon detector which is able to detect the α particles emitted by the ^{10}B after the irradiation with the neutron beam. The detector is a $9.5 \times 9.5 \times 0.041$ cm^3 not depleted silicon microstrip detector (Hamamatsu) with a 121 μm readout pitch [3] . It works in a self-triggering mode, vetoed by the bunch presence: it acquires data only in the inter-bunch period in order not to be blind by the primary γ beam of the Linac. It is used in a not depleted configuration to detect only the α particles and not the γ background present in the room. A simulation with GEANT3 has been performed to estimate the minimum layer from which the α particles can escape from the sample obtaining a value of 5 μm.

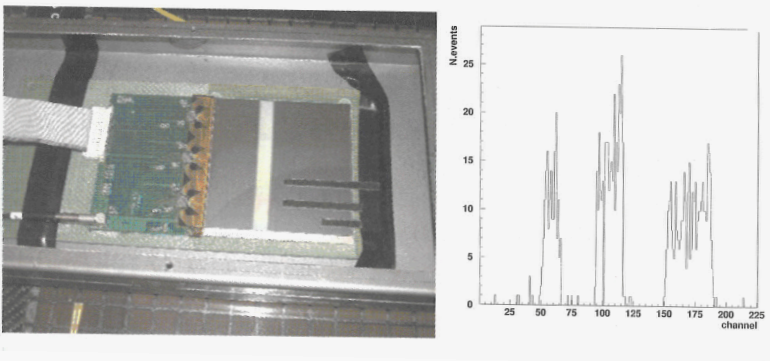

(a) (b)

Fig. 3. **Picture (a) and autoradiography** (b) of three samples made of boron resin positioned on the silicon detector.

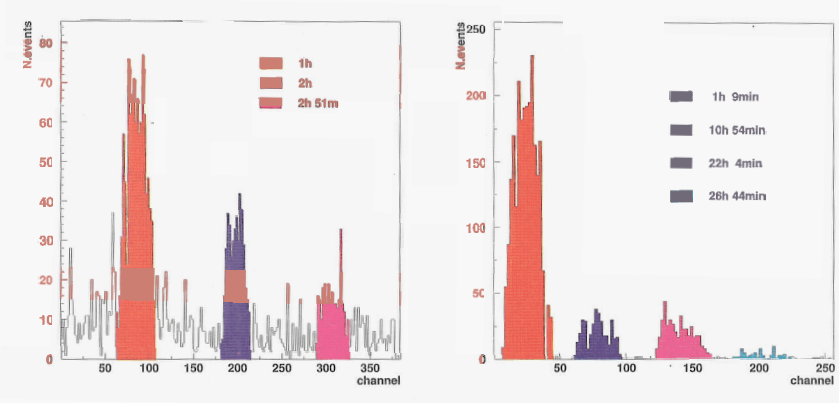

Fig. 4. Autoradiography of samples of urin doped with BPA and BSH taken at different times from the patient's uptake of the carrier.

3. Results

All the measurements were performed at the Radiotherapy division of the S. Anna Hospital in Como with a Varian Clinac 2100C/D accelerator.
The imaging detector has been tested with different samples: some boron resin samples such as the ones in fig. 3(a) whose results are shown in

fig. 3(b); some solutions of boric acid, with different concentrations of boron, deposited on 1 cm^2 spots on a plastic support which allowed to measure the minimum detectable concentration (1.91 $nmol/cm^2$). Measurements with biological samples were also performed and fig. 4 shows the autoradiographies of two different carriers used in BNCT: BPA and BSH. The samples of urin doped with the two carriers have been taken from the patients at different times from the uptake of the carriers themselves; the areas of the profiles of fig. 4 should be proportional to the boron concentrations.

4. Conclusions

The neutron imaging system developed within the INFN PhoNeS project has given good results. This real time system does not need a nuclear reactor to perform neutron imaging and it allows to study the concentration of boron in cells using different carriers to find the best one for BNCT treatments. The measurement uncertainty is <10% and can be improved using a better technique to deposit the samples on the support. The detection limit is <1 ppm and the spatial resolution can be easily improved to 50 μm even if this is not a constraint.

5. Aknowledgments

We would like to thank Dr. W. Sauerwein for having provided the biological samples to test our imaging system.

References

1. R. Bevilacqua et al., Nucl. Inst. and Meth. in Phys. Res. A572, 231-232 (2007).
2. V. Conti et al., "A time-of-flight detector for thermal neutrons from radiotherapy Linacs", Nucl. Inst. and Meth. in Phys. Res. A, doi: 10.016/j.nima.2007.07.145.
3. M. Prest et al., Nucl. Inst. and Meth. in Phys. Res. A501, 280-287 (2003).

IMPLEMENTATION OF IMAGE-GUIDANCE TECHNIQUES IN RADIATION THERAPY

MICHAEL THOMAS, BRENDA CLARK, MILLER MACPHERSON, LYNN MONTGOMERY, LEE GERIG

Medical Physics, The Ottawa Hospital Cancer Centre, 501 Smyth Ave. Box 927, Ottawa, ON K1H 8L6, Canada

For more than 100 years, physicists have been a vital part of the medical team required to deliver radiation therapy. Their role encompasses the verification of dose accuracy to the development and implementation of new techniques, the most recent of which is the incorporation of daily image guidance to account for inter- and intra-fraction target changes. For example, computed tomography (CT) integrated into radiotherapy treatment units allows the image-guided treatment of the prostate where the target location depends on the degree of rectal filling—a parameter that changes on timescales from minutes to weeks. Different technology is required for the adequate treatment of small lung tumours since respiration occurs on timescales of seconds. This presentation will review current image-guided techniques.

1. Introduction

Radiation therapy is the use of ionising radiation in the treatment of cancer and is most frequently delivered to the patient externally using megavolt photon beams generated by electron linear accelerators. Approximately half of all individuals diagnosed with cancer undergo radiation therapy as part of their treatment. Radiobiological considerations of the normal tissue surrounding the target, unavoidably irradiated during treatment, usually requires the dose to be delivered in multiple daily fractions over a period of up to eight weeks. Until relatively recently, the daily setup of the patient on the treatment couch was effected through the use of a combination of skin marks and bony anatomy, with a set of orthogonal radiographs taken on the one or more days to check positioning.

The recent incorporation of sophisticated imaging technology into the treatment delivery unit has enabled a dramatic increase in the precision of daily patient setup and prompted the implementation of image-guided radiation therapy (IGRT). A variety of technologies are currently available for pre-treatment volumetric imaging including helical tomotherapy, gantry mounted kilovolt conebeam CT (CBCT), megavolt CBCT, robotically mounted x-band

accelerator and ultrasound with many others under development[1]. The potential uses of image-guidance range from patient positioning, monitoring of anatomical changes over the course of treatment, monitoring of treatment response and target delineation in the presence of high Z material such as hip replacement prostheses to dose adjustment and dose guidance to correct inadequacies in dose distribution caused by reshaping of the target[2].

The clinical implementation of IGRT is a non-trivial exercise and also requires substantial investment in equipment. Image-guidance techniques must be tailored to the treatment site and disease[3,4,5]. For example, image registration processes are anatomy based but use different criteria for different treatment sites and in all cases, guidelines must be developed to ensure a standardised approach and appropriate delegation of decision making from the physician who is not present at the time of treatment to the treating therapists. While it is difficult to make a business case prior to implementation[6,7], recent publications have provided some indication of the potential improvement in tumour control to be obtained. For example, the prostate gland is known to move substantially and unpredictably during radiation therapy due to the movement of gas in the rectum. A study by De Crevoisier et al.[8] showed significant benefit in biochemical tumour control for patients with undistended rectum at the time of the treatment planning imaging as compared to those with substantial rectal distension, indicating a geographic miss of some or all of the radiation treatment fractions may have occurred. We present further details on tomotherapy and CBCT.

2. Helical Tomotherapy

Tomotherapy is an innovative technology that integrates megavolt volume imaging with treatment delivery by mounting a short linear accelerator on a ring gantry similar to a CT scanner as shown in Figure 1.

The advantages of tomotherapy include the elegant use of the ring gantry to give good quality volume imaging combined with helical radiation delivery, the fan beam modulated by a binary multi-leaf collimator, the continuous radiation delivery from 360 degrees around the patient, the integration of the treatment planning system with the treatment delivery system to provide dose information on the pre-treatment imaging and the relatively small footprint. In 2005, we installed a tomotherapy unit (TomoTherapy Hi-Art, TomoTherapy Inc., Madison, Wisconsin) in a pre-existing bunker too small for a modern accelerator. This installation has been so successful during the last two years of operation that we have recently installed a second unit in an adjacent bunker.

Traditional medical linear accelerators are equipped with two or more photon and several electron beam energies, requiring several weeks installation and physicists to perform up to 12 weeks of commissioning measurements prior to clinical use. In contrast, our second tomotherapy installation was complete in 2 weeks, one week for installation and one week for acceptance and commissioning. With only one 6 MV fan beam and pre-configured treatment planning software included as part of the purchase, the physics work was dramatically reduced compared to that for a traditional accelerator.

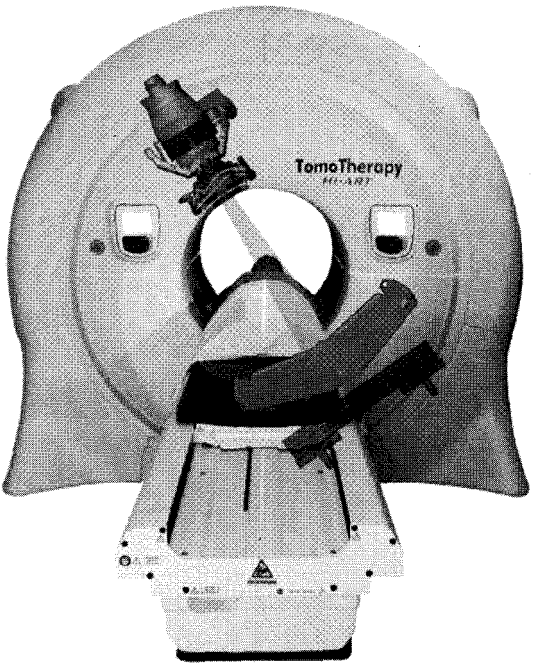

Figure 1. An image of a TomoTherapy Hi-Art system with a schematic diagram showing the gantry mounted linear accelerator, fan-beam, detector array and beam stopper (www.tomotherapy.com)

However, the main advantage of tomotherapy is not the reduction in physics effort required, but rather the exquisite conformality of dose distribution obtained through the use of helical, fan beam intensity modulated delivery combined with volume imaging immediately prior to treatment to ensure that the patient is aligned with the dose. Figure 2 shows an example of the value of image guidance for the treatment of locally advanced basal cell carcinoma immediately adjacent to the posterior aspect of the spinal cord. As seen in this figure, this patient also had disease on his anterior chest which was treated simultaneously, demonstrating an additional capability of helical tomotherapy

dose delivery not possible with a conventional accelerator. The ability of the system to show the calculated dose distribution superimposed on the pre-treatment imaging allows the treating therapists to optimise the geographic location of the dose deposition prior to treatment. Sites treated on our unit to date include brain, head and neck, pelvis and and full central nervous system, and most treatments are delivered according to pre-determined protocols to allow for assessment and quantification of clinical results. Table 1 gives the results of a timing study.

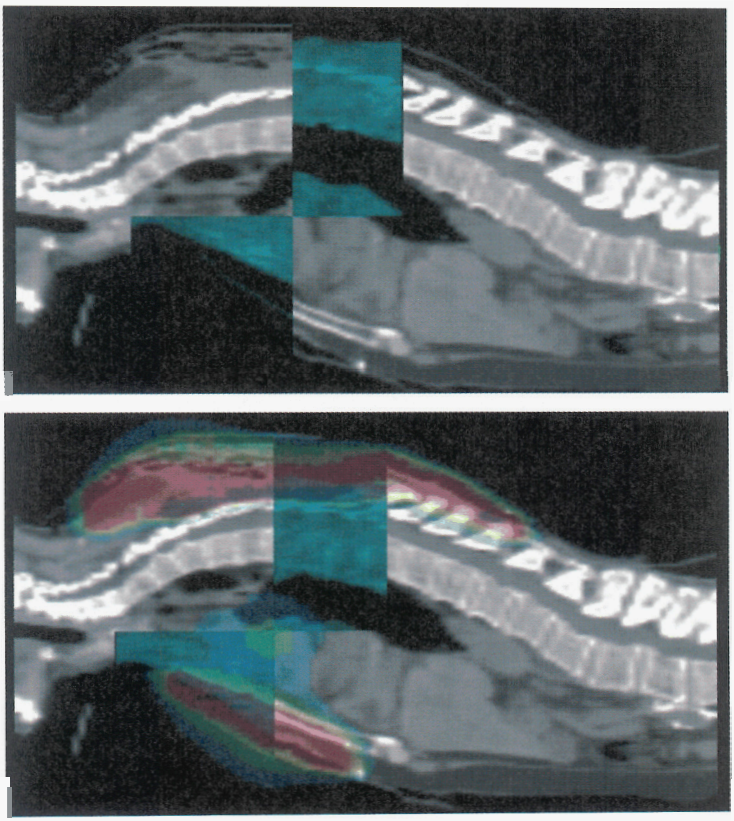

Figure 2. A sagital megavolt CT image from pretreatment imaging (inset) superimposed on the kilovolt CT planning image showing (top) misalignment of the patient and (bottom) after realignment. This patient was simultaneously treated for a posterior tumour which had invaded the paraspinal musculature and eroded the posterior spinal processes and a second tumour on his upper chest.

Recently, we agreed to act as a pilot site for clinical evaluation of the TomoTherapy Hi-ART StatRT® software, designed to enable the process of scan, plan and treat in a single session as little as 30 minutes. The time required to execute the individual sub-elements (setup, scan, contour, optimize, plan evaluation/accept, second scan + image registration, and treatment delivery) of the treatment session were timed from patient entry to exit from the treatment room. We found the system to be useful to quickly scan, plan and treat palliative patients in a single session with highly conformal dose distributions, allowing for critical organ and normal tissue sparing.

Table 1. Median (Mean) treatment time (minutes) by site for tomotherapy patients, first 10 months.

Site	*n*	Setup	Image acquisition & Registration	Total Treatment Time
Brain	52	3.0 (3.9)	6.0 (6.6)	22.0 (22.8)
Head & Neck	106	4.0 (4.9)	9.0 (9.6)	27.0 (27.9)
Pelvis	85	5.0 (4.6)	8.0 (8.1)	25.0 (25.6)

Service of the tomotherapy unit is provided by three in-house electronics technicians who are responsible for all maintenance and service activities and who share daily machine preparation duties with two physicists. The total time required for daily machine preparation and QA is currently one hour, our units operate 9 hours per day with an average patient appointment time of 25 minutes.

3. Conebeam CT

Gantry mounted kilovolt volume imaging is now available on both Elekta and Varian accelerators through kilovolt generators and associated detectors mounted orthogonally to the megavolt treatment delivery system as shown in Figure 3. Both megavolt and kilovolt systems use amorphous silicon detector panels and the image quality has been found acceptable[2]. However, by virtue of the increased scatter at megavolt energies, the kilovolt conebeam imaging has superior contrast and resolution compared to the MVCT of the tomotherapy system. The linac configuration is a somewhat cumbersome unit having a much slower gantry rotation compared to the tomotherapy system and also requiring more attention to the geometrical setup. Not only is there a centre of rotation (isocentre) of the MV radiation field, there is also a mechanical isocentre relating to the couch, gantry and collimator rotations plus a kV isocentre relating to the kV imager. The co-incidence of these isocentres must be calibrated and checked regularly if the unit is to be used for quantitative image guidance.

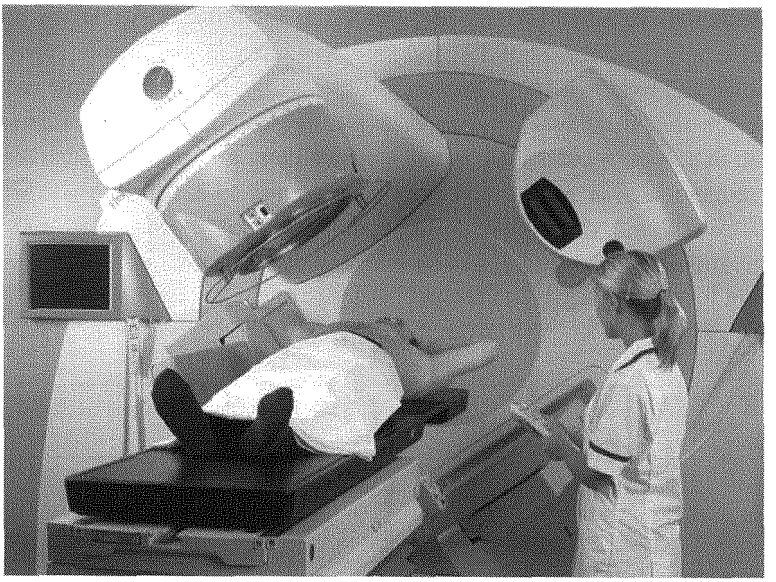

Figure 3. An Elekta Synergy accelerator showing the megavolt treatment delivery system on the upper left, the kilovolt x-ray tube on the upper right and two amorphous silicon detector panels mounted on the opposite side of the gantry, with the treatment couch positioned at the centre. (www.elekta.com)

These units have been used for patient repositioning for prostate cancer[4,9], extra-cranial stereotactic radiosurgery[10] and in the management of respiratory motion in lung cancer treatments[11]. The Ottawa Hospital Cancer Centre has two Elekta Synergy accelerators each with matching 4, 6 and 10 MV photon beams. Our experience with image guidance techniques has shown that planar MV imaging is almost equally effective as volume imaging at aligning patients for prostate treatments if the patient has fiducial markers implanted into the prostate prior to treatment, Figure 4. For those patients ineligible or unwilling to undergo fiducial implantation, we have found that megavolt planar imaging does not provide sufficient soft tissue discrimination to visualise the prostate and we use kilovolt volume CBCT for pre-treatment alignment, Figure 5. The results of a timing study comparing the two techniques is given in Table 2.

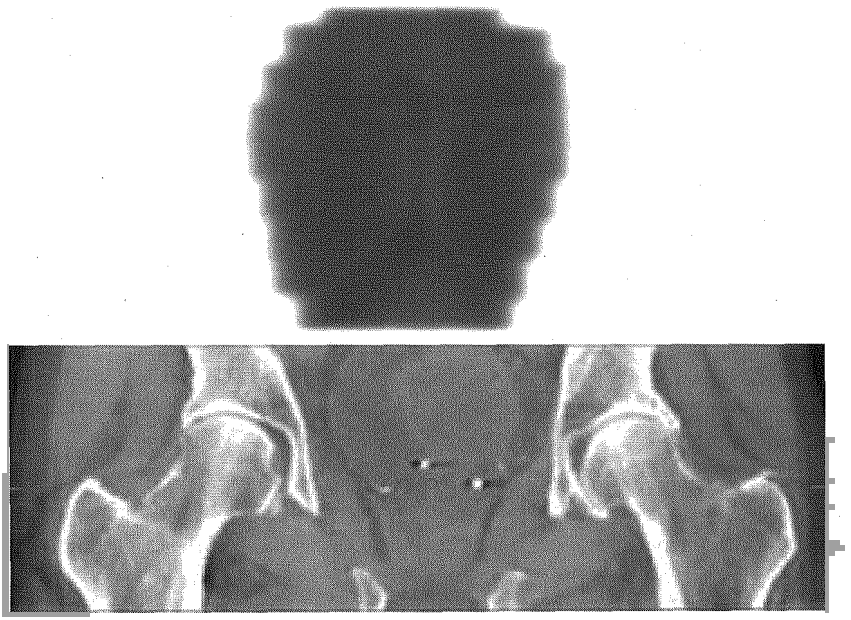

Figure 4. Top: a two-dimensional megavolt portal image showing the anterior-posterior view of a prostate treatment field with three fiducial markers visible in the field. **Bottom:** a coronal reconstruction of a conebeam CT volume image showing much increased anatomical information.

Figure 5. An axial reconstruction of a conebeam CT volume image of a prostate patient without implanted fiducial markers.

Table 2. Average (± standard deviation) of time (minutes) for image guidance process for planar MV imaging (EPID) and volume CBCT imaging.

	Patient Setup	Image acquisition, Registration and Setup Correction	Total Treatment Time
EPID (n=122)	3:59 (± 1:35)	4:30 (± 1:51)	14:31 (± 3:21)
CBCT (n=246)	3:48 (± 1:18)	6:43 (± 1:32)	20:30 (± 3:22)

4. Summary

This brief review has described some of the issues arising from the clinical implementation of image guidance in radiation therapy. The introduction of these new technologies is expected to result in a steady reduction in the volume of tissue irradiated as confidence in the ability to accurately target the cancerous tissue increases, thus providing an opportunity to either reduce toxicity to surrounding normal tissue or to increase dose delivered to the target and thereby increasing tumour control. Pre-treatment imaging also paves the way to modify the dose distribution to account for changes in target shape during the course of treatment, or even during a single treatment with intra-fraction motion. The potential uses of IGRT have yet to be fully realised and include the appication to some cancers presently considered incurable by escalating the dose to levels that would be highly toxic without a high degree of conformality to the target tissue and dramatic reduction of dose to surrounding normal tissue. However, the cost is considerable in such things as investment in the technology, increased treatment time, management of the image data generated and increased staffing. Thus it is imperative that the implementation of image guidance in radiation therapy is matched by appropriate resource allocation and management.

References

1. J. A. Purdy. *Front Radiat.Ther.Oncol.* **40**, 18. (2007).
2. L. A. Dawson and D. A. Jaffray. *J.Clin.Oncol.* **25**[8], 938. (2007).
3. P. A. Kupelian, C. Lee, K. M. Langen, O. A. Zeidan, R. R. Manon, T. R. Willoughby, and S. L. Meeks. *Int.J.Radiat.Oncol.Biol.Phys.* **In press.** (2007).
4. W. Y. Song, B. Schaly, G. Bauman, J. J. Battista, and D. J. Van. *Int.J.Radiat.Oncol.Biol.Phys.* **64**[1], 289. (2006).
5. O. A. Zeidan, K. M. Langen, S. L. Meeks, R. R. Manon, T. H. Wagner, T. R. Willoughby, D. W. Jenkins, and P. A. Kupelian. *Int.J.Radiat.Oncol.Biol.Phys.* **67**[3], 670. (2007).
6. T. H. Fox, E. S. Elder, I. R. Crocker, L. W. Davis, J. C. Landry, and P. A. Johnstone. *J.Am.Coll.Radiol.* **3**[1], 38. (2006).
7. M. D. Mills, W. J. Spanos, and R. J. Esterhay. *J.Am.Coll.Radiol.* **3**[4], 278. (2006).
8. de Crevoisier R., S. L. Tucker, L. Dong, R. Mohan, R. Cheung, J. D. Cox, and D. A. Kuban. *Int.J.Radiat.Oncol.Biol.Phys.* **62**[4], 965. (2005).
9. W. Y. Song, E. Wong, G. S. Bauman, J. J. Battista, and D. J. Van. *Med.Phys.* **34**[1], 352. (2007).
10. M. Fuss, J. Boda-Heggemann, N. Papanikolau, and B. J. Salter. *Med.Dosim.* **32**[2], 102. (2007).
11. P. J. Keall, G. S. Mageras, J. M. Balter, R. S. Emery, K. M. Forster, S. B. Jiang, J. M. Kapatoes, D. A. Low, M. J. Murphy, B. R. Murray, C. R. Ramsey, M. B. Van Herk, S. S. Vedam, J. W. Wong, and E. Yorke. *Med.Phys.* **33**[10], 3874. (2006).

A DOUBLE LAYER SILICON DETECTOR FOR SINGLE PHOTON COUNTING

E. VALLAZZA*, F. ARFELLI, F. BRUNI, E. CASTELLI, R. LONGO, C. PONTONI, L. RIGON, T. ROKVIC

INFN Sezione di Trieste and Department of Physics, Trieste University, Via Valerio 2, I-34127 Trieste, Italy
**E-mail: erik.vallazza@ts.infn.it*

A. BERGAMASCHI, B. SCHMITT

Paul Scherrer Institut, 5232 Villigen PSI, Switzerland

D. DREOSSI, R. H. MENK

Sincrotrone Trieste, Strada Statale 14 - km 163,5 in AREA Science Park I-34012 Basovizza, Trieste, Italy

The SYRMEP Beamline at the ELETTRA Synchrotron (Trieste, Italy) has already been performing clinical mammographic examinations using X-rays generated by one bending magnet. These examinations have been performed with traditional screen-film systems, but in order to exploit the characteristics of the beam (monochromatic in the energy range 8.5-35 keV, with a rate up to 7×10^7 photons/(mm^2·s) at 17 keV), a double layer Silicon detector has been developed within the INFN PICASSO project. This detector is the evolution of the single layer already deployed by the INFN MATISSE project, in collaboration with the Paul Scherrer Institut. This single layer was based on a microstrip Silicon sensor (50 μm pitch) coupled to the Mythen-II high-rate photon counting ASIC, used in the edge-on configuration to improve the detection efficiency. This contribution presents the development of a double layer with limited coverage (5.5 cm instead of 21 cm), used to verify all the steps in view of the construction of the full scale assembly. We present the results in terms of rate and of the imaging capability of standard phantoms, recorded in the phase contrast imaging modality.

Keywords: Digital Mammography, Synchrotron Radiation, Phase Contrast Imaging

1. Introduction

The ELETTRA Italian Synchrotron Radiation (SR) Facility in Trieste is provided with a dedicated bending magnet beamline for medical physics operated by the SYRMEP (Synchrotron Radiation for Medical Physics) collaboration. During 2006 the collaboration performed worldwide unique clinical mammographic examinations using a monochromatic laminar synchrotron radiation beam in the energy range from 17 keV to 35 keV with a cross section of 0.3×21 cm^2 at the patient position. The unique characteristics of synchrotron radiation allow the use of the so-called phase contrast imaging modality, pioneered by the collaboration.[1] This technique relies not only on the source characteristics but also on detection devices featuring high spatial resolution. Initially a traditional screen-film system has been employed for the clinical examinations providing good preliminary results.[2] However, the use of screen-film systems implies very well known limitations and therefore, in parallel to the development of the beamline infrastructure, the collaboration has developed a digital detector specifically designed to operate in single photon counting mode.

2. Detection system

The design is matched with the beam geometry and energy and it has to tolerate a high photon flux up to 7×10^7 photons/(mm^2·s) at 17 keV.
To meet these requirements in combination with high absorption efficiency, a Silicon microstrip detector in edge-on geometry has been employed, resulting in a pixel size defined by the detector thickness of 300 μm and the strip pitch of 50 μm. A single-layer detector assembly consisting in 2368 strips and thus covering approximately a beam width of 12 cm has been built and operated within the INFN MATISSE project in collaboration with the Detector Group of the Paul Scherrer Institut. This single layer detector is based on a Hamamatsu Silicon detector ($12 \times 0.03 \times 2$ cm^3) coupled to the Mythen-II ASICs and its associated read out boards developed at PSI; preliminary results on the performance of this device have been already presented.[3]

The main requirements in the evolution from the single layer are:

- Very precise mechanical structure in order to have a planarity of the detector, used in the edge-on configuration, better than 20 μm.
- Capability to cover the full width of the beam, 21 cm, by using two detectors side by side, one 9 cm wide and the other 12 cm wide, for a total of 33 ASICs and 4224 channels per layer.

To fulfill these requirements, a mechanical structure based on an Aluminum frame holding both the Silicon detector ($9 \times 0.03 \times 1.5$ cm^3) and the PCB that houses the readout ASICs, has been developed. Two of these structures could then be stacked with high precision. It has been decided to build a limited coverage (5.5 cm overlap) version of the assembly to verify this assembly scheme and that the stringent mechanical requirements could be met. The schematic view of the two layer assembly seen from the side is shown in Fig. 1.

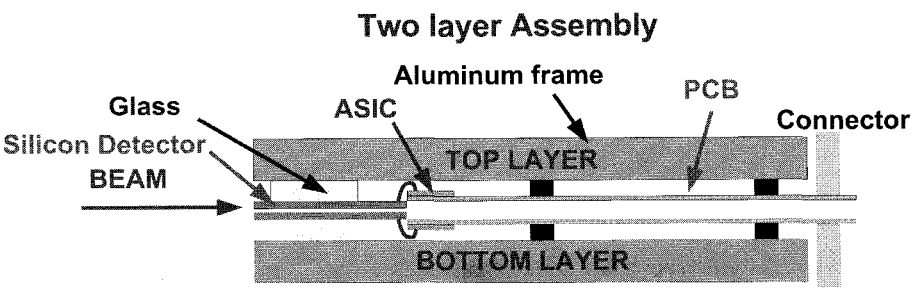

Fig. 1. Drawing of the two layer assembly showing the components (not to scale).

In order to insure a very good planarity, the Silicon detector is glued, after bonding, to a glass bar which in turn is glued to the Aluminum frame, together with the PCB. The two prototype frames are shown on the left in Fig. 2. The PCBs holding the Mythen-II ASICs are seen from the bottom allowing to see the Silicon detectors. The assembly with the two layers stacked with the detectors back to back is shown on the right in Fig. 2.

3. Results

The detector has been taking data at the SYRMEP beamline in four periods between April and September 2007. The first measurement performed, by exposing the two layer assembly to moving vertical slits, were the ones on the distance between the center of the two layers and on the planarity of each layer. In the first case, the distance has been measured as 572 μm on average, as shown on the left of Fig. 3, that has to be compared to the design goal of 600 μm, i.e. 300 μm gap between the two detectors. The alignment can be improved with a system of micrometric screws to adjust the distance between the layers. The deviation of the top layer from the planarity is shown on the right of Fig. 3. The RMS of the distribution is

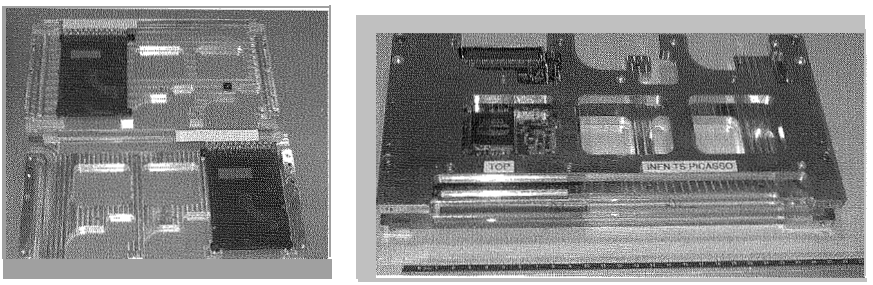

Fig. 2. On the left, picture of the two frames with PCB and Silicon detectors, seen from the bottom. On the right, picture of the detector assembly. The two frames holding the Silicon detectors are shown after the assembly.

3.8 μm and 98.3% of the channels are within ± 10 μm. For the bottom detector the RMS is 3.1 μm and 99.7% the channels are within ± 10 μm.

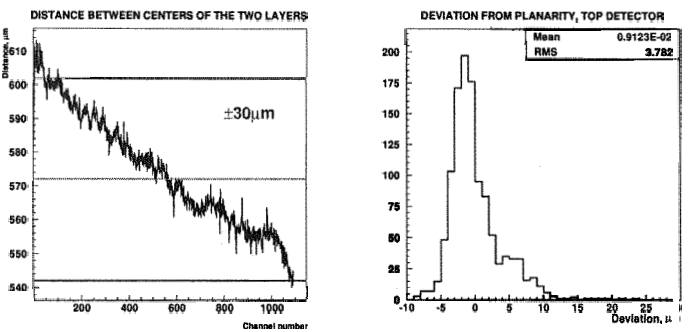

Fig. 3. On the left, measured distance between the centers of the two layers as a function of the channel number (50 μm pitch i.e. about 5.5 cm total); on the right, measured deviation from planarity of the channels of the top layer.

In order to evaluate the Detective Quantum Efficiency (DQE) of the system, i.e. the capability to produce an output count able to follow the number of incoming photons, a set of flat fields with different filtering have been taken at various energies. As an example, Fig. 4 on the left presents the DQE at 17 keV, showing the contribution of the geometric efficiency (dead zone in front of the detector which influences the count at the limit of very low incident fluxes) corresponding to 48.7% and of the dead time of the counting system which has been fit with a poissonian paralysable

model:

$$\mathrm{DQE} = \frac{N_{out}}{N_{in}} = \varepsilon \times \exp(-\varepsilon\tau N_{in})$$

where N_{in} in the input rate, N_{out} is the measured rate, ε is the efficiency and τ is the dead time, measured to be 166 ns. The plot shows that even at 1.2 MHz, the count loss due to the dead time is <10%. This DQE has been measured at 17 keV where the flux is maximum, to stress the detector performance in terms of dead time and therefore the efficiency is low due to the dead zone. This can be improved given that in the final assembly the detectors will have 200 μm of dead zone instead of 400 and that the typical energy for mammography is above 20 keV where the geometrical efficiency is greater than 80% with a 200 μm dead zone. An important aspect of the data taking was to asses the capability to acquire an image with the two separate layers and then produce with the adequate corrections for the different positions of the layers a summed image. In Fig. 4 on the right an image of the Ackermann (RMI-160) phantom is presented, obtained by summing the two separate images of the two layers. The air entrance dose delivered to take this image was 6.9 mGy but an image of comparable quality could be obtained with a much smaller dose (below 1.5 mGy) by optimizing the energy and the scanning step. Finally, to show the phase contrast imaging capability of this system, in Fig. 5 the images taken in phase contrast mode of a phantom made by nylon wires of different sizes (from 100 to 600 μm) fixed on a Lucite slab 3 cm thick are presented: on the left, the image taken with the screen-film system with an air entrance dose of 1.5 mGy while in the middle and on the right are shown the images of the same phantom with the PICASSO detector, with a 150 μm scan step (dose 0.9 mGy) and a 50 μm scan step (dose 2.53 mGy) respectively. These images show that phase effects along the 50 μm pixel pitch can be easily seen with a lower dose with respect to the screen-film system while by oversampling in the 300 μm pixel pitch direction some effects can be seen with a moderate increase of the dose.

4. Conclusions

The PICASSO project has shown the feasibility of a novel assembly system that can be used to build a detector able to fully exploit the characteristics of the beam provided by the SYRMEP beamline at ELETTRA. The first results in terms of planarity and quality of the assembly for the small size prototype are very satisfactory and the steps to develop a full scale two layer assembly for the startup of ELETTRA in March 2008 have been taken.

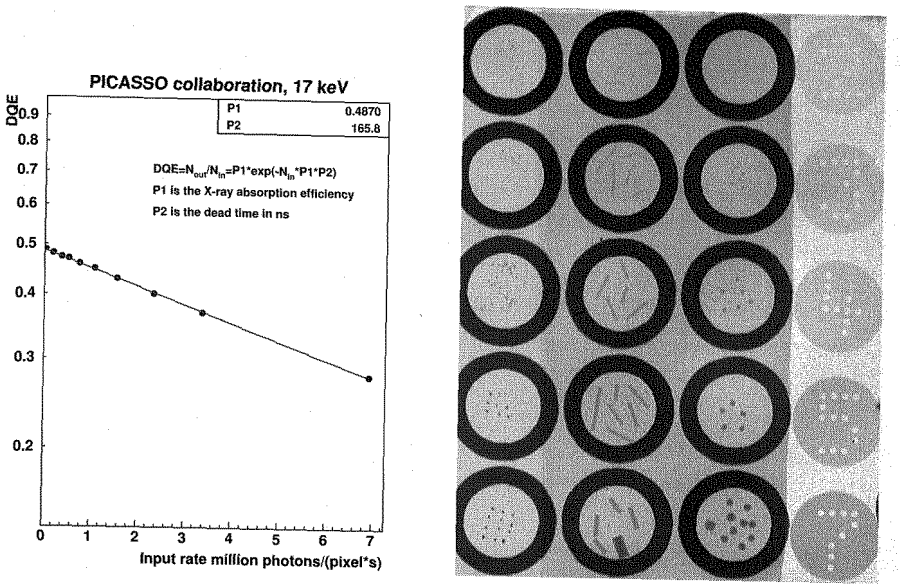

Fig. 4. On the left, measured DQE; on the right, picture of the Ackermann phantom, obtained by summing the top and bottom layer, with an air entrance dose of 6.9 mGy.

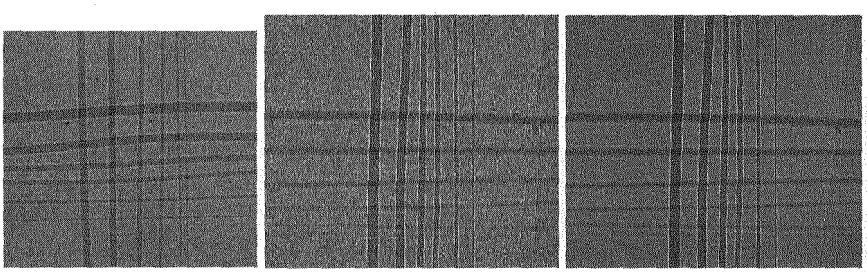

Fig. 5. Images of the nylon wire phantom (described in the text): on the left with the screen-film system; in the middle, with the PICASSO detector, 150 μm scan step; on the right again the PICASSO detector with a 50 μm scan step.

References

1. F. Arfelli et al., Radiology 215 (1) (2000) 286.
2. E. Castelli et al., Nucl. Instr. Methods A 572 (2007) 237-240.
3. D. Dreossi et al., Nucl. Instr. Methods A 576 (2007) 160-163.

IMAGING OF ABSORBED DOSE IN RADIOTHERAPY BY A POLYMER GEL DOSIMETER

E. VANOSSI[1,4], G.GAMBARINI[3,4], M.CARRARA[2], M. MARIANI[1], A. NEGRI[3,4]

[1] *Dipartimento di Ingegneria Nucleare, Politecnico di Milano,Via Ponzio 34/3, 20133 Milano, Italy*

[2] *S.C. Fisica Sanitaria, Fondazione IRCCS "Istituto Nazionale Tumori", Via Venezian 1, 20133 Milano, Italy*

[3] *Dipartimento di Fisica, Università di Milano, Via Celoria 16,20133 Milano, Italy*

[4] *INFN - Istituto Nazionale di Fisica Nucleare, Sezione di Milano, Italy*

Optical imaging of polymer gel dosimeters in form of layers was investigated to enquire their reliability for in-phantom dose measurements in photon or thermal neutron fields. The obtained dose measurements were compared with those achieved by means of Fricke gel dosimeters. Reliability of Fricke gel dosimeters was confirmed, whereas it has been shown that a conspicuous improvement of the adopted polymer gel dosimeters is necessary.

1. Introduction

In recent radiotherapy techniques, aimed at achieving high dose release in volumes conformal to the tumours and low dose in the surrounding healthy tissues, the high non-uniformity of the dose spatial distribution makes imperative to perform reliable 3-D dose measurements. In last years, a growing up interest was focussed on gel dosimetry that is considered a very promising technique for accomplishing 3-D imaging of absorbed dose.

The method is based on the analysis of a tissue-equivalent gel medium that acts by itself as continuous dosimeter. Such a dosimetric matrix is obtained by incorporating a chemical dosimeter into a tissue-equivalent gel [1]. The absorbed dose is not affected by the chemical compounds constituting the dosimeter, because they are always present in millimolar amount. After irradiation, absorbed dose is obtained analysing the variation of certain physical parameters of the system such as the relaxation rates of hydrogen nuclei, measurable by nuclear magnetic resonance (NMR) imaging, or the visible light optical absorption, measurable by spectrophotometry.

In the last decade, Fricke gel (FG) dosimetry has been studied as a technique to achieve 3D dose distribution and as a reliable alternative to film or

semiconductors array dosimetry [2]. These dosimeters are obtained by infusing a ferrous sulphate solution in the gel. The chemical reactions occurring after exposure to ionising radiation give rise to oxidation of ferrous ions Fe^{2+} to ferric ions Fe^{3+} and the ferric ion yield is proportional to the absorbed dose.

The metal ion indicator Xylenol Orange (XO) is incorporated in order to allow reliable optical analysis. The complex XO - Fe^{3+} gives rise to light absorption at 585 nm and the absorbed dose is proportional to the measured difference in optical density. Dose images are obtained by detecting light transmittance images, for example by means of a CCD camera supplied with an optical filter [3].

Owing to the diffusion of ferric ions in the gel matrix, with the consequent necessity of performing optical imaging within a short time after irradiation, new kind of gel dosimeters is currently under study. The main advantage of these gels is that the measured changes correlated to the absorbed dose do not involve diffusive ions. Many studies are in development, in particular concerning gel matrices in which ionising radiation induces a polymerisation process that increases the opacity of the medium and makes optical imaging possible. The research on polymer gel dosimeters is in particular turned to find a stable system, with both high sensitivity to radiation and good reliability.

The opportunity of performing in-phantom dose imaging and profiling is of great importance for treatment planning validation not only in conformal radiotherapy, but also in BNCT (Boron Neutron Capture Therapy). The method for spatial determination of absorbed doses in thermal or epithermal neutron fields, based on gel dosimeters in form of layers, has been proven to be very reliable [3]. In fact, gel dosimeters in form of layers permit not only to obtain spatial dose distributions, but also to achieve measurements of each dose contribution in neutron fields separately. A properly studied procedure based on the analysis of polymer gel dosimeters with a suitably modified composition has been developed to this aim [4]. The layer-geometry has the advantage of avoiding significant alteration of neutron transport, even if the elemental gel composition is changed adding isotopes having high cross section for thermal neutrons. This is the case for instance of ^{10}B, which is added to achieve separation of its dose contributions from the total dose [5].

2. Materials and methods

Polymer gel layers are synthesized and stored overnight in a fridge as described elsewhere [6]. The dosimeters are in form of layers with a thickness of 3 mm and a rectangular shape. The day after the preparation, they are irradiated at different

calibration doses. Light transmittance images before and after irradiation are acquired with a CCD camera and the variation of the optical density, proportional to the absorbed dose, is obtained by pixel-to-pixel manipulations of the couples of images of each dosimeter. The absorbed dose images are finally obtained and the dosimeter response vs. the absorbed dose is studied.

In our study, the reliability of the designed polymer gel dosimeters for in-phantom dose determination in radiotherapy fields has been investigated. To this aim, depth dose profiles extracted from the dose images have been compared with the corresponding profiles obtained by FG dosimeters. Although FG dosimeters had already shown high reliability [1], as a further verification they have been adopted to measure the percentage depth dose (PDD) profiles of a 10×10 cm^2 size X-ray field produced with a linear accelerator (Varian LINAC 2100c) in 18 MV modality. The prescribed dose at the isocentre was 10 Gy, whereas the source surface distance was 100 cm. The obtained PDD profiles were finally compared with measurements obtained with a cylindrical ionisation chamber.

In order to investigate the reliability of polymer gel layer dosimeters to measure the absorbed dose, some gel layers have been irradiated with an ^{192}Ir brachytherapy high dose rate (HDR) system (Nucletron Microselectron-HDR). A dose of 5 Gy at a 3 cm distance from source was planned.

Finally, some dose measurements in BNCT neutron fields have been carried out. The dosimeters were put in phantoms and exposed in the thermal column of a research nuclear reactor. After one half of the exposure time, the phantoms were rotated of 180°. In-phantom 3D images of both gamma and boron doses were achieved.

3. Results

Fig. 1 shows an example of the comparison between PDD profiles obtained with a FG layer dosimeter and the measurements obtained by a ionisation chamber. In Fig. 2, three dimensional dose images achieved by means of Polymer (a) and Fricke (b) gel dosimeters are represented. A picture of two polymer gel dosimeters after exposure at the brachytherapy unit has been as well reported in figure 2 (c). In Fig. 3, the PDD profiles along the axis passing perpendicularly through the centre of ^{192}Ir source are reported.

The gamma dose images obtained by means of the dosimeters put in phantoms exposed in a thermal column of a nuclear reactor are shown in Fig. 4. The extracted dose profiles are reported in Fig. 5.

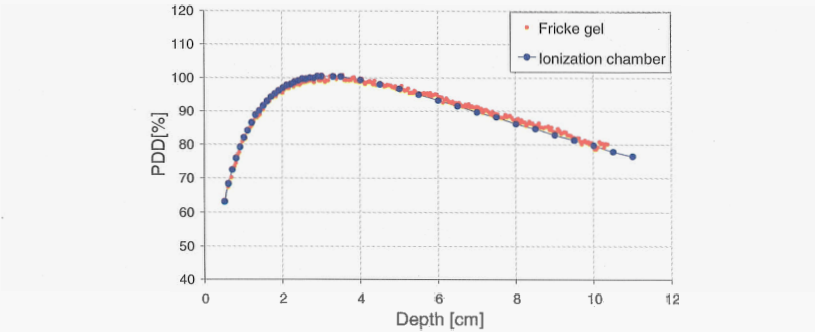

Figure 1. Percent depth doses in a phantom irradiated with X-rays from a linear accelerator measured with FG dosimeter and with ionisation chamber.

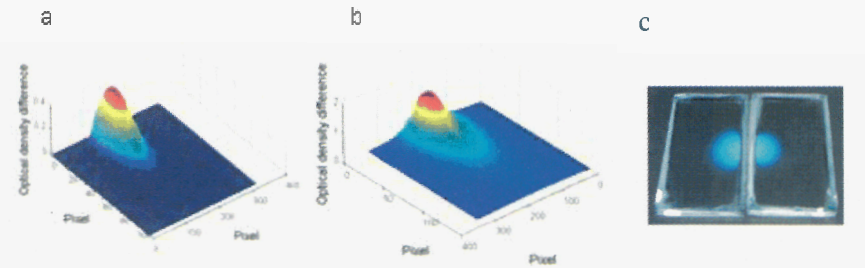

Figure 2. Dose images obtained by polymer gel (a) and a FG (b) layers irradiated with a HDR brachytherapy source. c) Picture of the polymer gel layers irradiated with a brachytherapy source;

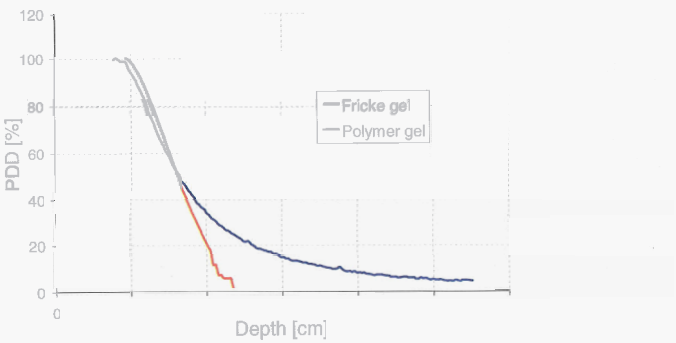

Figure 3. Percent depth dose profiles obtained by polymer gel and a FG layers irradiated with a HDR brachytherapy source.

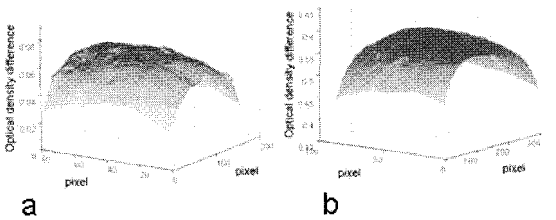

Figure 4. Gamma dose images achieved by polymer (a) and Fricke (b) gel dosimeters.

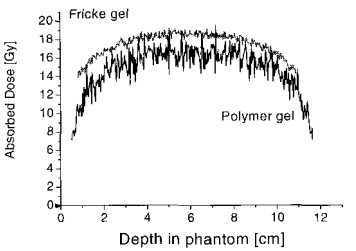

Figure 5. Gamma dose profiles extracted from polymer and FG dose images.

4. Conclusion

Fricke gel dosimeters are reliable, whereas the adopted polymer gel dosimeters would need a conspicuous improvement. Different polymer gels might be more suitable to our aims.

References

1. R.J. Schulz, A. deGuzman, D. Nguyen and J. C. Gore, *Phys. Med. Biol.* **35**, 1611 (1990).
2. S. Tomatis, M. Carrara, G. Gambarini, R. Marchesini and M. Valente, *Nucl. Instrum. Meth. A* **580,** 506 (2007).
3. G. Gambarini, G. Gomarasca, R. Marchesini, A. Pecci, L. Pirola and S. Tomatis, *Nucl. Instrum. Meth. A* **422,** 643 (1999).
4. G. Gambarini, S. Agosteo, M. Carrara, S. Gay, M. Mariani, L. Pirola and E. Vanossi, *Journal of Physics: Conference Series* **41**, 275 (2006).
5. G. Gambarini, V. Colli, S. Gay, C. Petrovich, L. Pirola and G. Rosi, *Appl. Radiat. Isotopes* **61**, 759 (2004).
6. M. Mariani, E. Vanossi, G. Gambarini, M. Carrara and M. Valente, *Radiat. Phys. Chem.* **76**, 1507 (2007).

RADIOCHEMICAL SEPARATIONS: USEFUL METHODS FOR THE PREPARATION OF *NO–CARRIER–ADDED* SOLUTIONS OF DIFFERENT RADIONUCLIDES FOR METABOLIC RADIOTHERAPY

C. ZONA, F. GROPPI, E. PERSICO, L. CANELLA, M. L. BONARDI
LASA, Università degli Studi di Milano and INFN-Milano, via F.lli Cervi 201 Segrate,I- 20090, Italy

M. CHINOL
Istituto Europeo di Oncologia, via Ripamonti 435, I-20141 Milano, Italy

K. ABBAS, U. HOLZWARTH, N. GIBSON
IHCP, Institute for Health and Consumer Protection, JRC-Ispra, via E. Fermi Varese, I-21020, Italy

In Nuclear Medicine, radionuclides are used in the detection and the treatment for cancers and others diseases. We must obtain, for therapeutic purposes, solutions of radionuclides in the required chemical form, with an high specific activity (A_S). To reach our goal we must, first, obtain *no–carrier–added* (NCA) solutions. In this work we present different methods for the production of NCA radionuclides, based on either wet–chemistry, or thermo– and radio–chromatography. We set up four different methods: two for the preparation of the alpha emitter ^{211}At, and two for the beta emitters ^{186g}Re and ^{90}Y. These radionuclides had been chosen because of their chemical and nuclear properties as their half–life, type, abundance and energy of emissions, that make them among the most promising radionuclides to label compounds for the metabolic radionuclide therapy.

1. Introduction

It is well known that the first radionuclide to be artificially produced was ^{30}P, obtained by Pierre and Marie Curie in 1934 using nuclear reaction ^{27}Al(α,n)^{30}P; in this reaction α particles (from the a decay of ^{210}Po) react with stable ^{27}Al, neutrons are emitted and the short–lived ($t_{1/2}$ ~ 2.6 min) ^{30}P product nuclide is formed.

Today, the most manmade radionuclides are produced by charged particle, like protons, deuterons or α particles, accelerated in a compact cyclotron: in general the radionuclides generated by charged particle bombardment are neutron deficient isotopes, and so tend to be those isotopes which decay by β^+ emission or electron capcture (EC).

A second source of manmade radionuclides has become available since the development of nuclear fission reactors, during the 1950s; thus a nuclear reactor

can be used as a plentiful source of neutrons, and through (n,γ), (n,fission) and (n,charge particle) reactions a very wide range of radionuclides can be produced. In general, reactor produced radionuclides are neutron rich isotopes which tend to decay by β^- emission.

Another method of obtaining a limited number of short–lived isotopes in a laboratory uses nuclide–generator. A nuclide generator is little more than a supply of a moderately long–lived parent radionuclide which decays to produce a required short–lived isotope. In most nuclide generators the parent isotope is adsorbed onto a support material, such as ion exchange resin, which is packed in a column; the daughter radionuclide may be obtained simply by pumping a proper buffer solution, that dissolves only the daughter nuclide, from the generator tube.

After the production, a radiochemical separation is mandatory to prepare solutions of the radionuclides of interest; an important goal, for a good separation technique, is to obtained the radionuclides in a *no–carrier–added* (NCA) form, although without the presence or the addition of isomorphous isotopic carrier.

We present four different methods based on wet–chemistry, on thermo– and radiochromatography: two for the preparation of the alpha emitter ^{211}At, and two for the beta emitters ^{186g}Re and ^{90}Y. These radionuclides had been chosen because of their chemical and nuclear properties as their half–life, decay mode, abundance and energy of emissions, that make them some of the most promising radionuclides to label compounds for the metabolic radionuclide therapy (radiopharmaceuticals).

2. Astatine–211 (^{211}At)

Between the radionuclides of At, the ^{211}At is the most promising to label compounds for the hi–let metabolic radionuclide therapy; this aspect is due to its half–life of 7.214 h that is long enough to label radiocompounds and to the α particles of the ^{211}At/^{211g}Po system (energy from 5 868 keV to 7 451 keV)[1], that have a range from 60 to 67 μm in water (or soft animal tissues) and a LET_∞ from 100 to 130 eV·nm^{-1}, which is nearly the maximum of the RBE curve for energetic ions[2]. There are, however, some problems with the production and the purification of the ^{211}At from the target and/or from radionuclidic impurities.

^{211}At has been obtained via ^{209}Bi(α, 2n) reaction by α–cyclotron irradiation, using α energies larger than the reaction threshold of 20.72 MeV. Bi targets were irradiated by using α particles beam with energy higher than 28.61 MeV, in order to produce also small amounts of the γ emitter ^{210}At, via ^{209}Bi(α,3n) reaction.

The presence of a small amount of ^{210}At does facilitate the radiochemical processing of irradiated target, because ^{211}At/^{211g}Po is an almost pure α emitting system, with emission of X–rays of energy not optimal for high–purity

germanium (HPGe) spectrometry. ^{210}At decays on the long–lived impurity ^{210}Po, which can settle irreversibly in the body tissue with undesired radiation damage; nonetheless the activity produced under the irradiation conditions adopted, is negligibly small compared to ^{211}At one, due to the favorable ratio of the half–lives.

We present two different methods, useful in this step of production of the *NCA* ^{211}At/^{211g}Po, obtained from ^{209}Bi target by an α beam irradiation in a cyclotron.

The "wet–method" is a selective separation of At radionuclides, based on the dissolution of the irradiated target with HNO_3, the drying and the dilution with HCl, the extraction with DIPE (di–*iso*–propyl–ether) with a radiochemical yield larger than 98 % and the back–extraction with NaOH at various concentrations with an yield greater than 95 % in a range from 0.75 M to 2.00 M.

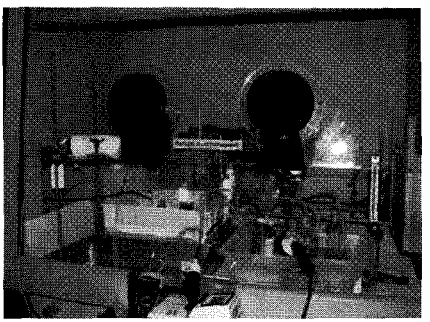

Figure 1. Dry distillation system.

In Fig. 1 it is shown the dry–distillation system developed by our research group. It is based on the sublimation of At radionuclides and Po radioimpurities in air–flux at 1.2 atm, the reaction of these elements with a chemical filter of CaO for the purification, and finally the trapping of At radionuclides in a acetone/dry CO_2 cryotrap down to –90 °C. This method allowed to obtain a radiochemical recovery yield larger than 64% with a radioimpurities concentration smaller than $3 \cdot 10^{-3}$ %; in these separations we obtained the first thermochromatogram for this type of method, carried out in Italy.

These methods are effective for the production of a very high specific activity ^{211}At/^{211g}Po system, characterized by a radionuclidic purity close to 100 %. Some studies are mandatory in order to improve the radiochemical yield of the dry–distillation method.

3. Rhenium–186g (^{186g}Re)

In Nuclear Medicine, especially in the metabolic radiotherapy, β^- emitting radionuclides are used in the treatments for cancers and others diseases. In our

case, the attention is focused on the ^{186g}Re[1], a β^- emitter ($t_{1/2}$ = 90.64 h, E^{max}_{β} = 1.07 and 0.93 MeV, E_γ = 137 keV) used for pain palliation of bone metastases[5]. The goal, however, consists in the extension of its applications to therapeutic purposes. The first step to succeed in our objective is to obtain *NCA* ^{186g}Re in order to increase its specific activity (A_S = activity on mass of isotopic carrier). To obtain the *NCA* ^{18x}Re, a separation of the Re radioisotopes from irradiated W target is mandatory, without any addition of either isotopic or isomorphous carrier. The wet–chemistry method is a selective radiochemical separation based on the dissolution, under heating and stirring, of the W target with a HNO_3(14.5 M)/HF(24 M)~3/1 solution, the addition of pre-heated H_2O and warming to remove HF. The last step is the separation of Re with a radiochromatographic method, using an activated aluminium oxide (acidic–AAO) minicolumn, that retains tungsten and elutes ^{18x}Re only. The eluate is collected in different vials, whose analysis was carried out by HPGe and NaI(Tl) detectors. It was possible obtaining a radiochromatogram from the collection of the spectra.

In Fig. 2 it is shown the fitted radiochromatograms obtained during different separations; in this experiments we used two different amount of AAO and we saw that the quantities of AAO influences only the position and the shape of the chromatographic peaks. In fact, in different experiments, we obtained radiochemical yields greater than 99% and less than 1% of ^{18x}Re remained onto the column.

The wet–chemistry method is effective for the production of very high specific activity ^{18x}Re, characterized by a radionuclidic purity close to 100 %. Some quality controls are necessary to study the presence of non–isotopic and non–radioactive residuals eluted from AAO column.

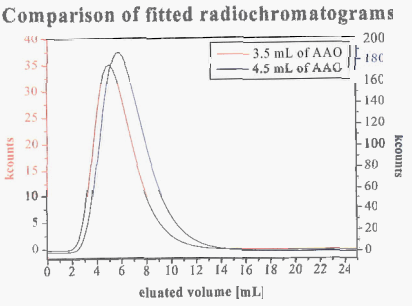

Figure 2. Fitted radiochromatograms.

4. Yttrium–90 (^{90}Y)

^{90}Y is often believed to be one of the most useful radionuclides that have been considered for radioimmunotherapeutic applications. This radionuclide has a half–life ($t_{1/2}$ = 64.1 h) consistent with the rate of antibody accumulation in tumour, that is not accompanied by gamma–ray emission in its decay, beta particles of high (E^{max}_{β} = 2.3 MeV), to a stable daughter. It is significant that ^{90}Y could be available conveniently and inexpensively as a radionuclide "generator" by decay of its parent, ^{90}Sr (a pure β^- emitter, $t_{1/2}$ = 28.1 a, E^{max}_{β} = 0.5 MeV). Nevertheless, the most present and planned clinical applications with [^{90}Y]labelled compounds employ activities that are not obtained from a "self–made" generator, but from commercial sources. So we evaluated a radiochemical separation method based on Eichrom's Sr–resin minicolumn, either as an "in–home" generator or as a fast QC tool for ^{90}Y solution. The extractant system in this resin is 1.0 M 4,4'(5')–di–*t*–butylcyclohexano 18–crown–6 (crown ether) in 1–octanol. The uptake of strontium by Sr–Resin increases with the increasing of nitric acid concentration. Starting on these information we studied and developed a method based on the loading of HNO_3 8 M solutions, containing ^{90}Sr/^{90}Y or ^{85}Sr (a pure γ emitter with a single γ emission at 514 keV), on a minicolumn, 2 elutions with HNO_3 8 M for the recovery of "pure" ^{90}Y solutions and 2 elution with HNO_3 0.01 M for the recovery of radioSr.

In particular, for the development as a generator, we research the percentage of the radioSr (^{90}Sr or ^{85}Sr as a γ spike) in the first 8 M HNO_3 eluate: in this fraction the concentration of ^{90}Sr must be smaller than 10^{-5}% (Pharmacopea recommendations for safe administration to humans). For fast QC tool, we analyzed the concentration of ^{90}Y in all the fraction containing "only" radioSr: ^{90}Y must not be in these eluates. After the collection of β^- and γ spectra and analysis of them, we concluded that, at this level, Sr–resin can not give us the results expected, neither as generator, nor as fast QC tool: it is able to separate the 2 radioelements, but not with the expectations demanded by international Pharmacopea or by users of commercial solutions.

References

1. R.B. Firestone, C.M. Baglin, F.S.Y. Chu, *Table of Isotopes*, 8-th Ed., Update on CD-ROM, John Wiley and Sons, New York, USA, 1998.
2. F. Groppi, M.L. Bonardi, *et al.,* Appl. Radiat. Isot., **63** (2005) 621.
3. Special Issue of Radiochimica Acta on Astatine Chemistry, **47** (1989).
4. B. L. Zhuikov, J. Radioanal. Nucl. Chem., **263** (2005) 65
5. A.N. Serafini, J. Nucl. Med., **42** (2001) 895.
6. M. Chinol, D.J. Hnatowich, J. Nucl. Med., **28** (1987) 1465.
7. J. J. M. de Goeij, M. L. Bonardi, J. Radioanal. Nucl. Chem., **263** (2005) 13

This page intentionally left blank

Software Applications

Organizers:

P. Binko
S. Giani

M. Asai	GEANT4 Applications in Space
V. Beckmann	INTEGRAL - Operating High-Energy Detectors for Five Years in Space
A. Bocci	ATLAS Inner Detector Alignment
M.J. Boschini	New generation Data Transfer for AMS02
D. Brogioli	Finite state automa for parallelization of time-expensive operations
S.G. de la Hoz	ATLAS Distributed Analysis Tools
M. Ellis	MICE Software Design and Physics Performance
M. Fahrer	The Control System for the CMS Strip Tracking Detector
I. Fedorko	The Message Reporting System in the ATLAS DAQ System
K.K. Galvào	Management of Equipment Databases at CERN for the ATLAS Experiment
S. Giani	GEANT4 Parametrization and Modeling of Pion Production in Proton-Nucleus Interactions based on HARP Experimental Data: Incident Proton Momenta are from 3 GeV/c to 12.9 GeV/c
K. Hayatsu	Environmental Radiation Dose on the Moon
N. Marinelli	Track Finding in Gamma Conversions in CMS
Z. Marshall	The GEANT4-based ATLAS Fast Electromagnetic Shower Simulation
J. Perl	North American Medical Physics Applications of the GEANT4 Simulation Toolkit
R. Preghenell	Tools to monitor the quality of the ALICE-TOF detector data
C. Rovelli	The detailed simulation of the CMS detector
M. Verducci	ATLAS Conditions Database Experience with the COOL Project
N. Yamashita	Intensity Variation of Gamma Rays due to Water Concentrations on the Lunar Surface

This page intentionally left blank

GEANT4 APPLICATIONS IN SPACE

MAKOTO ASAI
Stanford Linear Accelerator Center, Stanford University
Menlo Park, California 94025, U.S.A.

The use of Geant4 is rapidly expanding in the domain of space applications. I try to give an overview three major application areas of Geant4 in space, which are apparatus simulation for pre-launch design and post-launch analysis, planetary scale simulation for radiation spectra and surface and sub-surface explorations, and micro-dosimetry simulation for single event study and radiation-hardening of semiconductor devices. Recently, not only the mission-dependent applications but also various multi-purpose or common tools built on top of Geant4 are also widely available. I overview some of these tools as well. The Geant4 Collaboration identifies the space applications now-as one of the major driving forces of the further developments and refinements of Geant4 toolkit. Highlights of such developments are given.

1. Apparatus simulation

Apparatus simulation is essential for both pre-launch design studies and post-launch analyses. Geant4 [1,2] is widely and commonly used for various current and future science missions including XMM-Newton [3], GLAST [4], LISA and LISA Pathfinder [5], RHESSI [6], ACE [7], JWST [8], INTEGRAL [9], Bepi Colombo [10], Messenger [11], Herschel [12], Cassini and Huygens [13], Astro-E2 [14], ConeXpress [15], SELENE [16], SWIFT [17] and modules of ISS (International Space Station) including Columbus [18], AMS [19] and MAXI [20]. In the following sections, I will give an overview of how Geant4 is used for some of these missions.

1.1. *GLAST LAT*

GLAST[4] is to be launched in early 2008 and measures the direction, energy and arrival time of celestial gamma rays. The LAT (Large Area Telescope) instrument measures gamma rays in the energy range from about 20 MeV up to greater than 300 GeV. In addition, the GBM (Gamma-ray Burst Monitor) instrument provides correlative observations of transient events in the energy range between 20 KeV and 20 MeV. GEANT4 was adopted since 1999 for the test beam simulations and the balloon flights [21].

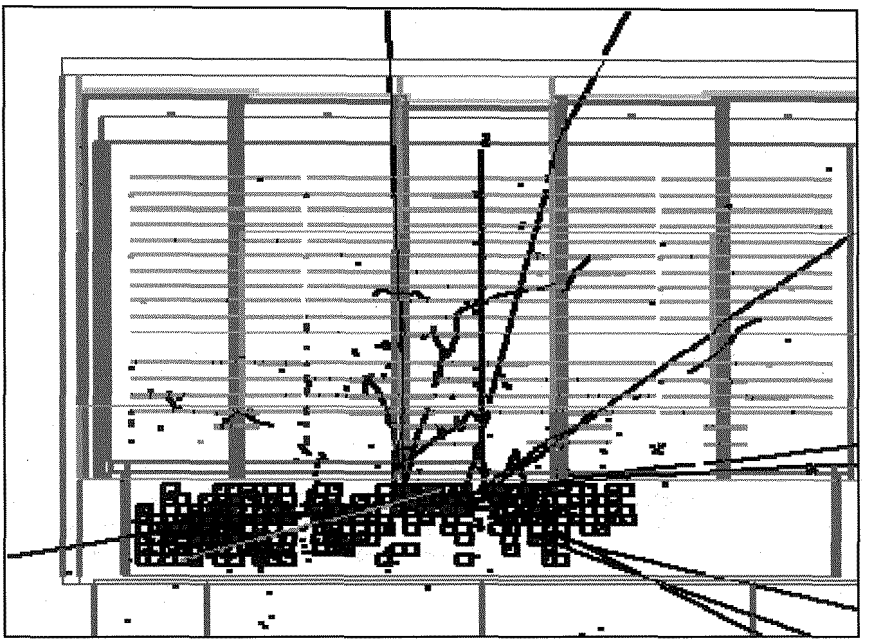

Figure 1. Simulated background hadronic event in GLAST LAT[4]. Courtesy of F. DeBois (SLAC) and F. Longo (INFN/Trieste).

For GLAST mission, simulation of background events is even more important than simulation of signal events. Figure 1 shows a proton incident hadronics event in a CsI crystal calorimeter which causes EM particles leak into the silicon tracker and fakes a signal event. They are now processing 50 billion background events of cosmic proton, neutron and electron and earth albedo backgrounds prior to proceed to the simulation of one full year signal events.

1.2. *Cassini LEMMS*

LEMMS (Low Energy Magnetospheric Measurement System) is on board of the Cassini spacecraft to measure the energy and spatial distribution of energetic particles (electrons and ions separately) in the interplanetary medium and in the magnetosphere of Saturn. LEMMS consists of low energy detector head with collimator, high energy detector head with collimator, and programmable turntable. The measurements of energetic particles are based on the loss of energy in semiconductor detectors. LEMMS has 11 different detectors. These detectors and collimators are modeled in Geant4 and studied as shown in Fig.2 [14].

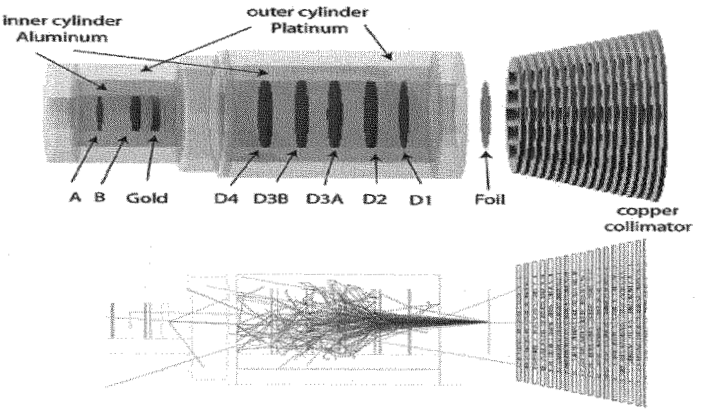

Figure 2. Geant4 geometry model of LEMMS and simulation of a 2 MeV electron pencil beam. Courtesy of D.K. Haggerty (JHUAPL).

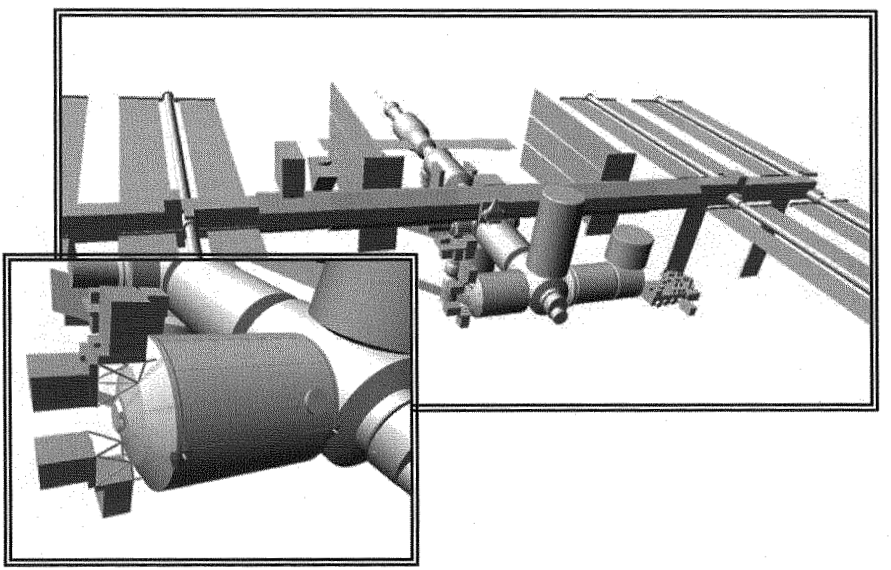

Figure 3. Geant4 geometry model of the International Space Station (up) and the Columbus module (left). Courtesy of T. Ersmark (KTH Stockholm).

1.3. *ISS Columbus*

Full geometry model of ISS (International Space Station) and particularly detailed apparatus structure of the European Columbus module are built to accurately calculate radiation fluxes and doses inflicted to astronauts inside the Columbus module [18]. Incident radiation includes trapped protons, galactic cosmic rays, solar particle events and Earth albedo neutrons.

2. Planetary scale simulation

Planetary scale simulation is essential for both radiation spectra calculation and surface and sub-surface explorations. Full-scale geometrical and magnetosperic structure of a planet is modeled in Geant4 to simulate the trapped solar particles to the Earth [22], Mercury [23], Mars [24] and Jupiter [25]. Geant4 is also used successfully for simulation of even larger scale and at higher energies such as particle accelerations in solar flare [26] and gamma-ray burst [27].

Interactions of solar particles on the (sub-)surface are simulated with Geant4 for mineralogical survey of Mercury by Bepi Colombo mission [28] and for water search of Moon by SELENA mission [29].

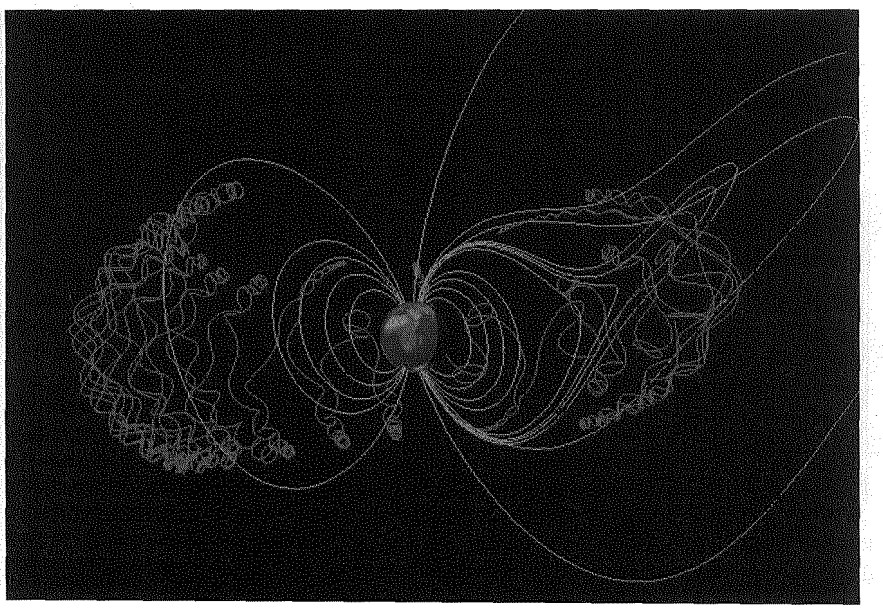

Figure 4. Simulated trajectory of a proton trapped in the Earth magnetosphere. Courtesy of L. Desorgher (U. Bern).

3. Micro-dosimetry simulation

Three sources in natural space environment contribute to various effects on microelectronics. These are solar particles (protons and heavier ions), galactic cosmic rays, and particles trapped in the Earth's radiation belts. Due to these radiations, there are three basic effects that occurs when components are exposed, single event effects (SEEs) [30], total ionization dose and charge deposit [31], and displacement damage [32].

Single event upset (SEU) is one of SEEs. SEU observations recorded by ISS show clear patterns of temporal and spatial dependence. SEUs are mainly due to two ionization cases, direct ionization caused by incident particle and indirect ionization caused by secondary particles generated by the interaction of the primary particle. In all cases, charge collected on a sensitive node of electrical circuit causes unwanted change in the information stored in the circuit. Commercial Technology Computer Aided Design (TCAD) [33] tool alone is unable to predict indirect ionization case. Also, a classical method with CREME96 [34] does not give satisfactory results [35]. Combining Geant4-based Monte-Carlo Radiative Energy Deposition (MRED) tool with TCAD and SPICE, energy partitioning information simulated by MRED is transferred to TCAD to model the electron-hole transportation, and then whole-circuit response to SEU is calculated by SPICE [36]. Similar approach is taken by other applications [37].

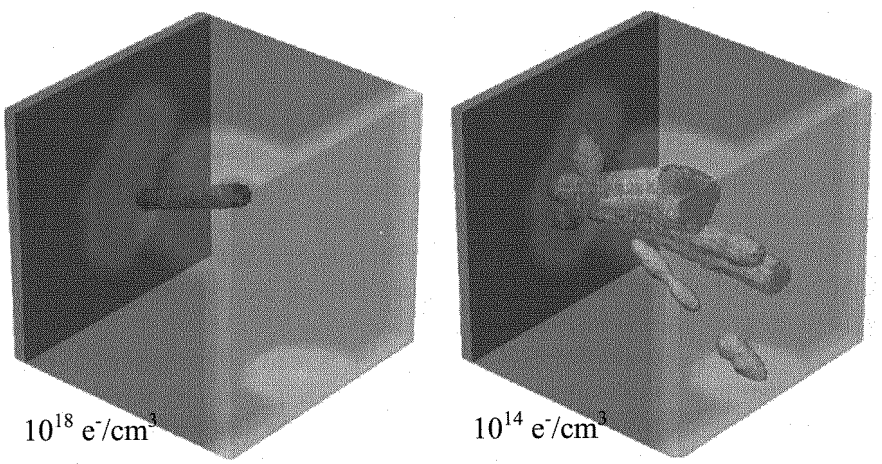

Figure 4. Electron density distribution caused by secondary particles of proton-tungsten interaction simulated by MRED. Courtesy of R. Reed (Vanderbilt Univ.) .

4. General-purpose tools

There are many general / multipurpose tools built on top of Geant4 available for space applications. These include the following tools.

- General Framework
  - GRAS [38]
- Plug-in Physics Model
  - G4LECS [39]
- Sector Shielding Analysis
  - MULASSIS [40]
  - Open Frontier [41]
- Radiation on planets
  - PLANETOCOSMICS [42]
- Dosimetry on semiconductor devices
  - MRED [36]
  - GEMAT [43]
  - FASTRAD [44]

Geant4 offers flexibility and robustness of kernel, powerful capability of geometrical modeling and comprehensive coverage of physics models, which are all essential to these diverse variations of application tools.

5. Recent developments in Geant4 toolkit

The Geant4 Collaboration [45] identifies domain of space applications now as one of the major driving force of the further developments and refinements of Geant4 toolkit. In this section I introduce some of these developments which are driven mainly, if not solely, by the requirements from the space application domain.

5.1. *Tessellated solid*

Tessellated solid is a kind of solid newly supported by Geant4 since 2006. It is a solid consists of arbitrary number of facets. Each facet can be triangular or quadrangular. This solid shape is of particular importance for conversion from CAD system bounded with generic surfaces into an approximate description with facets of defined dimension (Fig. 5).

To import geometrical models from CAD, it is required to convert first the CAD shapes into tessellated surfaces. A way to do this is to save the shapes in the geometrical model as STEP [46] files and convert them using a tool like STViewer [47] to tessellated (faceted surfaces) solids. This strategy allows one

to import any shape with some degree of approximation; the converted CAD models can then be imported through GDML (Geometry Description Markup Language) [48] into Geant4 and be represented as tessellated solid shapes.

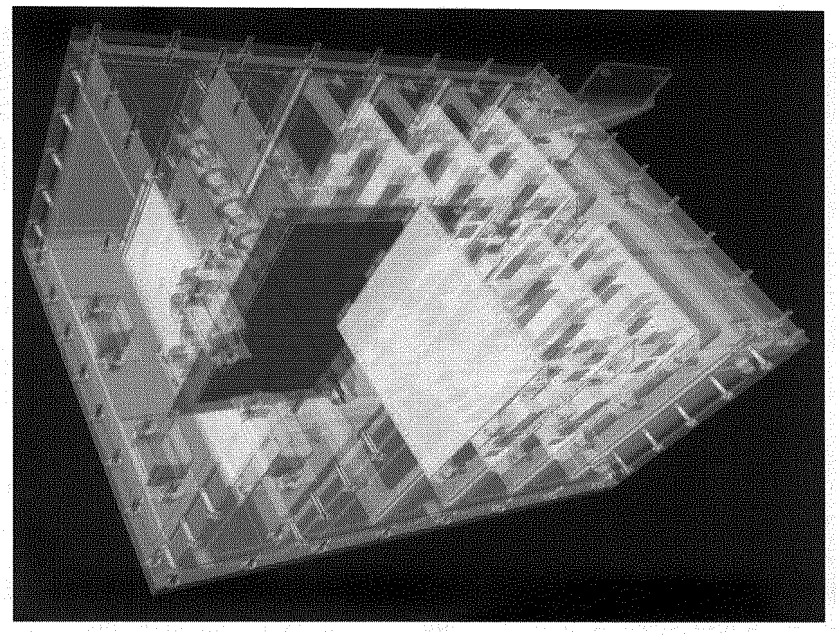

Figure 5. Geometry of a module imported from CAD into Geant4 tessellated solid. Courtesy of G. Cosmo (CERN)

5.2. *Quantum Molecular Dynamics code*

Radiation in space includes considerable amount of heavy nuclides and they are particularly important for simulating dose and also SEEs. Geant4 currently has Binary Light Ion Cascade model [49] and Wilson Abrasion and Ablation model [50], both of which work mainly for relatively light nucleus [51]. By the end of 2007, Geant4 is releasing its new Quantum Molecular Dynamics (QMD) model [52], which firstly works for most nuclides of up to 300 MeV/n (Fig. 6), and it is foreseen to be extended up to several GeV/n.

5.3. *Built-in scoring tools*

For recording detector responses, Geant4 originally offered only the abstract classes with various ready-to-reuse examples. Thus, the user had to implement his/her detector responses. It is a reasonable requirement for a large-scale HEP experiment, but it is a burden for space/medical users who just need to score

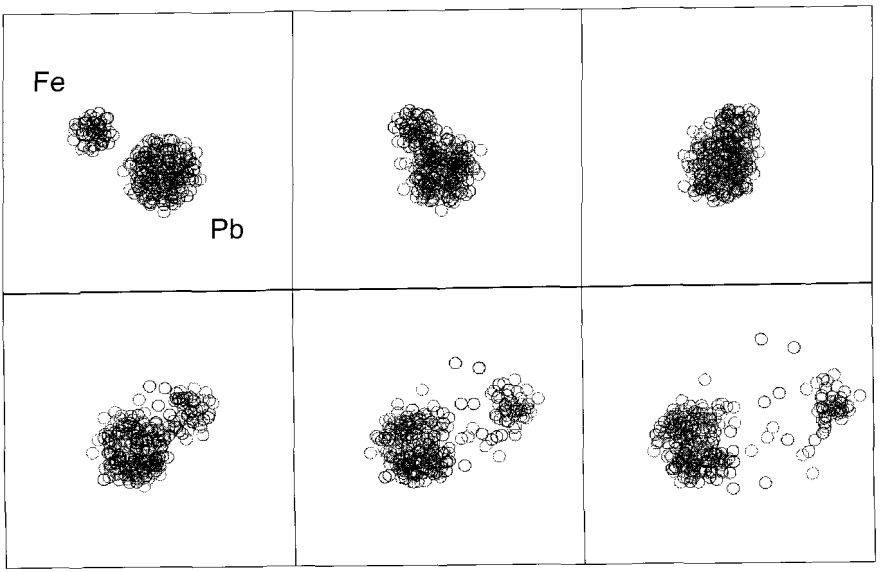

Figure 5. A collision of 290 MeV/n iron onto lead simulated by Geant4 QMD code. A blue circle represents proton and a red circle represents neutron. Courtesy of T. Koi (SLAC)

most common quantities such as dose or flux. By the end of 2005, Geant4 released built-in concrete implementation of scorers for common quantities, which include energy, dose and charge deposition, surface flux and current, and number of secondary generation [53]. It is foreseen that all of such scorers will be defined with simple interactive commands regardless of the geometrical model of actual materials.

6. Conclusions

In 2008, Geant4 will be in 10 years of its public releases. It had been addressing mainly the requirements from HEP experiments, and Geant4 is nowadays well adapted to most of the current and future HEP experiments as their simulation engine [54]. Use of Geant4 is quite rapidly expanding in space application domain. I gave an overview of such Geant4 applications, in particular for apparatus simulation, planetary scale simulation, micro-dosimetry simulation and general-purpose tools for space missions. I have to note here that my overview is quite incomplete, and much richer list of Geant4 applications in the domain of space can be found at the Geant4 Space Users home page [55]. Robust and flexible kernel structure, comprehensive coverage of physics models

and powerful geometrical modeling capability provided by Geant4 were proven to be suitable for mission critical simulations.

References

1. S. Agostinelli *et al., NIM* A506, 250 (2003)
2. J. Allison *et al., IEEE Trans. Nucl. Sci* 53, 270 (2006)
3. R. Nartallo *et al., IEEE Trans. Nucl. Sci* 48, 1815 (2001)
4. L. Baldini *et al., Nucl. Phys. Proc. Suppl.* 150, 62 (2006).
   N. Omodei *et al., AIP Conf. Proc.* 906, 1 (2007)
   R.M. Kippen *et al., AIP Conf. Proc.* 921, 590 (2007)
5. M. Henrique *et al., Astropart. Phys.* 22, 451 (2005)
   H.M. Araujo, *et al., Class. Quantum Grav.* 20, S311 (2003)
6. C. Wigger *et al., Astrophys. J.* 613, 1088 (2004)
7. D.K. Haggerty *et al.,* Advances in Space Research 32, 423 (2003)
8. G. Santin *et al., IEEE Trans. Nucl. Sci* 52, 2294 (2005)
9. C. Ferguson *et al.,* presentation at 4th INTEGRAL workshop (2000).
10. A. Owens *et al.,* presentation at Round Table on 21st Century Monte Carlo Methods for Space Applications, Noordwijk, 2001
11. D.K. Haggerty, presentation at Conference of Solar and Space Physics and the vision for Space Exploration (2005)
12. C. Bongardo, *et al., Exp. Astro.* 21, 67 (2006)
13. D.K. Haggerty *et al.,* Advances in Space Research 33, 2303 (2004)
14. M. Ozaki *et al., IEEE Trans. Nucl. Sci* 53, 1310 (2006)
15. http://space-env.esa.int/ProjectSupport/ConeXpress/ConeXpress.htm
16. O. Okudaira *et al.,* Proceedings of 9th Conference on Astroparticle, Particle and Space Physics, Detectors and Medical Physics Applications, 490 (2005)
17. M. Suzuki *et al., IEEE Nucl. Sci. Symp. Conf. Rec. vol.5,* 3550 (2003)
18. T. Ersmark *et al., IEEE Trans. Nucl. Sci* 51, 1378 (2004)
    T. Ersmark, Ph.D. thesis, ISBN 91-7178-398-9, KTH Stockholm, June 2006
19. M.C. Espirito-Santo *et al., IEEE Trans. Nucl. Sci.* 51, 1373 (2004)
20. H. Tomida *et al., Proc. SPIE vol.*4851, 993 (2003)
21. T.H. Burnett *et al., IEEE Trans. Nucl. Sci* .49, 1898 (2002)
22. L. Desorgher *et al.,* Proceedings of 28th International Cosmic Ray Conference, 4281 (2003)
    F. Lei *et al., IEEE Trans. Nucl. Sci* 51, 3442 (2004)
    M.D. Looper *et al.,* Presentation at 4th Geant4 Space Users' Workshop, (2005)
23. M. Gurtner *et al.,* Advances in Space Research 37, 1759 (2006)
24. A. Keating *et al., IEEE Trans. Nucl. Sci* 52, 2287 (2005)
25. R.F. Elsner *et al.,* Icarus 178, 417 (2005)

26. J. Kotoku *et al,* e-Print: arXiv:0708.0057 (2007)
27. K. Murase and S. Nagataki, *Phys. Rev.* D73:063002 (2006)
28. A. Mantero *et al., IEEE Nucl. Sci. Symp. Conf. Rec. vol.3,* 1527 (2003)
29. K. Hayatsu *et al.,* Presentation at 10th Conference on Astroparticle, Particle and Space Physics, Detectors and Medical Physics Applications (2007) N. Yamashita *et al.,* Presentation at 10th Conference on Astroparticle, Particle and Space Physics, Detectors and Medical Physics Applications (2007)
30. P.E. Dodd *et al., IEEE Trans. Nucl. Sci* 50, 583 (2003)
31. T.R. Oldham and F.B. McLean *et al., IEEE Trans. Nucl. Sci* 50, 483 (2003)
32. J.R. Srouor *et al., IEEE Trans. Nucl. Sci* 50, 653 (2003)
33. http://www.synopsys.com/products/tcad/tcad.html
34. A.J. Tylka *et al., IEEE Trans. Nucl. Sci* 43, 2758 (1996)
35. R.A. Reed *et al., IEEE Trans. Nucl. Sci* 50, 622 (2003)
36. K.M. Warren *et al., IEEE Trans. Nucl. Sci* 53, 2125 (2005) A.S. Kobayashi *et al., IEEE Trans. Nucl. Sci* 53, 2189 (2003)
37. I. Jun *et al,* JPL R&TD Annual Report 06-128, Pasadena, CA (2006)
38. G. Santin *et. al., IEEE Trans. Nucl. Sci* 52, 2294 (2005)
39. R.M. Kippen, New Astronomy Reviews 48, 221 (2004)
40. F. Lei *et al., IEEE Trans. Nucl. Sci* 49, 2788 (2002)
41. H. Sdunnus *et al.,* Presentation at 20th European Workshop on Thermal and ECLS Software (2006)
42. http://cosray.unibe.ch/~laurent/planetocosmics/
43. G. Santin *et al.,* Nuclear Physics B – Proceedings Supplements vol.125, 69 (2003)
44. T. Beutier *et al.,* Proceedings of 7th European Conference on Radiation and its Effects on Components and System, 181 (2004)
45. http://cern.ch/geant4/
46. http://www.tc184-sc4.org/SC4_Open/SC4_Standards_Developers_Info/ Files/ STEP_application_handbook_63006.pdf
47. http://www.steptools.com/products/stviewer/
48. R. Chytracek *et al., IEEE Trans. Nucl. Sci* 53, 2892 (2006)
49. G. Folger *et al., Eur. Phys. J.* A21, 407 (2004)
50. P. Truscott *et al.,* Proceedings of Monte Carlo 2005 Topical Meeting ISBN:0-89448-695-0 (2005)
51. T. Koi *et al.,* Proceedings of Monte Carlo 2005 Topical Meeting ISBN: 0-89448-695-0 (2005)
52. J.Z.H. Zhang, ISBN 981-02-3388-4, (1998)
53. T. Aso *et al., IEEE Nucl. Sci. Symp. Conf. Rec. vol.2,* 978 (2005)
54. http://geant4.web.cern.ch/geant4/collaboration/Geant4-Review2007.html
55. http://geant4.esa.int/

INTEGRAL - OPERATING HIGH-ENERGY DETECTORS FOR FIVE YEARS IN SPACE

V. BECKMANN* on behalf of the INTEGRAL collaboration

INTEGRAL Science Data Centre, Ch. d'Ecogia 16,
1290 Versoix, Switzerland
**E-mail: Volker.Beckmann@obs.unige.ch*
http://isdc.unige.ch/~beckmann

The *INTEGRAL* satellite, which studies the Universe in the hard X-ray and soft Gamma-ray domain, has been operational for 5 years now. The X-ray telescopes, which use the coded mask technique, provide unprecedented spectral and imaging resolution. This led to a number of discoveries, such as the distribution of diffuse emission in the Galaxy, the discovery of highly absorbed sources in the Galactic Plane, localization of $\sim$ 50 Gamma-ray bursts, and the resolution of the cosmic X-ray background around its peak at 30 keV. About 300 previously known X-ray sources have been detected and in addition more than 200 new sources have been discovered. *INTEGRAL* provides spectra starting at 3 keV and ranging up to several hundred keV. This article gives a brief overview about the major discoveries of *INTEGRAL*.

Keywords: Astrophysics; Gamma-rays; X-rays.

1. The INTEGRAL Mission

ESA's *INTEGRAL* space mission [1] hosts two major hard X-ray instruments, IBIS and SPI, both coded-mask telescopes. IBIS [2] provides imaging resolution of 12 arcmin, while SPI [3] is optimized for spectroscopy. Both instruments operate at energies from 15 keV up to several MeV. Co-aligned with these main instruments are the two X-ray monitors JEM-X [4], which provides spectra and images in the 3–30 keV band, and the optical camera OMC [5], which provides photometry in the V filter. *INTEGRAL* was launched on October 17, 2002 from Baikonur into a highly eccentric orbit with a perigee of 9,000 km and an apogee of 150,000 km, which avoids as much as possible the Earth's radiation belt and allows for un-interrupted observations of up to 3 days [6].

2. Data processing for INTEGRAL and the ISDC

Data from the *INTEGRAL* mission is made available to the community via the *INTEGRAL Science Data Centre* (ISDC [7]). The telemetry of the satellite is sent in a constant data flow of $\sim 90\,\mathrm{kbit\,s^{-1}}$ to the Mission Operations Center. From there the data are then sent to the ISDC. Incoming data are searched for transient sources and Gamma-Ray bursts within a few seconds after arrival by the *INTEGRAL Burst Alert System* (IBAS [8]). The telemetry data are pre-processed, which means that they are decoded and data are stored into a fits file data structure. Afterwards the data are analysed by a scientist on duty in order to look for scientifically interesting events, such as the occurance of new sources, and to inform the astrophysical community. The data are then archived together with standard analysis results and distributed to the scientific community. In addition, the ISDC provides scientific analysis software to the community, in collaboration with the instrument teams. The software, documentation and *INTEGRAL*'s data are available through the ISDC web-page[a].

3. Scientific Highlights

Within the first five years of the mission *INTEGRAL* related research led to several hundreds of scientific publications. Below I will present a few of them, focussing on most recent discoveries. This list is obviously incomplete and biased, and I refer the reader to the list of *INTEGRAL* related publications maintained at ESA/ISOC[b].

3.1. *The Galactic Centre*

Using ISGRI [9], the soft γ-ray detector of IBIS, it was for the first time possible to resolved the Galactic Centre above 20 keV. A new source, IGR J1745.6–2901, was found to be the hard X-ray counter part of Sgr A*, which appears to be a faint but persistent source at this energy with a spectrum which apparently originates from a two temperature plasma with $kT \simeq 1.0\,\mathrm{keV}$ and $kT \simeq 6.6\,\mathrm{keV}$ [10]. The source seen by *INTEGRAL* is also detected at TeV energies by HESS [11]. ISGRI also detected another new source close by, which has been accociated with the giant molecular cloud Sgr B2 [12]. This cloud might reflect the emission of Sgr A* in the

[a]The ISDC web page is located at http://isdc.unige.ch/
[b]http://www.sciops.esa.int/index.php?project=INTEGRAL

X-rays and therefore function as a "Compton mirror" [13]. If this hypothesis is true, the emission of the central black hole of our Galaxy was much higher about 300 – 400 years ago than it appears today.

3.2. *Compact Objects*

Galactic compact objects are the brightest persistent sources seen by *INTEGRAL*. Therefore during the first five years of the mission, the majority of observing time was used to cover the Galactic Centre and the Galactic Plane, revealing not only a large number of new sources, but also allowing for the first time to monitor in detail the spectral evolution of known hard X-ray sources. Within the class of black hole candidates especially Cygnus X-1 led to many new results, such as the detection of a hard tail in the spectrum in excess of the thermal Comptonization [14], and the complex nature of the physical processes involved in state transitions [15,16]. In the case of GRO J1655–40, the interpretation of a bright burst observed in 2005 is still ongoing, as some studies find evidence for a spectral cut-off at high energies [17], whereas others find an undisturbed power law up to several hundreds of keV [18,19]. In addition the number of black hole candidates with well studied spectra increased significantly with *INTEGRAL*. This includes the cases of XTE J1550–564 where an underluminous outburst was observed [20], XTE J1817–330, in which the ISGRI data indicate a thermal accretion disk and a comptonizing hot corona [21], 4U 1630-47 shows a variety of high-amplitude variability occuring at the highest disk luminosities [22], and also newly discovered black hole candidates like IGR J17464–3213 [23].

Extending the spectra into the soft γ-ray range, *INTEGRAL* shows that many low mass X-ray binaries (LMXB) indeed have variable "hard tails" [24], which most likely originate in the Compton cloud located inside the neutron star's magnetosphere [25]. Concerning the pulsars, the enigmatic rotating neutron stars, cyclotron lines can now be measured in greater detail, e.g. in A 0535+26 [26], or in the anomalous X-ray Pulsar 4U 0142+614, which shows a complex spectrum and timing behaviour in the hard X-rays [27]. The anomalous X-ray pulsars show very hard and pulsed X-ray emission, which indicates that these sources are indeed magnetars [28]. The observation of the outburst of the pulsar V0332+53 [29] has led to the discovery that the brightness decline is accompagnied by a change in the extent of the cyclotron scattering region [30], gave detailed insight into its orbital parameters [31] and geometry [32], and revealed that the energies at which the cyclotron lines appear change linearly with

the source luminosity [33]. Several pulsars have been shown to be accretion powered, such as the newly discovered pulsars IGR J00370+6122 [34] and IGR J18483-0311 [35], and 4U 1954+319 turned out to be a symbiotic LMXB with the slowest wind-accreting X-ray pulsar ever observed [36]. On the other hand, *INTEGRAL* also discovered the fastest millisecond pulsar ever known, the new source IGR J00291+5934 [37]. The accreting Be/X-ray pulsar SAX J2103.5+4545 has been a puzzling object, as it was seen exhibiting hard/high and soft/low states [38] and large spin-up rate [39,40].

Microquasars have been also studied in great detail. GX 339–4 displays a variable high energy cut-off which might suggest that the low- and high-energy components in this source have a different origin [41]. The X-ray binary LSI +61 303 also seems to host a microquasar, but does not reveal the presence of a cut-off, and the observed spectrum and spectral variability can be explained if the compact object in the system is a rotation powered pulsar [42]. LS 5039, the only persistently detected X-ray binary at TeV energies, has been detected by IBIS/ISGRI and the data hint to a break in the spectral behaviour at hard X-rays [43]. For GRS 1915+105 new variability patterns have been discovered [44], whereas the case of Cyg X-3 and whether or not it hosts a microquasar remains a question of debate [45,46].

3.3. *New Sources found by INTEGRAL*

Since the launch of the mission, *INTEGRAL* has discovered more than 200 previously unknown hard X-ray sources[c]. As most of the new sources were discovered along the Galactic Plane, optical identification of the counter part is often difficult. Several projects aim at this problem, for example by comparing the *INTEGRAL* sources with photometric catalogues [47] or with the ROSAT catalogues [48], by optical spectroscopy (e.g. [49,50]), or by simultaneous multi-telescope follow-up observations (e.g. [51]). Despite these efforts, more than 50% of the new discoveries remain unclassified. Among the Galactic sources, *INTEGRAL* discovered a number of highly absorbed high mass X-ray binaries (HMXB), in which the binary system is obscured by the strong stellar wind originating from the massive donor star [51–53]. Another study suggests that the obscured sources may be microquasars like SS 433, but with slightly lower mass transfer rate [54]. The majority of the new sources seems to be distributed in the Galactic Plane

[c]See the webpage listing the new sources discovered by *INTEGRAL* under http://isdc.unige.ch/~rodrigue/html/igrsources.html

rather like the LMXB than the HMXB population [55]. The extended mission of *INTEGRAL* allows now also to detect fainter sources, like the magnetic CV IGR J00234+6141 of the intermediate polar type. The discovery of this type of object confirms earlier conclusions that intermediate polars contribute significantly to the population of galactic X-ray sources and represent a significant fraction of the high energy background [56]. Lately it has also been shown that several unidentified sources detected in the TeV range are counterparts of *INTEGRAL* sources [57,58]. While for point-like and variable TeV sources the correspondence with the *INTEGRAL* sources is almost sure, we seem to observe different acceleration sites in the case of extended sources like supernova remnants and pulsar wind nebula [59].

In the extragalactic sky *INTEGRAL* detected more than 160 AGN, mainly Seyfert galaxies, of which many were not known to be hard X-ray emitters [55].

3.4. *Active Galactic Nuclei and the CXB*

With the wide spectral coverage, *INTEGRAL* was used to study in detail several bright AGN. The AGN detected by IBIS/ISGRI above 20 keV are on average low luminous and near-by ($\bar{z} = 0.02$) Seyfert galaxies [60–62]. In the hard X-rays the absorption by Galactic hydrogen does not affect the spectra, thus *INTEGRAL* can observe AGN shining through the Galactic Plane [63,64]. In most of the AGN it appears that the spectral turn-over from a simple power law is located at energies $\gg 100\,\mathrm{keV}$, as shown in the Seyfert 2 galaxy NGC 4388 in which the absorbing material is probably far from the central engine [65], NGC 4151 [66], NGC 2992, the most variable Seyfert of the bright AGN seen by *INTEGRAL* [67], Cen A [68], and in a spectral study of 72 AGN combining data from all three X-ray instruments on board the satellite [60]. The objects with sufficient sufficient signal-to-noise show though signatures of Compton reflection [66,69], but only a dozend AGN have been detected by IBIS/ISGRI above 100 keV so far [70]. Only about 10 blazars have been detected and studied so far, such as S 0716+714 [71], 3C 454.3 [72], which both were observed after an outburst. The lowest redshift quasar 3C 273 shows a historic minimum in its X-ray emission [73,74], which allows to study the spectral features usually hidden by the strong jet emission [75], and lately the farthest object seen so far by *INTEGRAL* has been detected: IGR J22517+2218 which is spatially coincident with MG3 J225155+2217, a quasar at $z = 3.668$ [76].

Related to the compilation of AGN surveys in the hard X-rays is the question of what sources form the cosmic X-ray background (CXB) which

peaks at an energy of about 30 keV. An early study seemed to indicate that a large fraction of low luminous AGN contributes to the CXB [77], but apparently these source detections were spurious and could not be confirmed by later studies. Number counts of AGN and the construction of the X-ray luminosity function remains one of the major aspects of current *INTEGRAL* related AGN research. The first luminosity function derived in this energy range indicated that the *INTEGRAL* detected AGN cannot explain the CXB without evolution of the AGN population [78], and a recent study indicates that the CXB can be explained when considering luminosity dependend density evolution [62]. On the contrary, a study on the *XMM*-LSS field came to the conclusion that an evolution in absorption (towards stronger absorbed sources at higher redshifts) has to be assumed in order to connect the CXB to INTEGRAL detected AGN [79]. In all these studies it has to be taken into account that the exact strength of the CXB is still under debate. *INTEGRAL* measurements of the CXB through Earth-occultation technique seem to indicate that the actual flux is higher by $\sim 20\%$ when compared to earlier HEAO-1 measurements [80].

3.5. *Gamma-Ray Bursts and the IBAS system*

The *INTEGRAL* Burst Alert System (IBAS [8]) monitors the incoming data for events in the Anti-Coincidence System (ACS [81]) of the spectrometer SPI and in the field of view of IBIS. For the latter events which have the signature of a Gamma-Ray Burst (GRB), the coordinates are determined automatically with high precision (usually $\sim$ 2 arcmin uncertainty) and distributed within $\sim$ 20 seconds to the astronomical community. As of October 2007, *INTEGRAL* has detected 47 GRB in the field of view[d]. Among those GRB, only one event is a so-called short burst [82,83]. Because of the high sensitivity of IBIS/ISGRI, even faint GRBs are detected and thus *INTEGRAL* was able to see the sub-energetic GRB 031203, the closest to Earth determined so far [84,85]. Thanks to IBAS, *INTEGRAL* was the first satellite in 2004 to report the giant flare from the soft gamma-ray repeater SGR 1806-20 [86]. The bright flare of this magnetar, i.e. a strongly magnetized neutron star, can be explained by magnetic reconnection caused by crust breaking of the neutron star's surface [87].

The GRB detected by the SPI-ACS are also made public immediately through the web[e]. Although no localization is available for these bursts, the

[d] see http://ibas.iasf-milano.inaf.it
[e] For all alerts from the IBAS system see http://isdc.unige.ch/index.cgi?Soft+ibas

ACS provides 50 ms lightcurves for on average one burst every 3 days [88].

3.6. *Diffuse Galactic Emission*

The Ge detectors of the SPI spectrometer [3] provides a resolution of about 2.5 keV at 1.3 MeV. This is sufficient to resolve Gamma-Ray lines of the Galactic diffuse emission. A prominent line is the 511 keV annihilation line of cosmic positrons. SPI measurements demonstrate that the positrons mainly annihilate with free electrons and that the medium must be at least partially ionized [89]. Another finding is that most of the emission seems to arise from the Galactic bulge and not from the Galactic disk [90], which led to speculations that the source of the diffuse emission is the Galactic black hole Sgr A* [91] or that it might origin from electroweak scale WIMPs [92], from WIMP candidates with an "excited state" [93], or from pulsar winds [94]. Another bright Gamma-ray line at 1808.65 keV arises from the decay of radioactive ^{26}Al. Analysis of SPI data led to the finding that ^{26}Al source regions corotate with the Galaxy, supporting its Galaxy-wide origin and revealing a core collapse supernovae rate of 1.9 ± 1.1 per century in our Galaxy [95]. Other gamma-ray lines which have been observed from nucleosynthesis sites include ^{44}Ti [96] and ^{60}Fe [97]. Gamma-ray lines from point sources, as they were reported from previous Gamma-ray missions with less sensitivity, have so far not been detected and also no "unexpected" lines have been found [98].

Another mystery solved by *INTEGRAL* is the origin of the Galactic background emission at 20–60 keV, which has been demonstrated to arise from compact sources [99], whereas the Galactic ridge emission at soft γ-rays (200 keV – 1 MeV) has been shown to be indeed a diffuse or unresolved emission component which might be caused by in-situ electron acceleration or by an unresolved population of weak sources with hard X-ray spectra [100].

4. Outlook

All instruments of the *INTEGRAL* mission are in good health. The recent results have shown that many science projects are only possible through the very deep exposures, available after several years of observation. Not only will the study of the diffuse emission benefit from an on-going *INTEGRAL* project, as it will reveal the true distribution of the positrons, ^{26}Al, ^{60}Fe and other elements resulting from nucleosynthesis in the Galaxy. Especially for source population studies, like for X-ray binaries like LMXB,

HMXB, and CVs, and of course for AGN, the continuous observation of the sky with high spectral and spatial resolution above 20 keV will be crucial. Concerning the AGN the question what causes the CXB will be answered, and the true physics in the central engine of Seyfert galaxies and what role Compton reflection plays in there, will be revealed. For Galactic sources the observations of the X-ray binary population will help us to understand the formation of accretion disks around black holes, and their contribution to the Galactic Ridge emission. This will help to disentangle the source mix apparent in our Galaxy. Finally, obscured sources, both Galactic and extragalactic will be discovered, helping us to peer through the obscuring material into the true nature of the most violent physical processes.

Acknowledgments

INTEGRAL is an ESA project funded by ESA member states (especially the PI countries: Denmark, France, Germany, Italy, Spain, Switzerland), Czech Republic and Poland, and with the participation of Russia and the USA.

References

1. Winkler, C., Courvoisier, T. J.-L., Di Cocco, G., *et al.* 2003, A&A, 411, L1
2. Ubertini, P., Lebrun, F., Di Cocco, G., *et al.* 2003, A&A, 411, L131
3. Vedrenne, G., Roques, J.-P., Schönfelder, V., *et al.* 2003, A&A, 411, L63
4. Lund, N., Budtz-Jørgensen, C., Westergaard, N., *et al.* 2003, A&A, 411, L231
5. Mas-Hesse, J. M., Giménez, A., Culhane, J. L., *et al.* 2003, A&A, 411, L261
6. Eismont, N. A., Ditrikh, A. V., Janin, G., *et al.* 2003, A&A, 411, L37
7. Courvoisier, T.J.-L., Walter, R., Beckmann, V., et al. 2003, A&A, 411, L53
8. Mereghetti, S., Götz, D., Borkowski, J., *et al.* 2003 A&A, 411, L291
9. Lebrun, F., Leray, J. P., Lavocat, P., *et al.* 2003, A&A, 411, L141
10. Bélanger, G., Goldwurm, A., Renaud, M., et al. 2006, ApJ, 636, 275
11. Aharonian, F., Akhperjanian, A. G., Aye, K.-M., *et al.* 2004, A&A, 425, L13
12. Revnivtsev, M. E., Churazov, E., Sazonov, S. Y., *et al.* 2004, A&A, 425, L49
13. Hinton, J. A., & Aharonian, F. A. 2007, ApJ, 657, 302
14. Cadolle Bel, M., Sizun, P., Goldwurm, A., *et al.*, 2006, A&A 446, 591
15. Fritz, S., Wilms, J., *et al.* 2007, A&A accepted, astro-ph/0706.2137
16. Malzac, J., Petrucci, P.O., Jourdain, E., *et al.* 2006, A&A 448, 1125
17. Shaposhnikov, N., Swank, J., Shrader, C. R., *et al.*, 2007, ApJ, 655, 434
18. Caballero-García, M. D., Miller, J.M., Kuulkers, E., *et al.* 2007, ApJ accepted, astro-ph/0706.1302
19. Díaz Trigo, M., Parmar, A.N., Miller, J., *et al.* 2007, A&A, 462, 657
20. Sturner, S.J., & Shrader, C.R., 2005, ApJ, 625, 923
21. Sala, G., Greiner, J., Ajello, M., *et al.* 2007, A&A, 473, 561
22. Tomsick, J.A., Corbel, S., Goldwurm, A., & Kaaret, P. 2005, ApJ, 630, 413

23. Capitanio, F., Ubertini, P., Bazzano, A., *et al.* 2005, ApJ, 622, 503
24. Farinelli, R., Titarchuk, L., & Frontera, F. 2007, ApJ, 662, 1167
25. Paizis, A., Farinelli, R., Titarchuk, L., *et al.* 2006, A&A, 459, 187
26. Caballero, I., Kretschmar, P., Santangelo, A. et al. 2007, A&A 465, L21
27. Rea, N., Nichelli, E., *et al.*, 2007, MNRAS accepted, astro-ph/0707.3363
28. Kuiper, L., Hermsen, W., den Hartog, P., Collmar, W. 2006, ApJ, 645, 556
29. Kreykenbohm, I., Mowlavi, N., Produit, N., et al. 2005, A&A, 433, L45
30. Mowlavi, N., Kreykenbohm, I., Shaw, S. E., *et al.* 2006, A&A, 451, 187
31. Zhang, S., Qu, J.-L., Song, L.-M., & Torres, D.F. 2005, ApJ, 630, L65
32. Schönherr, G., Wilms, J., Kretschmar, P., et al. 2007, A&A 472, 353
33. Tsygankov, S. S., Lutovinov, A., Churazov, E., *et al.* 2006, MNRAS, 371, 19
34. in 't Zand, J.J.M., Kuiper, L., den Hartog, P.R., *et al.* 2007, A&A 469, 1063
35. Sguera, V., Bazzano, A., Bird, A.J., *et al.* 2007, A&A 467, 249
36. Mattana, F., Götz, D., Falanga, M., *et al.* 2006, A&A, 460, L1
37. Shaw, S., Mowlavi, N., Rodriguez, J., *et al.* 2005, A&A, 432, L13
38. Camero Arranz, A., Wilson, C. A., Finger, M. H., *et al.* 2007, A&A, 473, 551
39. Sidoli, L., Mereghetti, S., Larsson, S., *et al.* 2005, A&A, 440, 1033
40. Blay, P., Reig, P., Martinez Nunez, S., *et al.* 2004, A&A, 427, 293
41. Joinet, A., Jourdain, E., Malzac, J., *et al.* 2007, ApJ, 657, 400
42. Chernyakova, M., Neronov, A., Walter, R., et al. 2006, MNRAS, 372, 1585
43. Goldoni, P., Ribó, M., di Salvo, T., *et al.* 2007, Ap&SS, 309, 293
44. Hannikainen, D.C., Rodriguez, J., Vilhu, O., *et al.* 2005, A&A 435, 995
45. Beckmann, V., Soldi, S., *et al.* 2007, A&A accepted, astro-ph/0708.0473
46. Hjalmarsdotter, L., *et al.* 2007, MNRAS submitted, astro-ph/0707.2032
47. Negueruela, I., & Schurch, M.P.E. 2007, A&A, 461, 631
48. Stephen, J.B., Bassani, L., Malizia, A., *et al.* 2006, A&A, 445, 869
49. Masetti, N., Morelli, L., Palazzi, E., et al. 2006, A&A, 459, 21
50. Masetti, N., Pretorius, M.L., Palazzi, E., et al. 2006, A&A 449, 1139
51. Beckmann, V., Kennea, J.A., Markwardt, C., et al. 2005, ApJ, 631, 506
52. Walter, R., Zurita Heras, J., Bassani, L., et al. 2006, A&A, 453, 133
53. Leyder, J.-C., Walter, R., Lazos, M., *et al.* 2007, A&A, 465, L35
54. Begelman, M. C., King, A. R., & Pringle, J. E. 2006, MNRAS, 370, 399
55. Bodaghee, A., Courvoisier, T.J.-L., Rodriguez, J., *et al.* 2007, A&A, 467, 585
56. Bonnet-Bidaud, J. M., de Martino, D., *et al.* 2007, A&A, 473, 185
57. Ubertini, P., Bassani, L., Malizia, A., *et al.* 2005, ApJ, 629, L109
58. Malizia, A., Bassani, L., Stephen, J.B., *et al.* 2005, ApJ, 630, L157
59. Walter, R. 2007, Ap&SS, 309, 5
60. Beckmann, V., Gehrels, N., Shrader, C. R., Soldi, S. 2006, ApJ, 638, 642
61. Bassani, L., Molina, M., Malizia, A., et al. 2006, ApJ, 636, L65
62. Sazonov, S., Revnivtsev, M., Krivonos, R., et al. 2007, A&A, 462, 57
63. Soldi, S., Beckmann, V., Bassani, L., *et al.* 2005, A&A, 444, 431
64. Molina, M., Malizia, A., Bassani, L., *et al.* 2006, MNRAS, 371, 821
65. Beckmann, V., Gehrels, N., Favre, P., *et al.* 2004, ApJ, 614, 641
66. Beckmann, V., Shrader, C. R., Gehrels, N., et al. 2005, ApJ, 634, 939
67. Beckmann, V., Gehrels, N., Tueller, J. 2007, ApJ, 666, 122
68. Rothschild, R. E., Wilms, J., Tomsick, J., *et al.* 2006, ApJ, 641, 801

69. Molina, M., Giroletti, M., *et al.* 2007, MNRAS accepted, astro-ph/0709.1895
70. Bazzano, A., Stephen, J. B., Fiocchi, M., *et al.* 2006, ApJ, 649, L9
71. Foschini, L., Tagliaferri, G., Pian, E., *et al.* 2006, A&A, 455, 871
72. Pian, E., Foschini, L., Beckmann, V., *et al.* 2006, A&A, 449, L21
73. Courvoisier, T., Beckmann, V., Bourban, G., *et al.* 2003, A&A, 411, L343
74. Chernyakova, M., Neronov, A., Courvoisier, T., *et al.* 2007, A&A, 465, 147
75. Türler, M., Chernyakova, M., Courvoisier, T.J.-L., *et al.* 2006, A&A, 451, L1
76. Bassani, L., Landi, R., *et al.* 2007, ApJL accepted, astro-ph/0709.3023
77. Krivonos, R., Vikhlinin, A., Churazov, E., *et al.* 2005, ApJ, 625, 89
78. Beckmann, V., Soldi, S., Shrader, C. R., *et al.* 2006, ApJ, 652, 126
79. Treister, E., Virani, S., Urry, C.M., *et al.* 2007, A&A submitted
80. Churazov, E., Sunyaev, R. A., Revnivtsev, M., *et al.* 2007, A&A, 467, 529
81. von Kienlin, A., Beckmann, V., Rau, A., *et al.* 2003, A&A, 411, L299
82. Beckmann, V., Ricci, C., Beck, M., *et al.* 2007, GRB Circular Network, 6605
83. Götz, D., Beckmann, V., Mereghetti, S., *et al.* 2007, GCN, 6607
84. Sazonov, S. Yu., Lutovinov, A. A., Sunyaev, R. A. 2004, Nature, 430, 646
85. Soderberg, A. M., Kulkarni, S. R., Berger, E., *et al.* 2004, Nature, 430, 648
86. Mereghetti, S., Götz, D., von Kienlin, A., *et al.* 2005, ApJ, 624, L105
87. Hurley, K., Boggs, S.E., Smith, D. M., *et al.* 2005, Nature, 434, 1098
88. Rau, A., von Kienlin, A., Hurley, K., & Lichti, G.G., 2005, A&A, 438, 1175
89. Jean, P., Knödlseder, J., Gillard, W., *et al.* 2006, A&A, 445, 579
90. Weidenspointner, G., *et al.* 2007, proc. of the 6th INTEGRAL Workshop "The Obscured Universe" (3-7 July 2006, Moscow), astro-ph/0702621
91. Cheng, K.S., Chernyshov, D.O., Dogiel, V. A., *et al.* 2007, A&A, 473, 351
92. Pospelov, M., & Ritz, A. 2007, PhLB, 651, 208
93. Finkbeiner, D. P., & Weiner, N. 2007, Phys. Rev. D submitted, astro-ph/0702587
94. Wang, W., Pun, C. S. J., & Chenk, K. S. 2006, A&A, 446, 943
95. Diehl, R., Halloin, H., Kretschmer, K. *et al.* 2006, Nature 439, 45
96. Renaud, M., Vink, J., Decourchelle, A., *et al.* 2006, ApJ, 647, L41
97. Wang, W., Harris, M. J., Diehl, R., *et al.* 2007, A&A 469, 1005
98. Teegarden, B.J. & Watanabe, K. 2006, ApJ, 646, 965
99. Lebrun, F., Terrier, R., Bazzano, A., *et al.* 2004, Nature, 428, 293
100. Knödlseder, J., Lonjou, V., Weidenspointner, G., *et al.* 2007, AIPC 921, 130

ATLAS INNER DETECTOR ALIGNMENT

A. BOCCI

Duke University,
Durham, NC, USA
**E-mail: bocci@fnal.gov*

on behalf of the ATLAS Collaboration

The ATLAS experiment is a multi-purpose particle detector that will study high-energy particle collisions produced by the Large Hadron Collider at CERN. In order to achieve its physics goals, the ATLAS tracking requires that the positions of the silicon detector elements have to be known to a precision better than 10 μm. Several track-based alignment algorithms have been developed for the Inner Detector. An extensive validation has been performed with simulated events and real data coming from the ATLAS. Results from such validation are reported in this paper.

Keywords: Style file; LaTeX; Proceedings; World Scientific Publishing.

1. The ATLAS Inner Detector

The ATLAS detector[1] is a general-purpose experiment actually being assembled at CERN for the Large Hadron Collider (LHC). The LHC will provide proton-proton collisions with a center-of-mass energy of nearly 14 TeV, a frequency of 40 MHz and a nominal luminosity of 10^{34} cm^{-2}s^{-1}. Particle reactions at the design luminosity produce up to 1500 charged tracks per event. These tracks originate from several primary interactions within one bunch crossing. The reconstruction of charged tracks and the identification primary and secondary vertices is performed by the inner detector of the ATLAS experiment. The ATLAS Inner Detector[2] is composed of three complementary technologies designed to have an optimum performance of track reconstruction in the high-multiplicity high-frequency LHC (Large Hadron Collider) environment: a silicon pixel detector closest to the interaction point, followed by a silicon microstrip detector, and the outermost straw-tube tracker, surrounded by a superconducting solenoid providing a 2 T axial field. The Pixel detector consists in a barrel region with three

cylindrical layers and two symmetric end-caps each containing three disks for tracking in the forward region. All pixel modules are identical, with a sensor segmented in 50 μm $\times$ 400 μm pixels providing a 2D readout with a binary resolution of 14 μm $\times$ 115 μm in the azimuth ($r\phi$) and transverse planes (z) respectively. The SCT is made of four layers in the barrel region and nine disks in each of the two end- caps. SCT modules are composed by two pairs of single-sided silicon microstrip detectors glued back-to-back with a relative stereo angle of 40 mrad. The strip pitch is 80 μm for the barrels and varying from $\sim$ 55 μm to $\sim$ 90 μm for end-cap modules. The resolution in the direction perpendicular to the strips is $\sim$23 μm. The Transition Radiation Tracker (TRT) consists of approximately $\sim 3 \times 10^5$ straw tubes arranged in three barrel layers and 14 end-cap wheels on each side. A resolution of 140 μm is provided by a 30 μm thick gold-plated tungsten wire at the center of each straw of 2 mm radius. However, the initial position of these modules is only known to a scale of 100 μm, which makes it necessary to perform an alignment procedure.

2. Strategy and tests for track-based alignment of the Inner Detector

The requirements of the alignment precision are set by demanding that misalignment effects should not degrade the resolution of the track parameters by more than 20%. To fulfill this requirement the position of the modules has to be known with an accuracy of 7 μm for the pixel and 12 μm for the SCT modules in the precision coordinate. Several track-based alignment algorithms have been developed for the Inner Detector and are already implemented under the ATLAS software framework. All track-based alignment methods share the principle of optimizing distributions of residuals, defined as the distance between the intersection of the fitted track with a detector element and the hitpoint read out by this detector element. A misaligned detector geometry leads to an increased width and a shifted mean value from which the displacements of the detector elements are determined. A $\chi 2$ value is calculated for all hits:

$$\chi^2 = \sum_{tracks} r^T V^{-1} r$$

where $r(a, \pi)$ is the vector of hit residuals depending on both alignment (a) and track parameters (π), and V is the covariance matrix of the hit measurements including the contribution from Multiple Coulomb Scattering (MCS). The correlations between the different modules can be taken

into account by iterating the procedure until convergence is reached (local approach) [3] or by correlating the different modules using the reconstructed track (global approach).[4] In general to extract the alignment parameters a $n \times n$ symmetric matrix needs to be inverted, where n is the total number of alignment degrees of freedom (DoFs) of the system. For the ATLAS silicon system (Pixel and SCT) n is about 35000. In the case of the local approach the correlations between the various detector modules are neglected, leading to a block-diagonal matrix. For the global approach different methods to solve large systems of linear equations have been investigated in terms of time performance and accuracy. The MA27 solver[5] offers the possibility to solve the set of linear equations without diagonalizing or inverting the matrix. However, the MA27 solver works only for sparse matrices. The different alignment approaches have been extensively tested with simulated events and real data coming from the ATLAS Combined Testbeam and cosmic runs recorded in the surface assembly area. The results are shown in what follows.

2.1. *Alignment of the ATLAS Combined Test Beam (CTB)*

The ATLAS Combined Testbeam (CTB) took place at CERN H8 beamtest area during 2004. Detectors from all different ATLAS subsystems were used in the final setup in order to reproduce a barrel slice of the ATLAS experiment starting from the interaction point at $\eta = 0$. The detector setup used mimics a slice of the ID barrel, with 6 pixel, 8 SCT and 6 TRT modules. Here only the alignment of the silicon-part of the setup with 84 degrees of freedom is discussed. Due to the particularities of the incoming beam distribution (particles come parallel with almost perpendicular incidence on the detector planes), some degrees of freedom were not considered. The mean and the width of the hit residual distribution agree quite well for all four alignment approaches. A Gaussian fit to the final distributions leads to sigmas of ~ 12 μm and ~ 22 μm for Pixel and SCT respectively, being the mean centered around zero within a micron. Figure 1 shows a comparison of the momentum resolution obtained for a 100 GeV π^+ pion run before and after alignment. The recover of the correct momentum distribution is evident.

2.2. *Alignment with cosmics tracks*

Cosmic-rays were recorded on the SR1 assembly area with the already assembled SCT and TRT barrels and with one of the two SCT and TRT

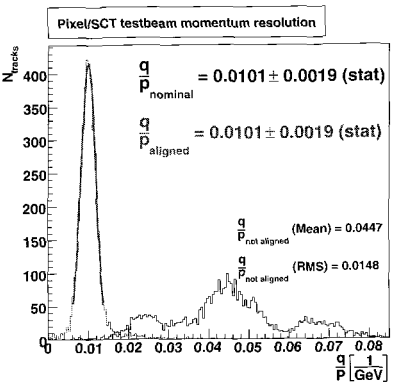

Fig. 1. Momentum resolution of Pixel and SCT modules for a run of 100 GeV π^+ pion before (not fitted histogram) and after alignment corrections (Gaussian-fitted histogram).

end-caps. For the barrel test, two sectors of the SCT and TRT were cabled for readout, representing $\sim$ 22% and $\sim$ 13% of the entire SCT and TRT barrel detectors. The muon trigger was given by several scintillators on top and bottom of the setup placed according to the angular distribution of cosmic ray muons. A slab of concrete allowed a momentum cutoff of about 170 MeV. This cutoff however allows large effects from MCS that dominate the hit residual resolution. The collected data are used to test the different alignment approaches. At this stage a framework was also developed to align *simultaneously* the TRT and SCT module using extended SCT-TRT tracks.[6] For the SCT results are consistent, in term of residuals to those obtained with SCT stand alone tracks. After the alignment procedure The mean value are correctly centers around zero.

2.3. *Alignment with simulated data*

To exercise the alignment approaches with the full ATLAS detector setup a large sample of tracks with a misaligned detector setup is simulated.

A special *as-built* geometry was employed where misalignments of the different subsystems, distorted material and distorted (tilted and shifted) magnetic field were included. The misalignments range from about 1mm for big structures going down to 100 μm for individual modules. With a blind knowledge of the alignment constants embedded in the simulation, a first set of calibration and alignment parameters is derived and then applied in a subsequent data reconstruction. Fig. 3 shows the impact of residual

misalignments on the measurement of the Z^0-mass. The difference between the reconstructed and true Z^0-mass shows no bias and the width of the distribution is only slightly wider compared to the uncertainty obtained using a not-misaligned detector.

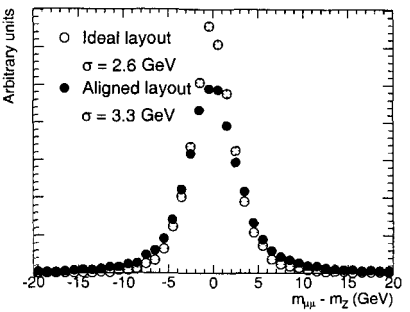

Fig. 2. The difference between the reconstructed and the true Z^0-mass for the not-misaligned geometry (empty circles) and after the alignment (full circles).

3. Summary

The alignment of the ATLAS inner detector is a crucial task in the commissioning of the detector. A number of algorithms have been developed to align the ATLAS Inner Detector. Extensive validation and testing are being performed and algorithms are continuously being improved. These have shown that the ID components have been assembled better than design standards. Full scale tests are being performed on nominal and misaligned detector simulations and are proving to be vital to our understanding of systematical errors.

References

1. ATLAS Technical Proposal, CERN/LHCC/94-43 (1994).
2. ALTAS Inner Detector Tecnical Design Report, CERN/LHCC97-16 (1997).
3. Goettfert T., MPP-2006-118 (2006)
4. Bruckman, de Renstrom P. et al., ATL-INDET-PUB-2005-002 (2005).
5. I.S. Duff *et al.*, Report R-10533, AERE Harwell Laboratory, UK (1982)
6. Bocci A. and Hulsbergen W., *TRT alignment for SR1 cosmics and beyond*, ATL-INDET-PUB-2007-009 (2007)

New generation Data Transfer for AMS02

M. J. Boschini

CILEA
Via R. Sanzio, 4,
Segrate, MI-Italy
E-mail: boschini@cilea.it

D. Brogioli, D. Grandi and P.G. Rancoita

INFN-Milano
P.zza Scienza, 3,
Milano, Italy

In this paper we present the new generation of the Data Transfer system for the AMS02 experiment. In particular we show how using a finite state automa and XML, the data flow of the system has been greatly simpliefied. Futhermore we will show the use of parallel queues and multiple threads to enhance overall throughput. The system has also been modified in order to be grid-aware. Finaly, we will show results of several months of real-life usage.

1. Introduction

Accurate measurements of cosmic ray spectra, particularly of protons, are important because of their close connection with the foundation of the theories of elementary particles, Grand Unified Theory and Dark Matter. The Alpha Magnetic Spectrometer AMS is a space-bourne experiment dedicated to investigate and measure with high precision such spectra, with particular attention to the detection of primordial anti-matter. AMS-01 was flown on the Space Shuttle Discovery on flight STS-91 in June 1998. This was primarily a test flight that enabled the AMS team to gather data on background source and adjust and verify the spectrometer performance for the actual data taking, known also as AMS-02.

The AMS-02 experiment, described in greater detail elsewhere[1] , is scheduled to start data taking by the second half of year 2009 on board of the International Space Station Alpha (ISSA).

The data flow, which is described in greater detail elsewhere[2] , can be summarized as follows: data will be recorded on board of International Space Station (ISS) and transmitted to Marshall Space Flight Center (MSFC) Alabama and therefrom to AMS ground centers: Payload Operation and Control Center and Science Operation Center. From there, data will be sent over the Internet to the *Science Operation Center and Central Production Facility (SOC)*,

located at CERN, where it will be processed and analyzed. Furthermore, the *Master Copy* of the whole data sample, both raw, reconstructed and simulated, expected to be around 45 Tbytes per year, will be stored at the *Italian Ground Segment Data Storage (IGSDS)*. The *IGSDS* will act not only as a master copy, but also as a "distribution center", in order to allow fast access to data to all collaborators without interfering with the *CPF* activity.

Facing the long running time and the way how the data will be transmitted from the detector to the analysis and production facilities, the development of a secure and reliable way of data transferring and organization is one of ground data handling vital issues. In particular, consistency between the *CPF* and the *IGSDS* data samples and data catalogs is of prominent importance.

2. AMS02 Italian Data Transfer

One major component of AMS Ground Data Handling system is the Data Transfer (*DT*), whose goal is moving data efficiently from *SOC* to *IGSDS* without interfering with *SOC* activities and keeping track of what has been moved and if successfully or not. The *DT* must also be capable of moving data from remote locations to *SOC* with exactly the same code and architecture. The *DT* has been developed and maintained by the authors, on behalf of the AMS collaboration, since 2004. Described in greater detail elsewhere[3] , the system has been succesfuly used to transfer 9 Tbytes from *SOC* to *IGSDS* and 3 Tbytes from remote locations to *CPF*, with an overall throughput of 40 Mbit/sec. This value satisfies the initial requirement of a throughput not less than 36 Mbit/sec, but analysis of the general behaviour showed there was room for great enhancements.

First of all, an overall re-design of AMS02 data handling and data storage policies at *SOC* could allow direct access to the central database, which could be queried to get an updated and comprehensive catalog of datasamples.

Furthermore, analysis of the processing of individual files by the Data Transfer System (henceforth called *DT*) reveals that the overall throughput is dominated by time lost in waiting for some resources, like available bandwidth or CPU, while some other resources are idle. Just to clarify, suppose that the network bandwidth needed to transfer file `F1` is not available: nothing happens, but in the meantime a resource needed to process `F2`, say CPU to calculate `F2`'s chekcsum[a] is idle.

Finaly, some *Grid Computing* tools could be leveraged, or at least tested, to enhance *SOC* to *IGSDS* comunications, relying on the fact that both CERN and CNAF, who host *SOC* and *IGSDS* respectively, adhere since the beginning to the grid/egee[6] project

3. The New Generation Data Transfer System

These factors induced us to radically change the *DT* in terms of resource usage. Other sub-components of the *DT* , like, for example, the book-keeping mechansim, based on a relational database, or the communication between the two sites, based on a custom SSL client/server architecture, were not modified

[a] Henceforth called *CRC*

in their overall architecture[b].

The basic starting point was that the process main bottlenecks are the data transfer through networks and CRC calculations[c]. Different bottlenecks refer to different resources; for example, CRC calculation is mainly computational and CPU time-consuming, while network transfer is mainly a I/O consuming operation. So, increasing data throughput is achieved by performing as many operations as possible in parallel, on those different resources: for example, we can transfer a file File1, F1 through a local network from *SOC* to *IGSDS* and in the meanwhile process another file's (F2) *CRC* or book-keeping or validation process. This parallelization mechanism requires a considerable level of coordination: for example, we cannot start to transfer file F3 before its CRC has been calculated.

Additional tasks concern errors and exceptions handling (for example, what should be done when a CRC is found to be wrong?) and report generation (statistics, error log and so on). Finally, the new system to be implemented has to be as "strong" as possible, that is, it must rely on persistent structures that are not lost in case of hardware failures.

We tackled the problem dividing it into a lower level, generic problem, parallelization and coordination of time-expensive processes, and a higher level, specific problem implementation of specific AMS02 Data Transfer subcomponents.

We thus decided to develop a generic program, with the following characteristics:

- acts on a definite set of items
- performs a user-defined program on each item
- steps of the user-defined program can be forced to be performed in sequence or in parallel
- the progress of the whole process is stored in a power-off safe way
- steps can be conditionally defined
- optimization, that is, highest pressure in each queue, is obtained by an algorithm that is transparent to the user

Items are the unique file names, and the user-defined program is the sequence of file transfers and CRC calculations. The conditional definition of steps is useful to handle an error in transfer; for exemple, if a CRC is found to be wrong, the file must be transferred again, while if it is right, it can be defined as corretly transferred.

We describe the process to be performed on each item through a finite state automa (FSA), so that the user-defined program becomes a transition action of the finite state automa, described in a dedicated "configuration" file (*FSAD*). We decided to use a programming language based on XML, since its parsing is well standardized, generic handling tools are available, and extensions are easily possible. Rule definition include income and outcome states, and a shell

[b]Obviously, some changes had to be introduced, in order to integrate those "old" subcomponents with the new process management.

[c]Not only in terms of CPU, but also in terms of I/O access to the variuos storage systems, which can be quite critical in an HPSS like CASTOR[5]

command to be performed on the item; the outcome state will depend on the exit status of the shell command.

With long rule lists and many allowed states, it is possible to express very complex operations. With this approach, the FSA includes the algorithm that decides when each command must be run, so that it performs in parallel the operations using different resources, and in series what uses the same resources; the user must only implement the commands, perhaps, through a simple Perl script. The FSA itself is written in Python. Each item, at each time, is associated to its state; in order to have a permanent (power-off safe) database of items and states, we decided to use a MySQL database; it works also as a book-keeping mechanism.

The following picture is a simplified block diagram of the FSA implemented for the AMS02 *DT* .

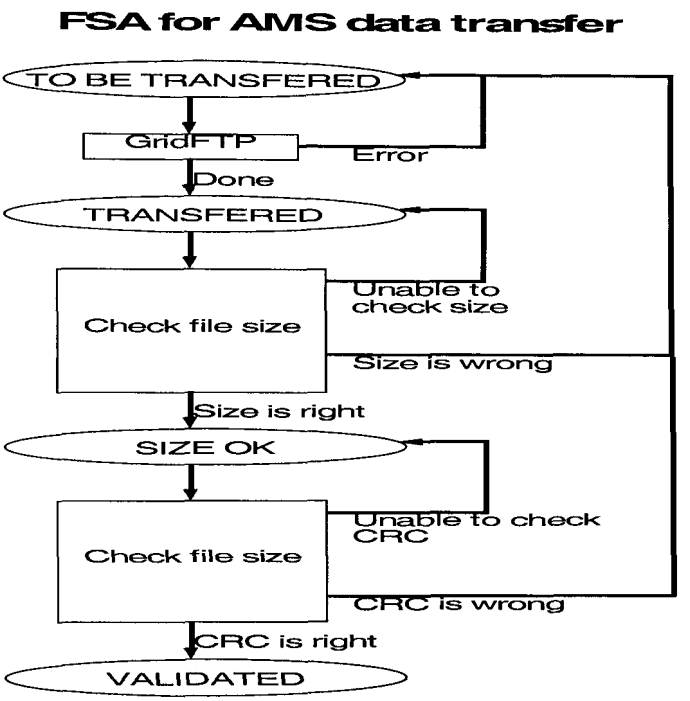

Fig. 1. Block diagram of the new Data Transfer.

The following is an excerpt of the FSAD file for AMS02 *DT* which clearly shows how queues are defined and used: if commands in two different rules share the same resource, it is useful to impose that they are not parallelized, defining the rules inside a queue.

As soon as an item is available for being processed through the rule, or through one of the rules of a queue, the process immediately starts. As many

processes are started in time-sharing as possible; at most, we can have as many simultaneus processes as much as the rules and the queues are.

```
<queue>
  <rule>
    <status>CRC_DONE</status>
    <command>
      perl check_transf.pl $name $size $vc_crc
    </command>
    <if code="0" status="VALIDATED" />
    <if code="1" status="TO_BE_TRANSFERED" />
  </rule>
  <rule>
    <status>VALIDATED</status>
    <command>
      perl processa_trasferiti.pl $name
    </command>
  </rule>
</queue>
```

Search for new files to be transferred is by default[d] performed through a search in the AMS02 data catalog stored at *SOC*, based on Oracle RDBMS, but can also be performed browsing through the storage systems. Items returned by this step are then looked-up in the DT data catalog, based by default on a MySQL RDBMS. If items are found to be new, i.e `TO BE TRANSFERRED`, they are pushed in the corresponding queue. Since queues are high pressure ones, items are processed as soon as they enter the queue. A further check, based on grid technologies, namely `grid-ftp-ls`, checks directly from *SOC* if and how taht given file is present at *IGSDS* .

This step, or transition in FSA terminology, as well as all the following ones, is made persistent by saving the actions that were being performed on the specified item in temporary files. In case of a system crash, those temporary files are processed by a dedicated thread, automaticaly spawned by the FSA when restarted. This makes the system robust against harware failures.

The actual transfer through the network is performed (by default) by means of grid `globus-url-copy` directly on CASTOR's Storage Resource Management(SRM). In this way we make full use of CASTOR's capabilities, without worrying of CASTOR's internals. Some tests we performed show that using directly SRM instead of moving data to CASTOR's stage area enhance performance of approximately a 20%. As in the case of `grid-ftp-ls`, another benefit of using grid technologies is the fact that no particular authentication mechanism has to be implemented, relaying on grid's authentication architecture.

Coordination bewteen *SOC* and *IGSDS* , involving the steps that check the file size and eventualy its *CRC* , is implemented by means of an SSL client/server system. Inherited from the old AMS02 DT^4 , it has been greatly improved. Mainly, the server is now able to respond with file size or *CRC* , while the client waits for the answer[e].

[d] i.e. defined by default in the configuration file.
[e] Which can be quite off-time if the CRC has to calculated.

Currently, *CRC* calculation is disabled since the file is directly transferred via SRM, which does not give direct and immediate access to the file, since its stored inside CASTOR; *CRC* is thus checked, comparing the one at *SOC* with the one declared by CASTOR after the file has been moved to tape, as a separate step in the FSA, with its own dedicated queue ran on files in status `TRANSFERRED` but not yet `VALIDATED`. Nevertheless, the *DT* already implements a mechanism that can handle files not directly moved to SRM or a CASTOR configuration which will move files to tape rarely[f]. In this case, the system, once a file is in status `TRANSFERRED` since a (configurable) time τ, runs it in a queue which tells *IGSDS* 's CASTOR to stage the file out and calculate its *CRC* , and then gives the result back. This is a good example to understand the usefulness of the 'parallized queues': this last operation is quite heavy in terms of CPU and I/O. Shouldn't there be any parallelization, the whole system will be stuck, or at least slowed down, while waiting for these tasks to complete.

Finally, the *DT* has been provided with a detailed logging facility, which provides useful data both for monitoring the whole system and for debugging it.

4. Performance

The *DT* system descrived above, has been put in production mid 2007. At the time of writing it has succesfully transferred more than 3500 files from *SOC* to *IGSDS* , amounting to 3 Tbytes worth of data[g]. The *DT* has also been used to move 0.6 Tbyte worth of simulated data, contained in approximately 200 files, from remote locations to *SOC*, fullfilling the requirement to be poortable and transparent.

The system robustly survived various hardware failures (mainly due to prolungated electrical power outages), proving the persistency mechanism to be reliable.

Fig. 2 is a pictorial view of 1000 seconds of *DT* , using data from the log files. The plot clearly shows that the system performs serially the various operations on a given file, while at same time other files undergo other operations.

A more exhaustive plot (Fig. 3), showing data from a longer period, clearly shows that all queues are efficiently populated and processed.

In order to verify that the overall throughput of the *DT* has improved using the parallel queues and the FSA, we calculate it for the whole sample we transferred, To do this, we get from the log file the time elasped since a file `F1` is found, and thus taken charge of, till another file,`F2`, is taken charge of and/or `F1` is put in `VALIDATED` state, depending on which happens later. We evaluate the overall throughput, for the more that 3500 files transferedd so far, to be $61.7 \pm 16.3 Mb/s$.

We also run network bandwidth estimation tools, like `pathload`[7] and `iperf`,[8] in order to compare the throughput of the *DT* with the available bandwidth; we found that *DT* 's throughput is 85% of the time only 10% lower that the raw available bandwidth, thus proving that the *DT* is as efficient as can be. Data for the whole sample is pictured in Fig.4.

[f]Namely, a CASTOR configuration with a vey large staging area and/or very high staging watermarks.

[g]Mainly Montecarlo simulated events

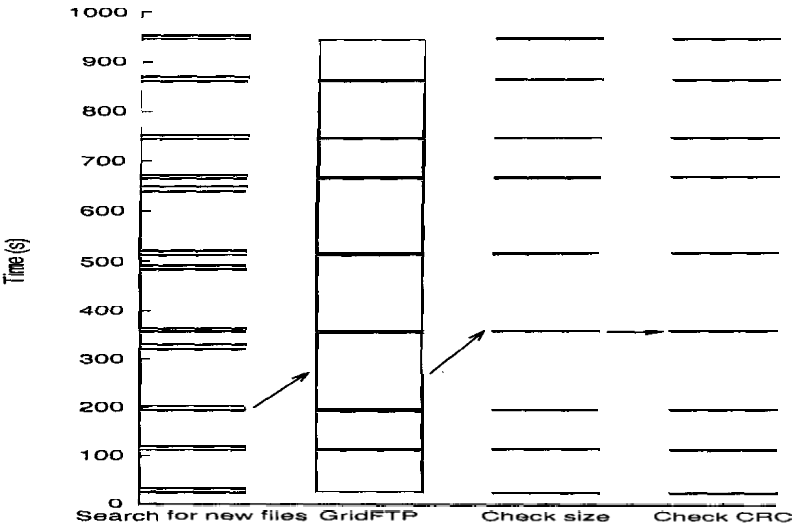

Fig. 2. **Pictorial view of 1000s** of DT running. Excerpt from log file. History of a peticular file is outlined with arrows

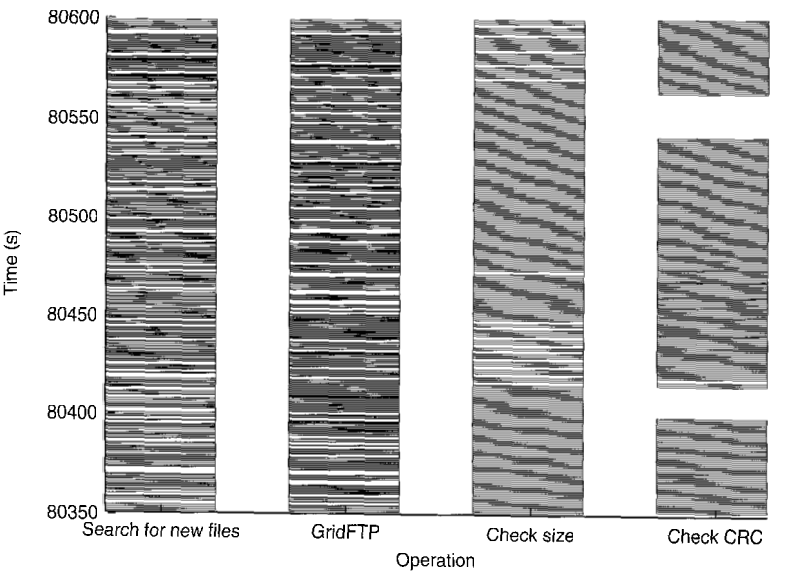

Fig. 3. Pictorial view of long run.

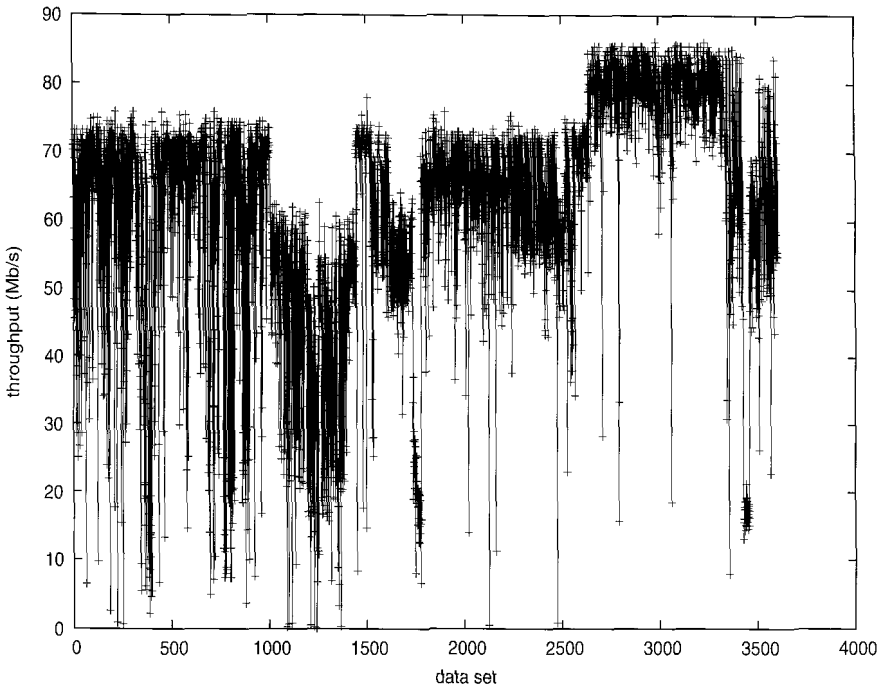

Fig. 4. Overall throughput for the more than 3500 files transferred using the New Generation *DT*. $Average = 61.7 \pm 16.3 Mb/s$

5. Conclusions

We developed a Finite State Automa to improve performance of AMS02 Data Transfer. The FSA implements parallel queues, in order to perform same operations on different files in parallel and at the same time process the same file serialy, thus preserving coordination of the file's various handling stages. We also introduced grid technologies, taking advantage of grid's authentication mechanism as well as of its transparency to underlying storage architectures. The New Generation AMS02 *DT* proved robust against hardware failures and has full logging funcionalities. Several months of its use in production, during which a total of 4 Tbytes of data were processed, show that the parallel queues mechanism if fully deployed, enhancing the overall throughput to nearly two times the required one, reaching an average of 61 Mb/s on a not-dedicated 100 Mb/s network.

Acknowledgments

We wish to aknowledge the continuous support received by CILEA and its director, Prof. A. Cantore.

References

1. AMS Collaboration *Physics Reports*, **366/6**, 331 (2002)
2. V. Choutko, A. Klimentov *Proceedings of Computing in High Energy Physics (CHEP 2001), Sep. 2001.*
3. M. J. Boschini et al, *Proceedings of 9th ICATPP Conference* (2006).
4. M. J. Boschini et al, *Proceedings of 8th ICATPP Conference* (2004).
5. http://castor.web.cern.ch/castor/
6. http://public.eu-egee.org/
7. http://www.cc.gatech.edu/fac/Constantinos.Dovrolis/pathload.html
8. http://dast.nlanr.net/Projects/Iperf/

Finite state automa for parallelization of time-expensive operations

M.J. Boschini[1], D. Brogioli[2], D. Grandi[2], P.G. Rancoita[2]

[1] *CILEA, Via R. Sanzio, 4,Segrate, MI-Italy*
[2] *INFN Milano-Bicocca, P.zza Scienza, 3,Milano, Italy*
E-mail: doriano.brogioli@mib.infn.it

We describe a finite state automa simulator (FS), aimed at coordinating the symultaneous processing of many items. The automa was developed for improving the performances of the Data Transfer system for the AMS02 experiment, but its applications are generic. FS is programmed through a XML file, with an abstract language describing a finite state automa. FS implementation includes the logics needed to perform the operations in parallel threads, as soon as processing is required. FS allows to coordinate the execution of different time-consuming operation; moreover, it handles error conditions, and performs logging and book-keeping.

1. Introduction

In this paper, we describe a programmable finite state automa and its programming language, aimed at the coordination and parallelization of time-expensive programs.

It was developed at first to solve the specific problem of enhancing the performance of the AMS02 experiment[1] Data Transfer System.[2]

The process main bottlenecks are the data transfer through networks and CRC calculations. Different bottlenecks refer to different resources; for example, CRC calculation is mainly computational and CPU time-consuming, while network transfer is mainly a I/O consuming operation. So, increasing data throughput is achieved by performing as many operations in parallel, on different resources: for example, we can transfer a file F1 through a local network from a remote host A to local host B; in the meanwhile, we can transfer another file, F2, though a different network, from local host B to another remote host C, and simultaneously perform a CRC calculation on file F3 on the localhost. This parallelization process requires an amount of coordination: for example, we cannot start a the transfer of

file F3 before its CRC has been calculated. Additional tasks concern the handling of errors and exceptions (for example, what should be done when a CRC is found to be wrong?) and report generation (statistics, error log and so on). Finally, must be as "strong" as possible, that is, it must rely on structures that are not lost when a PC is accidentally powered off.

It is often useful to tackle the problem by dividing it into a lower level, generic problem (in this case, parallelization and coordination of time-expensive processes), and a higher level, specific problem (implementation of specific transfer and CRC calculation programs). This approach has two distinct advantages: the first is that the generic part can be shared with other developers, that will provide further improvements, independently from the specific use; the second is that changes in higher level details will not affect the lower level.

We decided to develope a generic program, with the following characteristics: acts on a definite set of items; performs a user-defined program on each item; steps of the user-defined program can be forced to be performed in sequence or in parallel; performs a log for each step of the user-defined program; the progress of the whole process is stored in a power-off safe way; steps can be conditionally defined; optimization, that is, highest pressure in each queue, is obtained by an algorithm that is transparent to the user

In our case of data transfer, items are the unique file names, and the user-defined program is the sequence of file transfers and CRC calculations. The conditional definition of steps is useful to handle an error in transfer; for exemple, if a CRC is found to be wrong, the file must be transfered again, while if it is right, it can be defined as corretly transfered.

We decided to describe the process to be performed on each item through a finite state automa (FSA), so that the user-defined program becomes the definition of the finite state automa (FSAD). We decided to use a programming language based on XML, since its parsing is well standardized, generic handling tools are available, and extensions are easily possible. Rule definition include income and outcome states, and a shell command to be performed on the item; the outcome state will depend on the exit status of the shell command. With long rule lists and many allowed states, it is possible to express very complex operations. With this approach, the FSA includes the algorithm that decides when each command must be run, so that it performs in parallel the operations using different resources, and in series what uses the same resources; the user must only implement the commands, perhaps, through a simple Perl script. The FSA itself is written in Python.

Each item, at each time, is associated to its state; in order to have a permanent (power-off safe) database of items and states, we decided to use a MySQL database; it works also as a book-keeping mechanism. Each record can contain more fields than name and state; they will be accessible by the FSA. For example, the name field can be the unique name of a file, and another field can contain the full path.

2. Language description

In order to use the FSA, the user must write a FSAD, in XML language, following the language description detailed below. The FSAD is mainly a sequence of rules. Each rule includes an income status list, a shell command, and an outcome status list.

The general structure of the FSAD is as follows:

```
<finitestates>
  <database data....> </database>
  <rule>
     ... definition...
  </rule>
  ... other rules...
</finitestates>
```

In order to use the FSA, we need a database table on which it will be run, that is, a table containg at least the two fields name and status; the user must have read and write privileges on the table. The `database` tag is used to define the required parameters (host, user, ,passwd, database, table); it also allows to define the fields to be used as unique name and status. Moreover, it allows to declare the names of the fields that can be accessed by the FSA, and an optional insert time field, for statistics and optimizations.

After the `database` definition, there is the list of rules. Here's an example. We want to implement this rule: for each item in status `FILE` or `DIR`, run the command `ls`, using the item name as argument; then update the status of the item as `FOUND` or `NOT_FOUND` depending on the exit code of the command. Here's how the rule looks like in the XML file:

```
<rule>
  <status>FILE</status>
  <status>DIR</status>
  <command> ls $name </command>
```

```
    <if code="0" status="FOUND" />
    <if code="1" status="NOT_FOUND" />
  </rule>
```

The FSA runs continuously, as a daemon; when it finds an element with a given status in the database table, it looks for a rule that can be applied to it and runs the shell command. When the command returns, the FSA updates the status in the DB, depending on the return code of the shell command. Then, the FSA looks for other rules that can be applied to items with status=FOUND or status=NOT_FOUND.

It's worth noting that there are no limits on the shell command. It can be something like `perl cheese.pl`, so that Perl scripts can be used with FSA. Obviously, many commands can be put together, separated by ";". There are situations in which the shell command must be able to interact with the database fields; at least, it can require the name field of the record. This is obtained easily, since field values are passed as environment variables by the FSA. For example, consider a table with a field named `path`, together with `status` and `name`; the shell command can be `ls $path`. In this case, FSA defines the environment variable `$path` with the value of the field `path`, and passes the value to the subshell. In a similar way, it is possible to alter the values of the fields.

Some of the operations must be run continuously; among them, commands to look for new items and insert them in the DB, and consistency checks. Such kind of commands are expressed as rules without any `<status>` tag. This kind or rules is handled in a different way, with respect to the previous ones: the command is repeatedly run at given intervals of time. The exit code if the shell command is then used to inform the FSA about which kind of new items have been added: this will be used by FSA optimization algorithm, that will immediately start looking for rules for processing the new items.

Generally, the FSA tries to run simultaneously, in different shells, one command for each rule, as soon as items are available for processing. This means that commands from different rules are executed in parallel, on different items, and sequences of commands coming from the same rule, on different items, are performed in series. If the commands in two different rules share the same resource, it is useful to impose that they are executed in series; this is done by putting the rule definition inside the tags `<queue>` ... `<queue>`.

The FSA automatically generates a log file, that can be sent to a user-defined file. Each time a command is executed or terminates, a row is added

to the log, with time, date, the string `starting` or `finished`, the shell command. Moreover, the standard output and standard error of the shell command are redirected, and sent to the log file.

3. Optimization of operations

The above described behaviour of the FSA refers to the user-programmable logic sequence of the operations that will be performed on the DB items. Instead, the exact timing of the operation is determined by the FSA, that runs continuously as a daemon, and runs the shell commands in an optimized way, transparent to the user.

Each rule is considerd a bottleneck. This means that, as soon as an item is available for being processed through the rule, the processing immediately starts. As many processes are started in time-sharing as possible; at most, we can have as many simultaneus processes as are the rules. For each running command, there's a running Python thread that waits its end, so that no time is lost in looking for ended processes.

The operation of looking for new items to be processed is quite critical. It requires particular care when no new items are avaliable, since we cannot perform continuously a DB SQL `select` command. Instead, the `select` is issued at given time-steps. It is possible that a new item with the required status becomes available during the sleep between two consecutive DB queries, as a conseguence of the execution of a rule; in this case, the sleep is interrupted, and the required processing immediately starts.

Other kind of problems arise when a command fails. This is expressed, in the FSAD, by the fact that the status of the item is not changed after the shell command execution. This forces the command to be repeated, but this is not what we generally want, since, probably, it will fail again. In this case, the FSA looks for other items to be processed and tries to process them. After all the other items have been processed, or no other item is available for processing, the FSA tries to run again the failed command. Moreover, the failed command is not issued before a given time has elapsed. All this requires that the FSA keeps a list of processed items; in the meanwhile, when required, it looks for new items in the DB, as described before.

References

1. AMS Collaboration *Physics Reports*, **366/6**, 331 (2002)
2. M. J. Boschini et al, *Proceedings of 9th ICATPP Conference* (2006).

ATLAS DISTRIBUTED ANALYSIS TOOLS*

SANTIAGO GONZALEZ DE LA HOZ, LUIS MARCH RUIZ†
IFIC – Instituto de Física Corpuscular, Centro Mixto Universitat de València – CSIC, Valencia, Apartado de Correos 22085, E-46071, Spain

DIETRICH LIKO
CERN – European Organization for Nuclear Research, CH-1211 Geneva, CH-1211, Switzerland

The ATLAS production system has been successfully used to run production of simulation data at an unprecedented scale. Up to 10000 jobs were processed in one day. The experiences obtained operating the system on several grid flavours was essential to perform a user analysis using grid resources. First tests of the distributed analysis system were then performed. In the preparation phase data was registered in the LHC File Catalog (LFC) and replicated in external sites. For the main test, few resources were used. All these tests are only a first step towards the validation of the computing model. The ATLAS management computing board decided to integrate the collaboration efforts in distributed analysis in only one project, GANGA. The goal is to test the reconstruction and analysis software in a large scale Data production using Grid flavors in several sites. GANGA allows trivial switching between running test jobs on a local batch system and running large-scale analyses on the Grid; it provides job splitting and merging, and includes automated job monitoring and output retrieval.

1. Introduction

The primary goal of the distributed analysis is to bring computation power to individual ATLAS physicists. This is achieved by providing easy access to the computing resources of the various Grids.

The distributed analysis model is included on the ATLAS computing model [1] and stipulates that data is distributed in various computing facilities. User jobs are in turn routed depending on the availability of relevant data. A typical analysis job consists of a Python [2] script that configures and executes a user defined algorithm in Athena (ATLAS software framework). The script specifies the input data and produces one or more files containing plots and histograms. The expected volume of data recorded for offline reconstruction and analysis

* This work is supported by the Spanish National Research Council (CSIC)
† Work partially supported by Marie Curie grant MERG-CT-2006-44258 of the European Union.

will be of the order of 1 PB (10^{15} bytes) per year. Due to the size of this expected data volume it is necessary to use distributed resources all over the world to perform reconstruction and analysis of the data.
The ATLAS Computing Model covers all aspect of this operation. It includes organized production of simulated data, and also user analysis. In this paper we describes our experience running ATLAS distributed analysis tools.
The ATLAS production system has been developed to perform the production of the experiment. It provides a robust framework to execute a large number of jobs in the grid infrastructures.
This experience will allow us to compare the execution of analysis task using such a system versus using direct submission to the infrastructure. This activity was part of the Data Challenges (DC's) that were organized to validate the Computing Model to ensure the correctness of the technical choices.
The collaboration decided to perform these DC's in the context of the LHC Computing Grid project, LCG [3], which contains the majority of ATLAS resources, but also to use both the middleware and the resources of two other Grid projects, OSG [4] and NorduGrid [5]. The aim is to prepare the computing infrastructure for the simulation, processing and analysis of the LHC data.

1.1. *Atlas Production System*

In order to handle the task of DC's an automated system was designed. The production system [6] is implemented in a modular way to enable ATLAS to use resources out of these three infrastructures. All jobs are defined in a specific schema and stored in a central database. A supervisor agent picks them up, and sends their definition as an XML message to the various executors. Executors are specialized agents, able to convert the ATLAS specific XML job description into a Grid specific language. Three executors were developed, for LCG (Lexor and CondorG), NorduGrid (Dulcinea) and OSG (Capone). All the data management operations are performed using a central service, Don Quijote (DQ) [7]. DQ moves files from their temporary output locations to their final destination on some Storage Element and registers this location in the Replica Location Service of the corresponding Grid flavor. This allows operating the different replica catalogues of the three Grid flavors in a similar way.

The ATLAS production system has been successfully used to run production jobs at an unprecedented scale for a system deployed on about 100 sites around the world. On successful days there were more then 10000 jobs processed.

2. Distributed Analysis Strategy

ATLAS has adopted a multi-pronged approach to distributed analysis by exploiting its existing Grid infrastructure (see figure 1).

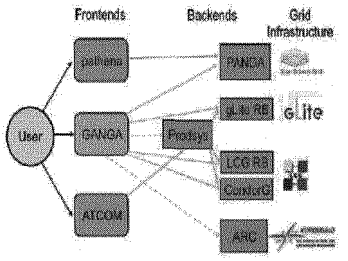

Figure1. Various front-end clients are intended to perform distributed analysis on the existing Grid infrastructure. These front-end are PanDA/Pathena, ATCOM and GANGA.

PanDA [8] is a job management system associated with OSG designed specifically for both distributed production and analysis. PanDA has native support for the ATLAS Distributed Data Management (DDM) system allowing accepting datasets as input and producing datasets as output. PanDA offers users a comprehensive system view presenting heterogeneous distributed resources as a single uniform resource, accessible via a standard interface. It also has extensive web-based job monitoring and browsing capabilities. Panda looks to GANGA [9] in order to provide a graphical job definition and submission interface. Pathena is a python script designed to submit analysis jobs to the PanDA system.

ATCOM [10] was the dedicated graphical user interface front-end to the production system, designed to be used in large-scale organized production of data. It had the potential to be used for distributed analysis purposes as well. The Computing Board decided to integrate the collaboration efforts in distributed analysis in only one project, GANGA. It is a powerful user friendly front-end tool for job definition and management. GANGA provides distributed analysis users easy access to the whole Grid infrastructure. Two user interface clients are provided: a Command Line interface (CLI) and a Graphical User Interface (GUI). GANGA allows switching between testing on a local batch system and large-scale processing on the Grid, and helps to keep track on results.

A GANGA job is constructed from a set of building blocks. All jobs have to specify the software to be run and the processing system (back-end) to be used.

2.1. *Distributed analysis using the production system and GANGA*

Distribution of data on several sites and local access to the data is a very important issue to minimize failures. In total 155 GB of merged datasets were used for distributed analysis. The dataset were registered at CERN in Logical File Catalog (LFC) and were replicated in the several sites.

The algorithm of choice has been a $Z_H \rightarrow ttbar$, a heavy Z decaying into tops in the Little Higgs model. A total of 400 Analysis Object Data (AOD's) were produced using the Athena full simulation chain, each one containing 50 events. The analysis has been performed using the production system and GANGA.

Despite the possibility to run analysis jobs via the production system, not all functionalities to support distributed analysis were currently available. In the following, the technical issues that had to be addressed are discussed in turn.

A dedicated database was setup for analysis jobs to separate private work from the ongoing production. A generic analysis transformation was created, that compiles user code or the user package on the worker node, processes AOD input files and produces histograms as output. ATCOM was used to define jobs. It was also used to monitor the status.

To perform an analysis the user has to define a task and associated jobs according to the conventions of the ATLAS production system. The task contains summary information about the jobs to be run (input/output datasets, transformation parameters, resource and environmental requirements), while individual jobs are defined by their specific parameters needed for execution.

We defined the same jobs using GANGA. It provides a set of ATLAS-specific features such as application configuration based on the Athena framework and input data location based on DDM. Users need to enter just a few commands to set application properties and submit jobs to run the application on selected back-ends (Grid flavours or local batch system).

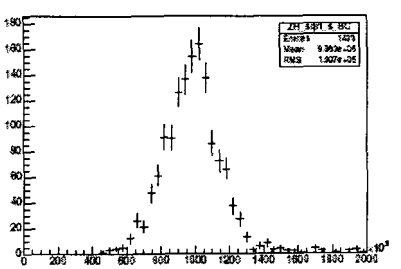

Figure 2: $Z_H \rightarrow tt$ invariant mass distribution after merging the output files (GeVunits in the y axis).

The jobs were running at several sites and were instructed to save output at one single Storage Elements close to the user. The ROOT package was used to merge the histogram output files and to analyze the results (see. figure 2).

All these tests are only a first step towards the validation of the computing model and distributed analysis. More realistic tests have to involve many physicists working in concurrent mode. This requires not only progress in the application, but also progress in the Grid middleware and the site configurations.

3. Conclusions

The ATLAS production system and GANGA have been used to submit physics analysis jobs to LCG Grid flavor. Using the production framework for analysis has the advantage to profit from the experience of the large scale production..
For the main test few resources were used. The system was able to process 10k events jobs in about 10 minutes. It is fair to say that it was difficult to achieve this performance due to the instability of the major components of the software that were still in a development phase. Nevertheless we consider this first test as encouraging and promising.
Comparing the production system with GANGA, we could observe a more robust execution and we were also profiting from the advanced monitoring capabilities of the production system. A drawback is that such a system represents an additional infrastructure, which has to be operated by the experiment.
Distributed Analysis is still work in progress. With the startup of LHC in the next year we expect a dramatic increase of the data volume. This will requires the general ATLAS user to use resources on the grid to perform his analysis.

References

1. ATLAS Computing Technical Design Report, CERN-LHCC-2005-022.
2. G. Van Rossum and F.L. Drake, Jr (eds.) Python Reference Manual 2.4.3
3. M. Lamana,et al,"The LHC computing grid project", NIM **A 534** (2004) 1-6
4. R. Gardner, "Grid3," in Proc. CHEP04, p 1318 (2 vol)
5 M.Ellert et al.,"The NorduGrid. Project", NIM **A (502)** (2003) 407-410.
6. L. Goossens, "Production System in ATLAS DC2," in Proc. CHEP04, p501.
7. M. Branco, "Don Quijote" CERN Yellow Report 2005-002, p 661.
8. PanDA (http://twiki.cern.ch/twiki/bin/view/Atlas/Panda).
9. GANGA (http://ganga.web.cern.ch/ganga)
10. ATCOM (http://uimon.cern.ch/twiki.cern.ch/twiki/bin/view/Atlas/AtCom).

MICE SOFTWARE DESIGN AND PHYSICS PERFORMANCE

MALCOLM ELLIS

Electronic & Computer Engineering Department, Brunel University, Uxbridge, Middlesex, UB8 3PH, United Kingdom.

The design philosophy and key features of the Muon Ionisation Cooling Experiment (MICE) software (G4MICE) is presented. The performance of the analysis is demonstrated through a number of Monte Carlo simulations.

1.1. *The Muon Ionisation Cooling Experiment*

1. The purpose of the Muon Ionisation Cooling Experiment [1] (MICE) is to demonstrate the feasibility of building and operating a section of ionisation cooling channel and measure the performance of this channel. The measurements made in MICE will be used to validate Monte Carlo simulations and extrapolated to optimise the performance of a cooling channel for use in a Neutrino Factory.

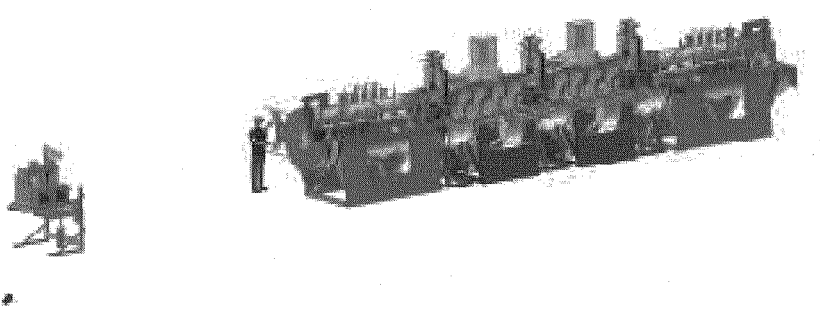

Figure 1. The instrumentation and cooling channel of the MICE experiment.

Muons will pass through MICE one at a time. Position, momentum and time measurements will be made as the muon enters and exits the cooling channel. Bunches will be constructed offline from the individual measurements of up to 10^6 particles.

The layout of the MICE experiment, including the upstream time of flight and cherenkov detectors and downstream time of flight and calorimeters for particle ID, input and output spectrometers either side of the cooling channel are shown in Figure 1.

The experiment mixes conventional particle physics instrumentation with accelerator physics technology and requires a mixture of tools from both fields in the simulation, reconstruction and analysis software.

2. G4MICE

The software developed for the MICE experiment was originally conceived to perform GEANT4 simulations of the experimental concept for the purposes of designing the experiment and gaining funding. As a result, the software has come to be known as G4MICE [2].

The software now provides a wider range of services beyond simulation and continues to be developed as the experiment nears completion and the beginning of data-taking in early 2008.

The domains diagram for G4MICE is shown in Figure 2.

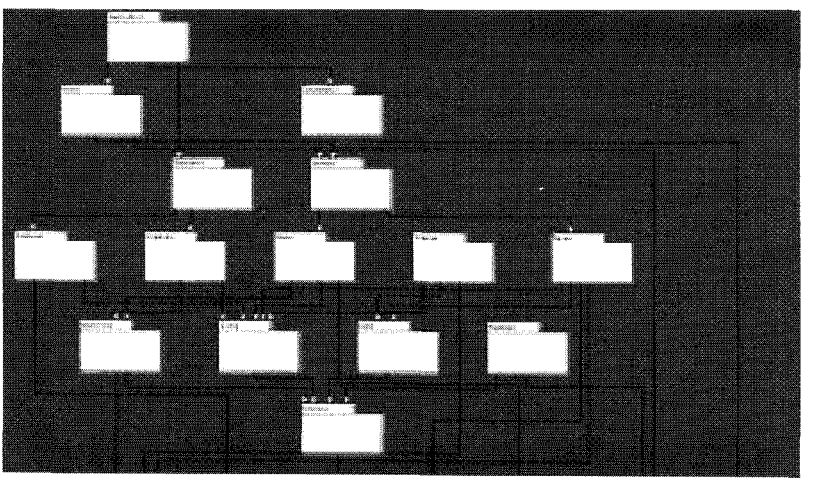

Figure 2. The G4MICE domains diagram

2.1. *Applications*

The highest level domain, Applications, is where executables are contained. For each Use Case, one or more applications exist which are linked with one or more of the libraries that are built from the remaining G4MICE domains.
A perl script which knows the dependencies implied by the domains diagram creates Makefiles on the basis of a list of input source code files (one of which must contain the main() routine) and a list of one or more G4MICE domains and external libraries. The script follows the dependency tree and so if, for example, Config is requested, Interface will also be included, whether it was explicitly listed or not.

The existing applications include a set of Simulation, Digitisation and Reconstruction tools as well as numerous special purpose programmes written for specific test beams, quality control and characterisation of the instrumentation as well as examples of how to build an analysis application to make histograms, Ntuples or trees for use in PAW or ROOT.

2.2. *Event Model*

The design philosophy has been to separate as much as possible classes representing models of the experiment, detector response and reconstructed physical quantities from any files or file formats.

Each detector has a "digit" class which represents the lowest level of calibrated information produced by the device. The reconstruction is performed by taking these classes and building others to represent the higher level information that results from cluster finding, space point reconstruction, pattern recognition, track fitting and matching.

The Simulation produces hits which are used to generate digits by the Digitisation application. Due to the wide range of data formats already seen in MICE for research and development, test beams and characterisation of detectors, the digit classes are not dependent on an assumption of the file formats. A converter has been written for each unique format that contains the code required to decode the specific file format. Each of these converters results in the same C++ digit classes being present in the event for subsequent reconstruction and analysis.

2.3. *Persistency*

Each of the classes that represent simulated hits, digits, low and higher level reconstructed information are made persistent through a scheme developed for the HARP experiment [3].

The technique employed is that of writing a converter class for every transient class and for every method of making the class persistent. This class knows the internal structure of the transient class as well as the means by which the method of persistency reads and writes the class information.

This design ensures that the transient classes have no dependence on any of the means through which they may be made persistent and decouples each method of persistency from any other. It also has the advantage that it does not impose any constraints on the class design (for example it does not require only uni-directional pointers).

The current means of persistency used in G4MICE is through a gzipped text file (using the Zlib library), however this technique has also been used through a MySQL database and can be extended to any other desired medium.

Conversion from one form of storage to another is easily achieved by using the reader code of the original format and then the writer method of the new format.

2.4. *Data files and formats*

The "RealData" domain takes care of the many different data formats that have been used in MICE to date and will continue to be extended as new formats come into use.

For each format, the classes that define the event model (in the "Interface" domain) are created by a special purpose converter written for that format.

Each of these converters as well as the reader classes for each means of persistency are derived from an abstract interface which defines a generic data reader. This reader can be instantiated using a common framework which allows the data type to be selected at run time. In this manner, an application can be developed without any regard to the file format that may be used and as an example, allows an application to analyse simulated and real data without any compile time dependence on which type of data is being analysed.

2.5. *Experimental models*

The experimental model needs to cope with a range of conventional high energy physics detectors as well as beam line elements including dipole, quadrupole and solenoidal magnets and RF cavities.

Each experimental configuration is modeled using a single class which contains information about the shape, location, orientation and properties of each component. The complete model is built up as a tree of instances of this class. Standard volume shapes such as boxes, cylinders and tubes can be

selected and in addition, special purpose volumes have been added as required such as wedges, poly-cones (for safety windows) and various magnet types.

The class is mostly ignorant of what it is storing (other than the volume type, dimensions, location and orientation). Most of the information is contained through properties which are stored as STL maps from the property name to the value. Properties can be a range of types, including boolean, integer, double precision float, string and the CLHEP Hep3Vector class.

CLHEP is used to provide the geometrical transformations (translation, rotation and scaling) as well as the SystemOfUnits definition. The use of units in G4MICE has been extended through a class which keeps track of the numerical value of a unit as a function of its name. This class allows units to be used whenever user input is required, such as the command line, model definitions and the data cards system which is used to specify running conditions.

An additional class similarly maintains a set of materials which can be interrogated by the material name and return the physical properties of that material. In the case where an application is built with GEANT4, this class will also return a pointer to the G4Material class corresponding to the material and so is used in the Simulation's representation of the model. In all other cases, the physical properties of the material are still available for use (for example, so that the track fit can include the radiation length information in the calculation of multiple scattering).

Electromagnetic fields are modeled using the "BeamTools" domain. These tools include the ability to model solenoidal magnets, multi-pole magnets (for example dipoles, quadrupoles and sextupoles) and RF cavities.

The beam tools allow any representation to know the electromagnetic field at any position within the experiment and at any time. This has been used to implement correct time varying EM fields inside the RF cavities inside the GEANT4 simulation of the ionisation cooling channel.

2.6. *Representations*

For each specific use of a model, a representation is built that depends on the model and any G4MICE or external libraries that are needed. This division allows the models to be completely independent of any external libraries (other than CLHEP) and ensures complete decoupling between, for example, the Simulation and Reconstruction, where it would not be desirable for the track fitting code to depend on GEANT4.

A representation takes the information contained in the model that is relevant to the particular task and performs the necessary tasks to implement that

model in the appropriate framework. The Simulation representation builds the GEANT4 geometry, electro-magnetic fields and sets sensitive detectors on the basis of the description in the model and is the sole location for code that depends on GEANT4. Similarly, the reconstruction representation initialises the RecPack Kalman fitting package with the necessary geometrical information and the visualisation representation produces a HepRep format file.

3. Software Performance

G4MICE has been used to simulate a range of input beams, ranging from very small emittance (0.5 π mm rad) to the largest beams that could be measured in the experiment (9.5 π mm rad). Following digitisation and track reconstruction, virtual bunches were generated of 1 million muons per beam and the beam emittance before and after the cooling channel determined from the Monte Carlo truth information and the reconstructed track information. Figure 3 shows the MICE cooling channel performance as a function of the input beam emittance as well as the emittance resolution achieved by the reconstruction.

In addition to measuring the emittance of a beam through the measurement of the phase space volume occupied by an ensemble of particles, it is also possible to measure the single particle emittance, which is a quantity that can be applied to each individual muon. Figure 4 shows the distribution of single particle emittance from truth and reconstructed tracks from the tracker measuring the beam going into and coming out of the cooling channel. The cooling effect of the ionisation cooling channel can be seen through the reduction in the number of particles that have a large single particle emittance and an increase in those with a small single particle emittance.

In both cases, the reconstruction can be seen to be correctly reporting the properties of the beam and the simulation is predicting that the cooling channel will perform in a similar manner to that expected as a result of earlier calculations.

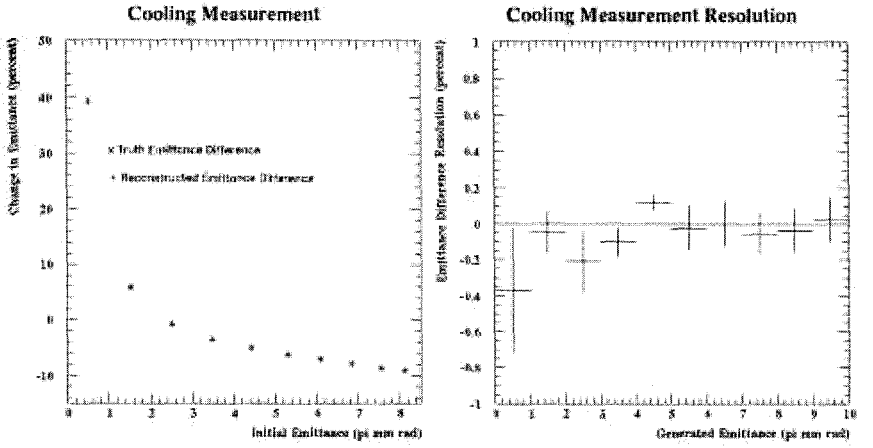

Figure 3. Simulated and reconstructed change in emittance as a function of input beam emittance (left) and reconstructed emittance resolution as a function of input beam emittance (right).

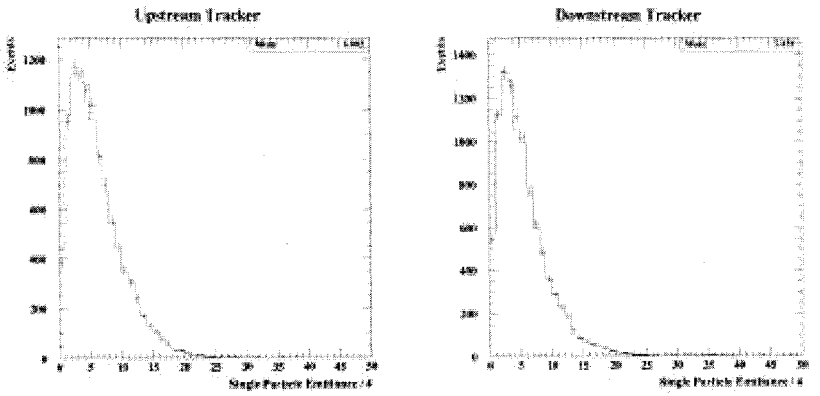

Figure 4. Single Particle Emittance distributions in the upstream tracker (left) and downstream tracker (right). The distribution of truth values are shown in the solid histograms, reconstructed values are shown as points with error bars.

4. Conclusions

The G4MICE software has been developed over the past few years into a powerful tool for the simulation and analysis of the Muon Ionisation Cooling Experiment. Through the implementation of simple modeling and analysis tools, it has come to be used outside of the MICE experiment and is now being used to

develop the MANX 6D cooling experiment as well as ongoing studies of Neutrino Factory cooling channels (both linear and circular).

G4MICE will face additional challenges in the coming year as MICE data taking begins.

References

1. M. Ellis, *Int.J.Mod.Phys.* **A20**, 3843-3846 (2005).
2. C. Rogers & R. Sandstrom, EPAC06 Proceedings, 2400-2402 (2006).
3. M.G. Catanesi *et al.*, *Nucl.Instrum.Meth.* **A571**, 527-561 (2007).

The Control System for the CMS Strip Tracking Detector

Manuel Fahrer*[,1,2], Frank Hartmann**[,1,2], Jie Chen[1], Alexander Dierlamm[2], Martin Frey[2], Lorenzo Masetti[1,3], Otilia Militaru[4], Yousaf Shah[1], Robert Stringer[1,5], Andromachi Tsirou[1]

[1] *CERN, Meyrin, Switzerland*
[2] *University of Karlsruhe, Germany*
[3] *University of Florence, Italy*
[4] *University of Louvain, Belgium*
[5] *University of Riverside, CA, USA*
* *E-mail: manuel.fahrer@cern.ch*
** *E-mail: hartmann@iekp.fzk.de*

The Tracker of the CMS silicon strip tracking detector covers a surface of 206 m^2. 9648128 channels are available on 75376 APV front-end chips on 15232 modules, built of 24328 silicon sensors. The power supply of the detector modules is split up in 1944 power supplies with two low voltage for front end power and two high voltage channels each for the bias voltage of the silicon sensors. In addition 356 low voltage channels are needed to power the control chain. The tracker will run at -20°C at low relative humidity for at least 10 years. The Tracker Control System handles all interdependencies of control, low and high voltages, as well as fast ramp downs in case of higher than allowed temperatures or currents in the detector and experimental cavern problems. This is ensured by evaluating 10^4 power supply parameters, 10^3 information from Tracker Safety System and 10^5 information from the tracker front end.

1. CMS Tracking Detector

The Tracker is composed out of four major parts: inner barrel (TIB), outer barrel (TOB), and two end caps (TEC). The barrel parts are structured in layers and the end caps in disks. Substructures are (from larger to smaller) cooling loops for all parts, sectors for the end caps and control groups and power groups for all parts. More exhaustive descriptions and design considerations are given in.[1] The physical structure of the tracker as well as its power supply is reflected in the control system's hierarchies.

2. The Tracker Safety System

The control and safety systems of the CMS Tracking Detector are well separated, but information is frequently interchanged. The Tracker Safety system (TSS) is a PLC based, self-contained system operating on the information provided by 1004 hardwired sensors. It monitors those sensors and acts depending on the monitored values, consisting of temperatures, humidities and cavern information. The TSS will interlock the tracker power following a user defined scheme when one or a group of temperatures goes above or below user defined limits or when the cavern systems malfunction. The interlock system is realized with relays cutting the power of power supply crates in case of an incident. Six independent PLC systems serve each side (plus and minus) of the three major sub detectors having made slightly different sensor choices and positioning. One additional PLC system serves as supervisor. The TIB, being closer to the interaction point, uses a high number of temperature probes (240) and interlocks based on the temperature measured per cooling segment. The TEC uses the temperature measured on the hottest silicon modules per petal (288) in order to engage interlocks (see for example the sensor distribution of TEC in Fig. 1). The TOB uses five temperature sensors for each of its 44 cooling segments and combines this information with its air temperature that then sums up to 264 temperature informations. The measurements of the humidity probes that are homogenously distributed inside the detector's volume combined with the air temperature sensor measurements will provide the detector with valuable dewpoint information. The PLC programs are kept as simple as possible, allowing flexibility and interconnectivity. Each sensor holds its dedicated upper and lower limit, including an enable/disable flag. The users are free to define, within some minima imposed directly by the PLC, a number of sensors or groups of sensors that need to be off limits in order to release a certain number of intelock relays. Also basic information from the racks, the beam condition monitors (BCM), the cooling plant (CP), thermal screen (TS) and dry gas system can evoke an interlock. TSS is ultimately reporting to the global CMS control system and reacting on pre-warnings, like pending power cuts.

3. The Tracker Control System

The main task of the tracker control system (TCS)[4] is the safe switch-on and -off of the whole detector or parts of it, taking into account the PLC information, coming via the native Siemens S7 driver and using information

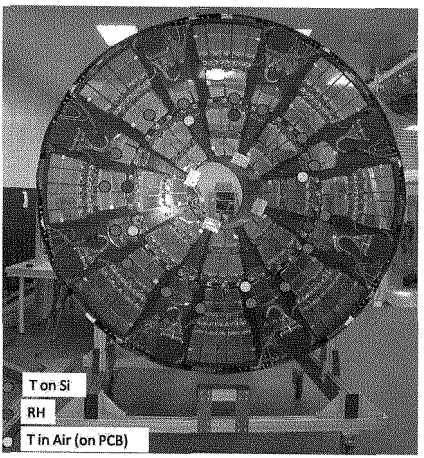

Fig. 1. *The distribution of hardwired sensors in the TEC outermost disk are shown. Each of the 288 petals routes a temperature sensor sitting on the hottest sensor spot to provide an interlock signal. In addition 12 pairs of relative humidity measurements and air temperature probes are equally distributed to allow a dewpoint monitoring.*

of the approx. 15000 detector control units (DCUs) of all the individual modules, provided by the detector front end and transfered to the TCS via SOAP. The information and commands to the CAEN power system are managed through the OPC protocol. Communications of the BCM and CP are realized via SCADA to SCADA messaging, while the TS, controlled by a PLC system communicates via S7. The dataflow and hardware connections are visualized in Fig. 2. An earlier description can also be found in.[2]

3.1. *Hierarchy and Finite State Machine*

The control systems of all LHC experiments reflect detector and hardware in a hierarchical structure. Autarkic functioning sub parts can be included or excluded in the given hierarchy. An excerpt of the Tracker hierarchy is shown in Fig. 3. All commands travel down the hierarchy, while information and error messages are reported upwards. The main TOP FSM node is the CMS node followed by the sub detectors Muon, HCAL, ECAL and the Tracker. The Tracker itself is again divided into TIB, TOB, TECplus and TECminus, the next children are the 132 cooling loops and TEC sectors, which father the 356 control groups. The lowest units are the 1944 power groups representing one power supply with two low voltage and two high voltage channels each. Thus, this hierachy then controls 8132 channels

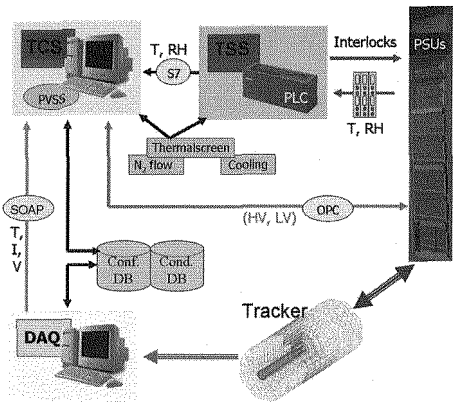

Fig. 2. *A simplified scheme of hardware and corresponding dataflow is given above.*

in total with an overall number of OPC address items of 180000. Major sub detectors routines are running on a supervisor PC, while cooling loop's programs and their corresponding children are distributed on four PCs to share load. The concept is based on defined transitions from finite state to

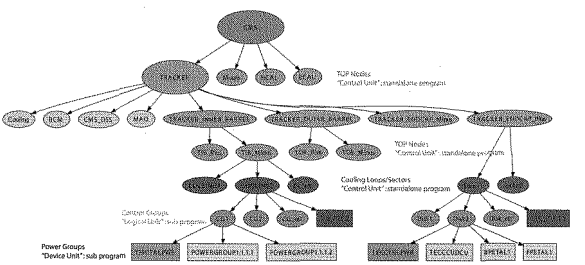

Fig. 3. *An excerpt of the tracker hierarchy is shown. The main node CMS is followed by the CMS sub detectors, here the tracker. The TOP node's (TEC+, TEC-, TIB, TOB) states are used to enable the corresponding HLT. The further distinction in plus and minus represents connectivity schemes. The 132 cooling loops and sectors are the lowest standalone programs, so called control units, in the hierarchy, distributed on four computers. The 356 control groups are sub routines, so called logical units. The device units are representing the power supply channels.*

finite state, true for all types of elements of the hierarchy. The state machine is implemented in the SMI++[3] language. The hierarchical approach facilitates summary information, especially error reporting of sub nodes and summary commanding to large parts of the detector. Also inclusion

and exclusion of detector parts is manageable in a defined way. In addition, the high level trigger (HLT) needs clear discrete states of the sub detector parts TEC+, TEC-, TIB and TOB.
The basic software building block is the professional SCADA software PVSS by ETM. It has been extended by CERN to a framework to adjust it for the LHC project's needs and to gain from experiment's developments. PVSS allows archiving of values and treatment of alarms, warnings and error messages. All controls are restricted by access handling.

3.2. *Majority Voting*

The simple approach of a discrete FSM will not be sufficient in some cases during normal detector operation. The reason is, that its current implementation generates mixed states in the parent node when at least one node is in a different state from the siblings nodes, causing the tracker being not-on when only one power supply is switched off or being in error when only one is in error. This behaviour is unwanted since the tracker should stay operable and continue taking data also with a small fraction of the tracker being off or in error.
The solution is a majority voting algorithm that counts the numbers of all power supply status in any level of the FSM hierarchy online. A simple mechanism that propagates any change up through the whole FSM hierachy would overload the system. To solve this performance issue, at each node, changes are collected during a specific timeout and then propagated up as a sum of changes. Data integrity is cared for by synchronizing access to node data from different threads, which is possible since PVSS version 3.6.

References

1. Gian Mario Bilei, Status of the CMS Silicon Tracker and cosmic test results & Guido Dirkes, Construction of the CMS silicon strip tracker, NIM A 581 (2007) 299-302
2. M. Frey for the collaboration, The CMS-tracker detector control system. Published in *Como 2005, Astroparticle, particle and space physics, detectors and medical physics applications* 1067-1071
3. SMI++ object oriented framework for designing and implementing distributed control systems / Franek, B J; Gaspar, C 1998 - Published in: IEEE Trans. Nucl. Sci. 45 (1998) 1946-1950
4. L. Masetti et. al., The CMS Tracker Control System, to be published in Canada in Journal of Physics: conference series (Conference Proceedings of CHEP 2007, Victoria)

The Message Reporting System in the ATLAS DAQ System

M. Caprini

National Institute of Physics and Nuclear Engineering, Bucharest, Romania

I.Fedorko*

CERN, Geneva CH-1211, Switzerland
** Corresponding author E-mail: ivan.fedorko@cern.ch*

S.Kolos

University of California, Irvine, California, USA

The Message Reporting System (MRS) in the ATLAS data acquisition system (DAQ) is one package of the Online Software which acts as a glue of various elements of DAQ, High Level Trigger (HLT) and Detector Control System (DCS). The aim of the MRS is to provide a facility which allows all software components in ATLAS to report messages to other components of the distributed DAQ system. The processes requiring a MRS are on one hand applications that report error conditions or information and on the other hand message processors that receive reported messages. A message reporting application can inject one or more messages into the MRS at any time. An application wishing to receive messages can subscribe to a message group according to defined criteria. The application receives messages that fulfill the subscription criteria when they are reported to MRS. The receiver message processing can consist of anything from simply logging the messages in a file/terminal to performing message analysis. The inter-process communication is achieved using the CORBA technology. The design, architecture and the used technology of MRS are reviewed in this paper.

Keywords: ATLAS, DAQ, Online software, Message Reporting System

1. Introduction

The ATLAS experiment [1] is designed to observe the outcome of collisions between protons of 7 TeV provided by the Large Hadron Collider (LHC), which will start to operate in 2008 at CERN and deliver collisions at a rate

of 40MHz. The designed luminosity value is $10^{34} cm^{-2} s^{-1}$. ATLAS experiment covers huge spectrum of physics research with main focus on Higgs boson and supersymetry search and precise measurement of W-boson and t-quark. Atlas records about 2MB of information per event at rate of ~200 events per second. The event selection is performed via a three-stage trigger system. The first level is based on custom-made electronics. The second and third level are software triggers. The ATLAS DAQ [2] system is composed of ~ 25000 applications running on more then 2600 interconnected computers. The Online Software as a part of the DAQ is responsible for configuring, controlling and monitoring the data taking system, provides many services to DAQ and detectors system, is responsible for synchronization of entire system and supervision of processes. For diagnostic purpose applications inform about their states or report error condition and Online Software has to provide transport mechanism for such messages. Due to fact that ATLAS DAQ is a large distributed system the transport system has to offer also sufficient scalability. The Message Reporting System facility, as a part of Online Software, is providing the means to exchanging unique information and error messages across different DAQ applications.

2. System architecture

2.1. *General view*

The MRS system is responsible for transport, distribution and filtering of messages. It has been designed following the client-server paradigm. The processes of the DAQ requiring service of the MRS are on one hand applications that report specific information or error conditions and on the other hand message processors that receive reported messages. A message reporting application can inject messages into the MRS at any time. The message is composed of the message name, the severity, optional text, parameter values, optional parameter values, qualifiers (time stamp, process ID, etc.) and optional qualifiers. An application wishing to receive messages can subscribe to a message group according to criteria based on logical expression of the message name, severity and qualifiers. The application receives messages that fulfil the subscription criteria when they are reported to MRS. The MRS server can receive messages from one or more MRS senders. It searches the MRS message database (MD) for the message name. After a successful search the corresponding database information is added to the message instance. If the message is not found in the database, the information as received from the sender is passed to the client. Using of MD

provides centralized message content management and reduce amount of data sent over the network. The MRS server keeps a list of subscribed applications, the receivers, and their corresponding subscription criteria. In the server can be set a filter to stop reporting messages of a set of messages, according to the filter criteria. If the message has passed the filter then it is distributed to those receivers in this internal list, which have matching subscription criteria. The client library, which is used by processes to send and to subscribe to messages, which has been issued by other processes, is implemented in C++ and Java while the server side has been implemented in C++. The inter-process communication is achieved using the CORBA technology [3].

2.2. *System implementation*

The MRS server has been initially implemented as a single Linux process, dealing with the reception of all messages and their redistribution to any subscribers. Nevertheless, the large number of applications involved in the DAQ, combined with the need of publishing many messages during the debugging phase of the experiment, has led recently to a complete redesign of this part of the MRS. The server functionality has been distributed over a publicly accessible MRS server process and a variable number of private MRS workers which are performing the actual work of receiving each a sub-set of the messages and to forwarding them to the subscribers. The number of installed private servers can be adjusted according to the size and complexity of the DAQ system and the required message throughput. Having been started up the private MRS servers join the public MRS server sending a handle (self handle) which can be used later to access the methods of the private MRS servers.

The sender API provides the MRS stream interface and offer possibility to create MRS message by user. In the ATLAS DAQ the error reporting is done using the Error Reporting System (ERS) package. Output from ERS can be linked to MRS stream and the MRS is used as transport mechanism of the ERS messages. A user application wishing to report messages has to connect to the public MRS server via the MRS sender API and get handle to a particular private MRS server. Therefore the message will automatically be sent directly to the private MRS server. For the case where the MRS server is not present in the system, the MRS sender writes the message to a local log file. An application wishing to receive messages must subscribe to the public MRS server with the help of the MRS receiver interface. Subscription includes the request to receive messages, implemented as a call-

back mechanism, and the subscription criteria. The public MRS server then transmits this subscription to all private servers. All private MRS servers report any corresponding message directly to the MRS receiver application interface (MRS receiver API). When an application wants to unsubscribe from a particular message group it sends this request in the same way to the public MRS server, which transmits it to all the private MRS servers. The DAQ expert can initiate set of command via the MRS command API, e.g. command can adjust the filter criteria for messages on their way through the private MRS servers.

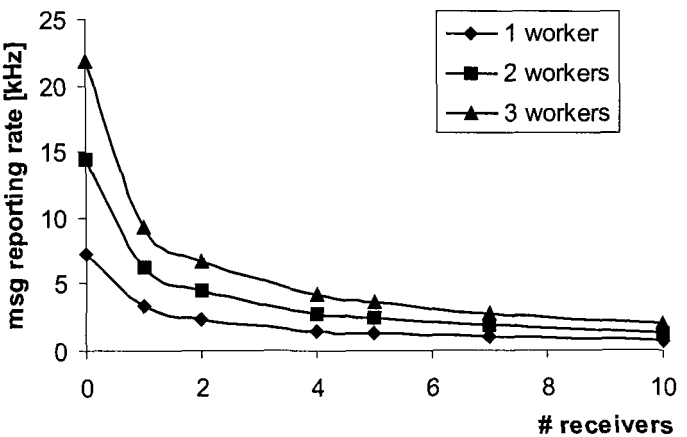

Fig. 1. The average message reporting rate as a function of number of subscribed receivers. The throughput of the system growths with number of the active private servers.

3. Performance

The functionality tests showed that the implementation of the MRS library fulfils the test requirements and that the component functionalities correspond to the specification. The MRS system is regularly used during commissioning phase and proved that the MRS is able to fulfil expected functionality and reliability. With latest version of system we measured mean message reporting time for a distributed configuration. The servers, senders and receivers are running at different machines to emulate condi-

tions as used in final DAQ system. For configuration when one public server and one private server are running on the same machine (4-core Intel Xeon CPU 3GHz, 2GB RAM), no receiver subscribed, and applications sending typical message at maximum rate we measured average message reporting rate at the server with a value of ~9kHz. For more parallel sending applications the saturation value was observed at ~17KHz. For the scalability test the private servers have been distributed on separate machine of the same type (2-core Intel Xeon CPU 2GHz, 500MB RAM). Applications sending messages at maximum rate were running on PCs with 2-core Intel Xeon CPU 3GHz and 500MB RAM. For the receivers were used PCs with 1-core Intel Xeon CPU 3GHz and 500MB RAM and reported message was written to file. The good scalability in expected range of active receivers was observed, see Fig 1.

4. Conclusion

We reported the design and implementation of the Message Reporting System as a part of the DAQ Online Software. The aim of the MRS is to provide a facility which allows all software components in the ATLAS DAQ system and related processes to report messages to other components of the distributed DAQ system. The MRS provides the functionality to transport, to filter and route messages. Usage of the MRS during detector and trigger commissioning phase demonstrated expected system functionality and usage of design with public and private servers provide requested scalability.

References

1. ATLAS Collaboration, Detector and Physics Performance Technical Design Report, CERN/LHCC 99-14/15,CERN, (Geneva, Switzerland, 1994).
2. High-Level Trigger Data Acquisition and Controls, CERN/LHCC/2003-022, (CERN, Geneva, Switzerland, 2003).
3. R. Jones *at al*, Applications of CORBA in the ATLAS prototype DAQ, IEEE Transactions on Nuclear Science, volume 47, Issue 2, Part 1, (April 2000), Page(s):244 - 249.

MANAGEMENT OF EQUIPMENT DATABASES AT CERN FOR THE ATLAS EXPERIMENT*

KAIO KARAM GALVÃO
CERN, Geneva, Switzerland
Federal University of Rio de Janeiro, Brazil

KATHY POMMÈS, JORGE MOLINA-PÉREZ
CERN, Geneva, Switzerland

CARMEN MAIDANTCHIK, FELIPE FINK GRAEL
Federal University of Rio de Janeiro
Rio de Janeiro, Brazil

The ATLAS experiment is about to finish its installation phase, entering into operation on the summer of 2008. This installation has represented an enormous challenge in terms of developing, setting up, and administrating the Equipment Databases, due to the large complexity of the detector, its associated services, and the necessary infrastructure. All major equipment is registered prior to installation including its electronic description and interconnectivity. This information is stored in Oracle databases. 3D visualization tools, user interfaces for portable devices, and generic retrieval/updating mechanisms have been developed in order to carry out the management of the sub-detectors databases. The full traceability of all installed equipment is crucial from ATLAS organizational point of view, and it is also a requirement by the French authorities to fulfill the INB (*Installation Nucléaire de Base*) protocol.

1. Introduction

ATLAS is one of the four experiments under construction to be operated with the Large Hadron Collider (LHC) at CERN [1]. The detector consists of four major subsystems: inner tracker, electromagnetic and hadronic calorimeters, muon spectrometer and magnet system [2]. The outer dimensions of the barrel-shaped detector are 46 m in length and 22 m in diameter [3], and it is located 100 m underground. More than 93000 items compose the overall detector, which are manufactured all over the world by research institutes and the industry. The ATLAS Technical Coordination is responsible for the final installation at CERN.

* This work is run by the ATLAS Technical Coordination.

The main activities of this process are: assure that the sub-detector and off-detector electronics objects are assembled in the correct positions; implement and maintain the connection between the front end and back end electronics; realize survey measurements to monitor the sub-detector parts displacements from their nominal positions.

During the production and installation phases, each sub-system stores large amounts of data under different modeling schemes. Individual database solutions are implemented with distinct storage technologies. The successful installation of the experiment depends critically on organizing the equipment information. This involves sharing data in an easy and transparent way, as well as integrating related information located in multiple repositories.

2. Equipment databases management

Databases are established to register and maintain equipment information. Figure 1 shows the general concept employed in the databases definition. Every physical object going to the underground area is called *equipment*. A *functional position* represents a function to be fulfilled by an equipment [4]. The following rules apply: only functional positions are cabled; functional positions are not moved; equipments can be moved; history is kept for both equipments and functional positions.

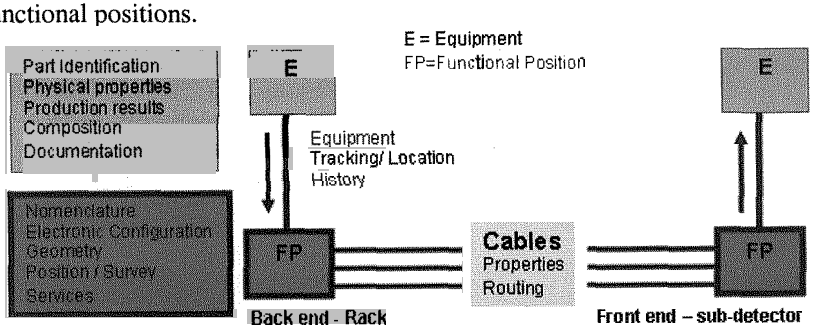

Figure 1. Equipment management general concept.

The Technical Coordination and subsystems leaders are responsible for filling in the information into the databases for every unit they plan to install and its associated functional position. The Web is the common access platform for this data. Access through handheld devices is also provided. Next, the equipment databases are described, together with the software tools managed by Technical Coordination to interact with the information.

2.1. *Manufacturing and test folder*

All equipment installed in ATLAS, up to the board level, is labeled and entered into an Oracle database through the Manufacturing and test folder (MTF). The MTF application [5] is used in ATLAS for equipment inventory. MTF underlies on D7i, a commercial database from Datastream [6] used for maintenance management and asset tracking. Within MTF, each item has a unique ID corresponding to its serial number, which is referenced in the Functional Positions database.

2.2. *Rack Wizard*

The Rack Wizard [7] is a Java tool, firstly developed for the CMS experiment at CERN, used to manage the substantial amount of electronics used in the ATLAS experiment. It offers a graphical view of the off-detector electronics layout in a drag and drop style. It stores in an Oracle database the electronics configuration and location of each functional position. The interconnectivity between the back end and the front end objects is done through access to the cable database.

2.3. *AtlasEditor3D*

The AtlasEditor3D [8] is a graphical software tool, implemented in Java3D, used in the management of equipment geometry and positioning. It allows the synthesis of the ATLAS detector starting from 3D shapes, such as boxes, tubes, cones, and trapezoids. This tool supports the sub-detector objects registered in the database, together with their geometrical properties and nominal positions. It is integrated into Rack Wizard.

2.4. *Cable Database*

The Cable Database contains data on interconnectivity between the back-end racks and the sub-detector objects. It stores on Oracle information to support the cable installation team (e.g. purpose, physical characteristics, routing, start-point, endpoint, and status of each cable). The Cable Interface [9] runs also on handheld devices, allowing users to update the Cable Database while working in the ATLAS underground area.

2.5. *Survey Database*

A large amount of survey data is being accumulated during sub-detectors integration and installation. This survey data is stored into an Oracle database to monitor existing displacements of the sub-detectors objects from their nominal

positions in the ATLAS Interaction Point reference system. This information is displayed through the Java3D tool AtlasSurvey3D [10], which shows a 3D visualization of the sub-detectors and axis deviations.

2.6. *The Glance Project*

The Glance [11] interacts to all the equipment data stored in Oracle databases. This system manages interface descriptions stored using the XML markup language. It provides data retrieval and insertion/update engines on distinct and geographically spread repositories. The system connects to several storage technologies, such as Oracle, MySQL and Microsoft SQL Server. Glance automatically recognizes and displays to the user the internal structure of the databases. It allows the creation of customized Search Interfaces (SI) and Insertion Interfaces (II), without the necessity of previously knowing the data modeling of each data set. Each interface can integrate information sets coming from multiple data sources. Retrieved information can be delivered to the requester in different formats, such as HTML, XML and CSV. Glance has a user Web interface and can also be accessed by other software applications.

3. Results

The MTF database stores records from more than 93000 equipment parts located in the experimental cavern. This data is accessed via 10 Search Interfaces created with the Glance system. About 4000 items were inserted in this database in the last 6 months, with the support of 10 Glance Insertion Interfaces.

The Functional Positions database contains data on 670 racks, 15000 crates/boards, 13000 sensors, and others. This information is managed by the Rack Wizard and also retrieved by 17 Glance Search Interfaces. The Cable database holds information regarding 55600 cables. The Glance system exports all the cable data in an interval of time of less than 30 seconds.

People from the 164 institutes in more than 35 countries participating in the ATLAS collaboration [2] interact with all this data in a transparent way using the software tools previously described.

4. Conclusions and future work

The ATLAS detector, as soon as it enters into operation, must satisfy the French government requirements for the INB (*Installation Nucléaire de Base*) protocol. That means guaranteeing the traceability and history of all the equipment exposed to radiation. Therefore, some data will be required on a long-term basis

to track the movement of equipment in and out of the experimental cavern throughout the life of ATLAS.

Besides fulfilling the INB requirements, the Equipment Databases are used by the Technical coordination and sub-detectors groups during the integration and installation phases of the experiment, and will in many cases be used to initialize other databases, e.g. the online configuration and conditions databases.

The off-detector systems, such as trigger and data acquisition systems, rely on the cabling information. Cabling updates are entered into the database using a barcode reader, and this data will then be exported to the online configuration/conditions databases, allowing channel mapping information to be automatically updated in the online and offline software. This facility is particularly important during the commissioning phase, when many re-cabling operations are expected.

Analyses and calculations are performed on the acquired data relatively to the ATLAS Interaction Point reference system. The Survey data is used to verify that such displacements will not affect the experiment results.

References

1. A. Salzburger, "TRACK EXTRAPOLATION WITH INTRINSIC NAVIGATION IN THE NEW ATLAS TRACKING SCHEME", Paper presented at 9th ICATPP Conf. 2005, Como, Italy.
2. The ATLAS Experiment, http://atlas.ch/
3. H.J. Burckhart and B. Hallgren, "Front-end I/O of the ATLAS Detector Control System", Paper presented at ICALEPCS'99, Trieste, Italy.
4. K.Pommès, M. Sharpp, F.Dittus, J-C. Guillaume, "Equipment Registration Conventions" https://edms.cern.ch/cedar/plsql/doc.info?document_id=345996&version=1.
5. C. Delamare, A. Jimeno, S. Mallón Amérigo, E. Manola-Poggioli, P. Martel, B. Rousseau, D. Widegren, "MANUFACTURING AND TEST FOLDER: MTF", Proceedings of EPAC 2002, Paris.
6. Enterprise Asset Management Software, http://www.datastream.net/
7. F. Glege, "The Rack Wizard - a graphical database interface for electronics configuration", Paper presented at LECC 2003, Amsterdam.
8. K. Pommès, J. Molina-Pérez, AtlasEditor3D; http://cern.ch/AtlasEditor3D/
9. F. Glege, K. Pommès, J. Molina-Pérez, Cable Interface, https://oraweb.cern.ch/pls/atlasintegration/EMT_main.main_menu
10. K. Pommès, J. Molina-Pérez, AtlasSurvey3D, http://cern.ch/AtlasSurvey3D/
11. C. Maidantchik, F. F. Grael, K. K. Galvão, K. Pommès, "Glance Project: a database retrieval mechanism for the ATLAS detector", Proceedings of CHEP 2007, Victoria BC, Canada.

GEANT4 PARAMETRIZATION AND MODELING OF PION PRODUCTION IN PROTON-NUCLEUS INTERACTIONS BASED ON HARP EXPERIMENTAL DATA: INCIDENT PROTON MOMENTA ARE FROM 3 GEV/C TO 12.9 GEV/C

SIMONE GIANI[†], VLADIMIR IVANCHENKO, JAAP PANMAN
CERN
Geneva, 23, CH1211, Switzerland

VLADIMIR GRICHINE
Lebedev Physics Institute
Moscow, 53 Lenin Prospekt, 117924, Russia

Expeimental data of HARP (the hadron production experiment at CERN-PS, PS214) describing inclusive spectra of pions produced in proton-nucleus interactions in the momentum range 3-12.9 GeV/c were compared versus Geant4 model predictions. No special tuning of Geant4 models was done. In addition the data were parameterized in the form suitable for Geant4 and their parameterization is proposed to be used in Geant4 hadron generators.

1. Introduction

The HARP experiment [1] was designed for systematic study of hadron production for beam momentum range 1.5 – 15 GeV/c. The results of the measurements of the double differential inclusive production cross sections of pions were published elsewhere [2-5]. The typical accuracy of the obtained cross sections is about 10%. The data of HARP have been already used for decreasing the systematic uncertainty on the neutrino oscillation result by K2K [6] and will affect Neutrino Factory physics studies. These data are relevant to many HEP experiments at LHC and ILC. The Geant4 toolkit [7] is adopted as a main simulation engine for future LHC experiments and is used in many other applications. The systematic comparison between HARP data and Geant4 predictions allows validation of Geant4 hadronic generators and provides feedback to hadronic models developers. In the current work we show

[†]simone.giani@cern.ch

comparison results without tuning of released Geant4 models (run prior to HARP data publication).

2. Comparison of HARP data and Geant4 generators

For the validation and comparison of Geant4 hadronic generators with HARP data a special software package has been developed [8]. The following Geant4 models have been used for comparisons:

- the Low Energy Parameterized model (LHEP) [9];
- the Binary cascade (BIC) [10];
- the Bertini cascade (BERT) [11, 12];
- the Quark-Gluon String model with the PreCompound model backend (QGSP) [11, 13];
- the Quark-Gluon String model with the CHIPS generator backend (QGSC) [11, 14];
- the Fritiof fragmentation model with the PreCompound model backend (FTFP) [13].
-

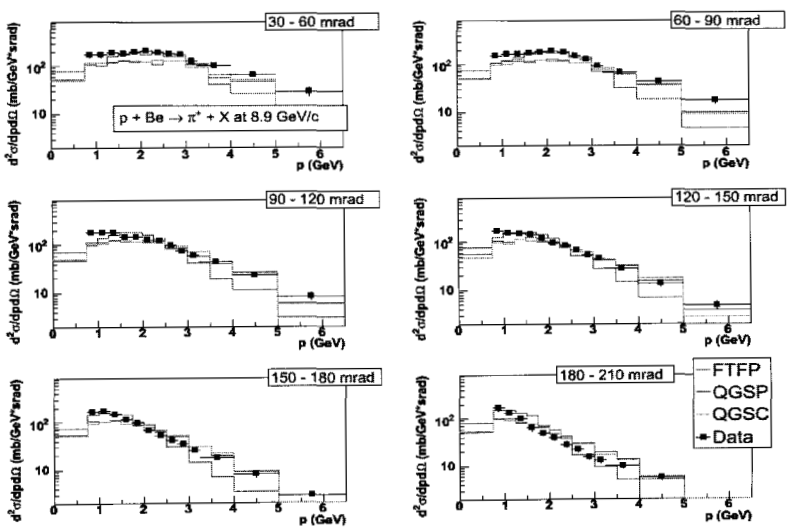

Figure 1. The forward inclusive production cross sections of π^+ by 8.9 GeV/c proton beam off Be target [3] are compared with Geant4 string models FTFP, QGSP, QGSC. Geant4 version 9.0ref01.

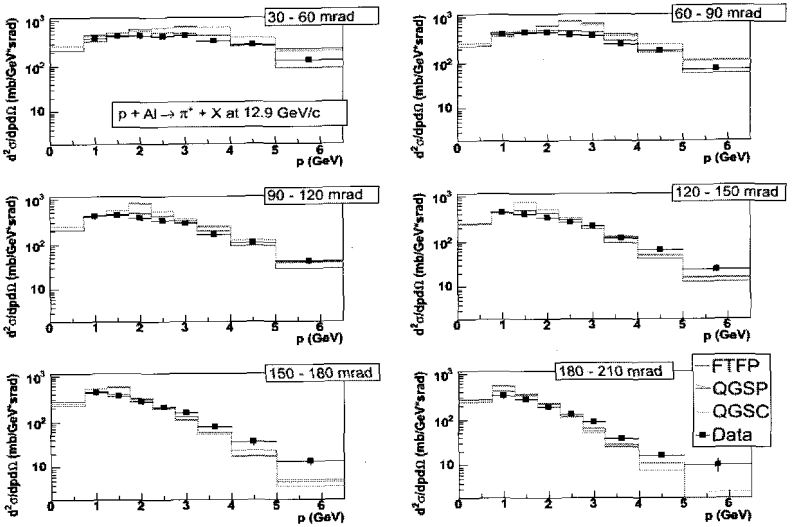

Figure 2. The forward inclusive production cross sections of π^+ by 12.9 GeV/c proton beam off AL target [2] are compared with Geant4 string models FTFP, QGSP, QGSC (Geant4 version 9.0ref01).

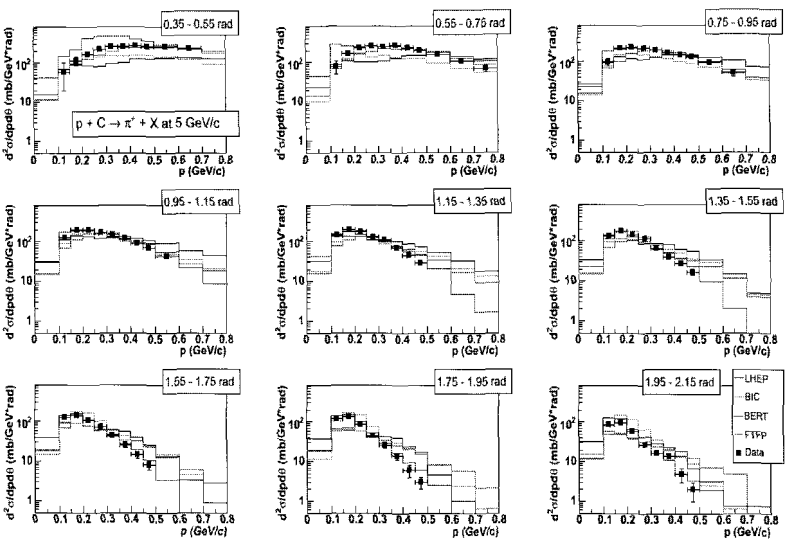

Figure 3. The comparison of the data [5] and different Geant4 models (version 9.0) for the large angle inclusive production of π^+ in carbon target by 5 GeV/c proton beam.

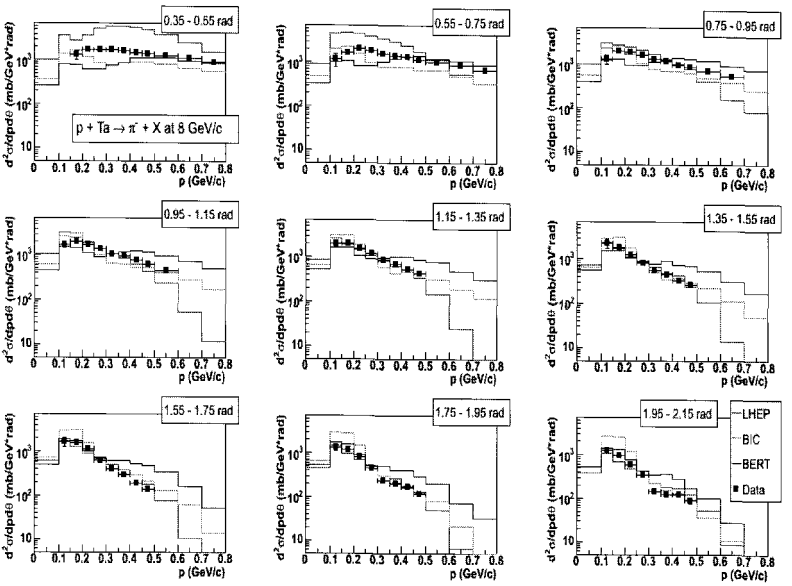

Figure 4. The comparison of the data [4] and different Geant4 models (version 9.0) for the large angle inclusive production of π^- in tantalum target by 8 GeV/c proton beam.

For the forward π+ production in the beryllium target at 8.9 GeV/c (Fig.1) FTFP model shows the best agreement for pions up to about 3 GeV/c, while QGSP and QGSC describe the tail of the pion distribution above 4 GeV/c more accurately. FTFP shows very precise agreement for forward π+ production in the aluminum target at 12.9 GeV/c (Fig.2). For large angle production in the carbon target at 5 GeV/c (Fig.3) FTFP is still working well for pion momenta up to 400 MeV/c, the cascade models are on average applicable, and LHEP gives the best description of the pion distribution tail above 400 MeV/c, in particular for angles greater than 1.15 rad. Finally, the BIC cascade model provides the most adequate spectra for large angle production in tantalum at 8 GeV/c (Fig.4), showing precise agreement with the data at different pion momenta and angles.

3. Sanford-Wang parameterization

The Sanford-Wang parameterization [15] was used for evaluating HARP forward pion production data [2, 3]. We extend the scope of this parameterization by fitting HARP data at large angles (Fig.5). As a result the parameterizations are provided for different targets and projectile beam. This multi – parameters fit was found to be the most stable using PAIDA fitting [16].

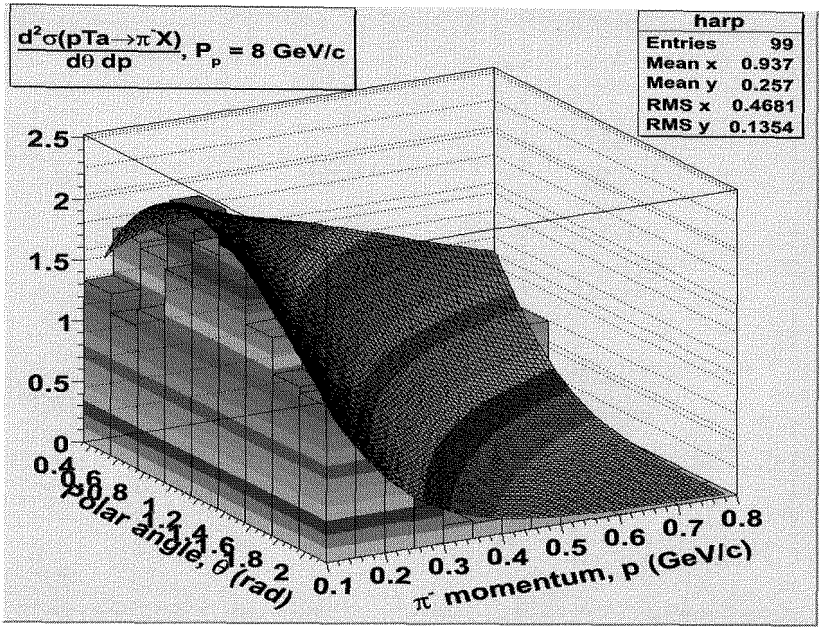

Figure 5. The profile view of the result of the parameterization of the double differential inclusive production cross section of π^- in tantalum target by 8 GeV/c proton beam [4].

4. Conclusions

The results of systematic comparisons of HARP data and Geant4 hadronic models are shown for Geant4 version 9.0. Agreement between at least a suitable Geant4 model and experimental data is observed in general without special tuning of such models, confirming that Geant4 simulation can be used in predictive mode for simulation in HEP. The parameterization provided in this work also allows a direct use of HARP data in Geant4 models.

References

1. M. G. Catanesi et al., *Nucl. Instrum. Meth. A* **572** 899 (2007).
2. M. G. Catanesi et al., *Nucl. Phys. B* **732** 1 (2006).
3. M. G. Catanesi et al., hep-ex/0702024
4. M. G. Catanesi et al., *Eur. Phys. J. C* **51** 787 (2007).
5. M. G. Catanesi et al., *hep-ex/0709.3464, Submitted Eur. Phys. J. C*
6. M. H. Ahn et al., *Phys. Rev. D* **74** 072003 (2006).

7. S. Agostinelli et al. *Nucl. Instrum. Meth. A* **506** 250 (2003).
8. V. N. Ivanchenko and A. Ivantchenko, *CHEP'07, poster #283*
9. D. H. Wright et al., *AIP Conf. Proc.* **867,** 479 (2006).
10. G. Folger et al., *Eur. Phys. J.* A **21** 407 (2004).
11. D. H. Wright et al., *AIP Conf. Proc.* **896** 11 (2007).
12. A. Heikkinen et al., *CHEP-2003-MOMT008, physics/0306008*
13. G. Folger et al., *CHEP'03: CHEP-2003-MOMT007, physics/0306007*
14. P. V. Degtyarenko et al., *Eur. Phys. J.* A **8** 216 (2000).
15. J. R. Sanford and C. L. Wang, *Phys. Rev. Lett.* **25** 1068 (1970).
16. http://paida.sourceforge.net/

ENVIRONMENTAL RADIATION DOSE ON THE MOON

K. HAYATSU, S. KOBAYASHI, N. YAMASHITA, M. HAREYAMA, K. SAKURAI, AND N. HASEBE

Research Institute for Science and Engineering, Waseda University, 3-4-1 Okubo, Shinjuku, Tokyo 169-8555 Japan

Ambient dose equivalent on the lunar surface is estimated as contribution from galactic cosmic rays, secondary neutrons and γ rays from the lunar surface. Since the cosmic ray flux on the lunar surface varies with the phase of the solar activity, radiation doses on the surface are calculated of the three cases of this activity; the maximum, the minimum and the average. To estimate the doses of the secondary particles, Monte Carlo simulation library Geant4 is applied. As a result, total annual dose equivalent of about 225 mSv/yr on the lunar surface is expected during the quiet time of solar activity. The dose of neutrons and γ rays reaches to 50 mSv/yr and 2 mSv/yr, respectively. In particular, fast neutrons have the largest contribution to the total neutron dose. The dependency of total neutron dose for mare and highland region of the Moon is small on the lunar surface as comparing with that for solar activity.

1. Introduction

Human activities on the Moon are expected to begin with the construction of lunar bases in the near future. Before the beginning of these activities, it is necessary to survey the environmental condition as related to background radiation over the lunar surface. The environment condition on the lunar surface is much different from that on the Earth's surface because neither atmosphere nor magnetic field is existent over the Moon. This means that the lunar surface is always exposed to the direct bombardment of galactic cosmic rays (GCRs). GCRs generate nuclear cascade in thick lunar soils and effectively produce neutrons and γ rays. A part of those neutrons and γ rays leak from the lunar surface. However, the doses of such secondary particles were not considered in detail because of complicated processes of nuclear reactions.

In this work, thus complicated production and transportation of secondary neutrons and γ rays in the Moon are calculated by the Geant4 code improved by Yamashita et al. [1]. The original code has a lot of difficult problems to satisfactorily reproduce such line γ ray for the application of the planetary γ ray spectroscopy. However, this problem was overcome by introducing new nuclear data such as inelastic scattering cross sections of neutrons from JENDL-3.3 [2] and branching ratios of nuclides after neutron capture reactions [3] to the calculation code. Finally, a quantitative study of the dose on the lunar surface

during solar quiet period of the solar activity is studied for lunar habitants, by taking not only contribution from primary GCRs into account, , but also from the secondary neutrons and the γ rays produced by primary GCRs. In particular, we focus the doses of those secondary particles in this paper.

2. Method for Calculating Ambient Dose Equivalent on the Moon

2.1. *Radiation dose on the Moon*

In order to estimate the dose on human from space radiation on the Moon, we calculate an ambient dose equivalent, $H^*(10)$ [Sv], which is defined as a dose at depth of 10 mm in the ICRU sphere. Total ambient dose equivalent on the Moon is defined as

$$H^*(10)\ [\mathrm{Sv}] = H^*(10)_{GCR} + H^*(10)_N + H^*(10)_\gamma \qquad (2\text{-}1),$$

where $H^*(10)_{GCR}$ [Sv] represents a contribution from GCRs and $H^*(10)_N$ and $H^*(10)_\gamma$ represents a contribution from neutrons and γ rays on the lunar surface, respectively. Each $H^*(10)$ is calculated from each fluence on the lunar surface and its quality factor or conversion factor [4]. GCR fluence at the Moon is assumed based on the empirical formula given by the references [5,6] for proton and helium, which include the dependency of solar cycle activity, and the GCR abundance given by Simpson [7] for heavy ions. The fluence of leakage neutrons and γ rays on the lunar surface are calculated by the Geant4 code as described in next section.

2.2. *Production and transportation of secondary particles in the lunar subsurface*

Penetrative GCRs to the lunar surface interact successively with lunar material and produce many secondary particles such as neutrons and continuous γ rays. These secondary neutrons also produce line γ rays by inelastic scattering or neutron capture of various nuclei in the lunar soil. These line γ rays also produce continuous γ rays by Compton scattering in the lunar soils.

The intensities of GCR-induced neutrons and γ rays on the lunar surface are calculated numerically by simulating their production and transportation in the Moon using a Monte Carlo simulation library Geant4 release 8.0.p01 [8] with the modified nuclear data library G4NDL3.9 [1] and the hadronic interaction model called QGSP_BERT_HP. In the Monte Carlo calculations, the lunar subsurface is modeled as 50 x 50 x 50 m^3 cubes, whose center on a surface is isotropically irradiated with only GCR protons with an energy spectrum [5,6]. The cubes are composed of materials with average composition of soils found at each landing site of Apollo 11 in typical mare region or Apollo 16 in highland

region relatively far from mare region [9]. The materials at mare is mainly composed of basalt which are rich in Fe and Ti, while highlands is mainly composed of ferroan anorthosite (FAN) rich in Al and Ca. Fe and Ti have a large cross section of neutron production and thermal neutron capture as compared with Al and Ca as shown in Table 1 [10]. Thus, as shown in Fig.1 calculated by Yamashita et al. [1], it is expected that fast neutrons will leak larger in mare region (A11) at the lunar surface than that in highland region (A16). Leakage neutron and γ rays on the surface are counted in each energy bin and then their fluences are calculated. The neutron fluence at the highland region on the lunar surface is shown in Fig. 2.

Table 1. The capture cross section at thermal neutron and the production cross-section at 3 GeV proton for Al, Ca, Ti and Fe.

	capture cross-section at thermal neutron (mbarn)	production cross-section at 3 GeV proton (mbarn)
Al	231	902
Ca	431	1398
Ti	6080	2279
Fe	2560	2522

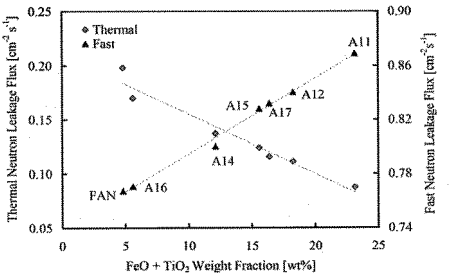

Figure 1. Leakage fluxes of fast and thermal neutrons as a function of the weight fraction of FeO and TiO_2.

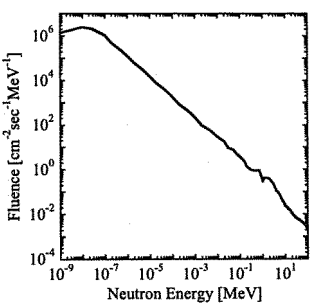

Figure 2. Energy spectrum of neutrons emitted from lunar surface. Apollo 16 soil sample is targeted in Monte Carlo simulation. Irradiated particle is proton at solar average flux.

To take contribution of production from GCR particles heavier than proton into account, the production rate of neutrons and γ rays by proton are multiplied by 1.5 [11]. The γ ray dose from the natural radioactive isotopes is assumed to be the same as that on the Earth; it is 0.48 mSv/yr [12].

3. Results and discussion

The ambient dose equivalents on the lunar surface are shown in Table 2 under the condition of the solar minimum, average and maximum in highland

region and of the solar average in mare region. An annual dose equivalent to the human is about 225 mSv/yr on the lunar surface at the solar average, which is approximately 90 times as large as natural dose on the Earth of about 2.4 mSv/yr. The neutron doses are divided three energy regions based on their interactions with matter; thermal (< 0.4 eV), epithermal (0.4 eV < E < 1 MeV), and fast (> 1 MeV). The contribution of neutron dose is about 23~24% in the total dose and that of γ ray dose is about 1~2 % in the total dose. Therefore the dose of secondary neutron on the Moon is not ignored, while the dose from γ rays is not so important.

Table 2. The ambient dose equivalents on the lunar surface.

particle	H*(10) [mSv/yr] in highland (A16)			in mare (A11)
	Solar Min.	Solar Ave.	Solar Max.	Solar Ave.
Fast neutron	52.9	37.8	18.5	40.2
Epithermal neutron	19.6	13.9	6.8	16.0
Thermal neutron	0.35	0.24	0.13	0.15
Neutron total	72.9	51.9	25.4	56.3
GCR	233.8	168.6	65.8	168.6
Gamma ray	3.3	2.5	1.6	2.5
total	310.0	223.0	92.8	227.4

Neutron dose versus its kinetic energy is presented in detail in Fig.3. The conversion coefficient [Sv/ $sec^{-1}cm^{-2}$] at the energy range between 1 and 100 MeV neutron is a few orders of magnitude larger than the other energy region [4] Neutron fluence in unit of $cm^{-2}s^{-1}$ is also larger in fast region than that in thermal and epithermal region as estimated from Fig.2. Therefore, fast neutrons largely contribute to the total neutron dose as shown in Table 2.

As expected in the previous section, the dose of fast neutrons in mare is larger than that in highland, while opposite situation is appeared in the thermal neutron. This is due to the dependency of lunar soil composition. In fact, neutron fluences in both local lunar soils are clearly different from each other as shown in Fig.4, in particular for thermal neutron. Moreover, neutron fluences in the Moon are larger than those on the surface. These results suggest that the neutron dose is rather important for human activity under the lunar surface such as lunar bases. However this dependency is negligible on the lunar surface as comparing with that for solar activity.

The variation of total neutron dose for solar activity is a little bit smaller than that of GCRs. This is due to the reasons that the cross section of neutron production for proton projectile is effectively large in GeV energy region and the solar modulation effect for GeV GCRs is relatively smaller than those for sub-GeV GCRs, though sub-GeV GCRs are the most abundant in energy spectrum of GCR proton.

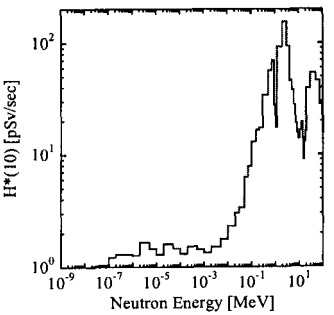

Figure 3. Ambient dose equivalent of neutron. Apollo 16 soil sample is targeted in Monte Carlo simulation. Irradiated particle is proton at solar average flux.

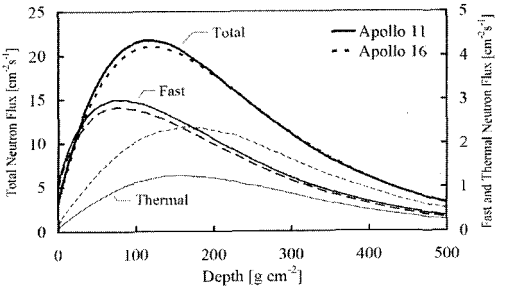

Figure 4. Distribution of calculated neutron flux within the subsurface of the Moon. In this figure, the energy of fast neutron is more than 1 MeV, and that of thermal neutron is below 0.4 eV.

4. Conclusion

The dose effect of space radiation for the human activity on the Moon calculated numerically with precisely contribution from secondary products by the improved Geant4 code. Total annual dose equivalent to the human on the lunar surface is expected as about 225 mSv/yr during the quiet time of the average phase of solar activity. The total neutron dose is about 23 % in total dose; in particular, fast neutrons have most contribution to the total neutron dose. The variation of total neutron dose for mare and highland region is negligible on the lunar surface as comparing with that for solar activity.

5. Reference

1. Yamashita, N. *et al., Earth Planets Space* (2007) submitted.
2. Shibata, K. *et al., J. Nucl. Sci. Technol.* **39**, 1125 (2002).
3. Reedy, R. C. and S. C. Frankle, *Atomic data and nuclear data tables,* **80**, 1-34 (2002).
4. International Commission on Radiological Protection, ELSEVIER (1997).
5. Masarik, J. and R. C. Reedy *Geochimica et Cosmochmica Acta,* **58**, 5307-5317 (1994).
6. Castagnoli, G. and Lal. D. *Radiocarbon*, **22**, 133–158 (1980).
7. Simpson, J. A. *Ann. Rev. Nucl. Part. Sci.* **33**, 323-381 (1983).
8. Agostinelli, S. *et al., Nucl. Inst. Meth.* **A506**, 250-303 (2003).
9. Heiken, G. *et al.,* Cambridge University Press (1991).
10. JENDL3.3: Japan Evaluated Nuclear Data Library, http://wwwndc.tokai-sc.jaea.go.jp/jendl/Jendl_J.html
11. Ishizaki, T. *et al., Space Radiation*, **5**, No.2, in Japanese (2006).
12. United Nations Scientific Committee on the Effects of Atomic Radiation, United Nations Pubns. (2000).

TRACK FINDING IN GAMMA CONVERSIONS IN CMS

N. MARINELLI

Physics Department, University of Notre Dame,
Notre Dame, Indiana, USA
**E-mail: nancy.marinelli@cern.ch*

A track finding algorithm has been developed for reconstruction of e^+e^- pairs. It combines the information of the electromagnetic calorimeter with the information provided by the Tracker. Results on reconstruction efficiency of converted photons, as well as on fake rate are shown for single isolated photons and for photons from H$\rightarrow \gamma\gamma$ events with pile-up events at 10^{33} cm^{-2} s^{-1} LHC luminosity.

1. Introduction

The need for high granularity and an adequate number of measurements along the charged particle trajectories, in order to obtain excellent momentum resolution and pattern recognition in the congested environment of LHC events, has lead to a CMS Tracker design having an unprecedented large area of silicon detectors with a very large number of front-end readout channels. The resulting amount of material is large and comprises active layers, support structures, general services as well as an impressive cooling system.

The relatively massive Tracker results in a large probability of photon conversion and electron bremsstrahlung radiation in the Tracker volume. The fraction of photons converting in the Tracker material, integrated over the acceptance, has been estimated from a simulated sample of single photons with P_T=35 GeV (Fig. 1).

The number of gamma conversions in CMS is not negligible and it is important to reconstruct the e^+e^- tracks. Major examples of the use of track reconstruction of gamma conversions are:

- Photons from neutral pion decays constitute a very large background to prompt photons. In the case of converted photons the rejection of the background using the electromagnetic shower shape becomes ineffective. The information added by dedicated track finding improves the available rejection factor. Moreover the information from the tracks can be used to refine the electromagnetic energy clustering in the ECAL hence improving the energy measurement.
- Gamma conversion reconstruction is also a tool for electron reconstruction validation, i.e. asymmetric conversions occurring very early in the Tracker are unwanted background to genuine electrons.

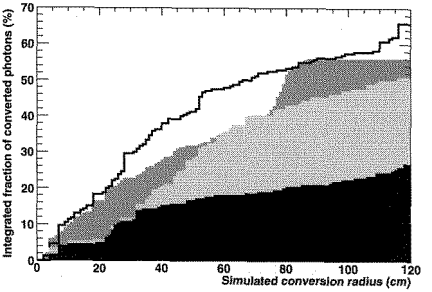

Fig. 1. Fraction of photons converting in the Tracker, integrated over all radii. The four histograms correspond to 0.1 slices in η around $|\eta| = 0.2$ (black), $|\eta| = 0.9$ (light grey), $|\eta| = 2.0$ (dark grey) and $|\eta| = 1.2$ (hollow).

• The reconstruction of conversion vertices provides, once the reconstruction efficiency is taken into account, a "radiography" of the Tracker and allows the mapping of the material with data.

This paper summarizes the work described in Ref. [1, 2]. A detailed description of the CMS Electromagnetic Calorimeter and of the Pixel and Silicon Strip Tracker is provided in Ref. [3] and Ref. [4, 5] respectively.

2. Electron-positron pair track reconstruction

CMS track reconstruction is divided into four separate steps; a) trajectory seed generation; b) trajectory building (i.e. seeded pattern recognition); c) trajectory cleaning which resolves ambiguities and d) trajectory smoothing (i.e. the final track fit).

In CMS, the standard seed and track finding algorithm (Chapter 14, Sec.4.1 of Ref. [6]) was developed and optimized for tracks originating from the primary interaction vertex, with pattern recognition starting from track seeds built in the pixel detector. For electron tracks, instead, the match between a super-cluster energy deposit in the ECAL and hits in the pixel detector is used for building seeds (Ref. [7]).

Neither of these approaches are suitable for tracks originating from vertices that are significantly displaced with respect to the primary vertex such as those from converted photons. Different seed finding and pattern recognition algorithms are necessary.

Recently, after a major re-working of the CMS Reconstruction software took place (Ref. [8]), additional track seed finding methods were developed which no longer rely on the Pixel information. However they were developed for general usage and do not combine information from ECAL for specific conversion reconstruction.

This paper describes the combination of an inward ECAL seeded track finding method with a subsequent outward track finding step.

The electron bending in the CMS 4 Tesla magnetic field and the large emission probability of bremsstrahlung photons in the Tracker material leads to a spray of energy in the ECAL extending mainly in the transverse plane. When dealing with single, high-energy electrons the electron energy is collected by clusters of clusters extended along a ϕ road called super-clusters

(SC). Different clustering algorithms (Ref. [7]) are used for the ECAL barrel and endcaps. The same clustering procedure is applied here when dealing with converted photons.

The initial assumption is made that the bulk of energy arising from converted photons is contained in one super-cluster, however allowance is made for tracks falling outside its boundaries. The energy of the sub-clusters within a SC and the magnetic field are used to give a first rough estimate of a trajectory path, assuming that the initial photon vertex is the origin of the reference frame. Compatible hits are then sought for in the three outermost layers of Tracker. If compatible hits are found they are used to re-evaluate the seed parameters releasing the initial hypothesis on the initial vertex. Seeds are built out of pairs of hits and used for pattern recognition, trajectory building and final fitting proceeding inward in the Tracker, using the Kalman Filter formalism (Ref. [9]).

The average radiation energy loss (bremsstrahlung) experienced by electrons traversing the Tracker material is described by the Bethe-Heitler parametrization (Ref. [10, 11]). With the Kalman filter (which is a linear least-squares estimator), the radiation energy loss is taken into account at each propagation step by correcting the track momentum by an amount corresponding to the predicted mean value of the energy loss and by increasing the track momentum variance with the predicted variance of the energy loss under the assumption that its distribution is Gaussian.

The two oppositely charged tracks with the largest number of hits reconstructed with the inward tracking are used in turn, independently from one another, as the basis for the outward seed and track finding procedure. If only one track was found it is used by default. Given an inward track, its innermost hit is assumed to be the e^+e^- vertex and is used as the starting point for seed finding of the other conversion arm.

The first hypothesis of the outgoing track is made based on the presence of a basic cluster within a suitable ϕ range from the presumed conversion vertex and the fact that the two tracks must be parallel at the vertex. Pairs of hits compatible with the estimated track path are sought in the next two layers moving outwards along the helix. These pairs are used as seeds for the forward trajectory building. After this step, trajectories are cleaned according to the number of shared hits and smoothed with the backward fit to obtain the parameters of the tracks at their innermost state. The description given before concerning the treatment of radiation energy losses applies here as well.

The two sets of tracks reconstructed in the inward and outward tracking procedures are merged together. All combinations of oppositely charged tracks are fitted to a common vertex and are considered as possible converted photon candidates.

2.1. *Results*

The algorithmic efficiency was measured normalizing the number of reconstructed conversions to the simulated conversions with the vertex located before the third-outermost Tracker layer (R$\sim$ 85 cm). Figure 2 shows the efficiency as a function of the radius and of η; the total efficiency is broken down into two contributions arising from candidates with two reconstructed

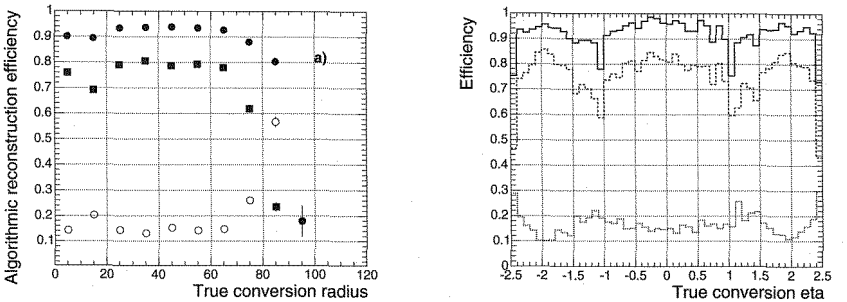

Fig. 2. Reconstruction efficiency measured with single photons with fixed P_T=35 GeV/c as a function of the simulated conversion-point position. (left) Total (black dots), two-tracks (black squares) and single track (open dots); (right) Total (solid line), two-tracks (dashed line) and single track (dotted line).

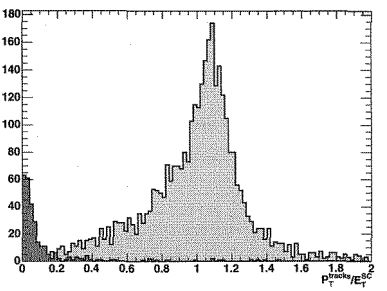

Fig. 3. The ratio P_T(tracks)/E_T(SC) for reconstructed converted photons in a sample of H$\rightarrow\ \gamma\gamma$ events with low luminosity pile-up. The dark grey histogram shows the contribution from fake pairs.

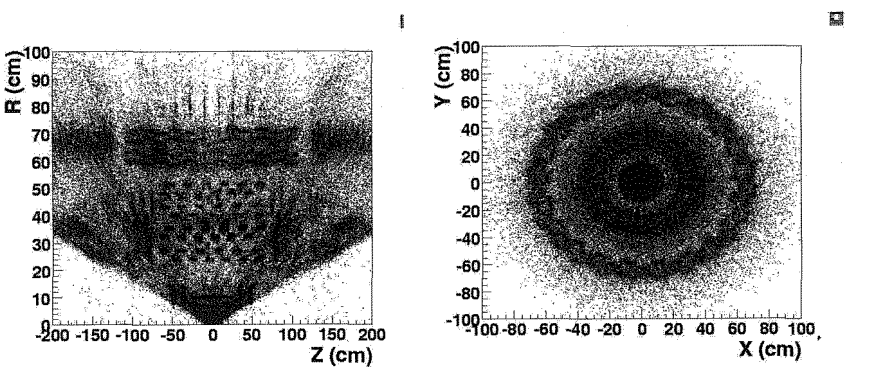

Fig. 4. Reconstructed converted photon vertices.

tracks and those with only one track. At this point it is important to check that the photon momentum measured from the tracks matches the energy collected in the ECAL super-cluster. The ratio P_T(tracks)/E_T(SC) is shown in Fig. 3 for signal and background (dark grey) from fake pairs. The fraction

of fake pairs was measured in a sample of Higgs-to-two-photon decays with low LHC luminosity (10^{33} cm^{-2} s^{-1}) pile-up events; it amounts to about 5%, easily reducible with a cut on P_T(tracks)/E_T(SC). Finally the position of the fitted conversion vertices is shown in Fig. 4. It is worth emphasizing that the results presented here were obtained with a non-final simulation of the Tracker material and are likely to change in a future update.

3. Conclusions

A baseline reconstruction method for converted photons in CMS has been described. It gives very encouraging results. This tracking method, designed specifically for reconstruction of converted photons has recently been ported to the new CMS Software environment (CMSSW) (Ref. [8]), where the final Tracker geometry description is being finalized.

Acknowledgments

I wish to thank all CMS colleagues who, over the years, contributed to the development of the ECAL clustering and the basic tracking tools used for this work. A special thank is for R. Ruchti who constantly provides me with sound advices. Finally I would like to acknowledge the US National Science Foundation for financial support under grants PHY-0355340 and PHY-0735119.

References

1. N. Marinelli, *Track finding and identification of converted photons*, CMS Note 2006/005.
2. The CMS Collaboration *CMS - Detector performance and software*, Physics Technical Design Report Vol. 1, CERN/LHCC 2006-001, CMS TDR 8.1 (2006).
3. The CMS Collaboration, *The Electromagnetic Calorimeter Project*, Technical Design Report,CERN/LHCC 97-33, CMS TDR 4.
4. The CMS Collaboration, *The Tracker Project*, Technical Design Report, CERN/LHCC 98-6, CMS TDR 5.
5. The CMS Collaboration, *The Tracker Project*, Technical Design Report, CERN/LHCC 2000-016, CMS TDR 5, Addendum 1 (2000).
6. The CMS Collaboration, *The Trigger and data acquisition project* , Vol 2 Technical Design Report, CERN/LHCC 2002-026, CMS TDR 6.2; *Track reconstruction in the CMS tracker*, W.Adam, B.Mangano, T. Speer, T. Todorov, CMS NOTE 2006-041.
7. *Electron reconstruction in CMS*, S. Baffioni et al., CMS NOTE 2006/040.
8. CMSSW, The CMS Software for Simulation and Reconstruction, https://twiki.cern.ch/twiki/bin/view/CMS/SWGuideFrameWork; https://twiki.cern.ch/twiki/bin/view/CMS/Reco.
9. R. Fruhwirth, Nucl. Instrum. and Methods A 262, 444 (1987).
10. H. Bethe and W. Heitler, Proc. R. Soc. London A 146 (1934) 83.
11. D. Stampfer, M. Regler and R. Fruhwirth, Comp. Phys. Comm. 110 (1994) 157.
12. The CMS Collaboration, *The CMS High Level Trigger*, hep-ex/0512077.

THE GEANT4-BASED ATLAS FAST ELECTROMAGNETIC SHOWER SIMULATION

E BARBERIO[1], J BOUDREAU[2], B BUTLER[3], S L CHEUNG[4], A DELL'ACQUA[5], A DI SIMONE[5], W EHRENFELD[6,7], M V GALLAS[5], A GLASOW[7], E HUGHES[8], Z MARSHALL[8,9], J MUELLER[2], R PLACAKYTE[7], A RIMOLDI[10], P SAVARD[4], V TSULAIA[2], A WAUGH[11], C C YOUNG[3]

[1]*School of Physics, University of Melbourne, Parkville, Victoria, 3010, Australia*
[2]*Department of Physics and Astronomy, University of Pittsburgh, 3941 O'Hara Street, Pittsburgh, PA 15260, USA*
[3]*Stanford Linear Accelerator Center, 2575 Sand Hill Road, Menlo Park, CA 94025, USA*
[4]*Department of Physics, University of Toronto, 60 Saint George Street, Toronto, M5S 1A7, Ontario, Canada*
[5]*European Laboratory for Particle Physics, CERN, 1211 Geneva 23, Switzerland*
[6]*Institut für Experimentalphysik, Universität Hamburg, Luruper Chaussee 149, 22761 Hamburg, Germany*
[7]*Deutsches Elektronen-Synchroton, DESY, Notkestrasse 95, 22603 Hamburg, Germany*
[8]*Nevis Laboratory, Columbia University, 136 So. Broadway, Irvington, NY 10533, USA*
[9]*Physics Department, California Institute of Technology, Pasadena, CA 91125, USA*
[10]*Instituto di Fisica Nucleare, Universita di Pavia and I.N.F.N., Via A Bassi 6, 27100 Pavia, Italy*
[11]*Falkiner High Energy Physics Group, School of Physics, University of Sydney, Sydney, NSW 2006, Australia*

We present a three-pronged approach to fast electromagnetic shower simulation in ATLAS. Parameterisation is used for high-energy, shower libraries for medium-energy, and an averaged deposition for very low-energy particles. We present a comparison between the fast simulation and full simulation in an ATLAS Monte Carlo production.

1. Introduction

ATLAS [1], one of two general-purpose experiments designed to collect data from the Large Hadron Collider, has implemented a detector simulation within the Athena software framework [2] based on GEANT4 [3]. However, owing to the complexity of both GEANT4 itself and the ATLAS detector geometry, the standard simulation ("full simulation") takes upwards of twenty minutes to simulate single physics events. The fast simulation package speeds up the simulation of electromagnetic (EM) showers within the calorimeters.

2. Motivation

The time spent for simulating the ATLAS subdetectors motivated the development of a fast simulation. Table 1 shows the CPU time spent during simulation of various particles as they passed through the subdetectors for QCD dijet events. The vast majority of time is spent on EM particles in the calorimeters. No other detector element contributes more than 6% of the total CPU time.

Energy spectra of particles entering the sampling portion of the calorimeters in the same dijet events were used to determine the most important energies to study in the fast simulation. Several orders of magnitude more particles enter the calorimeter with energies of a few tens of MeV than at energies over 500 MeV; the simulation of low-energy particles drives the total simulation time. An order of magnitude more photons below 10 MeV appear in typical events than all other particles combined. At high energies, photons pair produce after only a few steps, so that treating the subsequent electron-positron pair suffices to speed up the simulation. Below about 10 MeV, this is no longer the case.

Table 1. CPU time per event for full and fast simulation by subdetector and particle type for simulation of a QCD dijet sample with a 280-560 GeV leading jet. Systematic and statistical uncertainties are each at the few percent level. Timer overhead, ~5%, was removed. "Other Systems" mostly comprises beam pipe, detector services, and shielding. Neutrons dominate "Other Particles" (~90%).

Detector Subsystem	**Full Sim. Time [kSI2Ks]**	**Fast Sim. Time [kSI2Ks]**
Tracker	44	38
EM Barrel Calorimeter	91	23
EM Endcap Calorimeter	393	107
Forward Calorimeter	155	55
Hadronic Barrel Calorimeter	29	27
Hadronic Endcap Calorimeter	50	47
Muon System	21	21
Other Systems	124	89
Total Event	**907**	**406**
Particle Type	**Full Sim. Time [kSI2Ks]**	**Fast Sim. Time [kSI2Ks]**
Electrons and Positrons	344	124
Photons	259	88
Other Particles	304	194
Total Event	**907**	**406**

3. Fast Simulation

The fast shower framework comprises three methods: a high-energy (~10 GeV) parameterisation based on [4]; a medium-energy (~100 MeV) shower library approach, consisting of pre-simulated particle showers; and a "killing" approach that recreates the average energy and position of the one hit typically created by sufficiently low-energy (few MeV) particles.

As a particle moves through the detector, each is separately examined by the fast simulation package. When a particle enters the homogeneous sampling region of a calorimeter, its type is checked. Only photons, electrons, and positrons can trigger the fast simulation. If the shower's energy is more than 95% contained, longitudinally and transversely, in that region, and the initial particle's energy is in the chosen range, the fast simulation triggers. If any test fails, GEANT4 moves that particle one more step, and the particle is retested.

If the particle satisfies all criteria, one of the three fast shower methods is applied. The original direction of the particle determines the core of the eventual shower; systematic effects from the magnetic field are taken to be small.

Each method was studied individually to assess its impact on the simulation time and accuracy in reproducing the full simulation. Because of the spectrum of particles entering the calorimeters and the high minimum energy for parameterisation, the shower libraries and "killing" are applied more frequently than the parameterisation.

4. Parameterisation Method

For electrons and positrons above a sufficiently high energy, around 10 GeV, the detector appears sufficiently homogeneous to apply a shower parameterisation. The parameterisation takes small steps in the direction of the original particle, depositing energy according to several tuned functions as it goes.

The longitudinal profiles of showers were parameterised as in [4,5] and normalized with an energy scale for each subdetector. The radial profile is a 2-dimensional function of radius and depth in the shower, as in [4-6], normalized by the longitudinal profile. Energy is deposited in GEANT4 hits [3] in order to mimic full simulation. Fluctuations are introduced in three separate places, representing the random characteristics of shower length and shape, the sampling resolution of the calorimeter, and the geometric fluctuations in the energy collected.

5. Shower Libraries Method

Particles captured by the fast simulation in the appropriate energy range are replaced by a shower from a pre-simulated library, rotated and scaled to match the primary particle. Shower libraries are generated in bins of pseudorapidity and energy for electrons and photons. Only hits in the sensitive detectors are stored. The binning reproduces the fine structure in the calorimeters.

6. "Killing" Method

Low-energy (~10 MeV) electrons deposit only one hit in the sensitive detector volumes. The properties of that hit are all that must be reproduced. A step is taken in the direction of the original particle, with a varied length. The particle's energy is scaled to recreate the energy response of the calorimeter. Absorber and active material are not separated, providing a geometric energy fluctuation. The containment test was removed to avoid a bias near detector cracks.

7. Full and Fast Simulation Comparison

The fast simulation has been tuned to and compared with full simulation Monte Carlo in Athena release 13.0.30. Simulation time for dijet events is reduced by a factor of two to three, as seen in Table 1.

Average energy deposition in the sensitive detector is well reproduced by the fast simulation. Figure 1 displays fast and full simulation energy depositions in the forward calorimeter for primary electrons of several initial energies and several initial pseudorapidities. The ratio of the energy deposited in the first sampling of the EM calorimeter to that in the second provides an important

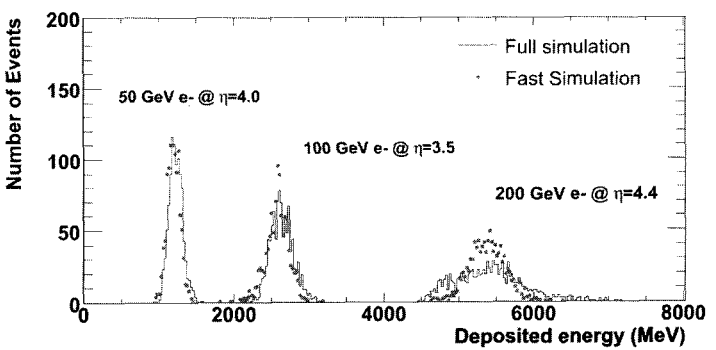

Figure 1: Energy deposition in the ATLAS forward EM calorimeter for primary electrons of various energies. Full simulation is presented in black (solid) and fast simulation is in red (dots).

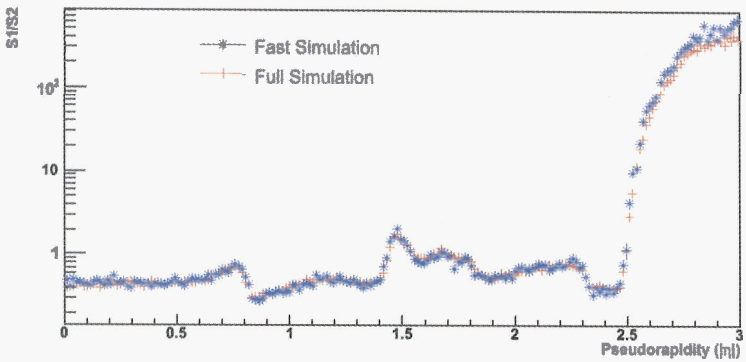

Figure 2: The ratio of energy deposition in the first sampling layer of the ATLAS EM calorimetry to that in the second layer for 50 GeV primary electrons, as a function of pseudorapidity, is presented for full (red pluses) and fast (blue stars) simulation. The EM barrel calorimeter ends at $|\eta|=1.4$.

check pertaining to electron and photon identification. The quantity is reproduced at the few percent level, except at high pseudorapidity. Figure 2 displays the ratio of this variable from fast simulation to that in full simulation.

8. Conclusions

We have presented a fast simulation approach for the ATLAS EM calorimetry, comprising parameterisation of high-energy particles, shower libraries for medium-energy particles, and "killing" for low-energy particles. A comparison with full simulation of physics observables and CPU time is included.

Work is ongoing to improve physics agreement and reduce simulation time. The extension of several of these models to additional subdetectors and particles is currently being tested. More information is available in [5].

References

1. **ATLAS** Collaboration, *The ATLAS Experiment at the CERN Large Hadron Collider*, 2007.
2. **ATLAS** Collaboration, Athena - The ATLAS Common Framework, Version 8, http://atlas-computing.web.cern.ch/atlascomputing/documentation/swDoc/AthenaDeveloperGuide-8.0.0-draft.pdf, CERN, 2006.
3. J. Allison et al., IEEE Transactions on Nuclear Science **53** 270 (2006).
4. G. Grindhammer, M Rudowicz, S. Peters, *NIM* **A290**, 469 (1990); G. Grindhammer, S. Peters, hep-ex/0001020.
5. E. Barberio, A. Straessner, ATL-COM-PHYS-2004; Fast Simulation Working Group, https://twiki.cern.ch/twiki/bin/view/Atlas/AtlasShowerParam.
6. J. del Peso, E. Ros, *NIM* **A306**, 485 (1991).

NORTH AMERICAN MEDICAL PHYSICS APPLICATIONS OF THE GEANT4 SIMULATION TOOLKIT*

JOSEPH PERL
Stanford Linear Accelerator Center
Menlo Park, CA 94025, USA

Geant4 is a toolkit for the simulation of the passage of particles through matter. While Geant4 was originally developed for High Energy Physics, applications now include Nuclear, Space and Medical Physics. Medical applications include characterizing machines and sources, calculating dose and the development of imaging technology. This paper surveys Geant4 medical applications in North America, explains why users choose Geant4 and discusses the challenges of bringing Geant4 to this community.

1. Why Geant4 is Used in Medical Physics

The Geant4 Simulation Toolkit[1,2] began in 1994 as a research project for a new general-purpose simulation code for High Energy Physics (HEP). One of the first large object-oriented software applications in physics, Geant4 has become the standard simulation package for most HEP experiments including three of the four experiments at the Large Hadron Collider. Geant4 was chosen for these applications because of its ability to handle very complex constructive geometry and to handle all particles. In the US, the BaBar collaboration, which was the first major HEP user of Geant4, has by now simulated over 5 x 10^9 events.

1.1. *The Place of Monte Carlo in Medical Physics*

Within Medical Physics, Monte Carlo has been used for many years to characterize machines and sources, to calculate dose and to develop imaging technologies. In treatment planning, where the workflow involves imaging, then planning, then simulation of the plan, with the latter steps often iterated several times, time constraints generally lead to use of parameterized models rather than Monte Carlo, but a hybrid approach may use parameterized models for the first few iterations and Monte Carlo for subsequent iterations. Monte Carlo is superior to parameterized models in cases of material inheterogeneity, such as at

* This work is supported by the U.S. Department of Energy under contract DE-AC02-76SF00515.

the tissue/air interfaces of the lung, in the complicated tissue/bone interfaces in the head and neck, or near implants made of high atomic weight materials.

Retrospective studies are computationally similar to treatment planning but are done after the fact, to look at whether the dose calculated by parameterized models is correct. Some studies involve actual patient data, other studies use simulated patients (hardware or software models called "phantoms").

Medical imaging technology is in a period of rapid advance, moving towards higher resolution, higher speed, lower dose and better ability to differentiate tissue types. Monte Carlo is used to evaluate new designs.

1.2. *Why Some Medical Physicists Choose Geant4*

Geant4 is still quite new to Medical Physics. Other codes, such as EGSnrc, XVMC, MCNP, PENELOPE and FLUKA have a longer history in this field. However use of Geant4 is increasing rapidly. Frank Verhaegen of McGill University, titled an article for MedicalPhysicsWeb[3] "GEANT4: a new giant in medical physics."

Why do medical physicists choose Geant4 given the availability of other well established codes? A first reason is that Geant4 can handle all types of particles, as opposed to the "Gold Standard" in Medical Physics, EGSnrc, which handles only electron and gamma. With the growth of proton and ion therapy, due to the appealingly sharp dose depth cutoff of the Bragg Peak, there is significant interest in "all-particle" codes.

A second reason users turn to Geant4 is its ability to handle complex geometry. Geant4 offers the most flexible geometry description of any Monte Carlo. Medical Physics applications include complex parts of proton intensity modulated radiotherapy machines (IMRT), multileaf collimators (MLCs) and brachytherapy sources.

Another unique aspect of Geant4 is that it can model sources and geometries in motion, such as the rotating parts of an IMRT beam line, dynamic MLCs, a brachytherapy source moving through a catheter, moving parts of imaging systems and even the motion of patient organs from respiration, etc.

Geant4 has the ability to handle fields, both electric and magnetic. This can be helpful in simulation of the treatment head or in novel, real-time imaging treatment modalities where the treatment is performed in a magnetic field.

Another appealing quality of Geant4 is its use of modern programming techniques (object-oriented, C++). All other codes currently in use are in FORTRAN. Finally, Geant4 is open and free - Geant4 source code is

distributed to the user who is welcome not only to add user code but to modify the source code and even to repackage, redistribute or sell that source code.

2. Some Medical Physics Applications of Geant4 in North America

We will now discuss some of the recent Geant4 medical applications in North America. Space does not allow a complete list of such efforts, but an assortment of projects are described to give a sense of the breadth and depth of activities.

2.1. *Characterizing Machines and Sources*

Geant4 has been used for design and quality assurance for beam therapies, brachytherapy and even for a novel form of therapy, "electronic brachytherapy." Therapeutic beams may be x-rays (from bremsstrahlung of electrons on a high Z target, typically 4 to 25MeV), electrons (for skin or small depth treatments, special cases of whole body irradiation, and for inter-operative radiotherapy, 4 to 25 MeV) and protons or ions (from a cyclotron, typically around 160 MeV).

Work by Paganetti, Jiang, Lee and Kooy[4] at Harvard/Massachusetts General Hospital used Geant4 to simulate the treatment head for a proton linac including complexities such as the motion of intensity modulator wheels and the varying fields of steering magnets. At MD Anderson Cancer Center, Peterson, Polf, Frank, Bues and Smith[5] used Geant4 to study variations in scanned beam proton therapy doses due to random magnetic beam steering errors.

On the other end of the proton therapy suite, a collaboration of University of Texas, M. D. Anderson and Université Laval, including Archambault, Polf, Beaulieu and Beddar[6], chose Geant4 to study the scintillation detectors used for dose measurement. Flanz and Paganetti[7] used Geant4 to study overall radiation protection issues for proton therapy suites.

Brachytherapy (from the Greek for "short", referring to short distance therapy) typically involves gamma and beta emitters placed outside the body close to the skin (for superficial tumors), temporarily inserted into the body through catheters or permanently implanted ("seeds"). Geant4's flexible geometry has made it popular for modeling such applicators and seeds and calculating the resulting dose. Examples of such studies include modeling of an Iridium 192 source by Poon, Reniers, Devic, Vuong and Verhaegen[8] of McGill University, an Iodine 125 source by Carrier[9] of Université Laval and the "Active Mammosite" device by Winston, Black and Cudjoe[10] at Hampton University.

A novel treatment system, "electronic brachytherapy," mixes qualities of beam therapy with qualities of brachytherapy. A device is temporarily inserted through a catheter, but the device is not a radioactive seed but a miniature x-ray

tube. A group at McGill University, including Liu, Poon, Bazalova, Reniers, Evans, Seuntjens and Verhaegen, in collaboration with Rusch[11] from the equipment manufacturer Xoft Inc, used Geant4 to model this "Axxent x-ray tube", choosing Geant4 for its ability to handle complex geometry.

2.2. *Treatment Planning and Retrospective Studies*

Jiang, Seco and Paganetti[12] at Harvard/Massachusetts General Hospital have used Geant4 to study dose from proton therapy to the head and neck region to see where the dose calculated by Monte Carlo differs from that calculated by analytical methods. Also at Harvard, Paganetti, Jiang and Trofimov[13] used Geant4's ability to handle moving geometries to study dose to the lung in breathing patients. Treatment plans that incorporate this dimension of movement in time are referred to as "4D plans." While many Monte Carlo codes can handle a single motion (such as the beam angle changing during treatment), Geant4 puts no limit on how many parts of the geometry may be in motion (beam position, multileaf collimator motion, respiration, etc.). In the absence of this 4D ability, time-slicing can allow one to build up a moving geometry's dose calculation by summing dose from several static setups, but such an approach can require an unwieldy number of slices if there are multiple simultaneous motions, and interplay effects must be handled carefully to avoid time-binning artifacts.

Yet another study from Harvard/Massachusetts General, in collaboration with University of Florida and Rensselaer Polytechnic, by Zacharatou Jarlskog, Lee, Jiang, Bolch, Xu and Paganetti[14], used Geant4's all-particle capabilities to study the risk associated with neutron radiation in proton therapy. The issue here is that while the primary proton beam's shape can be well controlled, the interaction of these protons in the patient's body results in secondary neutron radiation generated within the body and heading in many directions. In studying the risk from this secondary dose, the team created five separate patient models, ranging from a 9 month to 14 year old, and including both genders, to account for significant differences among these patient groups.

In prostate brachytherapy, treatment planning involves decisions about where in the prostate to place on order of 100 small radioactive seeds. Standard calculation techniques look at each seed individually and then sum the resulting dose. A retrospective study by Carrier, D'Amours, Verhaegen, Reniers, Martin, Vigneault and Beaulieu[15], of CHUM, used imaging to determine the actual location of seeds after implant and then used Geant4 to calculate the effects of

"interseed attenuation," the effect each seed has in blocking some dose from surrounding seeds.

2.3. *Imaging*

Many developers of imaging technology use Geant4 by way of GATE, the Geant4 Application for Emission Tomography, which wraps around Geant4 to simplify use and add imaging features. Within the North American community, a group at UCLA's Crump Institute for Molecular Imaging, including Taschereau, Chatziioannou, Vu and Douraghy use GATE in small animal studies. To facilitate their work they developed a very high resolution voxelized mouse phantom. They use this phantom, for example, to study dose from 18-flourine compounds[16]. Another study at the Crump Institute by Douraghy, Rannou, Alexandrakis, Silverman and Chatziioannou[17] uses GATE to study dual modality optical PET (OPET), which combines optical tomography with positron emission tomography. And a Crump Institute group including Vu, Yu, Silverman, Farrell, Shah, Tseng and Chatziioannou[18] uses GATE to study specialized beta detectors for use with microfluidic chips.

Other developers studying imaging use Geant4 directly rather than through GATE. At Emory University, Sechopoulos, Suryanarayanan, Vedantham, D'Orsi and Karellas[19] used Geant4 for the first comprehensive study of radiation dose to different organs from x-ray scatter during mammography and breast CT.

2.4. *Validation Studies*

Before any particular Monte Carlo can be used for treatment planning, validation studies must be published in appropriate journals. A variety of studies have been undertaken by Geant4 developers and medical physicists to validate Geant4 against measured data and other Monte Carlo codes. Faddegon of UCSF, in collaboration with Asai, Perl and Tinslay of SLAC, have calculated such benchmarks as large field electron dose distributions[20], variation reduction techniques (bremsstrahlung splitting)[21] and thick target bremsstrahlung[22].

3. Challenges for Geant4 in Medical Physics Applications

3.1. *Technical Challenges*

Because the Geant4 toolkit was originally developed for a different field, HEP, changes were needed to make it more usable for medical applications. The original applications of Geant4 involved highly specialized detector

development. Geant4 was therefore set up with the assumption that users would write their own "hit" classes (user code called when a particle enters a given detector volume which then models an electronics readout, scores dose, charge, etc.). Writing such classes was a burden for those medical physics users who just wanted to score standard quantities. Accordingly, Geant4 now provides ready-to-use scoring capabilities - the user just specifies what quantity to score along what geometry (plane, spherical surface, etc.). The object-oriented design of Geant4 made it fairly easy to add these capabilities to the toolkit.

A second challenge for Geant4 was to improve physics results at energy scales appropriate for Medical Physics. To the original developers of Geant4, the energies typical for radiation treatment were considered "low energy" and of low priority. With a very significant part of the Geant4 user community now coming from Medical Physics and Space Physics, new focus has been applied to improving performance at these lower energies (refinements to scattering, etc.). The modular design of Geant4 has proven useful here.

A third technical challenge involved the geometries to be modeled. While Geant4 boasts the worlds most flexible geometry for the hierarchical, constructive solid geometry typical of HEP spectrometers, HEP beamlines, medical linacs and brachytherapy sources, the medical physics world adds the requirement to model a different kind of geometry - patient geometry, read in from scan data as very large three dimensional arrays of densities. Such geometries are not complex in the same way as HEP detectors, but can involve very large numbers of voxels (3 million is common). To accommodate this geometry required changes to particle navigation, memory management and visualization. Geant4's software design has made such changes feasible.

3.2. *Funding Challenges*

Geant4 core development has been primarily funded by the HEP community. To bring more resources to bear on the technical challenges for medical physics applications, there is a corresponding challenge for funding. Some funding for Geant4 has recently emerged from the Space Physics community (ESA, JAXA and NASA), however dedicated medical funding for core Geant4 development has been limited (coming from Japan and Italy). Given Geant4's demonstrated usefulness in Medical Physics, it is hoped that funding will come from the North American medical community. An interesting parallel is that the current "Gold Standard" Monte Carlo for medical physics, EGSnrc, though currently maintained by Canada's National Resource Council, primarily for the medical

physics community, has its own roots in another HEP project begun at SLAC in the 1970s, the EGS Monte Carlo.

3.3. *Sociological Challenges*

Bringing Geant4 from HEP to Medical Physics has involved communication challenges. Some issues simply involve terminology (what HEP calls an "event", medical physics calls a "history"). Each field has its own set of acronyms, and terms like "low energy" have orders of magnitude different meaning between the two fields. A greater issue is that the two communities don't attend the same conferences and don't subscribe to the same journals.

HEP experiments often involve large collaborations (thousands of people). Such collaborations may assign several people to spend nearly full time learning about Geant4, digging into its details, discussing with Geant4 developers and optimizing performance. Medical Physics studies are typically by single individuals or very small collaborations. One cannot expect them to devote such manpower to understanding Geant4. Technical improvements, such as ready-to-use scoring classes, are a help, as are applications like GATE that wrap Geant4 for specialized uses, but a greater issue is that someone needs to provide easy-to-access guidance on how to tailor Geant4 for medical applications (such as what parameters are appropriate for what use cases).

The Geant4 North American Medical Users Organization (G4NAMU)[23] was launched in 2005 to address such guidance issues. Work is now under way to form international working groups, combining medical physics users with Geant4 developers to further address these issues. An initial group will focus on recommendations for Geant4 physics Lists (the code that specifies which physics processes to model and what parameters to use). Another group will explore strategies for assembling various reusable components into easier-to-use medical applications.

4. Conclusion

Medical applications of Geant4 in North America and throughout the world have been increasing rapidly due to the overall growth of Monte Carlo use in Medical Physics and the unique qualities of Geant4 as an all-particle code able to handle complex geometry, motion and fields with the flexibility of modern programming and an open and free source code. Work has included characterizing beams and brachytherapy sources, treatment planning, retrospective studies, imaging and validation. Challenges from the technical to the sociological have been addressed.

That software originally designed for HEP has found so many applications in Medical Physics should not come as a surprise - the histories of both fields go back to the same particle physics roots. Indeed, the first medical linac in the western hemisphere grew from the very institution, Stanford University, that also gave birth to the world's longest HEP accelerator. The first treatment from that medical linac was performed exactly fifty years ago this year. The transfer of technology between HEP and Medical Physics continues today.

References

1. S. Agostinelli et al, *NIM Phys. Research A.* **506**, 250-303 (2003).
2. J. Allison et al, *IEEE TNS* **53**, 270-278 (2006).
3. F. Verhaegen, *medicalphysicsweb.org/cws/article/opinion/25856* (2006).
4. H. Paganetti, H. Jiang, S.Y. Lee and H.M. Kooy, *Med. Phys.* **31(7)**, 2107-2118 (2004).
5. S. Peterson, J. Polf, S. Frank, M. Bues and A. Smith, *Med. Phys.* **34(6)**, 2627-2628 (2007).
6. L. Archambault, J. Polf, L. Beaulieu and S. Beddar, *Med. Phys.* **34(6)**, 2336 (2007).
7. J. Flanz and H. Paganetti, *Aust. Phys. Eng. Sci. Med.* **26(4)**, 156-161 (2003).
8. E. Poon, B. Reniers, S. Devic, T. Vuong and F. Verhaegen, *Med. Phys.* **33(12)**, 4515-4526 (2006).
9. J-F. Carrier, *PhD Thesis,* Université Laval.
10. J. Winston, R. Black and T. Cudjoe, *G4NAMU Meeting*, SLAC (2006).
11. D. Liu, E. Poon, M. Bazalova, B. Reniers, M. Evans, J. Seuntjens, T. Rusch, F. Verhaegen, www.medphys.mcgill.ca/~mcworkshop2007/talks/Liu.ppt
12. H. Jiang, J. Seco and H. Paganetti, *Med. Phys.* **34(4)**, 1439-1449 (2007).
13. H. Paganetti, H. Jiang, A. Trofimov, *Phys. Med. Biol.* **50(5)**, 983-90 (2005).
14. C. Zacharatou Jarlskog, C. Lee, H. Jiang, W. Bolch, X.G. Xu and H. Paganetti, *AAPM Annual Meeting* (2007).
15. J-F. Carrier, M. D'Amours, F. Verhaegen, B. Reniers, A.G. Martin, E. Vigneault and L. Beaulieu, *IJROBP* **68(4)**, 1190-1198 (2007).
16. R. Taschereau and A.F. Chatziioannou, *Med. Phys.* **34(3)**, 1026-36 (2007).
17. A. Douraghy, F.R. Rannou, G. Alexandrakis, R.W. Silverman and A.F. Chatziioannou, *AAMI-SMI Conference,* Providence RI (2007).
18. N.T. Vu, Z.T.F. Yu, R.W. Silverman, R. Farrell, K.S. Shah, H.R. Tseng and A.F. Chatziioannou, *IEEE NSS-MIC Conference*, Honolulu HA (2007).
19. I. Sechopoulos, S. Suryanarayanan, S. Vedantham, C.J. D'Orsi and A. Karellas, *Radiology*, in press (2007).
20. B. Faddegon, J. Perl and M. Asai, *Phys. in Med. Biol.*, in press (2007).
21. J. Tinslay, B. Faddegon, J. Perl, M. Asai, *Med. Phys.* **34(6)**, 2504 (2007).
22. B. Faddegon, J. Tinslay, J. Perl, M. Asai, *Phys. Med. Biol.*, in press (2007).
23. J. Perl, *geant4.slac.stanford.edu/g4namu*

Tools to monitor the quality of the ALICE-TOF detector data

A. Akindinov[a], A. Alici[b,c], P. Antonioli[c], S. Arcelli[b,c], M. Basile[b,c], G. Cara Romeo[c], L. Cifarelli[b,c], F. Cindolo[c], A. De Caro[d], D. De Gruttola[d], S. De Pasquale[d], M. Fusco Girard[d], C. Guarnaccia[d], D. Hatzifotiadou[c], H.T. Jung[e], W.W. Jung[e], D.S. Kim[e], D.W. Kim[e], H.N. Kim[e], J.S. Kim[e], S. Kiselev[a], G. Laurenti[c], K. Lee[e], S.C. Lee[e], M.L. Luvisetto[c], D. Malkevich[a], A. Margotti[c], R. Nania[c], A. Nedosekin[a], F. Noferini[c,f], P. Pagano[d], A. Pesci[c], R. Preghenella[b,c,*], G. Russo[d], M. Ryabinin[a], E. Scapparone[c], G. Scioli[b,c], A. Silenzi[b,c], Y. Sun[g], M. Tchoumakov[a], K. Voloshin[a], M.C.S. Williams[c], B. Zagreev[a], C. Zampolli[c,f], A. Zichichi[b,c,f].

[a] *Institute for Theoretical and Experimental Physics, Moscow, Russia*
[b] *Dipartimento di Fisica dell'Università, Bologna, Italy*
[c] *Sezione INFN, Bologna, Italy*
[d] *Dipartimento di Fisica dell'Università and INFN, Salerno, Italy*
[e] *Department of Physics, Kangnung National University, Kangnung, Republic of Korea*
[f] *Museo Storico della Fisica e Centro Studi e Ricerche "Enrico Fermi", Rome, Italy*
[g] *World Laboratory, Lausanne, Switzerland*

Since the beginning of commissioning of the ALICE-TOF detector, one of the most crucial aspects has been to check the quality of the data produced. Both during last November tests at the CERN PS and in the cosmic-ray test facility, running since more than one year, the data taking of assembled TOF "modules" has been continuously monitored in order to detect as quickly as possible faulty conditions or bad detector configurations. The tools developed for these purposes, which are currently also used for the commissioning of TOF "supermodules", and the new under-development automatic data quality monitor will ensure the highest possible TOF data quality during its operation.

Keywords: ALICE; MRPC; Data acquisition; Data quality monitor.

1. Introduction

The ALICE experiment [1,2] has been designed to study the strongly interacting matter embedded in the extreme temperature and energy-

*Corresponding author.
email address: Roberto.Preghenella@bo.infn.it (R. Preghenella)

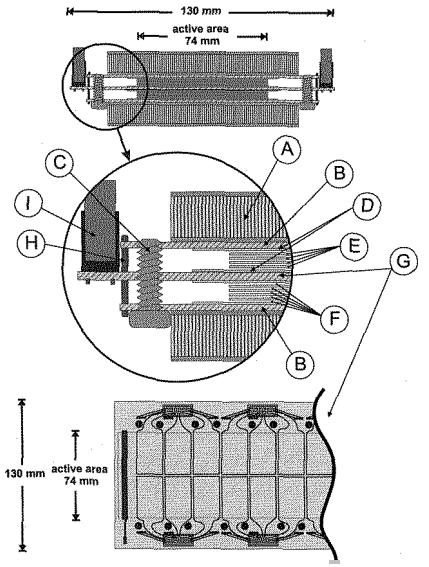

Fig. 1. Schematic cross section of a ALICE-TOF MRPC. (A) 10 mm thick honeycomb panel; (B) PCB with cathode pick-up pads; (C) plastic pins to hold the spacer; (D) 0.55 mm thick external glass plates; (E) 0.4 mm thick internal glass plates; (F) 250 μm wide gas-gap; (G) central PCB with anode pick-up pads; (H) metallic connections to bring cathode signals to the central PCB; (I) connector to take signals to the front-end electronics.

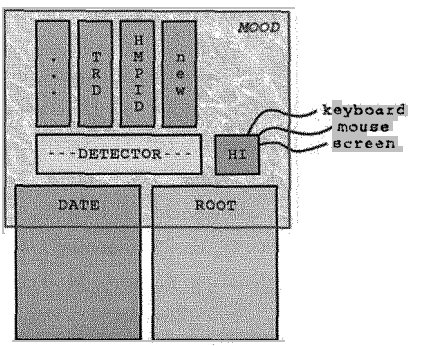

Fig. 2. MOOD plugable design. The ROOT and DATE libraries provide the GUI, the analysis tool and the interface to the DAQ. The executable is a GUI in which detector specific modules are loaded at runtime. TRD and HMPID are acronyms for two ALICE detectors.

density environment produced in the LHC ultra-relativistic Pb–Pb collisions ($\sqrt{s}$ = 5.5 TeV per nucleon pair). The Time-Of-Flight (TOF) system [3] will be one of the most powerful ALICE detectors capable to identify charged hadrons in the mid-momentum region. It consists of a large cylindrical surface 3.7 metres away from the interaction point covering a pseudorapidity acceptance of $|\eta| \lesssim 0.9$. The very good time-resolution performances required for such a system have been obtained by using as the basic detector element a MRPC (Multigap Restistive Plate Chamber) [4] strip detector (Fig. 1), divided into two rows of 48 readout pads, each one having an area of about 9 cm^2. The signals coming from the MRPCs are readout by low-jitter Front-End Electronic (FEE) cards, based on NINO ASIC chips [5], and digitized by high-resolution Time-to-Digital converters (HPTDC ASIC chips) embedded in the so called TDC Readout Modules

(TRM) [6]. To complete the full TOF detector a total of 1638 MRPC strips have already been produced in Bologna and most of them have been integrated inside large modules which are giving shape to the 18 TOF azimuthal sectors: the TOF "supermodules".

2. MOOD: an interactive monitoring tool

The online data quality monitoring is an important part of the ALICE data acquisition (DAQ) sofware framework (DATE, Data Acquisition and Test Environment) [7]. It allows to detect faulty conditions or bad detector configurations as soon as possible during data taking. Moreover it is also very useful to have a quick look into the detector behaviour during detector commissioning. For these purposes, an online monitoring application called MOOD (Monitor Of Online Data) has been developed within the ALICE collaboration. MOOD is written in C++ and it is based on the ROOT framework [8] which provides the Graphical User Interface (GUI) and the analysis tools such as histograms and graphs. The use of the DATE monitoring library provides the needed interface to the DAQ and therefore to the raw data stream.

MOOD is an interactive application with a plugable structure (Fig. 2) in which classes containing the detector specific functionalities are loaded at runtime. Specialized MOOD "modules" have been developed in order to monitor the TOF raw data stream produced in a wide set of test environments and have been heavily used since more than one year. All MOOD-TOF modules share a fast and error-safe[a] decoder and a light interactive GUI to present in a set of online histograms the detector status.

3. Monitoring the ALICE-TOF detector data

The very large mass production both of detectors and readout electronics ($\sim 10^5$ readout channels) for the ALICE-TOF system requires a strict set of quality tests [9]. One of the most crucial ones concerns the readout of the detectors through the complete final electronic chain; this has been done during the last November tests with the CERN PS beam and it is currently under way in the module cosmic-ray test facility [10], running since more than one year. Moreover, readout tests are part of the commissioning programme of the TOF detector.

[a]The ALICE-TOF decoding routines have been developed in order to detect data inconsistencies. This functionality prevents unpredictable decoder behaviours due to wrong or corrupted data.

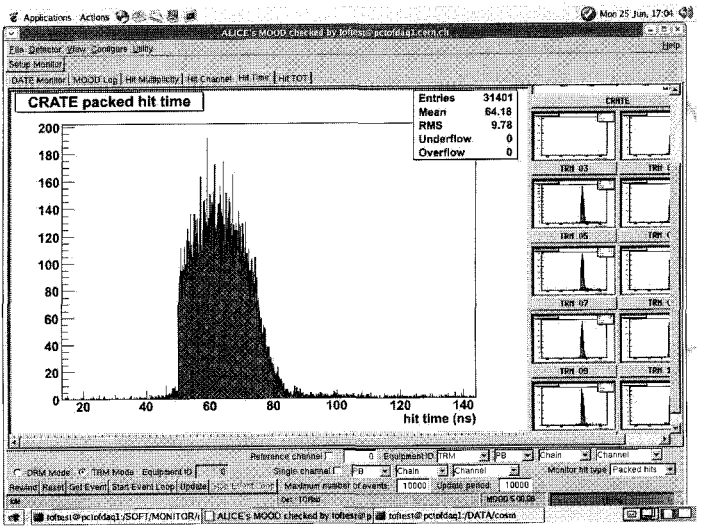

Fig. 3. Screenshot of MOOD-TOF module while monitoring the data taking in the cosmic-ray test facility. The main histogram shows the time distribution of the channels under test. A clearly visible sharp cut in the spectrum signals that the readout electronics has not been properly configured.

A special MOOD-TOF module has been developed to monitor the data taking for the last November tests at the CERN PS. It showed to be very helpful both in finding the beam position with respect to the MRPC readout pads and in promptly evaluating the time resolution of the channels under test, that is looking at the RMS of the online time distributions. The final MOOD-TOF module has also been developed and it is continuously monitoring the data coming from the module cosmic-ray test facility since its very beginning. Some user-related bad configurations (Fig. 3) as well as some electronics-related faults have been encountered, understood and fixed since the first cosmic-ray run and the quality of the data has always been restored as soon as the user detected a bad condition. The same final MOOD-TOF module is also being used for the commissioning of the ALICE-TOF supermodules on which readout tests are carried out sending an external pulse into the MRPC readout pads. As a matter of fact, it has been demonstrated that MOOD is a very useful tool in finding quickly badly plugged-in electronic cards and cables as well as in discovering faults in the VME boards installed in the supermodule crates.

4. The automatic data quality monitor

Although the most striking feature of these tools is their capability in detecting that something is going wrong without running any analysis application, they have a strong limit: they need a user to watch at the histograms. For this reason, the ALICE collaboration is developing a new monitoring tool, called AMORE (Automatic MOnitoRing Environment), that will be used already at the first run of LHC. The main difference with respect to MOOD is that AMORE will be an automatic monitoring application which aims at informing that something is going wrong with messages, so that the user can execute the corrective operations. For the TOF detector a special AMORE module is under developement following the traces of the MOOD-TOF one. It will be able to automatically detect both detector- and electronic-related faulty conditions and user-related bad detector configurations as quickly as possible in order to ensure the highest possible TOF data quality.

5. Conclusions

The tools developed to monitor the ALICE-TOF detector raw data stream during its operation have demonstrated to be able to detect faulty conditions and bad detector configurations in a wide set of test environments. These tools and the upcoming automatic monitoring application will therefore ensure the highest possible quality of the data produced by the TOF detector.

References

1. ALICE Collaboration, *J. Phys.* **G30**, 1517 (2004).
2. ALICE Collaboration, *J. Phys.* **G32**, 1295 (2006).
3. ALICE Collaboration, Addendum to the technical design report of the time of flight system (TOF), CERN–LHCC–2002–016, (2002).
4. E. Cerron Zeballos *et al.*, *Nucl. Instrum. Meth.* **A374**, 132 (1996).
5. F. Anghinolfi *et al.*, *Nucl. Instrum. Meth.* **A533**, 183 (2004).
6. A. N. Akindinov *et al.*, *Nucl. Instrum. Meth.* **A533**, 178 (2004).
7. ALICE DAQ Project, ALICE DAQ and ECS user's guide, ALICE–INT–2005–015.
8. R. Brun *et al.*, ROOT users guide 5.16, http://root.cern.ch.
9. A. Akindinov *et al.*, *Nucl. Phys. Proc. Suppl.* **158**, 78 (2006).
10. R. Preghenella, *Nuov. Cim.* **B121**, 789 (2006).

The detailed simulation of the CMS detector

C. Rovelli

on behalf of the CMS Collaboration

INFN Roma1, c/o dip. di Fisica Università 'La Sapienza', P.le Aldo Moro 2, 00185 Roma, Italy

**E-mail: chiara.rovelli@roma1.infn.it*

The CMS Collaboration developed a detailed simulation of the detector which is integrated in the software framework CMSSW. The simulation is based on the Geant4 tool for the description of particles interactions with the detector material. Care is given to the detailed description of the detector geometry. The simulation software is fully operational and it is currently under validation using real data from testbeams and from commissioning with cosmic rays.

1. Introduction

The experiments which will take date at the Large Hadron Collider will make use of Monte Carlo samples to generate large amounts of signal and background events for physics analyses and to develop and validate methods for the detectors calibration, for efficiency and resolution estimation and so on. Having an accurate, faithful and data driven simulation is therefore really important. The CMS Collaboration [1] has recently reimplemented its simulation, reconstruction and analysis software in the new CMSSW framework. The porting of the code was the occasion for a revision of several packages of the software. In this report the implementation of the full simulation is discussed, together with its validation through the comparison with real data collected at testbeams and during the commissioning with cosmic rays.

2. The simulation chain

The simulation inputs are collision events produced by some events generator. Several general-pourpose generators are currently interfaced to CMSSW (Pythia, Herwig, Alpgen, ...) and generator configuration cards embedded in full configuration files are implemented, as well as particle

guns. The format of the Monte Carlo events throughout CMSSW is a wrapper around generator informations recorded in the HepMC format. The CMS full simulation is based on the Geant4 simulation toolkit [2] which provides a rich set of physics processes describing electromagnetic and hadronic interactions in detail. Geant4 also provides tools for modelling the full geometry and the interfaces required for retrieving informations from particle tracking through the subdetectors. It also allows the description of the magnetic field. The Geant4 functionality is interfaced to the core of CMSSW throught one single module coming with a set of parameters which are configurable at run time. Among them, one of the most relevant is the physics list for the processes to be simulated; up to now many physics lists for both hadronic and electromagnetic interactions have been tested (LHEP, QGSP, QGSC...) together with different particle production cuts. An interface for the possible tuning of the Geant4 objects at any simulation time is also implemented. The detector description involves the geometrical properties of the components, their relative positions and the materials description. The approach followed in CMS is the unification under a single architecture implemented via a Detector Description Database (DDD). In this package the detector is represented as a multigraph structure with a compactified description; such a view can be traslated into an expanded one with a tree structure of volumes contained into higher level ones. XML is used as a language to encode the description itself through the DDD schema, but the whole structure is actually independent on the language used for the practical detector implementation. The simulation is currently implemented for all the central subdetectors including the field map for the 4T solenoid. The porting to the new framework was also the occasion to revisit the detector geometry implementation: all the subdetectors are updating their geometry to the latest engeneering drawings of the detector, both for sensitive regions and for dead materials. Forward subdetectors have been also ported to the new framework and their simulation is currently being tested. During the low luminosity and high luminosity phases of its operation, the LHC accelerator will produce respectively an average of about 3 and 20 inelastic pp collisions per bunch crossing that will pile-up on top of the signal collisions. Both in-time and out-of-time pile-up with respect to the trigger are taken into account in the simulation. At present signal and pile-up events are simulated in different streams and then merged at the hit level through a dedicated mixing module. A new project is on the way to mixup real data pile-up with simulated events, to get a more realistic description of the underlying events. The mixing module provides the input for the digitization

module, which constitutes the simulation of the electronic readout. Care is given to all the details of the electronics, according to the different subdetector configurations. Fluctuations in the energy deposits are taken into account; also, an accurate description of detector noise, drift times, cross talk and any other detector characteristic is simulated. Where needed zero suppression algorithms are also implemented. The digitization software has been ported to the CMSSW framework for all the subdetector and it is fully operational. Most of the work is now related to possible improvements in the algorithms in order to speed up the digitization itself and to improve the software performances. The goal of the digitization is providing an output as close as possible to the real data coming from CMS. Such an output is then passed to the reconstruction software, which builds up reconstructed hits for all subdetectors and then produces higher order physics objects.

3. Simulation validation

A data driven and as faithful as possible simulation is important to be ready for the CMS physics at startup and a big effort is therefore currently ongoing to validate the simulation output versus the available data. In recent years modules of both the electromagnetic and hadron calorimeters have been exposed to testbeams with pion and electrons over a large energy range and a detailed comparison with dedicated testbeam simulations is currently ongoing. The output from the tracker simulation is being compared with the data collected during a cosmic campaing during summer 2006 and at the Tracker Integration Facility at CERN. Also, the response to cosmic data during the commissioning of the muon detectors is being compared with the simulation exploiting a dedicated cosmic rays generator. In general a good agreement between data and simulation is found and an effort is ongoing to understand the remaining discrepancies where any. Some examples are shown in figure 1. The tuning of the simulation and digitization of the various subdetectors is on the way profiting from the output of such validations in order to better match the real data; also, feedback from these validations is provided to the Geant4 Collaboration. A dedicated effort is also devoted to compare the results obtained with different Geant4 versions and physics lists and to validate one software release versus another.

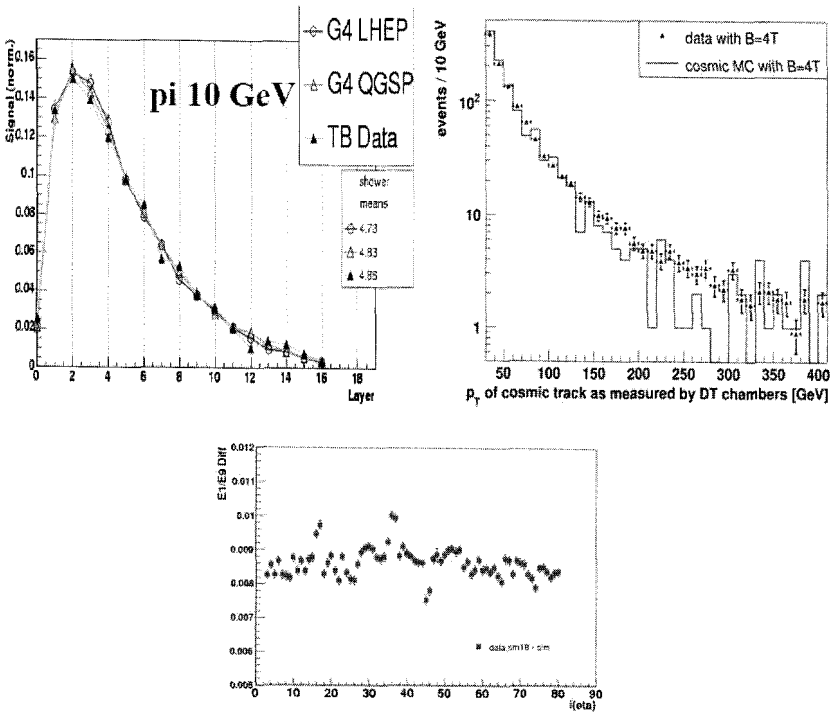

Fig. 1. Validation of the CMS simulation versus data. On the top left, pions shower profile in HCAL: comparison between two different Geant4 physics lists and testbeam data; right, muons transverse momentum in drift tubes: comparison between cosmic rays collected during the commissioning and simulation. On the bottom: difference between the transverse profile of electromagnetic showers in ECAL with simulated electrons and data collected at testbeam.

4. Conclusion

The full simulation of the CMS detector has been integrated in the new CMSSW framework and many its components have been improved. The simulation software is fully operational and it is currently under validation using real data from testbeams and from commissioning with cosmic rays.

References

1. The CMS Collaboration, "The Compact Muon Solenoid Technical Proposal", CERN/LHCC 94/38, LHCC P1 (1994)
2. S.Agostinelli et al., *Nuclear Instruments and Methods in Physics Research A* **506**, 250 (2003)

ATLAS CONDITIONS DATABASE EXPERIENCE WITH THE COOL PROJECT

MONICA VERDUCCI
ON BEHALF OF THE ATLAS COLLABORATION
CERN 1211 Meyrin, Geneve, Switzerland and
CNAF via Viale Berti Pichat 6/2, Bologna, Italy

The COOL conditions database will be one of the most challenging and heavily used database applications for ATLAS, both in terms of data volumes and rates, but also in the variety of data stored. One of most challenging tasks in the ATLAS experiment will be the storage of non-event data produced by calibration and alignment stream processes into the Conditions Database at the Tier0 (located at CERN) using the COOL technology. In this work, the ATLAS Conditions Database and the conditions data (in particular the data coming from the calibration and alignment processes) are described.

1. Introduction on the ATLAS experiment at LHC

The accelerator LHC (Large Hadron Collider) is a proton-proton collider that will run at 14 TeV in the center of the energy mass.
Along the 27 Km ring, four different detectors are placed: ATLAS (A Toroidal LHC ApparatuS), CMS (Compact Muon Solenoid), ALICE (A Large Ion Collider Experiment) and LHCb (Large Hadron Collider bphysics).
The protons, coming in roughly cylindrical bunches of few centimeters long and few microns in radius and separated in time by 25 ns, will collide in a 110 m long region, without any magnetic field. At the designed high luminosity (10^{34} cm^{-2} s^{-1}), the two proton beams will be made of 2835 bunches, with a total number of produced events per unit time (Rate) of about 1 GHz, according to the proton-proton inelastic cross section of $\sigma = 70$ mb.
The major problem of data management, that the LHC experiments, and in particular ATLAS, are going to face, is the huge quantity of data each year of about few PBytes, that must be stored and made available to all physicists of the collaboration, distributed world-wide. The distributed architecture based on Grid infrastructure has been chosen to resolve problems related to data storage capacity and data transfer among computing centers, spread in different countries, to assure data access only to the authorized users and to ensure remote resources are used effectively.

2. Event Selection (Trigger) and Streams

The major challenge faced at ATLAS is to reduce the interaction rate of about 1 GHz at the design luminosity of 10^{34} cm^{-2} s^{-1} online by about seven orders of magnitude to an event rate of O(100) Hz going to mass storage.
Divided in different levels of increased latency and complexity, the trigger chain operates a selection in the event, according to the pre-defined trigger menu. The final output, after the Event Filter (EF), consists of several streams with a well defined scope; see for details [1].
The output data from the EF requires an average 320 MB/s bandwidth connecting it to the first-pass processing facility.
Four types of streams come from the Event Filter: a ***Primary Stream***, containing all the physics events from EF divided into five sub-streams, a ***Calibration and Alignment Stream*** dedicated to the calibration and about 10% of the entire EF output, an ***Express-line Stream*** dedicated to a rapid processing, and a ***Diagnostic Stream*** for events causing problems at EF level. While the option of "streaming data" at the EF should be retained; the baseline model assumes a single primary stream containing all physics events flowing from the Event Filter to Tier-0.
Several other auxiliary streams are also planned, the most important of which is a calibration hot-line containing calibration trigger events (which would most likely include certain physics event classes). This stream is required to produce calibrations of sufficient quality to allow a useful first-pass processing of the main stream with minimum latency. A working target (which remains to be shown to be achievable) is to process 50% of the data within 8 hours and 90% within 24 hours and all the data within 48 hours.
Two other auxiliary streams are planned. The first is an express-line of physics triggers containing about 10% of the full data rate and processing as soon as possible and anyway within 8 hours. This stream has been also included to do calibration and alignment studies as well as the calibration stream; moreover, it will allow the tuning of physics and detector algorithms and also a rapid alert on some high-profile physics triggers. It is to be stressed that any physics based on this stream must be validated with the "standard" versions of the events in the primary physics stream. However, such a hot-line should lead to improved reconstruction. It is intended to make much of the early raw-data access in the model point to this and the calibration streams. The fractional rate of the express stream will vary with time, and will be discussed in the context of the commissioning.

The other auxiliary stream contains pathological events, for instance those that cause problems for the EF processing. These may pass the standard Tier-0 processing, but if not they will attract the attention of the development team. They will be strongly rate-limited.

2.1. *Calibration and Alignment Process*

Calibration and alignment processing refers to the processes that generate "non-event" data that are needed for the reconstruction of the event data, including processing in the trigger/event filter system, prompt reconstruction and subsequent later reconstruction passes.

These "non-event" data (i.e. calibration or alignment entries) are generally produced by processing some raw data from one or more sub-detectors, rather than full raw data. The input raw data can be in the event stream (either normal physics events or special calibration triggers) or can be processed directly in the sub-detector read-out systems in special calibration runs. The output calibration and alignment data will be stored in the conditions database, and may be fed back to the online system for use in subsequent data taking, as well as being used for later reconstruction passes, [2].

Various types of calibration and alignment processing can be distinguished:

1. Processing directly in the sub-detector read-out system (the RODs
2. Processing in the EF system, with algorithms either using dedicated calibration triggers (identified in the level 1 trigger or HLT).
3. Processing after the event filter, but before prompt reconstruction.
4. Processing offline after prompt reconstruction.

3. Conditions and Configuration Databases

Many types of non-event data will be used during the ATLAS data taking, reconstruction and subsequent processing.

These data have many different origins, and are stored in many different types of databases.

In the ATLAS experiment there are two database systems to store these non-event data: a Configuration Database and a Condition Database, see [2].

The Configuration Database will store all the data needed at the start of the run, including sub-detector hardware and software configuration. The Conditions Database will store all the parameters describing run conditions and logging, all the data which will be accessed offline, i.e. by the reconstruction or analysis software.

The conditions database is closely related to Configuration Database, needed to set up and run the detector hardware and associated online and event selection software.
Conditions data varies with time, and is usually characterized by an "interval of validity" (IOV). It includes data archived from the ATLAS detector control system (DCS), online book-keeping data, online and offline calibration and alignment data, and monitoring data characterizing the performance of the detector and software during any particular period of time.

3.1. *Conditions Database*

The ATLAS Condition Database is based on Oracle DB, all the Condition Database, in particular for the offline reconstruction, is implemented using COOL technology, an LCG product, that allows database applications to be written independently of the underlying database technology (this means that COOL databases can be stored in Oracle, SQLite or MySQL), see for more details [3].
Moreover, the COOL API has been integrated into the ATLAS online software. Several special-purpose higher level interfaces are also being developed, including the Condition Database Interface (CDI) for archiving information system (IS) data to COOL, the PVSS to COOL interface for archiving Detector Control System (DCS) data, and specialized interfaces for saving monitoring data.
The objects stored or referenced in COOL have an associated start and end time between which they are valid, the data are stored via an Interval of Validity (IoV).
COOL data is stored in folders, which are themselves arranged in a hierarchical structure of folder sets. Within each folder, several objects of the same type are stored, each with his interval of validity range. These times are specified either as run/event, or as absolute timestamps, and the choice between formats is made according to meta-data associated with each folder. The objects in COOL folders can be optionally identified by a channel number (or channel ID) within the folder. Each channel has its own intervals of validity, but all channels can be dealt with together in bulk updates or retrieves.

COOL implements each folder as a relational database table, with each stored object corresponding to a row in the table. COOL creates columns for the start and end times of each object, and optionally the channel ID and tag if used. Several other columns are also created (e.g. insertion time and object ID), to be

used internally by the COOL system, but these are generally of no concern to the user.

The payload columns (where the data are stored) are defined by the user when the table is created. In ATLAS, the payload data can be stored in the three following ways.

The payload data can be stored directly in one or more payload columns (inline data), where the columns directly represent the data being stored (e.g. a mixture of float and integer values in the columns representing status and parameter information).

In second way, the payload data (in this case a single column) can be used to reference data stored elsewhere. This reference can be a foreign key to another database table, or a reference to something outside of COOL - e.g. a POOL object reference allowing an external object to be associated to intervals of validity.

A third approach involves storing the data as an inline CLOB in the database, i.e. defining the payload to be a large character object (CLOB) which has an internal structure invisible to the COOL database. COOL is then responsible only for storing and retrieving the CLOB, and its interpretation is up to the client code.

The retrieving and storing of the data inside a reconstruction job in the Athena framework (offline reconstruction framework) is possible using the IOVService, a software interface between the COOL DB and the reconstruction algorithms via IOV range. Extensive tests are foreseen during the Computing and Detector Commissioning.

Acknowledgments

Many thanks to the INFN section of the University of Rome "La Sapienza" for the grant given me to attend the 10th ICATTP Conference.

References

1. ATLAS Collaboration, ATLAS High-Level Triggers, DAQ and DCS Technical Proposal, CERN/LHCC/2000-17, (2000)
2. ATLAS Collaboration, ATLAS Computing Technical Design Report, CERN/LHCC/2005-022, (2005)
3. A. Valassi, COOL web page, Available at http://lcgapp.cern.ch/project/CondDB/

INTENSITY VARIATION OF GAMMA RAYS DUE TO WATER CONCENTRATIONS ON THE LUNAR SURFACE

K. IWABUCHI, N. YAMASHITA, S. KOBAYASHI, K. HAYATSU, M. HAREYAMA, Y. KAROUJI, K. SAKURAI AND N. HASEBE

Research Institute for Science and Engineering, Waseda University, 3-4-1 Ohkubo, Shinjuku, Tokyo 169-8555, Japan

Fluxes of gamma rays emitted from the lunar surface consisting from ferroan anorthosite with various concentration of water (H_2O) were calculated with Geant4. They are useful to the current and future lunar missions for the projects to search for the existence of water in the lunar polar regions with a gamma-ray spectrometer. The result thus obtained indicates that the flux of gamma-rays with 2223 keV due to the reactions $^1H(n, \gamma)^2D$ has a monotonous dependence on the concentration of H_2O from 0.1 to 20 wt% and the flux of 4934 keV gamma-rays due to the reactions $^{28}Si(n, \gamma)^{29}Si$ is remarkably correlated with the abundance of H_2O. The variation of these gamma-ray fluxes dependent on the concentration of H_2O is also discussed with the neutron density profile in the lunar subsurface.

1. Introduction

One of the most attractive and interesting topics about the Moon is the existence of water on the lunar polar regions, since the work of Watson et al.[1] was published. The recent results obtained by the neutron spectrometer aboard Lunar Prospector, LP, show that the abundance of hydrogen near the lunar polar regions is of 100 ~ 150 ppm H in average and 0.18 ~ 40 wt% H_2O in localized area[2]. These results seem to request for us to obtain more confident evidences. The most suitable method to reach for them is a gamma-ray spectroscopy by using a high-purity germanium detector to be on board SELENE (KAGUYA) mission[3]. The reason is that hydrogen nuclei emit 2223 keV gamma ray due to the reactions $^1H(n, \gamma)^2D$ by absorbing neutrons produced by galactic cosmic ray ,GCR incidence on the lunar surface, and the detection of 2223 keV peak in gamma-ray spectra will become a firm confidence for the existence of water.

The foregoing study by Brückner et al.[4] should be mentioned here. They calculated gamma-ray spectra on the Mercury surface and found that fluxes of gamma-ray emissions due to inelastic and capture reactions from major elements are varied by water content. This means that the existence of water can

be shown by measuring ordinary gamma rays without direct signal of 2223 keV from hydrogen. Based on this idea, possible variation of fluxes of hydrogen peak (2223 keV, $^{1}H(n, \gamma)^{2}D$) and silicon peak (4934 keV, $^{28}Si(n, \gamma)^{29}Si$) with different concentration of water from lunar soil made of ferroan anorthosite, FAN, is considered in detail by using the calculation by Geant4.

2. Calculation method

In order to simulate the production and transportation of gamma rays and neutrons due to incident GCRs into the lunar subsurface, the simulation code based on Geant4.8.0.p01 was used.

In the simulation for neutron production, GCR-protons with the spectra used in reference[5], 4π flux of GCR = 2.90 cm^{-2} s^{-1} (solar modulation parameter ϕ = 550 MV) and an energy range from 0.1 to 100 GeV were irradiated on lunar soils made from ferroan anorthosite, FAN, (see Table I) containing various concentrations of water (0 ~ 50%). Although gadolinium and samarium that have large capture cross sections influence the transportation of neutrons at low energy, they were not included in this calculation for simplicity. Whole of neutrons generated in the lunar soil were traced until they ended in capture reactions, escapes from lunar surface to space, nuclear reactions such as (n, p) or decays. Then, distributions of the positions of capture reactions in the subsurface, depth profile, were obtained as shown in the next section. The depth profile is multiplied by a factor of 1.3 to include the contribution by alpha particles in GCR according to discussion in refference[6].

Table I. The composition of ferroan anorthosite

	Na_2O	MgO	Al_2O_3	SiO_2	CaO	FeO
wt%	0.2	3.6	30.3	44.5	17.7	3.7

Since the nucleus of hydrogen is only excited by neutron capture reactions, the flux of gamma rays by this capture is calculated. The production rates of gamma ray as a function of depth in the lunar surface are calculated by using capture gamma ray emission cross sections[7], the abundance of elements in the soil and the above depth profile, assuming that the capture cross sections stringently obey the $1/v$ law. This hypothesis introduces a major error (~10 %) for our calculation because we were not concerned with the effects of resonance peaks and of cross sections at high energy (> 100 eV).

Gamma rays were isotropically generated by a Monte Carlo code by using the production rates. Fluxes of line gamma ray on the lunar surface were

obtained, assuming that the gamma rays were exponentially attenuated with the mass attenuation coefficients[8, A]. The mean free path of gamma rays by using them is shown in Fig. 1.

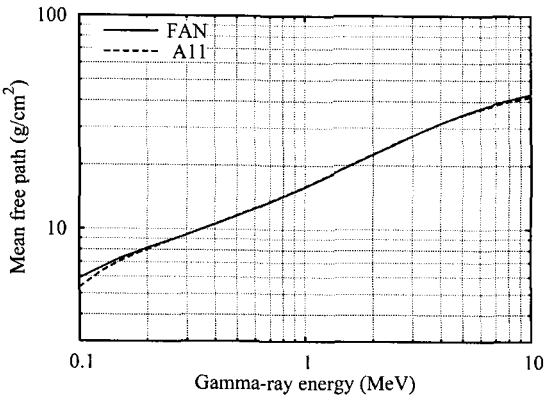

Fig. 1. Mean free path of gamma ray in the soil made of FAN and Apollo 11 landing sites.

3. Results

3.1. *Depth profiles of neutron capture reactions in the lunar subsurface*

The depth profiles of capture reactions are shown in Fig. 2. For dry soil, i.e. FAN with no water, the peak position is around 170 g/cm^2, and the peak shifts shallower with increase of the water contents. According to the result of McKinney et al.[8] the neutron production is the most intense at the depth less than 25 g/cm^2, and so it follows that this peak shift is attributed to the moderation of water. The concentration of water increasing, it become too difficult for the neutrons produced from interactions of GCR with the lunar soil to proceed deeper because of effective energy loss by collisions with hydrogen atoms.

This depth profile indicates that gamma rays due to capture reactions are generated at all depths. The mean free path of gamma ray, however, is 5 ~ 40 g/cm^2, thus, the effective capture reactions contributing on the surface flux of gamma rays should also be occurred less than 40 g/cm^2. As shown in Fig. 2, the number of capture reaction shallower than 40 g/cm^2 increases with the increase of water contents. It is expected that gamma rays due to the capture reactions,

---

[A]XCOM: http://physics.nist.gov/PhysRefData/Xcom/Text/XCOM.html

such as the reaction ^{28}Si (n, γ) ^{29}Si, become intense as the contents of water is high.

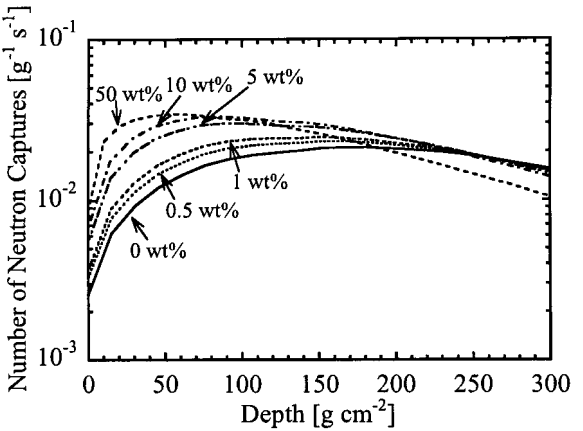

Fig. 2. Depth profile of capture reactions in the lunar subsurface.

3.2. *Gamma-ray flux due to $^{1}H(n, \gamma)^{2}D$ and $^{28}Si(n, \gamma)^{29}Si$*

By using the depth profile in Fig.2, the gamma ray flux at the surface is calculated by the method mentioned in Sec. 2. The gamma ray flux at the lunar surface as a function of mass fraction of H_2O is shown in Fig. 3.

The flux of 2223 keV monotonically increases with the increase of the concentration of water (C_{H2O}). The average abundance of H in the equatorial region, 50 ppm (C_{H2O} ~ 0.045 wt% H_2O equivalent), is 10^{-2}~10^{-3} photons cm^{-2} min^{-1}. On the other hand, if the mass fraction of H_2O is above 10 wt%, the flux of 2223 keV is comparable to that of 1461 keV from ^{40}K (= 2.6 cm^{-2} min^{-1})[9] that is one of the strongest gamma rays on the lunar surface.

The flux of 4934 keV due to ^{28}Si(n, γ)^{29}Si shows a characteristic response. The flux is constant while C_{H2O} is less than 0.1 wt%. It can be understood from the fact that the depth profile of capture reaction in Fig. 2 is not affected in this range of the concentration. When C_{H2O} is 0.1 ~ 5 wt%, the flux increases as expected from the calculation done in previous section. The maximum of the flux of the gamma ray from silicon is at 5 wt% and is 1.5 times higher than that in no water. If C_{H2O} is greater than 5 wt%, the flux decreases with C_{H2O} since water become the most major material in the soil and the absolute abundance of silicon is decreased.

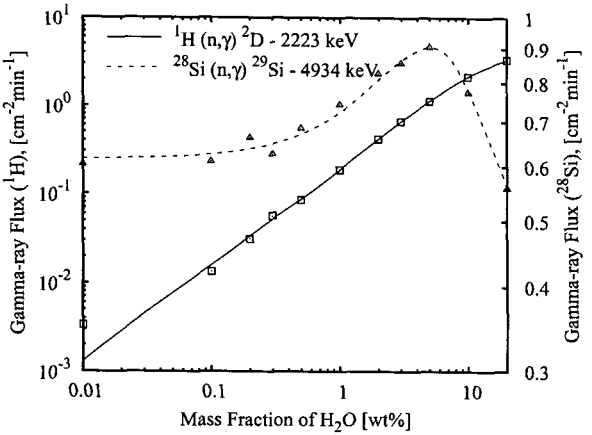

Fig. 3. Fluxes of gamma ray as a function of mass fraction of H_2O in the FAN Soil.

4. Summary

The responses of the flux of gamma rays due to $^{1}H(n, \gamma)^{2}D$ and $^{28}Si(n, \gamma)^{29}Si$ to the concentrations of water in a lunar soil were studied by Geant4. Both of the flux depend well on the concentration of water in the soil. The fluxes of gamma ray due to $^{28}Si(n, \gamma)^{29}Si$ are correlated with the depth profile of neutron capture reaction that easily varies with the presence of water. Considering these results, vertical distribution of water in the lunar soil could be inferred by measuring both of the capture gamma-rays from hydrogen and silicon, because localization of water at a depth could cause the distinctive fluxes depending on the water distribution.

References

1. K. Watson, B. Murray and H. Brown, *J. Geophys. Res.* **66**, 1598 (1961).
2. D. J. Lawrence et al., *J. Geophys. Res.* **111**, E08001 (2006).
3. N. Hasebe et al., "Gamma-Ray Spectrometer (GRS) for Lunar Polar Orbiter SELENE," *Earth Planets Space,* submitted.
4. J. Brückner and J. Masarik, *Planet. Space Sci.* 45, **39** (1997).
5. J. Masarik and R.C.Reedy, *Geochimica et Cosmochimica Acta* **58** 5307 (1994).
6. G.. W. McKinney et al. J. Geophys. Res. **111**, E06004 (2006).
7. G. L. Molnar "Handbook of Prompt Gamma Activation Analysis with Neutron Beams", Kluwer Academic Publishers (2004).
8. M.J. Berger et al., XCOM: Photon Cross Sections Database
9. R. C. Reedy, *Proc. Lunar Planet. Sci. Conf. 9th* 2961 (1978).

This page intentionally left blank

Space Experiments and Heliosphere

Organizers:

K. Kudela
Particles in Heliosphere and Earth Magnetosphere
S. Volontè
Space Experiments

This page intentionally left blank

REENTRANT HELIOSPHERIC PARTICLES IN 2D DRIFT MODEL[1]

BOBIK PAVOL, KUDELA KAREL
Institute of Experimental Physics SAS
Košice, 04001, Slovak Republic

BOSCHINI MATTEO, GRANDI DAVIDE, GERVASI MASSIMO, RANCOITA PIER GIORGIO
Instituto Nazionale di Fisica Nucleare
Milano, 20126, Italy

We developed 2D time dependent heliospheric model where particles trajectory are reconstructed back in time. The model is time dependent due to drifts in the heliosphere. We followed particles also after escaping the heliosphere in the interstellar space to found the fraction of them that reenter back again into the heliosphere. We show how this effect can change the modulation of particles in the heliosphere for different solar periods and for different orientation and strength of interstellar magnetic field. The dependence of modulation process in the heliosphere from reentrant particles is discussed in connection to particles mean free path in the interstellar space.

1. Introduction

Transport and distribution of Galactic Cosmic Rays in the heliosphere and interstellar space is described by the Fokker-Planck equation (FPE hereafter) [1][2]. In previous decades was introduced many methods to solve the FPE [3][4]. One of the commonly used is the solutions of the FPE by the Monte Carlo method [5]. The time reversal process is also possible [6]. Particles of GCR from interstellar space penetrating the heliosphere are affected by outgoing solar wind and lose energy adiabatically. Particles outside the heliosphere diffuse in the interstellar space without any energetic losses. It may happen that a particle escaping the heliosphere reenter later back again. Almost in all present models of GCR modulation in the heliosphere, particles escaping the heliosphere are no longer considered.

2. Diffusion in heliosphere and in the interstellar space

Model consist from two parts. First is a particles diffusion in heliosphere. 2D

[1] This work is supported by the Slovak Research and Development Agency under the contract No. APVV51053805.

model of particle diffusion in the heliosphere including drift effects [7] and working with a time reversal process. Particles are injected uniformly with energy at 1AU. Particle with injection energy T_0 during its way back in time in the heliosphere can gain energy. After injection the particle is followed back in time inside the heliosphere to the moment when it crosses the heliosphere border at 100AU. Kinetic energy T_1 of the particle at the moment of first heliopause crossing is recorded. Main parameters of model inside heliosphere are diffusion coefficient, tilt angle and solar wind velocity. The radial diffusion coefficient is $K_r = K_\Pi \cos^2\psi + K_\perp \sin^2\psi$, where ψ is the angle between radial and magnetic field directions. The latitudinal coefficient is $K_{\theta\theta} = K_\perp$. The parallel and the perpendicular diffusion coefficients are

$$K_{II} = K_0 \beta K_P(\Re)\frac{B_0}{3B}, \quad K_\perp = (K_\perp)_0 K_{II} \tag{1}$$

$K_0 = 2 - 5\ 10^{22}\ cm^2\ s^{-1}$, β is the particle velocity in units of light velocity, $K_P(\Re) = \Re$ take into accounts the dependence on rigidity ($\Re$ in GV), $(K_\perp)_0 = 0.025$ is the ratio between parallel and perpendicular diffusion coefficient, $B_0 = 5$ nT is the value of heliospheric magnetic field at the Earth orbit, and B is the Parker field. Second part of model is description of particles diffusion in the interstellar space. Because the probability that a particle reenter back to the heliosphere should depend on the particle mean free path in interstellar space, we use a parallel diffusion coefficient K_{II}^{IS} in interstellar space constructed in following way [8].

$$K_{II}^{IS} = \eta K_B \sim K_0^{IS}\,\eta Z^{-1}\left(\frac{E}{GeV}\right)\left(\frac{B}{1\,\mu G}\right)^{-1} cm^2 s^{-1} \tag{2}$$

where diffusion coefficient in the interstellar space $K_0^{IS} = 3.3 x 10^{22} cm^2 s^{-1}$. η is the ratio of the mean free path of the particle to the Larmor radius, K_B is the Bohm diffusion coefficient $K_B = Ec/(3ZeB)$ where E is total energy, Z is the atomic number and B is the magnetic field intensity in the interstellar space. η is a parameter of simulation in interstellar space. We used a set of values η from 10 to 1000. Perpendicular diffusion coefficient $K_\perp^{IS} = (K_\perp^{IS})_0 K_{II}^{IS}$ where $(K_\perp^{IS})_0$ is a parameter which influence to model result was test in range from 0.01 to 1. Magnetic field in the interstellar space is the second parameter of the simulation outside the heliosphere.

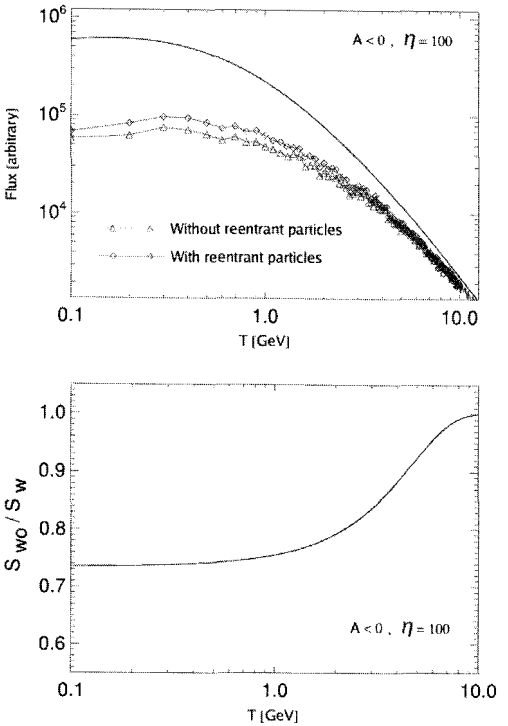

Figure 1: Upper panel show a modulated spectra at 1AU for η = 100 together with a local interstellar spectrum (LIS). Line with triangles denote a spectrum without reentrant particles, solid line with diamonds denote spectrum with a reentrant particles. Bottom panel of figure show a ratio between both proton spectra (S_{WO}/S_W) for A < 0.

For calculations in interstellar space we choosed a locally constant (in the test domain) homogenous magnetic field oriented wit angle δ to ecliptic plane of the heliosphere described as $B_r = B_0 \sin(\theta + \delta)$ and $B_\theta = B_0 \cos(\theta + \delta)$ where value B_0 = 1 μG. Particle diffuse in the interstellar space. Finally when particle crosses the border 1 parsec we record its kinetic energy T_2. In this moment we evaluate two flux values. First for modulated spectrum at 1AU not affected by reentrant particles, and second affected by reentrant particles. Then, next particle is injected and the process is repeated.

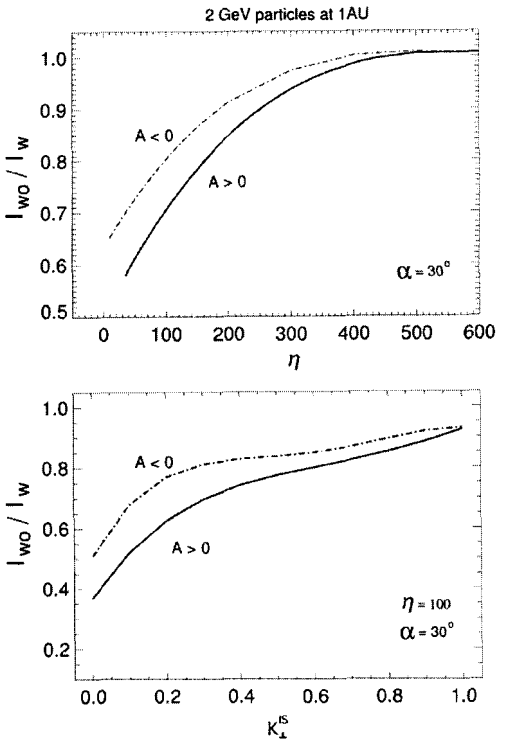

Figure 2: Upper panel show I_{WO}/I_W ratio dependence on η for A > 0 and A < 0 . Bottom panel show I_{WO}/I_W ratio dependence on $(K_{perp}^{IS})_0$ for A > 0 and A < 0.

3. Results

Influence of reentrant particles to different energies of modulated spectra is presented on figures 1. and 2. Situation for negative solar period A < 0 with η = 100, δ = 0°, α = 30° and $(K_{\perp}^{IS})_0$ = 0.25 is showed at Figure 1. At upper panel is the spectrum containing reentrant particles (S_W) compared with the spectrum without reentrant particles (S_{WO}) both calculated for same parameters in the heliosphere. Bottom panel of Figure 1. shows ratios between both spectra (S_{WO}/S_W) for negative solar period A < 0 and η = 100. We made calculation for a set of η values for particles registered at 1AU with energy 2 GeV. Dependence of ratio between intensity of particles without taking into account a reentrant particles (I_{WO}) and with a reentrant particles (I_W) for a different values of η is showed at upper panel of Figure 2. Effect of reentrant particles to registered intensity inside heliosphere also depend on a ratio between parallel and perpendicular coefficient in the interstellar space.

To show the effect we made a calculation for a particles registered at 1AU in a ecliptic plane with kinetic energy 2GeV. Dependence of ratio between intensity of 2GeV particles without taking into account a reentrant particles (I_{WO}) and with a reentrant particles (I_W) for a different values of $(K_{\perp}^{IS})_0$ is presented at the bottom panel of Figure 2.

4. Conclusions

The effect of reentrant heliospheric particles to energy spectra at 1AU depends on many factors: particles mean free path in the interstellar space, the interstellar magnetic field, the ratio between parallel and perpendicular diffusion coefficients in the interstellar space, the solar period and solar period parameters as polarity and tilt angle. Reentrant particles have stronger influence during positive solar periods. Decreasing the ratio between parallel and perpendicular diffusion coefficient in the interstellar space increase the effect of reentrant particles to spectra modulation. The effect of reentrant particles increases with decreasing the particles mean free path in the interstellar space.

Acknowledgments

This work is supported by the Slovak Research and Development Agency under the contract No. APVV51053805.

References

1. E. N. Parker, *Planetary and Space Science* **13**, 9 (1965).
2. S. Chandrasekhar, *Rev. Mod. Phys.* **15**, 1 (1943).
3. L. A. Fisk, *J. Geophys. Res.*, **76**, 221 (1971).
4. J. R. Jokipii, A. J. Owens, *J. Geophys. Res.*, **80**, 1209 (1975).
5. Krülls, W. M.; Achterberg, A., Astron. Astrophys., **286**, 314 (1994).
6. J. Kóta, *Proc. of 15 ICRC*, **11**, 186 (1977).
7. P. Bobik, M. Gervasi, D. Grandi, P.G. Rancoita, I.G. Usoskin, *Proceedings of ICSC 2003*, **ESA SP-533**, 637 (2003).
8. H. Muraishi, S. Yanagita, T. Yoshida, *Progress of Theoretical Physics*, **113**, 721 (2005).

The INFN-LNF Space Climatic Facility

D. Arnold[1], G. Bellettini[2], A. Boni[3], C.Cantone[3], I. Ciufolini[4], D. G. Currie[5]
S. DellAgnello[3], G. O. Delle Monache[3], M. A. Franceschi[3], M. Garattini[3]
N. Intaglietta[3], A. Lucantoni[6], M. Martini[3], T. Napolitano[3], A. Paolozzi[6], R. Tauraso[2]
and R. Vittori[7]

[1] *NASA-GSFC*
[2] *Università Roma Tor Vergata*
[3] *Laboratori Nazionali di Frascati (LNF) dell'INFN*
[4] *Università e INFN Lecce*
[5] *University of Maryland at College Park*
[6] *Università di Roma "La Sapienza", Scuola di Ingegneria Aerospaziale*
[7] *Aeronautica Militare Italiana*

The Space Climatic Facility (SCF) is an experimental apparatus built in 2006 at the Frascati National Laboratory of INFN to study the thermal thrusts acting on the LAGEOS I and II satellites and to perform integrated thermal and optical characterization of retro-reflector (CCR) arrays for laser ranging. The latter include the new LARES satellite, whose main scientific goal is to improve the measurement accuracy of the frame dragging of the Earth (Lense-Thirring effect) predicted by General Relativity and reach a relative accuracy of the order of 1%. The SCF is also devoted to make the same tests on CCR arrays deployed on GNSS constellations (especially on GALILEO) within an approved INFN experiment, ETRUSCO. The SCF is a cylindrical cryostat where a realistic space environment is established in terms of pressure (10^{-6}–10^{-7} mbar), temperature (down to 77 K) and e.m. radiation (Sun simulator and infrared Earth simulator). Thermal simulations are well advanced and laser-optical simulations are making good progress.

1. Introduction

The LAGEOS/LARES program is addressing the significant issue of thermal Non Gravitational Perturbations (NGP), with two main goals: climatically characterize LAGEOS prototypes to reduce NGP errors on the determination of frame dragging, design a new mission and build a fully characterized satellite, which avoids as much as possible the weaknesses of LAGEOS and is capable of reaching 1% accuracy on the Lense-Thirring effect [1]. The SCF has been designed to measure the CCR thermal relaxation time of the, τ_{CCR}, at $\leq 10\%$ accuracy. In 2006 an engineering prototype of

LAGEOS I (a polar sector built in 1992) was sent to LNF by NASA-GSFC for an SCF test. In September 2007 INFN gave the final approval of the LARES experiment.
The SCF turned out to be well suited to characterize the thermal and laser-ranging performance of CCR arrays deployed on GNSS, like the existing US GPS-2, the imminent European GALILEO and the future GPS-3. For each CCR of the arrays, the characterization will include the measurement of the thermo-optical parameters (emissivity, ϵ, and reflectivity, ρ), τ_{CCR} and the variation of the laser far field diffraction pattern (FFDP) in a realistic space environment. This SCF-test will improve the long-term stability and the accuracy of the determination of the GALILEO orbits down to ≤ 1 cm [2].

2. The Space Climatic Facility

The SCF is a cylindrical cryostat (1 m diameter, 2 m length) where a realistic space environment is established in terms of pressure, temperature and e.m. radiation (solar constant and Earth infrared emission). During the measurements a copper shield, black painted with a high emissivity paint, is cooled down with liquid nitrogen to $T = 77K$ and the vacuum is typically $10^{-7} \div 10^{-6}$ mbar. A side Germanium window allows for taking thermograms of the prototypes with an infrared (IR) digital camera [3]. Recently we added a fused silica window (deformations of transmitted wavefront $< \lambda/10$) for FFDP measurements in the space environment.

3. Thermal Measurements and Simulations

The IR camera measures temperatures of external components only. For the camera calibration and for internal componnents we use a 2nd temperature acquisition system made of National Instrument compact Fieldpoints and PT100/PT1000 probes.
Thermal SCF tests have been made on August 30th 2007 using a LAGEOS prototype built at LNF: an aluminum block with 9 CCRs, arranged in a 3x3 matrix [3]. On the top-left CCR temperature sensors have been glued to monitor the temperatures of all the mounting rings. The aluminum block is kept at $\sim$ 300K, the LAGEOS average temperature in space, with a series of 4 Thermo Electric Coolers (Peltier cells), driven by a Electrondynamics TCM controller. Measurements were performed with only the Solar Simulator turned on for three hours in front of the prototype; data were also taken for the next three hours during the cooling phase. The results are pre-

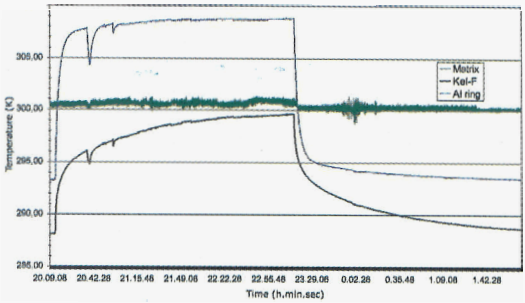

Fig. 1. Measurement of the T variation of the CCR assembly parts using the PT100 sensors.

sented in Fig. 1 and 2. These tests, never performed before, gave important preliminary results:

- Al retainer rings have a significantly smaller temperature variation than expected from all previous calculations [4,5].
- τ_{CCR} is longer than expected.

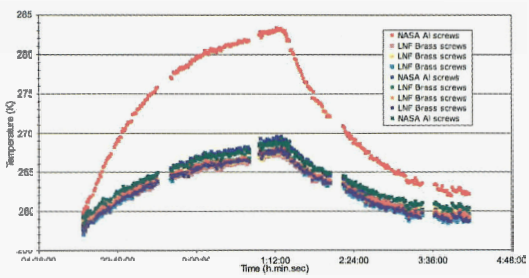

Fig. 2. Measurement of the T variation of all CCR top surfaces using the IR camera.

As we expected, the sensors glued on the CCR destroy locally its Total Internal Reflection and cause a higher temperature variation (red line in Fig. 2). τ_{CCR} will be estimated using the other 8 unperturbed CCRs (with no PT100s glued on). Data taken from Figure 2 were used to make simulations of thermal thrusts of a simplified 3D model of LAGEOS during fully simulated orbits using Thermal Desktop and Sinda Fluint (by Cullimore & Ring Tech.). Results presented in Fig. 3 show good qualitative agreement with previous calculations [5], while the absolute values of the thrusts are lower than in [5]. New full-blown 3d models of LAGEOS and LARES are

nearing completion.

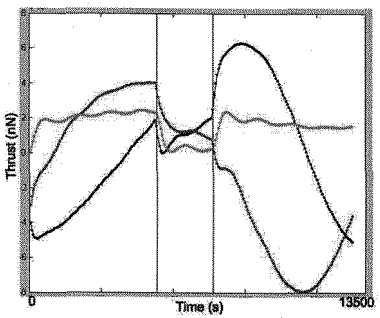

Fig. 3. Thermal thrusts acting on LAGEOS in an orbit of Jan. 1, 2000.

4. Optical Measurements and Simulations

Laser ranging performances depend on the absolute angular size and intensity of CCRs FFDPs. The angular size is important for the phenomenon of the *Velocity Aberration*, due to the relative motion between the satellite and the LR station. Simulations have been performed with CodeV (by Optical Research Associates), an optical CAD modeling software used for the optimization, analysis and toleracing of optical systems. The FFPD measured for a LAGEOS-type CCR with 0 arcsec dihedral angle offset, with one edge up and for a normal horizontally polarized laser beam is shown in Fig. 4 along with the simulated pattern. The measured CCR belongs to the GSFC polar sector. A CCR with 0 arcsec dihedral offset has most

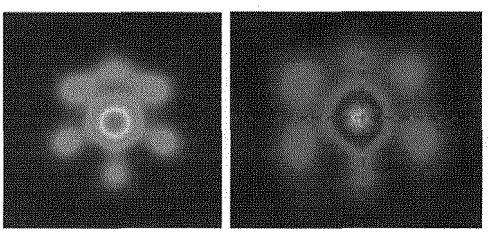

Fig. 4. FFDP of an uncoated CCR with 0 arcsec angle offset. laser beam with $\lambda = 632.8$ nm. Plot size is $\pm 50\,\mu$rad. (Simulated pattern, measured pattern)

of the energy concentrated in the center; an increase in angle offset causes

the zone of higher energy to move towards external radii. To correct for the LAGEOS velocity aberration an offset of 1.25 ± 0.5 arcsec was used. For LARES satellite an offset of 1.5 ± 0.5 arcsec has been chosen due to the lower altitude. Figure 5 shows the simulated FFDP of a single LARES CCR, the simulated coherent pattern of the whole LARES (preliminary) and a simulated incoherent FFDP of the whole LARES.

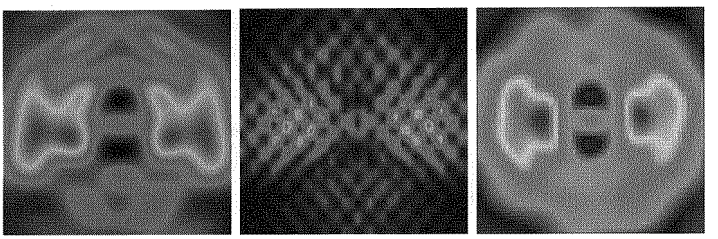

Fig. 5. FFDP of a LARES under a normal horizontally polarized laser beam with λ=632.8 nm. Plot size is $\pm 50\,\mu$rad

5. Conclusions

We are currently working on the SCF-test of the *flight model* of the GPS-2 CCRs array. The SCF-test of the LAGEOS polar sector will then follow. Integrated thermal and laser tests are now possible thanks to the new prototype positioning system (rotation+tilt) and to the 2nd optical table and FFDP circuit set-up next to the cryostat.

We deeply thank Prof. M. Calvetti (INFN-LNF Director), Dott. F. Ronga (Pres. of the INFN CSN2) and Prof. U. Bottigli (Pres. of INFN CSN5) for their support and encouragement.

References

1. I. Ciufolini, "Dragging of Inertial frames", *Nature* 449, 41-47 (Sept 6, 2006) Review.
2. R. Vittori *et al.*, "ETRUSCO: Extra Terrestrial Ranging to Unified Satellite COnstellations", LNF-07-(IR),(2007).
3. A. Bosco *et al.* "Probing Gravity in Neo with High-Accuracy Laser-Ranged Test Masses", LNF-06-24(P), (2006).
4. V. J. Slabinski, "Anumerical solution for LAGEOS thermal thrust: the rapid spin case", *Celestial Mechanics and Dynamical Astronomy*, **66**, N. 2, June 1996.
5. J. I. Andres, "Numerical simulation of the LAGEOS thermal behaviour and thermal accelerations", *Jou. of Geophys. Reas.*, 111(b9), (2006).

PARTICLE BEAM TESTS FOR THE GLAST-LAT CALIBRATION

M.BRIGIDA[†], A.CALIANDRO, C.FAVUZZI, P.FUSCO, F.GARGANO[†], N.GIGLIETTO, F.LOPARCO, M.N.MAZZIOTTA, C.MONTE, S.RAINÒ AND P.SPINELLI FOR GLAST-LAT COLLABORATION

Dipartimento Interateneo di Fisica "M.Merlin"
Università degli Studi e Politecnico di Bari
I.N.F.N. Sez. Bari
Via Amendola 173, 70126 Bari, Italy

The calibration strategy of the GLAST Large Area Telescope combines analysis of cosmic ray data with accelerator particle beams measurements. To validate the LAT simulation and to study its performance, a massive campaign of particle beam tests was performed, in parallel with the LAT integration and test, on the LAT Calibration Unit (CU). This is a detector built with two complete flight spare modules, a third spare calorimeter module, five anticoincidence tiles located around the telescope and flight-like readout electronics.
The CU was exposed to different kinds of beams, representing the whole spectrum of the signal that will be detected by the LAT, using the CERN and the GSI accelerator facilities. Beams of photons (0-2.5GeV), electrons (0.5-300GeV), hadrons (pions and protons, 6GeV-100GeV) and ions (C, Xe, 1.5GeV/n) were shot through the CU to measure the physical processes taking place in the detector and eventually fine-tune their description in the LAT Monte Carlo simulation. This talk describes the motivations and goals of the test runs, the many different experimental setups used to select the required particles and trigger the CU, the measured performance of the CU and the results of the LAT Monte Carlo validation.

1. Introduction

The Gamma-Ray Large-Area Space Telescope (GLAST) is a next generation high-energy observatory, to be launched by NASA in early 2008 with a lifetime of five years. The payload includes two different instruments: the Large Area Telescope (LAT) and the GLAST Burst Monitor (GBM). The LAT is sensitive to photons in the energy range between 20 MeV ad 300 GeV and consists of three subsystems: a solid state detector tracker (TKR), a CsI calorimeter (CAL), and a plastic scintillator anticoincidence system (ACD). The GMB is optimized for the detection of transients photon events at low energy (10 keV – 20 MeV). The combined detectors will observe the entire sky not occulted by Earth in all-sky survey and pointing mode.

[†] Corresponding authors: monica.brigida@ba.infn.it and fabio.gargano@ba.infn.it

2. Goals of beam tests for GLAST

After LAT integration, dedicated tests must be performed in order to study the instrument response, to test the calibration procedures and to improve the predictions of the current Monte Carlo simulation, based on GEANT4.
The whole LAT, now integrated and delivered for launch, was not available for these tests. However, since most laboratories do not provide beams facilities to irradiate the full instrument and the simulation shows that most of events in orbits will be contained in two towers, a test on a smaller unit (Calibration Unit" or CU) of the full LAT has been performed. The CU is composed of two complete LAT tower modules (TKR and CAL) and one additional CAL module, integrated in a 1×4 aluminum grid. Five flight-like ACD tiles complete the assembly. A mechanical interface with the remotely controlled *XY* table was used to set the CU position and orientation with respect to the beam line [1].
In this paper we will discuss the main features of the beam test set-ups and the low level performance.

3. Beam test setup

The CU was exposed to different kinds of beams, representing the whole spectrum of the signal that will be detected by the LAT, using the CERN and the GSI accelerator facilities. Beams of photons (0-2.5GeV), electrons (0.5-300GeV), hadrons (pions and protons, 6GeV-100GeV) and ions (C, Xe, 1.5GeV/n)

3.1 Cern PS set-up

The T9 line of the CERN-PS provides a mixed beam of electrons, positrons, pions and protons between 500 MeV/c and 10 GeV/c. Figure 1 shows a schematic view of the experimental setup.

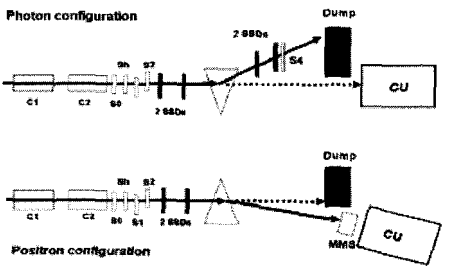

Figure 1. Schematic view of the experimental setup at the CERN PS-T9 line.

Two gas threshold Cherenkov counters ($C1$ and $C2$) were used for particle identification, while a set of plastic scintillators (S_0, S_h, S_1, S_2, S_4) provided the

external trigger/veto signal for the different data acquisition configurations. S_0 was used to monitor the total number of particles in the beam; S_h had a hole of 2.4 cm diameter in the center and was used as a veto to reject the halo beam; S_1 and S_2 had a small cross-section to select a small area of the beam; S_4 was used to select electrons inside the spectrometer acceptance.
Bremstrahlung photons are produced by electrons in matherials through the beam line. The photon tagger is a two-armed spectrometer composed of two Silicon Strips Detectors (SSDs) hodoscopes with two XY detection planes each: it is used to evaluate the photon momentum by mesuring the charge particle deflection in a magnet (triangle in the picture). The dipole magnet had a maximum bending power of 50cm×1T and deflected electrons into the second arm of the spectrometer and eventually onto the beam dump. The curved tracks measured by the spectrometer provide the energy of the deflected electron and, by difference with the nominal beam energy, that of the photon hitting the CU.
Different electron beam momenta (0.5; 1; 1.5; 2.5 GeV/c) were used to cover the photon bremsstrahlung spectrum between 50 MeV/c and 1.5 GeV/c, required for the CU calibration. Runs with e^+/e^-, π and protons have been also performed to ensure the instrument calibration and a proper ovelap with SPS data.

3.2 Cern SPS setup

The high-precision H4 line has been used for CERN SPS tests. This line provides secondary beams (e^+,e^-, p, π) with momenta from 10 GeV/c until 300 GeV/c, corresponding to the high energy range covered by the LAT, with low hadron contamination (lower than 1% beyond 50 GeV). The discrimination between electron and hadron has been performed by two Cherenkov counters and a set of three plastic scintillators has been also placed upstream to provide the trigger/veto signal.

3.3 GSI setup

The CU was exposed to heavy ion beams ($^{12}_{6}C$ and $^{131}_{54}Xe$), with energies of 1 and 1.5 *GeV/n*, and impacting the detector at 0, 30 and 60 degrees. Various rates were explored (10-1000 Hz/cm^2) around the expected average ion rate inorbit to make sure that test results were not influenced by rate effects such as event pileup. Because the purity of the beam line, the CU was mostly operated in self-trigger mode.

4. The CU Performance

4.1 Tracker

The TKR trigger efficiency, hits and clusters have been analyzed to study the low level performance of the TKR and to compare experimental and

simulated data. Figure 2 left shows the TKR trigger efficiency as a function of the beam electron energy and incident angle for real data and MC simulations. The agreement between data and MC is quite good, and the small discrepancies at normal incidence are due to the differences in the impact point. In fact, at normal incidence the gaps between the ladders introduce dead regions in the TKR. Figure 2 right shows the multiplicities of fired strips in the TKR planes for electrons with momenta from 1 GeV/c to 280 GeV/c and for 6 GeV/c protons, all at normal incidence. The beam direction is from the top plane (35) to the bottom one (0). The hit strip multiplicity is roughly constant for non-interacting protons, but it increases along the beam direction for electrons, following the development of the electromagnetic shower in the tracker.

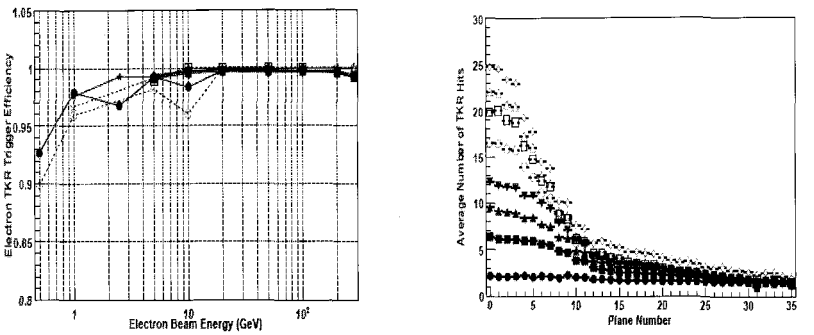

Figure 2. *Left*: Tracker electron trigger efficiency vs beam energy and incident angle. Real data: solid line and full symbols, MC data: dashed line and empty symbols. Circles: beam at normal incidence; squares: beam incidence 10 deg; triangles: beam incidence 20 deg; stars: beam incidence 30 deg. *Right*: Average number of TKR hits as function of the plane number: full circles: 6 GeV/c protons; other symbols: electrons of different momenta, from the bottom to the top 1; 2.5; 5; 20; 50; 100; 280 GeV/c.

4.2 Calorimeter

To calibrate the CU calorimeter the following procedure has been followed. The pedestals in all channels were measured using random trigger events, when no energy is deposited in the calorimeter crystals. The non-linearity of each channel was measured using the charge injection system. The energy scale of each channel was calibrated using the signals produced by cosmic muons. After path-length correction, the energy deposits of cosmic muons in a single crystal have the peak with most probable value of 11.2 *MeV*. To see this signal in the high energy ranges a special muon gain setting was used providing an output signal ten times bigger than for normal flight gain. The exact ratio between the flight and muon gains was calibrated using charge injection. At the beginning of each beam test data taking period the calorimeter was exposed to the electron beam (5 *GeV* for the PS and 100 *GeV* at the SPS) and a set of runs was collected

with four-range readout and different incident points in order to provide a broad spectrum of energy deposits in all crystals.
Figures 3 show the energy distributions measured by the CU and by the tagger with 2.5 *GeV/c* electrons. In the left plot, the blu-dotted line shows the energy distribution of photons measured with the CU, the red-dashed line shows the energy distribution of deflected electrons measured with the spectrometer tagger, and the white full line shows the distribution of the sum of photon and electron energies. As expected, the total energy distribution is peaked around the nominal energy of the incoming beam. Figure 3-right shows a linear dependence beteewn the photon energy mesured by the CU and the energy mesured by the tagger spectrometer.

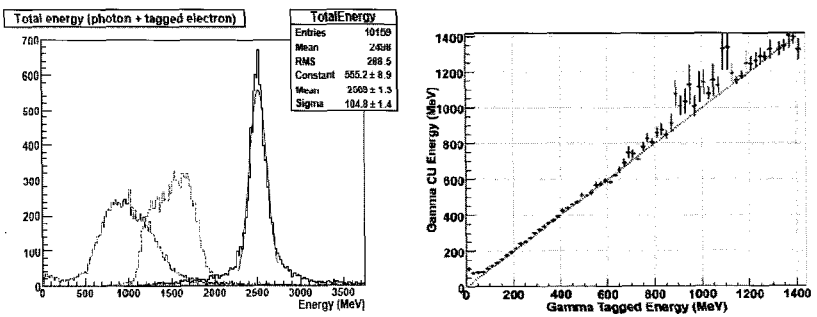

Figure 3. *Left*: Energy distributions: photon energy measured with the CU (blue-dotted); deflected electron energy measured with the tagger spectrometer (red-dashed); total energy (full white line). *Right*: The energy mesured in the CU vs energy mesured by the tagger spectrometer.

5. Conclusion

A massive beam test campaign on a GLAST Calibration Unit made with spare flight modules was performed in 2006 to validate the LAT Monte Carlo simulation and to verify the actual response of the whole detector. In particular the angular dispersion of the TKR and the energy resolution of the CAL fulfil the requirements of the missions and are in good agreement with the simulation.

References

1. L.Baldini et al., "Preliminary results of the LAT Calibration Unit beam tests", Proceedings of the first GLAST symposium, AIP Conference Proceedings Vol. 921 (2007) 190-204

SIMULATION OF A TIME-OF-FLIGHT TELESCOPE FOR SUPRATHERMAL IONS IN THE HELIOSPHERE

R. BUČÍK, A. KORTH, U. MALL
Max-Planck-Institut für Sonnensystemforschung
37191 Katlenburg-Lindau, Germany

G. M. MASON
JHU, Applied Physics Laboratory
Laurel, MD 20723, USA

A Monte Carlo code based on Geant 3.21 has been used for simulations of energy losses and angular scattering in a time-of-flight Suprathermal Ion Telescope (SIT) on the Solar-Terrestrial Relations Observatory (STEREO). A hemispherical isotropic particle distribution, a monoenergetic or power law in energy is used in these simulations. The impact of scattering, energy losses and system noise on the instrument mass resolution is discussed.

1. Introduction

A Monte Carlo simulation of the SIT telescope aboard the STEREO spacecraft was performed by Geant 3.21 [1]. This is a powerful code which allows to simulate the whole experimental setup and tracks the particle within the setup taking into account the primary interaction of those particles with matter.

In the present paper we study effects of the angular scattering and energy losses in the time-of-flight (TOF) telescope on the mass resolution. Monte Carlo simulations are needed to understand the response of the SIT instrument, especially for masses and energies not covered by calibration measurements.

2. Experiment

The SIT sensor is a TOF mass spectrometer, which measures ions (from hydrogen up to iron) from ~20 keV/n to several MeV/n [2]. The instrument identifies the incident ion mass and the energy by measuring the TOF τ and the residual kinetic energy E_{SSD} of the particle that enters the telescope through a thin nickel foil and stops in the silicon solid state detector (SSD) at the rear of the telescope. The TOF is determined by start and stop pulses from micro

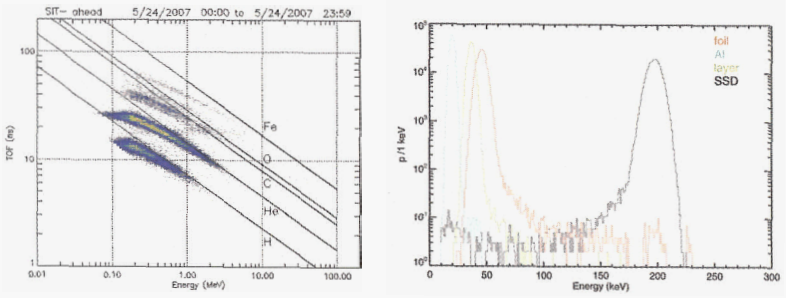

Figure 1. (Left) TOF versus the total kinetic energy for particles measured by the SIT sensor. Over-plotted are straight lines for five species using Eq. (1). (Right) Energy loss histograms for 300 keV protons for different absorbers in the SIT telescope.

channel plates (MCPs) that detect secondary electrons that are emitted from the foil and the surface of the SSD. The mass m of the ion is obtained from:

$$m = 2E_{SSD}\left(\frac{\tau}{L}\right)^2, \qquad (1)$$

where L is the distance between the foil and the SSD. In the range ~ 0.1 -1.0 MeV/n, the mass resolution σ/m is 0.1 measured during calibrations by α-sources. The TOF for SIT ranges from ~ 2.5 to 125 ns. The SSD threshold energy is set at 0.24 MeV and the total energy deposit is 163 MeV.

As can be seen in Eq. (1), when E_{SSD} is plotted versus τ on a log-log scale, the various atomic species are organized along straight lines with slopes of (-2) and offsets given by the mass. This can be seen in Figure 1 (left), which shows data from the SIT sensor. Each point represents the measurements of one ion.

3. Overview of the simulations

The simple mass model of the SIT telescope consists of four absorbers: the two nickel entrance foils, each 1000 Å, are replaced by one 40.7x15.5 mm nickel foil, 0.2 μm thick; a 40x15 mm silicon SSD, with thickness of 500 μm, at a distance of L=10 cm behind the foil; adjacent to the SSD an aluminum surface metallization, 0.2 μm thick and a silicon junction dead layer, 0.35 μm thick. The MCPs rates are not implemented in the simulations, only the foil and SSD responses are taken into consideration. The telescope housing was not modeled; we neglected any additional effects scattering off the surrounding structure. The sunshade with its additional role of limiting the solid angle was not included in model geometry.

In our analysis 10^8 particles were simulated which isotropically incident on SIT from the upper hemisphere. The simulated species include the following fully ionized ions: H, ^{3}He, ^{4}He, C, N, and O. The species are monoenergetic or with a power law spectrum with an index of (-2) for a total kinetic energy between 240 keV and 163 MeV. Except for ionization energy loss, simulations include energy straggling and multiple Coulomb scattering. The non-ionizing nuclear energy losses important for <100 keV/n heavy ions [3], are not considered in the present simulations.

4. Results and discussion

4.1. *Angular and energy distribution*

Energy losses in the four absorbers are given for 300 keV protons in the right panel of Figure 1. As shown later, the high energy losses in the foil correspond to high incident angles. The low energy tail in the SSD is a result of reduced ion energy by the absorbers above the SSD. On the average, 15% (3%) energy is deposited in the foil by 300 (900) keV protons. The same amount of energy is stored in the adjacent to the SSD Al metallization and dead layer.

Figure 2 (left) is an example of the number distribution of 300 keV protons as a function of the energy loss in the SSD and the angle between incident direction and normal of the foil. We see that particles with incident angles outside of the nominal telescope field-of-view (44° x 17°) can hit the SSD. In this figure lower energy deposit in the SSD corresponds to higher incident angles, which can be explained by a high energy lost in the foil, when a particle strikes it in a high incident angle and traverses through higher amount of material. Figure 2 (right) shows the distribution of a number of protons as a

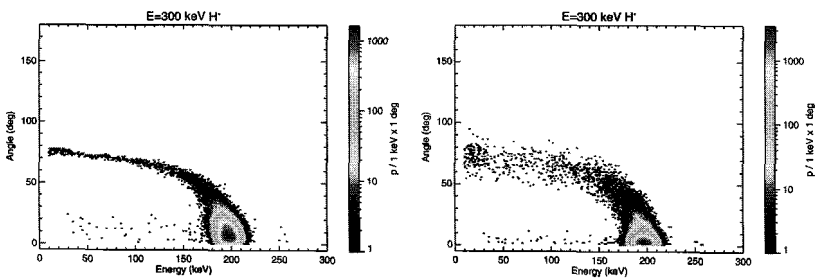

Figure 2. The simulated number distribution of 300 keV protons as a function of energy stored in the SSD and angle between incident direction and normal of the entrance foil (Left) or angle between incident and scattering direction (Right).

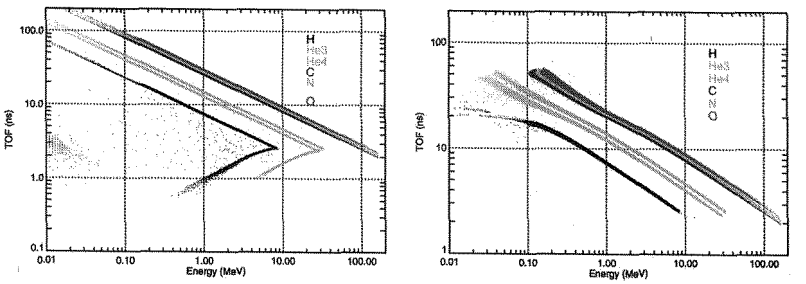

Figure 3. Simulated data in the TOF-Energy plane for different ions with a power law energy distribution.

function of energy deposited in the SSD and the angle between incident and scattering direction. Particle which hit the SSD can be scattered to a high degree only for large incident angles. Those particles, however, store small amount of energy in the SSD. This fits well with the simulations.

4.2. *Mass resolution*

The TOF in Figure 3 (left) is calculated using a modified Eq. (1) with $L/\cos\alpha$ instead of L, where α is scattering angle to the foil normal. The energy losses in Al-dead layers are turned off. Theoretical straight tracks are reproduced for ions stopped in the SSD with a small smear in the TOF caused by scattering in the foil. For particles stopping in the SSD, the σ/m, calculated for the whole simulated energy range and for all elements is about 0.03.

Since there is no anticoincidence detector in the back of the SSD, fast light ions which are not stopped in SSD can trigger the telescope. As can be seen in Figure 3 (left), for TOF of > ~ 2.5 ns this effect does not contribute to the uncertainty in the TOF. Penetrating heavy elements storing energy above the upper threshold value in the SSD do not produce an energy signal.

In Figure 3 (right), the energy losses in the surface metallization and the dead layer were taken into account in the simulations. The simulated data in TOF-Energy plane still produce distinctive tracks although deviating from the nominal one in the low energy region. In the energy range of 0.1-1.0 MeV/n the σ/m is ~ 0.10 for six species.

Finally, we investigate the effect of the system noise in the SIT instrument with a full width at half maximum (FWHM) of ~ 50 keV and dispersion in TOF with FWHM of ~ 1 ns. The system noise includes effects due to system electronics noise and the SSD FWHM. The uncertainties in the TOF measurement result from a combination of the TOF dispersion of secondary

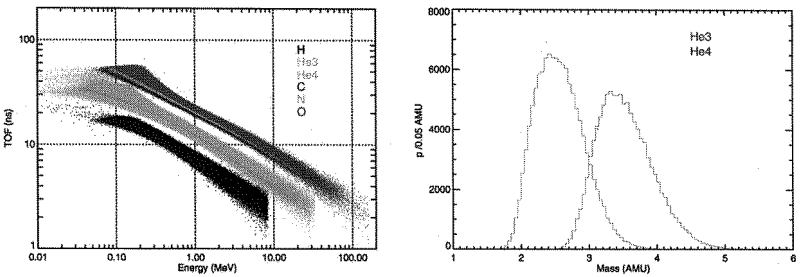

Figure 4. (Left) Same as Figure 3 with added energy and TOF dispersion. (Right) Mass histograms shown for helium ^{3}He and ^{4}He isotopes.

electrons and the noise in the MCPs and associated electronics [4]. Results are shown in Figure 4 (left). In comparison with previous TOF-Energy diagram added dispersions cause significant mass broadening, however, the helium isotopes are still distinguishable as well as oxygen from carbon ions. Mass distribution histograms in the energy range from 0.1-1.0 MeV/n for helium isotopes are shown in right panel of Figure 4. Adding effects of energy and TOF dispersions, the average mass does not change, but the mass resolution decreases to an average value of $\sigma/m \sim 0.14$ for all simulated ions. Particularly, the simulated mass resolution for ^{4}He is 0.12, close to the calibration value of 0.10. The relative statistical error of the obtained masses for all elements is well below 0.01 at 95% confidence level.

5. Conclusion

The Monte Carlo simulations of angular scattering and energy losses in the SIT telescope show that:

- Angular scattering in the entrance foil of the telescope is responsible for intrinsic TOF dispersion, and for the increase of the nominal instrument field-of-view which leads to high energy losses in the foil.
- Energy losses in both the SSD surface metallization and the junction dead layer contribute to the same amount to the mass resolution as the dispersion in energy and TOF measurements. Scattering in the entrance foil has a minor effect, about 30% of the previous contributors.
- Penetrating particles do not form an identifiable component of the background in the simulated instrument.

Although a further improvement in modelling of the SIT system is still needed, the present simulations can be still helpful in the experimental data analysis.

Acknowledgments

This work is supported by the Max-Planck-Gesellschaft zur Förderung der Wissenschaften and the Bundesministerium für Bildung und Forschung (BMBF) under grant 50 OC 0501.

References

1. GEANT, CERN Program Library Long Writeup W5013 (1993).
2. G. M. Mason *et al.*, *Space Sci. Rev.* **130**, in press (2007).
3. F. M. Ipavich *et al.*, *Nucl. Instr. Meth.* **154**, 291 (1978).
4. G. Gloecker and, K. C. Hsieh, *Nucl. Instr. Meth.* **165**, 537 (1979).

The PAMELA space mission

O. Adriani[1], M. Ambriola[2], G. C. Barbarino[3], A. Basili[4], G. A. Bazilevskaja[5], R. Bellotti[2], M. Boezio[6], E. A. Bogomolov[7], L. Bonechi[1], M. Bongi[1], L. Bongiorno[8], V. Bonvicini[6], A. Bruno[2], F. Cafagna[2,*], D. Campana[3], P. Carlson[9], M. Casolino[4], G. Castellini[10], M. P. De Pascale[4], G. De Rosa[3], N. De Simone[4], V. Di Felice[4], D. Fedele[1], A. M. Galper[11], P. Hofverberg[9], S. V. Koldashov[11], S. Y. Krutkov[7], A. N. Kvashnin[5], J. Lundquist[6], O. Maksumov[5], V. Malvezzi[4], L. Marcelli[4], W. Menn[12], V. V. Mikhailov[11], M. Minori[4], S. Misin[5], E. Mocchiutti[6], A. Morselli[4], N. N. Nikonov[7], S. Orsi°5, 9, G. Osteria[3], P. Papini[1], M. Pearce[9], P. Picozza[4], M. Ricci[8], S. B. Ricciarini[1], M. F. Runtso[11], S. Russo[3], M. Simon[12], R. Sparvoli[4], P. Spillantini[1], Y. I. Stozhkov[5], E. Taddei[1], A. Vacchi[6], E. Vannuccini[1], G. Vasilyev[7], S. A. Voronov[11], Y. T. Yurkin[11], G. Zampa[6], N. Zampa[6] and V. G. Zverev[11]

1 *INFN, Structure of Florence and Physics Department of University of Florence, Via Sansone 1, I-50019 Sesto Fiorentino, Florence, Italy*

2 *INFN, Structure of Bari and Physics Department of University of Bari, Via Amendola 173, I-70126 Bari, Italy*

3 *INFN, Structure of Naples and Physics Department of University of Naples Federico II", Via Cintia, I-80126 Naples, Italy*

4 *INFN, Structure of Rome Tor Vergata" and Physics Department of University of Rome Tor Vergata", Via della Ricerca Scientifica 1, I-00133 Rome, Italy*

5 *Lebedev Physical Institute, Leninsky Prospekt 53, RU-119991 Moscow, Russia*

6 *INFN, Structure of Trieste, Padriciano 99, I-34012 Trieste, Italy*

7 *IOFFE Physical Technical Institute, Polytekhnicheskaya 26, RU-194021 St. Petersburg, Russia*

8 *INFN, Laboratori Nazionali di Frascati, Via Enrico Fermi 40, I-00044 Frascati, Italy*

9 *KTH Department of Physics, Albanova University Centre, SE-10691 Stockholm, Sweden*

10 *IFAC, Via Madonna del Piano 10, I-50019 Sesto Fiorentino, Florence, Italy*

11 *Moscow Engineering and Physics Institute, Kashirskoe Shosse 31, RU-11540 Moscow, Russia*

12 *Universitat Siegen, D-57068 Siegen, Germany*

* *E-mail: francesco.cafagna@ba.infn.it*

The PAMELA (a Payload for Antimatter-Matter Exploration and Light-nuclei Astrophysics) experiment, is a satellite-borne particle spectrometer. It was launched on 15^{th} June 2006 from the Baikonur cosmodrome in Kazakhstan, is installed into the Russian Resurs–DK1 satellite. PAMELA is composed of a

time-of-flight system, a magnetic spectrometer, a silicon-tungsten electromagnetic calorimeter, an anticoincidence system, a shower tail catcher scintillator and a neutron detector. Among the PAMELA major objectives are the study of charged particles in the cosmic radiation, the investigation of the nature of dark matter, by mean of the measure of the cosmic-ray antiproton and positron spectra over the largest energy range ever achieved. PAMELA has been in a nearly continuous data taking mode since 11^{th} July 2006. The status of the apparatus and performances will be presented.

1. Introduction

The PAMELA (a Payload for Antimatter Matter Exploration and Light-nuclei Astrophysics) experiment[1] was launched into space on the 15^{th} June 2006. PAMELA is a particle spectrometer housed inside a pressurized container attached to the Russian satellite Resurs–DK1 . Launched by a Soyuz-U rocket, from the Baikonur cosmodrome in Kazakhstan, is deployed in a semi-polar (70°) elliptical orbit at alitidude in the range 350–600 km. PAMELA was switched on for the first time on 21^{st} June 2006 and has been in a nearly continuous data taking since 11^{th} July 2006. Until September 2007, the total acquisition time has been ~380 days, for a total of ~800 million triggers and 6.4 TByte of down–linked data.[2] The mission is foreseen to last for at least three years.

2. PAMELA scientific objectives

PAMELA major scientific goal is the measurement of antiparticle — mainly $\overline{p}$ and e^+ — spectra in cosmic rays. The high energy part of these spectra, well beyond the present limit of ~50 GeV, will be explored for the first time. Both $\overline{p}$ and e^+ can be produced from exotic sources providing hints of new physics. Moreover, PAMELA will have sensitivity for antihelium search at the level of $\sim 10^{-8}$; detection of antinuclei would prove direct evidence of antistellar nucleosyntesis providing an extremely important result.

Besides PAMELA has been designed to measure in detail the spectra of primary and secondary components of the cosmic radiation. The long term period of data taking provides unprecedented statistics with no atmospheric overburden reducing the systematic uncertainties of previous measurements obtained by balloon-borne experiments.

Concomitant goals include: the study of solar physics[3] and solar modulation during the 24^{th} solar minimum, and the study of trapped particles in the radiation belts. The semi-polar orbit allows PAMELA to investigate the various particles and nuclei in a wide energy range and different condition of geomagnetic cutoff.

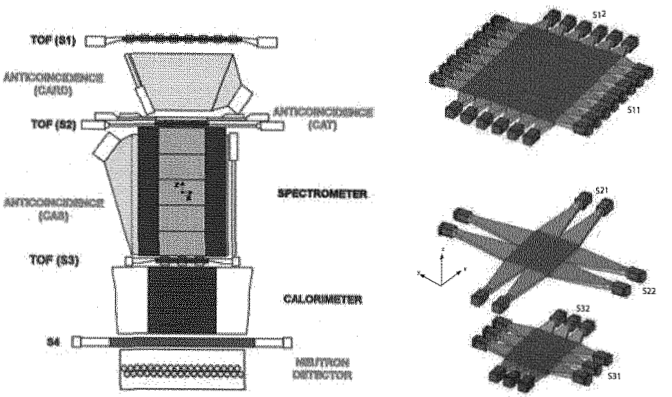

a) b)

Fig. 1. **a) Sketch of the PAMELA apparatus. b) The PAMELA** ToF system. S1 is housed on PAMELA top; S2 above and S3 below the spectrometer.

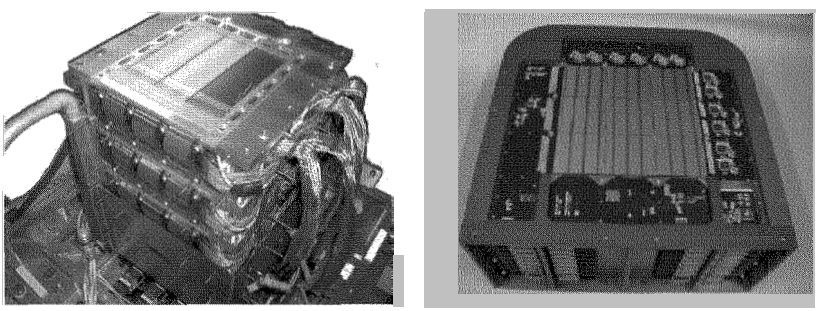

a) b)

Fig. 2. a) The PAMELA tracking system. The first silicon plane is visible inserted into the permanent magnet canister. b) The PAMELA electromagnetic imaging calorimeter.

3. The PAMELA apparatus

The PAMELA apparatus is composed of the following sub-detectors, stacked, as in Fig. 2a, from top to bottom: a time of flight system (ToF) (S1,S2,S3), a magnetic spectrometer, an anticoincidence system (CARD, CAT, CAS), an electromagnetic imaging calorimeter, a shower tail catcher scintillator (S4), and a neutron detector.

The ToF is used for the first–level trigger and is made out of 3 double–layer plastic scintillator paddles[4] as shown in Fig. 2b. Measuring particle β and dE/dx , does help in particle identification, for rigidity (R) <1GV,

and in rejecting albedo particles.

Particle rigidity and charge is determined by the spectrometer.[7] Six layer of double–side silicon sensors are stacked in between five permanent magnet modules. Thanks to spatial resolution of $3 \div 4$ μm and $8 \div 13$ μm, in bending and not bending view respectively, it is possible to reach a maximum detectable rigidity (MDR) of ≈ 1 TeV/c. Particle identification is also possible thanks to the dE/dx measurements. A picture of the tracking system is shown in Fig. 2a.

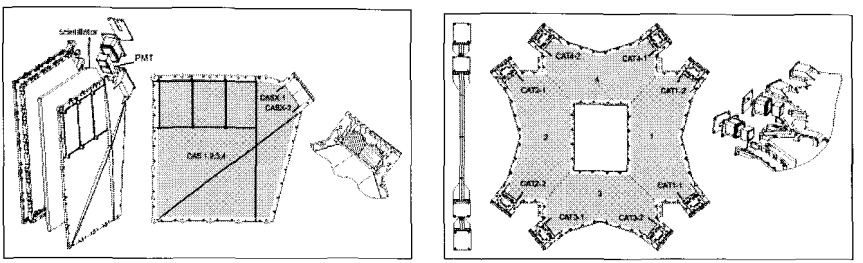

a) b)

Fig. 3. Exploded views of the PAMELA anticoincidence system. a) the CAS, shielding the lateral sides of the spectrometer; b) the CAT, covering the top of the spectrometer.

The PAMELA anticoincidence system[6] shields the spectrometer, covering the magnet top (CAT) and lateral sides (CAS), and the upper part of the detector(CARD). Made up of 9 plastic scintillator paddles, this system rejects events triggered by particles interacting with the apparatus or the pressurized container. In Fig. 3 CAT and CAS drawing are shown.

The electromagnetic imaging calorimeter comprises 44 single–sided silicon sensor planes, orthogonally arranged, interleaved with 22 plates of tungsten absorber.[5] Each layer has a thickness which corresponds to 0.74 X_0 for a total depth of 16.3 X_0 and 0.6 nuclear interaction lengths. Combining the topological information of the two views with the dE/dx , make it possible to to achieve a proton rejection factor of at least 10^5 above 10 GeV/c while maintaining an electron selection efficiency of $\sim$90%. Besides a self–trigger system was implemented in the read–out to measure high–energy electrons crossing at least 10 X_0 in the calorimeter, increasing by a factor 30 the acceptance for this component. A picture of this detector is shown in Fig. 2b.

The shower tail catcher scintillator,[8] is attached at the calorimeter bottom, just above the neutron detector. It does participate to the trigger for

high energy events and the neutron detector.

The neutron detector[9] consists of 36 ^{3}He counters, inserted into a polyethylene moderator. It will help in hadrons and leptons discrimination in the high energy events.

PAMELA overall size is about 130×70×70 cm^3, corresponding to a geometric factor of 21.5 cm^{2}sr (for R>1GV), for a total mass of ~470 kg, and a maximum power consumption of 360 W.

PAMELA in flight operations are handled by the PAMELA Storage and Control Unit (PSCU).[10] The PSCU manages the data acquisition, the communication between the satellite CPU and continuously checks for proper operation of the apparatus. During data acquisition it does recover the error conditions due to alarms in the detectors electronics.

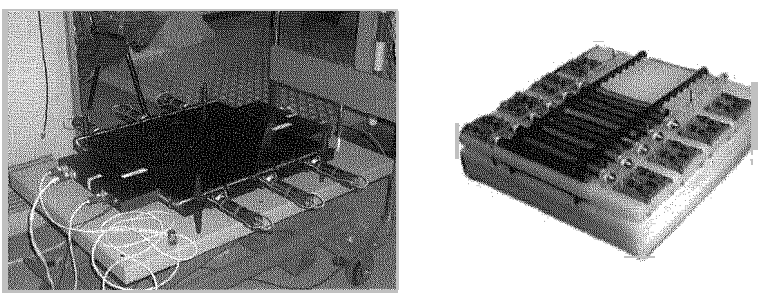

a) b)

Fig. 4. a) A picture of shower tail catcher scintillator. b) A picture of the neutron detector, without the aluminum cover box, during the installation of the ^{3}He counters.

4. In Flight operations, data handling and analysis

Since the first days of operation, PAMELA, is transmitting to ground about 16 GB of data every day. The receiving station is located at the Research Center for Earth Operative Monitoring (NTsOMZ) in Moscow, Russia. Here data are received, unpacked, checked and transferred to various institutions for further data processing and analysis.[11]

After a quick look to check the status of the detector, data are reduced and calibrated. In the calibrated data, information from each detector are registered in a format suited to permit an identification of the particle type and to measure the energy spectrum of the various components. Due to the long term exposure and the possibility of spanning different location, alti-

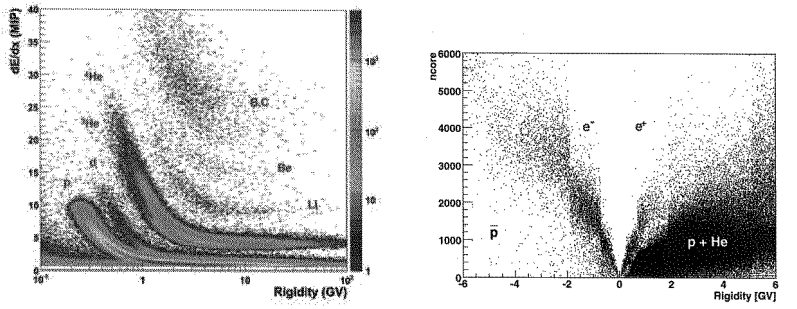

a) b)

Fig. 5. a) The dE/dx in the tracking system. b) Distribution of a variable combining the topological information with the dE/dx in the calorimeter.

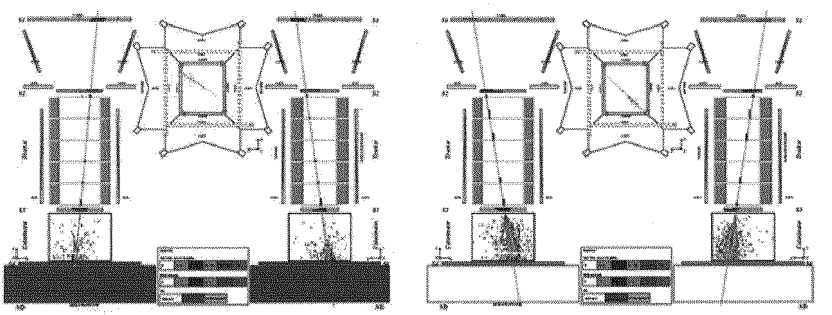

a) b)

Fig. 6. a) A 84 GV $\overline{p}$ candidate. b) A 92 GV e^+ candidate. It is possible to notice the different response of the neutron detector (the red box in a)), and the different shower topology in the calorimeter.

tudes and solar activities periods, a long term monitor and precise mapping of these spectra can be determined.

After a first selection of the down-going particles, using ToF data, particles not cleanly entering the PAMELA acceptance are rejected using the anticounter system. Then the charge is identified and the rigidity determined, using the spectrometer. The final identification is provided by the combination of the calorimeter and neutron detector information plus the β measurements from the ToF and ionization losses in the tracker system at low momenta. In this way, several tens of thousand events have been identified as e^+ and about a thousand of events as $\overline{p}$. Distributions of the

dE/dx in the tracker system, along with the one of a variable combining the topological information with the dE/dx in the calorimeter, are shown in Fig. 4. A 84 GV $\overline{p}$ candidate, interacting in the calorimeter, along with a 92 GV e^+ candidate are shown in Fig. 4.

5. Conclusions

The PAMELA experiment was successfully launched on the 15^{th} of June 2006 and it has been continuously taking data since then. It is smoothly collecting data, $\sim 8 \times 10^8$ triggers have been registered so far allowing for precise measurement of cosmic-ray spectra over a wide energy range, candidating PAMELA to be a permanent cosmic ray laboratory in space. Up to now, PAMELA has recorded the largest antiparticle statistic ever and results will be published soon.

References

1. Picozza, P. *et al.* , *Astropart. Phys.* **27**, 296–315 (2007).
2. Boezio, M. *et al.* , The PAMELA space experiment: first year of operation, *Proc. HEP2007, Manchester*, England (2007).
3. Casolino, M. *et al.* , Solar cosmic ray observations with PAMELA experiment, *Proc. 30^{th} Int. Cosmic Ray Conf. Merida*, Mexico (2007).
4. Menn, W. *et al.* , The ToF System of the PAMELA Experiment: In-orbit Performance, *Proc. 30^{th} Int. Cosmic Ray Conf. Merida*, Mexico (2007).
5. Mocchiutti, E. *et al.* , The PAMELA Electromagnetic Calorimeter: Flight Status, *Proc. 30^{th} Int. Cosmic Ray Conf. Merida*, Mexico (2007).
6. Orsi, S. *et al.* , A Study of the In-Orbit Particle Rate with the PAMELA AC System, *Proc. 30^{th} Int. Cosmic Ray Conf. Merida*, Mexico (2007).
7. Bongi, M. *et al.* , In–orbit performances of the magnetic spectrometer of PAMELA, *Proc. 30^{th} Int. Cosmic Ray Conf. Merida*, Mexico (2007).
8. Malvezzi, V. *et al.*, Performance of neutron detector and bottom trigger scintillator of the space instrument PAMELA, *Proc. 9^{th} ICATPP Como*, Italy (2005)
9. Stozhkov, Y.I. *et al.* , The in-flight performance of the PAMELA Neutron Detector, *Proc. 30^{th} Int. Cosmic Ray Conf. Merida*, Mexico (2007).
10. Casolino, M. *et al.* , *Nucl. Instr. and Meth. A* **572**, Issue 1, 349–350 (2007)
11. Mikhailov, V.V. *et al.* , PAMELA experiment: Flight data receiving and quicklook, *Proc. 30^{th} Int. Cosmic Ray Conf. Merida*, Mexico (2007).

A LARGE CAVITY GAMMA-RAY SPECTROMETER FOR MEASUREMENT OF COSMOGENIC RADIONUCLIDES IN ASTROMATERIALS BY WHOLE ROCK COUNTING

C. TARICCO, P. COLOMBETTI*, N. VERMA and G. VIVALDO

Dipartimento di Fisica Generale, Università di Torino,
Via Pietro Giuria 1, 10125 Torino, Italy
and Istituto di Fisica dello Spazio Interplanetario (IFSI), INAF
Corso Fiume 4, 10133, Torino, Italy
**E-mail: paolo.colombetti@ph.unito.it*
www.ph.unito.it, www.ifsi-torino.inaf.it

N. BHANDARI

Physical Research Laboratory and Basic Sciences Research Institute,
Navrangpura, Ahmedabad, India
E-mail: nnbhandari@yahoo.com

For resolving the ongoing debate that the Earth's climate may respond to solar activity variations, it is necessary to reconstruct a high resolution time series of heliospheric magnetic field in the past and correlate it to climatic records. The solar magnetic activity modulates the galactic cosmic ray flux, which is responsible for producing radioactive nuclides in rocks on planetary surfaces and in meteorites. To measure the minute quantity of γ emitting cosmogenic radionuclides, we have set up a low background, highly specific and selective γ-ray spectrometer. Using this spectrometer, we have reconstructed the solar activity over the past 3 centuries by measuring ^{44}Ti and ^{26}Al in meteorite falls; in particular we have shown that the intensity of cosmic rays has linearly decreased, in agreement with some models proposed for the past solar activity. In order to improve the Ge-NaI coincidence spectrometer, crucial for selective ^{44}Ti detection, we have developed a multiparametric acquisition system. The flexibility of optimizing appropriate energy channels allows more reliable measurement of the small activity present in meteorites.

Keywords: Gamma ray spectroscopy; Cosmogenic radionuclides; Meteorites; Cosmic ray flux; Solar activity; ^{44}Ti; Coincidence techniques; Multiparametric data acquisition.

1. Introduction

Over the past two decades it has been increasingly recognized that energetic particle precipitation can lead to changes in atmospheric composition and structure. Recent investigations indicate that these processes are controlled by phenomena such as the mesospheric polar vortex and transport from the thermosphere to the stratosphere. The energetic particles in the near Earth space consist of particles of both solar as well as galactic origin. Whereas the solar energetic particle emission is sporadic and the frequency of solar flares increases in phase with the sunspot cycle, the more energetic galactic cosmic rays are modulated by the heliospheric magnetic field and their intensity is anticorrelated with the sunspot cycle. The amount of radioactivity induced by these radiations in Earth's atmosphere or in rocks in the interplanetary space also varies likewise.

Extensive studies on cosmogenic ^{10}Be and ^{14}C produced in Earth's atmosphere and deposited subsequently in terrestrial archives, such as ice cores and tree rings, have been carried out during the past few decades.[1] These isotopes are however affected by geomagnetic field variations and exchange rates between various terrestrial reservoirs, whereas the radioactivity produced in meteorites records the solar activity more faithfully since they are free of interferences by terrestrial processes.

One of the main interests is to know solar activity changes back to the time of the Maunder Minimum (1645–1705), when the exceptionally low magnetic activity of the Sun was concomitant with a cold period, known as Little Ice Age. Because of its half life, ^{44}Ti ($T_{1/2}$ = 59.2 years) has been proposed as an index tracer for the study of solar activity variation on centennial scale. ^{44}Ti is mainly produced by spallation reactions between cosmic ray protons and meteoritic iron and nickel. Resulting ^{44}Ti γ activity in meteorites is very low (~1 dpm/kg) and there is strong interference by ^{214}Bi γ's from the decay chain of the naturally occurring ^{238}U (also in meteorite itself). On the basis of the decay scheme (β^+-γ in coincidence) of ^{44}Sc, short-lived daughter of ^{44}Ti, a germanium γ-ray spectrometer has been set up. The same configuration can be used for ^{26}Al measurement which also emits a positron and a γ-ray in coincidence.

2. Experimental set-up

The main detector is a p-type close-end coaxial HPGe crystal (~3 kg; 91 mm dia x 88.4 mm high; GEM 150, Ortec). It has a relative efficiency of 147%, a resolution of 1.85 keV and a peak-to-Compton ratio of 104 for

the 1332.5 keV ^{60}Co γ-rays. The HPGe works in coincidence with a surrounding NaI(Tl) annular single crystal (13.5 cm internal diameter, 10 cm thick and 30 cm high) and by a NaI(Tl) cylindrical plug; the total mass of the scintillator is ~90 kg and it is coupled to 7 photomultipliers, as shown in Fig. 1. The assembly is housed in a 20 cm thick high-purity lead shield,

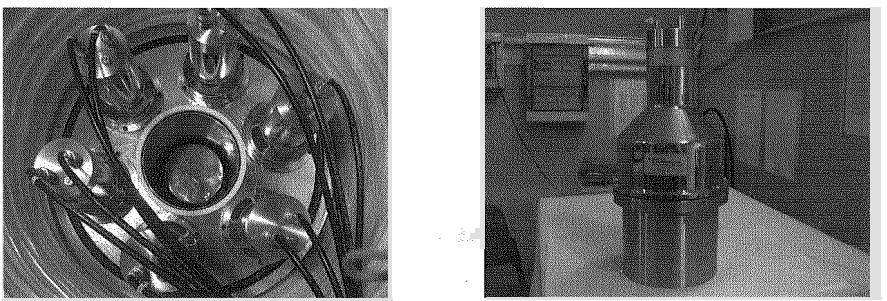

Fig. 1. **The** HPGe detector surrounded by the NaI(Tl) *annulus* (left) and the NaI(Tl) plug (right).

internally lined with 1 mm of Cd, 5 cm OFHC copper and the surrounding empty space is filled with polythene to reduce the amount of ambient radon emanating from the ground. The spectrometer has a large cavity in which a rock of about 1 kg weight can be placed for coincidence and anticoincidence γ-counting. This spectrometer[2] is located at the underground (70 m.w.e.) Laboratory of Monte dei Cappuccini in Torino (Italy). The μ meson rate in the cave is 14000 particles/m^2 h, ~30 times less than at the surface level.

We have so far measured ^{44}Ti and ^{26}Al activity in 20 meteorites which fell during the last 235 years.[3,4] These measurements show a linear decreasing trend of ~43% in ^{44}Ti activity during the past 235 years, superimposed on an 87 year oscillation, with amplitude (peak to trough) of ~25%. These measurements of ^{44}Ti in chondrites have also been used to validate different solar activity reconstruction models.[5]

3. New data acquisition system

Recently we have developed and installed a multiparametric Ge-NaI acquisition system, which allows more flexibility in the choice of the NaI coincidence energy windows, crucial for selective ^{44}Ti detection. Moreover, we developed the managing software embedded in the control electronics module in order to allow autonomous acquisition and storage of the data

for the long-lasting meteorite measurements.

In order to compare the results obtained by the new coincidence system with those obtained before, we have remeasured Dhajala meteorite, which fell in 1976. Figure 2 shows the 2-dimensional spectrum of Dhajala meteorite corresponding to the Ge energy region ~1750–1850 keV. The co-

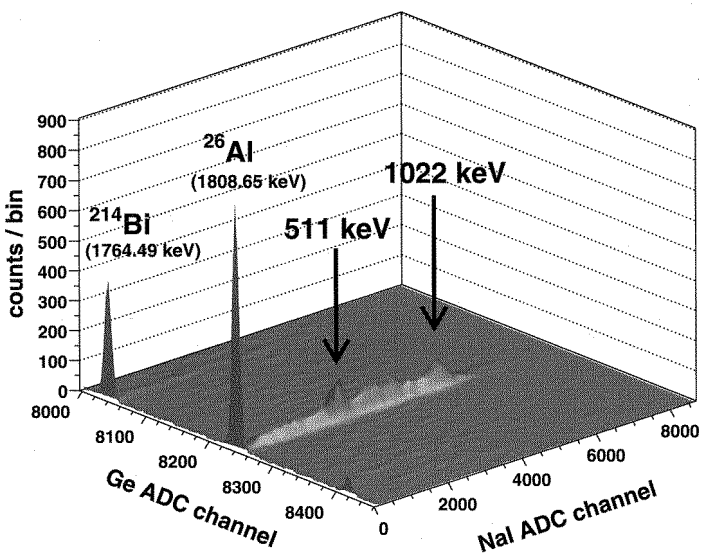

Fig. 2. Dhajala meteorite Ge-NaI 2-dimensional spectrum in the Ge energy region around ^{26}Al 1808.65 keV peak, for which corresponding NaI detection of β^+-annihilation γ's is visible, as opposed to mostly single-γ ^{214}Bi 1764.51 keV γ.

incidence between the 1808.65 keV γ from ^{26}Al revealed by the Ge detector and the NaI revealed annihilation γ's (giving peaks at 511 and 1022 keV) is clearly seen. In the same region the 1764.49 keV γ peak from ^{214}Bi, coming from mostly single-γ events, is not associated with relevant NaI events.

By considering the NaI events in coincidence with Ge events in the 1808.65 keV peak region, we obtain the NaI sub-spectrum shown in Fig. 3(a), which gives information on suitable NaI energy intervals for selective ^{44}Ti detection. Interference from the 1155.19 keV ^{214}Bi γ's is not completely eliminated if the coincidence settings do not exclude the contemporary emitted 609.31 keV γ's (close to 511 keV) which may mimic an annihilation event. The 609.31 keV peak is shown in Fig. 3(b), representing the NaI sub-spectrum corresponding to the Ge 1120.19 keV peak due to

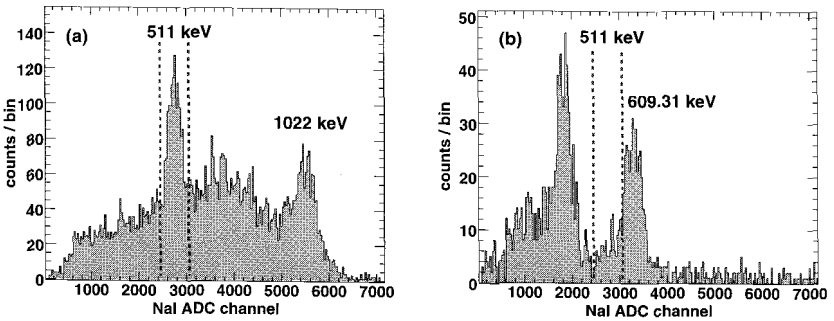

Fig. 3. NaI spectrum of Dhajala meteorite acquired in coincidence with Ge events in the region of ^{26}Al 1808.65 keV peak (a) and of ^{214}Bi 1120.52 keV peak (b) respectively.

^{214}Bi. The optimum selection of ^{44}Ti peak has to be based on eliminating the overlapping of 511 keV and 609.31 keV peaks (see region marked by dotted lines in Fig. 3).

The tests performed with the multiparameter system indicate that we should be able to measure other meteorites which fell more than 200 years ago.

Acknowledgements

We are grateful to Prof. Sami K. Solanki (Max-Planck-Institut für Sonnensystemforschung, Katlenburg-Lindau, Germany) for his support which allowed us to improve the acquisition system of the spectrometer. We thank curators of various museums namely Vaticano, Berlin, Vienna, Paris, Modena and Dublin who graciously made the meteorite samples available for our work. We thank Mr. A. Romero for careful technical assistance. N.B. thanks Indian national Science Academy for INSA Honorary Scientist grant.

References

1. J. Beer, A. Blinov, G. Bonani, H. J. Hofmann and R. C. Finkel, *Nature* **347**, 164 (1990).
2. C. Taricco, N. Bhandari, D. Cane, P. Colombetti, N. Verma and G. Vivaldo, *Nucl. Inst. Methods Phys. Res. A* **572**, 241 (2007).
3. G. Bonino, G. Cini Castagnoli, N. Bhandari and C. Taricco, *Science* **270**, 1648 (1995).
4. C. Taricco, N. Bhandari, D. Cane, P. Colombetti and N. Verma, *J. Geophys. Res.* **111**, p. A08102 (2006).
5. I. G. Usoskin, S. M. Solanki, C. Taricco, N. Bhandari and G. A. Kovaltsov, *Astron. & Astroph.* **457**, L25 (2006).

A NEW APPROACH TO LAGEOS SPIN ORIENTATION AND ITS ROLE IN GENERAL RELATIVITY MEASUREMENTS

DOUGLAS CURRIE
Department of Physics, University of Maryland, College Park, MD, 20742, USA

SIMONE DELL'AGNELLO, GIOVANNI DELL MONACHE, ROBERTO TAURASO
LARES-GRUPPO 2, INFN/LFN, via E. Fermi, 40, Frascati, Italy

The two LAGEOS Satellites have addressed a variety of issues in Geophysics (GP) and General Relativity (GR). The extreme accuracy of laser ranging (currently approaching millimeter accuracy) now means that very small error sources act upon LAGEOS and have become important, affecting the study of GP (e.g., the tides) and GR (e.g., Lenses-Thirring Effect). Initial measurements and analysis of the spin orientation were first performed at the in the early 1990s at the University of Maryland. However, the spin rate of LAGEOS has slowed to the point that this method is no longer effective. A new observing approach (the "Pocket Modulation Effect") to determine the spin axis has been proposed by the first author. Data that addresses this method has been collected at various sites and is being analyzed at LNF/INFI. We will report on the physics involved in the PME and describe the laboratory data and simulations performed to validate the proposed approach, the LAGEOS data obtained at sites, the new analysis procedures and then address the impact of this new information.

1. Science Motivation

1.1. *M ach's Principle and General Relativity (GR)*

Mach's Principle addresses the fact while we cannot distinguish the physics in frames in relative linear motion, we can clearly distinguish a rotating frame. Earnest Mach addressed this problem in 1893, and hypothesized that a "non-rotating" frame was established by the distant matter in the universe, that is, the distant matter of the universe affects the physics in a local frame. Within the framework GR, such an effect may exist, related to the measurement of the so-called Lense-Thirring effect.

1.2. *Lense-Thirring Effect – (L-TE)*

Many parameters of GR have been experimentally addressed. However, almost all of these experiments address static effects, that is, the effects on experiments of a static configuration of masses. The dynamical effects, that is, the effects of the effects caused by moving masses has only recently been addressed. The L-TE is the effect of the mass current of the rotating earth, i.e., as it twists space-time and alters the orientation of a gyroscope. Using the LAGEOS satellite, Ciufolini has evaluated the L-TE at the 10% level. GPB is another experiment expected to address the measurement of the L-TE.

1.3. Gravito-Electro-Magnetics

The L-TE can be understood by noting the close relationship between these aspects of L-TE and the theory of Electrodynamics. Just as an electric current in a closed loop generates a dipole magnetic field that causes a compass needle to twist, the mass current generated by the rotation of a finite size spinning body such as the earth and its rotation generates effects in L-TE that causes a twist in a local frame outside the earth. This is the L-TE for a satellite such as LAGEOS. Another effect that can be addressed with respect to the Gravito-Electro-Dynamics approach as the interaction of two parallel currents. In electrodynamics this is referred to as Ampere's Law. The "mass currents" generated by the motion of the earth and moon about the sun also cause an effect on the moon's orbit. This should be measurable with the new accuracy expected with the APOLLO Lunar Ranging Station and the even higher accuracy of the proposed new arrays for the moon proposed by the University of Maryland.

1.4. Chern-Simons Gravity

Within the structure of String Theory, Chern & Simons have proposed a modification of the GR equations. It has recently been shown by Smith et. al. that using the measurements of the L-TE with the LAGEOSs they can place interesting limits on the magnitude of the coupling coefficients. This addresses such recently discovered phenomena as Dark Energy.

2. Technology Aspects

We now address some technology aspects of the measurements using LAGEOS and future similar satellites. We will review the methods of measurements and then the possible error sources and finally the methods to correct these forces. However, most of the material will be review very briefly and we shall concentrate on the effects of photon thrust. That is, the emission of photons from the heated surface of the satellite and the reaction that moves the satellite into an new orbit.

2.1. Laser Ranging Accuracy

The orbits of the satellites are determined by laser ranging, using a very narrow laser pulse is sent from a ground station, reflected directly back to the ground stations by special mirrors, the Cube Corner Retro-reflectors, (CCRs). Photo-detectors then receive the reflected pulse and determine the time since the transmission. From such repeated measurements, one determines the orbit of the satellite. Currently, for most of the interesting measurements, the limiting accuracy is not the precision to which this time can be measured, but other more systematic effects to be addressed in the next sub-sections.

2.2. Gravitational Forces

Of course the dominate "force" on the satellites is the gravitational force of the earth, the "force" that assures the satellite moves on a geodesic from the view of GR. The higher moments in the gravitational field must be known very accurately in order to form a basic reference orbit. Recent satellite measurements have reduced the gravitational field uncertainties to a level that is acceptable.

2.3. Non-Gravitational Forces

In addition to the gravitational forces, there are a number of non-gravitational forces that must be addressed. These consist of solar pressure, atmospheric drag due to both neutral particles and charged particles. Again, these are manageable. However, the photon thrust or thermal thrust is a force that must be addressed in order to make the accurate measurements of the perturbations that are of interest.

2.4. Satellite Motions

We now briefly review the rotational effects on LAGEOS. It is essentially a metal ball rotating in the magnetic field of the earth so electrical currents are generated within the satellite. The energy of these currents, which comes from the rotational energy, is converted to heat, so the rotation rate of the satellite slows. Further, the earth's magnetic field acting on these currents twists the orientation of the spin axis.

2.5. Photon Thrust

Photon Thrust is the effect caused by the combination of the solar heating of the satellite and the rotation of the satellite. Thus as the sun heats the satellite on one side, an excess of infra-red photons are emitted. However, this warm side is rotated away from the sun and the direction of the reaction force now depends upon the rotation of the satellite. A more detailed analysis shows that for a rapidly rotation satellite, the force is along the axis of rotating. Thus is critical to determine the orientation of the spin axis in order to make these corrections.

3. Determination of the Direction of the Photon Thrust

3.1. Background – Solar Glint Approach (SGA)

There is a cluster of theoretical estimates of the spin rate, the orientation of the spin axis. However, the first determinations of the orientation based upon observations were conducted in the 1990s at the University of Maryland. The orientation of the spin axis has been determined by the observation of the sun glints reflecting from the front surface of the CCRs. These photometric records can be used to determine the orientation of the spin axis. Andres was the first incorporate the measurements into an orbital determination program LOSSAM. In recent years, other stations have been performing the photometry to contribute to the improved orbit evaluated by Andres.

3.2. Current Challenges

After launch, the rapid rotation of LAGEOS I permitted the SGA to be used very effectively. However, it now has a period of thousands of seconds and the SGA is no longer a feasible approach. The reason for the difficulty with slow rotation is that the reflected image of the sun is a narrow beam as it sweeps across the earth. Unless the apparent axis of rotation (primarily changing due to the geometry of the pass) remains within one degree for a quarter of a rotation period, the SGA cannot effectively be used. Thus the combination of the narrow beam of the solar reflection and the slow rational period causes the problem. For this reason, a new method is required.

4. Pocket Effect Approach

4.1. Theoretical Pocket Effect Approach (PEA)

In order to understand the PEA, consider the LAGEOS satellites as a shiny ball with no CCRs. Viewed in the sunlight, we see a small (a few millimeters) image of the sun on the surface. As the ball rotates, the brightness of the image remains the same, yielding a constant photometric signature. Now consider a shiny ball that his many holes or pockets so much of the surface is covered with pockets. Now as the shiny ball with pockets rotates, when the image of the sun is on the remaining shiny surface, we again see the constant photometric signature. However, as a hole rotates into the image of the sun, the intensity of the reflection will go to zero. During the rotation, we expect to see no intensity for about 8 degrees of rotation and the bright surface signature during abut 2 degrees of rotation. Thus due to the larger angles of rotation covered by the PEA, one has several hundred times better coverage for the rotation information. In fact, since more than half of the surface is covered with pockets so we always get signatures, unlike the SGA. Now consider a CCR in each of the pockets. If the image of the sun passes very precisely over the center of the pocket, we will get a Fresnel reflection and a very bright signal. However, this will happen only occasionally for LAGEOS II and never twice for the same band for LAGEOS I due to the latter's slow rotation.

4.2. Experimental Laboratory Test

To confirm these theoretical expectations of the satellite behavior, we have obtained a GSFC engineering model that was built with LAGEOS I. It is a sector of the LAGEOS satellite that has been loaned to INFN for these tests. A video taken as the sector rotates confirms the above expectations.

4.3. LAGEOS II observations

In 2004, LAGEOS II was observed on the 3.6 meter telescope at the Starfire Optical Range in New Mexico, USA using the RULLI camera built by LANL.

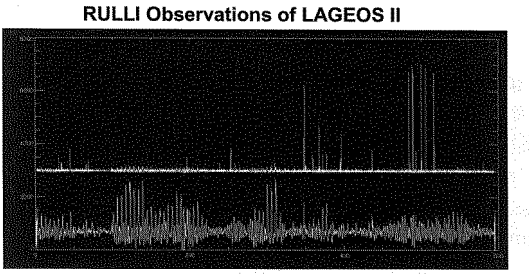

The upper plot displays the solar glints recorded by the RULLI Camera These solar glints have been used at the University of Maryland to determined the orientation of the spin axis. The lower curve illustrates the variation in the diffuse reflection. It is the latter we are now using to test the new method to determine the orientation.

This camera records the time of arrival of individual photoelectrons extreme precision. The figure shows a 600 second recording of the solar reflection of LAGEOS II.

4.4. Data Reduction

The development of the analysis algorithms is in progress. This data will initially be treated in the same manner as the SGA data. However the results are obviously less accurate in the angle than the SGA. The PEA will predict and/or identify when a SGA glint will occur. Thus with a single SGA glint, we can identify its source and use it to the upgrade the accuracy to the SGA level.

6. Conclusions

The use of artificial and natural satellites has already yielded most of the most accurate tests of GR. In the future, they should lead to a better understand of the dynamical effects in GR, especially w.r.t. the L-TE, String theory in the Chern-Simons approach and torsion effects. A critical aspect is to retain the ability to measure the orientation of the spin axis of the LAGOES-type satellites during the time that they are slowing. The PEA is providing such an observational and analytic approach. An expanded version of this paper with figures, videos and references may be found at http://www.physics.umd.edu/rgroups/astrometro.html and at http://www.lnf.infn.it/acceleratori/lares/LAGEOS%20article%20list.htm

7. Acknowledgements

The author thanks David Thompson of LANL, Mark Davis of NRL and Ron Dantowitz of the Clay Center Observatory for LAGEOS observations. The first author also thanks INFN for travel support to coordinate the analysis of this data.

Evaluation of the flux of CR nuclei inside the magnetosphere

G. Boella[a], M.J. Boschini[b], M. Gervasi[a,*], D. Grandi, S. Pensotti[a], and P.G. Rancoita

INFN Milano Bicocca, Milano, Italy
[a] and Physics Department, University of Milano Bicocca
[b] and CILEA, Segrate - Milano, Italy
** E-mail: massimo.gervasi@mib.infn.it*

P. Bobik, and K. Kudela

Institute of Experimental Physics, Department of Space Physics, Slovak Academy of Science, Kosice, Slovak Republic

We have evaluated Cosmic Ray trajectories inside the magnetosphere and defined a Transmission Function (TF) for the CR penetration. We have then computed the TF for Helium, Carbon and Iron nuclei. Finally the flux of primary CR Helium, Carbon and Iron has been evaluated inside the magnetosphere. The results have then been compared with calculations for protons and also with experimental data collected by AMS-01 and HEAO-3.

Keywords: Cosmic Rays; Propagation in magnetosphere; Geomagnetic cut-off.

1. Cosmic abundances and experimental data

Among the Galactic Cosmic Rays (GCR), protons are largely the most abundant, but also the amount of Helium nuclei and electrons is relevant. In addition the presence of heavier nuclei, like Carbon, Nitrogen, Oxygen and Iron, is not negligible, in particular taking into account the amount of energy they can deposit on a target. For this reason it is important to evaluate the relative abundance of the several components of the Cosmic Rays in relation to the radiation damage and radiation dose in space.

An accurate evaluation of these effects is even more important for long duration space missions, as it can be an interplanetary journey or for a permanent orbiting station like the International Space Station (ISS). An accurate evaluation of the radiation and its effect is unavoidable in particular for the manned missions.

In the present paper we consider the data of protons and Helium taken by the AMS-01 detector in June 1998[1] , while the data of Carbon and Iron

were measured by the HEAO-3-C2 experiment from October 1979 to June 1980[2]. Data were collected by the two detectors during periods of similar solar activity and polarity. Experimental conditions were also comparable: altitude and inclination of the orbit, angular acceptance of the detectors.

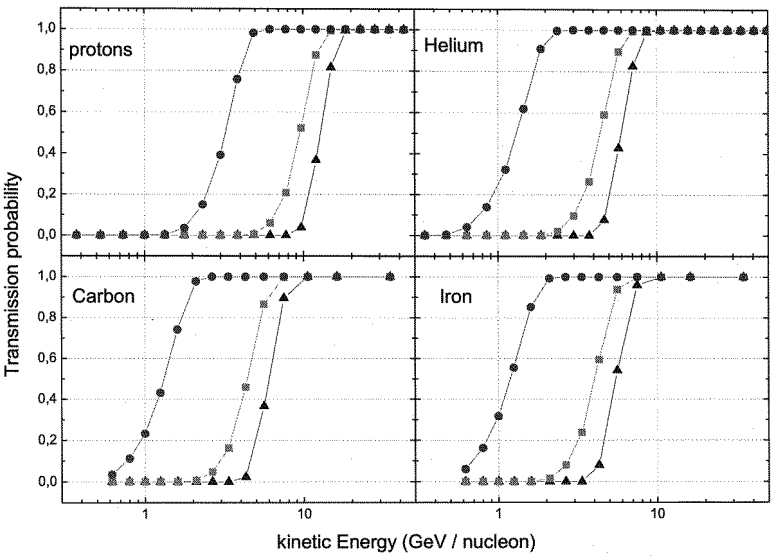

Fig. 1. The Transmission Function of p, He, C and Fe, in the geomagnetic regions M1 (triangles), M4 (squares) and M7 (circles).

2. Magnetospheric Transmission Function

In the space region around the Earth, the Geomagnetic field provides a shield against the penetration of CR down to the Earth surface[3] . Trajectories calculations in the geomagnetic field are usually performed to estimate the particles approaching to a ground station or to an orbiting satellite. This study can be done by using a software code reproducing the interaction between a charged particle and all the magnetic fields along the whole path. We developed a code to reconstruct the Cosmic Rays trajectory in the Earth magnetosphere[4] . This code solves the Lorentz equation and propagates a particle backward in time[5] . The total magnetic field is evaluated by using the International Geomagnetic Reference Field (IGRF) 2000-2005[6] , representing the main contribution due to the inner Earth,

and the external magnetic field Tsyganenko-96[7] , representing all the other contributions, like particle currents in the magnetosphere[8] .

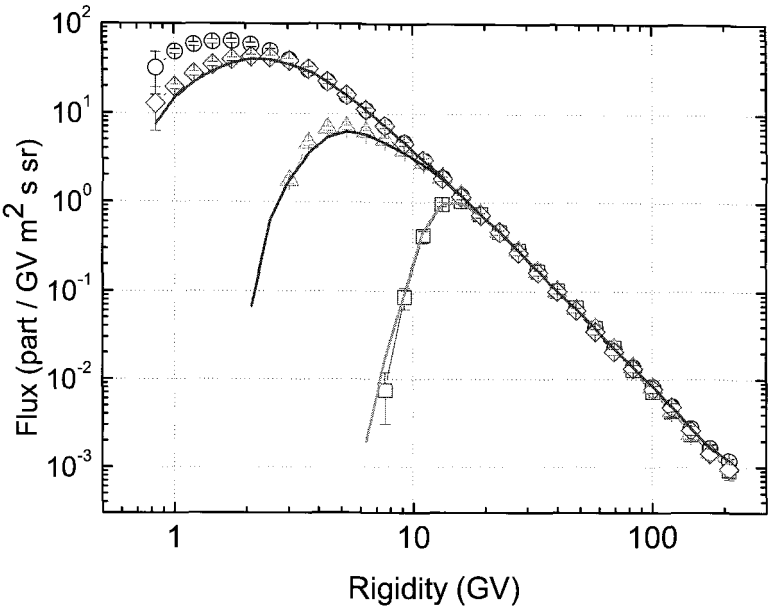

Fig. 2. Fluxes of He primaries: comparison of calculations with AMS-01 data. regions M1 (circles) and M7 (triangles).

The magnetospheric Transmission Function (TF) was calculated evaluating the probability for particles with rigidity P to reach some geographic position coming from outside the magnetosphere[5] . In particular we considered the AMS-01 geomagnetic regions[1] , defined as functions of the geomagnetic latitude, at the altitude of AMS or HEAO-3. In every region **M** a particle with a rigidity (P) lower than a threshold value (usually called rigidity cut-off, P_{cut}) can not enter the magnetosphere. For $P << P_{cut}$ we obtain $TF_M = 0$, while for $P >> P_{cut}$ we have $TF_M = 1$. This threshold value is decreasing going towards the magnetic poles, but is nearly independent from the nuclear kind considered. Besides, looking at the TF_M in terms of kinetic energy, instead of rigidity, we can find a shift in the cut-off region for the nuclei respect to protons. This effect arises because the ratio $Z/A \simeq 1/2$ for almost all the nuclei (like He, C and Fe) except the H (protons) for which the ratio $Z/A \simeq 1$. In figure 1 the TF of H, He, C and Fe

is shown, for three geomagnetic regions.

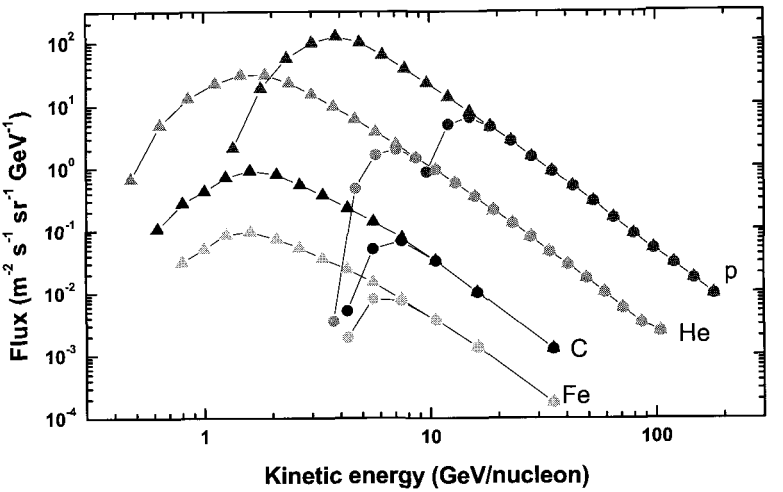

Fig. 3. Fluxes of primaries p, He, C and Fe, in the geomagnetic regions M1 (circles) and M7 (triangles).

3. Ions fluxes and abundances inside the magnetosphere

We computed the flux of primary CR entering each geomagnetic region **M** ($\Phi_M^{pri}(E_i)$). Using the TF calculated ($TF_M(E_i)$) we obtain the component of primary CR from the AMS-01 cosmic flux for p and He and from HEAO-3-C2 flux for C and Fe ($\Phi^{cos}(E_i)$):

$$\Phi_M^{pri}(E_i) = \Phi^{cos}(E_i) \cdot TF_M(E_i) \tag{1}$$

In figure 2 the comparison of calculation and AMS-01 data is shown for Helium in three geomagnetic regions.

As for the Transmission Function, the flux cut-off in the same geomagnetic region occurs at the same value of rigidity, but at different values of kinetic energy. This effect is shown in figure 3 for p, He, C and Fe, in two geomagnetic regions.

In order to evaluate the relative abundance of He, C and Fe, respect to the protons, inside the several geomagnetic regions, the integral flux above a certain value of kinetic energy has been computed. In fact inside the

magnetosphere all the particles above the local rigidity cut-off are present and contribute to the radiation. The relative abundance was defined as the ratio of the integral flux of ions (i) Helium, Carbon, Iron, respect to the flux of protons (p):

$$\Re_{i/p}(E) = \frac{\int_E^\infty \Phi_i^{pri}(E')\, dE'}{\int_E^\infty \Phi_p^{pri}(E')\, dE'} \tag{2}$$

This ratio ($\Re_{i/p}(E)$) is shown in figure 4 for He, C and Fe in the three geomagnetic regions. In this plot the limit at high energy is equal to the ratio as measured outside the magnetosphere: the cosmic abundance. On the other hand, the limit at low energy is the ratio as obtained considering all the particles penetrated inside the magnetosphere in that geomagnetic region. The transition between the two regimes occurs around the rigidity cut-off and it changes with the geomagnetic region.

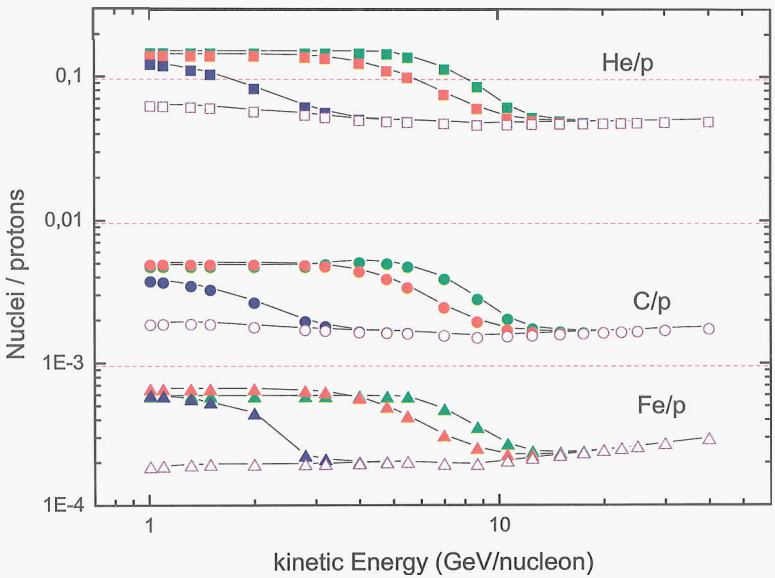

Fig. 4. **Flux ratio ($\Re_{i/p}(E)$) for He, C and Fe in the geomagnetic** regions M1 (green), M4 (red) and M7 (blue), and for cosmic abundance (open symbols).

Below the cut-off, the relative abundance inside the magnetosphere is larger than the cosmic one. This effect is due mainly to the different energy

cut-off obtained for the nucleons, respect to the protons. In fact the energy cut-off for nuclei is shifted by a factor of $2 - 3$ towards lower values.

Furthermore we evaluated the abundance enhancement inside the magnetosphere, comparing the abundance of the several nuclei inside the magnetosphere with the cosmic abundance, which take into account the flux outside the magnetosphere. This was done comparing the solid symbols in the low energy limit with the open symbols in figure 4: at this effective energy the differential primary fluxes are null and the abundance is computed using the whole population of nucleons and protons. The enhancement values range from 2.5 for He/p and C/p ratios to 3.1 for Fe/p ratio.

References

1. AMS collaboration - M. Aguilar et al., *Phys. Rep.*, **366**, 331 (2002).
2. J.J. Engelmann et al., *Astron. & Astrophys.*, **233**, 96 (1990).
3. K. Stoermer, *Z. Astroph.*, **1**, 237 (1930).
4. P. Bobik et al., *AGU Geophysical Monograph Series*, **155**, 301 (2005).
5. P. Bobik et al., *J. Geophys. Res.*, **111**, A05205 (2006).
6. Barton, C.E., International Geomagnetic Reference Field: The Seventh Generation, *J. Geomag. Geoelectr.*, **49**, 123 (1997).
7. N.A. Tsyganenko, *J. Geophys. Res.*, **100**, 5599 (1995).
8. N.A. Tsyganenko, and D.P. Stern, *J. Geophys. Res.*, **101**, 27187 (1996).

2D Stochastic Monte Carlo to evaluate the modulation of GCR for inner and outer solar system planets

P. BOBIK[1] , M.J. BOSCHINI[2]*, M.GERVASI[2,3], D.GRANDI[2] AND P.G. RANCOITA[2]

[1] *Institute of Experimental Physics, Kosice, Slovak Republic*
[2] *INFN Istituto Nazionale di Fisica Nucleare sezione di Milano-Bicocca, Milano Italy*
[3] *and University of Milano Bicocca, Italy*
E-mail: Davide.Grandi@mib.infn.it

We developed a 2D Stochastic Monte Carlo model for Cosmic Rays propagation in the Heliosphere. The model solves numerically the transport equation of particles in the heliosphere, including major processes affecting the heliospheric particle transport: diffusion, convection, adiabatic energy losses and drift of particles. We evaluated the modulated flux at several distances from the Sun (i.e. at planetary distances) and compared our results for both solar polarities with measurements of CR protons at the Earth distance, 1 AU.

Keywords: Heliosphere; Cosmic Rays; Modulation

1. Introduction

Accurate models for the propagation of Galactic Cosmic Rays (GCR) in the Heliosphere should take into account all the solar cavity features, in order to reproduce the observed fluxes. We can mention, for example, the complex structure of the heliospheric magnetic-field (HMF)[1] , after the measurements performed by the Ulysses satellite. We used, in particular, the Parker field model for the HMF[2] , that becomes time dependent due to the measurements associated with drift effects[3] , the values of the solar wind velocity in the ecliptic plane (V) and the tilt angle (α). We developed a two dimensional (radius and heliolatitude) model[4] , including curvature, gradient and current sheet drifts, which are depending on the charge sign of particles. With our model we reproduced the primary CR flux at the Earth and at the planet locations.

*also CILEA, Segrate Milano

2. Stochastic 2D Monte Carlo model

We used a stochastic Monte Carlo to study the Cosmic Rays propagation in the Heliosphere, based on the Fokker–Planck equation (hereafter FPE) for GCR transport in the heliosphere without drift terms[5,6] :

$$\frac{\partial f}{\partial t} = \frac{1}{r^2}\frac{\partial}{\partial r}\left(r^2 K_{rr}\frac{\partial f}{\partial r}\right) + \frac{1}{r^2\sin\theta}\frac{\partial}{\partial\theta}\left(K_{\theta\theta}\sin\theta\frac{\partial f}{\partial\theta}\right)$$
$$+\frac{1}{3r^2}\frac{\partial}{\partial r}\left(r^2 V\right)\frac{\partial}{\partial T}\left(\Gamma T f\right) - \frac{1}{r^2}\frac{\partial}{\partial r}\left(r^2 V f\right), \qquad (1)$$

θ is the heliolatitude f is phase space distribution function, t is the time, T is the kinetic energy (per nucleon) r is the heliocentric radial distance, V the solar wind velocity and $\Gamma = (T + 2T_0)/(T + T_0)$, where T_0 is proton's rest energy. The first two terms in Eq. 1 describe the diffusion of GCR in the heliosphere, the third term is adiabatic energy loss and the last one is convection by the outgoing solar wind. A mathematical proof by Ito[7] set an exact equivalence between the FPE and a set of stochastic differential equations (SDE), so we can solve ordinary differential equations equivalent to Eq. 1, written as:

$$\Delta r = \frac{1}{r^2}\frac{d(r^2 K_{rr})}{dr} + V\Delta t + R_g\sqrt{2K_{rr}\Delta t}$$
$$\Delta\mu = \frac{d}{d\mu}\left[\left(1-\mu^2\frac{K_{\theta\theta}}{r^2}\right)\right]\Delta t + R_g\sqrt{2\left(1-\mu^2\right)\frac{k_{\theta\theta}}{r^2}\Delta t}$$
$$\Delta E = -\frac{2VT\Gamma}{3r}\Delta t, \qquad (2)$$

where $\mu = cos\theta$ and so $\Delta\mu = \Delta cos\theta$ is the latitudinal variation of the particle, V is the solar wind velocity, R_g is the Gaussian distributed random number with unit variance, Δt is the time step of calculation. The radial diffusion coefficient is $K_{rr} = K_{||}cos^2\psi + K_{\perp}sin^2\psi$, ψ is the angle between radial and magnetic field directions[5] , the latitudinal coefficient is $K_{\theta\theta} = K_{\perp}$. The parallel and the perpendicular diffusion coefficients are

$$K_{||} = K_0\beta K_P(P)\frac{B_\oplus}{3B}$$
$$K_{\perp} = (K_{\perp})_0 K_{||}, \qquad (3)$$

$K_0 = 1-6\times10^{22}$ cm^{2}s^{-1} (from[8]), β is the particle velocity, $K_P(P)$ depends on rigidity P (in GV), $(K_{\perp})_0$, the ratio between parallel and perpendicular diffusion coefficients, is typically in the range $0.01 - 0.05$, $B_\oplus \sim 5$ nT is the heliospheric magnetic field at Earth, and B is the Parker field[9] . In our

model the solar wind speed $V(\theta)$ is a function of θ[10] : $V = V_0(1 + sin\theta)$, for $0^o < \theta < 60^o$ and $V = 750$ kms^{-1}, for $60^o < \theta < 90^o$. V_0 is the velocity of solar wind in ecliptic plane. Drift effects are included through analytical effective drift velocities[11] . The average drift velocity is $v_d = \nabla \times (\frac{\beta \Re}{3B})$. In this spiral field we added to the previous formulas (Eq. 2), the three components of drift, the gradient, the curvature and drift along the neutral sheet to calculate the position of a test particle during a time step Δt:

$$\Delta r_d = \Delta r + (v_g + \overline{v_d^{ns}})\Delta t$$

$$\Delta \mu_d = \cos\left[\arccos(\Delta\mu) + \arctan\left(\frac{v_\theta \Delta t}{r}\right)\right], \qquad (4)$$

Δr_d is the radial variation with drift effect, $\Delta\mu_d$ is the latitudinal variation of the particle due to drift, v_g is the velocity of gradient drift, v_d^{ns} is the velocity of neutral sheet drift and v_θ is the velocity of curvature drift. As Local Interstellar Spectrum of protons (LIS) we used Burger's model[12] .

3. Study of the modulation parameters

We evaluated the modulation dependence from the diffusion terms of Eq. 1. The GCR flux as a function of the diffusion coefficient follows the expected behavior, so higher values of K_0 corresponds to a lower modulation and vice versa. We also considered the dependence of our model on, $(K_\perp)_0$: as expected the modulation effect on the LIS is higher for lower values of $(K_\perp)_0$. For positive periods we evaluated the effect on the model by changing the solar wind speed and the tilt angle α, the main parameter for the level of the solar activity (see for complete description[4]): the higher the value of α the lower the expected GCR flux, and a higher value of V is related to higher solar activity.

4. Results

We estimated the GCR flux at 1 AU in relation with three different experiments: AMS-01, IMAX and CAPRICE (see[13–15]). To obtain the starting value of the diffusion coefficient we used the force field (FF) long-term modulation study (see[16]). We chose $(K_\perp)_0 = 0.025$, and we obtained V_{sw} and α for the related periods from data (see[17,18]). In Fig.1 left and Fig.2 we present our results in comparison with data. Fine tuning of the parameters showed that different values of K_0 must be taken to reproduce the measured flux. This probably underline that the heliosphere description of the FF approach is incomplete, and that its complexity may be described

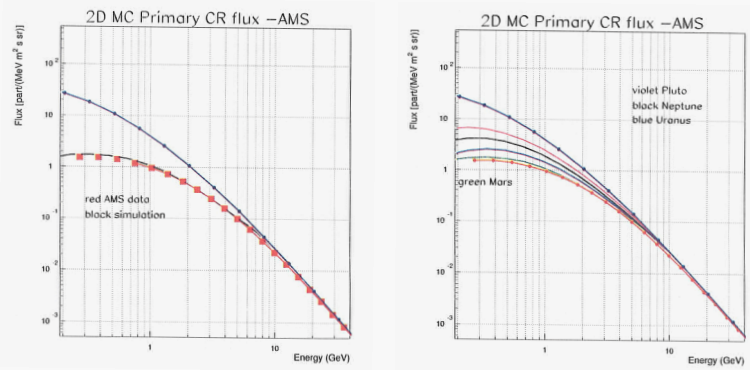

Fig. 1. **Left:2D model: diffusion coefficient effect on the modulated CR** flux at Earth, no NS drift. Right: Modulated CR flux for 3 planets of the Solar System

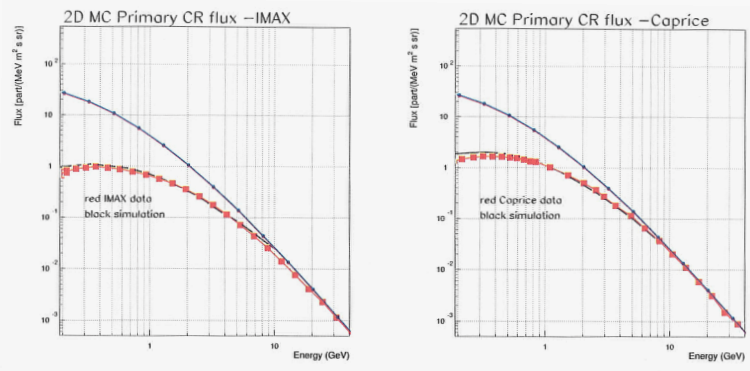

Fig. 2. **Left:2D model: diffusion coefficient effect on the modulated CR** flux at Earth, no NS drift. Right: Modulated CR flux for 3 planets of the Solar System

with a deeper insight by the 2D (and soon 3D) model. We present also the modulated CR spectrum for solar system planets (here with the same parameters used for AMS-01), As shown in Fig. 1 right, the solar modulation is decreasing with increasing heliospheric distance (in agreement with integral spectrum of CR from Voyager I and II and Pioneer, see[19]).

5. Conclusions

We built a 2D stochastic model of particles propagation in the heliosphere with drift effects and show quantitatively good agreement with measured

values. Proton spectra, as predicted by the model, are decreasing with increasing tilt angles and solar wind velocity. The model must be tested with data in different solar conditions, we thus expect the next AMS-02 mission for more than 3 years data taking, in ascending solar phase and negative polarity. We implemented in the 2D model the possibility to calculate a modulated proton spectra at different heliospheric distancies (corrispondent to the solar system planets radii) and we evaluated for the same positive period of AMS-01 the primary CR flux at different planets.

References

1. L.A. Fisk, *J. Geophys. Res.* 101, 15547-15553, (1996).
2. R. A. Burger et al., *Amer. Geophys. Un.* SH71A-04, Fall Meeting (2002).
3. G. Wibberenz, et al., *Space Science Rev.*, 97, 373 (2001).
4. P. Bobik et al.,*Proceedings of ICSC* 2003ESA SP-533, 2003.
5. M. S. Potgieter, et al., *The Astrophys. J.*, 403, 2, 760 (1993).
6. L. A. Fisk, *J. Geophys. Res.* 81, 4646, (1976).
7. Gardiner, C.W., *Handbook of Stochastic Methods*, Springer Verlag, (1989).
8. M. S. Potgieter, J. A. Le Roux, *The Astrophys. J.* 423, 817, (1994).
9. R.A. Burger and M.S. Potgieter, *The Astrophys. J.* 339, 501, (1989).
10. J. P. L. Reinecke, et al., *Adv. Space. Res.* 19, Issue 6, 901, (1997).
11. M. Hatting and R.A. Burger, *Adv. Space. Res.* 16, No. 9, 213, (1995).
12. R. A. Burger, et al., *J. Geophys. Res.* , 105, A12, 27447, (2000).
13. J. Alcaraz et.al., *Physics Letters B* 490, 27 (2000).
14. Menn, W. et al.*The Astrophys. J.*, 533, 1, (2000)
15. Boezio, M. et al. *The Astrophys. J.*, 518, 1, (1999).
16. Usoskin, I. et al. *Jour. of Geoph. Res.*, 110, A12, (2005)
17. http://wso.stanford.edu/
18. http://omniweb.gsfc.nasa.gov/form/dx1.html
19. http://pds-rings.seti.org/voyager/

The PoGOLite balloon-borne soft gamma-ray polarimeter

M. Kiss*

for the PoGOLite collaboration

Particle and Astroparticle Physics, Royal Institute of Technology, SE-106 91 Stockholm, Sweden

** E-mail: mozsi@kth.se*

PoGOLite is a balloon-borne experiment that will measure the polarization of soft gamma-rays between 25 keV and 80 keV through detection of coincident Compton scattering and absorption in a close-packed array of 217 well-type phoswich detector cells. The potential observation targets include pulsars, accreting compact objects and astrophysical jets. The polarization properties of such radiation can reveal important new information on the geometry, magnetic fields and emission mechanisms of these sources.

Keywords: Polarimetry, X-rays, Gamma-rays, Well-type phoswich detectors

1. Introduction

X-ray and gamma-ray polarimetry is expected to provide important new information about astronomical sources, *e.g.* on the physical state and geometry of compact objects and the intervening material. Although potential targets for polarimetric measurements are numerous, only one significant detection of polarization in the X-ray band has been reported so far, from an experiment where the polarization of 2.6 keV and 5.2 keV photons from the Crab nebula was studied [1,2]. One of the biggest difficulties with polarimetry in the X-ray band is the high levels of background, e.g. atmospheric gamma-rays and neutrons, charged cosmic rays and neutrons produced in cosmic ray interactions with the payload mechanics. We are therefore constructing a polarimeter based on phoswich detector cell technology and several active and passive systems for background rejection. This balloon-borne instrument, PoGOLite (the Polarized Gamma-ray Observer — light-weight version) [3], operates in the energy range 25 keV to 80 keV and will be able to measure a 10% polarization from a 200 mCrab source in a single six hour at an altitude of about 40 km. Sources of interest include pulsars, accreting black holes and neutron stars, as well as galactic

binaries and jets from active galaxies. Since photons have a higher probability to scatter perpendicular than parallel to the polarization vector [4], the distribution of azimuthal scattering angles observed in a segmented detector is modulated by the polarization, thus enabling the polarization characteristics (degree and angle) to be reconstructed [5]. The PoGOLite instrument (Fig. 1) employs a close-packed array of 217 well-type phoswich detector cells (PDCs) to detect Compton scattering and photoabsorption in order to reconstruct azimuthal scattering angles of incident photons. A 54-segment side anticoincidence shield (SAS) made of BGO crystals surrounds the array and is used to detect charged particles and photons entering the instrument from the side. The neutron-induced background is reduced by a 10 cm thick polyethylene shield, which covers the side and the bottom of the detector. To minimize systematical bias, the instrument is also rotated around the viewing axis.

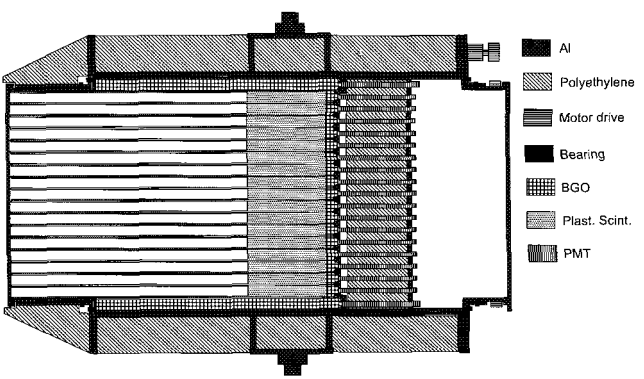

Fig. 1. Axial cross-section of the PoGOLite instrument, which measures about 1.5 m in length. The inner cylinder houses the active detector components, *i.e.* the phoswich detector cells and the side anticoincidence shield. The outer cylinder contains the polyethylene neutron shield and provides an interface for the mechanisms which enable the instrument to rotate around the viewing axis as well as pivot for elevation pointing.

Each PDC [6,7] in the array consists of a hollow slow plastic scintillator (60 cm), a solid fast plastic scintillator (20 cm) and a BGO crystal (4 cm) and is viewed by a single photomultiplier tube. The slow scintillator is an active collimator which narrows the field of view to about 5 square degrees. Photons from the observed source enter cleanly through the hollow slow scintillator and undergo Compton scattering or photoelectric absorption in the solid fast scintillator, which is the active detector component. The bottom BGO crystal is part of the anticoincidence system and identifies back-

entering charged particles and photons. Pulse shape discrimination is used to distinguish between signals in the different detector components [6].By measuring a Compton scattering in one cell and a photoelectric absorption in a separate cell, the azimuthal scattering angle of the incident photons can be reconstructed. The relative energy deposition is used to distinguish between scattering sites and absorption sites. Multiple-site events triggering more than two cells can also occur. Monte Carlo simulations based on the Crab pulsar spectrum show, however, that the polarization can be reliably reconstructed by including up to three-site events, and that less than 20% of the triggered events involve more than three cells [8,9].

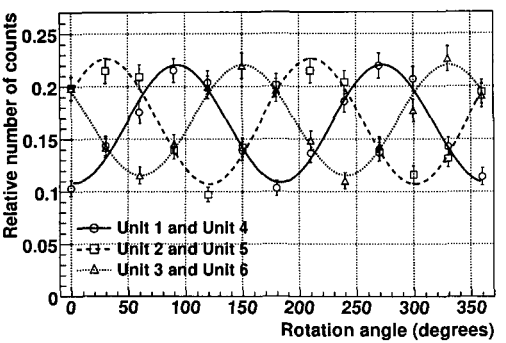

Fig. 2. Observed modulation for the 50 keV measurement. Units 1–6 are symmetrically placed around a central unit, which is directly irradiated and acts as a scatterer. As the detector array is rotated relative to the fixed beam polarization, a modulation is seen in the relative number of counts in the six surrounding units. The modulation is more pronounced the higher the polarization degree of the incident beam is. Results shown here have been pairwise averaged for opposing detector cells to account for intrinsic differences between the cells. Sinusoidal curves have been fitted to the data.

2. The PoGOLite prototype

In March 2007, a 7-unit prototype was tested at the KEK "Photon Factory" in Japan [10]. The instrument was irradiated with a beam of photons with a polarization degree of $(91 \pm 1)\%$. Using flight-version front-end electronics, the scattering angles were measured at 25 keV, 50 keV and 70 keV. The detector array was rotated 360° around the beam axis in 15° steps while the polarization of the incident photon beam was kept constant. In-flight, the detector will be rotated in a similar fashion. Figure 2 shows the modulation obtained for the 50 keV measurement. The modulation factor (amplitude

of the fitted modulation curve divided by the average value of the curve) was found to be (33.7 ± 1.3)%, in accordance with our expectations. To test the background rejection capability, the detector array was irradiated by 662 keV photons from ^{137}Cs through a segment of the side anticoincidence BGO shield. The modulation caused by the polarization could still be clearly measured, even with this added source of background. In this case, the obtained modulation factor was (31.8 ± 0.7)%.

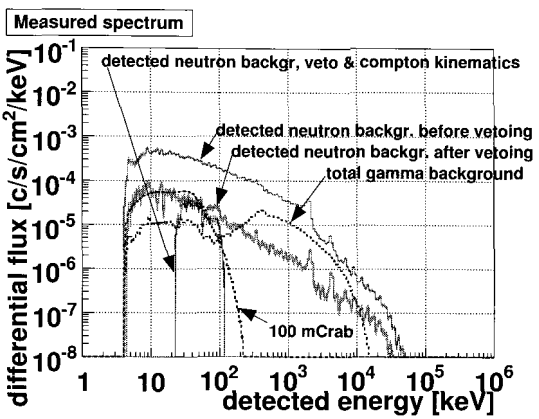

Fig. 3. Simulations of atmospheric and structure-induced contributions to the background. The energy range relevant for PoGOLite is 25 keV to 80 keV.

3. Background suppression

Sources of background have been carefully studied using Geant4 simulations [8,11]. Several measurements have also been made with charged particles such as 392 MeV protons from a beam line irradiating the fast scintillator [12] or minimum ionizing electrons with energies up to 2 MeV from ^{90}Sr irradiating the slow scintillator of a single detector cell [9]. A signal from 59.5 keV photons from ^{241}Am could be seen even with a background greater than that expected in-flight by more than an order of magnitude. Simulations [11] show that the biggest contribution to the background is from atmospheric neutrons. The side and the bottom of the PoGOLite instrument are therefore surrounded by a polyethylene shield which either prevents the neutrons from entering the detector array at all or moderates the neutrons to energies where the probability for fake triggers is low. Figure 3 shows the simulated background from neutrons as measured by the

instrument. By using the veto systems and Compton kinematics of the involved processes, the background can be reduced to less than a 100 mCrab level in the relevant energy range, 25 keV to 80 keV. Simulations also show that the background from neutrons produced when cosmic rays hit the gondola is much smaller than the other backgrounds.

4. Mission plans and outlook

The first flights (2009, 2010) will focus on the Crab pulsar, the main northern hemisphere target, and will enable the correct high-energy emission model to be identified from the three currently proposed models [3]. Other targets of interest on the northern hemisphere include Cygnus X-1, which is an X-ray binary system [13], and Hercules X-1, an accretion-powered pulsar [14]. Polarimetric measurements of Cygnus X-1 with PoGOLite will provide important new information about the emission mechanism and the accretion geometry of the binary system, whereas for the case of Hercules X-1, the measurements will give insight into the magnetic field orientation radiative processes in accretion flows onto the pulsar [3]. Long-duration flight from Sweden to Canada are also planned, during which it will be possible to observe multiple targets and study time variations of the sources. Furthermore, thanks to the simple instrumental design, PoGOLite can quickly be brought from stand-by to full operation. Future observations may therefore also focus on "targets of opportunity" such as transient events detected by GLAST, SWIFT or other instruments.

References

1. M. C. Weisskopf, *et al.*, ApJ, 208 (1976) L125.
2. M. C. Weisskopf, *et al.*, ApJ, 220 (1978) L117.
3. T. Kamae, *et al.*, arXiv:0709.1278v1 [astro-ph].
4. T. Mizuno, *et al.*, Nucl. Instr. and Meth. A 540 (2005) 158.
5. F. Lei, *et al.*, Space Sci. Rev. Vol. 82 (1997) 309.
6. Y. Kanai, *et al.*, Nucl. Instr. and Meth. A 570 (2007) 61–71.
7. M. Kiss, KTH Master's Thesis (2006), www.particle.kth.se/pogolite
8. O. Engdegård, KTH Master's Thesis (2006), www.particle.kth.se/pogolite
9. M. Kiss, M. Pearce, Nucl. Instr. and Meth. A 580 (2007) 876-879.
10. M. Ueno, *et al.*, manuscript in preparation for publication
11. J. Kazejev, KTH Master's Thesis (2007), www.particle.kth.se/pogolite
12. Y. Kanai, Tokyo Institute of Technology Master's thesis (2007), kipac.stanford.edu/pogolite/collab
13. D. R. Gies, C. T. Bolton, ApJ, 304, 371 (1986).
14. P. Mészáros, *et al.*, ApJ, 324, 1056 (1988).

PERFORMANCE THE GLAST-LAT: BEAM TEST RESULTS

M.BRIGIDA, A.CALIANDRO, C.FAVUZZI, P.FUSCO, F.GARGANO, N.GIGLIETTO, F.LOPARCO, M.N.MAZZIOTTA[†], C.MONTE[†], S.RAINÒ AND P.SPINELLI

FOR THE GLAST COLLABORATION

Dipartimento Interateneo di Fisica "M.Merlin"
Università degli Studi di Bari and Politecnico
and I.N.F.N. Sez. Bari
Via Amendola 173
70126 Bari, Italy

Between July and November 2006, the LAT Collaboration has performed a massive campaign of particle beam test on a Calibration Unit (CU), in order to study the performance of the LAT and validate the LAT Geant4 based simulation. We have tested the LAT Calibration Unit at CERN, both at PS and SPS accelerators, and at GSI. The Calibration Unit is a detector built with two complete flight spare modules, a third spare calorimeter module, five antocoincidence tiles located around the telescope and flight-like readout electronics. The LAT response to minimum ionizing particles, high energy electrons, gamma ray and ions (C,Xe) in a wide energy range, has been studied. This large amount of data allowed to determine the LAT performance, such as the capability to reconstruct the direction of the incident gamma-rays.

1. Introduction

The Gamma-ray Large Area Telescope (GLAST) is a satellite-borne observatory to study the high-energy gamma-ray sky. The Large Area Telescope (LAT) is the main instrument on board GLAST. It is a pair-conversion telescope which will survey the sky in the energy range from 20 MeV up to 300 GeV. The LAT has a modular structure, consisting of a 4x4 array of identical towers, supported by a low-mass grid. Each tower is composed by a silicon strip detector (SSD) tracker (TKR), a CsI calorimeter (CAL) and data acquisition module (DAQ). A plastic segmented scintillator anticoincidence system (ACD) covers all the towers and provides most of the rejection of the charged particle backgrounds.
A second instrument, the GLAST Burst Monitor (GBM) will provide spectra and timing in the energy range from 8 keV to 30 MeV for Gamma-Ray Bursts (GRB) [1,2].

[†] Corresponding author: mazziotta@ba.infn.it and claudia.monte@ba.infn.it

2. The GLAST LAT Beam test

As a part of the LAT calibration strategy, a beam test campaign was performed between July and November 2006 on a reduced scale LAT prototype (Calibration Unit, CU). The CU is a detector consisting of two complete flight towers, a third calorimeter module and five anticoincidence tiles. The CU was exposed at the CERN (PS and SPS) and GSI accelerator facilities, to beams of photons, electrons, hadrons (pions and protons) and ions (C, Xe) with different momenta (see Table 1) and incoming direction, representing the whole spectrum of the signal that will be detected by the LAT [3].

Particle	*PS*	*SPS*	*GSI*
γ	0.5,1,1.5,2.5 GeV/c (electron beam)		
e^-	0.5,1,1.5,2.5,5 GeV/c	10,20, 50, 100, 200, 280 GeV/c	
e^+	0.5,1 GeV/c		
π-	5 GeV/c	20 GeV/c	
p	6,10 GeV/c	20,100,150 GeV/c	
^{12}C			1.5 GeV/n
^{131}Xe			1.5 GeV/n

Table 1. Features of the beams at CERN-PS and SPS and at GSI facilities.

3. Beam test data analysis

3.1. Photon Angular Dispersion

For angular dispersion studies, photon data from runs in both tagged and non-tagged mode have been used [4]. The runs in non-tagged mode were taken with a 2.5 GeV/c electron beam; the runs in tagged mode were taken with electron momenta ranging from 0.5 to 2.5 GeV/c. The gamma direction for non-tagged mode runs was assumed to be coincident with the nominal electron beam direction. The systematic errors in the evaluation of the angular dispersion in non-tagged mode runs are due to the electron incoming beam divergence (4 mrad at 2.5 GeV/c), to the uncertainty of the CU position with respect to the beam (0.1 degrees), and to the photon production angle by bremsstrahlung with respect to the electron (0.1 degrees).

We have classified all acceptable events into three classes, using the output of the tracking and vertexing algorithms: events with a single vertex, events with two vertices, and events with more than two vertices. In addition, since one or

two tracks can be associated to a vertex, it is possible to introduce sub-classes in each of these classes. For our analysis we selected events with a single vertex and two associated tracks. Figure 1 shows a comparison between data and Monte Carlo simulation for the angle dispersion at 68% containment value for events at normal incidence.

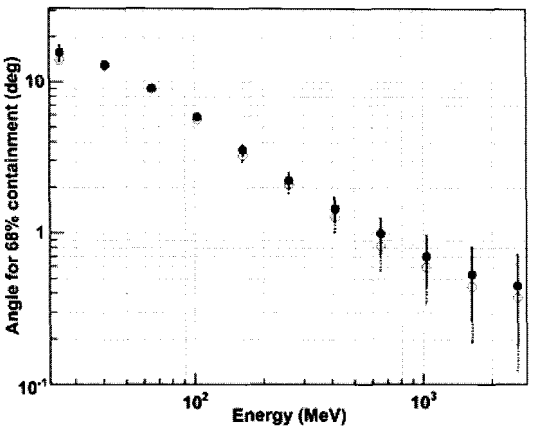

Figure 1: Angular dispersion at 68% containment. Full circles: real data; open circles: simulation predictions.

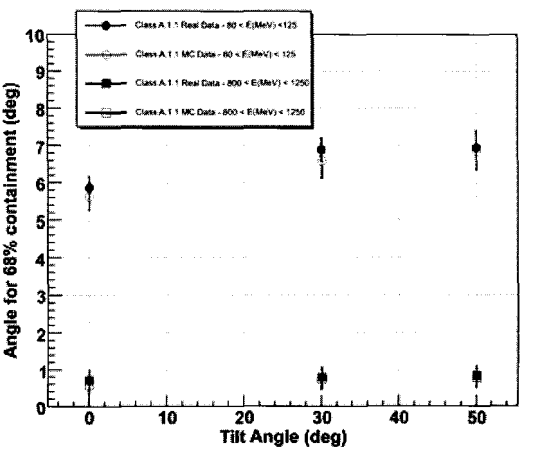

Figure 2: Angular dispersion at 68% containment at different photon incidence angles. Full symbols: real data; open symbols: simulation predictions. Circles: energy in the range 80-125 MeV; squares: energy in the range 800-1250 MeV.

Figure 2 shows the dependence of the 68% containment angle on the tilt angle of the CU with respect to the normal direction at different photon energies. Experimental data are well reproduced by the Monte Carlo simulation.

3.2. *Detector response to electrons*

Using the electron set-up [4], we collected a large set of electron runs with different configurations (different momenta and incoming directions with respect to the CU). We selected electron events with at least one vertex and one track reconstructed in the TKR and an energy deposition in the CAL greater than 300 MeV (to reject hadrons).

Figure 3 shows the average energy deposited in CAL layers by electrons of different energies entering the CU with normal incidence. For increasing electron energies, the electromagnetic showers tend to develop deeper inside the CAL and at high energies the showers are not fully contained.

The electron energy is reconstructed taking into account the information from both the TKR and the CAL. For each configuration (incident electron energy and direction) we have compared the CU reconstructed energy to the nominal beam energy. Figure 4 shows this comparison in the case of vertical electrons: the CU reconstructs correctly the energies of incoming electrons.

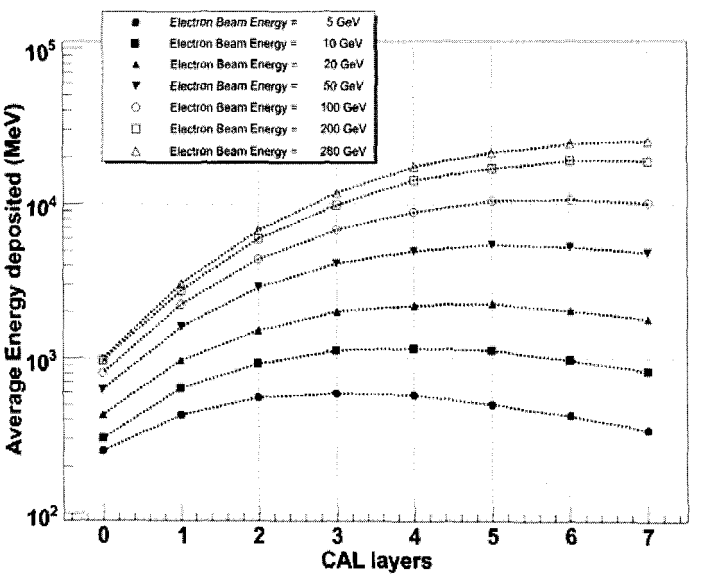

Figure 3: Average energy deposited in the CAL layers by electrons of different energies with normal incidence.

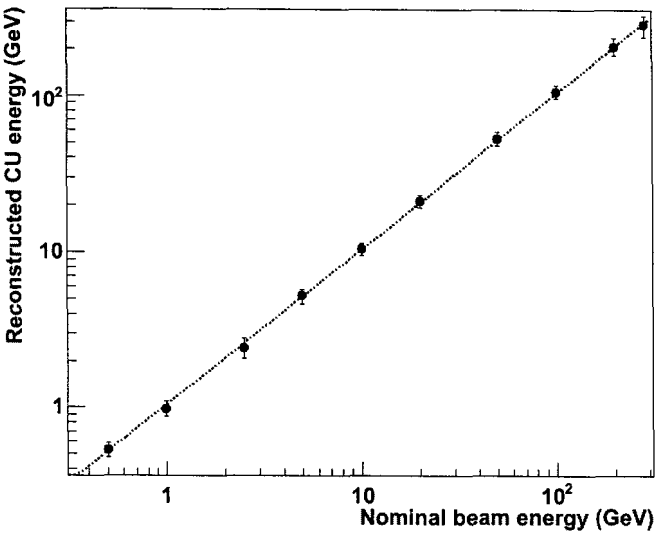

Figure 4: Reconstructed CU energy Vs Nominal beam energy for vertical electrons. The dotted line is drawn as a guide for the eye.

4. Conclusions

A beam test campaign on a GLAST-LAT Calibration Unit was performed in 2006. During the test, a large set of configurations (particles, energies and angles) have been explored.
The measured photon angular resolution is well reproduced by the Monte Carlo simulation. Preliminary results also confirm that the apparatus correctly reconstructs the energy of incoming particles.

References

1. http://glast.gsfc.nasa.gov/
2. "GLAST-LAT – Scientific and Technical Plan", AO 99-OSS-03 (2000)
3. L. Baldini et al. – "Preliminary results of the LAT Calibration Unit beam tests", proceedings of the first GLASST symposium, AIP Conference Proceedings Vol. 921 (2007) 190-204
4. M. Brigida et al. – "Particle beam tests for the GLAST-LAT calibration", these proceedings

The Alpha Magnetic Spectrometer on the International Space Station

M. Paniccia*, on behalf of the AMS Collaboration

Departement de Physique Nucleaire et Corpusculaire, Université de Genéve, 24 quai E. Ansermet, CH-1211 Geneva, Switzerland

**E-mail: mercedes.paniccia@physics.unige.ch*

The Alpha Magnetic Spectrometer (AMS) is a particle physics detector designed to measure charged cosmic rays spectra up to TV region, with high energy photon detection capability up to few hundred GeV. With the large acceptance, the long duration (3 years) and the state of the art particle identification techniques, AMS will provide the most sensitive search for the existence of antimatter nuclei and for the origin of dark matter. The detector is being constructed with an eight layers Silicon Tracker inside a large superconducting magnet, providing a $\backsim 0.8$ Tm^2 bending power and an acceptance of $\backsim 0.5$ m^2sr. A Transition Radiation Detector and a 3D Electromagnetic Calorimeter allow for electron, positron and photon identification, while independent velocity measurements are performed by a Time of Flight scintillating system and a Ring Image Cherenkov detector. The overall construction is due to be completed by 2008.

Keywords: AMS; Antimatter; Cold Dark Matter; Cosmic rays.

1. Introduction

The Alpha Magnetic Spectrometer is a particle physics experiment designed to perform high accuracy measurements of charged and neutral high energy radiation in space. A prototype detector, AMS-01,[1] has flown on board the NASA Space Shuttle Discovery during the STS-91 Mission in June 1998. In addition to validating the AMS concept analysis of the collected events led to significant physics results on rates and spectra of charged cosmic rays and provided the most precise upper limit at the time on the ratio of the flux of antihelium to the flux of helium. Following the experience gathered during the precursor flight, the AMS collaboration is constructing a more ambitious detector, AMS-02, for installation on the International Space Station (ISS) for at least three years of data taking.

2. The AMS-02 detector

The core of the AMS-02 detector is a spectrometer with a superconducting magnet, providing a rigidity range for charged particle up to the multi-TV region. A view of the detector is shown in Fig. 1.

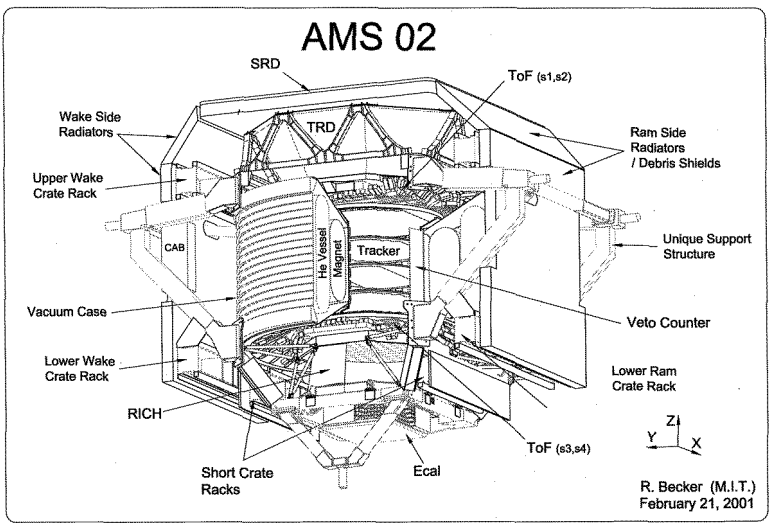

Fig. 1. The AMS-02 detector as it will appear on the ISS.

2.1. *Cryomagnet*

The magnet system[2] consists of superconducting coils, a superfluid helium vessel and a cryogenic system, all enclosed in a toroidal vacuum tank with inner diameter of 1.1 m, outer diameter of 2.7 m and a length of the central cylinder surrounding the Tracker of 0.9 m. The magnet operates at a temperature of 1.8 K, cooled by superfluid helium stored in the vessel. It is launched at the operating temperature, with the vessel full of 2500 litres of superfluid helium, sufficient to assure the magnet operation for at least three years. The coil systems consists of two Helmholtz coils and two series of six smaller racetrack coils arranged in a magic ring configuration around the inner cylinder of the vacuum tank. The single pair of Helmholtz coils generates the magnetic dipolar field perpendicular to the experiment axis. The flux return coils control the stray field and, with this geometry, they also contribute to the useful dipolar field. The magnetic flux density at the

geometric centre of the system is 0.8 T.

2.2. *The Silicon Tracker*

The AMS-02 Silicon Tracker is composed of double-sided silicon micro-strip sensors. Close to 2500 silicon sensors are assembled in 192 ladders of variable number of sensors (7 to 15) to match the circular geometry of the Tracker. The ladders are arranged in 8 layers of about 1 m^2 mounted on 5 planes of an ultra-light support structure. The Silicon Tracker provides a tracking resolution of 10 μm in the bending direction and of 30 μm in the orthogonal direction. The good tracking resolution together with the magnet bending power ($BL^2 = 0.86$ Tm^2) allows to measure particle rigidity with an accuracy better than 2% up to 30 GV and to extend the range of detectable rigidities up to the TV region. The measurement of the specific energy loss, $dE/dx \backsim Z^2$, allows the identification of nuclei up to $Z = 24$.

Furthermore the Tracker measures the direction and the energy of photons converted in the material above the first Tracker layer, with excellent directional resolution and good energy resolution. Accurate knowledge of the instrument orientation will be provided by the Star Tracker system, mounted on the upmost Tracker plane supporting structure. Systematic errors in the pointing accuracy of the AMS Tracker for converted photons are reduced performing frequent checks of the Tracker geometry with the Tracker Alignement System (TAS).[3] The presence of the superconducting magnet requires an active cooling system for the Tracker. It consists of evaporator cooling loops connected to radiator panels facing the deep space.

The AMS-02 Silicon Tracker is surrounded by a layer of scintillation counters fitting tightly inside the inner bore of the superconducting magnet. These AntiCoincidence Counters (ACC) detect particles which enter the Tracker laterally, outside the main acceptance, providing the veto for these unwanted particles with high efficiency.

2.3. *The Time of Flight system*

The Time of Flight (TOF) system is composed of four roughly circular planes of 12 cm wide scintillator paddles, one pair of planes above the magnet and one pair below. Each plane has a sensitive area of 1.2 m^2 and within one plane the paddles are overlapped by 0.5 cm to avoid geometrical inefficiencies. The paddles in the two adjacent planes are perpendicular. Each paddle is instrumented with two Photo Multiplier Tubes (PMTs) at

each end.

The TOF provides the fast trigger for charged particles and converted photons, selection, at the trigger level, of particles within the main AMS acceptance, measurement of the particle velocity including the discrimination between upward and downward going particles and a measurement of the absolute charge which complements those made in the other detectors. Timing resolution of $\backsim$ 180 ps for protons and of $\backsim$ 100 ps for light ions is expected.

2.4. *The Ring Imaging Cherenkov*

Below the spectrometer, a Ring Imaging Cherenkov detector (RICH)[4] provides further velocity and charge measurements. Light emitted in the combined Aerogel n = 1.05 and sodium-fluoride n = 1.334 radiators on the top is detected as a circle of photons by an array of position sensitive photomultiplers on the bottom, occasionally after reflection off a conical mirror. The emission angle measures the particle velocity and the number of photoelectrons measures the energy loss and thus the charge. The RICH detector will perform the identification of isotopes of mass A $<$ 25 over its momentum range (5 – 13 GeV), and it will identify chemical elements up to iron and up to the upper rigidity limit of the spectrometer.

2.5. *The Electromagnetic Calorimeter*

The Electromagnetic Calorimeter (ECAL) is a fine grained lead-scintillating fiber sampling calorimeter, that allows precise three-dimensional imaging of the longitudinal and lateral shower development, providing high ($\geq 10^6$) electron/hadron discrimination in combination with the other AMS-02 subdetectors. The expected energy resolution for electromagnetic showers is $\delta E/E \approx 12\%/\sqrt{E(GeV)} \oplus 1.5\%$. The calorimeter also provides a standalone photon trigger capability to AMS. The light collection system and electronics are optimized for the calorimeter to measure electromagnetic particles over a wide range, from GeV up to TeV.

2.6. *The Transition Radiation Detector*

Separation between light and heavy particles is also provided by the Transition Radiation Detector (TRD) placed on top of the set-up, which measures the radiation emitted by particles upon changes in the index of refraction of the traversed medium. A fleece is used as radiator. The transition radiation

photons are detected in straw tubes, filled with a Xe : CO_2 (80%:20%) gas mixture and operated at 1600 V. In total 328 TRD modules, each containing 16 straws, of lenghts between 0.8 and 2 m are arranged in 20 layers each with 20 mm of 0.06 g/cm^3 polypropylene/polyethylene 10 μm fiber fleece. The lower and upper four layers are oriented parallel to the AMS-02 magnetic field while the middle 12 layers run perpendicular to provide 3D tracking. The proton rejection power is well above 100 for proton energies up to 300 GeV.

3. Conclusions

The high precision detectors described above will enable AMS to perform a direct search for antimatter, such as anti-He and anti-C, an indirect search for dark matter and a measurement of cosmic rays and photons spectra in space, with higher sensitivity and in an extended energy domain in comparison to previous experiments. Dark matter annihilation in the galactic halo could produce structures in γ-ray, positron and anti-proton spectra; simultaneous measurement of the spectra of these particles will strongly constrain dark matter models. In addition a high statistics study of light nuclei and isotopes will be performed. Unstable isotope ions with long lifetime like ^{10}Be and ^{26}Al are of particular interest because they provide a measurement of the confinement time of charged particles in galaxies.[5,6]

Construction of the AMS-02 detectors, support structures and electronics has been completed and shipping to CERN, where a dedicated facility for integration has been installed, has presently started in order to perform an assembly test. The final integration will take place in early 2008, afterwards the detector will undergo thermal vacuum tests at ESTEC (Netherlands). Finally by December 2008 the AMS-02 detector will be delivered to NASA Kennedy Space Center, ready to be launched on the ISS.

References

1. M. Aguilar *et al.*, *Physics Reports* **366**, 331 (2002).
2. S. M. Harrison *et al.*, *AIP Conf. Proc.* **823**, 1315 (2006).
3. W.Wallraff, AMS02 tracker alignment verification during integration, in *these proceedings*,
4. R.Pereira, The RICH detector of the AMS-02 experiment: status and physics prospects, in *these proceedings*,
5. R. Battiston, *Nucl. Phys. Proc. Suppl.* **113**, 9 (2002).
6. A. Jacholkowska *et al.*, *Phys. Rev.* **D74**, p. 023518 (2006).

The RICH detector of the AMS-02 experiment: status and physics prospects

RUI PEREIRA, on behalf of the AMS RICH collaboration

LIP/IST
Av. Elias Garcia, 14, 1° andar, 1000-149 Lisboa, Portugal
e-mail: pereira@lip.pt

The Alpha Magnetic Spectrometer (AMS), whose final version AMS-02 is to be installed on the International Space Station (ISS) for at least 3 years, is a detector designed to measure charged cosmic ray spectra with energies up to the TeV region and with high energy photon detection capability up to a few hundred GeV. It is equipped with several subsystems, one of which is a proximity focusing RICH detector with a dual radiator (aerogel+NaF) that provides reliable measurements for particle velocity and charge. The assembly and testing of the AMS RICH is currently being finished and the full AMS detector is expected to be ready by the end of 2008. The RICH detector of AMS-02 is presented. Physics prospects are briefly discussed.

1. The AMS-02 experiment

The Alpha Magnetic Spectrometer (AMS),[1] whose final version AMS-02 is to be installed on the International Space Station (ISS) for at least 3 years, is a detector designed to study the cosmic ray flux by direct detection of particles above the Earth's atmosphere, at an altitude of $\sim$ 400 km, using state-of-the-art particle identification techniques. AMS-02 is equipped with a superconducting magnet cooled by superfluid helium. The spectrometer is composed of several subdetectors: a Transition Radiation Detector (TRD), a Time-of-Flight (ToF) detector, a Silicon Tracker, Anticoincidence Counters (ACC), a Ring Imaging Čerenkov (RICH) detector and an Electromagnetic Calorimeter (ECAL). A preliminary version of the detector, AMS-01, was successfully flown aboard the US space shuttle Discovery in June 1998.

The main goals of the AMS-02 experiment are: (i) a precise measurement of charged cosmic-ray spectra in the rigidity region between $\sim$ 0.5 GV and $\sim$ 2 TV and the detection of photons with energies up to a few hundred GeV; (ii) a search for heavy antinuclei ($Z \geq 2$), which if discovered would signal the existence of cosmological antimatter; (iii) a search for dark matter

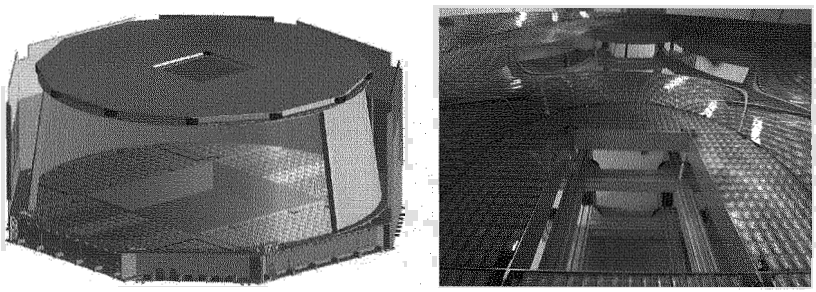

Fig. 1. **The RICH** detector of AMS-02 *(left)*. View of the assembled RICH detector at CIEMAT *(right)*.

constituents by examining possible signatures of their presence in cosmic ray spectra. The long exposure time and large acceptance (0.5 $m^2 \cdot sr$) of AMS-02 will enable it to collect an unprecedented statistics of more than 10^{10} nuclei.

2. The AMS RICH detector

AMS-02 includes a proximity focusing Ring Imaging Čerenkov (RICH) detector, shown in Fig. 1, placed in the lower part of the spectrometer between the lower ToF counters and the ECAL. A dual radiator configuration with silica aerogel ($n = 1.050$) and sodium fluoride (NaF, $n = 1.334$) has been chosen for the RICH. The geometrical acceptance of the central NaF square corresponds to $\sim 10\%$ of the total RICH acceptance.

A high reflectivity ($> 85\%$ at $\lambda = 420$ nm) lateral conical mirror made of aluminium-nickel-coated silica has been included to increase photon collection. The detection matrix at the bottom of the detector has 680 multianode photomultiplier tubes (PMTs) (4×4) coupled to light guides with a pixel size of 8.5 mm.

Charged particles crossing a radiator of refractive index n with a velocity $v > c/n$ emit Čerenkov radiation in a cone with an aperture $\theta_c = \arccos(\frac{1}{\beta n})$. The intensity of radiation is proportional to the square of particle charge and also increases with velocity. The impact of photons in the PMT matrix produces a ring which, combined with data on particle tracks obtained from the Silicon Tracker, allows to determine the Čerenkov angle θ_c and therefore the particle's velocity. Particle charge may be determined from the total signal collected by the PMTs taking ring acceptance into account.

The analysis of RICH data involves the identification of the Čerenkov ring in a hit pattern which usually includes several scattered noise hits and an eventual strong spot in the region where the charged particle crosses the

detection plane.

The RICH detector will provide a very accurate velocity measurement (in aerogel, $\Delta\beta/\beta \sim 10^{-3}$ and 10^{-4} for $Z = 1$ and $Z = 10 - 20$, respectively) and charge identification of nuclei up to iron ($Z = 26$). RICH data, combined with information on particle rigidity from the AMS Silicon Tracker, enable the reconstruction of particle mass. The accuracy of the RICH velocity measurement is essential for mass reconstruction due to the growth of relative errors when $\beta \sim 1$ ($\frac{\Delta m}{m} = \frac{\Delta p}{p} \oplus \gamma^2 \frac{\Delta \beta}{\beta}$). The RICH detector also plays a major role in the exclusion of upward going particles (albedo). Additional information on the RICH detector may be found in Ref. 3. The assembly of the AMS RICH detector is coming to an end at CIEMAT in Madrid. The integration of the RICH and the other subdetectors of AMS-02 will take place at CERN and should be finished by the end of 2008.

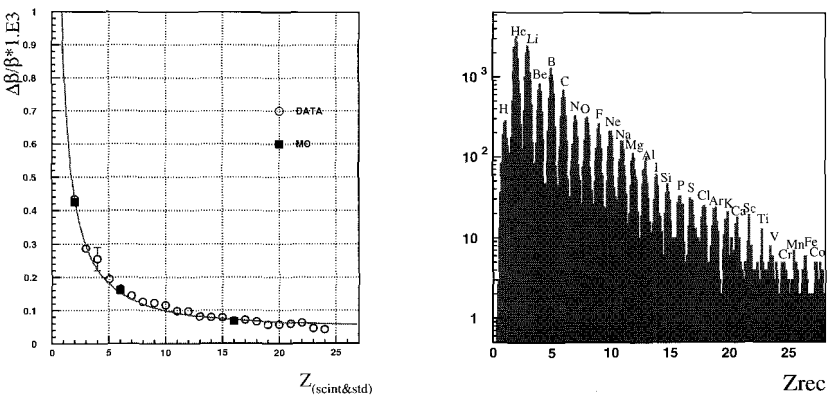

Fig. 2. Results from RICH prototype tests: velocity resolution *(left)* and charge distribution *(right)* for aerogel events.

3. RICH prototype tests

Tests on RICH particle detection were performed using a prototype corresponding to a fraction of the final detector (96 PMTs). The first prototype tests were performed in mid-2002 at LPSC in Grenoble by exposing the detector to the cosmic-ray flux at ground level. Later, in-beam testing took place at CERN SPS in October 2002 and October 2003 using secondary beams of nuclear fragments.[2] The 2002 beam was produced by bombarding a Be target with Pb ions having a momentum of 20 GeV/c/nucleon, while the 2003 beam was obtained from the bombardment of a Pb target with In ions having a momentum of 158 GeV/c/nucleon. During the 2003 tests a

mirror segment corresponding to a 30° sector (1/12 of total) was included in the experimental setup.

Fig. 2 shows prototype results for velocity and charge reconstruction with the aerogel radiator chosen for the final detector. A velocity resolution $\Delta\beta/\beta = 8.7 \times 10^{-4}$ for $Z = 1$ and $\Delta\beta/\beta \simeq 0.6 \times 10^{-4}$ for $Z > 20$ was found. A good agreement between data and Monte Carlo results was observed. Charge separation was possible up to $Z \sim 26$, with a charge resolution $\Delta Z = 0.16$ charge units for low Z. Further details on velocity and charge reconstruction can be found in Ref. 4.

4. System monitoring and pre-assembly testing

A detailed monitoring of all components of the RICH detector is necessary to ensure that systematic errors are at the level required for good velocity and charge reconstruction. A good velocity measurement requires a knowledge of the aerogel's refractive index with a precision of 10^{-4}. The quality of charge measurement constrains several variables: required knowledge of detector properties is at the level of 0.4 mm for aerogel thickness, 3% for aerogel clarity, 1% for mirror reflectivity and 5% for PMT gain and unit cell efficiency. Extensive testing has been performed on the RICH detector and its individual components to fulfill these requirements. A detailed mapping of each aerogel tile's thickness and refractive index was performed at LPSC in Grenoble with participation from LIP and UNAM. Mirror reflectivity was measured for several incidence angles. Studies for the characterization of PMTs and unit cells took place at CIEMAT.

Additional tests focused on the response of detector components to the conditions expected to occur during detector transportation into orbit and operation at the ISS. One rectangular grid, corresponding to approximately one-fifth of the detection matrix, underwent magnetic field testing at CERN and at LCMI in Grenoble to determine if PMT response would change significantly under a stray magnetic field of up to 300 G. Thermal and vacuum testing, which included individual PMTs being subject to temperatures between −35°C and 55°C and a rectangular grid undergoing temperatures between −20°C and 40°C, took place at CIEMAT. Vibration tests of the radiator container (including all NaF tiles and 1/4 of aerogel tiles) took place at SERMS in Terni, while one rectangular grid underwent similar testing at INTA in Madrid. Individual unit cells also underwent vibration tests. Monitoring and testing will continue during the detector assembly period.

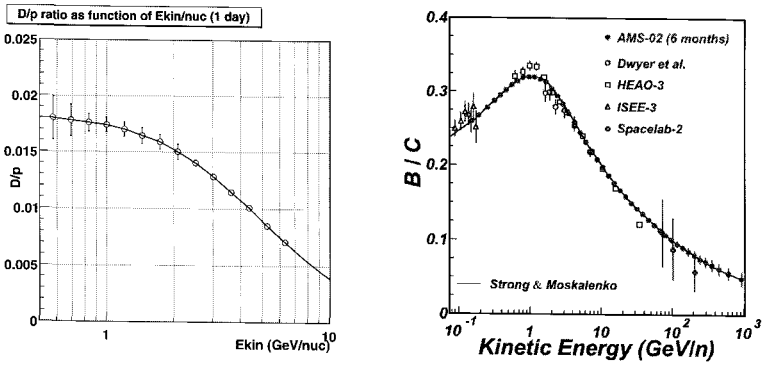

Fig. 3. Expected sensitivity of AMS: D/p ratio with one day of data *(left)* and B/C ratio with six months of data *(right)*.

5. Physics prospects

The capacities of the RICH detector for velocity and charge reconstruction will play a major role in particle identification with AMS-02. RICH data will provide charge separation up to $Z \sim 26$. Mass measurements obtained from the combination of RICH velocity with Tracker rigidity data will make possible the isotopic separation of light elements such as H, He and Be.

AMS data will provide new insights on cosmic ray physics. Secondary to primary ratios such as D/p, ^{3}He/^{4}He and B/C will provide information on cosmic ray propagation, while the ratio between the abundances of radioactive isotope ^{10}Be and stable ^{9}Be will provide data on galactic confinement times and help improve the accuracy of existing halo models.

6. Conclusions

AMS-02 will provide a new insight on the cosmic-ray spectrum by collecting precise data for an unprecedented number of particles above the Earth's atmosphere. The RICH detector will play a key role in the operation of AMS due to its capabilities for velocity reconstruction, charge determination and albedo rejection. Extensive testing has been performed on the RICH detector and its components. The assembly of the RICH detector is currently being finished and the full AMS detector is expected to be ready by the end of 2008.

References

1. S. P. Ahlen *et al.*, *Nucl. Instrum. Methods A* **350**, 34 (1994).
   V. M. Balebanov *et al.*, *AMS proposal to DOE*, approved April 1995.
2. P. Aguayo *et al.*, *Nucl. Instrum. Methods A* **560**, 291 (2006).
3. F. Barao *et al.*, Proceedings of 29th ICRC, Pune, India, 349-352 (2005), arXiv:astro-ph/0603852.
4. F. Barao *et al.*, Proceedings of 30th ICRC, Merida, Mexico (2007), arXiv:0709.2154 [astro-ph].

STUDY OF THE PERFORMANCE OF THE GLAST LAT AS A GROUND-BASED COSMIC RAY OBSERVATORY

M. BRIGIDA, G.A. CALIANDRO, C. FAVUZZI, P. FUSCO,
F. GARGANO, N. GIGLIETTO, F. GIORDANO, F. LOPARCO,
M.N. MAZZIOTTA, C. MONTE, S. RAINÒ, P. SPINELLI
For the GLAST Collaboration

Dipartimento Interateneo di Fisica "M.Merlin",
Università degli Studi e Politecnico di Bari, Italy
I.N.F.N. Sezione di Bari,
Via Amendola 173, 70126 Bari, Italy
E-mail: silvia.raino@ba.infn.it

The Gamma-ray Large Area Space Telescope (GLAST) is scheduled for launch in 2008. The Large Area Telescope (LAT) on board GLAST aims at performing gamma-ray astronomy in the energy range from 20 MeV up to 300 GeV. The potential of the LAT instrument and its scientific return will greatly depend on how accurately its performance is known and on the capability of monitoring it. The LAT is now integrated in the spacecraft and it has been tested as a cosmic-ray observatory. At present, it is undergoing the final environmental testing. This talk presents the results of studies of the performance of the LAT using cosmic-ray data obtained during ground testing. The analysis methods will carry over for studies of the in-flight performance of the LAT in the LAT Instrument Science Operations Center (ISOC), which supports mission operations and data processing for the LAT.

1. Introduction

The Gamma-Ray Large Area Space Telescope (GLAST) is a satellite-based observatory that will study the gamma-ray sky in a wide energy range from a few keV up to 300 GeV, allowing the investigation of many fields of the gamma-ray astrophysics. It will be launched in 2008.
Two instruments are on board GLAST [1]: the Large Area Telescope (LAT) and the GLAST Burst Monitor (GBM) for high variability phenomena studies (i.e. gamma-ray bursts) in an energy range from a few keV up to 30 MeV. The LAT is a wide field-of-view high energy gamma-ray telescope that will cover the higher energy range, from about 30 MeV up to 300 GeV. The LAT is a pair conversion telescope that consists of three subsystems: a precision silicon strip detector tracker (TKR), a CsI calorimeter (CAL) and a segmented anti-coincidence detector (ACD) shield of plastic scintillators that provides the rejection of the charged cosmic-ray background.

The LAT has a modular structure consisting of an array of 4x4 identical towers. Each tower is composed by one tracker module, consisting of a stack of 18 x-y single-sided silicon strip detectors interleaved with tungsten foils that provided the conversion of photons in electron-positron pairs, a calorimeter module composed by 96 CsI(Tl) bars corresponding to 8.6 radiation lengths (normal incidence), and a data acquisition module (DAQ) [1].

2. Cosmic-Ray Observatory Data Taking

The LAT and the GBM have been integrated into the spacecraft at "General Dynamics" in Gilbert, Arizona and the whole instrument has been tested there as a cosmic-ray observatory. The data collected at ground after the integration give a good opportunity to test the LAT instrument performance, to validate the Monte Carlo simulation of the instrument response and complete the verification of the Science Requirements for the LAT combining the results of cosmic-ray data taking at ground-level with the ones provided by both simulations and beam tests analysis [2].

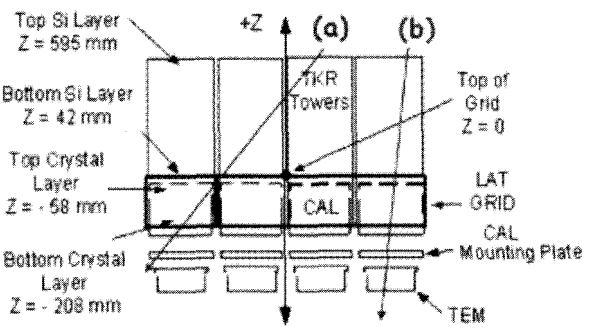

Figure 1: Geometrical selection criteria: arrow (a): tracks crossing the whole LAT; arrow (b) almost straight single tower tracks.

The analysis was performed on about $2*10^6$ total events. The events selection was done by considering the following cuts:

- events triggered by both the TKR and the ACD;
- single muon tracks;
- events fully contained in the LAT, i.e. crossing the instrument from the TKR top layer to the CAL bottom layer.
- energy deposited in the CAL layers consistent with that of a MIP.

About 16% of the total events survived to the "full LAT" cuts. A further cut has been considered, selecting all the events completely crossing a single tower, from the top TKR layer to the CAL layer. In this case, the events selected were 4% of the total.

Figure 1 shows a front view of the TKR and the CAL and two arrows pointing out the possible single muon tracks, crossing the whole LAT (a, more inclined tracks) or crossing a single tower (b, almost straight tracks).

3. Analysis of the TKR Performance

The TKR performance has been monitored by studying the distributions of the fired strips (TKR hits) for full LAT events and single tower events. Figure 2 shows the distribution of the hit strips for events fully contained in the LAT.

The dependence of the hit strips multiplicity has also been studied as a function of the zenith angle θ. Figure 3 reports the hit strip multiplicity profile as a function of $1/\cos\theta$, a function proportional to the track length in the silicon strip detectors. The number of hits increases with the track length, i.e. with the inclination of the track itself.

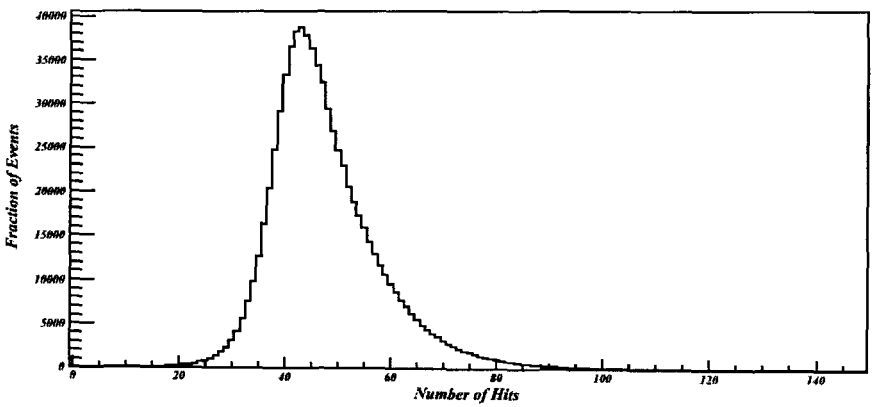

Figure 2: Hit strips multiplicity distribution for events fully contained in the LAT.

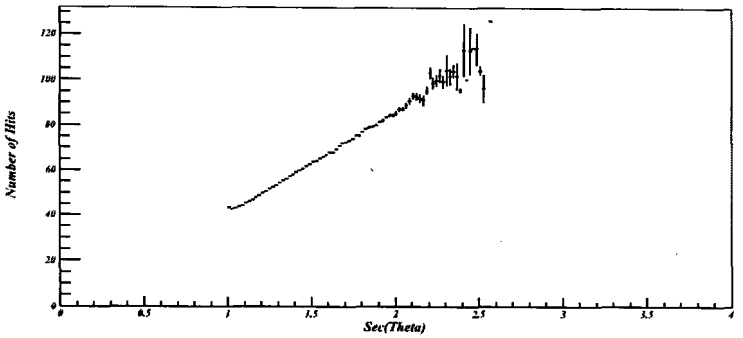

Figure 3: Average number of hit strips as a function of 1/cosθ.

The response of the CAL has also been evaluated. The energy distribution for events crossing a single tower in the CAL is shown in Figure 4. The peak of the distribution, for particles passing through the CAL, is around 110 MeV. Finally, Figure 5 shows that the energy deposited in the CAL for events contained in a single tower, as an increasing trend with 1/cosθ: the energy deposited in the CAL layers is directly proportional to the track length.

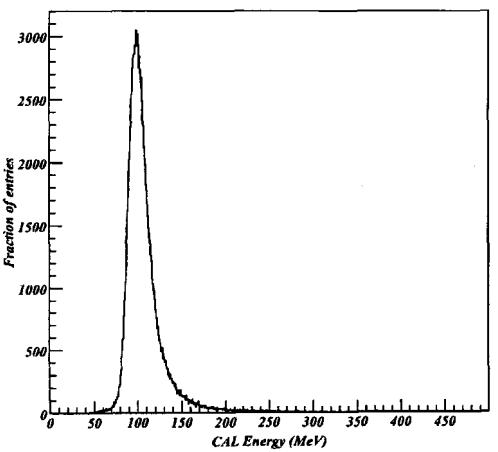

Figure 4: CAL energy distribution for one tower events.

4. Instrument Science Operations Center

The analysis methods used for the cosmic ray data analysis are carrying over for the studies of the in-flight performance of the LAT. A preliminary map of the instrument capability is being implemented by the GLAST LAT Instrument

Science Operations Center (ISOC) whose main scope will be to support the mission operations and real-time activities during GLAST satellite-to-ground contacts.

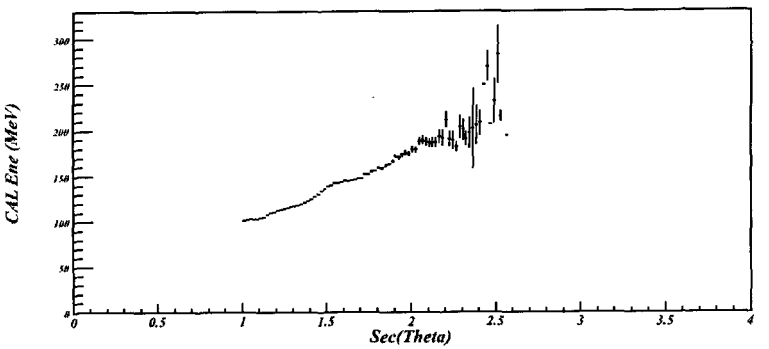

Figure 5: Trend of increase of the energy deposited in the CAL as a function of $1/\cos\theta$.

The ISOC will be devoted to data-processing, calibration and configuration of the detectors, as well as the monitoring of the instruments response and the data analysis [3]. A GLAST LAT portal is being developed including numerous plots for the on-line monitoring of the data quality and on-line analysis. Before GLAST launch all the tools developed by the ISOC group will be tested and improved during the weeks dedicated to the simulation of real data and rehearsals of operation shifts and related activities.

5. Conclusions

The LAT performance has been monitored with cosmic rays, after the integration of the instruments in the spacecraft. The results obtained are a good input for the final tuning and improvement of the Monte Carlo simulation. At present, the spacecraft is undergoing the environmental testing before launch in 2008.

References

1. P. Michelson "GLAST: the next generation gamma ray observatory " – these proceedings
2. M. Brigida et al., "Particle beam tests for the GLAST-LAT Calibration Unit" and C.Monte et al. "Performance of the GLAST-LAT TKR: beam test results" – these proceedings
3. http://glast-isoc.slac.stanford.edu/

THE CALET SPACE OBSERVATORY FOR JEM-EF ON THE INTERNATIONAL SPACE STATION

J.P.WEFEL[17], S.TORII[1], Y.SHIMIZU[1], K.KASAHARA[1], N.HASEBE[1], M.HAREYAMA[1], S.KODAIRA[1], O.OKUDAIRA[1], N.YAMASHITA[1], M.MIYAZIMA[1], T.MIYAJI[1], M.TKAYANAGI[2], S.UENO[2], H.TOMIDA[2], Y.SAITO[2], H.FUKE[2], T.YAMAGAMI[2], J.NISHIMURA[2], T.TAMURA[3], N.TATEYAMA[3], K.HIBINO[3], S.OKUNO[3], A.SHIOMI[4], M.TAKITA[4], T.YUDA[4], F.KAKIMOTO[5], Y.TSUNESADA[5], T.TERASAWA[5], T.KOBAYASHI[6], A.YOSHIDA[6], K.YAMAOKA[6], Y.KATAYOSE[7], M.SHIBATA[7], M.ICHIMURA[8], S.KURAMATA[8], Y.UCHIHORI[9], A.KITAMURA[9], K.YOSHIDA[10], H.MURAKAMI[11], Y.KOMORI[12], K.MIZUTANI[13], K.MUNAKATA[14], R.E.STREITMATTER[15], J.W.MITCHELL[15], L.M.BARBIER[15], A.A.MOISEEV[15], J.F.KRIZMANIC[15], J.F.ORMES[16], G.CASE[17], M.L.CHERRY[17], T.G.GUZIK[17], J.B.ISBERT[17], W.R.BINNS[18], M.H.ISRAEL[18], H.S.KRAWCZYNSKI[18], P.S.MARROCCHESI[19], G.BIGONGIARI[19], K.BATKOV[19], M.Y.KIM[19], M.G.BAGLIESI[19], P.MASESTRO[19], V.MILLUCCI[19], R.ZEI[19], O.ADRIANI[20], P.PAPINI[20], E.VANNUCCINI[20], L.BONECHI[20], J.CHANG[21], J.YAN[21], W.GAN[21], G.CHEN[22], Y.MA[22], H.WANG[22]

[1]Research Institute for Science and Engineering, Waseda University, Japan; [2]Institute of Space and Astronautical Science, Japanese Aerospace Exploration Agency, Japan; [3]Faculty of Engineering, Kanagawa University, Japan; [4]Institute for Cosmic Ray Research, University of Tokyo, Japan; [5]Department of Physics, Tokyo Institute of Technology, Japan; [6]Department of Physics, Aoyama Gakuin University, Japan; [7]Department of Physics, Yokohama National University, Japan; [8]Department of Earth and Environmental Sciences, Hirosaki University, Japan; [9]National Institute of Radiological Sciences, Japan; [10]Department of Electronic Information Systems, Shibaura Institute of Technology, Japan; [11]Department of Physics, Rikkyou Univeristy, Japan; [12]Kanagawa University of Human Services, Japan; [13]Department of Physics, Saitama University, Japan; [14]Department of Physics, Shinshu University, Japan; [15]Goddard Space Flight Center, NASA, USA; [16]Denver Research Institute, University of Denver, USA; [17]Department of Physics & Astronomy, Louisiana State University, USA; [18]Washington University in St. Louis, USA; [19] University of Siena and INFN, Italy; [20] University of Florence and INFN, Italy; [21]Purple Mountain Observatory, Chinese Academy of Sciences; [22]Institute of High Energy Physics, Chinese Academy of Sciences, China.

e-mail: Wefel@phunds.phys.lsu.edu

The CALorimetric Electron Telescope, CALET, is a new Space Observatory being developed for the Japanese Experiment Module Exposed Facility, JEM-EF, of the International Space Station. Major scientific objectives are to search for nearby cosmic ray sources and dark matter by carrying out a precise measurement of the electron spectrum from 10's of GeV - 10 TeV and of gamma rays in the range 20 MeV - several

TeV. CALET has a unique capability to observe electrons and γ-rays over 1 TeV, with a hadron rejection power better than 10^5 and an energy resolution of a few % beyond 100 GeV. Moreover, CALET will follow PAMELA, GLAST and other experiments and can both extend and refine the observations made by those missions. The main instrument, to be described, consists of an imaging calorimeter combined with a total absorption calorimeter. With auxiliary detectors, the CALET Observatory will also monitor solar activity and study γ-ray bursts. The phase A/B study is underway for a proposed 2013 launch on the H-II Transfer Vehicle (HTV) for 3- 5 years of observation on JEM-EF.

Keywords: Electrons, Gamma Rays, Space Station, Cosmic Ray Sources, Dark Matter

1. Introduction

The CALET (**CAL**orimeteric **E**lectron **T**elescope) mission will investigate the High Energy Universe, extending observations and discoveries made by GLAST, AGILE, Atmospheric Cherenkov Telescopes (ACT), PAMELA and balloon instruments. CALET will have superior energy resolution and excellent separation between hadrons and electrons and gamma rays. With these capabilities, it will be possible to address many of the outstanding questions in High Energy Astrophysics (HEA) including (1) signatures of dark matter, in either the high energy electron or gamma ray spectrum, (2) the nature of the sources of high energy particles and photons, through the high energy electron spectrum, and gamma ray observations of sources, and (3) the details of particle propagation in the galaxy

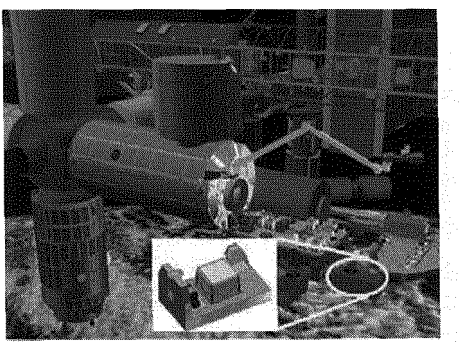

Fig. 1: CALET on the JEM exposed facility.

CALET is a Japanese led international mission proposed as part of the ISS (International Space Station) utilization plan. CALET will be launched by an H2 rocket utilizing the Japanese developed HTV (H-IIA Transfer Vehicle). The instrument will be robotically emplaced upon the Exposure Facility attached to the Japanese Experiment Module (JEM-EF), as illustrated in Figure 1. The Japanese Space Agency (JAXA) has selected CALET for Phase A/B studies in 2007-09, leading to a 2013 projected launch.

2. The CALET Project

CALET will address many of the important outstanding HEA questions, and extend the work of preceding balloon (ATIC, CREAM, TRACER, CREST) and space (GLAST, AGILE, PAMELA, AMS) missions. A schematic of the

CALET detector concept is shown in Figure 2. The instrument is composed of two major subsystems: the Imaging Calorimeter (IMC) and the Total Absorption Calorimeter (TASC) (Torii et al., 2004) plus two additional subsystems: Silicon Detector Array (SIA) and Anti-coincidence Detector (ACD).

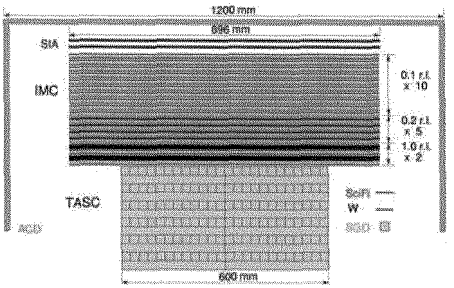

Fig. 2: Exploded view of the CALET instrument.

The **IMC** consists of 17 layers of lead plates each separated by 2 layers of 1 mm square cross section scintillating fiber (SciFi) belts arranged in the x and y direction for a total thickness of 4 radiation lengths (X_0), about 0.13 proton interaction lengths (λ). This provides the precision necessary to 1) separate the incident particle from backscattered particles, 2) precisely determine the starting point for the shower, and 3) determine the incident particle trajectory.

The **TASC** measures the development of the shower to determine the total energy of the incident particle and to separate electrons and gamma-rays from hadrons. The TASC is composed of 12 layers of Bismuth Germanate (BGO) "logs" where each log has dimensions of 2.5 cm x 2.5 cm x 30 cm, viewed by a triple segmented photodiode (Katayose et al., 2003). Alternate layers are orientated 90^0 to each other to track the shower core. The total area is 0.36 m^2 and the vertical depth is 30 cm or 26.8 X_0.

On top of the IMC is a double layer, pixellated Si detector array, containing ~6400 pixels per layer. Each pixel is a square 1.125 cm on a side, and is 500 micron thick. The **SIA** is designed to provide superior charge resolution (0.1e for H to 0.35e for Fe). Surrounding the entire detector is a segmented scintillator array, the **ACD**, to provide anti-coincidence protection for low energy gamma ray measurements. A separate Gamma Ray Burst monitor completes the instrumentation.

CALET must efficiently identify high energy electrons within the "sea" of background cosmic ray hadronic events. The calorimeter exploits two principal differences between proton and electron/gamma ray showers. First, proton induced showers are wider than electron showers due to the spread of secondary particles in nuclear interactions. Second, an electron induced shower will start and die off earlier than a proton cascade as only a fraction of the hadron total energy (~40%) is deposited in the calorimeter. A model of the CALET instrument was exposed to electron and proton beams at the CERN-SPS

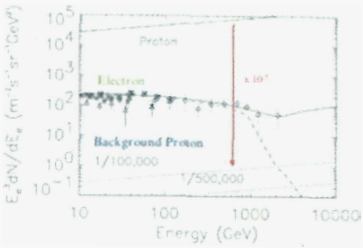

Fig. 3. Expected proton rejection power.

accelerator, and these experimental data were used to validate the simulation calculations (Katayose, et al., 2005), showing an electron detection efficiency above 95% and a proton rejection factor of 1 in 5 x 10^5 (Chang et al. 2005). Figure 3 shows the relationship between the measured electron flux, the cosmic ray proton spectrum (top curve) and proton rejection factors of 1 in 10^5 and 1 in 5 x 10^5 (bottom dotted curves).

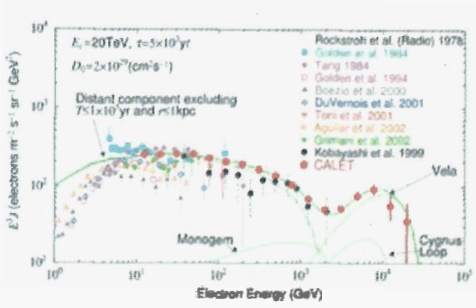

Fig 4: Expected CALET electron measurement compared with previous data.

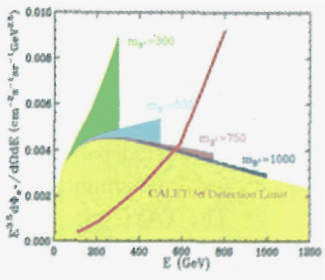

Fig 5: Predicted positron signal from annihilation of Kaluza-Klein dark matter candidate particles, from Cheng, Feng and Matchev (2002).

3. High Energy Astrophysics from CALET

3.1. *Nearby Cosmic Ray Source(s)*

Evidence that particle acceleration is taking place at astrophysical sites such as SNRs is provided by electron synchrotron and gamma-ray emission measurements (Koyama et al., 1995, Aharonian et al., 2004). Cosmic ray transport through the galaxy is a diffusion process during which the hadronic component may traverse large distances during their lifetime. High energy electrons, however, suffer radiative energy loses that limit their lifetime and, consequently, the distance they can diffuse away from their source. The highest energy electrons that we see at Earth likely originate in sources younger that 10^5 years and less than 1 kpc from the Solar System. Since there are only a handful of candidate SNRs which meet these requirements, the electron energy spectrum around 1 TeV could show structure and allow these energetic particles to be associated with a specific source. Figure 4 shows the calculated electron spectra

compared to a compilation of previous electron measurements (Kobayashi et al., 2004). The possible contributions of Vela, Monogem and the Cygnus Loop are shown as examples. Adding these three sources to the "distant component" gives the top most curve with the anticipated CALET measurements superposed.

3.2. *Dark Matter Signatures*

Electrons and positrons are products of the annihilation of many exotic particles speculated as dark matter candidates and could appear as excesses in the cosmic ray electron (negatron + positron) spectrum over the energy range of 200 GeV to 1000 GeV. Experimental and theoretical work has essentially eliminated all known particles as dark matter candidates leaving only a few exotic species as possibilities. Such candidates include weakly interacting particles from supersymetric theories, such as neutralinos, which can annihilate and produce both gamma rays and electrons as a signature. Another candidate, suggested by Cheng, Feng and Matchev (2002), are particles resulting from theories involving compactified extra dimensions – the so-called Kaluza-Klein (KK) particles. Like neutralinos, KK particles can annihilate and produce electrons. Unlike neutralinos, however, direct annihilation of KK particles to e, μ, and τ is not suppressed and, consequently, the KK "signal" is enhanced relative to that from neutralinos. Figure 5 shows just the predicted positron signal for possible KK particle masses (dark shaded regions) with the estimated background flux (light shaded region) of secondary particles. Significant is the sharp cutoff at the KK mass, which could produce a detectable "feature" in the electron energy spectrum.

References

1. Aharonian, F.A. et al., *Nature*, **432**, 75 (2004)
2. Chang, J. et al., *Proc. 29th Intl Cosmic Ray Conf (Pune)*, **3**, 273 (2005)
3. Cheng, H.C., Feng, J.L., and Matchev, K. T., *Phys. Rev. Lett.*, **89**, 211301 (2002)
4. Katayose, Y. et al., *Proc. 28th Intl Cosmic Ray Conf (Tsukuba)*, **4**, 2197 (2003)
5. Katayose, Y. et al., *Proc. 29th Intl Cosmic Ray Conf (Pune)*, **3**, 325 (2005)
6. Kobayashi, T. et al., J., *Ap. J.*, **601**, 340 (2004)
7. Koyama, K. et al., Nature, **378**, L255 (1995)
8. Torii, S. et al., Nuclear Physics (Proc. Suppl.), **134**, 23 (2004)

This page intentionally left blank

Tracking Devices

Organizer: D. Abbaneo

This page intentionally left blank

SPATIAL RESOLUTION STUDIES OF MICRO PATTERN GAS DETECTORS USING THE CHARGE DISPERSION SIGNAL

A. BELLERIVE

Ottawa-Carleton Institute for Physics, Department of Physics, Carleton University, 1125 Colonel By Drive, Ottawa, K1S 5B6, Canada
E-mail: alain_bellerive@carleton.ca

The Time Projection Chamber (TPC) for the International Linear Collider will need to measure about 200 track points with a spatial resolution close to 100 μm. A Micro Pattern Gas Detector (MPGD) readout TPC could achieve the desired resolution with existing techniques using sub-millimeter pad width at the expense of a large increase in the detector cost and complexity. A new MPGD readout concept of charge dispersion developed in Canada has been recently applied to small prototypes MPGD-TPC. Using cosmic-ray tracks, it demonstrated the feasibility of achieving good resolution with pads similar in width to the ones used for the proportional wire TPC. The charge dispersion technique was used with GEM and micromegas and results on resolution studies are presented. The TPC resolution with GEM and micromegas readout are compared to the earlier results without charge dispersion. First results of performance with charge dispersion in a magnetic field of strength comparable to that for the ILC detector are presented. An unprecedented 50 μm resolution has been achieved, which is an important step toward demonstrating the feasibility of meeting the challenging ILC TPC goal.

Keywords: Gaseous Detectors; Position-Sensitive Detectors; Micro Pattern Gas Detectors; Gas Electron Multiplier; Micromegas; ILC.

1. Introduction

Large volume time projection chambers (TPC) have been used as high precision tracking detectors in many high energy physics experiments since the 1970's. A large volume TPC is also a prime track detector candidate for future experiments at the international linear collider (ILC). However for the ILC application, it will be important to improve the spatial resolution capability for the TPC. A promising possibility is the replacement of the traditional wire-pad readout by a micro pattern gas detector (MPGD) like the gas electron multiplier (GEM) or micromegas (μMegas). This would

eliminate one of the major systematic errors which results from the so called $\mathbf{E} \times \mathbf{B}$ effect that degrades the spatial resolution.

The readout of a TPC with MPGD has several advantages but also some drawbacks, both of which are related to the confinement of the signal charge to a quite small spatial region. The advantage is that the localization has the potential to improve the double track resolution. The disadvantage is that it may lead to difficulties with the determination of the signal position. With a standard pad size of $\sim$2 mm some signals may be confined to one or two pads only, making a centroid calculation less precise. A smaller pad width would lead to a better resolution but also to a large number of readout channels which is costly and difficult to manage for a large detector.

One possibility to improve the signal centroid determination and thus achieve good resolution with relatively wide pads is to use a MPGD with a resistive anode which disperses the charge after amplification and allows the signal to be reconstructed on several pads. The principle of charge dispersion has been proven previously[1] for a point X-ray source. Details of the concept can be found there. In this paper, results of track resolution measurements with charge dispersion for cosmic-ray particles are presented. The spatial resolution is measured as a function of the drift distance. First results in a strong magnetic field are summarized.

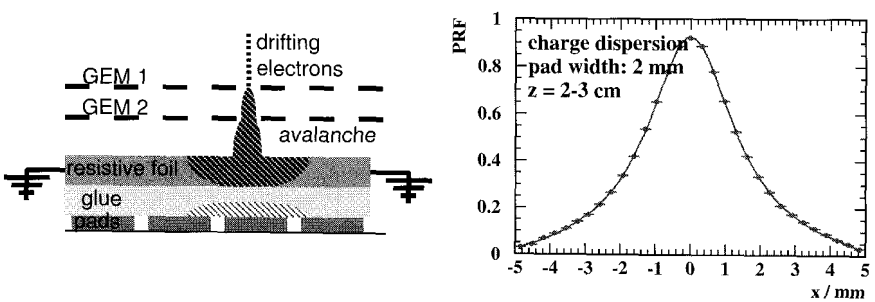

Fig. 1. Principle of charge dispersion with a resistive foil laminated on top of the readout pads (left). Pad response function for $z = 2 - 3$ cm from charge dispersion on a 2 mm wide pad (right).

2. Concept of charge dispersion

As depicted in Fig. 1 (left) a resistive foil is glued on top of the readout PCB. With the insulating glue as spacer this forms a 2-D resistive-capacitive network with a characteristic RC time constant. The resistive anode structure

is fabricated by laminating a 25 μm thick film of carbon loaded Kapton with an effective surface resistivity of about 530 K$\Omega/\Box$ to the readout pad PCB using a double sided insulating adhesive. The adhesive provides a 50 μm gap between the resistive anode and the PCB. Taking the dielectric constant of the glue into account, the gap results in a capacitance density of C $\simeq$ 0.22 pF/mm^2. After the amplification from the GEM or the μMegas the avalanche charge arriving at the foil surface disperses with the system RC time constant.

While for a charge distribution arising from gas diffusion a Gaussian profile can be assumed, the pad response function (PRF) in the case of dispersion on a resistive foil is not a priori known. Figure 1 (right) shows the pad response function as determined from the data. The shape can be described with a generalized Lorentzian with parameters that depends on the drift distance z. In theory, a first principle determination of the track pad response function is possible.[2] For the present, the PRF is determined empirically from the internal consistency of cosmic-ray track data.

The time evolution of the dispersion leads to significant differences in the pulse shapes depending on the distance between the pad and the position of the charge deposited. Figure 2 (left) shows the raw charged observed as a function of the distance on a rectangular pad for specific timestamps t = 10, 50, 100, 250 and 1000 ns. Figure 2 (right) shows the pulse shapes observed on the same rectangular pads located at the position of charge deposition. The amplitude of the primary signal falls much faster and the secondary signal reaches its maximum about 250–300 ns later. Potentially these characteristics can provide information about the position. However, for the current analysis only the amplitude, reconstructed as the maximum of the pulse, is used.

3. Experimental setup

We detect cosmic rays passing through a small volume TPC which has a 15 cm long drift region. The ionization signals are amplified by the GEM or μMegas readout. When the chamber is not being operated in a magnetic field, a low diffusion Ar:CO_2(90:10) gas mixture is used to mimic the small transverse diffusion properties encountered when a TPC is used in a solenoid magnet. In a strong magnetic field, an argon with CF_4 and isobutane Ar:CF_4:Iso(95:3:2) mixture is preferred. The layout of the readout pad system contains inner rows (pad size: 2 mm $\times$ 6 mm), together with two large area outer pads whose signals are used for selecting cosmic events for analysis. Charge signals on the pads are read out using Aleph

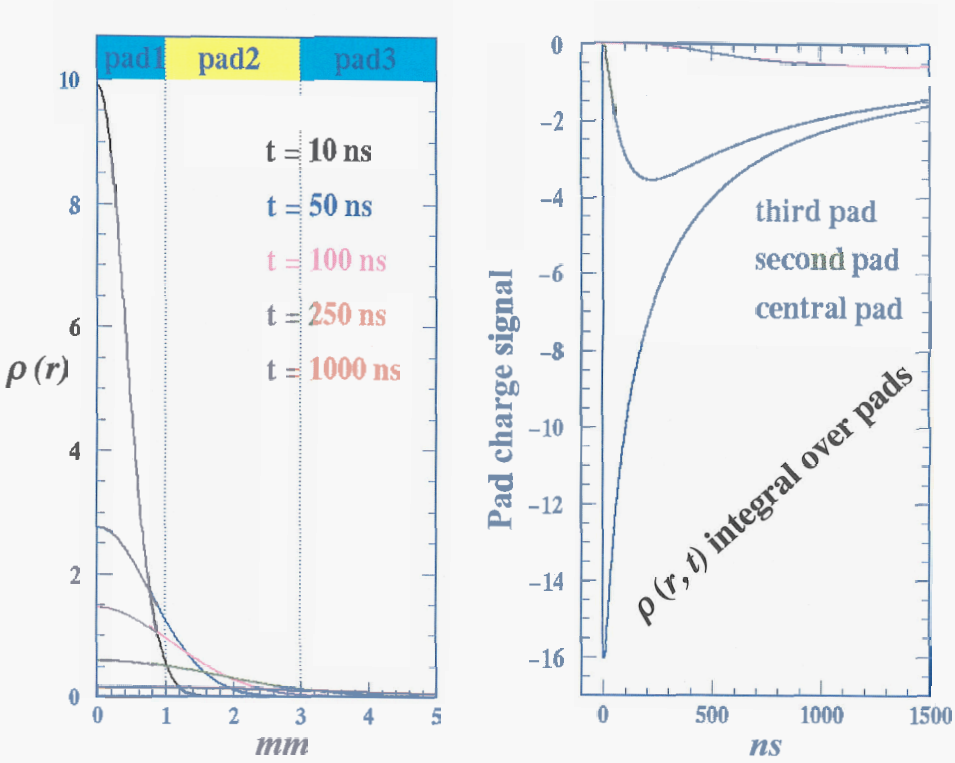

Fig. 2. **The raw space charge $\rho(r)$ at different timestamps for 2 mm** wide pads (left). Pulse signals $Q(t) = \int \rho(r,t)dr$ for the central, second and third pads.

wire TPC preamplifiers and digitized directly using 200 MHz custom built 8 bit FADCs.

4. Experimental Results

Details of the data analysis method are described in selected publications. Here the results of data collected with cosmic-rays are summarized.

A priori the small 15 cm Carleton-TPC prototype took cosmic data with Ar:CO_2(90:10) and was not operated in a magnetic field. First the chamber was instrumented with a GEM that did not used the charge dispersion technique.[3] This was an important step in demonstrating the spatial reso-

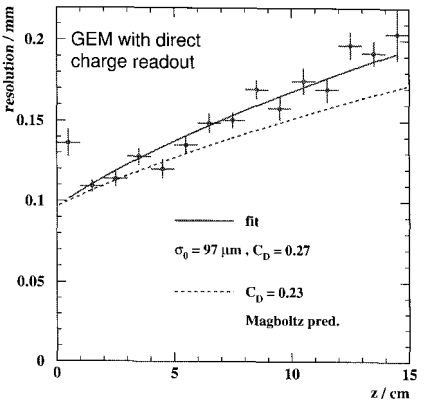

Fig. 3. Cosmic data taken without magnetic field and with Ar:CO_2(90:10). For standard GEM with direct charge collection: measured resolution as a function of drift distance with a fit to the data compared to the Magboltz prediction assuming the same σ_0.

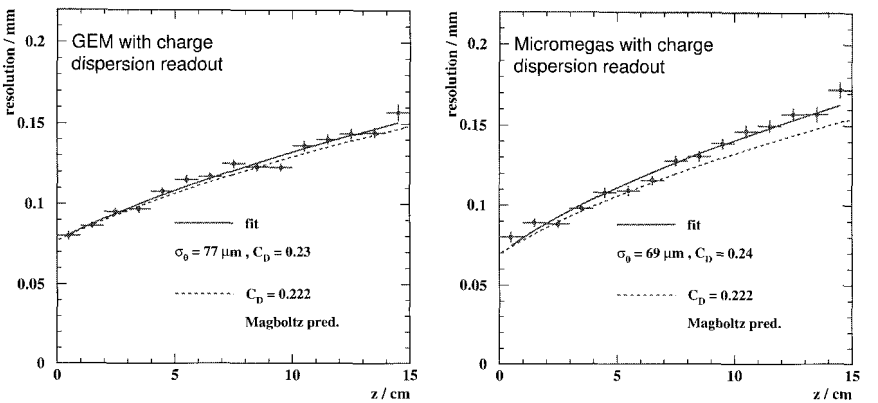

Fig. 4. Cosmic data taken without magnetic field and with Ar:CO_2(90:10). For GEM (left) and μMegas (right) with charge dispersion signal: measured resolution as a function of drift distance with a fit to the data compared to the Magboltz prediction assuming the same σ_0.

lution with a standard MPGD. Then, GEM[4] and μMegas[5] readouts were instrumented with a resistive foil. In each case, the spatial resolution as a function of drift distance was extracted and fitted to the function

$$\sigma = \sqrt{\sigma_0^2 + \frac{C_D^2\, z}{N_{\text{eff}}}}\,, \tag{1}$$

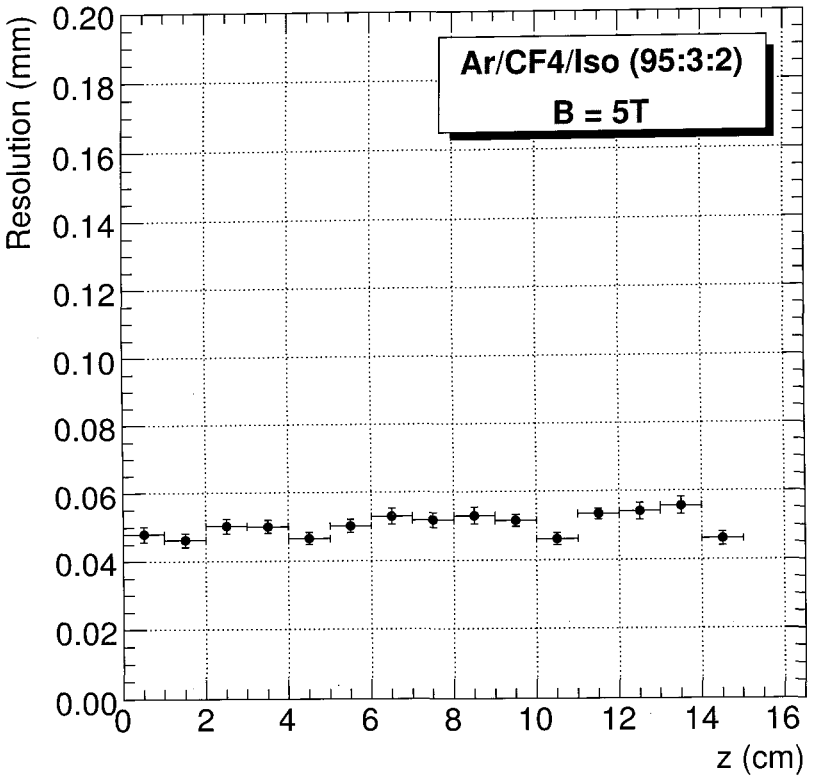

Fig. 5. Cosmic data taken with a strong magnetic field of 5 Tesla and with Ar:CF_4:Iso(95:3:2). Measured resolution as a function of drift distance for a μMegas readout instrumented with a resistive anode.

where σ_0 is the resolution at $z = 0$, C_D is the diffusion constant and N_{eff} is the effective number of electrons along the track on a pad row.

Figure 3 shows the results with the standard GEM that used direct charge readout; while the results with the charge dispersion technique on GEM and μMegas are shown in Fig. 4. In each case the transverse diffusion constant C_D given by the Magboltz simulation package are listed. The comparison of the results with and without a resistive foil shows that charge dispersion improves the TPC resolution over that from direct charge reconstruction. When the data obtained is compared to the prediction of propagation from Magboltz, it confirms that the charge dispersion is reach-

ing the limit set by transverse diffusion in the gas.

Finally, cosmic-ray data were taking in a 5 Tesla magnetic field at DESY.[6] Results of the measured spatial resolution as a function of drift distance for a μMegas readout instrumented with a resistive foil are shown in Fig. 5.

5. Conclusion

Using the charge dispersion signal, the spatial resolution obtained with a GEM-TPC are very comparable with the one using a μMegas-TPC, and clearly better than the conventional direct charge readout for 2 mm wide pads. With no magnetic field, the measured dependence of resolution on drift distance reaches the behavior expected from transverse diffusion in the gas.

Cosmic data were then taken with μMegas in a strong magnetic field. The new readout concept of charge dispersion achieved an unprecedented 50 μm resolution, which is an important step toward demonstrating the feasibility of meeting the challenging 100 μm ILC TPC resolution goal over large drift distances.

Three out of the four present ILC detector concepts include a large volume TPC for tracking. The Linear Collider TPC (LC-TPC) collaboration has been formed recently with first task to construct and test a large 1 meter prototype TPC by 2010. The goal will be to establish the system performance in a magnetic field of strength comparable to the ILC TPC. The LC-TPC collaborators have the plan to design and construct charge dispersion readout panels for the 1 meter TPC.

References

1. M.S. Dixit, J. Dubeau, J.P. Martin and K. Sachs, NIM **A**518, 689, 2004.
2. M.S. Dixit and A. Rankin, NIM **A**566, 281 (2006).
3. R.K. Carnegie, M. S. Dixit, J. Dubeau, D. Karlen, J. P. Martin, H. Mes and K. Sachs, NIM **A**538, 372, 2005.
4. K. Boudjemline, M. S. Dixit, J.P. Martin and K. Sachs NIM **A**574, 22, 2007.
5. A. Bellerive, K. Bouldjemine, R.K. Carnegie, M.S. Dixit, J.P. Martin, J. Miyamoto and K. Sachs, Physics 0510086, International Linear Collider Workshop, Stanford, USA, 2005. To be submitted to NIM.
6. M. Dixit, D. Attié, A. Bellerive, K. Boudjemline, P. Colas, A. Giganon, I. Giomataris, V. Lepeltier, S. Liu, J.-P. Martin, K. Sachs, Y. Shin and S. Turnbull, arXiv:physics/0703263v1, NIM **A** (in press).

THE LHCB MUON SISTEM

SIMONE BRUSA, ON BEHALF OF THE LHCB COLLABORATION
Università degli studi di Ferrara, Via Saragat 1, Ferrara, 44100, Italy

In this paper is described the LHCb muon detector, which plays a fundamental role in the Level-0 (L0) trigger and muon identification for the high-level trigger (HLT) and offline analysis. After a short review of the detector structure and of the required performances, we will describe, with some detail, the construction procedures and the relative quality control tests of the single chambers. The results of the quality control tests performed in the production centers , and the tests with fully equipped chambers performed at CERN before the installation on the experiment site, will also be reported.

1. Introduction

LHCb is an experiment dedicated to precision studies of CP-violation and rare decays in the $b\bar{b}$ sector.

The LHCb muon system [1,2,3] is made of five Stations (M1-M5) of rectangular shape, covering an acceptance of 300 rnrad (bending plane) and 200 rnrad (non bending plane). Its main task is to provide fast L0 triggering and offline muon identification.

The first station, M1, is placed in front of the calorimeter. M2-M5 follow it, and are separated by iron filters. The stations cover a total area of about 435 m^2. Each station is divided into four regions (R1-R4), with increasing distance from the beam axis and with approximately the same particle acceptance. The detector readout provide a space point measurements (x,y) of the tracks. Its granularity is higher in the bending plane, and gives an accuracy $\delta P_t/P_t \sim 20\%$.

Since the trigger scheme uses a five-fold coincidence among all the stations, the efficiency of each station must be enough to obtain a trigger efficiency of at least 95 %, within a time window smaller than 25 ns in order to unambiguously identify the bunch crossing. This is ensured by the use of a fast gas mixture (40:55:5 MWPC, 40:15:40 GEM of $Ar/CO_2/CF_4$) and of an optimized charge collection geometry both for the MWPC and GEM detectors. Given the large active area to be covered, the detector should be relatively cheap and modular but, at the same time, robust, in order to guarantee stable working conditions for 10 years in high radiation environment.

2. Detector Description

The muon detector is built with 1368 4(2 in M1)-gap MWPCs and 12 triple GEM detectors (each of them consists of two triple GEM OR-ed).

In the MWPCs a wire-cathode distance of 2.5 mm ensures a fast charge collection (about 10 ns) while a wire spacing of 2 mm has been chosen to have a time resolution of 5 ns (or less) and a good mechanical stability [4]

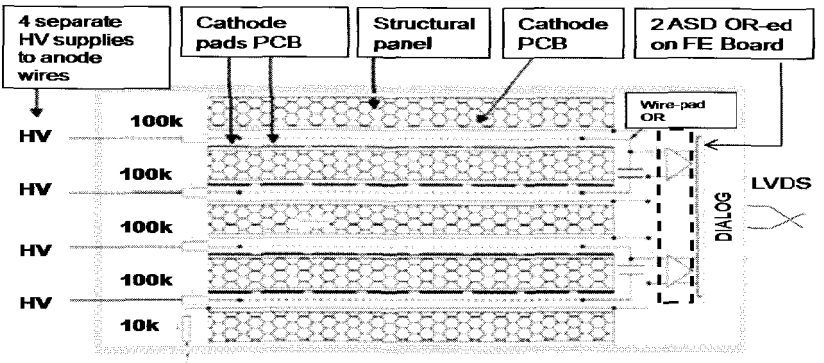

Figure 1. Schematic side view of a 4-gap MWPC of the LHCb muon detector, wire readout. Two contiguous gaps are hard-wired together in OR to form a Double Gap layer. The readout electrodes of this Double Gap (either wires or cathode pads) are connected to separate FE channels and then OR-ed by the FE electronics.

A chamber, Figure 1, is made of four identical gas gap (two in M1, to reduce the material budget on front the calorimeters) superimposed and rigidly stacked together, each constituting an elementary detector. The structural elements of the chamber are the panels, each formed of an insulating core sandwiched between two conducting planes. The panels are stacked with two frames of 2.5 mm which support the wires while the 5 mm gas gap is ensured by several precise spacers placed on the panels. The front-end boards, the LV voltage regulators and the HV filters are mounted inside the Faraday cage to minimize electrical pickup. The general design and construction is the same for all chambers and is discussed in detail in [5].

The triple-GEM detector consists of three gas electron multiplier (GEM) [6] foils sandwiched between anode and cathode planes. The detector were built piling up and gluing together, on a reference plane machined to high precision, the single detector parts in the following order: cathode panel, the first GEM foil (GEM1) glued on a 3 mm thick fiberglass frame, the second GEM foil (GEM2) glued on a 1 mm thick frame, the third GEM foil (GEM3) glued on a 2 mm thick

frame and then the last 1 mm thick frame that, followed by the pad panel, that closes the induction gap.

To satisfy the requirements on spatial resolution and rate capability, on the MWPC we have three different readout methods (anode wire, cathode pads, mixed), with pad sizes from (1 x 2.5) cm^2 to (25 x 30) cm^2.

The use of multiple gaps with independent HV supplies, provides a high degree of redundancy, and in addition an improved time resolution.

3. The Front End Electronics

The large number of channels (~126k) in the Muon System, the need to synchronize all the channels in a 20 ns window, the high radiation expected led us to develop dedicated rad-hard ASICs using IBM 0.25 micron technology.

The chamber readout is performed via the CARIOCA chip [7], which is an amplifier–shaper–discriminator frontend chip. In order to achieve a good time resolution at a reasonably low gas gain, the amplifier has a short peaking time (t_p < 15ns) and low noise (< 2fC) for detector capacitances between 20 and 220 pF. Since we expect a rate per channel of up to 1MHz and we want to minimize the inefficiency due to signal pile-up, a tail cancellation circuit is implemented.

The DIALOG chip receives the outputs from two CARIOCA chips, and performs the logical OR of the corresponding two layers of a chamber, forming the so called logical channels. The DIALOG is equipped with adjustable delays on every input, to allow the time matching of the various input signals. In addition, the DIALOG also allows the CARIOCA thresholds setting and the masking of its input.

A special version of the CARIOCA chip, CARIOCAGEM, has been produced for use on the GEMs, with lower threshold and without tail cancellation circuit.

4. Detector Quality Control and Testing

In order to have a uniform quality of the detectors produced in the various sites, stringent quality tests of the individual chamber components and of the assembled chamber have been carried out.

All the panels were individually measured at production and then before assembly. Despite the tight tolerances the yield of good panels was 90 %. At the production sites two automated tables were used to measure the wire pitch [8,9], and the wire mechanical tension [10, 11]. In Figures 2,3 are shown, respectively, the distributions of the pitch and of the wire tension , measured on about 250 chambers.

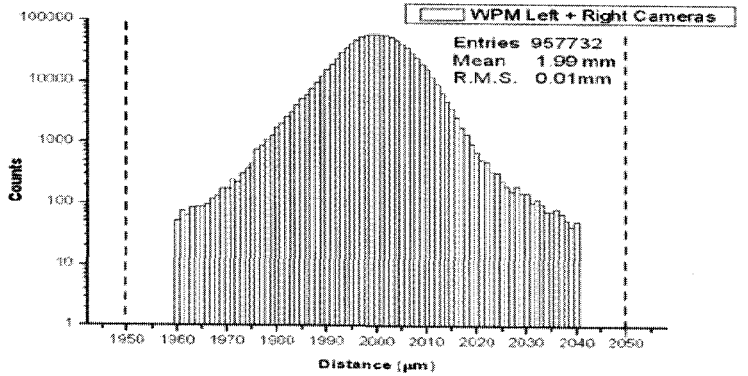

Figure 2. Distribution of wire pitch measured with a system based on two digital cameras .The average value is 1.99 mm with an r.m.s. of 0.01 mm. The two dashed lines defines the interval which must comprise 95 % (100 % in ±100 μm) of all the wires.

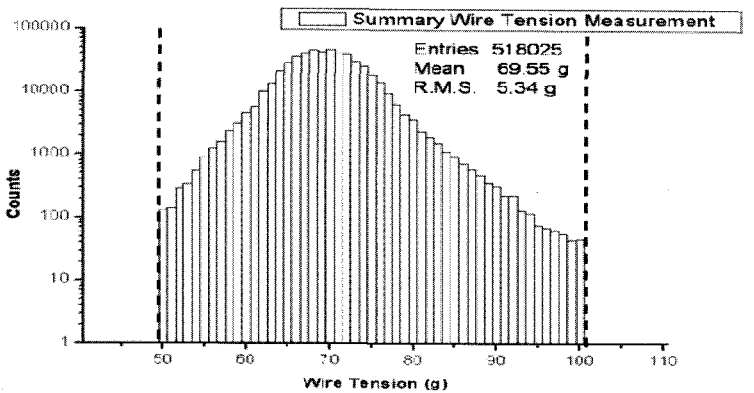

Figure 3. Distribution of wire mechanical tensions obtained from a measure of the wire mechanical resonant frequency. The mean value of the tension is 69.55 g with an r.m.s. of 5.34 g.

The checks on the assembled chambers consisted in a gas leak test and a HV test at 2800 V using the standard gas mixture. The uniformity of the gas gain in the gaps was systematically checked using radioactive sources mounted on automated tables which performed an (x,y) scan over the complete chamber surface (Figure 4).

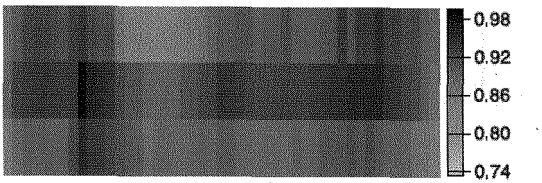

Figure 4. Gain uniformity measurements for a single gap of an M5R4 chamber, performed with a movable radioactive source.

Chambers with local gain deviations of at least one Double Gap exceeding a factor $(1.7)^{\pm 1}$ with respect to the average were rejected. All the above checks were performed without the readout electronics installed.

Finally all chambers, fully equipped with the front-end electronics, underwent a final test with cosmic rays prior to installation. The electronics noise was again checked after the chambers were mounted on the detector. A database allows us to retrieve at anytime the results of all quality control and chamber data.

Several quality checks were performed also on Triple-GEMs before the chamber assembly, on different detector components. Since the cathode and anode panels are the main mechanical structure of the detector, they were checked for planarity. Also the GEM foils were checked via optical inspection with a microscope. If the GEM foil passed the visual inspection, a high voltage test was performed.

After the chamber construction, the detector gas leakage was measured. In order to check the uniformity response two kinds of tests were carried out. The first test was performed on a single chamber, while the second was executed on the two GEM detectors superimposed. The uniformity gas gain test checked both, the mechanical tolerance and the uniformity response of a single chamber. This test was performed with an X-ray gun. The current signal induced on each pad (192 pads per chamber), was corrected for the temperature and the pressure variations. The current deviations from the average were all below 20% in a detector surface scan, with a typical RMS < 10%.

Finally, a cosmic rays test was performed on all chambers fully equipped with the front-end electronics.

5. Detector Performances

Extensive tests have been performed on prototypes and final MWPCs both, on beam tests and with cosmic rays at the production sites, to measure the main

chamber parameters. Figure 5 shows the efficiency in a 20 ns window as a function of the applied voltage, for a chamber with anode readout (M5R4) and one chamber with cathode readout (M4R2). Figure 5 also shows that the design criteria concerning the required intrinsic cluster size (should be less than 1.2), are well satisfied [12].

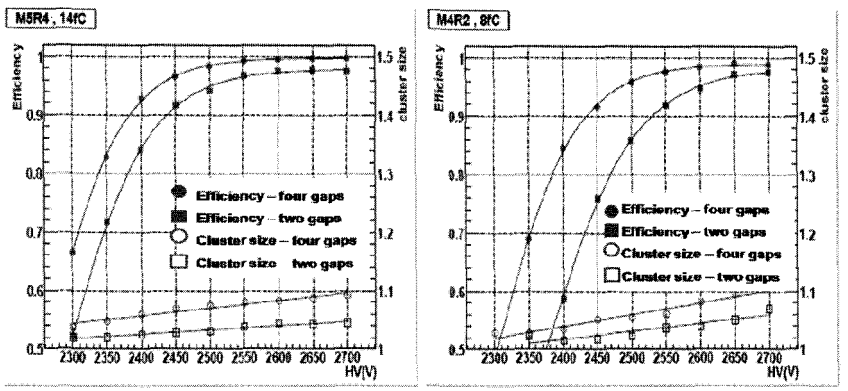

Figure 5. Efficiency and cluster size for the four-gap and double-gap configurations vs. HV. Anode readout-type chamber (left) and cathode readout-type chamber (right).

Cosmic rays have also been used to check the gas gain uniformity on final chambers [13]. Special tests have been performed also at the CERN Gamma Irradiation Facility (GIF) [14]. Up to a photon flux of 10 kHz/cm2 (70% of the M2R1 rate/cm) there was no visible space-charge effect on the chamber efficiency and time performance. An extensive aging test was performed on MWPC [15] and GEM [16] prototypes, showing no detector performances deterioration by the large dose expected in the experiment in several years of operation (10^8 s) at full luminosity.

Triple-GEM detectors with the final FE electronics (CARIOCAGEM) have been tested both in a dedicated 40 MHz test beam and with cosmics in the lab. Efficiency and cluster size of the chambers in a 20 ns window as a function of the gain, for each single triple-GEM detector and the logical OR, are shown in Figure 6. Thanks to the longer shaping time of the CARIOCAGEM with respect to the CARIOCA chip, the beginning of the efficiency plateau has moved from a detector gain of 6000 to 4000 with the choice of this electronics. This does not only decrease by 30% the integrated charge in the detectors, but it also allows the detectors to be operated in even safer conditions with respect to discharges.

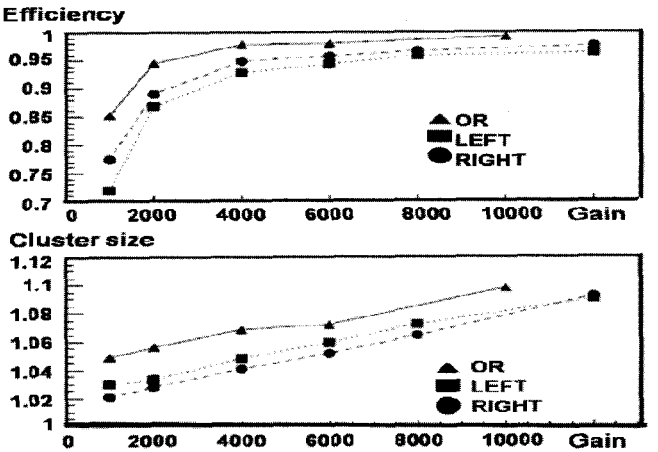

Figure 6. Efficiency and cluster size for a 3-GEM chamber as a function of the gain.

References

1. LHCb Collaboration, "LHCB Muon System Technical Design Report", CERN-LHCC-2001-010, (2001).
2. LHCb Collaboration, "LHCb Addendum to the Muon System Technical Design Report", CERN-LHCC-2003-002, (2003).
3. LHCb Collaboration, "LHCb Second Addendum to the Muon System Technical Design Report", CERN-LHCC-2005-012, (2005).
4. W. Riegler, Note LHCb-Muon 2000-060, (2000).
5. A. Kachtchouk et al., Note LHCb-MUON 2001-026, (2001).
6. F. Sauli, *Nucl. Instr. and Meth. in Phys. Res.* **A386** (1997) 531.
7. W. Bonivento et al, Development of the CARIOCA front-end chip for the LHCb muon detector, *Nucl. Instr. and Meth* **A491** (2002) 233-243.
8. M. Anelli et al., IEEE *Trans. Nucl. Sci.* **53** (2006) 330.
9. A. Franconieri, PhD Theses (2007), Università degli Studi di Ferrara; "Quality assurance and Quality control on the MWPCs for the LHCb Experiment".
10. P. Ciambrone et al, Nucl. *Instr. and Meth. in Phys. Res.* **A545** (2005) 156.
11. W. Baldini et al., "Wire Tension Measurement System with Laser Readout Technique", Note LHCb-MUON 2007-120, (2007).
12. G. Sabatino et al., Note LHCb-Muon 2006-011, (2006).
13. S. de Capua et al., Note LHCb-Muon 2006-010, (2006).
14. M. Anelli et al., Note LHCb-Muon 2005-003, (2005).
15. M. Anelli et al., "Extensive aging test of two prototypes of four-gap MWPC for the LHCb Muon System", Note LHCb-Mon 2004-029, (2004).
16. M. Alfonsi et al., IEEE *Trans. Nucl. Sci.* **52** (2005) 2872.

DESIGN AND CHARACTERIZATION OF A MONOLITHIC ACTIVE PIXEL SENSOR IN 0.25 μm TECHNOLOGY

A. BULGHERONI*

Physics Department, University of Rome 3, and I.N.F.N. Sect. of Rome 3 Rome, Italy
**E-mail: antonio.bulgheroni@roma3.infn.it*

E. SPIRITI, J. MLYNARCZYK

I.N.F.N. Sect. of Rome 3, Rome, Italy

Since few years Monolithic Active Pixel Sensors (MAPS) are actively developed all around the word and are becoming a valuable alternative to hybrid pixel sensors in high energy physics applications. Those sensors, designed using the standard technology for consumer electronics (CMOS), are integrating on the same substrate both the sensitive layer and the readout electronics; this is allowing very high granularity and excellent spatial resolution, limited material budget and easiness of integration. This paper is about the MimoRoma1 chip designed, produced and commissioned in 0.25 μm CMOS technology by the authors. The chip was submitted as a multiproject run to TSMC through the MOSIS consortium. The sensor design was meant to investigate which performance can be achieved in this scaled technology featuring a very narrow sensitive volume (the epitaxial layer) compared to other traditional hybrid detectors and to test the radiation hardening via enclosed transistors. The results of the chip characterization with radioactive sources are presented.

Keywords: Vertex detectors; MAPS; Silicon

1. Introduction

Future High Energy Physics (HEP) experiments at the next International Linear Collider (ILC) will be characterized by a highly demanding physics program, focused on an extremely precise calorimetry and on an accurate heavy quark flavour tagging. While the former is realized by a sampling calorimeter featuring an important lateral and longitudinal segmentation, the latter is achieved by a billion channel, ultralight and compact vertex detector; this is featuring an unprecedented spatial resolution with a ma-

terial budget for each sensor plane below 0.1% χ_0.
The increased level of system complexity and the advantages arising from the development in the field of silicon technology are driving the detector physicists toward a monolithic approach in which both the sensitive part and the front end electronics are integrated on the same silicon substrate, therefore avoiding critical and expensive hybridization procedure and allowing pixel sizes as small as 20 μm by 20 μm.
One possible monolithic implementation called Monolithic Active Pixel Sensor (MAPS) based on the standard CMOS technology and resembling the one adopted by visible light CMOS imager is offering several advantages with respect to other technologies. Due to the limited space for this paper, the reader is invited to refer to Refs. 1 and 2 for a detailed description of the sensor working principle and a comparison with other monolithic technologies.
This paper is about a MAPS prototype called *MimoRoma1* designed and characterized by the authors in the INFN laboratory in Rome 3. The chip design along with the sub–matrices characteristics is outlined in section 2, while the results obtained exposing the sensor to ionizing radiation and X-rays are reported in section 3.

2. MimoRoma1 design

The MimoRoma1 chip has been designed using the 0.25 μm TSMC[a] technology by a team of electronic designers in the last years and submitted for production through the MOSIS[b] consortium as a multiproject run.
Among others, the main objectives of the design were the following:

(1) Explore the technology properties in terms of the most important figures of merit such as the Charge to Voltage conversion Factor (CVF) and the Charge Collection Efficiency (CCE).
(2) Improve the charge collection efficiency reducing the charge spreading among neighbouring pixels.
(3) Study the radiation hardening via the design of enclosed transistors and compare their performance against the standard linear design.

To reach all these targets, the overall area of 4×3.2 mm^2 of the chip has been divided into five sub–arrays implementing different front end archi-

[a]This is the acronym of Taiwan Semiconductor Manufacturing Company (`http://www.tsmc.com`)
[b]`http://www.mosis.com/`

tectures, pixel pitches and collecting diode sizes. A summary of the main properties of the five sub–matrices are given in Table 1.

Table 1. Main properties of the five sub–matrices implemented into the MimoRoma1 chip.

Sub–matrix name	Size (pixel × pixel)	Pixel pitch (μm × μm)	Diode size (μm × μm)	Architecture[a]
4DIO	32 × 32	34 × 34	2 × 2 [b]	**3T, 4D, ENC**
5x5	32 × 32	34 × 34	5 × 5	**3T, 1D, ENC**
SB	64 × 64	17 × 17	5 × 5	**SB, 1D, ENC**
Mixed0	64 × 32	17 × 17	1.2 × 1.2	**3T, 1D, STD**
Mixed1	64 × 32	17 × 17	1.2 × 1.2	**3T, 1D, ENC**

Note: [a] Possible values are: **3T** meaning standard three transistor cell, **SB** meaning self biased, **ENC** enclosed transistor design, **STD** standard linear transistor, **1D** meaning one collecting diode instead of **4D** with four diodes.
[b] This surface must be multiplied by the number of collecting elements.

The **Mixed** matrices were especially design to compare the different behavior of enclosed and linear transistor geometry, in fact **Mixed0** and **Mixed1** are the two halves of one sub–matrix with one single output stage and the only difference is the transistors implementation. This was a strong point of the design, because the enclosed design reveals itself to be inadequate introducing too much parasitic capacitance and increasing the noise level; this problem was clearly spotted through the use of the mixed matrix.

3. Sensor characterization

As soon as the sensor prototypes were back from the foundry, a characterization system composed by an interface board steering the pixel addressing and generating the readout sequence, and a commercial VME ADC board was commissioned. The standard characterization procedure is made by the following steps:

(1) **Noise evaluation** with different readout clock frequencies and reset pulse lengths (not for the self biased matrix).
(2) **System check-up** illuminating the sensor surface with an α emitting isotope. The α particle interaction is producing a large signal on a rather big cluster of pixels. The right readout sequence is found when the cluster is properly reconstructed with a reasonably symmetric shape.

(3) **Sensor calibration** exposing the sensor to a strong ^{55}Fe source emitting soft X-rays as described in Ref. 3. From this measurement it is possible to measure all the most important figures of merit of the sensor as the charge to voltage conversion factor, the charge collection efficiency and the equivalent noise charge.
(4) **Sensitivity to charged particles** exposing the sensor to β emitting sources.

This procedure has been systematically repeated on all the sub-matrices and the results collected and compared.

3.1. *Detailed measurement results for the Mixed matrix*

Due to the limited space, in this paper only the results obtained with the two mixed matrices will be reported in details, while for the other arrays only a brief summary is given in Sec 3.2.
The main results of the characterization procedure on the Mixed0 matrix can be summarized in Figs. 1 and in Tab. 2.

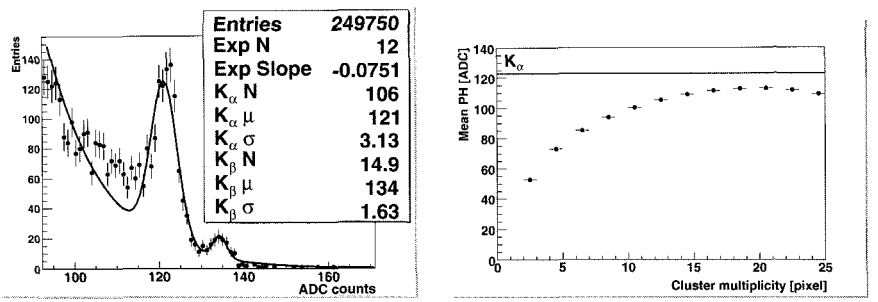

(a) *Seed pixel calibration peaks* (b) *Charge collection efficiency*

Fig. 1. *(a) The calibration peaks in the seed pixel spectrum corresponding to 100% CCE. Both the K_α and K_β lines of the emitting radioisotope are clearly visible and can be used to obtain the CVF of this architecture. (b) Integrating the charge collected by the pixels surrounding the seed pixel the average CCE can be estimated.*

All the relevant results have been found in agreement with the expected results from technological simulations. A charge collection efficiency in excess to 90% has been obtained summing the signal contribution of 18 pixels.
The difference in the response of standard and enclosed transistor layout becomes clear comparing the seed pixel spectra obtained during the same long lasting calibration run (Fig. 2). The main differences in the two spectra

Table 2. Mixed0 and Mixed1 calibration summary.

	Calibration constant (e^-/ADC)	DAQ conversion (ADC/mV)	CVF (mV/e^-)	Reciprocal CVF (e^-/mV)	ENC e^- r.m.s.
Mixed0	13.43	2.05	0.036	27.53	23.21
Mixed1	37.27	2.05	0.013	76.41	61.20

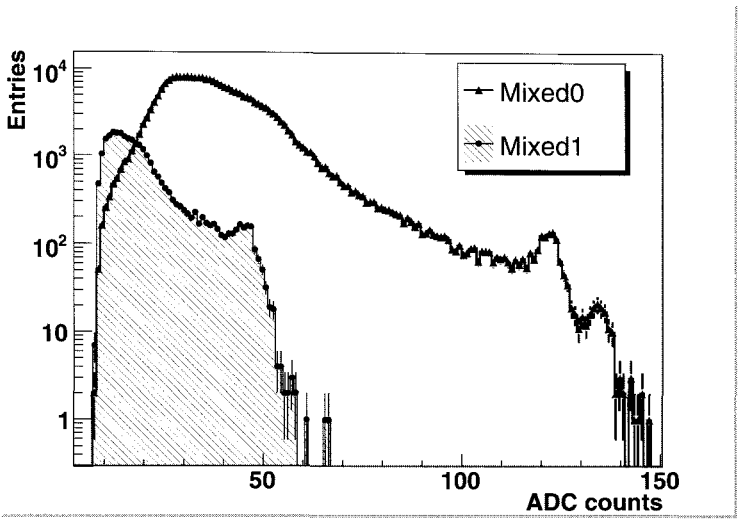

Fig. 2. *Seed pixel spectrum comparison for standard and enclosed transistor layout.*

are: (1) the lower position of the calibration peak of Mixed1 and (2) the lower number of entries in the incomplete collection peak. The two spectra are normalized by definition because the two matrices were exposed to the same flux of photons and this is also clear looking at the number of entries below the calibration peaks. The different CVF is caused by the parasitic contribution of in the input capacitance of the enclosed layout while the lesser number of detected photons is due to the higher ENC for Mixed1. In fact, both matrices have the same voltage noise level at the ADC inputs, but Mixed1 having roughly three time lower CVF results into a three time larger ENC value, thus making the SNR selection criterion stronger for Mixed1.

3.2. *Brief summary of the other sub-matrices results*

Unfortunately, the use of the enclosed layout for transistor implementation in all the other matrices is making the evaluation of their properties very difficult and not conclusive. For instance, since the calibration peak was not visible on both the **4DIO** and the $\mathbf{5 \times 5}$ matrices, it is not possible to say whether it is better to increase the diode size or to increase the number of collecting elements.
It was also impossible to test the self biased structure because of the too low polarization diode resistance making the baseline restoring too fast.

4. Conclusion

A MAPS prototype called MimoRoma1 was designed in 0.25 μm TSMC technology, produced in a multiproject run, commissioned and tested according to a well defined characterization procedure. The main goals of this prototype were the study of the technology properties, in particular the comparison of enclosed rad-tol and standard linear rad-soft transistor layout and the different techniques to improve the CCE.
Only the sub-array designed with standard rad-soft transistors is behaving as expected while the enclosed layout is suffering from a high parasitic capacitive load making the overall performance inadequate as a pixel detector.

5. Acknowledgment

The authors would like to thank Marco Belfiori and Fabio Bartolucci for their contribution in the chip design.

References

1. E. R. Fossum, *IEEE Transactions on Electronics Devices* **44 (10)**, p. 1689 (1997).
2. R. Turchetta, J. D. Brest, B. Casadei, G. Claus, C. Colledani, W. Dulinski, Y. Hu, D. Husson, J. P. Le Normand, J. L. Riester, G. Deptuch, U. Goerlach, S. Higueret and M. Winter, *Nucl. Instrum. Meth. A* **458**, 677 (2001).
3. W. Dulinski, A. Braem, M. Caccia, G. Claus, G. Deptuch, D. Grandjean, C. Joram, J. Séguinot and M. Winter, *Nucl. Instrum. Meth. A* **546**, 274 (2005).

The CMS Silicon Strip Tracker: from integration to start-up

V. Ciulli*

Università and INFN Firenze,
via G. Sansone 1, Sesto F. (FI), 50019, Italy
**E-mail: vitaliano.ciulli@fi.infn.it*

The CMS Silicon Strip Tracker (SST) integration has been completed. After an extensive period of testing with cosmic muons the detector is ready for the final installation inside the CMS magnet. This paper will review the integration procedures and the tests completed to ensure that SST performs according to specifications.

Keywords: CMS, Tracker, Silicon, Microstrip, Integration, Commissioning

1. Introduction

The CMS tracker is the largest silicon microstrip detector ever designed. Consisting of three main sub-assemblies, Tracker Inner Barrel and Disks (TIB/TID), Tracker Outer Barrel (TOB) and Tracker End Caps (TEC), it is 5.5 m long and is 2.4 m in diameter (Fig. 1). The total detector surface is an unprecedented 200 m^2 with more than 15000 detector modules such as that shown in Fig. 2.

The CMS solenoid provides a homogeneous magnetic field of 4 Tesla over the full volume of the tracker. The tracker is operated at or slightly below $-10°C$. At the LHC design luminosity of 10^{34} cm^{-2} s^{-1} there will be on average about 1000 particles from more than 20 overlapping proton proton interactions traversing the acceptance of the tracker for each bunch crossing, i.e. every 25 ns. A detailed description of the SST is given in Refs. 1 and 2.

2. Integration procedures

Even though the SST is an all-silicon device with the same front-end electronics (FEE) and same type of auxiliary chips, it is essentially three independent sub-detectors put together as a single assembly. The mechanical

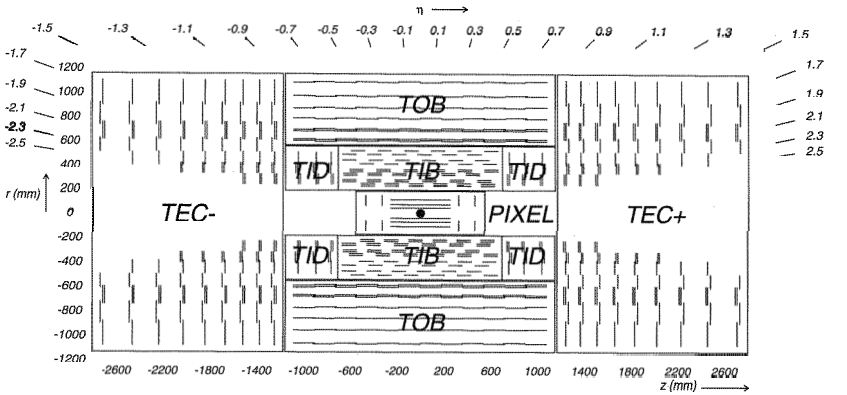

Fig. 1. **Schematic cross section of the CMS tracker. Each line represents a** detector module. Double lines indicate back-to-back modules which deliver stereo hits.

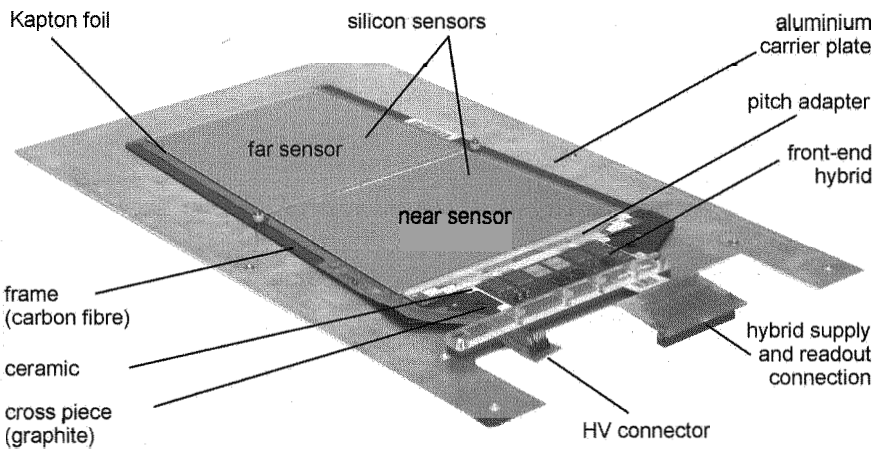

Fig. 2. Picture of a TEC module. The other three sub-assemblies use similar pieces for integration. The main difference with TIB modules is the use of two sensors instead of one (TIB modules are smaller). Roughly 15000 of these modules are integrated in the CMS SST.

support structures for all three sub-assemblies are made from carbon fibre. In the case of TOB and TEC the silicon detector modules are first integrated in rods (containing 12 modules) or petals (containing either 23 or 28 modules). These are later integrated in the actual TOB or TEC. Rods and petals are self contained units which have all the electrical and cool-

ing services for the silicon detector modules. A TOB rod with 12 modules is shown in Fig. 3. The TIB/TID on the other hand has no intermediate structure and modules are assembled directly on shells or disks (up to 150 modules at a time).

All three detectors followed a similar sequence of integration steps, the basic tenet of the integration paradigm being an in depth test at all levels so as not to rework integrated structures. Thus all the required pieces arrived at the integration facilities having already undergone extensive testing and burn-in procedures.

Counting everything, from tiny screws to inserts to cable holders to hybrids etc., the number of pieces needed was of the order of 10^5. The logistics governing the flow of these objects was a major undertaking in itself.

Once a rod or petal is fully equipped, tests are made on electrical connectivity, control signal response and finally noise characterization. For the TIB, since the number of modules in a shell is huge, the connectivity tests are made each time a single interconnect board is fully equipped while the noise characterization is made at the level of a full control ring. In general

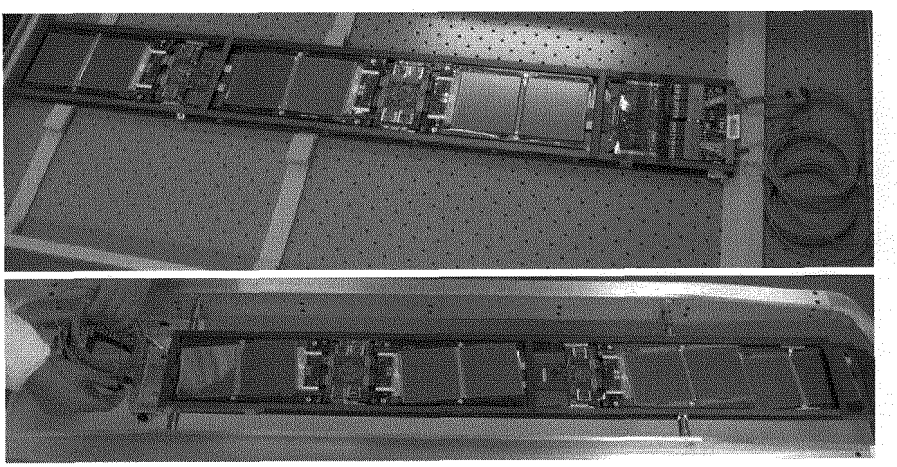

Fig. 3. A TOB rod completed with 12 modules. The top picture shows the $r\phi$ side where the strips are parallel to the beam axis. The bottom picture shows the stereo side, with strips rotated by 0.1 rad to measure the z coordinate along the beam axis.

the number of dead/noisy channels for all three sub-structures is at the per mil level, an amazing achievement which testifies to the care placed in

handling all components during the integration phase.

Rods and petals were also separately tested at cold temperatures. For TIB special procedures were made because of the size of the structure to be tested. A climate chamber of a large enough dimension was equipped with a chiller and sufficient electronics to service a TIB half-layer.

Once ready, TIB and TEC were shipped to CERN and integrated with TOB, assembled on site, in the Tracker Integration Facility (TIF). The complexity of the final integration of the three sub-detector is evident from the channel and service densities shown in Tab. 1.

Table 1. Channels density in the detector volume and service area for the different tracker subsystems. Density on service area is a relevant parameter only for TIB and TOB, due to their access through the barrel end-flanges. For TEC and TID, instead, services do not have access problems.

	# of channels	Volume [m^3]	Channel Density [$\times 10^6$ m^{-3}]	Service Area [m^2]	Ch. Density on Serv. Area [$\times 10^6$ m^{-2}]
TIB	1 787 904	0.82	2.2	1.6	1.11
TID	565 248	0.5	1.1		
TOB	3 096 576	5.9	0.52	5.7	0.54
TEC	3 866 624	11	0.35		

The tracker will be transported to the experimental area and inserted into CMS in November. Meanwhile, services deployement in the cavern is ongoing. A great care is applied to test each single cooling pipe, cable or fibers ribbon, since it would be difficult, if not impossible, to repair a faulty one after tracker insertion.

3. Tests with cosmic muons

A period of commissioning of the full CMS experiment with cosmic muons is foreseen between December 2007 and the LHC start-up next year. Several tests of this kind were already done in the past. Among them, two were particularly important for the quality and the amount of data they provided: the Magnet Test and Cosmic Challenge (MTCC) and the Slice Test at the TIF.

3.1. *Magnet Test and Cosmic Challenge*

In the summer of 2006, the CMS collaboration took advantage of the magnet commissioning tests and of the partial installation of some of the sub-

detectors in the above ground hall to do the MTCC. A fraction of all subdetectors (with the exception of the pixel systems) was operated with an up-to 4 T magnetic field delivered by the superconducting solenoid and read out with a downscaled, final design global data acquisition system (DAQ). Cosmic muon triggering was provided by the Level-1 trigger electronics of the muon detectors. The tracker front-end chip, the APV25,[3] was operated in "slow" read-out mode, because cosmic muons are not synchronous with 40 MHz read-out design. As shown in Fig. 4, the cluster signal in the TIB for different latency values was consistent with a CR-RC shape. The timing constant of 50 ns was in agreement with APV specifications.

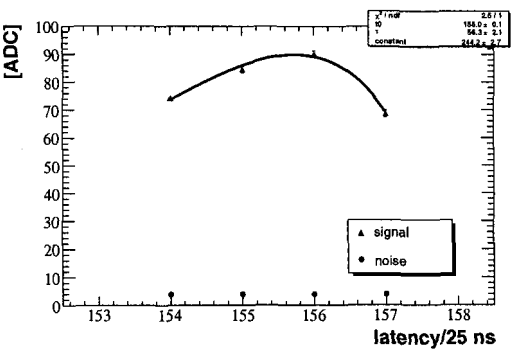

Fig. 4. Cluster charge and noise in TIB modules for different latency at MTCC. Sampling time is delayed as latency decrease.

Despite the fact that the MTCC tracker setup represented only about 1% of the final system, most of the selected hardware and software systems were prototypes of the final versions. The MTCC, therefore, offered the unique opportunity of testing the performance of the tracker in the presence of the 4 T magnetic field. No increase was observed in the strip noise because of the magnetic field or interference with other subdetectors. The Lorentz drift of the charge carriers in the silicon was measured using reconstructed tracks. The Fig. 5 shows the fit to the cluster width versus the track incident angle: the minima correspond to the drift direction of the charge carriers without and with magnet on. The results are in agreement with values expected for holes in silicon detectors.[4]

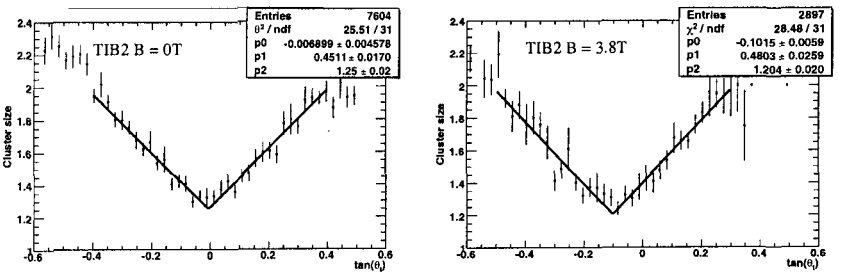

Fig. 5. *Cluster width vs track incident angle, without (left) and with (right) 3.8 T magnetic field.*

3.2. *Slice Test at TIF*

Once the integration was completed in the TIF, a slice of about 90° of the plus side was connected to power units, cooling and control and read-out electronics. Plastic scintillators were laid above and below the tracker to provide the trigger for cosmic muons. A layer of lead 5 cm thick on top of ground scintillators filtered the very low momentum muons, hence reducing the effect of multiple scattering for the triggered ones.

About 5 million events were collected in four months of operations. Different conditions where tested, including changing the temperature of the cooling fluid from 15°C to −15°C. To prevent condensation and ice formation, which could have seriously damaged the system, the tracker was enclosed in a sealed volume flushed with dry air. Temperature sensor and humidity probes on the cooling manyfolds and inside the tracker volume provided a constant monitoring of the dew point for the Detector Safety System. Furthermore, 150 thermistors and humidity sensors on the modules were read-out by the Detector Control System and also sent to the Safety System, in particular to avoid overheating and consequent damage of the hybrids.

The quality of data collected was excellent. About one event out of ten was reconstructed online, providing immediate feedback about the system behaviour. Overall more than 90% of the runs were considered good for further analyses.[5] Figure 6 shows the stability over time and temperature variations of signal-to-noise values for the three subsystems. The numbers of dead and noisy strips were found to be at per mil level, as obtained at the end of subsystems integration. Hence, no evidence of any degradation of the performance because of the final assembly was found.

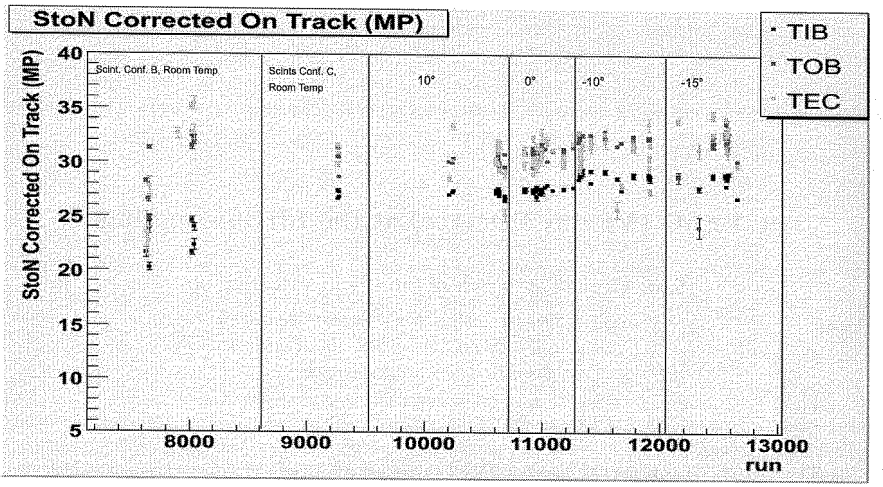

Fig. 6. Signal-to-noise values for the three subsystems during the slice test at TIF. In the first period a non-optimal latency value was used.

4. Conclusions

The construction of the CMS Silicon Strip Tracker is approaching completion. So far the quality of the detector has been nothing short of exceptional. The SST fully meets design specifications. Still it remains to be seen how it will interact with the rest of the CMS environment, but all tests done showed no relevant interferences with external sources of noise. This author is confident that the excellent quality achieved will be maintened throughout the installation and commissioning process.

References

1. *CMS: The Tracker Project Technical Design Report*, **CERN-LHCC-98-06** (1998).
2. *Addendum to CMS Tracker TDR*, **CERN-LHCC-2000-016** (2000).
3. M. Raymond et al., *The CMS Tracker APV25 0.25 μm CMOS Readout Chip*, 6th Workshop on Electronics for LHC Experiments, Cracow, Poland (2000).
4. V. Bartsch, W. de Boer, J. Bol, A. Dierlamm, e. Grigoriev, F. Hauler, S. Heising, L. Jungermann, *Nucl.Instrum.Meth.***A497**, 389 (2003).
5. D. Kcira, *Results from the Commissioning Run of the CMS Silicon Strip Tracker*, 10^{th} ICATPP Conference, Como, Italy (2007).

The VELO (VErtex LOcator) at the LHCb experiment

S. de Capua* on behalf of the LHCb VELO group

European Organization for Nuclear Research,
CERN, CH-1211 Genéve 23, Switzerland
** E-mail: sdecapua@cern.ch*
www.cern.ch

The LHCb silicon vertex locator (VELO) is an array of silicon planes installed in a retractable roman pot system, which will enable the LHCb experiment to reconstruct and trigger on b-hadrons produced in collisions at the LHC. The VELO will be also used to attempt measuring the absolute luminosity with a novel method based on vertex reconstruction of beam gas interactions. In this paper the VELO system, its construction and the results from the commissioning phase are presented. The options for a possible upgraded detector are also discussed.

Keywords: Silicon micro-strip; Vertex detector; Absolute luminosity; Radiation hardness;

1. Introduction

The LHCb experiment [1] is dedicated to the precise measurement of CP-violating processes and rare decays in the B-meson sector in order to constrain the elements of the CKM matrix [2] and to probe for physics beyond the Standard Model.

The VErtex LOcator (VELO) [3] is the LHCb sub-detector situated closest to the interaction region with the purpose of reconstructing primary and (displaced) secondary vertices with a resolution of several tens of micrometers. The VELO plays a fundamental role both in the on-line event selection and in the off-line reconstruction. A part of VELO, the Pile-Up VETO, participates in the first level trigger to reject bunch crossings with multiple interactions. The VELO is included in high level trigger where displaced vertices and transverse momentum information are used in the selection. Furthermore, the proper lifetime of the b-mesons is measured from the primary and secondary vertices reconstructed by the VELO.

2. The Vertex Locator

The VELO detector (Fig. 1) features a series of 42 silicon micro-strip modules placed perpendicurarly to the beam around and downstream the interaction region; each module consists of two 300 μm thick half-circular silicon sensors, one measuring the radial distance r from the beam axis and the other measuring the azimuthal angle ϕ. The R-sensors have 2048 circular

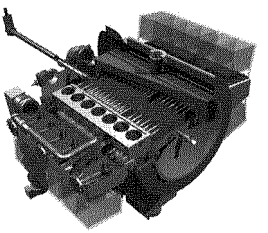

Fig. 1. Overview of one VELO half.

strips with a linearly increasing pitch from 40 μm at r=8.2 mm to 102 μm at r=42 mm, each strip covering 45° in ϕ. The Φ-sensors have 2048 radial strips with a small stereo angle. There are 683 inner strips covering low radii and 1365 outer strips covering large radii. The pitch of the Φ-sensors varies from 36 to 97 μm.

The great challenge for the LHCb vertex detector is an accurate reconstruction of displaced vertices. This requires that the sensors are placed close to the interaction region, with a minimum amount of material between them and the interaction point. Therefore the VELO will operate in a harsh non-uniform radiation environment where the expected fluence r=8 mm; the severe radiation environment has led to the choice of diffusion oxygenated float zone sensors with n^+ strips in n-bulk and a p^+ rectifying contact on the back side.

To minimise the amount of material between the interaction point and the silicon sensors, the detector modules are operated in a secondary vacuum. In order to protect the beam vacuum from possible outgassing of the detector modules and also to shield the sensors from the strong wakefields generated by the intense LHC beams, the detector is separated from the beam vacuum by a 300 μm thick aluminum foil (RF-box). During the injection of the beams the two detector halves are retracted by 30 mm in order to allow for injection and ramping of the proton beams and reduce

the risk of radiation damage to the sensors (Figure 2). The 2048 strips on

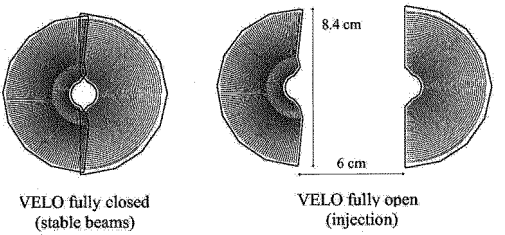

Fig. 2. Position of the r and ϕ sensors with respect to the beam during physics running conditions (left) and injection (right).

each sensor are routed via a second metal layer on the sensor to 16 analog Beetle [4] front-end chips, which are especially developed in a radiation tolerant 0.25 μm technology; the nominal power consumption is 20 W per module. The electronic components are mounted on polyimide (kapton) circuits which have excellent radiation hardness and vacuum properties. The kapton circuits are glued back to back on a carbon fibre substrate with a Thermal Pyrolytic Graphite (TPG) core for heat conduction.

In addition to the 21 $r-\phi$ stations, four stations with only R-sensors, located backward with respect to the experiment, form the Pile-up system which is part of the first level trigger. The detector modules are cooled by a CO_2 circuit: stainless steel tubes carrying the bi-phase CO_2 are cast into aluminium cooling blocks clamped with thermally conductive pads onto the base of the hybrid : a temperature of -30 °C in the tubes results in a silicon temperature of about -5 °C at a heat load of 30 W per module.

3. Luminosity measurement

With the advent of precise microvertex detectors, a novel method of measuring the absolute luminosity emerges [5]. The method relies on beam-gas interactions for measuring the individual beam shapes and determining the beam overlap integral which enter the luminosity. The luminosity L for two counter-rotating bunches with density function $\rho_i(\mathbf{x},t)$ and uniform velocity $\mathbf{v}_i$ is given by [6]:

$$L = fN_1N_2\sqrt{(\mathbf{v}_1-\mathbf{v}_2)^2-\frac{(\mathbf{v}_1\times\mathbf{v}_2)^2}{c^2}}\times\int\rho_1(\mathbf{x},t)\,\rho_2(\mathbf{x},t)\,\mathrm{d}^3x\,\mathrm{d}t$$

where f is the revolution frequency and N_i the total number of particles in the bunches. Assuming the velocities and the total number of particles in the bunches can be precisely measured by independent means, the method aims at measuring the densities ρ_i from beam-gas collisions. An estimation of the rate of inelastic beam-gas collisions, taking xenon as target gas and at a residual gas pressure of 10^{-7} mbar, gives approximately 30 Hz per bunch, which will allow mapping the bunch profile within minutes with a statistical precision below 1%. Moreover, once calibrated by this method, any given reaction can be used later to measure the absolute luminosity in a continuous way without the addition of target gas and at any luminosity.

4. VELO closing strategy

The unique feature of the VELO, whereby the silicon modules can be retracted from the beam by up to 3 cm, while remaining fully powered and operational, allows the continuous monitoring of the LHC beams even before stable collisions are established. For physics conditions the VELO must be centered around the beam, and thus the foil approaches the beam to a distance of 5 mm. The beam position may move by several millimeters from fill to fill, so the VELO is designed to overshoot the nominal centered position if necessary. This means that great care must be taken when approaching the beams, and a strategy, to ensure the process is accurately and quickly completed, must be defined. For this goal, several Pattern Recognition and Vertexing algorithms have been characterised [7], with the aim of deciding on a combination of algorithms which precisely and quickly visualizes the beam. This study demonstrated the beam can be imaged to within a precision of 50 μm when the VELO is in open position ($\pm$20 mm) and 15 μm when the closure is achieved and the VELO is centered around the beam. Furthermore, the study has proven the sample data can be collected and displayed in a short time compared to the mechanical closing time, which represents the major factor in deciding the VELO closing time.

5. Ugrade

The lifetime of the VELO detector is expected to be about three years at the nominal luminosity (2×10^{32} cm^{-2}s^{-1}) which corresponds to about 6 fb^{-1}. Nevertheless, since during the first year of LHC running, which is expected to begin in May 2008, the luminosity will be much lower than the nominal value, a replacement of the VELO is not expected before 2011. Because of this limited lifetime, various upgrade scenarios are under study.

The main motivation behind a technology upgrade is the need for sensors with increased radiation hardness, considering the wish to reduce the distance to the beam from the current 7.2 mm to 5 mm to improve on the impact parameter resolution. A second reason for upgrades is to improve the performance of the VELO and also the LHCb experiment as a whole. Most notably is the wish for an increase in luminosity by a factor of 5: this requires a substantial fraction of the front-end electronics to be redesigned and also an increase in the radiation dose by the same factor.

Good spatial precision, low material budget and extreme radiation tolerance would be required for any future technology and performance upgrade. Several technologies are presently being explored: n-in-p sensors [8,9], Magnetic Czochralski silicon [10,11], 3D silicon [12] and pixel detectors [13].

6. Status

In order to achieve powerful vertex reconstruction and high quality data the detector is undergoing a complete and thorough commissioning phase. In May 2006 the VELO vacuum vessel, the vacuum and positioning control system of the two detector halves and the CO_2 cooling machine have been installed in the LHCb experimental hall; the electronics components including the front end boards, analog links, and digitisation boards have been fully characterised and installed. The commisioning of the readout and control system is ongoing. The module production and assembly has finished in March 2007 and the two detector halves have been installed in November 2007. The VELO is on schedule for the first data in spring 2008.

References

1. LHCb Technical Design Report, CERN/LHCC 2003-030 (2003).
2. M. Kobayashi, T. Maskawa, *Prog. Theor. Phys.* **49**, 652 (1973).
3. LHCb VELO Technical Design Report, CERN/LHCC 2001-011 (2001).
4. N. van Bakel et al., LHCb-2001-046 (2001).
5. M. Ferro-Luzzi *Nucl. Instr. and Meth.* **A 553**, 388 (2005).
6. See e.g. in O. Napoly, *Part. Acc.* **40**, 180 (1993); W. Herr, B. Muratori, Concept of Luminosity, CERN-2006-002 (2006).
7. S. Redford, LHCb-2007-117 (2007).
8. G. Casse et al., *Nucl. Instr. and Meth.* **A 487**, 465 (2002).
9. G. Casse et al., *Nucl. Instr. and Meth.* **A 579**, 623 (2007).
10. J. Härkönen, *Nucl. Instr. and Meth.* **A 541**, 202 (2005).
11. A. Gouldwell Bates, CERN-THESIS-2006-003 (2006).
12. S.I. Parker, C.J. Kenney, J. Segal, *Nucl. Instr. and Meth.* **A 395** 328 (1997).
13. L. Moroni, *Nucl. Instr. and Meth.* **A 446** 235 (2000).

The CDF II eXtremely Fast Tracker Upgrade

I.Fedorko*

CERN,
Geneve CH-1211, Switzerland
** Corresponding author E-mail: ivan.fedorko@cern.ch*

A. Abulencia,D. Errede,H. Gerberich, T. Junk, M. Kasten ,S. Levine, R. Mokos, K. Pitts, E. Rogers, G. Veramendi

University of Illinois, Urbana, Illinois 61801 USA

P. Azzurri, S. Donati, A. Staveris-Polykalas

Istituto Nazionale di Fisica Nucleare Pisa, Universities of Pisa, Siena and Scuola Normale Superiore, I-56127 Pisa, Italy

E. Cochran, J. Efron, J. Gartner, R. Hughes, M. Johnson, B. Kilminster, K. Lannon, J. McKim, D. Olivito, B. Parks, J. Slaunwhite, B. Winer

The Ohio State University, Columbus, Ohio 43210

J. Dittmann, S. Hewamanage, N. Krumnack, J. S. Wilson

Baylor University, Waco, Texas 76796

R. Erbacher, R. Forrest, A. Ivanov, A. Soha

University of California, Davis, Davis, California 95616

G. Flanagan, T. Jones

Purdue University, West Lafayette, Indiana 47907

S. Holm, R. Klein, E. E. Schmidt, L. Scott, T. Shaw, P. J. Wilson

Fermi National Accelerator Laboratory, Batavia, Illinois 60510 USA

The CDF II eXtremely Fast Tracker (XFT) is the trigger processor which reconstructs charged particle tracks in the transverse plane of the central tracking chamber. The XFT tracks are also extrapolated to the electromagnetic calorimeter and muon chambers to generate trigger electron and muon candidates. The XFT is crucial for the entire CDF II physics program: it detects

high p_T leptons from W/Z and heavy flavor decays and, in conjunction with the Level 2 processors, it identifies secondary vertices from beauty decays. The XFT has thus been crucial for the recent measurement of the B_s^0 oscilation and Σ_b discovery. The increase of the Tevatron instantaneous luminosity demanded an upgrade of the system to cope with the higher occupancy of the chamber. In the upgraded XFT, three dimensional tracking reduces the level of fake tracks and measures the longitudinal track parameters, which strongly reinforce the trigger selections. This allows to mantain the trigger perfectly efficient at the record luminosities $2\text{–}3 \cdot 10^{32}$ cm^{-2} s^{-1} and to mantain intact the CDF II high luminosity physics program, which includes the Higgs search. The architecture, the used technology, the performance and the impact of the upgraded XFT on the entire CDF II trigger strategy are reviewed.

Keywords: CDF,XFT,Trigger

1. Introduction

The eXtremely Fast Tracker [1] finds tracks in the transverse plane of the CDF II drift chamber, the COT [2], in time for the Level 1 trigger decision. The XFT tracks are also matched to electromagnetic clusters for online electron identification, and to stubs in the muon chambers for muon identification. The role of the XFT in the trigger is to reduce the raw collision rate (1.7 MHz) to a maximum of about 30 KHz of interesting physics events which can be processed by the Level 2 trigger. The XFT uses hit data from the 4 axial superlayers of the chamber, arranged in cells of 12 wires each. A charged particle passing through an axial layer generates a characteristic pattern of 12 hits, one per wire, with a characteristic timing. Track identification is performed in two steps by the Finder boards, which search for track segments in each of the 4 axial layers of the chamber, and by the Linker boards, which search for 4/4 matches among segments in the 4 layers, consistent with a track exiting from the interaction point. The XFT measures the p_T and ϕ of all the tracks with $p_T > 1.5$ GeV/c with $\epsilon > 96$ % per track, $\sigma_{p_T}/p_T^2 \sim 2\%$ (GeV^{-1}) and $\sigma_\phi \sim 6$ mR. The XFT is essential for the CDF II physics program, it selects high pT leptons from W/Z and top decays, as well as soft leptons from b decays, and, in conjunction with the Level 2 processors, hadronic displaced tracks from b decay vertices. The hadronic trigger has been crucial for the recent $B_s^0 - \overline{B^0}_s$ mixing measurement and Σ_b discovery.

2. The Axial XFT System

The XFT system architecture is presented schematically in Fig. 1. The XTC (acronym of XFT TDC Card) mezzanine cards reside on the COT

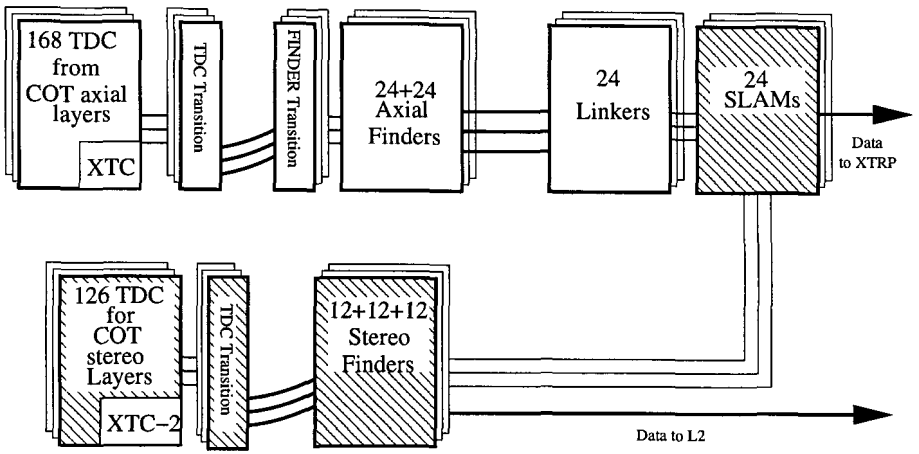

Fig. 1. Schematic diagram of the XFT system architecture. The white boxes indicate the original axial system, and the shaded boxes depict the new components introduced with the upgrade. The new Stereo Linker Association Modules (SLAMs) replace the Linker Output Modules (LOMs), which are not shown.

TDC's. The cards take in pulses from the COT and convert them into a digital output using a "2-time-bin" algorithm. The hits are classified as prompt or delayed, whether the time of hit is smaller or larger then 44 ns, respectively. These data are sent to a transition module on the back of the COT TDC crate and from there are are transmited at 45.5 MHz as LVDS signals to the Finder module crates, where they are received by transition modules and go to the Finder modules (9U VME) through a customized backplane. The pixel finding code is loaded on PLD. From Finder modules the data (track segments) are transmitted to the Linker modules (9U VME) which find the tracks and the associated parameters p_T and ϕ. One Linker covers 15° of azimuthal angle and each of 12 Linker's PLD's looks for tracks in a 1.25° slice. Track information is driven by transition modules to the extrapolation unit (XTRP) which extrapolates the tracks to the electromagnetic calorimeter and the muon chambers and distributes the data to the Level 1 and Level 2 triggers. At Level 2 the XFT tracks are used as seeds by the Online Silicon Vertex Tracker [3] which performs a combined track reconstruction in the tracking chamber and in the silicon vertex detector.

3. The upgrade of the system

The upgrade mantains the existing axial system, and new Stereo Finder boards are added to find track segments also in the three outer stereo layers of the chamber. Fake axial tracks are rejected by associating the axial tracks to the stereo segments. The 3D track as result of the upgraded XFT system provide the track parameters as cot θ and z_0, which can be used to require the XFT track to point in the z-direction towards the calorimeter tower or the muon stub involved in electron or muon triggers.

The upgraded system architecture is presented schematically in Fig. 1, where the shaded boxes indicate the new components. The XTC-2 mezzanine cards reside on the TDC's that process data from the COT stereo layers. The card classifies the hits in 6 time windows with programmable edges, set around 55, 79, 103, 127, 151 and 255 ns. Data are transmitted through additional mezzanine cards installed at the back of the TDC crates to the Stereo Finders using optical fibers. The cards are design according to the Common Mezzanine Card standard [4]. The fiber transmitter uses TLK1501 [5] devices to serializes and deserializes the transmitted data.

The Stereo Finder boards identify track segments in the stereo layers of the COT. Each board covers a 30° azimuthal angle slice, so a total of 36 boards is necessary to instrument the 3 outer stereo layers. The number of 12 wire cells processed by each board is respectively 20/28/36 for the internal/central/external stereo layers. The software compares imput hit patterns, from core 4 cells plus 2 neigbouhr cells from both sides of core, with the segments of tracks simulated with uniform distribution of curvature and rapidity. The Stereo Finder logic is implemented with two Altera Stratix EP2S60 Programmable Gate Arrays. The Stereo Finders output the list of found pixels, which indicate the position and slope of an identified track segment. The pixels exist in two formats output through two independent data streams on optical fibers. The first one has each COT cell divided in 12 pixels, with 6 azimuthal bins and 2 slope bins, and is directed to the Stereo Linker Association Modules (SLAM), which perform the matching between the axial XFT tracks and the stereo pixels. The second one, less compressed, has each COT cell divided in 90 pixels, with 18 azimuthal bins and 5 slope bins, and is directed to the Level 2 trigger processors, where the extra time available allows the use of more refined information. Each SLAM receives the axial track data from one

Linker Module, which covers a 15° azimuthal angle slice, and the stereo pixels from a slice of 45° azimuthal angle covered by two Stereo Finders and centered on the region covered by the Linker Module. The association

algorithm is implemented using one Altera Stratix EP1S25 per module. The format of the data output from the SLAM to the extrapolation unit (XTRP) is identical to the original output of the Linker Output Modules, with the insertion of the "matched/unmatched track" information and the "positive/negative z direction" in two presently spare bits. At high luminosity only matched tracks will be used in the trigger selection. The more precise stereo pixels transmitted to the Level 2 trigger are matched to the axial XFT tracks, and are used to measure the track cot θ and z_0, respectively with a resolution of ~ 0.1 and 10 cm, sufficient to improve the quality of the Level 2 selection.

The efficiency of hadronic trigger (see part 1) using 2D tracks were dramaticaly droping at luminosities $> 130{\cdot}10^{30}$ cm^{-2} s^{-1}. With upgraded system the trigger works up to $180{\cdot}10^{30}$ cm^{-2} s^{-1}. For muons in region with high occupancies ($0.6< |\eta| <1.0$), where muon triggers were dominated by fake tracks, the reduction factor of trigger rates achieved value of 4 requiring stereo confirmation.

4. Conclusions

In this paper we review the upgrade of the eXtremely Fast Tracker, which reconstructs tracks in the transverse view of the CDF II Central Outer Chamber in time for the Level 1 trigger decision. The upgraded system is designed to perform a three dimensional track reconstruction. Using 3D tracks provided by upgraded XFT system improved the purity of tracks used in Level 1 trigger and provides the possibility of 3D tracking with greater precission on Level 2 trigger.

References

1. E. J. Thomson *et al.*, IEEE Trans. Nucl. Sci. 49, 1063 (2002)
2. T. Affolder *et al.*, Nucl. Instrum. Meth. A526: 249, (2004)
3. W. Ashmanskas *et al.*, Nucl. Instrum. Meth. A518: 532, (2004)
4. IEEE Standard for Common Mezzanine Card Family:CMC, Document 1386-2001,ANSI Pub., 2001
5. Texas Instruments, TLK1501:0.6 to 1.5 GPBS Tranceiver, Data Sheet 2004

The DEPFET Active Pixel Sensor as Vertex Detector for the ILC

P. Fischer for the DEPFET collaboration *†

Institute of Computer Science, Mannheim University,
B6, 26, 68131 Mannheim, Germany
E-mail: peter.fischer@ti.uni-mannheim.de

Large matrices of DEPFET sensors are a promising technology for the ILC Vertex Detector. Pulse-cleared MOS-based DEPFET pixels of $\approx 25\,\mu\text{m} \times 25\,\mu\text{m}$ size are arranged in modules with an active area of $\approx 1.3\,\text{cm} \times 10\,\text{cm}$. This part can be as thin as $50\,\mu\text{m}$. A thicker silicon frame provides stability for a self-supporting module. The readout is performed by sequentially addressing pixel rows with analog multiplexer chips located at the module edge and by digitizing the drain currents with specialized readout chips at a rate of several 10 MHz. This concept can provide a low mass tracker with low power dissipation in the active area and with good radiation tolerance.

Keywords: ILC; Vertex Detector; Tracker; DEPFET

1. Introduction

Large arrays of depleted field effect transistor (DEPFET) pixels are a promising technology for the vertex detector of the planned International Linear Collider ILC. Other candidates are, to name a few, Charge Coupled Devices (CCDs), In-situ Storage Image Sensors (ISIS[1]) and Active Pixel Sensors.[2,3] This paper summarizes the present status of the DEPFET development and gives an outlook on how an ILC compatible demonstrator module could be built. The next section summarizes briefly the DEPFET principle, matrix readout and some important properties and performance figures of pixels, matrices and thin sensors. Section 3 describes a possible module geometry, Sec. 4 presents the new *SWITCHER* chip followed a brief outlook to our next steps.

*see appendix

†This work was supported by the German Federal Ministry for Research BMBF under grants No. 05HS6PD1 and 05HS4VM1 and by the Humboldt foundation.

2. DEPFET Operation and Properties

2.1. *Operating Principle*

The depleted field effect transistor[4] is a device with built in amplification: The electrostatic field in a fully sideward depleted silicon structure is shaped such that all electrons generated by ionizing particles, Xrays or photons are collected in a small volume which is located under the channel of an integrated p-channel field effect transistor. The negative charge in this 'internal gate' leads to an increase of the channel current according to the small signal charge gain $g_q \approx 0.5\,\mathrm{nA}$ per electron. The current can be completely switched off with an additional, 'external' gate. Charge collection is fully efficient also while the device is switched off, so that a low power operation is possible. The accumulated charge can be measured as a voltage change at the source in 'source follower' readout, or as a current signal at the drain in 'drain readout'.[5] The charge accumulated in the internal gate can be removed through a clear contact with a positive voltage pulse of $\approx 7\,\mathrm{V}$.

2.2. *Matrix Readout*

Two dimensional arrays are constructed by connecting gates and clears in rows and the drains in columns, holding all sources at a common potential. After a charge accumulation period, a row is turned on by pulling its external gate line low. The current in all drain columns is measured and compared to the current with empty internal gate, which is obtained by pulsing the clear line. This sequence is repeated periodically for all rows. In order to cope with the high occupancy at the innermost ILC layer, several readout frames must be taken during one ILC burst. This imposes a row readout rate of 10 MHz or more. At these frequencies, readout noise is dominated by thermal noise of the electronics and not by the intrinsic noise of DEPFET devices, which can be below 2 electrons (enc) at room temperature for slow shaping times of $10\,\mu\mathrm{s}$. Small matrices with 64×128 pixels are being operated routinely with fully integrated gate/clear steering and drain readout electronics.

2.3. *Some Key Properties of DEPFETs*

The *size* of one DEPFET pixel is presently limited by the manufacturing technology available at the Semiconductor Laboratory of the Max-Planck Institute in Munich to $\approx 24 \times 24\,\mu\mathrm{m}^2$ but there is no fundamental limit which excludes smaller devices. Pixels can be made very large with nearly

no noise penalty by adding drift rings so that the DEPFET acts as the collecting anode of a silicon drift detector.[6] This feature makes the devices well suited for many special applications like X-ray satellite missions.

The *thickness* of the device can vary over a wide range: Our standard devices are manufactured on 450 μm thick wafers. As the full sensor thickness is depleted, these devices are well suited for detection of X-rays with moderate energies. On the the other hand, a thinning technology compatible to DEPFET manufacturing has been developed which makes possible devices of 50 μm thickness or less. The thinning procedure described in Ref. 7 is based on *local* back-etching of a two layer sandwich structure down to an etching barrier. This makes it possible to still have some thick silicon structures for mechanical stability so that self supporting thin modules with a thicker frame are possible.

The (small signal) *charge gain* g_q quantifies the drain current increase induced by charge in the internal gate. Present devices have gains of $0.3 \ldots 0.5\,\mathrm{nA/electron}$, but we hope to reach up to $1\,\mathrm{nA/electron}$ in the near future. Large charge gain is often associated which higher clear voltages, which is another important parameter, so that an optimum balance must be found here. One straight forward way to increase g_q is the reduction of the gate length which must be traded against manufacturing yield. A high charge gain is of utmost importance, as the system noise is obviously reduced by providing more current for a given charge.

The *noise* of the DEPFET can be as low as 2 electrons (enc) at room temperature for shaping times of 10 μs due to the very low input capacitance of the internal gate. At the high speed required for ILC, however, this number increases due to the higher bandwidth. One of the dominant noise contributions is the regulated cascode circuit in the drain readout chip required to keep the long drain busses at a constant potential, so that the DEPFETs see a sufficiently low impedance input (required for high speed). When reserving $\approx 2\,\mathrm{mW}$ of power for this part, the noise contribution is still $100 - 200$ electrons, depending on g_q.

The *radiation tolerance* of DEPFETs has been studied in several irradiations. Due to the high electric field in the bulk present for charge collection, no severe bulk damage effects are expected and this is confirmed by comparing proton/neutron and gamma irradiations. Surface charge effects lead to shifts of the threshold of the external MOSFET in the order of $-4\,\mathrm{V}$ (which can be compensated for by adjusting the external potentials) but not - more important - to a degradation of the transconductance, which is required for speed. The noise of a device irradiated up to almost

1 Mrad (Si) increased by only 2 electrons (for the same slow shaping time of 10 μs). This is negligible compared to other noise components caused by high speed readout. The latest results on irradiations will be presented at the NSS/MIC conference 2007. It should be noted here that the two types of readout ASICs required - the gate/clear steering chips and the drain readout chips - are using manufacturing technologies and design techniques to achieve a sufficient radiation tolerance as well.

The *spatial resolution* has been measured in recent test beams using a telescope made of five DEPFET planes. A preliminary analysis resulted in a resolution of $\lesssim 2\,\mu$m for the device with best track prediction. This is no big surprise given the excellent signal/noise ratio of ≈ 110 as obtained for the minimum ionizing particles in 450 μm thick sensors. Further results of this analysis have been submitted to IEEE and will also be presented at the NSS/MIC conference 2007. The test beam results have been used to successfully verify a DEPFET detector simulation framework which allows us to predict the performance of thin devices within ILC. Depending on the detector layout and the magnetic field, we expect $r-\varphi$ resolutions between 3 μm and 4.3 μm for pixels of $25 \times 25\,\mu\text{m}^2$.

The *frame rate*, i.e. the time required to cycle once through the matrix is determined by the number of rows and by the row speed, where we aim at $20-40$ MHz. For the anticipated size of ≈ 2000 rows (per half module), the frame rate will be $50-100\,\mu$s, i.e. 10-20 frames per bunch train can be read out. The limiting factors for speed are the power dissipation in the drain readout chips which must live with a drain bus capacitance of ≈ 40 pF and, possibly, RC time constants in the matrix itself.

3. Possible ILC Module Geometry

Figure 1 shows a possible geometry for an ILC *half*-module.[8] The actual module is twice as large, mirrored at $z = 0$, with readout at both ends. The active area (of the *half module*) is subdivided into 512×2048 pixels of $24 \times 24\,\mu\text{m}^2$ size, covering $12.3 \times 49.2\,\text{mm}^2$. This part is thinned to 50 μm except for some support bars. The edges are made from thicker ($\approx 300\,\mu$m) silicon. One side is wider to support two rows of *SWITCHER* chips which steer gate and clear rows. These chips are thinned and bump bonded directly to the sensor. Two adjacent pixels on the matrix are grouped to a *double pixel* so that the double row chip pitch for gate and clear is 48 μm. This pixel arrangement, shown schematically in Fig. 1 leads to a very narrow drain column pitch of 12 μm which enforces bump bonding for the readout chips as well. The steering signals and power for the *SWITCHER* chips is

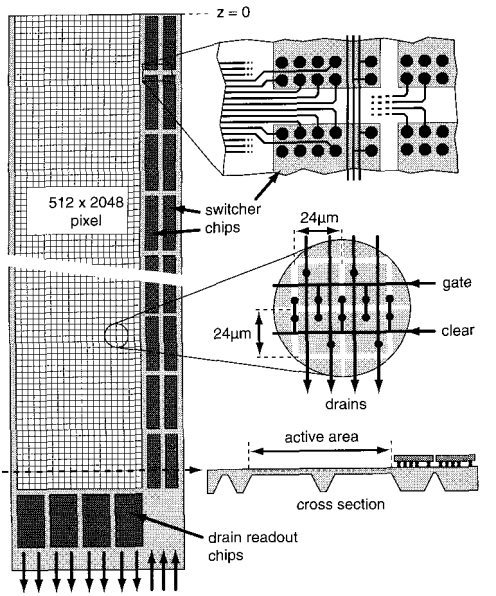

Fig. 1. Sketch of half an ILC module showing *SWITCHER* and readout ASICs, the double pixel structure and a cross section of the thin sensor.

routed on the two metal layers available on the silicon, so that no further interconnect is required. This makes a very thin module possible.

4. The new *SWITCHER* Chip

The steering signals for gate- and clear rows are provided by '*SWITCHER*' chips which are basically fast analogue multiplexers with an intelligent sequencer. The most important requirements for these chips are:

- They must be as small (long and slim) and thin as possible to keep the amount of dead material small. Their pads must be compatible to the anticipated bump bonding procedure.
- Power dissipation must be minimal to eliminate the need for massive cooling of the inner region.
- The chips must be sufficiently radiation tolerant. The expected dose remains to be determined by simulation of the background at ILC, but several Mrad should be required at least. This requirement complicates a lot the switch design, where high voltage tolerant devices with thick gate oxides would normally be used. Measure-

ments on a 0.8 μm HV technology have confirmed that these devices suffer from severe threshold shifts after only 30 krad, as expected.

- They must be able to switch voltages of up to $\approx$ 10 V. This value includes some safety margin in particular for the clear signals where a step of 7 V only is presently required.
- They must achieve rise/fall times of < 10 ns for a load of 20 pF.
- Only a minimal number of power and control signals can be routed along the narrow 'balcony' of the module.
- The switching patterns (the sequence of channels) must be programmable and flexible to cope, for instance, with broken rows or with very inhomogeneous occupancy where more frequent readout of some areas may be beneficial. Many chips must be operated in parallel with no overhead.

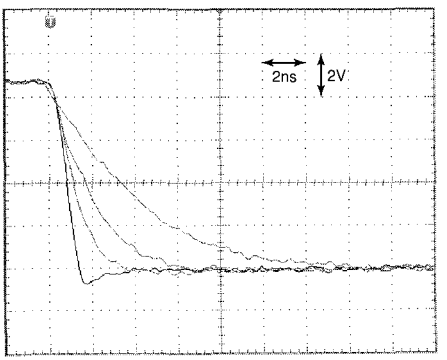

Fig. 2. Measured falling edges of 9 V swing generated by *SWITCHER*3 for load capacitances of 0 pF, 10 pF, 22 pF, 47 pF (2 ns/div, 2 V/div).

These requirements have lead to the design of the *SWITCHER*3 chip using a 0.35 μm CMOS technology. It contains 128 channels, arranged in 4 rows suited for bump bonding. Enclosed transistors and guard rings are used throughout the design. The analogue switches use three stacked transistors, each operated at 3.3 V only, so that 10 V are reached in this technology. They are sufficiently fast, as illustrated in Fig. 2. The power consumption of the switch part is dominated by the load capacitance. A very flexible sequencer has been implemented. The digital consumption when clocked at 20 MHz and supplied with 3 V is $\approx$ 18 mW and can be further reduced in the next iteration.

5. Outlook

A new sensor production has just been finished and will be characterized. It includes modules of full ILC width and length. The new *SWITCHER3* chips will be used and a new drain readout chip will be completed.

Appendix: The DEPFET collaboration

The members of the DEPFET collaboration, as of October 2007, are: RWTH Aachen, Germany (L. Feld, W. Karpinski, K. Klein), Bonn University, Germany (G. Hanninger, R. Kohrs, H. Krüger, P. Lodomez, M. Mathes, L. Reuen, M. Koch, E. v. Törne, J. J. Velthuis, N. Wermes), Charles University, Prague, Czech Republic (Z. Doleal, Z. Drsal, P.Kody, P. Kvasnicka, D. Scheirich), Instituto de Fisica Corpuscular, University of Valencia, Spain (I. Carbonell Pascual, J. A. Fuster, C. Lacasta Llcer, M. Vos). Karlsruhe University, Germany (W. de Boer, A. Sabellek), Mannheim University, Germany (P. Fischer, F. Giesen, Ch. Kreidl, I. Peric), MPI for Physics and MPI Semiconductor Laboratory, Munich, Germany (L. Andricek, X. Chen, A. Frey, G. Lutz, H. G. Moser, A. Raspereza, R. H. Richter, S. Rummel),

References

1. C. J. S. Damerell: CCD-based vertex detectors, Nucl. Inst. Meth. **A541** (2005) pp. 178–188
2. G. Varner et. al.: Development of a super B-factory monolithic active pixel detector - the Continuous Acquisition Pixel (CAP) prototypes, Nucl. Inst. Meth. **541** (2005) pp. 166–171
3. G. Deptuch et al.: Monolithic active pixel sensors adapted to future vertex detector requirements, Nucl. Inst. Meth. **A535** (2004) pp. 366–369
4. J. Kemmer and G. Lutz: New Semiconductor Detector Concepts, Nucl. Inst. Meth. **A253** (1987) pp. 365–377
5. P. Fischer et al.: Readout Concepts for DEPFET Pixel Arrays, Nucl. Inst. Meth. **A512** (2003) pp. 318–325
6. J. Treis et. al.: DEPMOSFET Active Pixel Sensor Prototypes for the XEUS Wide Field Imager, IEEE Trans. on Nucl. Science **Vol. 52, No 4** (2005) pp. 1083–1091
7. L. Andricek, G. Lutz, M. Reiche and R. H. Richter: Processing of Untra-Thin Silicon Sensors for Future e^+e^- Linear Collider Experiments, IEEE Trans. on Nucl. Science **Vol. 51, No. 3** (June 2004) pp. 1117–1120
8. P. Fischer et. al.: Progress towards a large area, thin DEPFET detector module, Presentation at the vertex 2006 conference, submitted to NIM 2006

Integration and Commissioning of the ATLAS Muon Spectrometer

Masaya ISHINO

ICEPP, University of TOKYO, Tokyo 113-0033, Japan

On behalf of the ATLAS Muon Collaboration

The ATLAS experiment at Large Hadron Collider (LHC) has a characteristic muon spectrometer with toroidal magnetic-field for the purpose of stand-alone precision tracking and momentum selective trigger. By the combination of four types of detector technologies, the pseudo-rapidity range of $|\eta| < 2.7$ is covered by tracking chambers and $|\eta| < 2.4$ by trigger chambers. The tracking system is designed to achieve momentum resolution of better than 10% up to transverse momenta of 1 TeV. Based on the matrix-coincidence logic, the trigger system generates level-1 trigger signal and sends it to global DAQ system. Up to now, most of the system has been installed into the ATLAS pit, and all the system will be completed by the end of 2007. In the mean time, detector commissioning is intensively performed with cosmic-rays. We present the results from this activity.

Keywords: ATLAS, Muon Spectrometer, Detector Commissioning

1. Introduction

The ATLAS muon spectrometer has a characteristic concept to perform stand-alone momentum analysis of muon tracks by introducing the large superconducting air-core toroid magnets and triggering high/low P_T momentum muons with dedicated chambers whose time jitter is less than the bunch space of 25nsec. [1]

The barrel toroid and two end-cap toroids cover the pseudo rapidity range of $|\eta| < 1.0$ and $1.4 < |\eta| < 2.7$ respectively. Each of the three toroids consist of eight superconducting coils assembled radially and symmetrically around the beam axis. By rotating endcap system by 22.5 degrees respect to barrel, radial overlap can be made and magnetic field is available also in the transition region of $1.0 < |\eta| < 1.4$. The bending power of 2 to 6 Tm is available in barrel, and 4 to 8 Tm in the endcap region.

For the precision measurement of muon tracks, Monitored Drift Tube

(MDT) chambers are used in the most of the place except at the high pseudo-rapidity region ($2.0 < |\eta| < 2.7$) of the inner endcap station, Cathode Strip Chambers (CSC) have high granularity strips to cope with high particle flux and background rate. The precision measurement of the muon tracks is done in a direction parallel to the bending direction of the toroidal magnetic field. The axial coordinate Z is measured in the barrel and the radial coordinate R in the endcap. Three stations are arranged along the muon paths and momentum is determined from sagitta in the barrel region, instead point-angle measurement gives the best possible resolution in the endcap.

For the muon trigger, Resistive Plate Chambers(RPC) in the barrel region and Thin Gap Chamber(TGC) in the endcap are used. To identify the bunch crossing which contains high momentum muon(s), better time jitter than 25 nsec of the LHC bunch space is required. The typical time jitter of RPC is a few nsec and of TGC is around 20 nsec depends on the incident angle. The trigger logic is based on the matrix-coincidence of multi chamber layers. By the bending power of toroidal magnets and order of 1cm space resolution, the hit pattern between three stations has difference according to the transverse momentum of muons. This information is built in look-up-table of the trigger logic, and number of muon candidates is sent to central-trigger-processor with labeling estimated transverse momentum of muon track. Typical set of threshold boundary is 4, 6, 10, 15, 20, 40 GeV, and it can be changed flexibly. This feature enables to create variety of trigger menu which is requested for physics study.

2. ATLAS Muon Detectors and its integration

2.1. *MDT ; Monitored Drift Tube*

The outer structure of MDT is an aluminum tube of 30mm diameter having thickness of 300 μm. There is 50 μm W-Re wire at the center of the tube, the length is ranged from 0.7m to 6.3m. The tubes are arrayed and stacked as three or four multi-layer. One station consists two multi-layers and it is the unit of assembly on surface. The operation gas is a mixture of Argon CO_2 (93:7) at 3bar absolute pressure. The high-voltage of 3080V is normally then the gas gain is 2×10^4. The single tube resolution of 80 μm is expected.

2.2. *RPC ; Resistive Plate Chamber*

The basic structure of RPC unit is a narrow gas gap formed by two parallel 2mm thick plate made of resistive Bakelite and they are separated by 2mm

thick insulating spacers made of polycarbonate. The internal surface Bakelite plate is treated with linseed oil. The gas mixture of $C_2H_2F4(94.7\%) + iso-C_4H_{10}(5\%) + SF_6(0.3\%)$ is used and high-voltage of 9600V is applied to the 2mm gas gap. The gas amplification is done in avalanche mode and typically the pulse of 0.5pC is produced. The signal is picked up by two orthogonal readout strip panels with a pitch of a few cm. Two gas gaps are combined mechanically and form doublet plane, and assembled together with MDT barrel station.

2.3. *TGC ; Thin Gap Chamber*

The basic structure of TGC is a Multi Wire Proportional Chamber (MWPC) with a graphite cathode having a surface resistivity of 1MΩ per square. The distance of anode wire and cathode strip is 1.4 mm, smaller than the space between anode wires of 1.8mm. The diameter of anode wire is 50 μm to give high electric field for over all space in the cell. The gas mixture is CO2 (55%) and n-Pentane (45%) which has strong quenching qualities to avoid the production of streamers. The timing jitter is less than 25 nsec corresponding to the bunch space of LHC. The hit signals are read from both anode wires and cathode strips made of a copper foil arrayed in orthogonal to the wires. Each chamber has an effective area of 1 to 2 m^2, and two or three single layers are glued as doublet or triplet unit. In total 3600 chambers were produced in Israel, Japan and China.

All the chambers were tested with cosmic-rays under normal operation condition and the overall efficiency was measured. The cut criteria was set to the layer efficiency of 95% , and most of the chambers have efficiency better than 99% in the active region. About 70% of the chambers were tested with high rate gamma-ray flux of 200 to 1000 Hz/cm^2 depending on the η region to be installed. The operation stability and comparison of leak current, single rate before and after irradiation were checked. After the shipment to CERN, again all chambers were operated for 3 weeks and each noise level is checked with self trigger.

Finally chambers are installed into fan-shaped mechanical structure which forms a 1/12th of the station. The structure is made of aluminum, 10 I-profiles length of 10m, 8 rectangle transversal-bars and one thick outer beam. These pieces are aligned with a precision of 2mm within the tolerance for the connection between sectors. All the services, gas tubes, signal cables, high-voltage cables, trigger signal cables (CAT6), low-voltage cables, CAN control cables, slow monitor cables and their support structures are installed in the first stage. The on-sector trigger electronics for taking the

first coincidence are mounted on the same structure. Then 22 chambers are installed and each service is connected to them.

The final commissioning on the surface is performed using test pulses and cosmic-rays. The functionality of the readout chain starting from Amplifier-Shaper-Discriminator (ASD) on chambers, followed by the signal cables and on-sector electronics is verified by test pulses injected at the ASD. Following this test, the chambers are made operational by turning the high-voltage and cosmic-ray data is taken in a self-trigger made by a coincidence of multi layers. The hit-profile, noise level and functionality of the trigger path are checked in situ. All 72 sectors were tested and installed in the ATLAS experiment. The rate of dead channels was found to be at the level of 10^{-4} for the 320k channels of the system. In total six wheels, three on each side were completed by September 2007.

3. Commissioning status and results

In September 2007, as a series of system commissioning program, the ATLAS global run with cosmic-rays was performed including MDT chambers, RPC and TGC triggers, central Trigger and DAQ system.

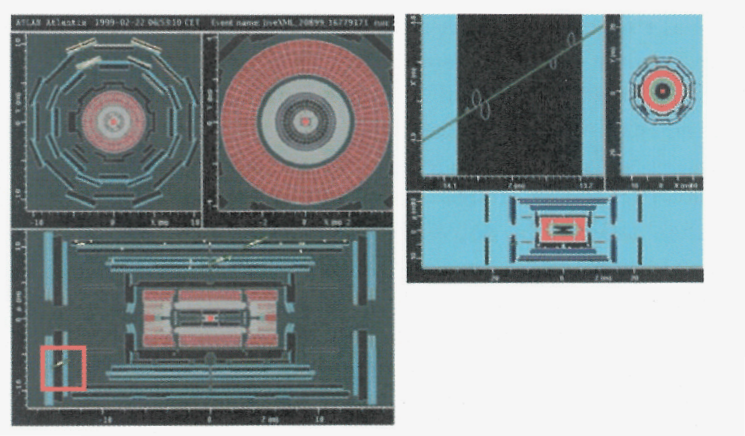

Fig. 1. An example event taken by TGC trigger is shown. The associated hits seen in both MDT endcap and barrel chambers (left). The drift circle of MDT endcap middle station is shown. (right) Straight line is fit well on the line of drift circle.

An event example taken during this combined run is shown in Fig. 1. The event is triggered by TGC in the endcap region. Associated hits are seen in MDT endcap chambers and also track segment is found in barrel

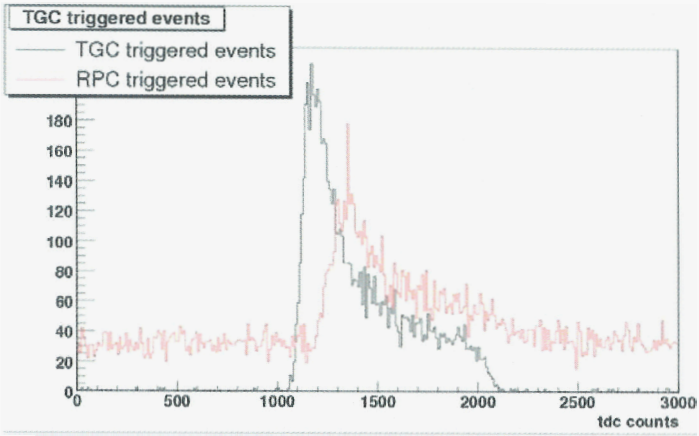

Fig. 2. **The TDC spectrum of MDT endcap chambers. Events** taken by TGC trigger is shown in black line and by RPC trigger is shown in red line.

region. The drift circles are well fit by straight line.

The TDC spectrum of drift tube is shown in Fig. 2. It is the time spectrum of MDT endcap chambers and events taken by TGC trigger is shown in black line and by RPC trigger is shown in red line. Because of the better geometrical matching, there is no jitter of time-of-flight between MDT endcap and TGC, so sharp rising edge is seen with very good signal to noise ratio.

4. Summary

Most of the ATLAS Muon system is successfully assembled and installed into the pit. The system commissioning has been intensively performed. By the end of 2007, rest of the muon system, endcap small wheels including CSC and outer MDT wheel will be installed.

In September 2007, ATLAS global commissioning run with cosmic-rays was performed and the muon system is well integrated into global Trigger and DAQ system. Part of the system from each detector is used for this commissioning run and data is taken successfully with muon triggers generated by TGC and RPC.

References

1. ATLAS Muon Collaboration, ATLAS Muon Spectrometer Technical Design Report, CERN/LHCC/97-22, CERN (1997).

Results from the Commissioning Run of the CMS Silicon Strip Tracker

Dorian Kcira *

Université catholique de Louvain, Center for Particle Physics and Phenomenology, Louvain-La-Neuve, Belgium. dorian.kcira@cern.ch

Results of the CMS Micro Strip Silicon Tracker performance are presented as obtained in the setups where the tracker is being commissioned.

Keywords: Silicon Strip Tracker, Compact Muon Solenoid, CERN, HEP

The CMS Micro Strip Silicon Tracker,[1] referred from here on as the Tracker, was commissioned using cosmic muons in two main setups: the Magnet Test Cosmic Challenge (MTCC) and the Tracker Integration Facility (TIF).[2] A large number of studies of the tracker performance and offline data analysis has been performed and many others are still ongoing. Only few of these studies for both setups are presented here.

1. Signal Properties

In figure 1 (right) the noise in ADC counts is plotted versus the length of the micro strips for different subsets of the detector modules at the TIF. As expected, this dependence is linear and the dependence on other effects, like number of readout chips per module, is small. The signal-to-noise ratio (S/N) for hits associated to reconstructed cosmic muon tracks (Combinatorial Track Finder, section 2) at the TIF was measured and is shown in figure 1 (left) for the TIB. The achieved (most probable) values for the S/N are very good, larger than 27 for all substructures of the tracker. For the TIF data taking the slower readout mode of the chip was used as the trigger timing was not precise enough to use the fast one. Using the fast readout mode will lead to a reduction by a factor of 2/3 of S/N. Measurements have shown that values of the noise and of the S/N were stable and had

*Supported by the Belgian Interuniversity Attraction Pole, PAI, P6/11.

only small variations with time over the period of the commissioning run at TIF.

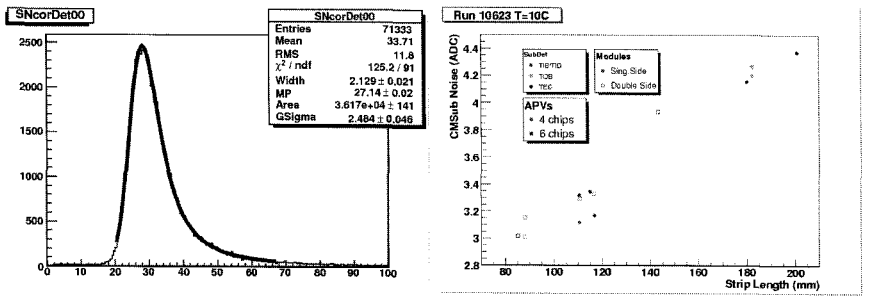

Fig. 1. Left plot: Signal to Noise ratio for TIB. Right plot: Noise versus strip length.

2. Tracking

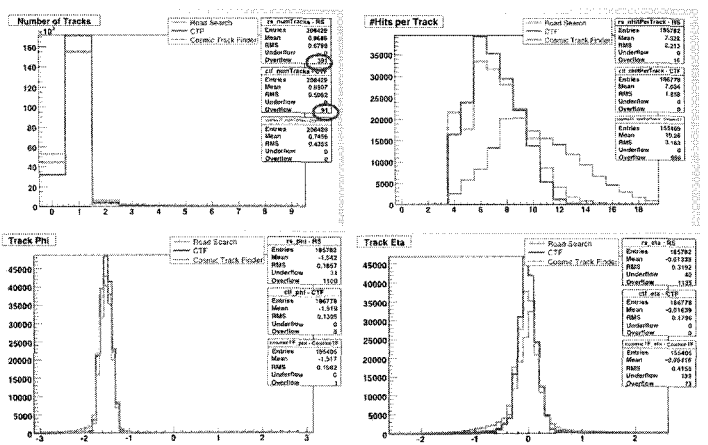

Fig. 2. Track quantities for the three different track algorithms used at TIF and MTCC.

Three tracking algorithms were applied to TIF and MTCC data: the standard Combinatorial Track Finder, Road Search and the Cosmic Track Finder, specialized for single-track cosmic events. They use the reconstructed hits, i.e. position estimates based on clusters found in the modules

of the tracker. In addition a reconstruction geometry describing the location of the modules and the distribution of passive material and condition information about the status of the different modules were needed. In figure 2 some track quantities are shown for all algorithms. The Cosmic Track Finder has a larger number of hits per track because it treats hits from stereo detectors as two separate hits. A general agreement is seen between the different algorithms.

3. Detector Efficiency Measurement

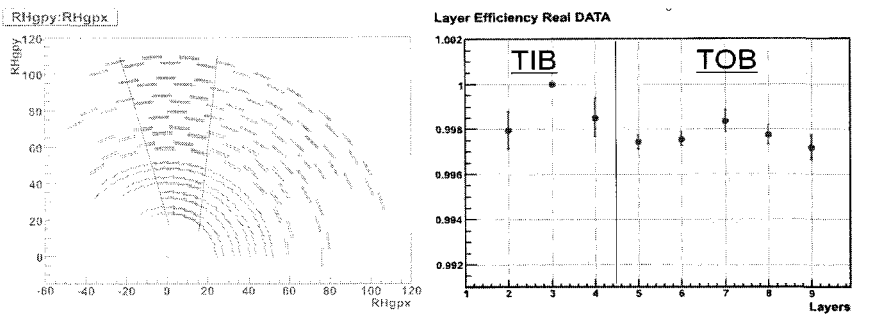

Fig. 3. Left: the shaded area between the two lines shows the selected region for determining the detector efficiency. Right: detector efficiency for TIB and TOB layers at the TIF.

During the integration procedure the number of dead or noisy channels was determined to be low, around 0.2% of the total. The tracker layer and module response efficiency was cross-checked using cosmic muon data taken at the TIF. For this the Combinatorial Track Finder was run and hits associated to the tracks were selected. For each layer (or module) crossed by the track the number of valid hits, S and invalid hits, B were computed, where valid means that the track built excluding that layer / module finds the hits in the expected position, within a certain range (dependent on the track / hit uncertainty and the tracker alignment precision). The efficiency was then calculated as $S/(S+B)$. Events with only one track were selected in order to avoid high occupancy and tracks were selected almost perpendicular to the modules to avoid uncertainties in the module assignment during track propagation. The selected region for performing the study and the measured efficiencies for TIB/TOB are shown in figure 3. The layer efficiency is more than 99.7% for both single sided and double sided layers.

4. Gain Measurement

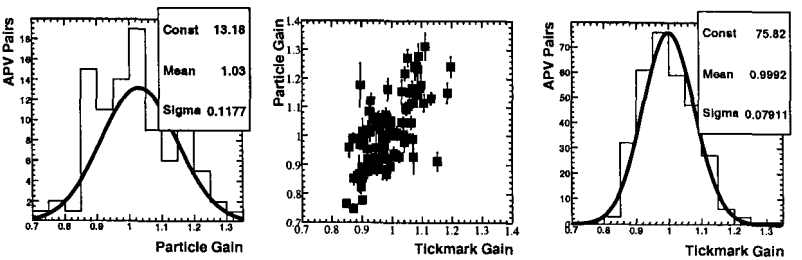

Fig. 4. Distribution of gain inter-calibration constants for APV pairs calculated with the particle and tickheight methods as well as the correlation between the two.

Charged particles passing through the silicon material of the tracker release charge that translates into ADC counts assigned to the set of channels that make up a cluster. Non-uniformities both in the charge collection and in the readout chain affect the aplification and the linearity of the primary charge.[3] Linearity and uniformity of the amplification (gain) across the channels of a silicon module is fundamental for the ultimate space resolution of these detectors. Also, the performance of particle identification technique with energy loss (Section 5) depends both on the absolute calibration and on gain non-uniformities. Two complementary methods are used to perform the inter-calibration of the APV pairs. The tickmark method uses a signal with constant height generated by each APV. The particle method uses hits from tracks crossing the silicon material and takes into account also non-uniformities in the silicon, amplification chain preceding the LLD and non-perfect synchronization of the readout. The gain correction factors for both methods applied to MTCC data and their correlation on an APV pair basis are shown in figure 4. A correlation between the methods is observed. The particle gain values are larger than the tick-height ones.

5. Particle Identification with the Energy Loss Technique

The energy deposit into the silicon layers of the tracker can be used for particle identification. The signal height from a single microstrip (or pixel) is related to the number of electron-hole pairs created by the traversing particle in the bulk of the silicon module. The dE/dx of the track can provide information for identification of electrons in jets and will be able to

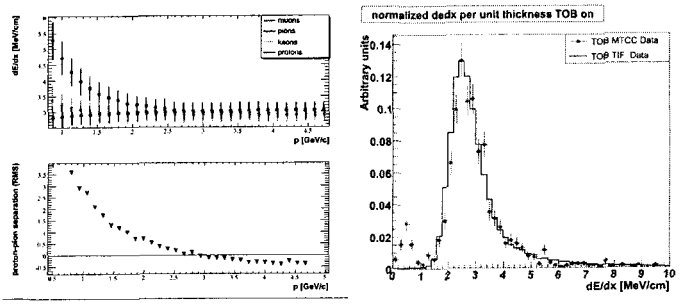

Fig. 5. Left: most probable values for dE/dx from a Landau fit and proton/pion separation as function of the track momentum. Right: Comparison of the dE/dx for TIF and MTCC.

discriminate between different hadron species. This is important particularly for low p_T jets, for which correcting the energy of the proton using its mass instead of the pion mass makes a difference of around 1 GeV. Another important motivation for the development of dE/dx measurements is that a large energy loss is one of the most characteristic signatures of long-lived massive charged particles. The left side of figure 5 illustrates the proton-pion separation at low momenta. Simulated data from a particle gun and the full tracker simulation are used. The right side of figure 5 shows a comparison of dE/dx measurements for the MTCC and the slice test of the TOB at the TIF. No difference is visible in this comparison. The dE/dx in both cases is normalized to the path the particle travels in the silicon.

6. Conclusions

The commissioning run at the TIF and MTCC has been an important experience for the tracker. The tracking system has been successfully commissioned with local and global DAQ and operated together with all other subdetectors of CMS. The tracker perfomance has been excellent and a large sample of data has been gathered. Detailed offline studies are ongoing. Results of some of these studies have been presented.

References

1. CMS Collaboration, CERN/LHCC 98-6, CERN/LHCC 2000-16
2. V. Ciulli, *"The CMS Silicon Strip Tracker: from Integration to Start-Up"*, *Proceedings 10th ICATPP Conference*, (2007)
3. S. Dris, K. Gill, F. Vasey *CMS Note* **2006 / 145** (2006)

TRB for HADES and FAIR experiments at GSI

I. FRÖHLICH , C. SCHRADER, H. STROEBLE, J. STROTH, A.TARANTROLA

Institut fur Kernphysik, Johann Goethe-Universitat, 60486 Frankfurt, Germany

M. KAJETANOWICZ

Nowoczesna Elektronika Pl-30-109 Cracow, Poland

K. KORCYL, W. KRZEMIEŃ*, M. PALKA, P. SALABURA, R. TRĘBACZ

Institute of Physics, Jagiellonian University, Pl-30-059 Cracow, Poland
**E-mail: wojciech.krzemien@if.uj.edu.pl*

P. SKOTT, M. TRAXLER

Gesellschaft fur Schwerionenforschung mbH 64291 Darmstadt, Germany

TRB module is a multi-purpose Trigger and Readout Board with on-board DAQ functionality developed for the upgrade of the HADES experiment. It contains single computer chip (Etrax) running Linux and the 100 Mbit/s Ethernet interface. It has been orginally designed as the 128-channel Time to Digital Converter based on the HPTDC chip from CERN. The new version of TRB contains 2 Gbit/s optical link and interface connector (15 Gbit/s) implementing the add-on card concept and making the board more flexible. Moreover, FPGA chip (Xilinx, Virtex 4 LX 40) and TigerSharc DSP provide new computing resources which can be used to run on-line analysis algorithms. The TRB is proposed as a prototype of base readout module for the planned detector systems PANDA and CBM at the future FAIR facility at GSI-Darmstadt.

Keywords: Triggering; Data acquisition.

1. Introduction

HADES is a high resolution dilepton spectrometer for hadron and heavy ion physics at the SIS18 accelerator facility of GSI, Germany.[1] Its main goal is the study of in-medium modification of light vector mesons proper-

ties. PANDA[2] and CBM[3] are detector systems which will operate at new Facility of Antiproton and Ion Research (FAIR) at GSI. The large research program of PANDA and CBM will address the questions of the generation of mass, spontaneous breaking of chiral symmetry, the limits of hadronic existence and the transition to de-confined matter.[4] To provide access to rare decay channels the experiments will be operated at high luminosity. The cross sections and branching ratios of interesting processes are low and the background will be of orders of magnitude higher in yields[4] Therefore, to collect statistically relevant data, the detector systems should operate with the interaction rates above 10 MHz. This is a real challenge in the data acquisition domain. HADES experiment implements classical two-level trigger system whereas the PANDA and CBM plan to design their DAQ systems without the central trigger. The data generated by subdetectors are time stamped and sent to the event builder. In this approach a large amount of data has to be handled and so there is a need for a high level data reduction mechanisms. A universal readout electronics for various detectors need to be developed. Trigger and Readout Board (TRB) is a general-purpose electronic device which can be used as base readout module for the development of the future DAQ systems in the FAIR experiments.

2. TRB board version 1

TRB version 1 (TRBv1) has been orginally developed as a 128-channel Time to Digital Converter based on the HPTDC chips. It contains 4-input connectors (high density 80 pins). Each connector permits to sample 31 LVDS timing signals. Four 32-channel HPTDC chips perform time to digital conversion. 32th channel of each HPTDC is connected to the external reference timing signal. The HPTDC chips are highly configurable.[5] The TDC binnig could be chosen in the range of 25 to 780 ps. The HPTDC allows to measure rising and falling edges, and to define a matching window. TRBv1 contains also FPGA Controller (Xilinx Spartan 2), FIFO queue and dual ported RAM memory. The Slow control and the DAQ functionality is done via Etrax - single computer chip running Linux operation system.[6] The data acquisition is started by external level one trigger (LVL1). FPGA controller initiates the readout and the selected data from HPTDC is stored in the FIFO queue where it is waiting for the level two trigger (LVL2). If the LVL2 signal is positive data is moved to the dual ported RAM. The data is then read out by the Etrax and send via UDP protocol over 100 Mbit/s Ethernet to the event builder.

The time resolution between two channels from different HPTDC chips

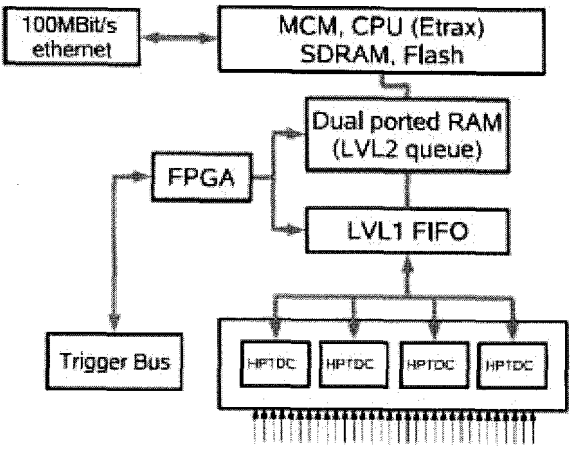

Fig. 1. TRBv1 block diagram. The readout of the data is started via the signal on the trigger bus. The data is stored in the FIFO queue until the LVL2 decision arrives. Final data formatting is done by Etrax chip.[4]

resulted 40 ps (with 100 ps binning).[4] The crosstalk influence to resolution has been estimated to be less than 20 ps. The maximum data transport rate via UDP has been measured: 8 MB/s.[6] The maximum LVL2 trigger rate was about 18 kHz. TRBv1 has been tested and succesfully used in the new RPC detector as a part of the upgrade of HADES detector system.

3. TRB board version 2

The enhanced version of TRB module (TRBv2) has been developed. The TRBv2 has been designed as multi-purpose readout module which could be used for all types of detectors. It uses Etrax-FS processor with Linux operation system for DAQ and slow-control functionality. It has three integrated I/O co-processors (each 200 MHz) which allow to use the bandwidth more efficentally without using too much CPU computing resources. It eliminates the bottelneck observed in the TRBv1. The TRBv2 has in addition an optical link 2 Gbit/s which can be used for data transmission in the future applications. The FPGA in the TRBv2 has been upgraded to Xilinx Virtex 4 LX40 with 128 MB RAM. The new version of the board provides place for the TigerSharc DSP which may be used to implement

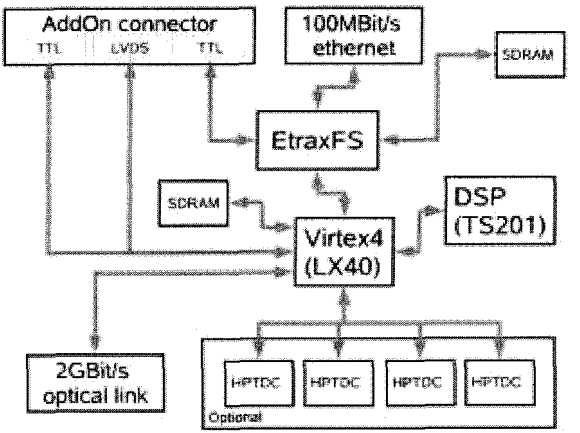

Fig. 2. TRBv2 diagram block. It consists of 4 HPTDC chips (optional), Etrax-FS processor with 128 MB, Ethernet interface, 2 Gbit/s optical link, FPGA Virtex 4,and TigerSharc DSP.[4]

on-line analysis algorithms. To broaden the spectrum of the applications TRBv2 is equipped with a high data-rate digital interface connector (32 LVDS lines, 15 GBit/s) which allows to connect add-on boards with the TRB. The concept of add-on boards is explained in the next section.

4. Add-on cards

TRBv2 has been designed as a detector-independent base readout module. All detector-specific FEE, interfaces and connectors are placed on the add-on cards which can be easily mounted on the TRB. Additional computing resources such as FPGA or DSP could be added to the add-on card. The first add-on card for the MDC readout has been developed. It has 10 connectors. Each connector has 50 pins and 2 RS485 transcivers. The operation of the MDC-add-on card is controlled by the FPGA (Xilinx, XC4VLX-10FF1148) chip. MDC-add-on board is connected back to back to the TRBv2 via two connectors (SAMTEC QSE-040-01, 80 pins each) and allows to read out each MDC-chamber by one single TRB board. The concept of add-on boards provides a possibility to mount specific-detector resources in a flexible way, using the same base readout module for every detector.

5. Conclusion

The multi-purpose trigger and readout board with the on-board DAQ functionality(TRB) has been presented. TRB has been designed for the HADES readout system. However, it can be used also in new CBM and PANDA detector systems which will operate at FAIR facility at GSI. TRB version 1 has been designed as a 128-channel Time to Digital Converter based on the HPTDC chip. The module has been succesfully implemented to readout of the RPC detector. It has been also used in the prototype drift chamber tests for PANDA. TRB version 2 has an 2 GBit/s optical link, add-on card connectors, as well as a place for the TigerSharc DSP. Add-on board for MDC, PreShower and for other types of detectors are currently being tested. It is planned to use add-on board which will serve to the readout the MAPS sensors for the CBM experiment. TRB module is proposed as a standard base readout module for the new FAIR experiments.

Acknowledgments

This work has been supported by the EU under the contracts CNI DIRAC-PHASE-1 (515876) and Hadron Physics (RII3-CT-2004-506078), the BMBF, the Helmholtz Research School, the Polish MEEN (158/E-338/SPB/6.PR UE/DIE 455/2004-2007) and GSI.

References

1. *High Acceptance Dilepton Spectrometer*, http://www-hades.gsi.de/
2. M. Kotulla *et al.*[PANDA Collaboration], *Strong interaction studies with antiprotons. Letter of intent for PANDA (Antiproton Annihilations at Darmstadt).*
3. *The Compressed Baryonic Matter Experiment at FAIR*, http://www.gsi.de/fair/experiments/CBM
4. M. Traxler *et al., A General Purpose Trigger and Readout Board for HADES and FAIR-Experiments.*
5. J. Christiansen, Digital Microelectronics Group, CERN.
6. R. Trebacz, *Single-Chip-Linux-Computer for the HADES-experiment Data-Acquisition*, GSI Summer Student Programm 2004.

LOW AND HIGH INTENSITY BEAM MONITORING AND TRACKING

D.LIETTI[a], A.BERGAMASCHI[d], D.BOLOGNINI[b], J.COLOMBO[a], S.HASAN[b], A.MATTERA[a], A.MOZZANICA[c], M.PREST[b], B.SCHMITT[d], E.VALLAZZA[e]

[a] *Università degli Studi dell'Insubria, Como, Italy*
[b] *Università degli Studi dell'Insubria e INFN sezione di Milano Bicocca, Italy*
[c] *Università degli Studi di Milano e INFN sezione di Pavia, Italy*
[d] *PSI, Villigen, Switzerland*
[e] *INFN sezione di Trieste, Italy*

Several detector types have been designed and assembled in order to monitor charged particle beams in a wide range of intensities: silicon microstrip detectors for high precision tracking (spatial resolution better than 5 μm), a scintillating fiber tracker with multianode photomultiplier readout for coarse but fast monitoring, a microstrip silicon detector readout by a counting ASIC to monitor very high intensity beams.
These detectors and their readout electronics have been characterized at the BTF (Beam Test Facility) of the INFN National Laboratories of Frascati and used on the H8 line at the CERN SPS as tracking media for the data taking of the H8RD22 collaboration.
The paper describes the results obtained in terms of spatial resolution and maximum counting rates.

Keywords: silicon microstrip detectors, scintillating fiber tracker, channeling

1. Introduction

Scintillating fiber (SciFi) and silicon microstrip detectors are used in high energy physics for their excellent characteristics: the fast response of SciFi makes them ideal for triggering while the high resolution of silicon is the right key for tracking purposes.
This article describes the design, assembly and test of three different types of detectors developed to monitor charged particle beams in a wide range of intensities: a silicon microstrip telescope for high precision monitoring, a SciFi tracker for coarse but fast tracking, and a silicon profilometer for high intensity beam monitoring. Each detector has been characterized in February '07 at the BTF (Beam Test Facility) at the INFN National Laboratories of Frascati (Rome) and used on the H8-line at the CERN SPS (May '07) for bent silicon crystal channeling measurements. Sec. 2 describes the detectors layout and electronics while Sec. 3 is

dedicated to the experimental results.

2. Detectors description

2.1. *TELESCOPE: the silicon microstrip detector*

It consists of 4 modules built in 1995 by INFN TS along the lines described in [1] for the commissioning of the BaBar detectors [2], each one enclosed in an Al box which houses part of the readout electronics. The detector is a double sided high resistivity silicon microstrip detector, 300 μm thick and with an effective area of 1.92×1.92 cm^2 (Fig. 1(a)). The p-side has a p+ implantation strip every 25 μm and a readout pitch of 50 μm. The n-side has n+ implantation strips every 50 μm, spaced with p+ blocking strips. Each side is divided in 768 strips connected to the readout ASICs with external quartz capacitors. The readout low noise VA2 ASICs are glued on a substrate of ceramic providing the digital control signals and the routing of the analog ones. Fig. 1(b) shows one of the telescope modules on the H8 SPS beam line.

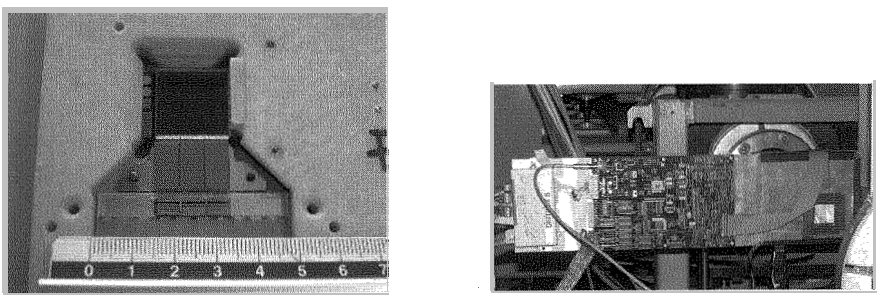

(a) (b)

Fig. 1. *The silicon telescope detector (a) and the complete module (b) positioned on the H8 beam line.*

2.2. *ERPA: the SciFi tracker*

ERPA is a detector for coarse but fast monitoring, consisting in 2 modules with two x-y layers with 64 channels each; each layer is composed of 1 mm diameter fibers (BCF-10, Bicron) arranged as in fig. 2(a) in order to reduce dead regions and obtain a better spatial resolution. The effective sensitive area is 6.4×6.4 cm^2. The

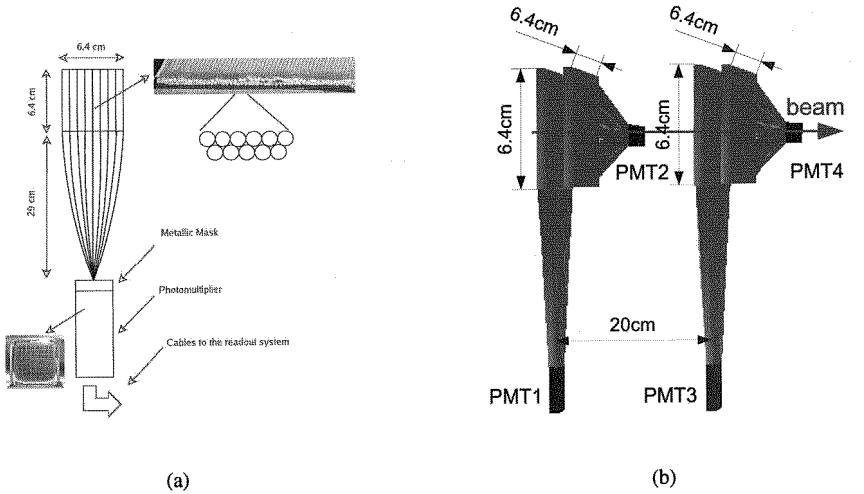

(a) (b)

Fig. 2. *Fiber layout (a) and overall tracker design (b).*

mechanical support for the fibers and the readout electronics is a 0.5 cm thick PVC plane (55×55 cm^2). The fibers are 35 cm long and have been covered with a thin layer of dark plastic to avoid light. They have been polished with sandpaper and abrasive grease, and connected to a multianode PMT (H5746B, HAMAMATSU). Fig. 2(b) shows the overall design scheme of the detector.

The coupling beetween the fibers and the PMT was performed with a 3×3 cm^2 metallic mask with 64 2×2 mm^2 square holes (mod.A) with 2 fibers each and with a similar mask with 8 2×20 mm^2 slits (mod.B). The net result is a readout pitch of 1 mm in mod.A and 1.3 mm in mod.B.

The SciFi tracker readout electronics is based on the VA64TAP2.1 ASIC (IDEAS, Norway), which amplifies and shapes the analog signals of the PMT, and on the LS64_2 that shifts the trigger outputs. The fiber tracker can work in analog mode, with a multiplexed readout, or in full digital mode in two different ways:

- with each channel acting as a counter, thus behaving as a profilometer,
- with a sampling clock to tag the arrival time, as shown in [3] .

2.3. *The silicon profilometer*

The Si profilometer [4–6] detector (PSI-INFN TS) consists in a single side silicon microstrip detector (HAMAMATSU), 12 cm long and 300 μm thick with 2368

50 μm pitch strips (fig. 3(a)).

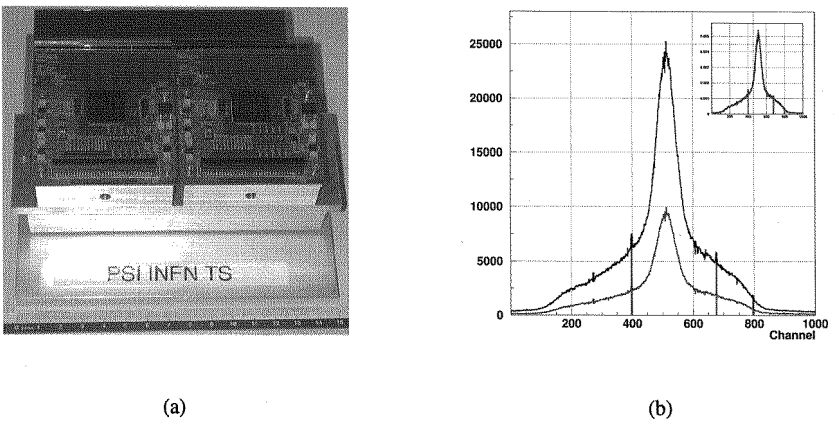

(a) (b)

Fig. 3. *The silicon profilometer readout by 19 Mythen-II ASICs (a) and the beam profile for two different particles fluxes (b); the insert shows the two profiles rescaled to their total entries to demonstrate that no saturation effect is present.*

This detector is readout by a "counting" electronics (it counts the signals over threshold in a given time window), the 128 channels Mythen-II ASIC consisting in a charge preamplifier, two shapers, a discriminator with a global threshold for the ASIC and a 6 bit trim DAC per channel and a 24 bit counter. The Mythen-II ASIC is linear up to 3 MHz per channel. The silicon profilometer is readout by 19 Mythen-II ASICs.

The VME readout system is the same for the silicon telescope and the scintillating fiber tracker, while the silicon profilometer works in a standalone mode.

3. Measurements

Several measurements were performed to characterize the detectors in terms of spatial resolution and efficiency both at the BTF with a 463 MeV electron beam (in which case multiple scattering effects had to be taken into account) and at the CERN SPS with a 400 GeV/c proton beam.
The spatial resolution has been measured using the residual distribution obtained reconstructing the tracks with a set of silicon chambers (with a spatial resolution of 20 μm) for the SciFi at the BTF and for one of the telescope planes sandwiched

between the other two at the SPS H8-line. Table 1 presents the spatial resolution of the SciFi modules, while the resolution of the telescope on the SPS beam line resulted of 3.38±0.05 μm. Both the systems have an efficiency greater than 99%.

Table 1. SciFi tracker spatial resolution.

Mod.	x (μm)	y (μm)
A	613.28±0.09	665.15±0.09
B	716.01±0.01	639.38±0.01

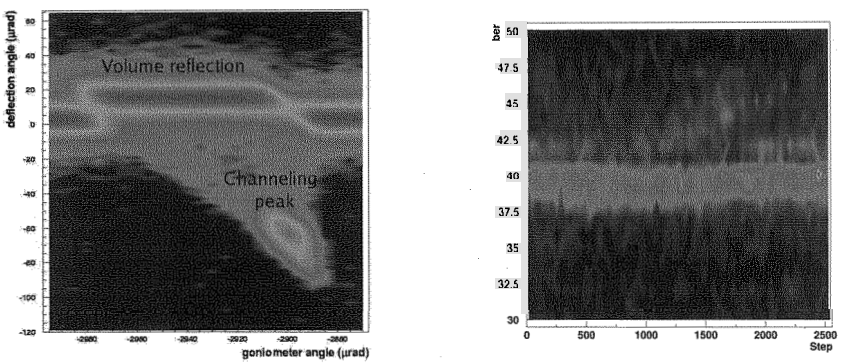

(a) (b)

Fig. 4. *QM2 silicon crystal channeling: the deflection angle, computed as the difference between the reconstructed tracks with the telescope modules before and after the crystal, as a function of the goniometer angle (a) and the same plot for the beam profile obtained with the SciFi tracker (b) with the vertical axis upside down.*

As far as the silicon profilometer is concerned, fig. 3(b) shows the beam profiles measured at the H8 beam line with two different fluxes: $4.8 \cdot 10^6$ (black) and $1.8 \cdot 10^6$ (red) particles in a 4 s spill. The insert presents the two profiles each one rescaled to its total entries: no saturation effect is present since the two shapes are perfectly the same.

The 3 detectors have been used at the SPS by the H8RD22 collaboration to check the beam intensity and profile and for channeling measurements [7]. In fig. 4(a)

the beam deflection angle caused by a Quasi-Mosaic Crystal (a crystal that was cut parallel to its lattice and then bent) as a function of the rotational angle of the crystal with respect to the beam is reported. Thanks to the high resolution of the telescope it is possible to distinguish the volume reflection region, that corresponds to the particles that were reflected into the crystal lattice, from the amorphous beam (the particles that see the crystal as an amorphous material). The scan with the SciFi tracker (fig. 4(b)), even if with a worse resolution, allows anyway to see the details. The resolution will be improved using 250 μm diameter fibers, while the maximum allowable rate can be increased from a few kHz to several hundred kHz per channel just switching from the analog to the digital readout; in this way a fast scan of several crystals for a mass test can be foreseen.

4. Conclusions

Three different detectors with very different features and goals have been developed and tested: a high resolution silicon telescope for beam monitoring with a spatial resolution better than 4 μm and a 99% efficiency; a fast SciFi tracker with a good enough spatial resolution (650 μm) and an efficiency of 99%; a silicon profilometer for very high intensity beam monitoring. The detectors operated successfully at the H8 SPS beam line for the measurements of channeling effects in bent crystals.

References

1. M.de Palma et al., *A high resolution beam telescope built with double sided silicon strip detectors*, NIM A 381 (1996) 49-56
2. M.Bari et al., *Results form the BaBar Silicon Vertex Tracker Test Beam*, BaBar Note #278 (1996)
3. V.Mascagna et al., *FAST: a compact scintillating fiber detector for Antiproton cross section measurements*, ICATPP Conference 2007
4. B.Schmitt et al., *Mythen detector system*, NIM A 501 (2003) 267-272
5. B.Schmitt et al., *Development of single photon counting detector at the SLS*, NIM A 501 (2004) 436-439
6. D.Dreossi et al., NIM A 576 (2007) 160-163
7. S.Hasan et al., *Bent Silicon Crystals for the LHC collimation: test with 400 GeV/c protons*, ICATPP Conference 2007

DEVELOPMENT OF A DETECTOR (ALFA) TO MEASURE THE ABSOLUTE LHC LUMINOSITY AT ATLAS

A. MAPELLI[a], F. ANGHINOLFI[a], S. ASK[a], P. BARRILLON[b], G. BLANCHOT[a], S. BLIN[b], A. BRAEM[a], C. CHEIKLALI[b], C. DE LA TAILLE[b], B. DI GIROLAMO[a], I. EFTHYMIOPOULOS[a], J. FAUSTINO[c,d], D. FOURNIER[b], S. FRANZ[a], P. GRAFSTRÖM[a], L. GURRIANA[d], M. HAGUENAUER[e], V. HEDBERG[f], M. HELLER[b], S. HOFFMANN[g], W. IWANSKI[a,h], C. JORAM[a], A. KOCNÁR[i], B. LAVIGNE[b], B. LUNDBERG[f], A. MAIO[d,j], M.J.P. MANEIRA[c], C. MARQUES[d], U. MJÖRNMARK[g], P. CONDE MUÍÑO[c,d], P. PUZO[b], M. RIJSSENBEECK[k], J.P. SANTOS[d], J.G. SARAIVA[d], N. SEGUIN-MOREAU[b], S. SOARES[d,j], H. STENZEL[g], M. THIOYE[k], E. VALLADOLID-GALLEGO[a], V. VOROBEL[i]

[a]*CERN, PH Department, Geneva, Switzerland*
[b]*LAL, Univ. Paris-Sud, CNRS/IN2P3, Orsay, France*
[c]*CEFITEC/Faculdade de Ciências da Universidade de Lisboa, Lisbon, Portugal*
[d]*LIP – Laboratorio de Fisica Experimental e Instrumentacão em Partículas, Lisbon, Portugal*
[e]*Ecole Polytechnique, Palaiseau, France*
[f]*University of Lund, Lund, Sweden*
[g]*II. Physikalisches Institut, Justus-Liebig- Universität, Giessen, Germany*
[h]*IFJPAN. Krakow, Poland*
[i]*Faculty of Mathematics and Physics, Charles University in Prague, Czech Republic*
[j]*CFNUL/Faculdade de Ciências de Universidade de Lisboa, Lisbon, Portugal*
[k]*Stony Brook University, New York, USA*

The ATLAS collaboration plans to determine the absolute luminosity of the CERN LHC at Interaction Point 1 by measuring the trajectory of protons elastically scattered at very small angles (μrad). A scintillating fibre tracker system called ALFA (Absolute Luminosity For ATLAS) is proposed for this measurement. Detector modules will be placed above and below the LHC beam axis in roman pot units at a distance of 240 m on each side of the ATLAS interaction point. They allow the detectors to approach the beam axis to millimeter distance. Overlap detectors also based on the scintillating fibre technology, will measure the precise relative position of the two detector modules. Results obtained during beam tests at DESY and at CERN validate the detectors design and demonstrate the achievable resolution. We also report about radiation hardness studies of the scintillating fibres to estimate the lifetime of the ALFA system at different operating conditions of the LHC.

1. Introduction

The ATLAS experiment will determine the absolute luminosity of the CERN LHC at Interaction Point 1 (IP1) to a precision $\Delta L/L \sim 3\%$ by measuring the

trajectories of elastically scattered protons at very small angles in the limit of the Coulomb Nuclear interference region[1]. A tracker system called ALFA (Absolute Luminosity For ATLAS) is proposed for this measurement. It is based on scintillating fibres and will be located in Roman Pots above and below the LHC beam axis at a distance of 240 m on each side of IP1. The first ALFA detector prototypes were tested at DESY in 2005[2], demonstrating that the main requirements of the fibre tracker can be achieved with the current design. A further test beam was carried out at CERN in 2006[3], with the main objectives of testing the first prototype of the dedicated Front-End (FE) electronics[4] and the alignment method using overlap detectors[5] (ODs). During the summer of 2007, plastic scintillating fibres have been irradiated in a proton beam at CERN and characterized[6].

2. Requirements on the detector

In order to approach the beam at mm distance the tracker should not have any sizeable inactive region (< 100 μm). The spatial resolution should be significantly smaller than the size of the beam spot at the detector; a resolution of 30 μm or better is required. The vertical distance between the upper and lower tracker must be known with a precision of about 10 μm. The detectors have to be insensitive to RF emitted by the LHC beam and to possible magnetic stray fields from nearby magnets. They need to operate in a secondary vacuum inside the roman pots and need to stand an accumulated dose of 100 Gy/yr.

3. The ALFA system

A tracking detector based on plastic scintillating fibres fulfills the requirements in a simple and cost effective way. As shown in Figure 1 it will be inserted in a roman pot together with an OD that is also a scintillating fibre tracker that reconstructs only the vertical coordinate for the precise relative alignment of the top and bottom pot. Trigger scintillators[a] define the active areas of the tracker and the ODs. The baseline fibres[b] of the ALFA tracker and the overlap detector are coated with an Al film to avoid cross talk. They are routed inside the roman pot to fibre connectors and coupled to MAPMTs[c]. The fibre connectors are inside the vacuum flange that closes the roman pot and the MAPMTs are inside

[a] 3 mm thick Bicron BC-404

[b] Kuraray SCSF-78, S-type, 0.5 × 0.5 mm^2 square section

[c] Multi-Anode PhotoMultiplier Tube R7600 from Hamamatsu

a mu-metal shield. The very compact FE electronics is mounted directly on the back of the MAPMT.

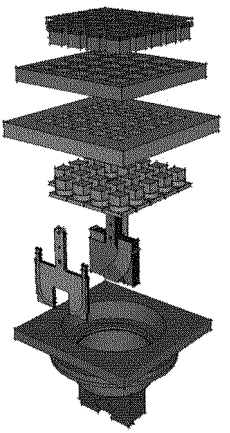

Figure 1. Exploded view of one detector unit of the ALFA system. From bottom to top we see the roman pot, the overlap detector and the tracker, the fibre connectors, the vacuum flange, the mu-metal shield and the MAPMTs with the PMFs. Not shown on the drawing are the trigger scintillator tiles.

The tracker consists of 10 ceramic plates (170 μm thick) supporting 2 layers of 64 fibres arranged in UV geometry under an angle of ±45° relative to the vertical axis. The planes are staggered by multiples of (500μm/10) × √2 = 70.7 μm to obtain an effective fibre pitch of 50 μm and a theoretical spatial resolution of $\sigma_{x,y}$ = (500μm/10)/√12 = 14.4 μm. Recently an alternative design has been proposed where titanium plates are used instead of ceramics. A prototype of a tracker based on this new design is under construction.

Each Roman Pot unit (upper and lower pots) will house in special extrusions two ODs (one in each pot) to determine the precise relative position of the upper and lower pot. They consist of 3 planes vertically staggered by multiples of (500μm/3) = 166.7 μm. Horizontal fibres define an active area of 6 × 15 mm^2. The ODs will be precisely positioned relative to the tracker.

Due to space limitations a very compact system design[4] is adopted where a large part of the binary FE electronics is mounted directly at the back of the MAPMTs. The so-called PMF (PhotoMultiplier Front-end) is a stack of three PCBs. The first board from the MAPMT is a custom voltage divider, the second board routes the signals to the third board which contains the MAROC[7] chip (Multi-Anode Readout Chip) and an FPGA called ALFA-R[8] (ALFA Readout) on the other side. The MAROC chip contains variable gain preamplifiers to correct for the MAPMT non-uniformity and transmits binary information to the ALFA-R which stores it in a pipeline until it receives an ATLAS Level 1 Accept

trigger signal via the TTC (Timing, Trigger & Control) system. The data is then sent to the Roman Pot mother board which formats it and sends it to the common ATLAS readout system[9] through a Gigabit Optical Link.

4. Beam tests of prototype ALFA detectors

The results obtained during the beam tests confirmed the detector's design. The baseline fibre gave an average light yield of approximately 4 photoelectrons for an efficiency of 95% leading to a tracking efficiency of the detector superior to 99%. The spatial resolution of the tracker was of 36 μm during the first test beam with 6 GeV electrons. During the second test beam a spatial resolution of 23 μm was found with 230 GeV protons in agreement with the 30 μm required. No significant dead space at the edge of the detector was identified.

In addition to the ALFA prototype trackers two prototype ODs were built and tested. One OD consisted of 2 staggered layers with 30 fibres each. The ODs, as well as the alignment method, were tested for the first time in the CERN test beam achieving a vertical relative alignment with a precision better than 15 μm.

5. Characterization of irradiated scintillating fibres

Scintillating fibres of various types[d] were irradiated with 24 GeV/c protons with fluences ranging from 6.78×10^{11} p·cm^{-2} to 8.40×10^{15} p·cm^{-2} in the IRRAD1 facility[10] in the T7 beam line of the CERN PS accelerator. A specially designed tooling allowed simultaneous irradiation of fibres along the beam axis and fibres perpendicular to the beam. The irradiation campaign lasted 1 month and 7 batches of fibres were irradiated to doses ranging from about 100 Gy to more than 2 MGy. The light yield of fibres was measured by exciting them with a Sr-90 source. The fibre under test was coupled to a silicon photomultiplier[e]. An Al-coated reference fibre coupled to a photomultiplier tube[f] served as trigger. From the spectra obtained we determined the average number of photoelectrons for each fibre and calculated the detection efficiency which is plotted in Figure 2 as a function of the accumulated dose. The analysis[6] is ongoing and preliminary results show that the ALFA baseline fibre's efficiency starts decreasing for doses greater than 3 kGy. This confirms the full suitability of the scintillating fibre technology for luminosity measurements and indicates its potential for

[d] Kuraray SCSF-78 with and without Al-coated, Kuraray 3HF, Bicron BCF-12; all fibres have a square section of 0.5×0.5 mm^2.

[e] Hamamatsu MPPC (Multi Pixel Photon Counter) S10362-11-100U

[f] Hamamatsu R647-01

physics runs up to a luminosity of 10^{31} $cm^{-2}s^{-1}$ assuming that proton-proton interactions dominate over background of the beam halo[6].

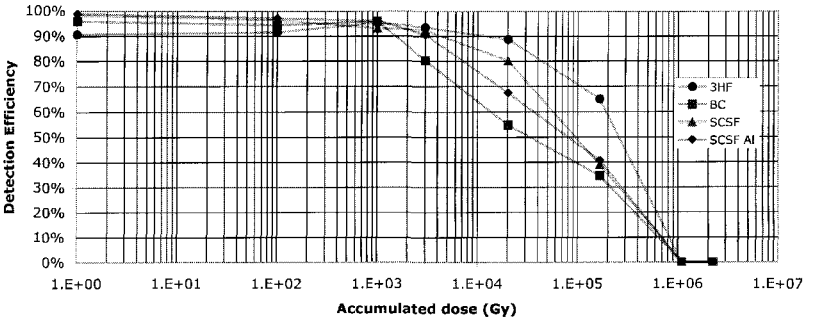

Figure 2. Detection efficiency of single fibres as a function of the dose (preliminary results).

6. Conclusions

Two beam test experiments have allowed us to validate the design of the ALFA tracker and to confirm that it meets the requirements for a precise measurement of the absolute luminosity at Interaction Point 1 where the ATLAS detector is located. The alignment method of the roman pots with overlap detectors has proven to provide the required precision. The next step is to build a full-size detector of 10 planes with 2 layers of 64 fibres each that will be integrated in a Roman Pot unit together with the overlap detectors and the trigger counters. The aim is to obtain a full system including also the front-end electronics to evaluate its performance and address integration issues such mounting and alignment precision.

References

1. ATLAS, CERN-LHCC/04-10, LHCC I-014.
2. S. Ask et al., *NIM* **A568**, 588 (2006).
3. F. Anghinolfi et al., *Jinst* **2** P07004 (2007).
4. G. Blanchot et al., presented at the 1st TWEPP, Prague, Czech Republic, 3-7 Sep 2007.
5. A. Mapelli et al., ATL-LUM-PUB-2007-004, 2006.
6. A. Mapelli et al., ATL-COM-LUM-2007-009, 2007.
7. P. Barrillon et al., presented at the 2006 IEEE NSS, San Diego, USA, 29 Oct - 2 Nov 2006.
8. W. Iwanski, presented at the 1st TWEPP, Prague, Czech Republic, 3-7 Sep 2007.
9. ATLAS, CERN/LHCC/2003-022, 2003.
10. M. Glaser et al., *NIM* **A426**, 72 (1999).

The Tracker–Muon Hardware Alignment System of CMS

Celso Martínez Rivero
(on behalf of the CMS Hardware Alignmment Group)
Instituto de Fisica de Cantabria (CSIC-UC),
Avda. de los Castros s/n, 39005 Santander. Spain.

The CMS detector has been instrumented with an optical and mechanical system that allows to perform a link between the central Tracker of the detector with the outer Barrel and Endcap muon chambers in order to relate the local alignments of these subsystems in a common reference frame.In this paper the system will be described in detail and preliminary resuls of its operation under different magnetic conditions during the MTCC done in 2006 will be reported

1. Introduction

The CMS Magnet Test and Cosmic Challenge -MTCC- took place in two different phases during Summer and Autumn 2006 in SX5 at CERN. Several components of the muon system were tested, amongst them a fraction of the hardware alignment system.

This document describes the basic setup of the Alignment Hardware installed during the MTCC followed by the reconstruction methods used for the analysis. Finally some prelimary results obtained from the Link subsystem both from direct observation of analog data and offline reconstruction of data coming from digital sensors are presented.

2. General description of the Muon Alignment system

The Muon Hardware Alignment system consists of three different subsystems, which are described below.

The Barrel Alignment system [1] measures the positions of the barrel muon chambers with respect to each other and the whole barrel muon spectrometer. Each barrel muon chamber is equipped with light sources (LEDs, more than 9000 in total). The LEDs are observed by small video-cameras (600 in total) mounted on rigid carbon-fiber structures called MABs (Module for the Alignment of the Barrel). There are direct observations between

the MABs called diagonal connections. The system is completed with long carbon bars called z-bars fixed to the vacuum-tank of the magnet.The z-bars (12 in total, 6/side) are also equipped with LED light sources and observed by video-cameras mounted on the MABs. The MABs (36 altogether) are fixed to the return yoke in the gaps between the barrel wheels (6 per gap) and on both ends of the barrel (6 per side). The MABs on the two ends, containing Link and Endcap elements are used to connect the three alignment subsystems to each other. During the MTCC the two bottom sectors of the full barrel were equipped (10 MABs, 4 z-bars).

The Endcap Alignment system [1] is designed to monitor the relative positions of the CSC chambers. The system consists of different components: the axial transfer lines, consisting of laser lines connecting end-cap to the external MAB's using DCOPS (Digital CCD optical position sensor); a straight-line monitoring measuring the relative position of chambers in the same disk; Z and R-monitoring sensors. The muon end-cap ME+ on the positive z-side of the CMS detector was fully instrumented with alignment sensors for the MTCC.

The purpose of the link alignment system is to measure the relative positions of the muon spectrometer and the tracker in a common CMS coordinate system. It is designed to work in a challenging environment of very high radiation and magnetic fields, meet tight space constrains, and provide high precision measurements over long distances. A distributed network of opto-electronic position sensors placed around the muon spectrometer and tracker volumes are connected by laser lines. The ASPD 2D sensors (Amorphous Silicon Position Detector) consist of two groups of 64 silicon micro-strips with a pitch of 430 microns oriented perpendicularly.

The entire system is divided into three ϕ-planes 60° apart. Each plane consists of four independent quadrants, resulting in 12 laser paths, or lines: 6 on each side (positive or negative z) of the CMS detector, matching the 12-fold segmentation of the barrel muon spectrometer. Rigid carbon fiber annular structures are placed at both ends of the tracker (Alignment Rings) and at the YE+1 and YE-1 wheels of the end-cap muon spectrometer (Link Disks). Rigid structures called MABs are also attached to the barrel yokes. These are the reference structures for the alignment of the muon spectrometer. The ME1/1 and ME1/2 disks of the end-cap muon spectrometer are also linked to the corresponding MAB via an opto-mechanical transfer plate. The link measurement network is complemented by electrolytic tiltmeters, proximity sensors (optical and mechanical), magnetic probes and temperature sensors.

One can see in figure 1 a sketch of the position of the analogical proximity sensors –indicated by broad arrows– (left) and the direction followed by the three laser paths active during the MTCC (right).

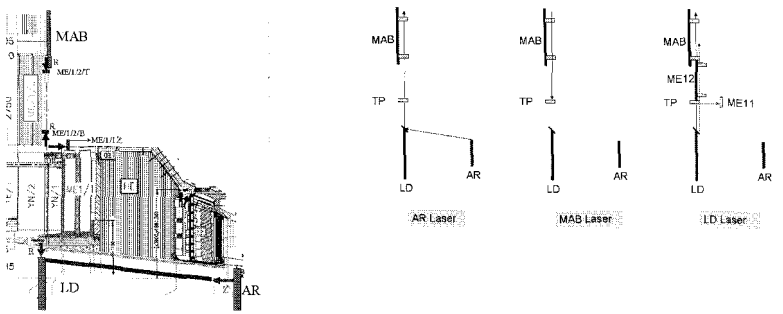

Fig. 1. Sketch of the position of the analogical proximity sensors of the Link System (left) and of the three laser paths of the Link System (right).

3. Link Hardware Alignment MTCC Results

Only three light paths, or lines (out of a total of 12), were instrumented for the MTCC: 75+,255+ and 315+, where the number refers to the ϕ angle and the sign to the z side of the detector. Each light path contains three lasers, one in the Alignment Ring (AR), one in the MAB and one in the Link Disk (LD) (see figure 1 for a sketch). The readout sequence for the link is the following: all lasers from the AR turn on simultaneously and stay on for two minutes –impacting over the TP and MAB sensors–. After this, the AR lasers are turned off and all MAB lasers turn on for two minutes –impacting over the MAB and TP sensors– and finally the MAB lasers are turned off while the LD lasers are turned on for two minutes –impacting over TP, ME11, ME12 and MAB sensors–. This six-minute reading cycle –called an event– is repeated starting again with the AR lasers.

The global reconstruction of the muon alignment events is handled by COCOA [2], which obtains positions and orientation angles of defined reference points or structures from a non linear least-squares fit of the data. In addition to the measurement files described above, the system description has to be provided. This includes the interconnection of elements (which laser points to which sensor, for example) and hierarchy (which elements are attached mechanically to which structure), together with an approxi-

mation of the geometry provided with previous measurements (calibrations or photogrammetry). Supplying a good estimation of the geometry is not necessary, but speeds the convergence, ensures the goodness of the result and avoids falling in local minima.

Before attempting a full geometry reconstruction, the data from the different sensors in the system allow to measure the relative displacements and deformations of the yoke structures for the different magnet field values. Two effects were observed. The first is the change in the original positions of the structures (the positions before any magnet operation). The displacements of the structures along the z direction towards the solenoid, of about 3 mm for the barrel iron and about 5 mm for the endcap disks, seem to stabilize after the first 2.5–3 T are reached. This compression is permanent, meaning it is not reversed/recovered in subsequent magnet off states, and it is interpreted as the final closing of the structures due to the magnetic forces acting on the iron. The magnitude of the measured displacement are undestood as specific to the fist CMS closing experience and can not be extrapolated to other scenarios. The second effect is the almost perfectly elastic deformations between magnet-on and magnet-off states. The strong magnetic forces pull the central part of the endcap disks towards the solenoid. At 4 T the nose of YE+1 is pulled approximately 16 mm towards the interaction point. This displacement follows , as expected, a quadratic behaviour with the magnet intensity.

A preliminary study on geometry reconstruction of the Link system data has been performed with COCOA. The full system geometry was coded for the MTCC configuration: including 24 ASPD 2D sensors and the data coming from the analog proximity sensors -15 in total-.

An initial geometry was defined based on the calibrated positions and orientations of all the pieces cited above. In order to get the best possible description of the system an exhaustive use of photogrammetry, laboratory 2D and 3D measurements and calibrations were included in COCOA's description file. The photogrammetry of our system taken at SX5 -see [3] as reference document- allowed to put in place the main mechanical structures which support the ASPD's and other devices.

Fits to data taken in different magnetic field configurations were performed in order to compare the variation of positions and orientations monitored by the system. The result of the reconstruction at B=0T at the end of Phase I was taken as input in the reconstruction program as a better estimation of the geometry.

The comparison of two sets of results monitors the displacements of the

different components during the MTCC cycle. Preliminary results show good agreement with the results discussed above and based on the independent analysis of analog sensors response. Table 1 shows the difference in position/orientation for the YE+1, YB+2 and LD disks between the data fit at B=4.0T and the fitted position/orientation at B=0T at the end of Phase I.

Table 1. Preliminary results on the difference in position (in mm) and orientation (in mrad) between the fitted values at B=4.0T and B=0T.

Phase I. B=4.0T	Δ_X	Δ_Y	Δ_Z	Δ_{AngX}	Δ_{AngY}	Δ_{AngZ}
YE+1	-0.13	0.90	-14.66	0.21	0.23	-0.74
YB+2	0.19	3.47	-2.08	-0.07	1.59	-0.89
Link Disk	-0.04	0.43	-0.65	-0.37	-0.12	-0.30

As a first preliminary conclusion from these numbers, the compressed distance between the Link Disk and the Alignment Ring can be directly obtained adding the two Z shifts towards CMS center of the YE+1 disk and the LD disk from table 1: 14.66 + 0.65 = 15.31mm which can be compared with the analogical values of the three distancemeters placed between these two structures giving a compression of 15.5, 15.1 and 15.6 mm respectively for the distancemeters placed at 195, 315 and 75 degrees.

4. Conclusions

A quarter of the Link Hardware Alignment system was installed and operational during CMS MTCC. A first attemp to reconstruct the 3–D geometry of this system was performed by means of a cross–check of data reconstruction at B=0T against photogrammetry survey of some reference points, resulting in a good undestanding of the system. Furthermore, data taken by this system were analysed at different field conditions to get an estimate of the global movements of different detector structures like Endcap or Barrel disks.

References

1. CMS Technical Design Report "The Muon Project", CERN/LHCC 97-32, CMS TDR 3, 15 December 1997
2. P.Arce and A.L.Virto, "CMS Object Oriented Code for Optical Alignment (COCOA)", CMS Note 2002/060
3. J.F.Fuchs, R.Goudard and J.D.Maillefaud, "CMS-YE+1 Photogrammetry of the YE+1", CMS-SG-UR-0058

FAST: A COMPACT SCINTILLATING FIBER DETECTOR FOR ANTIPROTON CROSS SECTION MEASUREMENTS

V. MASCAGNA*, D. BOLOGNINI, M. PREST

Università degli Studi dell'Insubria, Como, Italy — INFN Milano-Bicocca
**E-mail: valerio.mascagna@gmail.com*

M. CORRADINI, M. LEALI, E. LODI-RIZZINI, A. MOZZANICA, L. VENTURELLI, N. ZURLO

Università degli Studi di Brescia, Italy — INFN Pavia, gr. coll. Brescia

E. VALLAZZA

INFN Trieste

A novel tracking detector (FAST, Fiber Antiproton Scintillating Tracker) has been developed for the measurement of the annihilation cross section of slow antiprotons at the CERN Antiproton Decelerator. FAST has to reconstruct the charged pion tracks produced in the antiproton annihilation in gaseous and solid targets. The cylindrical (diameter: 30 cm, length: 50 cm) detector consists of 2 axial and 4 stereo layers of 1 mm BCF-10 scintillating fibers readout by 42 multianode photomultipliers (64 channels) whose signals are amplified and discriminated by the VA64TAP2.1+LS64 VLSI ASICs and sampled at 320 MHz by a Cyclone II Altera FPGA. The fast sampling allows to distinguish annihilation events at the ns level as required by the pulsed nature of the AD beam ($10^6\bar{p}$ in a 40 ns bunch for 6 bunches every $\sim$ 110 s).
The paper describes the detector design, its commissioning with cosmic rays and its performance in the 2007 data taking.

Keywords: scintillating fiber, tracker, antiproton annihilation.

1. Introduction

The antiproton annihilation cross section on different nuclei was measured mainly by the OBELIX collaboration at LEAR (CERN) during the '80s – '90s; its dependence on the atomic mass number A, in the momenta range 200–800 MeV/c, was found to be $\sigma_{\text{ann}} = \sigma_0 A^\nu$ with $\nu \simeq 2/3$ [1,2].
More recent measurements at lower energies ($p \lesssim 60$ MeV/c) showed that the annihilation cross section value is almost constant for light nuclei (H,

D, He) [3]. Low statistics annihilation data on ^{20}Ne at 57 MeV/c [4] and on ^{3}He [5] seem to confirm a saturation effect of the annihilation cross section with a decreasing A at low energies.
In order to achieve a deeper knowledge in the $\overline{p}$-nucleus annihilation dynamics, and more in general in the strong interactions, new experiments with a higher statistics are needed.
For these reasons, a new $\overline{p}$ cross section experiment has been proposed and a scintillating fiber tracker has been built. In the following, the detector will be described and the results from the commissioning phase will be shown and discussed (Sec. 2). At last, some preliminary results from the July 2007 data taking will be presented (Sec. 3).

2. The detector

The detector (Fig. 1) has a cylindrical geometry and consists of 2 axial and 4 stereo layers of scintillating fibers (1 mm diameter Bicron BCF-10). It covers a sensitive volume 50 cm long and ~30 cm in diameter. The scintillation light is readout, with a 2 mm pitch, by Hamamatsu multianode photomultipliers (H7546-series): 42 PMTs with 64 channels each are used, for a total of ~2500 readout channels. The signals from the PMTs are amplified, shaped and discriminated by VLSI ASICs (VA64TAP2.1 and LS64_2 by IDEAS, with 50 ns peaking time), and the digital discriminated signal is sampled on both edges by a 320 MHz clock with a Cyclone II FPGA by Altera.
The goal of the FAST tracker is the measurement of the annihilation cross section of slow antiprotons (100 MeV/c) on different nuclei: the low energy antiprotons provided by the Antiproton Decelerator at CERN (6 bunches of 40 ns FWHM every ~2 min with ~10^6 $\overline{p}$/bunch) are delivered at the ASACUSA beam line and enter the vessel (Fig. 2) that is connected to the beam pipe. The fraction of antiprotons that annihilate on the solid target within the sensitive region of the tracker is, for the used elements (Pt, Sn and Ni) and thicknesses (15–400 nm), of the order of 10^{-6}–10^{-5}, thus a few annihilations per bunch are expected. Each annihilation originates 2–6 charged π-mesons (in the 200–900 MeV/c range of momenta) that cross the layers of the detector. The fast sampling allows to associate the hits on the fibers with the correct annihilation event, both in time and in space.
The cross section can be computed counting the number of the reconstructed vertices in the target fiducial volume with respect to the total number of particles in the bunch, measured at the end of the vessel with an integration detector.

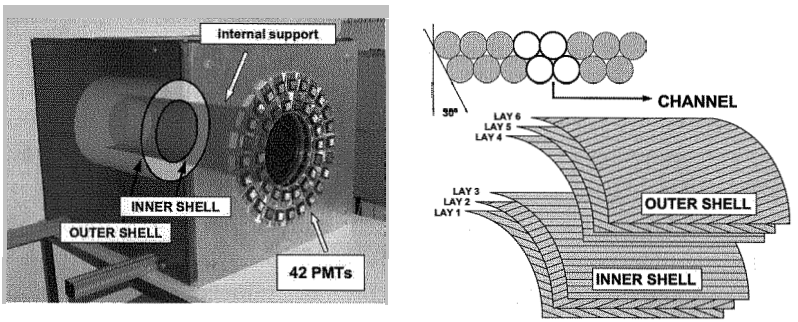

(a) (b)

Fig. 1. **(a) Scheme of** the FAST detector. (b) Layout of the six layers; the direction of the fibers is indicated.

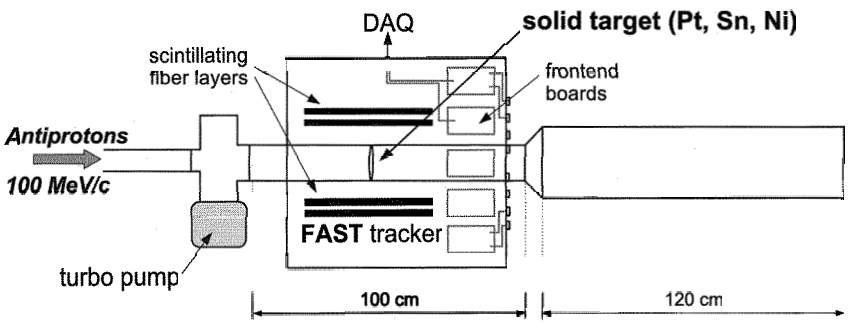

Fig. 2. **Experimental setup of** the data taking in the ASACUSA area at the AD (Antiproton Decelerator) – CERN.

3. The commissioning phase results

The performances of the detector have been measured during two cosmic ray runs in 2006 and 2007. Two silicon strip detectors (40 μm of spatial resolution [6]) have been used as a tracking reference, and a trigger system based on plastic scintillators (a few hundreds of ps of time resolution) allowed a measurement of the time resolution of the whole readout system. The acquisition electronics tests were satisfactory: the entire set of the 25 produced frontend boards showed a minimum gain spread (4%) and a negli-

gible number of dead channels (less than 10). The obtained time resolution was 3 ns (RMS) [7].
The average efficiency was ~95% while the optical crosstalk (when the collected light spreads over the PMT pads that are not really hit) was rather large (~60%); anyway the analysis showed that this did not prevent a good track reconstruction.
Some imperfections in the mechanical assembly have been found and partially solved via software (offline shifting of two layers and correction by means of a montecarlo simulation).

4. Preliminary results of the 2007 data taking

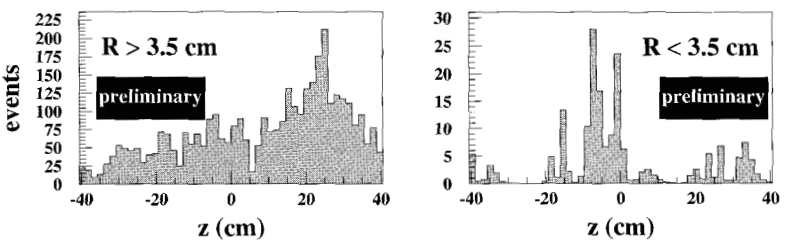

Fig. 3. Reconstructed vertex position along the z direction. The events are divided on the base of their distance from the beam axis (R parameter).

The 2007 data taking started in July 2007 and lasted 10 days. After having faced some unfit characteristics of the beam (an early "pre-bunch" of antiprotons arrived up to ~300 ns before the main bunch, saturating the detector), about 7000 AD shots were successfully acquired with three different targets (Sn, Ni and Pt), with the empty vessel and with only the mylar diskette (the 0.9 μm thick support on which the target materials were sputtered).
The first annihilation events have been reconstructed. Up to now, only some qualitative considerations can be made. Fig. 3 shows the z distribution of the reconstructed vertices, dividing them depending on their distance from the beam axis. Looking at the ones positioned at R greater than 3.5 cm (Fig. 3 on the left), the distribution is the one of the (unwanted) annihilations on the vessel walls since the target is sputtered on the support

within a circle of $\sim$1 cm of diameter. Moreover, the shape, considering that the antiprotons come from the negative z, suggests that they are all due to Rutherford scatterings, forward and backward, in the target itself. The beam size is enlarging towards positive z, causing an increasing number of wall-annihilations.
On the other hand, if only those vertices placed close to the beam axis are considered (Fig. 3 on the right), the annihilations are mainly reconstructed at the target position (z=-10 cm). This is a promising result and the analysis is ongoing.

5. Conclusions

A compact scintillating fiber tracker for the $\overline{p}$-N annihilation cross section measurements has been built. A dedicated electronics has been developed and the tests demonstrated it fulfills completely the requirements. As far as the tracker is concerned, the commissioning phase revealed some problems related to the assembly procedure that have been partially solved. The 2007 data taking period has just ended and some encouraging results have been obtained, since the first annihilations have been reconstructed in the target. Anyway, no quantitative indications concerning the cross section measurement can be made at this level. In order to exploit the full set of collected data, the analysis software has to be tuned to time-tag each event, that is to assign hits to tracks based on the instant they have been sampled. This will suppress almost all the wrong reconstructions which, in these preliminary phase, are present together with the annihilations in the target.
In 2008 a data taking period at lower energy is scheduled. For this reason, some modifications have been added to the analysis software to improve its time-tag capabilities, as well as some hardware upgrades are under investigation to achieve a higher spatial resolution to reject wrong events with more effectiveness.

References

1. D. Bendiscioli and D. Kharzeev, *La Rivista del Nuovo Cimento* **17**, p. 1 (1994).
2. V. G. Ableev *et al.*, *Il Nuovo Cimento* **107 A**, p. 943 (1994).
3. CERN Courier, July–August 2000.
4. A. Bianconi *et al.* , Phys. Lett. **B 481**, 194 (2000).
5. A. Bianconi *et al.* , Phys. Lett. **B 492**, 254 (2000).
6. M. Prest *et al.*, *Nucl. Instr. and Meth.* **A 520**, 280 (2003).
7. A. Mozzanica *et al.*, *Nucl. Instr. and Meth.* **A 567**, 315 (2006).

DESIGN OF A MONOLITHIC ACTIVE PIXEL SENSOR IN ST 0.13UM TECHNOLOGY

JANUSZ MLYNARCZYK[X,Y], ELEUTERIO SPIRITI[X], ANTONIO BULGHERONI[X]

[X] *National Institute of Nuclear Physics, Roma Tre Section, via della Vasca Navale 84, Roma, Italy*

[Y] *Department of Electronics, AGH University of Science and Technology, al. Mickiewicza 30, Krakow, Poland*

This paper presents the architecture of a new Monolithic Active Pixel Sensor chip designed in ST Microelectronics 0.13um CMOS technology at the Roma Tre University INFN Section. The two goals of the chip are: technology characterization and test of data sparsification architecture, implemented to fulfil requirements of the future high energy physics experiments. In the intended applications the commonly used 'off-line' and 'off-chip' signal processing is not possible due to a huge bandwidth needed to read out all pixels at a satisfactory speed. The authors propose a new approach for the on-line data sparsification which consists in implementation of the full on-pixel signal processing. The difficulties that had to be overcame are: limited on-pixel silicon area for fitting all the necessary electronic circuitry, forced use of only NMOS transistors in the sensing area, current and threshold mismatch typical for CMOS submicron technologies. Finally special care had to be taken to avoid crosstalk from digital to analog signals.

1. Introduction

Monolithic Active Pixel Sensors are of great interest for the experimental physics due to their promising tracking performances: high spatial resolution, high detection efficiency and 100% fill factor. Before MAPS detectors could be effectively applied to the new high energy physics experiments, such as the future colliders, some important issues must be solved. One of the most important problems of the "classical" MAPS configuration is the data bandwidth required to read out all the pixels at the satisfactory speed. The signal occupancy (the percentage of pixels on which the signal is detected at a time) in the intended physics experiments is of the order of few percent only, then the 'off-line' and 'off-chip' signal processing is obviously not effective.

The possibility of a selective reading of the pixels - i.e. reading for the 'off-chip' analysis only those areas where the signal was detected - would be a considerable step forward for MAPS detectors. It would greatly reduce the bandwidth and enable high pixel read out frequency.

This paper presents a new approach for the on-line data sparsification which consist in implementation of the complete on-pixel signal processing, including not only correlated double sampling operation but also signal discrimination and analog information storing.

Implementation of the full on-pixel signal processing is a great challenge for the designer due to the current and threshold mismatch in the modern sub-micron CMOS technologies and highly limited area available for the electronics on a single pixel. Additional difficulty comes from the principle of operation of the detector: the MAPS sensor must integrate on the same substrate the detecting layer and the signal processing electronics. In order not to degrade the detector performance, only NMOS transistors should be used, which makes the implementation of the required functionalities more complex and introduce an additional trade off between the area and the power consumption.

2. The chip

2.1. *Overview of the chip structure*

The chip developed at INFN (National Institute of Nuclear Physics) at Roma Tre University, named MIMOROMA2 consists of several matrixes of MAPS sensors. It is composed of two main parts, subdivided into smaller testing matrixes.

The purpose of the first part of the chip is to characterize the STMicroelectronics 0.13 um technology. It includes standard 3T pixel structures and self-biased structures[1]. The difference between the different structures consist in power supply voltage used (1.2V or 2.5V) as well as in the collecting diode and pitch dimensions. Based on the set of parameters shown in Table 1, ten arrays were build: five 32x16 pixels arrays with 20x20um^2 pitch and five 64x32 pixels arrays with 10x10um^2 pitch.

Table 1. Set of parameters for different arrays implemented in the non sparsified part of the chip in order to characterise the technology.

Parameter	Value 1	Value 2
Pixel Structure	3T	Self-biased
Pitch	20um x 20um	10um x 10um
Diode dimensions	1um x 1um	1.5um x 1.5um
Power supply	2.5 V	1.2 V

The goal of the second part of the chip was to test the proposed implementation of the on-line data sparsification. In this part one can find some matrixes with all the feature implemented as well as some matrixes where only

some of the important functionalities are tested. To accommodate all the on-pixel components the pitch was set to 25um x 25um.

The signal from the matrixes of pixels are read out by selecting the required row and column. For that purpose, the decoders were implemented on the periphery of the chip and the analog signal coming from the pixel is amplified by a CMOS OTA designed on purpose and featuring 80dB open loop gain and 150 MHz gain-bandwidth product with the load of 10pF.

2.2. *Architecture of the on-pixel signal processing*

The block schematic of the on-pixel signal processing implemented in the sparsified matrix is presented in Figure 1.

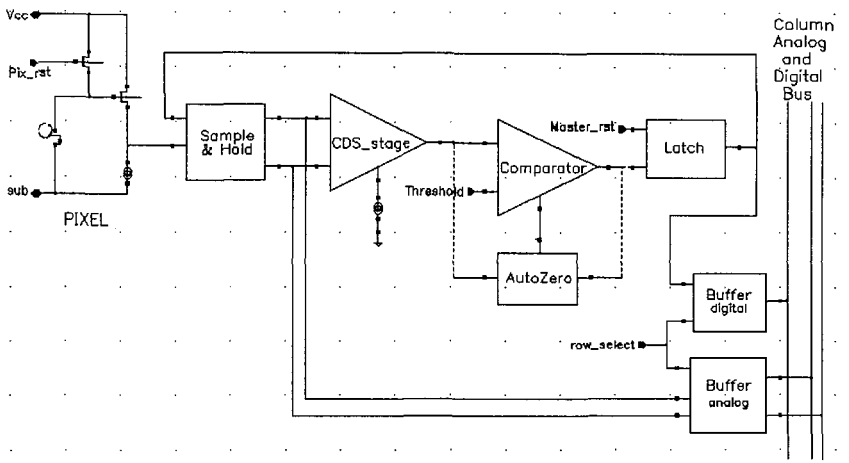

Figure 1. Architecture of the proposed on-pixel signal processing.

One can clearly see the pixel structure with N-well/Psubstrate collecting diode, reset transistor and source follower. Then the signal is fed to the sample and hold circuit, where the voltage signal, related to the diode collected charge from two consecutive time slots is memorised. The two values are then processed by the CDS stage which combines signal amplification and correlated double sampling. The resulting signal, proportional to the difference of the two samples, is then compared with a threshold in the comparator and the result is stored in the latch which provides also the necessary control signals. If the signal was detected the values stored in the sample and hold circuit are frozen and read out during the reading cycle with a help of the buffers.

All the blocks were implemented using only NMOS transistors. This made good logic levels more difficult to obtain and forced us to trade off between power consumption and area for the latch and the digital logic.

Lack of the PMOS transistors is also a serious constrain for the gain performance of the amplifier. Moreover, having in mind the leakage current in the 3T pixel structure, difficult to estimate in absence of a reliable Nwell/Psubstrate diode model, the designer must trade off between the gain and the input dynamic range of the amplifier. Then the amplifier must be prepared for the worst case in the first run in this technology.

The heart of the signal processing architecture is the comparator, that appeared also the most difficult sub-block to design. It operates on currents and not on voltages, so the circuit includes also some voltage to current converters. Minimizing current and threshold mismatch in the comparator was crucial for its operation as it influence directly the sensitivity of the signal processing circuitry.

Figure 2 presents the simulated pixel-to-pixel signal processing response to a signal equivalent to a charge of 10^3 e^- injected on the collecting diode, which is a rough estimation of the seed pixel collected charge.

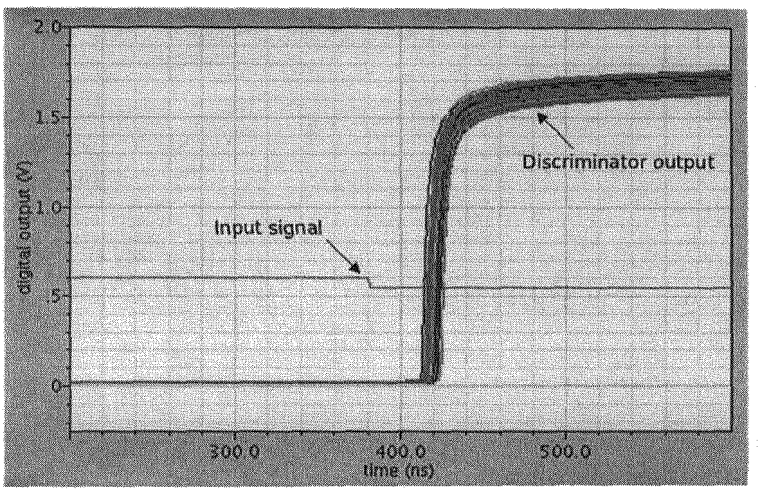

Figure 2. Simulated pixel-to-pixel signal processing response to a signal equivalent to a charge of 1000 e-.

In the pixel-to-pixel dispersion simulation minimum signal required to get right discriminator output in all 100 cases (100% efficiency) was equivalent to 250 e^-. The threshold was defined as the minimum value needed to get no false discriminator trigger with no signal at the input.

Even it the current mismatch in the comparator was reduced by one order of magnitude and reached the value which seems to be the limit for the available area, it could still be not enough for the expected signal level. In order to improve further the performance an implementation of the auto-zero technique[2]

will be tested in one of the matrixes of the chip. The simulation results are promising, but their must be confirmed by the laboratory tests after chip fabrication.

2.3. *Layout considerations*

Special care was taken to design the layout of the chip. To reduce the threshold mismatch in all the sensitive blocks cross-coupled configuration for the transistors layout were used and other layout design recommendations[3] were respected. The layout of the chip, and of the whole matrix, was also organized in the way to minimize the crosstalk between digital and analog signals. As the pixels is composed of the analog part and the digital part, the power supplies and the grounds of the two parts were separated and additional guard rings were applied.

3. Conclusions

The paper presents a new concept of a MAPS detector developed at INFN Roma Tre section. It was driven by the highly demanding performances of the vertex detectors for the future colliders. The presented approach consist in including full on-pixel signal processing in order to allow very efficient on-line data sparsification. Due to the area limitation the implemented electronic circuitry must be simple but effective. The on-pixel circuitry was designed without use of the PMOS transistors. But the main difficulty the authors had to deal with was related to the current and threshold mismatch in the used CMOS submicron technology. Finally a care had to be taken to separate digital and analog signal crosstalk. The authors were able to overcome all those difficulties and implement the required signal processing functionalities at the level of the chip design and simulation. The chip is now ready for submission through the CMP service[4] and the test board will be developed.

References

1. G. Deptuch et al., *Monolithic active pixel sensors with on-pixel amplification and double sampling operation*, Nucl. Instr. & Meth. A512, 299-309 (2003).
2. C. Enz and G. Temes, *Circuits techniques for reducing the effects of the op-amp imperfections: Autozeroing, correlated double sampling, and chopper stabilization*, Proc. IEEE, vol. 84 (1996).
3. A.Hastings, "The Art of Analog Layout", Prentice Hall (2001).
4. Circuits Multi-Projects, http://cmp.imag.fr/.

A Triple-GEM Detector with Pixel Readout for High-Rate Beam Tracking in COMPASS

T. Nagel*, A. Austregesilo, F. Haas, B. Ketzer,
I. Konorov, M. Krämer, A. Mann, S. Paul

Physik-Department E18,
Technische Universität München,
85748 Garching, Germany
**E-mail: thiemo.nagel@ph.tum.de*
www.e18.physik.tu-muenchen.de

For its physics program with a high-intensity hadron beam of $2 \cdot 10^7$ particles/s, the COMPASS experiment at CERN requires tracking of charged particles scattered by very small angles with respect to the incident beam direction. While good resolution in time and space is mandatory, the challenge is imposed by the high beam intensity, requiring radiation-hard detectors which add very little material to the beam path in order to minimise secondary interactions.

To this end, a set of triple-GEM detectors with pixel readout in the beam region and 2-D strip readout in the periphery is currently being built. The pixel size has been chosen to be $1 \times 1\,\mathrm{mm}^2$, which constitutes a compromise between the spatial resolution achievable and the number of readout channels. Surrounding the pixel area, a 2-D strip readout with a pitch of 400 μm has been realised on the same printed circuit foil. In total an active area of $10 \times 10\,\mathrm{cm}^2$ is covered using 2048 readout channels. Analogue readout by the APV25 ASIC has been chosen in order to profit from amplitude measurements which help to improve the spatial resolution by clustering neighbouring hit strips or pixels. A detector prototype has been tested successfully in the $5 \cdot 10^7$ particles/s COMPASS muon beam, as well as in a focused hadron beam. The design of the detector and first results concerning its performance as a beam tracker will be presented.

Keywords: GEM, pixel readout, high-rate tracking, micropattern gas detector, APV25, COMPASS.

1. Introduction

COMPASS (**CO**mmon **M**uon and **P**roton **A**pparatus for **S**tructure and **S**pectroscopy)[1] is a two-stage magnetic spectrometer, built for the investigation of the gluon and quark structure of nucleons and the spectroscopy of hadrons using high-intensity muon and hadron beams from

CERN's Super Proton Synchrotron (SPS). Scattering a polarised beam of 160 GeV/c muons/s from a polarised deuterium target, results on the deuteron spin-dependent structure function g_1^d,[2–4] on transverse spin asymmetries,[5,6] and on the gluon polarisation in the nucleon[7] have been obtained from the first phase of data taking between 2002 and 2004.

After upgrading the spectrometer in 2005 and resuming operation in 2006, the muon beam program will be completed in 2007 by taking data with a polarised proton target. From 2008 onward, experiments with a hadron beam of $2 \cdot 10^7$ particles/s are foreseen to perform spectroscopy of mesons and baryons in the light quark sector. For these experiments the tracking of charged particles in the beam region requires fast detectors providing good resolution in space and time in order to disentangle pile-up and multi-track events. Further demands of the high hadron flux density are radiation hardness and minimal material in order to avoid secondary interactions. Based on the experience with large-area triple-GEM tracking detectors in COMPASS[8,9], a set of triple-GEM beam trackers with combined pixel readout in the central region and 2-D strip readout in the periphery has been proposed ("PixelGEM"). After a successful prototype test in high-intensity muon and hadron beams in 2006, a total of five detectors is being built and tested.

2. Design of the PixelGEM Detector

Figure 1 shows a top view of a first full-size detector prototype. The detector is mounted on a light honeycomb sandwich structure serving as base panel carrying the high voltage distribution, the front-end electronics, the readout foil, and the GEM stack. The GEM stack consists of three GEM foils, stretched and glued onto spacer frames of glass fiber material. It is enclosed on the top by another smaller honeycomb panel carrying the drift foil. Both honeycomb panels have holes in the center to minimise the material where the beam passes through. The triple amplification, together with a number of other features taken over from the large-size COMPASS GEM detectors, like segmented GEM foils and asymmetric gain distribution, allows operation without electrical discharges even in a high-intensity particle beam.

The electron signal emerging from the triple GEM amplification stack of the PixelGEM detector is read out by a 100 μm thin, Kapton-based flexible printed circuit foil with three conductive layers, carrying both the pixel and the strip structure, and the signal lines from the pixel region. Pixels of 1×1 mm^2 size have been chosen since they yield an average cluster

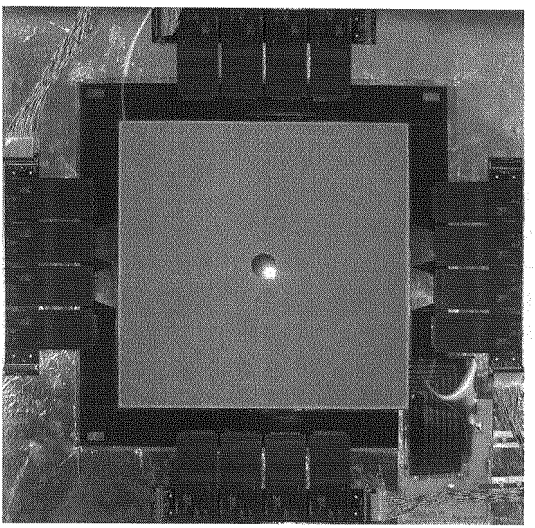

Fig. 1. Photograph of a PixelGEM detector prototype.

size larger than one, thus allowing to improve the spatial resolution by applying clustering algorithms. With a total of 32×32 pixels the beam region is fully covered. At the same time it is still technologically feasible to route, on a single metal layer, the signals from the pixels to the front-end electronics mounted 15 cm from the active area, thus minimising the material exposed to the beam. Surrounding the central square of pixels a strip readout, delivering two projections of a particle penetration point, has been realised on the same thin film printed circuit. The strip pitch is 400 μm, with all strips cut in the middle and read out from both sides in order to keep capacitance variations between different strips at a minimum. A strip width of 80 μm for the top and 340 μm for the bottom strips has been chosen to achieve an equal charge sharing between the two strip layers. The total active area of the detector is $10 \times 10\,\mathrm{cm}^2$, which guarantees sufficient overlap with other tracking detectors.

A total of 2048 channels are read out through 16 APV25 preamplifier/shaper ASICs with an analog pipeline with a depth of 160 25 ns-spaced samples. Each chip is mounted on a separate printed circuit board, which also includes a protection circuit in case of electrical breakdowns, and which is mounted upside down on the support honeycomb panel, the electrical connection to the readout electrode being made via high-density 0.5 mm pitch connectors. For each trigger, the chip forwards three samples to digitisa-

tion and further processing, so that pulse shape analysis allows to determine the time of a hit relative to the trigger, a feature of great importance in a high-intensity environment.

Owing to the described design choices, for $r<1.5\,\mathrm{cm}$, i.e. in the center of the detector, the amount of detector material could be reduced to a total thickness of 0.4 % of a radiation length (X_0) and 0.09 % of a nuclear interaction length (λ_I), respectively. Utilisation of GEM foils with Cu layer thickness of 1 μm instead of 5 μm is currently being investigated and may result in an even lower thickness of 0.2 % X_0 and 0.08 % λ_I, respectively.

3. Prototype Test

The prototype detector was characterised in the laboratory using various ionisation sources, and then installed upstream of the COMPASS target in the immediate vicinity of a beam telescope made up of 12 planes of silicon microstrip detectors and four planes of scintillating fibers, providing precise tracks to evaluate the performance of the PixelGEM as a beam tracker. For most of the tests the nominal COMPASS muon beam of $4 \cdot 10^7\,\mu/\mathrm{s}$ with a maximum flux density of $\sim 1.2 \cdot 10^5\,\mathrm{mm}^{-2}\mathrm{s}^{-1}$ was used. For a short period also a 190 GeV/c pion beam with an intensity of $1 \cdot 10^6\,\pi/\mathrm{s}$ was focused at the position of the PixelGEM, resulting in a local intensity about 5 times smaller than with the muon beam.

The detector performance was first determined at a low muon flux density of $\sim 2.5 \cdot 10^3\,\mathrm{mm}^{-2}\mathrm{s}^{-1}$. For the pixel region a plateau of efficiency is found at a value of 99% starting at a drift voltage of 3900 V, corresponding to a gain of $\sim$7000. This setting was chosen as the operating point, as a larger gain yields larger clusters, which on the one side improves the spatial resolution, but on the other side increases the probability for overlapping clusters at high intensity. For the calculation of the efficiency clusters within a roadwidth of 1 mm from the reconstructed track position have been taken into account, corrected for the probability of a background hit, i.e. a hit caused by out-of-time tracks or noise, within this roadwidth.

The spatial resolution has been determined by fitting a double-Gaussian plus constant background to the residual distribution of all clusters with respect to the tracks reconstructed in the beam telescope, taking into account the contributions of different cluster sizes to the distribution. The detector spatial resolution is then calculated by taking the weighted mean of the two standard deviations, and is found to be $\sigma_\mathrm{s} = 95\,\mu\mathrm{m}$. From the pulse shape analysis of the analogue signals a temporal resolution of rms = 9.9 ns is determined. The probability for a background hit is only $b = 0.1$ % per

pixel at low intensity.

In the high intensity muon beam with up to $\sim 1.2 \cdot 10^5\,\mathrm{mm}^{-2}\mathrm{s}^{-1}$ flux density the performance of the detectors was found to be slightly degraded due to pile-up of events. For the pixel area the detector exhibits a spatial resolution of $\sigma_s = 135\,\mu\mathrm{m}$ at an efficiency $\epsilon = 96\,\%$ and an average probability of a background hit per pixel of $b = 2\,\%$. The clustering algorithm—which works well in low intensity conditions—still leaves room for improvement of these preliminary numbers in the high flux density environment.

4. Summary and Outlook

A new ultra-light beam tracker for the COMPASS experiment based on a triple GEM detector with combined pixel and strip readout was proposed and realised. A full-size prototype test in high-intensity muon and hadron beams proved the stability of the detector and showed good performance in terms of efficiency and resolution. No electrical instabilities or discharges were observed during these tests, making this type of detector a promising candidate for a low-mass, radiation-hard beam tracker in high-rate hadron beams.

Recently, a second prototype with $1\,\mu\mathrm{m}$ Cu layer thickness has been built. While it has not yet been characterised completely in terms of gain uniformity, first measurements indicate that it is fully functional. For the COMPASS physics program with hadron beams, a set of five PixelGEM detectors is currently being built and commissioned.

References

1. COMPASS collaboration, P. Abbon *et al.*, *Nucl. Instrum. Meth. A* **577**, 455 (2007).
2. COMPASS collaboration, E. S. Ageev *et al.*, *Phys. Lett. B* **612**, 154 (2005).
3. COMPASS collaboration, V. Y. Alexakhin *et al.*, *Phys. Lett. B* **647**, 8 (2007).
4. COMPASS collaboration, V. Y. Alexakhin *et al.*, *Phys. Lett. B* **647**, 330 (2007).
5. COMPASS collaboration, V. Y. Alexakhin *et al.*, *Phys. Rev. Lett.* **94**, p. 202002 (2005).
6. COMPASS collaboration, E. S. Ageev *et al.*, *Nucl. Phys. B* **765**, 31 (2007).
7. COMPASS collaboration, E. S. Ageev *et al.*, *Phys. Lett. B* **633**, 25 (2006).
8. C. Altunbas, M. Capeáns, K. Dehmelt, J. Ehlers, J. Friedrich, I. Konorov, A. Gandi, S. Kappler, B. Ketzer, R. D. Oliveira, S. Paul, A. Placci, L. Ropelewski, F. Sauli, F. Simon and M. van Stenis, *Nucl. Instrum. Meth. A* **490**, 177 (2002).
9. B. Ketzer, Q. Weitzel, S. Paul, F. Sauli and L. Ropelewski, *Nucl. Instrum. Meth. A* **535**, 314 (2004).

Track Reconstruction at the LHCb Experiment

K. RINNERT* for the LHCb Collaboration

Department of Physics, The University of Liverpool,
Liverpool, L69 7ZE, United Kingdom
**E-mail: kurt.rinnert@cern.ch*
www.liv.ac.uk

The LHCb experiment will perform high-precision measurements of CP violation parameters and rare phenomena in B meson decays. It requires an excellent track reconstruction efficiency, particle identification and the precise measurement of secondary vertex positions in LHC collisions. We will discuss the methodology for the global reconstruction of tracks, using the ensemble of tracking detectors arranged on both sides of the LHCb dipole magnet. Hardware features of the tracking detectors that affect the tracking strategy will be outlined. We will describe the design and performance of the track reconstruction algorithms.

Keywords: LHCb; Tracking; Vertexing; Reconstruction

1. Introduction

The LHCb experiment[1] is designed to perform high-precision measurements of CP violation parameters and rare phenomena in B meson decays. The results will improve our understanding of quark flavour physics in the Standard Model. In addition the measurements may reveal evidence for physics beyond the Standard Model. The LHCb detector is a single-arm spectrometer that reconstructs the decay products of particles produced by LHC proton-proton collisions in the forward region. It comprises a silicon microstrip vertex detector, RICH and muon detectors for particle identification, calorimeters and tracking detectors (Fig. 1). A dipole magnet with a bending power of 4 Tm bends charged particle trajectories in the x-z plane.

Charged particle tracks are the backbone of event reconstruction at LHCb. Firstly they measure essential particle properties on their own: production vertices and particle momenta, the latter being derived from the track curvature in the magnetic field. Secondly they are the only means by which the information from different detector components can be linked

together.

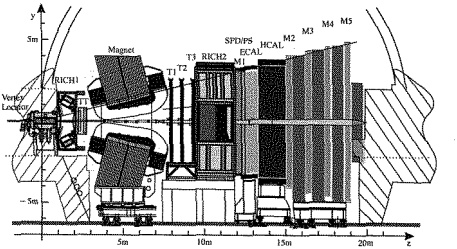

Fig. 1. Overview of the LHCb detector.

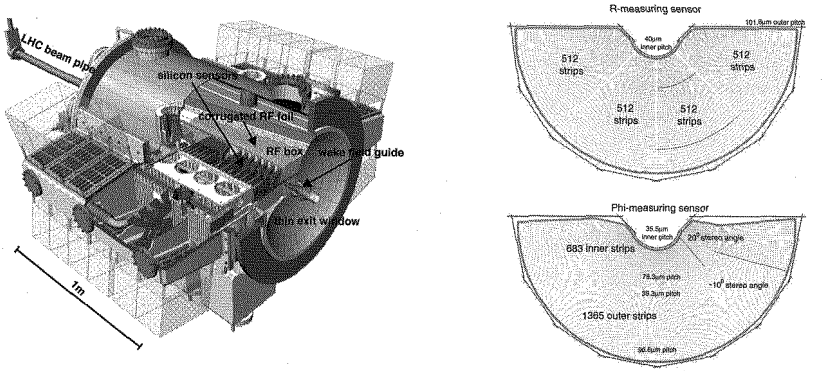

Fig. 2. The VELO vacuum vessel (left) and the R (top right) and Phi (bottom right) silicon sensor layout.

2. The VELO

The primary purpose of the VELO (VErtex LOcator)[1,2] is to provide high-precision measurements of primary and secondary vertex positions. It consists of 88 silicon micro-strip sensors mounted in retractable halves in a vacuum vessel around the interaction region. There are two different types of sensors designed to measure r and ϕ coordinates, respectively (Fig. 2). In the closed position the sensitive region starts at a distance of 8 mm from the beam. A corrugated aluminium foil shields the sensors from RF radiation and separates the beam and detector vacuum. The production of the

VELO modules was completed in early 2007 and commissioning at CERN is underway.

3. The Trigger Tracker

The Trigger Tracker (TT)[1] is located between the VELO and the dipole magnet. It serves to obtain a momentum estimate, which is important for the trigger decision. The layout of the detector is shown in Fig. 3. The TT is a silicon strip detector with a strip pitch of 183 μm. The strip orientations with respect to the y axis in the four 140 cm $\times$ 120 cm wide detector planes are 0°, −5°, +5° and 0°. The TT will be ready for global commissioning in January 2008.

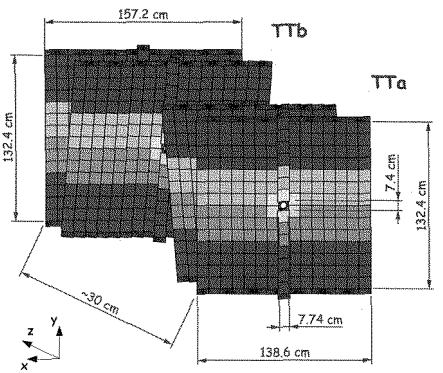

Fig. 3. Layout of the Trigger Tracker (TT).

4. The Tracking Stations

The three tracking stations behind the magnet feature two different detector technologies.[1,3,4] As illustrated in Fig. 4, there is the Inner Tracker (IT) close to the beam and the Outer Tracker (OT) covering the acceptance area further away from the beam. The IT is again a silicon detector with a strip pitch of 198 μm. The OT is a straw tube detector with a straw tube diameter of 5 mm. Both detectors are primarily designed to measure particle coordinates in the bending plane of the dipole magnet. Both, OT and IT, have four layers in each station. With respect to the y axis the strips (drift cell wires) in the IT (OT) are at the angles 0°, +5°, −5°

and 0°. This is referred to as the *xuvx* layout. This configuration provides sufficient vertical resolution via the *uv* stereo angles while at the same time maintaining a precise measurement of track coordinates in the bending plane for momentum determination.

The IT module production is completed and it will be ready for global commissioning in early 2008. Several OT components are undergoing final testing while it is prepared for taking cosmic data and for global commissioning.

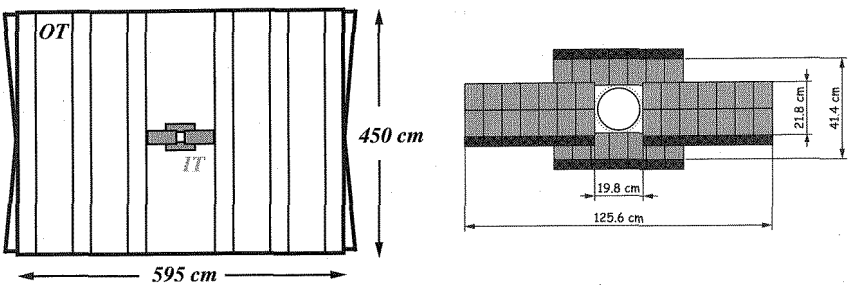

Fig. 4. Layout of a tracking station (T-Station) with OT and IT modules (left) and details of the IT station layout (right).

5. Track Reconstruction Strategies and their Performance

A suite of algorithms is used to reconstruct the different types of tracks illustrated in Fig. 5. The tracks providing the most information are the Long Tracks. These have measurements in all tracking detectors. They are reconstructed in two different ways. The first strategy is to reconstruct line segments in the VELO only (VELO Tracks), propagate them through the magnetic field and add measurements in the tracking stations. The second strategy starts from track seeds in the tracking stations which are propagated backwards and matched with VELO Tracks. Upstream Tracks are VELO Tracks with additional hits in the TT. They are useful for pattern recognition in RICH1. Similarly, Downstream Tracks have measurements in the T-Stations and the TT only. They enhance the reconstruction efficiency for long lived particles like K_S^0. Finally the VELO-only tracks are used for primary vertex reconstruction and the T-Station seeds help the pattern recognition in RICH2.

A further complication arises in the VELO. During beam injection the VELO halves a retracted to a position 3 cm away from the beam. In this

position the sensor layout does no longer correlate well with the r and ϕ coordinates. A specialised algorithm is used to monitor the beam in this phase until the VELO has moved to the closed position for physics data taking.

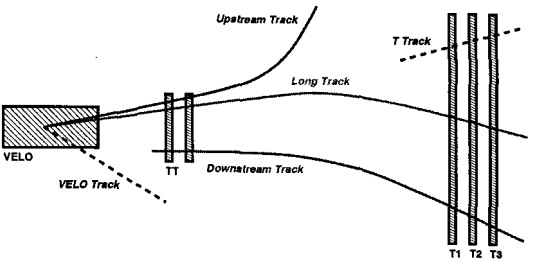

Fig. 5. The different types of tracks reconstructed at LHCb.

Recently the track reconstruction software was subjected to a thorough review in order to further improve its performance, robustness and maintainability. Its performance was evaluated using a realistic detector simulation. With a momentum resolution of $\delta p/p = 0.4\%$, a vertex resolution of 15 μm and an efficiency of 96% for high momentum tracks it performs well within the design specifications outlined in Ref. 1.

6. Conclusion

The efficient and precise reconstruction of charged particle tracks is essential for the success of the LHCb experiment. The hardware components of the LHCb tracking detectors are in the process of being commissioned at CERN. The track reconstruction software is stable, robust and performs well within design specifications. LHCb will be ready for data taking and processing when the LHC starts up in 2008.

References

1. The LHCb Collaboration, *LHCb reoptimized detector design and performance Technical Design Report* (CERN, Geneva, 2003). CERN-LHCC-2003-030.
2. The LHCb Collaboration, *LHCb VELO (VErtex LOcator) Technical Design Report* (CERN, Geneva, 2001). CERN-LHCC-2001-011.
3. The LHCb Collaboration, *LHCb outer tracker Technical Design Report* (CERN, Geneva, 2001). CERN-LHCC-2001-024.
4. The LHCb Collaboration, *LHCb inner tracker Technical Design Report* (CERN, Geneva, 2002). CERN-LHCC-2002-029.

PROTOTYPE DRIFT CHAMBER FOR TRACKING AT SMALL ANGLES IN THE PANDA EXPERIMENT

J. SMYRSKI, P. HAWRANEK, W. KRZEMIEŃ, P. SALABURA, A. WROŃSKA

Institute of Physics, Jagiellonian University
ul. Reymonta 4, 30-059 Cracow, Poland

A prototype drift chamber for tracking at small angles in the high rate environment of the PANDA experiment has been built. The chamber contains 1 cm x 1 cm drift cells arranged in two double layers. The most central wires are mounted on insulating rings surrounding the beam pipe. Results of the chamber tests with a beam of up to $5 \cdot 10^6$ protons per second indicate a drop of detection efficiency by about 5% at the highest measured flux of 0.2 MHz/cm^2.

1. Forward tracking at PANDA

PANDA [1, 2] is a fixed target experiment proposed for studies of reactions induced by antiproton beams on hydrogen as well as on nuclear targets at the Facility for Antiproton and Ion Research (FAIR) at GSI-Darmstadt. The general layout of PANDA is based on two spectrometers. The Target Spectrometer surrounds the interaction region and has a 2 T superconducting solenoid as momentum analyzer. The most forward scattering angles – $\pm 10^\circ$ horizontally and $\pm 5^\circ$ vertically – are covered by the Forward Spectrometer using a 1 m gap dipole magnet for momentum analysis of the forward-going particles.

For tracking of charged particles in the field of the PANDA solenoid, either a straw tube tracker or a time projection chamber surrounding the interaction point will be used. For tracking at forward angles - below 22° - which are not covered fully by the straw tube tracker we propose to use two planar drift chambers placed 1.8 m and 2.1 m downstream the target. The chambers have to stand a high counting rate of particles peaked at the most forward angles due to the relativistic boost as well as due to the small angle $\overline{p} - p$ elastic scattering. With the envisaged maximum $\overline{p} - p$ interaction rate of 20 MHz and at the maximum momentum of the antiproton beam of 15 GeV/c, the expected particle flux in the chambers in the vicinity of the 5 cm diameter beam pipe is about 0.02 MHz/cm^2. Besides, the chambers have to work in the 2 T magnetic field produced by the PANDA solenoid. In order to fulfill these requirements quadratic drift cells with an active area of 1 cm^2 were chosen. Each chamber will

contain four pairs of detection planes with wires mounted on frames of octagonal shape and oriented at 0°, 90°, +45° and -45°.

Drift chambers with 1 cm^2 cells are also considered for tracing particle trajectories in the Forward Spectrometer. In this case one pair of drift chambers will be installed before and the other after the dipole magnet allowing measurement of the deflection of the particle trajectories in the magnetic field. Additionally, for tracing of low momentum particles being bent inside the dipole magnet towards the magnet yoke, a third pair of drift chambers will be installed inside the gap of the magnet.

2. Prototype drift chamber

In order to test the mechanical construction of the proposed drift chambers and to investigate their high rate behavior we constructed a prototype chamber. The chamber contains 1 cm x 1 cm quadratic drift cells arranged in double-layers as it is shown in Fig. 1. The electric field in the cells has approximately cylindrical symmetry, and thus the relation between distance from wire and drift time depends only weakly on the particle angle of incidence. The sense wires are made of 20 μm thick gold-plated tungsten, whereas for the 110 μm field and cathode wires gold–plated molybdenum was used. The cathode as well as the field wires are grounded and the sense wires are set at a positive voltage.

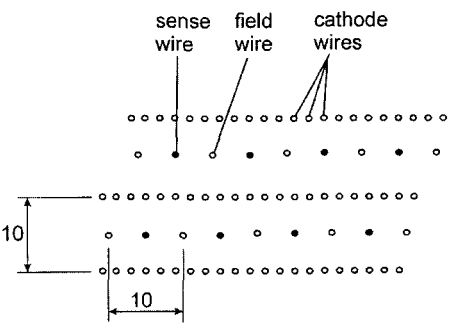

Figure 1. Double layer of drift cells.

The prototype chamber contains two double-layers with vertical wires. This arrangement is sufficient for testing a reconstruction of tracks in the horizontal plane. The wires are stretched on frames of octagonal shape made of 5 mm thick Stesalit 4411W epoxy-fiberglass composite. Each double layer consists of five frames with glued printing boards containing pads for soldering the wires. Three frames are used for mounting the cathode wires, the other two support sense and

field wires. The cathode wires were wound up with a winding machine on auxiliary frames equipped with combs for fixing the relative distance of the wires. Then the auxiliary frames were placed on the fiberglass frames and the wires were soldered on the printing boards. The sense and the field wires were stretched individually. The wire positions are defined by Ø=2 mm plastic pins which are fixed at the printing boards near the soldering pads. The most central wires in each plane are mounted on insulating rings which will surround the beam pipe in the PANDA experiment. The rings are made of 1.5 mm thick printing boards. A drawing of the ring for mounting the sense and the field wires is shown in Fig. 2. The sense wires, which are soldered to the pads in the upper part of the ring, are connected electrically to corresponding wires soldered in the lower part of the ring. In this way it is sufficient to connect the read out electronics either to the sense wires in the upper or in the lower part of the ring.

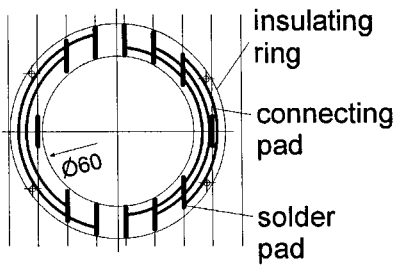

Figure 2. Ring for mounting the sense wires and the field wires in the central part of the chamber.

The stack of five epoxy-fiberglass frames with wires forming a double layer is screwed to an auxiliary ring-shaped frame made of 10 mm thick aluminum. With a mechanical tension of 0.05 kG for the sense wires and of 0.11 kG for the field and cathode wires, the total load coming from wires in one double layer is about 250 kG. This force is partly taken over by the aluminum frame. The alignment of the epoxy-fiberglass frames and the aluminum frame in one double layer is achieved by means of eight Ø=12 mm stainless steel pins penetrating the frames. The double layers mounted on the aluminum support frames form independent mechanical units. The prototype chamber is a pack of two such units. These units are positioned with respect to chamber support by means of four linear bearings which are fixed to the support. The diameter of the active area of the chamber is equal to 120 cm. The chamber is closed from both sides with 20 μm Kapton windows glued to the aluminum support frames. The gas tightness is guaranteed by Ø=2 mm rubber O-rings placed in grooves machined in the frames. In the neighborhood of the beam pipe, the chamber volume is

limited by an aluminum cylinder with a wall thickness of 0.1 mm. A photograph of the chamber equipped with preamplifiers is shown in Fig. 3.

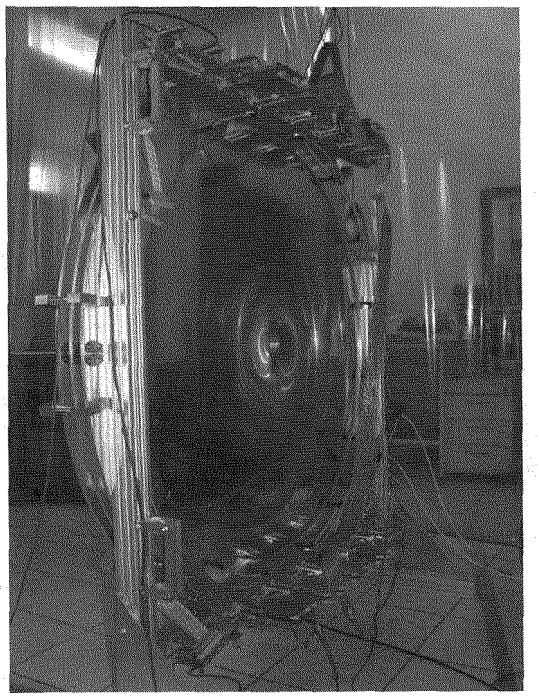

Figure 3. Prototype drift chamber for PANDA. The chamber contains four detection planes with square 1 cm x 1 cm cells. The central opening is foreseen for the beam pipe.

3. Chamber tests

The prototype drift chamber was tested using the external proton beam of the COSY accelerator in the Research Center - Jülich. The beam momentum was 2.9 GeV/c and the maximum intensity in the spill was $5 \cdot 10^6$ protons per second. The width of the beam intensity profile at the chamber position was about 4 cm (FWHM) horizontally and 8 cm (FWHM) vertically. The maximum particle flux was $0.2 \cdot MHz/cm^2$. During the test we used a chain of read out electronics containing 16 channel preamplifier-discriminator cards [3] based on the Fujitsu MB13468 amplifier chip and the LeCroy MVL407S comparator chip, converters of ECL to LVDS pulses and 128 channel TDC-boards [4] based on the HPTDC chips. The read out electronics worked properly even at the highest hit rate per channel of 1.5 MHz. The rate of events written to tape was limited by the 100 Mb Ethernet link used to transfer the data from the TDC board to a Personal

Computer. The chamber was operated with 90% Ar + 10% CO_2 gas mixture at atmospheric pressure. The gas flow through the chamber was 18 l/h. The detection efficiency was determined by selecting events with one and only one hit in a given detection plane, chosen as the reference. For the neighboring planes, the efficiency was calculated as the percentage of events, in which there was a hit in at least one cell adjacent to the fired cell in the reference plane. The efficiency plateau was observed for voltages above 1700 V. We observed a drop of the detection efficiency from 96% to 91% when increasing the particle rate from 0.012 MHz/cm^2 to 0.2 MHz/cm^2. We reconstructed tracks of particles registered in the chamber using a straight line fit. With chamber calibration determined by means of the uniform irradiation method we obtained a position resolution of $\sigma = 300$ μm per detection plane. Test of the chamber will be continued with respect to the aging effects. Results of the present and planned tests will allow to make a final choice between the drift detectors and the GEM detectors which are considered as an alternative solution for the forward tracking in the Target Spectrometer of the PANDA detector.

Acknowledgments

We acknowledge the support of the European Community under the contracts "DIRACsecondary-Beams" (grant 515873-RIDS) and "Hadron Physics" (grant RII3-CT-2004-506078) and the Polish Ministry of Science and Higher Education (grant SPUB 158/E-338/6.PR UE/DIE 455/2004-2007 and SPUB 65/6.PR UE/2006/7).

References

1. PANDA Collaboration, Technical Progress Report, http://www.panda.gsi.de/archive/public/panda_tpr.pdf.
2. J. Smyrski, "PANDA: a detector for research with antiprotons", Proceedings of the 9th ICATPP Conference on Astroparticle, Particle, Space Physics, Detectors and Medical Physics Application, Como, 17-21 October 2005.
3. L. Jarczyk et al., Annual Report 1990 IKP-KFA, 1991, p. 219.
4. I. Fröhlich et al., contribution to these proceedings.

Production and Quality Assurance of Detector Modules for the LHCb Silicon Tracker

Dmytro Volyanskyy and Olaf Steinkamp on behalf of the LHCb Silicon Tracker group*

Physik-Institut, Universität Zürich,
Winterthurerstr. 190, CH-8057 Zürich, Switzerland
E-mail: volyanskyy@physik.uzh.ch , olafs@physik.uzh.ch

The LHCb experiment, which is currently under construction at the Large Hadron Collider (CERN, Geneva), is designed to study CP violation and find rare decays in the B meson system. To achieve the physics goals the LHCb detector must have excellent tracking performance. An important element of the LHCb tracking system is the Silicon Tracker, which covers a sensitive surface of about 12 m^2 with silicon microstrip detectors and includes about 272k readout channels. It uses up to 132 cm long detector modules with readout strips of up to 38 cm in length and up to 57 cm long Kapton interconnects in between sensors and readout hybrids. The production of detector modules has been completed recently and the detector is currently under installation. A rigorous quality assurance programme has been performed to ensure that the detector modules meet the mechanical and electrical requirements and study their various characteristics. In this paper, the detector design, the module production steps, and the module quality assurance programme are briefly described.

1. Introduction

Since $b\bar{b}$ hadrons at the LHC will be predominately produced at low polar angles in the same forward cone, the LHCb spectrometer[2] is designed as a single-arm, forward spectrometer with an angular coverage from 10 mrad to 300(250) mrad in the horizontal (vertical) plane. The Silicon Tracker is part of the LHCb tracking system. It comprises two sub-detectors: the Trigger Tracker (TT) and the Inner Tracker (IT). Both use single-sided silicon sensors and a common readout[a] and infrastructure, such as high voltage, low voltage and cooling. Around 30 physicists from five universities and laboratories from four countries are currently involved in the LHCb Silicon Tracker project.

*For the full list of authors, see[1] .

[a]Both detectors use the same readout chip (Beetle[3]) and readout link[4] .

The TT is a 150 cm wide and 130 cm high planar tracking station, which is located just in front of the entrance of the LHCb dipole magnet. Charge particle fluxes of about $5\times10^5\text{cm}^{-2}\text{s}^{-1}$ are expected in the innermost region of the TT. The detector consists of four planar detection layers of silicon microstrip sensors that cover the complete LHCb acceptance. The detection layers are arranged according to the x–u–v–x configuration: the first and the last layer have vertical strips, while the second and third have strips which are rotated by an angle of $+5°$ and $-5°$, respectively. The layers are enclosed in a common thermally-insulating box that also provides electrical and optical shielding and mechanical support. A detailed description of the TT detector layout can be found in[5] .

The IT covers a roughly 120 cm wide and 40 cm high cross-shaped area around the beam pipe in the centre of three planar tracking stations downstream of the magnet. Although the IT covers only 1.3% of the sensitive surface of the tracking stations, approximately 25% of all charged particles from the *pp* interaction point that reach the tracking stations will pass through the IT. Charge particle fluxes of about $1.5\times10^5\text{cm}^{-2}\text{s}^{-1}$ are expected in the innermost region of the IT. There are four separate IT boxes in each of the tracking stations: above, below, to the left and to the right of the beam pipe. They provide electrical and thermal shielding for the silicon sensors and readout electronics. Each IT box contains four detection layers of silicon microstrip detectors with a x–u–v–x topology, as in the TT. A detailed description of the IT detector layout can be found in[6] .

2. Module design

The basic detector unit of the TT is the half-module. It consists of seven 500 μm thick silicon sensors[b] and a stack of readout hybrids located at one end. To provide mechanical stability two carbon fibre rails are glued along the sensor edges. By bonding the strips on adjacent sensors, the half-module is segmented into two or three readout sectors. This allows to limit the hit occupancy and to decrease the total load capacitance at the input of a readout amplifier. There are two different types of half-modules: LMK and LM half-modules. The LMK half-modules are placed in the innermost part of the detector around the beam pipe, where the occupancy is highest. In these half-modules, the seven silicon sensors are electronically divided into three independent readout sectors: an outer four-sensor long readout sector,

[b]TT sensors are 9.64 cm wide and 9.44 cm long, and carry 512 readout strips with a strip pitch of 183 μm.

an intermediate two-sensor long readout sector and an inner readout sector consisting of a single silicon sensor. The LM half-modules are placed outside the beam pipe region. These half-modules are electronically divided into two readout sectors: an outer four-sensor long readout sector and an inner three-sensor long readout sector. Each readout sector is independently read out by a front-end hybrid located at the end of the half-module. This leads to two (three) stacked readout hybrids for the LM (LMK) half-module. The four-sensor long readout sectors are directly connected to their front-end readout hybrids via a short pitch adapter. In order to connect the three-sensor and two-sensor readout sectors of the LM and LMK half-modules to the corresponding readout hybrids, an interconnect Kapton cable[c] with a length of 39.1 cm is used. A similar cable with a length of 58 cm is employed to connect the one-sensor readout sectors of the LMK half-modules to their readout hybrids.

IT detector modules consist of one 320 μm thick or two 410 μm thick silicon sensors[d] that are connected via a short pitch adapter to a single readout hybrid. Silicon sensor(s), pitch adapter and readout hybrid are glued onto a flat backplane that consists of a thin layer of polyetherimide foam sandwiched in between two sheets of carbon fiber of high thermal conductivity. A thin Kapton foil is used to insulate the silicon sensors from the carbon-fibre sheets. To provide a direct heat path between the readout hybrid and a thin aluminium cooling rod onto which the modules will be mounted, a small aluminium insert ("cooling balcony") is embedded into the backplane at the location of the readout hybrid.

3. Module production

The series production of TT modules was launched in September 2005 and was completed in December 2006. Including 15% spares, 148 half-modules have been produced: 116 LM half-modules and 31 LMK half-modules. The production of TT modules proceeded in two or three stages, depending on the module type. During the first production step the seven silicon sensors and the lowest readout hybrid were placed on an assembly template, the two carbon fibre rails were glued along the sensor edges, the bias voltage cable was connected to the sensors, and the readout strips and the ground

[c]The interconnect Kapton cable has a thickness of 0.010 cm and a width of 6 cm and carries 512 signal lines with a fan-in section which reduces the sensor pitch of 183 μm to the 112 μm pitch of the cable.

[d]IT sensors are 7.8 cm wide and 11 cm long, and carry 384 readout strips with a strip pitch of 198 μm.

connections of the four-sensor readout sector were bonded. After this stage, the four-sensor sector was fully operational. At the next production step, the readout hybrid and a 39.1 cm long interconnect Kapton cable for the three-sensor and two-sensor readout sectors of the LM and LMK half-modules were mounted and the sensors within these sectors were bonded together. After this step, the assembly of a LM half-module was completed. For the LMK half-modules, a third production stage was performed to attach and bond the readout hybrid and a 58 cm long interconnect Kapton cable of the one-sensor readout sector.

The series production of IT modules was launched in January 2006 and was completed in September 2007. In total, about 415 modules have been produced. The production of IT modules proceeded in several steps. At first, the pre-fabricated support backplane was placed on an assembly template and the readout hybrid and pitch adapter were positioned and glued onto the support. Then, a first readout test was performed to assure the functionality of the readout hybrid. Depending on the module type, one or two silicon sensors were further positioned on a second template, transfered to the assembly template using a vacuum transfer jig, and glued onto the support using a silicone-based glue. At the next step, bias voltage and ground connections were bonded and a first HV test was performed. Finally, the readout strips were bonded.

4. Quality assurance

A crucial role in the quality assurance programme for the detector modules was played by the comprehensive "burn-in" test, through which each detector module passed at least once during its assembly. This test allowed to investigate the long-term behaviour of the detector modules at different thermal conditions, to study their electrical characteristics and to search for defective channels. The burn-in setups and programmes for IT and TT differed in details, however their main features were similar. The typical burn-in programme took around 36 hours for TT and 48 hours for IT and included temperature cycling between room temperature and +5°C in case of TT and between +40°C and -5°C in case of IT. During the cycling, the modules were continuously biased at 500V and leakage currents were monitored as a function of temperature and time. Furthermore, the leakage currents were measured as a function of the applied bias voltage at cold and warm temperature. These measurements provided a search for the breakdown voltages of the silicon sensors. In order to investigate the noise performance of the detectors, pedestal runs were repeatedly taken at

cold and warm temperatures. Measurements of the signal pulse shapes were performed at both temperatures using an internal test pulse implemented in the Beetle readout chip and, in case of the TT setup, using an array of infra-red laser beams that permitted to generate charges at predefined locations on each readout sector. This allowed to verify the optimal timing settings of the readout electronics and to study pulse shape characteristics as a function of different parameters. In particular, the dependence of the signal amplitude on the applied bias voltage was investigated and the charge-collection efficiency curves were obtained. In case of TT, the burn-in programme was running fully automatically. This was achieved by using the LabView programming language that allowed to control all components of the burn-in test-stand, including readout electronics and data taking. An extensive and uninterrupted measurement programme was running even overnight and over the weekends. The need for operator intervention was limited to searching of defective channels at the beginning and at the end of the test and to exchanging the half-modules.

The overall quality of the modules is very good. The fraction of defective channels (interrupts, shorts, pinholes) is only 0.13% for TT and approximately 0.1% for IT. Leakage currents at 500 V and at room temperature are typically below 0.4 μm. However, a small number of modules were graded as spares due to higher or unstable leakage currents at 500 V. Around 2 TByte of data have been accumulated in the TT burn-in tests alone.

5. Outlook

The production of detector modules for the LHCb Silicon Tracker has been completed. The results of the quality assurance programme demonstrate that the detectors meet the mechanical and electrical requirements for the LHCb Silicon Tracker. The detector installation has been started and will be completed by the end of 2007.

References

1. LHCb note 2007-131
2. LHCb Reoptimized Detector Design and Performance - Technical Design Report, CERN/LHCC-2003-030
3. LHCb note 2005-105
4. A. Vollhardt et al., Proc. LECC 2005, CERN/LHCC-2005-038 (2005) 187-191
5. D.Volyanskyy, The Trigger Tracker and a Monte Carlo Study of the $B_s^0 \rightarrow J/\psi\eta'$ Decay in the LHCb Experiment, CERN-THESIS-2007-065
6. LHCb Inner Tracker - Technical Design Report, CERN-LHCC/2002-029

Managing Bias Leakage Currents and High Data Rates in the *BABAR* Silicon Vertex Tracker *

J. Garra-Tico[1], V. Re[2], M. Bondioli[3], M. Bruinsma[3], S. Curry[3], D. Kirkby[3], S. Burke[4], D. Callahan[4], C. Campagnari[4], A. Cunha[4], D. Hale[4], S. Kyre[4], J. Richman[4], T. Beck[5], A.M. Eisner[5], J. Kroseberg[5], W.S. Lockman[5], G. Nesom[5], A. Seiden[5], P. Spradlin[5], L. Winstrom[5], D. Brown[6], S. Dardin[6], F. Goozen[6], L.T. Kerth[6], G. Lynch[6], N.A. Roe[6] J. Anderson[7], C. Chen[7], C. K. Lae[7], D. Roberts[7], G. Simi[7], J. Tuggle[7†], A. Lazzaro[8], V. Lombardo[8], F. Palombo[8], L. Ratti[9], C. Angelini[10], G. Batignani[10], S. Bettarini[10], F. Bosi[10], F. Bucci[10], G. Calderini[10,19], M. Carpinelli[10], M. Ceccanti[10], R. Cenci[10], A. Cervelli[10], F. Forti[10], M.A. Giorgi[10], A. Lusiani[10], P. Mammini[10], P.F. Manfredi[10], G. Marchiori[10], M, Mazur[10], M. Morganti[10], F. Morsani[10], N. Neri[10], E. Paoloni[10], A. Profeti[10], M. Rama[10,20], G. Rizzo[10], J. Walsh[10], P. Elmer[11] O. Long[12] E. Charles[13], A. Perazzo[13], P. Burchat[14], A.J. Edwards[14], T. S. Miyashita[14], S. Majewski[14], B.A. Petersen[14,21], M. Bona[15,21], F. Bianchi[15], D. Gamba[15], P. Trapani[15], M. Bomben[16], L. Bosisio[16], C. Cartaro[16], S. Dittongo[16], L. Lanceri[16], L. Vitale[16], V. Azzolini[17], N. Lopez-March[17], Y.Y.Gao[18], A.V.Gritsan[18], Z.J.Guo[18],

[1]Universitat de Barcelona, Spain
[2]INFN-Pavia and Università di Bergamo
[3]University of California, Irvine
[4]University of California, Santa Barbara
[5]University of California, Santa Cruz
[6]Lawrence Berkeley National Laboratory
[7]University of Maryland
[8]INFN-Milano and Università di Milano
[9]INFN-Pavia and Università di Pavia
[10]INFN-Pisa and Università di Pisa
[11]Princeton University
[12]University of California, Riverside
[13]Stanford Linear Accelerator Center, Stanford
[14]Stanford University
[15]INFN-Torino and Università di Torino
[16]INFN-Trieste and Università di Trieste
[17]IFIC, Universitat de Valencia-CSIC, Valencia
[18]Johns Hopkins University, Baltimore, Maryland
[19]Now at Laboratoire de Physique Nucleaire et de Hautes Energies, IN2P3/CNRS, Paris

*Presented by J. Tuggle at the 10^{th} ICATPP Conference
†Corresponding author, jtuggle@slac.stanford.edu

[20]Now at Laboratori Nazionali di Frascati, INFN, Frascati
[21]Now at CERN, Geneva

The silicon vertex tracker at the *BABAR* experiment is the primary device used in measuring the distance between B^0 and $\overline{B}^0$ meson decay vertices for the extraction of *CP* asymmetries. It consists of five layers of double-sided, AC-coupled silicon modules, read out by custom integrated circuits. It has run well consistently for eight years. I report on three years of experience in managing problematic bias leakage currents in the fourth layer. In addition, I report on recent success in decreasing the data acquisition time by reducing the readout window.

1. The *BABAR* Experiment

The *BABAR* experiment at the PEP-II collider at SLAC was designed to study *CP* violation in decays of B mesons. Precision measurements of B decay rates and asymmetries yield information critical to the determination of the parameters of the Cabibbo-Kobayashi-Maskawa matrix of the standard model. To date, *BABAR* has recorded over 475×10^6 $\Upsilon(4S) \rightarrow B\overline{B}$ decays produced in e^+e^- collisions with a center-of-mass energy of 10.58 GeV. The full details of the *BABAR* detector are described elsewhere [1].

To study time-dependent *CP* asymmetries, the *BABAR* detector must be able to determine the proper time difference between the decays of two B^0 mesons. This is done by boosting the B^0 mesons in the laboratory frame so that their decay time differences can be inferred from the spatial separation of the decay vertices. The 9 GeV e^- beam on a 3.1 GeV e^+ beam yields a boost such that the B^0 decays have an average spatial separation of 250 μm along the e^- beam direction. The innermost layer of the *BABAR* detector, the silicon vertex tracker (SVT), is crucial in measuring that separation. It is also the primary tracking device for low-momentum particles ($p_T <$ 120 MeV/c), which do not travel far enough to be measured by the drift chamber.

2. Silicon Vertex Tracker

The SVT consists of five layers of double-sided, AC-coupled silicon strip detectors, located in the region 3.2–14.4 cm from the beam line, inside a magnetic field of 1.5 T. Each silicon module is 300 μm thick and has strips oriented parallel to the beam axis on one side (ϕ strips) and perpendicular on the other (z strips). For layers 1–3 the ϕ strips are n^+ implants and the z strips are p^+ implants. The situation is reversed for layers 4 and 5. The total active area of the detector is 0.96 m^2. Modules are organized into 208

readout sections, each containing 7–10 chips, with approximately 150,000 readout channels in total. The readout strip pitch varies from 50–210 μm.

Readout is accomplished using a customized integrated circuit, known as A Time Over Threshold Machine (ATOM) [2]. Signals from the detector are converted to a pulse such that the width is logarithmically proportional to the deposited charge. The pulse is then compared to a programmable threshold and the resulting digital signal stored in a 193-bin circular buffer. This is updated at 15 MHz for up to 128 channels associated with a single ATOM chip.

Individual hit resolution for normally-incident tracks is about 10–15 μm in the first three layers, and 20–30 μm in the outer two. This leads to a resolution for the separation of B decay vertices of about 80 μm, meeting the design goal. After running for eight years, the average SVT hit efficiency for active readout sections is approximately 92%. Further details about the SVT may be found in Ref. [3].

3. Experience in Bias Leakage Currents

At the previous meeting of this conference it was reported that *BABAR* had encountered and successfully mitigated an unexpected increase in bias leakage currents in layer 4 of the SVT. Over the course of several months, the problem was eventually diagnosed to result from positive ions, likely created by the PEP-II beams, collecting on the passivated surface of the layer-4 modules, on the side containing the p^+ implants. This extra charge induces a breakdown at the junction between the p^+ implant and the n-type substrate of the SVT wafer by amplifying the already-greater electric field at that point. This same problem does not occur among modules in layers 1–3 because the n- and p-sides are swapped, with the p-sides shielded by a layer of fanout circuts.

This leakage currents were handled by adjusting the reference voltage in modules of layers 4 and 5 to minimize the electric field between the layers, while keeping all relative voltages within a module the same. After a period of discharge, a high-current module returns to a stable state with no permanent damage. The progression from low to high bias currents and the subsequent fix is shown in Fig. 1, which shows the effect of unplugging a reference voltage cable. Since the initial onset, we have found that occasionally — a few times per year — the bias current in a module will begin to rise. Such problems are quickly corrected by adjusting the reference voltage of the affected module as well as the adjacent ones.

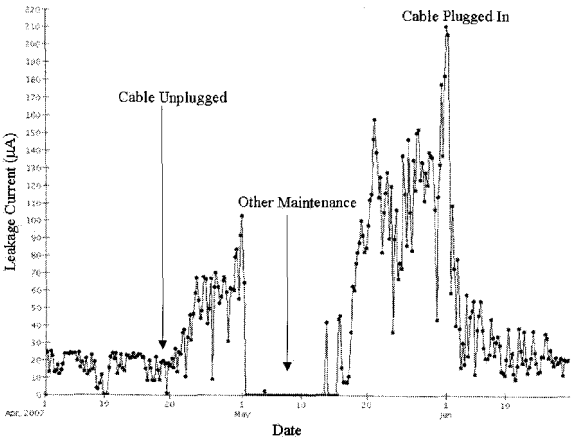

Fig. 1. Bias leakage current from April – June 2007 in the module described in the text.

4. Managing High Data Rates

The SVT data acquisition (DAQ) system completely saturates at trigger rates of about 4 kHz. At the beginning of 2006, worst-case predictions of the trigger rate in that year reached 5.5 kHz, which is an upper limit on the *BABAR* readout capability. In order not to lose good data during periods of high background, the SVT and dataflow crews began examining the viability of reducing the SVT readout window.

The SVT DAQ system associates a timestamp relative to the trigger time for each hit it records. False hits due to electronic noise have a flat timestamp distribution, while hits associated with a charged particle passing through the SVT peak at about 5-6 clock ticks (333–400 ns). The default window is 15 clock ticks wide, and reducing it is expected to decrease the readout time without significantly degrading performance.

In the summer of 2006 *BABAR* took two hours of data with a window shortened by two ticks in front, and four in back. The deadtime due to SVT during this period was reduced by about 40%, as expected. After processing, it was found that the overall track reconstruction efficiency dropped by 0.5%, similar to simulations. There was almost no degradation in the hit resolution. In the last week of August this year, the reduced window was activated for all new data. With respect to the original readout window, the new one has been reduced by one tick in front and three in back for layers 1-3; and one in front, two in back for layers 4-5.

The results of the reduced-window runs are encouraging. For the first

time, *BABAR* was able to run at 4.8 kHz with only 1.8% deadtime during a period of poor backgrounds. Figure 2 shows a clear reduction in the deadtime at high trigger rates. On the other hand, although the deadtime has been reduced, it was not as low as expected during normal conditions. We are currently investigating this discrepancy. Based on the simulations, the window could be further reduced without any significant impact on data quality, if necessary.

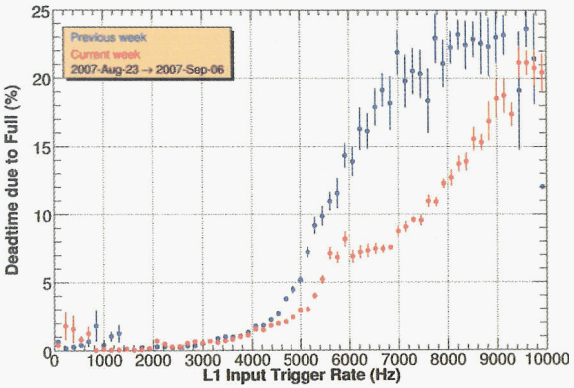

Fig. 2. **Deadtime versus Level 1 trigger rate for the week before** (blue) and the week after (red) the implementation of the reduced SVT readout window.

5. Conclusion

The *BABAR* SVT continues to meet its design requirements. Bias leakage currents have been successfully managed since their onset in 2004. The data acquisition readout time has been reduced, producing a reduction of the deadtime. The DAQ system is now more robust in the event that the trigger rate increases sharply due to poor background conditions as PEP-II pushes for higher luminosity. Other studies to further reduce the SVT deadtime are ongoing. The system is expected to perform well through the end of data-taking next year.

References

1. B. Aubert *et al.*, *Nucl. Instrum. Meth.* **A479**, 1 (2002).
2. V. Re *et al.*, *Nucl. Instrum. Meth.* **A409**, 354 (1998).
3. V. Re *et al.*, *IEEE Trans. Nucl. Sci.* **49**, 3284 (2002).

Precision Calibration of the STAR TPC

G. Van Buren*, for the STAR Collaboration

*Brookhaven National Laboratory, Upton, NY 11973-5000, USA
E-mail: gene@bnl.gov

The STAR Experiment's Time Projection Chamber (TPC) was designed to efficiently reconstruct charged particle tracks in the high multiplicity environment of the original RHIC specifications with the spatial precision to topologically identify weak decays of strange hadrons. The evolving physics program of the experiment has driven the calibration requirements to exceed those design goals to handle higher luminosities and accurately reconstruct track positions with even finer precision for optimal cooperation with silicon detectors. We discuss the challenges involved in the calibration of the TPC and the efforts which have successfully realized these goals.

Keywords: Calibration; Time projection chamber

1. Introduction and Design

When the STAR TPC and solenoidal magnet systems were designed, many of the necessary calibrations and distortion corrections for optimal track reconstruction were understood.[1] Software tools to calibrate and correct these distortions were developed to allow the TPC to achieve its design performance. But time has brought challenges to the calibration tasks, new operating conditions, and new goals for the physics capabilities. It is worthwhile to assess & review the experience gained from nearly 10 years of operation.

In the initial design, the performance was seen as divisible into two general physics categories of track measurements: soft, characterized by 2% momentum resolution at a p_T of 1.5 GeV/c using the TPC alone, and hard, desiring 5% resolution at 10 GeV/c for tracks fit to the collision vertex. The geometrical layout of the detector translates these into requirements of 400 μm and 300 μm sagitta resolutions, and subsequent azimuthal hit resolutions of approximately 700 μm. Space charge (buildup of ions in the TPC, due to their slower drift) was originally expected not to be a factor at the design luminosity of RHIC (2×10^{26} cm^{-2}s^{-1}).

Other desired performance from the TPC included particle identification through energy loss (dE/dx) in the $1/\beta^2$ region (low p_T). And topological reconstruction of strangeness decays was planned via the precision of inner silicon tracking, the matching of TPC tracks to which was expected to be unproblematic.

2. Calibrations and Distortions

The calibrations necessary to achieve the design goals of the TPC include alignments, drift velocity and T0, gains, and distortions caused by non-uniformities in the E and B fields. For the E fields, sources of the distortions include irregularities in the potentials on surfaces as well as space charge in the gas volume. Not all calibrations will be discussed in this paper; focus will be given to those which have provided significant challenges.

Equations useful in correcting for field distortions have been previously developed and solved.[2] A baseline calibration is to determine the value of $\omega\tau$ in these equations. This was done by introducing specific modifications to the E field and measuring the difference in reconstructed hit positions of laser tracks.[3] We measured in both the radial and azimuthal directions and obtained different values: $\omega\tau_r = 2.32 \pm 0.02$ and $\omega\tau_{r\phi} = 2.82 \pm 0.04$, supporting a tensor description of the electron mobility.[4]

2.1. *Ions in the TPC*

Perhaps the foremost of challenges encountered in achieving the desired performance arrived in the form of space charge. In addition to having under-predicted the amount of space charge which would be present at design luminosity, RHIC was also exceeding this luminosity within a few years of running. As an example, during Run VII RHIC delivered on average six times its design luminosity, and reached 15 times as much at peak. RHIC II might deliver a factor of 50 above design at nearly all times.

Studies of zero-bias data (triggers independent of beam crossings) confirmed that usual operating conditions did at least present the expected shape of the charge distribution, permitting our solutions to the distortion equations for it. Using the errors on tracks pointing to the primary vertex as a measure, we also confirmed that the charge amount scaled linearly with luminosity. Removal of the distortion was then a relatively simple matter of subtracting a correction scaled by luminosity.

Unfortunately, some zero-bias data showed abnormal collections of charge in the TPC, and almost all data began presenting fluctuations in the

track pointing errors, indicative of luminosity fluctuations on the time scale of one second or less. Uncertainties about the abnormal charge distributions lead to either exclusion of such data in notable cases, or no treatment for mild cases. The luminosity fluctuations forced us to develop a novel on-the-fly calibration technique during data processing which builds a statistically significant measure of the distortion from events which are close in time.[5] This technique is aided by the increases in DAQ rates which STAR has developed and is pursuing.[6]

Furthermore, track residuals in the TPC showed a significant distortion at the radii between the inner and outer padrows. Characteristics of the distortion revealed it to be a sheet of positive charge flowing out of gaps in the gated grid at these radii. GARFIELD simulations of the detection plane near these gaps confirmed it to be a design flaw. However, the amount of charge from this leak has been found to be at a near constant proportion to the amount of primary ionization space charge in the TPC across years of operation and different collision species, allowing us to scale its correction in parallel with the standard space charge correction. Additional smaller leaks were later discovered in other locations which are believed to be at gated grid wires which have lost their electrical contact and are at a floating potential. By good fortune, these leaks can be sealed by reversing the polarity of the gated grid for the surrounding portion of the TPC.

2.2. *Field Cage Shorts*

Another serious problem has been the development of fluctuating resistivity drops in the field cage chains. These appear to be initially due to contaminants on the surfaces of the field cages between potential-bearing rings. Cleaning these surfaces can only be performed during down periods of the experiment, and have not always solved the shorting. One persistent fluctuating short was patched with a permanent fixed short and additional resistance between neighboring rings, but new shorts developed. The current through the resistive chain can tell us the amount of missing resistance, but measures of the distortion are needed to tell us the location(s). The difficulty of this task is compounded by more than one location of missing resistance for one of the field cages.

We tackled this problem by using a least-chi-squared fit of modeled pairs of shorts (note that there may be more than two, but that the data is insensitive to shorts within a couple rings of each other) to laser data, and confirming reasonable correction in physics data. Because currents can only be measured every 15 seconds in the present setup, deviations on

shorter time scales allow this to remain a sizable contribution to the hit reconstruction error.

3. Drift Velocity

At small drift distances, the dominant contribution to the longitudinal hit position error comes from the large dip angles of the tracks. But drift velocity has played the primary role for long drift distances in the past, simply because further precision was unnecessary when not matching to any other detectors. Inclusion of the inner tracking detectors mandated an upgrade to our initial method of using only a few select laser tracks, which achieved 0.2% drift velocity resolution (compensated in part by the T0 calibration).

An effort was made to utilize all available information (e.g. all laser tracks, propagation time of lasers and physics tracks, empirical fits to environment dependencies), culminating in 0.03% resolution, confirmed by longitudinal residuals in the silicon. Of note, different drift velocities are observed between the two TPC halves.

4. dE/dx

Energy loss and dE/dx measurements in the TPC have been modeled using the Bichsel formalization,[7] from which we have set our goal as 7.6% resolution for straight non-dipping tracks crossing all padrows. Careful attention to environmental dependencies of the gains has allowed us to meet or exceed this performance in past datasets. Unfortunately, high occupancies (due to high luminosity) in recent data have caused TPC signal pulses to overlap undershoot tails of prior pulses. Considerable work will be necessary to reclaim the degradation to the resolution and it is under investigation. An electronics upgrade will remedy this situation in the near future.[6]

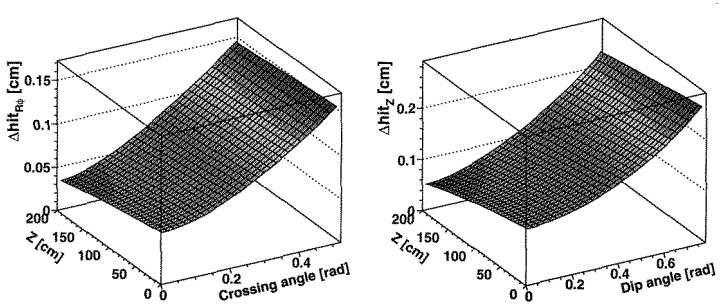

Fig. 1. Reconstructed hit errors in the $r\phi$ and Z directions as a function of Z, and track crossing and dip angles respectively (where Z is the distance from the central membrane in the drift direction) for outer TPC pads. Inner pads are slightly better.

5. Results and Summary

Pulls from track reconstruction have allowed us to determine that we are achieving hit errors which vary from ~300 μm near the central membrane to ~550 μm near the endcaps for tracks with 0° crossing angles (rising to as much as 1.5 mm for 30° crossing angles), as shown in Fig. 1. This translates into sagitta errors of ~600 μm averaged over all TPC tracks when using the TPC alone, and ~400 μm when including the vertex. The end result is that despite numerous challenges, we are very close to our design goals with ~2% momentum resolution for the soft physics point at $p_T = 1.5$ GeV/c, and ~5-6% for hard physics with the vertex at 10.0 GeV/c.

The needs for pointing resolution have been driven by two factors: topological strangeness physics without (preceding the utility of) silicon, and an increasing interest in topological heavy quark physics. The TPC has performed sufficiently to meet the strangeness goals through resolutions of just under 3 mm near the primary vertex. Attaining the goals of heavy quark decay reconstruction requires maximal precision in calibrating the silicon and hit matching to TPC tracks. We have achieved millimeter scale resolution in projecting TPC tracks to the outermost layer of silicon, which we believe is opening the door to this physics.

Additionally, dE/dx resolution has generally met or exceeded the design, allowing determination of separate species contributions to the dE/dx spectrum at high momenta (in the relativistic rise regime).

As RHIC continues to attain luminosity increases, and the component hardware continues to age, it is clear that the role of precision calibration of the TPC will remain paramount for STAR. We hope that our experiences and accomplishments will prove useful to the design, operation, and calibration of other time projection chamber experiments.

References

1. J. W. Harris and the STAR Collaboration, "Conceptual Design Report for the Solenoidal Tracker At RHIC", LBL Pub-5347 (1992).
2. M. Anderson *et al.*, Nucl. Instr. and Meth. **A499** (2003) 659.
3. J. Abele *et al.*, Nucl. Instr. and Meth. **A499** (2003) 692.
4. W. Blum and L. Rolandi, *Particle Detection with Drift Chambers* (Springer, Berlin) (1993).
5. G. Van Buren *et al.*, Nucl. Instr. and Meth. **A566** (2006) 22.
6. B. Surrow *et al.*, Nucl. Instr. and Meth. **B241** (2005) 293.
7. H. Bichsel, *Proceedings of the 8th ICATPP Conference on Astroparticle, Particle, Space Physics, Detectors and Medical Physics Applications*, eds. M. Barone *et al.*(World Scientific, Singapore) (2004).

ATLAS PIXEL DETECTOR SYSTEM TEST AND COSMICS RUN

JIAHANG ZHONG[†]
Institute of Physics, Academia Sinica, Nankang
Taipei, 11529, Taiwan

The pixel Detector is the innermost sub detector of ATLAS (A Toroidal LHC ApparatuS) experiment, a general purpose detector at LHC (Large Hadron Collider). People kept working on the Atlas Pixel Detector for a decade, while the most recent action was the so-called "system test". This series of work was aimed to verify that the integrated assembly will have expected performance upon installation into ATLAS. Here we will introduce the whole procedure of the system test, including peripheral service test, optoboard and module calibration, cosmics data taking, and connectivity test.

1. ATLAS pixel detector

The pixel detector is a critical component of the inner tracking detector of ATLAS [1], as its essential resolution can help to achieve precise and efficient identification and reconstruction of primary and secondary vertices. It is expected to provide efficient pattern recognition over the pseudo-rapidity range $|\eta|<2.5$, at the luminosity of the LHC as $10^{34}cm^{-2}s^{-1}$ [2].

The ATLAS pixel detector consists of a 3-layer barrel and two 3-disk endcaps. There are overall 1744 detector modules with approximately 80 million pixels. The size of each pixel is 50 microns in φ direction and 400 microns in z (barrel region) or r (endcap region) direction. These make an active area of about $1.7m^2$. As the innermost tracker of the whole detector, the ATLAS pixel detector had to meet very challenging design requirements. First, it must sustain over 300kGy of radiation over ten years of operation. Second, high track-multiplicity per bunch crossing, as well as desired impact resolution, requires high granularity and low mass. Third, high-rate bunch crossing at the LHC demands fast preamplifier rise time (25ns). Finally, the slow level 1 trigger (~2.5μs) necessitates on-detector buffering.

[†] On behalf of the Atlas pixel detector collaboration

2. System Test

After testing and calibration of single modules during the production phase, it is necessary to verify that the integrated assembly will perform as expected upon installation into ATLAS. To meet this goal, the scale of tests rose to O(100) modules , and extended to both the peripheral services and the control software. The system test was carried out in a laboratory above ground at CERN. We first tested with a complete end-cap, consisting of 3 disks for a total of 144 modules, or roughly 10% of the whole detector. With cooling system and scintillator trigger running, this system underwent data taking to track cosmic muons. Afterwards we launched another campaign called "connectivity test", as a quality assurance check of the assembly of the whole detector.

2.1. *Service Test*

Though the pixel detector is relatively small, the peripheral service system is no less complicated. As showed in figure 1, the detector requires stable DC power, including high voltage for pixel sensor depletion (150V~600V), low voltage for detector module front-end and control chips (analogue ~1.6V, digital ~2.0V), etc. In addition, cooling services shared with SCT [3] are needed to dissipate heat generated from front-end electronics, while keeping the modules at -10°C for radiation hardness. For this purpose and safety reason, an interlock system is implemented also.

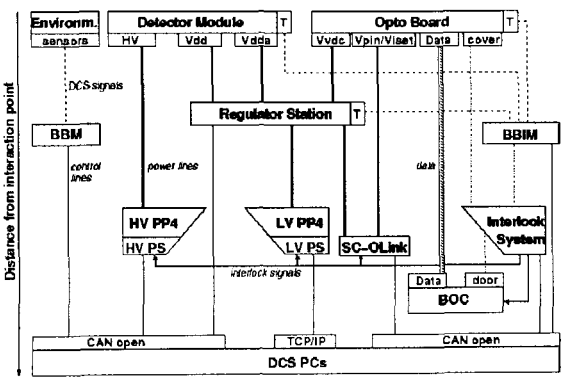

Figure 1. Pixel Detector Service System [4]

The service test was aimed to qualify the service chain from power supplies down to patch panel 1 interface at the detector and back, including interlock

functions. It was mainly focused on catching malfunctioning of the low voltage regulators and protection circuits. We used a dummy detector consisting of active resistance loads to mimic a pixel module. The voltages and currents were monitored with both external multimeters and detector control software (PVSS2, an ETM product). Bugs were spotted and fixed much more easily with this setup. Currently it is being used in the pit for the last test before the Pixel Detector is connected to ATLAS services.

2.2. *Calibration*

Following the service tests, modules and opto-boards were calibrated. For a good pixel detector, the output of all channels should be uniform, to provide track energy information with Time over Threshold (ToT). Several parameters were tuned for this purpose, see figure 2. The most important are the VIset current of laser power for optoboard, and the RX Threshold of signal discrimination for each channel.

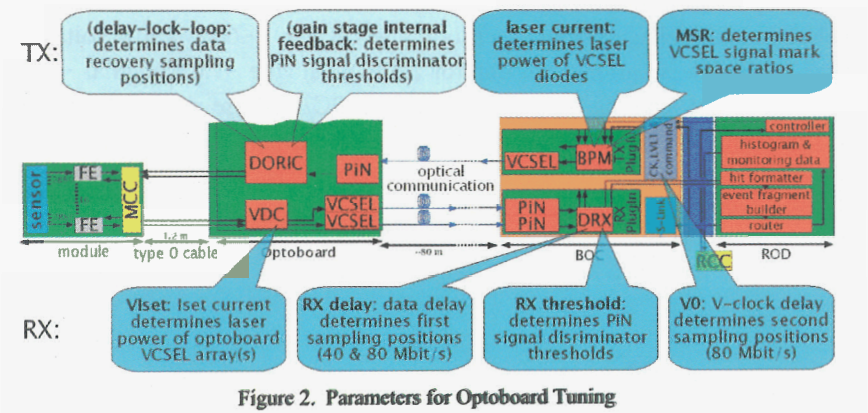

Figure 2. Parameters for Optoboard Tuning

Data then was taken from a complete endcap setup with random triggers, from which a map of noisy and dead pixels was obtained. This turned out to be only 0.074% of the whole detector.

In addition, through the test it was realized that the performance of some of the opto-boards degrades significantly when the temperature drops below 5°C . However the nearby detector sensors do need working temperature as low as -10°C. Additional opto-boards heater was designed and implemented later, to keep the opto-boards running at 20°C.

2.3. *Cosmics Run*

With a set of scintillators as trigger (figure 3), cosmic rays were detected and reconstructed using one complete pixel endcap. According to GEANT4 simulation, cosmic muons with sufficient energy will interact with our setup at a rate of 18Hz. This was a complete exercise of the data-taking path, including event data storage and decoding. Through this procedure, we measured single pixel efficiency and tracking efficiency, and completed first alignment studies.

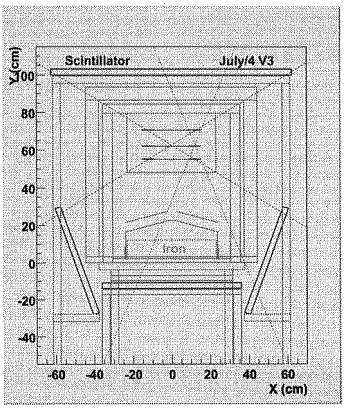

Figure 3. Cosmics Run Trigger Setup

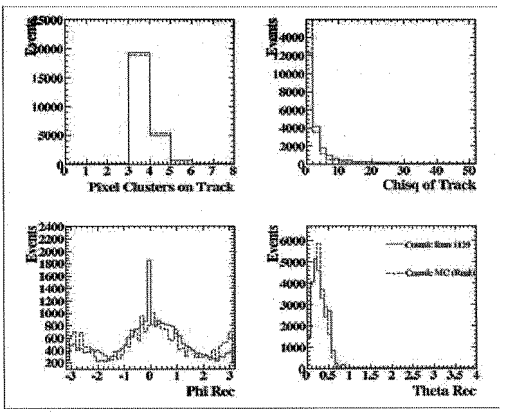

Figure 4. Cosmics track data

Soon after the cosmics run was launched, the first evidence of reconstructed tracks appeared, in the form of different module trigger timing and ToT distributions between events with random triggers and cosmic triggers [5]. About O(10k) cosmic tracks were recorded and reconstructed, most of which seems reasonable. 29 out of 144 modules were disabled during operation for various reasons, fortunately only one is caused by the module itself, while the others are all related to the services.

2.4. *Connectivity Test*

After the cosmics run, the endcap was integrated into the pixel detector. All pixel modules from endcap disks and barrel cylinders were then connected permanently to the service quarter panels. A series of tests and scans were performed, in order to check all possible connections to the detector, and to diagnose any errors before lowering the pixel detector into the cavern, where repair is not possible due to accessibility constraints.

Another purpose of the connectivity test was to check various steps of the integration and installation themselves. Through this test, many problems were spotted and fixed. In the end, only two dead modules and three chips were unrecoverable at last. Fortunately they are not in the innermost layer.nd dead pixels was obtained. This turned out to be only 0.074% of the whole detector.

3. Summary

The system test since 2006 made a lot of improvement of our system. DAQ and DCS chains were qualified and debugged extensively. The cosmics run with 10% of the detector confirmed the expected performance, and provided a good chance to exercise both online data-taking and offline tracking. Later the pixel detector assembly was lowered into the pit, and is ready to be connected with ATLAS service now. With experience gained from system test, many similar actions will be performed, such as service test and cosmics run. The pixel detector will be ready before the scheduled LHC run in middle 2008.

References

1. ATLAS Collaboration, ATLAS Inner Detector, Technical Design Report, Volume I and Volume II,(CERN/LHCC, 97-16 and 97-17).
2. ATLAS Pixel Collaboration, ATLAS Pixel Detector, Technical Design Report, (CERN/LHCC, 98-13).
3. M. Olcese, et al., ID Evaporative Cooling System, (ATL-IC-ES-006, 2003).
4. T. Henss, et al., The Hardware of the ATLAS Pixel Detector Control System, (JINST 2 P05006, 2007).
5. PixelCosmicsAnalysisResults, https://twiki.cern.ch/twiki/bin/view/Atlas/PixelCosmicsAnalysisResults

LIST OF PARTICIPANTS

ABBANEO	Duccio	CERN	Switzerland
ACCARDO	Lucio	INFN	Italy
AHARONIAN	Felix	Dublin Institute fuer Advanced Studies	Ireland
ALFONSI	Matteo	Laboratori Nazionali di Frascati - INFN	Italy
ALICI	Andrea	Bologna University and INFN Bologna	Italy
AMBROSIO	Michelangelo	INFN	Italy
ANDREOLI	Claudio	Università degli Studi di Pavia	Italy
ANGARANO	Matteo	CAEN SpA	Italy
ANTONELLI	Vito	Univ.degli Studi di Milano	Italy
APOLLONIO	Marco	University of Oxford	U.K.
ASAI	Makoto	SLAC	USA
BACCARO	Stefania	ENEA	Italy
BARBIER	Rami	IPNL / UCB Lyon IN2P3	France
BARNEY	David	CERN	Switzerland
BARONE	Michele	DEMOKRITOS	Greece
BARTESAGHI	Giacomo	Univ. Degli Studi di Milano	Italy
BARWICK	Steven	University of California	USA
BATTISTON	Roberto	University of Perugia	Italy
BAUDOT	Jerome	IPHC - University Strasbourg	France
BECKMANN	Volker	INTEGRAL Science Data Centre	Switzerland
BELLERIVE	Alain	Carleton University	Canada
BIKIT	Istvan	Dept. Of Physics, University of Novi Sad	Serbia
BINKO	Pavel	ISDC & University of Geneva	Switzerland
BOBIK	Pavol	Institute of Experimental Physics SAS	Slovak Republic
BOCCI	Andrea	Duke University	USA
BONACORSI	Daniele	INFN-CNAF	Italy
BONI	Alessandro	INFN - Laboratori di Frascati	Italy
BOSCHINI	Matteo	CILEA	Italy
BOZZA	Cristiano	Università degli Studi di Salerno	Italy
BRIGIDA	Monica	University and INFN-Bari	Italy
BRINET	Mariane	CNRS/L.P.S.C.	France
BROGIOLI	Doriano	INFN - Milano Bicocca	Italy
BRUSA	Simone	Università di Ferrara - INFN	Italy
BUCIK	Radoslav	Max Planck Institute for Solar System	Germany
BULGHERONI	Antonio	INFN - sezione di Roma 3	Italy
CAFAGNA	Francesco	INFN - Sezione di Bari	Italy
CAFORIO	Davide	INFN di Bologna	Italy
CAMPI	Domenico	CERN	Switzerland
CAMPORESI	Tiziano	CERN	Switzerland
CAPONE	Antonio	Università La Sapienza e INFN sez. Roma	Italy
CAPONERI	Benedetta	Università degli Studi di Perugia	Italy
CAPONERO	Michele Arturo	ENEA	Italy
CAPPELLINI	Chiara	Università dell'Insubria	Italy
CARILLO	Viviana	INFN - sezione di Napoli	Italy
CARR	John	CPPM/IN2P3/CNRS	France
CARSON	Laurence	University of Glasgow - Dept.of Physics & Astronomy	Scotland
CAVALLARI	Francesca	INFN Roma	Italy
CEMMI	Alessia	ENEA R.C. Casaccia	Italy

CHIOCHIA	Vincenzo	University of Zurich	Switzerland
CHIOSSO	Michela	INFN - sezione di Torino	Italy
CHMILL	Valery	Insubria University	Italy
CICALESE	Roberta	INFN	Italy
CIULLI	Vitaliano	INFN - Firenze	Italy
COLOMBETTI	Paolo	Università di Torino	Italy
CONSOLANDI	Cristina	INFN Milano Bicocca	Italy
CONTI	Valentina	INFN Milano	Italy
CORDA	Christian	INFN	Italy
CORTIANA	Giorgio	INFN - Università di Padova	Italy
CROSETTO	Dario	3D-Computing, Inc.	USA
CUCOANES	Sebastian	IIIB Physics Institute, RWTH Aachen	Germany
CURRIE	Douglas	University of Maryland - Dept.of Physics	USA
CUSANNO	Francesco	INFN Gruppo Sanità Collegato Sezione di Roma	Italy
DAI	Hongliang	Institute of High Energy Physics	China
DAMAZIO	Denis	Brookhaven National Laboratory	Switzerland
DAMMER	Jiri	Czech Technical University in Prague	Czech Republic
DANU	Andrea	Institute of Space Science	Romania
DE CAPUA	Stefano	CERN	Switzerland
DE CATALDO	Giacinto	INFN Sezione di Bari e CERN	Switzerland
de la Hoz	Santiago	IFIC-Valencia	Spain
DE LELLIS	Giovanni	Università di Napoli - Dip. di Fisica	Italy
DE LEO	Raffaele	Physics Dep. University of Bari	Italy
DESPEISSE	Matthieu	CERN	Switzerland
DI MAIO	Gianni	CAEN SpA	Italy
DI SARCINA	Ilaria	ENEA C.R. Casaccia	Italy
DI SIMONE	Andrea	CERN and INFN/CNAF	Switzerland
DITTUS	Fido	CERN	Switzerland
DORO	Michele	Università di Padova - INFN	Italy
ELLIS	Malcolm	Brunel University	U.K.
EREDITATO	Antonio	University of Bern	Switzerland
FAHRER	Manuel	Institut fuer Experimentelle Kernphysik - Univ. Karlsruhe	Germany
FANFANI	Alessandra	University of Bologna - INFN	Italy
FANTECHI	Riccardo	INFN - sezione di Pisa	Italy
FARINA	Fabio	INFN Milano-Bicocca	Italy
FARUQI	A.R.	MRC Laboratory of Molecular Biology	U.K.
FEDORKO	Ivan	CERN	Switzerland
FERRONI	Fernando	Università Roma La Sapienza & INFN	Italy
FETFATZIS	Prodromos	National Technical University of Athens	Greece
FINOCCHIARO	Giuseppe	Laboratori Nazionali di Frascati dell'INFN	Italy
FISCHER	Peter	University of Mannheim	Germany
FOGGETTA	Luca	INFN - Milano Bicocca, Università dell'Insubria	Italy
FOKITIS	Emmanuel	National Technical University of Athens	Greece
FORKAPIC	Sofija	Dept. Of Physics, University of Novi Sad	Serbia
FUOCHI	Piergiorgio	Ist. per la sintesi organica e la fotoreattività - CNR	Italy
GADDI	Andrea	CERN	Switzerland
GAIA	Daniele	FN SpA - Nuove Tecnologie e Servizi Avanzati	Italy
GAN	K.K.	The Ohio State University	USA
GARIBALDI	Franco	Italian National Institute of Health	Italy

GAUZZI	Paolo	Università La Sapienza e INFN sezione di Roma	Italy
GEHRELS	Neil	NASA-GSFC	USA
GEKTIN	Alex	Institute for Scintillation Materials	Ukraine
GEMME	Claudia	CERN/INFN Genova	Italy
GERVASI	Massimo	University of Milano Bicocca	Italy
GIANI	Simone	CERN	Switzerland
GIORGINI	Miriam	Bologna University and INFN	Italy
GORETTI	Augusto Mario	Princeton University	Italy
GRAH	Christian	DESY	Germany
GRANCAGNOLO	Sergio	INFN Lecce & Università del Salento	Italy
GRANDI	Davide	INFN - Milano	Italy
GRATTA	Giorgio	Stanford University	USA
GRINYOU	Boris	Institute for Scintillation Materials	Ukraine
GULMEZ	Erhan	Bogazici University	Turkey
HAGOPIAN	Sharon	Florida State University	USA
HAGOPIAN	Vasken	Florida State University	USA
HASAN	Said	Università dell'Insubria	Italy
HASEBE	Nobuyuki	Waseda University	Japan
HAYATSU	Kanako	Waseda University, Research Inst. for Science and Engineering	Japan
HOEPFNER	Kerstin	RWTH Aachen, III Phys.Inst.A.	Germany
HOGAN	Craig	Max-Planck-Institut fuer Astrophysik	Germany
HSU	Ching-Cheng	Max-Planck Institute fuer Physik	Germany
IANNI	Andrea	Princeton University - INFN	Italy
IPPOLITOV	Mikhail	RRC	Russia
ISHINO	Masaya	ICEPP - Univ. Of Tokyo	Switzerland
JASTRZAB	Marcin	Università degli Studi dell'Insubria	Italy
KAGAN	Harris	Ohio State University - Dept. Of Physics	USA
KARAM GALVAO	Kaio	CERN/UFRJ	Switzerland
KCIRA	Dorian	University of Louvain	Belgium
KECSKEMETY	Karoly	KFKI Research Inst.for Particle and Nuclear Physics	Hungary
KISS	Mozsi	Royal Institute of Technology (KTH)	Sweden
KLINKBY	Esben	Niels Bohr Institute	Denmark
KRAFT-BERMUTH	Saskia	INFN Sezione Milano-Bicocca	Italy
KRIEGER	Peter	University of Toronto	Canada
KRZEMIEN	Wojciech	Institute of Physics, Jagiellonian University	Poland
KUCERA	Pavel	Ecole Polytechnique Federale de Lausanne	Switzerland
LAMBERT	Robert	University of Edinburgh, JCMB	U.K.
LAZANU	Sorina	National Institute of Materials Physics	Romania
LE DU	Patrick	DAPNIA CEA Saclay	France
LEARNED	John	University of Hawaii	Hawaii
LEE	Kerry	Lockheed Martin	USA
LEROY	Claude	University of Montreal	Canada
LESLIE	Dawn	Brunel University	U.K.
LIANG	Xiaoluan	Key Laboratory for Ultrafine Materials of Ministry of Education	China
LIETTI	Daniela	Università dell'Insubria	Italy
LOMBARDI	Paolo	INFN - sezione di Milano	Italy

LOPARCO	Francesco	Università di Bari e INFN	Italy
MAGLIOZZI	Maria Lucia	INFN - sezione Roma 1	Italy
MALTEZOS	Stavros	National Technical University of Athens	Greece
MAPELLI	Alessandro	CERN	Switzerland
MARINELLI	Nancy	University of Notre Dame	USA
MARSHALL	Zachary	Columbia University	Switzerland
MARTINEZ	Gustavo	CIEMAT	Spain
MARTINEZ RIVERO	Celso	IFCA (CSIC-UC)	Spain
MASCAGNA	Valerio	Università degli Studi dell'Insubria	Italy
MATTHIAE	Giorgio	Univ. Of Roma Tor Vergata	Italy
McNULTY	Peter	Clemson University	USA
MEDDI	Franco	INFN - sezione di Roma	Italy
MERLO	Jean-Pierre	University of Iowa	Switzerland
MICHELSON	Peter	Stanford University	USA
MLYNARCZYK	Janusz	INFN - Sezione di Roma Tre	Italy
MONTE	Claudia	Università degli Studi di Bari e INFN	Italy
MONTICELLI	Fernando	Universidad Nacional de La Plata	Argentina
MYERS	Stephen	CERN	Switzerland
NAGEL	Thiemo	TU Muenchen	Germany
NAPPI	Eugenio	INFN - sezione di Bari	Italy
NARDULLI	Alessandro	ETH Swiss Federal Institute of Technology	France
NASTEVA	Irina	University of Manchester, HEP Group, School of Physics and Astronomy	U.K.
NEGODAEV	Mikhail	Deutsches Elektronen-Synchrotron DESY	Germany
NEILSON	Russell	Stanford University	USA
NESSI-TEDALDI	Francesca	ETH Zurich	Switzerland
NICOLAS	Estre	Institut de Physique Nucleaire de Lyon	France
NIKO	Hisko	Tokyo University	Japan
NILL	Simeon	German Cancer Research Center	Germany
NOBREGA	Rafael	INFN - sezione di Roma	Italy
ONEAL	Ray	Florida A&M University	USA
ORIMOTO	Toyoko	California Institute of Technology	USA
ORR	Robert	University of Toronto	Canada
OZAWA	Shunsuke	Institute of Cosmic Ray Research - Univ. of Tokyo	Japan
PANICCIA	Mercedes	University of Geneva	Switzerland
PAOLETTI	Claudia	ENEA C.R. Casaccia	Italy
PASTRONE	Nadia	INFN Torino	Italy
PAUL	Jacques	Laboratoire Astroparticult et Cosmologie - Univ. Paris Diderot	France
PELLICCIARI	Monica	Università dell'Insubria	Italy
PEREIRA	Rui	LIP-Lisbon / IST	Portugal
PERL	Joseph	Stanford Linear Accelerator Center	USA
PERNEGGER	Heinz	CERN PH Dept, CERN F03300	Switzerland
PERSICO	Elisa	Università degli studi di Milano, LASA and INFN	Italy
PIETRZYK	Uwe	Research Center Juelich	Germany
PINCI	Davide	INFN - sezione di Roma	Italy
PINFOLD	James	University of Alberta	Canada
PIPARO	Danilo	CERN / Università di Milano Bicocca	Italy
PLACKETT	Richard	Imperial College London	U.K.

POSPISIL	Stanislav	Inst. of Experimental and Applied Physics - Technical Univ.	Czech Republic
PREGHENELLA	Roberto	Università di Bologna, Dip. di Fisica - sez. INFN	Italy
PRICE	Lawrence	Argonne National Laboratory	USA
PSOROULAS	Serena	Università degli Studi di Milano	Italy
RAINO	Silvia	University and INFN-Bari	Italy
RANCOITA	Pier-Giorgio	INFN Milano-Bicocca	Italy
RANIERI	Antonio	INFN - Bari	Italy
REDONDO F.	Ignacio	Fermilab	USA
RICCI	Fulvio	Univ. La Sapienza di Roma	Italy
RICCOBENE	Giorgio	INFN/LNS	Italy
RIJSSENBEEK	Michael	Stony Brook	USA
RINNERT	Kurt	The University of Liverpool	U.K.
ROPER YEAR-WOOD	G.	RWTH Aachen	Germany
ROVELLI	Chiara	INFN Roma 1	Italy
RUCHTI	Randy	National Science Foundation and Univ. Of Notre Dame	USA
RUZIN	Arie	Tel Aviv University	Israel
RYAN	Matt	Imperial College	U.K.
SACCO	Donatella	INFN Roma 3	Italy
SALA	Silvano	INFN - Milano Bicocca	Italy
SALERNO	Roberto	Università Milano Bicocca - INFN	Italy
SALESA	Francisco	IFIC - Instituto de Fasica Corpuscular	Spain
SCAZZI	Selene	Università degli Studi dell'Insubria	Italy
SCHMITT	Udo	Forschungszentrum Karlsruhe	Germany
SCHNEIDER	Peter	Univ. Bonn - Argelander Institut fuer Astronomie	Germany
SCIOLI	Gilda	Bologna University and INFN Bologna	Italy
SEGUINOT	J.	College de France	France
SERVOLI	Leonello	INFN Perugia	Italy
SMYRSKI	Jerzy	Institute of Physics, Jagiellonian University	Poland
SOPCZAK	Andre	Lancaster University	U.K.
SOSSI	Vesna	University of British Columbia	Canada
SPIRITI	Eleuterio	INFN sezione Roma 3	Italy
STEINKAMP	Olaf	Universitaet Zuerich	Switzerland
STORACI	Barbara	CERN / Università degli Studi Milano Bicocca	Switzerland
STROM	David	University of Oregon	USA
TACCONI	Mauro	INFN Milano Bicocca	Italy
TAIUTI	Mauro	Università di Genova e INFN	Italy
TANCINI	Valentina	Università Milano Bicocca e INFN	Italy
TAVANI	Marco	IASF-INAF	Italy
THOMAS	Michael	The Ottawa Hospital Regional Cancer Centre	Canada
TIMMERMANS	Charles	NIKHEF/Radboud University Nijmegen	The Netherlands
TODOROVIC	Natasa	Dept. Of Physics, University of Novi Sad	Serbia
TOJO	Junji	KEK	Japan
TRENTADUE	Raffaello	Università degli Studi di Bari	Italy
TUGGLE	Joseph	SLAC	USA
TZAMARIAS	Spyros	Hellenic Open University	Greece
UGOLINO	Ugo	INFN - sezione di Napoli	Italy
UOZUMI	Satoru	Shinshu University	Japan

VALA	Ladislav	Czech Technical University in Prague	Czech Republic
VALLAZZA	Erik	INFN Sezione di Trieste	Italy
VAN BUREN	Gene	Brookhaven National Lab	USA
VANOSSI	Elena	Politecnico di Milano	Italy
VASILEV	Andrey	RRC	Russia
VERDUCCI	Monica	CERN/CNAF-INFN	Switzerland
VOGEL	Julia	Albert-Ludwigs Universitaet Freiburg	Germany
VOLONTE	Sergio	ESA	France
VOLPE	Giacomo	INFN - sezione di Bari	Italy
WALLRAFF	Wolfgang	RWTH Aachen	Germany
WATTIMENA	Nanda	DESY	Germany
WEFEL	John	Louisiana State University	USA
WISCHNEWSKI	Ralf	DESY	Germany
XELLA	Stefania	Niels Bohr Institute, Copenhagen University	Denmark
XIE	Zhen	Princeton University	USA
YAMASHITA	Naoyuki	Waseda University	Japan
YANG	Yong	Caltech	Switzerland
ZABLOTSKY	Aleksey	Lomonosov Moscow State University	Russia
ZABOROV	Dmitry	Institute for Theoretical and Experimental Physics	Russia
ZHONG	Jiahang	Academia Sinica	Switzerland
ZHOU	Li	Institute of High Energy Physics of CAS	China
ZONA	Cristiano	Università degli studi di Milano, LASA and INFN	Italy

This page intentionally left blank

Proceedings of the 10th Conference

Astroparticle, Particle and Space Physics, Detectors and Medical Physics Applications

The exploration of the subnuclear world is done through increasingly complex experiments covering a wide range of energies and in a large variety of environments — from particle accelerators and underground detectors to satellites and space laboratories. For these research programs to succeed, novel techniques, new materials and new instrumentation need to be used in detectors, often on a large scale. Hence, particle physics is at the forefront of technological advancement and leads to numerous applications. Among these, medical applications have a particular importance due to the health and social benefits they bring. This volume reviews the advances made in all technological aspects of current experiments in the field.

World Scientific
www.worldscientific.com
6906 hc

ISBN-13 978-981-281-908-6
ISBN-10 981-281-908-8